Transactions of the ASME® Journal of Heat Transfer

Transactions of the ASME, Journal of Heat Transfer (ISSN 0022-1481) is published quarterly (Feb., May, Aug., Nov.) for $240.00 per year by The American Society of Mechanical Engineers, Three Park Avenue, New York, NY 10016. Periodicals postage paid at New York, NY and additional mailing offices. POSTMASTER: Send address changes to Transactions of the ASME, Journal of Heat Transfer, c/o THE AMERICAN SOCIETY OF MECHANICAL ENGINEERS, 22 Law Drive, Box 2300, Fairfield, NJ 07007-2300.

CHANGES OF ADDRESS must be received at Society headquarters seven weeks before they are to be effective. Please send old label and new address. **PRICES:** To members, $40.00, annually: to nonmembers, $240.00. Add $40.00 for postage to countries outside the United States and Canada.

INDEXED by Applied Mechanics Reviews and Engineering Information, Inc. Canadian Goods & Services Tax Registration #126148048.

Published Quarterly by The American Society of Mechanical Engineers

VOLUME 120 • NUMBER 3 • AUGUST 1998

537 Editorial

HEAT TRANSFER GALLERY

538 Heat Transfer Gallery
C. T. Avedisian

539 Impact and Solidification of Molten-Metal Droplets on Electronic Substrates
J. M. Waldvogel, G. Diversiev, D. Poulikakos, C. M. Megaridis, D. Attinger, B. Xiong, and D. B. Wallace

540 Flame-Vortex Interactions in a Counterflow Burner
I. Vihinen, J. R. Gord, J. M. Donbar, R. D. Hancock, W. M. Roquemore, G. J. Fiechtner, C. D. Carter, K. D. Grinstead, Jr., V. R. Katta, and J. C. Rolon

541 Swirl Distribution Effects on the Structure of Lean Premixed Flames Using PLIF Diagnostics
M. Birouk and A. K. Gupta

542 Enroute to Convection: Breakup of Conduction Layer
D. K. Mukherjee and V. Prasad

543 Direct Numerical Simulation of Film Boiling
D. Juric and G. Tryggvason

544 Soot Shell Structures of Fuel Droplet Flames in Microgravity
C. T. Avedisian, B. J. Callahan, and G. S. Jackson

545 Visualization of Flow Fields Near a Bubble in a Temperature Gradient
N. Rashidnia and M. Kassemi

546 Liquid Jet Impingement Using Visualization
S. C. Arjocu and J. A. Liburdy

TECHNICAL PAPERS

1997 Max Jakob Memorial Award Lecture

547 The Monte Carlo Method in Radiative Heat Transfer
J. R. Howell

Analytical and Experimental Techniques

561 Consecutive-Photo Method to Measure Vapor Volume Flow Rate During Boiling From a Wire Immersed in Saturated Liquid
C. N. Ammerman and S. M. You

568 Sensitivity Analysis for Thermophysical Property Measurements Using the Periodic Method
A. Haji-Sheikh, Y. S. Hong, S. M. You, and J. V. Beck

577 Frequency Response Characteristics of an Active Heat Flux Gage
C. Dinu, D. E. Beasley, and R. S. Figliola

Conduction Heat Transfer

583 Computation of Anisotropic Conduction Using Unstructured Meshes
J. Y. Murthy and S. R. Mathur

592 Exact Solution of Heat Conduction in Composite Materials and Application to Inverse Problems
C. Aviles-Ramos, A. Haji-Sheikh, and J. V. Beck

Forced Convection

600 Effects of Temperature-Dependent Viscosity Variations and Boundary Conditions on Fully Developed Laminar Forced Convection in a Semicircular Duct
T. M. Harms, M. A. Jog, and R. M. Manglik

(Contents continued on Outside Back Cover)

This journal is printed on acid-free paper, which exceeds the ANSI Z39.48-1992 specification for permanence of paper and library materials.∞ ™

♲ 85% recycled content, including 10% post-consumer fibers.

(Contents continued)

606 Two-Dimensional Modeling of Heat Transfer Through Sandwich Plates With Inhomogeneous Boundary Conditions on the Faces
Y. Murer and P. Millan

617 An Analytical Model for Turbulent Compression-Driven Heat Transfer
F. J. Cantelmi, D. Gedeon, and A. A. Kornhauser

624 Effect of Channel Orientation of Local Heat (Mass) Transfer Distributions in a Rotating Two-Pass Square Channel With Smooth Walls
C. W. Park and S. C. Lau

Natural and Mixed Convection

633 Free Convection Limits for Pin-Fin Cooling
T. S. Fisher and K. E. Torrance

Boiling Condensation

641 Near-Wall Microlayer Evaporation Analysis and Experimental Study of Nucleate Pool Boiling on Inclined Surfaces
G. F. Naterer, W. Hendradjit, K. J. Ahn, and J. E. S. Venart

Phase Change and Multiphase Heat Transfer

654 The Effects of Sublimation-Condensation Region on Heat and Mass Transfer During Microwave Freeze Drying
Zhao Hui Wang and Ming Heng Shi

Combustion

661 Numerical Modeling of Fire Walls to Simulate Fire Resistance Test
Zhao-Fen Jin, Yutaka Asako, Yoshiyuki Yamaguchi, and Minoru Harada

Porous Media, Particles and Droplets

667 Flow and Heat Transfer Characteristics Inside Packed and Fluidized Beds
C. C. Wu and G. J. Hwang

674 Transient Heat Transfer From a Particle With Arbitrary Shape and Motion
Zhi-Gang Feng and E. E. Michaelides

682 Effect of Drop Deformation on Heat Transfer to a Drop Suspended in an Electrical Field
M. A. Hader and M. A. Jog

Heat Exchangers

690 A Complementary Experimental and Numerical Study of the Flow and Heat Transfer in Offset Strip-Fin Heat Exchangers
N. C. DeJong, L. W. Zhang, A. M. Jacobi, S. Balachandar, and D. K. Tafti

699 Heat and Moisture Transfer in Energy Wheels During Sorption, Condensation, and Frosting Conditions
C. J. Simonson and R. W. Besant

Heat Transfer Enhancement

709 Heat Transfer-Friction Characteristic Comparison in Rectangular Ducts With Slit and Solid Ribs Mounted on One Wall
Jenn-Jiang Hwang

717 Direct Numerical Simulation of Three-Dimensional Flow and Augmented Heat Transfer in a Grooved Channel
M. Greiner, G. J. Spencer, and P. F. Fischer

724 Heat Transfer in Turbulent Flow Past a Surface-Mounted Two-Dimensional Rib
S. Acharya, S. Dutta, and T. A. Myrum

Micro-Scale Heat Transfer

735 Thermal Bubble Formation on Polysilicon Micro Resistors
Liwei Lin, A. P. Pisano, and V. P. Carey

743 Capillary Performance of Evaporating Flow in Micro Grooves: An Approximate Analytical Approach and Experimental Investigation
G. P. Peterson and J. M. Ha

(Contents continued on p. 632)

(Contents continued)

752 Transient Thermocapillary Flows Induced by a Droplet Translating in an Electric Field
Chun-Liang Lai and Wen-Lang Tang

758 Theoretical Analysis of Thermocapillary Flow in Cylindrical Columns of High Prandtl Number Fluids
Y. Kamotani and S. Ostrach

765 Electronic Desorption of Surface Species Using Short-Pulse Lasers
L. M. Phinney and Chang-Lin Tien

TECHNICAL NOTES

772 A Periodic Transient Method Using Liquid Crystals for the Measurement of Local Heat Transfer Coefficients
J. W. Baughn, J. E. Mayhew, M. R. Anderson, and R. J. Butler

777 Thermal Diffusivity Determination of High-Temperature Levitated Oblate Spheroidal Specimen by a Flash Method
F. Shen and J. M. Khodadadi

781 Effective Thermal Conductivity Model of Flame Spread Over a Shallow Subflash Liquid Fuel Layer
M. Epstein and J. P. Burelbach

784 Thermal Transport Phenomena in Turbulent Gas Flow Through a Tube at High Temperature Difference and Uniform Wall Temperature
Shuichi Torii and Wen-Jei Yang

787 Means to Improve the Heat Transfer Performance of Air Jet Arrays Where Supply Pressures are Limiting
H. S. Sheriff and D. A. Zumbrunnen

789 Enhancement of Saturated Flow Boiling Heat Transfer on Cylinders Using Interference Sleeves
S. Madhusudana Rao and A. R. Balakrishnan

792 A New Method for Tracking Radiative Paths in Monte Carlo Simulations
B. M. Shaughnessy and M. Newborough

795 Heat Transfer Coefficient Enhancement With Perforated Baffles
S. Dutta, P. Dutta, R. E. Jones, and J. A. Khan

797 Second-Law Analysis on Wavy Plate Fin-and-Tube Heat Exchangers
W. W. Lin and D. J. Lee

DISCUSSION

801 Analysis of Matrix Heat Exchanger Performance, by G. Venkatarathnam and S. Sarangi—Discussion by V. Ahuja and R. K. Green

ANNOUNCEMENTS

576 NSF/ASME Workshop—Announcement

653 Visualization of Thermal Phenomena—Call for Photographs

689 Change of Address Form for Subscribers

764 Periodicals on ASMENET

806 33rd National Heat Transfer Conference—Call for Papers

807 1999 ASME Mechanics and Materials Conference

808 Information for Authors

Journal of Heat Transfer Editorial

Journal Activities

This issue marks the completion of three years of my five-year appointment as Technical Editor of the Journal, and it is timely to report on some Journal activities.

This issue also marks the second year in which the Journal has published a section on Heat Transfer Visualization, and we intend to make this an annual event. Professor Tom Avedisian of Cornell University has taken the lead in organizing sessions at the IMECE each year at which authors present various forms of visualization, and the Journal is pleased that we can provide an outlet for the best of this material.

Associate Editors Ted Bergman, Adrienne Lavine, Peter Simpkins, Satish Ramadhyani, and Manohar Sohal have completed their three-year terms. A good Associate Editor sometimes finds frustration as well as a sense of accomplishment in the job, and they receive far too little recognition for their efforts. In keeping with the Heat Transfer Division policy of encouraging broad participation of the Division membership, the Journal normally does not reappoint Associate Editors for a second consecutive term, so I wish to thank these editors for their service.

New editors beginning their three-year appointments in July, 1998 are Christoph Beckermann, B. T. F. Chung, Deborah Kaminski, Roop Mahajan, Arunava Majumdar, and David Zumbrunnen. You might note that there are five editors retiring and six joining the editorial board. This marks an effort to expand the editorial staff and reduce the workload on the individual editors.

A special issue of the Journal is planned for November of this year. If all goes as planned, we will feature papers by industrial and academic co-authors that address unresolved heat transfer problems in various areas of application of our field. We hope that this will open new research opportunities, and initiate some dialogue on the future of the field.

You may have received an inquiry from Debbie Mullins, the Journal's Executive Secretary, requesting information on your areas of interest in reviewing for the Journal. We are updating our reviewer information base so that the Associate Editors can better direct requests for reviews to those with an interest and expertise in the necessary area. If you were not contacted but wish to review for the Journal, you can contact Mrs. Mullins at jht@uts.cc.utexas.edu.

This is part of an effort to provide timely reviews. We continue to suffer from inordinately long response times from some reviewers. We are trying to target reviewers who will provide timely and complete feedback to us and to their colleagues on behalf of the Journal.

The Journal backlog has been greatly reduced, chiefly by the increase in page allotment by ASME to 1200 pages per year. We presently carry about a one and one-half issue (three-to-five month) backlog of papers that have been accepted, down from as much as seventeen months a few years ago.

If you have not looked the JHT web page, it may be of interest. Aside from material on Instruction for Authors, you can examine and download JHT policies on determination of experimental and numerical accuracy that must be part of a Journal paper. We also list upcoming meetings of interest to the heat transfer community, and show photos and short biographical sketches of the pioneers in heat transfer. You can access the web page via http://www.asme.org/divisions/jht.

We are working with ASME in a broad effort at putting the Journal, along with other ASME journals, into accessible online format for subscribers, and hope to be able to announce a firm date in the near future.

If you have suggestions for improving the Journal, please contact me.

John R. Howell
Technical Editor

Journal of
Heat Transfer

Heat Transfer Gallery

C. T. Avedisian[1]. The second "Heat Transfer Gallery" was held at the International Mechanical Engineering Congress and Exhibition in Dallas last November. At this session, photographs were displayed that depicted various processes occurring in the presence of temperature gradients. The session attracted 19 photo displays which were evaluated based on subjective judgments of the visual impact of the photographs and the original contributions they were thought to make to the understanding of a thermal process. Eight of the highest rated displays were selected for publication in this special section of the ASME *Journal of Heat Transfer*.

The purpose for publishing these photographs is to draw attention to the aesthetic qualities of thermal processes. The text is kept to a minimum to focus on the visualizations. The photographs include phenomena of natural and forced convection, phase change processes, and combustion. One purely computational study is also included. Reproductions in color are intended to enhance the visualizations. It is hoped that the readership of the Journal enjoys browsing through this collection of photographs.

The editorial assistance of Ms. Judith Sierant of ASME is appreciated in the production of this photo collection. Thanks also go to the following who participated in the judging: P. S. Ayyaswamy, K. Ball, R. O. Buckius, S. M. Cho, J. N. Chung, V. J. Dhir, M. Faghri, J. R. Howell, K. Khim, J. Kim, T. J. Kom, H. Y. Kwak, J. H. Lienhard, A. G. Levine, R. Mahajan, P. Ooosthuizen, S. Ostrach, O. A. Plumb, P. G. Simpkins, L. C. Witte, and S. M. You.

References

Arjocu, S. C., and Liburdy, J. A., 1997a, "Analysis of Flow Structures Occurring in Impingement of Elliptic Jet Arrays," AIAA 97-1993, 28th AIAA Fluid Dynamics Conference.

Arjocu, S. C., and Liburdy, J. A., 1997b, "Influence of Elliptical Structure on Impingement Jet Array Heat Transfer Performance," *Optical Technology in Fluid, Thermal, and Combustion Flow, III,* SPIE, Vol. 3172, pp. 130–140.

Birouk, M., and Gupta, A. K., 1998, "Lanar Laser Induced Fluorescence Imaging of OH Distribution in Lean premixed Swirling Flames," paper to be presented at ASME International Joint Power Generation Conference, Baltimore, MD, Aug. 24–26.

Kassemi, M., and Rashidnia, N., 1997, "Steady and Oscillatory Flows Generated by a Bubble in 1-G and Low-G Environments," paper AIAA-97-0924.

Katta, V. R., Carter, C. D., Fiechtner, G. J., Roquemore, W. M., Gord, J. R., and Rolon, J. C., 1998, "Interaction of a Vortex with a Flat Flame Formed between Opposing Jets of Hydrogen and Air," *27th Symposium (International) on Combustion,* The Combustion Institute, accepted for publication.

Mukherjee, D. K., Prasad, V., and Tan, H., 1997, "Measurement of Thermal Gradients and Fluctuations Using Liquid Crystals," *Proceedings of the ASME Heat Transfer Division,* Vol. 3, HTD-Vol. 353, ASME, New York, pp. 81–95.

Rashidnia, N., 1997, "Bubble Dynamics on a Heated Surface," *Journal of Thermophysics and Heat Transfer,* Vol. 11, No. 3, July–Sept., pp. 477–480.

Rolon, J. C., Aguerre, F., and Candel, S., 1995, "Experiments on the Interaction between a Vortex and a Strained Diffusion Flame," *Combustion and Flame,* Vol. 100, pp. 422–429.

Sparrow, E. M., Husar, R. B., and Goldstein, R. J., 1970, "Observations and Other Characteristics of Thermals," *Journal of Fluid Mechanics,* Vol. 41, Part 4, pp. 793–800.

Waldvogel, J. M., and Poulikakos, D., 1997, "Solidification Phenomena in Picoliter Size Solder Droplet Deposition on a Composite Substrate," *International Journal of Heat and Mass Transfer,* Vol. 40, pp. 295–309.

Xiong, B., Megaridis, C. M., Poulikakos, D., and Hoang, H., 1998, "An Investigation of Key Factors Affecting Solder Microdroplet Deposition," ASME JOURNAL OF HEAT TRANSFER, Vol. 120, pp. 259–279.

---

[1] Sibley School of Mechanical and Aerospace Engineering, Cornell University, Ithaca, NY 14853-7501.

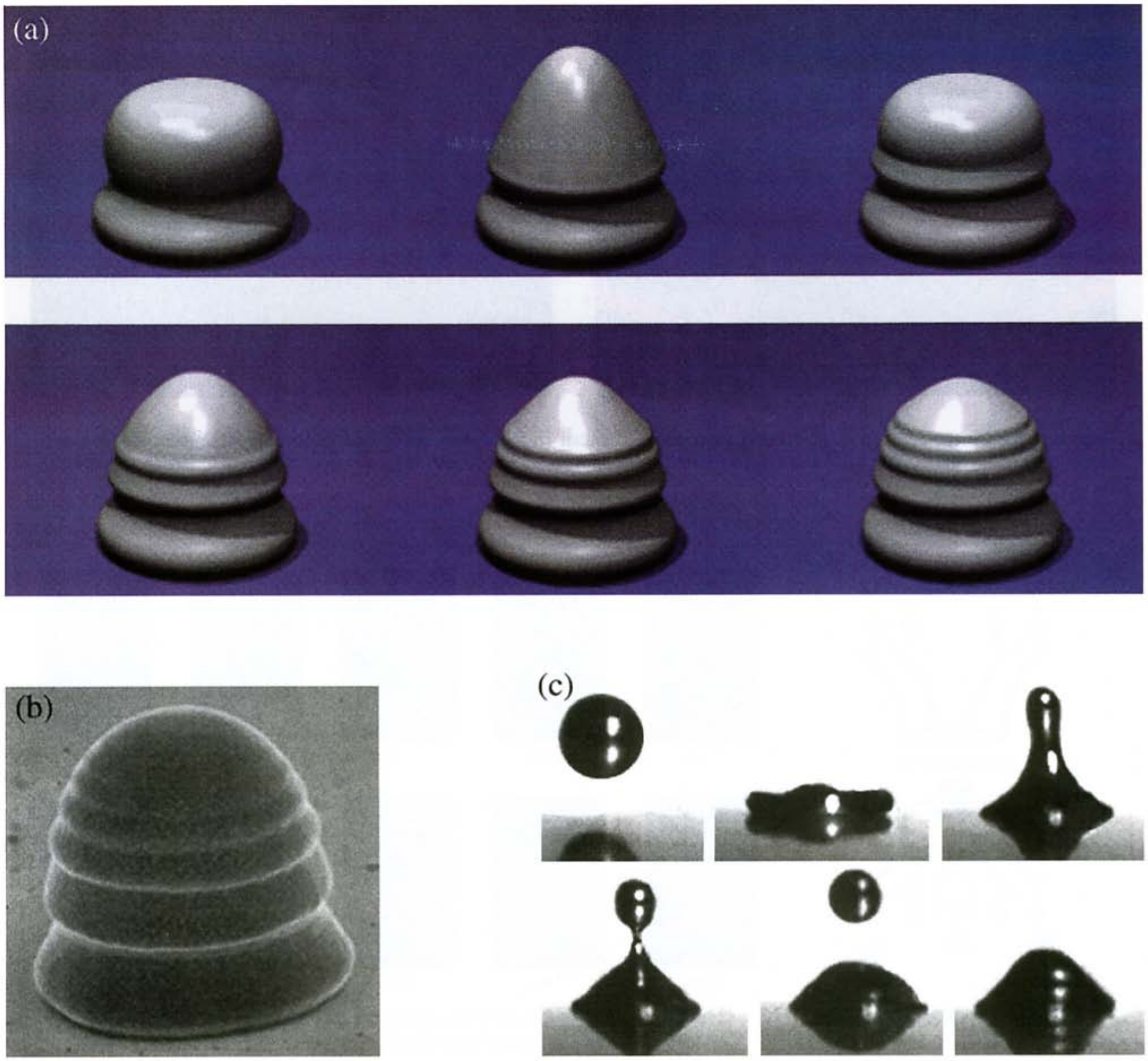

IMPACT AND SOLIDIFICATION OF MOLTEN-METAL DROPLETS ON ELECTRONIC SUBSTRATES

J. M. Waldvogel[1], G. Diversiev[2], D. Poulikakos[3], C. M. Megaridis[2], D. Attinger[3], B. Xiong[2] and D. B. Wallace[4]

[1] Motorola, Schaumburg, Illinois
[2] Department of Mechanical Engineering, University of Illinois at Chicago, Chicago, Illinois
[3] Institute of Energy Technology, Swiss Federal Institute of Technology, CH-8092 Zurich, Switzerland
[4] MicroFab Technologies, Plano, Texas

(a) Rendering of temporal shape variation of a 50 μm solder droplet impacting on a flat Ni/Si substrate. This sequence was obtained using the numerical model of Waldvogel and Poulikakos (1997). The bottom right frame in the sequence defines the shape of the solidified bump. The rings result from the interaction between the droplet oscillation and the upward propagation of the solidification front. Time proceeds from left to right and from top to bottom.

(b) Scanning electron micrograph of a 50 μm solder bump, as produced by a solder jetting apparatus; see Xiong et al. (1998). Note the remarkable resemblance between the predicted bump shape (final frame in a), and that obtained experimentally (b).

(c) Experimental images obtained via high-speed video when a 1 mm solder droplet impacted on a flat copper substrate. Note the breakup and subsequent reattachment of the secondary droplet during the recoiling after impact. Again, time proceeds from left to right and from top to bottom.

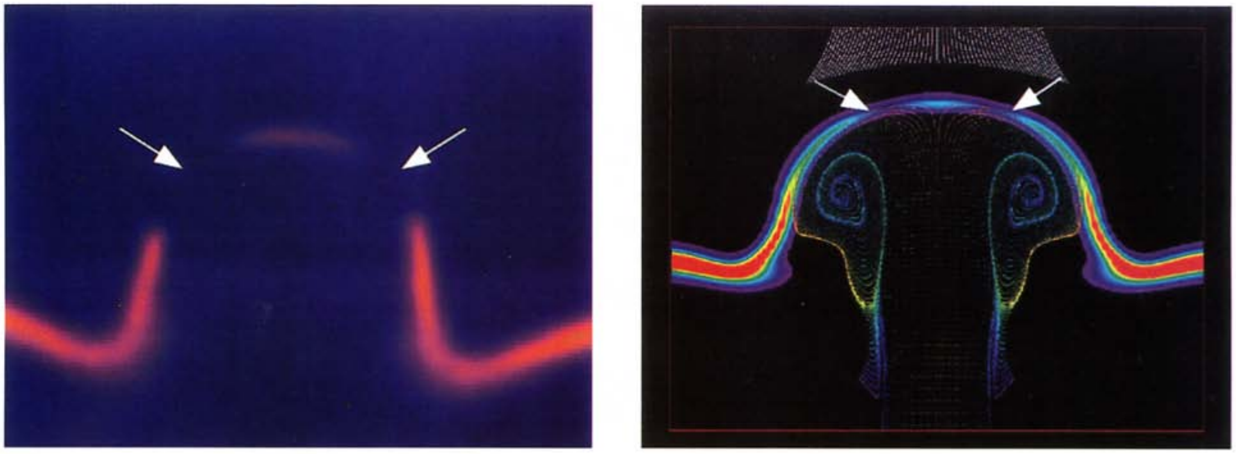

Figure 1. Agreement between Experimental (left) and Computed (right) Flame (OH) Distributions in a Counterflow Burner. Arrows indicate region of local flame extinction; streaklines (color coded with injection location) are shown in the computed image.

Figure 2. Experimental Setup (Red=Flame, Green=Vortex).

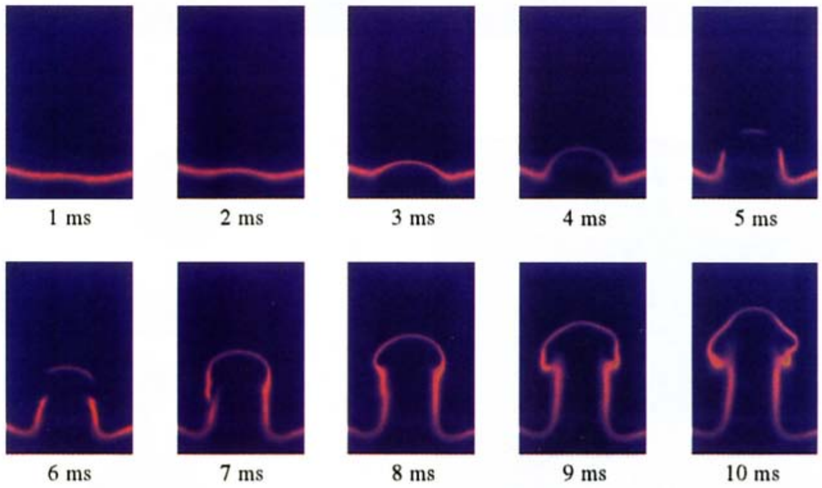

Figure 3. Evolution of the Flame (OH) Distribution in a Counterflow Burner Showing Local Extinction (5 ms), Separation (6 ms), and Reattachment (7 ms).

FLAME-VORTEX INTERACTIONS IN A COUNTERFLOW BURNER

I. Vihinen, J. R. Gord, J. M. Donbar, R. D. Hancock, W. M. Roquemore
Air Force Research Laboratory, Wright-Patterson AFB, Ohio
G. J. Fiechtner, C. D. Carter, K. D. Grinstead, Jr., V. R. Katta
Innovative Scientific Solutions, Inc., Dayton, Ohio
J. C. Rolon
Laboratoire EM2C, CNRS, Ecole Centrale Paris, France

In a rare instance when computational predictions (Katta et al., 1998) precede experimental results, we find that local extinction of a non-premixed hydrogen/nitrogen/air counterflow diffusion flame occurs at the sides and not the center of the impinging vortex. In a counterflow burner (Rolon et al., 1995), hydrogen and nitrogen diluent flow from above at 6 and 15 lpm, while air flows from below at 15 lpm, producing a global strain rate of 20 s^{-1}. The computational image is obtained using a third-order-accurate, time-dependent, computational fluid dynamics with chemistry code with detailed chemical kinetics (14 species, 74 reactions). The experimental images are recorded at 1-ms intervals using planar laser-induced fluorescence of OH with an intensified CCD camera. The evolution of the flame showing local extinction, separation, and reattachment is obtained by delaying the laser pulses and camera timing relative to the motion of the vortex-producing piston.

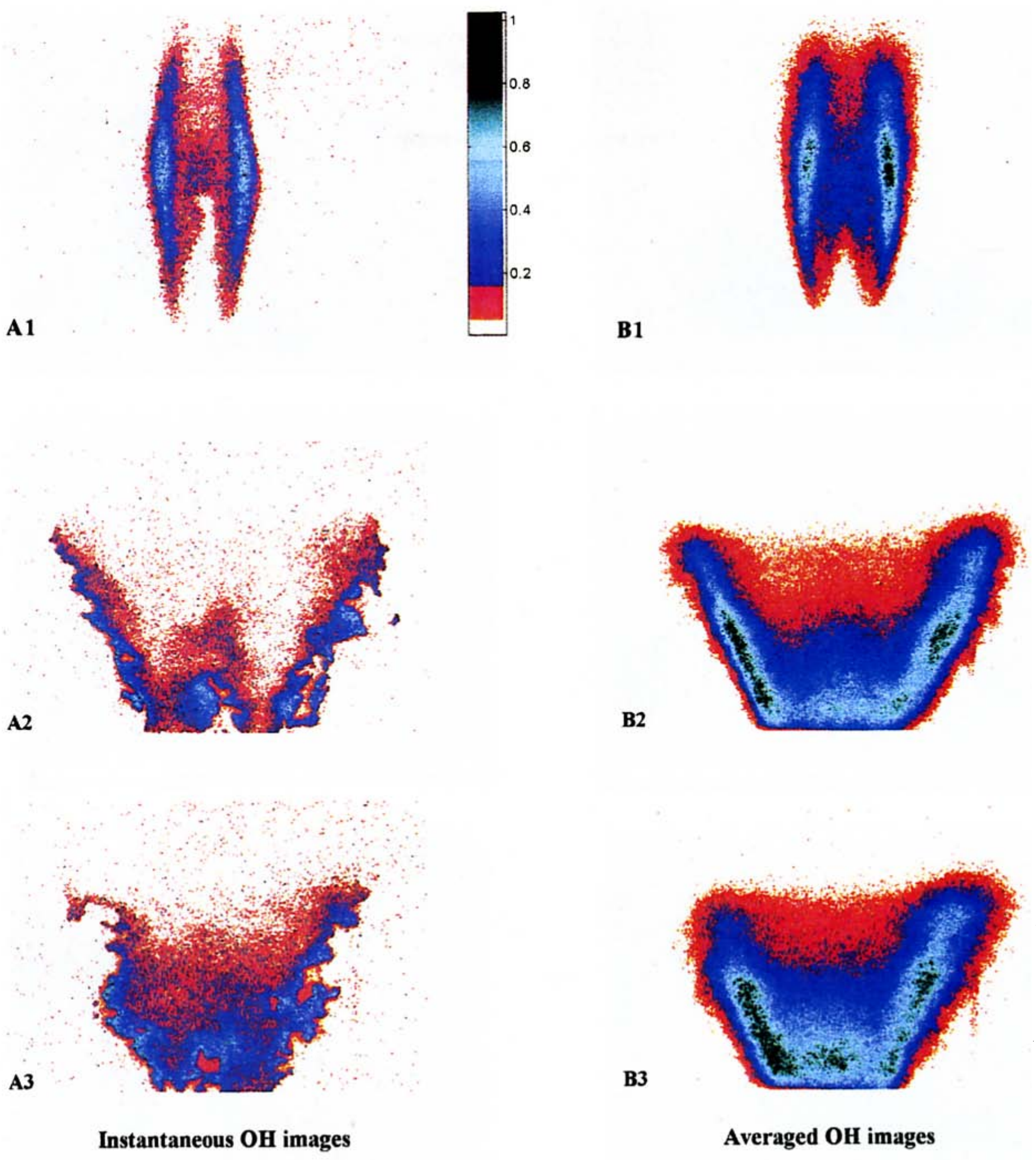

SWIRL DISTRIBUTION EFFECTS ON THE STRUCTURE OF LEAN PREMIXED FLAMES USING PLIF DIAGNOSTICS

M. Birouk and A. K. Gupta, The Combustion Laboratory, University of Maryland, College Park, Maryland

Planar Laser Induced Fluorescence (PLIF) images, at a vertical cross-section (through the centerline) in methane-air flames shows the effect of swirl on the distribution of OH concentration in premixed flames. The double concentric burner enabled one to change the radial distribution of swirl in the burner. The photos shown are with co- or counter-swirl in the outer annulus and co-swirl in the inner annulus of the burner. The left column (Photos A) shows the distribution of instantaneous OH images while the right column (Photos B) shows ensemble averaged OH images. The vertical color bar scale given on the right side of photo A1 gives the color code used here. Instantaneous OH distribution for the non-swirling case (Photo A1) shows a uniform reaction zone. Introduction of swirl to the mixture (co-swirl in both the outer and the inner annulus) provided a uniform, a wider (divergent) and fragmented reaction zone (Photo A2). A change in swirl from co- to counter- in the outer annulus provided a significant change in the flame structure. Photo A3 shows that the use of counter-swirl in the outer annulus results in a nonsymmetric, narrower, and somewhat less fragmented image. This nonsymmetric feature can also be seen from the ensemble averaged photo B3. The global structure of the flames remained unchanged at all the fuel-lean mixture conditions examined here except for the enhanced fragmentation of reaction zone under very lean mixture conditions. Enhanced fragmentation of the reaction zone under leaner conditions affects flame stability, combustion dynamics, and emission of pollutants. Further details on the PLIF diagnostics are described in Birouk and Gupta (1998).

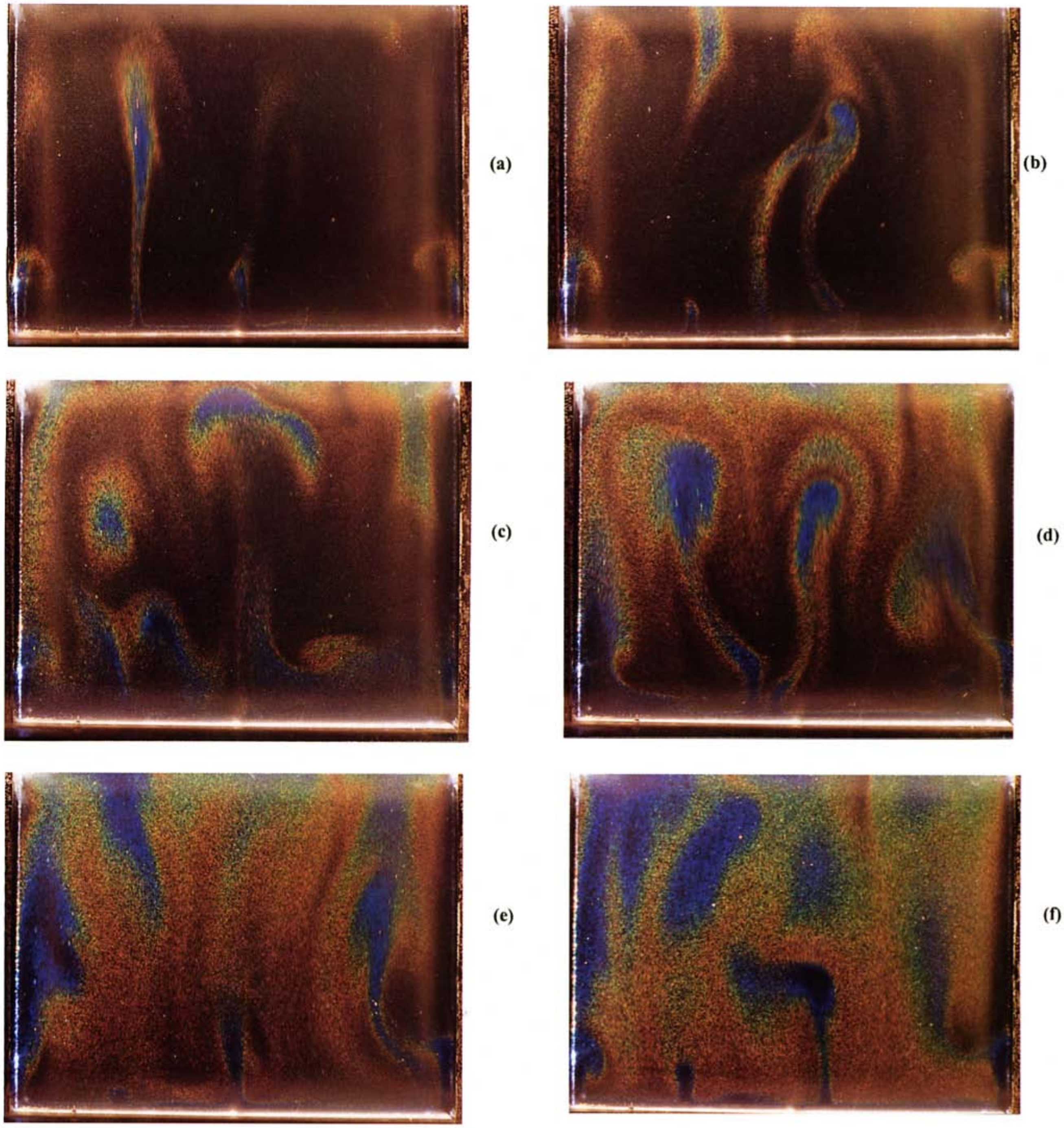

ENROUTE TO CONVECTION: BREAKUP OF CONDUCTION LAYER

D. K. Mukherjee and V. Prasad
State University of New York at Stony Brook, Stony Brook, New York

The sequence of photos illustrates the transition from a conductive to a convective mode of heat transfer. This is achieved by ramping the bottom plate temperature from 22°C to 38°C at 4°C/10 min; thus introducing varying temperature gradients in the fluid (Water/Glycerol; Pr ~ 1140). Flow tomoscopy, with liquid crystals as the dispersion agent, is used on a cubic cavity (Mukherjee et al., 1997). The progression of colors (red, green, and blue for two separate temperature ranges, 24–30°C and 31–36°C) captures the periodic process of: a conductive phase, break off and then mixing (Sparrow et al., 1970). An 85 mm. lens (aperture at f/4 with a 1 sec. exposure time) is used to image (a) the generation of thermals and wall jets, (b) merging of two thermals, (c) mushrooming due to viscous and thermal resistance, (d) movement of thermals towards each other due to radial pressure gradient, and (e, f) emergence of several convective rolls.

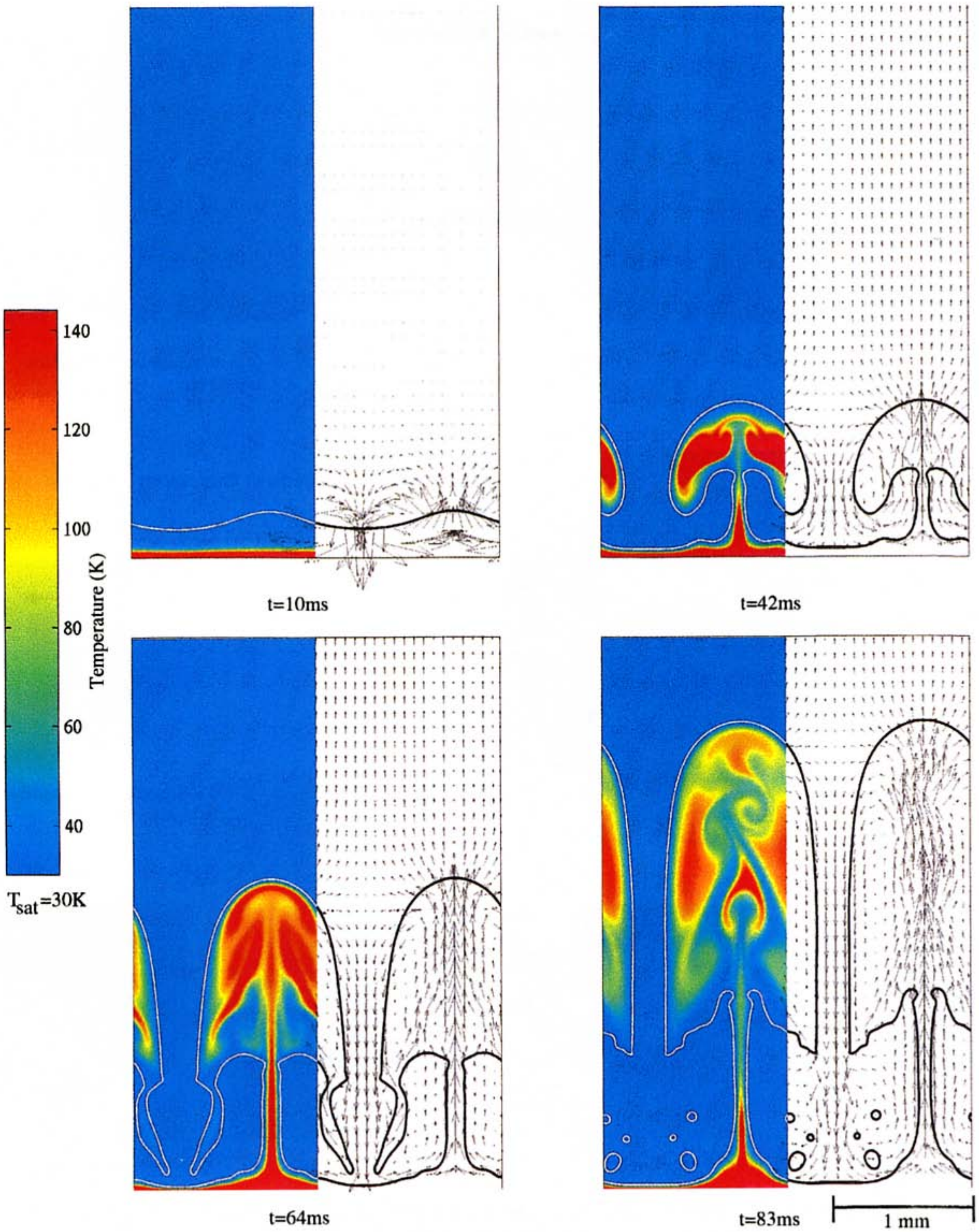

DIRECT NUMERICAL SIMULATION OF FILM BOILING

D. Juric, Theoretical Division, Los Alamos National Laboratory, Los Alamos, New Mexico
and
G. Tryggvason, Department of Mechanical Engineering and Applied Mechanics, University of Michigan, Ann Arbor, Michigan

Direct simulations of film boiling are carried out using a numerical method based on explicit tracking of the liquid-vapor interface. This front-tracking technique couples the solution of the unsteady Navier-Stokes and energy equations to the complex dynamics of the phase interface, interphase mass transfer, latent heat, surface tension and jumps in material properties. Shown above are four frames from a two-dimensional simulation of film boiling of hydrogen at 8 atm. resolved by a 300 × 600 uniform grid, periodic in the transverse direction. The left and right halves of each frame illustrate the temperature and velocity fields, respectively. Initially the liquid is separated from a heated wall (Q = 44 W/cm^2) by a thin vapor layer. At later times the unstable vapor layer evolves into a rising plume with vortical mixing of the hot and cold vapor. The results compare quite well with some simple exact solutions and correlations of experimental data on wall heat transfer in film boiling. More details of the method and its applications can be found at http://www.lanl.gov/home/djuric. This work was supported by DOE, NASA, and NSF.

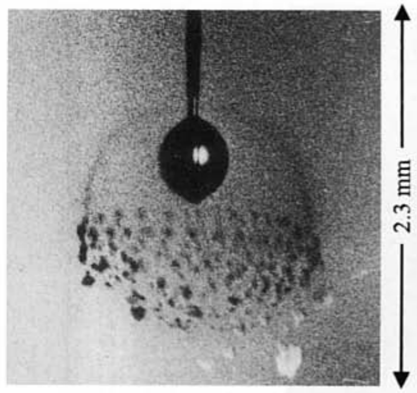

(1a) n-heptane burning on 57 μm fiber. t=ignition+0.45 sec

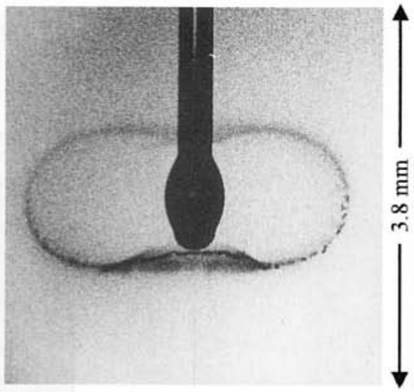

(1b) n-heptane on 330 μm fiber. t=0.45 sec

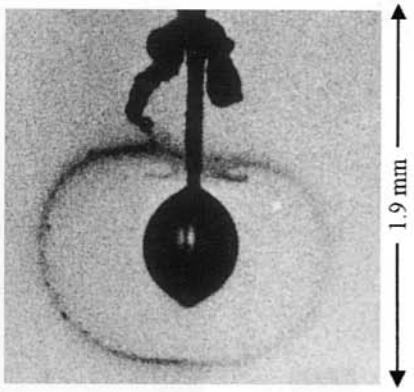

(1c) n-nonane on 63 μm fiber. t=0.60 sec

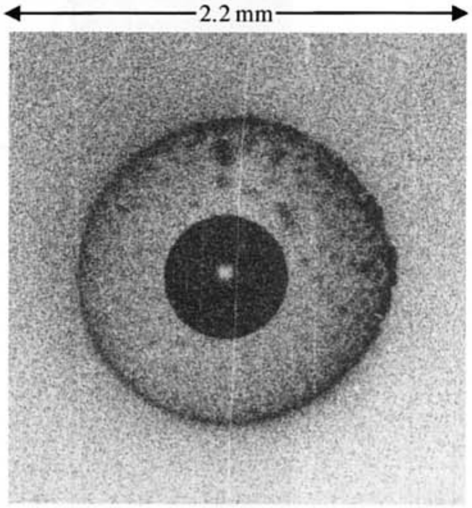

(2) n-heptane without fiber support. t=0.25 sec

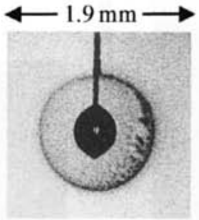

(3) n-heptane on 30 μm fiber. t=0.25 sec

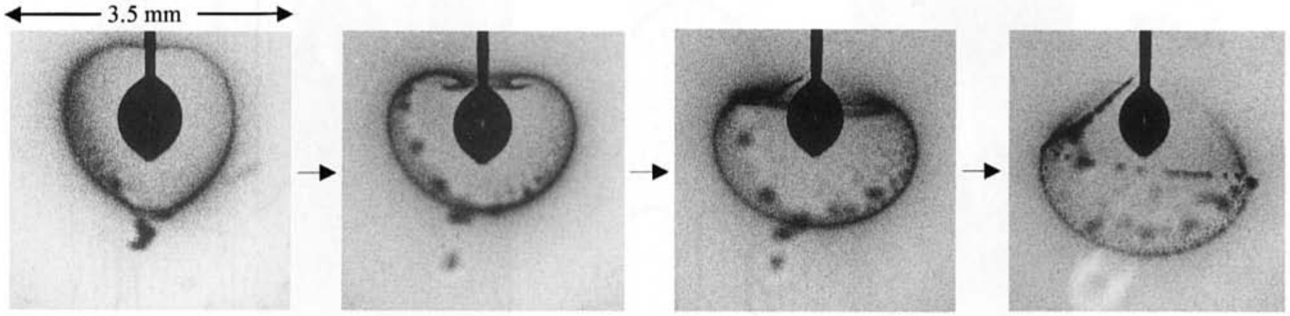

(4a) n-heptane on 57 μm fiber. t=0.34 sec

(4b) t=0.49 sec

(4c) t=0.54 sec

(4d) t=0.66 sec

SOOT SHELL STRUCTURES OF FUEL DROPLET FLAMES IN MICROGRAVITY

C. T. Avedisian and B. J. Callahan, Sibley School of Mechanical and Aerospace Engineering,
Cornell University, Ithaca, New York
G. S. Jackson, Department of Mechanical Engineering, University of Maryland, College Park, Maryland

These photographs show various shapes of trapped soot particles in droplet flames with low external convection. A balance of drag and thermophoretic forces trap the soot aggregates into the black ''shell'' or ''ring'' structure. Disturbances in the flow field around the droplet, or a large fiber for anchoring the droplet affect the shape of the shell. In the above photos, the times after ignition and the dimensions are given.

In Fig. (1a), downward convection ''peels'' the soot shell away late in the burning process to create an ''umbrella'' with soot aggregates dripping from the rim. The 330 μm fiber in Fig. (1b) pinches the soot shell into a ''donut'' shape. In Fig. (1c), the fiber curls the shell top into a ''vortex'' and upward convection stacks soot onto the fiber.

With no fiber (a ''free'' droplet) and minimum convection, the burning configuration approaches the ideal case of spherical symmetry, which appears as a ''bulls eye'' in Fig. 2. A bulls eye can also be realized for a fiber-supported droplet, as in Fig. 3, if the fiber diameter is small relative to the droplet diameter.

Figure 4 shows a soot shell undergoing changes as burning progresses. The shell curls into a ''heart'' shape in Fig. (4b), then progresses to a ''bowl'' shape from Fig. (4c) to (4d).

For all of the photographs, the lighting and magnification is such that the flame is dim and out of view.

This work was supported by NASA grant NAG3-1791.

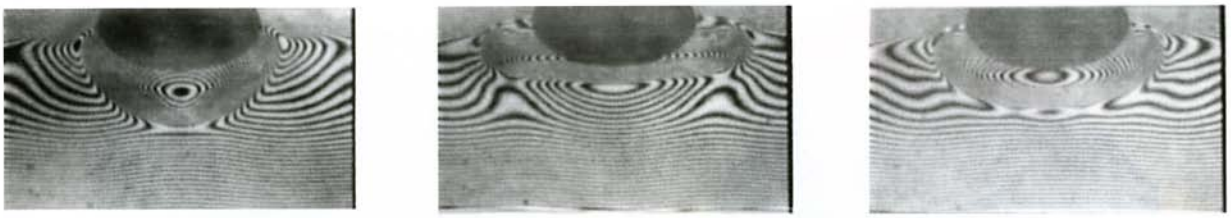

Sequence of Interferograms near The Bubble During One Period of Oscillation

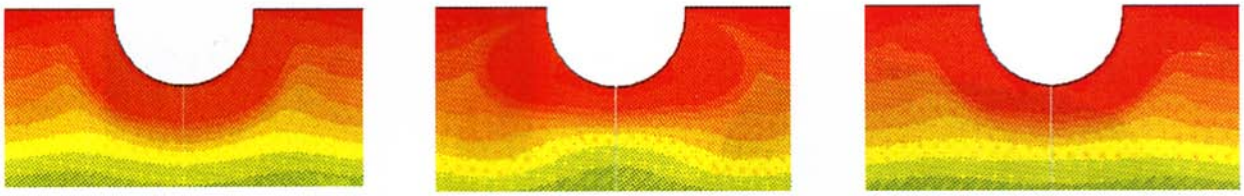

Numerical Predictions of Temperature Contours near The Bubble During One Period of Oscillation

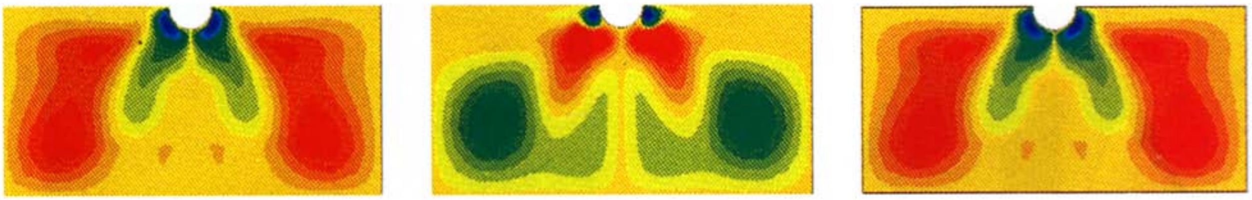

Numerical Predictions of Streamline Contours in The Enclosure During One Period of Oscillation

VISUALIZATION OF FLOW FIELDS NEAR A BUBBLE IN A TEMPERATURE GRADIENT

N. Rashidnia and M. Kassemi
NCMR, NASA Lewis Research Center, Cleveland, Ohio

Interaction between gas and vapor bubbles with the surrounding fluid is of great interest for both space and ground-based processing. A combined experimental and experimental approach is adopted here to study thermocapillary flow generated by a bubble on a heated surface. The experiment is conducted by using a test enclosure with inside dimensions of 38 mm × 19 mm × 19 mm with transparent optical quality windows. Top and bottom copper plates are heated and cooled with two constant temperature circulating baths (Rashidnia, 1997). The temperature field is visualized using Mach-Zehnder interferometry. A finite element numerical model is developed which solves the transient two-dimensional momentum and energy equations and includes the effects of bubble surface deformation (Kassemi and Rashidnia, 1997). Above the critical Marangoni number, both the model and the experiment indicate an oscillatory flow and temperature fields as indicated in the figures for $Pr = 8.4$, $Ma = 90{,}000$, and $Ra = 50{,}000$.

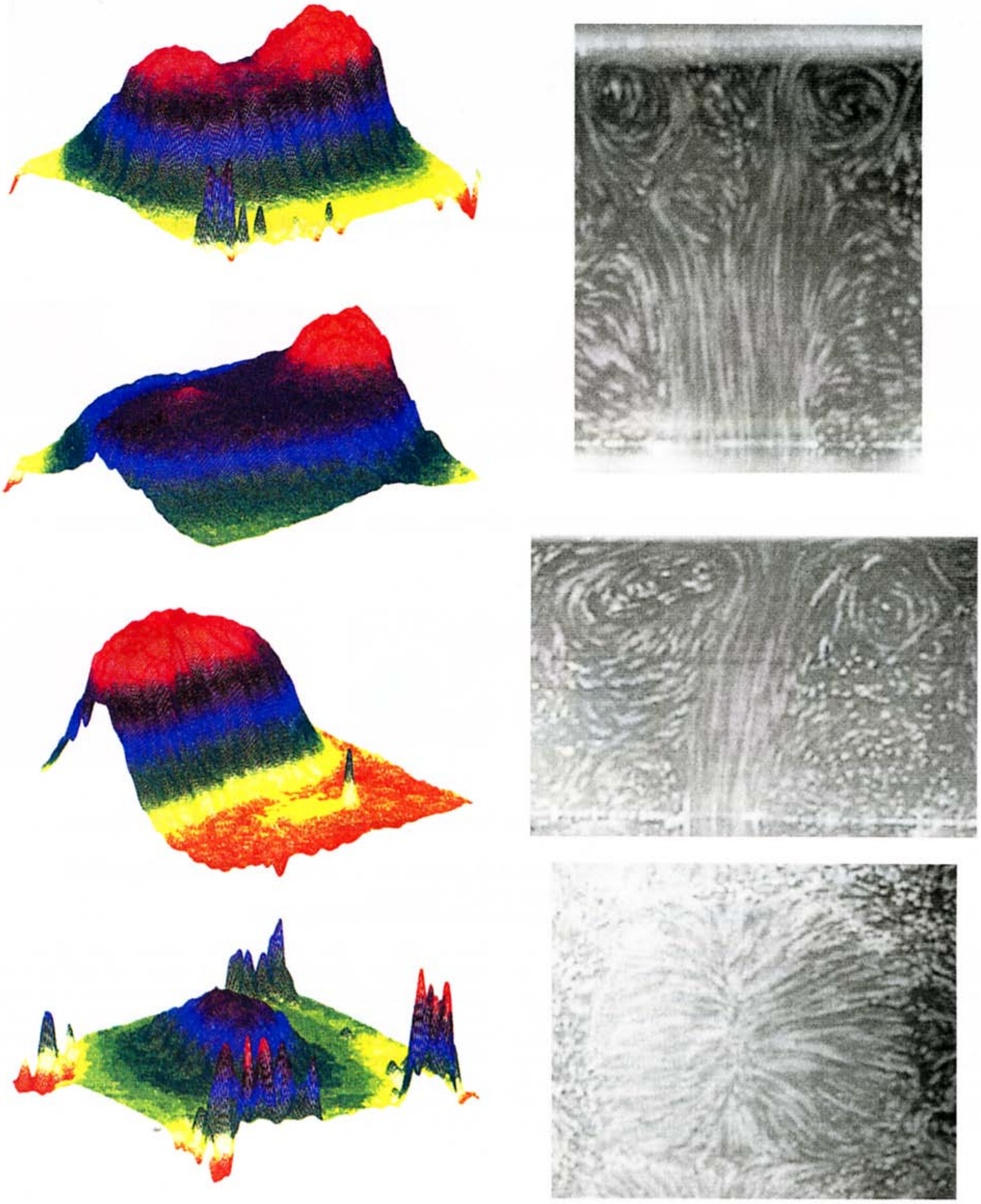

LIQUID JET IMPINGEMENT USING VISUALIZATION

S. C. Arjocu, Medical University of South Carolina, Charleston, South Carolina
J. A. Liburdy, Oregon State University, Corvallis, Oregon

Shown are instantaneous, local distributions of the heat transfer coefficient (left) from liquid crystal studies and flow visualization (right) for the center jet of an array of impinging elliptical jets. Several large-scale instability modes are present in this flow. The top two heat transfer distributions and top flow visualization illustrate bimodal heat transfer distributions that oscillate due to unstable vortical structures at the surface.

The center images illustrate jet swaying and a resultant skewed heat transfer distribution. The bottom images, where the flow visualization is viewed from beneath the impingement surface, show the result of a switching of the major and minor axes of the central jet when impingement surface is beyond four jet hydralic diameters from the jet exit (Arjocu and Liburdy 1997a, b).

1997 Max Jakob Memorial Award Lecture

The Monte Carlo Method in Radiative Heat Transfer

J. R. Howell
Department of Mechanical Engineering,
The University of Texas at Austin,
Austin, TX 78712-1063
e-mail: jhowell@mail.utexas.edu
Fellow ASME

The use of the Monte Carlo method in radiative heat transfer is reviewed. The review covers surface-surface, enclosure, and participating media problems. Discussion is included of research on the fundamentals of the method and on applications to surface-surface interchange in enclosures, exchange between surfaces with roughness characteristics, determination of configuration factors, inverse design, transfer through packed beds and fiber layers, participating media, scattering, hybrid methods, spectrally dependent problems including media with line structure, effects of using parallel algorithms, practical applications, and extensions of the method. Conclusions are presented on needed future work and the place of Monte Carlo techniques in radiative heat transfer computations.

Introduction

The Monte Carlo method is a class of numerical techniques based on the statistical characteristics of physical processes, or of analogous models that mimic physical processes. The method was developed by early workers trying to analyze the potential behavior of nuclear weapons, where experiments were difficult and the methods of analysis available at that time were not sufficient to provide accurate prediction of behavior. Directly simulating the behavior of individual neutrons and then following the history of many such neutrons allowed prediction of the average behavior of the weapon. Metropolis and Ulam (1949) provide an early exposition of the philosophy behind the approach.

In this review, consideration is restricted to applications of the method to problems in radiative heat transfer. There are many closely related applications in atmospheric physics, astrophysics, remote sensing, and others, which have the same basis in mathematics and statistics, but space precludes such a broad review.

General reviews of the Monte Carlo method in radiative heat transfer are available in many sources, which provide the details for implementation. These include Howell (1968), Haji-Sheikh (1988), Brewster (1992), Siegel and Howell (1992), Modest (1993), Walters and Buckius (1994), and Howell and Mengüç (1998). Because these reviews provide the details and derivations of the functions necessary to implement a Monte Carlo analysis, this level of detail can be omitted here. However, a short example is presented to provide background to the reader who is unfamiliar with the Monte Carlo approach.

Consider the geometry shown in Fig. 1. Elements dA_1 and dA_2 are strip elements of infinite length in the z coordinate, and surface A_2 is a plane of finite width and infinite length into the page. Howell (1998) shows that the fraction of energy leaving an infinitely long strip and striking a parallel infinite strip depends only on the angle β between the strips. The *configuration factor*, dF_{d1-d2} for this two-dimensional differential strip-to-differential strip geometry is given by

$$dF_{d1-d2} = \frac{\cos\beta d\beta}{2} = \frac{d(\sin\beta)}{2}. \qquad (1)$$

Suppose it is desired to find the fraction of radiation leaving the element dA_1 on surface 1 that is incident on the entire surface A_2. In conventional analysis, this is done by integrating across the receiving surface A_2 to give

$$\begin{aligned} F_{d1-2} &= \int_{A_2} dF_{d1-d2} = \int_{\beta=\beta_{\min}}^{\beta_{\max}} \frac{d(\sin\beta)}{2} \\ &= \frac{1}{2}(\sin\beta_{\max} - \sin\beta_{\min}) \\ &= \frac{1}{2}\left\{\frac{W-x}{[(W-x)^2+H^2]^{1/2}} + \frac{x}{(x^2+H^2)^{1/2}}\right\} \qquad (2) \end{aligned}$$

where $\beta_{\min}$ in this case is negative. For the particular case of $W = 2$, $H = 1$, and $x = 0.5$, Eq. (2) gives $F_{d1-2} = 0.6396$.

Now, let us apply the Monte Carlo technique to find F_{d1-2} for this geometry. Imagine that a very large number of photons leaves surface 1, and many of these intercept surface 2. We will model a large number of these photons by simulating their behavior with a smaller number of energy packets that mimic the behavior of photons. First, we ask what is the probability dP that radiation leaving surface element dA_1 will strike a parallel element oriented at angle β from dA_1. Because of the definition of the configuration factor, the probability dP in this case is equal to the configuration factor, so

$$dP = dF_{d1-d2} = \frac{d(\sin\beta)}{2}. \qquad (3)$$

To simulate the radiative transfer process, imagine that the radiative energy is made up of discrete packets of energy leaving dA_1. If we can determine the fraction of the total packets of energy that strike anywhere on A_2, this will be the configuration factor. In straightforward Monte Carlo, we will shoot a large number of energy packets from dA_1 and simply see how many strike A_2. However, we must be very sure that the directions at which the packets leave dA_1 obey the laws governing radiation. Further, in more complex problems than this example, we must be sure that every event is independent of preceding events. Thus, we would like to choose the outgoing directions *at random from the correct distribution* of outgoing directions. This is done by relating the outgoing direction to a number R chosen at random from a uniform set of numbers in the range $0 < R < 1$. The governing relation between a random number and a known probability distribution is (Kalos and Whitlock, 1986)

Contributed by the Heat Transfer Division for publication in the JOURNAL OF HEAT TRANSFER and presented at the AIAA/ASME Heat Transfer Conference, Albuquerque. Manuscript received by the Heat Transfer Division, Feb. 17, 1998; revision received, Mar. 13, 1998. Keywords: Computational, Emitting, Heat Transfer, Radiation, View Factors. Associate Technical Editor: J. R. Howell.

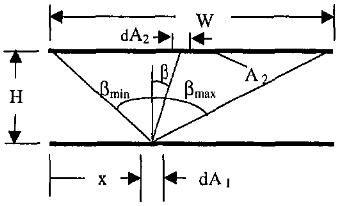

Fig. 1 Geometry for configuration factor between strip element and plane

$$R = \int_{\xi^*=-\infty}^{\xi} dP(\xi^*). \tag{4}$$

This relation is often called *the fundamental theorem of Monte Carlo.* If the probability of occurrence of any event is known, then random choices from this distribution can be made by applying Eq. (4), and then choosing random numbers to determine successive values of the variable ξ. When enough values of ξ are chosen, the chosen values are guaranteed to have the probability distribution $dP(\xi)$. So, for this example,

$$R = \int_{\beta_{\min}=-\pi/2}^{\beta} dP(\beta^*) = \int_{\sin\beta^*=-1}^{\sin\beta} \frac{d(\sin\beta^*)}{2}$$
$$= \frac{1}{2}(\sin\beta + 1). \tag{5}$$

Then the angle β for an individual energy packet leaving dA_1 can be found by choosing a random number R and recasting Eq. (5) as

$$\sin\beta = 2R - 1. \tag{6}$$

When a large enough sample of packets is sent forward, they are guaranteed by this procedure to have the probability distribution $dP(\beta)$. Now, to determine the value of F_{d1-2}, we follow the histories of a large number of packets, and for each one we check to see whether the value of β from Eq. (6) lies between $\beta_{\min}$ and $\beta_{\max}$. If so, the packet strikes A_2. A computer flow chart for this problem is shown in Fig. 2. It is apparent that this flow chart will result in a quite short and simple program.

Using the chart in Fig. 2 as a basis, a simple program was written to determine the value of F_{d1-2} for the particular case of $W = 2$, $H = 1$, and $x = 0.5$. Substituting these values into Eq. (2) gives the analytical value of $F_{d1-2} = 0.6396$. The values generated by the Monte Carlo program depend on the number of sample packets N chosen for the simulation. Some results are shown in Table 1. These results are all generated starting with the same initial random number and random number sequence.

The results show many of the typical characteristics of Monte Carlo analysis. First, because of their statistical nature, the results become more accurate as more packets are included in the simulation. These statistical characteristics are at once a drawback and a blessing. The drawback is that it may take a very large number of samples to obtain acceptable results, resulting in long computational times. The advantage is that statistical tests can be used so that the uncertainty in the results can be measured, an advantage that is often not present in other more deterministic methods. For example, dividing the computation for 100,000 packets into ten simulations of 10,000 packets, the mean $\bar{F}_{d1-2}$ and standard deviation γ of the ten simulations can be computed, resulting in $F_{d1-2} = \bar{F}_{d1-2} \pm \gamma = 0.6395 \pm 0.0145$. This indicates that the actual value of F_{d1-2} lies within ± 0.0145 of the mean value with a probability of 63.2 percent, and within $2\gamma = \pm 0.029$ with a probability of 95 percent.

Clearly, if the value of H/W were larger, the value of F_{d1-2} would be smaller. Because a smaller fraction of the packets would strike A_2, the uncertainty as expressed by the standard deviation γ would probably increase for a given number of packets, N. Thus, the uncertainty in Monte Carlo results depends on the particular geometry under study.

Another characteristic is that accuracy tends to depend on the square root of the increase in sample packet number; i.e., running four times the number of packet histories will reduce the uncertainty in the result by one-half.

This example does not include one important aspect of Monte Carlo techniques. This is that each succeeding event is independent of the previous history of the packet. For example, if surface A_2 were nonblack, we might wish to determine the fate of energy reflected from that surface. We could choose an angle of reflection from surface 2, and find the final location where the packet ends its history; back on surface 1, or through one of the edge openings. If surface 2 is diffusely reflecting, then we should choose the angle of reflection as being independent of the angle of incidence, because the reflectivity of a diffuse surface is usually assumed to be independent of incident direction. Therefore, we could choose the angle of reflection by invoking the fundamental theorem of Monte Carlo (Eq. (4)) to relate the angle of reflection to a random number. This independence of a given event on prior events is characteristic of Monte Carlo analysis. A sequence of events, each of which is independent of prior events, is called a *Markov chain* (Billings et al., 1991a, b).

Note that the independence of succeeding events is determined by the use of random numbers chosen in the range $0 < R < 1$. Most programming languages have arithmetic random number generators that provide a sequence of random numbers. These generators are called in the same manner as common functions such as sine or natural log. The generators have been tested to show that the sequence of random numbers produced pass common tests required of random numbers. The first is the necessary (but not sufficient) test that a sequence of generated random numbers indeed is uniformly distributed; that is, any equal increment between zero and unity will have the same fraction of random numbers. However, the generator must pass other tests; for example, all even and all odd random numbers must also be uniformly distributed; sets of every second, every

Nomenclature

A = area, m^2
a = absorption coefficient, m^{-1}
e = emissive power, W/m^2
F = configuration factor
H = perpendicular distance between parallel surfaces, m
N = number of sample packets
n = packet index
P = probability
R = random number chosen in range $0 \leq R \leq 1$
S = number of absorbed packets
T = absolute temperature, K
t = CPU run time, s
W = width of plane, m
x = coordinate along plane width, m

Greek Symbols

β = angle with respect to normal in plane perpendicular to strip element
γ = standard deviation
λ = wavelength, μm
σ = Stefan-Boltzmann constant, 5.667×10^{-8} $W/(m^2 K^4)$

Subscripts

b = blackbody
max = maximum value
min = minimum value

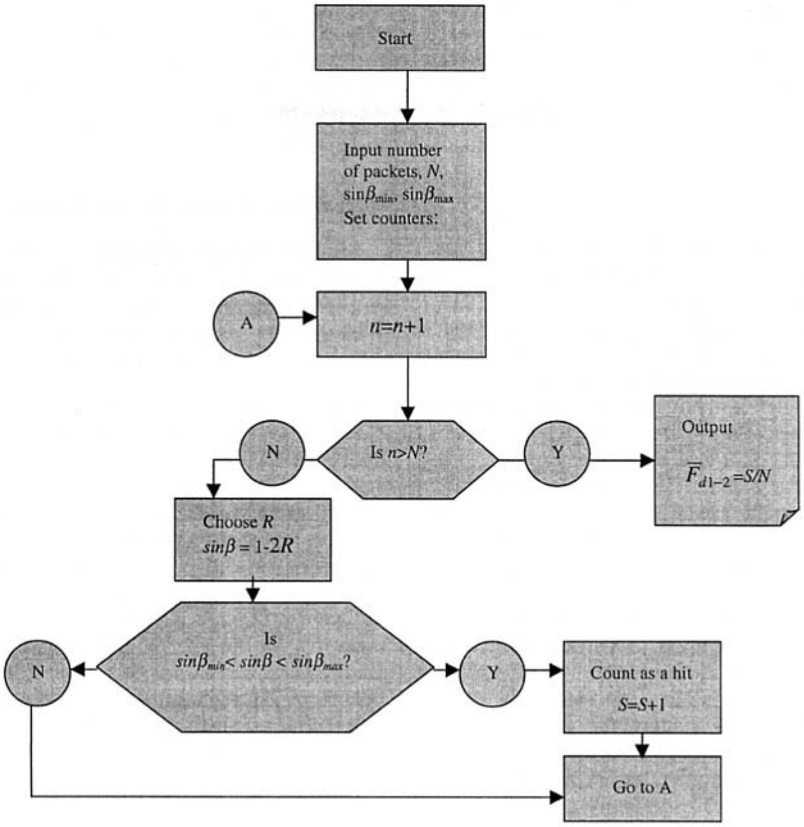

Fig. 2 Monte Carlo flow chart for determining the configuration factor

third, every fourth, etc., random numbers must be uniformly distributed. Further, these sets cannot be correlated such that succeeding numbers follow a sequence; i.e., pairs of generated random numbers cannot follow a large-large, small-small or large-small, large-small sequence. In fact, to prove true randomness, a generator must pass an infinite number of tests.

Hayes (1993) provided a thought-provoking review of the various attempts to produce true random number generators for computers. He noted that some recent large-scale computations have shown interactions between the models being processed and the particular random number generator being used. For the radiative heat transfer problems solved to date, no mention has been made in the literature of inadequacy in standard random number generators provided as part of programming languages. However, Hayes quoted John von Neumann: "Anyone who considers arithmetical methods of producing random digits is, of course, in a state of sin."

The example of Fig. 2 does show important characteristics of the Monte Carlo approach. First, simple relations that are repeated many times replace a degree of mathematical sophistication. This allows quite complex physical problems to be easily programmed. The price for programming simplicity may be lengthy computational time. However, with the rapid increase in computer speed and the implementation of massively parallel architecture in computers, the importance of this drawback is diminishing.

Table 1 Results of Monte Carlo simulation for the configuration factor

Number of packets, N	Mean value of configuration factor, $\bar{F}_{d1-2}$
100	0.65
1,000	0.640
10,000	0.6302
100,000	0.6395

Because the method outlined above simulates the actual behavior of radiative transfer, it is often referred to as *direct simulation of radiation by Monte Carlo* (DSRMC).

Monte Carlo in Radiative Heat Transfer. The Monte Carlo technique is important in radiative heat transfer for the same reasons it was introduced in neutron diffusion problems. The governing mathematical equations describing radiative heat transfer are complex and difficult to solve with accuracy. In addition, many physical effects are important to radiative transfer (e.g., spectral dependence of surface and participating medium properties, anisotropic scattering distributions, directional surface properties, variation of properties with location and temperature), and these further complicate calculations based on deterministic mathematical models.

The common techniques for solving the mathematical models of radiative transfer generally rely on various degrees of approximation. For example, the discrete ordinates technique approximates integrals over direction by a numerical quadrature technique, and it is then assumed that the radiative intensity is constant within each quadrature direction. The solution will approach exactness as the number of quadrature elements is increased.

The P-N or spherical harmonics method describes the radiative intensity as an orthogonal infinite series expansion in terms of distance and angle, and then truncates the series to a set that can be conveniently solved.

Some attempts have been made at exact solution of the complete radiative transfer equation by using finite element solutions; these again incorporate a degree of approximation in the choice of element basis functions and shape. There are essentially no exact analytical solutions available to the radiative transfer equation except for quite simplified choices of geometries and property variations.

The Monte Carlo method is able to incorporate all important effects in a radiative transfer simulation without approximation, and this is its major attribute.

Review of Literature

General Reviews. Various reviews of the Monte Carlo method have appeared over the years. Because of its wide use, most recent texts and handbooks cover the fundamentals of the method, and those are not reviewed here.

Howell (1968) reviewed the method as applied to heat transfer problems, with emphasis on radiative transfer. Haji-Sheikh and Sparrow (1969) provided an overall review of the method, and considered in some detail the generation of probability distribution-random number relations for cases where the variables to be chosen depend on more than one variable. They provided some methods for biasing the single-variable choice techniques to account for multivariate dependence. Haji-Sheikh (1988) provided a comprehensive review of the literature dealing with Monte Carlo in heat transfer through the date of publication.

Walters and Buckius (1994) gave a comprehensive and readable review of the method as applied to participating media with scattering. They provide a bibliography of references in collateral fields where scattering is also important.

Farmer and Howell (1998) have attempted to quantify and compare the various common strategies available for use in programming Monte Carlo simulations, and provided comparisons for classes of problems that are typically attacked.

Statistical Characteristics. The nature of the Monte Carlo method is that the results inherently possess statistical behavior. This can be a benefit in that the uncertainty (in terms of variance or standard deviation) in the results can always be determined as shown in the example; however, in certain cases, the predicted uncertainty may be so large that the results are useless. The obvious solution is to follow more packets; however, if the particular problem being run is very expensive in machine time, this may not be a feasible strategy. For example, in a given simulation, the radiative flux at a particular location may be required to high accuracy. If a very small fraction of sample packets reaches that location, then it may be difficult to obtain a sufficiently large packet sample to obtain low uncertainty in the flux. In such a situation, variance reduction procedures of various kinds have been employed. The use of a reverse Monte Carlo technique may be valuable in this case.

Haji-Sheikh and Sparrow (1969) covered the fundamental statistical measures needed to determine the accuracy of Monte Carlo solutions, along with a relation for determining the variance in the results as the number of packets or packet groups is increased so that "on-line" determination of solution accuracy can be monitored. Shamsundar et al. (1973) showed that partitioning the energy carried by packets after each event in the path, and then following the partitioned energy portions individually, can greatly reduce the variance in some cases. This was particularly the case in "open" configurations, i.e., enclosures with one open boundary exposed to the environment. Haji-Sheikh (1988) discussed various techniques for biasing direct Monte Carlo results to reduce variance, along with methods for computing expected variance.

Almazan (1994) used the variance in successive runs to control the number of packets used in successive iterations.

Farmer and Howell (1998) defined the "performance" of various Monte Carlo methods as the product of run time t and variance γ^2 of the solution, or

$$\text{Performance} = \gamma^2 t. \tag{7}$$

The method or strategy in a Monte Carlo simulation that minimizes the value of this quantity is assumed to be the best choice. Farmer (1995) and Farmer and Howell (1998) showed comparisons of performance for a wide variety of Monte Carlo strategies, along with comparisons for various problems that exercise these strategies for problems with participating media in enclosures.

References Using Monte Carlo Analysis

Surface-Surface Exchange. The use of Monte Carlo for surface-surface exchange actually came after the method was employed in participating medium problems. The method probably is most useful in problems with complex geometries, or where directional surface properties must be treated.

Direct Computation in Complex Geometries. Polgar and Howell (1966a, 1966b) used Monte Carlo to determine the bidirectional reflectivity of conical cavities with diffuse internal surfaces exposed to collimated incident radiation. Corlett (1966) used Monte Carlo to analyze radiative exchange in enclosures with surfaces with specified bidirectional reflectance. Examples for some simple enclosures with specular-diffuse surfaces were carried out. Toor and Viskanta (1968) examined radiative exchange between some simply arranged sets of surfaces by Monte Carlo, and compared the effects of various assumptions as to the directional properties of surface reflectance. They examined diffuse, specular, and bidirectional reflectivities, and found that the differences in radiative transfer ranged from negligible to very large, depending on surface arrangement. Vossbrecker (1970) used Monte Carlo to find the radiative exchange within a cylindrical container closed at one end, and also determined the effective emissivity of cylindrical cavities.

Howell and Durkee (1971) made experimental measurements of the incident flux on the surfaces of an enclosure with an aperture exposed to collimated incident radiation. The enclosure had a diffuse, a specular, and a highly directional surface of known bidirectional reflectance. A Monte Carlo analysis for predicting incident flux on each surface provided results that compared well with experiment.

A practical application by Blechschmidt (1974) was the determination of the fraction of incident radiation that is transmitted through a specular tube. This work was applicable to determining the radiative transfer to or from a vacuum chamber through an access port. Effects of the assumed directional distribution of incident energy were shown. This work neglected the effect of polarization on the specular reflectivity, which is known to be important in determining radiative transfer when multiple specular reflections are present (Edwards and Tobin, 1967).

Egan and Hilgeman (1978) applied Monte Carlo to determining the spectral characteristics of the reflectivity of spherical particles of known complex refractive index. They applied this information to find the predicted reflectance of a surface composed of spherical particles. They found good comparison with the measured reflectance of meteorites of known complex refractive index.

Maltby and Burns (1991) gave an in-depth analysis of variance in Monte Carlo calculations applied to enclosures with nonparticipating media, with a good review of the literature. Effects of various parameters on variance and run time were investigated.

McHugh et al. (1992) analyzed the use of various arrangements of specular and diffuse surfaces to funnel daylight into interior building spaces. Although the code they developed was capable of handling spectral effects, only results for gray surfaces were given.

Palmer et al. (1996) and Antoniak et al. (1996) used direct Monte Carlo simulation to determine radiative transfer between opaque elements with triangular and cylindrical cross sections in fixed two-dimensional arrays. Shading and blocking were accounted for, and the surface properties of the elements were diffuse or specular. Zaworski et al. (1996) modeled the radiative transfer through a gap with directionally reflecting boundaries using Monte Carlo, and compared their results with experiment. They observed that the assumption of diffuse reflection becomes particularly poor for cases where the intensity is incident at near-grazing angles to the surface. In such cases, a specular spike in reflectivity becomes pronounced and must be accounted for to retain accuracy.

Calculation of Configuration and Exchange Factors. From the simple example problem presented in Figs. 1 and 2, it is apparent that Monte Carlo presents a useful method for finding the values of configuration factors. For simple geometrical arrangements of surfaces, over 250 factors have been presented in the literature (Howell, 1998). However, when the arrangement of surfaces and shapes is arbitrary, it is often necessary to compute the configuration factors for the particular geometry and arrangement of surfaces at hand. Weiner et al. (1965) discussed how Monte Carlo can be used, and the expected statistical errors that result. Yarbrough and Lee (1986) presented a comprehensive review of the use of Monte Carlo for finding configuration factors, and compared results with known analytical values for a number of shapes. They also presented results for two configurations not previously in the literature. Bushinskii (1976) presented exchange factors for some simple two-dimensional geometries and compared with analytical solutions. Modest (1978) treated the calculation of exchange factors among nongray, nondiffuse curved surfaces in enclosures and open geometries. He also noted that for open geometries, the energy partitioning approach of Shamsundar et al. (1973) was very effective in reducing computational time.

Because configuration factors computed by Monte Carlo show the usual statistical fluctuations, the mean values found from a series of calculations do not necessarily meet the requirements that all factors from a particular surface sum to unity, or of reciprocity. Various methods for adjusting the factors to meet one or both requirements have been proposed by Sowell and O'Brien (1972), Vercammen and Froment (1980), Larsen and Howell (1986), van Leersum (1989), and Taylor et al. (1995).

Inverse Design. Thermal designers often face problems where they know the outcome required of a design. For example, the temperature distribution and radiative flux necessary to bake foods passing continuously through an oven is known; the design problem is where to place the heating elements in the oven and how much power to provide to them. This is the reverse of the way most thermal design problems are solved; in conventional solution methods, the heater placement and temperature or power input are prescribed, and the heat flux or temperature on the oven rack is found. If they don't match the requirements, some aspect of the prescribed conditions is changed, and the solution is run again. This is repeated until a satisfactory solution is found. *Inverse design methods* seek to use the required outcome as a problem input, and then a satisfactory design is computed without iteration. Unfortunately, the relations describing inverse solutions are mathematically *ill-posed*, resulting in requirements for solution techniques that are more difficult than for forward problems. The state of inverse thermal design was recently reviewed for surface-surface radiation problems by França et al. (1997) and for enclosures with participating media by França et al. (1998).

Monte Carlo can be used in inverse design. Wu and Mulholland (1989) used a method of statistical least squares optimization of multiple Monte Carlo forward solutions to determine the best solution from a set. They examined two-dimensional surfaces radiating to one or more radiation detectors, with a known signal. The objective was to find the surface temperature distribution. They fit the Monte Carlo solution set with Legendre polynomials, and then optimized the polynomial coefficients to find the best solution for the temperature distribution. This is not a design solution method, but could probably be adapted for design purposes.

Oguma and Howell (1995) solved a radiative inverse problem in a two-dimensional enclosure by using a modified reverse Monte Carlo procedure. Packets were emitted diffusely from the heated design surface in proportion to the desired incident flux distribution, and were traced to their point of origin. The forward problem was then solved using the outgoing flux from the heaters found by the reverse procedure to see how close the solution was to the required solution. The forward solution and reverse requirements differed because the heaters were assumed to emit diffusely, but the inferred outgoing flux from the reverse algorithm was not diffuse. The solution for the heater net radiative flux was then adjusted until an acceptable solution was found. Oguma et al. (1998) extended the algorithm to an inverse problem in which it was desired to find the necessary two-dimensional enclosure geometry to produce a given heat flux and temperature on the oven rack.

Packed Beds and Fiber Layers. Ray tracing and Monte Carlo techniques have been successfully applied to problems of radiation transfer through regular and random arrays of particles and fibers. Yang (1981) and Yang et al. (1983) derived the statistical attributes of a randomly packed bed of identical cold (nonemitting) spheres (distribution of number of contact points between spheres and the conditional distributions of contact angles for spheres with a given number of contact points.) These were found by using a zero-momentum random packing model modified from that of Jodrey and Tory (1979). This model has the inherent difficulty that the upper layer of spheres in a randomly packed container is not level (as is true in a real packed bed). Thus, defining the bed thickness is somewhat arbitrary, especially for beds that are only a few sphere diameters in depth. Wavy container boundaries were assumed so that the radial dependence of packing characteristics present in rigid containers could be ignored. Yang (1981) and Yang et al. (1983) used the bed packing distributions to construct a ray-tracing algorithm for specularly reflecting spheres, and computed the fraction of incident diffuse radiation that was transmitted through the bed. Comparisons with the experimental results of Chen and Churchill (1963) were made, and although similar trends of transmittance versus bed thickness were shown, exact agreement was not attained.

Abbasi and Evans (1982) adapted a Knudsen gas diffusion code to compute the transfer of photons through a plane layer of porous material, using the porosity as the only parameter in determining fraction transmitted vs. reciprocal penetration depth.

Kudo et al. (1991b) used a model similar to that of Yang for determining transmittance, and added further experimental results for comparison. They simulated random packing by perturbing a regular packing within a bounded region and then removing those spheres that overlapped the boundary after perturbation. This produced a low-density region near the boundary, which was found to introduce a considerable increase in bed radiative transmissivity. Both specularly and diffusely reflected spheres were modeled.

Singh and Kaviany (1991, 1992, 1994) and Kaviany and Singh (1993) extended the Monte Carlo analysis of packed beds of spheres to consider semitransparent and emitting spheres, and in particular to show that dependent scattering effects are quite important even for quite large bed porosities. Near-field dependent-scattering effects are inherently included in these Monte Carlo analyses of packed beds, but are difficult to include in many other methods. Kaviany and Singh (1993) provided a quite complete discussion of radiation in packed beds up to the time of publication. They pointed out that the results of the earlier analyses by Yang and Kudo did not account for the nondiffuse nature of the incident radiation in the Chen and

Churchill experiments, and thus tended to underpredict the experimental bed transmittance. They also gave a comprehensive discussion of the effect of dependent scattering.

Argento and Bouvard (1996) revisited the work of Yang et al. (1983), and were able to derive a more accurate method for determining the effective bed radiative properties by using Monte Carlo results evaluated in the bed interior. The method eliminated the problem of indeterminate bed height in random packing.

Kudo, Li, and Kuroda (1995) and Li et al. (1996) analyzed transfer through a bed of randomly oriented fibers, and a bed of fibers that are randomly oriented but lie in planes parallel to the bed surface. Mie scattering was assumed to occur from individual fibers. Comparison with available experimental results for transmission through fiber beds was quite good.

Applications to Practical Systems. Many practical problems have been solved by the methods discussed in this paper. For surface-surface exchange, typical applications were given by Howell and Bannerot (1976), who analyzed the absorption in trapezoidal moderately concentrating solar collectors for various angles of incidence using Monte Carlo. They compared the predicted radiative flux distribution on the concentrator with measured values. Omori et al. (1990) analyzed radiant transfer in a complex enclosure to predict the behavior of human comfort in a floor-heated room; Villeneuve et al. (1994), used Monte Carlo as a design tool to compute and suppress IR signatures from jet engines; and Mochida et al. (1995) used combined-mode analysis to predict the behavior of a vacuum furnace heated by radiant tube burners.

Participating Media. When a medium that absorbs, emits, and scatters radiation is present in an enclosure, the treatment of radiation is more complex. For Monte Carlo analysis, packets of energy will now undergo additional events in their histories, but the treatment of these events adds little to the Monte Carlo flow chart. Thus, Monte Carlo has significant advantages in many cases over other techniques for treating participating media. In fact, the initial application of Monte Carlo to radiation heat transfer was for such problems (Fleck, 1961; Howell and Perlmutter, 1964a, 1964b; Perlmutter and Howell, 1964).

The first engineering application to participating media was determining the temperature distribution in a gray absorbing-emitting medium between infinite parallel plates of given temperature and emissivity (Howell and Perlmutter, 1964a), for which numerical solutions were available for comparison. This paper served to provide the basis of the method for this class of problems. A follow-on paper applied the technique to the more complex geometry of concentric cylinders enclosing a gray gas for which no analytical solution was available at that time (Perlmutter and Howell, 1964). Finally, the case of a nongray gas between parallel plates was treated to show the applicability of the method to problems with spectral dependence (Howell and Perlmutter, 1964b).

Campbell (1967) discussed methods for using Monte Carlo in time-dependent multimode problems with frequency-dependent properties.

House and Avery (1969) provided a detailed derivation of the necessary functions for treating radiative transfer in a participating medium. Of most interest is their discussion of biasing techniques applied to packet path lengths in the medium, so that highly attenuating media can be treated without the extreme computational times necessary if straightforward path-length calculations are used.

Howell (1973) provided an extension of Monte Carlo analysis to general thermal analysis problems by noting that for most thermal systems, there are uncertainties in dimensions, properties, configuration factors, and other design variables. If the mean value and standard deviation of these factors is known or can be estimated, then a Monte Carlo analysis of the thermal system can be performed by choosing from the distributions of each variable to construct an individual sample system and analyze its thermal behavior. By building enough such sample systems, the mean thermal behavior and standard deviation of the design system can be predicted. This is a viable and effective alternative to worst-case analysis of thermal (or other) systems.

Steward and Guruz (1974) studied a medium with spectrally dependent absorbing and anisotropically scattering particles between gray infinite parallel planes. They considered cases with and without the presence of gases with band absorption.

Al Abed and Sacadura (1983) and Mishkin and Kowalski (1983) analyzed a combined radiation/combustion problem for a gray medium between parallel plates, using Monte Carlo for the radiative terms in a finite difference analysis of the energy equation.

A comparison of a P-1 and Monte Carlo solution for radiation from a gray isothermal medium to an enclosing conical surface was given by Kaminski (1989).

For iterative calculations as typically found in multimode heat transfer problems involving radiation in participating media, Kobiyama (1989) provided alternative formulations to conventional Monte Carlo. These methods are particularly useful for problems where temperature-dependent properties are present.

Martin and Pomraning (1990) used Monte Carlo to determine the fraction of emitted radiation from an infinite plane that is scattered back to the plane by a sphere of purely scattering medium located at some distance from the plane. Results are only given for a point on the plane directly beneath the sphere. Some variance reduction techniques are employed.

An interesting exercise of the Monte Carlo method was initiated by Tong and Skocypec (1992), who provided the parameters for solution of a set of radiative transfer problems. Solutions by various methods were solicited for comparison in a special session of the 1992 National Heat Transfer Conference. The problem set ranged from one to three-dimensional geometries, enclosing a medium with spectrally dependent anisotropic scattering and a specified set of parameters for use in a wide-band spectral treatment of gas absorptance. The medium temperature distribution was specified. Solutions were requested for local flux divergence and heat flux. Monte Carlo solutions to the problem were submitted by Yuen et al. (1992) and Farmer and Howell (1992). The results differed significantly among the methods, including between the two Monte Carlo solutions. This was apparently due to differences in the treatment of spectral effects. Some final results were later presented by Farmer and Howell (1994a).

Parthasarathy et al. (1994) showed applications of Monte Carlo to complex geometries enclosing participating anisotropic media, and presented some solutions for rhombic and other quadrilateral enclosures, and for some configurations with curved boundaries. Henson et al. (1996) used Monte Carlo to benchmark solutions by the discrete transfer method.

Scattering. Scattering is relatively easy to treat in Monte Carlo problems compared with methods that solve the equation of radiative transfer. If the scattering distribution (phase function) is specified, the relation of angle of scatter to a random number is found as for the other random choices in a packet path. Walters and Buckius (1994) provided a comprehensive review of scattering algorithms in Monte Carlo, and also gave a discussion of treatments for inhomogeneous media and the use of backwards Monte Carlo algorithms. The reader should consult that work for a review of literature up to the date of publication.

Kudo et al. (1993b) and Taniguchi and Mochida (1994) investigated anisotropic scattering effects by comparing anisotropic and isotropic scattering results in a gray slab and in a slab with spectrally dependent gas absorption/emission using a wide-band model.

Farmer (1995) and Farmer and Howell (1998) have investigated the performance of various strategies for carrying out

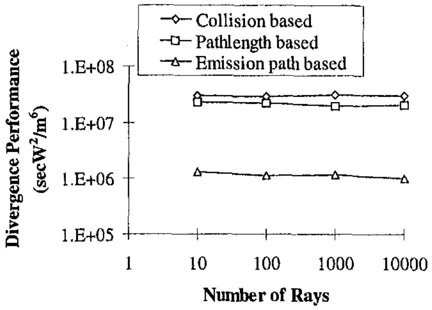

Fig. 3 Performance of various scattering strategies versus number of packets followed: gray gas of optical thickness 10 between parallel black cold plates (Farmer, 1995)

scattering calculations. For example, the packet energy can be held constant and the path length to a scattering event found. In this case, all packet energy is redirected at the point of scatter and the packet is followed until the energy is deposited at a radiative sink. This technique is easy to program and fast to execute, but has poor statistics in that the scattering points are widely separated. It is called the *collision-based method.*

Another strategy is to deposit a portion of the packet energy in each volume element traversed. The portions are in proportion to the logarithmic decrement of energy caused by the scattering coefficient in that element. Each portion is then tracked as if it scattered from the "center of scatter" of the element. This technique has good statistics in that the scattering more nearly simulates the physical process of continuous scattering along the packet path; however, the memory and computation overhead is high. This method includes the continuous attenuation due to absorption, and is referred to as the *pathlength method.*

Finally, the reverse method introduced by Walters and Buckius (1992, 1994) (called the *emission path method*) can be used. This method traces packet histories in reverse, beginning at the point of origin; it has been found to be very efficient for problems where local conditions are required.

Each method has a tradeoff between the variance in the results due to differing statistical properties, and the time of solution. Generally, the methods with lower variance require longer CPU time, so the choice of method is not obvious. Farmer (1995) therefore compared the methods for some simple problems using the performance definition of Eq. (7). Variations and combinations of these methods were compared for the case of an isothermal gray absorbing-emitting-scattering medium between parallel black cold boundaries. The pathlength and emission path methods were generally found to be superior to the collision-based methods. The forward pathlength method worked best at small optical thickness, while the emission path method performed best at large optical thickness.

Figure 3 shows the performance defined in Eq. (7) for the various strategies.

For each of the three methods, it is clear that the performance is nearly independent of the number of packets (rays) followed. The variance is reduced in proportion to the number of packets, so the product is nearly constant. For this particular optically thick case, as noted, the emission-based method has the best (lowest) performance values.

Reverse and Inverse Techniques. Modifications of Monte Carlo have been proposed for particular purposes. Dunn (1983) proposed an inverse Monte Carlo technique to determine the albedo distribution in a plane layer from observed measurements. Subramaniam and Mengüç (1991) used an inverse Monte Carlo technique to recover information on both the albedo and phase function of a particulate-laden medium from optical diagnostic data.

Walters and Buckius (1992, 1994) presented the basis for a reverse Monte Carlo technique that has many advantages as an alternative to straightforward Monte Carlo for certain problems. The technique is based on a reciprocity principle, and appears to be especially useful when the conditions optically close to a surface or volume element with known conditions must be determined. Ambirajan and Look (1996) used a backward Monte Carlo method to analyze the problem of multiply scattered radiation from a "searchlight" beam obliquely incident on a plane scattering layer.

Applications to Practical Systems. The Monte Carlo technique has been widely applied to practical problems with participating media. Initial practical applications for systems with participating media were probably in analysis of space nuclear propulsion. Howell et al. (1965) examined the radiative flux expected along the surfaces of a rocket nozzle exposed to radiation from the face of a high-temperature nuclear reactor, and included the effects of spectrally absorbing/emitting dissociated hydrogen. Because of the high predicted flux values, Howell and Renkel (1965) examined the effect of injecting particles to form a high-opacity region along the nozzle wall. The results are summarized in Howell et al. (1966). Industrial furnaces have also received considerable attention. Taniguchi (1967) applied Monte Carlo to a one-dimensional slab with an absorbing-emitting gray medium, with temperature-dependent properties and uniform internal generation. He then extended the work to a three-dimensional enclosure with gray walls at equal uniform temperature (Taniguchi, 1969). Taniguchi and Funazu (1970) further extended the three-dimensional enclosure analysis to include two regions of differing radiative properties and spectral characteristics to approximate the flame and combustion products regions of a fired furnace. They also included a simple model of advection in the gas. Later comparisons were made between predictions and experimental data (Taniguchi et al., 1974).

Steward and Cannon (1971) analyzed radiant transfer in an end-fired cylindrical furnace, and found results that were comparable to zonal analysis. They describe the method as being more flexible, but suggested ways to minimize statistical variance in the results.

Monte Carlo was used by Vercammen and Froment (1980) to compute view factors and exchange areas for the zoning method for application in furnaces. They also provided an algorithm for smoothing the statistical variations in the calculated factors. Lockwood and Shah (1981) in their initial explanation of the discrete transfer method (DTM) noted that it is closely related to Monte Carlo techniques, but that they expected to sidestep some of the shortcomings of Monte Carlo. Malalasekera and James (1995) used a ray-tracing technique in a nonorthogonal grid to find the transfer among discrete elements for use in the DTM. Gupta et al. (1983) and Farag et al. (1986) used Monte Carlo to account for the anisotropic scattering present in fired furnaces. Kudo et al. (1991a) developed a three-dimensional code for furnace analysis, Omori et al. (1991) used a Monte Carlo/zonal method to study the behavior of a heat-treating furnace. Duic et al. (1996) used Monte Carlo to compute the radiative flux divergence in the energy equation to analyze the effect of tube leakage on heat transfer into a combustion chamber.

Radiative transfer in a circulating fluidized bed was analyzed by Kudo et al. (1990) and Taniguchi et al. (1993), and Tamura et al. (1995) analyzed the interaction between convection, combustion, and radiation in a radiant tube burner.

Radiation from high-temperature gas jets has been another area of application. Galanova and Shashina (1981) used Monte Carlo methods to evaluate the triple integral describing the radiative flux on an arbitrary object from an axisymmetric free jet; this is one of the few cases in radiative heat transfer where this technique is used instead of direct simulation. Sumarsono et al. (1993) and Taniguchi et al. (1995) analyzed the coupled radiative-convective heat transfer in a nongray free jet, and predicted the spectral flux emitted to a cylindrical surface parallel to the jet axis.

Related Algorithms and Comparisons. Edwards (1985) presented a formulation of radiative transfer that used Monte Carlo to compute shape factors and exchange factors between volume and surface elements. He then used standard matrix inversion techniques to solve the radiative transfer, and presented examples in planar and cylindrical shell geometries. Emissivities of isothermal layers were predicted for absorbing-scattering isothermal layers.

READ. A similar approach to that of Edwards (1985) was presented by Yang et al. (1995). They gave a detailed description of the Radiant Energy Absorption Distribution (READ) method. This technique has the objective of combining the advantages of Monte Carlo techniques with reduced computational time. Effectively, this method also computes exchange factors among all medium and surface elements using Monte Carlo, and then uses these factors in a standard energy matrix formulation to determine radiative transfer. Computer programs and examples are provided for two and three-dimensional systems.

REM^2. The Radiation Element Method by the Ray Emission Model (REM^2) technique has been modified through a series of papers as finally outlined in Maruyama and Aihara (1996). This method also uses rays emitted from volume and surface elements to determine factors that describe radiative exchange, and these are then used to compute radiative exchange. Results are shown for a complex toroidal geometry.

These methods can treat inhomogeneous media as long as the properties are not temperature dependent; if they are, then the matrix of exchange factors must be recomputed at each iteration, and the advantage of the method is lost.

The READ and REM^2 techniques have the same advantages and limitations as other methods based on exchange factors; once the factors are computed, different sets of boundary conditions (temperatures or fluxes) can be imposed, and these cases each can be run without recomputing the exchange factors. Thus, many cases can be run parametrically and quickly. If a combined-mode problem is being run, this has significant advantages in computer time and algorithm convergence. However, if radiative properties are temperature dependent, or if nongray gases are considered (so that an exchange factor matrix must be computed for every spectral interval considered), or if parametric studies of the effect of properties are the objective, then the method may not be a practical choice.

Markov Chains. Some methods closely related to direct physical simulation as used in Monte Carlo have also been proposed. Esposito and House (1978) indicated that a Markov Chain formalism could be implemented that would allow general treatment of a large class of radiative transfer problems, where Monte Carlo simulation must often be reformulated for each geometry. They implement a Markov chain formalism to the problem of unidirectional radiation incident on a Henyey-Greenstein scattering plane layer, and show that the layer reflectance can be quickly and easily computed. In this method, a transition matrix is precomputed. This matrix relates the scattering interactions between plane volume elements within the plane layer. The multiple scattering is then computed as a chain of implementations of the exchange matrix.

Naraghi and Chung (1984) showed how a transition matrix can be found for the case of an enclosure with diffuse, specular, or specular-diffuse surfaces. When specular surfaces are present, the reflection process is not truly Markovian, as the reflected energy distribution is dependent on the incident distribution. The authors showed how to partially account for this effect, and their technique approached higher accuracy as more and more multiples of the transition matrix were used. In Naraghi and Chung (1985), the method was extended to treat participating media. It was shown that the transition matrix could be generated from Hottel's exchange areas. The method was further extended to bidirectional surfaces in Naraghi and Chung (1986).

Billings et al. (1989) treated enclosures with participating media by a general Markov chain formalism, and solved the problem of radiative exchange through a participating medium between concentric cylinders. In Billings et al. (1991a, 1991b), a two-parameter Markov chain method was introduced so that the effect of history on specular and general bidirectional reflections could be accurately handled.

Sivathanu and Gore (1993, 1994, 1996) have introduced the Discrete Probability Function (DPF) method, which is in a sense a hybrid of Monte Carlo and Markov chain methods. Rather than direct simulation of each individual packet path, the probabilities of dispersion of energy after each event are computed; these are closely related to the transition matrices of Markov chain methods. Increased efficiency of calculation was noted, particularly for cases where low probability events are of interest such as absorption in optically thin media or on high reflectivity surfaces.

The chief drawback of the Markov chain methods is that the transition matrix must be precalculated. This matrix must contain all of the effects of factors such as anisotropic scattering and bidirectional reflectivities for exchange between every pair of surface and volume elements in an enclosure, and may be different for each spectral range considered. The necessary amount of precomputation destroys much of the advantage gained over the direct simulation Monte Carlo method during the actual calculation of radiative transfer. It is not clear that Markov chain methods possess an advantage for complex problems, although the methods probably deserve more research.

Treatment of Extended Problems.

Variable Properties. Participating media with properties that vary spatially are tedious to treat by any technique. Monte Carlo is really no exception, and variable property problems are a major challenge. Because packet paths may go in any direction, the distance to absorption or scattering for each packet must be individually computed along a vector with varying absorption and/or scattering coefficients. A few papers have addressed this problem.

Montagnino (1968) noted that for media with a refractive index that varies spatially, Monte Carlo sample packets should follow a curved path, and this will affect the calculation of energy distribution on receiving surfaces. A Taylor series expression for the curvature vector near a particular point was derived and implemented in a ray-tracing procedure. He presented some examples of error induced by neglecting this effect.

Maltby (1994) examined the ASME test problems suggested by Tong and Skocypec (1992) using a three-dimensional Monte Carlo code. He varied the mesh size in one-eighth of a three-dimensional parallelepiped enclosure from $5 \times 5 \times 5$ to $9 \times 9 \times 9$. Properties and temperature were assumed to be constant within each element. Because the properties and temperature in the medium both vary in a prescribed way in these problems, the results are expected to be grid-dependent to some degree. He found that the results for wall flux and local flux in the medium did not vary significantly with grid size in the range tested, but the flux divergence did vary, particularly near the cold bounding walls. He also found very strong dependence on the way the spectrum was averaged.

Because of the observation that differences in treatment of spectral effects apparently introduced considerable differences among solutions by many methods in the 1992 ASME problem comparison, Hsu and Farmer (1995) took one of the three-dimensional problems from the problem set, and reduced it to a gray linearly anisotropically scattering medium problem with

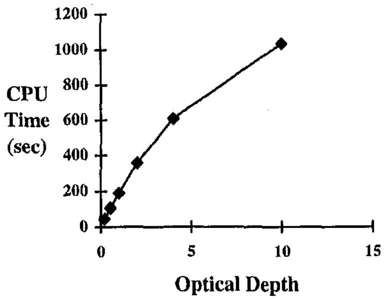

Fig. 4 Relation between optical depth and CPU time for a gray medium with parabolic temperature distribution between infinite parallel black plates (Farmer and Howell, 1994c)

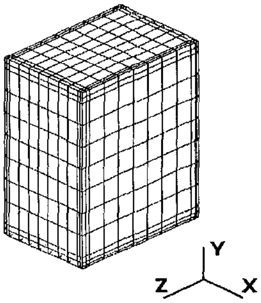

Fig. 5 Grid system for hybrid diffusion-Monte Carlo solution (Farmer and Howell, 1994c)

spatially varying properties. In this way, all aspects of the problem except the spectral effects could be examined and compared. They used a Monte Carlo and a modified discrete ordinates (YIX) method with an S-16 quadrature set to solve the problem, and compared results for eight different cases of property variation across a cubical enclosure. The results of the two methods were in very good agreement (within one percent) except for cases where discontinuities in properties were present; in these latter cases, the well-known "ray effect" apparently introduced error (up to six percent) in the YIX results. However, the YIX method ran considerably faster than the Monte Carlo solutions. To remove the ray effects from the cases where significant disagreement occurs would require a higher-order quadrature set, which might well make the CPU times comparable. Hsu and Tan (1996) further extended the YIX method and continued to compare with Monte Carlo results for validation.

Farmer (1995) and Farmer and Howell (1998) compared various strategies for handling problems with variable properties. For example, if a volume is divided into volume elements, then it can be assumed that both temperature and radiative properties are constant within the element. If this is done, the distribution of calculated properties becomes more precise in space if more volume elements are chosen as shown by Maltby (1994), but the variance in results for each element increases unless the number of packets is increased. An alternative is to allow linear, quadratic, or higher-order variations of temperature, properties, or both within each volume element, thus allowing fewer volume elements to be used. The price is increased computational complexity in determining packet paths. Comparisons of the performance of the various strategies were given in Farmer and Howell (1998).

Hybrid Methods. Straightforward Monte Carlo tends to become quite long running when a participating medium becomes optically thick in either a spectral or geometric region, so various methods have been introduced to eliminate this disadvantage. Optical thickness can become large within spectral regions because of band and line absorption, and in spatial regions because of the generation of combustion products or other spatially varying effects. The relationship between CPU time and optical depth for a particular single processor is shown in Fig. 4 for a one-dimensional homogeneous, gray medium with specified parabolic temperature distribution between cold black walls. CPU time is that required to calculate the uncertainty in the surface radiative flux to within one percent of analytical results.

Some methods are quite accurate for optically thick media. These are generally the methods based on series expansions in terms of optical thickness, which can be accurate when only a few terms are retained. These include the diffusion and P-N methods. It follows that a hybrid technique that uses one of these methods in the optically thick portions of the spectrum or geometry, and uses the Monte Carlo method in the moderate-to-small optical thickness regions should be quite accurate and efficient. Farmer and Howell (1994b, 1994c) used this approach, defining two hybrids that combine the diffusion solution (Deissler, 1964) and Monte Carlo.

In the *coupled hybrid* method, each spectral interval is tested for the product of the shortest side of a volume element times the optical thickness. All optically thick elements are set aside for treatment by the diffusion method. The rest are analyzed by Monte Carlo. Optically thick elements that abut boundaries and thin elements are treated by Monte Carlo so that adjustments such as jump boundary conditions need not be imposed.

The *adjusted hybrid* method is a faster but more crude method. For each spectral interval, the smallest volume element dimension throughout the medium is multiplied by the smallest extinction coefficient. If this product gives a value larger than some specified optical thickness, then the entire medium is treated as optically thick, and the diffusion solution with jump boundary conditions is applied. Otherwise, the medium is treated by Monte Carlo. This allows efficient treatment of problems with spectral bands and windows.

Farmer and Howell (1994c) presented hybrid solutions for a three-dimensional 2 × 5 × 3 m enclosure containing an absorbing-emitting spectrally dependent and anisotropically scattering medium (CO_2 plus carbon particles). This is one of the problems from the 1992 specification by Tong and Skocypec (1992). The grid system used is shown in Fig. 5.

Figure 6 shows a comparison between the exact solution (generated by the pure Monte Carlo method), a solution by the discrete-ordinates-YIX method, and the two forms of the hybrid Monte Carlo-diffusion solution. Comparison of CPU time is given in Table 2. The reductions for this particular problem are significant but not startling. This is because the spectral bands cover a relatively small portion of the spectrum, so most of the problem is run using Monte Carlo, and the diffusion solution is only imposed in the optically thick portion of the bands.

Note that the variation in the precision of the results (mean standard deviation in the flux divergence throughout the volume) is reduced as more of the problem is treated by the diffu-

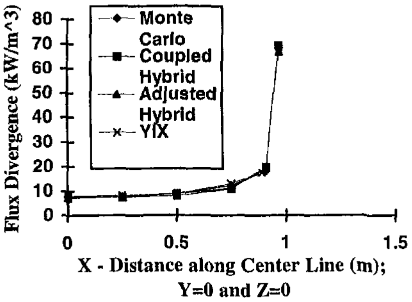

Fig. 6 Flux divergence along centerline of parallelepiped enclosure containing nongray scattering medium by four methods (Farmer and Howell, 1994c)

Table 2 Computation time for the results of Fig. 6 (Farmer and Howell, 1994c)

Precision (kW/m^3)	Solution method	CPU time (hr.)
1.64	Pure Monte Carlo	11.8
1.16	Coupled Hybrid	7.5
0.6	Adjusted Hybrid	4.7

sion solution. More details and examples of some other hybrid approaches can be found in Farmer (1995).

Spectral Dependence. The effects of spectral dependence of the absorption and scattering properties of participating media remain difficult to handle in radiative transfer analyses. Because the addition of spectral effects to a Monte Carlo code adds a few programming steps, it is not conceptually difficult to include them. Indeed, adding detailed consideration of spectral effects may add little to the run time of Monte Carlo codes, and this is a most attractive feature of the method.

For many methods of analysis (for example, the zone and READ method), exchange areas or their equivalents are dependent on optical thickness, and it may be necessary to carry out significant additional calculation to handle a spectrally dependent problem. For Monte Carlo, however, the number of sample packets needed to treat a problem that includes spectral dependence need be no larger than the number required for an equivalent gray problem. This is because the intent of most analyses is to determine total heat flux (i.e., heat flux integrated over the entire spectrum), total flux divergence, or temperature. These quantities depend on total energy; that is, the *total* number of packets that is absorbed locally. So long as a method is used that appropriately distributes the total number of packets among the spectral regions, no increase in packet number is necessary over that for a gray solution. However, in certain cases, particularly where a medium is highly emitting and has many spectral lines, many of the emitted packets may be in spectral regions with high optical thickness; in this case, run time may be greatly increased over the gray case, and the variance of the solution may be greater for an equal number of packets compared with a gray case. If the details of the spectral distribution of radiant energy are needed, then it may be necessary to increase the number of packets so that sufficiently accurate statistics are generated in each portion of the spectrum.

Howell and Perlmutter (1964) included the spectral characteristics of the absorption coefficient a_λ of high-temperature hydrogen in a calculation of radiative transfer between parallel plates. Because the hydrogen line structure was overridden by the continuum spectrum at the very high temperatures considered, line structure was neglected. In this case, a straightforward application of the relation between a random number and the wavelength was obtained by numerical integration of Eq. (4) applied to this case, which takes the form

$$R = \frac{\int_{\lambda^*=0}^{\lambda} a_\lambda(\lambda^*) e_{\lambda b}(\lambda^*, T) d\lambda}{\sigma T^4} . \qquad (8)$$

The objective was to choose R and determine the corresponding value of the wavelength, λ. To do this, Eq. (8) was integrated from zero to various values of the upper limit λ, and the resulting R versus λ relation was curve-fit in the form

$$\lambda = AR + BR^2 + CR^3 + \ldots . \qquad (9)$$

In this particular case, a different curve-fit must be obtained for various temperatures which the medium may attain. Because the absorption coefficient was highly temperature-dependent for the temperature range considered in this paper, and the temperature distribution was unknown and to be determined, this problem was iterative and the properties varied across the medium. Thus, the path length calculation for energy packets was done piecewise across each medium volume element.

Haji-Sheikh and Sparrow (1969) and Modest (1993) have presented algorithms for determining the wavelength of emission from a blackbody as a function of a random number. Hadji-Sheik's method is a straightforward set of curve fits of the form of Eq. (9), while Modest uses a more efficient technique based on a cubic spline.

Campbell (1967) treated a frequency-dependent absorption coefficient. Again, line structure was omitted. Comparisons between the complete frequency-dependent Monte Carlo solution and solutions based on Planck mean and Rosseland mean absorption coefficients showed large differences.

A wide-band spectral model was used by Farmer and Howell (1992, 1994a, 1994b, 1994c) and Yuen et al. (1992) because it was specified for the Tong and Skocypec (1992) comparison problems. In these problems, the temperature distribution was specified.

A much more complex case is encountered when the detailed line structure that forms absorption bands must be considered. A number of researchers (Modest, 1992; Taniguchi et al., 1992; Kudo et al., 1993a; Liu and Tiwari, 1994; Cherkaoui et al., 1996; Surzhikov and Howell, 1998) have applied Monte Carlo using narrow-band models of line structure.

Modest (1992) used a narrow-band approach, and verified the method by comparing with exact solutions for isothermal slab emission and transfer between parallel plates. He carefully points out the difference in mean packet path lengths that occur for emission from boundaries and emission from the medium. Packets emitted from surfaces have a high probability of having a wavelength that lies in a spectral window, with correspondingly long path length. Emission from the gas, however, will have a high probability of emission near a spectral line center, and thus will have an associated wavelength that will place it in a highly absorbing region of the spectrum with correspondingly short path length. This correlation of gas emission wavelength with wavelengths where the medium has high absorption causes radiative transfer to have characteristics that are difficult to handle in many analytical techniques.

Taniguchi et al. (1992a) used the Elsasser narrow band model with Edwards' wide-band parameters for CO_2 and water vapor in nitrogen, and predicted the energy exchange between parallel plates through the gas mixture. Variations in gas properties across the layer were considered, although the gas was divided into only five volume elements. They compared with various equivalent gray-gas models using spectrally averaged gas properties.

Kudo et al. (1993a) extended the Taniguchi work by noting that the first event in a Markov chain can be chosen deterministically as long as succeeding events are chosen randomly. By choosing the first event as the determination of spectral variable (wavelength or wave number), the tedious stochastic choice procedure can be replaced by a sequential choice across the spectrum. Savings of a factor of nine were observed in computational time.

Liu and Tiwari (1994) used a narrow band model with an exponential-tailed inverse intensity distribution to simulate gas spectral properties. They showed that the effect of considering the correlation of spectral lines can be quite large, and if it is ignored the radiative transfer can be greatly overestimated. They indicated that Monte Carlo is one of the few techniques that allow easy inclusion of correlation effects.

A narrow-band approach coupled with an exchange factor calculation by Monte Carlo evaluation was invoked by Cherkaoui et al. (1996). Using this method, reciprocity of exchange factors was assumed, and some of the statistical fluctuations in the Monte Carlo results were avoided.

A reduction in Monte Carlo computational time was the objective of the work by Surzhikov and Howell (1998). They observed that CPU time is greatly affected by the presence of extremely large absorption coefficient near line centers (and therefore very short path lengths and long CPU times for correlated-line problems). They examined various averaging techniques for handling line absorption using narrow-band approaches. The methods were found to be accurate and effective for small-to-moderate optical thickness (less than order 1), but became quite inaccurate at larger optical thickness in comparison with exact line-by-line calculations.

Parallel Processing. Monte Carlo is particularly suited to parallel computation. Each sample packet can be treated individually, so that individual bundle histories can be handled on a single processor. The more processors that are available, the more packets can be handled simultaneously.

The usual measures of the efficacy of parallel computing for a particular application are the *speedup,* defined by

$$\text{speedup} = \frac{\text{CPUtime}_{\text{serial}}}{\text{CPUtime}_{\text{parallel}}} \tag{10}$$

and the *efficiency,* defined as

$$\text{efficiency} = \frac{\text{speedup}}{\text{number of processors}} . \tag{11}$$

Because there is little or no required communication among processors during history generation, there is little overhead in using multiple processors, and the speedup in Monte Carlo calculation in radiative transfer should be very nearly inversely proportional to the number of processors (i.e., the efficiency should approach 1.0). This potential advantage of the method has been recognized by many researchers.

Burns and Pryor (1989) showed the effects of vectorizing a Monte Carlo code for surface-surface interaction, and discuss the probable advantages of parallel computation. Taniguchi et al. (1992b) presented results for a nongray medium in a simple geometry using a particular 64 processor computer, and showed that computational time was essentially inversely proportional to the number of processors used. Using a farming algorithm in which tasks are assigned to individual processors by a central processor as needed, they showed the fraction of total computation time taken for following packet histories, communication, and idle time. By far the greatest fraction was for packet histories, so that communication overhead and idle time were small and speedup was indeed nearly proportional to the number of processors. For 64 processors, efficiency was 98.4 percent.

Al-Bahadili and Wood (1993) presented a quite good comparison of the speedup and efficiency provided by various types of computer architecture. They solved three rather complete radiative transfer problems on a variety of serial computers and two parallel computers with differing characteristics. They indicated that speedup is nearly ideal with up to 16 processors with efficiency of over 90 percent. They discussed a method of distributing random numbers among the processors, and showed some techniques for rapid random number generation. They compared the accuracy of results from the Monte Carlo calculation with solutions from a finite element and S-8 solution, but unfortunately did not compare the CPU times among the various solution techniques.

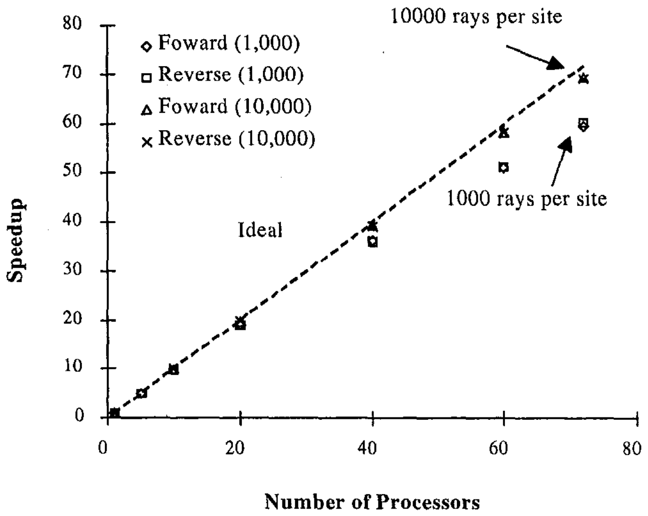

Fig. 7 Speedup versus number of parallel processors for isothermal optically thick medium (optical thickness = 10) between cold black surfaces (Farmer, 1995)

Farmer (1995) and Farmer and Howell (1998) examined the various parallel architectures for computers, and their relative advantages for Monte Carlo calculations. They discussed the advantages of various programming strategies, including domain decomposition, farming, and pipelining. Most attention was paid to domain decomposition, where portions of the problem are given to each processor. Various modes of domain decomposition were considered; decomposition by portions of the total number of packets; decomposition of the spectrum; decomposition of the geometry; and decomposition by number of trials to be run. The potential for a hybrid method using two or more forms of decomposition was discussed. It was concluded that domain decomposition by fraction of packets was simplest, and also has historically shown near-ideal speedup. An isothermal gray slab between black boundaries was used as a test case. They pointed out that using the performance measure $\gamma^2 t$ and then running cases to the same variance level on sequential and parallel machines, the speedup can be defined as

$$\text{speedup} = \frac{\gamma^2 \times \text{CPUtime}_{\text{serial}}}{\gamma^2 \times \text{CPUtime}_{\text{parallel}}} = \frac{\text{CPUtime}_{\text{serial}}}{\text{CPUtime}_{\text{parallel}}} \tag{12}$$

which is the same definition as Eq. (10). Thus, the speedup and the ratio of serial to parallel performance are the same. The optical thickness was varied, and the speedup (performance ratio) was measured for various numbers of parallel processors up to 72. The speedup for an optical thickness of 10 is shown in Fig. 7.

The speedup was seen to be quite close to the ideal. When a larger number of packets was used, the speedup was even closer to ideal (efficiency over 90 percent for any number of processors up to 72). This happened because the time spent in initialization, communication, final data output, and other front and back-end tasks became a small portion of the total CPU time. Speedup and efficiency dropped off with decreasing optical thickness; this effect was ascribed to the load imbalance that occurred because a processor may rapidly complete the assigned packet histories and become idle. This effect was especially severe for regions near an absorbing boundary, because many packets leaving such regions could reach the boundary immediately and end their histories. Regions far from a boundary have fewer packets with such curtailed histories. For an optically thick case, there is less unbalance because each packet will on average have paths that end in one mean free path before reaching a boundary. Each processor will then on average spend about the same time to complete its packet histories. The use of a farming algorithm could reduce this unbalance problem for optically thin cases.

It is clear that parallel algorithms will greatly benefit Monte Carlo calculations of radiative transfer. Further research in this area may give definitive answers to the questions of best strategy for implementation, but the use of parallel computation is clearly indicated.

Conclusions

It is clear that a large volume of literature has appeared over the last 30 years on the fundamentals and applications of the

Monte Carlo method. This is strong evidence of both the continuing development of the method and its immediate usefulness. Despite the tongue-in-cheek description of the method as one in which random numbers are put in and random answers come out, the method clearly fulfills some definite needs.

Monte Carlo can be used to solve tedious and difficult problems in radiative transfer. This can be done by the analyst without a large investment in learning methods that are heavily steeped in mathematics. Monte Carlo has therefore been applied to many practical applications where a heat transfer analyst requires an accurate answer quickly, but the time to learn more arcane methods can't be invested. Because the method is known to produce accurate results if enough sample packets are used, Monte Carlo is often used to validate the results of other methods.

Probably the single most difficult problem in using the method is the inherent tradeoff between statistical accuracy (variance) and computational grid size. If radiative flux divergence is to be calculated for use in the energy equation, then the grid necessary for resolving the energy equation probably governs the problem. However, in many problems involving convection, this grid size must be quite fine, and it may not be suitable for a Monte Carlo flux divergence calculation. This incompatibility is not insurmountable. Radiative flux divergence often varies slowly over a region where convective effects are varying rapidly. In that case, a courser radiation grid can be used for radiative calculations, and the results can be overlaid on the convective grid.

A related problem is the potential statistical variation from volume element to element. This could potentially induce convergence problems in a finite difference or finite element solution of the energy equation. Variance reduction methods can ameliorate this problem.

The author of this review is an advocate of the Monte Carlo method, and the following should be considered in that light: Computer speed is increasing rapidly. Monte Carlo has proven to adapt nearly ideally to massively parallel computation, while other methods generally have much lower speedup and efficiency. The cost of CPU time will soon be negligible compared with the cost of programming time. That may already be the case. If and when it is the case, it will make little sense to apply approximate numerical methods simply to save computer time; and indeed, these methods may not have a computer time advantage over Monte Carlo on massively parallel machines.

Because it allows the accurate treatment of spectral properties, inhomogeneous media, anisotropic scattering, complex geometries, and indeed all of the important effects in radiative transfer, the Monte Carlo method stands an excellent chance of emerging as the dominant choice for treating radiative heat transfer.

References

Abbasi, M. H., and Evans, J. W., 1982, "Monte Carlo Simulation of Radiant Transport Through an Adiabatic Packed Bed or Porous Solid," *AIChE J.*, Vol. 28, No. 5, pp. 853–854.

Al Abed, A., and Sacadura, J.-K., 1983, "A Monte Carlo-Finite Difference Method for Coupled Radiation-Conduction Heat Transfer in Semitransparent Media," ASME Journal of Heat Transfer, Vol. 105, pp. 931–933.

Al-Bahadili, H., and Wood, J., 1993, "Calculation of Radiative Heat Transfer Through a Grey Gas on Parallel Computer Architecture," *Parallel Computation*, A. E. Fincham and B. Ford, eds., Clarendon Press, Oxford, pp. 135–157.

Almazan, P., 1994, "Accuracy Control in Monte Carlo Radiative Calculations," *Proc. 5th Annual Thermal and Fluids Analysis Workshop*, NASA Lewis Research Center, pp. 47–62.

Ambirajan, A., and Look, D. C., Jr., 1996, "A Backward Monte Carlo Estimator for the Multiple Scattering of a Narrow Light Beam," *J. Quant. Spectrosc. Radiat. Transfer*, Vol. 56, No. 3, pp. 317–336.

Antoniak, Z. I., Palmer, B. J., Drost, M. K., and Welty, J. R., 1996, "Parametric Study of Radiative Heat Transfer in Arrays of Fixed Discrete Surfaces," ASME Journal of Heat Transfer, Vol. 118, pp. 228–230.

Argento, C., and Bouvard, D., 1996, "A Ray Tracing Method for Evaluating the Radiative Heat Transfer in Porous Media," *Int. J. Heat Mass Transfer*, Vol. 39, No. 15, pp. 3175–3180.

Billings, Ronald J., Barnes, J. Wesley, Howell, John R., and Singh, Sanjay K., 1989, "Using Markov Chains to Analyze Thermal Radiation Heat Transfer in Participating Media," *Proc. ORSA/TIMS Conference*, Vancouver.

Billings, Ronald L., Barnes, J. Wesley, and Howell, John R., 1991a, "Markov Analysis of Radiative Transfer in Enclosures with Bidirectional Reflections," *Num. Heat Transfer*, Part A, Vol. 19, No. 3, pp. 101–114.

Billings, Ronald L., Barnes, J. Wesley, Howell, John R., and Slotboom, O. Erik, 1991b, "Markov Analysis of Radiative Heat Transfer in Specular Enclosures," ASME Journal of Heat Transfer, Vol. 113, pp. 429–436.

Blechschmidt, D., 1974, "Monte Carlo Study of Light Transmission Through a Cylindrical Tube," *J. Vac. Sci. Technol.*, Vol. 11, No. 3, pp. 570–574.

Brewster, M. Quinn, 1992, *Thermal Radiative Transfer and Properties*, John Wiley and Sons, New York.

Burns, P. J., and Pryor, D. V., 1989, "Vector and Parallel Monte Carlo Radiative Heat Transfer Simulation," *Num. Heat Transfer*, Part B, Vol. 16, pp. 97–124.

Bushinskii, A. V., 1976, "Determination of the Geometric-Optics Coefficients of Thermal Radiation by the Monte Carlo Method," *Inzhenerno-Fizicheskii Zh.*, Vol. 30, No. 1, pp. 160–166.

Campbell, Philip M., 1967, "Monte Carlo Method for Radiative Transfer," *Int. J. Heat Mass Transfer*, Vol. 10, No. 4, pp. 519–527.

Chen, J. C., and Churchill, S. W., 1963, "Radiant Heat Transfer in Packed Beds," *AIChE J.*, Vol. 9, No. 1, pp. 35–41.

Cherkaoui, M., Dufresne, J.-L., Fournier, R., Grandpiex, J.-Y., and Lahellec, A., 1996, "Monte Carlo Simulation of Radiation in Gases with a Narrow-Band Model and a Net-Exchange Formulation," ASME Journal of Heat Transfer, Vol. 118, pp. 401–407.

Corlett, R. C., 1966, "Direct Monte Carlo Calculation of Radiative Heat Transfer in Vacuum," ASME Journal of Heat Transfer, Vol. 88, pp. 376–382.

Deissler, R. G., 1964 "Diffusion Approximation for Thermal Radiation in Gases with Jump Boundary Condition," ASME Journal of Heat Transfer, Vol. 86, No. 2., pp. 240–246.

Duic, N., Bogdan, Z., Schneider, D. R., Šerman, N., and Afgan, N., 1996, "Tube Leakage Effect on Radiative Heat Flux in Boiler," *Radiative Transfer I—Proc. First Int. Symp. Radiation Transfer*, M. Pinar Mengüç, ed., Begell House, New York, pp. 610–619.

Dunn, W. L., 1983, "Inverse Monte Carlo Solutions for Radiative Transfer in Inhomogeneous Media," *J. Quant. Spectrosc. Radiat. Transfer*, Vol. 29, No. 1, pp. 19–26.

Edwards, D. K., and Tobin, R. D., 1967, "Effect of Polarization on Radiant Heat Transfer through Long Passages," ASME Journal of Heat Transfer, Vol. 89, No. 1, pp. 132–138.

Edwards, D. K., 1985, "Hybrid Monte-Carlo Matrix-Inversion Formulation of Radiation Heat Transfer with Volume Scattering," *Proc. 23rd Natl. Heat Trans. Conf., Denver*, pp. 273–278.

Egan, W., and Hilgeman, T., 1978, "Spectral Reflectance of Particulate Materials: A Monte Carlo Model Including Asperity Scattering," *Appl. Optics*, Vol. 17, No. 2, Jan. 15, pp. 245–252.

Esposito, L. W., and House, L. L., 1978, "Radiative Transfer Calculated from a Markov Chain Formalism," *Astrophs. J.*, Vol. 219, Feb. 1, pp. 1058–1067.

Farag, I. H., Hemming, M. K., and Reicker, E., 1986, "Effects of Radiative Scattering on a Monte-Carlo Semi-Infinite Furnace Slab," *Heat and Technology*, Vol. 4, No. 1, pp. 33–46.

Farmer, J. T., and Howell, J. R., 1992, "Monte Carlo Solution of Radiative Heat Transfer in a Three-Dimensional Enclosure with an Anisotropically Scattering, Spectrally Dependent, Inhomogeneous Medium," *Developments in Radiative Heat Transfer*, S. T. Thynell et al., eds., ASME, New York, pp. 301–309.

Farmer, J. T., and Howell, J. R., 1994a, "Monte Carlo Prediction of Radiative Heat Transfer in Inhomogeneous, Anisotropic, Non-gray Media," *J. Thermophys. Heat Trans.*, Vol. 8, No. 1, pp. 133–139.

Farmer, J. T., and Howell, J. R., 1994b, "Hybrid Monte Carlo/Diffusion Method for Enhanced Solution of Radiative Transfer in Optically Thick Non-Gray Media," *Radiative Transfer: Current Research*, Y. Bayazitoglu et al., eds., ASME, New York, pp. 203–212.

Farmer, J. T., and Howell, J. R., 1994c, "Monte Carlo Algorithms for Predicting Radiative Heat Transport in Optically Thick Participating Media," *Proc. 10th International Heat Transfer Conference*, Vol. 2, Brighton, Aug., pp. 37–42.

Farmer, Jeffery T., 1995, "Improved Algorithms for Monte Carlo Analysis of Radiative Heat Transfer in Complex Participating Medium," Ph.D. dissertation, Department of Mechanical Engineering, The University of Texas at Austin, Austin, TX.

Farmer, Jeffery T., and Howell, John R., 1998 "Monte Carlo Strategies for Radiative Transfer in Participating Media," *Advances in Heat Transfer*, Vol. 31, J. P. Hartnett and T. Irvine, eds., Academic Press, San Diego, pp. 1–97.

Fleck, J. A., 1961, "The Calculation of Nonlinear Radiation Transport by a Monte Carlo Method: Statistical Physics," *Methods in Computational Physics*, Vol. 1, pp. 43–65.

França, Francis, Morales, Juan C., Oguma, Masahito, and Howell, John R., 1997, "Inverse Design of Engineering Systems Dominated by Radiative Transfer," *Radiative Transfer II: Proc. Second Int. Symp. on Radiative Heat Trans.*, M. Pinar Menguç, ed., Begell House, New York.

França, Francis, Morales, Juan C., Oguma, Masahito, and Howell, John R., 1998, "Inverse Design of Thermal Systems with Participating Radiating Media," *Proc. 13th Int. Heat Trans. Conf.*, Vol. 1, KyongJu, Korea, Aug.

Galanova, Z. S., and Shamshina, G. A., 1981, "Calculation of Thermal Radiation from Jets by the Monte-Carlo Method," *Fluid Mechanics–Soviet Research*, Vol. 10, No. 2, pp. 33–38 (originally published 1981 in *Gazodinamika i Teploobmen,* No. 6, pp. 184–190.)

Gupta, R. P., Wall, T. F., and Truelove, J. S., 1983, ''Radiative Scatter by Fly Ash in Pulverized-Coal-Fired Furnaces: Application of the Monte Carlo Method to Anisotropic Scatter,'' *Int. J. Heat Mass Transfer,* Vol. 26, No. 11, pp. 1649–1660.

Haji-Sheikh, A., and Sparrow, E. M., 1969, ''Probability Distributions and Error Estimates for Monte Carlo Solutions of Radiation Problems,'' *Progress in Heat and Mass Transfer,* Vol. 2, Thomas F. Irvine, Warren E. Ibele, James P. Hartnett, and Richard J. Goldstein, eds., Pergamon, Oxford, pp. 1–12.

Haji-Sheikh, A., 1988, ''Monte Carlo Methods,'' *Handbook of Numerical Heat Transfer,* Wiley Interscience, New York, pp. 673–722.

Hayes, Brian, 1993, ''The Wheel of Fortune,'' *Am. Scientist,* Vol. 81, May–June, pp. 114–118.

Henson, J. C., Malasekekera, W. M. G., and Dent, J. C., 1996, ''Comparison of the Discrete Transfer and Monte Carlo Methods for Radiative Heat Transfer in Three-Dimensional, Nonhomogeneous Participating Media,'' *Solution Methods for Radiative Transfer in Participating Media,* R. D. Skocypek, S. T. Thynell, D. A. Kaminski, A. M. Smith, and T. Tong, eds., ASME, New York.

House, L. L., and Avery, L. W., 1969, ''The Monte Carlo Technique Applied to Radiative Transfer,'' *J. Quant. Spectrosc. Radiat. Transfer,* Vol. 9, pp. 1579–1591.

Howell, John R., and Perlmutter, Morris, 1964a, ''Monte Carlo Solution of Thermal Transfer Through Radiant Media Between Gray Walls,'' ASME JOURNAL OF HEAT TRANSFER, Vol. 86, pp. 116–122.

Howell, John R., and Perlmutter, Morris, 1964b, ''Monte Carlo Solution of Radiant Heat Transfer in Nongrey Nonisothermal Gas with Temperature Dependent Properties,'' *AICHE J.,* Vol. 10, No. 4, pp. 562–567.

Howell, John R., Strite, Mary K., and Renkel, Harold, 1964c, ''Analysis of Heat Transfer Effects in Rocket Nozzles Operating with Very High-Temperature Hydrogen,'' NASA Technical Report TR-220, Feb.

Howell, John R., and Renkel, Harold E., 1965, ''Analysis of the Effect of a Seeded Propellant Layer on Thermal Radiation in the Nozzle of a Gaseous-Core Nuclear Propulsion System,'' NASA Technical Note TN D-3119, Dec.

Howell, John R., and Strite, Mary K., 1966, ''Heat Transfer in Rocket Nozzles Using High-Temperature Hydrogen Propellant with Real Property Variations,'' *J. Spacecraft and Rockets,* Vol. 3, No. 7, pp. 1063–1068.

Howell, John R., 1968, ''Application of Monte Carlo to Heat Transfer Problems,'' *Advances in Heat Transfer,* Vol. 5, J. P. Harnett and T. Irvine, eds., Academic Press, San Diego, pp. 1–54.

Howell, John R., and Durkee, R. E., 1971, ''Radiative Transfer Between Surfaces in a Cavity with Collimated Incident Radiation: A Comparison of Analysis and Experiment,'' ASME JOURNAL OF HEAT TRANSFER, Vol. 93, pp. 129–135.

Howell, John R., 1973, ''The Treatment of Data Uncertainties in Thermal Analysis,'' *J. Spacecraft and Rockets,* Vol. 10, No. 6, pp. 411–414.

Howell, John R., and Bannerot, R. B., 1976, ''Trapezoidal Grooves as Moderately Concentrating Solar Energy Collectors,'' *Radiative Transfer and Thermal Control,* (AIAA Progress in Aeronautics and Astronautics Series, Vol. 49), A. E. Smith, ed., pp. 277–289.

Howell, John R., 1998, *A Catalog of Radiation Configuration Factors,* 2nd Ed., electronic version, available at http://www.me.utexas.edu/howe.

Howell, John R., and Mengüç, M. Pinar, 1998, ''Radiation,'' *Handbook of Heat Transfer Fundamentals,* J. P. Hartnett and T. J. Irvine, eds., McGraw-Hill, New York, Chapter 7, in press.

Hsu, P-f., and Farmer, J. T., 1995, ''Benchmark Solutions of Radiative Heat Transfer within Nonhomogeneous Participating Media using the Monte Carlo and YIX Methods,'' *Proc. 1995 Natl. Heat Transfer Conf.,* Vol. 13, Y. Bayazitoglu, D. Kaminski, and P. D. Jones, eds., ASME, New York, pp. 29–36.

Hsu, P.-f., and Tan, Y., 1996, ''Recent Benchmarkings of Radiative Transfer within Nonhomogeneous Participating Media and the Improved YIX Method,'' *Radiative Transfer I—Proc. First Int. Symp. Radiation Transfer,* M. Pinar Mengüç, ed., Begell House, New York, pp. 107–126.

Jodrey, W. S., and Tory, E. M., 1979, ''Simulation of Random Packing of Spheres,'' *Simulation,* Jan., pp. 1–12.

Kalos, M. H., and Whitlock, P. A., 1986, *Monte Carlo Methods. Volume 1: Basics,* John Wiley and Sons, New York.

Kaminski, Deborah A., 1989, ''Radiative Transfer From a Gray, Absorbing-Emitting, Isothermal Medium in a Conical Enclosure,'' ASME *Journal of Solar Energy Engineering,* Vol. 111, pp. 324–329.

Kaviany, Massoud, and Singh, B. P., 1993, ''Radiative Heat Transfer in Porous Media,'' *Advances in Heat Transfer,* Vol. 23, Hartnett, J. P. and Irvine, T., eds., Academic Press, San Diego, pp. 133–186.

Kobiyama, M., 1989, ''Reduction of Computing Time and Improvement of Convergence Stability of the Monte Carlo Method Applied to Radiative Heat Transfer with Variable Properties,'' ASME JOURNAL OF HEAT TRANSFER, Vol. 111, pp. 135–140.

Kudo, K., Taniguchi, H., Kaneda, H., Yang, W. J., Zhang, Y. Z., Guo, K.-H., and Matsumura, M., 1990, ''Flow and Heat Transfer Simulation in Circulating Fluidized Beds,'' *Circulating Fluidized Bed Technology III: Proc. Third Int. Conf. on Circulating Fluidized Beds,* P. Basu, M. Horio, and M. Hasatani, eds., Nagoya, Oct., Pergamon Press, Oxford, pp. 269–274.

Kudo, K., Taniguchi, H., Kuroda, A., Sasaki, T., and Yamamoto, T., 1991a, ''Development of General Purpose Computer Code for Two/Three Dimensional Radiation Heat Transfer Analysis,'' *Proc. Seventh Int. Conf. on Numerical Meths. in Thermal Problems,* R. L. Lewis, J. H. Chin, and G. M. Homsy, eds., Vol. VII, Pt. 1, Pineridge Press, Swansea, pp. 698–708.

Kudo, K., Taniguchi, Hiroshi, Kim, Yong-Mo, and Yang, Wen-Jei, 1991b, ''Transmittance of Radiative Energy through Three-Dimensional Packed Spheres,'' *Proc. 1991 ASME/JSME Thermal Engineering Joint Conf.,* J. Lloyd and Y. Kurosoki, eds., ASME, New York, pp. 35–42.

Kudo, K., Taniguchi, H., Kuroda, A., Oath M., and Dakota, H., 1993a, ''Improvement of Analytical Method on Radiative Heat Transfer in Nongray Media by Monte Carlo Method,'' *Heat Transfer—Japanese Research,* Vol. 22, pp. 559–572.

Kudo, K., Taniguchi, H., Kuroda, A., Sumarsono, M., and Fukuchi, T., 1993b, ''Analysis of Radiative Characteristics of Heat-Generating Particles Dispersed in Non-Gray Combustion-Gas Slab,'' *Proc. JSME-ASME Intl. Conf. On Power Engineering: ICOPE-93,* JSME, Tokyo.

Kudo, K., Li, B., and Kuroda, A., 1995, ''Analysis on Radiative Energy Transfer through Fibrous Layer Considering Fibrous Orientation,'' *Proc. 1995 Natl. Heat Transfer Conf.,* ASME, New York. pp. 37–43.

Kudo, K., Taniguchi, H., Kuroda, A., Otaka, M., Ushijima, T., and Obata, M., 1995, ''Analysis on Radiative Characteristics of High-Temperature Nongray-Gas Jet,'' *Proc. 1995 ASME/JSME Thermal Engineering Joint Conference,* Vol. 3, L. S. Fletcher and T. Aihara, eds., ASME, New York, pp. 273–278.

Larsen, Marvin E., and Howell, John R., 1986, ''Least-Squares Smoothing of Direct Exchange Factors in Zonal Analysis,'' ASME JOURNAL OF HEAT TRANSFER, Vol. 108, pp. 239–242.

Lewis, E. E., and Miller, W. F., Jr., 1984, *Computational Methods of Neutron Transport,* John Wiley and Sons, New York.

Li, B., Kudo, K., and Kuroda, A., 1996, ''Study on Radiative Heat Transfer through Fibrous Layer,'' *Proc. Third KSME-JSME Thermal Eng. Conf.,* Vol. III, KyongJu, Korea, Oct., pp. 279–284.

Liu, J., and Tiwari, S. N., 1994, ''Investigation of Radiative Transfer in Nongray Gases Using a Narrow Band Model and Monte Carlo Simulation,'' ASME JOURNAL OF HEAT TRANSFER, Vol. 116, pp. 160–166.

Lockwood, F. C., and Shah, N. G., 1981, ''A New Radiation Solution Method for Incorporation in General Combustion Prediction Procedures,'' *Eighteenth Symposium (International) on Combustion,* The Combustion Inst., Pittsburgh, PA, pp. 1405–1414.

Malalasekera, W. M. G., and James, E. H., 1995, ''Calculation of Radiative Heat Transfer in Three-Dimensional Complex Geometries,'' *Proc. 1995 Natl. Heat Transfer Conf.,* Vol. 13, Y. Bayazitoglu, D. Kaminski, and P. D. Jones, eds., ASME, New York, pp. 53–61.

Maltby, J. D., and Burns, P. J., 1991, ''Performance, Accuracy, and Convergence in a Three-Dimensional Monte Carlo Radiative Heat Transfer Simulation,'' *Numer. Heat Transfer,* Part B, Vol. 19, pp. 191–209.

Maltby, J. D., 1994, ''Evaluation of Property-Induced Uncertainty in a Monte Carlo Simulation of Radiative Heat Transfer in a Participating Medium,'' *Radiative Heat Transfer: Current Research,* Y. Bayazitoglu et al., eds. pp. 161–170.

Martin, W. R., and Pomraning, G. C., 1990, ''Monte Carlo Analysis of the Backscattering of Radiation from a Sphere to a Plane,'' *J. Quant. Spectrosc. Radiat. Transfer,* Vol. 43, No. 2, pp. 115–126.

McHugh, J., Burns, P. J., Hittle, D., and Miller, B., 1992, ''Daylighting Design via Monte Carlo,'' *Developments in Radiative Heat Transfer,* S. T. Thynell et al., eds. ASME, New York, pp. 129–136.

Metropolis, Nicholas, and Ulam, S., 1949, ''The Monte Carlo Method,'' *J. Am. Statistical Assoc.,* Vol. 44, No. 247, pp. 335–341.

Mishkin, M., and Kowalski, G. J., 1983, ''Application of Monte Carlo Techniques to the Steady-State Radiative and Conductive Heat Transfer Problem Through a Participating Medium,'' ASME Paper 83-WA/HT-27.

Mochida, A., Kudo, K., Mizutani, Y., Hattori, M., and Nakamura, Y., 1995, ''Transient Heat Transfer Analysis in Vacuum Furnace by Radiant Tube Burners,'' *Proc. RAN 95: Int. Symp. on Adv. Energy Conversion Systems,* Soc. Chemical Engineers—Japan, Nagoya, Dec.

Modest, M. F., 1978, ''Three-Dimensional Radiative Exchange Factors for Nongray, Nondiffuse Surfaces,'' *Num. Heat Transfer,* Vol. 1, pp. 403–416.

Modest, M. F., 1992, ''The Monte Carlo Method Applied to Gases with Spectral Line Structure,'' *Num. Heat Transfer,* Part B, Vol. 22, pp. 273–284.

Modest, M. F., 1993, *Radiative Heat Transfer,* McGraw-Hill, New York.

Montagnino, L., 1968, ''Ray Tracing in Inhomogeneous Media,'' *J. Opt. Soc. Am.,* Vol. 59, pp. 1667–1668.

Maruyama, S., and Aihara, T., 1996, ''Radiative Heat Transfer of Arbitrary 3-D Participating Media and Surfaces with Non-Participating Media by a Generalized Numerical Method REM^2,'' *Radiative Transfer I—Proc. First Int. Symp. Radiation Transfer,* M. Pinar Mengüç, ed., Begell House, New York, pp. 153–167.

Naraghi, M. H. N., and Chung, B. T. F., 1984, ''A Stochastic Approach for Radiative Exchange in Enclosures with Nonparticipating Medium,'' ASME JOURNAL OF HEAT TRANSFER, Vol. 106, pp. 690–698.

Naraghi, M. H. N., and Chung, B. T. F., 1985, ''A Unified Matrix Formulation for the Zone Method: A Stochastic Approach,'' *Int. J. Heat Mass Transfer,* Vol. 28, No. 1, pp. 245–251.

Naraghi, M. H. N., and Chung, B. T. F., 1986, ''A Stochastic Approach for Radiative Exchange in Enclosures with Directional-Bidirectional Properties,'' ASME JOURNAL OF HEAT TRANSFER, Vol. 108, pp. 264–270.

Oguma, Masahito, and Howell, John R., 1995, ''Solution of Two-Dimensional Blackbody Inverse Radiation by an Inverse Monte Carlo Method,'' *Proc. 4th ASME/JSME Joint Symposium,* Maui, Mar.

Oguma, Masahito, Mizuno, Masayuki, and Howell, John R., 1998, ''Solutions of Variable Geometry Inverse Radiation Problems by An Inverse Monte Carlo Method (Variable Geometry Problems for Flat-Plates Enclosures),'' *Proceedings of the 1998 Int. Heat Trans. Conf.,* Seoul, Aug.

Omori, T., Taniguchi, H., and Kudo, K., 1990, "Monte Carlo Simulation of Indoor Radiant Environment," *Int. J. Num. Meths. In Engineering,* Vol. 30, No. 4, pp. 615–627.

Omori, T., Nagata, T., Taniguchi, H., and Kudo, K., 1991, "Three-Dimensional Heat Transfer Analysis of a Steel Heating Furnace," *Proc. Seventh Int. Conf. on Numerical Meths. in Thermal Problems,* R. L. Lewis, J. H. Chin, and G. M. Homsy, eds., Vol. VII, Pt. 2, Pineridge Press, Swansea, pp. 1346–1356.

Palmer, Bruce J., Drost, M. Kevin, and Welty, James R., 1996, "Monte Carlo Simulation of Radiative Heat Transfer in Arrays of Fixed Discrete Surfaces Using Cell-to-Cell Photon Transport," *Int. J. Heat Mass Transfer,* Vol. 39, No. 13, pp. 2811–2819.

Parthasarathy, G., Patankar, S. V., Chai, J. C., and Lee, H. S., 1994, "Monte Carlo Solutions for Radiative Heat Transfer in Irregular Two-Dimensional Geometries," *Radiative Heat Transfer: Current Research,* Y. Bayazitoglu et al., eds. ASME, New York, pp. 191–201.

Perlmutter, Morris, and Howell, John R., 1964, "Radiant Transfer Through a Gray Gas Between Concentric Cylinders Using Monte Carlo," ASME JOURNAL OF HEAT TRANSFER, Vol. 86, pp. 169–179.

Polgar, L. G., and Howell, John R., 1966a, "Directional Thermal-Radiative Properties of Conical Cavities," *Progress in Astronautics and Aeronautics,* Vol. 18, Academic Press, San Diego, pp. 311–323.

Polgar, L. G., and Howell, John R., 1966b, "Directional Thermal-Radiative Properties of Conical Cavities," NASA TN D-1929.

Shamsundar, N., Sparrow E. M., and Heinisch, R. P., 1973, "Monte Carlo Solutions-Effect of Energy Partitioning and Number of Rays," *Int. J. Heat Mass Transfer,* Vol. 16, No. 3, pp. 690–694.

Siegel, R., and Howell, J. R., 1992, *Thermal Radiation Heat Transfer,* 3rd Ed., Taylor and Francis, Washington, DC.

Singh, B. P., and Kaviany, M., 1991, "Independent Theory versus Direct Simulation of Radiative Heat Transfer in Packed Beds," *Int. J. Heat Mass Transfer,* Vol. 34, No. 11, pp. 2869–2881.

Singh, B. P., and Kaviany, M., 1992, "Modeling Radiative Heat Transfer in Packed Beds," *Int. J. Heat Mass Transfer,* Vol. 35, No. 6, pp. 1397–1405.

Singh, B. P., and Kaviany, M., 1994, "Effect of Solid Conductivity on Radiative Heat Transfer in Packed Beds," *Int. J. Heat Mass Transfer,* Vol. 37, No. 16, pp. 2579–2583.

Sivathanu, Y. R., and Gore, J. P., 1993, "A Discrete Probability Function Method for the Equation of Radiative Transfer," *J. Quant. Spectrosc. Radiat. Transfer,* Vol. 49, No. 3, pp. 269–280.

Sivathanu, Y. R., and Gore, J. P., 1994, "A Discrete Probability Function Method for Radiation in Enclosures and Comparison with the Monte Carlo Method," *Radiative Heat Transfer: Current Research,* Y. Bayazitoglu et al., eds., ASME, New York, pp. 213–218.

Sivathanu, Y. R., and Gore, J. P., 1996, "Radiative Heat Transfer Inside a Cylindrical Enclosure with Nonparticipating Media Using a Deterministic Statistical Method," *Proc. ASME Heat Transfer Div.,* Vol. 1, P.D. Jones, eds., ASME, New York, pp. 145–152.

Sowell, E. F., and O'Brien, P. F., 1972, "Efficient Computation of Radiant-Interchange Factors within an Enclosure," ASME JOURNAL OF HEAT TRANSFER, Vol. 49, pp. 326–328.

Steward, F. R., and Cannon, P., 1971, "The Calculation of Radiative Heat Flux in a Cylindrical Furnace Using the Monte Carlo Method," *Int. J. Heat Mass Transfer,* Vol. 14, No. 2, pp. 245–262.

Steward, F. R., and Guruz, K. H. 1975, "Radiative Heat Transfer in Absorbing, Emitting and Scattering Media Using the Monte Carlo Method," *Trans. Canadian Soc. Mech Engng.,* Vol. 3, No. 1, pp. 10–16.

Subramaniam, S., and Mengüç, M. P., 1991, "Solution of the Inverse Radiation Problem for Inhomogeneous and Anisotropically Scattering Media Using a Monte Carlo Technique," *Int. J. Heat Mass Transfer,* Vol. 34, No. 1, pp. 253–266.

Sumarsono, M., Taniguchi, H., Kudo, K., Kuroda, A., Ohtaka, M., Li, B., 1993, "Radiation Heat Transfer Analysis on High Temperature Free Jet of Nongray Gas," *Proc. 3rd Int. Symp., Short Courses and Exhibition on Rotating Machinery,* Bandung, pp. 53–62.

Surzhikov, Sergey, and Howell, John R., 1998, "Mathematical Simulation of the Emittance of Light-Scattering Volumes with Regard to Line Structure," *AIAA J. Thermophysics Heat Trans,* Vol. 12, No. 2, pp. 278–281.

Tamura, M., Nakamura, Y., Mochida, A., and Kudo, K., 1995, "Heat Transfer Analysis in a Radiant Tube Burner," *Proc. Int. Symp. on Adv. Energy Conv. System and Related Technologies: RAN95,* Japan Soc. Chem. Engineers, pp. 1175–1180.

Taniguchi, H., 1967, "Temperature Distributions of Radiant Gas Calculated by Monte Carlo Method," *Bull. JSME,* Vol. 10, No. 42, pp. 975–988.

Taniguchi, H., 1969, "The Radiative Heat Transfer of Gas in a Three Dimensional System Calculated by Monte Carlo Method," *Bull. JSME,* Vol. 12, No. 49, pp. 67–78.

Taniguchi, H., and Funazu, M., 1970, "The Numerical Analysis of Temperature Distributions in a Three Dimensional Furnace," *Bull. JSME,* Vol. 13, No. 66, pp. 1458–1468.

Taniguchi, H., Sugiyama, K.-I., and Taniguchi, K., 1974, "The Numerical Analysis of Temperature Distribution in a Three Dimensional Furnace (2nd Report: The Comparison with Experimental Results)," *Heat Transfer-Japanese Research,* Vol. 3, No. 4, pp. 41–54 (originally published 1973, *Trans. JSME,* Vol. 39, pp. 324–347.)

Taniguchi, H., Kudo, K., Otaka, M., Sumarsono, M. and Obata, M., 1992a, "Development of a Monte Carlo Method for Numerical Analysis on Radiative Energy Transfer through Non-Grey-Gas Layer," *Int. J. Num. Meths. Engineering,* Vol. 35, pp. 883–891.

Taniguchi, H., Kudo, K., Kuroda, A., Ohtaka, M., Mochida, A., Komatsu, T., Kosaka, S., and Fujisaki, M., 1992b, "Monte Carlo Simulation of Non-Gray Radiation Heat Transfer on Highly Parallel Computer AP1000," *Proc. 3rd Int. Symp. On Heat Transfer,* Beijing, Oct.

Taniguchi, H., Kudo, K., Kuroda, A., Kaneda, H., Fukuchi, T., and Song, K. K., 1993, "Effects of Several Parameters on Heat Transfer in Circulating Fluidized Bed Boiler," *Proc. 6th Int. Symp. on Transport Phenomena in Thermal Engineering,* J. S. Lee, S. H. Chung, and K. H. Kim, eds., Vol. IV, KSME, Seoul, p. 54.

Taniguchi, H., and Mochida, A., 1994, "Radiative Heat Transfer in the Mixture of Gas and Particle with Anisotropic Scattering Effect," *Proc. Pacific Rim Conf. on Environmental Control of Combustion Processes,* pp. 13–31.

Taylor, Robert P., Luck, Rogelio, Hodge, B. K., and Steele, W. Glenn, 1995, "Uncertainty Analysis of Diffuse-Gray Radiation Enclosure Problems," *J. Thermophys. Heat Trans.,* Vol. 9, No. 1, pp. 63–69.

Tong, W. T., and Skocypec, R. D., 1992, "Summary on Comparison of Radiative Heat Transfer Solutions for a Specified Problem," *Developments in Radiative Heat Transfer,* S. T. Thynell et al., eds., ASME, New York, pp. 253–258.

Toor, J. S., and Viskanta, R., 1968, "A Numerical Experiment of Radiant Heat Interchange by the Monte Carlo Method," *Int. J. Heat Mass Transfer,* Vol. 11, No. 5, pp. 883–897.

van Leersum, J., 1989, "A Method for Determining a Consistent Set of Radiation View Factors from a Set Generated by a Nonexact Method," *Int. J. Heat Fluid Flow,* Vol. 10, No. 1, p. 83.

Vercammen, H. A. J., and Froment, G. F., 1980, "An Improved Zone Method Using Monte Carlo Techniques for the Simulation of Radiation in Industrial Furnaces," *Int. J. Heat Mass Transfer,* Vol. 23, No. 2, pp. 329–337.

Villeneuve, P. V., Chapman, D. D., and Mahan, J. R., 1994, "Use of the Monte-Carlo Ray-Trace Method as a Design Tool for Jet Engine Visibility Suppression," *Radiative Heat Transfer: Current Research,* Y. Bayazitoglu et al., eds. ASME, New York, pp. 59–71.

Vossbrecker, H., 1970, "On the Calculation of Heat Transfer by Radiation using the Monte Carlo Method," *Wärme- and Stoffübertragung,* Vol. 3, pp. 146–152 (in German).

Wu, W. J., and Mulholland, G. P., 1989, "Two-Dimensional Inverse Radiation Heat Transfer Analysis Using Monte Carlo Techniques," *Developments in Radiative Heat Transfer,* S. T. Thynell et al., eds. ASME, New York, pp. 181–190.

Walters, D. V., and Buckius, R. O., 1992, "Rigorous Development for Radiation Heat Transfer in Nonhomogeneous Absorbing, Emitting and Scattering Media," *Int. J. Heat Mass Transfer,* Vol. 35, No. 12, pp. 3323–3333.

Walters, D. V., and Buckius, R. O., 1994, "Monte Carlo Methods for Radiative Heat Transfer in Scattering Media," *Annual Review of Heat Transfer,* Chang-Lin Tien, ed., CRC Press, Boca Raton, pp. 131–176.

Weiner, M. M., Tindall, J. W., and Candell, L. M., 1965, "Radiative Interchange Factors by Monte Carlo," ASME Paper 65-WA/HT-51.

Yang, W.-J., Taniguchi, H., and Kudo, K., 1995, "Radiative Heat Transfer by the Monte Carlo Method," *Advances in Heat Transfer,* Vol. 27, J. P. Hartnett and T. F. Irvine, eds., Academic Press, San Diego, pp. 1–215.

Yang, Y. Sam, 1981, "Heat Transfer through a Randomly Packed Bed of Spheres," Ph.D. dissertation, Department of Mechanical Engineering, The University of Texas-Austin, Austin, TX.

Yang, Y. Sam, Klein, Dale E., and Howell, John R., 1983, "Radiative Heat Transfer through a Randomly Packed Bed of Spheres by the Monte Carlo Method," ASME JOURNAL OF HEAT TRANSFER, Vol. 105, pp. 325–332.

Yarbrough, David W., and Lee, Chon-Lin, 1986, "Monte Carlo Calculation of Radiation View Factors," *Integral Methods in Science and Engineering,* Fred R. Payne, C. C. Corduneanu, A. Haji-Sheikh, and T. Huang, eds., Hemisphere, Washington, DC, pp. 563–574.

Yuen, W. W., Ma, A. K., and Takara, E. E., 1992, "Evaluation of Radiative Heat Transfer using the Generalized Zonal Method and the Absorption Mean Beam Length Concept," *Developments in Radiative Heat Transfer,* S. T. Thynell et al., eds. ASME, New York, pp. 265–273.

Zaworski, J., Welty, J. R., Palmer, B. J., and Drost, M. K., 1996, "Comparison of Experiment with Monte Carlo Simulations on a Reflective Gap Using a Detailed Surface Properties Model," ASME JOURNAL OF HEAT TRANSFER, Vol. 118, pp. 388–393.

C. N. Ammerman
Faculty Research Associate,
e-mail: ammerman@uta.edu,
Assoc. Mem. ASME

S. M. You
Associate Professor,
e-mail: you@uta.edu,
Mem. ASME

Department of Mechanical and
Aerospace Engineering,
The University of Texas at Arlington,
Arlington, TX 76019-0023

Consecutive-Photo Method to Measure Vapor Volume Flow Rate During Boiling From a Wire Immersed in Saturated Liquid

A photographic measurement technique is developed to quantify the vapor volume flow rate departing from a wire during boiling. The vapor flow rate is determined by measuring the volume of bubbles after departure from the boiling surface in consecutive frames of high-speed video. The measurement technique is more accurate and easier to implement than a previously developed photographic/laser Doppler anemometry (LDA) method. Use of the high-speed camera in place of a standard video camera eliminates the requirement for LDA-acquired bubble velocity measurements. The consecutive-photo method requires relatively few video images to be analyzed to obtain steady-state vapor volume flow rates. The volumetric flow rate data are used to calculate the latent heat transfer and, indirectly, sensible heat transfer which comprise the nucleate boiling heat flux. The measurement technique is applied to a 75-μm diameter platinum wire immersed in saturated FC-72.

Introduction

In fully developed, saturated nucleate boiling, latent heat transport and convection are the primary heat transfer mechanisms. Latent heat transport occurs when liquid vaporizes and leaves the surface. Convection heat transfer results from sensible energy being removed by entrainment of the superheated liquid in the departing bubble's wake. A knowledge of these boiling heat transfer mechanisms will aid in the development of empirical and analytical correlations for boiling heat transfer.

Previous investigators (e.g., McFadden and Grassmann, 1962; Rallis and Jawurek, 1964; Paul and Abdel-Khalik, 1983; Barthau, 1992) have employed various photographic techniques to determine key boiling parameters such as bubble departure diameter, departure frequency, and nucleation site density. These investigators have presented experimental results of these key boiling parameters and most have used them to calculate contributions to total heat flux from a heated surface. Despite their merits, however, the methods used by these investigators require the analysis of a large number of individual photographic frames at each heat flux.

A single-photo method was developed by Ammerman et al. (1996) to enable rapid quantification of latent heat flux from a heated wire. Their method combined a single video image with laser-Doppler anemometry (LDA) bubble velocity data to determine the volumetric flow rate of vapor above a heated wire. The advantage of this over previous methods was that it required the analysis of only a few photographs at each heat flux. Another advantage of the single-photo method was that it evaluated bubbles departing from multiple cavities instead of focusing on an individual nucleation site.

In the present investigation, a new consecutive-photo method is presented and explained. The consecutive-photo method requires relatively few video images to be analyzed to obtain steady-state vapor volume flow rates. This new method is a simplification of the single-photo method and provides more accurate vapor volume flow rate measurements. The consecutive-photo method is used to determine the boiling heat transfer mechanisms for a 75-μm diameter, electrically heated, platinum wire immersed in saturated FC-72. Results from the consecutive-photo measurement technique are compared with data taken using the photographic/LDA method.

Experimental Apparatus and Procedure

The experimental apparatus for this study is shown in Fig. 1. The test section consisted of an electrically heated, 75-μm diameter platinum wire mounted between two copper terminals spaced 2 cm apart. A voltmeter and power supply were connected to the heater via the copper terminals. The direct-current power supply was connected to the heater in series with a precision resistor which was used to determine the electrical current. The precision resistor had a resistance of 0.1 Ω with an accuracy of ±0.05 percent. This equipment was interfaced via IEEE-488 cables and controlled by a personal computer. Since platinum has a repeatable temperature-versus-resistance relationship, the wire itself was used to measure heater temperature. The wire was calibrated prior to testing and was checked after the test to ensure that it had not been damaged during the experiment. The heater was immersed in saturated FC-72 at atmospheric pressure. Liquid temperature was measured using a copper-constantan thermocouple which was calibrated with a precision thermometer. The experimental uncertainties in total heat flux and wall superheat for a 95 percent confidence level were ±4.1 percent and ±0.25 K, respectively.

The wire heater was contained in a 1-cm thick aluminum test vessel equipped with a 0.65-cm thick aluminum cover plate bolted into place and sealed with a rubber gasket. The test section could be viewed and illuminated through 1.3-cm thick lexan viewports built into the sides of the vessel. The bulk liquid was heated using three strip heaters attached to the outside of the vessel (two mounted to opposite sides and one mounted to the bottom). The bottom and sides of the test vessel (except for the viewports) were insulated with 2.5-cm thick styrofoam and the top with 1.3-cm thick foam rubber. The vessel was connected to a water-cooled condenser which vented the test section to ambient pressure. Electrical wiring entered through a sealed port on top.

Contributed by the Heat Transfer Division for publication in the JOURNAL OF HEAT TRANSFER and presented at IMECE '97, Dallas. Manuscript received by the Heat Transfer Division, June 30, 1997; revision received, Mar. 23, 1998. Keywords: Boiling, Flow Visualization, Measurement Techniques. Associate Technical Editor: M. Sohal.

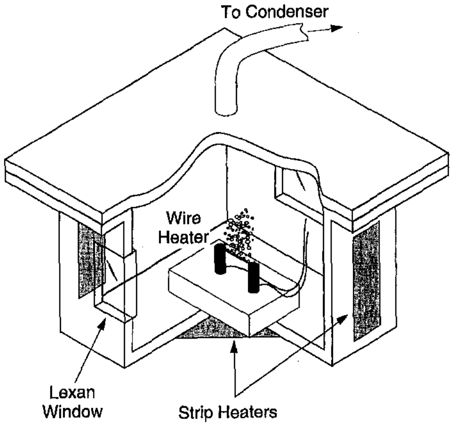

Fig. 1 Pool boiling test facility

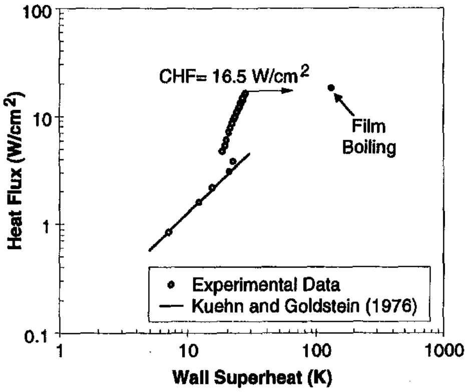

Fig. 2 Boiling curve

A high-speed digital camera was used to obtain images of the boiling bubbles during the experiment. The frame rate and shutter speed were set at 240 frames per second and 1/10,000th of a second, respectively. The camera was connected to a personal computer where digitized images were directly downloaded into the computer's memory as they were acquired. The camera was equipped with a 200 mm lens to magnify the viewing area. The wire heater was illuminated from the back side with a high-intensity 150 W halogen lamp. Light from the lamp was diffused using an imperfect diffuser (tracing paper) placed outside the test vessel. Lunde and Perkins (1995) found that using a perfect (Lambert) diffuser could cause bubble diameters to be significantly underestimated. They determined that the reflected image of the background in the bubble surface would be indistinguishable from the background itself, causing the outer portion of the bubble to appear invisible. However, the use of tracing paper as a diffuser resulted in highly accurate diameter measurements.

Prior to performing the experiment, power was supplied to the strip heaters to heat the test liquid to its saturation temperature of 56°C. The test liquid remained at saturation conditions for three to four hours to remove noncondensable gases. During this time, a magnetic stirrer was activated to expedite the degassing process. Following this degassing process the test was initiated. A heat-flux controlled boiling curve (shown in Fig. 2) was generated by incrementally advancing the power supplied to the wire heater. The boiling curve started in the natural convection region, progressed through the nucleate boiling region, and was extended just beyond critical heat flux (16.5 W/cm^2) into the film boiling region. The solid line indicates the single-phase natural convection correlation of Kuehn and Goldstein (1976) and compares well with the test data.

Vapor Volume Flow Rate Measurement Methodology

A new photographic measurement technique was developed to quantify the vapor volume flow rate departing from a wire during boiling. The vapor flow rate was determined by measuring the volume of bubbles after departure from the boiling surface in consecutive frames of high-speed video. This consecutive-photo method is a major improvement over the single-photo measurement technique previously developed by the present authors (Ammerman et al., 1996).

Image Length Scale and Gray Level Calibration. Image processing software was used to measure the size of individual bubbles. The images were divided into 256 gray levels from black to white (0 to 255). However, before the bubbles could be sized, the image length scale and threshold gray level (gray level which separates the edge of a bubble from the background) had to be determined. Lunde and Perkins (1995) determined the threshold gray level by examining a histogram of gray levels within an image. Two peaks were observed within their histograms: one peak representing mean gray level of bubble pixels and a much larger peak representing mean background gray level. They typically set the threshold gray level to be halfway between these two peaks. Ammerman et al. (1996) determined threshold gray level by computing an average value of gray level for pixels which were clearly in the background (no bubbles nearby). Both of these methods for determining threshold gray level are somewhat arbitrary, therefore a more rigorous method was established for this study.

Several calibration photos were taken of a millimeter-scale ruler and a 1.59-mm diameter ($\frac{1}{16}$th-inch diameter) ball bearing, each with a different background grey level. A calibration photo was selected such that the background grey level in the region surrounding the ball bearing was nearly equal to the background grey level in the bubble images. Image length scale was directly obtained from the ruler and fixed within the image processing software. Equipped with the length scale, the image processing software could then be used to find the diameter of the ball bearing. Thus, the threshold gray level was determined by iteratively varying its value until the measured diameter of the ball bearing matched the known diameter.

Bubble Sizing. Once the length scale and threshold gray level were determined, bubble sizes were obtained from the photographic images. Due to differences in rise velocity, one bubble sometimes partially obstructed the view of another bubble within an image. When bubbles appeared to touch or overlap, they were divided into separate objects with a thin white line prior to sizing. When overlap of bubbles occurred, bubbles with a two-dimensional area approximately equal to the obstructed area were counted twice to correct for the obstruction.

Nomenclature

a = semi-major axis of bubble (mm)
b = semi-minor axis of bubble (mm)
CHF = critical heat flux (W/cm^2)
D = wire diameter (cm)
h_{fg} = latent heat of vaporization (J/kg)
L = length of wire examined (cm)
LDA = laser Doppler anemometry
q_{LH} = latent heat flux (W/cm^2)
V_b = bubble volume (mm^3)
$\dot{V}_g$ = vapor volumetric flow rate (mm^3/s)
ρ_g = vapor density (kg/m^3)

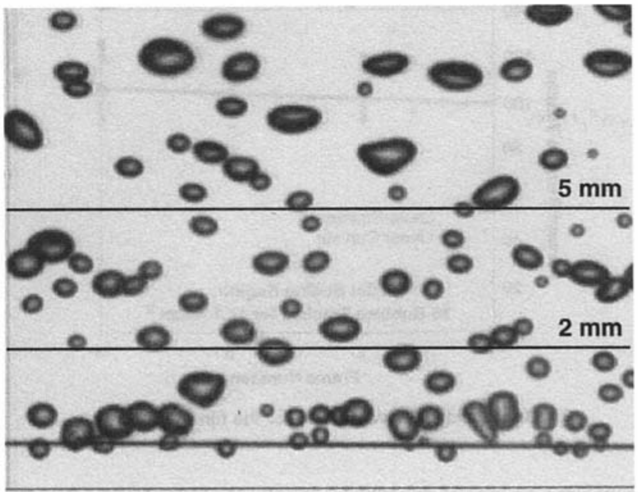

Fig. 3(*a*) 8.6 W/cm²

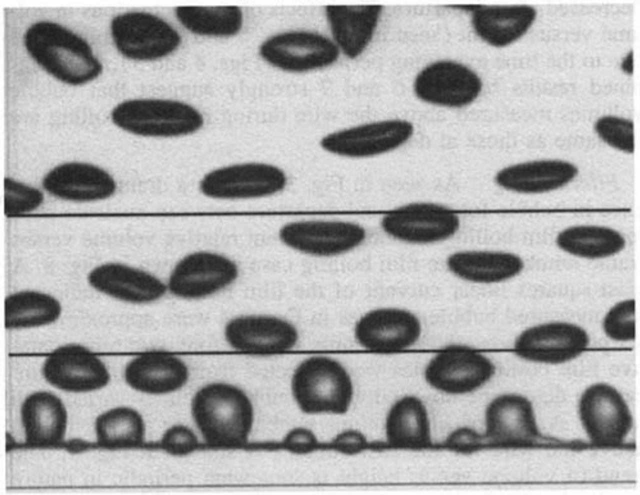

Fig. 3(*b*) 18.1 W/cm²

Fig. 3 Sample nucleate and film boiling photos

While the shapes of the bubbles were slightly irregular, most bubbles appeared elliptical in two dimensions. This was due to the initially spherical bubble being flattened between the opposing buoyancy and drag forces. Based on this flattening phenomenon, the bubble volume was determined from the two-dimensional image. First, the image processor mathematically transformed the slightly irregular two-dimensional bubble shape into an equivalent-area two-dimensional ellipse (semi-major and minor axes of a and b, respectively) with identical second moments about the center of gravity. Then, based on the flattening phenomenon, the three-dimensional bubble was assumed to resemble an ellipsoid with semi-axes, a, a, and b, so that the bubble volume was calculated as

$$V_b = \tfrac{4}{3}\pi a^2 b. \tag{1}$$

Volume Flow Rate Measurement. A series of several hundred photographs was acquired at each of three different fully developed nucleate boiling heat fluxes (8.6, 11.6, and 14.5 W/cm²) and one film boiling heat flux (18.1 W/cm²). Sample photographs are shown in Fig. 3 for the 8.6 and 18.1 W/cm² cases. For the present experiment (bubble velocities on the order of 0.1 m/s), a filming rate of 240 frames per second was chosen to enable tracking of individual bubbles from frame to frame. Therefore, the time interval between successive frames was 4.17 ms.

Each series of photographs was examined, four frames at a time, to count and size individual bubbles. A control line was drawn parallel to the wire in each frame as a reference location for counting bubbles (shown in Fig. 3). The control line was bounded by the edges of the photographic image. It was not uncommon to observe bubbles merging just prior to, or just after, departure from the wire. Therefore, the control line was placed 2.0 mm above the wire to avoid sizing two bubbles in the process of merging. The first frame in a series was used as a reference frame (time = 0 s) to start bubble counting. The second and third frames were used to identify and track bubbles as they crossed the control line. In the fourth frame (time = 0.0125 s), all bubbles which had completely crossed the control line during the time interval were sized. (No bubble in this study exceeded a height of 5 mm prior to being sized.) The sum of the individual bubble volumes was computed and divided by the time interval between the first and fourth frames (0.0125 s). The resulting value represents the instantaneous vapor volume flow rate for the sequence of four frames examined. The fourth frame of the first sequence then became the first (reference) frame for the next sequence of four frames, and the process of computing instantaneous vapor volume flow rate was repeated.

A plot of vapor volume flow rate versus time is shown in Fig. 4 for a heat flux of 8.6 W/cm². The open squares represent values of instantaneous vapor volume flow rate. The scatter in the instantaneous data occurs, in part, due to the requirement that the bubbles must completely cross the control line before being sized. Also shown in Fig. 4 (represented by the connected open circles) is the cumulative time average of the instantaneous values. The cumulative time average settles quickly near the steady-state value in approximately 0.1 s. An analysis of 0.1 s of video required sizing bubbles in only eight frames (out of 25 frames examined). The measurement time was extended to 0.25 s to obtain greater accuracy. However, even at 0.25 s, bubble sizing was performed in only 20 video frames (out of 61 frames examined). Figure 5 shows a plot of cumulative time average vapor volume flow rate for each of the four heat fluxes examined. All four heat fluxes show a similar trend of settling near their steady-state values within 0.1 s.

Volume Versus Height Investigation. To investigate the possibility of additional vaporization or condensation after departure, individual bubble volumes were measured in successive frames and compared. Fifteen bubbles were selected at random from each heat flux for this purpose. The bubbles selected were located below the control line in the reference frame of a given four-frame sequence. The bubble's volume was measured in each of the four frames as it rose and crossed the control line. Then each of the four volumes in a sequence were divided by the reference-frame volume to determine the percent change from frame to frame.

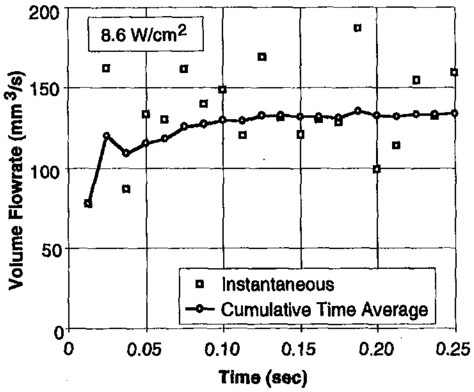

Fig. 4 Instantaneous and cumulative time average volume flow rates for 8.6 W/cm²

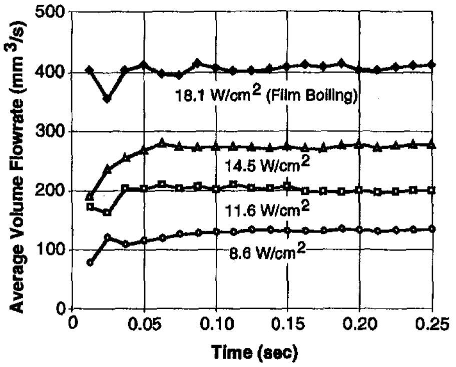

Fig. 5 Cumulative time average volume flow rate

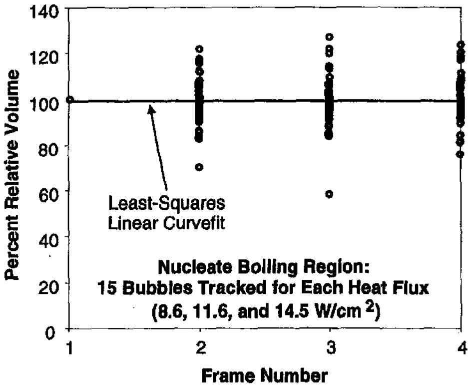

Fig. 6 Percent relative volume for the three nucleate boiling cases

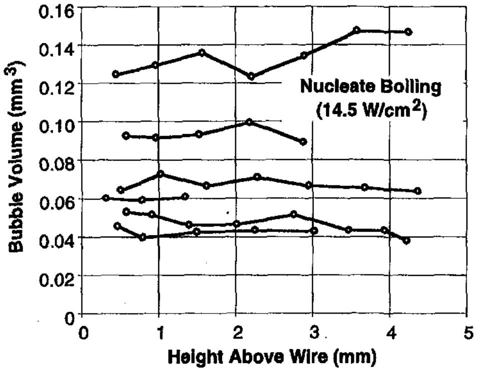

Fig. 7 Individual bubble volume versus height for nucleate boiling (14.5 W/cm^2)

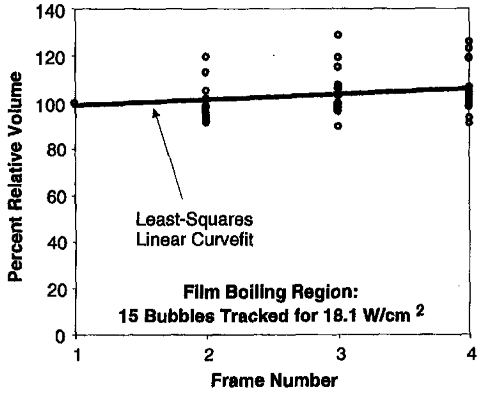

Fig. 8 Percent relative volume for the film boiling case

Nucleate Boiling. Data for the three nucleate boiling heat fluxes are shown in Fig. 6 in a plot of percent relative volume versus frame number. As seen in Fig. 6, volume fluctuations did occur from frame to frame due to irregularities in bubble shape (not perfectly ellipsoidal as assumed). However, a least-squares linear curvefit of the data (included in Fig. 6) indicates that the average bubble's volume does not change as it rises.

To further investigate this volume-versus-height trend in the nucleate boiling region, six bubbles of various size were selected at random from the 14.5 W/cm^2 case. The bubbles were tracked and sized in successive frames. Results of how their volume varied with height above the wire are shown in Fig. 7. (Bubble height is defined as the height of the bubble's center of gravity above the wire.) The first frame captured these bubbles just after the moment of departure. The bubble was then followed until it reached the edge of the four-frame measurement area or was obstructed by another bubble. Figure 7 indicates that, on average, bubble volume neither increased nor decreased after departure. The effects of the fluctuations in volume versus height (seen in both Figs. 6 and 7) are minimized due to the time averaging performed (Figs. 4 and 5). The combined results of Figs. 6 and 7 strongly suggest that bubble volumes measured above the wire during nucleate boiling are the same as those at departure.

Film Boiling. As seen in Fig. 3, there is a dramatic difference in bubble formation and departure between nucleate boiling and film boiling. Results of percent relative volume versus frame number for the film boiling case are shown in Fig. 8. A least-squares linear curvefit of the film boiling data indicated that measured bubble volumes in Frame 4 were approximately six percent above those in Frame 1. Therefore, two representative film boiling bubbles were selected from the 18.1 W/cm^2 case to determine how individual bubble volumes varied with height. A plot of film boiling bubble volume versus height above the wire for the two bubbles is shown in Fig. 9. The trend of volume versus height is somewhat periodic in nature due to the fluctuation in shape after departure. The first frame in each series is taken just prior to the moment of departure as the base of the bubble is necking. Since the bubble is necking from a thin wire, the bubble shape is not symmetrical but is elongated in the direction parallel to the wire (see Fig. 3(*b*)). Therefore, in the image, the bubble appears to be larger than its actual size. The second frame is taken just after departure when the bubble is in transition to a more uniform shape. By the third frame, the bubble has attained a fairly stable, uniform shape. The third frame in each series is representative of the Frame 1 bubbles identified in Fig. 8. Then, between approximately 2 to 5 mm above the wire, the measured volume increases. (Bubbles in the latter portion of this region are typical

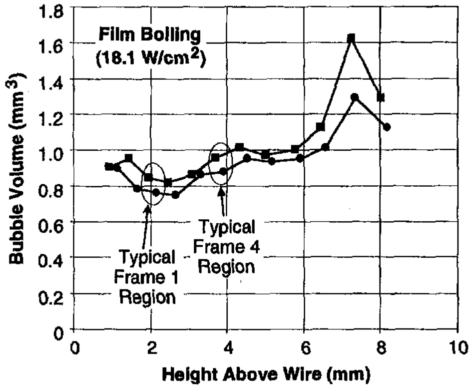

Fig. 9 Individual bubble volume versus height for film boiling

Table 1 Uncertainties in vapor volume flow rate

Total heat flux (W/cm^2)	Volume flow rate uncertainty (percent)
8.6	±8.4
11.6	±8.6
14.5	±7.3
18.1	±8.2

of Frame 4 bubbles identified in Fig. 8.) In this region, the bubbles are accelerating. Because of their size and speed, they begin to deform, becoming slightly cup shaped. This deformation may account for the increase in measured volume in this region. This increase in individual bubble volume between 2 and 5 mm above the wire accounts for the volume increase seen between Frames 1 and 4 in Fig. 8. Above 6 mm, the bubbles generally begin to tilt back and forth as they travel upward (see Fig. 3(*b*)). When they tilt, they expose their flattened top (or bottom) sides toward the camera making their volumes appear even larger.

The present authors believe that the volumes measured in the region near 2 mm above the wire are representative of departure volumes. This region is selected because bubble shapes are more uniform and bubble speeds are relatively low. Therefore, to estimate departure volumes for the film boiling case, the measured (Frame 4) volumes were decreased by six percent according to the curvefit shown in Fig. 8.

Volume Flow Rate Uncertainty. Uncertainties in the nucleate and film boiling volume flow rate measurements are shown in Table 1 versus total input heat flux for a 95 percent confidence level. These uncertainties are due mainly to image resolution and bubble shape irregularity. Image resolution determines the bubble diameter uncertainty since the diameter can only be measured to within one pixel width. The scale of the calibration photo determines the size of a pixel within the image processing software.

Bubble shape irregularity accounts for the fluctuation in the individual bubble volume as illustrated in Figs. 7 and 9. Increasing the measurement time (number of frames examined) will decrease the uncertainty due to bubble shape irregularity as seen in Fig. 5. An additional six percent uncertainty was included in the film boiling calculation due to the variation in size versus height, as discussed earlier with Fig. 8.

Comparison With the Single-Photo Method. In order to explain the benefits of the consecutive-photo method compared with the single-photo method, a brief summary of the single-photo method will be provided. (A more detailed explanation can be found in Ammerman et al., 1996.) Video images of bubbles departing a heated wire immersed in a saturated liquid were recorded at selected heat fluxes. Bubble volumes in these images were measured in a manner similar to that used for the consecutive-photo method. Based on these volumes, an average bubble diameter was obtained for each heat flux. However, since high-speed photography was not used, bubbles could not be tracked from frame to frame. Therefore, even though bubble volumes were acquired, no time scale existed with which to determine volume flow rate. To provide this time scale, laser velocimetry was used to measure bubble velocity at each heat flux. Because bubbles accelerate upon departure, velocities were measured at various heights and numerically integrated to obtain an average velocity within the video image for each heat flux. Next, the average velocity per heat flux was plotted versus the average diameter per heat flux to obtain a velocity-versus-diameter trend. This trend was used to estimate the velocity of individual bubbles within the video images at each heat flux. Finally, the individual bubble volumes and velocities were combined to determine volume flow rate.

The primary advantage of the consecutive-photo method over the single-photo method is the ability to determine volume flow rates without measuring bubble velocities. Velocities measured with the laser were assumed to be representative of average bubbles departing the wire. However, it is not clear whether the average bubble velocity measured statistically corresponds to the bubble with the average diameter. This potential velocity-diameter mismatch adds an unknown uncertainty to the single-photo measurements. Another advantage of the consecutive-photo method over the single-photo method is the manner in which gray level threshold was determined. As mentioned previously, image gray level threshold calibration for the single-photo method was not performed using a known-diameter sphere. Therefore, even though estimates of gray level threshold level uncertainty can be made, they are difficult to justify. These two advantages of using the consecutive-photo method provide much greater confidence in volume flow rate measurements.

Boiling Heat Transfer Mechanism Analysis

Experiments were conducted in both the fully developed nucleate boiling and film boiling regimes under saturation conditions. Natural convection is not present in fully developed boiling, Marangoni flow (surface tension-driven flow) is negligible in saturated boiling, and radiation is not significant until much larger wall superheats exist. Therefore, the primary heat removal mechanisms in both of these regimes are latent and sensible heat removal. Latent heat fluxes can be determined using the measured vapor volume flow rates and the sensible heat component can be assumed to make up the difference.

The steady-state vapor volume flow rates measured with the consecutive-photo method were used to determine the latent heat contribution to the total heat removal from the wire. The following equation was used to calculate latent heat flux:

$$q_{LH} = \frac{\rho_g \dot{V}_g h_{fg}}{\pi D L} . \tag{2}$$

The density (13.49 kg/m^3) and heat of vaporization (94.176 kJ/kg) were evaluated at the saturation temperature of the liquid. Support for this assumption can be found in Figs. 6–9 which showed that with increasing height above the wire, bubble volumes either remained constant (nucleate boiling) or possibly increased (film boiling). If the vapor within a bubble had been superheated, it would have had a density lower than the density of saturated vapor. Upon cooling, the density would have increased and the bubble's volume would have decreased. Since no decrease in volume was observed, the vapor properties within a bubble were assumed to be at saturation conditions.

A plot of latent heat flux versus total heat flux is shown in Fig. 10. The closed circle represents the film boiling point. The heavy solid line indicates the total heat flux, and therefore, the

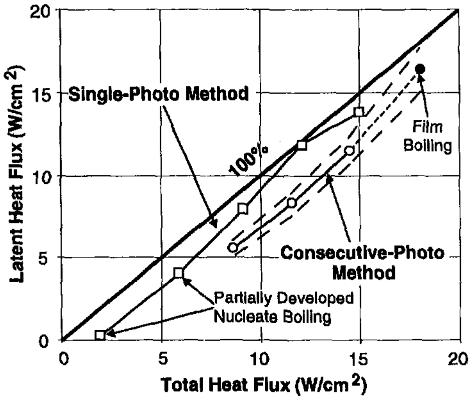

Fig. 10 Latent heat flux versus total heat flux

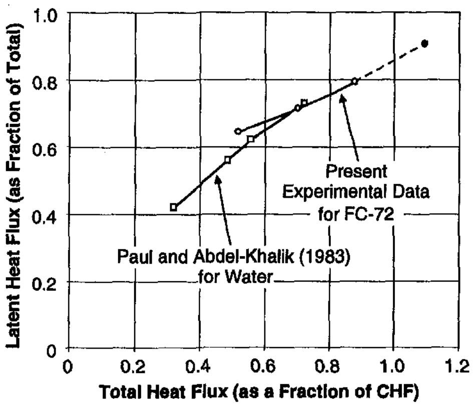

Fig. 11 Latent heat flux (as a fraction of total)

theoretical upper limit of the latent heat flux. The latent heat flux data exhibit a smooth increase with total heat flux, even into the film boiling regime. An experimental uncertainty band is shown with the data using dashed lines. Uncertainties in latent heat flux result from uncertainties in vapor volume flow rate and wire heater surface area. Also shown in Fig. 10 is the latent heat flux determined by Ammerman et al. (1996) measured using the single-photo method. The test conducted by Ammerman et al. examined a 75-μm platinum wire immersed in saturated FC-72. Therefore, a direct comparison can be made between the two data sets. (Also included in the data of Ammerman et al. are two partially developed nucleate boiling heat fluxes.) Latent heat flux data measured using the single-photo method are larger than those measured using the consecutive-photo method. The data measured by Ammerman et al. were the best that could be obtained within the limitations of the single-photo method. However, the single-photo data fall outside the measured uncertainty band of the consecutive-photo data. As discussed previously, the present authors place a high level of confidence in the consecutive-photo data since potential sources of error involved with the single-photo method have been eliminated.

Figure 11 shows a plot of latent heat flux as a fraction of total heat flux versus the total heat flux as a fraction of the experimental critical heat flux (CHF). Also shown in Fig. 11 are pool boiling data of Paul and Abdel-Khalik (1983) for a 300-μm diameter wire immersed in saturated water at atmospheric pressure. Both sets of data show surprisingly similar magnitudes in view of the significant property differences between FC-72 and water, and the differences in wire diameter. The present data, however, exhibit a lower slope than the water data. This slope appears to remain constant even as conditions change from nucleate to film boiling. This is interesting since some previous investigators (e.g., Paul and Abdel-Khalik, 1983; Zuber, 1959) have expected that heat transfer in the film boiling regime (at relatively low wall superheats) would be almost entirely due to latent heat transport. However, latent heat transport for the present film boiling case (wall superheat = 133 K) is approximately 89 percent of the total heat flux.

A value of 89 percent latent heat transport indicates that approximately 11 percent of the film boiling heat transfer is due to sensible heat removal. In film boiling, this sensible heat component could take the form of liquid-solid contact. There is evidence in the literature for liquid-solid contact during film boiling. Chang and Witte (1990) detected liquid-solid contact during film boiling from a 6.35-mm OD thin-walled Hastelloy-C cylindrical heater immersed in saturated Freon-11 at atmospheric pressure. They observed dramatic evidence of liquid-solid contact near the minimum heat flux at a wall superheat of 115 K. The occurrence of liquid-solid contact gradually decreased with increasing temperature up to a wall superheat of 179 K where almost none occurred. Lee et al. (1985) measured the frequency of occurrence of liquid-solid contact on the face of a 10.2-cm diameter copper disk immersed in saturated water. They measured contact frequencies ranging from approximately 2 Hz at a superheat of 200 K up to 50 Hz at a superheat of 100 K. Chang et al. (1998) investigated film boiling from smooth and microporous-coated flat surfaces immersed in saturated FC-72 and FC-87 at atmospheric pressure. They showed that the film boiling curve was enhanced, including the increase of the minimum heat flux, due to the addition of the microporous surface coating. Since the microporous coating enhances boiling by generating an increased number of nucleation sites, the enhancement in film boiling could only come from liquid contact with the surface.

Comparing film boiling at 18.1 W/cm^2 with nucleate boiling at 14.5 W/cm^2 in Fig. 11, the sensible heat component only decreases by approximately ten percent of the total heat flux. Therefore, in the present experiment, there is a strong possibility that liquid-solid contact is responsible for the sensible heat component during film boiling. In nucleate boiling, there are obviously large liquid-solid contact areas combined with large liquid contact durations. In contrast, both the film boiling liquid-solid contact area and contact duration must be much smaller. However, the wall superheat that drives the sensible energy exchange is nearly five times larger for the film boiling case. This large wall superheat is what enables 11 percent of the total energy to be removed in the form of sensible energy.

The seemingly smooth transition of the latent heat transport curve in Fig. 11 from nucleate to film boiling indicates the possibility that the latent heat component at CHF may not be 100 percent of the total heat flux. If this is true, then the analytical reasoning behind the development of Zuber's (1959) hydrodynamic CHF correlation could be challenged. Zuber theorized that when a sufficient quantity of vapor was departing from the surface, hydrodynamic instabilities would occur which would trigger the collapse of the vapor onto the surface, resulting in vapor blanketing. In the development of his CHF prediction correlation, Zuber assumed that 100 percent of the heat dissipated at CHF would be due to latent heat transport. By interpolation of the curve in Fig. 11, the latent heat component at CHF could be slightly less than 85 percent. No firm conclusions can be drawn from these results, however, because Zuber's analysis was conducted assuming the heated surface was an infinite flat plate. Therefore the present test results with regard to CHF are not conclusive and additional testing is needed to further investigate this region.

Conclusions

A new consecutive-photo measurement technique was developed to quantify the vapor volume flow rate departing from a wire during boiling. The vapor flow rate was determined by measuring the volume of bubbles after departure from the boiling surface in consecutive frames of high-speed video. The measurement technique is applied to a 75-μm platinum wire immersed in saturated FC-72 to determine the nucleate boiling and film boiling heat transfer mechanisms.

1 Bubble volumes measured after departure in the region above the wire are indicative of departure volumes. This observation is based on frame-to-frame volume measurements for individual bubbles starting just after departure and on a bubble heat transfer analysis.

2 The consecutive-photo method is more accurate and easier to implement than a previously developed single-photo method. The single-photo method required bubble velocity measurements in order to obtain a time scale for volume flow rate calculation. These velocity measurements introduced additional error into the resulting volume flow rates.

3 Based on the measured vapor volume flow rates, the latent heat and (indirectly) the sensible heat components of the fully

developed nucleate boiling and film boiling heat fluxes were determined. The latent heat flux values in nucleate boiling were lower than those measured previously using the single-photo method. However, the latent heat transport as a fraction of the total heat flux data were similar to data obtained in a previous investigation for water boiling from a wire.

4 The latent heat component for a film boiling condition was 89 percent of the total heat flux. This observation indicates a significant sensible energy component for the film boiling case examined. It is likely that liquid-solid contact is responsible for the sensible energy removal.

Acknowledgments

This study was funded under Advanced Research/Technology Program grant number 003656-014 provided by the Texas Higher Education Coordinating Board. The authors would like to thank Mr. Y. S. Hong for his technical support during testing.

References

Ammerman, C. N., You, S. M., and Hong, Y. S., 1996, "Identification of Pool Boiling Heat Transfer Mechanisms From a Wire Immersed in Saturated FC-72 Using a Single-Photo/LDA Method," ASME JOURNAL OF HEAT TRANSFER, Vol. 118, pp. 117–123.

Barthau, G., 1992, "Active Nucleation Site Density and Pool Boiling Heat Transfer—An Experimental Study," *Int. J. Heat Mass Transfer,* Vol. 35, pp. 271–278.

Chang, K.-H., and Witte, L. C., 1990, "Liquid-Solid Contact in Pool Film Boiling From a Cylinder," ASME JOURNAL OF HEAT TRANSFER, Vol. 112, pp. 263–266.

Chang, J. Y., You, S. M., and Haji-Sheikh, A., 1996, "Film Boiling Incipience at the Departure From Natural Convection On Flat, Smooth Surfaces," ASME JOURNAL OF HEAT TRANSFER, Vol. 120, pp. 402–409.

Kuehn, T. H., and Goldstein, R. J., 1976, "Correlating Equations for Natural Convection Heat Transfer Between Horizontal Circular Cylinders," *Int. J. Heat Mass Transfer,* Vol. 19, pp. 1127–1134.

Lee, L. Y. W., Chen, J. C., and Nelson, R. A., 1985, "Liquid-Solid Contact Measurement Using a Surface Thermocouple Temperature Probe in Atmospheric Pool Boiling Water," *Int. J. Heat Mass Transfer,* Vol. 28, No. 8, pp. 1415–1423.

Lunde, K., and Perkins, R. J., 1995, "A Method for the Detailed Study of Bubble Motion and Deformation," *Proc. 2nd Int. Conf. Multiphase Flow,* Kyoto, pp. 395–405.

McFadden, P. W., and Grassmann, P., 1962, "The Relation Between Bubble Frequency and Diameter During Nucleate Pool Boiling," *Int. J. Heat Mass Transfer,* Vol. 5, pp. 169–173.

Paul, D. D., and Abdel-Khalik, S. I., 1983, "A Statistical Analysis of Saturated Nucleate Boiling Along a Heated Wire," *Int. J. Heat Mass Transfer,* Vol. 26, pp. 509–519.

Rallis, C. J., and Jawurek, H. H., 1964, "Latent Heat Transport in Saturated Nucleate Boiling," *Int. J. Heat Mass Transfer,* Vol. 7, pp. 1051–1068.

Zuber, N., 1959, "Hydrodynamic Aspects of Boiling Heat Transfer," Ph.D. thesis, University of California at Los Angeles, Los Angeles, CA.

A. Haji-Sheikh
Fellow ASME

Y. S. Hong

S. M. You
Mem. ASME

Department of Mechanical and
Aerospace Engineering,
The University of Texas at Arlington,
Arlington, TX 76019-0023

J. V. Beck
Department of Mechanical Engineering,
Michigan State University,
East Lansing, MI 48824-1226
Fellow ASME

Sensitivity Analysis for Thermophysical Property Measurements Using the Periodic Method

The frequency domain provides an interesting alternative platform for measuring thermophysical properties. The resulting measurement technique produces reasonably accurate thermophysical data from imprecise surface information. Having a periodic heat flux input at one surface, the thermal diffusivity is obtainable if temperature produces a measurable periodic effect at another location. The analysis shows that only the phase shift is necessary to produce needed information while the boundary conditions can affect the experimental results. This method was tested near room temperature using two different materials: Delrin and 304 stainless steel. The experiments yield accurate thermal diffusivity data for both materials but the data for Delrin exhibit smaller errors. Before performing the experiments, a sensitivity analysis was carried out to determine the best range of frequencies for an experimental investigation.

Introduction

This work addresses a procedure for accurately measuring thermal conductivity and/or thermal diffusivity of different solids. The details of the theoretical procedure leading to the analysis of experimental data are well known and are available in most thermal conduction textbooks (Carslaw and Jaeger, 1986). Only a few studies of temperature response to periodic surface temperature or surface heat flux are referenced here. Zubair and Chaudhry (1995) discussed the steady-state and transient temperature variations in a semi-infinite solid. Caulk (1990) assumed temperature variations are confined within a thin layer and calculated temperature distributions. This assumption is valid for a periodic boundary condition of high frequency. A study of temperature oscillation in a solid cylinder was reported by Khedari et al. (1992). Rouault et al. (1987) used this concept to measure thermal diffusivity of alumina at high temperature. They compared sinusoidally modulated temperature at the outer surface of a cylinder with temperature at interior points. This technique is equally useful for measuring thermophysical properties of thin films. Feldman et al. (1989) measured thermal diffusivity of diamond film by this method.

The measurement procedure evolves from the classical solution of the diffusion equation. The use of a periodic temperature field to measure thermal conductivity of a metal rod has been known for over a century (Ångström, 1861). With the proliferation of modern computer-based data acquisition systems, it is possible to design a strategy for accurately computing thermophysical properties from the measured temperature data. Thermal property measurement by this technique is simple and relatively inexpensive; however, for thin and/or high thermal conductivity materials, sophisticated instrumentation is needed.

A plate having a periodic heat flux at one surface will have a periodic temperature field throughout the plate after initial transients. However, depending on the frequency, the amplitude of the periodic temperature decreases in the direction away from the heat flux source. In principle, one can modulate the heat flux until there is a detectable temperature signal at a site and determine the phase delay between the heat flux and temperature signals. A one-to-one relation exists between this phase delay and the thermal diffusivity of the plate. Also, the difference between phase delays of temperature signals at two different sites depends on the thermal diffusivity. Generally, the phase delay is independent of the exact value of the measured temperature.

The phase delay in the frequency method is useful for measuring thermal diffusivity when it is difficult to obtain accurate temperatures; e.g., temperatures above 1200 K. Any measurable property that changes with temperature is a candidate for phase delay determination. The objective of this work is to perform sensitivity analysis and to demonstrate the useful range of frequencies for a specific application. This narrow range of frequencies depends on the thickness of the material and its thermal diffusivity. A sensitivity analysis is carried out to show the set of parameters that can be adjusted to provide accurate results. An experimental study was performed near room temperature where the measurement environment can be accurately controlled. The test materials used were Delrin (a polymer) and 304 stainless steel. The analysis and experiments showed interesting results and identified the limitations of this measurement technique. This theoretical and experimental study paves the way for a more effective utilization of this type of measurement technique.

Analysis

The objective is to develop a measurement technique for thermal diffusivity and thermal conductivity under periodic quasi-steady-state conditions. The geometry is a one-dimensional slab and the governing equation is

$$\frac{\partial^2 T}{\partial x^2} = \frac{1}{\alpha}\frac{\partial T}{\partial t} \tag{1}$$

with the boundary condition at $x = 0$ being $q = q_a + q_0 \sin \nu t$ where q_a is the average or mean value of heat flux over one period. The boundary condition at $x = L$ depends on the design of the experiment. First, a constant heat flux is used, $q \cong q_a$, until the steady condition is achieved. Then, the temperature at the onset of periodic heat flux condition, or the initial condition

---

Contributed by the Heat Transfer Division for publication in the JOURNAL OF HEAT TRANSFER and presented at '96 IMECE, Atlanta. Manuscript received by the Heat Transfer Division, Feb. 7, 1997; revision received, Mar. 2, 1998. Keywords: Conduction, Measurement Techniques, Thermophysical Properties. Associate Technical Editor: R. Boyd.

is $T(x, 0) = T_i(x) = T_{i0} - (T_{i0} - T_{i1})x/L$, where T_{i0} is initial temperature at $x = 0$ and T_{i1} is initial temperature at $x = L$. The transformation, $\theta(x, t) = T(x, t) - T_i(x)$, introduces the following system of equations:

$$\frac{\partial^2\theta(x, t)}{\partial x^2} = \frac{1}{\alpha}\frac{\partial\theta(x, t)}{\partial t}. \qquad (2)$$

The initial condition is $\theta(x, 0) = 0$; the boundary condition at $x = 0$ is $q = q_0 \sin \nu t$, and, the boundary condition at $x = L$ may be of the first, second, third, or fifth kind.

The solution of this equation using the Green's function solution method (Beck et al., 1992) is

$$\theta(x, t) = \frac{\alpha}{k}\int_{\tau=0}^{t} G(x, t|0, \tau)q(\tau)d\tau \qquad (3)$$

where $G(x, t|0, \tau)$ is the Green's function. Integrating Eq. (3) gives

$$\frac{k\theta(x, t)}{q_0L} = \sum_{m=1}^{\infty}\frac{\cos(\beta_m x/L)}{N_m}\left\{\frac{\omega e^{-\beta_m^2\alpha t/L^2}}{\beta_m^4 + \omega^2} + \frac{\beta_m^2 \sin(\omega\alpha t/L^2)}{\beta_m^4 + \omega^2} - \frac{\omega\cos(\omega\alpha t/L^2)}{\beta_m^4 + \omega^2}\right\} \qquad (4a)$$

where $\omega = \nu L^2/\alpha$ and β_m depends on the boundary condition at $x = L$. Only the values β_m and N_m in Eq. (4a) are to be computed for each of the boundary conditions of the first, second, third, or fifth kind at $x = L$ (Beck et al., 1992). For example, the boundary condition of the first kind at $x = L$ requires $\beta_m = (2m - 1)\pi/2$ and $N_m = \frac{1}{2}$. The eigenvalues, β_m, and norm, N_m, for boundary conditions of the third kind and fifth kind at $x = L$ were obtained from Beck et al. (1992, pp. 495–496, 499). These solutions were examined during experimental studies. However, for the initial study, the boundary condition at $x = L$ is of the second kind (Beck et al., 1992, Eq. X22.3), $\beta_m = (m - 1)\pi$, and when n replaces $m-1$, Eq. (4a) reduces to

$$\frac{k\theta(x, t)}{q_0L} = 2\sum_{n=1}^{\infty}\cos(n\pi x/L)\left\{\frac{\omega e^{-(n\pi)^2\alpha t/L^2}}{(n\pi)^4 + \omega^2} + \frac{(n\pi)^2 \sin(\omega\alpha t/L^2)}{(n\pi)^4 + \omega^2} - \frac{\omega\cos(\omega\alpha t/L^2)}{(n\pi)^4 + \omega^2}\right\} + \frac{1}{\omega}[1 - \cos(\omega\alpha t/L^2)]. \qquad (4b)$$

The last term is the contribution of the $n = 0$ term. For quasisteady state operation, t is large and the exponential term disappears. The solution after replacing $\alpha t/L^2$ by $\bar{t}$ is

$$\frac{k\theta(x/L, \bar{t})}{q_0L} = \left[2\sum_{n=1}^{\infty}\cos\left(\frac{n\pi x}{L}\right)\cdot\frac{(n\pi)^2}{(n\pi)^4 + \omega^2}\right]\sin(\omega\bar{t}) - \left[2\sum_{n=1}^{\infty}\cos\left(\frac{n\pi x}{L}\right)\cdot\frac{\omega}{(n\pi)^4 + \omega^2}\right]\cos(\omega\bar{t}) + \frac{1}{\omega}[1 - \cos(\omega\bar{t})]. \qquad (5)$$

This equation is rewritten as

$$\frac{k[T(x/L, \bar{t}) - T_i(x/L)]}{q_0L} = B\sin(\omega\bar{t}) - C\cos(\omega\bar{t}) + \frac{1}{\omega} = \sqrt{B^2 + C^2}\left[\frac{B}{\sqrt{B^2 + C^2}}\sin(\omega\bar{t}) - \frac{C}{\sqrt{B^2 + C^2}}\cos(\omega\bar{t})\right] + \frac{1}{\omega} \qquad (6a)$$

where

$$B(x/L) = \left[2\sum_{n=1}^{\infty}\cos\left(\frac{n\pi x}{L}\right)\cdot\frac{(n\pi)^2}{(n\pi)^4 + \omega^2}\right] \qquad (6b)$$

and

$$C(x/L) = \left[2\sum_{n=1}^{\infty}\cos\left(\frac{n\pi x}{L}\right)\cdot\frac{\omega}{(n\pi)^4 + \omega^2}\right] + \frac{1}{\omega}. \qquad (6c)$$

The term $1/\omega$ in Eq. (6a) is an offset value that appears since the first eigenvalue is zero in this specific case. Equation (6a) can be rewritten in terms of an offset angle φ by using $\cos(\varphi) = B/\sqrt{B^2 + C^2}$; then Eq. (6$a$) becomes

$$\frac{k(T - T_i)}{q_0L} = \sqrt{B^2 + C^2}\sin(\omega\bar{t} - \varphi) + \frac{1}{\omega}. \qquad (7)$$

For convenience, Eq. (7) can take a different form when both sides are multiplied by ω,

Nomenclature

Ampl(·) = amplitude
Bi = Biot number, hL/k
B, C = functions, Eqs. (6b) and (6c)
c_p = specific heat, J/kg·K
C_t = contact conductance, W/m^2·K
C_h = mc_p for the heater, J/m^3·K
f = frequency, Hz
k = thermal conductivity, W/m·K
L = plate thickness, m
m = mass, kg
m, n = summation indices
q = heat flux, W/m^2
q_0 = amplitude of $q(0)$, W/m^2
q^* = heat flux amplitude at heater site, W/m^2
q_a = mean heat flux, W/m^2
R = relative sensitivity coefficient
SC = sensitivity coefficient
SD = standard deviation
t = time, s
$\bar{t}$ = dimensionless time, $\alpha t/L^2$
t_o = period of oscillation, s
$t^*(x)$ = time delay at x, s
T = temperature, K
T_a = mean temperature, K
T_∞ = ambient temperature, K

Greek

α = thermal diffusivity, m^2/s
β = eigenvalues
$\delta(x - x')$ = Dirac delta function, m^{-1}
θ = temperature difference, $T - T_i$, K
$\bar{\theta}$ = dimensionless temperature, $\rho c_p \nu L(T - T_i)/q_0$
ν = $2\pi f$, rad/s
ρ = density, kg/m^3
τ = dummy variable
$\varphi(x)$ = phase delay at x, rad
ψ = amplitude of $\bar{\theta}$
ω = dimensionless frequency, $\nu L^2/\alpha$

Subscripts

0 = at $x = 0$
1 = at $x = L$
a = average or mean
d = for time delay
i = initial condition

$$\bar{\theta}(x/L, \bar{t}) = \frac{\rho c_p \nu L(T - T_i)}{q_0}$$
$$= \omega\sqrt{B^2 + C^2}\,\sin(\omega\bar{t} - \varphi) + 1 \qquad (8)$$

where $\varphi = \varphi(x/L)$ is the phase delay, and it is related to the time delay by the relation $t^*(x/L) = \varphi(x/L)/\nu$.

The convergence of Eqs. (6*b*) and (6*c*) is enhanced by using certain identities (Hansen 1975, p. 239),

$$B = \frac{1}{2}\left(\frac{x}{L}\right)^2 - \frac{x}{L} + \frac{1}{3} - 2\sum_{n=1}^{\infty} \frac{\cos(n\pi x/L)}{n^2\pi^2 + n^4\pi^4(n\pi/\omega)^2} \qquad (9)$$

and

$$C = -\omega\left[\frac{1}{24}\left(\frac{x}{L}\right)^4 - \frac{1}{6}\left(\frac{x}{L}\right)^3 + \frac{1}{6}\left(\frac{x}{L}\right)^2 - \frac{1}{45}\right.$$
$$\left. + 2\sum_{n=1}^{\infty} \frac{\cos(n\pi x/L)}{n^4\pi^4 + n^6\pi^6(n\pi/\omega)^2}\right] + \frac{1}{\omega}. \qquad (10)$$

Consider again the quasi-steady-state solution given by Eq. (8). Note that the local temperature and heat flux are harmonic functions, and there is an offset function equal to 1 that has no effect on the phase delay or amplitude. The amplitude of $\bar{\theta}$ is $\psi(x/L) = \omega(B^2 + C^2)^{1/2}$ and the phase delay is $\varphi(x/L) = \tan^{-1}(C/B)$. For the surface at $x = 0$, $\psi(0)$ and $\varphi(0)$ are plotted in Fig. 1 for Bi values of 0, 1, 10, and 100. Notice that the amplitude, $\psi(0)$, increases as ω increases while $\varphi(0)$ rapidly approaches a constant value when $\omega > 10$. When Bi = 0, an examination of Eqs. (6*b*) and (6*c*) shows that the solid lines in Fig. 1 have limiting values of $\varphi(0) = \pi/2$ and $\psi(0) = 1$ when $\omega = 0$. According to this figure, the phase delay at $x = 0$ is not generally sensitive to frequency change when $\omega > 10$. This will be demonstrated in the study of sensitivity coefficients.

When the surface at $x = L$ is exposed to ambient conditions or is not perfectly insulated, the hypothesis of using the boundary condition of the second kind is satisfactory if the temperature amplitude at $x = L$ is small. For example, the estimated error assuming boundary conditions of the second kind at $x = L$ instead of the third kind is about $100 \times \text{Ampl}[T(L, t)]/[T_a(L) - T_\infty]$ percent. However, the heat transfer coefficient also may depend on temperature. For example, in the presence of natural convection, the heat transfer coefficient depends on $[T_a(L) - T_\infty]^\sigma$ with $\sigma \cong \frac{1}{3}$ to $\frac{1}{4}$ and the error is of the order of $(100) \times \text{Ampl}[T(L, t)]/\{\sigma[T_a(L) - T_\infty]\}$ percent. The solution using Eq. (4*a*) for boundary conditions of the third kind, at $x = L$, requires numerically finding eigenvalues, β_m, from the relation $\beta_m \tan\beta_m = \text{Bi}$ (Beck et al., 1992). Using dimensionless parameters, Fig. 2 shows $\omega^{1/2}$ as a function of the ratio of time delay, $t^*(1) - t^*(0)$, to period of oscillation, t_o, for different values of Bi. The abscissa in this figure is $[t^*(1) - t^*(0)]/t_o = [\varphi(1) - \varphi(0)]/2\pi$. The graph shows three distinct regions: small ω, large ω, and an intermediate range. The intermediate and large ranges of ω are perhaps the best regions to design a measurement technique while keeping the time delay less than one period. Figure 3 shows the ratio of amplitude at $x/L = 1$ to amplitude at $x/L = 0$. The amplitude ratio rapidly reduces as the signal frequency increases. A small-temperature amplitude at $x/L = 1$ implies that the solution becomes insensitive to the boundary condition at $x = L$. This observation is discussed in the section on experimental studies.

The influence of convection at $x = L$ is represented by the Biot number, $\text{Bi} = hL/k$, and the influence of the Biot number becomes small for $\omega > 5$ and is negligible when $\omega > 10$. Data for different $\text{Bi} = hL/k$ values are computed and included in Figs. 1–3. The data in Fig. 2 exhibit a remarkable feature; that is, the lines are nearly linear when $\omega > 5$; however, the slope of the lines depends on the Biot number. Therefore, one can write,

$$\omega^{1/2} = \sqrt{\frac{\nu}{\alpha}}\,L \cong c_1 + c_2\left[\frac{t^*(1) - t^*(0)}{t_o}\right] \qquad (11)$$

where $t^*(1) - t^*(0)$ is the time delay between $x/L = 0$ and $x/L = 1$. A nonlinear regression yields $c_1 = 1.11 - 1.15\exp(-0.376\,\text{Bi}^{0.76})$ and $c_2 = 9.89 - 4.58/(1 + \text{Bi})^{1/4} + 3.63/(1 + \text{Bi})^{1/2}$. If there is a sensor at $x = x_1$, a plate between $x = x_1$ and $x = L$ has a thickness of $L - x_1$ and Eq. (11) becomes

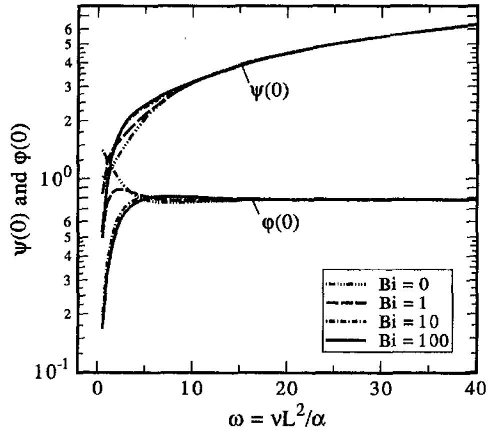

Fig. 1 Dimensionless amplitude and phase delay for the surface at $x = 0$

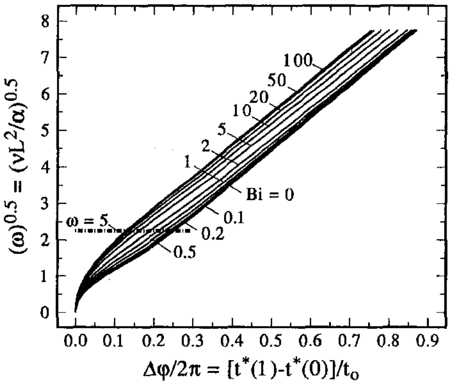

Fig. 2 Variation of time delay with ω for different Biot numbers

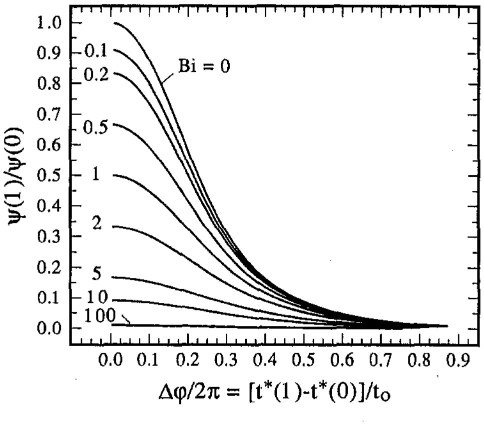

Fig. 3 Ratio of amplitude at $x = L$ to amplitude at $x = 0$ as a function of time delay for different Biot numbers

$$\sqrt{\frac{\nu}{\alpha}}\,(L - x_1) \cong c_1 + c_2\left[\frac{t^*(1) - t^*(x_1/L)}{t_o}\right] \qquad (12)$$

where c_1 and c_2 are constant when Bi = 0. Equation (12) is valid when $\nu\,(L - x_1)^2/\alpha > 5$. Further simplification is attainable when Bi = 0. Subtracting Eq. (12) from Eq. (11) provides the relation $\alpha \cong \nu[2\pi x_1/(c_2\Delta\varphi)]^2$ where $\Delta\varphi = \varphi(x_1) - \varphi(0)$.

Sensitivity Coefficients

The theoretical information described earlier is useful for implementing an experimental procedure that can produce measured values of thermal diffusivity. The test directly produces thermal diffusivity if the time delay between two different signals from two different sites is known. In addition, the amplitude of the harmonically varying temperature can directly produce thermal conductivity if the amplitude of the surface heat flux is available. Therefore, two independent sets of information are obtainable: the first is the amplitude and the second is the frequency shift. It is necessary to calculate the sensitivity coefficients for both cases.

The amplitude sensitivity coefficient, SC, to thermal diffusivity, α, assuming fixed ρc_p, is

$$SC(x/L, \omega) = \alpha\left[\frac{\partial\psi(x/L, \omega)}{\partial\alpha}\right] = -\omega\left[\frac{\partial\psi(x/L, \omega)}{\partial\omega}\right]. \qquad (13a)$$

To conduct an optimal experiment, for standard statistical assumptions, independent of the frequency, it is necessary to maximize the ratio

$$R(x/L, \omega) = \frac{\alpha}{\psi(0, \omega)}\left[\frac{\partial\psi(x/L, \omega)}{\partial\alpha}\right]. \qquad (13b)$$

The sensitivity coefficient, SC, and relative sensitivity, R, at $x/L = 1$ are plotted in Fig. 4 as a function of ω. The relative sensitivity is also plotted as a function of x/L and ω in Fig. 5. Figure 5 shows that the magnitude of R reduces at higher x/L and ω. The value of R, Fig. 5, is negative at $x = 0$, then passes through zero and assumes small positive values at $x = L$, see in Fig. 4. The dot-dash line in Fig. 4 shows a pair of x/L and ω that makes $R = 0$, indicating a poor sensitivity zone. This implies that the magnitude of amplitude will not provide useful information far beyond $x = 0$.

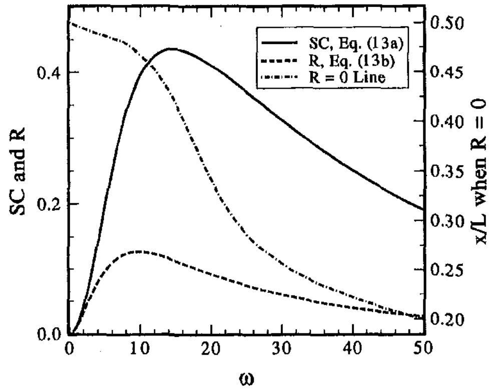

Fig. 4 Sensitivity coefficient, SC, and relative sensitivity, R, for amplitude

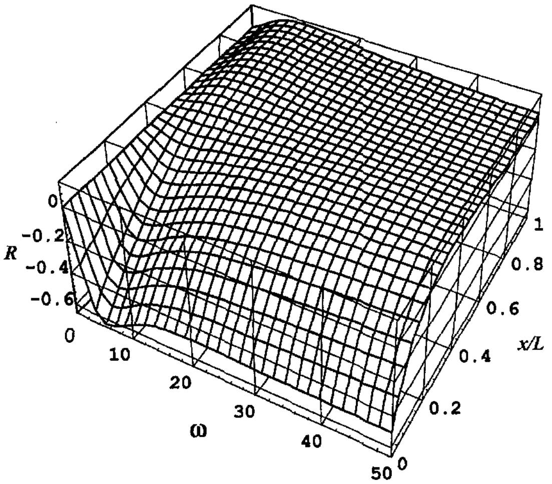

Fig. 5 Relative sensitivity for amplitude, R, as a function of x/L and ω

Alternatively, the sensitivity of the signal delay between $x = 0$ and any x, $\Delta\varphi(x)/2\pi = [t^*(x) - t^*(0)]/t_o$, also depends on the value of ω. The phase-delay sensitivity coefficient is defined as

$$SC_d = \alpha\,\frac{\partial[\Delta\varphi(x)]}{\partial\alpha} = -\omega\,\frac{\partial[\Delta\varphi(x)]}{\partial\omega} \qquad (14a)$$

that can also be written as

$$R_d = -\left(\frac{\omega}{2\pi}\right)\frac{\partial[\Delta\varphi(x)]}{\partial\omega}. \qquad (14b)$$

The function R_d is computed as a function of x and ω and the results are plotted in Fig. 6. The value of R_d is small when either x or ω is small. Based on the data in Fig. 6, the frequency should be chosen when R_d is sufficiently large, e.g., $\omega > 3$. However, based on Figs. 3 and 5, large x/L and ω values reduce both amplitudes and sensitivity R at the sites.

Experimental Studies

The theoretical study shows that the time delay between a sensor at $x = 0$ and at $x = L$ can produce the value of α. Furthermore, the analysis indicates that the boundary condition at $x = L$ can affect the time delay between $x = 0$ and $x = L$. However, as stated earlier, one can find an optimum value of ω, so that the time delay between $x = 0$ and $x = L/2$, for example, becomes insensitive to the boundary condition at $x =$

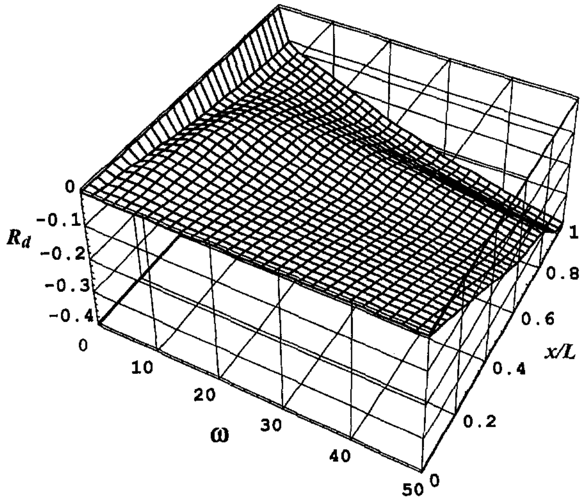

Fig. 6 Relative sensitivity for time delay, R_d, as a function of x/L and ω

L. When this condition exists, losses due to the finiteness of the sample size should not influence the measured time delay. These interesting theoretical observations will be demonstrated experimentally using two test plates with different thermal conductivities: one low and the other moderately high. Theoretical studies are verified using two different materials: Delrin and stainless steel.

Experiments Using Delrin. A simple test apparatus was constructed that consists of two Delrin plates 0.1508 m × 0.0503 m and $L = 0.01966$ m thick. Delrin or poly(oxymethylene) is an engineering thermoplastic with the chemical formula $(\text{—}CH_2\text{—}O\text{—})_n$ that is machinable and has low thermal conductivity. A heater was placed between the two Delrin plates. Two thermocouples were embedded, one at $x = L/2$ and one at $x = 0.0165$ m from the hot surface. Two additional thermocouples were affixed at $x = 0$ and $x = L$. The location of the thermocouples and the plate are in the inset of Fig. 7. A quasi-steady condition was obtained by providing a heat sink while maintaining the one-dimensionality of heat flux. To accomplish this, the Delrin plates and the heaters were sandwiched between two aluminum plates; each 0.0065 m thick. This provides a spatially uniform temperature field at $x = L$. However, the aluminum plates did begin to influence the frequency shift and provide an interesting phenomenon. Equation (4a) also describes the temperature solution except the eigenvalues, β_m, must include the effect of heat capacity of the aluminum plates (Beck et al., 1992). This type of boundary condition is classified as a boundary condition of the fifth kind. The heater and thermocouples were connected to a National Instrument data acquisition board. Prior to the onset of the experiment, direct current was supplied to the heater until a steady-state condition was reached. The steady-state condition yields the values of heat transfer coefficient using the relation $h = q_a/(T_{i1} - T_\infty)$ where T_∞ is the ambient temperature and T_{i1} is temperature at $x = L$. The heat transfer coefficient, h, is assumed to be constant for boundary conditions of the third and fifth kind at $x = L$; and, the respective eigenvalues β_m are computed using equations $\beta_m \tan \beta_m = hL/k$ and $\beta_m \tan \beta_m = hL/k - \beta_m^2 (mc_p)_{\text{Al}}/(mc_p)_{\text{Delrin}}$. Then, the computer is programmed to provide power to the heater so that the applied power has the form

$$q = q_a + q^* \sin \nu t \tag{15}$$

where q_a and q^* are the mean value and amplitude of heat flux at the heater site. There will be a phase shift for the heat flux entering the Delrin plate due to the heat capacity of the heater. Also, the contact resistance can cause a reduction in the amplitude of the heat flux from q^* to q_0. However, it is shown that the only factor that determines the thermal diffusivity is the phase delay between the thermocouples, e.g., at $x = 0$ and another thermocouple. Figure 7 demonstrates the influence of different thermocouple locations on the results. The symbols in the figure represent the measured thermal diffusivity data using the time delay between a thermocouple signal at $x = 0$ and a thermocouple signal at another location; $x = 0.5\ L$, $0.84\ L$ or L. Also, they are for different mean plate temperatures and for boundary conditions of the third and fifth kind. The data show remarkably good agreement and the worst discrepancy is about ±10 percent.

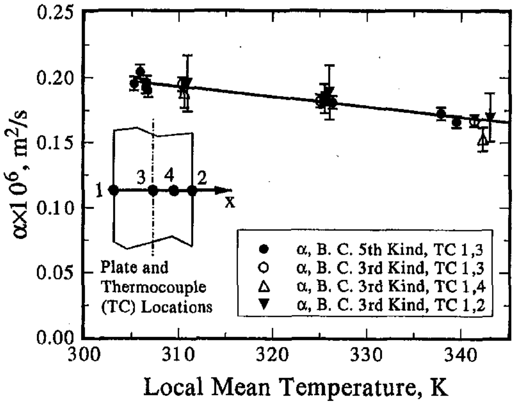

Fig. 7 Thermal diffusivity using signals at different locations and the best fit line, $\alpha \times 10^6 = d_1 + d_2T$ where $d_1 = 0.435$ m²/s and $d_2 = -7.80 \times 10 - 4$ with SD = ±0.004 m²/s

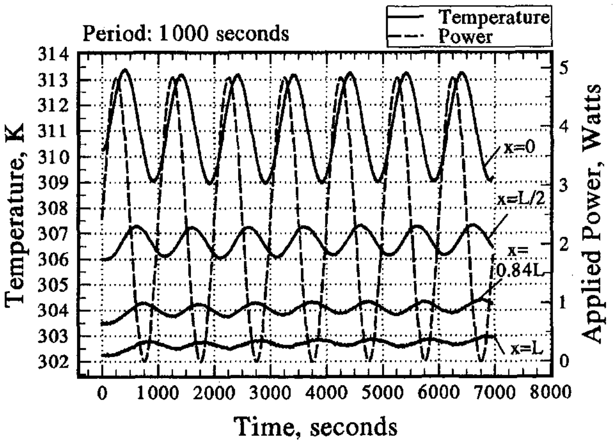

Fig. 8(a) A sample of measured temperature and heat flux for Delrin, $t_o = 1000$ s

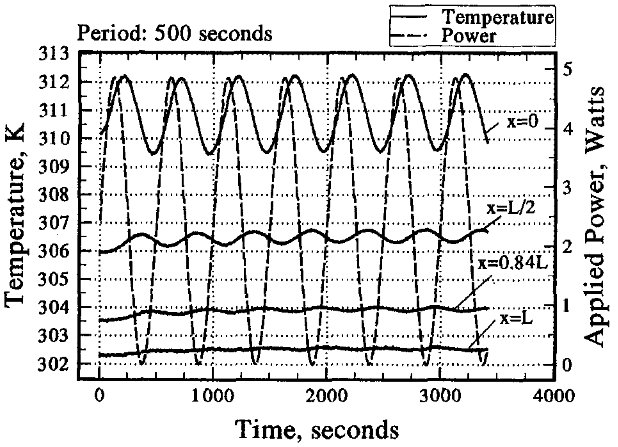

Fig. 8(b) A sample of measured temperature and heat flux for Delrin, $t_o = 500$ s

Two experiments for periodically applied power and the resulting temperature data are shown in Figs. 8(a) and 8(b). The periods for the data are 500 and 1000 seconds corresponding to $\nu = 0.004\pi$ and 0.002π rad/s and frequencies of $f = 0.002$ and 0.001 Hz. The time delay for each trace in Figs. 8(a) and 8(b) is calculated by curve fitting the data using basis functions $1, t, \ldots, \sin \nu t, \cos \nu t$. The value of the relative time delay, $\Delta t^*(x/L)/t_o$, provides input to a computer program that calculates ω. In numerical calculations, Eq. (12) provides the initial guess for an iterative method to obtain the value of ω and then $\alpha = \nu L^2/\omega$.

Figure 9 shows the influence of different signal frequencies on the results. From theoretical observations, at relatively high frequencies, a boundary condition at $x = L$ will not significantly affect the measured thermal diffusivity. In contrast, at a relatively low frequency, the temperature amplitude at $x = L$ is high and the boundary condition will affect the output of the thermocouple at other interior locations, e.g., $x = L/2$. The presence of the 0.0065 m thick aluminum plates, at $x = L$,

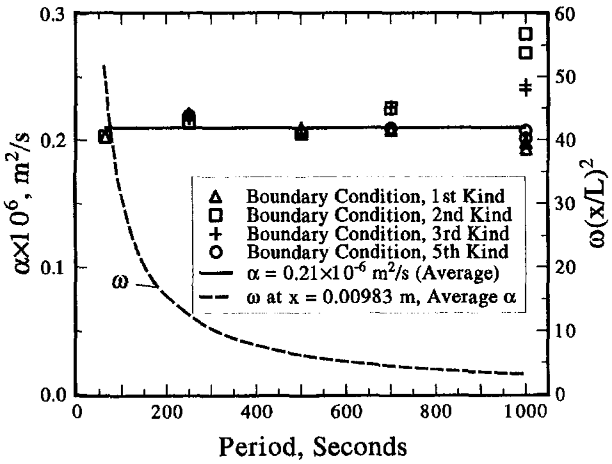

Fig. 9 Influence of period, t_o, or frequency, $f = 1/t_o$, on the measured thermal diffusivity using TC #1 and #3; see Table 2 for errors

permits evaluation of the boundary condition of the fifth kind (zero contact conductance) as well as boundary conditions of first, second, and third kinds. When $t_o = 1000$ seconds, the frequency is low and the temperature amplitude at $x = L$ is relatively large. At this frequency, only the boundary condition of the fifth kind provides the best accuracy; see circular data in Fig. 9. The data presented in Fig. 9, using TC# 1 and 3, are for periods of $t_o = 62.28$, 250, 500, 700, and 1000 seconds. When $t_o = 1000$ seconds, the value of $\nu(L - L/2)^2/\alpha$ is less than five and only the analysis using the boundary condition of the fifth kind (Beck et al., 1992) at $x = L$ produces consistent results. However, results using a boundary condition of the first kind are only slightly lower while convective and insulated boundary conditions provide higher results. For periods of 500 seconds and less, all approximations for the boundary condition at $x = L$ yield nearly identical results. Figures 8(*a*) and 8(*b*) confirm this since the temperature amplitude at $x = L$ is very small; negligible amplitude at $x = L$ implies that temperature is nearly uniform and boundary conditions of the first, second, or third kind are acceptable. This confirms the theoretical reasoning that there is a frequency range where a boundary condition will not influence the measurement results when using sensors away from this boundary. Accordingly, one can adjust the input frequency so that the thermal diffusivity data become insensitive to the effect of an imperfect boundary condition at a remote boundary. According to Fig. 9, the optimum frequency range, using thermocouples 1 and 3, is 0.0014 to 0.002 Hz.

In the presence of a heat sink at $x = L$, there is a temperature drop across the plate. To verify the quasi-steady condition, the thermal conductivity is calculated using temporal mean values of heat flux and temperature according to equation $q_a = k\Delta T_a/\Delta x$. The plus and diamond symbols in Fig. 10 represent the thermal conductivities computed from the temporal mean values. The open circles in the same figure are thermal conductivities computed under steady-state conditions when $q^* = 0$. The curve-fitted data plotted in Fig. 10 agree with a standard deviation of $SD = 0.0034$ W/m·K. A good agreement between steady-state and quasi-steady-state data validates the experimental accuracy. The agreement between the two sets of data is satisfactory. The measured thermal conductivity of Delrin is approximately 20 percent higher than the values reported in the literature (Hawthorne et al., 1969). The difference is due to variance in the number of polymer chains, in manufacturing, and in heat treating.

The heat flux modulation to accurately determine thermal diffusivity is useful for applications when it is impractical to obtain accurate temperature data. Such conditions exist when temperatures are extremely high or when materials are extremely thin. Measuring the thermal diffusivity by this method does not require accurately calibrated temperature since it only uses the phase shift, not the amplitude. Nonetheless, the method requires high heat flux amplitude and becomes demanding for thin films, especially when thermal conductivity is high. This point is demonstrated when this technique is used to measure the thermal diffusivity of 304 stainless steel.

Experiments Using 304 Stainless Steel. Type 304 stainless steel has well-known thermophysical properties, and a moderately high thermal conductivity sought to demonstrate the peculiarities of this measurement technique. The experiment using Delrin is repeated except the Delrin plates are replaced by two 304 stainless steel plates, each 0.01275 m thick. Thermocouples, as thin as 40 gauge, placed at the surfaces of a plate next to the heater were influenced by the heater and showed temperature differences that are too high for reasonable accuracy. To improve the measurement accuracy, thermocouples were embedded within the stainless steel plates. The main plate has three embedded thermocouples; one at $x = 0.00256$ meter (TC#1) from the hot surface, one at the center (TC#2), and one at $x = 0.01019$ meter (TC#3). The other stainless steel plate has a centrally located thermocouple, mainly to verify the symmetry conditions of the temperature field. If the thermal diffusivity is of the order of 4×10^{-6} m²/s, then for $\omega = 5$ the value of ν is 0.123 rad/s and the corresponding period is 50 seconds. A periodic heat flux within this time period is not difficult to implement. Figure 11(*a*) shows temperature traces at three thermocouple sites when $t_o = 50$ seconds. When $\omega \cong 5$, the amplitude of the temperature at the thermocouple site farthest from the heater is only 0.175 K. As the period of harmonically varying heat flux reduces to 30 seconds, see Fig. 11(*b*), the amplitude reduces to 0.071 K. Accordingly, the temperature amplitude at the surface farthest from the heater is negligibly small; hence, a boundary condition of the third kind with a constant heat transfer coefficient at $x = L$ is a suitable approximation.

At the sample's mean temperature, Table 1 contains the measured values of thermal diffusivity, assuming a boundary condition of the second kind at $x = L$. Also, this table contains the measured values of thermal diffusivity for the same data but uses a boundary condition of the third kind at $x = L$. The deviation between the two sets of data is within the expected deviations of experimental data discussed earlier. The numbers included in the parentheses in Columns 3 and 4 are the values of ω for the corresponding thermal diffusivity data. There is a remarkable agreement between thermal diffusivity data when ω values are in the neighborhood of 5. The temperature data at $x = L$, Fig. 11(*b*), are noticeably noisier than corresponding

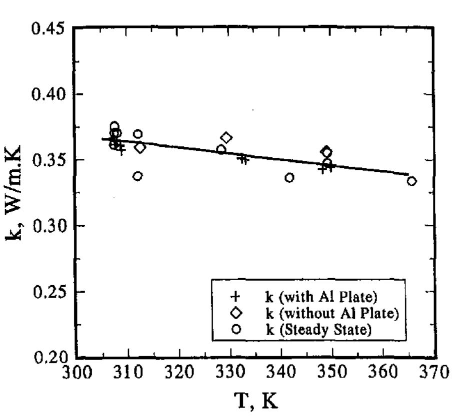

Fig. 10 A comparison of measured thermal conductivity of Delrin using mean values of periodic signals and steady-state measurements and best-fit line, $k = d_3 + d_4T$ where $d_3 = 0.38$ W/m·K and $d_4 = -4.52 \times 10^{-4}$ W/m·K²

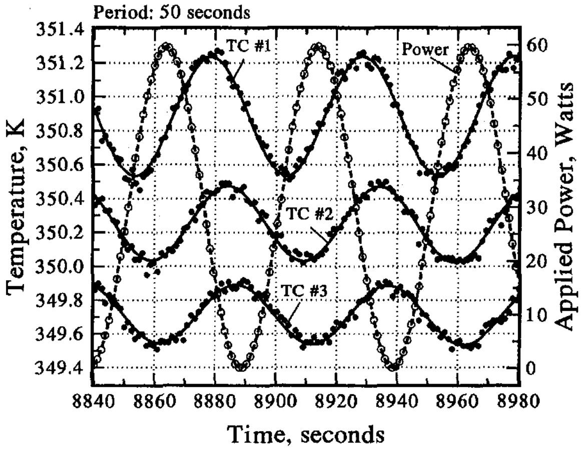

Fig. 11(*a*) A sample of measured temperature and heat flux for 304 stainless steel, t_o = 50 s

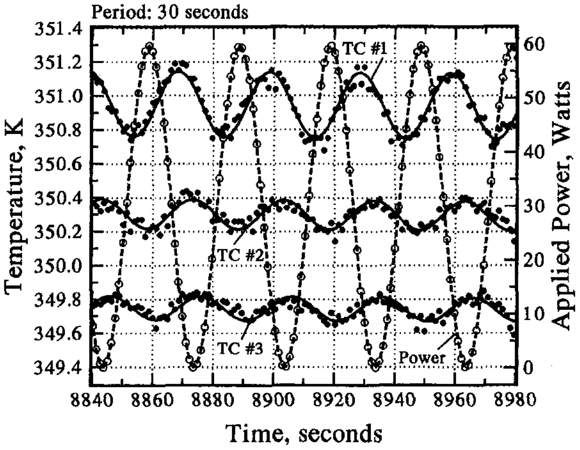

Fig. 11(*b*) A sample of measured temperature and heat flux for 304 stainless steel, t_o = 30 s

data in Fig. 11(*a*). The noisy data is likely to increase the error in the measured values of thermal diffusivity when $t_o = 20$ and 30 s; further discussion of errors is in a separate section. The data in column 4, for t_o of 40, 50, and 60 seconds, agree well with the reported value of thermal diffusivity (Incropera and DeWitt, 1990), column 6, especially for the more realistic boundary condition of the third kind at $x = L$. The thermal diffusivity values, when $\omega \leq 6.5$, are within 4.4 percent of available data (Incropera and DeWitt, 1990). To check the robustness of the measured temperature data, the thermal conductivity is computed using mean temperature and mean heat flux values. The measured values are lower than expected, within $k = 11.9$ to 12.9 W/m·K. The error is likely due to transient noise in the periodic data, discussed in the next section.

Table 1 Measured thermal diffusivity and thermal conductivity

Period, seconds	Mean Temp., K	$\alpha(\omega)\times10^6$, m^2/s		$\alpha\times10^6$ m^2/s†
		BC 2nd Kind	BC 3rd Kind	
20	346.8	3.34 (15.3)	3.24 (15.3)	4.16
30	350.1	3.72 (9.14)	3.59 (9.48)	4.18
40	347.0	4.26 (6.00)	4.01 (6.36)	4.17
40	349.6	4.59 (5.56)	4.36 (5.85)	4.18
50	345.7	4.63 (4.42)	4.29 (4.76)	4.16
50	350.1	4.35 (4.69)	4.14 (4.93)	4.18
60	346.9	4.59 (3.71)	4.25 (4.00)	4.17

† Incropera and DeWitt (1990)

To verify this, the steady-state technique, $q^* = 0$, is also used to measure the thermal conductivity of the test samples. The measured thermal conductivity increased to 14.2 W/m·K but remains nine percent lower than the reported data (Incropera and DeWitt, 1990).

Error Analysis

An important feature of using phase modulation is that the temperature calibration has no effect on the results. The location where the temperature effect is measured has significant effect on the computed thermal diffusivity since α is related to L^2. The determination of the exact sensor location depends on the specific experiment and material being used, e.g., front and back surfaces of a thin film. In this study, it is assumed that the thermocouple is at the geometrical center of the hole drilled by a milling machine. The recorded coordinate of the thermocouple is verified by examining the temperature linearity prior to the onset of experimentation.

An important and interesting factor that is inherent in the measurement of phase delay is the random error. This becomes significant as the amplitude of temperature decreases. One can show that the error in phase delay is directly related to the error in the measured sensor signal. For a harmonic temperature signal $T = \psi \sin(\omega t + \varphi)$, any change in φ and ψ influences the value of T. Differentiating T and then casting the results in the difference form shows

$$\Delta T = \frac{\partial T}{\partial \psi}\Delta\psi + \frac{\partial T}{\partial \varphi}\Delta\varphi$$

$$= [\sin(\omega t + \varphi)]\Delta\psi + [\psi \cos(\omega t + \varphi)]\Delta\varphi \qquad (16)$$

when $\Delta\psi$ and $\Delta\varphi$ are small. Since the phase is computed by setting $\sin(\omega t + \varphi) = 0$, then

$$\Delta\varphi = \Delta T/\psi. \qquad (17)$$

This simple relation is a primary contributor to the error in thermal diffusivity data.

In numerical processing of the data for phase and amplitude, the standard deviation describes the data noise. Based on Eq. (17), the standard deviation represents the error in the phase angle. Table 2 shows a sample of errors for Delrin. Measured temperature data, similar to those in Figs. 8 and 11, were curve fitted to extract temperature amplitude and phase angle, columns 3 and 5. The standard deviation of the curve fit is in column 4. When the temperature amplitude is much larger than the standard deviation, the random error is quite small. Only data that show a signal amplitude larger than the standard deviation were processed. For example, the data for TC#2 and 4 when t_o = 250 s show the effect of the aluminum plate at $x = L$ and they are not suitable for processing. Depending on the frequency and amplitude of the input signal, the error with 95 percent

Table 2 Estimated error in Delrin sample data at thermocouple locations for different frequencies, $f = 2\pi/t_o$

Period, t_o, s	TC#	Amplitude Degree K	SD, K	φ(x), s	Estimated Error%
1000	1	2.075	0.020	1.06	2
	2	0.111	0.018	3.57	9
	3	0.571	0.016	2.28	2.4
	4	0.231	0.016	3.07	4.4
700	1	1.681	0.019	1.13	3
	2	0.0536	0.016	4.08	14
	3	0.366	0.013	2.60	2.6
	4	0.131	0.014	3.51	6
250	1	0.805	0.018	1.29	4
	2	0.0022	0.014	6.80	190
	3	0.0646	0.013	3.73	10
	4	0.0128	0.012	5.44	34

probability, column 6, varies over a broad range, typically between 2 to over 100 percent. The error in the values of thermal diffusivity is indicated by error bars in Fig. 7. The data are curve fitted to ascertain systematic and other random errors. The solid line fits the experimental data with standard deviation of 0.004 between 305 to 345 K, and it is within the range of error bars for most of the data. Equation (17) appears to over estimate the error when ψ is larger than but of the order of random noise. Perhaps the elimination of higher order terms in Eq. (16), when $\Delta\varphi$ is large, is responsible for this effect. Signals from thermocouples 1 and 3 were used to evaluate data shown in Fig. 9. Except for the low range of periods, the error is less than the size of the data shown in the figure.

In the evaluation of thermal diffusivity for Delrin, a power variation between 0 and 4.8 Watts produces temperature amplitudes of larger than 1.0 K. However, for 304 stainless steel, according to Fig. 11, for a peak power of 60 Watts, the largest amplitude is 0.35 K in Fig. 11(*a*) and 0.19 K in Fig. 11(*b*). Again, the standard deviation of temperature data is a measure of random noise. It is used to calculate the error in phase angle according to Eq. (17). The estimated errors due to random noise and system limitation for t_o = 20, 30, 40, 50, and 60 seconds data in Table 1 are 30 percent, 20 percent, 12 percent, 9.5 percent, and 8.9 percent, respectively. These estimated errors are remarkably consistent with the trend of data in Table 1, column 4, and their agreement with published data. The standard deviation of the curve fit to extract amplitude and phase angle varies between 0.026 K and 0.04 K, larger than those for Delrin for the same mean temperatures (see Table 2). This is responsible for the weak comparison between the thermal conductivity data using the mean periodic temperature with the steady-state measurements and indicates a larger systematic error due to the limitation of system resolution.

Conclusion and Remarks

The technique for measuring thermal conductivity and thermal diffusivity presented here is broadly classified as an inverse method. The experimental data only addresses the measurement of thermal diffusivity using the change between the phase angles at two different sites. The analysis shows that the specific heat is obtainable from the amplitude information. This requires an accurate knowledge of the input signal. The input signal could be surface heat flux or volumetric heat source. Except for the error analysis, the amplitude is only used in the Appendix to provide system information.

When it is not possible to use conventional measurement techniques, a measurement of the change in the phase angle can be used to produce reasonably accurate thermal diffusivity data from imprecise information. To properly design an experiment requires a knowledge of the theoretical studies presented here. Primarily, the sensitivity data serve as a guide when designing a new experiment. The thermal diffusivity is obtainable if the temperature produces a measurable, periodic effect at the surface. Since only the phase shift is used, it is not necessary to know the actual value of the temperature. The sensitivity and other mathematical analyses indicate a frequency range that can improve the accuracy of data. A boundary condition can severely influence the results unless the measurements are made away from that boundary.

According to Eq. (8), the value $\mathrm{Ampl}[\rho c_p \nu L(T - T_i)/q_0]$, for a given value of ω, is fixed at any given spatial location. Since the thermal diffusivity of stainless steel is much higher than Delrin, for the same value of ω, the selected amplitude of heat flux must be substantially higher to provide detectable temperature signals. It then follows that for thin materials with higher thermal conductivities, an experiment of this type requires heat flux with high amplitude.

Acknowledgment

The authors wish to acknowledge the support of the Mechanical and Aerospace Engineering Department at the University of Texas at Arlington and the National Science Foundation, Grant No. CTS-9400647.

References

Ångström, A. J., 1861, "Neue Methode, das Wärmeleitungsvermögen der Körper zu bestimmen," *Annalen der Physik und Chemie, Lpz,* Vol. 114, pp. 513–530.

Beck, J. V., Cole, K. D., Haji-Sheikh, A., and Litkouhi, B., 1992, *Heat Conduction Using Green's Functions,* Hemisphere, Washington, DC.

Carslaw, H. S., and Jeager, J. C., 1986, *Conduction of Heat in Solids,* 2nd Ed., Clarendon Press, Oxford, UK.

Caulk, D. A., 1990, "A Method for Analyzing Heat Conduction With High Frequency Boundary Conditions," ASME JOURNAL OF HEAT TRANSFER, Vol. 112, pp. 280–287.

Feldman, A., Frederikse, H. P. R., and Ying, X. T., 1990 "Thermal Wave Measurements of the Thermal Properties of CVD Diamond," *Diamond Optics II,* A. Feldman and S. Holly, eds., Proceedings of the 1989 SPIE—The International Society for Optical Engineering, Vol. 1146, pp. 78–84.

Hansen, E. R., 1975, *A Table of Series and Products,* Prentice-Hall, Englewood Cliffs, N.J.

Hawthorne, J. M., Heffelfinger, C. J., and Knox, K. L., 1969, "Polyester Films," *Encyclopedia of Polymer Science,* H. F. Mark and N. G. Gaylord, eds., Vol. 11, Interscience, New York, p. 42.

Incropera, F. P., and DeWitt, D. P., 1990, *Fundamentals of Heat and Mass Transfer,* John Wiley and Sons, New York.

Khedari, J., Benign, P., Rogez, J., and Mathieu, J. C., 1992, "A Solution of the Heat Conduction Equation in the Finite Cylinder Exposed to Periodic Boundary Conditions: The Case of Steady Oscillation and Constant Thermal Properties," *Proc. Roy. Soc. London,* Vol. A438, pp. 319–329.

Rouault, H., Khedari, J., Arzoumanian, C., and Rogez, J., 1987, "High-Temperature Diffusivity Measurements by Periodic Stationary Method," Tenth European Conference on Thermophysical Properties, *High Temperature-High Pressure,* Vol. 19, No. 4, pp. 357–363.

Sextro, G., 1989, "Physical Constants of Poly(oxymethylene)," *Polymer Handbook,* 3rd ed., J. Brandrup and E. H. Immergut, eds., John Wiley and Sons, New York.

Zubair, Syed M., and Chaudhry, M. Aslam, 1995, "Heat Conduction in a Semi-Infinite Solid Subject to Steady and Non-Steady Periodic-Type Surface Heat Fluxes," *Int. J. Heat Mass Transfer,* Vol. 38, No. 18, pp. 3393–3397.

APPENDIX

It is possible to predict the contact resistance between the heater and plates, and the value of $C_h = (mc_p)$ for the heater assembly using a simplified analysis. One can conveniently compute q_0 and the phase delay between applied power and heat flux at $x = 0$. Both amplitude and phase information can produce the value of contact resistance between the heater assembly and the plates in addition to the value of mass times specific heat of the heater assembly. Assuming the spatial temperature variation in the heater assembly is negligible, one can use the fluctuating component of heat flux and write

$$q^* \sin \nu t - q_0 \sin(\nu t - \varphi^*) = C_h \frac{dT^*}{dt}, \qquad \text{(A1)}$$

where q_0 is the amplitude of heat flux entering the plate, φ^* is the phase shift between applied power and power transferred to the plate, and T^* is the temperature of the heater. Integration of Eq. (A1) yields

$$T^* = -\frac{q^*}{\nu C_h}\cos \nu t + \frac{q_0}{\nu C_h}\cos(\nu t - \varphi^*) + T_{ah} \qquad \text{(A2)}$$

where T_{ah} is the constant of integration equal to the temporal mean temperature of the heater over one period. The contact conductance, C_t is computed from the following relation between amplitudes:

$$q_0 \sin(\nu t - \varphi^*) = C_t \times \left[-\frac{q^*}{\nu C_h}\cos \nu t \right.$$

$$\left. + \frac{q_0}{\nu C_h}\cos(\nu t - \varphi^*) - T_{p0}\sin(\nu t - \varphi^*) \right] \qquad \text{(A3)}$$

where $\varphi_0 = \varphi^* + \varphi(0)$ and $T_{p0} = \mathrm{Ampl}[T(0, t)]$. After matching the amplitudes and phase shifts, both sides of Eq. (A3) yield,

$$C_t = q_o \Big/ \left[\left[-T_{a0} \cos(\varphi_0) + \frac{q_0}{\nu C_h} \sin(\varphi^*) \right]^2 + \left[\frac{q}{\nu C_h} - \frac{q_0 \cos(\varphi^*)}{\nu C_h} - T_{a0} \sin(\varphi_0) \right]^2 \right]^{1/2} \quad \text{(A4)}$$

and

$$C_h = \frac{q^* - q_0 \cos(\varphi^*) - q_0 \sin(\varphi^*) \tan(\varphi^*)}{\nu T_{a0}[\sin(\varphi_0) - \cos(\varphi_0) \tan(\varphi^*)]} . \quad \text{(A5)}$$

The average values for contact conductance and $C_h = mc_p$ of the heater assembly are 210 W/m$^2\cdot$K and 40 J/K, respectively. They were computed using the data for Delrin.

Frequency Response Characteristics of an Active Heat Flux Gage

C. Dinu
e-mail: cdinu@ces.clemson.edu

D. E. Beasley
e-mail: goblue@ces.clemson.edu,
Mem. ASME.

R. S. Figliola
e-mail: fgliola@ces.clemson.edu,
Fellow ASME.

Thermal-Fluid Sciences
Research Laboratory,
School of Mechanical and
Industrial Engineering,
Clemson, SC 29634

The transient response and frequency response of a constant-temperature platinum film gage are computationally modeled for application to heat flux measurement. The probe consists of a thin platinum film (sensor) deposited on a Pyrex substrate, and coated with aluminum oxide. The probe is exposed to a convective environment, and the power required to maintain the sensor at a constant temperature is a direct indication of the local, instantaneous heat transfer rate. In application, the probe is mounted in a heated, high thermal conductivity material, creating an isothermal heat transfer surface. A two-dimensional numerical model was developed to represent the sensor, the Pyrex substrate and the coating. Ideally, the probe would be operated with the platinum at identically the same temperature as the isothermal surface. In the present study, the effects of non-ideal operating conditions, resulting in differences between the sensor and surface temperature, are examined. Frequency response characteristics are presented in a nondimensional form. The results of this modeling effort clearly indicate the importance of precise control over the sensor temperature in employing the present method for heat flux measurement. With the sensor temperature equal to the isothermal surface temperature, the probe calibration is insensitive to the heat transfer rate over a wide range of heat transfer coefficients. However, a 0.5°C difference between the sensor and surface temperatures yields a change in the calibration of approximately 20 percent over a range of heat transfer coefficient of 500 W/m^{2}K. At an input frequency of 10 Hz and an average heat transfer coefficient of 175 W/m^{2}K, amplitude errors increase from 3 percent to 35 percent as the temperature difference changes from zero to 1°C. These results are useful guide to calibration, operation, and data reduction in active heat flux measurement.

Introduction

The measurement of a time-varying local heat flux presents significant challenges in probe design and selection, calibration, and data analysis. Passive gages that sense temperature gradient have experienced recent advances, and inverse methods for heat flux measurement are common. Current heat flux measurement techniques have been described in the review by Diller (1995). In addition to these passive methods, heat flux can also be measured by employing a probe employing a thin-film sensor operated in a self-heated, constant temperature mode, in a manner similar to a hot-film anemometer. Such a probe can be mounted flush with a heated surface, thereby allowing for the possibility of creating an isothermal heat transfer surface. This active measurement technique has been employed in the Thermal-Fluid Sciences Laboratory at Clemson, primarily for the measurement of heat flux from a submerged surface to a fluidized bed.

In previous papers, theoretical limits were established for active heat flux probes employed in the measurement of both constant and time-varying heat fluxes (Beasley and Figliola, 1988; Figliola, Swaminathan and Beasley, 1993). Liang and Cole (1992) examined the transient response of a heated film sensor under unsteady conditions, and Park and Cole (1994) investigated substrate effects in constant current operation.

The issues which arise in the measurement of heat flux using a heated gage include the calibration of the gage, the bandwidth or frequency response of the measurement system, and the ability to control the temperature of the platinum film and the substrate. In previous studies, the steady-state calibration of a film sensor for heat flux measurement has been expressed in terms of the effective area of the probe. This concept provides a physical interpretation of the heat flow and resulting data reduction technique required for accurate measurement of heat flux using this technique. Further study examined the step response and frequency response of the probe in the case when the platinum sensor temperature and the heat transfer surface temperature were exactly equal. In practice, this operating condition cannot be achieved. Figliola and Swaminathan (1996) examined the steady response of a local heat flux probe under nonideal operating conditions.

The present paper examines in detail the calibration, operation, and frequency response characteristics of a heated platinum film probe for the measurement of heat flux. The probe is assumed to be operating under the limitations associated with actual implementation of the measurement technique using a constant temperature bridge anemometer. It will be assumed in the present discussion that the heat flux probe is mounted in a heat transfer surface, and that the objective is to measure time-varying convective heat flux from this constant temperature surface. Ideally, the platinum film and the heat transfer surface would be at identically the same temperature during measurement. However, due to uncertainties in the temperature-resistance calibration of the sensor, and the inability to create a perfectly isothermal heat transfer surface, the platinum film must be operated at a temperature slightly higher than the heat transfer surface to ensure bridge stability. As such, the power required to maintain the platinum film at a constant temperature is strongly dependent on the amount of energy that flows to or from the sensor as a result of temperature differences between the platinum film and the heat transfer surface. The sensitivity of the measurement system is greatly reduced as the heat transfer to

---

Contributed by the Heat Transfer Division for publication in the JOURNAL OF HEAT TRANSFER. Manuscript received by the Heat Transfer Division, May 16, 1997; revision received, Mar. 27, 1998. Keywords: Analog Techniques, Instrumentation, Measurement Techniques. Associate Technical Editor: M. Kaviany.

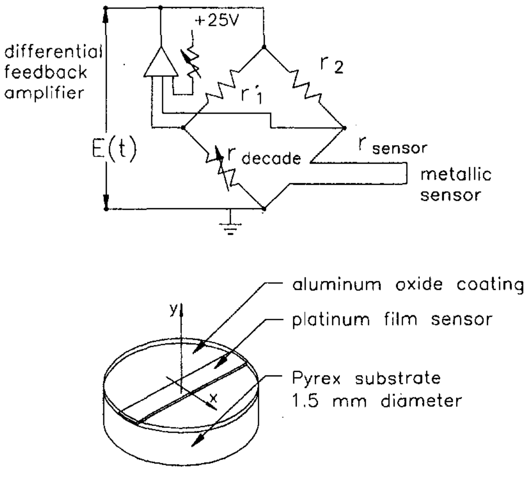

Fig. 1 Schematic representation of platinum film probe geometry and constant temperature bridge circuit

or from the probe becomes significant compared to the heat transfer to the convective environment. The present paper examines the operation of a representative probe under conditions where there are experimental uncertainties in the sensor temperature. A two-dimensional numerical model is formulated and a reasonable range of the design modifications described. Steady response, step response, and frequency response are discussed.

Operation and Calibration

A brief description of the operation and calibration of a platinum film probe for heat flux measurement will be provided. In the applications under consideration here, a probe coated with aluminum oxide is employed. Such a probe and the associated electronics are shown in Fig. 1. The probe is mounted flush with the heat transfer surface, and appropriate electrical connections provided. Clearly, during calibration it is desired to determine the steady-state ratio of the bridge voltage and the local heat transfer coefficient. The following equation describes such a relationship in terms of the effective area, for a typical constant-temperature anemometer bridge circuit,

$$h(t) = \frac{E(t)^2 r_S}{(r_S + r_b + r_c)^2 A_{\rm eff}(T_S - T_\infty)} . \tag{1}$$

Approaches to determining the static calibration, in terms of the effective area, of such probes include using stagnation air flows or radiative techniques. An approach which has proved successful in this laboratory for time-resolved heat flux measurement equates the time-average value of heat transfer measured independently to the average signal from the constant-temperature bridge circuit.

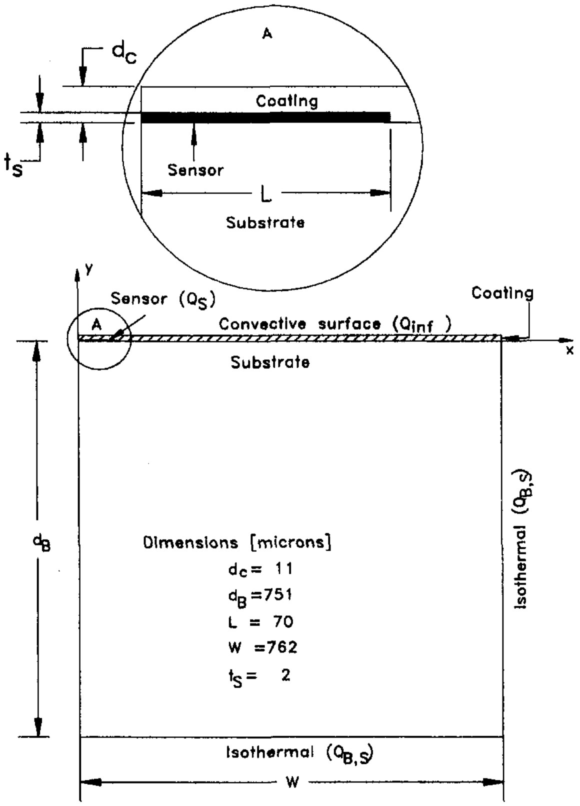

Fig. 2 Two-dimensional model of heat flux probe

Modeling

The fundamental effects of temperature differences between the sensor and the heat transfer surface cannot be identified experimentally, but are essential to operation for the present technique. The nomenclature associated with probe geometry can be seen in Fig. 2. Defining the following nondimensional

Nomenclature

$A_{\rm eff}$ = effective area of heat flux probe (m^2)
A_S = sensor area (m^2)
Bi_C = Biot number
d_C = thickness of the coating (μm)
d_B = thickness of the substrate (μm)
$E(t)$ = time-varying bridge circuit voltage (Volts)
Fo = Fourier number
f = frequency (Hz)
h = convective heat transfer coefficient (W/m^{2}K)
k = thermal conductivity (W/mK)
L = length of the sensor (μm)
m = nondimensional length of the probe
m_S = nondimensional thickness of the sensor
m_C = nondimensional thickness of the coating
m_B = nondimensional thickness of the substrate
$\dot{Q}_\infty$ = convective heat transfer rate (W)
$\dot{Q}_{B,S}$ = heat transfer rate to the substrate (W)
$\dot{Q}_S$ = heat transfer rate from the sensor (W)
r_b = bridge circuit equivalent resistance (Ω)
r_c = cable resistance (Ω)
r_s = sensor resistance (Ω)
t = time (sec)
T_B = temperature in the substrate (°C)
$T_{B,S}$ = temperature at the substrate boundary (°C)
T_C = temperature in the coating (°C)
T_S = sensor temperature (°C)
t_S = thickness of the sensor (μm)
T_∞ = average temperature of the convective environment (°C)
W = width of the probe (μm)
x = Cartesian coordinate
$\bar{x}$ = nondimensional Cartesian coordinate
y = Cartesian coordinate
$\bar{y}$ = nondimensional Cartesian coordinate
α = thermal diffusivity (m^2/s)
Θ = nondimensional temperature

parameters (with the subscripts C and B referring to the coating and substrate, respectively),

$$\bar{x} = \frac{x}{L}; \quad \bar{y} = \frac{y}{d_C}; \quad \Theta_C = \frac{T_C - T_S}{T_S - T_\infty};$$

$$\Theta_B = \frac{T_B - T_S}{T_S - T_\infty}; \quad \Theta_{B,S} = \frac{T_{B,S} - T_S}{T_S - T_\infty} \tag{2}$$

$$\mathrm{Fo} = \frac{\alpha_C t}{d_C^2}; \quad \mathrm{Bi}_C = \frac{h(t) d_C}{k_C}; \quad m_s = \frac{t_S}{d_C};$$

$$m_C = \frac{d_C}{L}; \quad m_B = \frac{d_B}{L}; \quad m = \frac{W}{L} \tag{3}$$

the governing equations, and initial and boundary conditions are

$$\frac{\partial \Theta_C}{\partial \mathrm{Fo}} = m_C^2 \frac{\partial^2 \Theta_C}{\partial \bar{x}^2} + \frac{\partial^2 \Theta_C}{\partial \bar{y}^2} \tag{4}$$

$$\Theta_C(0 \le \bar{x} \le 1, 0 \le \bar{y} \le m_S, \mathrm{Fo}) = 0 \tag{5}$$

$$\frac{\partial \Theta_C(\bar{x} = 0, m_S < \bar{y} \le 1, \mathrm{Fo})}{\partial \bar{x}} = 0 \tag{6}$$

$$\Theta_C(\bar{x} = m, 0 \le \bar{y} \le 1, \mathrm{Fo}) = \Theta_{B,S} \tag{7}$$

$$-\frac{\partial \Theta_C(0 < \bar{x} < m, \bar{y} = 1, \mathrm{Fo})}{\partial \bar{y}} = \mathrm{Bi}_C[\Theta_C(0 < \bar{x} < m, \bar{y} = 1, \mathrm{Fo}) + 1]. \tag{8}$$

For the substrate, analogous expressions are

$$\frac{\alpha_C}{\alpha_B} \frac{\partial \Theta_B}{\partial \mathrm{Fo}} = m_C^2 \frac{\partial^2 \Theta_B}{\partial \bar{x}^2} + \frac{\partial^2 \Theta_B}{\partial \bar{y}^2} \tag{9}$$

$$\Theta_B(0 \le \bar{x} \le m, \bar{y} = -m_B, \mathrm{Fo}) = \Theta_{B,S} \tag{10}$$

$$\frac{\partial \Theta_B(\bar{x} = 0, -m_B < \bar{y} < 0, \mathrm{Fo})}{\partial \bar{x}} = 0 \tag{11}$$

$$\Theta_B(\bar{x} = m, -m_B \le \bar{y} \le 0, \mathrm{Fo}) = \Theta_{B,S} \tag{12}$$

$$\frac{\partial \Theta_C(1 < \bar{x} < m, \bar{y} = 0, \mathrm{Fo})}{\partial \bar{y}} = \frac{k_B}{k_C} \frac{\partial \Theta_B(1 < \bar{x} < m, \bar{y} = 0, \mathrm{Fo})}{\partial \bar{y}}. \tag{13}$$

In these equations the following material properties were used $k_S = 1.2$ W/m-K, $k_C = 19.2$ W/m-K, $\alpha_C = 8 \times 10^{-6}$ m^2/s and $\alpha_S = 61 \times 10^{-6}$ m^2/s.

The nondimensional governing equations and boundary conditions were discretized based on a control-volume approach that yielded a fully implicit set of difference equations to represent the temperature distribution in the coating and the substrate. Variable grid spacings in both directions were employed, with much finer grid spacings used in the areas of highest temperature gradients. The resulting matrix system was solved using matrix operations in the software Matlab, which uses a Gauss elimination numerical technique to perform both left and right matrix division. When these operations are performed, a test for ill-conditioning is applied and in the case of an ill-conditioned system warning messages are displayed. No ill-conditioning problems were detected.

The accuracy of the present numerical solution was assessed in several ways. Overall energy balances for the steady-state solutions allowed comparison of the convective heat transfer rate with the heat transfer rates at the boundaries of the probe, and that entering the domain from the sensor. The energy balance was accurate to approximately ±4–6 percent for the grid used to generate the present results (1496 nodes) with the convective heat flux as a reference. Comparison between the present formulation and results from previous studies confirmed the accuracy of the step-response for ideal boundary conditions where the temperature of the sensor and the heat transfer surface were equal. Grid independence of the transient and steady temperature fields was also examined. Very small absolute and relative errors were observed in the temperature field. The heat fluxes were more sensitive to the grid refinement. The overall heat transfer rate balance was considered as appropriate to evaluate the error levels with the convective heat transfer rate as a reference. Table 1 presents the predicted nondimensional heat transfer rates coming from the substrate, supplied by the sensor, and removed by the convective fluid, for $\Theta_{B,S} = 0$ and $\mathrm{Bi}_C = 10^{-4}$. The numerical results are dependent on the grid size and on the distribution of the grid nodes within the computational domain. It was decided that the grid with 1496 nodes leads to a good compromise between the numerical accuracy and the computational effort. Most of the results presented here were performed on a Sparc 20 workstation, with a typical run requiring three minutes for a steady-state analysis and about 20 hours for a transient case as that shown in Fig. 8. The effect of grid refining on the predicted results under transient conditions was also investigated. Predicted amplitude distortion and phase shift were within two percent for all grids presented in Table 1. For $\mathrm{Bi}_C = 3 \times 10^{-4}$ the error decreased from nine percent to two percent as the number of grid points increased from 624 to 1496. However, these estimations are greatly dependent on the Biot number and six percent was a representative error for the range of Biot number investigated here.

The Effective Probe Area. Let us denote by $\dot{Q}_{B,S}$ the heat transfer rate entering or leaving the computational domain at the interface with the isothermal heat transfer surface. Taking as positive the heat flux entering the domain, the heat transfer rate balance over the whole domain gives

$$\dot{Q}_S + \dot{Q}_{B,S} + \dot{Q}_\infty = 0. \tag{14}$$

Then h can be expressed as

$$h = \frac{\dot{Q}_S}{A_{\mathrm{eff}}(T_S - T_\infty)} = \frac{-\dot{Q}_\infty(1 + \dot{Q}_{B,S}/\dot{Q}_\infty)}{A_{\mathrm{eff}}(T_S - T_\infty)}. \tag{15}$$

In a numerical simulation, with h taken as an input, and from the above equation, A_{eff} is evaluated as

$$A_{\mathrm{eff}} \equiv \frac{\dot{Q}_S}{h(T_S - T_\infty)} \equiv \frac{-\dot{Q}_\infty(1 + \dot{Q}_{B,S}/\dot{Q}_\infty)}{h(T_S - T_\infty)}. \tag{16}$$

When a numerical algorithm is applied to solve the analytical model, the three heat fluxes involved in this equation are approximately computed. If we designate by a prime these approximate quantities, the effective probe area can be expressed as

$$(A'_{\mathrm{eff}})_S = \frac{\dot{Q}'_S}{h(T_S - T_\infty)} \tag{17}$$

or

$$(A'_{\mathrm{eff}})_B = \frac{-\dot{Q}'_\infty(1 + \dot{Q}'_{B,S}/\dot{Q}'_\infty)}{h(T_S - T_\infty)}. \tag{18}$$

The effective area is computed from the arithmetic average of the two values:

$$(A'_{\mathrm{eff}})_{\mathrm{ave}} = \frac{(A'_{\mathrm{eff}})_B + (A'_{\mathrm{eff}})_S}{2}. \tag{19}$$

Results

The present results are computed with the TSI Model 1471 platinum film probe as the nominal case. The dimensions of this probe are shown in Figs. 1 and 2. Figure 3 shows nondimen-

Table 1 The influence of the grid refinement on the predicted nondimensional heat fluxes

Mesh	No. of grid points	Sensor $\frac{\dot{Q}_S}{A_S h(T_S - T_\infty)}$	Substrate $\frac{\dot{Q}_{B,S}}{A_S h(T_S - T_\infty)}$	Convective boundary $\frac{\dot{Q}_\infty}{A_S h(T_S - T_\infty)}$	Error [%] $\frac{\dot{Q}_S + \dot{Q}_{B,S} + \dot{Q}_\infty}{\dot{Q}_\infty} x100$
26x24	624	3.933	5.917	-10.718	8.1
35x26	910	3.976	5.955	-10.713	7.3
35x34	1190	4.130	5.942	-10.717	6.5
44x34	1496	4.223	5.958	-10.715	5.0
39x50	1950	4.234	5.962	-10.716	4.9
43x54	2322	4.314	5.970	-10.715	4.0
50x60	3000	4.331	5.968	-10.716	3.9

sional isotherms in the probe under the heat transfer conditions described in the caption. Energy flows from the sensor to the substrate and along the coating. It can be seen that the minimum temperature is located on the convective boundary as expected. Also it should be noted that a portion of the energy removed by the convective fluid comes from the heat transfer surface through the substrate. Therefore the heat flux at the convective boundary consists of two parts: the heat flux supplied (partially) by the sensor and the net heat flux coming from the substrate. The ratio between the two components varies with the temperature difference between the sensor and the heat transfer surface, the convective heat transfer conditions, and the size of the probe. It should be noted, however, that only the sensor power is measured to provide a heat flux signal. This complexity of the heat transfer suggests that precise control of the sensor and heat transfer surface temperatures are imperative during calibration. In the present model, these heat transfers can be determined explicitly, and used as described in Eqs. (15), (18), and (19). When time-varying conditions are present at the convective boundary, the calibration is yet more difficult. The precise control over the sensor and heat transfer surface temperature eliminates one of those dependencies, and its importance is apparent. The figure clearly suggests that the effective area of the probe will be significantly larger than the sensor area. In this case the nondimensional effective area of the probe is 5.1.

For this measurement technique to be effectively employed, it is necessary that the probe be operated under conditions where the calibration is not greatly affected by the heat transfer rate. Figure 4 illustrates the effective area dependence on the coating Biot number, with the nondimensional temperature between the sensor and the heat transfer surface as a parameter. As Bi_C increases, the sensitivity of the effective area to the rate of heat transfer decreases. For the nominal probe, a value of Bi_C of 0.0001 corresponds to a heat transfer coefficient of 175 W/m^{2}K. Figure 5 illustrates the linear dependence of the effective area on the temperature difference between the sensor and the heat transfer surface. These results are similar to those obtained by Figliola and Swaminathan (1996) for a larger probe design. As the convective heat transfer rate increases, corresponding to an increasing Bi_C, the sensitivity of the effective area to $\Theta_{B,S}$ is reduced. In the limit of ideal boundary conditions ($\Theta_{B,S} = 0$) the probe calibration is insensitive to the heat transfer rate over a wide range of the heat transfer coefficient. This plot also shows the necessity of controlling as precisely as is possible the temperatures of the sensor and the heat transfer surface. While it is neither possible, nor desirable for operation of the bridge electronics, to set these temperatures exactly the same, it is an absolute requirement that the difference be constant during calibration and measurement. Note that a change in $\Theta_{B,S}$ of 0.015 yields a change in the calibration of 20 percent over a range of Bi_C of 0.0004. For the nominal probe dimensions and materials, and $T_S - T_\infty = 30°\mathrm{C}$ these conditions correspond to a temperature difference between the sensor and the heat transfer surface of about 0.5°C and a range of the heat transfer

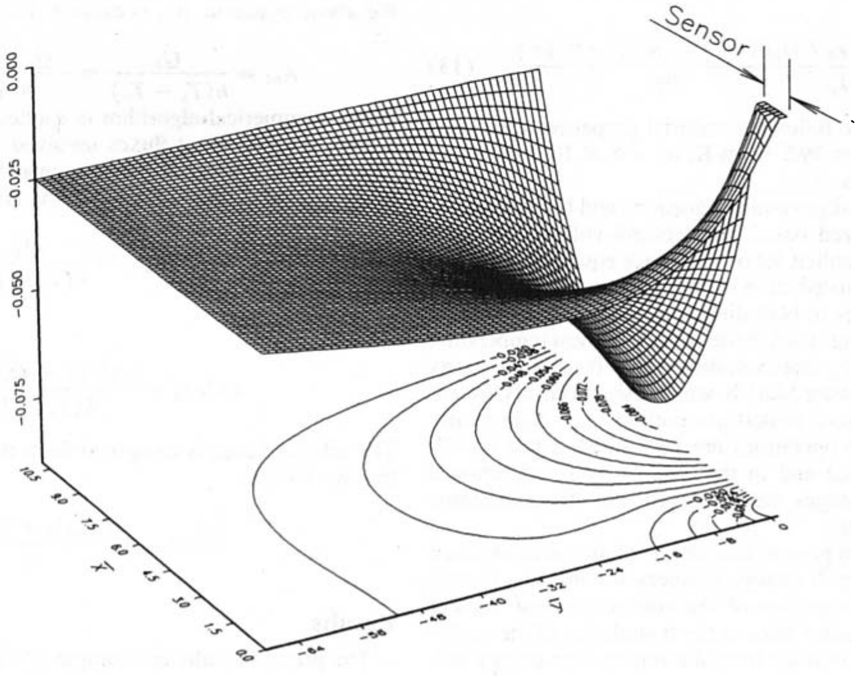

Fig. 3 Steady-state isotherms for the nominal probe and nonideal boundary conditions ($\mathrm{Bi}_C = 3 \times 10^{-4}$; $\Theta_{B,S} = -0.025$)

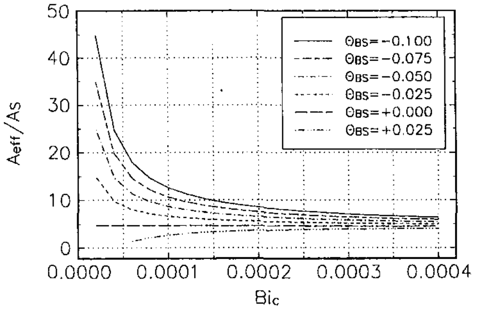

Fig. 4 Effective area of the nominal probe as a function of operating conditions and heat transfer coefficient

coefficient of about 500 W/m^{2}K. Note that in the present analysis, the temperature of the platinum sensor was assumed uniform. In actual operation, such a condition cannot rigorously be maintained. Park and Cole (1996) showed that a thin metal sensor has a nonuniform temperature that is $T_S = T_S(x)$. In their model heat was introduced to the sensor by uniform heat generation throughout the metal volume. In the present application, however, it was found that the spatial variation of the sensor temperature can be neglected. The coating plays an important role in this regard. For different convective heat transfer conditions, the heat dissipated by the sensor evaluated for T_S = constant was determined (for the nominal probe dimensions). To determine the degree of nonuniformity in the sensor temperature, in subsequent simulations heat was introduced to sensor through uniform heat generation. The results indicated a maximum temperature difference throughout the sensor material of 0.25°C. The same difference was observed at the convective boundary in the vicinity of the sensor, while for the rest of the boundary the temperature distribution was practically unaffected. This temperature difference may cause an error in the estimated sensor temperature T_s of about 0.1°C which is about 0.3 percent in the temperature difference $T_s - T_\infty$ and will have a negligible impact on the estimation of $A_{\rm eff}$ for the range of operating conditions investigated here.

Figure 6 illustrates the step-response of the probe, and also illustrates the effects of modifications to the probe geometry. The error fraction shows how fast the probe responds to a step change in the heat transfer coefficient. It is defined as $(h(t) - h_f)/(h_o - h_f)$ where h_o; h_f, and $h(t)$ are the initial, final and transient (probe response) heat transfer coefficients, respectively. The probe is subjected to a step change in Bi_C from 5 $\times$ 10^{-5} to 3 $\times$ 10^{-4}. For the nominal case this corresponds to a step-change in the heat transfer coefficient from 87 to 523 W/m^{2}K. Whereas the plot given in Fig. 6 in logarithmic scale shows in greater detail the initial transient, the uniform scale plot in Fig. 7 can be used to determine the rise time of the probe. The 95 percent response time for the nominal probe is 8 ms (Fo = 520). A reasonable increase in the coating thickness (m_C = 0.2) slightly increases the response time to 9 ms (Fo = 370). When the length of the probe is augmented (m increases from 10.886 to 12, which corresponds to more than one sensor length) the 95 percent response time increases to 14 ms (Fo = 740).

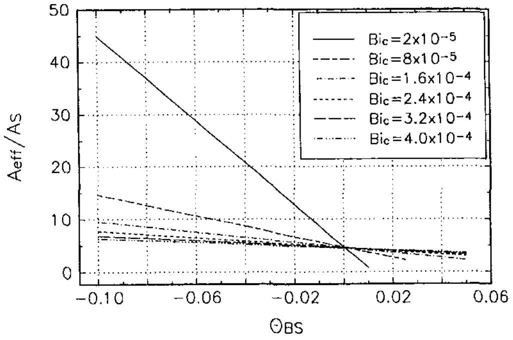

Fig. 5 Effect of Biot number and operating conditions on the nondimensional effective area

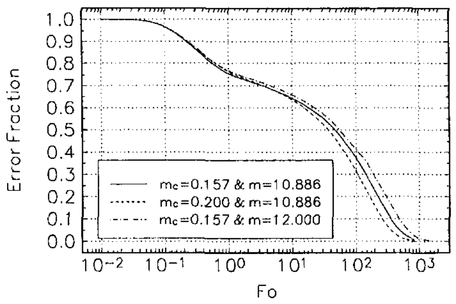

Fig. 6 Influence of the probe dimensions on the time response to a step change in the Biot number ($\Theta_{B,S}$ = −0.025)

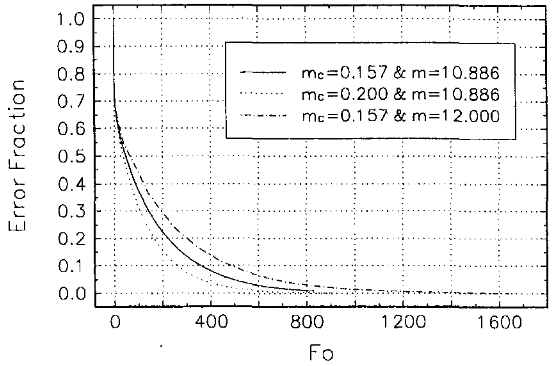

Fig. 7 Influence of the probe dimensions on the time response to a step change in the Biot number ($\Theta_{B,S}$ = −0.025; f = 150 Hz)

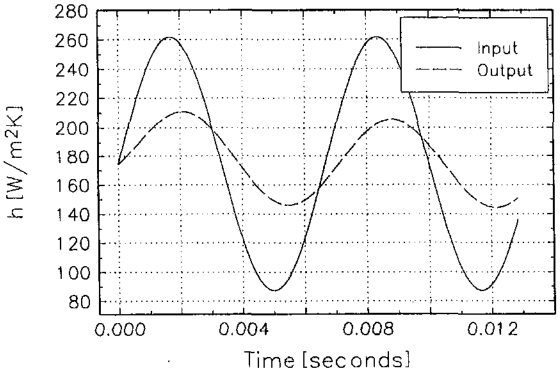

Fig. 8 Amplitude distortion and time delay for the nominal probe under steady-periodic conditions ($\Theta_{B,S}$ = −0.025; f = 150 Hz)

If the probe is subjected to a periodic input, the output signal is attenuated and delayed. The attenuation is described by the ratio of the amplitudes of the input and output signals, termed the magnitude ratio. This effect is illustrated in Fig. 8 for steady-periodic conditions. The amplitude distortion and phase shift depend on the frequency of the input signal. Note that after two periods of the input signal the response of the probe is stabilized in the computational model. However, our computations showed that at higher frequencies the number of periods needed for the output signal to stabilize increases gradually. Correspondingly, the computer time needed to accurately represent

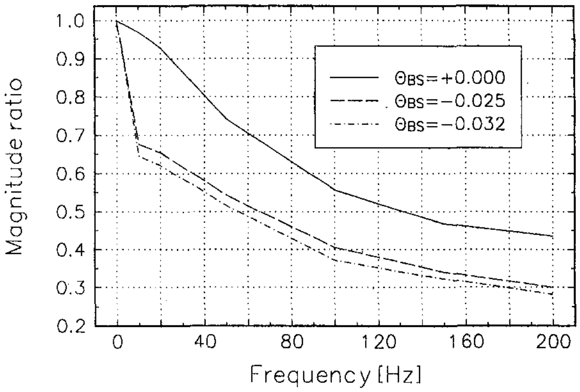

Fig. 9 Amplitude response of the nominal probe for nonideal boundary conditions

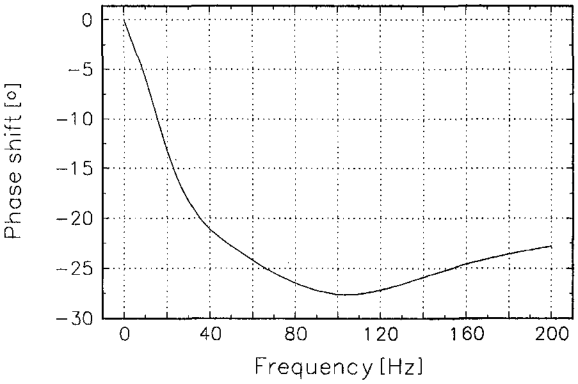

Fig. 10 Phase shift of the nominal probe for nonideal boundary conditions ($\Theta_{B,S}$ = −0.08; −0.06; −0.04; −0.02; 0.00)

the frequency response of the probe increases. The magnitude ratio versus frequency of the input signal, with the nondimensional temperature difference between the sensor and the heat transfer surface as a parameter is shown in Fig. 9. The amplitude error is larger when a temperature difference between the sensor and the heat transfer surface exists. Note that this decrease is more important at low frequencies. At 10 Hz a decrease in $\Theta_{B,S}$ from 0 to −0.032, which for the nominal case and $T_S - T_\infty$ = 30°C corresponds to about 1°C, the amplitude error exceeds 35 percent. It should also be noted that at a frequency of about 200 Hz the amplitude errors approach 60 percent even for ideal case ($\Theta_{B,S} = 0$). Frequencies beyond this range are important only from a theoretical point of view for the measurement technique analyzed here. Figure 10 presents the dependence of the phase shift on the frequency of the input signal. Runs were performed for the values of the nondimensional temperature difference between the sensor and the heat transfer surface shown in Fig. 9. This plot shows that the phase shift depends on frequency of the input signal and not on the temperature difference between the sensor and the heat transfer surface. The time delay increases when the frequency increases, reaches a maximum and then decreases and eventually will reach zero at very high frequencies. It should be noted that the maximum time delay is reached at a frequency about 100–130 Hz. One additional design modification was examined, that of a very thick coating ($m_C = 1$). The amplitude error increases from zero to 85 percent and stays approximately constant for the frequency range 10–200 Hz.

Conclusions

A two-dimensional computational model has been employed to examine the steady and dynamic response characteristics of a local heat flux probe. The effect of uncertainties in the heat transfer surface and sensor temperature are examined in terms of a steady calibration and for the frequency response effects. Nondimensional steady-state isotherms illustrate the effects of heat transfer from the boundaries of the probe (the heat transfer surface) on the effective area. These effects are quantified in terms of a nondimensional effective area of the probe. This effective area serves as the calibration constant, and is shown to be strongly dependent on the temperature difference between the sensor and the heat transfer surface. The frequency response of the probe is affected through a reduction in the magnitude ratio as the difference between the temperature of the heat transfer surface and that of the sensor increases. The phase shift was shown to depend on the frequency of the input signal and not on the temperature difference between the sensor and the heat transfer surface.

Acknowledgments

The support of the South Carolina Energy Research and Development Center and MTCI, Inc. are gratefully acknowledged. This research was conducted in conjunction with a DOE demonstration of Pulsed-Atmospheric Fluidized Bed Combustion on the campus of Clemson University.

References

Beasley, D. E., and Figliola, R. S., 1988, "A Generalised Analysis of a Local Heat Flux Probe," *Journal of Physics E: Scientific Instruments*, Vol. 21, pp. 316–322.

Diller, T. E., 1993, "Advances in Heat Flux Measurements," *Advances in Heat Transfer*, Vol. 23, Academic Press, San Diego, CA, pp. 279–369.

Figliola, R. S., Swaminathan, M., and Beasley, D. E., 1993, "A Study of the Dynamic Response of a Local Heat Flux Probe," *Measurement Science and Technology*, Vol. 4, pp. 1052–1057.

Figliola, R. S., and Swaminathan, M., 1996, "Boundary Condition Influences on the Effective Area of a Local Heat Flux Probe," *Measurement Science and Technology*, Vol. 7, pp. 1439–1443.

Liang, P. W., and Cole, K. D., 1992, "Conjugated Heat Transfer from a Rectangular Hot-Film with the Unsteady Surface Element Method," *AIAA J. of Thermodynamics and Heat Transfer*, Vol. 6, pp. 349–355.

Park, C. H., and Cole, K. D., 1994, "Unsteady Heat Transfer from a Thick-Film Sensor," *AIAA J. of Thermodynamics and Heat Transfer*, Vol. 8, pp. 797–799.

Park, C. H., and Cole, K. D., 1996, "One Point Calibration of a Glue-on Shear Stress Sensor," Proceedings of at the 1996 IMECE, Atlanta, GA, paper 96-WA/HT-19.

J. Y. Murthy
Mem. ASME.

S. R. Mathur

Fluent, Inc.,
Ten Cavendish Court,
Lebanon, NH 03766

Computation of Anisotropic Conduction Using Unstructured Meshes

This paper presents a conservative finite volume scheme for computing conduction heat transfer in materials with anisotropic conductivity. Unstructured solution-adaptive meshes composed of arbitrary convex polyhedra are used. Discrete energy balances are written over these polyhedra. Temperature gradients required for the evaluation of secondary diffusion fluxes are found by linear reconstruction. A fully implicit scheme is used for unsteady problems. The resulting discrete equations are solved using an algebraic multigrid scheme. Schemes for hanging-node and conformal adaption are implemented. Computations are performed using a variety of triangular and quadrilateral meshes. The results are compared to published analytical and numerical solutions and are shown to be satisfactory.

Introduction

Anisotropic conduction heat transfer occurs in a number of important industrial applications. In the manufacture of composite materials, for example, the presence of directional reinforcements results in anisotropic conduction (Beyeler and Guceri, 1988; Nejhad et al., 1991). Other applications include solidification (Weaver and Viskanta, 1989), conduction in porous media (Howle and Georgiadis, 1994), and electronics cooling. In most industrial processes, the geometric configurations involved are complex and difficult to address using conventional numerical tools. An efficient computational methodology is required for the analysis of anisotropic conduction in practical industrial geometries.

The majority of available computational methods for anisotropic conduction employ structured body-fitted meshes. Katayama and Saito (1974) employed a finite difference discretization of the governing equations. To avoid dealing with cross derivatives, they aligned their coordinate system with the principal directions of the conductivity tensor. Such a methodology is not easy to use in problems with multiple anisotropic materials. Methods for computing anisotropic conduction have been devised for composites applications by Beyeler and Guceri (1988) and Nejhad et al. (1991) using a finite difference scheme. In Beyeler and Guceri (1988), anisotropic heat transfer was modeled using a nonconservative formulation, with the diffusion term being decomposed in both first and second gradients of temperature. Though Beyeler and Guceri obtained good comparisons with experiment, the creation of first derivatives could lead to numerical difficulties. A conservative finite volume formulation was developed for cylindrical coordinates in Nejhad et al. (1991) to model heat transfer in filament winding. Weaver and Viskanta (1989) modeled anisotropic conduction during solidification using a finite volume scheme. An interface tracking algorithm was used, and the nonorthogonal domain resulting from a nonplanar melt interface was mapped to computational space using a body-fitted grid. Recently, Keyhani and Polehn (1995) devised a conservative finite volume technique for Cartesian meshes, and employed special interpolation procedures for the computation of secondary gradients resulting from cross-ply conduction terms. However, the procedure did not lead to substantial improvement over conventional linear interpolation.

During the last decade, unstructured grid methods have been the focus of a considerable amount of computational fluid dynamics research. With these methods, mesh generation for complex, realistic geometries is greatly simplified. Because the mesh does not require line structure, it is possible to dynamically adapt it to local features of interest, such as sharp gradients of temperature at material discontinuities. Literature on the computation of anisotropic conduction using unstructured meshes is relatively sparse. Galerkin finite element solutions of conduction have been reported by Padovan (1974) and others. Because of the success of finite element approaches in dealing with geometric complexity, attempts have been made to combine aspects of finite element methodology with the conservative property of finite volume schemes. The control-volume finite element method (CVFEM) (Baliga and Patankar, 1983; Schneider and Raw, 1987), stores solution variables at element vertices. Polyhedral control volumes are constructed around each vertex, and conservation enforced on the control volume. Finite element-like shape functions are used for discretization. Conduction heat transfer has been computed using this methodology by Banaszek (1984) and Blackwell and Hogan (1993); the computations compared favorably with traditional Galerkin finite element approaches.

More recently, unstructured cell-based finite volume schemes for fluid flow are beginning to appear (Jiang and Przekwas, 1994; Demirdzic and Muzaferija, 1995; Davidson, 1996; Mathur and Murthy, 1997) which are more closely related to traditional methods for structured body-fitted meshes (Peric, 1985; Karki and Patankar, 1989). Here conservation is enforced on the basic cell itself, and not on the cell-dual, as in Baliga and Patankar (1983). In these methods, gradient determination does not employ element-specific shape functions; consequently they have the potential for use with arbitrary polyhedral meshes. In this paper, we develop a conservative finite volume scheme for anisotropic conduction problems based on the methodology of Mathur and Murthy (1997). We address the proper decomposition of primary and secondary diffusion fluxes in the presence of anisotropy, making sure that the formulation defaults to the familiar form for structured body-fitted meshes and isotropic problems. Treatment of general nonlinear boundary conditions and conjugate heat transfer is also addressed. Issues specific to the formulation, such as the deferred computation of secondary gradients, are also discussed.

The next two sections present the governing equations and details of the numerical method, respectively. For completeness,

---

Contributed by the Heat Transfer Division for publication in the JOURNAL OF HEAT TRANSFER. Manuscript received by the Heat Transfer Division, Sept. 9, 1996; revision received, Mar. 30, 1998. Keywords: Computational, Conduction, Heat Transfer, Modeling, Numerical Methods. Associate Technical Editor: J. R. Howell.

we present a generalized development for unsteady anisotropic heat transfer including convection. Results obtained using this methodology are compared with analytical and numerical solutions in the literature and found to be satisfactory.

Governing Equations

The equations for conservation of energy for incompressible flow in an anisotropic medium are

$$\frac{\partial}{\partial t}(\rho C_p T) + \frac{\partial}{\partial x_i}(\rho u_i C_p T) = \frac{\partial}{\partial x_i}\left(k_{ij}\frac{\partial T}{\partial x_j}\right) + S_h. \quad (1)$$

The summation convention is used. For solids, the convective term is dropped except when solid body motion exists (Beyeler and Guceri, 1988). In fluid regions, anisotropic conduction is usually not important. One exception is the computation of the temperature field for flows through porous media, where the directional properties of the porous medium impose different volume-averaged conductivities in different coordinate directions.

Numerical Method

The domain is discretized into arbitrary unstructured convex polyhedra called cells. The boundaries surrounding the cells are called faces and the vertices of the polyhedra are referred to as nodes. Each internal face has two cells on either side; these are referred to as the face neighbors. The neighbors of a cell are defined to be those cells with which it shares a common face. Line segments joining the nodes are termed edges (and are identical to faces in two dimensions). Meshes with hanging nodes, such as the one shown in Fig. 1(*a*), are permitted. The coordinates of the cell center are the average of the nodal coordinates.

Temperature and thermal conductivity are stored at cell centers. This arrangement is preferred over node-based storage for several reasons. With cell-based storage, conservation can be ensured for arbitrary control volumes with nonconformal interfaces without special interpolation techniques. On triangular and tetrahedral meshes, cell-based storage also enjoys better resolution than node-based storage (since the ratio of number of cells to nodes is between 3 and 5) for roughly the same amount of work, which is typically proportional to the number of faces. In addition, temperature is also stored at the centers of boundary faces.

Discretization of the Energy Equation. Integration of the energy equation about the control volume C0 shown in Fig. 1(*a*) yields:

$$\frac{\rho C_p (T_0^{n+1} - T_0^n)\Delta\mathcal{V}_0}{\Delta t} + \sum_f J_f T_f = \sum_f D_f + (S_h \Delta\mathcal{V})_0 \quad (2)$$

where J_f is the mass flow rate (defined to be positive if flow is leaving C0), D_f is the transport due to diffusion through the face f and the summations are over the faces of the control volume. T_f is the temperature at the face. T_0^{n+1} and T_0^n are temperatures in the C0 cell at the current and previous time-steps respectively.

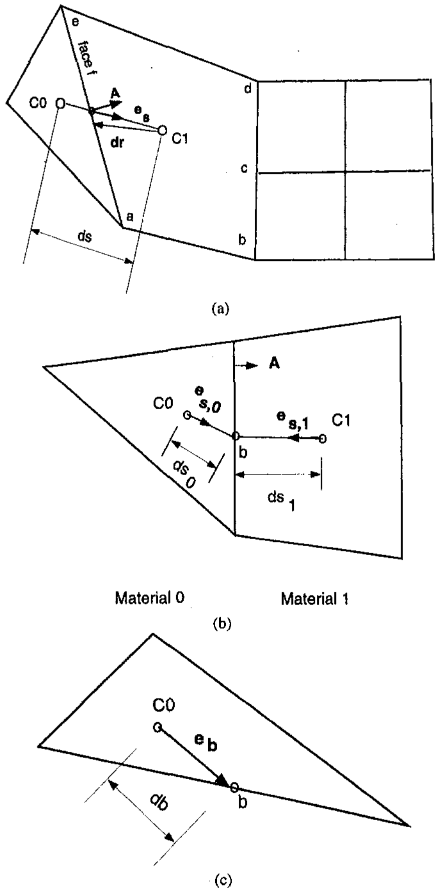

Fig. 1 Control volume; (*a*) interior, (*b*) interface, (*c*) boundary

A fully-implicit scheme is used for time discretization (Patankar, 1980). Thus, the convective, diffusive and source terms in the above equation are computed at time-step $n + 1$. The time discretization used above is first-order accurate; generalization to second-order schemes is straightforward and is not presented here.

Convection Term. The face mass flow rate J_f is assumed to be known from the solution of the flow field (Mathur and Murthy, 1997). When fluid properties are a function of temperature, J_f is a function of temperature. In such a case, it is based on the current iterate of temperature. Therefore the task of evaluation of the convective flux reduces to determining the face value, T_f. As in Mathur and Murthy (1997), a first-order approximation is to use the value at the upwind cell

$$T_f = T_{\text{upwind}} \quad (3)$$

A higher-order value at the face can be obtained as

Nomenclature

a_p, a_{nb} = coefficients of discrete equation
$\mathbf{A}$ = area vector
A_i = components of **A**
C_p = specific heat
D_f = diffusion flux on face f
g = acceleration due to gravity
k_{ij} = components of the conductivity tensor
k_s = conductivity of the solid
k_f = conductivity of the fluid
$\mathbf{q}$ = heat flux vector
q_i = components of **q**
q = heat flux
S_h = energy source per unit volume
S_p = source term in discrete equation
$\mathcal{S}$ = secondary diffusion flux
t = time
T = temperature
x_i = coordinate direction
α_f = thermal diffusivity of the fluid
β = thermal expansion coefficient
ν_f = kinematic viscosity of the fluid
$\Delta\mathcal{V}$ = volume of control volume
ρ = density

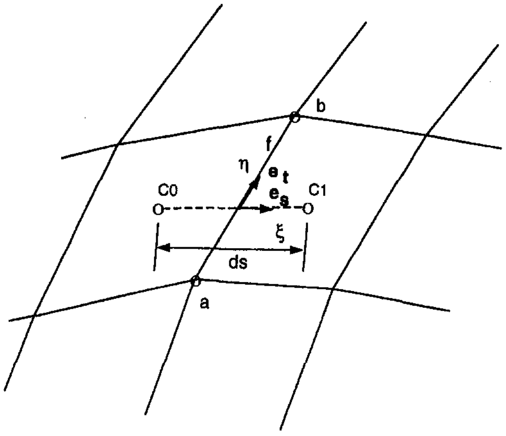

Fig. 2 Local coordinate system

$$T_f = T_{\text{upwind}} + \nabla T_{r\text{upwind}} \cdot \mathbf{dr} \tag{4}$$

where $\nabla T_{r\text{upwind}}$ is the *reconstruction gradient* at the upwind cell (Mathur and Murthy, 1997) and $\mathbf{dr}$ is the vector directed from the center of the upwind cell to the center of the face. The first term in Eq. (4) is treated implicitly and the second term is included explicitly.

Diffusion Term and Treatment of Anisotropy. The diffusion term at the face is

$$D_f = \mathbf{q} \cdot \mathbf{A}. \tag{5}$$

In two dimensions

$$\mathbf{q} = \left(k_{xx} \frac{\partial T}{\partial x} + k_{xy} \frac{\partial T}{\partial y} \right) i + \left(k_{yx} \frac{\partial T}{\partial x} + k_{yy} \frac{\partial T}{\partial y} \right) j \tag{6}$$

$$\mathbf{A} = A_x i + A_y j. \tag{7}$$

Consider the face f in Fig. 2. The ξ direction is aligned with the vector joining cell centers; the η direction lies in the direction joining the vertices of the face. We may write

$$\begin{aligned} \mathbf{q} \cdot \mathbf{A} = {} & T_\xi[(A_x k_{xx} + A_y k_{yx}]\xi_x + (A_x k_{xy} + A_y k_{yy})\xi_y] \\ & + T_\eta[(A_x k_{xx} + A_y k_{yx})\eta_x + (A_x k_{xy} + A_y k_{yy})\eta_y]. \end{aligned} \tag{8}$$

The transformation metrics can be written in terms of derivatives of (x, y) as

$$\xi_x = \mathcal{J} y_\eta \tag{9}$$

$$\xi_y = -\mathcal{J} x_\eta \tag{10}$$

$$\eta_x = -\mathcal{J} y_\xi \tag{11}$$

$$\eta_y = \mathcal{J} x_\xi \tag{12}$$

where $\mathcal{J}$, the Jacobian of the transformation, is given by

$$\mathcal{J} = \frac{1}{x_\xi y_\eta - x_\eta y_\xi}. \tag{13}$$

Substituting in Eq. (8) yields

$$\begin{aligned} \mathbf{q} \cdot \mathbf{A} = {} & T_\xi[(A_x k_{xx} + A_y k_{yx})\mathcal{J} y_\eta - (A_x k_{xy} + A_y k_{yy})\mathcal{J} x_\eta] \\ & + T_\eta[-(A_x k_{xx} + A_y k_{yx})\mathcal{J} y_\xi + (A_x k_{xy} + A_y k_{yy})\mathcal{J} x_\xi] \end{aligned} \tag{14}$$

For the mesh shown in Fig. 2, writing consistent approximations for the derivatives, we have the following expressions:

$$T_\xi = T_1 - T_0$$

$$x_\xi = x_1 - x_0$$

$$y_\xi = y_1 - y_0$$

$$T_\eta = T_b - T_a$$

$$x_\eta = x_b - x_a$$

$$y_\eta = y_b - y_a.$$

Further, from the geometry in Fig. 2, it is clear that

$$A_x = (y_b - y_a) \tag{15}$$

$$A_y = -(x_b - x_a). \tag{16}$$

We also note that the unit vector in the direction joining the two cell centers is

$$\mathbf{e}_s = \frac{(x_1 - x_0)i + (y_1 - y_0)j}{ds} \tag{17}$$

where ds is the distance between the cell centers. The tangent vector along the face has the components

$$\mathbf{e}_t = \frac{(x_b - x_a)i + (y_b - y_a)j}{A}. \tag{18}$$

Next, we substitute Eqs. (15), (16), (17), and (18) into Eq. (14). Using the summation convention, we may then write Eq. (14) as

$$q_i A_i = \frac{(T_1 - T_0)}{ds} \frac{(A_i k_{ij} A_j)}{(A_j e_{sj})} + \frac{(T_b - T_a)}{A} \frac{(A_i k_{ij} n_j A)}{(A_j e_{sj})}. \tag{19}$$

Here, n_j are the components of the unit vector normal to $\mathbf{e}_s$.

Equation (19) defaults to the standard form (Peric, 1985) for isotropic conduction on structured meshes. The first term on the right-hand side of Eq. (19) represents the primary gradient. The discretization is equivalent to a second-order central difference representation. As in typical structured mesh formulations (Peric, 1985), this term is treated implicitly and leads to a stencil that includes all neighboring cells.

The second term is the secondary or cross diffusion term. For the isotropic case, this term is zero when $A_j n_j$ is zero (e.g., on an orthogonal quadrilateral mesh or on a mesh of equilateral triangles). For the anisotropic case, this term can be significant. In a structured grid formulation the node values T_a and T_b are typically found by averaging the values at cell centers and the entire secondary gradient component is treated explicitly. For two-dimensional unstructured meshes, it is possible to evaluate these node values using a variety of methods (Jiang and Przekwas, 1994; Davidson, 1996). However, many of these methods are shape dependent, and extending them to three-dimensional polyhedra of arbitrary shape is not straightforward. In three dimensions, the faces of the control volume consist of arbitrary polyhedra with an arbitrary number of edges and nodes. There are no unique face tangential directions that can be used to

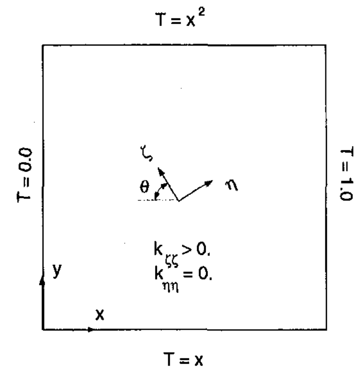

Fig. 3 Steady anisotropic conduction—schematic

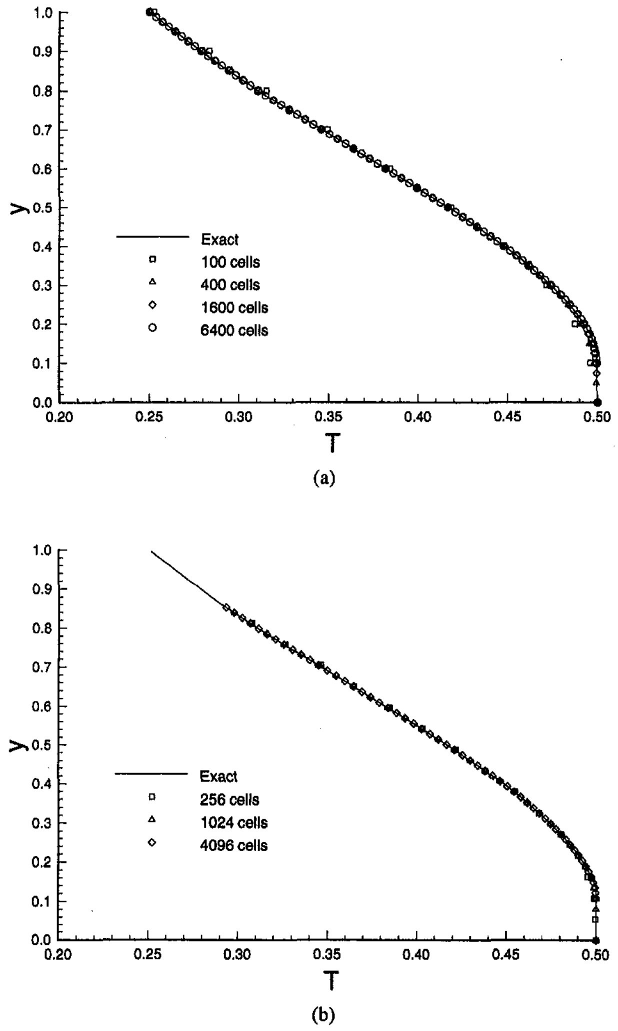

Fig. 4 Steady anisotropic conduction—centerline temperature; (*a*) quadrilateral mesh, (*b*) triangular mesh

represent $\mathbf{e}_t$; similarly the points a and b are not unique. (In structured grids the underlying grid directions supply the decomposition directions; corner nodes are used for the differencing stencils).

To avoid the use of face tangents and nodes, Eq. (19) can be written as

$$q_iA_i = \frac{(T_1 - T_0)}{ds}\frac{(A_ik_{ij}A_j)}{(A_je_{sj})} + \mathcal{S}_f \tag{20}$$

where

$$\mathcal{S}_f = A_ik_{ij}\overline{\frac{\partial T}{\partial x_j}} - \overline{\frac{\partial T}{\partial x_k}}\, e_{sk}\frac{(A_ik_{ij}A_j)}{(A_je_{sj})}\,. \tag{21}$$

The quantity $\mathcal{S}_f$ is the secondary diffusion term at the face and is written as the difference between the total diffusion term and the primary component. The quantity ($\overline{\partial T/\partial x_j}$) is taken to be the average of the temperature derivatives at the two adjacent cells. If the cell derivative is second-order accurate, the diffusion term representation is second-order accurate. A second-order representation of the cell-derivative using linear reconstruction has been presented in Mathur and Murthy (1997) and is repeated here for completeness. The derivative computation procedure is independent of cell shape, and can thus be used for meshes composed of arbitrary convex polyhedra. The formulation is applicable without modification to three-dimensional situations.

A deferred computation of the secondary diffusion term is used. $\mathcal{S}_f$ is evaluated from prevailing values of T and updated through a global iteration procedure, as described below. This treatment is different from that used in CVFEM or finite element method schemes, where the cross terms are included implicitly through the use of shape functions. Deferred computation of secondary diffusion terms does require several global iterations for convergence. However, the computational stencil is kept small, and the resulting nominally linear equations are diagonally dominant and amenable to iterative linear solvers. In any case, global iteration is required for conjugate problems and to resolve nonlinearities.

Gradient Computation. Previous finite element and CVFEM discretizations on unstructured meshes employed shape functions to write the derivatives of temperature in terms of nodal values. We employ linear reconstruction to obtain temperature derivatives (Barth, 1992). The *reconstruction gradient* is estimated as

$$\nabla T_r = \frac{\alpha}{\Delta\mathcal{V}}\sum_f(\bar{T}_f\mathbf{A}) \tag{22}$$

where the summation is over all the faces of the cell. The face value of T is obtained by averaging the values at the neighboring cells, so that for the face f in Fig. 1(a)

$$\bar{T}_f = \frac{T_0 + T_1}{2}\,. \tag{23}$$

α is a factor used to ensure that the reconstruction does not introduce local extrema. The limiter proposed by Venkatakrishnan (1993) is used.

Using the reconstruction gradient, the value at any face of the cell can be reconstructed as

$$T_{f,c} = T_c + \nabla T_r\cdot\mathbf{dr}. \tag{24}$$

The cell derivatives used for the secondary diffusion terms in Eq. (20) are computed by again applying the divergence theorem over the control volume and using the averaged reconstructed values at the faces

$$\nabla T = \frac{1}{\Delta\mathcal{V}}\sum_f(\tilde{T}_f\mathbf{A}) \tag{25}$$

where, for face f in Fig. 1(a), $\tilde{T}_f$ is given by

$$\tilde{T}_f = \frac{T_{f,0} + T_{f,1}}{2}\,. \tag{26}$$

If convective fluxes are present, they may be evaluated to second-order accuracy by taking the face value T_f as the reconstructed value from the upwind cell. This results in an upwind-biased second-order representation of the convective term.

Conjugate Heat Transfer. Heat transfer across the interface between two different materials is treated implicitly, similar to the procedure described in Kelkar (1990) for isotropic conduction on structured meshes. Consider the interface between two different materials, shown in Fig. 1(b). Writing the heat balance at the interface,

$$q_f = (q_iA_i)_0 = (q_iA_i)_1 \tag{27}$$

where q_f is the interface heat transfer from cell C_1 to cell C_0. We discretize the heat balance as

$$h_0(T_b - T_0) + \mathcal{S}_0 = h_1(T_1 - T_b) - \mathcal{S}_1 \tag{28}$$

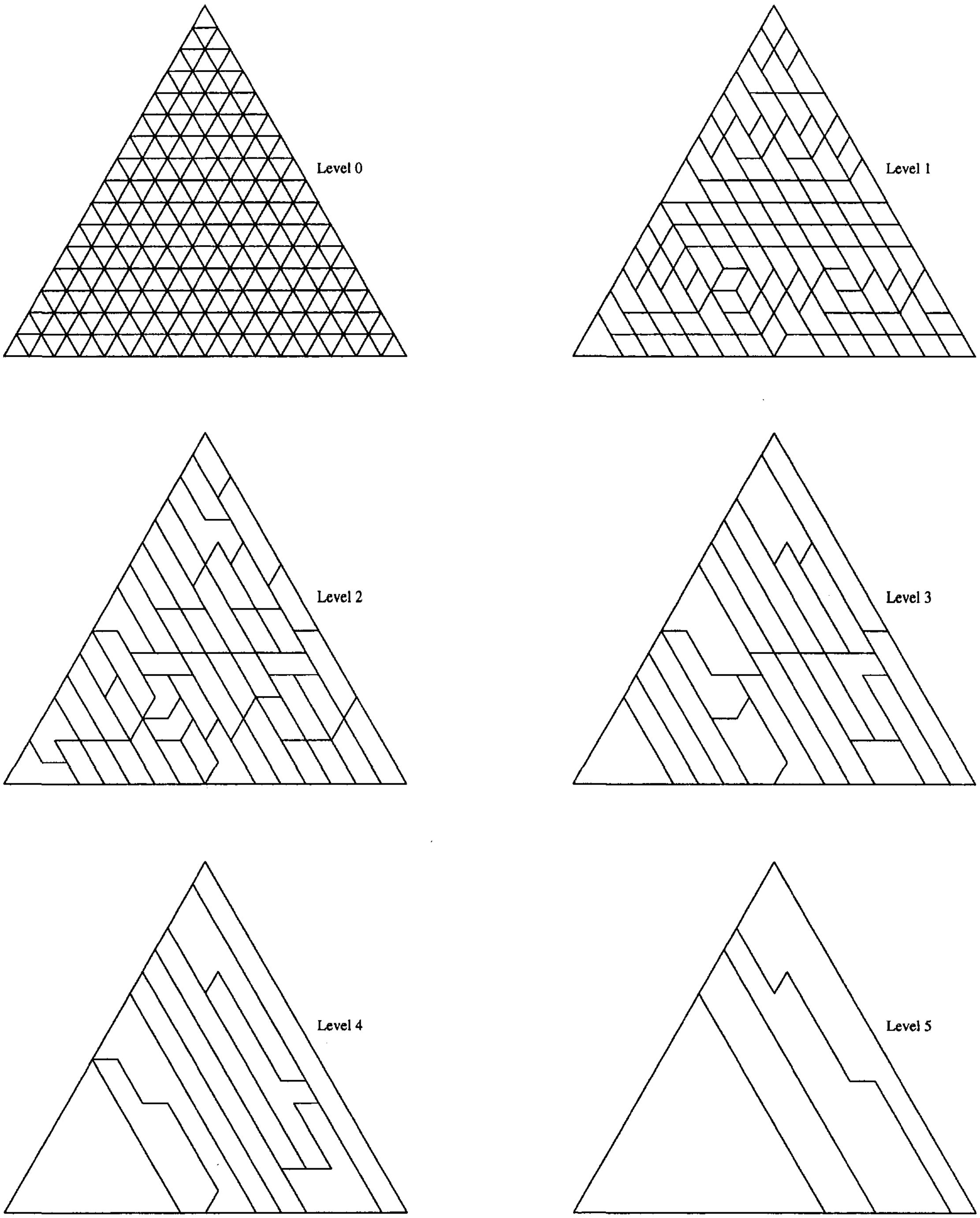

Fig. 5 Steady anisotropic conduction—multigrid coarsening with triangular mesh

where the heat transfer resistances h_0 and h_1 are given by

$$h_0 = \frac{(A_i k_{ij,0} A_j)}{(A_j e_{sj,0} ds_0)} \qquad (29)$$

and

$$h_1 = -\frac{(A_i k_{ij,1} A_j)}{(A_j e_{sj,1} ds_1)} . \qquad (30)$$

We may thus write T_b as

$$T_b = \frac{h_0 T_0 + h_1 T_1}{h_0 + h_1} - \frac{\mathcal{S}_0 + \mathcal{S}_1}{h_0 + h_1} . \qquad (31)$$

We may then write the interface heat transfer rate q_f as

$$q_f = \frac{h_0 h_1}{h_0 + h_1} (T_1 - T_0) - \frac{(\mathcal{S}_0 h_1 - \mathcal{S}_1 h_0)}{h_0 + h_1} . \qquad (32)$$

This expression is similar in structure to that derived for Cartesian meshes (Kelkar, 1990). It is included implicitly in the heat balance for the cells C_0 and C_1. The secondary diffusion terms $\mathcal{S}_0$ and $\mathcal{S}_1$ are computed using cell temperature gradients. The interface temperature T_b is updated using Eq. (31) and is used in evaluating cell derivatives and reconstruction gradients.

The development presented above may be applied even if one of the materials is isotropic or if one of the materials is a fluid. In the presence of turbulent fluid flow, the heat transfer resistance h_0 (or h_1) may be replaced by the equivalent thermal resistance resulting from the turbulence model.

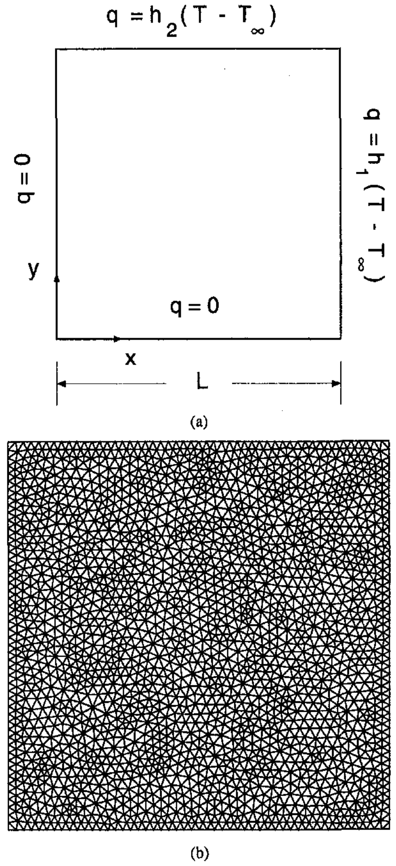

Fig. 6 Unsteady anisotropic conduction—(*a*) schematic, (*b*) grid

Boundary Conditions. Boundary conditions are treated in a manner similar to the treatment of conjugate heat transfer. In addition to cell centers, temperature is also stored on boundary face centers. Referring to Fig. 1(*c*), the boundary heat flux is written as

$$q_i A_i = \frac{(T_b - T_0)}{db}\frac{(A_i k_{ij} A_j)}{(A_j e_{bj})} + \mathcal{S}_0. \tag{33}$$

When the temperature is given, Eq. (33) provides the boundary heat transfer for the near-boundary control volume balance. The primary term is included implicitly and the secondary term explicitly. For heat-flux, convective, radiative, and mixed boundary conditions, the boundary heat transfer rate entering the control volume may be written in the general nominally linear form

$$q_b = C(T_b^*) - D(T_b^*)T_b. \tag{34}$$

The heat balance at the boundary is written as

$$h_0(T_b - T_0) + \mathcal{S}_0 = C - DT_b \tag{35}$$

where $h_0 = (A_i k_{ij} A_j)/(A_j e_{bj} db)$. As with conjugate heat transfer, we may write T_b and q_b as

$$T_b = \frac{C + h_0 T_0}{h_0 + D} - \frac{\mathcal{S}_0}{h_0 + D} \tag{36}$$

$$q_b = \frac{Ch_0 - Dh_0 T_0}{h_0 + D} + \frac{\mathcal{S}_0 D}{h_0 + D}. \tag{37}$$

As before, q_b is included implicitly in the heat balance for the boundary control volume. The boundary temperature T_b is updated using Eq. (36). $\mathcal{S}_0$ is the secondary diffusion term evaluated using the temperature gradient at the cell C0. The prevailing value of T_b is used in evaluating cell derivatives and reconstruction gradients.

Discretized Equations. The discretization procedure yields the following linear system of equations for T at the cell centers:

$$a_p T_p = \sum_{nb} a_{nb} T_{nb} + S_p. \tag{38}$$

Here the summation is over all the neighbors nb of cell p. The source term S_p contains any volumetric sources of T, the second-order contributions for the convective flux, as well as the secondary diffusion fluxes. Contributions from the boundaries are also included in S_p. Equation (38) is underrelaxed in the manner described in Patankar (1980).

Linear Solver. Since the mesh is unstructured, familiar line iterative solvers cannot be used to solve Eq. (38). As explained in Mathur and Murthy (1997), an algebraic multigrid procedure similar to that of Hutchinson and Raithby (1986) is used. Coarse levels are created by by grouping a fine level cell with n of its neighboring ungrouped cells for which the coefficient a_{nb} is the largest (Lonsdale, 1991), leading to unstructured polyhedral

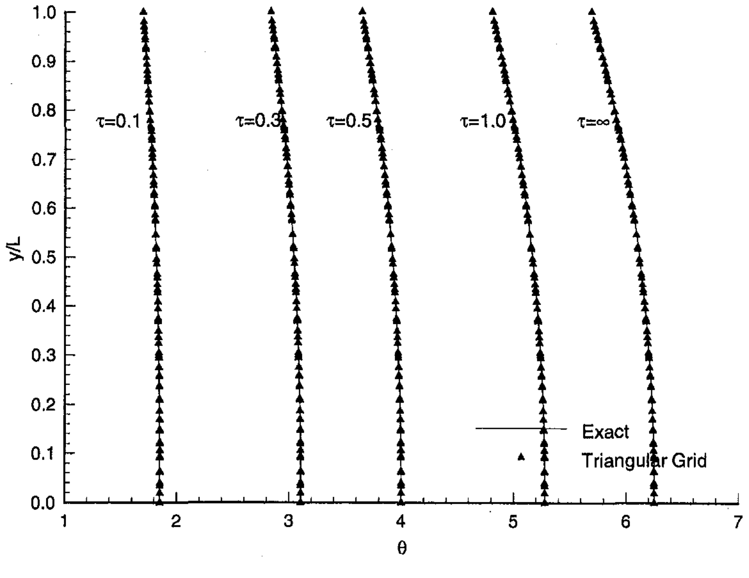

Fig. 7 Unsteady anisotropic conduction—temperature profiles at $x/L = 0.5$

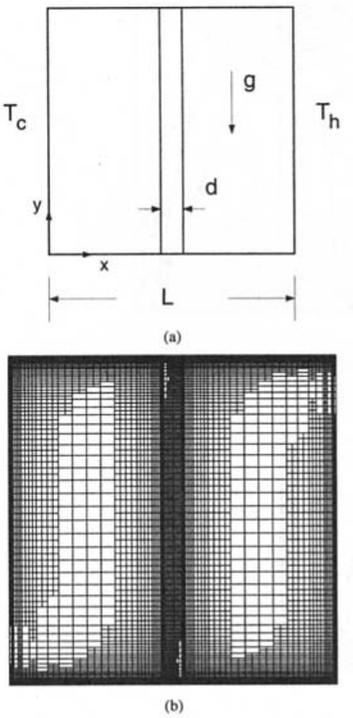

Fig. 8 Conjugate heat transfer in a partitioned enclosure—(*a*) schematic, (*b*) grid

meshes at the coarse levels as well. Best performance is observed when the group size is two, leading to a coarse level that is roughly half the size of the fine level. This procedure is recursively applied until no further coarsening is possible. At each level, Gauss-Seidel iteration is used as the relaxation method. A variety of multigrid cycles, such as the V, W and Brandt cycle (Brandt, 1977), have been implemented. For the examples in this paper, the Brandt cycle is used.

Agglomeration based on neighbor coefficients is critical for speedy convergence of conjugate heat transfer problems with large conductivity ratios. The agglomeration will tend to group cells with approximately the same temperature, and improves the efficiency of error removal across conjugate boundaries. The method used here is similar in philosophy to that of Kelkar (1990), where coarse level structured meshes were created by grouping cells with the same conductivity. For orthotropic conduction, the agglomeration tends to club together face neighbors whose shared-face normals are most closely aligned with the most-conducting principal direction. Thus coefficient-based agglomeration correctly captures the direction of information travel in the mesh.

Because of the deferred computation of secondary diffusion terms, a global iterative procedure is required to solve Eq. (38) even for linear problems. Thus, S_p, which contains the secondary gradients, is computed from the current iterative of T, and Eq. (38) is solved using the algebraic multigrid procedure. S_p is then updated, and the process repeated until the global iterations converge.

Grid Adaption. The discretization presented above permits both conformal refinement and adaption with "hanging" nodes. In the latter case, cells marked for adaption are subdivided by introducing midpoint nodes at edges and/or cell and face centers. Nonconformal interfaces created by hanging node adaption thus require no special treatment. For example, the undivided cell C1 in Fig. 1(*a*) next to a divided cell is simply considered to be a polyhedron, bounded by the five faces $a - b$, $b - c$, $c - d$, $d - e$ and $e - a$.

Results

In this section we apply the method developed above to three demonstration problems. The first two compare computations with standard analytical solutions, and establish the accuracy and convergence of the method. The third problem demonstrates the method for a conjugate heat transfer problem in a natural convection application. We define the r.m.s. error in a variable f as

$$1/N\left(\sum_{N}\left(\frac{f_n - f_{n,\mathrm{exact}}}{f_{n,\mathrm{exact}}}\right)^2\right)^{1/2} \qquad (39)$$

where f_n is the value of the variable f at point n, $f_{n,\mathrm{exact}}$ is the exact value at the same point, and N is the total number of points.

Steady Conduction in an Anisotropic Block. Keyhani and Polehn (1995) have generated an interesting two-dimensional solution for anisotropic conduction from a one-dimensional solution. Consider the unit square in Fig. 3. The material is orthotropic, with a nonzero conductivity $k_{\zeta\zeta}$ in the ζ direction, and a zero conductivity $k_{\eta\eta}$ in the η direction, perpendicular to ζ. The solution is one-dimensional in ζ. In (x, y) coordinates the solution is fully two-dimensional, and is given by Keyhani and Polehn (1995).

The problem is computed using both quadrilateral and triangular meshes for $\theta = \pi/3$. For quadrilaterals, the complete square domain is used. The problem is computed for 100, 400, 1600, and 6400 uniformly distributed cells. The temperature along the vertical centerline is plotted in Fig. 4(*a*). Mesh independence is established with a 1600-cell mesh. For triangular meshes the domain is chosen to be an equilateral triangle with the base on the $y = 0$ boundary of Fig. 3. Boundary conditions taken from the exact solution are applied on all boundaries. We start with a uniform equilateral mesh of 256 cells and subdivide each cell into four to generate finer meshes while keeping the cells equilateral. Computations are done for 256, 1024, and 4096 cells. Mesh independence is achieved with the 1024-cell mesh, as seen from the plot of temperature on the vertical centerline in Fig. 4(*b*). With the finest mesh, the r.m.s. error in the bottom-wall heat flux was less than 0.05 percent. The method shows the expected second-order convergence. The r.m.s. errors in temperature along the vertical centerline for the 100, 400, and 1600 cell quadrilateral meshes were 0.28 percent, 0.07 percent, and 0.017 percent, respectively. Thus, the error falls by approximately a factor of 4 with each halving of the grid spacing.

We note that secondary gradient terms are nonzero for both quadrilateral and triangular meshes because of anisotropy. As a result, several global iterations are required for convergence. Typically, about 50 global iterations are required for scaled residuals to drop to 10^{-7}. For isotropic conduction, secondary gradient terms would be zero for the meshes used here, and the solution could be obtained in one global iteration.

In the case of quadrilaterals, all control-volume faces have both primary and secondary fluxes. The horizontal faces have the largest a_{nb} coefficients, since their normals are most closely

Table 1 Conjugate heat transfer in a partitioned enclosure—dimensionless average heat flux

Case	Top wall	Left wall
Isotropic conduction, conducting interface	1.35 (1.31)	1.64 (1.64)
Isotropic conduction, adiabatic interface	0.53	0.86
Case A: Orthotropic conduction, $k_{xx} > 0$, $k_{yy} = 0$	1.28	1.61
Case B: Orthotropic conduction, $k_{xx} = 0$, $k_{yy} > 0$	0.48	0.84

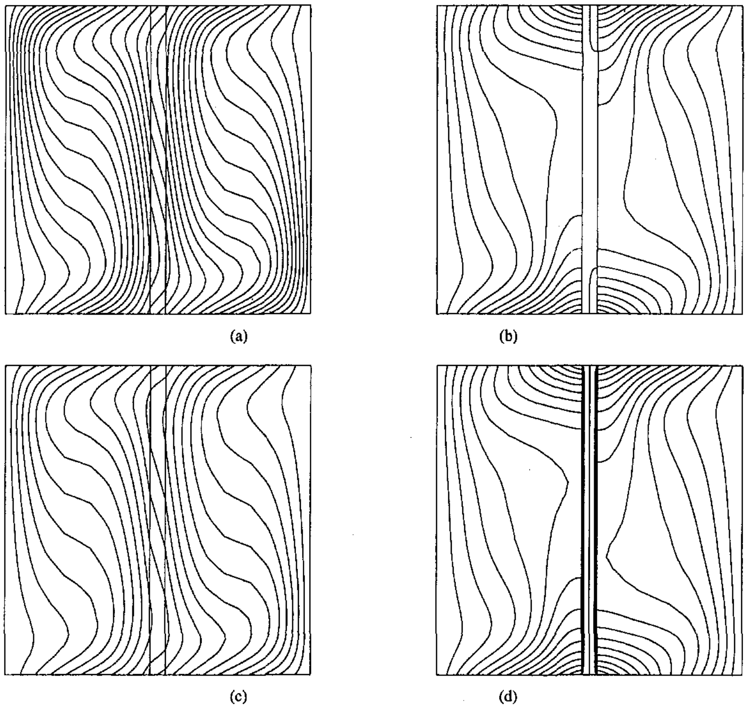

Fig. 9 Conjugate heat transfer in a partitioned enclosure—Isotherms; (*a*) isotropic partition, (*b*) adiabatic partition, (*c*) orthotropic partition case A, (*d*) orthotropic partition case B

aligned to the ζ-axis. For equilateral triangles, however, the ζ-axis is parallel to one set of control volume faces; for these faces, both primary and secondary fluxes are zero. For the other two faces, the a_{nb} coefficients are equal. As a result, coefficient-based multigrid agglomeration tends to produce coarse grid levels aligned in the ζ-direction, as shown in Fig. 5. This leads to efficient transfer of boundary information to the interior, and to fast convergence of the linear solver.

Unsteady Anisotropic Conduction. Here we consider unsteady orthotropic conduction in a rectangular slab of side L, as shown in Fig. 6(*a*). Initially, the slab is at a temperature T_0. For time $t \geq 0$, the $x = 0$ and $y = 0$ boundaries are kept insulated, and the boundaries at $x = L$ and $y = L$ lose heat by convection to an environment at T_∞, through heat transfer coefficients h_1 and h_2, respectively. In addition, a heat generation per unit volume, g_0, is also applied. The principal directions of the conductivity tensor are the x and y-axes, with conductivities k_1 and k_2, respectively. We choose $h_1L/k_1 = 1.0$, $h_2L/k_2 = 0.2$, $k_2/k_1 = 5.0$, and $g_0L^2/(k_1(T_0 - T_\infty)) = 10$. The conductivity ratio is typical of many thermoplastic matrix composites.

We compute the dimensionless temperature $\theta = (T - T_\infty)/(T_0 - T_\infty)$ as a function of dimensionless time $\tau = \alpha_1 t/L^2$ using an unstructured triangular mesh of 4198 cells. Care is taken to use a truly unstructured mesh as shown in Fig. 6(*b*), with no special alignment with the orthotropic axes. A dimensionless time step of 0.00125 is used. The results, shown in Fig. 7, are compared with the exact solution given by Ozisik (1980). The comparison at all time instants is good. To quantify the error, we compute the r.m.s. error in the temperature along $x/L = 0.5$ at different time instants. These are found to be 0.01 percent, 0.002 percent, 0.004 percent, 0.007 percent, and 0.007 percent at $\tau = 0.1, 0.3, 0.5, 1.0$, and at steady-state, respectively. The r.m.s. errors in the boundary temperature at steady state are 0.016 percent, 0.02 percent, 0.01 percent, and 0.015 percent on the left, right, bottom, and top boundaries, respectively.

Conjugate Heat Transfer in a Partitioned Enclosure. A square enclosure is partitioned into two equal halves by a conducting wall, as shown in Fig. 8(*a*). The left wall is at T_c and the right wall is at T_h, higher than T_c. The top and bottom walls have a linear temperature profile. The partition, of thickness d, is conducting. Yucel and Acharya (1991) have computed natural convection in the partitioned domain with and without participating radiation. In the absence of benchmarks solutions for conjugate heat transfer in anisotropic media, we use the work of Yucel and Acharya to establish the viability of our formulation.

We consider the case with no radiation for $Ra = g\beta(T_h - T_c)L^3/(\nu_f\alpha_f) = 10^5$, $\Pr = \nu_f/\alpha_f = 0.71$, $k_s/k_f = 2.0$, and $d/L = 0.05$. We first compare our solutions to the solutions of Yucel and Acharya for the case of an isotropic partition. Then we consider an orthotropic partition in two limits: (*i*) case A, where the partition is conducting only in the x-direction, with $k_{xx}/k_f = 2.0$ and $k_{yy}/k_f = 0.0$, and (*ii*) case B, where the partition is conducting only in the y-direction, with $k_{xx}/k_f = 0.0$ and $k_{yy}/k_f = 2.0$. Given the large aspect ratio of the partition and the fact that there is no net temperature difference between the top and bottom walls, we expect that case A will yield a solution very similar to the isotropic solution of Yucel and Acharya (1991). For case B, we expect the solution to be similar to the isotropic case with an adiabatic partition.

We start with a nonuniform 23 × 23 structured quadrilateral mesh, and adapt the mesh to $\partial T/\partial x$ using hanging-node adaption. Mesh-independence studies were carried out by starting with the structured mesh, and creating successively finer adapted meshes until the difference in the computed boundary heat fluxes between successive meshes was less than one percent. Final mesh sizes range from 6232 to 7564 cells. A typical mesh is shown in Fig. 8(*b*). The flow is computed using the Boussinesq assumption; details of the numerical scheme are available in Mathur and Murthy (1997).

Isotropic Partition. The dimensionless average heat flux on the top and left walls, $qL/(k_f(T_h - T_c))$, is shown in Table 1, along with the results of Yucel and Acharya (1991) in parentheses. Our computations are within one percent of their results. The isotherms in Fig. 9(*a*) show counterclockwise convection in both partitions. The isotherms in the conducting wall show that the primary direction of heat transfer is transverse to the partition, though some distortion of the isotherms occurs as a result of convection in the enclosure. These patterns are nearly identical to those presented by Yucel and Acharya.

We also computed convection in the enclosure for the case when the interface between the conducting wall and the fluid is adiabatic. Computed dimensionless heat fluxes on the top and left walls for this case are shown in Table 1. In this case, the conducting wall assumes a nearly uniform temperature since no transverse conduction is permitted by the adiabatic interface. Isotherms for this case are shown in Fig. 9(*b*).

Orthotropic Partition. The dimensionless average heat flux on the top and left walls for case A is shown in Table 1. Isotherms are shown in Fig. 9(*c*). Since the primary direction for heat transfer in the wall is transverse to the wall, this case yields a solution very similar to the case of the isotropically conducting wall described above.

Heat fluxes for case B are shown in Table 1. Corresponding isotherms are shown in Fig. 9(*d*). Since the transverse conductivity is zero, the partition acts like an adiabatic wall, and the patterns in the enclosure are similar to case of the adiabatic interface discussed above. Interestingly, however, the temperature solution in the partition wall is substantially different. For the orthotropic case, a temperature gradient in the transverse direction can be supported even though the solid/fluid interface is adiabatic, since the conductivity in the transverse direction is zero. This is not the case for isotropic conduction, and a nearly constant temperature is the only distribution consistent with an adiabatic interface.

Closure

A conservative finite-volume scheme has been developed for computing anisotropic conduction heat transfer on unstructured meshes. The discretization admits arbitrary convex polyhedra and solution-adaptivity. Though the method has been developed for conduction heat transfer, the formulation presented here can be used for other anisotropic diffusion equations, such as the pressure Poisson equation in porous media (Keyhani and Polehn, 1995). In conjunction with an unstructured mesh flow solver, the method may be used to analyze practical industrial applications.

Acknowledgments

We wish to acknowledge the contributions of J. Maruszewski and G. Spragle of Fluent Inc. to various aspects of this work. The use of Fluent Inc.'s software, FLUENT/UNS, TGrid, and PreBFC, is gratefully acknowledged.

References

Baliga, B. R., and Patankar, S. V., 1983, "A Control-Volume Finite Element Method for Two-Dimensional Fluid Flow and Heat Transfer," *Numerical Heat Transfer,* Vol. 6, pp. 245–261.

Banaszek, J., 1984, "A Conservative Finite Element Method for Heat Conduction Problems," *International Journal for Numerical Methods in Engineering,* Vol. 20, pp. 2033–2050.

Barth, T. J., 1992, "Aspects of Unstructured Grids and Finite-Volume Solvers for the Euler and Navier-Stokes Equations," Special Course on Unstructured Grid Methods for Advection Dominated Flow, AGARD Report 787.

Beyeler, E. P., and Guceri, S. I., 1988, "Thermal Analysis of Laser-Assisted Thermoplastic-Matrix Composite Tape Consolidation," ASME JOURNAL OF HEAT TRANSFER, Vol. 110, pp. 424–430.

Blackwell, B. F., and Hogan, R. E., 1993, "Numerical Solution of Axisymmetric Heat Conduction Problems Using Finite Control Volume Technique," *Journal of Thermophysics and Heat Transfer,* Vol. 7, pp. 462–471.

Brandt, A., 1977, "Multi-Level Adaptive Solutions to Boundary Value Problems," *Math. Comput.,* Vol. 31, pp. 333–390.

Davidson, L., 1996, "A Pressure Correction Method for Unstructured Meshes with Arbitrary Control Volumes," *International Journal for Numerical Methods in Fluids,* Vol. 22, pp. 265–281.

Demirdzic, I., and Muzaferija, S., 1995, "Numerical Method for Coupled Fluid Flow, Heat Transfer and Stress Analysis Using Unstructured Moving Meshes With Cells of Arbitrary Topology," *Comp. Meth. Appl. Mech. Eng.,* Vol. 125, pp. 235–255.

Howle, L. E., and Georgiadis, J. G., 1994, "Natural Convection in Porous Media with Anisotropic Dispersive Thermal Conductivity," *Int. J. Heat Mass Transfer,* Vol. 37, pp. 1081–1094.

Hutchinson, B. R., and Raithby, G. D., 1986, "A Multigrid Method Based on the Additive Correction Strategy," *Numerical Heat Transfer,* Vol. 9, pp. 511–537.

Jiang, Y., and Przekwas, A. J., 1994, "Implicit, Pressure-Based Incompressible Navier-Stokes Equations Solver for Unstructured Meshes," AIAA-94-0305.

Karki, K. C., and Patankar, S. V., 1989, "Pressure Based Calculation Procedure for Viscous Flows at all Speeds in Arbitrary Configurations," *AIAA Journal,* Vol. 27, No. 9, pp. 1167–1174.

Katayama, K., and Saito, A., 1974, "Transient Heat Conduction in Anisotropic Solids," *International Heat Transfer Conference,* Vol. 1, pp. 137–141.

Kelkar, K. M., 1990, "Iterative Method for the Numerical Prediction of Heat Transfer in Problems Involving Large Differences in Thermal Conductivities," *Numerical Heat Transfer,* Vol. 18, No. 1, pp. 113–128.

Keyhani, M., and Polehn, R. A., 1995, "Finite Difference Modeling of Anisotropic Flows," ASME JOURNAL OF HEAT TRANSFER, Vol. 117, pp. 458–464.

Lonsdale, R. D., 1991, "An Algebraic Multigrid Scheme for Solving the Navier-Stokes Equations on Unstructured Meshes," *Proceedings of the 7th International Conference on Numerical Methods in Laminar and Turbulent Flow,* pp. 1432–1442.

Mathur, S. R., and Murthy, J. Y., 1997, "A Pressure-Based Method for Unstructured Meshes," *Numer. Heat Transfer,* Vol. 31, No. 2, pp. 195–216.

Nejhad, M. N. Ghasemi, Cope, R. D., and Guceri, S. I., 1991, "Thermal Analysis of In-Situ Thermoplastic-Matrix Composite Filament Winding," ASME *Journal of Heat Transfer,* Vol. 113, pp. 304–313.

Ozisik, N., 1980, *Heat Conduction,* John Wiley and Sons, New York, pp. 632–638.

Padovan, J., 1974, "Steady Conduction of Heat in Linear and Non-Linear Fully Anisotropic Media by Finite Elements," ASME JOURNAL OF HEAT TRANSFER, Vol. 96, pp. 313–318.

Patankar, S. V., 1980, *Numerical Heat Transfer and Fluid Flow,* McGraw-Hill, New York.

Peric, M., 1985, "A Finite Volume Method for the Prediction of Three-Dimensional Fluid Flow in Complex Ducts," Ph.D. thesis, University of London, London, UK.

Schneider, G. E., and Raw, M. J., 1987, "Control-Volume Finite-Element Method for Heat Transfer and Fluid Flow Using Co-Located Variables—1. Computational Procedures," *Numerical Heat Transfer,* Vol. 11, pp. 363–390.

Venkatakrishnan, V., 1993, "On The Accuracy of Limiters and Convergence to Steady State Solutions," AIAA 93-0880.

Weaver, J. A., and Viskanta, R., 1989, "Effects of Anisotropic Conduction on Solidification," *Numerical Heat Transfer,* Vol. 15, pp. 181–195.

Yucel, A., and Acharya, S., 1991, "Natural Convection of a Radiating Fluid in a Partially Divided Enclosure," *Numerical Heat Transfer,* Vol. 19, pp. 471–485.

C. Aviles-Ramos

A. Haji-Sheikh
e-mail: haji@mecad.uta.edu
Fellow ASME

Department of Mechanical and
Aerospace Engineering,
The University of Texas at Arlington,
Arlington, TX 76019-0023

J. V. Beck
Department of Mechanical Engineering,
Michigan State University,
East Lansing, MI 48824-1226
Fellow ASME

Exact Solution of Heat Conduction in Composite Materials and Application to Inverse Problems

Calculation of temperature in high-temperature materials is of current interest to engineers, e.g., the aerospace industry encounters cooling problems in aircraft skins during the flight of high-speed air vehicles and in high-Mach-number reentry of spacecraft. In general, numerical techniques are used to deal with conduction in composite materials. This study uses the exact series solution to predict the temperature distribution in a two-layer body: one orthotropic and one isotropic. Often the exact series solution contains an inherent singularity at the surface that makes the computation of the heat flux difficult. This singularity is removed by introducing a differentiable auxiliary function that satisfies the nonhomogeneous boundary conditions. Finally, an inverse heat conduction technique is used to predict surface temperature and/or heat flux.

Introduction

The transient and steady-state temperature distribution in composite configurations consisting of several distinct thermally anisotropic subdomains have numerous applications to heat transfer problems in reentry vehicles, air frames, nuclear reactors, etc. The increased use of composite materials in the automotive and aerospace industries has motivated research into experimental techniques and solution methods to determine the thermal properties of these materials. The main purpose of this study is to find the surface heat flux from the knowledge of interior temperature histories when the composite bodies are heated by unknown, or partially known, surface conditions. This problem is solved by finding the exact solution of the direct heat conduction problem and subsequently using it as a model to solve the inverse heat conduction problem.

The analytical solutions of heat conduction problems in composite media have been investigated by several authors. Tittle (1965) developed a one-dimensional orthogonal expansion for a composite medium while Padovan (1974) surveyed the earlier work and developed a generalized Sturm-Liouville procedure for composite and anisotropic domains in transient heat conduction problems. Ozisik (1980, Chapter 14) discussed the application of the integral transform technique for the solution of heat conduction problems in composite media. Salt (1983) investigated the transient temperature solution in a two-dimensional isotropic-composite slab which is coupled to its environment through the surface of one layer only, after the temperature of the environment has suffered a step change. Mikhailov and Ozisik (1986) analyzed the three-dimensional version of the problem considered by Salt (1983). More recently, Yan et al. (1993) published exact series solutions for three-dimensional temperature distributions in two-layer bodies subject to various types of boundary conditions.

The specimen under consideration is composed of one carbon matrix-carbon fiber material (orthotropic) and a layer of mica (isotropic). Experimental measurements made on this specimen were reported by Dowding et al. (1996). The objective is to find the exact solution of the direct heat conduction problem, and to use it with the published thermal properties and temperature measurements to determine the spatially variable and time-dependent heat flux at the surface of the specimen. The emphasis of this work is to develop an alternative Green's function solution method that includes the quasi-steady-state solution as an auxiliary function (Beck et al., 1992). The quasi-steady-state solution should satisfy all homogeneous and nonhomogeneous boundary conditions of the temperature problem. For application to inverse heat conduction, the alternative Green's function solution leads to a well-behaved integral equation of the second kind.

In general, problems emerge in heat transfer where heat flux and/or temperature values at a heated or cooled surface are needed and it is often physically difficult to place sensors at the surface to measure surface temperature and heat flux. The study of heat transfer in a high-temperature environment underlines this problem. One can place temperature sensors in the material domain and use the response of the sensors to predict both surface temperature and surface heat flux. In theory, using minimization principles, it is possible to calculate thermophysical properties in addition to surface temperature and/or heat flux by this method.

The specific case studied here deals with heat conduction in a multidimensional two-layer body, one orthotropic and one isotropic, subject to boundary conditions of the second kind. First, transient and quasi-steady-state solutions are discussed. Next, the application of this exact solution to compute the surface heat flux is presented and the physical model employed is similar to that used in Dowding et al. (1996). The boundary conditions of the second kind make the exact solution a formidable problem. The completeness and orthogonality of the eigenfunctions are two important topics discussed here.

Analysis

Before discussing the inverse formulation, the exact series solution for the temperature distribution in a two-layer body, Fig. 1, will be presented. The orthotropic layer shown in Fig. 1 is carbon-carbon composite and the isotropic layer is mica. The diffusion equation in the carbon-carbon layer, region 1, is

---

Contributed by the Heat Transfer Division for publication in the JOURNAL OF HEAT TRANSFER and presented at '97 IMECE, Dallas. Manuscript received by the Heat Transfer Division, Aug. 18, 1997; revision received, Apr. 16, 1998. Keywords: Analytical, Composites, Conduction, Heat Transfer, Inverse, Properties. Associate Technical Editor: A. Lavine.

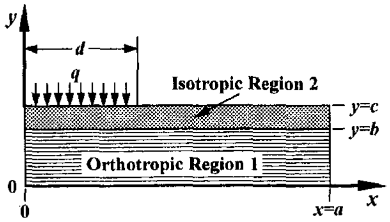

Fig. 1 Schematic of a two-layer body: an orthotropic layer and an isotropic layer

$$k_{1x}\frac{\partial^2 T_1}{\partial x^2}+k_{1y}\frac{\partial^2 T_1}{\partial y^2}+g_1(x,y,t)=\rho_1 c_{p1}\frac{\partial T_1}{\partial t}. \tag{1}$$

Now, consider an isotropic mica layer in perfect thermal contact with a carbon-carbon layer. The diffusion equation in the mica layer, region 2, is

$$k_2\frac{\partial^2 T_2}{\partial x^2}+k_2\frac{\partial^2 T_2}{\partial y^2}+g_2(x,y,t)=\rho_2 c_{p2}\frac{\partial T_2}{\partial t} \tag{2}$$

where $g_1(x, y, t)$ and $g_2(x, y, t)$ are volumetric heat source functions that could include the surface heat flux and a contribution from the quasi-steady-state temperature. Equations (1) and (2) are subjected to the following homogeneous boundary and interface conditions:

$$\frac{\partial T_i}{\partial x}=0 \quad \text{at} \quad x=0 \quad \text{and} \quad x=a \quad \text{for} \quad i=1 \text{ or } 2 \tag{3}$$

$$\frac{\partial T_1}{\partial y}=0 \quad \text{at} \quad y=0 \tag{4}$$

$$k_{1y}\left(\frac{\partial T_1}{\partial y}\right)_{y=b}=k_2\left(\frac{\partial T_2}{\partial y}\right)_{y=b} \tag{5}$$

$$T_1(x,b)=T_2(x,b). \tag{6}$$

The nonhomogeneous boundary condition at $y = c$ is

$$k_2\left(\frac{\partial T_2}{\partial y}\right)_{y=c}=q(x,t). \tag{7}$$

The initial temperatures in regions 1 and 2 are designated as $T_1(x, y, 0)$ and $T_2(x, y, 0)$. Using a standard transformation for orthotropic bodies

$$\bar{y}=y\sqrt{\frac{k_{1x}}{k_{1y}}}, \tag{8}$$

and a methodology based on the separation of variables similar to the one discussed by Yan et al. (1993), both solutions for T_1 and T_2 have the common forms,

$$T_1(x,y,t)=\sum_{n=0}^{\infty}\sum_{m=0}^{\infty}A_{mn}(t)\cos(n\pi x/a)\cos(\gamma_{mn}k_r y)\exp(-\lambda_{mn}^2 t) \tag{9}$$

and

$$T_2(x,y,t)=\sum_{n=0}^{\infty}\sum_{m=0}^{\infty}A_{mn}(t)\cos(n\pi x/a)[B_{mn}\sin(\eta_{mn}y)+C_{mn}\cos(\eta_{mn}y)]\exp(-\lambda_{mn}^2 t), \tag{10}$$

where $k_r = \sqrt{k_{1x}/k_{1y}}$ and γ_{mn} and η_{mn} are related to λ_{mn} by the equations

$$\gamma_{mn}=\sqrt{\lambda_{mn}^2/\alpha_{1x}-(n\pi/a)^2} \tag{11}$$

$$\eta_{mn}=\sqrt{\lambda_{mn}^2/\alpha_2-(n\pi/a)^2} \tag{12}$$

in which $\alpha_{1x} = k_{1x}/\rho_1 c_{p1}$ and $\alpha_2 = k_2/\rho_2 c_{p2}$. Notice that for γ_{mn} and η_{mn} to be real, λ_{mn} must be equal to or larger than the largest of the quantities $\{(n\pi/a)\sqrt{\alpha_{1x}}, (n\pi/a)\sqrt{\alpha_2}\}$. It is noted that γ_{mn} and η_{mn} can be real or imaginary depending on the values of α_{1x}, α_2, n, and m; further discussion concerning γ_{mn} and η_{mn} will appear later. The contact conditions at $y = b$ yield the values of B_{mn} and C_{mn} as

Nomenclature

a, b, c, d = dimensions in Fig. 1, cm
A, B, C = constants
$\bar{a} = a/b$
A_{mn} = Fourier coefficients, Eq. (28)
B_{mn} = coefficient, Eq. (13)
$\bar{c} = c/b$
C_{mn} = coefficients, Eq. (14)
c_{pi} = specific heat in region i = 1 or 2, J/kgK
d_j = coefficients in Eq. (47)
$\bar{d} = d/a$
D, E = constants
$\hat{\mathbf{D}}$ = vector of coefficients Eq. (49)
D_n = coefficient, Eq. (38)
E_n = coefficient, Eq. (39)
$F_{i,mn}$ = eigenfunctions, Eqs. (17), (18), i = 1, 2
$f(t)$ = a function of time
$\bar{g}_o$ = constant related to surface heat flux
g_i = volumetric heat source in region i, W/cm^3
$\bar{g}_i$ = constant related to heat source
G_{ij} = Green's function
$H(t)$ = Heaviside function
i, j = indices
k_{1x} = thermal conductivity in region 1 along x, W/cmK
k_{1y} = thermal conductivity in region 1 along y, W/cmK
k_2 = thermal conductivity in region 2, W/cmK
$k_r = (k_{1x}/k_{1y})^{1/2}$
l = index to designate thermocouple number
m, n = indices in eigenfunctions
M = number of temperature measurements
N = number of unknowns minus 1
N_{mn} = norm, Eq. (20)
q = input heat flux, W/m^2
$s(x)$ = spatial function
S_j = constants
t = time, s
T_j = temperature in regions 1 and 2, *K*
T_j^* = quasi-steady temperature in regions 1 and 2, K
$T_{l,i}$ = temperature, Eq. (31), *K*
$T_{G,i}$ = temperature, Eq. (32), K
V = volume, cm^3
x, y = coordinates, cm
$\bar{y} = yk_r$
$\mathbf{Y}$ = column vector of measured data

Greek

α_{1x} = thermal diffusivity along the x-direction in region 1, cm^2/s
α_2 = thermal diffusivity in region 2, cm^2/s
β_n = eigenvalue for x-direction, $n\pi/a$, cm^{-1}
δ = Dirac delta function
γ_{mn} = eigenvalue for y-direction in region 1, cm^{-1}
η_{mn} = eigenvalue for y-direction in region 2, cm^{-1}
λ_{mn} = eigenvalue for time, s^{-1}
Λ_{mn} = initial condition constant
θ_1, θ_2 = solutions of Laplace equation
ρ_1, ρ_2 = density of regions 1 and 2, kg/cm^3
$\hat{\sigma}^2$ = variance
ψ_n = notation, Eq. (40)
$\mathbf{\Phi}$ = matrix, Eq. (49)

$$B_{mn} = \cos(\gamma_{mn}k_r b)\sin(\eta_{mn}b) - (\gamma_{mn}/\eta_{mn})(\sqrt{k_{1x}k_{1y}}/k_2)\sin(\gamma_{mn}k_r b)\cos(\eta_{mn}b) \qquad (13)$$

$$C_{mn} = \cos(\gamma_{mn}k_r b)\cos(\eta_{mn}b) + (\gamma_{mn}/\eta_{mn})(\sqrt{k_{1x}k_{1y}}/k_2)\sin(\gamma_{mn}k_r b)\sin(\eta_{mn}b). \qquad (14)$$

A homogeneous boundary condition at $y = c$ yields a relation

$$\tan(\eta_{mn}c) = B_{mn}/C_{mn} \qquad (15)$$

that reduces to

$$\tan[\eta_{mn}(c-b)] = -(\gamma_{mn}/\eta_{mn})(\sqrt{k_{1x}k_{1y}}/k_2)\tan(\gamma_{mn}k_r b) \qquad (16)$$

for finding the eigenvalues. In a numerical scheme to calculate the eigenvalues, the parameters γ_{mn} and η_{mn} in Eqs. (13), (14), and (15) were replaced by λ_{mn} using Eqs. (11) and (12) and the roots of Eq. (15) are obtained numerically.

Orthogonality. In the subsequent formulations, the following shorthand notation will identify the eigenfunctions:

$$F_{1,mn}(x, y) = \cos(n\pi x/a)\cos(\gamma_{mn}k_r y) \qquad (17)$$

and

$$F_{2,mn}(x, y) = \cos(n\pi x/a)[B_{mn}\sin(\eta_{mn}y) + C_{mn}\cos(\eta_{mn}y)]. \qquad (18)$$

A study of orthogonality shows that

$$(\lambda_{\mu\nu}^2 - \lambda_{mn}^2)\left[\int_0^a\int_0^b \rho_1 c_{p1}F_{1,mn}F_{1,\mu\nu}dydx + \int_0^a\int_b^c \rho_2 c_{p2}F_{2,mn}F_{2,\mu\nu}dydx\right] = 0. \qquad (19)$$

According to Eq. (19), the term in the square bracket is equal to zero except when $\mu = m$ and $\nu = n$; therefore, the norm is

$$N_{mn} = \int_0^a\int_0^b \rho_1 c_{p1}(F_{1,mn})^2 dydx + \int_0^a\int_b^c \rho_2 c_{p2}(F_{2,mn})^2 dydx. \qquad (20)$$

Fourier Coefficients and Temperature Solutions. The solution is obtained by substituting Eqs. (9) and (10) into Eqs. (1) and (2) and making use of the two-dimensional eigenvalue problem

$$\frac{\partial^2 F_{1,mn}}{\partial x^2} + \frac{\partial^2 F_{1,mn}}{\partial y^2} + \frac{\lambda_{mn}^2}{k_{1x}}F_{1,mn} = 0 \qquad (21)$$

$$\frac{\partial^2 F_{2,mn}}{\partial x^2} + \frac{\partial^2 F_{2,mn}}{\partial y^2} + \frac{\lambda_{mn}^2}{k_2}F_{2,mn} = 0 \qquad (22)$$

for $m \geq 0$ and $n \geq 0$, to obtain

$$\sum_{m=0}^{\infty}\sum_{n=0}^{\infty} F_{1,mn}(x, y)\frac{dA_{mn}}{dt}\exp(-\lambda_{mn}^2 t) = \frac{\alpha_{1x}}{k_{1x}}g_1(x, y, t) \qquad (23)$$

$$\sum_{m=0}^{\infty}\sum_{n=0}^{\infty} F_{2,mn}(x, y)\frac{dA_{mn}}{dt}\exp(-\lambda_{mn}^2 t) = \frac{\alpha_2}{k_2}g_2(x, y, t). \qquad (24)$$

Both sides of Eqs. (23) and (24) are multiplied by $\rho_1 c_{p1}F_{1,\mu\nu}(x, y)$ and $\rho_2 c_{p2}F_{2,\mu\nu}(x, y)$, respectively, to obtain

$$\rho_1 c_{p1}\sum_{m=0}^{\infty}\sum_{n=0}^{\infty} F_{1,mn}(x, y)F_{1,\mu\nu}(x, y)\frac{dA_{mn}}{dt}\exp(-\lambda_{mn}^2 t) = g_1(x, y, t)F_{1,\mu\nu}(x, y) \qquad (25)$$

$$\rho_2 c_{p2}\sum_{m=0}^{\infty}\sum_{n=0}^{\infty} F_{2,mn}(x, y)F_{2,\mu\nu}(x, y)\frac{dA_{mn}}{dt}\exp(-\lambda_{mn}^2 t) = g_2(x, y, t)F_{2,\mu\nu}(x, y). \qquad (26)$$

Integrating Eqs. (25) and (26) over regions 1 and 2, respectively, adding the resulting equations, and applying the orthogonality condition, Eq. (19), and Eq. (20), one gets

$$\frac{dA_{mn}}{dt} = \frac{1}{N_{mn}}\left[\int_0^a\int_0^b g_1(x, y, t)F_{1,mn}(x, y)dydx + \int_0^a\int_b^c g_2(x, y, t)F_{2,mn}(x, y)dydx\right]\exp(\lambda_{mn}^2 t). \qquad (27)$$

Integrating Eq. (27) yields the value of the Fourier coefficients

$$A_{mn} = \Lambda_{mn} + \frac{1}{N_{mn}}\int_{\tau=0}^{t}\left[\int_0^a\int_0^b g_1(x, y, t)F_{1,mn}(x, y)dydx + \int_0^a\int_b^c g_2(x, y, t)F_{2,mn}(x, y)dydx\right]\exp(\lambda_{mn}^2\tau)d\tau. \qquad (28)$$

The integration constant, Λ_{mn}, is calculated by substituting Eq. (28) into Eqs. (9) and (10) and applying the initial conditions to obtain

$$T_i(x, y, 0) = \sum_{n=0}^{\infty}\sum_{m=0}^{\infty}\Lambda_{mn}F_{i,mn}(x, y) \quad \text{for} \quad i = 1, 2. \qquad (29)$$

For each i, multiplying Eq. (29) by $\rho_i c_{pi}F_{i,\mu\nu}$, integrating the resulting equations over the ith region, adding them, and applying the orthogonality relation, Eq. (19), yields the constant Λ_{mn}

$$\Lambda_{mn} = \frac{1}{N_{mn}}\left[\int_0^a\int_0^b \rho_1 c_{p1}F_{1,mn}(x', y')T_1(x', y', 0)dy'dx' + \int_0^a\int_b^c \rho_2 c_{p2}F_{2,mn}(x', y')T_2(x', y', 0)dy'dx'\right]. \qquad (30)$$

The final solutions are obtained by inserting Λ_{mn} from Eq. (30) in Eq. (28) and then substituting A_{mn} into Eqs. (9) and (10). The resulting equations satisfy the homogeneous boundary conditions over all surfaces and each equation has two parts. The first part is the fundamental solution that provides the contribution of the initial condition

$$T_{I,i} = \sum_{n=0}^{\infty}\sum_{m=0}^{\infty}\frac{F_{i,mn}(x, y)}{N_{mn}}\exp(-\lambda_{mn}^2 t)\left[\int_0^a\int_0^b \rho_1 c_{p1} \times F_{1,mn}(x', y')T_1(x', y', 0)dy'dx' + \int_0^a\int_b^c \rho_2 c_{p2}F_{2,mn}(x', y')T_2(x', y', 0)dy'dx'\right]; \quad \text{for} \quad i = 1 \quad \text{or} \quad 2. \qquad (31)$$

The second part accounts for the effect of the volumetric heat source while the initial temperature is zero; the heat flux at the wall multiplied by the Dirac delta function will be viewed as a volumetric heat source,

$$T_{G,i} = \sum_{n=0}^{\infty} \sum_{m=0}^{\infty} \frac{F_{i,mn}(x, y)}{N_{mn}} \int_{\tau=0}^{t} \exp[-\lambda_{mn}^2(t-\tau)] \times \left[\int_0^a \int_0^b g_1(x', y', \tau) F_{1,mn}(x', y') dy' dx' + \int_0^a \int_b^c g_2(x', y', \tau) F_{2,mn}(x', y') dy' dx' \right] d\tau;$$

$$\text{for} \quad i = 1 \quad \text{or} \quad 2. \qquad (32)$$

The final temperature solution is the sum of these two solutions

$$T_i(x, y, t) = T_{I,i}(x, y, t) + T_{G,i}(x, y, t); \quad \text{for} \quad i = 1 \quad \text{or} \quad 2 \qquad (33)$$

that includes the effect of initial condition and internal volumetric heat source. Equations (1) through (33) are for two-dimensional bodies and they can readily be modified for three-dimensional bodies. A two-dimensional analysis is employed for convenience of the presentation and to facilitate a comparison with the experimental data of Dowding et al. (1996).

For a solid illustrated in Fig. 1, a constant heat flux, q, is applied to the surface, $y = c$, within $0 \le x \le d$, at $t = 0$ and then cut off at time t_s. This condition is accounted for by considering Eq. (32) having the volumetric heat sources $g_1(x, y, t) = 0$ and $g_2(x, y, t) = q\delta(y - c)[H(t) - H(t - t_s)]$ where $\delta(y - c)$ is the Dirac delta function, and $H(t) - H(t - t_s)$ is the Heaviside function. Furthermore, Eq. (31) provides the contribution of the initial temperature. Because of an inherent singularity at the surface, Eq. (32) converges slowly to the solution. This can be improved by introducing an auxiliary differentiable function that satisfies both homogeneous and nonhomogeneous boundary conditions, such as the quasi-steady-state solution.

Quasi-Steady-State Solution. Under quasi-steady-state conditions, the temperature throughout the material domain changes linearly with time if the heat flux at the wall, q, is independent of time, i.e., $\partial T^*/\partial t = \bar{g}_o$. Using the energy balance, the value of $\bar{g}_o$ is

$$\bar{g}_o = \left[\int_0^d q(x) dx \right] \Big/ (a c \rho_e c_{pe})$$

where $\rho_e c_{pe} = [\rho_1 c_{p1} b + \rho_2 c_{p2}(c - b)]/c$. When $\partial T_i^*/\partial t = \bar{g}_o$, the homogeneous versions of Eqs. (1) and (2), $g_i = 0$, reduce to the following Poisson's equations:

$$k_{1x} \frac{\partial^2 T_1^*}{\partial x^2} + k_{1y} \frac{\partial^2 T_1^*}{\partial y^2} = \rho_1 c_{p1} \bar{g}_o \qquad (34)$$

$$k_2 \frac{\partial^2 T_2^*}{\partial x^2} + k_2 \frac{\partial^2 T_2^*}{\partial y^2} = \rho_2 c_{p2} \bar{g}_o. \qquad (35)$$

When $\bar{g}_1 = \bar{g}_o \rho_1 c_{p1}$, $\bar{g}_2 = \bar{g}_o \rho_2 c_{p2}$, the standard transformations $T_1^* = \theta_1 + \bar{g}_1 y^2/2k_{1y} + S_1 y + S_2$ and $T_2^* = \theta_2 + \bar{g}_2 y^2/2k_2 + S_3 y + S_4$ reduce the above Poisson's equations into two Laplace equations for θ_1 and θ_2. Because of boundary conditions of the second kind at $y = 0$ and $y = c$, either S_2 or S_4 is an arbitrary constant. The insulated boundary at $y = 0$ requires $S_1 = 0$ and to simplify the algebra, the arbitrary constant is $S_2 = -\bar{g}_1 b^2/2k_{1y}$. The contact condition at $y = b$ yields $S_3 = \bar{g}_1 b/k_2 - \bar{g}_2 b/k_2$ and $S_4 = \bar{g}_2 b^2/2k_2 - \bar{g}_1 b^2/k_2$; the transformations reduce to $T_1^*(x, y, t) = \theta_1 + \bar{g}_o t/\rho_e c_{pe} + \bar{g}_1 (y - b)^2/2k_{1y} + \bar{g}_1 b(y - b)/k_{1y}$ and $T_2^*(x, y, t) = \theta_2 + \bar{g}_o t/\rho_e c_{pe} + \bar{g}_2 (y - b)^2/2k_2 + \bar{g}_1 (y - b)/k_2$. Notice that the transformations are augmented by the term $\bar{g}_o t/\rho_e c_{pe}$. The substitutions of T_1^* in Eq. (34) and T_2^* in Eq. (35) yield two Laplace equations and the solutions for θ_1 and θ_2 result in the final equations for T_1^* and T_2^*,

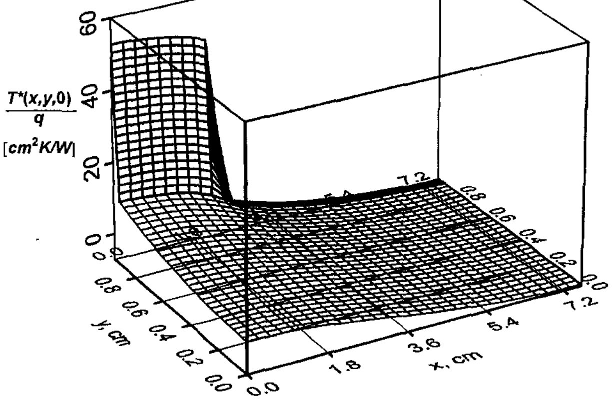

Fig. 2 Three-dimensional representation of the quasi-steady-state solution, $T^*(x, y, 0)/q$

$$T_1^* = \bar{g}_o t + \frac{\bar{g}_1 (y - b)^2}{2k_{1y}} + \frac{\bar{g}_1 b(y - b)}{k_{1y}} + \frac{2}{a} \sum_{n=1}^{\infty} \frac{q \sin(n\pi d/a)}{k_2 (n\pi/a)^2 \psi_n} \cos(n\pi x/a) \cosh(n\pi k_r y/a) \qquad (36)$$

and

$$T_2^* = \bar{g}_o t + \frac{\bar{g}_2 (y - b)^2}{2k_2} + \frac{\bar{g}_1 b(y - b)}{k_2} + \left(\frac{2}{a}\right) \sum_{n=1}^{\infty} \frac{q \sin(n\pi d/a)}{k_2 (n\pi/a)^2 \psi_n} \cos(n\pi x/a) \times [D_n \sinh(n\pi y/a) + E_n \cosh(n\pi y/a)] \qquad (37)$$

where $T_1^* = T_1^*(x, y, t)$ and $T_2^* = T_2^*(x, y, t)$. The contact conditions at $y = b$ and boundary condition at $y = c$ result in the relations

$$D_n = (\sqrt{k_{1x} k_{1y}}/k_2) \sinh(n\pi k_r b/a) \cosh(n\pi b/a) - \cosh(n\pi k_r b/a) \sinh(n\pi b/a) \qquad (38)$$

$$E_n = \cosh(n\pi k_r b/a) \cosh(n\pi b/a) - (\sqrt{k_{1x} k_{1y}}/k_2) \sinh(n\pi k_r b/a) \sinh(n\pi b/a) \qquad (39)$$

$$\Psi_n = D_n \cosh(n\pi c/a) + E_n \sinh(n\pi c/a). \qquad (40)$$

In the numerical computations, it is assumed that heat is entering the system and therefore q is negative. A three-dimensional plot of T^*, when $t = 0$, is presented in Fig. 2 that indicates a satisfactory behavior of the quasi-steady-state solution.

Equations (36) and (37) give the quasi-steady-state solution within a constant. This constant can be selected so that the temperature is the correct transient temperature for the transient problem after the initial transients have disappeared and it is found by making the volumetric heat-capacity-weighted temperature equal to zero at $t = 0$. The auxiliary functions T_1^* and T_2^* become the true quasi-steady-state temperature when the constant

$$\frac{\bar{g}_1 b^3}{3ck_{1y}} - \frac{\bar{g}_2 (c - b)^3}{6ck_2} - \frac{\bar{g}_1 b(c - b)^2}{2ck_2} \qquad (41)$$

is added to Eqs. (36) and (37). This constant has no influence on the value of T_1 and T_2 since it will reduce the coefficient A_{00} by exactly the same constant.

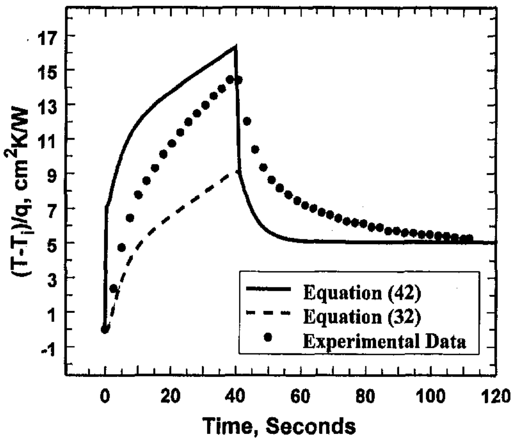

Fig. 3 A comparison of two temperature solutions at (0.889, 0.9144) with the experimental data, Dowding et al. (1996)

Now, the superposition of two solutions, Eq. (31) and Eq. (36) or (37) for $i = 1$ or 2 yields the transient temperature solution

$$T_i(x, y, t) = T_i^*(x, y, t) + T_{I,i}(x, y, t). \qquad (42)$$

The superposition of solutions requires using a new initial condition $T_i(x, y, 0) - T_i^*(x, y, 0)$ instead of $T_i(x, y, 0)$ in Eq. (31).

Solution Verification. Equations (42) and (32) are employed to solve for the effect of surface heat flux. To check the validity of these solutions, the following numerical values that are consistent with the experimental information, Dowding et al. (1996), are selected: $a = 7.62$ cm, $b = 0.9144$ cm, $c = 0.958$ cm, $d = 0.31a$ cm, $k_{1x} = 0.593$ W/cmK, $k_{1y} = 0.0484$ W/cmK, $\rho_1 c_{p1} = 2.509$ J/cm^{3}K, $k_2 = 0.001$ W/cm, and $\rho_2 c_{p2} = 2$ J/cm^{3}K.

It was noted that, for the above parameters, the imaginary values of γ_{mn} would significantly influence the temperature solution and a numerical study confirms this. For a solid shown in Fig. 1, Fig. 3 shows the effect of imaginary γ_{mn} values when using data obtained from Eqs. (42) and (32). The input heat flux is $q = 1$ W/cm^2 from $t = 0$ to 40 seconds and the solid is initially at a uniform temperature. Although the solid line, Eq. (42), and the dash line, Eq. (32), in Fig. 3 should be identical, the results are quite different and, in fact, unacceptable. A comparison with the experimental data of Dowding et al. (1996), for the referenced location, confirmed that neither solution is correct. A study of the basis functions revealed that this set is not complete since the solution excluded λ_{mn} values that will yield imaginary values for γ_{mn} when $n > 0$. An imaginary γ_{mn} value makes $\cos(\gamma_{mn} k_r y)$ in Eqs. (13) and (17) to become $\cosh(|\gamma_{mn}| k_r y)$, and $\cos(\gamma_{mn} k_r b)$ and $\gamma_{mn} \sin(\gamma_{mn} k_r b)$ in Eqs. (13) and (14) to become $\cosh(|\gamma_{mn}| k_r b)$ and $-|\gamma_{mn}| \sinh(|\gamma_{mn}| k_r b)$.

Table 1 A sample of convergence for $(T - T_i)/q$ within ±0.1 percent for (0.889, 0.9144) location in Fig. 4

Time, seconds	$T - T_i$, °C Exact	Eq. (43) Temp.	Eq. (43) N†	Eq. (33) Temp.	Eq. (33) N†
6	5.1525	5.1566	11	5.1551	46
12	8.2792	8.2822	3	8.2783	34
24	11.737	11.737	3	11.745	37
36	14.208	14.208	3	14.196	33
60	7.4233	7.4231	3	7.4231	3

† N is the number of terms for x and y-directions.

Figure 4 is prepared to show the solutions using Eqs. (42) and (32) when all eigenvalues are retained. The temperature at three surface locations with (x, y) coordinates of (1.270, 0), (0.889, 0.9144), and (1.905, 0.9144) and for $q = 1$ W/cm^2 is calculated using Eqs. (42) and (32) while retaining the contribution of imaginary γ_{mn}. The calculated temperature, $(T - T_i)/q$, is plotted in Fig. 4. The results show excellent agreement except for extremely small time. The difference in these two solutions is in the fifth significant figure when using 65 terms for both m and n. Typically, the solution that uses T^* converges faster at large time. The computed temperature converged using a smaller number of terms. For a typical set of data, Table 1 shows the number of terms needed for Eq. (42) to provide a temperature solution at $x = 0.889$ cm and $y = 0.9144$ cm within 0.1 percent of the exact solution. For comparison, Table 1 includes similar data using Eq. (32). For time larger than six seconds, only three terms for x and y directions will provide accurate results. For the same accuracy a solution that uses Eq. (32) needs significantly more terms.

A numerical study of the surface heat flux shows the reason for better convergence of Eq. (42). Unlike the temperature solution given by Eq. (32), Eq. (42) is free from singularities when calculating the surface heat flux. The value of the heat flux, when using Eq. (32), becomes equal to zero over the entire $y = c$ surface whereas Eq. (42) provides a surface heat flux equal to that of Eq. (37). Accordingly, the surface heat flux is calculated by differentiating T_2^* in Eq. (37) with respect to y and surface heat flux for $q = -1$ W/cm^2 is plotted in Fig. 5. Note that the summation in Eq. (37) contains n^2 in the denominator but following differentiation, the heat flux solution will have n in the denominator. Therefore, the convergence of the heat flux solution is slower than the convergence of the temperature solution. When 50 terms are used, the surface heat

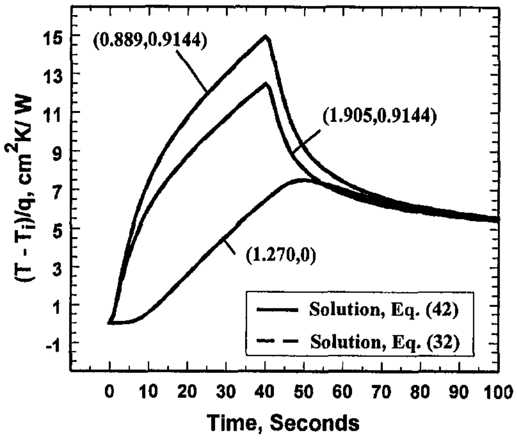

Fig. 4 A comparison of two solutions using Eqs. (42) and (32)

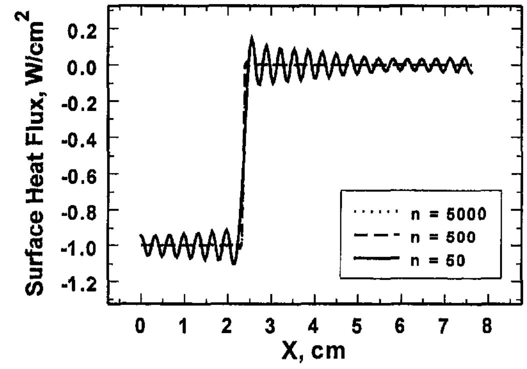

Fig. 5 Calculated surface heat flux using different number of terms

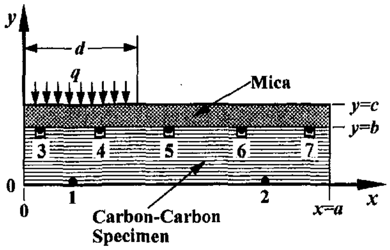

Fig. 6 Specimen with the location of the seven thermocouples, see Dowding et al. (1996)

flux visibly fluctuates about -1 and 0. Using 500 terms, the fluctuations are diminished and limited to the vicinity of $x = d$. There is no visible fluctuation when 5000 terms are used.

Green's Function.

One can generalize Eqs. (31) and (32) by expressing the solution in terms of the Green's function. Consider a single source $g_j(x, y, \tau) = \rho_j c_{pj} \delta(x - x^*)\delta(y - y^*)\delta(t - \tau^*)$ at (x^*, y^*) in region $j = 1$ or $j = 2$. Substitution of a source term $g_1(x', y', \tau)$ or $g_2(x', y', \tau)$ in Eq. (32) followed by the integrations using the properties of the Dirac delta function (Beck et al., 1992) yields the Green's function $G_{ij}(x, y, t | x^*, y^*, \tau^*)$. After replacing x^*, y^*, and τ^* by x', y', and τ, respectively, one obtains

$$G_{ij}(x, y, t | x', y', \tau) = \sum_{n=0}^{\infty} \sum_{m=0}^{\infty} \frac{\rho_j c_{pj} F_{i,mn}(x, y) F_{j,mn}(x', y')}{N_{mn}} \exp[-\lambda_{mn}^2 (t - \tau)] \tag{43}$$

where $i = 1$ or 2; and $j = 1$ and 2. Equations (31) and (32), in terms of the Green's function, become

$$T_{I,i}(x, y, t) = \sum_{j=1}^{2} \int_{V_j} G_{ij}(x, y, t | x', y', 0) T_j(x', y', 0) dV' \tag{44}$$

$$T_{G,i}(x, y, t) = \sum_{j=1}^{2} \frac{1}{\rho_j c_{pj}} \int_{\tau=0}^{t} d\tau \int_{V_j} G_{ij}(x, y, t | x', y', \tau) \times g_j(x', y', \tau) dV' \tag{45}$$

where $dV' = 1 \cdot dx'dy'$ and i takes the value of 1 or 2.

Often it is convenient to express the variables in dimensionless form. For instance, if b is the characteristic length, then, in dimensionless form, $\bar{x} = x/b$, $\bar{y} = y/b$, $\bar{c} = c/b$, $\bar{a} = a/b$, $\bar{d} = d/b$, $\bar{\gamma}_{mn} = \gamma_{mn} b$, $\bar{\eta}_{mn} = \eta_{mn} b$, and $\bar{\beta}_n = \beta_n b = (n\pi/a)b$. Accordingly, λ_{mn}^2 reduces to $\lambda_{mn}^2 = [(\bar{\gamma}_{mn})^2 + (\bar{\beta}_n)^2]\alpha_{1x}/b^2$ in region 1 and to $\lambda_{mn}^2 = [(\bar{\eta}_{mn})^2 + (\bar{\beta}_n)^2]\alpha_2/b^2$ in region 2.

The exact series solution obtained in this manner exhibited no peculiarities. However, computation of the eigenvalues using Eqs. (15) and (16) needs special attention since numerical truncation can produce false eigenvalues when some γ_{mn} values are imaginary and n is large.

Inverse Heat Conduction

The extension of the direct solution to inverse heat conduction is the final objective of this study. The inputs to the inverse problem are the experimentally obtained temperature data in Dowding et al. (1996). The calculation of the heat flux at the surface is carried out in the two-layer domain, Fig. 6. The computed heat flux is compared with available experimental information. An inverse technique uses temperature data within the domain to solve for the spatially variable and time-dependent surface condition. In general, this solution is found using the Green's function and an alternative Green's function solution (AGFS) formulation, Beck et al. (1992). The AGFS uses an auxiliary temperature function T^* that satisfies the homogeneous and nonhomogeneous boundary conditions. The functions, T_i^*, Eqs. (36) and (37), are constructed by solving an auxiliary quasi-steady-state problem defined using the same boundary conditions and physical properties of the original problem. Using the quasi-steady-state solution, Eq. (31) yields the AGFS solution,

$$T_i(x, y, t) = T_i^*(x, y, t) - \sum_{j=1}^{2} \int_{V_j} G_{ij}(x, y, t | x', y', 0) T_j^*(x', y', 0) dV'; \quad i = 1 \text{ or } 2 \tag{46}$$

for this inverse heat conduction study. In general, the value of temperature at a location designated by (x, y) and at time, t, is known and the unknown is the heat flux in the definition of $T_i^*(x, y, t)$. This formulation permits the heat flux to be a continuous or piecewise continuous function of spatial coordinates along the boundary. Also, the heat flux can be a continuous or a discrete function of time. In this inverse heat conduction study, $q(x, t)$ is the unknown to be determined and different methods of computation are discussed in Beck et al. (1996). In practice, one selects a complete set of independent basis functions to describe the variation of $q(x, t)$ and the size of the set depends on the complexity of the heat transfer process, the extent of the heated surface, and the duration of the process. For the experimental data of Dowding et al. (1996), the switch-on and switch-off process is adequately described by using the Heaviside function. It is assumed that the heat flux at the surface $y = c$ has the form $q = s(x)f(t)$ where $s(x) = (d_0 + d_1 x + d_2 x^2 + \ldots)[H(x) - H(x - d)]$, $f(t) = H(t) - H(t - t_s)$, the parameter d describes the size of the heated zone, Fig. 1, and t_s is the time when the power to the heater is switched off. These two Heaviside functions describe the abrupt changes in the spatial and temporal variation of the surface heat flux. Following appropriate substitutions, Eq. (46) reduces to a system of linear equations, each for a given set of $\{x, y; t\}$.

Matrix Representation. For simplicity in this presentation, let (x_l, y_l) designate the location of thermocouple l, and t_p be the time at which each temperature measurement is taken. Since all thermocouples were placed in the carbon-carbon composite, the left side of Eq. (46), $T_1(x_l, y_l, t_p)$, becomes a known quantity. The measured temperature is denoted as $Y_1(x_l, y_l, t_p)$ and it is an approximation to the temperature $T_1(x_l, y_l, t_p)$. By substituting q in Eqs. (36) and (37) to obtain T_1^* and T_2^* for inclusion in Eq. (46), the right side of Eq. (46) becomes $d_0\Phi_0 + d_1\Phi_1 + d_2\Phi_2 + \cdots + d_N\Phi_N$. Physically, Φ_j represents temperature at the location (x_l, y_l) and time t if the surface heat flux is equal to $x^j f(t)$ for $j = 0, 1, 2, \ldots, N$ and there is no internal heat source. In practical applications, the temperature measurements $Y_1(x_l, y_l, t_p)$ are known while the Φ_j values are obtained numerically. The least-squares estimate for the values of d_j is the one that makes the sum of squares for all seven thermocouples

$$\sum_{l=1}^{7} \sum_{p=1}^{M} [\sum_{j=0}^{N} d_j \Phi_j(x_l, y_l, t_p) - Y_1(x_l, y_l, t_p)]^2 \tag{47}$$

a minimum and this quantity is a minimum if

$$\frac{\partial}{\partial d_i} \{\sum_{l=1}^{7} \sum_{p=1}^{M} [\sum_{j=0}^{N} d_j \Phi_j(x_l, y_l, t_p) - Y_1(x_l, y_l, t_p)]^2\} = 0, \quad \text{for } i = 0, 1, \ldots, N \tag{48}$$

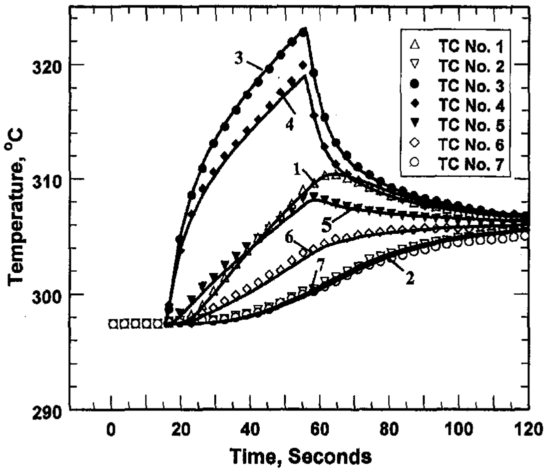

Fig. 7 A comparison of the calculated and measured temperatures at seven thermocouple locations using a spatially constant heat flux

where $N + 1$ is the number of constants to be determined. Equation (48) reduces to a set of linear equations described by

$$\mathbf{\Phi}\hat{\mathbf{D}} = \mathbf{Y} \tag{49}$$

where $\mathbf{Y}$ is a column vector of M measured temperature data, $\hat{\mathbf{D}}$ is a column vector that contains $N + 1$ unknown coefficients, d_j, and $\mathbf{\Phi}$ represents a matrix of calculated Φ_j values whose size is M by $(N + 1)$. Using standard least-squares algebra suggested by Eq. (49),

$$\mathbf{\Phi}'(\mathbf{\Phi}\hat{\mathbf{D}}) = \mathbf{\Phi}'\mathbf{Y} \tag{50}$$

where Φ' is the transpose of $\mathbf{\Phi}$. The solution for $\hat{\mathbf{D}}$ is

$$\hat{\mathbf{D}} = (\mathbf{\Phi}'\mathbf{\Phi})^{-1}(\mathbf{\Phi}'\mathbf{Y}) \tag{51}$$

Because of the measurement errors and the approximate nature of the product of $\mathbf{\Phi}$ by $\hat{\mathbf{D}}$, $\mathbf{\Phi}\hat{\mathbf{D}}$ does not equal $\mathbf{Y}$. The vector $\mathbf{Y} - \mathbf{\Phi}\hat{\mathbf{D}}$ represents the residual vector and the estimated variance, $\hat{\sigma}^2$, of the measured temperatures is obtained using

$$\hat{\sigma}^2 = (\mathbf{Y} - \mathbf{\Phi}\hat{\mathbf{D}})'(\mathbf{Y} - \mathbf{\Phi}\hat{\mathbf{D}})/M \tag{52}$$

where M is the total number of temperature data. In addition to random noise, other parameters, such as imperfection of heat flux modeling and thermophysical properties, will affect $\hat{\sigma}^2$.

Example. The temperature data for this numerical example are those of Dowding et al. (1996). Region 1 is a carbon-carbon composite layer and region 2 is a mica layer. Measured temperature data at the seven thermocouple sites shown in Fig. 6 are used during calculations. The location of thermocouples 1 through 7, using (x, y) axes shown in Fig. 6, are (1.270, 0), (6.35, 0), (0.889, 0.9144), (1.905, 0.9144), (3.175, 0.9144), (4.290, 0.9144), (6.731, 0.9144). It is assumed all thermocouples are located on both surfaces of the carbon-carbon composite layer and all units are in centimeters. The measured temperature data are shown in Fig. 7 and the mean variance for the measured temperatures is $\hat{\sigma}^2 = 0.0204$. This represents an error of ±0.2°C with 95 percent probability which is smaller than the size of the symbols shown in Figs. 7 and 8. The thermophysical properties mentioned earlier, reported by Dowding et al. (1996), are used in the inverse conduction calculations. The effective thermal conductivity (Dowding et al., 1996), k_2, includes the contribution of the contact conductance at the interface. First, it is assumed that the heat flux at $y = c$ has no spatial dependence in the interval $0 \leq x \leq d$. Using this assumption, the inverse heat conduction procedure described above produced a surface heat flux of 1.682 W/cm^2 using 50 × 50 eigenvalues. The calculated heat flux differs only 2.8 percent from an experimental heat flux of 1.730 W/cm^2 reported by Dowding et al. (1996). The temperature variance for this case is $\hat{\sigma}^2 = 0.078$. The temperatures at the seven thermocouple locations are calculated using the computed surface heat flux and the results are shown in Fig. 7.

The variation of the heat flux in the x-direction on the $y = c$ surface is investigated assuming an x-dependent heat flux of the form $q(x, t) = (d_0 + d_2x^2)[H(x) - H(x - d)][H(t) - H(t - t_s)]$. The constants d_0 and d_2 are computed using the thermocouple locations shown in Fig. 6. A comparison between experimental and calculated data is in Fig. 8. The constants and the variance for this case are $d_0 = 1.633$ W/cm^2, $d_2 = 0.0393$ W/cm^4, and $\hat{\sigma}^2 = 0.097$. This correction slightly improved the agreement between calculated and measured temperatures for thermocouple number 4 in Fig. 8. However, the variation in the heat flux is of the order of the data noise and is too small to be significant. The temperature variance for this case is slightly higher than the variance of the constant heat flux case.

Conclusion and Remarks

This paper presents a relatively convenient quasi-steady solution for the case of a two-layer material with one of the layers having orthotropic properties. Also, the transient solution for a two-dimensional problem with a surface partially heated is given. As a generalization, the Green's function for this problem is given and can be used for other problems. The numerical computations presented in this paper show that the exact analytical solution serves as a useful tool for solving an interesting class of inverse heat conduction problems. Furthermore, the solution was developed for insulated boundaries but the same methodology applies to other boundary conditions.

There are a few differences between the solution discussed earlier and classical solutions for isotropic bodies. First, a product solution (Beck, et al., 1992; p. 92) cannot be used as observed by Tittle (1965); also, the product solution cannot be used to obtain the Green's function. Second, a solution of this type, that uses the separation of variables, is restricted to the boundary conditions of the first or second kind on $x = 0$ and $x = a$ surfaces. However, there is no restriction on the type of boundary conditions at $y = 0$ and $y = c$. Third, contact resistance at the interface can be included in the solution with additional efforts.

This exact analysis serves as a powerful tool for solving inverse heat conduction problems and the inverse procedure combined with the exact analysis, described above, produces results with remarkable accuracy. This procedure satisfies all the criteria for the evaluation of the inverse heat conduction

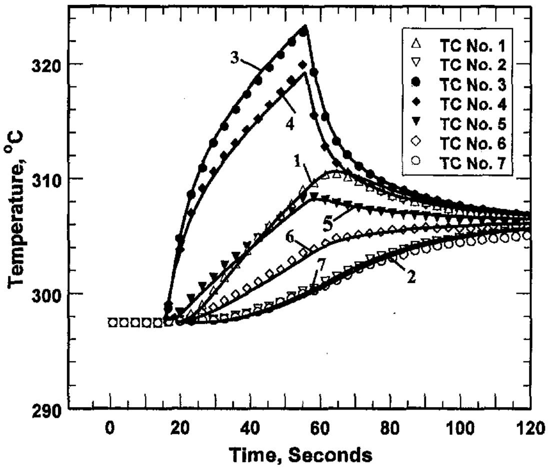

Fig. 8 A comparison of the calculated and measured temperatures at seven thermocouple locations using a spatially variable surface heat flux

problem (IHCP) solution methods outlined in Beck (1979) except for accommodating the temperature-dependent thermophysical properties. The temperature-dependent thermophysical properties need special attention not addressed here. This exact analysis is well suited to design experiments for the estimation of thermal properties as a part of IHCP studies. Also, the exact solution is ideal to calculate the sensitivity coefficients, to serve as a standard for evaluating approximate numerical methods, and to carry out simulations before performing the actual experiments.

Acknowledgment

The authors wish to acknowledge the support of the Mechanical and Aerospace Engineering Department at the University of Texas at Arlington and the National Science Foundation, Grant No. CTS-9400647.

References

Beck, J. V., 1979, "Criteria for Comparison of Methods of Solution of the Inverse Heat Conduction Problem," *Nucl. Eng. Desg.* Vol. 53, No. 1, pp. 11–22.

Beck, J. V., Blackwell, B., and Haji-Sheikh, A., 1996, "Comparison of Some Inverse Heat Conduction Methods Using Experimental Data," *International Journal of Heat and Mass Transfer,* Vol. 39, No. 17, pp. 3649–3657.

Beck, J. V., Cole, K. D., Haji-Sheikh, A., and Litkouhi, B., 1992, *Heat Conduction Using Green's Functions,* Hemisphere, Washington, DC.

Dowding, K. J., Beck, J. V., and Blackwell, B. F., 1996, "Estimation of Directional-Dependent Thermal Properties in a Carbon-Carbon Composite," *Int. J. Heat and Mass Transfer,* Vol. 39, No. 15, pp. 3157–3164.

Mikhailov, M. D., and Ozisik, M. N., 1986, "Transient Conduction in a Three-Dimensional Composite Slab," *Int. J. Heat and Mass Transfer,* Vol. 29, No. 2, pp. 340–342.

Ozisik, M. N., 1993, *Heat Conduction,* 2nd Ed., John Wiley and Sons, New York.

Padovan, J., 1974, "Generalized Sturm-Liouville Procedure for Composite Domain Anisotropic Transient Heat Conduction Problems," *AIAA Journal,* Vol. 12, No. 8, pp. 1158–1160.

Salt, H., 1983, "Transient Conduction in a Two-Dimensional Composite Slab—I. Theoretical Development of Temperature Modes," *Int. J. Heat and Mass Transfer,* Vol. 26, No. 11, pp. 1611–1616.

Salt, H., 1983, "Transient Conduction in Two-Dimensional Composite Slab—II. Physical Interpretation of Temperature Modes," *Int. J. Heat and Mass Transfer,* Vol. 26, No. 11, pp. 1617–1623.

Tittle, C. W., 1965, "Boundary Value Problems in Composite Media," *Journal of Applied Physics,* Vol. 36, No. 4, pp. 1486–1488.

Yan, Ling, Haji-Sheikh, A., and Beck, J. V., 1993, "Thermal Characteristics of Two-Layered Bodies With Embedded Thin-Film Heat Source," ASME *Journal of Electronic Packaging,* Vol. 115, No. 3, pp. 276–283.

Effects of Temperature-Dependent Viscosity Variations and Boundary Conditions on Fully Developed Laminar Forced Convection in a Semicircular Duct

T. M. Harms

M. A. Jog
Mem. ASME

R. M. Manglik
Mem. ASME

Department of Mechanical, Industrial,
and Nuclear Engineering,
University of Cincinnati,
Cincinnati, OH 45221-0072

Fully developed laminar flows in a semicircular duct with temperature-dependent viscosity variations in the flow cross section are analyzed, where the viscosity-temperature behavior is described by the Arrhenius model. Both the **T** *and* **H1** *boundary conditions are considered, as they represent the most fundamental heating/cooling conditions encountered in practical compact heat exchanger applications. Numerical solutions for the flow velocity and the temperature fields have been obtained by finite difference technique. The friction factor and Nusselt number results display a strong dependence on the viscosity ratio (μ_w/μ_b), and this is correlated using the classical power-law relationship. However, results indicate that the power-law exponents are significantly different from traditional values for circular tube. They are found to be functions of the flow geometry, boundary condition, and direction of heat transfer (heating or cooling).*

Introduction

Printed circuit or etched surface compact heat exchangers, that are increasingly being used for viscous media thermal processing applications, have semicircular flow channels as shown in Fig. 1(*a*). In practice, these channels have very small hydraulic diameters and relatively large (L/d_h). Because of these length scales and the viscous nature of the fluids being handled, the flows are generally laminar and both hydrodynamically and thermally fully developed.

Most fluids encountered in chemical, biochemical, and process industries are highly viscous in nature. The viscosity of these liquids is strongly dependent on temperature; the thermal diffusivity, however, remains relatively constant. For example, the viscosity of glycerin has a threefold decrease in magnitude for a 10 K rise in temperature (see Fig. 2). As a result, the constant property solutions most often given in the literature are inadequate, and they can grossly underpredict or overpredict the thermal-hydraulic performance. For such applications, forced convective solutions need to account for temperature-dependent viscosity variations.

Several different models have been used in the literature to account for the $\mu(\bar{T})$ behavior of viscous liquids. Some of the more commonly used constitutive relationships are listed in Table 1. While each of these equations provides reasonable $\mu(\bar{T})$ predictions for many liquids, the exponential (Arrhenius), modified exponential (Andrade), and logarithmic-polynomial models, Eqs. (1*c*)–(1*e*), perhaps give the best representation over a relatively large temperature range. However, even though Eqs. (1*d*) and (1*e*) may tend to have higher precision because of their form (for example, Eq. (1*e*) has more adjustable constants), the Arrhenius model, Eq. (1*c*), is very simple, provides a good representation for most common fluids (see Fig. 2), and is quite effective (Nakamura et al., 1979); as such, it has been the more popular model. An alternative approach has been to use a Taylor series expansion of $\mu(\bar{T})$ (Herwig, 1985; Herwig and Klemp, 1988).

The majority of earlier studies that have investigated the effects of temperature-dependent viscosity variations have primarily focused on the circular tube geometry (Bergles, 1983a, b). In an extended numerical study on fully developed flows in rectangular ducts, Nakamura et al. (1979) have evaluated the efficacy of the first four $\mu(\bar{T})$ equations listed in Table 1. Also, Herwig and Klemp (1988) have considered fully developed laminar flow heat transfer in concentric annuli. For the semicircular geometry, almost all previous results have been constant property solutions (Manglik and Bergles, 1994). In a recent work, Etemad and Mujumdar (1995) have reported results for the entrance region laminar flows of power-law (pseudoplastic and dilatant) liquids. Besides viscous dissipation and non-Newtonian effects, they have also considered temperature-dependent consistency variations in the developing flow regime. However, friction factor and Nusselt number solutions for fully developed laminar flow of Newtonian fluids in a semicircular duct, that account for the effects of $\mu(\bar{T})$ variations over a large range of heating and cooling conditions, do not appear to have been reported in the literature. This is addressed in the present study, and the results are of much significance to the design of printed-circuit heat exchangers.

Problem Formulation

Steady-state incompressible laminar flow of a Newtonian fluid in a semicircular duct (Fig. 1(*b*)) is considered. The flow is both hydrodynamically and thermally fully developed, with negligible viscous dissipation and axial conduction (Pe $\gg$ 1). Also, with the exception of temperature-dependent viscosity variations in the flow cross section, all fluid properties are con-

---

Contributed by the Heat Transfer Division for publication in the JOURNAL OF HEAT TRANSFER and presented at '97 ASME NHTC, Baltimore. Manuscript received by the Heat Transfer Division, Mar. 10, 1997; revision received, Mar. 3, 1998. Keywords: Forced Convection, Heat Exchangers, Thermophysical Properties. Associate Technical Editor: S. Ramadhyani.

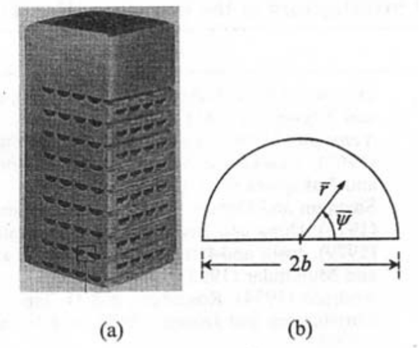

Fig. 1 Channel geometry: (*a*) typical section of an etched surface heat exchanger core (courtesy Heatric Ltd., UK), and (*b*) coordinate system in the duct flow cross section

sidered to be constant; the Arrhenius model, Eq. (1*b*), is taken to describe the viscosity-temperature behavior in the fully developed flow field. It may be noted that for highly viscous liquid flows in the small d_h channels of the present case, Gr would be insignificantly small ($\sim O[10]$) even under extreme heating/cooling conditions. For laminar flows in a horizontal semicircular duct, Lei and Trupp (1991) have shown experimentally that buoyancy effects become important only when $\mathrm{Gr} > 10^7$. Consequently, free-convection effects have been ignored.

For the cylindrical coordinate system and duct geometry described in Fig. 1(*b*), the following dimensionless variables are introduced:

$$r = (\bar{r}/b),\ \psi = \bar{\psi} \tag{2a, b}$$

$$\eta = (\mu/\mu_b) \tag{2c}$$

$$w = \bar{w}/[-(d\bar{p}/d\bar{z})(b^2/8\mu_b)] \tag{2d}$$

$$T = (\bar{T}_w - \bar{T})/[(d\bar{T}_b/d\bar{z})(b^2\bar{w}_b/\alpha)]. \tag{2e}$$

With the substitution of these variables, the governing dimensionless momentum and energy equations can be expressed as

$$\frac{1}{r}\frac{\partial}{\partial r}\left(\eta r\frac{\partial w}{\partial r}\right) + \frac{1}{r^2}\frac{\partial}{\partial \psi}\left(\eta\frac{\partial w}{\partial \psi}\right) + 8 = 0 \tag{3}$$

$$\frac{1}{r}\frac{\partial}{\partial r}\left(r\frac{\partial T}{\partial r}\right) + \frac{1}{r^2}\frac{\partial}{\partial \psi}\left(\frac{\partial T}{\partial \psi}\right) + S_T = 0 \tag{4a}$$

where (see Manglik and Bergles (1994) for details)

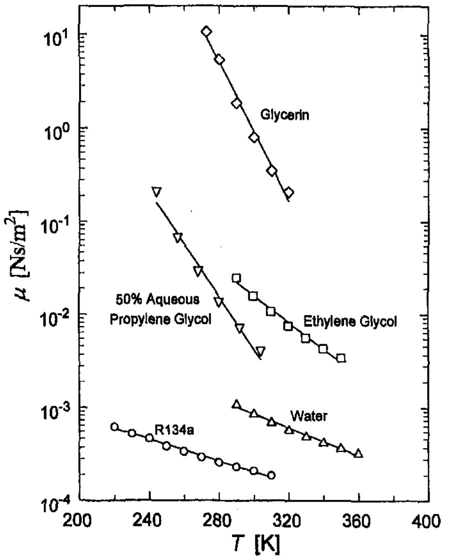

Fig. 2 Temperature-dependent viscosity variations of common liquids and their representation by the Arrhenius model of Eq. (1c)

$$S_T = \begin{cases} (w/w_b)(T/T_b) & \text{for } \mathbf{T} \\ (w/w_b) & \text{for } \mathbf{H1}. \end{cases} \tag{4b}$$

Equations (3) and (4) are subject to the following boundary conditions:

$$w(0, \psi) = w(1, \psi) = w(r, 0) = 0, \frac{\partial w}{\partial \psi}(r, \pi/2) = 0 \tag{5}$$

$$T(0, \psi) = T(1, \psi) = T(r, 0) = 0, \frac{\partial T}{\partial \psi}(r, \pi/2) = 0. \tag{6}$$

Note that symmetry allows the solution to be obtained by considering only half of the duct cross section, thereby requiring Neumann conditions at the duct centerline $(r, \pi/2)$. Also the viscosity function of Eq. (2*c*) can be expressed in dimensionless form as

$$\eta = (\mu_w/\mu_b)^{(1-T/T_b)}. \tag{7}$$

In Eq. (7), the ratio (μ_w/μ_b) becomes a known input depending upon the given heating/cooling conditions; values of $\mu_w/\mu_b <$

Nomenclature

b = semicircular duct radius, Fig. 1(*b*) m
c = empirical constant or exponent, Eq. (1)
d_h = hydraulic diameter, $(2b\pi)/(\pi + 2)$, m
f = Fanning friction factor, Eq. (10)
g = gravitational acceleration, m/s^2
Gr = Grashof number, $(g\beta\Delta T d_h^3/\nu^2)$
h = heat transfer coefficient, W/m$^2\cdot$K
H1 = axially uniform wall heat flux with peripherally uniform wall temperature
k = fluid thermal conductivity, W/m$\cdot$K
L = axial duct length, m
m, n = viscosity ratio exponents, Eqs. (14*a*, *b*)
Nu = Nusselt number, Eq. (11)
p = pressure, Pa
Pe = Peclet number, $\bar{w}_b d_h/\alpha$
r = dimensionless radial coordinate, Eq. (2*a*)
$\bar{r}$ = radial coordinate, m
Re = Reynolds number, $\rho\bar{w}_b d_h/\mu_b$
S_T = source term, Eq. (4*b*)
T = dimensionless temperature, Eq. (2*e*)
$\bar{T}$ = temperature, K
T = peripherally and axially uniform wall temperature
w = dimensionless axial velocity, Eq. (2*d*)
$\bar{w}$ = axial velocity, m/s
$\bar{z}$ = axial coordinate, m
α = fluid thermal diffusivity, m^2/s
β = volume expansion coefficient, K^{-1}
η = dimensionless fluid dynamic viscosity, Eq. (2*c*)
μ = fluid dynamic viscosity, Pa$\cdot$s
ν = kinematic viscosity, m^2/s
ρ = fluid density, kg/m^3
τ_w = wall shear stress, Pa
ψ, $\bar{\psi}$ = dimensionless circumferential coordinate, Eq. (2*b*)

Subscripts

ref = reference value at arbitrary reference temperature
b = bulk or mean
cp = constant property
w = wall

Table 1 List of viscosity-temperature models used by different investigators in the literature (Eq. (1))

	Model	Eq. No.	References
Power-Law	$\mu = \mu_{ref}(\bar{T}/\bar{T}_{ref})^{-c}$	(1*a*)	Deissler (1951), Nakamura et al. (1979), and Collins and Keynejad (1983)
Polynomial	$\mu = \mu_{ref}[1 + c(\bar{T} - \bar{T}_{ref})]^{-1}$	(1*b*)	Yamagata (1940), Yang (1962), Mizushina et al. (1967), Tanaka and Mitsuishi (1975), Gori (1978), and Nakamura et al. (1979)
Arrhenius/Exponential	$\mu = \mu_{ref}\ \exp[-c(\bar{T} - \bar{T}_{ref})]$	(1*c*)	Shannon and Depew (1969), Mahalingam et al. (1975), Hong and Bergles (1976a), Nakamura et al. (1979), Joshi and Bergles (1980, 1981), and Etemad and Mujumdar (1995)
Modified Exponential	$\mu = \mu_{ref}\ \exp[c([1/\bar{T}] - [1/\bar{T}_{ref}])]$	(1*d*)	Andrade (1934), Rosenberg and Hellums (1965), Christiansen and Jensen (1969), and Nakamura et al. (1979)
Log-Polynomial	$\ln(\mu - a) = (T/T_{ref})^n \ln(\mu_{ref} - a)$	(1*e*)	Test (1968) and Shome and Jensen (1995)

1 represent fluid heating, and $\mu_w/\mu_b > 1$ represents fluid cooling. A thermally and hydrodynamically fully developed flow implies that (w/w_b), $(T - T_w)/(T_b - T_w)$, and (μ/μ_b) are not functions of axial location. For the **H1** condition, $(T_w - T_b)$ as well as the corresponding (μ_w/μ_b) become constant; this holds for the **T** condition also, with T_b evaluated as the difference between the wall temperature and log-mean temperature difference. As such, a range of wall-to-bulk viscosity ratio $(0.02 \leq \mu_w/\mu_b \leq 50)$ has been considered in this study for each of the two boundary conditions.

The dimensionless bulk velocity and bulk temperature are obtained from their usual definitions as

$$w_b = \frac{4}{\pi}\int_0^{\pi/2}\int_0^1 wrdrd\psi \tag{8}$$

$$T_b = \frac{4}{\pi}\frac{1}{w_b}\int_0^{\pi/2}\int_0^1 wTrdrd\psi. \tag{9}$$

Finally, the global parameters of design interest, Fanning friction factor and Nusselt number, based on volumetric flow rate and enthalpy rise, respectively, are defined as

$$f = (2\tau_w/\rho\bar{w}_b^2) = [\pi/(\pi + 2)]^2(16/w_b\ \text{Re}) \tag{10}$$

$$\text{Nu} = (hd_h/k) = [\pi/(\pi + 2)]^2/T_b. \tag{11}$$

Numerical Solution Method

Numerical solutions for the coupled governing equations for axial velocity and temperature are obtained by finite difference methods, using a uniform grid and the Gauss-Seidel technique with SOR. The governing equations are discretized in conservative form by applying second-order accurate central differencing. This, however, results in the need to calculate viscosity at half-interval locations. A second-order accurate Lagrangian interpolation is used to determine the temperature, which is then used to calculate the viscosity at these locations. Dirichlet boundary conditions are set at the wall, while the symmetry conditions are approximated by second-order accurate forward or backwards difference formulae, as needed. For the numerical integration, algorithms based on Simpson's rule are employed.

All runs were performed with a 61 × 61 grid. This was adequate even for the extreme values of viscosity ratio. Grid independence was verified by running the most extreme heating case of $(\mu_w/\mu_b) = 0.02$ with a 91 × 91 grid for the **T** condition. For this test case, relative to the coarser grid, $f\text{Re}$ changed by only 0.3 percent, while the Nusselt number remained unchanged. The results for the **H1** condition show similar trends. The convergence criteria (maximum relative error in the values of the dependent variables between two successive iterations) in all test runs was set at 10^{-7}.

Accuracy of the numerical procedure was verified by comparison of the constant property results with those given in the literature. As shown in Table 2, the results obtained here are in excellent agreement with the available analytical (Sparrow and Haji-Sheikh, 1966) and numerical solutions. The numerical accuracy is further checked by comparing the friction factor and Nusselt number values of Eqs. (10) and (11) with the peripherally averaged values determined directly from the wall gradients given by

$$f\text{Re} = -\frac{4\pi}{(2 + \pi)^2}\frac{\mu_w}{\mu_b}\frac{1}{w_b}\left[\int_0^{\pi/2}\frac{\partial w}{\partial r}\bigg|_{r=1} d\psi - \int_0^1 \frac{1}{r}\frac{\partial w}{\partial \psi}\bigg|_{\psi=0} dr\right] \tag{12}$$

$$\text{Nu} = -\frac{4\pi}{(2 + \pi)^2}\frac{1}{T_b}\left[\int_0^{\pi/2}\frac{\partial T}{\partial r}\bigg|_{r=1} d\psi - \int_0^1 \frac{1}{r}\frac{\partial T}{\partial \psi}\bigg|_{\psi=0} dr\right] \tag{13}$$

Note that the circumferential gradients are singular when $r = 0$; however, they can be approximated by the radial gradients along $\psi = \pi/2$. The differences between the values obtained by Eqs. (10)–(11) and (12)–(13) were generally less than one percent, with a maximum of 3.7 percent for the case with $(\mu_w/\mu_b) = 0.02$.

Results and Discussion

In Fig. 3, the normalized axial velocity (w/w_b) contour plots for fully developed laminar flows are presented. As seen from this figure, because of temperature-dependent viscosity variations in the flow cross section under diabatic conditions, the velocity field (Figs. 3(*a*), (*b*), (*d*), and (*e*)) gets distorted significantly from the constant property case (Fig. 3(*c*)). For *wall heating*, the flow profiles in Figs. 3(*a*) and 3(*b*) tend to flatten and have a plug-like shape, relative to the constant property distribution. As a result, the velocity gradients become large near the wall and the maximum velocity decreases. The flow essentially tends to become uniform because of the fluid lubrication in the near wall regions. Also, the effect of boundary condition (**T** versus **H1**) appears to be small. For *wall cooling*, because the viscosity near the wall increases considerably, the profiles in Figs. 3(*d*) and 3(*e*) tend to elongate and become

Table 2 A comparison of the present constant property results with those available in the literature

	$f\text{Re}$	Nu_T	Nu_{H1}
Present study	15.768	3.321	4.093
Sparrow and Haji-Sheikh (1966)	15.767	—	4.089
Hong and Bergles (1976b)	—	—	4.108
Ben-Ali et al. (1989)	15.790	3.316	4.072
Manglik and Bergles (1994)	15.772	3.403	—

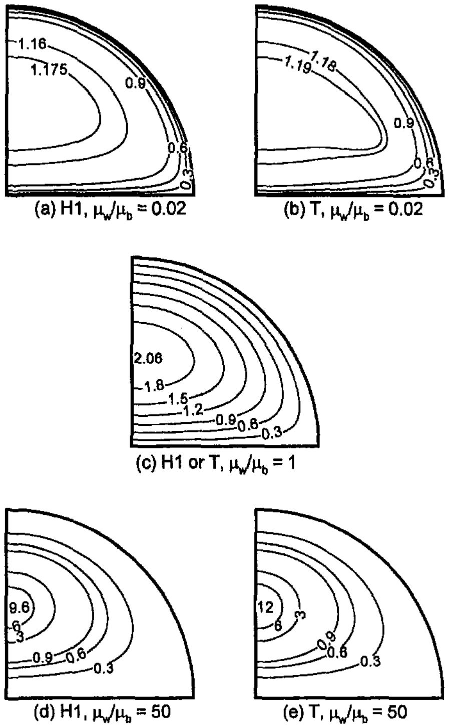

(a) H1, $\mu_w/\mu_b = 0.02$ (b) T, $\mu_w/\mu_b = 0.02$

(c) H1 or T, $\mu_w/\mu_b = 1$

(d) H1, $\mu_w/\mu_b = 50$ (e) T, $\mu_w/\mu_b = 50$

Fig. 3 Normalized axial velocity (w/w_b) contours for T and H1 conditions with (μ_w/μ_b) = 0.02, 1, and 50

almost conical. This in turn produces velocity gradients that are very small near the outer wall boundary with a dramatic increase in core velocity. In this case the boundary condition also has an effect, in that the maximum velocity for the **H1** condition (Fig. 3(d)) is approximately 21 percent less than that for the **T** condition (Fig. 3(e)). The effect of $\mu(T)$ variations are further illustrated in Fig. 4, where normalized axial velocity (w/w_b) profiles at the centerline ($\psi = \pi/2$) of the semicircular duct for the **H1** condition are shown as a function of the viscosity ratio. Most prominently, the maximum velocity is seen to dramatically increase with increasing (μ_w/μ_b).

The corresponding normalized temperature (T/T_b) contour plots for the two boundary conditions (**T** and **H1**) are given in Fig. 5. Reflecting the distortions in the velocity distribution for (μ_w/μ_b) < 1 and >1, the temperature profiles also deviate from the constant property solution. However, the differences in the temperature distributions are relatively small compared to the striking differences in the axial velocity distributions. For large values of the viscosity ratios (cooling), the temperature gradients near the wall are relatively small, compared to the constant property case, but increase significantly under heating conditions ($\mu_w/\mu_b < 1$). Also, as the viscosity ratio decreases ($\mu_w/\mu_b = 50 \rightarrow 1 \rightarrow 0.02$) the maximum fluid temperature decreases due to the convective effects in the core region of the duct. This effect is larger for the **T** condition than for the **H1** condition. Variations in the normalized temperature (T/T_b) distribution at the centerline ($\psi = \pi/2$) with (μ_w/μ_b) are given in Fig. 6 for the **H1** boundary condition. The temperature profiles, $T(r, \pi/2)$, are clearly seen to deviate from the constant property case for both heating and cooling. Again, the maximum fluid temperature is higher for heating than for cooling due to the convective effects.

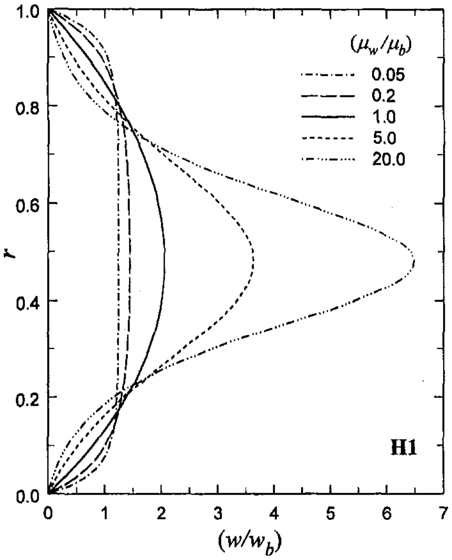

Fig. 4 The effect of viscosity ratio on the normalized axial velocity profile at the duct centerline ($\psi = \pi/2$)

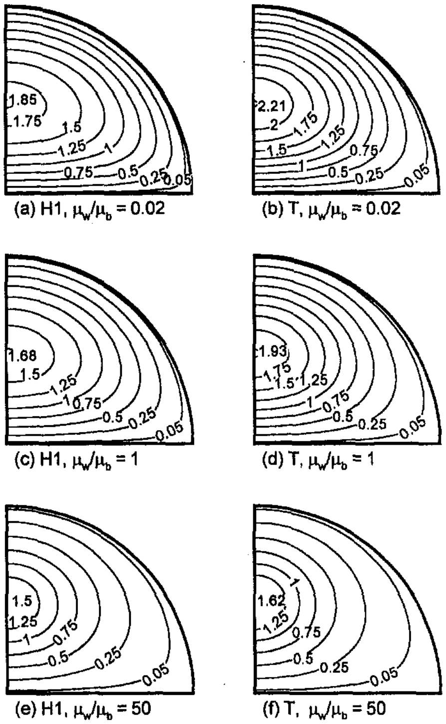

(a) H1, $\mu_w/\mu_b = 0.02$ (b) T, $\mu_w/\mu_b = 0.02$

(c) H1, $\mu_w/\mu_b = 1$ (d) T, $\mu_w/\mu_b = 1$

(e) H1, $\mu_w/\mu_b = 50$ (f) T, $\mu_w/\mu_b = 50$

Fig. 5 Normalized temperature (T/T_b) contours for T and H1 conditions with (μ_w/μ_b) = 0.02, 1, and 50

The friction factor and Nusselt number results for both **H1** and **T** conditions are presented in Figs. 7 and 8, respectively, in the form (f/f_{cp}) and ($\mathrm{Nu}/\mathrm{Nu}_{cp}$) versus ($\mu_w/\mu_b$). Wall heating conditions are seen to produce lower flow friction but higher heat transfer coefficient in comparison with the constant property solution; the converse is true for wall cooling. Depending upon the wall-to-bulk temperature differences, which in turn are reflected in the values for (μ_w/μ_b), the differences between $f - f_{cp}$ and $\mathrm{Nu} - \mathrm{Nu}_{cp}$ are seen to be quite significant. In fact, in design estimates based on constant property solutions, the relative errors in the predictions of $f \cdot \mathrm{Re}$ and Nu can be as much as 93.2 percent and 50.7 percent, respectively, for heating, and 909 percent and 51.7 percent, respectively, for cooling. Furthermore, the influence of the **H1** boundary condition on the variations in Nu with (μ_w/μ_b) is much greater than that of the **T** boundary condition; for the variations in f, the converse is true.

In much of the literature, based on the classical work by Sieder and Tate (1936), temperature-dependent viscosity variations are usually correlated in the form

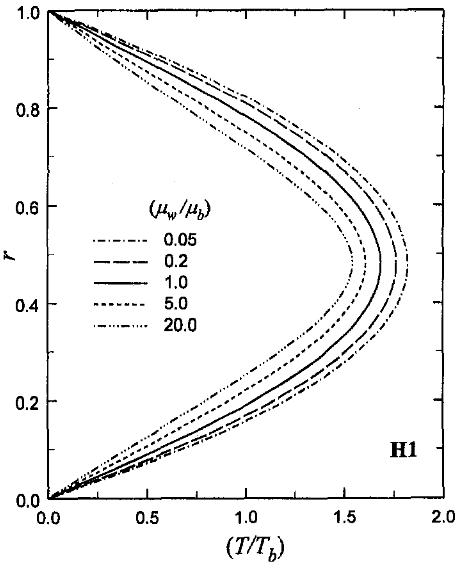

Fig. 6 The effect of viscosity ratio on the normalized temperature profile at the duct centerline ($\psi = \pi/2$)

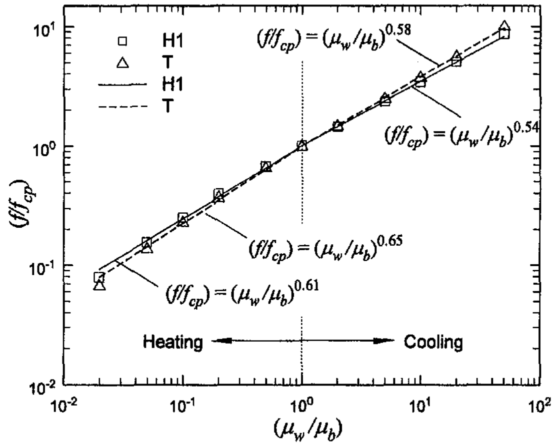

Fig. 7 Variation of (f/f_{cp}) with (μ_w/μ_b) for fully developed laminar flow in a semicircular duct

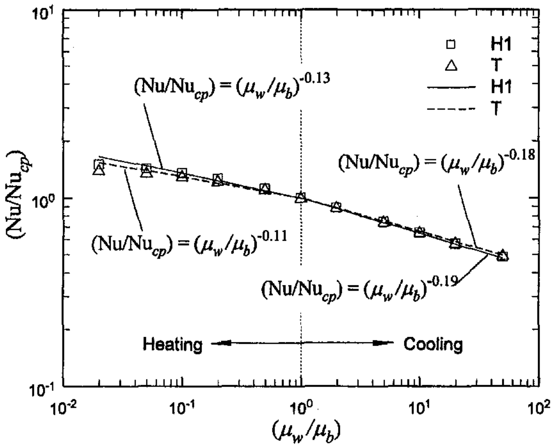

Fig. 8 Variation of ($\mathrm{Nu}/\mathrm{Nu}_{cp}$) with ($\mu_w/\mu_b$) for fully developed laminar flow in a semicircular duct

$$f/f_{cp} = (\mu_w/\mu_b)^m \tag{14a}$$

$$\mathrm{Nu}/\mathrm{Nu}_{cp} = (\mu_w/\mu_b)^n. \tag{14b}$$

While there is no unanimity over the values of m and n, even for circular tube flows (Kakaç et al., 1987; Manglik and Bergles, 1998), this form of correlation is perhaps the simplest and yet reliable. Such power-law representation of the present results are given in Figs. 7 and 8, respectively, for f and Nu. The exponents m and n are seen to be different not only for wall heating and cooling conditions, but for the **T** and **H1** boundary conditions as well. For the **H1** condition, $m = 0.54$ and $n = -0.19$ for cooling, and $m = 0.61$ and $n = -0.13$ for heating; the corresponding values for the **T** condition are $m = 0.58$ and $n = -0.18$ for cooling, and $m = 0.65$ and $n = -0.11$ for heating. Different exponents for heating, cooling, and boundary conditions have also been reported for the circular tube case in both experimental and computational results (Test, 1968; Joshi and Bergles, 1980, 1981; Marner and Bergles, 1989; Shome and Jensen, 1995; Manglik and Bergles, 1998). As seen from Fig. 7, the friction factor results are well correlated by Eq. (14a) and the indicated values of m, for both heating/cooling and **H1/T** boundary conditions. However, quite interestingly, the Nu results for very high heating conditions ($\mu_w/\mu_b < 0.1$) tend to deviate from the log-linear behavior; this is so for both **H1** and **T**. Similar deviations from the log-linear behavior are observed in the Nu results for rectangular ducts reported by Nakamura et al. (1979). Clearly, experimental data are needed to verify that this is indeed due to the convective characteristics of very viscous liquids under extreme wall heating conditions. Nonetheless, for practical applications, the power-law relationship of Eq. (14b) provides reasonably accurate results for Nu as well (the maximum relative error for $\mu_w/\mu_b = 0.02$ is 10.4 percent).

It may be noted that the **T** and **H1** boundary conditions represent the most common heating/cooling situations encountered in heat exchanger applications. The **T** condition simulates, for example, heating of the process fluid stream by condensing steam; the **H1** condition corresponds to heating or cooling in a two-fluid exchanger with equal heat capacity rates. Furthermore, because printed-circuit or etched-surface heat exchangers are compact units with large heat transfer surface area density, the precision in estimating the heat transfer and pressure loss has a significant impact on its design (Shah, 1981). For instance, a nominal ten percent underprediction of h, coupled with a ten percent overprediction of f (which would be the case with fluid heating when constant property estimates are used) would over size the heat exchanger and render it less compact. The present results provide more accurate predictions of Nu and f under both fluid heating and cooling conditions, and lend to more reliable design of such exchangers.

Conclusions

Numerical solutions for fully developed flows, with $\mu(\overline{T})$ variations modeled by the Arrhenius equation, in a semicircular duct have been presented. The **T** and **H1** wall boundary conditions with both heating and cooling are considered. Temperature-dependent viscosity variations are seen to produce significant distortions in both the velocity and temperature distributions in the fully developed flows. The corresponding f and Nu values deviate significantly from the constant property results. For the range of viscosity ratio variations considered here ($0.02 \le \mu_w/\mu_b \le 50$), f and Nu deviate by as much as a factor of 9 and 2, respectively. The dependence of friction factor and Nusselt number on the viscosity ratio (μ_w/μ_b) is reasonably correlated by the classical power-law relationships given in Eqs. (14a) and (14b), respectively. However, the power-law exponents are not only different from the circular tube values, but are found to be functions of heating, cooling, and the **T** and **H1** boundary conditions as well.

Acknowledgments

This work was partly supported by the Thermal-Fluids Laboratory. Also, the support of the National Science Foundation (Grant # CTS-9502128) to RMM is gratefully acknowledged.

References

Andrade, E. N., and Da, C., 1934, "A Theory of the Viscosity of Liquids," *Philosophical Magazine and Journal of Science,* Vol. 17, pp. 497–511, 698–732.

Ben-Ali, T. M., Soliman, H. M., and Zariffeh, E. K., 1989, "Further Results for Laminar Heat Transfer in Annular Sector and Circular Sector Ducts," ASME Journal of Heat Transfer, Vol. 111, pp. 1090–1093.

Bergles, A. E., 1983a, "Prediction of the Effects of Temperature-Dependent Fluid Properties on Laminar Heat Transfer," *Low Reynolds Number Flow Heat Exchangers,* S. Kakaç et al., eds., Hemisphere, Washington DC, pp. 451–471.

Bergles, A. E., 1983b, "Experimental Verification of Analyses and Correlation of the Effects of Temperature-Dependent Fluid Properties on Laminar Heat Transfer," *Low Reynolds Number Flow Heat Exchangers,* S. Kakaç et al., eds., Hemisphere, Washington DC, pp. 473–486.

Christiansen, E. B., and Jensen, G. E., 1969, "Laminar, Nonisothermal Flow of Fluids in Tubes of Circular Cross Section," *AIChE Journal,* Vol. 15, pp. 504–507.

Collins, M. W., and Keynejad, M., 1983, "Effects of Temperature Dependence of Viscosity and Viscous Dissipation on Laminar Flow Heat Transfer in Circular Tubes," *International Journal of Heat and Fluid Flow,* Vol. 4, pp. 33–42.

Deissler, R. G., 1951, "Analytical Investigation of Fully Developed Laminar Flow in Tubes with Heat Transfer with Fluid Properties Variable Along the Radius," National Advisory Committee for Aeronautics, Technical Note 2410.

Etemad, S. Gh., and Mujumdar, A. S., 1995, "Effects of Variable Viscosity and Viscous Dissipation on Laminar Convection Heat Transfer of a Power Law Fluid in the Entrance Region of a Semi-Circular Duct," *International Journal of Heat and Mass Transfer,* Vol. 38, pp. 2225–2238.

Gori, F., 1978, "Variable Physical Properties in Laminar Heating of Pseudoplastic Fluids With Constant Wall Heat Flux," ASME Journal of Heat Transfer, Vol. 100, pp. 220–223.

Herwig, H., 1985, "The Effect of Variable Properties on Momentum and Heat Transfer in a Tube with Constant Heat Flux Across the Wall," *International Journal of Heat and Mass Transfer,* Vol. 28, pp. 423–431.

Herwig, H., and Klemp, K., 1988, "Variable Property Effects of Fully Developed Laminar Flow in Concentric Annuli," ASME Journal of Heat Transfer, Vol. 110, pp. 314–320.

Hong, S. W., and Bergles, A. E., 1976a, "Theoretical Solutions for Combined Forced and Free Convection in Horizontal Tubes With Temperature-Dependent Viscosity," ASME Journal of Heat Transfer, Vol. 98, pp. 459–465.

Hong, S. W., and Bergles, A. E., 1976b, "Laminar Flow Heat Transfer in the Entrance Region of Semi-Circular Tubes with Uniform Heat Flux," *International Journal of Heat and Mass Transfer,* Vol. 19, pp. 123–124.

Joshi, S. D., and Bergles, A. E., 1980, "Analytical Study of Heat Transfer to Laminar In-Tube Flow of Non-Newtonian Fluids," *AIChE Symposium Series,* Vol. 76, pp. 270–281.

Joshi, S. D., and Bergles, A. E., 1981, "Analytical Study of Laminar Flow Heat Transfer to Pseudoplastic Fluids in Tubes with Uniform Wall Temperature," *AIChE Symposium Series,* Vol. 77, pp. 114–122.

Lei, Q. M., and Trupp, A. C., 1991, "Experimental Study of Laminar Mixed Convection in the Entrance Region of a Horizontal Semicircular Duct," *International Journal of Heat and Mass Transfer,* Vol. 34, pp. 2361–2372.

Mahalingam, R., Tilton, L. O., and Coulson, J. M., 1975, "Heat Transfer in Laminar Flow of Non-Newtonian Fluids," *Chemical Engineering Science,* Vol. 30, pp. 921–929.

Manglik, R. M., and Bergles, A. E., 1994, "Fully Developed Laminar Heat Transfer in Circular-Segment Ducts with Uniform Wall Temperature," *Numerical Heat Transfer, Part A,* Vol. 26, pp. 499–519.

Manglik, R. M., and Bergles, A. E., 1998, "Numerical Modeling and Analysis of Laminar Flow Heat Transfer in Non-Circular Compact Channels," *Computer Simulations in Compact Heat Exchangers,* B. Sundén and M. Faghri, eds., Computational Mechanics Publications, Southampton, UK, chapter 2.

Marner, W. J., and Bergles, A. E., 1989, "Augmentation of Highly Viscous Laminar Heat Transfer Inside Tubes with Constant Wall Temperature," *Experimental Thermal Fluid Science,* Vol. 2, pp. 252–267.

Mizushina, T., Ito, R., Kuriwaki, Y., and Yahikozawa, K., 1967, "Laminar Heat Transfer to Non-Newtonian Fluids in a Circular Tube, Constant Wall Heat Flux," *Kagaku Kogaku,* Vol. 31, pp. 250–255 (in Japanese).

Nakamura, H., Matsuura, A., Kiwaki, J., Matsuda, N., Hiraoka, S., and Yamada, I., 1979, "The Effect of Variable Viscosity on Laminar Flow and Heat Transfer in Rectangular Ducts," *Journal of Chemical Engineering of Japan,* Vol. 12, pp. 14–18.

Rosenberg, D. E., and Hellums, J. D., 1965, "Flow Development and Heat Transfer in Variable-Viscosity Fluids," *Industrial and Engineering Chemistry Fundamentals,* Vol. 4, pp. 417–422.

Shah, R. K., 1981, "Compact Heat Exchanger Design Procedures," *Heat Exchangers—Thermal-Hydraulic Fundamentals and Design,* S. Kakaç et al., eds., Hemisphere, Washington, DC, pp. 495–536.

Shannon, R. L., and Depew, C. A., 1969, "Forced Laminar Flow Convection in a Horizontal Tube With Variable Viscosity and Free-Convection Effects," ASME Journal of Heat Transfer, Vol. 91, pp. 251–258.

Shome, B., and Jensen, M. K., 1995, "Mixed Convection Laminar Flow and Heat Transfer of Liquids in Isothermal Horizontal Circular Ducts," *International Journal of Heat and Mass Transfer,* Vol. 38, pp. 1945–1956.

Sieder, E. N., and Tate, G. E., 1936, "Heat Transfer and Pressure Drop of Liquids in Tubes," *Industrial and Engineering Chemistry,* Vol. 28, pp. 1429–1435.

Sparrow, E. M., and Haji-Sheikh, A., 1966, "Flow and Heat Transfer in Ducts of Arbitrary Shape With Arbitrary Thermal Boundary Conditions," ASME Journal of Heat Transfer, Vol. 88, pp. 351–358.

Tanaka, M., and Mitsuishi, N., 1975, "Non-Newtonian Laminar Heat Transfer in Concentric Annuli," *Heat Transfer—Japanese Research,* Vol. 4, No. 2, pp. 26–36.

Test, F. L., 1968, "Laminar Flow Heat Transfer and Fluid Flow for Liquids With Temperature-Dependent Viscosity," ASME Journal of Heat Transfer, Vol. 90, pp. 385–392.

Yamagata, K., 1940, "A Contribution to the Theory of Non-Isothermal Laminar Flow of Fluids Inside a Straight Tube of Circular Cross Section," *Memoirs of the Faculty of Engineering, Kyushu Imperial University,* Vol. 8, pp. 365–449.

Yang, K. T., 1962, "Laminar Forced Convection of Liquids in Tubes With Variable Viscosity," ASME Journal of Heat Transfer, Vol. 84, pp. 353–362.

Y. Murer
yann.murer@onecert.fr

P. Millan
Pierre.Millan@onecert.fr

ONERA-DMAE,
2, avenue Edouard Belin,
BP 4025,
F-31055 Toulouse Cedex 4
France

Two-Dimensional Modeling of Heat Transfer Through Sandwich Plates With Inhomogeneous Boundary Conditions on the Faces

This paper presents a thermal model describing heat transfer in multispan sandwich rectangular plates. The model is time-dependent and two-dimensional. Complex thermal phenomena occurring in light cores (honeycomb) and thermal contact resistance are taken into account in the model. Particular attention is paid to the boundary conditions on the faces of the plate: radiative and nonuniform convective exchange are taken into account. The global temperature solution for stationary cases is developed on trigonometric and exponential functions bases. The properties of the Laplace transform are used to solve time-dependent cases. Validation experiments are carried out in a wind tunnel ring for two-span plates submitted to convective exchanges on one face; the same configuration is reproduced for an aluminum sandwich plate in an industrial set-up bench. Experimental results agree well with the numerical simulation.

Introduction

Multispan materials are of interest in many industrial fields, particularly for aeronautical and aerospace applications. Used in fuselage and engine cover panels, or in certain parts of combustion chambers, they are submitted to thermal constraints, which can be of importance during design or optimization phases. This is why the aerothermal team of the ONERA/DMAE decided to develop a model describing global heat transfer in these materials. Multilayer plates, composed of thin facings (metal sheets, multifold composites) flanking a thick, light core (honeycomb), are considered. The calculation of the temperature field of these panels requires the consideration of some particular points:

- the thermal behavior of honeycomb, the three heat transfer modes occur in such materials, conduction (along the cells walls), radiative exchanges (between the cell walls, the bottom and the top of the cell), and natural convection. In a first step, it is necessary to develop a reduced modeling of these phenomena.
- the modeling of interface conditions, the contact between the different layers of the panels is seldom perfect; glue, surface roughness, and air gaps lead to temperature jumps, which are usually described using contact conductances.
- the plates are generally submitted to specific flow exchanges (hot air on one side, cooling fluid on the other side for combustion chambers, external air flow for covering panels), which call for an appropriate modeling of boundary conditions.

Numerous publications have been devoted to heat transfer through multilayer plates, but papers dealing with global heat transfer through composites with thick cores are rare. Numerical methods allow a precise modeling of each phenomenon, and nodal methods present a more global approach. Some authors propose analytical models: Degiovanni (1993) and Houlbert (1992) use the quadripoles method to describe the different heat transfer phenomena in sandwich composites. For a cylindrical geometry, Özisik (1993) develops monodimensional time-dependent solutions for multispans with inhomogeneous boundary conditions. Considering the need of a global model for rectangular or parallelepipedic geometry with inhomogeneous boundary conditions, it was decided that we develop an analytical two-dimensional rectangular plate model (with the x-axis following the global direction of external flows, and the y-axis being across the layers). Stationary and time-dependent cases are considered. The considered temperatures range from the ambient to 423.15 K.

1 Model

Figure 1 sums up the different phenomena involved in the present study. They are treated inside a global multilayer conductive model: each heat transfer mode occurring inside the plate is modeled as a conduction phenomenon, or an interface condition between two layers. The boundary conditions of the model describe the thermal exchanges between the plate and its environment. The paper is structured as follows: first, the usual conductive phenomena in multispan plates are presented; second, the thermal properties of honeycombs are simplified so that the core can be described as an usual layer; then, the convective and radiative exchange on the plate faces are presented; and finally, the global model resolution is presented. Figure 2 indicates the coordinate system and the main nomenclature of the paper (layer number, etc.).

1.1 Conductive Phenomena in Multispans.

1.1.1 Orthotropic Conduction. The materials used in multispan plates range from simple metallic elements (aluminum, etc.) to complex composites (carbon, polyaramid). In general, each layer will be considered to be orthotropic for conduction. The conduction equation for layer i is then.

Contributed by the Heat Transfer Division for publication in the JOURNAL OF HEAT TRANSFER and presented at NHTC '97, Baltimore. Manuscript received by the Heat Transfer Division, June 18, 1997; revision received, Apr. 25, 1998. Keywords: Conduction, Forced Convection, Modeling and Scaling, Composite Materials. Associate Technical Editor: P. Menguc.

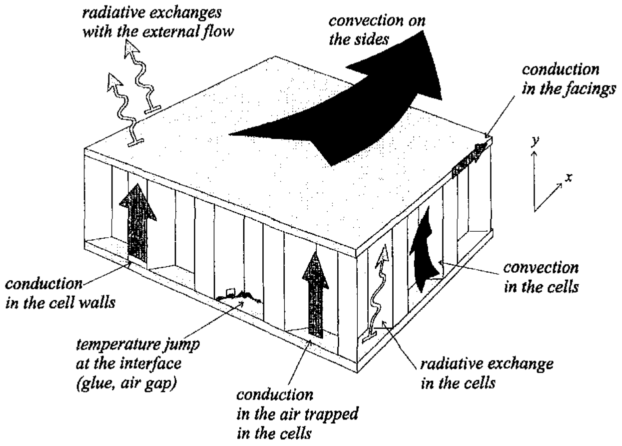

Fig. 1 Heat Transfer in honeycomb sandwiches

$$k_{ix}\frac{\partial^2 T_i}{\partial x^2}(x, y, t) + k_{iy}\frac{\partial^2 T_i}{\partial y^2}(x, y, t) = \rho_i c_i \frac{\partial T_i}{\partial t}(x, y, t), \quad (1)$$

c_i and ρ_i being constants calculated for the whole material in the case of heterogeneous materials (fibrous composite, for instance). It would be convenient to reduce this to the isotropic case. In order to avoid complications for interface conditions or boundary conditions in the x-direction, a new local variable Y_i is introduced for each layer. This leads to the following conduction equation:

$$\frac{\partial^2 T_i}{\partial x^2}(x, Y_i, t) + \frac{\partial^2 T_i}{\partial Y_i^2}(x, Y_i, t) = \frac{1}{\alpha_{ix}}\frac{\partial T_i}{\partial t}(x, Y_i, t) \quad (2)$$

with

$$Y_i = y\sqrt{\frac{k_{ix}}{k_{iy}}} \quad \alpha_{ix} = \frac{k_{ix}}{\rho_i c_i}. \quad (3)$$

Each orthotropic layer of thickness e_i is then replaced with an equivalent isotropic layer of equivalent diffusivity α_{ix}, conductivity K_i, and thickness E_i (calculations detailed by Murer, 1998):

$$K_i = \sqrt{k_{ix}k_{iy}} \quad E_i = e_i\sqrt{\frac{k_{ix}}{k_{iy}}}. \quad (4)$$

1.1.2 Interface Conditions. The imperfections of the contact between two layers (air gaps, microscopic geometry of the interface, glue or adhesive film) frequently give rise to temperature jumps at the interface, which are often described using thermal contact conductances.

Numerous works have been dedicated to contact conductances; a preliminary review of this literature (Degiovanni et al., 1990; Madhusudana and Fletcher, 1985; Fletcher, 1988; Stevenson et al., 1991; Sadhal, 1980, 1981) shows the complexity of the problem. Indeed, its microscopic aspect includes many different phenomena (convection, conduction and radiation in the gaps, presence of adhesive layer, etc.), depending on many different parameters (nature of the material, mean temperature of the contact, microscopic geometry of the contact, etc.). Even if some simplifications and global trends could be drawn from this review, microscopic contact conductance is too complex to be injected in a global model.

That is why it was decided to describe interface conditions in the stationary case with uniform non-temperature-dependent contact conductances, whose experimental values are extracted from the literature (for example, Stevenson et al., 1991). Considering the variable change in the y-direction for an orthotropic layer, the condition between layers i and $i + 1$ is written:

$$\begin{cases} -K_i \dfrac{\partial T_i}{\partial Y_i}(x, \tilde{Y}_i, t) \\ \quad = G_i(T_{i+1}(x, \tilde{Y}_i, t) - T_i(x, \tilde{Y}_i, t)) \\ -K_i \dfrac{\partial T_i}{\partial Y_i}(x, \tilde{Y}_i, t) & \forall x \in [0; L] \\ \quad = -K_{i+1}\dfrac{\partial T_{i+1}}{\partial Y_{i+1}}(x, \tilde{Y}_i, t) \end{cases} \quad (5)$$

with

$$\tilde{Y}_i = \sum_{j=1}^{i} E_i, \quad (6)$$

$\tilde{Y}_i$ being the beginning of the equivalent isotropic layer $i + 1$ in the y-direction and G_i the contact conductance between the two layers.

For the time-dependent case, two possibilities are proposed.

- The time scale of the interface phenomena is supposed to be negligible when compared to global heat transfer phenomena. In that case (microscopic gaps, etc.), only the temperature jump is to be considered, and contact conductances can be used directly in the global model.

Nomenclature

E = equivalent thickness of a layer (modified system)
G = thermal conductance
H, J, M = development orders
K = equivalent conductivity of a layer
L = length of the plate
N = number of layers
S = honeycomb cell cross section
T = temperature
U = mean velocity of the flow
c = specific heat
e = thickness of a layer
f_{bt} = configuration factor between top and bottom of a cell
h_c, h = convective and global heat exchange coefficients
k = thermal conductivity
s = Laplace variable
q = heat flux
(x, y, z, t) = space and time coordinates
u, v = fluid local velocities (x, y-direction)

Greek Symbols

α = thermal diffusivity
β_m = eigenvalue (x-direction)
ϵ = emissivity
γ_m = eigenvalue (y-direction)
θ = reduced temperature
$\overline{\theta}$ = laplace transform of the reduced temperature
ρ = density
σ = Stefan-Boltzman constant

Subscripts

c = core
f = fluid
i = layer index
m, j = development index
x, y = x, y-direction

Short scripts

LDV = laser Doppler velocimetry
ThIR = infraRed thermography

Dimensionless Numbers

Nu = Nusselt number
Re_x = Reynolds number for x

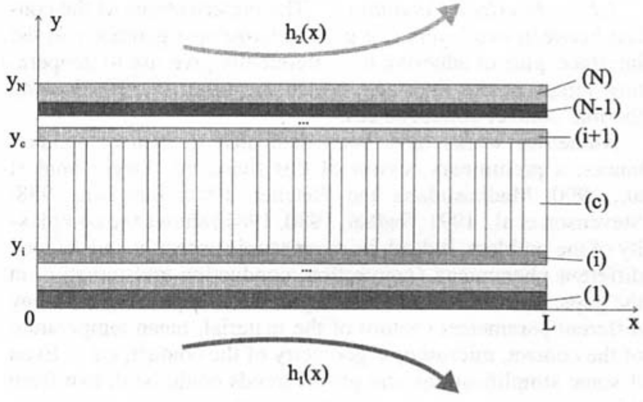

Fig. 2 Coordinate system and notations

- The time scale of the interface phenomena is not negligible (case of air film caused by nonflatness of pieces, glue layer). In that case, and if its geometrical characteristics are known, the interface is described as an additional layer.

1.2 Heat Transfer in Honeycomb Core. As stated before, a simplified modeling of heat transfer in honeycomb core is proposed here.

1.2.1 Convection in the Cells. According to the reviewed literature (Sunden, 1988; Chen and Hwang, 1989a, b), convection phenomena in honeycomb cells are ruled by the following parameters: nature of the cell walls (rather conductive or insulating materials), boundary conditions imposed on these walls (for the models); geometry of the cells (and mainly its aspect ratio); and the dimensionless number values characterizing the state of the system {cells walls + trapped air}: Nusselt, Rayleigh, and Prandtl numbers. Applying the results of various numerical, analytical, and experimental studies to the configurations considered in this paper, we may conclude that

- for cells with conductive walls (aluminum), there is no convection, or convection is negligible when compared with conduction in air and walls, or radiative exchanges (Houlbert, 1992; Lock and Zhao, 1992; Aggarwal and Manhapra, 1989).
- for cells with insulating walls (composites), the various models are not always in agreement, but the experimental works of Cane et al. (1977), Hollands (1973), and Buchberg et al. (1973) show that convection remains negligible.

Note that the problem of natural convection caused by apertures located at the interface facing/honeycomb is not considered in this study.

1.2.2 Conductive Exchanges. Very little literature is devoted to the description of conductive phenomena in honeycombs. Most of the time, when desired for industrial applications, conductive properties of honeycombs are measured or identified experimentally. Degiovanni (1993) and Houlbert (1992) describe the constriction phenomenon in the cells—that is, the conductive flux distribution between the cell walls and air trapped in the cell, depending on the wall conductivity compared with air conductivity. But this description is limited to the axial direction of the cell, and to a cylindrical geometry. However, to be easily incorporated in our model, honeycomb will be described using two conductivities and one specific mass:

- For a piece of honeycomb made with metallic ribbons (usually aluminum), values of orthotropic conductivities calculated by Hennis (1994), and based on the main assumption that the heat flux in air is negligible when compared with heat flux in the walls, were used as a first approximation.
- for honeycombs made with near insulating materials (polyethylene, polyaramid, etc.), the constriction hypothesis is not valid anymore. In that case, experimental or manufacturer conductivities were used.

In both cases, the specific heat is obtained from experimental or manufacturer data.

1.2.3 Radiative Exchanges in the Cells. Some authors have proposed analytical models of the radiative heat transfer in honeycomb cells (Tien and Yuen, 1975; Marcus, 1983), but, unfortunately, they cannot be integrated in a global conductive model. Another result of the experimental studies referenced above is of interest: uncoupling the radiative and conductive exchange in honeycomb cell modeling leads to consequent errors when compared with experimental results, particularly when the cell walls are highly absorbent (composite walls). On the contrary, for highly reflective walls (aluminum), radiative exchange can usually be neglected in comparison with conductive exchanges (Hennis, 1994). Making the same distinction, Houlbert (1992) introduces linearized radiative exchanges for one cell in a two-dimensional cylindrical geometry. A similar approach is followed here. These exchanges are introduced in the interface conditions between facings and honeycomb. Preliminary calculations show that the difference between the linearized and real flux are below two percent for the studied configuration; that is why the linearization hypothesis is retained. For highly reflective walls, the top and the basis of the cells are considered to be in total influence—that means all the flux emitted by one surface reaches the other, and vice versa. The flux and temperature conditions at the interface between layer i and the core then become

$$-K_i \frac{\partial T_i}{\partial Y_i}(x, \tilde{Y}_i, t) = -K_c \frac{\partial T_c}{\partial Y_c}(x, \tilde{Y}_i, t) + \frac{4\sigma S T_b^3}{\frac{1}{\epsilon_i} + \frac{1}{\epsilon_{i+1}} - 1}(T_i(x, \tilde{Y}_i, t) - T_{i+1}(x, \tilde{Y}_c, t)) \quad (7)$$

$$-K_c \frac{\partial T_c}{\partial Y_c}(x, \tilde{Y}_i, t) = G_i(T_c(x, \tilde{Y}_i, t) - T_i(x, \tilde{Y}_i, t)). \quad (8)$$

The conductance condition is to be applied only on the conductive flux transmitted in the core. The bulk temperature, T_b, is estimated from the global problem boundary conditions. For insulating walls, the top and the basis of the cells are considered to be in mutual influence; then, the flux condition becomes.

$$-K_i \frac{\partial T_i}{\partial Y_i}(x, \tilde{Y}_i, t) = -K_c \frac{\partial T_c}{\partial Y_c}(x, \tilde{Y}_i, t) + \frac{4\sigma S T_b^3}{\frac{1-\epsilon_i}{\epsilon_i} + \frac{1-\epsilon_{i+1}}{\epsilon_{i+1}} + \frac{2}{1+f_{bt}}}(T_i(x, \tilde{Y}_i, t) - T_b). \quad (9)$$

The temperature condition (Eq. (8)) remains unchanged. The configuration factor f_{bt} is between the bottom and the top of the cell; it is calculated using the D.A.R.C. code (Mavroukalis et al., 1996). The calculations are similar for the conditions at the interface between core and layer $i + 1$.

1.3 Boundary Conditions on the Faces of the Plate. The plate is subjected on both sides to fluid flows of different velocities and temperatures (which is the case in certain parts of combustion chambers, for example). Both radiative and convective exchanges on the plate faces are considered. This leads to the following boundary condition for the layer 1 in contact with the fluid):

$$-K_1 \frac{\partial T_1}{\partial Y_1}(x, 0, t) = h(x)(T_f - T_1(x, 0, t))$$

$$\forall x \in [0, L], \tag{10}$$

the expression being formally identical for the last layer. The coefficient $h(x)$ splits up into a radiative term and a convective term:

$$h(x) = \frac{4\sigma T_f^3}{\dfrac{1}{\epsilon_1} + \dfrac{1}{\epsilon_f} - 1} + h_c(x). \tag{11}$$

The radiative term is calculated assuming that the fluid and the layer 1 are in total influence, that both are gray bodies and that the considered temperature range allows the linearization of the radiative exchanges. As for the cells, this last hypothesis is verified through preliminary calculations.

For the estimation of the convective term, the flow is supposed to be parallel to the face plane, and to develop from a leading edge located upstream of the plate. The exchanges are then characterized by the evolution of the Nusselt number with x. Two cases are considered: laminar flow and turbulent flow. Simple flat-plate correlations are used in both cases (Cousteix, 1989a, b; Taine and Petit, 1989). Here they are expressed in the coordinate system (X-axis) whose origin is located at the leading edge. For laminar or turbulent flows with heat exchange only along the plate side (area before the plate thermally insulated),

$$\mathrm{Nu}(X) = \frac{0.324\ \mathrm{Re}_X^{0,5}\mathrm{Pr}^{1/3}}{(1 - (X_0/X)^{3/4})^{1/3}} \quad \text{(laminar case)} \tag{12}$$

$$\mathrm{Nu}(X) = \frac{0.324\ \mathrm{Re}_X^{0,5}\mathrm{Pr}^{1/3}}{(1 - (X_0/X)^{9/10})^{1/9}} \quad \text{(turbulent case)}. \tag{13}$$

The beginning of the plate on the X-axis is X_0. In both cases, the fluid properties are calculated for an estimated value of the film temperature since they are quasi-constant on the considered temperature range. With the relation

$$\mathrm{Nu}(X) = \frac{h_c(X)X}{k_f} \tag{14}$$

one can easily express h_c as a function of X, and then of x.

1.4 Resolution of the Problem.

1.4.1 Stationary Case. At this state of the process, heat transfer in each layer i is governed by three equations:

- the conduction equation and
- two interface conditions for internal layers ($Y_i = \tilde{Y}_{i-1}$, $Y_i = \tilde{Y}_i$), one Fourier condition and one interface condition for external layers.

With each layer being described by a rectangular domain, two more boundary conditions are necessary ($x = 0$, $x = L$). At this step of the study, two possibilities are proposed:

- Uniform homogeneous Neumann condition:

$$\frac{\partial T_i}{\partial x}(0, y) = \frac{\partial T_i}{\partial x}(L, y) = 0, \quad \forall i \in [1, N],$$

$$\forall Y \in [\tilde{Y}_{i-1}; \tilde{Y}_i]. \tag{15}$$

- Uniform inhomogeneous Dirichlet condition:

$$T_i(0, y) = T_i(L, y) = T_0, \quad \forall i \in [1, N],$$

$$\forall Y \in [\tilde{Y}_{i-1}; \tilde{Y}_i]. \tag{16}$$

Note that $\tilde{Y}_0 = 0$.

Let us explain the resolution of the considered system for the homogeneous Neumann conditions. Separation of variables is used to obtain an analytical approximation of the solution. Assuming that

$$T_i(x, Y_i) = \xi_i(x)\psi_i(Y_i), \tag{17}$$

the conduction equation for layer i leads to two separate problems, one with the variable x and homogeneous boundary conditions, and one with the variable Y_i and inhomogeneous boundary conditions. According to Özisik (1993), the homogeneous boundary conditions impose the form of the approximated solution (M order):

$$T_i(x, y) \approx \sum_{m=0}^{M} \sin(\beta_m x)[A_m^i e^{\beta_m Y_i} + B_m^i e^{-\beta_m Y_i}] \tag{18}$$

with

$$\beta_m = \frac{m\pi}{L}. \tag{19}$$

Writing the normalization integral for the interface or boundary conditions of all layers leads to a matrix system. In order to avoid numerical integration of the inhomogeneous boundary conditions on the faces of the multispan, the heat coefficients $h(x)$ are approximated on a Ritz-Rayleigh base using a least-square method:

$$h(x) = \sum_{j=0}^{J} h_j x^j. \tag{20}$$

The (A_m^i, B_m^i) are the solutions of the $2 \times N \times M$ system, which is solved using classical linear algebra methods.

The case of inhomogeneous Dirichlet boundary conditions is solved the same way, calling

$$\theta_i(x, y) = T_i(x, y) = T_0. \tag{21}$$

The problem for θ_i becomes homogeneous. The only difference is the global form of the solution

$$\theta_i(x, y) \approx \sum_{m=0}^{M} \cos(\beta_m x)[A_m^i e^{\beta_m Y_i} + B_m^i e^{-\beta_m Y_i}]. \tag{22}$$

The principle is also extended to other nonuniform inhomogeneous boundary conditions on the faces of the plate:

- nonuniform inhomogeneous Dirichlet condition

$$T_1(x, 0) = T_{\mathrm{imposed}}(x) \quad \forall x \in [0; L], \tag{23}$$

- nonuniform inhomogeneous Neumann condition

$$-k_1 \frac{\partial T_1}{\partial y}(x, 0) = q_{\mathrm{imposed}}(x) \quad \forall x \in [0; L]. \tag{24}$$

As above, the boundary conditions are approximated on a Ritz-Rayleigh basis and included in the matrix system once normalized.

1.4.2 Time-Dependent Solution. Let us assume that

$$\begin{cases} t = 0 \Rightarrow T_i(x, y, 0) = T_0 \\ \forall (x, Y_i) \in [0; L] \times [\tilde{Y}_{i-1}; \tilde{Y}_i], \quad \forall i \in [1, N] \end{cases}. \tag{25}$$

The boundary conditions on the edges of the plate remain the same as in the previous paragraph (homogeneous Neumann or inhomogeneous Dirichlet conditions). Note that in numerical procedure, the T_0 of the initial condition is the same as the T_0 of the inhomogeneous Dirichlet conditions.

The Laplace transform is used to reduce to the stationary case. Considering the following variable change:

$$\theta_i(x, y, t) = T_i(x, y, t) - T_0. \quad (26)$$

The Laplace transform of the heat equation for a layer i becomes

$$\frac{\partial^2 \bar{\theta}_i}{\partial x^2}(x, Y_i, s) + \frac{\partial^2 \bar{\theta}_i}{\partial Y_i^2}(x, Y_i, s) = \frac{s}{\alpha_{ix}} \bar{\theta}_i(x, Y_i, s). \quad (27)$$

Assuming that

$$\bar{\theta}_i(x, Y_i, s) = \bar{\xi}_i(x, s)\bar{\psi}_i(Y_i, s), \quad (28)$$

and writing the Laplace transform of the boundary conditions, one notes that the problem for $\bar{\theta}_i$ is formally identical to the stationary problem for T_i or θ_i. s is considered as a parameter of the solution, which leads to the following expression in the case of Neumann conditions on the edges (same calculations for Dirichlet conditions):

$$\bar{\theta}_i(x, y, s) \approx \sum_{m=0}^{M} \cos(\beta_m x)[A_m^i e^{\gamma_m^i Y_i} + B_m^i e^{-\gamma_m^i Y_i}] \quad (29)$$

with

$$\gamma_m^i = \sqrt{\left(\frac{m\pi}{L}\right)^2 + \frac{s}{\alpha_{ix}}}. \quad (30)$$

The Laplace transform of the temperature $\bar{\theta}_i$ is then calculated as for T_i or θ_i (truncation of the development, normalization of the boundary conditions on the faces and algebraic resolution of the obtained system), for any value of s.

The Stehfest algorithm (1970), suggested by Houlbert (1992), is used to transpose the solution in space-time coordinates.

1.4.3 Computational Values. Tests were conducted to estimate the optimal values for parameters such as M, J or the order of the numerical inverse Laplace transform H. Stationary and time-dependent temperature fields are calculated for two or three-span plates, with constituents of various isotropic or orthotropic conductions. Contact conductances were inserted between the layers, and the different boundary conditions combinations on ($x = 0$, $x = L$) and ($y = 0$, $y = y_N$) are tested.

Convergence value for J: For $J = 3$, the error between $h_c(x)$ and its approximation is always under 0.05 percent for the different correlations used (laminar and turbulent flows with velocity in the [0; 25 m/s] range, without adiabatic conditions before the plate). A 0.05 percent variation on an $h_c(x)$ correlation giving rise to negligible variations on temperature field results, an order 3 for $h_c(x)$, is considered to be sufficient. For plate with adiabatic conditions before the plate, $J = 5$ is recommended. Note that, for this case, $h_c(x)$ is supposed to take infinite values for $X = 0$. That is why it is rather difficult to estimate the error made for low values of X; but choosing an approximated finite value for $h_c(X = 0)$ leads to errors below five percent for the rest of the curve.

Convergence value for M: In most cases (stationary and time-dependent, two-span and three-span, nature of the materials, etc.), and for most of the boundary conditions on the faces, the difference between solutions for $M = 8$ and $M = 9$ is less than 5×10^{-3}°C in absolute value. This error value is considered to be small enough when compared to the temperature range of the study. Thus $M = 9$ is recommended. Nevertheless, some precautions had to be taken for cases coupling severe variations of the boundary conditions on the face with adiabatic conditions on the side. Discontinuity in the temperature gradient along x may occur and lead to typical "corner divergence" problems. When this happens, M should be drastically raised in order to reach for convergence. This can be the case for a composite plate including insulating materials (polyaramid, for instance) with adiabatic conditions on the sides, and $h_c(x)$ calculated using Eq. (13).

Table 1 Calculation parameter for the one-span/two-span test

Geometry	$L = 2 \times 10^{-1}$ m; $e_1 = 2 \times 10^{-2}$ m; $e_2 = 2 \times 10^{-2}$ m
Thermophysical properties	$k_1 = 200$ W/mK; $k_2 = 200$ W/mK
Interface conditions	$T_{2\infty} = 100$°C
Boundary conditions	$h_1(x) = 217.8 - 189.3x + 1207.5x^3$ W/m²K, $T_{f1} = 20$°C $h_2(x) = 149.6 - 27.9x + 76.8x^3$ W/m²K, $T_{f2} = 100$°C

Convergence value for H: A value of $H = 16$ is used. Stehfest (1970) recommends $H = 18$, but, in the present case, this higher value does not bring significant improvements. Note that numerical inverse Laplace transform gives satisfying results for damped systems periodically oscillating with time, but diverges for undamped ones. The inverse Laplace transform numerical algorithm does not converge until a minimum value of $t_{\min}$ is reached. This limit depends on the thermophysical properties of the components, and ranges from 0.01 s for thin conductive plates to 1 s for very insulating plates.

CPU times are negligible for the stationary case and below a few seconds for the time-dependent case (PC 486 system).

1.4.4 Numerical Validation. A numerical validation is also carried out. In a first step, the equivalence between one-span and multispan plates is checked. The temperature fields of simple plates of given characteristics are computed and compared with the temperature fields of two-spans plates of the same global characteristics, for various boundary conditions. The value of the thermal contact resistance between the two spans is $R = 10^{-7}$ m² K/W. If this value were exactly zero, the mathematical expression of the one-span and the two-span solutions would be the same and the test would not have any meaning. As an example, the results of the test are given for a one-span plate of global thickness equal to 0.04 m, with adiabatic conditions for $x = 0$ and $x = L$, and subjected to convective exchanges on both faces. The characteristics of the two-spans equivalent plate and the expression of the $h(x)$ are given in Table 1. Figure 3 shows the temperature field of the two-spans solution. The difference between the one-span and two-span solutions is given on Fig. 4. This difference is below 1.5×10^{-3} K, and is only generated by the introduction of the thermal contact resistance in the two-span calculation. For the other tested configurations the results are similar.

In a second step, the stationary solutions are compared with transient solutions for "infinite" time, for various materials (two-spans plates, sandwich materials) and various boundary conditions. Local divergences are observed at the corners or at the interface areas (for $x \approx 0$ or $x \approx L$, with Dirichlet conditions on the edges), but remain below 0.6°C for a temperature gradient above 100°C across the layers, and can be classified in the "typical corners problem."

The model is also compared with a numerical code using finite difference, developed at the ONERA/DMAE by Reulet (Reulet, 1997). This code calculates a stationary temperature field for two-dimensional rectangular multispan plates with any kind of boundary conditions on the faces, and Neumann or Dirichlet conditions on the side. It does not take thermal contact resistance into account. The test case is a two-span plate with adiabatic conditions on the sides, convective exchanges on the face $y = 0$, and Dirichlet conditions for the other face; the conductivity of the layer 2 is about 90 times greater than the conductivity of the layer 1. The convective exchange coefficient also presents a steeply slope for x near 0. Table 2 sums up the

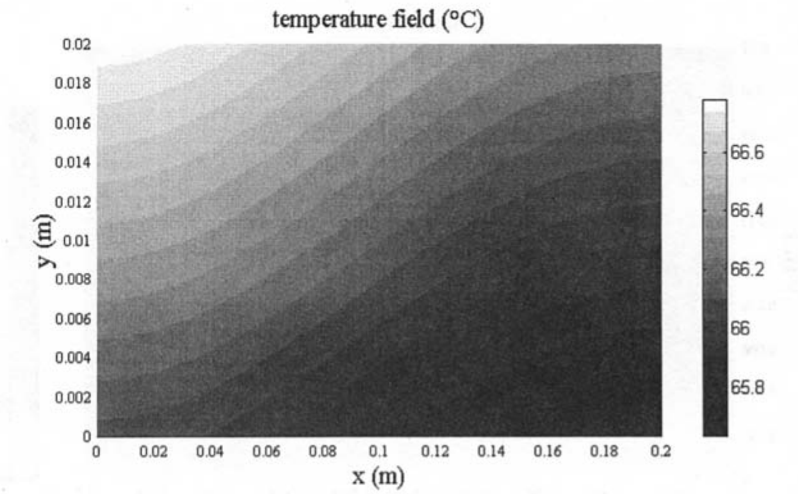

Fig. 3 Two-spans solution of the one-span/two-spans test

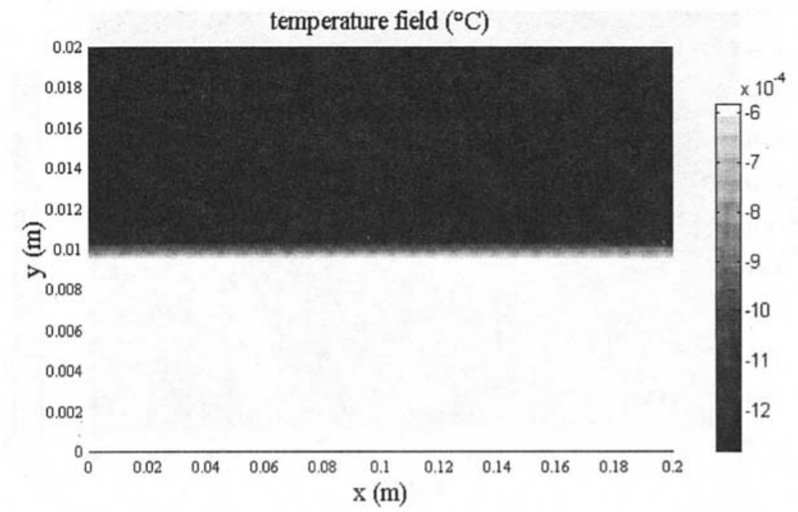

Fig. 4 Temperature difference between one-span and two-spans solutions—one-span/two-spans test

characteristics of the calculation. M is taken equal to 30 for the analytical calculation; a 4000 mesh discretization (101 nodes along the x-axis, and 41 nodes along the y-axis) is used for the numerical calculation. A very low thermal contact resistance is used to simulate perfect contact for the analytical model ($R = 10^{-8}$ m^{2}K/W). The results of the computation are detailed by Murer (1998). The comparison is excellent; the difference remains below 0.15×10^{-2} K, and is mainly caused by the residual oscillations of the trigonometric expansion of the analytical solution. For higher values of M ($M = 50$, for instance), these oscillations would almost disappear.

Table 2 Calculation parameters for the transient sandwich plate calculation

Geometry	$L = 0.2$ m; $e_1 = 0.6$ mm; $e_c = 19$ mm; $e_2 = 0.8$ mm
Thermophysical properties of the facings	Aluminum: $k_{cx} = 204$ W/mK; $k_{cy} = 204$ W/mK; $\alpha_c = 8.41 \times 10$-5 m^2/s
Thermophysical properties of the core	$k_{cx} = 2.77$ W/mK; $k_{cy} = 2$ W/mK; $\alpha_c = 9.09 \times 10$-5 m^2/s
Interface conditions	$G_1 = G_c = 2000$ W/m^{2}K
Initial conditions	Initial temperature: $T_0 = 323.15$ K
Boundary conditions	Adiabatic conditions on $x = 0$ and $x = L$; $h_{c1}(x) = 217.8 - 189.3x + 1207.5x^3$; $T_{f1} = 283.15$ K; $h_{c2}(x) = 149.6 - 27.9x + 76.8x^3$; $T_{f2} = 373.15$ K.

As an example, Fig. 5 gives three steps of the transient evolution of the temperature field for a sandwich plate {layer 1: aluminum—core: aluminum honeycomb—layer 2: aluminum} subjected to parietal flow on both faces. The calculation parameters are given in Table 2.

2 Validation Experiments

Validation experiments are carried out to check the validity of the model for some configurations. In a first step, this validation is limited to the stationary case. The implementation of a "real" situation on the model relies on the precise knowledge of a certain number of parameters:

- the thermal characteristics of nonhomogeneous materials, such as honeycomb: most of the time only global values are given (only one conductivity in one direction, etc.), which is not enough to validate the reduced descriptions;
- the contact conductances for plane contact between various materials (metal/metal, or composites/metal, etc.), in the considered temperature range;

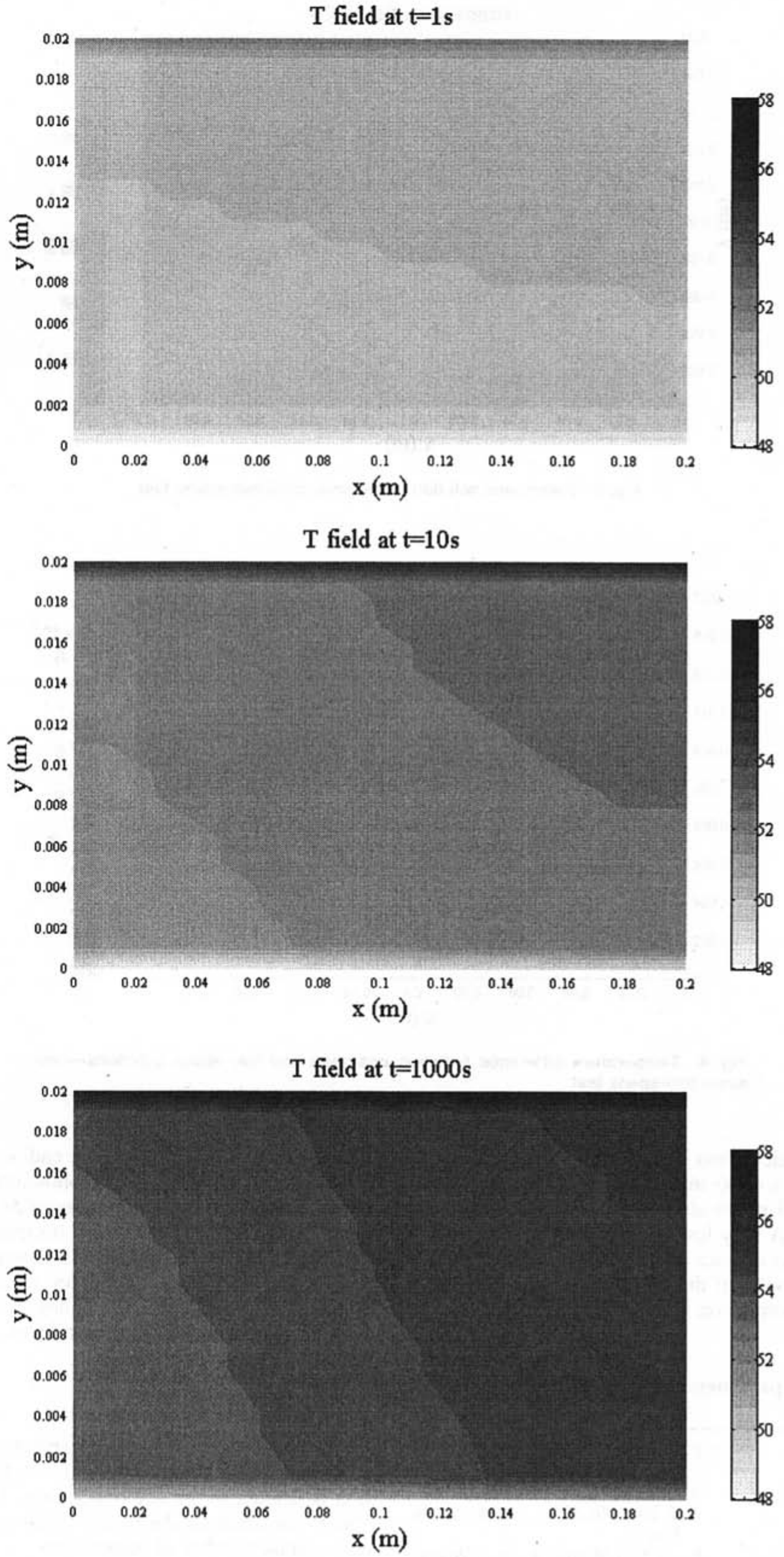

Fig. 5 Evolution of temperature field (°C) across an aluminum-aluminum honecomb-aluminum sandwich

- the estimation of convective exchanges on the plate faces; and
- *the exact boundary conditions imposed in the experimental* set-up.

Some of them are estimated through preliminary experiments (convective exchanges). Literature review, approximations or reduced models are used to determine the others. That is why this validation phase only aims to give trends. In a second step, these

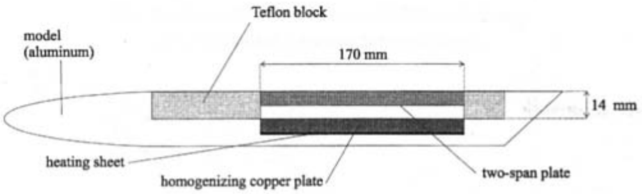

Fig. 6 First experiment: model geometry and dimensions

trends could lead to the refinement of weak points of the global model, and to the definition of more elaborated validation processes.

Two configurations are studied: a two-span plate with convective exchanges generated by a flow in a wind tunnel and a sandwich plate in an industrial set-up bench.

2.1 First Experiment.

2.1.1 Experimental Set-up. A profiled model containing a plexiglas-aluminum two-spans plate is placed inside a wind tunnel ring. The characteristics of its test section are 0.69 m length, 0.45 × 0.45 m^2 cross section. Velocities range from 2.5 m/s to 25 m/s.

The configuration and the dimensions of the profiled model are given in Fig. 6. The plate is 0.17 m × 0.014 m × 0.16 m; each span is 0.07 m thick; its bottom face temperature is regulated using a heating silicon fabric coupled with a regulation system. A copper plate of 0.005 m thickness is inserted between the silicon fabric and the plate, to reduce possible inhomogeneity of the heating flux. Thermocouples located in the plate, at the interface with the copper, give the temperature information for the regulation.

The aerodynamic parts of the model (leading edge, trailing edge, etc.) are made of aluminum; the plate is inserted in a Teflon block, in order to simulate adiabatic conditions on the sides. Particular attention is paid to make the plate, the Teflon and the leading edge flush.

2.1.2 Identification of Convective Exchanges. The convective heat transfer coefficients proposed in paragraph 1.3 are given for a flow developing over a theoretical flat plate. Our experimental set-up is slightly different, because the profiled model approaches a flat plate. Velocimetry measurements are then carried out, in order to identify the nature of the flow (global flow, boundary layer). These results are then correlated with a theoretical flat plate solution, whose associated Nusselt-Reynolds correlation leads to $h_c(x)$. The flow chart given in Fig. 7 sums up the processes, which is repeated for three different velocities: 4 m/s, 15 m/s and 23 m/s. The tested plate is heated ($T(x, y = 0) = 50°\mathrm{C}$).

A TSI two-dimensional fringe laser anemometer coupled to a 4W Argon laser is used to perform the measurements of the components u(x-direction) and v(y-direction) of the instantaneous velocity, and the calculation of the turbulence intensity, for different mean velocities. The air is seeded with incense particles. Thermocouples check the flow temperature.

For each mean velocity, two sets of measurements were performed:

- a global exploration of the upper part of the flow along the model, to check the uniformity of the flow in the test section and to estimate the thickness of the boundary layer; and
- an exploration of the boundary layer with 20 velocity profiles regularly distributed from the leading edge of the model to the end of the tested plate, the measurement grid is adjusted according to the estimated thickness of the boundary layer.

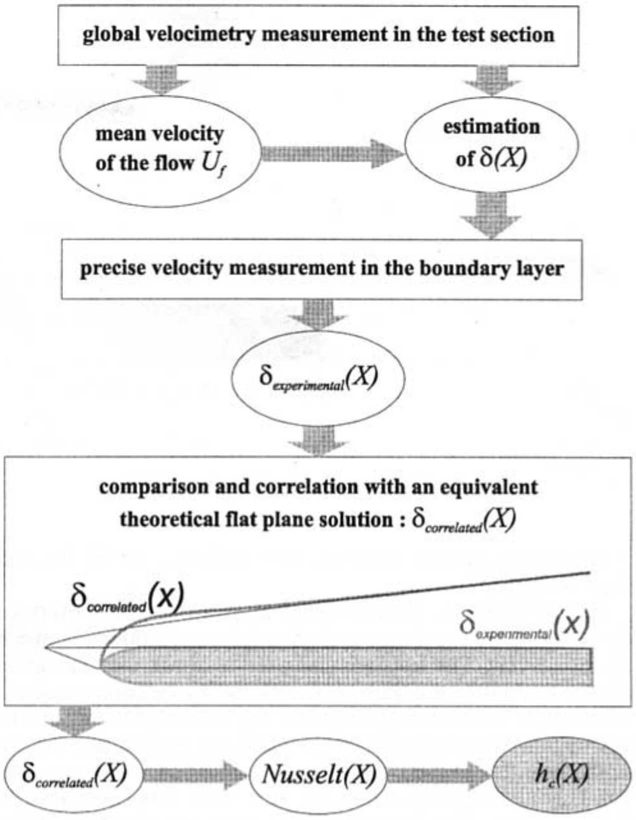

Fig. 7 Methodology of the convective exchange coefficient identification

The experimental profiles and the evolution of the boundary layer thickness are then compared to the classical laminar and turbulent theories (Cousteix, 1989a, b) for flat plates. The leading edge abscissa of an equivalent theoretical flat plane is then chosen in order to match theoretical and experimental results over the model. Knowing this theoretical equivalent solution, it is possible to calculate $\mathrm{Nu}(x)$ and $h_c(x)$. More details are given in reference Murer (1998).

Two main error sources were found: the first is the LDV system measurement error, which is under one percent of the measured mean velocity. The second is the wind tunnel mean velocity drifting (mostly caused by the engine heating during the experiment), which was estimated to be ±0.1 m/s. A short calculation shows that the maximum error on U_f leads to a ±0.3 percent maximum error on $h_c(x)$ (the error on the boundary layer thickness being less significant). Such a variation was incorporated in the model implemented with the studied configuration, and led to temperature variations which are negligible when compared with the temperature measurement errors (see below).

2.1.3 Infrared Thermography Measurement. The temperature field of the plate upper face was measured with an infrared camera (AGEMA 880 LWB) looking through a ZnS window; the observed scenery includes the whole face (see Fig. 8). Thermocouples were placed inside the plate and in the air flow, and complete the temperature measurement in the system. The ThIR measurement errors were the signal noise (about ±0.1°C for the used camera) and the different corrections made inside the acquisition process (air and wind tunnel wall absorption, etc.); the global error is estimated to be under 0.6°C (±0.3°C). The maximum error for thermocouples (after an in situ calibration) being under 0.5°C, the total error was taken to be approximately ±0.5°C.

In a first step, the stationary case is studied: the bottom face of the plate is temperature regulated and the upper face is submitted to the flow. Once the stationary state is reached, 4000

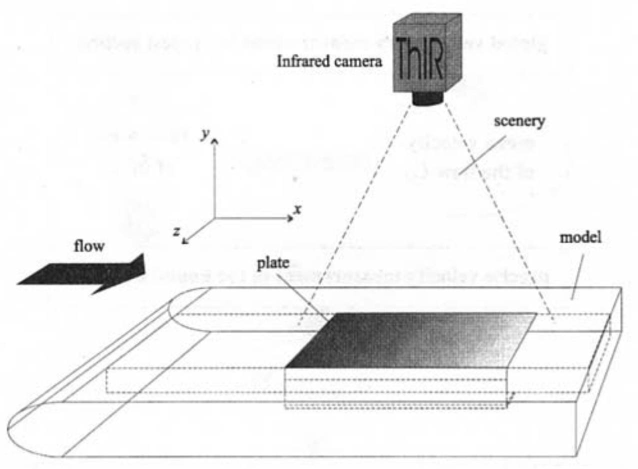

Fig. 8 ThIR visualization: first experiment

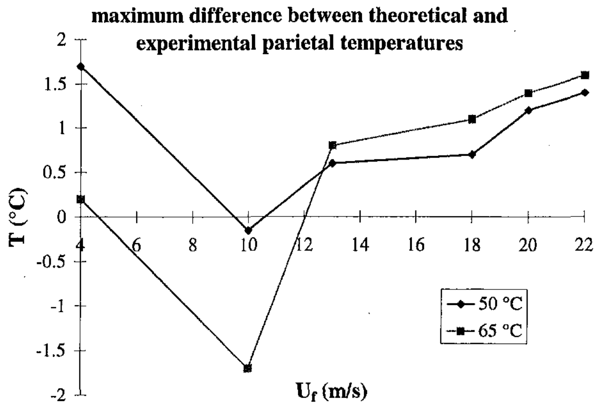

Fig. 9 Maximum difference between mode and experimental parietal temperature: first experiment

instantaneous images are taken, at a frequency of 60 Hz, and then averaged.

Preliminary tests are conducted to check the uniformity of the temperature regulation and of interface conditions between the two layers. The tests are also used to check the realization of the adiabatic conditions at $x = 0$ and L. Infrared measurements of the surface temperature for the Teflon insulating blocks upstream and downstream of the plate can lead to an estimate of the heat flux in the x-direction for $x = 0$ and $x = L$ (see Fig. 8). This flux is compared to the theoretical flux exchanged in the y-direction. The results are very satisfactory for the metallic layer, and acceptable for plexiglas layers (flux in the x-direction below 20 percent of the flux in the y-direction).

2.1.4 Comparison Between Model and Experiment. The stationary model is implemented with the description of the different experimental configurations (adiabatic boundary conditions at $x = 0$ and $x = L$, bottom face temperature and air temperature). J is taken equal to 3 and M to 9. Six different mean velocity (4, 10, 14, 18, 20 and 22 m/s) and two bottom-face temperature ($T_1(x, y = 0) = 50$ and 65°C) combinations are tested. The Reynolds number of the mean flow ranges from 5.2×10^4 to about 3×10^5 (taking the distance between the leading edge and the beginning of the plate as the characteristic length). The interface thermal conductance is estimated from the literature ($G = 500$ mK/W). The radiative exchanges between the plate upper face and its environment are estimated using Eq. (10). Analytical and experimental results are then compared on two points:

- evolution of the upper face temperature: $T_2(x, y = y_2)$, $x \in [0; L]$. The experimental temperature fields are averaged in the z-direction.
- temperature measured with thermocouples inside the two-span plate.

For the two temperature orders (50 and 65°C), the difference between analytical and experimental wall temperatures is below 1.7°C (see Fig. 9), and the theoretical trends are close to the experimental ones. As an example, Fig. 10 presents the parietal temperature field and the comparison between the analytic calculation and the mean evolution of this temperature with x, for $U_f = 4$ m/s and $T(x, y = 0) = 65$°C. Figure 11 shows another case ($U_f = 18$ m/s and $T(x, y = 0) = 50$°C). A parametric study reveals that

- the main cause of the difference between theory and experiment is an underestimation of the thermal contact resistance: a value of G equal to 50 mK/W reduces the mean error to about 0.2°C for "low" mean velocities ($U_f \leq 14$ m/s), which is below the experimental error.

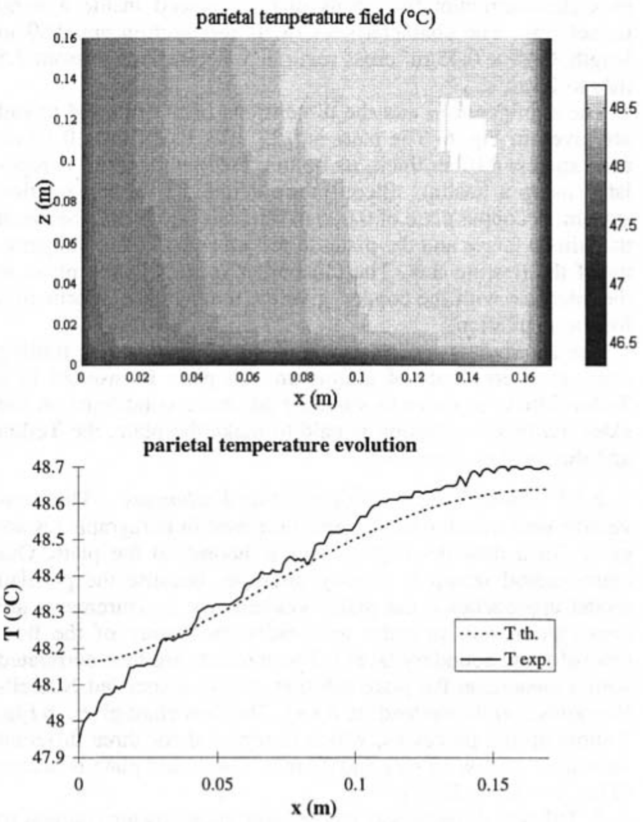

Fig. 10 Experimental and theoretical parietal temperature evolution for the two-span plate ($U_f = 4$ m/s, $T(x, y) = 65$°C)

- the convective coefficient is probably underestimated for "high" values of the velocity ($U_f \geq 18$ m/s). Note that the agreement is particularly satisfying for totally laminar flow ($U_f = 4$ m/s).

Other cases are tested, for higher bottom temperature ($T(x, y = 0) = 75$°C and 85°C). Thermomechanical phenomena (plexiglas plate buckling) dramatically modify the interface condition between the two span, which becomes rather difficult to estimate. But for "low" speed, the comparison between theory and experiment still gives encouraging results. Figure 12 gives an example for $U_f = 14$ m/s and $T(x, y = 0) = 85$°C.

2.1.5 Conclusion. The result of the first experimental validation is satisfying: for isotropic materials with known properties in a clearly identified environment (controlled boundary

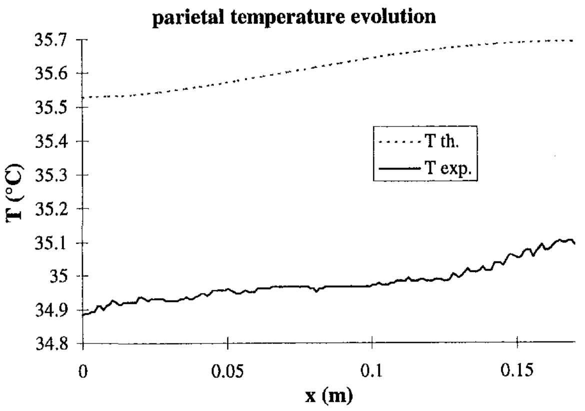

Fig. 11 Experimental and theoretical parietal temperature evolution for the two-span plate (U_f = 18 m/s, $T(x, y = 0)$ = 50°C)

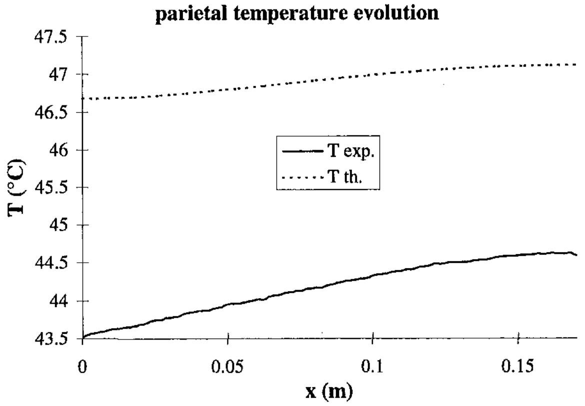

Fig. 12 Experimental and theoretical parietal temperature evolution for the two-span plate (U_f = 14 m/s, $T(x, y = 0)$ = 85°C)

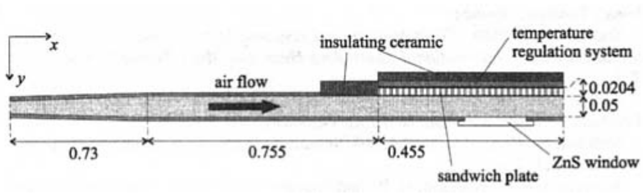

Fig. 13 Configuration of the second experiment

conditions), the agreement between model results and experiment is below 1.7°C. A parametric study also shows which parameters could explain the discrepancy (G, h_c), which falls below the experimental error once they are corrected.

2.2 Second Experiment.

2.2.1 Experimental set-up. The second experiment uses a bench-scale reproduction of an industrial configuration (combustion chamber). Figure 13 depicts the experimental configuration: an aluminum sandwich plate (length 0.455 m, width 0.16 m, thickness 0.0204 m) was submitted to an air flow parallel to the plate upper face. The flow is confined in a tunnel of rectangular cross section (0.16×0.05 m^2). A ZnS window on the side facing the sandwich allows ThIR measurements of the scenery for $0.15 \leq x \leq 0.325$. The bottom face of the plate is temperature regulated by a system including a copper plate with heating cartridges and thermocouples located at the copper/sandwich interface. A heater located upstream of the test section allows flow temperatures varying from the ambient temperature to 150°C, depending on the flow mean velocity. A more detailed description of the experimental set-up is given in the thesis of Dumoulin (1994). Thermocouples placed in the sandwich and in the flow complete the ThIR measurement. The errors on temperature measurement are similar to the previous experiment.

Table 3 calculation parameter for sandwich plate calculation (validation experiment)

Geometry	L = 0.47 m; e_1 = 0.8 mm; e_c = 19 mm; e_2 = 0.6 mm
Thermophysical properties of the facings	Duralumin: k_{cx} = 164 W/mK; k_{cy} = 164 W/mK
Thermophysical properties of the core	Aluminum honeycomb: k_{cx} = 0.4 W/mK; k_{cy} = 0.4 W/mK
Interface conditions	$G_{1\to c} = G_{c\to 2}$ = 1150 W/m^{2}K
Boundary conditions	Adiabatic conditions on $x = 0$ and $x = L$ $h_c(x) = 719 - 839.5x - 5786.2x^2 + 24326x^3 - 24088x^4$ $T(x, y = 0) = T_0$ (*temperature regulation order*)

The flow characteristics (mean velocity and different velocity profiles in the tunnel) are measured upstream of the test section using hot wire and hot film systems. The errors (about 0.1 m/s) are not significant considering the high turbulence level in the flow.

2.2.2 Estimation of the Experimental Parameters. The thermophysical characteristics of the sandwich plate are summed up in Table 3. The conductivities of the aluminum honeycomb core are estimated using Houlbert's (1992) results. The thermal contact conductances between the core and the facings are also extracted from the Houlbert results.

It is rather delicate to precisely define the boundary conditions on the sides of the plate: one side is in contact with an insulating ceramic, and the other is in contact with air. We admit that these conditions are not exactly adiabatic, because of the low thermal conductivity of the sandwich along the x-axis. Convective coefficients has been experimentally determined by Dumoulin (1994) for various fluid temperatures and velocities on the same experimental configuration; his results are used to approximate $h_c(x)$; $J = 4$ is enough to guarantee a precision of five percent. The convective exchange coefficient used for the presented calculation is also given in Table 3.

2.2.3 Comparison Between Experiment and Model: Conclusion. The stationary model is implemented with the parameters set. The calculations are compared to the wall temperature field measured on the ThIR scenery for two different bottom temperature order (120 and 150°C) and one mean flow velocity (U_f = 205 m/s); the Reynolds number related to the length of

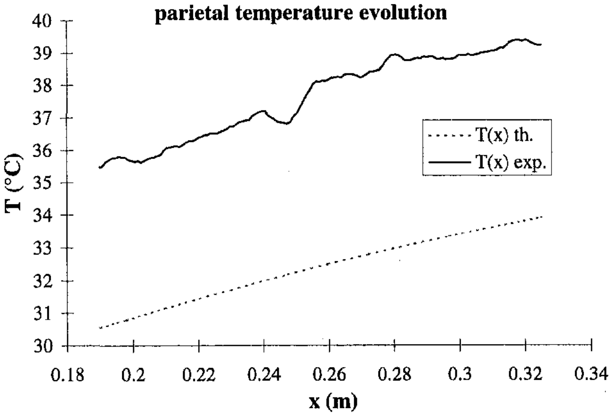

Fig. 14 Experimental and theoretical parietal temperature evolution for the aluminum sandwich plate (U_f = 205 m/s, $t(x, y = 0)$ = 120°C)

the tested plate is about 6.36×10^6. As for the previous experiment, the experimental parietal temperature is averaged along the z-axis. Figure 14 presents the theoretical and experimental curves for $T(x, y = 0) = 120°C$ and a flow temperature equal to 18°C. The difference between the calculations and the experimental results is about 5°C; and the trends (evolution with x) are similar. Following a parametric study, it is shown that the discrepancy is probably due to a coupled overestimation of the contact resistance and of the exchange coefficient. The same conclusions apply to the other tested case ($T(x, y = 0) = 150°C$). Even though the industrial set-up is producing an imperfect simulation of a Neumann condition on the edges, the experimental validation is considered to be very satisfactory.

3 Conclusions and Perspectives

A model describing two-dimensional time-dependent heat transfer in multispan or sandwich flat plates with inhomogeneous boundary conditions on the faces was developed. The different components are either isotropic or orthotropic for conduction; particular attention is paid to the reduction of different heat transfer modes in light cores (honeycomb). Contact conductances allow taking interface phenomena into account. Convective and radiative exchanges on the plate face are described using nonuniform inhomogeneous boundary conditions. Stationary solutions are developed on trigonometric and exponential function bases. Time-dependent cases are solved using the same principle and the properties of the Laplace transform. The CPU time on a PC system is negligible. Various tests show the validity of the model.

Validation experiments were carried out in different wind tunnels, and demonstrate satisfying agreement with the model trends for simple configurations (two-span plates and aluminum sandwich with convective exchanges on one face).

The study should be continued in the following perspectives:

- The analytical model should be developed to include time-dependent boundary conditions on the faces and nonuniform interface conductances; the superposition method should lead to a three-dimensional model with inhomogeneous boundary conditions on all faces.
- Other cases should be experimentally treated in order to improve the validation of the model. Thus, an experiment similar to the first presented in the present paper should be conducted with honeycomb sandwich plates. Moreover, experimental characterization of honeycomb cores should be carried out (comparative study of conduction and radiative exchanges in the cells).
- Finally, an experiment should be developed in order to validate the transient part of the model.

References

Aggarwal, S. K., and Manhapra, A., 1989, "Transient natural convection in a cylindrical enclosure non-uniformly heated at the top wall," *Numerical Heat Transfer,* Part A, Vol. 15, p. 341.

Buchberg, H., Catton I., and Edwards, D. K., 1973, "Natural Convection in Enclosed Spaces: A Review of Applications to Solar Energy Collection," ASME JOURNAL OF HEAT TRANSFER, Vol. 95, p. 182.

Cane, R. L. D., Hollands, K. G. T., Raythby, G. D., and Unny, T. E., 1977, "Free Convection Heat Transfer Across Inclined Honeycomb Panels," ASME JOURNAL OF HEAT TRANSFER, Vol. 99, p. 86.

Chen, R. S., and Hwang, G. J., 1989a, "Effect of Wall Conduction on Combined Free and Forced Laminar Convection in Horizontal Tubes," ASME JOURNAL OF HEAT TRANSFER, Vol. 111, p. 581.

Chen, R. S., and Hwang, G. J., 1989b, "Three-dimensional laminar natural convection in a honeycomb enclosure with hexagonal end walls," *Numerical Heat Transfer,* Part A, Vol. 15, p. 67.

Cousteix, J., 1989a, *Aérodynamique—Couche limite laminaire,* Editions CEPADUES.

Cousteix, J., 1989b, *Aérodynamique—Turbulence et couche limite turbulente,* Editions CEPADUES.

Degiovanni, A., 1993, "Conduction dans un "mur" multicouche avec sources: Extension de la notion de quadripôle," *International Journal of Heat and Mass Transfer,* Vol. 31, No. 3, p. 553.

Degiovanni, A., Lamine, A. S., and Moyne, C., 1990, "Thermal contact in transient states: A new model and two experiments," AIAA 90' Aerospace Sciences Meeting, Jan. 8–11, Reno, NV.

Dumoulin, J., 1994, "Méthode de détermination, par thermographie infrarouge, des coefficients d'échange de chaleur moyen et instationnaires en arérodynamique perturbée," thèse de l'INSA Toulouse, Toulouse, France.

Fletcher, L. S., 1988, "Recent Development in Contacts Conductance Heat Transfer," ASME JOURNAL OF HEAT TRANSFER, Vol. 110, p. 1059.

Hollands, K. G. T., 1973, "Natural Convection in Horizontal Thin-Walled Honeycomb Panels," ASME JOURNAL OF HEAT TRANSFER, Nov., p. 439.

Houlbert, A. S., 1992, "Caractérisation thermique des parois composites opaques—problèmes d'homogénéisation," thèse du LEMTA INP de Lorraine, Lorraine, France.

Lock, G. S. H., and Zhao, L., 1992, "Natural convection in honeycomb wall spaces," *International Journal of Heat and Mass Transfer,* Vol. 55, No. 1, p. 155.

Madhusudana, C. V., and Fletcher, L. S., 1985, "Contact Heat Transfer—the last decade," *AIAA Journal,* Vol. 24, No. 3, p. 510.

Marcus, S. L., 1983, "An approximate method for calculating the heat flux through a solar collector honeycomb," *Solar Energy,* Vol. 30, No. 2, p. 127.

Mavroukalis, A., Trombe, A., and Moisson, M., 1996, "Code de calcul D.A.R.C.," LETHEM, INSA Toulouse, Toulouse, France.

Murer, Y., 1998, "Caractérisation des comportements thermique et vibro-acoustique des composites multicouches et sandwichs," thèse de Doctorat de l'ENSAE Toulouse, Toulouse, France.

Özisik, M. N., 1993, *Heat Conduction,* 2nd Ed., John Wiley and Sons, New York.

Reulet, P., 1997, "Caractérisation expérimentale des échanges thermiques instationnaires en arérodynamique perturbée," thèse de Doctorat de l'ENSAE Toulouse, Toulouse, France.

Sadhal, S. S., 1980, "Transient thermal response of two solids in contact over a circular disc," *International Journal of Heat and Mass Transfer,* Vol. 23, p. 731.

Sadhal, S. S., 1981, "Unsteady Flow Between Solids With Partially Contacting Interface," ASME JOURNAL OF HEAT TRANSFER, Vol. 103, p. 32.

Stehfest, H., 1970, "Algorithm 368 Numerical inversion of Laplace transform," *ACM 13,* Vol. 1, p. 47.

Stevenson, P. F., Peterson, G. P., and Fletcher, L. S., 1991, "Thermal Rectification in Similar and Dissimilar Metal Contacts," ASME JOURNAL OF HEAT TRANSFER, Vol. 113, p. 30.

Sunden, B., 1988, "Transient conduction in a cylindrical shell with a time varying heat flux and convective and radiative surface cooling," *International Journal of Heat and Mass Transfer,* Vol. 32, No. 3, p. 575.

Taine, J., and Petit, J. P., 1989, "Cours de transferts thermique: Mécanique des fluides anisothermes," Dunod Université.

Tien, C. L., and Yuen, W. W., 1975, "Radiation characteristics of honeycomb solar collectors," *International Journal of Heat and Mass Transfer,* Vol. 18, p. 1409.

F. J. Cantelmi
Graduate Student,
Department of Mechanical and
Aerospace Engineering,
Rutgers, The State University of New
Jersey,
Piscataway, NJ 08855-0909
e-mail: cantel@jove.rutgers.edu

D. Gedeon
Principal,
Gedeon Associates,
16922 South Canaan Road,
Athens, OH 45701
Mem. ASME

A. A. Kornhauser
Associate Professor,
Department of Mechanical Engineering,
Virginia Polytechnic Institute
and State University,
Blacksburg, VA 24061-0238
e-mail: alkorn@vt.edu.
Mem. ASME

An Analytical Model for Turbulent Compression-Driven Heat Transfer

Compression-driven heat transfer is important to the performance of many reciprocating energy-conversion machines. For small pressure variations in cylinder spaces without inflow, heat transfer and power losses are well predicted using a simple heat transfer model which neglects turbulence. In actual engine cylinders, where significant turbulence levels can be generated by high-velocity inflow, a model which neglects turbulence may not be adequate. In this paper, a heat transfer model having an analytical solution is developed for turbulent cylinder spaces based on a mixing length turbulence model. The model is then used to develop expressions for heat-transfer-related power loss and heat transfer coefficient. Predicted results compare favorably with experimental data for two in-flow configurations.

Introduction

Compression-driven heat transfer is important to the performance of many reciprocating energy-conversion machines. It is particularly important to the performance of Stirling machines. Heat transfer in cylinder spaces takes place under conditions of oscillating pressure and oscillating flow. While under some operating conditions the heat transfer may be calculated from quasi-steady models such as Newton's Law of Cooling, there are many conditions for which this approach is inadequate.

Experimental work performed on closed piston-cylinder gas springs has shown that, for high nondimensional speeds, gas-wall heat transfer leads to gas-wall temperature differences of up to 45 deg. A theoretical model was proposed by Lee (1983) in which the heat transfer phase-shift was predicted through the use of a complex heat transfer coefficient. For a nearly sinusoidal temperature variation, a complex-valued heat transfer coefficient suggests that in addition to being proportional to the gas-wall temperature difference (as in quasi-steady models), compression-driven heat transfer has a component proportional to the rate at which the gas-wall temperature difference is changing. The relationship between the standard heat transfer coefficient and the complex heat transfer coefficient is analogous to that of resistance and complex impedance in circuit theory.

The complex heat transfer coefficient and heat-transfer-related power loss in closed gas springs can be well predicted by a theory which neglects turbulence. In actual engine cylinders, where significant turbulence levels may be generated by high velocity inflows, a model that neglects turbulence may not be adequate.

Gedeon (1989) and Kornhauser (1992) have proposed models for compression-driven heat transfer with inflow-generated turbulence. Existing models were unable to predict experimentally observed variations in the magnitude and phase of the heat transfer for different inlet conditions, indicating weaknesses in the models. The currently proposed model generalizes the models of Gedeon (1989) and Lee (1983) in an attempt to better predict the observed experimental trends.

Background

In an effort to present a theoretical basis for heat transfer related losses in gas springs, Lee (1983) modeled heat transfer for small-amplitude pressure fluctuation of an ideal gas in a one-dimensional geometry without turbulence. Lee solved the energy equation using a complex variable technique and obtained an expression for the heat-transfer-related power loss which agreed well with experimental results.

Lee's heat transfer model has been used to predict gas spring performance (Kornhauser, 1994; Kornhauser and Smith, 1993), to model hysteresis losses in Stirling engine codes (Huang, 1990), and to predict the performance of Stirling coolers (Wang and Smith, 1990). The model, however, was developed and tested for cylinder spaces without inflow or outflow. There is doubt as to its applicability to spaces with inflow-generated turbulence.

Gedeon (1989) modified Lee's analysis in an attempt to predict the effects of inflow-produced turbulence. Rather than using the molecular thermal diffusivity in the one-dimensional energy equation, he used a turbulent thermal diffusivity increasing linearly from the molecular value at the wall to some maximum value at the centerline of the space. The turbulent diffusivity was assumed to be constant in time, and its development was based on data for steady pipe flow and a simplistic turbulence model. Gedeon's analysis showed much greater heat transfer magnitudes and much smaller heat transfer phase shifts than Lee's. For typical Stirling engine conditions, the phase shift was negligible.

Kornhauser (1992) accounted for the effects of inflow-produced turbulence by extending a model developed by Pfriem (1943). Pfriem developed a model for compression-driven heat transfer much like those of Lee and Gedeon, but accounted for turbulence by setting the thermal diffusivity at the molecular level in a thin boundary layer and at infinity in a turbulent core. The temperature in the turbulent core was then uniform spatially but varied periodically in time. Kornhauser evaluated the bound-

---

Contributed by the Heat Transfer Division for publication in the JOURNAL OF HEAT TRANSFER. Manuscript received by the Heat Transfer Division, Aug. 4, 1997; revision received, Apr. 13, 1998. Keywords: Analytical, Energy Conversion, Heat Transfer, Periodic, Turbulent, Unsteady. Associate Technical Editor: M. Kaviany.

ary layer thickness based on steady flow heat transfer data for cylinder wakes. His analysis showed the same trends as Gedeon's, but with smaller heat transfer magnitude and larger heat transfer phase shift. By manipulating constants in the two models they could be made to give similar results.

The models of both Gedeon and Kornhauser were unable to predict experimentally observed variations in heat transfer magnitude and phase shift for different inlet conditions and both models predicted a much smaller phase shift than was observed experimentally. The currently proposed model extends Gedeon's model in order to rectify some of these weaknesses.

Gedeon's model describes the limiting case of a fully turbulent cylinder space. Experiments indicated that for nondimensional parameter ranges typical of Stirling machines, the heat transfer phase-shift was much larger than that indicated by the fully turbulent model. The current model attempts to generalize Gedeon's model so that it includes moderate and weak turbulence levels. The laminar and fully turbulent models then become limiting cases of the general model.

Heat Transfer Model

The heat transfer model considers the compression and expansion of an ideal gas between parallel walls. The energy equation, in nondimensional form, is given as (Cantelmi, 1995)

$$\frac{\partial T}{\partial t} = \frac{1}{2\beta^2}\frac{\partial}{\partial y}\left[\left(1+\frac{\varepsilon_H}{\alpha}\right)\frac{\partial T}{\partial y}\right] + \frac{\gamma-1}{\gamma}\frac{dP}{dt} \qquad (1)$$

for small pressure fluctuations. A sketch of the geometry is given in Fig. 1. The boundary conditions are that the wall temperature is held constant and that the solution is symmetric about the midplane, namely

$$T(0, t) = 1$$

$$\frac{\partial T}{\partial y}(1, t) = 0. \qquad (2)$$

The problem is driven by the pressure variation

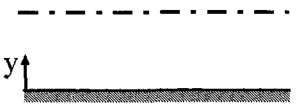

Fig. 1 Geometry

$$P = 1 + P_A \exp(it) \qquad (3)$$

where $P_A \ll 1$.

The parameter β is defined as

$$\beta = \frac{r_H}{\delta_L}. \qquad (4)$$

For actual engine spaces β is generally much larger than one, indicating that the thermal boundary layer thickness is much less than the hydraulic radius.

The spatial variation of the effective turbulent thermal diffusivity may be modeled by solving a simplified turbulence model such as that proposed by Gedeon (1989). The spatial variation of the diffusivity will be assumed to be of the form

$$\frac{\varepsilon_H}{\alpha} = \eta\beta y. \qquad (5)$$

The modeling of the eddy diffusivity is described in the Appendix.

Substituting the above expressions into the energy equation yields

$$\frac{\partial T}{\partial t} = \frac{1}{2\beta^2}\frac{\partial}{\partial y}\left[(1+\eta\beta y)\frac{\partial T}{\partial y}\right] + \frac{\gamma-1}{\gamma}\frac{dP}{dt}. \qquad (6)$$

The long-time periodic solution of this differential equation is assumed to be of the form

$$T = 1 + P_A\frac{\gamma-1}{\gamma}(1-\tilde{T}(y))\exp(it). \qquad (7)$$

Substituting into the energy equation yields

Nomenclature

A_{CYL} = cylinder cross-sectional area
A_{INLET} = inlet area
c_P = specific heat at constant pressure
C = empirical constant
D_H = hydraulic diameter = $4r_H$
F = parameter defined in text, a function of η
h = heat transfer coefficient, = $k\,\text{Nu}_R/D_H$, W/m^2 K
$i = \sqrt{-1}$
k = molecular thermal conductivity, turbulent kinetic energy per unit mass in the Appendix
L_M = Prandtl mixing length = κy^*
Nu_C = complex Nusselt number = $\text{Nu}_R + i\,\text{Nu}_I$
P = nondimensional pressure, P^*/P_0
P_0 = dimensional mean pressure, N/m^2
P_1 = dimensional pressure amplitude, N/m^2
P_A = nondimensional pressure fluctuation amplitude, P_1/P_0
Pr = Prandtl number = ν/α
Pr_t = turbulent Prandtl number
$\dot{q}''$ = heat flux rate, W/m^2
R = ideal gas constant
Re_{IN} = inlet Reynolds number = $u_{\text{IN}}D_H/\nu$
r_H = distance from wall to midplane (model), hydraulic radius = volume/surface area (experiment), m
T = nondimensional temperature, T^*/T_0
T_B = nondimensional bulk temperature, T_B^*/T_0
T_0 = dimensional wall temperature, K
t = nondimensional time, ωt^*
u_{IN} = maximum inlet velocity, m/s
v = nondimensional specific volume, v^*/v_0
v_0 = dimensional mean specific volume = RT_0/P_0, m^3/kg
y = nondimensional distance from wall, y^*/r_H
α = molecular thermal diffusivity = $k/\rho_0 c_P$, m^2/s
β = ratio of hydraulic radius to the laminar thermal boundary layer thickness = r_H/δ_L
γ = specific heat ratio
δ_L = laminar thermal boundary layer thickness = $(2\alpha/\omega)^{1/2}$, m
ε_H = eddy diffusivity for heat transfer = $\alpha\eta\beta y$, m^2/s
ε_M = eddy diffusivity for momentum transfer, m^2/s
θ = parameter defined in text, a function of η
η = model parameter = $C^*(A_{\text{CYL}}/A_{\text{INLET}})^*\beta$
κ = von Karman constant ≈ 0.41
ϕ = complex Nusselt number phase
ω = angular frequency, rad/s

Asterisks denote dimensional quantities.

Subscripts

0 = Reference or mean
1 = Amplitude

$$(1 + \eta\beta y)\tilde{T}'' + \eta\beta\tilde{T}' - (1 + i)^2\beta^2\tilde{T} = 0. \qquad (8)$$

Making the variable substitution

$$z = \theta\sqrt{1 + \eta\beta y} \quad \text{where} \quad \theta = (1 + i)\frac{2}{\eta} \qquad (9)$$

yields a modified Bessel equation of order zero, namely

$$\tilde{T}'' + \frac{1}{z}\tilde{T}' - \tilde{T} = 0 \qquad (10)$$

having the solution

$$\tilde{T} = c_1 I_0(\theta\sqrt{1 + \eta\beta y}) + c_2 K_0(\theta\sqrt{1 + \eta\beta y}). \qquad (11)$$

For actual engine cylinder spaces, β is generally large (Kornhauser et al., 1994). For the special cases when $\beta \gg \eta$, the solution displays an exponential-like decay to the centerline temperature. For such limiting solutions, c_1 can be taken to be zero and the final solution becomes simply

$$T(y, t) = 1 + P_A\frac{\gamma - 1}{\gamma}\left(1 - \frac{K_0(\theta\sqrt{1 + \eta\beta y})}{K_0(\theta)}\right)\exp(it). \qquad (12)$$

The form of the current temperature profile is similar in form to the result obtained by Lee (1983) for the fully laminar case which, when approximated for $\beta \gg 1$, is given as

$$T(y, t) = 1 + P_A\frac{\gamma - 1}{\gamma}(1 - \exp(-(1 + i)\beta y))\exp(it). \qquad (13)$$

The temperature profile can now be used to determine expressions for complex Nusselt number and heat-transfer-related power losses for turbulent cylinder spaces.

Complex Nusselt Number

The use of a complex Nusselt number was first proposed by Pfriem (1943). It has been used effectively for predicting compression-driven heat transfer without inflow (Kornhauser and Smith, 1994). When the wall-bulk gas temperature difference varies sinusoidally, the complex Nusselt number can be used to formulate an expression for the heat flux rate from the cylinder as follows:

$$\dot{q}'' = hT_0\left[(1 - T_B) + \tan\phi\,\frac{d}{dt}(1 - T_B)\right] \qquad (14)$$

where

$$h = \frac{\mathrm{Nu}_R\, k}{D_H} \quad \text{and} \quad \tan\phi = \frac{\mathrm{Nu}_I}{\mathrm{Nu}_R}. \qquad (15)$$

For quasi-steady heat transfer or if the phase of the complex Nusselt number is zero, the above expression reduces to Newton's Law of Cooling.

The complex Nusselt number based on the current model is formed by dividing the complex heat flux by the complex temperature difference. In terms of the current nondimensional variables the expression becomes

$$\mathrm{Nu}_C = \frac{H_c D_H}{k} = \frac{4\partial_y T(0, t)}{T_B(t) - 1} \qquad (16)$$

where the bulk temperature is defined as

$$T_B(t) = \int_0^1 T(y, t)dy. \qquad (17)$$

For the current model, the derivative of the temperature profile at the wall is

$$\partial_y T(0, t) = (1 + i)\beta P_A\frac{\gamma - 1}{\gamma}F(\eta)\exp(it) \qquad (18)$$

where $F(\eta)$ is defined as

$$F(\eta) = \frac{K_1(\theta)}{K_0(\theta)}. \qquad (19)$$

The expression for the bulk temperature becomes

$$T_B(t) = 1 + P_A\frac{\gamma - 1}{\gamma}\left[1 - \frac{1}{(1 + i)\beta}F(\eta)\right]\exp(it) \qquad (20)$$

where transcendentally small terms have been neglected. Noting that for $\beta \gg \eta$, $\beta \gg F(\eta)$ also, the expression for the complex Nusselt number then becomes, to leading order,

$$\mathrm{Nu}_C = 4(1 + i)\beta F(\eta) = 4\beta[(F_R - F_I) + i(F_R + F_I)]. \qquad (21)$$

It is interesting to note that this expression is very similar in form to the result obtained by Pfriem (1943) and Lee (1983) for the fully laminar case with $\beta \gg 1$, viz.

$$\mathrm{Nu}_C = 4(1 + i)\beta. \qquad (22)$$

Thus the effect of the turbulent diffusivity is contained in the $F(\eta)$ factor and the special case $F(\eta) = 1$ corresponds to the laminar solution.

In general, the real and imaginary parts of $F(\eta)$ may be evaluated in terms of Kelvin functions, viz.

$$F(\eta) = \frac{-kei_1(\sqrt{8}/\eta) + iker_1(\sqrt{8}/\eta)}{ker_0(\sqrt{8}/\eta) + ikei_0(\sqrt{8}/\eta)} \qquad (23)$$

where ker_0 and kei_0 are Kelvin functions of order zero and ker_1 and kei_1 are Kelvin functions of order one. These functions may be evaluated using the polynomial approximations given by Abramowitz and Stegun (1965).

Up until now the only assumptions regarding the magnitude of η was that $\beta \gg \eta$. At this point it is convenient to identify three separate regions which will be referred to as the fully turbulent region, the near-laminar region and the transition region. The fully turbulent region will correspond to solutions for which $\eta \gg 1$. The near-laminar region will correspond to solutions for which $\eta \ll 1$. Finally, the transition region will refer to solutions for which $\eta = O(1)$.

For the special case of the fully turbulent limit, namely when $\beta \gg \eta \gg 1$, limiting forms for small values of θ may be used and $F(\eta)$ takes on a somewhat simpler form, namely

$$\lim_{1/\eta \to 0} F(\eta) = F_{FT}(\eta) \cong \frac{1}{-\theta\ln(\theta)} = \frac{\eta}{\ln(\eta^4/64)} \times \left[(1 - i) + 2i\frac{\pi}{\ln(\eta^4/64)} + O\left(\frac{\pi^2}{\ln^2(\eta^4/64)}\right)\right] \qquad (24)$$

which upon substitution yields

$$\mathrm{Nu}_{C,FT} = 4\beta(1 + i)F_{FT}(\eta) = \frac{8\beta\eta}{\ln(\eta^4/64)} \times \left[1 - \frac{\pi}{\ln(\eta^4/64)}(1 - i) + O\left(\frac{\pi^2}{\ln^2(\eta^4/64)}\right)\right]. \qquad (25)$$

The leading order term for the fully turbulent limit corresponds to Gedeon's model (1989).

For the special case of the near-laminar limit, namely when $\beta \gg 1 \gg \eta$, asymptotic expansions for large values of θ may be used and $F(\eta)$ again takes on a somewhat simpler form

$$\begin{aligned}\lim_{\eta\to 0} F(\eta) &= F_{NL}(\eta)\\ &= (1 + \tfrac{1}{8}\eta - \tfrac{1}{256}\eta^3 + \tfrac{25}{8192}\eta^4 - \tfrac{13}{8192}\eta^5 + O(\eta^6))\\ &\qquad + i(-\tfrac{1}{8}\eta + \tfrac{1}{64}\eta^2 - \tfrac{1}{256}\eta^3 + \tfrac{13}{8192}\eta^5 + O(\eta^6)) \quad (26)\end{aligned}$$

which upon substitution yields

$$\begin{aligned}\mathrm{Nu}_{C,NL} &= 4\beta(1 + i)F_{NL}(\eta)\\ &= 4\beta(1 + \tfrac{1}{4}\eta - \tfrac{1}{64}\eta^2 + \tfrac{25}{8192}\eta^4 - \tfrac{13}{4096}\eta^5 + O(\eta^6))\\ &\qquad + i4\beta(1 + \tfrac{1}{64}\eta^2 - \tfrac{1}{128}\eta^3 + \tfrac{25}{8192}\eta^4 + O(\eta^6)) \quad (27)\end{aligned}$$

As $\eta \to 0$, the laminar result is recovered.

The power series representations for the real and imaginary parts of the complex Nusselt number in the near laminar limit diverge for $\eta > 1$. It is possible to extend this range by forming Pade approximants (Aziz and Na, 1984; Bender and Orszag, 1978). The [1, 1] Pade approximant for the above expression is

$$\mathrm{Nu}_C[1, 1] = 4\beta\left(\frac{1 + \frac{5}{16}\eta}{1 + \frac{1}{16}\eta} + i\right). \quad (28)$$

This approximation shows good qualitative agreement with the solution well into the transition region. Similarly, the [3, 2] Pade approximant

$$\begin{aligned}\mathrm{Nu}_c[3, 2] = 4\beta\Bigg(&\frac{1 + \frac{129}{100}\eta + \frac{1407}{3200}\eta^2 + \frac{417}{12800}\eta^3}{1 + \frac{26}{25}\eta + \frac{25}{128}\eta^2}\\ &+ \mathrm{i}\,\frac{1 + \frac{25}{14}\eta + \frac{639}{896}\eta^2 + \frac{9}{448}\eta^3}{1 + \frac{25}{14}\eta + \frac{625}{896}\eta^2}\Bigg) \quad (29)\end{aligned}$$

provides good qualitative agreement with the full result well into the fully turbulent region. While other approximants could be formed, these approximations are representative.

Figures 2(*a*) and 2(*b*) show plots of the real and imaginary parts of $\mathrm{Nu}_C/4\beta$. The asymptotic approximations are compared to the exact solution in the transition region evaluated using Kelvin functions. As expected, the approximate solutions for the near laminar and fully turbulent limits are in good qualitative agreement with the exact solution for limiting values of η.

Figures 3 and 4 show plots of the magnitude and phase of $\mathrm{Nu}_C/4\beta$. Once again, the asymptotic approximations are in good agreement with the exact solution for magnitude and phase. As the fully turbulent limit is approached the magnitude of the heat transfer coefficient becomes quite large relative to the laminar limit. In the laminar limit, the heat flux leads the wall-bulk temperature difference by 45 deg. As turbulence levels increase the phase shift decreases, asymptotically approaching zero. Thus, in the fully turbulent limit, the heat flux is nearly in phase with the temperature difference and quasi-steady models are adequate for representing cylinder heat transfer.

Heat-Transfer-Related Power Loss

The heat-transfer-related power loss, sometimes referred to as heat transfer hysteresis loss, provides a good global measure of a model's accuracy. It can also be used as a correction to Stirling machine performance codes that do not include direct modeling of compression-driven heat transfer (Kornhauser et al., 1994). Both Lee (1983) and Cooke-Yarborough and Ryden (1985) provided expressions for heat-transfer-related power loss in cylinder spaces without inflow.

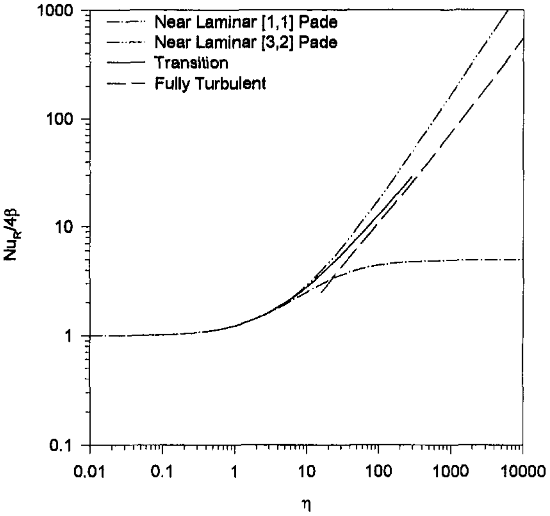

Fig. 2(*a*) Real part of $\mathrm{Nu}_c/4\beta$

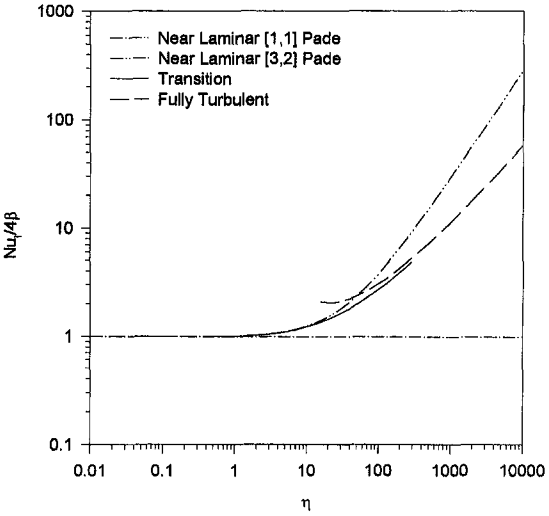

Fig. 2(*b*) Imaginary part of $\mathrm{Nu}_c/4\beta$

The power loss can be calculated from (Lee, 1983)

$$\frac{w_{\mathrm{LOSS}}}{P_0 v_0} = \int_0^{2\pi} P\,\frac{dv}{dt}\,dt = \int_0^{2\pi} \frac{T_B}{P}\,\frac{dP}{dt}\,dt \quad (30)$$

where P and T_B refer to the real parts of the pressure and bulk temperature, namely

$$\begin{aligned}T_B(t) = 1 + P_A\,\frac{\gamma - 1}{\gamma}\Bigg[1 - \frac{1}{2\beta}(F_R &\quad (31)\\ + F_I)\Bigg]\cos(t) - P_A\,\frac{\gamma - 1}{\gamma}\,\frac{1}{2\beta}(F_R - F_I)\sin(t)&\end{aligned}$$

and

$$P = 1 + P_A\cos(t). \quad (32)$$

Upon integration the expression for power loss becomes, to leading order,

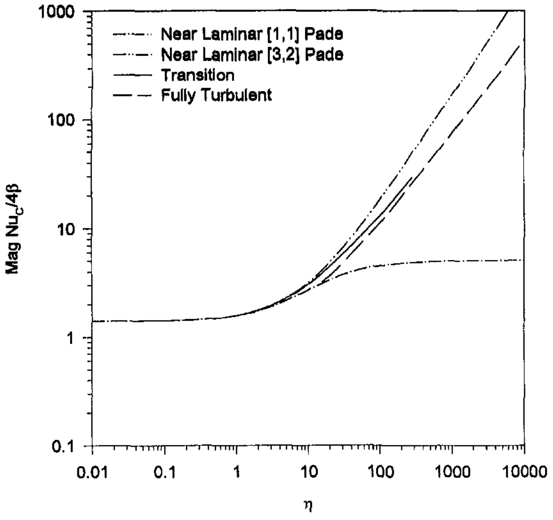

Fig. 3 Magnitude of Nu$_c$/4β

$$\frac{w_{\rm LOSS}}{P_0 v_0} = \frac{\pi}{2\beta} P_A^2 \frac{\gamma - 1}{\gamma} (F_R - F_I). \tag{33}$$

In previous experimental work (Kornhauser et al., 1994; and Cantelmi, 1995), loss results were reported in terms of the nondimensional lost work, defined as

$$\text{Loss}_{ND} \equiv \frac{w_{\rm LOSS}}{P_0 v_0 P_A^2 \dfrac{\gamma - 1}{\gamma}} = \frac{\pi}{2\beta} (F_R - F_I). \tag{34}$$

The case when $F_R - F_I = 1$ corresponds to the laminar results obtained by Lee (1983) and Cooke-Yarborough and Ryden (1985) for $\beta \gg 1$. The factor $F_R - F_I$ can be evaluated using the results in the previous section.

Figure 5 shows results for $\left(\frac{2\beta}{\pi}\right)\text{Loss}_{ND}$ calculated from the above expression. As the turbulence levels increase, heat-transfer-related power losses becomes large relative to the laminar power losses. Once again, the approximate solutions for the near laminar and fully turbulent limits are in good qualitative agreement with the exact solution for limiting values of η. It should be noted that the power loss is due to increased heat transfer only and does not include pressure drop losses from inflow.

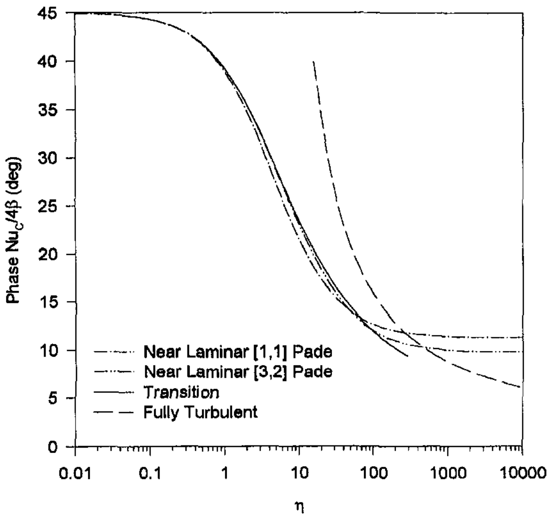

Fig. 4 Phase of Nu$_c$/4β

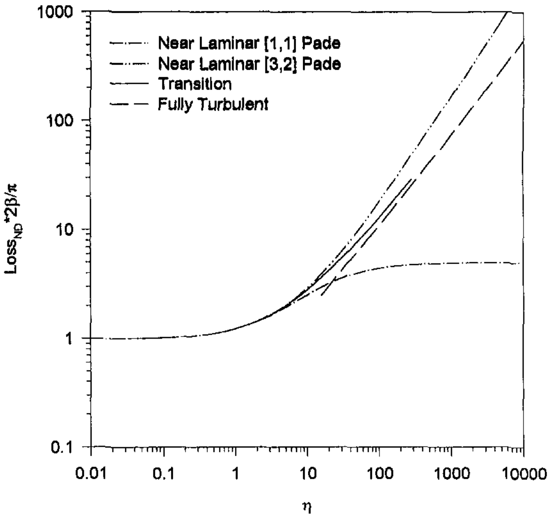

Fig. 5 $\left(\frac{2\beta}{\pi}\right)\text{Loss}_{ND}$

Preliminary Validation

Cantelmi (1995) performed experiments to measure the effects of inflow-produced turbulence on compression-driven heat transfer. Rather than measuring the effects of turbulence generated by high-velocity inflow and outflow on compression-driven heat transfer in actual engine cylinders (which would have required the measurement of both mass flow and enthalpy flow into and out of the cylinder), a novel experimental approach was taken. A closed piston-cylinder space was divide into two spaces connected by an orifice. A schematic of the experiment is shown in Fig. 6.

The orifice divided the cylinder into a varying volume space and a constant or fixed volume space. The movement of the piston-created pressure gradients across the orifice and induced flow between the two spaces. Due to the presence of the orifice, a high-velocity jet was introduced periodically into the relatively quiescent fluid of each space. This was meant to simulate the effects of inflow in actual engines. Both spaces were instrumented so that the pressure and volume could be measured throughout the cycle. From the pressure and volume data, the total heat transfer from both spaces was calculated.

Results for space-averaged complex Nusselt number and heat-transfer-related power loss were given for two inflow configurations: $A_{\rm CYL}/A_{\rm INLET} = 30$ and 60. The values β for the experimental runs were calculated based upon experimental geometry, mean pressure, piston frequency and material properties. The values of η for the experimental data are modeled as (see Appendix)

$$\eta = C \frac{A_{\rm CYL}}{A_{\rm INLET}} \beta \tag{35}$$

where C is an empirical constant. For the plots shown, a value of $C = 0.01$ was used to calculate η. Varying the value of C simply shifts the experimental data along the abscissa. For

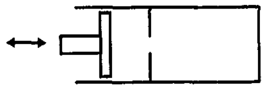

Fig. 6 Schematic of experiment

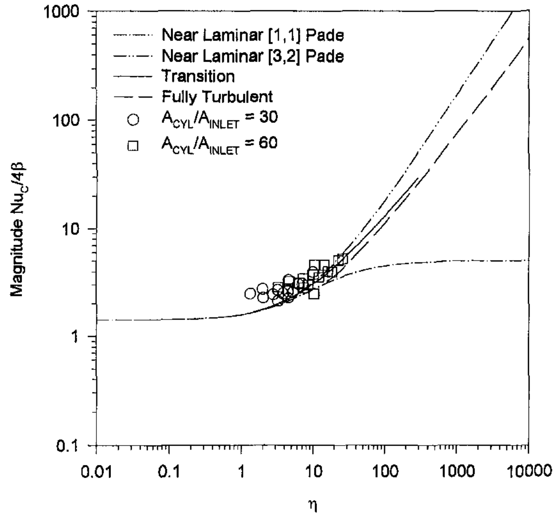

Fig. 7 Magnitude of $Nu_c/4\beta$ comparison with experiment

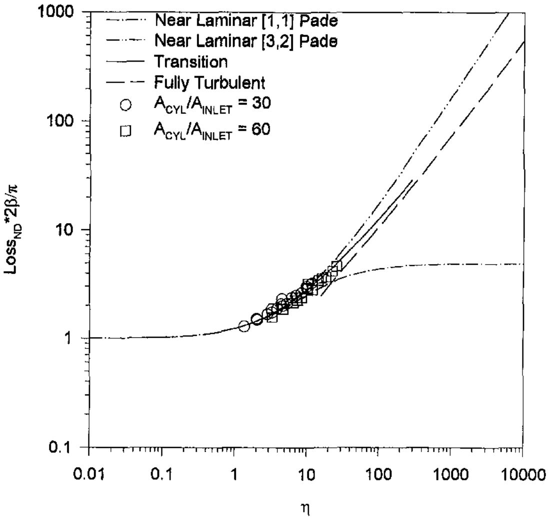

Fig. 9 $Loss^*_{ND}2\beta/\pi$ comparison with experiment

example, with $C = 0.1$, the experimental points shown would shift to the right by one order of magnitude.

Figures 7 and 8 compare the magnitude and phase of $Nu_C/4\beta$ predicted by the current model to those observed experimentally. The model predicted the proper variation of heat transfer magnitude for different inlet conditions. The experimental results for the phase were not well correlated but the overall qualitative trends are correct, namely that the effects of inflow would be to decrease heat transfer phase shift from the near laminar value of 45 deg.

It should be noted that the complex Nusselt number for the current model was developed for a single cylinder space with inflow while the experimental data were based on a complex Nusselt number averaged over the two spaces. A more direct comparison would require determination of separate Nusselt numbers for each space using an inverse, parameter optimization method. Previous attempts at using inverse techniques on experimental data, however, were unsuccessful (Kornhauser et al., 1994; Finkbeiner, 1994). The current model could be employed to prescribe relationships between some parameters, thereby reducing the number of parameters to be determined.

The total power loss in the experiment was a combination of the heat transfer related losses over the surface of the cylinder and the flow losses due to the presence of the orifice. Based upon the experimental data, the power loss due to entropy generation at the orifice was calculated using the approximate model described in Cantelmi (1995) and Kornhauser et al. (1994). The heat-transfer-related power loss was then calculated by subtracting the approximate flow loss from the total power loss.

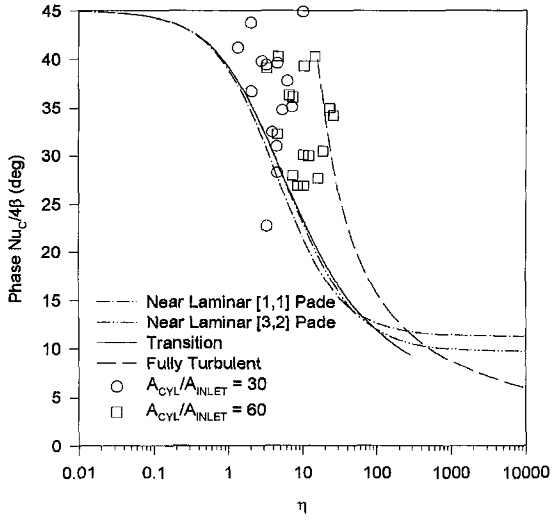

Fig. 8 Phase of $Nu_c/4$ comparison with experiment

Figure 9 compares $Loss^*_{ND}2\beta/\pi$ predicted by the current model to the experiment. The values of η for the experimental heat-transfer-related power loss data were determined using Eq. (35). The model agrees quite well with the experimental data and predicts the proper variation of power loss with inlet geometry. Further validation of the model and adjustment of the empirical constant would require comparison with actual Stirling performance data.

Conclusions

An analytical model for turbulent compression-driven heat transfer has been developed in an attempt to quantify the effects of inflow on compression-driven heat transfer. It generalizes the previous models of Lee (1983) and Gedeon (1989) whose models represented the limiting cases of laminar and fully turbulent conditions, respectively.

The model predicts that as turbulence levels increase, there is an increase in heat transfer magnitude and a decrease in heat transfer phase shift, agreeing with experimentally observed trends. It also predicts that heat-transfer-related power losses increase as turbulence levels increase.

When compared to experimental data, the model predicts the proper trends for power loss and heat transfer magnitude and phase shift for different inlet conditions. Further validation of the model and adjustment of the empirical constant would require comparison with actual Stirling performance data.

References

Abramowitz, M., and Stegun, I. A., 1965, *Handbook of Mathematical Functions*, Dover, New York.

Aziz, A., and Na, T. Y., 1984, *Perturbation Methods in Heat Transfer*, Hemisphere, New York.

Bender, C. M., and Orszag, S. A., 1978, *Advanced Mathematical Methods for Scientists and Engineers*, McGraw-Hill, New York.

Cantelmi, F. J., 1995, "Measurement and Modeling of In-Cylinder Heat Transfer with Inflow-Produced Turbulence," M.S. thesis, Virginia Polytechnic Institute and State University, Blacksburg, VA.

Cooke-Yarborough, E. H., and Ryden, D. J., 1985, "Mechanical Power Losses Caused by Imperfect Heat Transfer in a Nearly-Isothermal Stirling Engine," *Proc. 20th IECEC*, pp. 3.307–3.312.

Finkbeiner, D. L., 1994, "Calculation of Gas-Wall Heat Transfer from Pressure and Volume Data for Spaces with Inflow and Outflow," M.S. thesis, Virginia Polytechnic Institute and State University, Blacksburg, VA.

Gedeon, D., 1989, "A Cylinder Heat Transfer Model," memo to R. Tew, NASA-Lewis.

Huang, S. C., 1990, "HFAST Update," 3rd Stirling Thermodynamic Loss Workshop, Oct. 16–17, Cleveland, OH.

Kays, W. M., and Crawford, M. E., 1993, *Convective Heat and Mass Transfer*, 3rd Ed., McGraw-Hill, New York, pp. 198–200, 246–247.

Kornhauser, A. A., 1992, "A Model of In-Cylinder Heat Transfer with Inflow-Produced Turbulence," *Proc. 27th IECEC*, pp. 5.523–5.528.

Kornhauser, A. A., and Smith, J. L., Jr., 1993, "The Effects of heat Transfer on Gas Spring Performance," ASME *Journal of Energy Resources Technology*, Vol. 115, pp. 70–75.

Kornhauser, A. A., 1994, "Dynamic Modeling of Gas Springs," ASME *Journal of Dynamic Systems, Measurement, and Control*, Vol. 116, pp. 414–418.

Kornhauser, A. A., and Smith, J. L., Jr., 1994, "Application of a Complex Nusselt Number to Heat Transfer During Compression and Expansion," ASME JOURNAL OF HEAT TRANSFER, Vol. 116, pp. 536–542.

Kornhauser, A. A., Kafka, B. C., Finkbeiner, D. L., Cantelmi, F. J., 1994, "Heat Transfer Measurements for Stirling Machine Cylinders," Final Report for Grant NAG3-1285, National Aeronautics and Space Administration.

Launder, B. E., and Spaulding, D. B., 1972, *Mathematical Models of Turbulence*, Academic Press, San Diego.

Lee, K. P., 1983, "A Simplistic Model of Cyclic Heat Transfer Phenomena in Closed Spaces," *Proc. 18th IECEC*, pp. 720–723.

Pfriem, H., 1943, "Periodic Heat Transfer at Small Pressure Fluctuations," NACA TM-1048.

Wang, A. C., and Smith, J. L., Jr., 1990, "The Importance of Anchoring Cylinder Wall Temperature in Stirling Cyrocoolers," *Proc. 25th IECEC*, Vol. 5, pp. 386–391.

APPENDIX

This appendix describes the development of an expression for the thermal eddy diffusivity relevant to cylinder spaces with inflow. The development follows that of Gedeon (1989). First, using an eddy diffusivity based on Prandtl turbulent kinetic energy equation, the eddy diffusivity can be modeled as

$$\frac{\varepsilon_H}{\alpha} = \frac{\Pr}{\Pr_t}\frac{\varepsilon_M}{\nu} = \frac{\Pr}{\Pr_t}\frac{\sqrt{k}L}{\nu} \tag{36}$$

where k is a time-averaged turbulent kinetic energy per unit mass and L is a turbulent length scale. L is related to the Prandtl mixing length, L_M, by the expression (Launder and Spaulding, 1972)

$$\begin{aligned} L &= 0.53 L_M \\ &\approx \frac{\kappa}{2} y^* \end{aligned} \tag{37}$$

where y^* is the distance from the wall and $\kappa \approx 0.41$ is the von Karman constant (Kays and Crawford, 1993).

Based upon dimensional analysis, the turbulent kinetic energy may be scaled with the maximum velocity at the inlet, u_{IN}

$$k = C_1 u_{\mathrm{IN}}^2 \tag{38}$$

where C_1 is a constant of proportionality. Substituting yields

$$\begin{aligned} \frac{\varepsilon_H}{\alpha} &= \frac{C_1^{1/2}}{8}\frac{\Pr}{\Pr_t}\frac{u_{\mathrm{IN}} D_H}{\nu}\frac{L_M}{r_H} \\ &= \frac{C_1^{1/2}\kappa}{8}\frac{\Pr}{\Pr_t}\mathrm{Re}_{IN}\, y \end{aligned} \tag{40}$$

where $y = y^*/r_H$ is nondimensional distance from the wall. Finally, using an approximation for inlet Reynolds number developed by Kornhauser (1992) for free-piston Stirling engines,

$$\mathrm{Re}_{\mathrm{IN}} \Pr \approx 16 \frac{A_{\mathrm{CYL}}}{A_{\mathrm{INLET}}}\beta^2. \tag{41}$$

The final expression for the eddy diffusivity becomes

$$\begin{aligned} \frac{\varepsilon_H}{\alpha} &= \frac{2C_1^{1/2}\kappa}{\Pr_t}\frac{A_{\mathrm{CYL}}}{A_{\mathrm{INLET}}}\beta^2 y \\ &= \eta\beta y \end{aligned} \tag{42}$$

where β is defined as before and η is defined as

$$\begin{aligned} \eta &= \frac{2C_1^{1/2}\kappa}{\Pr_t}\frac{A_{\mathrm{CYL}}}{A_{\mathrm{INLET}}}\beta \\ &= C\frac{A_{\mathrm{CYL}}}{A_{\mathrm{INLET}}}\beta \end{aligned} \tag{43}$$

where is a constant to be determined empirically.

At the edge of the laminar thermal boundary layer, $y \approx 1/\beta$. Evaluating the eddy diffusivity at the edge of the thermal boundary layer yields

$$\frac{\varepsilon_h}{\alpha} \approx \eta. \tag{44}$$

Thus η is a measure of the magnitude of the eddy diffusivity in the thermal boundary layer. As $\eta \to 0$, the eddy diffusivity is small relative to the molecular diffusivity throughout the layer and the solution approaches the laminar solution. As $1/\eta \to 0$, the effective diffusivity increases rapidly through the layer. Beyond this thin thermal boundary layer, the spatial temperature variations are exponentially small. For this reason, the exact spatial variation of the eddy diffusivity beyond this layer is not important.

Effect of Channel Orientation of Local Heat (Mass) Transfer Distributions in a Rotating Two-Pass Square Channel With Smooth Walls

C. W. Park

S. C. Lau
e-mail: slau@mengr.tamu.edu
Mem. ASME

Department of Mechanical Engineering,
Texas A&M University,
College Station, TX 77843-3123

Naphthalene sublimation experiments have been conducted to study the effects of channel orientation, rotational Coriolis force, and a sharp turn, on the local heat (mass) transfer distributions in a two-pass square channel with a sharp turn and smooth walls, rotating about a perpendicular axis. The test channel was oriented so that the direction of rotation was perpendicular to or at a 45 deg angle to the leading and trailing walls. The Reynolds number was kept at 5,500 and the rotation number ranged up to 0.24. For the radial outward flow in the first straight pass of the diagonally oriented channel, rotation-induced Coriolis force caused large monotonic spanwise variations of the local mass transfer on both the leading and trailing walls, with the largest mass transfer along the outer edges of both walls. Rotation did not lower the spanwise average mass transfer on the leading wall and did not increase that on the trailing wall in the diagonally oriented channel as much as in the normally oriented channel. The combined effect of the channel orientation, rotation, and the sharp turn caused large variations of the local mass transfer distributions on the walls at the sharp turn and immediately downstream of the sharp turn. The velocity fields that were obtained with a finite difference control-volume-based computer program helped explain how rotation and channel orientation affected the local mass transfer distributions in the rotating two-pass channel.

Introduction

The geometry of a serpentine cooling passage in a gas turbine blade significantly affects the flow and heat transfer distributions in the cooling passage. Coriolis and buoyancy forces resulting from rotation produce secondary flows throughout the cooling passage. In and around the sharp turns, centrifugal forces also cause secondary flows. How the interactions of these secondary flows affect the heat transfer distributions on the various walls of the cooling passage depends on the directions of the secondary flows and the orientations of the walls with respect to the rotation direction. Thus, the flow in a turbine blade cooling passage is highly complicated. The main objective of this investigation is to study the effect of the orientation of a turbine blade cooling channel on the local heat transfer distribution in the channel.

The literature on heat transfer and pressure drop for turbulent flows in rotating multipass channels with smooth or rib-roughened walls was reviewed in Park et al. (1998a, 1998b). Wagner et al. (1991) investigated the effects of Coriolis and buoyancy forces on the regional heat transfer in a rotating serpentine square channel with smooth walls. Their results indicated a dependence of the regional heat transfer on several parameters: the streamwise location, the surface orientation, the main flow direction (inward or outward flow), the Reynolds number, the rotation number, and a buoyancy parameter. Han et al. (1993) studied the effect of wall temperature variation on the heat transfer in a rotating two-pass square smooth channel. Park et al. (1998a) presented local transfer distributions on the leading and trailing walls of a rotating two-pass square channel, and compared their local results with published regionally averaged heat transfer results.

Tse and McGrath (1995) and McGrath and Tse (1995) measured the local velocity distributions in a rotating serpentine channel with smooth walls, and compared their experimental results with distributions that were predicted numerically. Other relevant numerical studies on turbulent flow and heat transfer in rotating smooth channels include Prakash and Zerkle (1992), Dutta et al. (1994), and Tekriwal (1994).

In this investigation, naphthalene sublimation experiments are conducted with a rotating two-pass square channel with smooth walls that is oriented so that the direction of rotation is perpendicular to or at a 45 deg angle to the leading and trailing walls of the channel. The analogy between heat and mass transfer is applied to relate mass transfer distributions to heat transfer distributions. Since the test channel walls and the flow of naphthalene vapor-air mixture are both at room temperature, and the naphthalene vapor partial pressure and concentration at the test channel walls are very small, there is no significant density variation in the test channel. It may be shown that, the maximum variation of the density of the naphthalene vapor-air mixture that flows through the test channel is only about 0.05 percent of the density of the mixture. Thus, buoyancy effect in actual turbine blade cooling channels is not simulated.

The effect of density variation on the regional heat transfer in rotating channels has been discussed at length in Wagner et al. (1991), Prakash and Zerkle (1992), and Han et al. (1993). In an actual turbine blade cooling channel, the variation of density in the coolant flow may significantly affect the distributions of the local heat transfer coefficient on the channel walls as much as the coolant flow rate and direction, the channel geometry, and rotation.

Contributed by the Heat Transfer Division for publication in the JOURNAL OF HEAT TRANSFER. Manuscript received by the Heat Transfer Division, Sept. 22, 1997; revision received, Apr. 17, 1998. Keywords: Convection, Experimental, Heat Transfer, Mass Transfer, Rotating, Turbines. Associate Technical Editor: P. S. Ayyaswamy.

The naphthalene sublimation technique and the heat and mass transfer analogy have been employed in a number of previous local heat transfer studies, such as Sparrow and Tao (1983) and McMillin and Lau (1994). In Goldstein and Cho (1995), many of the naphthalene sublimation experiments were summarized and the analogy between heat transfer and mass transfer was discussed extensively.

A finite difference control-volume-based computer program is used to determine the velocity fields in a rotating two-pass square channel that has the same dimensions as the test channel and is subjected to the flow and boundary conditions of the experiments. The calculated velocity fields help explain how rotation and channel orientation affect the local heat (mass) transfer distributions in the two-pass test channel.

The experimental and numerical results of this study will enhance understanding of the momentum and thermal transport processes that take place in flows through rotating channels. The results will also enable turbine engine designers to develop improved computer codes to determine local temperature and thermal stress distributions in turbine blades under actual operating conditions. The experimental results will give engine designers detailed local data in the baseline cases of negligible density variation in flows through rotating channels for the validation of their computer codes.

Experimental Apparatus and Procedure

The test section was a 1.59 cm by 1.59 cm square two-pass channel constructed entirely of aluminum. It had a 180 deg turn with sharp corners and two straight sections, each of which was seven hydraulic diameters long. The distance between the tip of the inner wall and the tip wall in the turn, was one hydraulic diameter. The inner wall was one-half of a hydraulic diameter thick.

The test section consisted of seven wall segments: two principal walls (the leading and trailing walls), two inner side walls, two outer side walls, and a tip wall. The inner surface of each wall segment was coated with naphthalene in a casting process. After the wall segments were assembled, all inner surfaces of the test section were flat, smooth, and mass transfer active.

The test section was mated to an aluminum, mass transfer inactive, inlet and exit section assembly in an aluminum housing (see Fig. 1). The inlet and exit sections were 10 and 20 hydraulic diameters long, respectively. The downstream end of the exit section was affixed to a rotating pipe assembly of a rotation test rig in a protective cage. The distance from the middle of the test section to the rotation axis was 30 hydraulic diameters. Figure 1 also shows how the entire assembly of the test section, the inlet section, and the exit section may be rotated at a 45 deg angle about an axis that is perpendicular to the rotating shaft, so that the leading and trailing walls may be oriented at an angle to the rotation direction.

During an experiment, room air was drawn through the test section from the air-conditioned laboratory. Upon exiting the test section assembly, the air flowed through a calibrated orifice flow meter, and was then ducted to the outside of the laboratory. To determine the local mass transfer distribution, the elevation changes at 312 points on the naphthalene surface of each of the two principal walls, and 216 points on the tip wall were measured (see Fig. 1), and the overall weight losses from all seven wall segments were obtained.

Data Reduction

The local mass transfer coefficient at each measurement point is evaluated as

$$h_m = \dot{M}''/(\rho_w - \rho_b). \tag{1}$$

The naphthalene vapor density at the wall, ρ_w, is calculated according to Ambrose et al. (1975). The constant naphthalene vapor density value at the channel walls corresponds to the thermal boundary condition of uniform wall temperature.

The local Sherwood number is

$$\mathrm{Sh} = h_m D/\Lambda \tag{2}$$

The diffusion coefficient for naphthalene vapor in air, Λ, is calculated with Eq. (1) in Goldstein and Cho (1995). The Sherwood number is normalized by the Sherwood number for a corresponding fully developed flow in a stationary smooth tube, Sh_0. According to the analogy between heat and mass transfer,

$$\mathrm{Nu}/\mathrm{Nu}_0 = \mathrm{Sh}/\mathrm{Sh}_0. \tag{3}$$

The Reynolds number and the rotation number, both of which are based on the channel hydraulic diameter, are defined as $\dot{m}/\mu D$ and $\Omega D/U$, respectively.

Based on the method described in Kline and McClintock (1953), the maximum uncertainty of the Sherwood number is estimated to be 10.8 percent, which occurs at the test channel exit. The uncertainty of the Reynolds number is found to be 4.8 percent.

Readers are referred to Park et al. (1998a, b) for the detailed descriptions of the test apparatus and procedure, and the reduction of the experimental data.

Numerical Analysis

The main objective of the numerical analysis was to solve the governing conservation equations with a finite volume computer program to obtain approximate velocity distributions in a rotating two-pass channel. The numerical results helped explain how rotation and channel orientation affected the local mass transfer distributions in the rotating test channel in the experiments. The

Nomenclature

C_m = cumulative mass of naphthalene in air stream, kg/s
D = channel hydraulic diameter, m
h_m = local mass transfer coefficient, m/s
$\dot{m}$ = mass flow rate of air, kg/s
$\dot{M}''$ = local mass flux of naphthalene = $\rho_s \Delta z/\Delta t$, kg/(m$^2 \cdot$s)
$\underline{\mathrm{Nu}}$ = local Nusselt number
$\overline{\mathrm{Nu}}$ = spanwise averaged Nusselt number
Nu_0 = Nusselt number for fully developed flow
$\dot{Q}$ = volumetric flow rate of air, m^3/s
Re = Reynolds number based on channel hydraulic diameter, $=\dot{m}/\mu D$
Ro = Rotation number, $=\Omega D/U$
Sc = Schmidt number of naphthalene in air, ≅2.28
$\underline{\mathrm{Sh}}$ = local Sherwood number
$\overline{\mathrm{Sh}}$ = spanwise averaged Sherwood number
Sh_0 = Sherwood number for fully developed flow = $0.023\ \mathrm{Re}^{0.8}\mathrm{Sc}^{0.4}$
U = average air velocity, m/s
X = coordinate along main flow, X = 0.0 and 16.5 at channel inlet and exit, m
Δt = duration of test run, s
Δz = elevation change of naphthalene surface, m
Λ = diffusion coefficient of naphthalene, m^2/s
μ = dynamic viscosity of air, N$\cdot$s/m^2
Ω = angular velocity, rad/s
ρ_b = bulk naphthalene vapor density = $C_m/\dot{Q}$, kg/m^3
ρ_s = density of solid naphthalene, kg/m^3
ρ_w = naphthalene vapor density at wall, kg/m^3

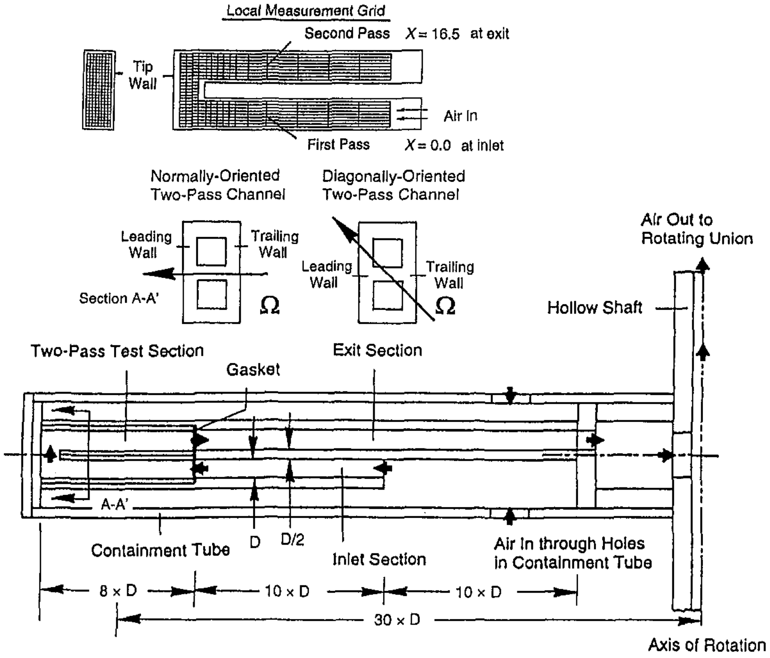

Fig. 1 Schematic of test apparatus, with local measurement grid

computational domain consisted of a ten-hydraulic-diameter-long entrance section, a two-pass channel, and a ten-hydraulic-diameter-long exit section, all of which had the same square cross section and smooth walls. The two-pass channel had the same dimensions as the test channel in the experiments. At the inlet of the entrance section, a uniform velocity (that is, no secondary flow), a turbulence intensity of ten percent, and a turbulence length scale of 3.5 percent of the hydraulic diameter were assumed. At the exit, local parabolic conditions (or zero diffusion fluxes) were imposed.

The variables in the three-dimensional governing differential equations were expressed in terms of Cartesian coordinates in a rotating reference frame. All properties were considered constant, including the density. Thus, rotational buoyancy was neglected. The equations were integrated over each of a structured grid of $17 \times 17 \times 217$ control volumes: a uniform grid of 17×17 control volumes at any cross section in the straight sections, progressively finer grid spacing in the streamwise direction approaching the sharp turn, and increasingly coarse grid spacing downstream of the turn. The SIMPLE (Semi-Implicit Method for Pressure-Linked Equations) algorithm, along with a nonstaggered grid, was used to couple the pressure and velocity fields. The power-law interpolation scheme was used to evaluate the values of variables at the control volume interfaces. The discretized equations were solved with a line-by-line and multigrid solver.

Since a highly swirling flow was expected in the rotating two-pass channel, the Reynolds stress model (Launder et al., 1975; Launder, 1989) was chosen over the k-ϵ turbulence model (which assumes that the turbulent viscosity is isotropic). At the walls where viscous effect dominated, the velocities were calculated using an empirical logarithmic wall function (Launder and Spalding, 1973). The 17×17 uniform grid at any cross section ensured that the values of y^+ at the near-wall control volumes were larger than 12.0, except in several small regions with back flow, along sharp edges, and at the corners in the turn in the computational domain.

All computations were performed on a supercomputer. Although only the velocity distributions in the case of constant fluid properties were computed and presented here, corresponding numerical results in the case of variable fluid properties might be obtained readily by expressing the local fluid property values in terms of the local temperatures.

Results

Naphthalene sublimation experiments were conducted with the test channel oriented so that the direction of rotation was perpendicular to or at a 45 deg angle to the leading and trailing walls. The Reynolds number was kept at 5500 and the rotation number ranged up to 0.24, corresponding to an average air flow velocity of 5.3 m/sec and rotational speeds up to 770 rpm. Attention was focused on the detailed local mass transfer distributions on the leading and trailing walls, and on the tip wall at the sharp turn.

The local mass transfer distributions are presented as contours of the normalized local Sherwood number. The computed flow fields are given as vector plots of the cross-streamwise velocities and the contour plots of the streamwise velocities at typical flow cross sections, along with discussions on how the flow fields affect the mass transfer distributions. First, however, the spanwise averaged Sherwood number ratios on the leading and trailing walls are presented along a streamwise coordinate, X/D. At the inlet and exit of the first straight pass, $X/D = 0.0$ and 7.0, respectively. In the turn, the measured local Sherwood number ratios are averaged over three regions: with areas of $D \times D$, $\frac{1}{2}D \times D$, and $D \times D$, respectively. These $\overline{\text{Sh}}/\text{Sh}_0$ values indicate the average mass transfer at $X/D = 7.5$, 8.25, and 9.0. At the exit of the turn, which is also the inlet of the second straight pass, $X/D = 9.5$.

Effects of Rotation and Channel Orientation on Regionally Averaged Mass Transfer.

First Straight Pass. Figure 2 shows the effect of varying the channel orientation on the streamwise $\overline{\text{Sh}}/\text{Sh}_0$ distributions on the leading and trailing walls, for $Ro = 0.24$ and $\text{Re} = 5{,}500$. In the figure, the streamwise $\overline{\text{Sh}}/\text{Sh}_0$ distributions in the no rotation case are also included. In the first pass with radial outward flow ($X/D < 7.0$), rotation lowers the spanwise averaged mass transfer on the leading wall in the diagonally oriented channel much less than on the leading wall in the normally oriented channel. The $\overline{\text{Sh}}/\text{Sh}_0$ values on the leading wall in the

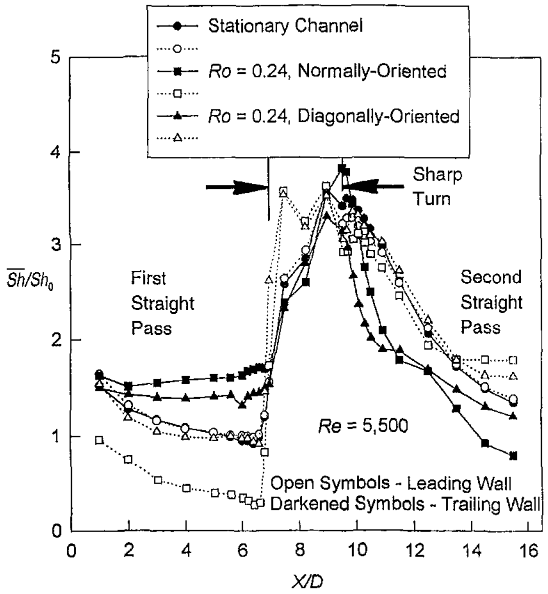

Fig. 2 Effects of rotation and channel orientation on streamwise $\overline{Sh}/Sh_0$ distributions

diagonally oriented channel are about the same as those in a stationary channel, with values dropping gradually toward the turn to about 1.0. The leading wall $\overline{Sh}/Sh_0$ values in the normally oriented channel are as low as 0.35.

Rotation increases the trailing wall mass transfer in the normally oriented channel by up to 1.60 times corresponding values for a stationary channel. Rotation does not increase the trailing wall $\overline{Sh}/Sh_0$ values as much in the diagonally oriented channel, with values of only up to 1.45.

In the normally oriented channel, the rotational Coriolis force pushes the core of the radial outward flow toward the trailing wall. When the leading and trailing walls are oriented at a 45 deg angle to the rotation direction, the rotation Coriolis force is directed at a 45 deg angle toward the outer edge of the trailing wall. It will be shown later that both the streamwise velocity distribution and the rotation-induced secondary flow contribute to the smaller difference between the average mass transfer on the leading and trailing walls in the diagonally oriented channel.

Sharp Turn. Entering the sharp turn, the mass transfer on the leading wall increases abruptly in both the normally oriented channel and the diagonally oriented channel cases. Although the $\overline{Sh}/Sh_0$ values are much higher at the turn entrance (at $X/D = 7.0$) in the diagonally oriented channel than in the normally oriented channel, the values are about the same on the leading walls in the sharp turns of the two channels. The leading wall $\overline{Sh}/Sh_0$ values in the middle region of the turn (at $X/D = 8.25$) of each channel are slightly lower than those in the upstream and downstream regions of the turn (at $X/D = 7.5$ and 9.0). On the other hand, the trailing wall mass transfer increases monotonically as the flow turns, in each channel. The trailing wall mass transfer in the upstream half of the turn is generally much lower than the leading wall mass transfer.

The generally large values of $\overline{Sh}/Sh_0$ on the leading and trailing walls in the turn of each channel are believed to be the result of the vigorous mixing of the flow in the turn, when the rotation-induced and turn-induced secondary flows interact.

Second Straight Pass. Immediately downstream of the turn ($X/D > 9.5$), the leading wall $\overline{Sh}/Sh_0$ values are higher and the trailing wall $\overline{Sh}/Sh_0$ values are lower in the diagonally oriented channel than in the normally oriented channel. The peak at the turn exit ($X/D = 9.5$) in the trailing wall $\overline{Sh}/Sh_0$ distribution for the normally oriented channel is not observed in the distribution for the diagonally oriented channel. Further downstream in the second straight pass, for $X/D \geq 13.5$, the trends are reversed in the radial inward flow: rotation increases the leading wall mass transfer and lowers the trailing wall mass transfer less in the diagonally oriented channel than in the normally oriented channel.

It will become clear shortly that the sharp turn causes the flow to swirl in the second straight pass of each channel, keeping the mass transfer high on both the leading and trailing walls immediately downstream of the turn in the second straight pass.

Effects of Rotation and Channel Orientation on Local Mass Transfer and Velocity Distributions. In this section, the local mass transfer and velocity distributions are presented. The local mass transfer distributions are presented as contours of the normalized local Sherwood number. The computed flow fields are given as vector plots of the cross-streamwise velocities and the contour plots of the streamwise velocities at strategic flow cross sections. The lengths of the vectors in each velocity vector plot give the relative magnitudes of the cross-streamwise velocities. The darker shade in the contour plots indicates higher streamwise velocity. At the turn, regions with back flow are circled.

Since it is not possible to present the computed three-dimensional flow fields in their entirety here, not all of the characteristics of the measured local mass transfer distributions may be explained with the computed flow fields. It should also be understood that, since measured local velocity data are not available to verify the numerical results, the computed velocity fields may only be considered as approximations of the actual velocity fields.

Figure 3 presents the Sh/Sh_0 contours on the leading and trailing walls of a diagonally oriented channel with Ro = 0.0, 0.09, and 0.24, along with the contours for a normally oriented channel with Ro = 0.24. Despite relatively small differences between the Sh/Sh_0 distributions on the leading and trailing walls in the stationary channel case, the two distributions are almost mirror images of each other. The local mass transfer increases abruptly at the turn entrance and continues to increase as the flow turns around. The local mass transfer is the highest along the outer edge of each wall near the exit of the turn. The turn-induced vortex pair forces the low concentration core flow to move outward in the turn, turn toward the leading and trailing walls, and then impinge on the outer portions of walls in the turn (Park et al., 1998a), causing the high mass transfer there.

First Straight Pass. In the first pass of the diagonally oriented channel, rotation causes the mass transfer to be high near the outer edges of both the leading and trailing walls and low near the inner edges of the two walls. In the Ro = 0.24 case, the Sh/Sh_0 values are up to about 2.0 along the outer edge of the trailing wall. On the leading wall, the Sh/Sh_0 values of between 1.5 and 1.75 along the outer edge are also quite high. The Sherwood number ratio drops monotonically toward the inner edges on both the leading and trailing walls, with the lowest values of below 0.5 on the leading wall. In contrast, in the first pass of the normally oriented channel, there is very little spanwise variation in the mass transfer distributions on both walls, and the mass transfer on the trailing wall is much higher than that on the leading wall.

Figure 4 presents the computed flow fields at $X/D = 6.0$ in the first straight passes of the normally oriented and diagonally oriented channels. The figure shows that, in the radial outward flow in the normally oriented channel, the rotation-induced Coriolis force pushes the high momentum core fluid toward the trailing wall and the resulting secondary flow is in the form of two symmetrical vortices. The numerical results show that the highest streamwise velocities are located near the inner and outer side walls, not in the middle of the channel. The higher mass transfer on the trailing wall and lower mass transfer on

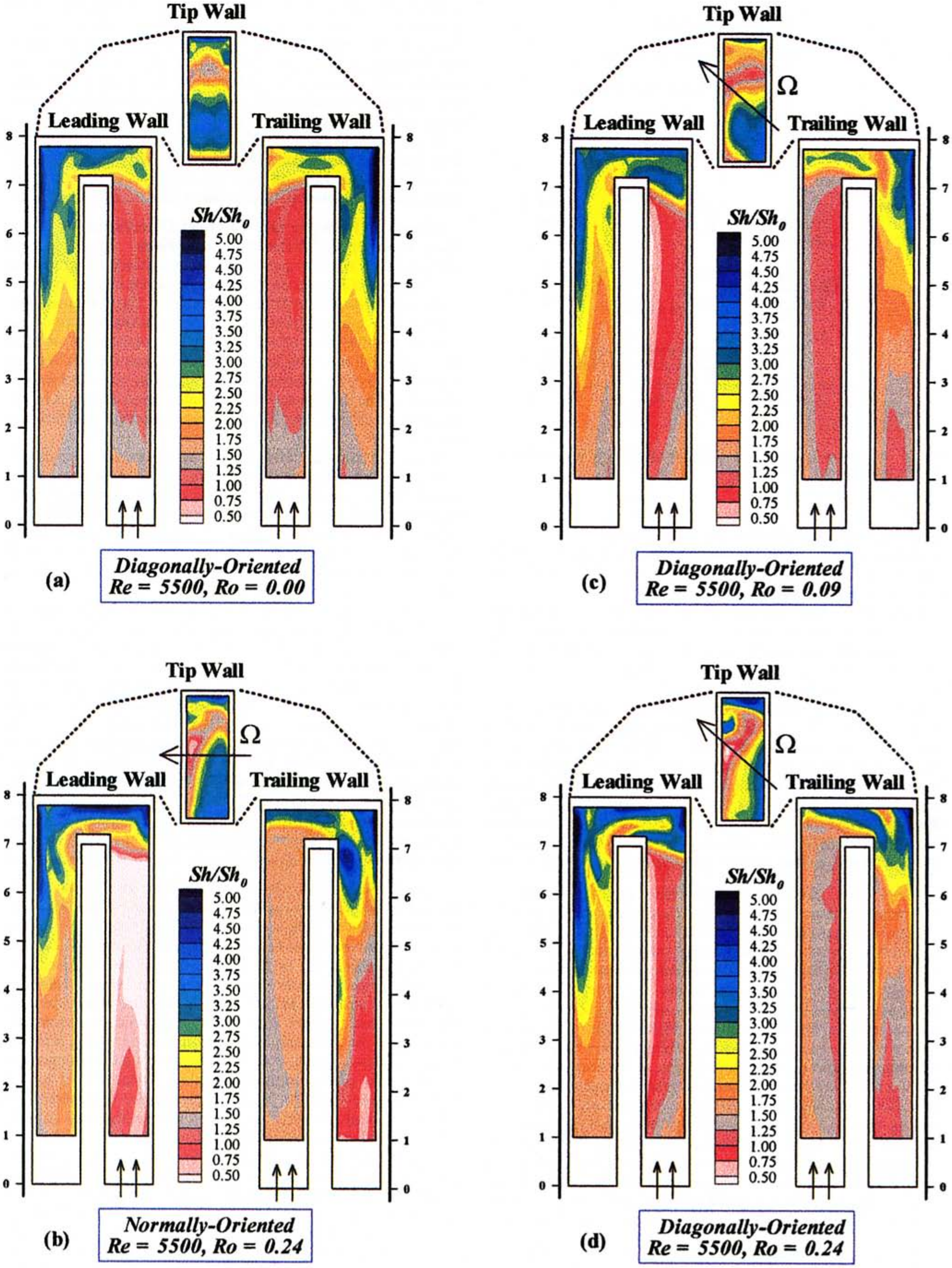

Fig. 3 Effects of rotation and channel orientation on Sh/Sh$_0$ distributions

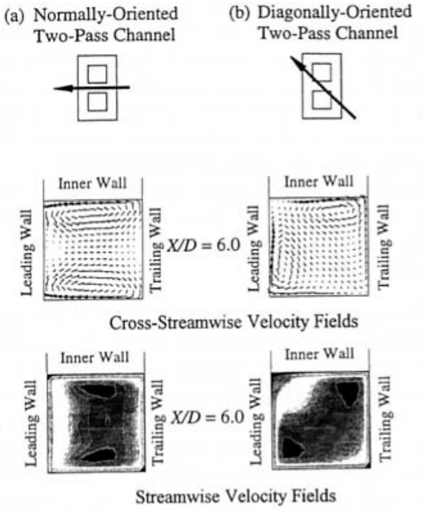

Fig. 4 Computed streamwise and cross-streamwise velocities at $X/D = 6.0$ in first straight pass

the leading wall, as shown in Fig. 3(*b*), are primarily due to the shift of the high-velocity low-concentration core flow toward the trailing wall, and the associated velocity and concentration gradients near the leading and trailing walls.

In the radial outward flow in the diagonally oriented channel, the rotational Coriolis force is directed at a 45 deg degree toward the outer edge of the trailing wall. Both the streamwise and cross-streamwise velocity distributions are symmetrical with respect to the diagonal plane between the inner edge of the leading wall and the outer edge of the trailing wall. The impingement of the secondary flow near the outer edge of the trailing wall and the shifting of the core flow toward the outer edge of the trailing wall cause the high mass transfer near the outer edge of the trailing wall, as shown in Fig. 3(*d*). Based on the experimental results, $Sh/Sh_0 \cong 1.75$ to 2.0 along the outer edge of the trailing wall. The secondary flow washes the trailing wall while turning toward the inner edge, causing the mass transfer to decrease monotonically in the spanwise direction. The values of Sh/Sh_0 near the inner edge of the trailing wall are only about 1.0, despite the relatively high streamwise velocities near the inner edge of the trailing wall.

Figure 3(*d*) shows that there is a larger spanwise Sh/Sh_0 variation on the leading wall of the diagonally oriented channel than on the trailing wall. Figure 4 shows that the relatively high leading wall mass transfer may be sustained by the impingement of the secondary flow after it sweeps the outer side wall and the large streamwise velocities near the outer edge of the wall. The mass transfer is the lowest near the inner edge of the leading wall where the secondary flow is weak and the streamwise velocities are very low.

Sharp Turn. Entering the sharp turn, the local mass transfer on the leading wall increases abruptly in both the diagonally oriented and normally oriented channels. Figure 3 shows that the leading wall mass transfer is generally high in the turn regions of both channels, except near the tip of the inner wall. A close examination of the leading wall mass transfer distributions in the turn in the two Ro = 0.24 cases reveals that the mass transfer in the diagonally oriented channel is not as low as that in the normally oriented channel near the tip of the inner wall, and not as high along the tip wall. In both channels, the highest leading wall mass transfer occurs along the tip wall and along the outer edge near the turn exit.

In both the diagonally oriented channel and the normally oriented channel, with Ro = 0.24, the trailing wall mass transfer increases abruptly in the upstream half of the turn and continues to increase as the flow turns. In the upstream half of the turn region and along the tip wall, the trailing wall mass transfer is quite low when it is compared with the leading wall mass transfer. At the downstream outer corner of each of the two channels, however, the trailing wall mass transfer is very high, although the high mass transfer region along the outer wall does not extend into the second straight pass, as in the case of the leading wall.

The local mass transfer on the tip wall is significantly affected by the turn geometry, rotation, and the channel orientation. The tip wall mass transfer distribution is almost symmetrical in the no rotation case, with large Sh/Sh_0 values of over 3.75 in the middle of the upstream half of the tip wall and very large Sh/Sh_0 values of over 4.5 along the downstream edge of the wall. The mass transfer is the lowest ($Sh/Sh_0 \cong 1.25$) near the middle of the downstream half of the tip wall.

In the normally oriented channel, rotation shifts the peak of the Sh/Sh_0 distribution in the middle of the upstream half of the tip wall toward the trailing wall and lowers the peak Sh/Sh_0 values. There is an isolated low mass transfer region near the leading wall, where the Sh/Sh_0 values are below 0.75. In the diagonally oriented channel, the tip wall mass transfer is high along the trailing wall and low along the leading wall in the upstream half of the tip wall. The Sherwood number ratio drops monotonically from a value of about 3.75 along the trailing wall to about 1.25 along the leading wall. In both rotating channels, the mass transfer distribution in the downstream half of the tip wall is characterized by a relatively large low mass transfer region in the middle and very high mass transfer near the downstream edge of the tip wall. The orientation of the channel with respect of the rotation direction does not appear to affect the shape of the local mass transfer distribution on the tip wall significantly.

Attention is now focused on the flow fields in the turns of the two channels. Figure 5 presents the cross-streamwise and

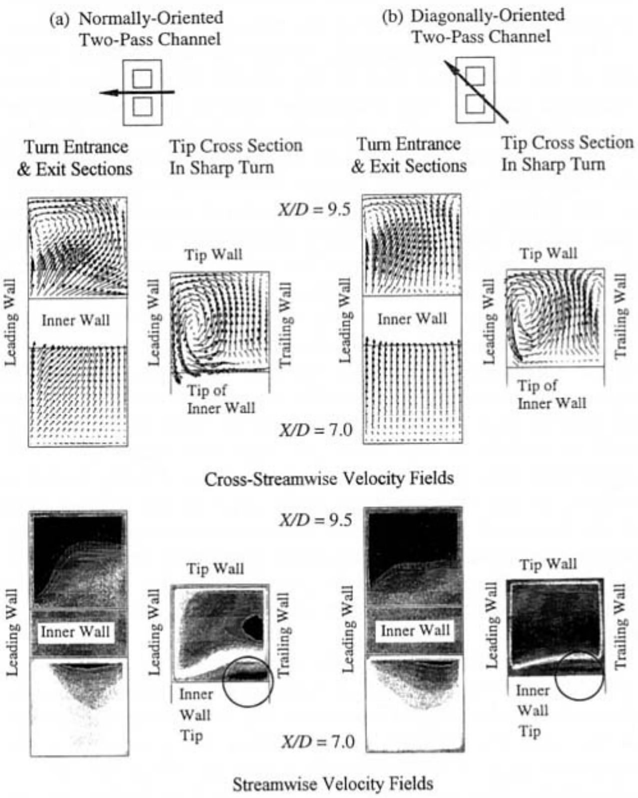

Fig. 5 Computed streamwise and cross-streamwise velocities at entrance, tip cross section, and exit of turn

streamwise velocities at three flow cross sections: at the turn inlet ($X/D = 7.0$), between the inner wall and the tip wall, and at the turn exit ($X/D = 9.5$). In the normally oriented channel, the flow turns toward the inner wall at the turn entrance ($X/D = 7.0$). Both the streamwise and cross-streamwise velocity distributions at the turn entrance are very different from those just a short distance upstream. The velocity distributions also show that the rotational Coriolis force appears to push the flow near the inner wall toward the trailing wall. Further downstream, in the cross section between the inner wall and the tip wall (or, the tip cross section), the streamwise velocity distribution clearly shows higher velocities near the trailing wall and flow recirculation near the trailing wall at the tip of the inner wall, both of which appear to be affected by the flow turning toward the trailing wall near the inner wall at the turn entrance.

The cross-streamwise velocity distribution at the tip cross section suggests that the turn-induced centrifugal force pushes the flow toward the tip wall. The low streamwise velocity of the flow near the leading wall may contribute to the swirling of the flow near the leading wall at the tip cross section. It should be pointed out that the cross-streamwise velocities at the tip cross section are comparable to the normal velocities at the tip cross section, and are much higher than the cross-streamwise velocities in the first straight pass, which are, at the most, equal to 15 percent of the mainstream bulk velocity. The very high leading wall mass transfer along the tip wall (see Fig. 3(b)) may be the result of the strong flow impingement on the outer edge of the leading wall. The low trailing wall mass transfer at the tip of the inner wall is caused by flow recirculation. Further out from the tip of the inner wall, the trailing wall mass transfer remains relatively high (although much lower than that in the very high mass transfer region on the leading wall directly across), since the streamwise velocity is high near the trailing wall.

The patterns of the streamwise and cross-streamwise velocities are consistent with the higher tip wall mass transfer near the trailing wall and the lower tip wall mass transfer near the leading wall, in the middle of the turn (see top of Fig. 3(b)).

The sharp turn dramatically affects the flow pattern at the exit of the turn (and that in the second straight pass, to be examined shortly). The streamwise velocity distribution at the turn exit of the normally oriented channel shows that the flow is thrown toward the outer wall by the centrifugal force, with the maximum streamwise velocity located near the outer edge of the trailing wall. The high streamwise velocities near the outer edge of the trailing wall are responsible for the high mass transfer along the outer edge of the wall. The cross-streamwise velocities near the inner wall are quite high (equal to about 50 percent of the mainstream bulk velocity) and are directed toward the trailing wall, continuing the trend in the cross section between the inner wall and the tip wall. The high mass transfer region on the trailing wall and the low mass transfer region on the leading wall immediately downstream of the tip of the inner wall, as shown in Fig. 3(b), are consistent with this cross-streamwise flow pattern at the exit of the turn. Finally, both the swirling of the flow near the outer edge of the leading wall at the turn exit (as shown in the cross-streamwise velocity distribution) and the relatively high streamwise velocities near the outer wall are believed to contribute to the high leading wall mass transfer along the outer edge of the wall (see Fig. 3(b)).

The streamwise and cross-streamwise velocity distributions at the three cross sections in the turn of the diagonally oriented channel are similar to the corresponding distributions in the turn of the normally oriented channel. Thus, the geometry of the sharp turn appears to affect the flow field more than the channel orientation. The measured mass transfer distributions in the turns of the two channels do not differ significantly. The rotational Coriolis force in the diagonally oriented channel, which is directed at a 45 deg angle to the leading and trailing walls, however, causes the velocity distributions to be slightly different from those in the normally oriented channel. With the Coriolis force directed at a 45 deg angle instead of normal to the leading and trailing walls, the cross flow toward the trailing wall near the tip of the inner wall is reduced or reversed. Without the flow impinging onto the trailing wall near the tip of the inner wall, the distinctive high mass transfer region immediately downstream of the tip of the inner wall on the trailing wall of the normally oriented channel is not observed in the diagonally oriented channel (Fig. 3(d)).

Second Straight Pass. In the second pass, the shapes of the local mass transfer distributions on the leading wall in the two $Ro = 0.24$ cases are very similar. The leading wall Sh/Sh_0 values are consistently higher in the diagonally oriented channel than in the normally oriented channel, except along the inner edge of the wall. It has already been pointed out that the very high mass transfer region immediately downstream of the tip of the inner wall on the trailing wall of the normally oriented channel is not apparent in the diagonally oriented channel. Further downstream, the trailing wall mass transfer in the diagonally oriented channel is higher along the outer edge and lower along the inner edge than that in the normally oriented channel. The trailing wall Sh/Sh_0 values in the diagonally oriented channel are lower in the first half of the second pass, and higher in the downstream half of the second pass than those in the normally oriented channel.

The sharp turn dominates the flow pattern in the second straight pass. Should the upstream sharp turn be replaced with a long square straight entrance section, the streamwise and cross-streamwise velocity distributions for the radial inward flow would be those presented in Fig. 4, except that the rotation directions would have to be reversed. Figure 6 gives the local

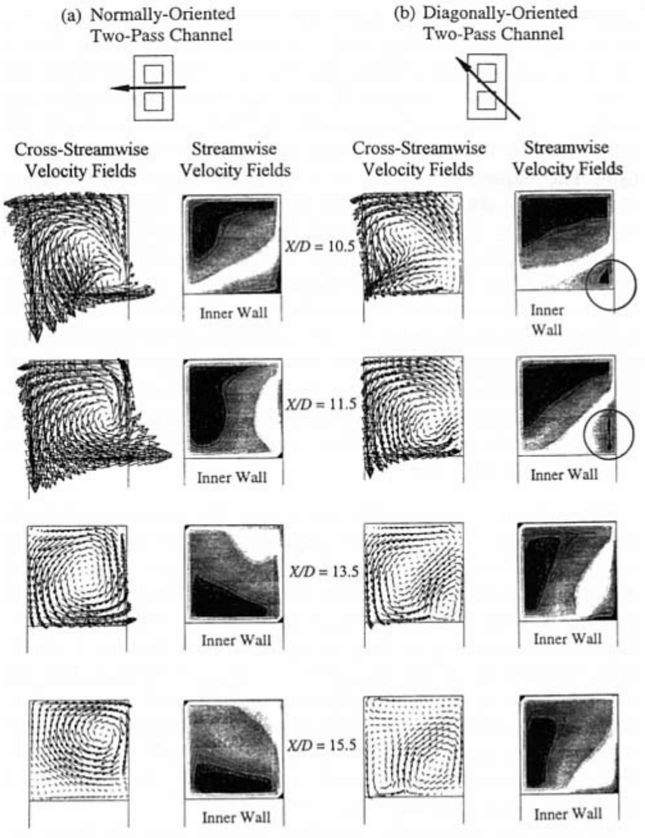

Fig. 6 Computed streamwise and cross-streamwise velocities at $X/D = 10.5$, 11.5, 13.5, and 15.5 in second straight pass

velocities at X/D = 10.5, 11.5, 13.5, and 15.5 in the second straight passes of the normally oriented and diagonally oriented channels. The figure shows that, in the normally oriented channel, rotation and the sharp turn cause the flow to swirl. The center of the vortex moves from a location near the outer edge of the leading wall at the turn exit (X/D = 9.5) to near the inner edge of the trailing wall one hydraulic diameter downstream in the second pass. The swirling flow impinges on the leading wall near the outer edge of the wall, and on the trailing wall near the inner edge of the wall. The cross-streamwise velocities are as high as one-half of the streamwise bulk velocity, substantially higher than the cross-streamwise velocities in the first pass. The strength of the vortex is reduced with distance from the turn exit. At four hydraulic diameters from the turn exit (X/D = 13.5), the maximum cross-streamwise velocity is only about one-fourth of the streamwise bulk velocity.

While the strength of the vortex gradually weakens downstream of the turn in the normally oriented channel, the high streamwise velocity region is shifted in the same direction of the swirl. The streamwise velocities are high near the outer wall one hydraulic diameter downstream of the turn exit (at X/D = 10.5). The highest streamwise velocities are near the leading wall at X/D = 11.5, and near the inner wall at X/D = 13.5. The high mass transfer on the outer edge of the leading wall and the inner edge of the trailing wall downstream of the turn is the result of the strength and the rotation direction of the vortex downstream of the turn. Except for the very high mass transfer region on the trailing wall immediately downstream of the tip of the inner wall, the generally higher streamwise velocities near the leading wall keep the mass transfer higher on the leading wall than on the trailing wall in the second straight pass of the normally-oriented channel (see Fig. 2). Note also that the mass transfer drops quite quickly along the outer edge of the trailing wall (see Fig. 3(*b*)) once the high streamwise velocity region moves away from the trailing wall.

With the channel oriented at a 45 deg angle to the rotation direction, a strong vortex still dominates the cross-streamwise velocity distribution immediately downstream of the turn. The shape of the vortex at X/D = 10.5, however, is different from that in the normally oriented channel: the cross flow impinges on the leading wall near both the outer and the inner edges of the wall. About one hydraulic diameter further downstream, the cross flow along the leading wall turns the impinging flow near the inner corner of the leading wall back toward the trailing wall. The cross-streamwise velocity distribution at X/D = 11.5 in the diagonally oriented channel is similar to the corresponding distribution in the normally-oriented channel. There are, however, two small vortices, both of which rotate in a direction opposite to that of the large vortex, near the inner and outer edges of the trailing wall. The small vortex at the outer edge of the trailing wall is also evident in the velocity distributions at X/D = 9.5 and 10.5.

At four hydraulic diameters downstream of the turn exit (X/D = 13.5) in the diagonally oriented channel, the large vortex becomes weaker, and the small vortex at the outer edge of the trailing wall has all but disappeared. The second small vortex, however, has gained strength and reverses the direction of the cross flow along the trailing wall near the inner edge of the wall.

In the second pass of the diagonally oriented channel, the high streamwise velocity region is also shifted in the same direction as the large vortex, but remains close to the leading wall beyond four hydraulic diameters downstream of the turn exit. Unlike in the case of the normally oriented channel, back flow near the inner edge of the trailing wall is apparent in the streamwise velocity distributions up to two hydraulic diameters downstream of the turn.

The computed velocity distribution in the second straight pass of the diagonally oriented channel is consistent with the measured mass transfer distributions on the leading and trailing wall of the channel presented in Fig. 3(*d*). Flow impingement on the leading wall and the large streamwise velocities near the leading wall are responsible for the high leading wall mass transfer downstream of the turn. Up to four hydraulic diameters downstream of the turn, the leading wall mass transfer is higher in the diagonally oriented channel than in the normally oriented channel, especially along the outer edge of the wall, apparently because the streamwise velocities remain high near the leading wall in the diagonally oriented channel. In addition to the lower streamwise velocities near the trailing wall, the back flow and the small vortex near the inner edge of the trailing wall cause the mass transfer in the upstream half of the second pass to be lower in the diagonally oriented channel than in the normally oriented channel.

Concluding Remarks

Naphthalene sublimation experiments have been conducted to study the effects of channel orientation, rotational Coriolis force, and a sharp turn, on the local heat (mass) transfer distributions in a two-pass square channel with a sharp turn and smooth walls, rotating about a perpendicular axis. The test channel was oriented so that the direction of rotation was perpendicular to or at a 45 deg angle to the leading and trailing walls. The following conclusions may be drawn:

1 The orientation of the rotating two-pass channel significantly affects the local mass transfer distribution in the first pass of the channel. Rotation does not lower the average leading wall mass transfer or increase the average trailing wall mass transfer in the diagonally oriented channel as much as in the normally oriented channel. The rotational Coriolis force in the diagonally oriented channel induces secondary flow and shifts the high streamwise velocity diagonally, resulting in the large monotonic spanwise variation of the mass transfer on both the leading and trailing wall.

2 The geometry of the sharp turn dominates the local mass transfer distributions in the turn and immediately downstream of the turn. The shapes of the mass transfer distributions in the normally oriented and diagonally oriented channels are similar, except for an isolated region on the trailing wall immediately downstream of the tip of the inner wall. The combined effect of the turn and rotation causes a strong swirling flow in both the normally oriented channel and the diagonally oriented channel, and flow impingement near the outer edges of the leading wall in the turn and immediately downstream of the turn.

3 Computed velocity distributions are useful in helping to explain how the flows affect the local mass transfer distributions. For instance, in the diagonally oriented channel, back flow keeps the trailing wall mass transfer low along the inner edge of the wall immediately downstream of the tip of the inner wall.

Acknowledgments

This research was sponsored by the NASA Lewis Research Center, Grant number NAG3-1980 and by the Energy Resources Center, College Station, TX.

References

Ambrose, D., Lawrenson, I. J., and Sprake, C. H. S., 1975, "The Vapor Pressure of Naphthalene," *Journal of Chem. Thermodynamics*, Vol. 7, pp. 1173–1176.

Dutta, S., Andrews, M. J., and Han, J. C., 1994, "Numerical Prediction of Turbulent Heat Transfer in a Rotating Square Duct with Variable Rotational Buoyancy Effects," ASME HTD-Vol. 271, ASME, New York, pp. 161–170.

Goldstein, R. J., and Cho, H. H., 1995, "A Review of Mass Transfer Measurements Using Naphthalene Sublimation," *Experimental Thermal and Fluid Science*, Vol. 10, pp. 416–434.

Han, J. C., Zhang, Y. M., and Kalkuehler, K., 1993, "Uneven Wall Temperature Effect on Local Heat Transfer in a Rotating Two-Pass Square Channel With Smooth Walls," ASME JOURNAL OF HEAT TRANSFER, Vol. 115, pp. 912–920.

Kline, S. J., and McClintock, F. A., 1953, "Describing Uncertainties in Single Sample Experiments," *Mechanical Engineering*, Vol. 75, pp. 3–8.

Launder, B. E., 1989, "Second-Moment Closure: Present. . .and Future?," *International Journal of Heat and Fluid Flow,* Vol. 10, pp. 282–300.

Launder, B. E., Reece, G. J., and Rodi, W., 1975, "Progress in the Development of a Reynolds-Stress Turbulence Closure," *Journal of Fluid Mechanics,* Vol. 68, pp. 537–566.

Launder, B. E., and Spalding, D. B., 1973, "The Numerical Computation of Turbulent Flows," Imperial College of Science and Technology, London, England, NTIS N74-12066.

McGrath, D. B., and Tse, D. G. N., 1995, "A Combined Experimental/Computational Study of Flow in Turbine Blade Passage: Part II—Computational Investigation," ASME Paper 95-GT-149.

McMillin, R. D. and Lau, S. C., 1994, "Effect of Trailing-Edge Ejection on Local Heat (Mass) Transfer in Pin Fin Cooling Channels in Turbine Blades," ASME *Journal of Turbomachinery,* Vol. 116, pp. 159–168.

Park, C. W., Lau, S. C., and Kukreja, R. T., 1998a, "Heat/Mass Transfer Distribution in a Rotating Two-Pass Square Channel—Part II: Local Heat Transfer, Smooth Channel," *International Journal of Rotating Machinery,* Vol. 4, No. 1, pp. 1–15.

Park, C. W., Lau, S. C., and Kukreja, R. T., 1998b, "Heat/Mass Transfer in a Rotating Two-Pass Square Channel With Transverse Ribs," *Journal of Thermophysics and Heat Transfer,* Vol. 12, pp. 80–86.

Sparrow, E. M., and Tao, W. Q., 1983, "Enhanced Heat Transfer in a Flat Rectangular Duct with Streamwise-Periodic Disturbances at One Principal Wall," ASME JOURNAL OF HEAT TRANSFER, Vol. 105, pp. 851–861.

Prakash, C., and Zerkle, R., 1992, "Prediction of Turbulent Flow and Heat Transfer in a Radially Rotating Square Duct," ASME *Journal of Turbomachinery,* Vol. 114, pp. 835–846.

Tekriwal, P., 1994, "Heat Transfer Predictions with Extended k-ϵ Turbulence Model in Radial Cooling Ducts Rotating in Orthogonal Mode," ASME JOURNAL OF HEAT TRANSFER, Vol. 116, pp. 369–380.

Tse, D. G. N., and McGrath, D. B., 1995, "A Combined Experimental/Computational Study of Flow in Turbine Blade Passage: Part I—Experimental Study," ASME Paper 95-GT-355.

Wagner, J. H., Johnson, B. V., and Yeh, F. C., 1991, "Heat Transfer in Rotating Serpentine Passages With Smooth Walls," ASME *Journal of Turbomachinery,* Vol. 113, pp. 321–330.

T. S. Fisher
e-mail: tsf3@cornell.edu
Assoc. Mem. ASME

K. E. Torrance
Sibley School of Mechanical and
Aerospace Engineering,
Cornell University,
Upson Hall,
Ithaca, NY 14853

Free Convection Limits for Pin-Fin Cooling

An analytical solution for a system consisting of a pin-fin heat sink and a chimney is presented. The result is applied to problems in which the size of the overall system is constrained. For a given heat dissipation and total system size, optimal values of the pin-fin diameter and heat-sink porosity are observed. The optima occur for systems with and without chimneys. The optimization is used to show that the minimum thermal resistance from a pin-fin heat sink is about two times larger than that of an idealized model based on inviscid flow.

1 Introduction

Heating from high-power electronic components can cause large increases in device and coolant temperatures. Often, components are cooled by mechanical fans or by other active devices. However, in many applications, active cooling may be undesirable due to power consumption, excessive noise, or reliability concerns. For some designs, it may be possible to exploit the buoyant forces created by fluid heating in order to cool electronic devices, and an understanding of the limits of free convection is necessary to design such systems. The present study uses analytical methods to predict the upper limits of heat transfer from pin-fin heat-sink/chimney systems.

Heat transfer from arrays of cylinders and pin fins has been reviewed by several authors. Armstrong and Winstanley (1988) reviewed heat transfer from staggered pin-fin arrays for Reynolds numbers (based on fin diameter) greater than 10^3. Zukauskas (1987) provided a thorough review of forced-convection heat transfer from arrays of in-line and staggered tubes. For in-line arrays, the recommended correlations for the average Nusselt number agree with the isolated cylinder correlations to within 20 percent.

Studies of forced-convection heat transfer from pin-fin heat sinks are common in the literature. Bejan and Morega (1993) used analytical methods to optimize heat transfer from cylindrical-fin arrays in the Darcy regime of low Reynolds numbers. Jubran et al. (1993) reported experimental results for in-line and staggered pin-fin arrays for Reynolds numbers of order 10^4. An optimal porosity of $\phi = 87$ percent was reported for both types of arrays. Square-fin array experiments under low-velocity forced flow ($\mathrm{Re} \sim 10^2$) were conducted by Shaukatullah et al. (1996), who described an optimal in-line pin-fin arrangement corresponding to $\phi = 92$ percent.

Ergun (1952) performed an early study of the drag characteristics of cylinder arrays for moderate Reynolds numbers. Ergun proposed an empirical correlation in which the streamwise pressure drop is a quadratic function of the fluid velocity. Sangani and Acrivos (1982) developed a high-porosity drag correlation for low Reynolds number flows. Flow through periodic arrays of cylinders has been studied by Koch and Ladd (1997), who used the lattice-Boltzmann numerical method to predict drag and pressure drop.

Experiments on combined free-convection/radiation from aligned and staggered arrays of fins with circular, elliptical, and square cross sections were performed by Taylor (1984). Sparrow and Vemuri (1985) studied the effects of shrouding and number of fins on overall heat transfer from staggered arrays of circular fins and found an optimal porosity of $\phi \approx 85$ percent for unshrouded fin arrays. Aihara et al. (1990) tested many heat sinks to determine an empirical correlation for heat transfer from unshrouded pin-fin arrays. Zografos and Sunderland (1990) experimentally found an optimal porosity of 90 percent among four heat sinks with porosities in the range 60 percent $\leq \phi \leq$ 90 percent. In the present work, the porosity and other variables can be varied continuously, thereby allowing a more precise optimization.

Previous work by Fisher et al. (1997) on plate-fin heat sinks with chimneys has shown that the plate spacing can be optimized for maximum heat transfer. Further, the plate-fin work suggested that, with the addition of a chimney, the heat-sink height can be reduced without a loss in thermal performance and without increasing the overall system height.

In the present work, we extend the heat-sink/chimney concept to systems with pin-fin heat sinks. Understandably, previous work has failed to generalize the optimization process due to difficulties in spanning parameter ranges with discrete experimental and computational models. The analytical approach enables easy parameter variations to identify regimes of maximum heat transfer. The parametric conditions for maximum heat transfer are then used to describe the upper limits of free convection from arrays of pin fins. Further, chimney enhancement, which has not been previously addressed for pin-fin heat sinks, is included in the analysis as a means of reducing the heat-sink height. Solutions are obtained by separately treating the fluid flow in the heat sink and chimney, and then matching pressure and velocity boundary conditions. In the following section, the analytical methodology is described, followed by a presentation and discussion of results.

2 Theory and Analysis

The problem geometry shown in Fig. 1 depicts a system with a pin-fin heat sink located beneath a chimney. The pin fins are circular in cross section. The total height H, width W, and length L (not shown) of the heat-sink/chimney system are fixed. For pin fins of sufficient length L, two-dimensional flow in the $X-Y$ plane of Fig. 1 can be assumed. A total amount of heat Q_{tot} is distributed *uniformly* among the pin fins, and the quiescent atmosphere outside the system is assumed to be isothermal at T_0 with a hydrostatic pressure variation $P = P_0 - \rho_0 g X$. Note that under the foregoing assumptions, the unfinned basal area of the heat sink is considered adiabatic.

The local pin-fin geometry, shown in Fig. 2, is defined by the fin diameter D and the fin spacing S. In general, the fin array may be aligned, as shown in Fig. 2, or staggered. Based on the work of Zografos and Sunderland (1990) for free-convection systems, only square aligned arrays are considered in the present work.

The working fluid (air) undergoes a series of processes in Fig. 1. Fluid is first inducted from the quiescent atmosphere into

---

Contributed by the Heat Transfer Division for publication in the JOURNAL OF HEAT TRANSFER and presented at '97 NHTC, Baltimore. Manuscript received by the Heat Transfer Division, Sept. 12, 1997; revision received, Apr. 21, 1998. Keywords: Electronics, Finned Surfaces, Heat Transfer, Natural Convection, Optimization. Associate Technical Editor: P. Simpkins.

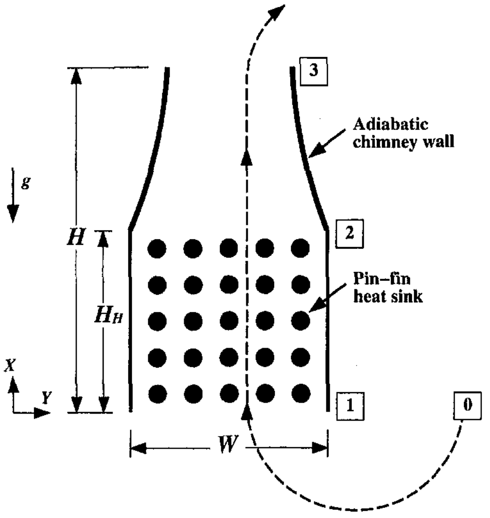

Fig. 1 Two-dimensional heat-sink/chimney system

the heat sink in process 0-1. In process 1-2, heat is transferred to the fluid while it is acted upon by viscous forces in the heat sink. The flow then proceeds through the chimney in process 2-3 and finally dissipates its acquired energy in the external atmosphere.

In order to obtain an analytical solution, several key assumptions are needed:

1 The flow inside the heat sink is two-dimensional in the $X - Y$ plane of Fig. 1, and the drag and heat transfer characteristics are reasonably described by forced-convection correlations. Further, a minimum fin surface efficiency of 85 percent is enforced for all results presented here to ensure a nearly uniform temperature along the length of each fin.

2 The flow outside the heat sink (processes 0-1, 2-3, and 3-0) is incompressible and inviscid.

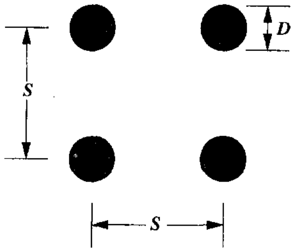

Fig. 2 Local pin-fin geometry

3 The fin surfaces are the only surfaces through which heat is transferred.

4 Radiative heat transfer to the surroundings is negligible due to the shroud surrounding the heat sink (Sparrow and Vemuri, 1985).

With the foregoing assumptions, the following sections describe the procedure for producing solutions.

2.1 Fluid Flow Analysis. Fluid flow in the heat sink is analyzed by considering an integral momentum equation. An exact Navier-Stokes solution is not possible. However, an overall force balance for the heat sink can be written as

$$P_1 - P_2 = \frac{\mathcal{F}\mu U n}{S} + \int_1^2 \rho g dX \qquad (1)$$

where

$$\mathcal{F} = \frac{F_D}{\mu U L} \qquad (2)$$

and U is the vertical freestream velocity just below the heat-sink entrance. In Eq. (1), n is the number of pin-fin rows in the streamwise (vertical) direction. Note that the velocity U can also be considered an average velocity over the entire heat sink volume, including the fluid and solid regions. The left side of Eq. (1) is the pressure force. The first term on the right side

Nomenclature

A, B = constants in Eq. (13)
c_0, c_1 = drag parameters, see Eq. (12)
C_i = parameters in Eq. (20), i = 1, 2, 3, 4
D = pin-fin diameter (m)
D^* = dimensionless pin-fin diameter, D/H
$\mathcal{F}$ = dimensionless drag force, see Eq. (2)
F_D = drag force per cylinder (kg m/s^2)
g = gravitational acceleration (m/s^2)
H = total system height (m), see Fig. 1
H_H = heat-sink height (m), see Fig. 1
H_H^* = dimensionless heat-sink height, H_H/H
k_f = fluid thermal conductivity (W/mK)
k_0 = drag factor, see Eq. (11)
K_i = parameters in Eq. (22), i = 1, 2, 3
L = fin length (m)
L^* = dimensionless fin length, L/H
n = number of pin-fin rows
P = fluid pressure (Pa)
Pr = Prandtl number, ν/α
Q_{tot} = total heat flow (W)
$\mathcal{R}$ = dimensionless thermal resistance, θ/Ra
Ra = modified Rayleigh number, $(g\beta Q_{\text{tot}}H^2/\nu\alpha k_f)$
Re = Reynolds number based on fin diameter, UD/ν
S = pin-fin spacing (m), see Fig. 2
S^* = dimensionless pin-fin spacing, S/D
T = temperature (K)
U = volume-averaged vertical velocity (m/s)
W = heat-sink width (m), see Fig. 1
W^* = dimensionless heat-sink width, W/H

Greek Symbols

α = thermal diffusivity (m^2/s)
β = coefficient of thermal expansion (1/K)
Γ = chimney contraction ratio
θ_{0-2} = dimensionless fluid temperature rise, $(g\beta(T_2 - T_0)H^2/\nu\alpha)$
θ_{f-b} = dimensionless fluid-to-base temperature rise, $(g\beta(T_b - T_f)H^3/\nu\alpha)$
$\theta_{\max}$ = maximum fluid-to-base temperature rise, $\theta_{0-2} + \theta_{f-b}$
κ = ratio of solid-to-fluid thermal conductivities
ν = fluid kinematic viscosity (m^2/s)
ρ = fluid density (kg/m^3)
ϕ = heat-sink porosity, (fluid volume in heat-sink)/(total volume fluid + solid)

Subscripts

0, 1, 2, 3 = system location, see Fig. 1
ave = average
b = heat-sink base
f = fluid
ideal = ideal
max = maximum
min = minimum
opt = optimal

represents the drag force from the pin-fin array, and the second term represents the buoyancy force. In Eq. (2), $\mathcal{F}$ is a dimensionless drag per unit length, the specific form of which is discussed in Section 2.2.

The buoyancy term of Eq. (1) can be evaluated by using a Boussinesq approximation, in which density in the energy equation is assumed constant. Consequently, the uniform distribution of heating in the heat sink produces a nearly linear fluid temperature rise. The fluid force balance then becomes

$$P_1 - P_2 = \frac{\mathcal{F}\mu U n}{S} + \rho_0 g H_H\left[1 - \frac{1}{2}\beta(T_2 - T_0)\right] \quad (3)$$

where β is the volumetric thermal expansion coefficient.

For chimney problems, the pressure drop $P_1 - P_2$ can also be calculated by analyzing the flow outside the heat sink. Fisher et al. (1997) previously analyzed the flow in the chimney and quiescent atmosphere as a series of incompressible Bernoulli processes. In the analysis, the dynamic head loss at the heat sink entrance is considered negligible due to the smooth contraction of the inflow streamlines. Conversely, the entire dynamic head of the flow at the chimney exit is assumed to be lost (Moore, 1976). For the outside flow loop, the pressure drop becomes

$$P_1 - P_2 = \frac{-\rho_0}{2} U^2\Gamma^2 + \rho_0 g H_H + \rho_0 g\beta(H - H_H)(T_2 - T_0) \quad (4)$$

where Γ is the ratio of cross-sectional flow areas at locations 2 and 3 of Fig. 1 and density variations have been included only in the buoyancy term.

Equations (3) and (4) provide separate expressions for the pressure drop $P_1 - P_2$. By equating the expressions, we arrive at a dimensional form of the draft equation

$$\frac{g\beta D^2(H - H_H)}{\nu^2}(T_2 - T_0) = \mathcal{F}\,\mathrm{Re}\frac{nD}{S} + \frac{1}{2}\mathrm{Re}^2\Gamma^2 \quad (5)$$

where $\mathrm{Re} = UD/\nu$. The temperature rise $T_2 - T_0$ and fluid velocity U are related by overall energy conservation

$$\rho_0 LWUc_p(T_2 - T_0) = Q_{\mathrm{tot}} \quad (6)$$

where again, density is assumed constant throughout the heat sink. Upon combining Eqs. (5) and (6), and using $n = H_H/S$, the dimensionless draft equation becomes

$$\frac{\mathrm{Ra}D^{*3}(1 - H_H^*/2)}{W^*L^*\mathrm{Pr}^2} = \mathcal{F}\frac{H_H^*}{D^*S^{*2}}\mathrm{Re}^2 + \frac{1}{2}\Gamma^2\mathrm{Re}^3 \quad (7)$$

where

$$\mathrm{Ra} = \frac{g\beta Q_{\mathrm{tot}}H^2}{\nu\alpha k_f} \quad (8)$$

$$H_H^* = \frac{H_H}{H}, \quad W^* = \frac{W}{H}, \quad L^* = \frac{L}{H}, \quad D^* \frac{D}{H}, \quad S^* = \frac{S}{D}. \quad (9)$$

The modified Rayleigh number Ra is a measure of the buoyant forces in the system, and for in-line arrays, the dimensionless fin spacing is related to the porosity by

$$S^*(\phi) = \sqrt{\pi/[4(1 - \phi)]}\,. \quad (10)$$

The dimensionless draft equation, Eq. (7), is central to the present work. In the following subsection, an empirical expression for the drag force $\mathcal{F}$ is developed, and subsequently, the draft equation is used to find an expression for the volume-averaged velocity U through the heat sink.

2.2 Drag Model. Various drag models have been proposed for flow over arrays of cylinders and circular pin fins (Ergun, 1952; Sangani and Acrivos, 1982; Gaddis and Gnielinski, 1985; Nield and Bejan, 1992; Shaukatullah et al., 1996). Bejan and Morega (1993) used the porous media Carman-Kozeny model in optimizing forced convection heat transfer from pin-fin arrays. However, for the present study, we find that the pore Reynolds number, $\mathrm{Re}\phi/(1 - \phi)$, generally falls in the range $10^2 - 10^3$, which exceeds by at least an order of magnitude the criterion for Darcy flow in a porous medium (Bejan and Morega, 1993).

Due to the absence of an existing drag model for high-porosity moderate Reynolds number flows, a drag correlation is developed in the present work. While the final form of the model is new, it is based on a combination of existing models. First, we assume that the porosity dependence of the model follows that predicted by the creeping-flow model of Sangani and Acrivos (1982):

$$\mathcal{F} = k_0(\phi) \equiv 4\pi\left[\frac{-0.5\ln(1 - \phi) + 0.262 - \phi}{-0.887(1 - \phi)^2 + 2.038(1 - \phi)^3}\right]. \quad (11)$$

Second, inertial effects are included with an Ergun-type correlation

$$\mathcal{F} = c_0 + c_1\,\mathrm{Re} \quad (12)$$

where the second term accounts for inertial effects. We also utilize the results of Koch and Ladd (1997) for random arrays that show $c_1 \sim c_0/(1 - \phi)$. Finally, we assume that $c_0 \sim k_0(\phi)$, and the resulting drag model becomes

$$\mathcal{F} = Ak_0(\phi) + B\frac{k_0(\phi)}{1 - \phi}\mathrm{Re} \quad (13)$$

where A and B are constants.

The numerical data of Koch and Ladd (1997) were used to estimate the values of A and B in Eq. (13). A regression analysis was performed over the ranges 80 percent $\le \phi \le$ 97.5 percent and $4 \le \mathrm{Re} \le 120$ to determine the values $A = 1.15$ and $B = 2.3 \times 10^{-4}$. The resulting errors are less than eight percent as compared to the reference numerical solutions. Figure 3 provides a graphical comparison of the present model with Koch and Ladd's data. Clearly, the proposed model closely matches the computational results for high porosities, $\phi \ge 80$ percent, over a wide range of Reynolds numbers.

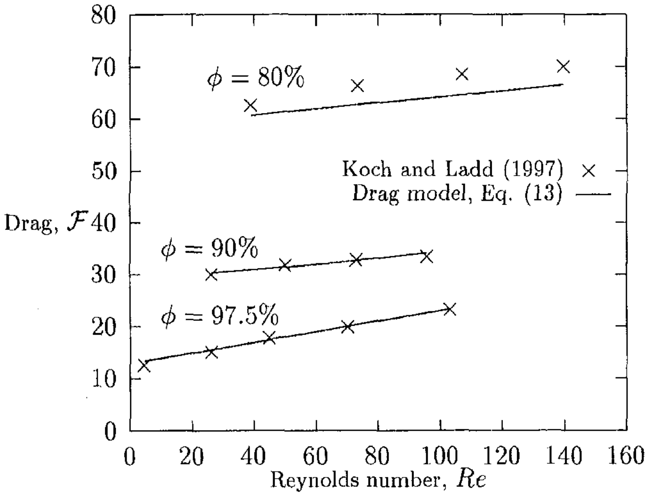

Fig. 3 Dimensionless drag, $\mathcal{F}$, as a function of Reynolds number, Re, and porosity, ϕ

2.3 Draft Equation. The draft equation, Eq. (7), can now be updated to include the drag model of Eq. (13). Upon combining the two equations and using $A = 1.15$ and $B = 2.3 \times 10^{-4}$, we find

$$\frac{\mathrm{Ra} D^{*3}(1 - H_H^*/2)}{W^* L^* \mathrm{Pr}^2} = 1.15 \frac{k_0(\phi) H_H^*}{D^* S^{*2}} \mathrm{Re}^2 + \left[2.3 \times 10^{-4} \frac{k_0(\phi) H_H^*}{D^* S^{*2}(1 - \phi)} + \frac{1}{2} \Gamma^2 \right] \mathrm{Re}^3. \quad (14)$$

An analytical solution to Eq. (14) exists for the Reynolds number in the form $\mathrm{Re} = \mathrm{Re}[\mathrm{Ra}/(W^* L^*), \mathrm{Pr}, H_H^*, D^*, \phi, \Gamma]$, and can be found with symbolic algebra software. Thus, the draft equation can be solved for the volume-average velocity, U, in the heat sink. Then, using Eq. (6), the mixed-mean temperature rise of the fluid is

$$\theta_{0-2} = \frac{\mathrm{Ra} D^*}{W^* L^* \mathrm{Pr}} \frac{1}{\mathrm{Re}} \quad (15)$$

where $\theta_{0-2} = g\beta(T_2 - T_0)H^3/(\nu\alpha)$.

2.4 Heat Transfer Analysis. The local heat transfer coefficient from arrays of pin fins can be obtained from tube-bundle correlations, which, like isolated-cylinder correlations, usually take the form $\mathrm{Nu} \sim \mathrm{Re}^m$. For moderate Re flows, m is a constant in the range $0.4 \le m \le 0.5$. The close correspondence of tube-bundle correlations with isolated cylinder correlations affirms the suitability of tube-bundle correlations for the present case of high-porosity arrays of pin fins, which in the limit $\phi \to 1$ become isolated cylinders. The following correlation recommended by Zukauskas (1987) for $1 \le \mathrm{Re}_{\max} \le 100$ is used

$$\mathrm{Nu} = 0.9\, \mathrm{Re}_{\max}^{0.4} \mathrm{Pr}^{0.36} \quad (16)$$

where, for square in-line arrays,

$$\mathrm{Re}_{\max} = \frac{S^*}{S^* - 1} \mathrm{Re}. \quad (17)$$

With the assumption of two-dimensional flow and a uniform heat transfer coefficient over the array of pin fins, the temperature rise from the bulk fluid (T_f) to the heat-sink base (T_b) can be described by a fin model. Using the correlation of Eq. (16) and an adiabatic fin-tip model, the temperature rise becomes

$$\theta_{f-b} = \frac{0.671 \dfrac{\mathrm{Ra}\, S^{*2} D^*}{W^* H_H^*}}{\sqrt{\kappa\, \mathrm{Re}_{\max}^{0.4} \mathrm{Pr}^{0.36}} \tanh\left(\dfrac{1.90 L^*}{D^*} \sqrt{\dfrac{\mathrm{Re}_{\max}^{0.4} \mathrm{Pr}^{0.36}}{\kappa}} \right)} \quad (18)$$

where $\theta_{f-b} \equiv [g\beta(T_b - T_f)H^3]/(\nu\alpha)$ defines a dimensionless temperature and κ is the ratio of solid-to-fluid thermal conductivities. The parametric dependence of the fluid-to-base temperature rise can be expressed as $\theta_{f-b} = \theta_{f-b}$ (Ra/W^*, Pr, κ, H_H^*, L^*, D^*, ϕ, Γ), where S^* has been replaced by a function of ϕ from Eq. (10).

For many heat transfer applications, the maximum solid temperature is the critical thermal parameter. In the following sections, we consider the effects of independent variables on the maximum base temperature $\theta_{\max}$, which occurs at the top of the heat sink (location 2 in Fig. 1). The maximum temperature can be expressed as the sum of the fluid temperature rise and the fluid-to-base temperature rise as

$$\theta_{\max}\left(\frac{\mathrm{Ra}}{W^*}, \mathrm{Pr}, \kappa, H_H^*, L^*, D^*, \phi, \Gamma \right) = \theta_{0-2}\left(\frac{\mathrm{Ra}}{W^* L^*}, \mathrm{Pr}, H_H^*, D^*, \phi, \Gamma \right) + \theta_{f-b}\left(\frac{\mathrm{Ra}}{W^*}, \mathrm{Pr}, \kappa, H_H^*, L^*, D^*, \phi, \Gamma \right). \quad (19)$$

According to the foregoing equation, the maximum temperature depends on eight independent variables. In subsequent sections, we will focus on three of the independent parameters, namely H_H^*, D^*, and ϕ.

The functional dependencies appearing in Eq. (19) may be somewhat misleading, because the terms on the right side depend on the Reynolds number. Thus, the draft equation, Eq. (14), must be used to solve for the Reynolds number before Eq. (19) can be applied. The following procedure is used to solve for the maximum temperature rise:

- Solve Eq. (14) for the Reynolds number, Re.
- Substitute the value of Re into Eq. (15) to solve for the fluid temperature rise, θ_{0-2}.
- Substitute the value of Re into Eq. (18) to solve for the fluid-to-base temperature rise, θ_{f-b}.
- Substitute the values of θ_{0-2} and θ_{f-b} into Eq. (19) to solve for the maximum temperature rise, $\theta_{\max}$.

2.5 Optimization. With an analytical solution from the foregoing sections, we can now differentiate the solution and obtain optimal configurations. The goal is to minimize the maximum base temperature $\theta_{\max}$ while varying the pin-fin diameter D^* and the porosity ϕ.

Noting that both the fluid temperature rise θ_{0-2} and the fluid-to-base temperature rise θ_{f-b} depend on the Reynolds number (see Eqs. (15) and (18)), the first step in the optimization is to differentiate the dimensionless draft equation, Eq. (14). Then, the partial derivative of Re with respect to D^* can be determined as

$$\frac{\partial \mathrm{Re}}{\partial D^*} = \frac{3C_1 D^{*2} + \dfrac{C_2}{D^{*2}} \mathrm{Re}^2 + \dfrac{C_3}{D^{*2}} \mathrm{Re}^3}{2 \dfrac{C_2}{D^*} \mathrm{Re} + 3\left(\dfrac{C_2}{D^*} + C_4 \right) \mathrm{Re}^2} \quad (20)$$

where

$$C_1 = \frac{\mathrm{Ra}(1 - H_H^*/2)}{W^* L^* \mathrm{Pr}^2}, \quad C_2 = \frac{1.15 k_0 H_H^*}{S^{*2}},$$

$$C_3 = \frac{2.3 \times 10^{-4} k_0 H_H^*}{S^{*2}(1 - \phi)}, \quad C_4 = \frac{1}{2} \Gamma^2. \quad (21)$$

Similarly, the derivative of Re with respect to ϕ is expressed as

$$\frac{\partial \mathrm{Re}}{\partial \phi} = \frac{\mathrm{Re}\left(2K_1 \dfrac{k_0}{S^{*3}} \dfrac{dS^*}{d\phi} - \dfrac{K_1}{S^{*2}} \dfrac{dk_0}{d\phi} - \mathrm{Re} K_2 \dfrac{dk_0}{d\phi} \right)}{2K_1 \dfrac{k_0}{S^{*2}} + \mathrm{Re}(3k_0 K_2 + 3K_3)} \quad (22)$$

where

$$K_1 = \frac{1.15 H_H^*}{D^*}, \quad K_2 = \frac{2.3 \times 10^{-4} H_H^*}{D^*(\pi/4)},$$

$$K_3 = \frac{1}{2} \Gamma^2. \quad (23)$$

In Eq. (22), the derivatives of S^* and k_0 with respect to ϕ can be determined by differentiating Eqs. (10) and (11), respectively.

The derivatives of the maximum base temperature with respect to D^* and ϕ can be calculated by differentiating Eq. (19). The resulting lengthy expressions involve derivatives of Re, k_0, and S^*, which are analytical, as shown above. We can thus obtain analytical solutions, not included here for brevity, for the derivatives of the maximum base temperature.

To find optimal solutions, the derivatives $\partial\theta_{\max}/\partial D^*$ and $\partial\theta_{\max}/\partial\phi$ are set to zero, and the corresponding D^* and ϕ are designated as optimal values D^*_{opt} and ϕ_{opt}. In the present work, the secant method is used to numerically compute optimal values to four significant figures. Note that the parameters can be optimized individually or in tandem. There are merits to each approach. For instance, one may be constrained by manufacturing constraints to use a specific pin-fin diameter, in which case only the porosity is optimized.

3 Results and Discussion

In the following paragraphs, the analytical solution is compared to existing experimental data. Then, the pin-fin diameter and porosity are optimized individually and in tandem. Throughout the latter section, the chimney effect is studied to determine its potential benefits in reducing the height and weight of the heat sink.

3.1 Comparison With Previous Work. Limited experimental or numerical data exist for free convection from in-line pin-fin arrays. Further, we have found no existing work on chimney enhancement from such heat sinks. However, the work of Zografos and Sunderland (1990) can be used to confirm the present model's predictions for a high-porosity configuration. Zografos and Sunderland (1990) conducted experiments, in which radiation was found to be insignificant, on heat sinks with porosities of 0.60, 0.77, and 0.90. Uniform heating conditions were experimentally confirmed in the experiment. Because of the present work's high-ϕ assumption, only the data for $\phi = 0.90$ are relevant here.

Figure 4 illustrates the variation of average heat-sink temperature rise θ_{ave} with the modified Rayleigh number Ra. Close agreement is observed over the range of Rayleigh numbers. The present model generally underpredicts the temperature rise by about ten percent. Some disagreement is expected because the experimental fin configuration was aligned in the stream-wise direction, but staggered in the span-wise direction. Also, a departure from two-dimensional flow may have been present in the experiment, as a shroud at the fin tips was not used. Despite the physical inconsistencies, the present model properly predicts both the magnitude of the temperature rise and its dependence on buoyancy through the Rayleigh number.

3.2 Regime Maps. The effects of porosity and pin-fin diameter on the maximum temperature rise are shown in the contour graphs of Fig. 5. The data in the figure were obtained with fixed values $\Pr = 0.7$, $\kappa = 7.5 \times 10^3$, $L^* = 0.2$, and $\Gamma = 1$. Figure 5(a) shows a system without a chimney ($H^*_H = 1$) and $\text{Ra} = 10^9$. The figure shows a pronounced region of minimum temperature rise traversing from the upper left to the lower right portion of the figure. In this optimal region, the temperature rise varies by less than ten percent. The optimal region is broad, covering porosity variations of up to five percent for a given pin-fin diameter, and diameter variations of up to 60 percent for a given porosity. Similar behavior is observed in Fig. 5(b) for a chimney system ($H^*_H = 0.5$) and $\text{Ra} = 10^{10}$.

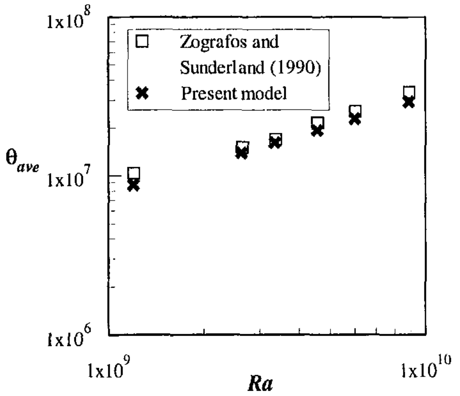

Fig. 4 Average temperature rise θ_{ave} as a function of modified Rayleigh number Ra. Comparison with experimental work (Zografos and Sunderland, 1990). $W^* = 0.888$, $\Pr = 0.7$, $\kappa = 6.8 \times 10^3$, $H^*_H = 1$, $L^* = 0.205$, $D^* = 0.017$, $\phi = 0.90$, $\Gamma = 1$.

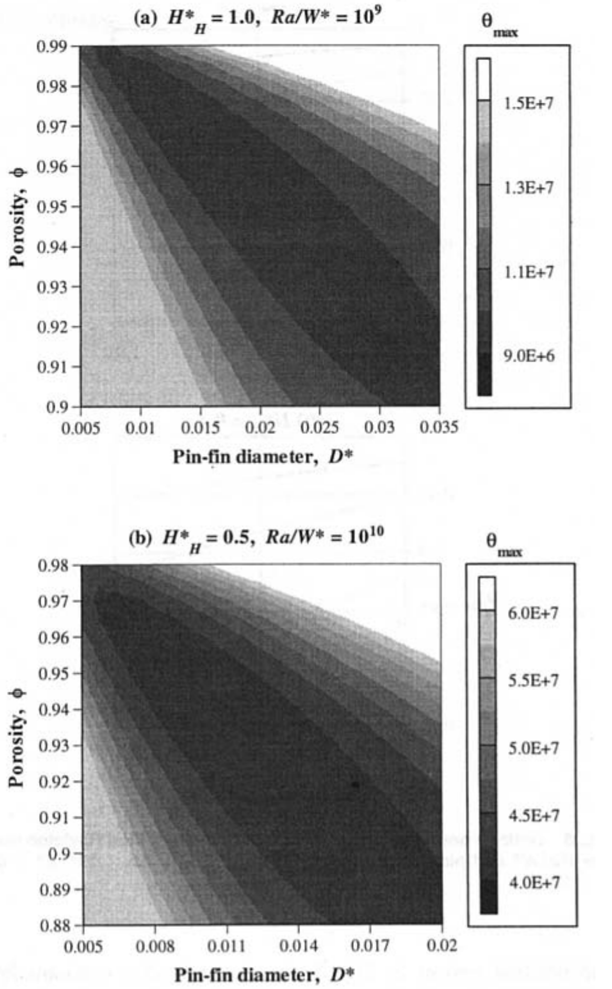

Fig. 5 Maximum heat-sink temperature $\theta_{\max}$ as a function of pin-fin diameter D^* and porosity ϕ. $\Pr = 0.7$, $\kappa = 7.5 \times 10^3$, $L^* = 0.2$, $\Gamma = 1$.

The optimal region of Fig. 5 reflects the best compromise between heat-transfer surface area and the local heat transfer rate from the fins. As the porosity or pin-fin diameter decreases away from the optimal region, the surface area increases, but the Reynolds number decreases, causing lower local heat transfer coefficients. Conversely, as the porosity or pin-fin diameter increases away from the optimal region, the local heat transfer coefficient increases, but the surface area is diminished.

A significant observation from Fig. 5 is that the pin-fin diameter and heat-sink porosity are strongly coupled in the search for optimal geometries. In general, larger pin-fin diameters produce smaller optimal porosities. This result can be explained by considering the functional dependence of the total heat-transfer area, $A_{\text{fins}} \sim H^*_H(1-\phi)/D^*$. Using a simplified analysis, Bejan and Ledezma (1996) suggested that there exists an optimal heat-transfer area for free-convection systems. To maintain a constant heat-transfer area for the present problem, the porosity must decrease as the pin-fin diameter increases. Considering

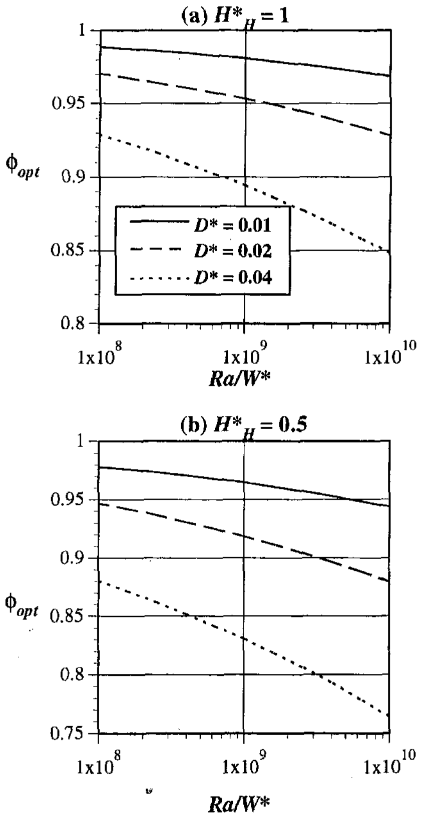

Fig. 6 Optimal porosity ϕ_{opt} as a function of the modified Rayleigh number Ra/W^* and pin-fin diameter D^*. Pr = 0.7, $\kappa = 7.5 \times 10^3$, $L^* = 0.2$, $\Gamma = 1$.

the optimal region in Fig. 5, the concept of a constant heat transfer area is valid in an approximate sense.

3.3 Single-Parameter Optimization. The regime map of Fig. 5 suggests that the temperature rise can be minimized with respect to the heat-sink porosity and the pin-fin diameter. For many designs, either of the foregoing parameters may be fixed. For instance, the pin-fin diameter may be fixed by manufacturing constraints, or the porosity may be constrained by weight considerations.

In the case of fixed pin-fin diameter, the temperature rise can be minimized with respect to the heat-sink porosity as described in Section 2.5. Figure 6(*a*) illustrates the variation of the optimal porosity for a system without a chimney ($H^*_H = 1$) and for several pin-fin diameters. The optimal porosity decreases with increasing Rayleigh number. Thus, as the buoyancy force increases, the compromise between surface area and local heat transfer shifts in favor of surface area. Similar behavior has been predicted for forced convection (Bejan and Morega, 1993), where the driving force is the applied pressure gradient.

For chimney systems (Fig. 6(*b*)) the optimal porosities are less than those for systems without chimneys (Fig. 6(*a*)). Again, the effect can be explained through the concept of heat transfer surface area. As a portion of the heat sink is replaced by a chimney, the total surface area for heat transfer decreases. In order to recoup some of the lost area, the optimal chimney system's porosity decreases.

The effect of the pin-fin diameter on the optimal porosity may explain some of the apparent inconsistencies in previous work. Zografos and Sunderland (1990) used $0.017 \leq D^* \leq 0.034$ and found an optimal porosity of about 0.90 (although higher-porosity heat sinks were not considered). Conversely, Sparrow and Vemuri (1985) used $D^* = 0.08$ and found an optimal porosity of about 0.85. Figure 6, in which decreasing optimal porosities are shown for increasing pin-fin diameters, provides some insight into the apparent disagreement. In general, the pin-fin diameter of a free-convection heat sink should be established before calculating the optimal porosity.

The temperature rise can also be minimized with respect to the pin-fin diameter, when the heat-sink porosity is fixed. Figure 7(*a*) illustrates the variation of the optimal pin-fin diameter for a system without a chimney and for several porosities. Again, as the buoyancy force increases, the compromise between surface area and local heat transfer shifts in favor of surface area, producing smaller optimal diameters for a given porosity.

For chimney systems (Fig. 7(*b*)) the optimal pin-fin diameters are less than those for systems without chimneys (Fig. 7(*a*)). Again, the effect can be explained by considering the total surface area for heat transfer, $A_{\text{fins}} \sim H^*_H(1 - \phi)/D^*$. As the heat-sink height H^*_H decreases, the pin-fin diameter D^* decreases to partially compensate for the lost area.

3.4 Upper Limits of Heat Transfer. Having shown that the heat-sink porosity ϕ and the pin-fin diameter D^* can be individually optimized, we now focus on optimizing both simultaneously. The objective here is not to provide extensive design curves for optimal designs, but rather, to define the upper limits of heat transfer, using optimization as a tool.

The results of a dual-parameter optimization are shown in Fig. 8. In the dual-parameter optimization, the variations of D^*_{opt} and ϕ_{opt} with respect to Ra/W^* are similar to those of the single-parameter optimization. In general, the optimal pin-fin diameters are smaller than those commonly used in actual applications, while the optimal porosities are larger than usual.

The variation of the maximum temperature rise with respect to the heat-sink height is shown in Fig. 9. In the figure, $\theta_{\text{max,opt}}$

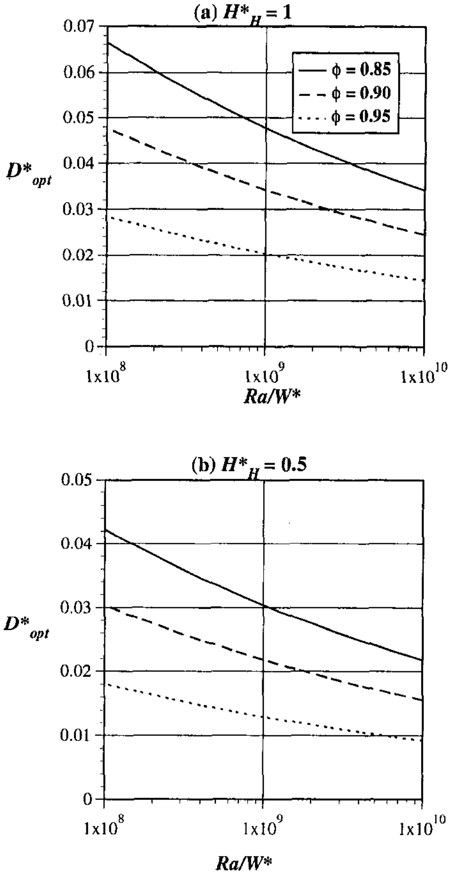

Fig. 7 Optimal pin-fin diameter D^*_{opt} as a function of the modified Rayleigh number Ra/W^* and porosity ϕ. Pr = 0.7, $\kappa = 7.5 \times 10^3$, $L^* = 0.2$, $\Gamma = 1$.

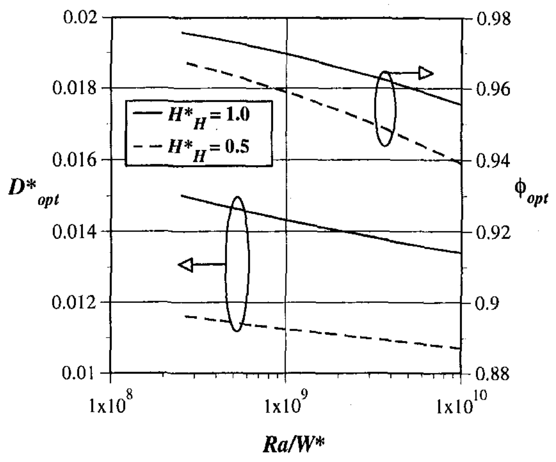

Fig. 8 Optimal pin-fin diameter D^*_{opt} and optimal porosity ϕ_{opt} as functions of the modified Rayleigh number Ra/W^*. Pr = 0.7, $\kappa = 7.5 \times 10^3$, $L^* = 0.2$, $\Gamma = 1$.

represents the maximum temperature rise under optimal geometric conditions, $D^* = D^*_{\mathrm{opt}}$ and $\phi = \phi_{\mathrm{opt}}$. In other words, $\theta_{\mathrm{max,opt}}$ represents the minimum value of the maximum heat-sink temperature rise. The variation of $\theta_{\mathrm{max,opt}}$ with H^*_H is shown for several Rayleigh numbers. Figure 9 illustrates that $\theta_{\mathrm{max,opt}}$ varies only slightly (less than ten percent) with the heat-sink height for all Rayleigh numbers considered. The invariance of $\theta_{\mathrm{max,opt}}$ with H^*_H suggests that, for a system of fixed overall height H, a portion of the heat sink can be replaced by a chimney without compromising thermal performance.

Finally, we compare the present results with previous work on plate-fin heat sinks to ascertain the upper limits of heat transfer from free-convection systems. Fisher et al. (1997) analytically studied free convection from isothermal parallel-plate fins and showed that a ridge of maximum heat transfer exists when the plate spacing and heat-sink height H^*_H are varied. The ridge described by Fisher et al. (1997) is analogous to the invariance of $\theta_{\mathrm{max,opt}}$ with respect to H^*_H (see Fig. 9) in the present study.

Because the previous work on plate fins considered isothermal boundary conditions, a direct comparison to the present work is not possible. However, a minimum thermal resistance can be defined as follows to provide an approximate basis of comparison

$$\mathcal{R}_{\min} = \frac{\theta_{\mathrm{ave,opt}}}{\mathrm{Ra}} = \frac{\Delta T_{\mathrm{ave,opt}} H k_f}{Q_{\mathrm{tot}}} \tag{24}$$

where $\Delta T_{\mathrm{ave,opt}}$ is the average temperature difference between the heat sink and the external ambient fluid. For the case of isothermal plates, $\Delta T_{\mathrm{ave,opt}}$ is simply the difference between the plate and ambient temperatures. For pin-fins, $\Delta T_{\mathrm{ave,opt}}$ is taken as the temperature at the vertical midpoint of the heat-sink base. In both cases, optimal geometric configurations are used. Noting that the "optimal" temperature for pin-fin heat sinks varies only slightly with heat-sink height (see Fig. 9), a representative value of $H^*_H = 0.6$ has been chosen for the comparisons with other types of heat sinks.

Fisher et al. (1997) showed that the optimal ridge for plate-fin heat sinks, assuming high-conductivity infinitesimally thin fins, is described by

$$\mathcal{R}_{\min} = [0.22\,\mathrm{Ra}\,\mathrm{Pr}(L^*W^*)^2]^{-1/3}. \tag{25}$$

A similar equation may be obtained by assuming ideal heat transfer with inviscid flow. Consider a chimney system in which all heat transfer occurs at the entrance. Taking the solid-to-fluid temperature rise within the infinitesimally thin heat sink to be zero, the contraction ratio Γ to be unity, and assuming zero pressure drop across the heat sink, Eq. (4) becomes

$$0 = \frac{-\rho_0}{2}U^2 + \rho_0 g\beta H(T_2 - T_0). \tag{26}$$

Then, using the energy balance of Eq. (6) and dimensionless variables, Eq. (26) can be written as

$$\mathcal{R}_{\min,\mathrm{ideal}} = [2\,\mathrm{Ra}\,\mathrm{Pr}(L^*W^*)^2]^{-1/3}. \tag{27}$$

The only difference between Eqs. (25) and (27) is the numerical coefficient preceding Ra. Thus, the minimum thermal resistance of the plate-fin system is a factor of $(2/0.22)^{1/3} = 2.1$ higher than the ideal system. For pin-fin systems, a concise equation describing the minimum thermal resistance has not been derived due to the numerical nature of the optimization procedure. Thus, the minimum resistance is computed using a representative heat-sink height as described above.

In Fig. 10, the variation of the minimum thermal resistance $\mathcal{R}_{\min}$ with the modified Rayleigh number Ra is shown for optimal pin-fin and plate-fin systems, as well as the ideal system. The figure shows that the pin-fin results closely match those of the previous plate-fin work. Thus, under optimal geometric

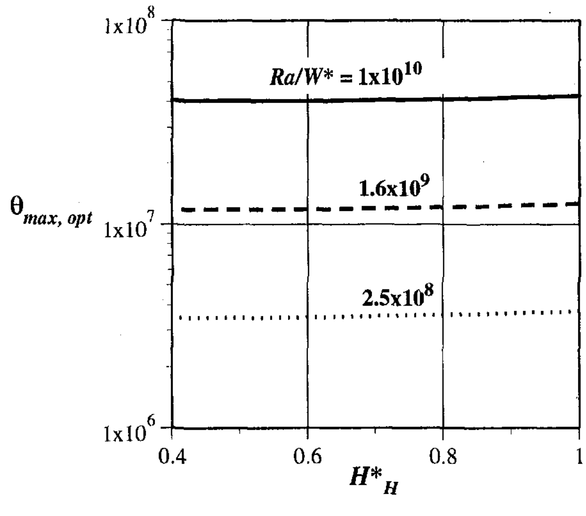

Fig. 9 Maximum temperature rise under optimal conditions $\theta_{\mathrm{max,opt}}$ as a function of the heat-sink height H^*_H and the modified Rayleigh number Ra/W^*. Pr = 0.7, $\kappa = 7.5 \times 10^3$, $L^* = 0.2$, $\Gamma = 1$.

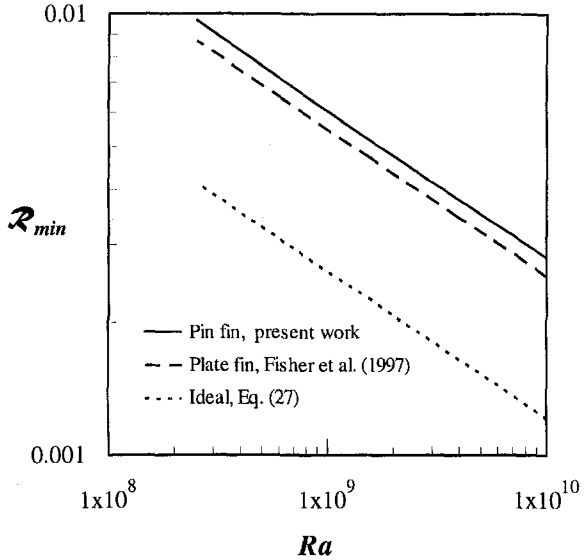

Fig. 10 Minimum thermal resistance $\mathcal{R}_{\min}$ as a function of the modified Rayleigh number Ra. Pr = 0.7, $\kappa = 7.5 \times 10^3$, $W^* = 1$, $L^* = 0.2$, $\Gamma = 1$.

conditions, the present results suggest that plate fins and pin fins can produce roughly equivalent thermal performance. Furthermore, the minimum thermal resistance of both heat-sink types is limited to about twice the ideal thermal resistance described by Eq. (27).

The foregoing results can be used in the design of cooling systems. For instance, one can use $\mathcal{R}_{\min} \approx 2\mathcal{R}_{\min,\mathrm{ideal}}$, with $\mathcal{R}_{\min,\mathrm{ideal}}$ obtained from Eq. (27), to determine whether or not a conventional heat sink in free convection will provide sufficient cooling for a given application.

4 Conclusions

The analytical nature of the present work allows broad parameter variations and a semi-analytical determination of optimal geometries. The results show that, for electronic packaging applications, the optimal heat-sink porosities are generally greater than 90 percent. However, the optimal porosity is strongly dependent on the pin-fin diameter, as shown in Fig. 6, with the optimal porosity decreasing with increasing pin-fin diameter and Rayleigh number.

The chimney effect was shown to enhance local heat transfer such that the minimum temperature rise remains approximately invariant while the height of the heat-sink relative to the total system height is reduced (see Fig. 9). In effect, this phenomenon would allow a designer to reduce the total heat-sink volume and weight without compromising thermal performance.

The present work has shown that the design of pin-fin heat sinks can be optimized by properly choosing the pin-fin diameter and the heat-sink porosity, and the resulting optimized heat transfer describes the limits of free-convection cooling. Also, when optimized, both plate-fin and pin-fin heat sinks can produce roughly equivalent thermal performance. The minimum thermal resistance for conventional heat sinks was shown to be about two times higher than the ideal limit based on inviscid flow with idealized local heat transfer. Consequently, thermal design engineers can assess the feasibility of free-convection cooling more easily and rapidly.

Acknowledgments

The present work was funded by the Industry-Cornell University Alliance for Electronic Packaging, with corporate support from AMP, DEC, IBM, and 3M. TSF was supported by a graduate fellowship from the Semiconductor Research Corporation. The authors thank Prof. F. K. Moore and Dr. K. K. Sikka for helpful conversations, and Prof. D. L. Koch for providing numerical data.

References

Aihara, T., Maruyama, S., and Kobayakawa, S., 1990, "Free Convective/Radiative Heat Transfer from Pin-Fin Arrays with a Vertical Base Plate (general representation of heat transfer performance)," *International Journal of Heat and Mass Transfer*, Vol. 33, No. 6, pp. 1223–1232.

Armstrong, J., and Winstanley, D., 1988, "A Review of Staggered Array Pin Fin Heat Transfer for Turbine Cooling Applications," ASME *Journal of Turbomachinery*, Vol. 110, pp. 94–103.

Bejan, A., and Ledezma, G. A., 1996, "Thermodynamic Optimization of Cooling Techniques for Electronic Packages," *International Journal of Heat and Mass Transfer*, Vol. 39, No. 6, pp. 1213–1221.

Bejan, A., and Morega, A. M., 1993, "Optimal Arrays of Pin Fins and Plate Fins in Laminar Forced Convection," ASME JOURNAL OF HEAT TRANSFER, Vol. 115, pp. 75–81.

Ergun, S., 1952, "Fluid Flow Through Packed Columns," *Chemical Engineering Progress*, Vol. 48, p. 93.

Fisher, T. S., Torrance, K. E., and Sikka, K. K., 1997, "Analysis and Optimization of a Natural Draft Heat Sink System," *IEEE Transactions on Components, Packaging and Manufacturing Technology—Part A*, Vol. 20, No. 2, pp. 111–119.

Gaddis, E. S., and Gnielinski, V., 1985, "Pressure Drop in Cross Flow Across Tube Bundles," *International Chemical Engineering*, Vol. 25, No. 1, pp. 1–15.

Jubran, B. A., Hamdan, M. A., and Abdualh, R. M., 1993, "Enhanced Heat Transfer, Missing Pin, and Optimization for Cylindrical Pin Fin Arrays," ASME JOURNAL OF HEAT TRANSFER, Vol. 115, pp. 576–583.

Koch, D. L., and Ladd, A. J. C., 1997, "Moderate Reynolds Number Flows Through Periodic and Random Arrays of Aligned Cylinders," *Journal of Fluid Mechanics*, in review.

Moore, F. K., 1976, "Dry Cooling Towers," *Advances in Heat Transfer*, Vol. 12, Academic Press, New York, pp. 1–74.

Nield, D. A., and Bejan, A., 1992, *Convection in Porous Media*, Springer-Verlag, New York.

Sangani, A. S., and Acrivos, A., 1982, "Slow Flow Past Periodic Arrays of Cylinders with Application to Heat Transfer," *International Journal of Multiphase Flow*, Vol. 8, No. 3, pp. 193–206.

Shaukatullah, H., Storr, W. R., Hansen, B. J., and Gaynes, M. A., 1996, "Design and Optimization of Pin Fin Heat Sinks for Low Velocity Applications," *SEMI-THERM XII*, Austin, TX, pp. 151–163.

Sparrow, E. M., and Vemuri, S. B., 1985, "Natural Convection/Radiation Heat Transfer from Highly Populated Pin Fin Arrays," ASME JOURNAL OF HEAT TRANSFER, Vol. 107, pp. 190–197.

Taylor, M. T., 1984, "Experimental Comparison of Pin Fin Configurations for Extended Surface Heat Transfer in Space Applications," *Proceedings of the 4th International Electronics Packaging Conference*, Baltimore, MD, pp. 441–467.

Zografos, A. I., and Sunderland, J. E., 1990, "Natural Convection from Pin Fin Arrays," *Experimental Thermal and Fluid Sciences*, Vol. 3, No. 4, pp. 440–449.

Zukauskas, A., 1987, "Convective Heat Transfer in Cross Flow," *Handbook of Single-Phase Convective Heat Transfer*, John Wiley and Sons, New York, Chapter 6.

G. F. Naterer
Assistant Professor of
Mechanical Engineering,
Lakehead University,
Thunder Bay P7B 5E1 Canada
Assoc. Mem. ASME

W. Hendradjit
Graduate Research Assistant

K. J. Ahn[1]
Ph.D. Candidate

J. E. S. Venart
Professor of Mechanical Engineering

University of New Brunswick,
Fredericton, NB E3B 5A3, Canada

Near-Wall Microlayer Evaporation Analysis and Experimental Study of Nucleate Pool Boiling on Inclined Surfaces

Boiling heat transfer from inclined surfaces is examined and an analytical model of bubble growth and nucleate boiling is presented. The model predicts the average heat flux during nucleate boiling by considering alternating near-wall liquid and vapor periods. It expresses the heat flux in terms of the bubble departure diameter, frequency and duration of contact with the heating surface. Experiments were conducted over a wide range of upward and downward-facing surface orientations and the results were compared to model predictions. More active microlayer agitation and mixing along the surface as well as more frequent bubble sweeps along the heating surface provide the key reasons for more effective heat transfer with downward facing surfaces as compared to upward facing cases. Additional aspects of the role of surface inclination on boiling dynamics are quantified and discussed.

Introduction

Boiling heat transfer along inclined surfaces arises in a variety of important industrial applications. For example, materials processing technologies encounter boiling problems during quenching mechanisms. Industrial problems involving chemical processing, pressure vessel transportation, plant thermalhydraulic problems, and electronic equipment design are further examples where boiling heat transfer on inclined surfaces occurs. In pool boiling problems, the fluid is initially quiescent near the heating surface and subsequent fluid motion arises from free convection and the circulation induced by bubble detachment and buoyancy. As the wall superheat, ΔT, increases (i.e., difference between wall and saturation temperature), the free convection and nucleate, transition, and film boiling modes along the boiling curve (Incropera and Dewitt, 1996) may be observed. A comprehensive historical review of the physical understanding of boiling phenomena is provided by Nishikawa (1984).

In the nucleate boiling region, vapor bubbles form and grow at nucleation sites on the surface. Early studies by Corty and Foust (1955) postulated that initial bubbles emerge from cavities where a gas or vapor phase already exists. As further heating occurs, more vapor forms and eventually a bubble emerges and departs from the cavity. Carey (1992) has reported that bubble growth occurs from evaporation of a liquid microlayer under or around the bubble and researchers such as Judd and Hwang (1976) have verified this mechanism. Studies by Han and Griffith (1965) postulated that each bubble carries away liquid superheat from a surrounding region $2D_b$ (D_b = bubble diameter) and heat transfer in the order of natural convection occurs between bubbles. Tien (1962) suggested that a boundary layer forms over the ascending bubble. After the bubble detaches, the liquid surges into the cavity and its higher heat capacity and conductivity leads to an increase in the local heat transfer rate. The liquid flow over the cavity traps the vapor remnant which then acts as the source for the next bubble. As the nucleation site density increases with further heating, discrete bubbles change to continuous vapor columns due to bubble coalescence; circulating liquid flows downward towards the surface between these vapor columns.

Many simultaneous mechanisms occur during bubble formation. At low (near or subatmospheric) pressures, major contributions to the heat flux occur when the microlayer evaporates and colder liquid rushes into contact with the heating surface. However, Cooper (1969) showed that at pressure above 1 atm for fluids such as water, hydrocarbons, and cryogens, this microlayer evaporation has a less significant influence on heat transfer in comparison to other effects such as sensible heat transfer. Researchers such as Liaw and Dhir (1989) have identified distinct regions of vapor transport for boiling on vertical and horizontal surfaces: (i) wall-dominated, (ii) intermediate, and (iii) vapor flow regions. Additional studies for vertical surfaces by Vijaykumar and Dhir (1992) employed holographic and interferometric techniques and observed the presence of ripples and waves along a finite vapor layer near the surface. Thermocapillarity may also occur. In subcooled liquids, small temperature differences across the bubble, due to evaporation on the hot side and conduction on the cold side, may lead to varying surface tension at the bubble's edge thereby inducing convection currents in the surrounding liquid and expediting microlayer evaporation. The relative importance of these simultaneously acting mechanisms is not well expressed by current theories despite significant recent approaches (i.e., see Mei, Chen, and Klausner (1995a, b)).

The influence of orientation on the nucleate boiling processes has only been recently examined. Jung, Venart, and Sousa (1987) as well as Hendradjit (1996) extended Rohsenow's (1952) early correlations to inclined surfaces. Fujita et al. (1988) also studied nucleate boiling between inclined rectangular surfaces. If the gap size between the surfaces decreases below a critical width, then heat transfer decreases because the liquid contact with the surface is obstructed by a compressed vapor layer near the surface. For inclined surfaces, bubble growth begins in a cavity and the bubble formed begins to slide

---

[1] deceased March 24, 1989.

Contributed by the Heat Transfer Division for publication in the JOURNAL OF HEAT TRANSFER. Manuscript received by the Heat Transfer Division, July 16, 1997; revision received, Apr. 23, 1998. Keywords: Analytical, Boiling, Experimental, Heat Transfer. Associate Technical Editor: M. Sohal.

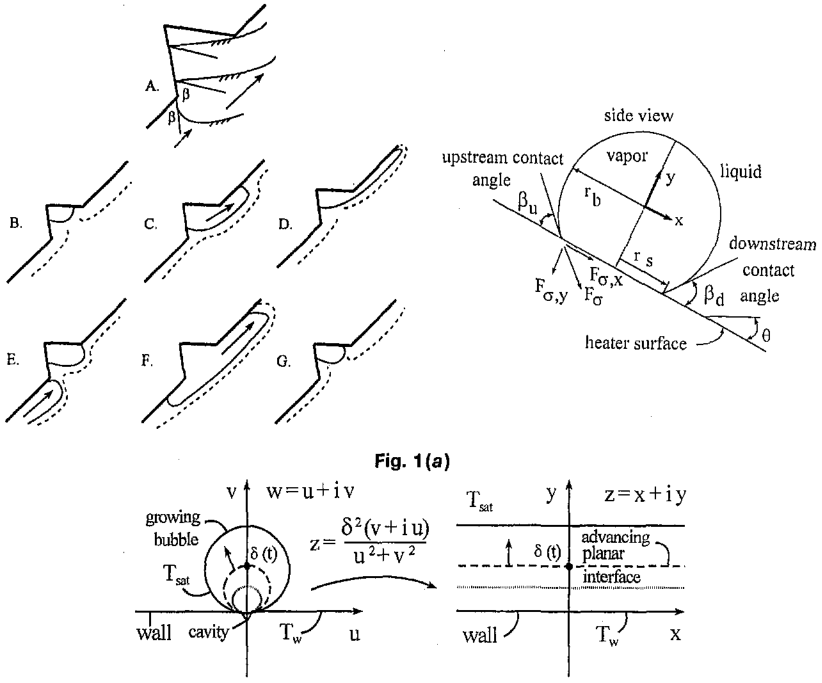

Fig. 1(*a*)

Fig. 1(*b*)

Fig. 1 (*a*) Buble growth schematic for inclined surfaces and (*b*) *w* and *z*-planes

along and away from the cavity's upper edge (Fig. 1(*a*) stages A–D). As the bubble expands and detaches from the wall, the lower vapor-liquid interface advances into the cavity (stages D–E). Adjacent bubbles rise under the action of buoyancy and merge with the remaining gas phase in the cavity (stages E–F). The newly formed larger bubble expands and moves along the surface (stage F). Then the wake of the passing bubble then mixes with the microlayer over the cavity and initiates the next sequence of bubble growth (stage G).

Heat transfer during nucleate boiling is generally attributed to transient conduction to the superheated liquid layer in contact with the heating surface and evaporation of the liquid layer beneath the growing bubble (Mikic and Rohsenow, 1969). Complicated interactions between these processes, such as bubble coalescence and vapor column interactions, have unfortunately limited analytical predictions of such boiling processes. Early work by Rohsenow (1952) predicted the effects of surface tension and pressure on nucleate boiling heat transfer. Vachon, Nix, and Tanger (1968) have modified Rohsenow's empirical exponents and other influences (i.e., surface conditions) have prompted different coefficients. Plesset and Zwick (1954) predicted bubble growth rates but these studies did not examine the resulting coupling with heat transfer. Nishikawa et al. (1984) defined liquid and vapor periods during which one-dimensional conduction solutions were applied for predictions of the nucleate boiling heat flux. Transient bubble growth and phase interface curvature were not considered in the heat transfer analysis. Mikic and Rohsenow (1969) also considered one-dimensional conduction to the liquid after bubble departure and expressed the average heat flux in terms of an empirical correlation for the frequency of bubble departure. Bhat, Prakash, and Saini (1983) apply an additional energy balance across the entire liquid layer to account for transient liquid consumption due to latent heat transfer during vapor generation. This control volume balance effectively transmits the wall heat flux instantaneously to the advancing liquid-vapor interface whereas an interfacial balance would instead balance the actual Fourier heat flux with the latent heat transfer rate at the phase interface. In the present work, the changing liquid layer thickness beneath the bubble is implicitly coupled with the temperature solution through boundary conditions at the wall and phase interface.

The focus of this paper is thus a new model which predicts nucleate boiling heat transfer on inclined surfaces by an analysis of alternating near-wall liquid and vapor periods. Two-dimensional aspects of bubble growth are considered through a transformation between circular and unidirectional planar regions. A transient conduction analysis coupled with an interfacial energy balance predicts the overall heat flux. The results are compared with experimental data for steady-state methanol boiling along a flat surface at various orientations. Further information and understanding of the influence of surface inclination for nucleate and film boiling heat transfer is also provided.

Nomenclature

f = frequency (1/s)
k = conductivity (W/mK)
h = convection coefficient (W/m^2 K)
L = latent heat (J/kg)
t = time (s)
T = temperature (K)
q = heat flux (W/m^2)
x, y = position (z-plane)
u, v = position (w-plane)

Greek

α = thermal diffusivity (m^2/s)
δ = bubble diameter (m)
$\lambda = \delta/(\pi \alpha t_l)$
σ = surface tension (N/m)
θ = wall tilt measured from upward horizontal plane

Subscripts

l, v = liquid, vapor
sat = saturation
w = wall

Heat Transfer Formulation

Rohsenow's (1952) early correlation is widely accepted for nucleate boiling predictions,

$$\frac{c_l(T_w - T_{\text{sat}})}{L} = C_{sf}\left[\left(\frac{q}{\mu_l L}\right)\left(\frac{\sigma}{g(\rho_l - \rho_v)}\right)^{1/2}\right]^r \text{Pr}^s \quad (1)$$

where c_l, L, μ_l, σ, ρ, and Pr refer to specific heat, latent heat, viscosity, surface tension, density, and Prandtl number, respectively. This correlation accounts for factors such as surface characteristics and fluid properties through the constants, C_{sf}, r and s. Jung, Venart and Sousa (1987) have proposed modified coefficients for R-11 on surfaces inclined at an angle θ,

$$r = 0.256 - 1.54 \times 10^{-4}\theta + 1.778 \times 10^{-5}\theta^2 - 7.16^{-8}\theta^3 \quad (2)$$

$$C_{s,f} = 7.218^{-3} - 1.74 \times 10^{-6}\theta. \quad (3)$$

These coefficients were obtained by correlating pool boiling data for inclined surfaces with the exponential form of Rohsenow's model in Eq. (1).

The current work presents an alternative model based on a transient conduction analysis during the alternating periods where liquid and vapor (growing bubble) phases contact the heating surface. The assumptions employed in the analysis are (i) constant wall and bubble temperatures are maintained at T_w and T_{sat} throughout the heating period; (ii) the proportion of time during which the surface is covered with a bubble is exponentially correlated to the degree of superheat between the initial appearance of bubbles and the onset of vapor slugs and columns; (iii) interference effects between adjacent bubbles are neglected except for a single correlation relating vapor phase duration to θ (inclination angle) and ΔT; (iv) the cavity width beneath a bubble is very much smaller than the bubble diameter; (v) the bubble shape may be approximated by a circular cross section; (vi) a lumped capacitance (negligible temperature gradient) approximation is valid within the growing bubble; and (vii) thermocapillarity effects on bubble growth are neglected. In addition, we will assume that two distinct regions in the problem (near-wall or inner diffusion-dominated layer and outer convection region) can allow us to decouple the momentum and energy equations. Inertial effects and bubble mixing cannot be neglected from the problem, but it will be assumed that their influences arise mainly in the outer region. In this way, since the answer of interest (heat flux) is controlled strongly by mechanisms in the inner region, we will examine the energy transport by transient conduction. Rather than a set of complicated interfacial constraints for closure of the inner-outer region solutions, we will use instead an increased vapor duration to include enhanced bubble mixing and convection effects on the inclined surfaces.

The vapor bubble initially emerges from a small cavity where a vapor phase already exists. In the present analysis, this growing circular bubble is modelled through a bilinear transformation (see Fig. 1(*b*)) between the w-plane (eccentric circular bubbles with radii a, δ) and the z-plane (one-dimensional planar regions) in complex coordinates.

$$z = x + iy$$
$$= \left(\frac{\delta^2}{a - \delta}\right)\left(\frac{au}{u^2 + v^2}\right) + i\left(\frac{\delta^2}{a - \delta}\right)\left(\frac{av}{u^2 + v^2} - 1\right) \quad (4)$$

where $i = \sqrt{-1}$. Letting $a \to \infty$ (i.e., outer bubble approximates the wall),

$$z = \left(\frac{\delta^2 u}{u^2 + v^2}\right) + i\left(\frac{\delta^2 v}{u^2 + v^2}\right). \quad (5)$$

In Eq. (5), δ represents the diameter of the growing bubble in the w-plane or the position of the advancing liquid-vapor planar interface in the z-plane. The wall, $v = 0$, and the attached bubble, $4u^2 + 4(v - \delta/2)^2 = \delta^2$, in the w-plane are mapped to the lines $y = 0$ and $y = \delta$, respectively, in the z-plane. Thus, once temperature profiles are determined in the one-dimensional case (z-plane), inferences back to the growing bubble geometry in the w-plane can be obtained.

The following correlations for the bubble departure diameter, frequency, and duration will be used in conjunction with the temperature results for subsequent predictions of the heat flux.

Bubble Departure Diameter (D_b) and Frequency (f). Many correlations have been proposed for the bubble departure diameter, D_b, and most models are based on a balance between buoyant and surface tension forces at the instant of departure. A widely used model that provides close agreement with a wide range of experimental data is

$$D_b = C_2\left[\frac{\sigma}{g(\rho_l - \rho_v)}\right]^{1/2}(\text{Ja})^{5/4} \quad (6)$$

where the empirical factor, $C_2 = 4.65 \times 10^{-4}$, and the Jacob number $\text{Ja} = \rho_l c_l T_{\text{sat}}/(\rho_v L)$ have been employed for a close fit with experimental data for a variety of liquids (Mikic and Rohsenow, 1969).

Previous studies on the bubble departure frequency, f, have generally identified two important regions: (i) the hydrodynamic region where buoyant and drag forces are dominant and (ii) the thermodynamic region where heat transfer effects on bubble growth are dominant. Although correlations for f and D_b are not extensively documented, Cole's model (1967) has been widely used for predictions in the heat transfer region.

$$fD_b = C_3\left[\frac{\sigma g(\rho_l - \rho_v)}{\rho_l^2}\right]^{1/4} \quad (7)$$

where $C_3 = 0.6$ is an average value which best accommodates certain experimental data (Mikic and Rohsenow, 1969); studies indicate that the value varies between $0.15 < C_3 < 0.6$ (Cole, 1967). The current work will show that the model's sensitivity to C_3 is weak and the final steady-state heat flux results do not show a strong dependence on C_3. Equation (7) will be used for the heat transfer region and it will be assumed that the bubble frequency, f, is interpreted as an average value over the entire heating surface.

Direct Trigonometric Model. Experimental findings of Nishikawa and co-workers (1984) have shown that the bubble departure frequency decreases as the surface approaches a downward-facing orientation (i.e., $\theta \to 180$ deg). This observation arises mainly from a larger effective bubble departure diameter in Eq. (7) at higher angles as the bubble elongates along the heating surface. Therefore, we will attempt to directly modify the above departure diameter, and thus indirectly influence the frequency, in order to account for stretching bubbles on inclined surfaces. Since the exact effects of surface angle are not well established (no general prediction method is available to the author's knowledge), the current approximation replaces g with $g \sin \theta$ in order to account for the changing gravitational effects in the force balance leading to Eq. (6). Although this simplification does not capture the detailed effects of bubble dynamics on inclined surfaces, it provides a useful first approximation of the modified role of gravitational forces on departing bubbles. In addition, a more detailed analysis, including the angle-dependent roles of surface tension and contact angles, is provided in the following analysis.

Angled Bubble Contour Model. In this case, consider a departing bubble along an inclined surface, with upstream and downstream contact angles varying with surface inclination (see

Fig. 1(a)). The contact angle between vapor and liquid at the wall (radians), β, varies from the upstream angle, β_u, to the downstream angle, β_d. Also, a linear approximation is employed for the variation of the contact angle along the circumference of the bubble base.

$$\beta_1(\phi) = \beta_u - (\beta_u - \beta_m)\frac{\phi}{(\pi/2)}; \quad \phi < \pi/2 \tag{8}$$

$$\beta_2(\phi) = \beta_m - (\beta_m - \beta_d)\frac{(\phi - \pi/2)}{\pi/2}; \quad \pi/2 < \phi < \pi \tag{9}$$

where ϕ is the circumferential angle around the bubble base (rad) and $\beta_m = (\beta_u + \beta_d)/2$. In the current angled bubble model, it will be assumed that the departing bubble retains the same Jacob number dependence as Eq. (6). Also, based on a variety of experimental results reported by Stephan (1992) the contact angles are assumed to vary linearly from $\beta = 40$ deg (up-facing) to a small angle, $\beta = 5$ deg (down-facing), where further results will be presented in order to assess the model sensitivity to the latter value.

Then, in a manner similar to the derivation of the earlier Rohsenow correlation, Eq. (6), we can perform a force balance, including surface tension, weight and buoyancy forces, in order to estimate the effective diameter of the departing bubble on the inclined surface. The total surface tension force in the x-direction along the front and back portions of the bubble, $F_{\sigma,x}$, acting in the plane of the heated wall, can be represented in the following manner:

$$F_{\sigma,x} = 2\sigma r_s \int_0^{\pi/2} \cos\,[\beta_1(\phi)]\cos\,(\phi)d\phi - 2\sigma r_s \int_{\pi/2}^{\pi} \cos\,[\beta_2(\phi)]\cos\,(\phi)d\phi \tag{10}$$

where r_s is the radius of the assumed circular bubble base. Performing the above integrations, including buoyancy and bubble weight terms, and rewriting the final force balance (x-direction) in terms of the bubble diameter,

$$D_b = C_2\left[\frac{\sigma}{g(\rho_l - \rho_v)}\right]^{1/2}(\mathrm{Ja})^{5/4}\left[\frac{(\beta_u - \beta_d)}{(\cos\beta_u - \cos\beta_d)}\right]^{1/2} \left[\frac{(\beta_u - \beta_d)(1 - \sin\beta_d) + 2\pi\cos\beta_m}{(\beta_u - \beta_d - \pi)(\beta_u - \beta_d + \pi)}\right]^{1/2} \tag{11}$$

where the empirical factors have been obtained by comparison of the analogous horizontal wall result (similar y-direction force balance for $\theta = 0$ deg) to the earlier bubble departure diameter in Eq. (6). Alternatively, the above equation can be obtained from the horizontal wall result, Eq. (6), by replacing g in the following manner.

$$g \rightarrow g\sin\theta\,\frac{(\cos\beta_u - \cos\beta_d)(\beta_u - \beta_d - \pi)(\beta_u - \beta_d + \pi)}{(\beta_u - \beta_d)((\beta_u - \beta_d)(1 - \sin\beta_d) + 2\pi\cos\beta_m)} \tag{12}$$

The factor $g \sin\theta$ illustrates the basis for the earlier approximation in the direct trigonometric model, and the current model effectively provides an additional g correction to account for the changing role of gravity in bubble stretching along the inclined surface. Varying contact angles and modified inclination-dependent forces on departing bubbles have been presented in this section as a possible prediction method for larger bubble departure diameters (departure frequency decreases in Eq. (7)) on inclined surfaces. Despite its limitations with the detailed dynamics of bubble coalescence and mixing, it will be shown that it still provides a reasonable and approximate method for capturing the overall aspects of stretching bubbles and heat transfer on inclined surfaces.

Liquid and Vapor Period Durations (t_l, t_v). The proportion of time during which the surface is covered with bubbles varies between 0 percent (onset of nucleate boiling, subscript onb) and 100 percent (continuous vapor slugs or columns, subscript sc). Assuming an exponential relationship in terms of the wall superheat,

$$\frac{t_{l,v} - C_4}{C_{5,l,v} - C_4} = \left(\frac{\Delta T - \Delta T_{\mathrm{onb}}}{\Delta T_{\mathrm{sc}} - \Delta T_{\mathrm{onb}}}\right)^{\chi(\theta)} \tag{13}$$

where the specific values of the constants C_4 and C_5 in Eq. (13) will be determined by matching the limiting cases at ΔT_{onb} and ΔT_{sc} to appropriate heat flux results. The exponent on the right side of Eq. (13), χ, will be allowed to vary with surface inclination, θ, in order to capture important bubble interaction processes. At a fixed ΔT, the duration and proportion of time during which vapor covers a particular location increases as θ increases.

This trend may be attributed to two factors, corresponding to moderate and high surface angles. For example, slower cessation of nucleating bubbles on downward-facing surfaces will increase the vapor period duration. Downward-facing surfaces inhibit bubble detachment because the bubble driving force for detachment and departure, upward buoyancy, is stalled by the opposing solid wall. In addition, at high inclination angles (i.e., $\theta \rightarrow 180$ deg), the opposing solid wall inhibits upward vapor motion and more bubbles must sweep along the surface. As a result, more upstream bubbles pass by any particular location; in other words, the overall proportion of time where vapor covers the location increases. The above effects act simultaneously to prolong t_v as θ increases.

The current analysis assumes that $\chi(\theta) = (1 - \theta/180)^2$. This formulation is based on earlier work by Nishikawa et al. (1984) where it was shown that the vapor period duration increases with surface inclination. The proportion of time during which a specific location is covered with a bubble is represented by the relative vapor proportion of total liquid and vapor periods, and therefore, if the vapor period increases, it occurs at the expense of a shorter liquid contact time. In other words, if the above vapor contact time increases, then the relative proportion of liquid contact time is reduced at higher angles. In addition, the experimental results (Nishikawa et al., 1984) indicate that the slope of the average vapor period with respect to the heat flux (or wall superheat in the nucleate boiling region) under a logarithmic scaling decreases in an approximately quadratic manner for increasing wall inclinations.

The individual liquid and vapor periods will now be considered. During the liquid period, sensible heat is extracted by transient conduction from the wall to the liquid. Bubbles then grow from surface cavities and the thin microlayer beneath the bubble evaporates during the vapor period.

(i) Liquid Period Analysis

Heat transfer during the liquid period is governed by the transient conduction equation.

$$\frac{\partial T}{\partial t} = \alpha\frac{\partial^2 T}{\partial y^2} \tag{14}$$

$$\text{subject to} \quad T(y, 0) = T_{\mathrm{sat}}; \quad T(0, t) = T_w \tag{15}$$

A similarity solution (Incropera and Dewitt, 1996) gives the temperature profiles and wall heat flux.

$$\frac{T - T_w}{T_{\mathrm{sat}} - T_w} = \mathrm{erf}\left(\frac{y}{2\sqrt{\alpha t}}\right) \tag{16}$$

$$q''_w = \frac{k(T_w - T_{\mathrm{sat}})}{\sqrt{\pi\alpha t}} \tag{17}$$

At the end of the liquid period, the slope of the temperature profile is $(T_{\text{sat}} - T_w)/\sqrt{\pi\alpha t_l}$. The initial condition for the vapor period is assumed to have a linear profile with this slope.

(ii) Vapor Period Analysis

In this period, the vapor bubble covers the heating surface and a function $\delta(t)$ represents the diameter of the growing bubble. Transient conduction within the microlayer beneath the bubble is governed by the heat conduction equation.

$$\frac{\partial T}{\partial t} = \alpha\frac{\partial^2 T}{\partial y^2} \tag{18}$$

subject to $T(y, t_l) = T_w - \lambda(T_w - T_{\text{sat}})\dfrac{y}{\delta}$;

$$T(0, t) = T_w; \quad T(\delta, t) = T_{\text{sat}} \tag{19}$$

where $\lambda = \delta/\sqrt{\pi\alpha t_l}$. Using Laplace transforms (see Appendix 1),

$$\frac{T_w - T}{T_w - T_{\text{sat}}} = (1-\lambda)\sum_{n=0}^{\infty}\left\{\operatorname{erf}\left[\frac{\delta(2n+1)+y}{2\sqrt{\alpha(t-t_l)}}\right] - \operatorname{erf}\left[\frac{\delta(2n+1)-y}{2\sqrt{\alpha(t-t_l)}}\right]\right\} + \lambda\left(\frac{y}{\delta}\right). \tag{20}$$

From Eq. (5), planar isotherms in Eq. (20) are mapped to circular isotherms about the growing bubble. Defining $T^* = (T_w - T)/(T_w - T_{\text{sat}})$ and extending Eq. (20) to the w-plane,

$$T^* = (1-\lambda)\sum_{n=0}^{\infty}\left\{\operatorname{erf}\left[\frac{\delta(2n+1)+\left(\dfrac{v\delta^2}{u^2+v^2}\right)}{2\sqrt{\alpha(t-t_l)}}\right] - \operatorname{erf}\left[\frac{\delta(2n+1)-\left(\dfrac{v\delta^2}{u^2+v^2}\right)}{2\sqrt{\alpha(t-t_l)}}\right]\right\} + \left(\frac{\lambda v\delta}{u^2+v^2}\right). \tag{21}$$

The wall heat flux is obtained by Fourier's Law and Eq. (20) with the following result.

$$q''_w = \frac{k(1-\lambda)\Delta T}{\sqrt{\pi\alpha(t-t_l)}}\sum_{n=0}^{\infty}\left\{\exp\left[\frac{-(2n\delta+\delta+y)^2}{4\alpha(t-t_l)}\right] + \exp\left[\frac{-(2n\delta+\delta-y)^2}{4\alpha(t-t_l)}\right]\right\} + \frac{k\lambda\Delta T}{\delta} \tag{22}$$

A similar calculation with Eq. (21) reveals that a relationship exists between the wall heat flux in the z-plane ($y = 0$ in Eq. (22)), $q''_{w,z}$, and the heat flux in the w-plane, $q''_{w,w}$.

$$q''_{w,z} = q''_{w,w}\left(\frac{\delta}{u}\right)^2 \tag{23}$$

In other words, the planar heat flux matches the wall heat flux at $u = \delta$ in the eccentric bubble domain. The importance of this observation is that a one-dimensional model represents a heat transfer approximation at a distance of 2 radii from the bubble contact point. A singularity at $u = 0$ exists in the solution because of different temperature specifications at the same location in the mathematical analysis. In the actual problem, this location represents the cavity position but the current analysis does not consider the microscopic nucleation processes within the indented cavity nor the actual three-dimensional bubble geometry.

The average heat flux during a cycle through a liquid to vapor period is then obtained by integration of the previous heat flux expressions over the appropriate time periods.

$$\bar{q}''_w = \frac{1}{t_v}\int_0^{t_l} q''_l(t)dt + \frac{1}{t_v}\int_{t_l}^{t_v} q''_v(t)dt \tag{24}$$

The interfacial constraint requires that the conduction heat transfer balances the rate of latent heat liberation.

$$-k\left.\frac{\partial T}{\partial y}\right|_{y=\delta_-} - \rho L\frac{d\delta}{dt} = -k\left.\frac{\partial T}{\partial y}\right|_{y=\delta_+} \tag{25}$$

where the latter term is neglected due to the lumped capacitance approximation used within the bubble. Using the result from Eq. (20) and rearranging terms,

$$\frac{d\delta}{dt} = \frac{k(1-\lambda)\Delta T}{\rho L\sqrt{\pi\alpha(t-t_l)}}\sum_{n=0}^{\infty}\left\{\exp\left[\frac{-\delta^2(n+1)^2}{\alpha(t-t_l)}\right] + \exp\left[\frac{-\delta^2 n^2}{\alpha(t-t_l)}\right]\right\} + \frac{k\lambda\Delta T}{\rho L\delta}. \tag{26}$$

It can be observed that higher-order terms become negligible in the above summation.

Case 1: $\lambda \ll 1$ (Early Stages of Bubble Growth). Considering the relative magnitude of terms in Eq. (26) by using characteristic values in Eqs. (6)–(7) and Appendix 2, then Eq. (26) can be simplified for the case $\lambda \ll 1$.

$$\frac{d\delta}{dt} = \frac{k\Delta T}{\rho L\sqrt{\pi\alpha(t-t_l)}} \tag{27}$$

subject to the initial condition $\delta(t = t_l) = 0$. Applying this condition and solving Eq. (27),

$$\delta(t) = 2\frac{k\Delta T}{\rho L}\sqrt{\frac{t-t_l}{\pi\alpha}}. \tag{28}$$

This expression is substituted into Eq. (22) to specify the heat flux in terms of the moving liquid-vapor interface.

Integrating Eqs. (17) and (22) and adding the results in Eq. (24),

$$\bar{q}''_w = 2k\Delta T\sqrt{\frac{t_l}{\pi\alpha t_v^2}} + \frac{4k\Delta T}{t_v}\sqrt{\frac{t_v - t_l}{\pi\alpha}}\exp\left[-\frac{1}{\pi}\left(\frac{k\Delta T}{\rho L\alpha}\right)^2\right]. \tag{29}$$

The form of Eq. (13) was constructed to ensure that it tends towards the appropriate limits at ΔT_{onb} at ΔT_{sc}. For example, since $q_l \to q_{\text{conv}}$ (free convection) and $q_v \to 0$ as $\Delta T \to \Delta T_{\text{onb}}$, then the following relationships must hold in Eq. (13).

$$C_4 = t_l(\Delta T_{\text{onb}}) = t_v(\Delta T_{\text{onb}}) = \frac{4}{\pi\alpha}\left(\frac{k}{h}\right)^2 \tag{30}$$

As $\Delta T \to \Delta T_{\text{sc}}$, then $t_l \to 0$ (i.e., $C_{5,l} = 0$) and $t_v \to 1/f$ (i.e., $C_{5,v} = 1/f$) where $1/f$ approximates the departure time (or the duration of a single liquid-vapor cycle). Substituting Eqs. (6)–(13) and (30) into Eq. (29) and rearranging terms allows us to write a single explicit expression for $\bar{q}''_w$ in terms of ΔT where f is as specified by Eq. (7).

$$\overline{q}''_w = \frac{2kf\Delta T}{\sqrt{\pi\alpha}} \left\{ \frac{2k}{h\sqrt{\pi\alpha}} \sqrt{1 - \left(\frac{\Delta T - \Delta T_{\text{onb}}}{\Delta T_{\text{sc}} - \Delta T_{\text{onb}}} \right)^{\chi}} + \frac{2}{\sqrt{f}} \sqrt{\left(\frac{\Delta T - \Delta T_{\text{onb}}}{\Delta T_{\text{sc}} - \Delta T_{\text{onb}}} \right)^{\chi}} \exp\left[-\left(\frac{2k\Delta T}{\rho L\alpha\sqrt{\pi}} \right)^2 \right] \right\} \quad (31)$$

The free-convection coefficient, h, for inclined upward facing surfaces ($0 \le \theta \le 60$ deg) is determined from vertical surface models by replacing g with $g \sin \theta$ (Incropera and Dewitt, 1996). Also, it should be emphasized that although bubble interaction effects are not considered in the above conduction analysis, bubble sweeping motion is modeled through the vapor period correlation in Eq. (13).

Case 2: λ ~ 1 (Late Stages of Bubble Growth). In this instance, the wall heat flux (Eq. (22)) may be simplified to

$$q''_w = 2\,\frac{(\sqrt{\pi\alpha t_l} - \delta)k\Delta T}{\pi\alpha\sqrt{t_l(t - t_l)}} \exp\left[\frac{-\delta^2}{4\delta(t - t_l)} \right] + \frac{k\Delta T}{\sqrt{\pi\alpha t_l}} \quad (32)$$

where the interface position is obtained from the solution of Eq. (26),

$$\delta(t) = \frac{\sqrt{\pi\alpha t_l}(\rho L\pi\alpha - 2k\Delta T)}{2k\Delta T} \left\{ \exp\left[-2\,\frac{k\Delta T}{\rho L\pi\alpha} \sqrt{\frac{t - t_l}{t_l}} \right] - 1 \right\} + \sqrt{\pi\alpha(t - t_l)}. \quad (33)$$

A similar expression to Eq. (31) can be obtained for this case by substituting Eqs. (6)–(13) into Eq. (32) and integrating the result over the entire cycle period. However, a closed-form solution is not available for this case and numerical integration is required in general.

Due to the complexity of the boiling process on inclined surfaces, the above models remain empirical in nature by virtue of their dependence on earlier correlations for bubble diameter and vapor period duration. Despite these limitations, the treatment of various processes, such as angle-dependent bubble forces, has provided a physically based correlating tool for nucleate boiling on inclined surfaces and a useful alternative to previous models for vertical or horizontal surfaces. As a result, it provides a physical basis from which future work with inclined surfaces can launch further developments in nucleate boiling predictions.

Experimental Apparatus and Procedures

Test Facility. Boiling experiments with methanol were conducted for a variety of surface inclinations and wall superheats. The working fluid, methanol, was selected because of its noncorrosive behavior, low boiling point ($T_{\text{sat}} \approx 65$°C), high thermal conductivity (see Appendix 2), good wetting characteristics, and importance in many industrial applications. The apparatus consisted of a heater assembly, fluid container, and additional external equipment. The heater assembly was mounted by a shaft through the walls of the fluid container where observation windows are located on three sides and the top side. These windows were constructed from 12.5-mm thick Lexan and sealed with silicon rubber O-rings. The hollow heater shaft allowed the heater assembly to be readily rotated to provide different surface inclinations. The shaft also provided access for the electrical power system and thermocouples. The external equipment consists of a 220 V three-phase electrical source, switch relay unit, data acquisition system, and auxiliary temperature controller. A heat exchanger in the container condensed the vapor formed during the boiling process and permited steady-state operation. Figure 2(*a*) illustrates the essential features of the equipment.

The heater block (200 mm × 40 mm × 70 mm) was machined from a copper block (see Fig. 2(*b*)). This block was vacuum-brazed to a stainless steel retaining plate and the inner space of the heater box was sealed from the surrounding fluid by a silicon rubber gasket. The space between the heater and the box was filled with ceramic fiber to provide insulation and minimize heat losses. The heater surface dimensions were 200 mm × 40 mm and the surface was polished to an average roughness of 0.0505 μm with an average waviness of 0.0237 μm. These surface roughness parameters for the heater surface were obtained from a survey with the Talysurf 5 System (Talysurf). Twenty cartridge heaters were implanted below the surface. Each cartridge heater had a maximum power and voltage of 450 W and 220 V, respectively, thus providing for surface heat fluxes up to 1 GW/m^2.

Also, 19 thermocouples were located along the lateral axis plane of the heater block on three levels. AWG 38 stainless steel sheathed type T thermocouples were employed. The thermocouples were positioned centrally in 0.5 mm diameter holes through one side of the block. Thermal contact between the thermocouple junction and the heater block was achieved by the use of a copper cement. Figure 2(*c*) illustrates the arrangement of thermocouples. The top view shows the locations of the cartridge heaters as well as the four off-axis and auxiliary thermocouples used to estimate heat losses from the block to the brazed stainless steel surrounding retainer. The side view shows each thermocouple row; the average depths of each row are 6.4 mm, 16.5 mm, and 26.4 mm, respectively.

An HP3497A data acquisition system was employed for thermocouple and power measurements. The HP3497A voltmeter was remotely programmed under the control of an HP 9000 Model 220 computer through an HP interface bus. The HP3497 unpacked the measurement data at the end of each period and converted it to voltages and temperatures. A switch relay unit was used to control the electrical power supply through the HP44422A unit. The watt transducers were F. W. Bell PX-2222BL units with voltage, current and power ratings of 220 V, 12 A, and 4000 W, respectively.

Test Procedures. A steady-state technique was used in the experiments. An incremental increase or decrease in the heater power provides a change of surface temperature, and at each increment, a selected block temperature is monitored until the conditions reach a steady-state. Temperatures below the heater surface are then measured at the steady-state and the heat flux is calculated from the temperature gradients in the block after external heat losses have been estimated.

For the initial nucleate boiling tests, the container was filled with the liquid through the bottom port until the heater was completely immersed for all possible surface orientations. A vent at the top of the container was opened for pressure relief. After a set of cold-run tests for system calibration, the liquid was then heated to a temperature near its saturation temperature at atmospheric pressure. Water was circulated through the condenser coils within the fluid container to condense the vapor formed. For each experiment, the switch relay unit was turned on and the input voltage, current, surface inclination, heater immersion depth, and container pressure noted. Measurements were then recorded at the steady-state; steady-state was assumed after the transient temperature variations of the reference thermocouple (TC#3) declined below $\Delta T = 0.0025$°C. The surface orientation was then altered for the next setting and after measurements were completed for all angles, the power level was increased or decreased and the process repeated.

Uncertainty Estimates. The method of Kline and McClintock (1953) was used to estimate the experimental uncertainty in the heat flux and temperature measurements. The measurement uncertainty, U_q, in the heat flux calculation, q, will be

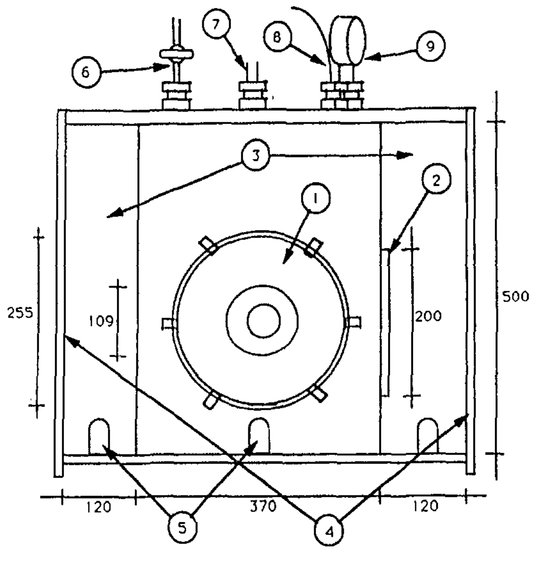

1. Side window and heater's shaft mounting.
2. Front window.
3. Outer perimeter space.
4. Outer shields.
5. Auxiliary heaters for outer perimeter space.
6. Vent pipe with gate valve.
7. Condenser ports.
8. Port for the liquid's temperature measuring thermocouples.
9. Pressure gage.

Fig. 2(*a*)

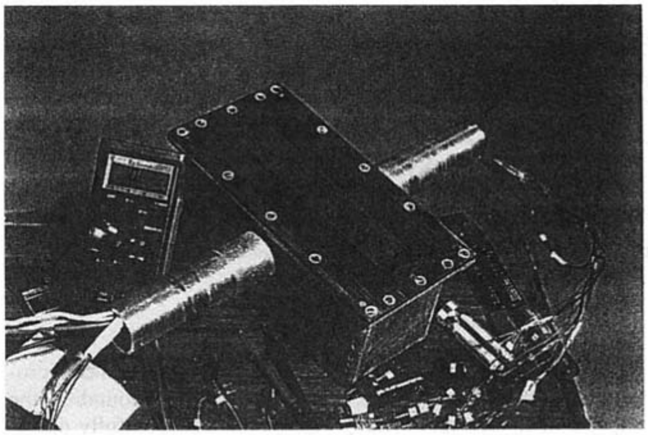

Fig. 2(*b*)

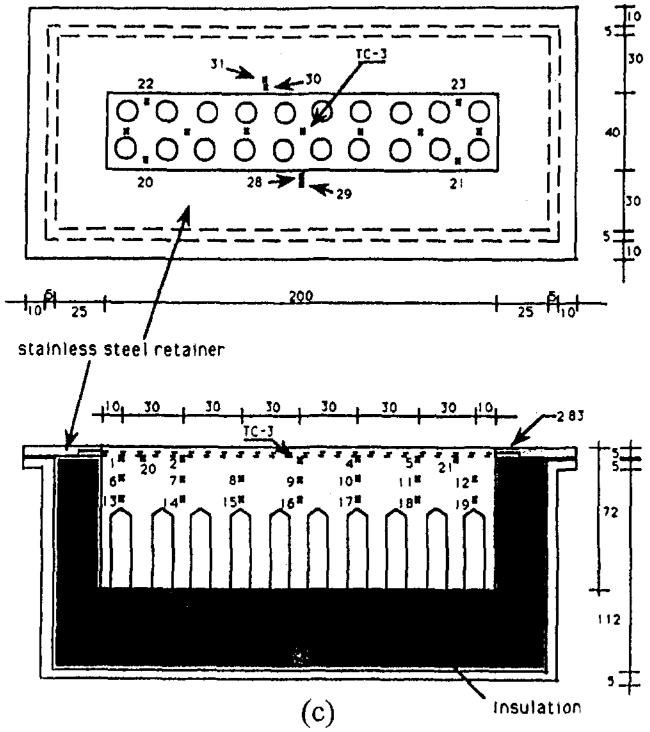

Fig. 2(*c*)

Fig. 2 (*a*) Fluid container with external dimensions (mm), (*b*) heater block, and (*c*) top/side views of heater block with thermocouple arrangement

estimated by the following combination of a precision (random) contribution, P_q, and a bias (fixed) contribution to the uncertainty, B_q,

$$U_q = \sqrt{P_q^2 + B_q^2} \tag{34}$$

A one-dimensional approximation in the heater block was employed for the heat flux calculations at the inclined surface. In the final calculations, the heat transfer rate for a specific surface angle was obtained by subtracting the heat losses through the steel retainer plate from the total heat input. With reference to Fig. 1(*c*), these approximations may be expressed as

$$q = k_{\mathrm{cu}}\left(\frac{T_2 - T_1}{d_2 - d_1}\right) - \left(\frac{T_3 - T_4}{d_3/k_{\mathrm{cu}} + d_4/k_{\mathrm{st}}}\right) \tag{35}$$

where d refers to the position of the thermocouple measurement. The subscripts 1 and 2 refer to row 1 and 2 measurements below the heater surface, respectively, such as locations 5 and 11 in Fig. 1(*c*). Also, the subscripts 3 and 4 refer to the thermocouple locations about the copper-steel interface, such as locations 3 and 28 in Fig. 1(*b*), because the latter term in Eq. (35) is an estimate of the heat loss through the steel retainer in Fig. 1(*c*). Also, the cu and st refer to copper and steel, respectively.

The individual terms in Eq. (34) can be calculated from the propagation equations of Kline and McClintock (1953),

$$P_q^2 = \left(\frac{\partial q}{\partial k_{\mathrm{cu}}}\right)^2 P_{k_{\mathrm{cu}}}^2 + \left(\frac{\partial q}{\partial \Delta d_{12}}\right)^2 P_{\Delta d_{12}}^2 + \left(\frac{\partial q}{\partial R}\right)^2 P_R^2 + \sum_{i=1}^{4}\left(\frac{\partial q}{\partial T_i}\right)^2 P_{T_i}^2 \tag{36}$$

where R refers to the thermal resistance between the copper block and the steel retainer. An equation similar to Eq. (36) is also constructed for the uncertainty in the resistance estimate, P_R. Individual derivatives in Eq. (36) can then be evaluated from Eq. (35), giving the following result:

$$\left(\frac{P_q}{q}\right)^2 = \left(\frac{P_k}{k}\right)^2 + \left(\frac{P_{T_1}}{\Delta T_{12}}\right)^2 + \left(\frac{P_{T_2}}{\Delta T_{12}}\right)^2 + \left(\frac{P_{\Delta d}}{\Delta d}\right)^2 + \left(\frac{P_R}{R}\right)^2 + \left(\frac{P_{T_3}}{\Delta T_{34}}\right)^2 + \left(\frac{P_{T_4}}{\Delta T_{34}}\right)^2. \tag{37}$$

An equation similar to Eq. (37) can also be constructed for the bias limit.

The temperature measurements were estimated to be reliable to ±0.1°C. This error includes the small variation of temperatures at the steady-state, temperature differences between columns at a fixed depth beneath the heating surface as well as

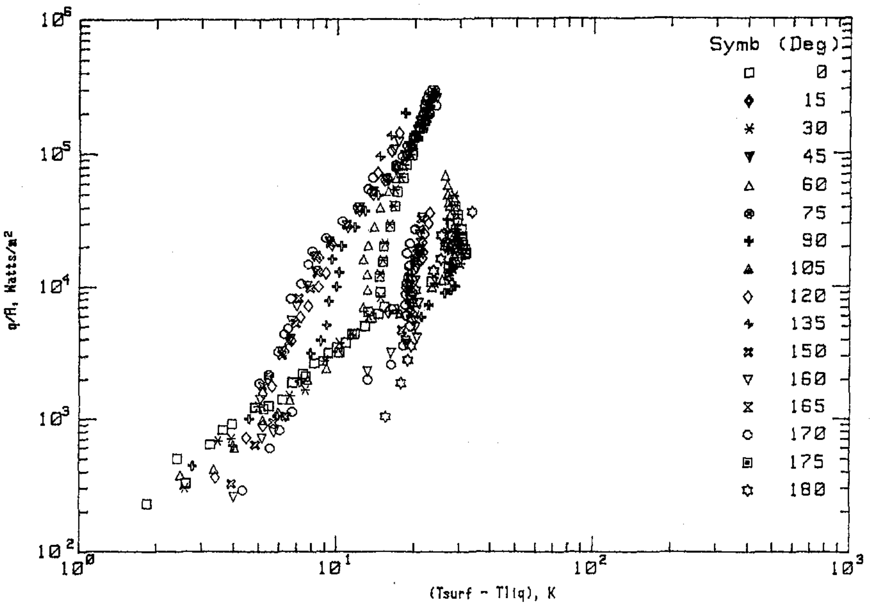

Fig. 3(*a*)

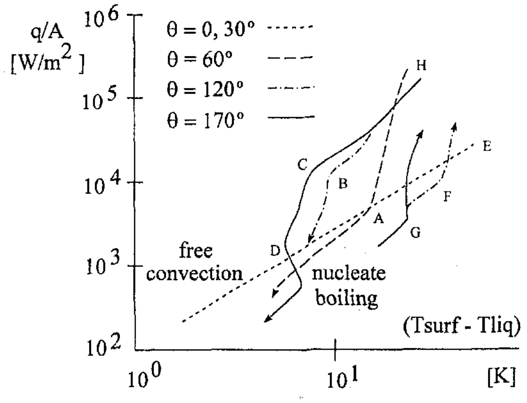

Fig. 3(*b*)

Fig. 3 (*a*) Boiling curve for methanol and (*b*) process sketch for free convection and nucleate boiling regions

discrepancies due to a fluctuating power source. The precision error due to random variations of the thermal conductivity is assumed to be negligible compared to the other precision terms in Eq. (36). The uncertainty in the thermal resistance is calculated under the same set of above estimates. The AWG 38 type T thermocouples were connected to the HP3497A unit through two HP44422A thermocouple acquisition terminal cards with a simulated thermocouple reference junction. The bias error provided by the manufacturer is ±1.0°C. Thermal conductivity data in tables are assumed to be accurate within two percent. The estimated percent bias error due to a constant thermal conductivity assumption over the extrapolation range in Eq. (35) is 3.7 percent. The thermocouple positioning is assumed to be reliable to ±5.9 μm. We can then substitute these error estimates in the above equations and use a set of representative values for typical experimental conditions in order to determine the precision, bias, and uncertainty estimates. As a result, the uncertainties with the extrapolated heater surface temperature and the corresponding heat flux when plotting the boiling curve points are estimated as ±3.7 percent and ±11.3 percent, respectively.

Results and Discussion

The growth, detachment, and movement of a bubble from a horizontal, upwards facing, nucleated site involves the heat transfer from the heated surface through both the liquid microlayer, adjacent to the surface, and the liquid surrounding the vapor dome. Judd and Hwang (1976) have successfully developed such models. The influence of the hydrodynamics of the liquid surrounding the growing bubble has been considered by Mikic, Rohsenow, and Griffith (1970). A basic model for the growth and detachment of bubbles on horizontal upward facing surfaces has been developed by Mei, Chen, and Klausner (1995). However, none of this work has been extended to consider the movement of bubbles along the surface as occurs with inclination. The current results will demonstrate that the use of alternating near-wall liquid and vapor periods provides an effective means to predict these bubble characteristics and resulting heat transfer for inclined surfaces.

The experimental results for the nucleate boiling section of the boiling curve appear in Fig. 3(*a*). Figure 3(*b*) illustrates the predominant trends of the boiling curve in the free-convection and nucleate boiling regions. Point D represents the cessation of nucleate boiling (CNB) for a set of experiments with gradual power reductions, or, alternatively, points below point D cover the free-convection region. For the upward-facing surface ($\theta = 0$), free convection occurs along the line DE even though some active nucleation sites appear during the experiments. At higher inclinations, nucleate boiling occurs and the

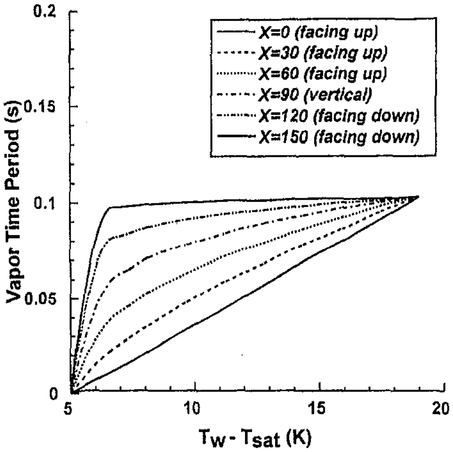

Fig. 4(a)

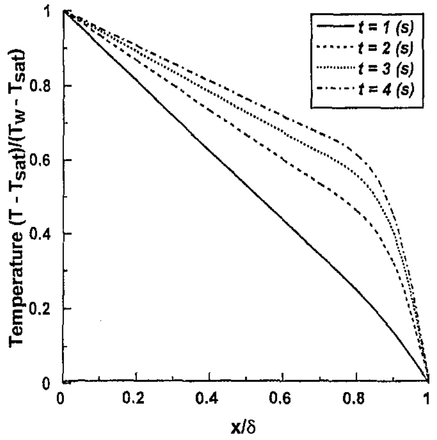

Fig. 4(b)

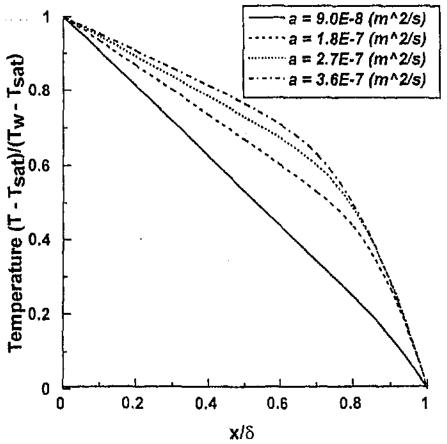

Fig. 4(c)

Fig. 4 Analytical predictions of (*a*) vapor period duration and (*b*)–(*c*) temperature profile sensitivity to different liquid period and thermal diffusivity values

line represents the transition from the CNB point to free convection. In the low heat flux region with nucleate boiling (ABCD), free convection plays an important role because the nucleation sites are sparsely distributed over the surface. A reversal of angular dependence appears below point D because higher inclinations promote the sweeping action of bubbles along the surface during nucleate boiling whereas they reduce the normal velocity components relative to the surface during free convection. In an analogous manner, a reversal appears with the cooling rate between regions AH and ABCD in the high heat flux

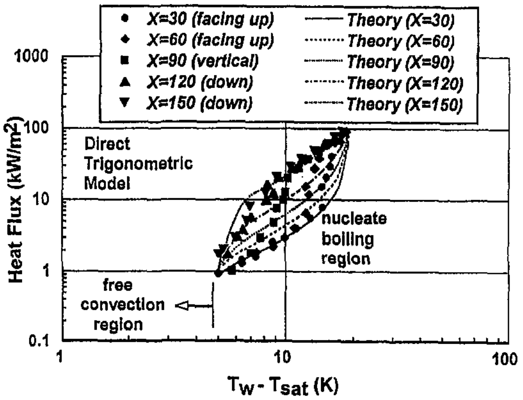

Fig. 5(*a*)

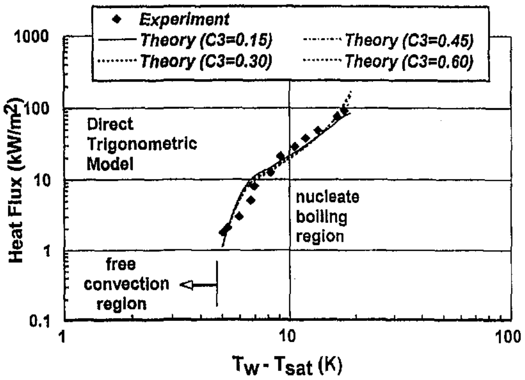

Fig. 5(*b*)

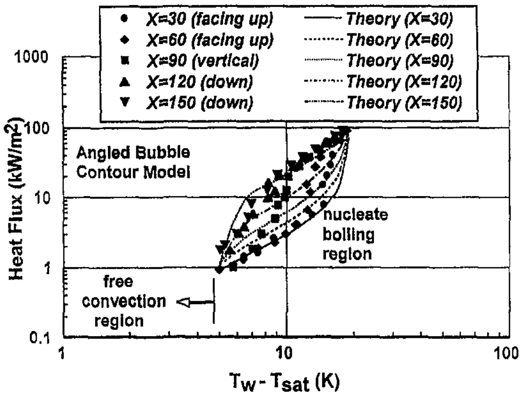

Fig. 5(*c*)

ΔT(°)	β_d = 5°	β_d =11°	β_d = 17°
5.0	1.13	1.13	1.13
6.6	9.78	9.75	9.73
8.1	14.67	14.67	14.67
9.7	20.21	20.26	20.30
11.2	26.59	26.73	26.84
12.8	33.93	34.22	34.44
14.3	42.36	42.87	43.29
15.9	51.92	52.78	53.48
17.4	62.26	63.61	64.73
19	66.26	67.95	69.38

Fig. 5(*d*)

Fig. 5 (*a*) Direct trigonometric models results, (*b*) sensitivity to model constant c_3, (*c*) angled bubble contour models results, and (*d*) heat fluxes (kW/m^2) at θ = 150° for various contact angles

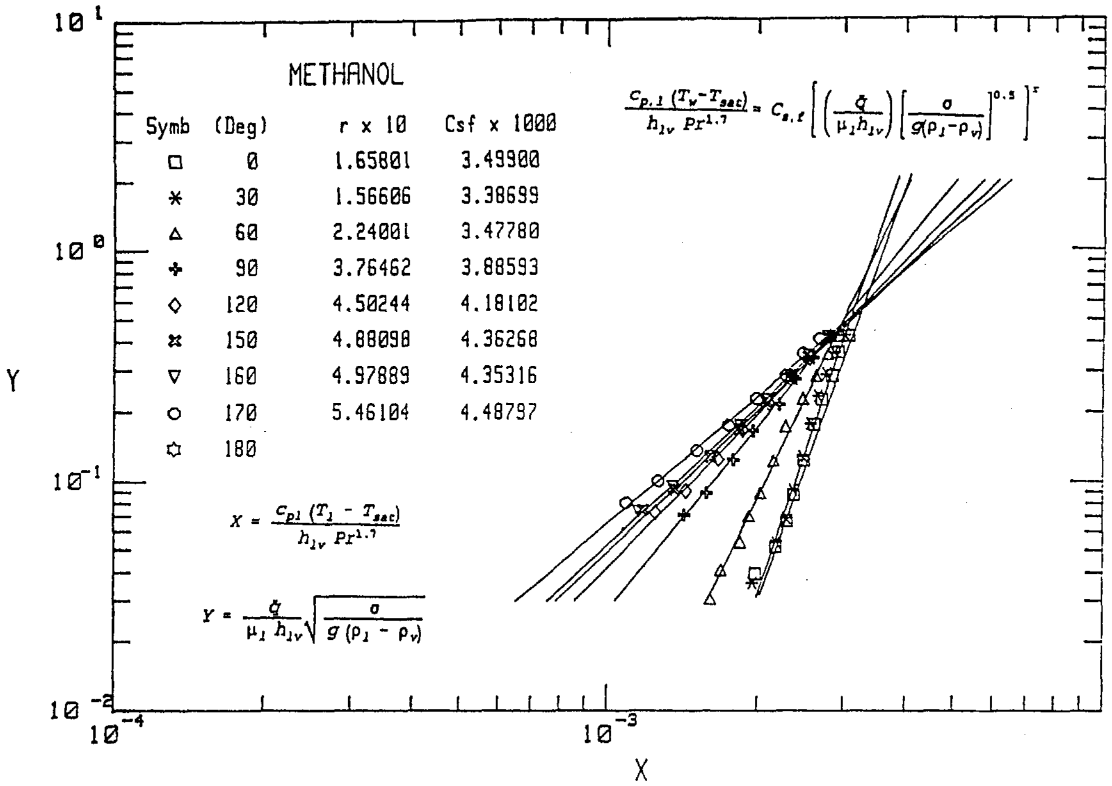

Fig. 6(*a*)

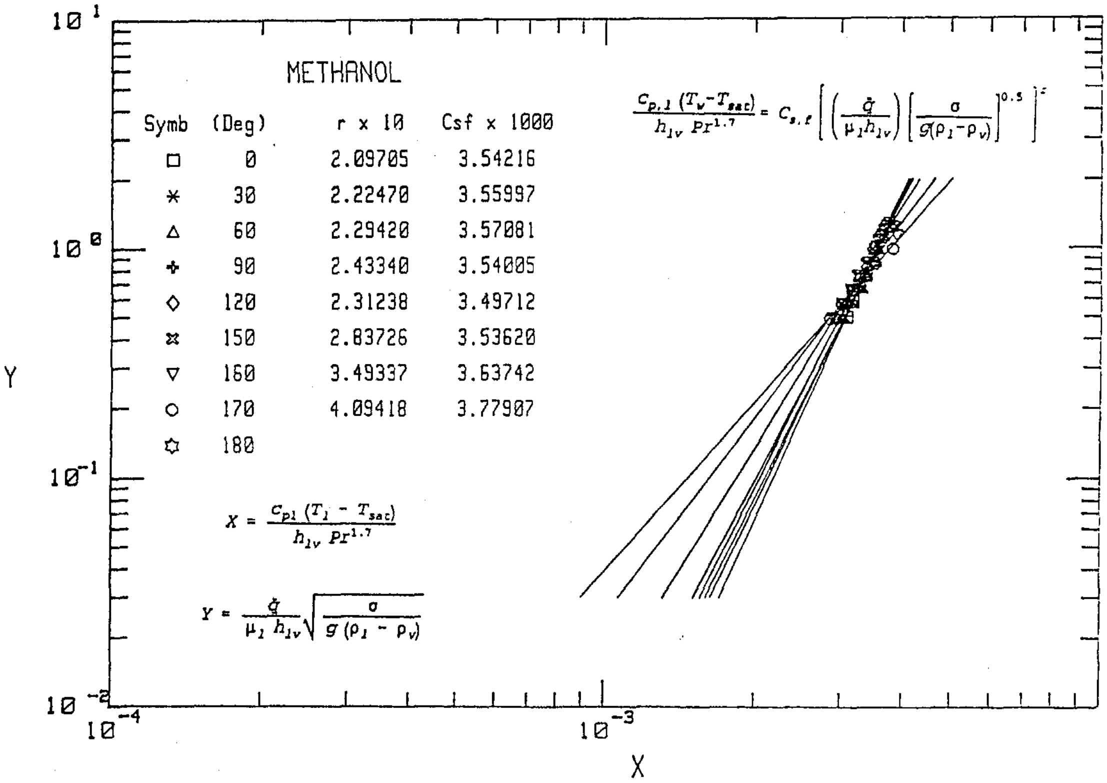

Fig. 6(*b*)

Fig. 6 Comparison between modified Rohsenow correlations and experiments (gradual power decrease procedure)

and low heat flux regions, respectively. In the former case, the most rapid decline of heat flux appears with the upward facing surfaces because bubbles are more easily swept along the surface by buoyancy forces. However, in the lower heat flux region, fewer nucleation sites imply a more active role for free convection. As a result, a more rapid decline of heat flux arises with the downward facing surfaces because small angular changes in these instances allow the flow to accelerate along the surface. These trends can be observed with the change in curvature at points A, B, and C.

Table 1 **(*a*) Free convection, nucleate boiling and (*b*) minimum heat flux and incipience hysteresis points (see Fig. 3(*b*) for process points *A* to *H*)**

Table 1(*a*)

Key point	q W/m^2	ΔT_e C°	h W/(m^2 C°)
A	8 930.	14.5	616.
B	15 920.	9.4	1 700.
C	18 290.	7.8	2 330.
D	~1 500.	~5.0	~300.
E	19 400.	30.8	630.
F	11 450.	27.3	419.
G	5 980.	18.6	322.
H	~100 000.	~19.0	~5 260.

Point **A**, **E**: $\theta = 0$ deg and 30 deg
Point **B**, **F**: $\theta = 90$ deg
Point **C**, **G**: 90 deg $< \theta \leq$ 170 deg
Point **D**: approximate final cessation
Point **H**: nucleate boiling transition

Table 1(*b*)

θ	q (kW/m^2)	h (W/m^2 C)	$\Delta T(e)$ (C)	$\Delta T(e$, icp) (C)	$\Delta T(e$, ces) (C)	$\Delta T(e$, hys) (C)
90	21.22	128.1	165.7	27.3	9.4	17.9
120	18.05	120.8	149.4	21.6	8.3	13.3
150	14.76	83.6	176.5	20.1	8.1	12.0
160	13.05	105.1	124.2	20.9	8.0	12.9
170	9.28	80.27	115.6	18.6	7.8	10.8

(i) Analytical Model of Nucleate Boiling on Inclined Surfaces. Results from the present analytical model appear in Figs. 4–5. Figure 4(a) illustrates the duration of the vapor period for different surface orientations using Eq. (13). The proportion of time during which vapor bubbles cover a particular location at a fixed superheat increases as θ increases because of enhanced bubble sweeping motion along the surface as well as the altered bubble detachment processes at the nucleation site. Examples of predicted dimensionless temperature profiles from Eq. (20) appear in Figs. 4(b–c) for the case $\delta = 0.5$ mm and $t - t_l = 0.01$ s. In Fig. 4(b), the temperature magnitude increases with larger values of the liquid period duration ($1 < t_l < 4$ s). The slope of the initial temperature profile increases for shorter liquid periods and this effect leads to steeper profile for $t_l = 1$ s (solid line). A similar trend is observed in Fig. 4(c) where a smaller thermal diffusivity leads to a steeper temperature profile ($t_l = 1$ s) because the slope of the initial profile increases in the vapor phase solution, Eq. (22).

Figure 5(a) illustrates a comparison between the theoretical predictions of the heat flux (direct trigonometric model) and the experimental data from the boiling curve in Fig. 3(a) for 5 different surface orientations (note: X refers to the surface inclination, θ). The sensitivity of the results to the model constant C_3 is minimal as Fig. 5(b) illustrates the similarity of results for the range of reported C_3 values. Good agreement is achieved in all cases and the correct physical trends are established. Figure 5(c) shows that the predictions yield similar accuracy with the angled bubble contour model, and in this model, the results are not strongly dependent on the specific value of the downstream contact angle (see Fig. 5(d)).

The bubble dynamics along the surface plays an important role in explaining the enhanced heat transfer for higher inclination angles. For example, consider an active nucleation site at stage A in Fig. 1(a). The bubble forms in the cavity (stage B) and its phase interface joins the wall with a contact angle β. The upper liquid-vapor interface rises above the nucleation site (stage C). As a result, the heat transfer decreases because the less conductive vapor covers the site. However, the bubble may elongate (stage D) and coalesce with ascending bubbles below its current position (stage E). The rear liquid-vapor interface surges into the cavity and the wake of the ascending bubble stirs and agitates the microlayer near the nucleation site (stage F). The bubble detachment (stage G) permits additional liquid to fill the cavity, extract heat through evaporation, and generate the next bubble growth sequence. The agitation of the microlayer, more vigorous mixing along the surface and frequent bubble sweeps along the nucleation sites provide the key reasons for the more effective heat transfer in the downward-facing positions. Although bubble interaction effects are neglected in the solution of the energy equation, Eq. (20), this equation effectively models the enhanced microlayer agitation and bubble sweeping motion at elevated inclination angles by defining the appropriate time duration of the vapor phase as θ increases.

In addition to the above analysis, the experimental data was approximated by a least-squares regression in order to examine the applicability of the Rohsenow correlation (1952).

(ii) Modified Rohsenow Equation for Nucleate Boiling on Inclined Surfaces. Using a least-squares regression and a linear approximation of the modified Rohsenow correlation, Eqs. (1)–(3),

$$\log(Y) = -\frac{1}{r}\log(C_{sf}) + \frac{1}{r}\log(X), \qquad (38)$$

where the constants follow from Eq. (1),

$$X = \frac{c_l(T_l - T_{\mathrm{sat}})}{L\,\mathrm{Pr}^{1.7}}; \quad Y = \frac{q}{\mu_l L}\sqrt{\frac{\sigma}{g(\rho_l - \rho_v)}}. \qquad (39)$$

Results from this analysis appear in Fig. 6. In these graphs, r represents the slope of the regression line in X-Y coordinates. In the high heat flux region (i.e., the slugs and columns region), a weak dependence between heat transfer and surface inclination appears as shown in Fig. 6(b). The variations of r and s increase with higher inclination angles but the value of C_{sf} is nearly constant for all angles. Previous studies on methanol have suggested $C_{sf} = 0.0059$ (Vachon, Nix, and Tanger, 1968) whereas the present regression produces results between $0.0035 \leq C_{sf} \leq 0.0045$. Also, Rohsenow determined an exponential value of $r = 0.33$ (1952) but the present regression indicates a large variation in r, i.e., $0.166 \leq r \leq 0.546$. Figure 6(a) indicates that the influence of surface inclination is weak for 0 deg $\leq \theta \leq$ 30 deg but increases significantly for 30 deg $< \theta \leq$ 90 deg. For the downward-facing positions, a small influence appears for 120 deg $\leq \theta \leq$ 160 deg whereas a greater change arises as the inclination approaches $\theta = 170$ deg. In the present analysis, the value $s = 1.7$ was maintained for agreement with Rohsenow's original work (1952) and the values of C_{sf} and r were altered to provide agreement with the experimental data.

Table 1(a) summarizes the key points in the boiling curve as well as the effective convection coefficients (column 4). If the steady-state measurements are observed by a gradual power reduction, then points A, B, and C (see Fig. 3(b)) represent the initial cessation of nucleate boiling (CNB) and point D represents the complete cessation of nucleate boiling and the transition to free convection. For power increases, the onset of nucleate boiling (ONB) initially appears at points F and G (nucleation incipience). An incipience hysteresis (i.e., difference between CNB and ONB points) arises because nucleation sites are inactive during the power increase procedure before the ONB but some sites remain sparsely distributed along the surface in the same region during power reduction. The differences between the superheat levels for nucleation incipience, $\Delta T(e$, icp), and the initial cessation of nucleate boiling, $\Delta T(e$, ces), indicate the observed incipience hysteresis, $\Delta T(e$, hys). These points, as well as the minimum heat flux values for different surface orientations, appear in Table 1(*b*). The hysteresis remains approximately uniform for the upward-facing positions (see Fig. 3(*a*)) but its magnitude declines as the surface approaches the downward-facing position. In the latter case, $\Delta T(e, \text{hys})$ declines because the free convection decreases and hence more heat transfer is directed towards earlier evaporation of the liquid near the heating surface.

Conclusions

An analytical and experimental study of methanol nucleate pool boiling on inclined surfaces has been conducted. The analytical method uses alternating near-wall liquid and vapor periods to estimate the steady-state heat flux from inclined surfaces during this boiling process. The heat flux is expressed in terms of the bubble departure diameter and frequency. Comparisons between the theories and experiments show good agreement in the low heat flux nucleate boiling region where surface inclination plays a dominant role. More vigorous mixing along the surface and more bubble sweeps along the nucleation sites lead to enhanced heat transfer as the surface inclination increases. Further quantitative results are revealed in the reported boiling curve for methanol on inclined surfaces. For example, at $q \approx 100$ kW/m^2, an approximate transition between the isolated bubbles region and the slugs and columns region occurs. In addition to visual confirmation of this transition, a "crossover" point occurs at the transition value where boiling curves at different angles criss-cross one another and spread to wider wall superheats at lower heat fluxes below the transition point.

Acknowledgments

The valuable suggestions from the manuscript review process are gratefully acknowledged.

References

Bhat, A., Prakash, R., and Saini, J., 1983, "Heat Transfer in Nucleate Pool Boiling at High Heat Flux," *Int. J. Heat Mass Transfer,* Vol. 26, pp. 833–840.

Carey, Van P., 1992, *Liquid–Vapor Phase-Change Phenomena,* Hemisphere Publishing Corporation, Washington, DC, pp. 169–298.

Cole, R., 1967, "Bubble Frequencies and Departure Volumes at Subatmospheric Pressures," *AIChE Journal,* Vol. 13, No. 4, pp. 779–783.

Cooper, M. G., 1969, "Microlayer and Bubble Growth in Nucleate Pool Boiling," *Int. J. of Heat Transfer,* Vol. 12.

Corty, C., and Foust, A. S., 1955, "Surface Variables in Nucleate Boiling," *Chemical Engineering Progress,* Symposium Series, Vol. 17.

Fujita, Y., Ohta, H., Uchita, S., and Nishikawa, S., 1988, "Nucleate Boiling Heat Transfer and Critical Heat Flux in Narrow Space Between Rectangular Surfaces," *Int. J. Heat Mass Transfer,* Vol. 31, No. 2, pp. 229–239.

Han, C. Y., and Griffith, P., 1965, "The Mechanism of Heat Transfer in Nucleate Pool Boiling—Parts I and II," *Int. J. Heat Mass Transfer,* Vol. 8, pp. 887–917.

Hendradjit, W., 1996, "Pool Boiling Heat Transfer of Methanol," M.Sc.E. thesis, University of New Brunswick, Fredericton, New Brunswick, Canada.

Incropera, F. P., and Dewitt, D. P., 1996, *Fundamentals of Heat and Mass Transfer,* 4th Ed., John Wiley and Sons, New York.

Judd, R. L., and Hwang, K. S., 1976, "A Comprehensive Model for Nucleate Pool Boiling Heat Transfer Including Microlayer Evaporation," ASME JOURNAL OF HEAT TRANSFER, pp. 623–629.

Jung, D. S., Venart, J. E. S., and Sousa, A. C. M., 1987, "Effects of Enhanced Surfaces and Surface Orientation on Nucleate and Film Boiling Heat Transfer in R-11," *Int. J. Heat Mass Transfer,* Vol. 30, No. 12, pp. 2627–2639.

Kline, S. J., and McClintock, F. A., 1953, "Description of Uncertainties in Single Sample Experiments," *Mechanical Engineering,* Vol. 75, pp. 3–8.

Liaw, S. P., and Dhir, V. K., 1989, "Void Fraction Measurements During Saturated Pool Boiling of Water on Partially Wetted Vertical Surfaces," ASME JOURNAL OF HEAT TRANSFER, Vol. 111, pp. 731–738.

Mei, R., Chen, W., and Klausner, J. F., 1995, "Vapor Bubble Growth in Heterogeneous Boiling—I. Formulation," *Int. J. Heat Mass Transfer,* Vol. 38, No. 5, pp. 909–919.

Mei, R., Chen, W., and Klausner, J., 1995, "Vapor Bubble Growth in Heterogeneous Boiling—II. Growth Rate and Thermal Fields," *Int. J. Heat Mass Transfer,* Vol. 38, No. 5, pp. 921–934.

Mikic, B. B., and Rohsenow, W. M., 1969, "A New Correlation of Pool-Boiling Data Including the Effect of Heating Surface Characteristics," ASME JOURNAL OF HEAT TRANSFER, pp. 245–250.

Mikic, B. B., Rohsenow, W. M., and Griffith, P., 1970, "On Bubble Growth Rates," *Int. J. Heat Mass Transfer,* Vol. 13, pp. 657–666.

Nishikawa, K., 1984, "Historical Developments in the Research of Boiling Heat Transfer," *JSME Int. J.,* Vol. 30, No. 9, pp. 1559–1571.

Nishikawa, K., Fujita, Y., Uchida, S., and Ohta, H., 1984, "Effect of Surface Configuration on Nucleate Boiling Heat Transfer," *Int. J. Heat Mass Transfer,* Vol. 27, pp. 1559–1571.

Plesset, M. S., and Zwick, S. A., 1954, "The Growth of Vapor Bubbles in Superheated Liquids," *J. of Applied Physics,* Vol. 25, No. 4, pp. 693–500.

Rohsenow, W. M., 1952, "A Method for Correlating Heat Transfer Data for Surface Boiling of Liquids," *Transactions of the ASME,* Vol. 74, pp. 969–976.

Stephan, K., 1992, *Heat Transfer in Condensation and Boiling,* Springer-Verlag, Berlin.

Talysurf 5, n.d., Operator's Handbook, Part 50, 240–50, Rank Taylor Hobson, England pp. 1–3.

Tien, C. L., 1962, "Hydrodynamic Model for Nucleate Boiling," *Int. J. Heat Mass Transfer,* Vol. 55, pp. 533–540.

Vachon, R., Nix, G., and Tanger, G., 1968, "Evaluation of Constants for the Rohsenow Pool-Boiling Correlation," ASME JOURNAL OF HEAT TRANSFER, Vol. 90, pp. 239–247.

Vijaykumar, R., and Dhir, V. K., "An Experimental Study of Subcooled Film Boiling on a Vertical Surface—Thermal Aspects," ASME JOURNAL OF HEAT TRANSFER, Vol. 114, pp. 169–178.

APPENDIX 1

Analytic Solution of Heat Equation

Define $T^* = (T_w - T)/(T_w - T_{\text{sat}})$, $x^* = x/\delta$, $\lambda = \delta/\sqrt{\pi \alpha t_l}$, $t^* = (t - t_l)/(t_v - t_l)$ and $a = \alpha \Delta t/\delta^2$. Writing the heat equation and dropping the * superscripts,

$$\frac{\partial T}{\partial t} = a \frac{\partial^2 T}{\partial x^2} \tag{40}$$

$$\text{subject to} \quad T(x, 0) = \lambda x, \quad T(0, t) = 0, \quad T(1, t) = 1. \tag{41}$$

Taking Laplace transforms of both sides in Eq. (41) and rearranging terms,

$$\frac{d^2\hat{T}}{dx^2} - \frac{s}{a}\hat{T} = -\frac{\lambda}{a}x, \tag{42}$$

and finding the complementary solution, $\hat{T}_c(x, s)$, and a particular solution, $\hat{T}_p(x, s)$,

$$\hat{T}_c(x, s) = a_1(s)e^{\sqrt{s/a}x} + a_2(s)e^{-\sqrt{s/a}x} \tag{43}$$

$$\hat{T}_p(x, s) = a_3x^2 + a_4x + a_5. \tag{44}$$

Taking Laplace transforms of Eq. (41) and then finding the unknown coefficients,

$$\hat{T}(x, s) = \left(\frac{1 - \lambda}{s}\right)\left[\frac{\cosh(\sqrt{s/a}x)}{\cosh(\sqrt{s/a})}\right] + \frac{\lambda}{s}x$$

$$= \frac{1 - \lambda}{s}\left[\frac{(e^{\sqrt{s/a}x} - e^{-\sqrt{s/a}x})e^{\sqrt{s/a}}}{(1 - e^{-2\sqrt{s/a}})}\right] + \frac{\lambda}{s}x. \tag{45}$$

A binomial expansion will present the results in an alternative form.

$$(1 - e^{-2\sqrt{s/a}})^{-1} = \sum_{n=0}^{\infty} e^{-2n\sqrt{s/a}} \tag{46}$$

$$\hat{T}(x, s) = \left(\frac{1 - \lambda}{s}\right)\sum_{n=0}^{\infty}\left\{\exp\left[-\sqrt{\frac{s}{a}}(2n + 1 - x)\right] - \exp\left[-\sqrt{\frac{s}{a}}(2n + 1 + x)\right]\right\} + \frac{\lambda}{s}x \tag{47}$$

Taking inverse Laplace transforms of both sides of the above equation,

$$T(x,t) = (1-\lambda)\sum_{n=0}^{\infty}\left\{\operatorname{erf}\left[\frac{2n+1+x}{2\sqrt{at}}\right] - \operatorname{erf}\left[\frac{2n+1-x}{2\sqrt{at}}\right]\right\} + \lambda x. \quad (48)$$

Rewriting this equation in a dimensional form gives the temperature in Eq. (20).

APPENDIX 2

Thermophysical Properties

For methanol, $T_{sat} = 64.7°\text{C}$, $L = 1101.1$ (kJ/kg), $c_p = 2.81$ (kJ/kg K), $k = 0.189$ (W/mK), $\rho_l = 751.035$ (kg/m^3), $\rho_v = 1.222$ (kg/m^3), $\mu = 3.31*10^{-4}$ Pas, $\sigma = 1.89*10^{-4}$ (N/m), and Pr = 5.0. The molecular weight of methanol (CH_3OH) is MW = 32.042.

The Effects of Sublimation-Condensation Region on Heat and Mass Transfer During Microwave Freeze Drying

Zhao Hui Wang[1]
e-mail: kezhwang@uxmail.ust.hk

Ming Heng Shi

Department of Power Engineering,
Southeast University,
Nanjing 210018, P. R. China

The sublimation-condensation model, developed for freeze drying of unsaturated porous media in the author's previous work, is analyzed numerically. The moisture redistribution in the sublimation-condensation region is taken into account in this model. The calculations show that the saturation of ice in the sublimation-condensation region will obviously decrease, and its effects on heat and mass transfer cannot be neglected for microwave freeze-drying of unsaturated porous media. The microwave freeze-drying tests of unsaturated beef are carried out. The experimental results show that the drying time is approximately proportional to the initial saturation of beef. Moreover the sublimation-condensation model is validated by the experimental results. These results show that the sublimation-condensation model agrees better with experimental results than the sublimation interface model.

Introduction

Freeze-drying has become a popular dehydration method for heat-sensitive materials, such as food and biological materials, because of the low temperature and no oxygen conditions during the process. On the other hand, the materials can keep their original pore's shape, nutrition, and have good rehydration; therefore, high-quality foods will be produced by this method. However, the low drying rate has been the main problem hampering its wider use. Freeze dehydration using microwave energy for volumetric heating has been developed to overcome the disadvantage of heat conduction in the materials.

Conventional freeze-drying has been investigated for many years. Arsem and Ma (1990) have given a comprehensive review of freeze-drying models before 1980. Based on the Luikov (1975) system, Lin (1981, 1982a, 1982b), and Fey and Boles (1987a, 1987b) have given some theoretical results by their exact analytical solutions. Peng and Chen (1994) analyzed the drying process considering a desorption mushy zone.

Microwave freeze-drying is different from conventional freeze-drying due to the internal generation of energy. Ma and Peltre (1975) carried out the first systematic study on freeze dehydration by microwave energy. A two-dimensional numerical analysis, reported by Ang et al. (1977), took into account the difference of the transport parameters with respect to grain orientation. Scott (1994) presented an analytical solution of microwave freeze-drying, and the sensitivity study was also conducted.

Of all the models above, a sublimation interface is assumed to separate a dried region from a frozen region where no vapor movement exists. Recently, Fey and Boles (1988) proposed a model of Luikov's theory for the freeze-drying of initially partially filled (or unsaturated) frozen porous media. In the model, there is vapor convection in the unsaturated frozen region, and some of the vapor flowing from the interface will be recondensed in this region since the temperature in the frozen region is lower than the interface temperature. However, just the opposite occurs during microwave freeze dehydration of unsaturated frozen materials because the temperature in the frozen region is higher than the interface temperature. As a result, the vapor will convect from the frozen region to the interface, and sublimation would occur in the frozen region. Thus, the saturation of the frozen region will decrease. In general, the frozen region can be called the sublimation-condensation region. In Fey and Boles' model (1988), the very small amount of vapor recondensation was assumed so that no change of moisture distribution was considered. Moreover, the model is limited in practical use because the transport properties in their equations of Luikov's system are difficult to obtained by experiments. Based on the volume-average theory (Whitaker, 1977), Wang (1996) developed a model which takes into account the sublimation or condensation caused by vapor transport in the unsaturated frozen region, and saturation change is considered. In the present work, the difference after including the new effect on the microwave freeze-drying process of unsaturated porous media will be studied by numerical calculations and experimental tests.

Statement of the Problem

An initially unsaturated porous infinite slab is exposed to a vacuum at a pressure below the triple point of frozen water substance. In the slab, the voids partially filled with frozen liquid and partially with gas are continuous so that convection may exist. In general, the vapor is the major component of gas and the noncondensable gases can be expected to be negligible. It is assumed that temperature, pressure, and vapor concentration of the gas-solid system are in local thermodynamical equilibrium, and the vapor pressure and concentration are functions only of the temperature. Initially, the temperature, frozen mass saturation, and vapor concentration are uniform. The physical model used to analyze the drying process is illustrated in Fig. 1.

As drying proceeds, a dried region forms on the side exposed to the vacuum. In previous work (Arsem and Ma, 1990), it was considered that there was no vapor movement in the frozen region and sublimation occurred in a very narrow region so that a sublimation interface was assumed. We call this model the sublimation interface model. But, in the case of unsaturated porous media, it is not the same in the frozen region because a temperature gradient will be created during drying and vapor pressure and concentration gradients will appear. The vapor will

---

[1] Current address: Department of Chemical Engineering, The Hong Kong University of Science and Technology, Clear Water Bay, Kowloon, Hong.

Contributed by the Heat Transfer Division for publication in the JOURNAL OF HEAT TRANSFER. Manuscript received by the Heat Transfer Division, May 12, 1997; revision received, Mar. 25, 1998. Keywords: Mass Transfer, Phase-Change Phenomena, Porous Media. Associate Technical Editor: P. Ayyaswamy.

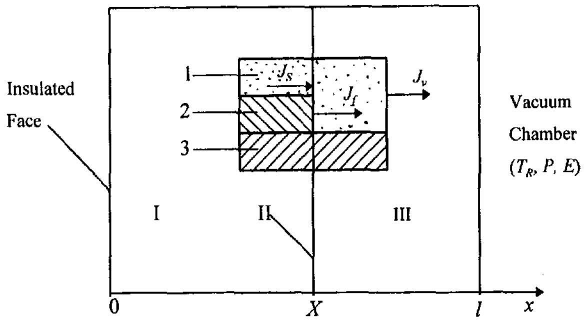

Fig. 1 Schematic description for microwave freeze drying of unsaturated frozen porous media. I-sublimation-condensation region; II-sublimation front; III-dried region 1-vapor($\epsilon(1-S)$); 2-frozen moisture (ϵS); 3-porous body ($1-\epsilon$).

convect in the voids due to Darcy's law and Fick's law. In order to satisfy the local thermodynamical equilibrium and mass balance of vapor, the ice will be sublimated or the vapor will be condensed in the voids. As a result, the saturation of frozen mass will decrease or increase. We call the region a sublimation-condensation region. The model describing this region is deduced by the author (Wang, 1996) based on volume-average theory, and the model is called a sublimation-condensation model in the mean time.

Between the sublimation-condensation region and dried region a sublimation front exists that is considered to be a plane as before. At the sublimation front, vapor may transfer from the sublimation-condensation region to the dried region or to the sublimation-condensation region. For conventional freeze-drying, heat is usually supplied from the surface of the body so that vapor will flow from the dried region to the sublimation-condensation region (Fey and Boles, 1988). For microwave freeze-drying the center of the body can be assumed to be insulated in general as shown in Fig. 1. On the other hand, the electric field can be considered uniform because the half-thickness of the slab in practice is usually much less than its penetration depth. Therefore, the temperature of the sublimation-condensation region will be higher than that of sublimation front, and the vapor will flow from the sublimation-condensation region to the dried region.

In order to describe the problem one-dimensional heat and mass transfer is supposed. For microwave freeze-drying of raw beef, the effect of absorption moisture in the dried region is usually neglected (Ma and Peltre, 1975; Ang et al., 1977). Also the ideal gas law is assumed to be valid for the vapor. The sublimation-condensation model developed in the author's previous work is presented as follows.

Mathematical Modeling

Sublimation-Condensation Region.

(1) Energy balance equation,

$$[\rho c]_e \frac{\partial T}{\partial \tau} = \frac{\partial}{\partial x}\left(\lambda_e \frac{\partial T}{\partial x}\right) + q, \tag{1}$$

here

$$[\rho c]_e = \rho c + \epsilon(1 - S)\frac{d\rho_v}{dT}\cdot \Delta H \tag{2}$$

$$\lambda_e = \lambda + \Delta H \cdot K_S. \tag{3}$$

$$K_S = \frac{K_D K_r}{\mu_v} R\rho_v^2 + \left[\frac{K_D K_r}{\mu_v} R\rho_v T + \epsilon(1 - S)D\right]\frac{d\rho_v}{dT}. \tag{4}$$

(2) Mass balance equation,

$$-u_{\text{sat}} \frac{\partial S}{\partial \tau} = -\frac{\partial}{\partial x}\left(K_S \frac{\partial T}{\partial x}\right) + f\frac{\partial}{\partial x}\left(\lambda_e \frac{\partial T}{\partial x}\right) + fq, \tag{5}$$

where

$$f = \frac{\epsilon(1 - S)}{[\rho c]_e}\cdot\frac{d\rho_v}{dT}. \tag{6}$$

Dried Region.

(1) Mass balance equation,

$$\epsilon \frac{\partial \rho_v}{\partial \tau} = \frac{\partial}{\partial x}\left(D_e \frac{\partial \rho_v}{\partial x}\right). \tag{7}$$

Nomenclature

c = specific heat of the material, J/(kg·°C)
D = diffusivity, m^2/s
D_e = effective diffusivity, m^2/s
E = electric field peak strength, V/cm
f = source conversion coefficient from heat to mass, kg/J
f_J = ratio of the vapor flux sublimated from sublimation-condensation region to the vapor flux in a dried region
f_m = moisture fraction of initial moisture
ΔH = latent heat of sublimation, J/kg
J_f = mass flux of vapor sublimated at sublimation front, kg/(m^2·s)
J_S = mass flux of vapor in sublimation-condensation region, kg/(m^2·s)
J_v = mass flux of vapor in dried region, kg/(m^2·s)
k = dissipation coefficient defined by Eq. (21), J/(s·m^3)·(V/cm)$^{-2}$
K_D = permeability of the dry material, m^2
K_r = relative permeability
K_S = effective coefficient of nonisothermal vapor motion in sublimation-condensation region, kg/(m·s·°C)
l = sample half-thickness, m
M = sample mass, g
M_{sat} = mass of saturated sample, g
P = vacuum pressure, Pa
P_M = precision limit of M, g
q = density of microwave power absorbed, J/(s·m^3)
R = water vapor gas constant, m^2/(s^2·°C)
S = saturation of ice in sublimation-condensation region
T = temperature, °C
U_{f_m} = experimental uncertainty of f_m
u_{sat} = moisture content of saturated frozen material, kg/m^3
U_T = experimental uncertainty of T, °C
x = space coordinate, m
X = position of sublimation front, m
α = heat transfer coefficient, J/(s·m^2·°C)
ϵ = porosity
λ = thermal conductivity, J/(s·m·°C)
μ = viscosity, kg/(m·s)
ρ = density, kg/m^3
τ = time, s
τ_d = drying time, min.

Subscripts

0 = initial value
d = of dried sample
D = in the dried region
i = of ice
R = vacuum chamber reference temperature
s = of solid body
S = in sublimation-condensation region
v = of vapor

(2) Energy balance equation

$$\rho c \frac{\partial T}{\partial \tau} = \frac{\partial}{\partial x}\left(\lambda \frac{\partial T}{\partial x}\right) - J_v c_v \frac{\partial T}{\partial x} + q, \qquad (8)$$

here,

$$J_v = -D_e \frac{\partial \rho_v}{\partial x}. \qquad (9)$$

Sublimation Front. If the vapor generated at the sublimation front can be written as

$$J_f = \left(-u_{\mathrm{sat}} S \frac{dX}{d\tau}\right)\bigg|_{x=X^-}, \qquad (10)$$

thus, the mass balance equation at the front is

$$\left(-D_e \frac{\partial \rho_v}{\partial x}\right)\bigg|_{x=X^+} - \left(-K_S \frac{\partial T}{\partial x}\right)\bigg|_{x=X^-} = J_f \qquad (11)$$

and the energy balance equation is

$$\left(-\lambda_e \frac{\partial T}{\partial x}\right)\bigg|_{x=X^-} - \left(-\lambda \frac{\partial T}{\partial x}\right)\bigg|_{x=X^+} = J_f \cdot \Delta H. \qquad (12)$$

Boundary Conditions. Due to symmetry of the material, the boundary condition at the center is

$$-\lambda_e \frac{\partial T}{\partial x}\bigg|_{x=0} = 0. \qquad (13)$$

The boundary conditions at the surface are

$$\left(-\lambda \frac{\partial T}{\partial x}\right)\bigg|_{x=l} = \alpha(T|_{x=l} - T_R) \qquad (14)$$

$$\rho_v|_{x=l} = \frac{P}{RT|_{x=l}}. \qquad (15)$$

Initial Conditions.

$$T|_{\tau=0} = T_0 \qquad (16)$$

$$S|_{\tau=0} = S_0 \qquad (17)$$

$$X|_{\tau=0} = l \qquad (18)$$

Physical Properties

Raw beef is selected as the freeze-drying material in this work. The physical properties of dried beef such as thermal conductivity and effective diffusivity are taken from the literature (Ma and Peltre, 1975).

For the sublimation-condensation region of frozen beef, the physical properties are different from those in previous models. Applying the experimental results of permeability (Harper, 1962), we can get the value of K_D for dried beef. With assuming $K_r = 1 - S$ and $D = D_e/\epsilon$, the expression of K_S can be obtained. It can be seen from Eq. (1) to Eq. (14) that their coefficients are an effective value. By volume averaging, the following is obtained:

$$\rho c = \rho_s c_s(1 - \epsilon) + \rho_i c_i \epsilon S + \rho_v c_v \epsilon(1 - S) \qquad (19)$$

$$\lambda = \lambda_s(1 - \epsilon) + \lambda_i \epsilon S + \lambda_v \epsilon(1 - S). \qquad (20)$$

Thus the coefficients in Eq. (1) to Eq. (14) are known.

The microwave heat generation, q, in Eqs. (1), (5), and (8) is given by

$$q = kE^2 \qquad (21)$$

where k is a coefficient, depending on the temperature and type of material, for saturated raw beef, k_F, and dried beef, k_D respectively (Ma and Peltre, 1975). After considering the effect of saturation variation on the microwave dissipation, the values of k in sublimation-condensation region can be obtained by volume averaging as follows:

$$k = k_F S + k_D(1 - S). \qquad (22)$$

It can be seen that the sublimation-condensation model becomes the sublimation interface model when $S = 1$; i.e., sublimation and condensation will not occur in the sublimation-condensation region when the porous media is fully filled with ice. If it is assumed that $K_S = 0$, $[\rho c]_e = \rho c$, and $f = 0$, the sublimation-condensation model becomes a sublimation interface model for any saturation.

Numerical Results

The mathematical model has been calculated numerically by applying a variable time-step finite difference method. The numerical error is tested by various space steps (×200, ×250) and shows that the difference of the total drying time is less than 10^{-4}. Table 1 shows the typical operation conditions for the numerical calculations.

It should be noted that in this paper it is assumed that $T_R = 20°\mathrm{C}$ and $T_0 = -15°\mathrm{C}$, and volume-averaged calculations give $\alpha = 6.7\ \mathrm{W/(m^2 \cdot °C)}$.

Figure 2 illustrates the temperature distribution during the drying. It is similar to the results of references Ma and Peltre (1975) and Ang et al. (1979) using a sublimation interface model for saturated raw beef. With the sublimation front propagating, the temperature decreases quickly, then increases gradually, and decreases again as the front position reaches 0.003 m. This is due to the variation of heating power and mass transfer resistance.

Figure 3 illustrates the ice saturation profiles of the beef sample during the drying process. It shows that the saturation keeps the initial value in the sublimation-condensation region before the first 572 seconds. This is because the temperature is relatively low in this period (Fig. 2) and K_S is so small (Eq. (4)) that the vapor transfer is slow, and there is nearly no sublimation. With the drying advancing, the temperature of sublimation-condensation region increases and sublimation in this region causes the saturation to decrease. It is seen that the maximum change of saturation occurs at the insulation interface where the maximum temperature of frozen ice exists. It seems that K_S plays a very important role in sublimation phenomena. However, there is little difference in the saturation between the sublimation front and the insulation interface. At the end of drying, the saturation at the front changes from the initial value of 0.7 to 0.4. This means that the sublimation-condensation region must be taken into account during the microwave freeze-drying of unsaturated porous media.

Figure 4 shows the ratio of the vapor flux sublimated from sublimation-condensation region to that flowing in dried region at different sublimation front positions. The ratio can be expressed as

$$f_J = \frac{J_S|_{x=X^-}}{J_v|_{x=X^+}}. \qquad (23)$$

It is indicated that for most time of the drying process more

Table 1 Typical operation conditions

$S_0 = 0.7$	$l = 0.008$ m
$E = 120$ V/cm	$P = 15$ Pa
$T_R = 20°\mathrm{C}$	$u_{\mathrm{sat}} = 685\ \mathrm{kg/m^3}$
$T_0 = -15°\mathrm{C}$	$\epsilon = 0.75$

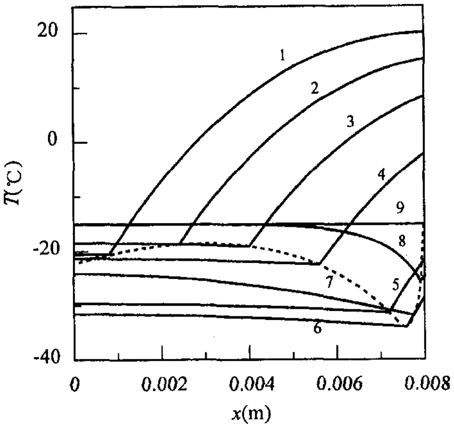

Fig. 2 Temperature profiles during microwave freeze drying. τ/s: 1-10434; 2-7489; 3-4950; 4-2714; 5-572; 6-76; 7-9; 8-0.1; 9-0. --- sublimation front.

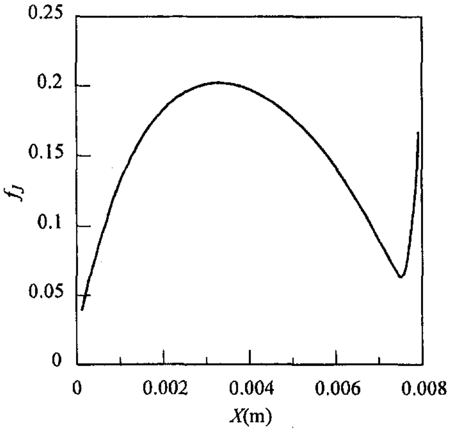

Fig. 4 Variation of f_J at different sublimation front positions

than ten percent of the vapor flowing from the material is sublimated from the sublimation-condensation region, i.e., the vapor sublimated from the sublimation-condensation region has a great contribution to drying rate. Therefore, the effect of the sublimation-condensation region on heat and mass transfer is significant to the drying process.

Since saturation changes with drying at the sublimation front, the drying time will be different from that of the sublimation interface model. Figure 5 shows the position of the sublimation front as a function of time in this model and the sublimation interface calculated by previous model as a function of time. It can be seen that the sublimation fronts are nearly the same during the first 60 minutes and then the results diverge. The total drying time for the sublimation interface model is about 240 minutes while it is about 200 minutes for the sublimation-condensation model.

Experimental Procedure

In order to study the drying characteristics of unsaturated porous media and validate the sublimation-condensation model experimental tests of microwave freeze-drying are carried out. The experimental apparatus is illustrated as Fig. 6. The sample mass is measured by a mass sensor with high precision. In each test, a large sample of more than 25 g mass is used to reduce the error in the sample mass determination due to the thermocouples. Due to of the shielding cavity for sensors, no obvious error was found in the determination of the sample mass, except when gas discharge occurred. The vacuum pressure is measured with two vacuum gauges. No effects of the microwave field were found on the pressure measurement or the sample mass.

The sample temperature is measured by several NiCr-NiSi thermocouples. The temperature measurement with thermocouples in a microwave field will be disturbed by the thermal and signal-coupling effects of a high-frequency electromagnetic field. On the other hand, the sample temperature will decrease quickly after microwave heating stops during the microwave freeze-drying process because of the sublimation of frozen moisture. As a result, it will also create a great error to measure the sample temperature by shutting off the microwave during the drying process. This is true especially for measuring the temperature of the ice core. The tests prove that it is suitable for thermocouples to measure the temperature with microwave heating in a weak electromagnetic field, but the microwave must be shut off when $E > 175$ V/cm. It seems that under lower electric field strength the sample temperature can be more precisely measured with microwave heating on than off. However, the thermocouples are not appropriate to measure the temperature during microwave freeze drying when the electric field strength is high enough (such as $E > 250$ V/cm) because they will cause gas discharge in the vacuum.

Several power controllers made of wood are located in the microwave cavity to absorb excess power and to ensure that the total load remains approximately steady. They are also used to make the electromagnetic field more homogenous by careful positioning, because the microwave power density distribution depends on the load distribution in the microwave cavity. Reasonably, the average microwave power density in the micro-

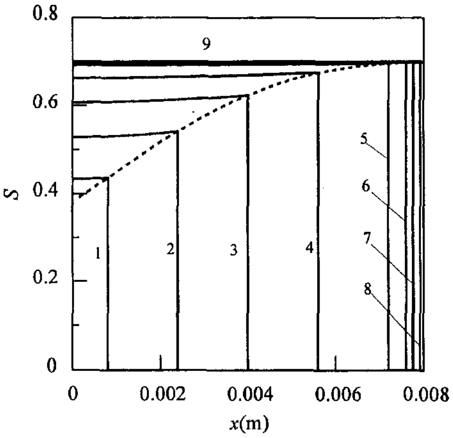

Fig. 3 Saturation profiles during microwave freeze drying. τ/s: 1-10434; 2-7489; 3-4950; 4-2714; 5-572; 6-76; 7-9; 8-0.1; 9-0. --- sublimation front.

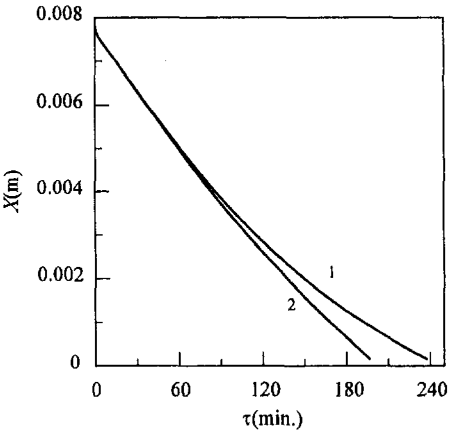

Fig. 5 Comparison of $X \sim \tau$ between two models. 1-sublimation interface model; 2-sublimation-condensation model.

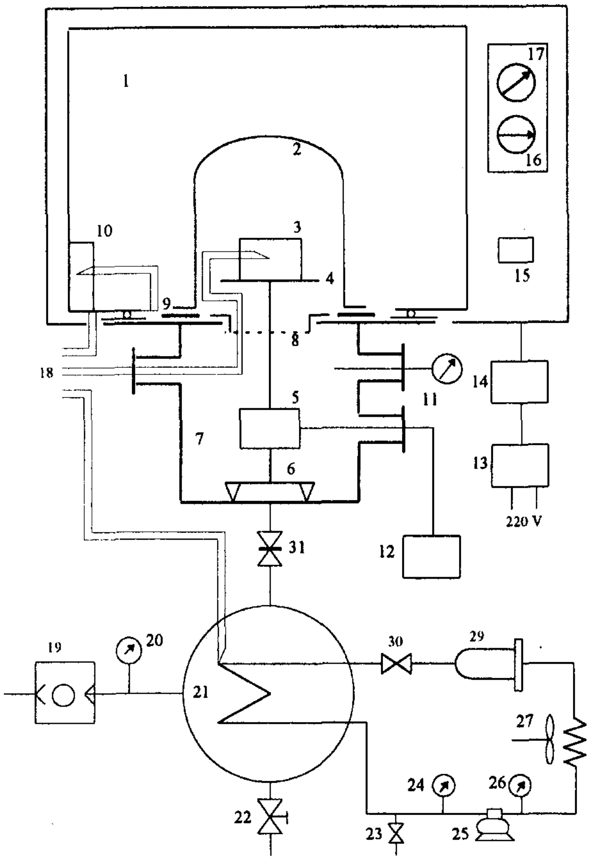

Fig. 6 Microwave freeze drying apparatus. 1-microwave cavity; 2-glass vacuum cover; 3-sample; 4-teflon sample tray; 5-mass sensor; 6-stand; 7-shielding cavity for sensors; 8-microwave shield; 9-teflon sealing washer; 10-microwave power controller; 11-vacuum gauge I; 12-mass meter; 13-voltage regulator; 14-voltage transformer; 15-microwave heating switch; 16-microwave power adjuster; 17-time register; 18-thermal couples; 19-vacuum pump; 20-vacuum gauge II; 21-vapor condenser; 22-gas valve; 23-inlet valve; 24,26-hydrostatic gauge; 25-compressor; 27-fan; 28-condenser; 29-drier; 30-capillary pipe; 31-butterfly valve.

wave cavity can be considered constant during the drying process if the absorbed power of the power controllers is held constant. Therefore, the average electric field strength of the cavity will be a function of the temperature of the power controllers. This relationship has been obtained at different input voltages of a microwave generator by measuring the temperature of the power controllers and the sublimation rate of an ice block which replaced the raw beef sample on the tray as illustrated in Fig. 6.

In each run the uniformity of the electric field strength is pretested. In order to keep the operation parameters constant during the microwave freeze-drying process, the electric field strength is controlled by the input voltage. The vacuum pressure is adjusted by the two valves, and the partial pressure of vapor in the vacuum chamber is obtained by measuring the temperature of vapor condenser and controlled by regulating the mass flow rate of the working fluid in the refrigerator. In this work the sample mass and temperature are measured simultaneously at different times in a same-sample test.

The test sample is prepared by preprocessing the unsaturated beef. The raw beef, which is considered to be saturated, is sliced to slabs perpendicular to muscle fiber orientation. First the beef slabs are freeze-dried and then rewetted to various moisture levels. If the volume change is neglected the saturation is 0.7 when the moisture content is 0.63 (wet basis). When the moisture is evenly distributed the rewetted beef slabs are frozen and put into a refrigerator for storage. Except the two biggest sides, the other sides of each slab are covered with a Teflon membrane and the slabs are prepared for the thermocouples holes.

An uncertainty analysis of experimental measurements was carried out by using Kline and McClintock's method (1953). The dimensionless moisture content f_m in the experimental tests was evaluated as

$$f_m = \frac{M_0 - M}{M_0 - M_d}. \tag{24}$$

After considering both the contributions of basis and random errors the 95 percent confidence uncertainty, U_{f_m}, can be calculated by the following relationship:

$$U_{f_m} = \sqrt{\frac{2P_M}{M_0 - M_d}(1 - f_m + f_m^2)}. \tag{25}$$

The sample mass was determined with a precision balance (1000 g, ±0.1 g). The mass of the dried sample is about 25 g. On the other hand, the average moisture content of the saturated raw beef is 70 percent (wet basis) and the following can be obtained:

$$M_0 - M_d = S_0(M_{\text{sat}} - M_d)$$
$$= S_0\left(\frac{1}{1-70\%} M_d - M_d\right) = \frac{7}{3} S_0 M_d. \tag{26}$$

Thus U_{f_m} is tabulated in Table 2.

Though the experimental uncertainty of f_m is greater especially for lower S_0 and lower f_m, the difference of calculated f_m are also greater enough between the sublimation-condensation model and the sublimation interface model to validate the calculated results with the experimental data. For example, under the operation condition $S_0 = 0.25$, $f_m = 0.2$ is obtained at $\tau = 45$ min. for the sublimation-condensation model while $f_m = 0.38$ for the sublimation interface model at the same time in the drying process as discussed below.

The temperature uncertainty is estimated by calibration tests that were conducted by measuring the temperature change of a wood block that occurred when the microwave power was turned off during microwave heating. The block placed in the vacuum chamber can be considered to be insulated and the heat capacity of thermocouples can be neglected. As a result the above change can be regarded as the temperature uncertainty. It was found that maximum change is less than ±5°C when $E < 150$ V/cm. In practice, the wet bulb temperature of the vacuum chamber is less than −40°C and the upper limit temperature of the material is 60°C. So the following is obtained:

$$\frac{U_T}{\Delta T} = \frac{U_T}{T_{\text{up}} - T_{wb}} = \frac{5}{60 - (-40)} = \text{five percent}. \tag{27}$$

The temperature measurement error is mainly due to the electromagnetic field. If large E is applied ($E > 175$ V/cm), the temperature difference will increase greatly, and thermocouples should not be used to measure the temperature in the electromagnetic field with microwave heating.

Table 2 f_m uncertainty estimates (95 percent confidence)

	f_m				
S_0	0	0.25	0.5	0.75	1
1	±0.059	±0.053	±0.051	±0.053	±0.059
0.7	±0.070	±0.063	±0.061	±0.063	±0.070
0.5	±0.083	±0.075	±0.072	±0.075	±0.083
0.25	±0.12	±0.11	±0.10	±0.11	±0.12

Experimental Results

Figure 7 shows the sample temperature variation during the drying ($S_0 = 0.7$, $E = 120$ V/cm, $P = 15$ Pa, $l = 0.008$ m). It can be seen that the sample temperature at different positions decreases quickly after starting the vacuum pump. In about ten minutes the temperature of both positions has nearly reached the same value, which is the wet bulb temperature of the vacuum chamber. Then microwave heating begins, and the time is considered to be zero in the time axis.

The temperature at different sample positions rises gradually after microwave heating and the change of both measured temperatures is the same. At 30 minutes the temperature near sample surface increases suddenly and rises quickly. The center temperature keeps changing gradually, remains flat for a time period, and decreases a little at 150 minutes. At 165 minutes the center temperature suddenly increases in a way similar to the surface temperature at 30 minutes. The time of the sudden change in the center temperature can be considered to be the end point of the drying process.

During microwave heating, the temperature change of frozen ice and the dried region in a beef sample is different. Due to the position error of the measured point, the measured results of surface temperature changes just like the center temperature before $\tau < 30$ minutes.

Figure 7 also indicates the numerical results for the temperature at different sample positions when calculated with the sublimation-condensation model under the same operation conditions. Both the numerical results and the experimental results show that the time is relatively short for the sample temperature to decrease from the initial value to the wet bulb temperature. As a result, the time when microwave heating begins in the experiment can be considered to be the starting point of microwave freeze drying in the calculation. It can be seen that the measured surface temperature is more like the calculated results of $x/l = 0.75$ than those of $x/l = 1$, while the temperature measured in the sample center is between the calculated results of $x/l = 0$ and $x/l = 0.25$.

Figure 8 shows the variation of the moisture fraction with various initial saturation conditions. Their operation conditions are listed in Table 3. The experimental results indicate that the moisture fraction decreases more quickly for the smaller initial saturation condition. This is because more energy is generated in the matrix per unit of ice. If the microwave dissipation coefficient of the matrix is rather small, such as glass, the unit ice will absorb nearly the same heating power. Then it is expected that the different initial saturation conditions will have the same drying time. An extreme example is that for a porous medium made of pure ice. Neither melting nor thermal degradation phenomenon is found during these tests.

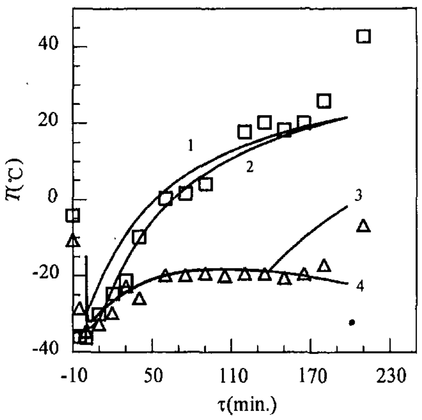

Fig. 7 Experimental and simulated temperature versus time. x/l: theoretical: 1–1; 2–0.75; 3–0.25; 4–0; experimental: □–1; △–0.

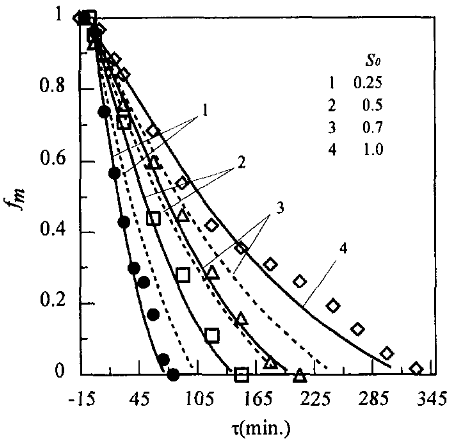

Fig. 8 Experimental and simulated fraction of initial moisture versus time. theoretical: ——— sublimation-condensation model; --- sublimation interface model. 1—run 1; 2—run 2; 3—run 3; 4—run 4. experimental: ●—run 1; □—run 2; △-run 3; ◇—run 4.

The numerical results for the moisture fraction calculated with both the sublimation-condensation model and the sublimation interface model are also illustrated in Fig. 8. Due to the saturation change in the sublimation-condensation region, the variation of the dimensionless position of the sublimation front cannot represent the change of the moisture fraction. The moisture as a fraction of initial moisture is obtained from

$$f_m = \int_0^{x^-} \frac{S}{S_0 l} dx. \tag{28}$$

It is seen that the experimental results agree better with the calculated results of the sublimation-condensation model than that of the sublimation interface model. This proves that the sublimation-condensation region does exist, and it has a great effect on heat and mass transfer during microwave freeze-drying of unsaturated porous media.

Though the measured temperatures fluctuate from the theoretical results illustrated in Fig. 7 due to the effect of the electromagnetic field, it seems that the point of the suddenly rising temperature clearly represents the location of sublimation front at this time. If the position error of the measured center point is neglected, the time when the measured center temperature suddenly increases can be considered to be the end of drying process. Because of the nonuniformity of the electromagnetic field and the material, it seems more reasonable to use the results of the measured center temperature to determine the experimental drying time. Figure 9 compares the experimentally and theoretically determined drying times (the drying conditions in Table 3). The starting period without microwave heating is not included in these experimental drying times. It can be seen that the drying time is approximately proportional to the initial saturation conditions. This means that the drying time at any initial saturation condition can be predicted by this linear relationship. The figure also indicates that the sublimation-condensation model is in better agreement with the experimental results than the sublimation interface model. However, the dimension and inside construct of the material and the position error of the center thermocouple still cause a relatively large

Table 3 Operating conditions

Run	S_0	E (V/cm)	l (m)	P (Pa)
1	0.25	120	0.008	15
2	0.5	120	0.008	15
3	0.7	120	0.008	15
4	1	120	0.008	15

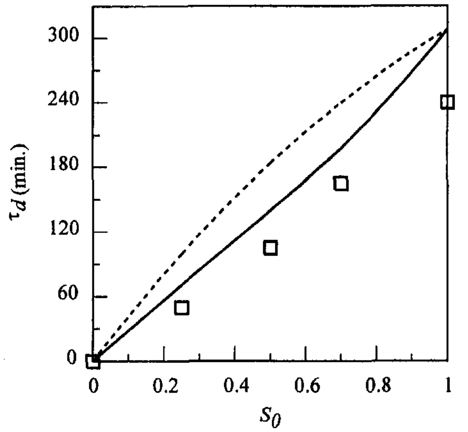

Fig. 9 Experimental and theoretical drying time versus initial saturation. theoretical:—sublimation-condensation model; --- sublimation interface model; experimental: □.

error of the drying time between the experimental data and the calculated results. Besides, the time-interval value used to collect the experimental data has an effect on determining the exact ending time of the drying process, and this will lead to the error of the drying time as well.

Conclusion

A sublimation-condensation region exists in freeze-drying of unsaturated porous. The saturation in the sublimation-condensation region will decrease greatly and this region has a significant effect on heat and mass transfer during microwave freeze-drying of unsaturated porous media. There is a great difference of numerical results between a sublimation-condensation model and a sublimation interface model. This analysis shows that the experimental results are in better agreement with the sublimation-condensation model. The experimental tests also indicate that the smaller initial saturation condition will have less drying time and the drying time is approximately proportional to the initial saturation.

Acknowledgment

The project is supported financially by the National Natural Science Foundation of China.

References

Ang, T. K., Ford, J. D., and Pei, D. C. T., 1977, "Microwave Freeze-Drying of Food: A Theoretical Investigation," *Int. J. Heat Mass Transfer*, Vol. 20, pp. 517–526.

Arsem, H. B., and Ma, Y. H., 1990, "Simulation of a Combined Microwave and Radiant Freeze Dryer," *Drying Technology*, Vol. 8, pp. 993–1016.

Fey, Y. C., and Boles, M. A., 1987a, "An Analytical Study of the Effect of Convection Heat Transfer on the Sublimation of a Frozen Semi-infinite Porous Medium," *Int. J. Heat Mass Transfer*, Vol. 30, pp. 771–779.

Fey, Y. C., and Boles, M. A., 1987b, "An Analytical Study of the Effect of the Darcy and Fick Laws on the Sublimation of a Frozen Porous Medium," ASME JOURNAL OF HEAT TRANSFER, Vol. 109, pp. 1045–1048.

Fey, Y. C., and Boles M. A., 1988, "Analytical Study of Vacuum-Sublimation in an Initially Partially Filled Frozen Porous Medium with Recondensation," *Int. J. Heat Mass Transfer*, Vol. 31, pp. 1645–1653.

Harper, J. C., 1962, "Transport Properties of Gases in Porous Media at Reduced Pressure with Reference of Freeze-Drying," *AIChE J.*, Vol. 8, pp. 298–302.

Kline, S. J., and McClintock, F. A., 1953, "Describing Uncertainties in Single-Sample Experiments," *Mechanical Engineering*, Vol. 75, Jan., pp. 3–8.

Lin, S., 1981, "An Exact Solution of the Sublimation Problem in a Porous Medium," ASME JOURNAL OF HEAT TRANSFER, Vol. 103, pp. 165–168.

Lin, S., 1982a, "An Exact Solution of the Sublimation Problem in a Porous Medium. Part II–With an Unknown Temperature and Vapor Concentration at the Moving Sublimation Front," ASME JOURNAL OF HEAT TRANSFER, Vol. 104, pp. 808–811.

Lin, S., 1982b, "An Exact Solution of the Desublimation Problem in a Porous Medium," *Int. J. Heat Mass Transfer*, Vol. 25, pp. 625–630.

Luikov, A. V., 1975, "Systems of Differential Equations of Heat and Mass Transfer in Capillary-Porous Bodies (Review)," *Int. J. Heat Mass Transfer*, Vol. 18, pp. 1–14.

Ma, Y. H., and Peltre, P., 1975, "Freeze Dehydration by Microwave Energy: Part I. Theoretical Investigation," *AIChE J.*, Vol. 21, pp. 335–344.

Peng, S. W., and Chen, G. Q., 1994, "Coupled Heat and Mass Transfer with One Discrete Sublimation Moving Interface and One Desorption Mushy Zone," ASME JOURNAL OF HEAT TRANSFER, Vol. 116, pp. 215–220.

Scott, E. P., 1994, "An Analytical Solution and Sensitivity Study of Sublimation-Dehydration within a Porous Medium with Volumetric Heating," ASME JOURNAL OF HEAT TRANSFER, Vol. 116, pp. 686–693.

Wang, Z. H., 1996, "Heat and Mass Transfer during Microwave Freeze Drying," Ph.D. thesis, Southeast University, Nanjing, China.

Whitaker, S., 1977, "Simultaneous Heat, Mass, and Momentum Transfer in Porous Media: A Theory of Drying," *Advances in Heat Transfer*, Vol. 13, Academic Press, New York, pp. 119–203.

Zhao-Fen Jin[1]

Yutaka Asako[2]
Mem. ASME

Yoshiyuki Yamaguchi

Department of Mechanical Engineering,
Tokyo Metropolitan University,
Minami-Osawa, Hachioji,
Tokyo 192-0397, Japan

Minoru Harada
Kumahira Safe Company,
Department of Research and Development,
Ujinahigashi,
Hiroshima 732, Japan

Numerical Modeling of Fire Walls to Simulate Fire Resistance Test

A fire wall is made of a mortar wall in which water storage materials are mixed. However, the mortar fire wall is relatively heavy. A nonorganic insulator for middle and high-temperature ranges such as a calcium silicate board is expected as a good material for the fire wall because of a light weight. Usually, a nonorganic insulator such as the calcium silicate board consists of a hydrate which contains free water, physically adsorbed water, and crystalline water. Behavior of such waters should be considered for a numerical model which is used to predict thermal responses of a fire wall. A simple one-dimensional numerical model to predict thermal response of a fire wall which is made of a nonorganic hydrate insulator, is developed. The numerical computations to simulate the thermal responses for a standard fire resistance test were performed for a sand wall of five percent volume of moisture and two calcium silicate boards which contains free water, adsorbed water, and crystalline water. The experiments for the sand wall and the calcium silicate boards were also performed. The numerical results were compared with experiments. The proposed model well predicts the thermal responses of the walls.

Introduction

It is empirically known that a humid fire resistance material shows good fire resistance performance. From this fact, a mortar wall in which water storage materials such as silica gels or humid perlites are mixed, is widely used for a fire wall of a safe. However, the mortar fire wall whose density ranges from 2000 to 2500 kg/m^3, is relatively heavy. Recently, there were increased demands to build safety storage rooms for magnetic media on a higher level in tall buildings. Therefore, a reduction of weight of the fire wall is strongly required. A nonorganic insulator for middle and high-temperature ranges, such as a calcium silicate board, is expected to be a good material for the fire wall because of a light weight and low thermal diffusivity. And a numerical model on a fire wall, which simulates the fire resistance test, is required to assist the development of a light-weight fire wall.

The evaporation of water in a fire wall will occur when the wall is intensely heated during a fire. Consequently, a vapor flow will form in the wall. Most of the nonorganic insulator consists of a hydrate which contains free water, adsorbed water, and crystalline water. Behavior of such waters should be considered for a numerical model which is used to predict thermal responses of a fire wall. The modeling for the humid porous material subjected to fires and the numerical prediction for the temperature response have been investigated by Sahota and Pagni (1979), Dayan and Gluekler (1982), and Huang and Ahmed (1991). However, a concrete wall or a light-weight concrete wall were objects of these investigations. Only the evaporation of the free water was considered in the model. We failed to disclose the modeling for the nonorganic hydrate insulators. This is the motivation of the present study.

A simple one-dimensional numerical model to predict thermal responses of a fire wall, which is made of a nonorganic hydrate insulator, such as a calcium silicate board, is developed. The numerical computations to simulate the thermal responses for a standard fire resistance test were performed for a sand wall of five percent volume of moisture and two calcium silicate boards containing free water, adsorbed water, and crystalline water. Fire resistance tests for the sand wall and the calcium silicate boards were also performed. Comparisons between the numerical results and experimental results were performed.

Formulation

Description of the Problem. The problem to be considered in this study is schematically depicted in Fig. 1. A one-dimensional fire wall of thickness L, which consists of a humid porous material whose pore is filled with air and water, is considered. The wall is initially kept at temperature T_i. At time, $t = 0$, the right surface of the wall (the heated surface) is exposed to the fire flame. The temperature of the heated surface instantaneously rises. It is assumed that the free water in the wall evaporates when the temperature reaches the saturation temperature of the water. Therefore, the moisture transfer will be excluded in the model. Under this assumption, a liquid-vapor interface is formed in the wall. The vapor generated at the interface flows in the wall from the right side of the interface to the heated surface. Note that the vapor flows in the opposite direction to the heat flow. And the interface moves to the left with time. The regions of the left and right sides of the interface will be called as "a liquid region" and "a vapor region," respectively. As mentioned above, in the case of a nonorganic hydrate insulator, it contains the adsorbed water and the crystalline water. Therefore, the evaporation of the adsorbed water and decomposition of the crystalline water occur at a temperature above the saturation temperature. Then, we consider three temperature ranges. The first temperature range is up to the saturation temperature from a room temperature. The second temperature range is up to a temperature where the decomposition of the crystalline water occurs. And the third temperature range is over the decomposition temperature. Constant thermophysical properties in each region are assumed. It is further assumed that the pores in the vapor region of the porous material are filled with vapor, and there is no liquid flow in the liquid region.

---

[1] Current address: Department of Thermal Engineering, Tsinghua University, Beijing 100084, China.

[2] Corresponding author. e-mail: asako@ecomp.metro-u.ac.jp.

Contributed by the Heat Transfer Division for publication in the JOURNAL OF HEAT TRANSFER and presented at '97 NHTC, Baltimore. Manuscript received by the Heat Transfer Division, Sept. 9, 1997; revision received, May 11, 1998. Keywords: Fire, Heat Transfer, Insulation, Modeling, Numerical Methods. Associate Technical Editor: M. Kaviany.

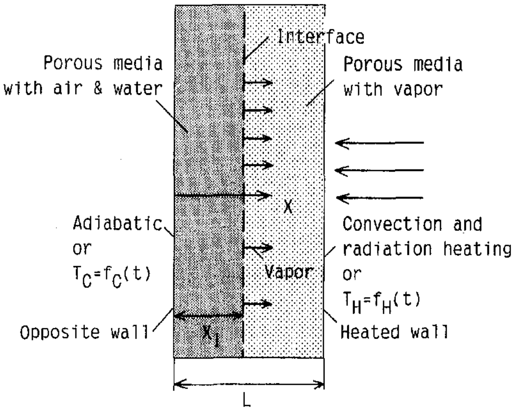

Fig. 1 Schematic diagram of a fire wall

Conservation Equations. The governing equations to be considered are the continuity, momentum, and energy equations. It is assumed that the vapor flow in the vapor region is governed by Darcy's model. The enthalpy transformed form of the energy equation for a phase-change problem proposed by Cao et al. (1989) is adopted. Then, the governing equations take the following form:

$$\frac{d(\rho_v U)}{dX} = 0 \tag{1}$$

$$0 = -\frac{dP}{dX} - \frac{\nu}{k}\rho_v U \tag{2}$$

$$\frac{\partial(\rho_{\mathrm{eff}} E_{\mathrm{eff}})}{\partial t} + \frac{\partial\left(\rho_v \dfrac{Cp_v}{Cp_{\mathrm{eff}}} U E_{\mathrm{eff}}\right)}{\partial X} = \frac{\partial^2(\Gamma E_{\mathrm{eff}})}{\partial X^2} + \frac{\partial^2 S}{\partial X^2} \tag{3}$$

where

$$\Gamma(E_{\mathrm{eff}}) = \begin{cases} K_{v\,\mathrm{eff}}/Cp_{v\,\mathrm{eff}} & (E_{\mathrm{eff}} > 0) \\ 0 & (-\gamma_{\mathrm{eff}} \le E_{\mathrm{eff}} \le 0) \\ K_{l\mathrm{eff}}/Cp_{l\mathrm{eff}} & (E_{\mathrm{eff}} < -\gamma_{\mathrm{eff}}) \end{cases} \tag{4}$$

$$S(E_{\mathrm{eff}}) = \begin{cases} 0 & (E_{\mathrm{eff}} > 0) \\ 0 & (-\gamma_{\mathrm{eff}} \le E_{\mathrm{eff}} \le 0) \\ K_{l\,\mathrm{eff}}\gamma_{\mathrm{eff}}/Cp_{l\,\mathrm{eff}} & (E_{\mathrm{eff}} < -\gamma_{\mathrm{eff}}) \end{cases} \tag{5}$$

and where E_{eff} is the effective enthalpy of the wall, and we have selected $E_{\mathrm{eff}} = 0$ at the situation where the pore of the porous material is filled with the vapor at the saturated temperature. K_{eff} and Cp_{eff} represent the effective thermal conductivity and the effective specific heat of the wall. Those physical properties will be discussed later. γ_{eff} represents as the effective latent heat of the free water. Therefore, the latent heat of the adsorbed water and the crystalline water are not included in γ_{eff}. γ is denoted as the latent heat of the free water, and the effective latent heat can be expressed as

$$\gamma_{\mathrm{eff}} = \frac{\phi_l \rho_l \gamma}{\rho_{l\,\mathrm{eff}}}. \tag{6}$$

Note that the second term of left-hand side of Eq. (3) represents the convection term which transports the enthalpy by vapor flow, and its value takes zero in the liquid region.

Initial and Boundary Conditions. The wall is initially kept at temperature T_i. Thus, the initial conditions are

$$t < 0: \quad T = T_i, \quad U = 0. \tag{7}$$

At time $t = 0$, the heated surface of the wall is exposed to the fire flame. In this case, the surface is heated by convection and radiation. And the left surface is insulated. Also the boundary condition for the case where the both surface temperatures are specified is considered. The boundary condition can be expressed as

$$t > 0, \quad X = L: \quad q_H = h_H(T_\infty - T_H) + \epsilon_H \sigma(T_\infty^4 - T_H^4) \tag{8}$$

$$\text{or} \quad T_H = f_H(t) \tag{9}$$

$$X = 0: \quad dT/dX = 0 \tag{10}$$

$$\text{or} \quad T_C = f_C(t) \tag{11}$$

where q_H is the heat flux on the heated surface and T_∞ is the fire temperature.

The Darcy velocity, U, becomes constant under the assumption of the constant vapor density and it can be expressed from the mass balance at the interface.

$$U = \frac{-\phi_l \rho_l}{\rho_v}\frac{dX_l}{dt}, \tag{12}$$

where dX_l/dt represents the moving velocity of the interface.

Numerical Solution. From the examination of Eqs. (1) and (2), it is obvious that the mass flux of the vapor, $\rho_v U$, is constant in the vapor region and the pressure changes linearly in that region. It is true that the saturated temperature depends on the pressure. Therefore, Eq. (3) should be solved coupling with Eqs. (1) and (2). However, the sensibility of the saturated temperature is low, and the permeability of the material, which could be used for the fire wall, is not so low. From these facts, the computations were performed for the fixed saturation temperature of 373.15 K. The capillary or surface tension may have

Nomenclature

A = coefficient defined in Eq. (16)
B = coefficient defined in Eq. (16)
C_1 = coefficient defined in Eq. (16)
C_2 = coefficient defined in Eq. (16)
C_p = specific heat, J/kg K
E = enthalpy, J/kg
h = heat transfer coefficient, W/m^{2}K
K = thermal conductivity, W/m K
k = permeability of porous medium, m^2
P = pressure, Pa
q = heat flux, W/m^2
S = coefficient in Eq. (3)
T = temperature, K
T_∞ = surrounding temperature of furnace, K
t = time, s or h
U = Darcy velocity, m/s
X = coordinate, m
X_l = interface location, m
ϵ = emissivity
ϕ = porosity
ϕ_a = volume fraction of air
ϕ_l = volume fraction of water
γ = latent heat, J/kg
Γ = coefficient in Eq. (3)
ν = kinematic viscosity, m^2/s
ρ = density, kg/m^3
σ = Stefan-Boltzmann constant, W/m^{2}K^4

Subscripts

a = air
C = opposite wall
eff = effective value
H = Heated wall
i = initial condition
l = water
s = solid particle
v = vapor

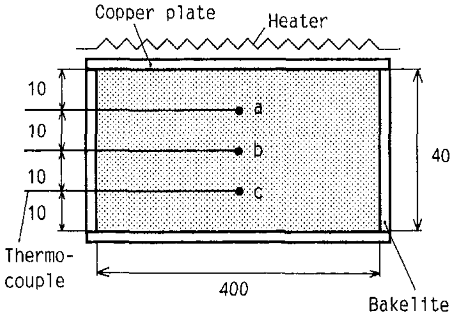

Fig. 2 Experimental setup for heating test of a sand wall

an effect on the saturation temperature. However, these effects are not considered.

The numerical methodology proposed by Cao et al. (1989) for the energy equation is adopted. Therefore, the discretized procedure of the equation is based on the control-volume-based upwind scheme. The computations were performed with 62 grid points and a time step of 10 sec.

Fire Resistance Test for Sand Wall

Experimental Setup. The first heated test was conducted for a humid sand wall to verify the validity of the proposed numerical model, since it can be considered that a humid sand wall contains only free water. A schematic diagram of the experimental setup is presented in Fig. 2. The size of the sand used is up to 1 mm diameter. The measured porosity of the sand layer was 46 percent. The sand was dried, and then five percent volume of water was uniformly added.

As shown in Fig. 2, the sand layer of 400 mm × 400 mm and 40 mm depth is placed horizontally between copper plates of 5 mm thick. An electric heater of 1.5 kW is placed behind the upper copper plate (heated plate). Exhausting holes for vapor flow are drilled on the upper copper plate. The side walls are made of bakelite plates and the equipment is insulated by the glass wool to minimize the heat loss. Using the copper and constantan thermocouples of 0.3 mmϕ, the heated wall temperature, the lower wall (opposite wall) temperature, and temperatures at three points with equal interval spacing of 10 mm in the sand layer were measured. The uncertain temperature is estimated to be 0.1 K.

The heated surface temperature rises gradually because of the heat capacity of the plate, and it reaches steady-state after 20 minutes. The measured temperatures of heated and opposite surfaces can be expressed by the following expressions:

$$T_H = \begin{cases} 287.1 + 0.281t - 7.06 \times 10^{-5}t^2 & (t \leq 1200) \\ 523.15 & (t > 1200) \end{cases} \quad (13)$$

$$T_C = \begin{cases} 288.6 - 7.194 \times 10^{-3}t + 4.935 \times 10^{-5}t^2 - 1.322 \times 10^{-8}t^3 \\ \qquad\qquad\qquad\qquad\qquad\qquad (t \leq 2100) \\ 373.15 \quad (t > 2100) \end{cases} . \quad (14)$$

The numerical computation was performed using Eqs. (13) and (14) for the boundary condition of the heated and opposite surfaces.

Thermophysical Properties. The thermophysical properties are estimated from the volume fraction of the sand particle $(1 - \phi_a - \phi_l)$, the volume fraction of the free water (ϕ_l), and the volume fraction of air (ϕ_a), using the properties of the sand particle, water, and air. The effective thermal conductivity in the liquid region of the sand layer, $K_{l\,\mathrm{eff}}$, is estimated from following equation proposed by Tanaka (1991) for humid porous materials:

Table 1 Thermal properties of elements

T (K)	Sand particle 400 K	Water 373 K	Vapor 400 K	Air 373 K
ρ (kg/m^3)	2650	958.4	0.555	0.916
Cp (J/kg·K)	891	4216	2000	1013
K (W/m·K)	4.70	0.682	0.0268	0.0323
υ (m^2/s)	—	—	24×10^{-6}	—
γ (J/kg)	—	2.182×10^6	—	—

$$K_{l\,\mathrm{eff}} = \frac{(1 - A)K_l}{2B(1 - K_l/K_s)} \ln \left\{ 1 + 2B \frac{(K_s/K_l - 1)C_1}{1 - A} \right\} + \frac{(1 - A)K_a}{2B(1 - K_a/K_s)} \ln \frac{1 + 2B(K_s/K_a - 1)}{1 + 2B(K_s/K_a - 1)C_1/(1 - A)} + \{A - (1 - C_2)\}K_l + (1 - C_2)K_a \quad (15)$$

where

$$A = 2\phi/(3 - \phi),\ B = \phi/3 \text{ and}$$

$$\phi_l \leq B(1 - A):\ C_1 = \{(1 - A)\phi_l/B\}^{0.5},\ C_2 = 1 - A$$

$$\phi_l > B(1 - A):$$

$$C_1 = 1 - A,\ C_2 = \phi_l + (1 - B)(1 - A). \quad (16)$$

The estimated value of $K_{l\,\mathrm{eff}}$ is 1.43 W/mK and this value is used for the computation. Also, the effective thermal conductivity in the vapor region of the sand layer, $K_{\upsilon\,\mathrm{eff}}$, is also estimated from the following equation proposed by Tanaka (1990):

$$K_{\upsilon\,\mathrm{eff}} = AK_\upsilon + (1 - A)K_\upsilon \frac{\ln\{1 + 2B(K_s/K_\upsilon - 1)\}}{2B(1 - K_\upsilon/K_s)} . \quad (17)$$

The estimated value is $K_{\upsilon\,\mathrm{eff}} = 0.234$ W/mK. The properties of each element of the sand layer used for the estimation of the effective values are listed in Table 1. The properties of a quartz particle at 400 K is used for the value of the sand particle.

Experimental and Numerical Results. Measured temperatures at point a, point b, and point c are plotted in Fig. 3 as a function of time. In the figure, dashed lines represent the temperatures of the heated and opposite walls. The initial temperature of the sand layer is 289.15 K, and the temperature of the sand layer rises and levels off as it reaches to 373.15 K. The temperature rises again after the water evaporates. The solid lines in the figure represent the numerical results. The numerical result is higher and lower than the experimental re-

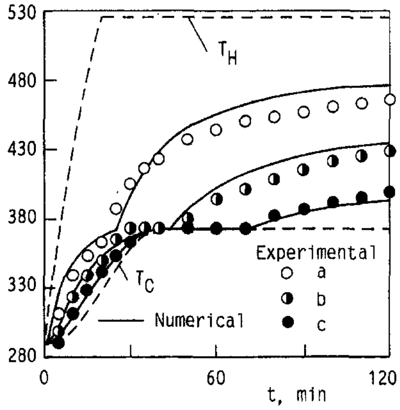

Fig. 3 Predicted and experimental temperatures

Table 2 Porosity, volume fractions of water and air

	Sample A	Sample B
ϕ	0.876	0.876
ϕ_l	0.012	0.018
ϕ_a	0.864	0.858

sults depending on the point. However, the time when the temperature rises again from 373.15 K agrees well with the experimental result.

In this numerical model, the saturation temperature is fixed at 373.15 K. To verify the validity of this assumption, the pressure in the sand layer is estimated from Eq. (2). The value of 1.8×10^{-10} m^2 (e.g., Nield, 1992) for the permeability of the sand layer is used for the estimation. The maximum pressure rise at the interface is 1 Pa. Therefore, the saturation temperature can be considered as 373.15 K.

Fire Resistance Tests for Calcium-Silicate Boards

Calcium-Silicate Boards. There are two types of calcium-silicate boards whose density ranges from 130 to 220 kg/m^3 and from 400 to 600 kg/m^3. The later is the pressed one of a low density board to reduce the thermal radiation. Low thermal conductivity and high heat capacity are required for the fire wall. Then, the numerical model for high density calcium-silicate boards, which contain different amount of the resin binder, will be presented. These two boards will be called a calcium-silicate board A and a calcium-silicate board B whose densities are about 400 kg/m^3.

The microphotograph for the boards are not presented here. But, the size of the void is less than 0.1 μm for both boards. Kunii et al. (1962) reported that the radiation heat transfer decreases with decreasing the size of the void. Therefore, the radiation heat transfer seems to be negligible small. Then, the radiation heat transfer is not included in the model.

The density and specific heat of the board change with temperature because of the evaporation of the adsorbed water and the decomposition of the crystalline water. Some measurements were done to obtain the thermal properties of the boards.

Measurement of Moisture Content. To measure the moisture content of the boards, the pieces of the calcium silicate boards of 30 mm cube were left in an electric furnace for 4.5 hours whose temperature was kept at 378.15 K. The moisture content of the boards was evaluated from the change in weight. The measured mass fractions of the free water in the test pieces are 2.82 and 4.04 wt% for the boards A and B, respectively. Using the density of water at 373.15 K, the volume fraction converted from the mass fraction is listed in Table 2. The effective density of the test pieces are, respectively, 405 and 406 kg/m^3. The porosity of the test pieces, ϕ_a, can be calculated from Eq. (16) using the effective density, $\rho_{v\,\mathrm{eff}}$, and the density of the crystal of the calcium-silicate, $\rho_s = 3270$ kg/m^3. The results are also listed in Table 2.

Thermogravimetry (TG) and Differential Thermal Analysis (DTA). The mass fractions of the adsorbed water, the crystalline water, and the resin binder were measured by using the thermogravity meter (Seiko Densi Co., TG/DTA 300). It is known that the heating rate within 5 ~ 20 K/min does not affect the results of TG and DTA. Then, the heating rate of 10 K/min was chosen. And the endothermic value of decomposition of the crystalline water was measured by using a differential thermal analyzer. The results of TG and DTA for the board A are plotted in Fig. 4. The solid line in the figure represents the result of TG and the dashed line represents DTA. As seen from the result of TG, the mass decreases gradually until 520 K, and the mass decreases twice in step fashion. The first mass reduction occurs in the temperature range from 570 to 720 K and the second reduction occurs in the range from 770 to 970 K. The reduction to 520 K is due to the evaporation of the adsorbed water, and the mass reduction from 570 to 720 K is due to the thermal decomposition of the resin binder. The last reduction from 770 to 970 K is due to the decomposition of the crystalline water.

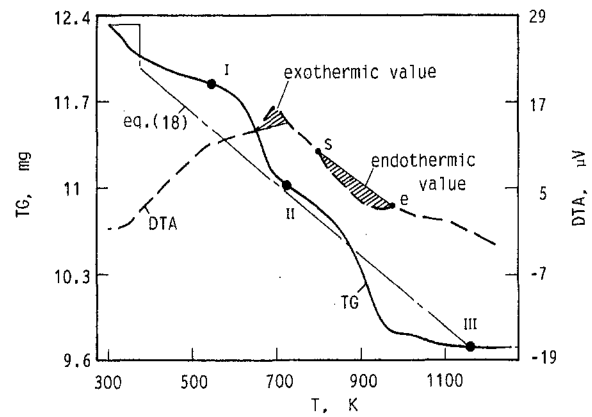

Fig. 4 Results of TG/DTA for calcium-silicate board A

As seen from Fig. 4, the mass reduction occurs continuously. Therefore, it is quite difficult to separate the masses of the adsorbed water, the resin binder, and the crystalline water exactly from the result of TG. Referring the result of DTA, the end point of the evaporation of the adsorbed water, denoted by I (the starting point of the decomposition of the resin binder), the end point of the thermal decomposition, denoted by II (the starting point of the decomposition of the crystalline water), and the end point of the decomposition of the crystalline water, denoted by III, are decided. The evaluated mass fractions of the free water, the adsorbed water, the resin binder, and the crystalline water are listed in Table 3.

Thermophysical Properties. Although the mass decreases in a step fashion as seen in Fig. 4, the mass reduction can be approximated by a liner function as

$$\rho_{\mathrm{eff}} = \begin{cases} \rho_0 & (T < 373.15) \\ c_1 - c_2 T & (373.15 < T < T_{\mathrm{III}}) \\ \rho_{\mathrm{III}} & (T_{\mathrm{III}} < T) \end{cases} \qquad (18)$$

where T_{III} represents the temperature of the end point of the decomposition of the crystalline water. The values of the coefficients c_1, c_2, ρ_0, and ρ_{III} are listed in Table 4. The correlation expressed by Eq. (18) is plotted in Fig. 4 by the dotted line.

Table 3 Mass fraction of water, adsorbed water, resin, crystalline water

	Sample A (wt%)	Sample B (wt%)
(a) Water	2.82	4.04
(b) Adsorbed water	1.03	1.79
(c) Resin	6.65	1.28
(d) Crystalline water	10.72	11.24

Table 4 Coefficients of Eq. (18)

	Sample A	Sample B
ρ_0 kg/m^3	417.0	423.1
c_1	441.2	432.8
c_2	0.09708	0.07195
ρ_{III} kg/m^3	328.6	345.5
T_{III} K	1136.85	1213.75

The peak of the DTA curve near 670 K represents the exothermic response due to the thermal decomposition of the resin binder. The shaded area in the figure represents the endothermic value due to the evaporation of the crystalline water. However, the area depends on the decision of the starting point s and the end point e. The endothermic value obtained from the figure is 2250 kJ/kg. The endothermic value due to the evaporation of the adsorbed water does not appear on the DTA curve in the figure, since the amount of adsorbed water is small. The latent heat of the free water at 373.15 K under the standard pressure, 2256.9 kJ/kg, is used for both endothermic values of the adsorbed water and the crystalline water. The exothermic values due to the decomposition of the binder obtained from the figure is 1900 kJ/kg. Therefore, the effective latent heat can be calculated by

$$\Delta\gamma = 2256.9 \times \{(b) + (d)\} - 1900 \times (c) \text{ kJ/kg}. \quad (19)$$

The effective specific heat of the calcium-silicate board is 838.4 J/kg K (catalog value). This value is considered as the value for the dried board. Then, the effective value for the board below 373.15 K, including the effect of the moisture, is

$$Cp_{l\,\mathrm{eff}} = \begin{cases} 930.6 & (\text{sample A}) \\ 973.6 & (\text{sample B}) \end{cases}. \quad (20)$$

Under the assumption that the decomposition of the resin binder, the evaporation of the adsorbed water, and the decomposition of the crystalline water occurs continuously from 373.15 K to T_{III}, those generated and absorbed heats could be included in the effective specific heat as

$$Cp_{v\,\mathrm{eff}} = \begin{cases} \dfrac{\{\Delta\gamma/(T_{\mathrm{III}} - 373.15)\}\rho_0}{\rho_{\mathrm{eff}}} + 838.4 \\ \qquad (373.15 < T < T_{\mathrm{III}}) \\ 838.4 \quad (T_{\mathrm{III}} < T) \end{cases}. \quad (21)$$

The effective thermal conductivities for both boards at room temperature were measured by the comparison method. Measured values are $K_{l\,\mathrm{eff}} = 0.105$ W/mK for the board A and $K_{l\,\mathrm{eff}} = 0.144$ W/mK for the board B, respectively. $K_{v\,\mathrm{eff}} = 0.070$ W/mK was used for the effective thermal conductivity in the range of $T > 373.15$ K. This value is the thermal conductivity of the calcium-silicate board at 400 K (e.g., Thermophysical Properties Handbook, 1990).

Comparisons With Experimental and Numerical Results. A schematic diagram of the experimental setup for the fire resistance test is presented in Fig. 5. Two calcium-silicate test boards of 210 mm × 210 mm × 60 mm were placed 8 mm apart. These two boards were insulated by a calcium-silicate insulator 60 mm thick whose density was 150 kg/m^3. These set of the boards were covered by a steel box of 1 mm thick. The box was set in an electric furnace. The air temperature of the furnace was controlled to follow the standard heating curve defined by JIS (Japanese Industrial Standard) S1037. The air temperature in the 8 mm gap was measured by K-type thermocouple of 0.65 mm ϕ. It can be considered that the measured temperature was slightly lower than that of the back surface of the board.

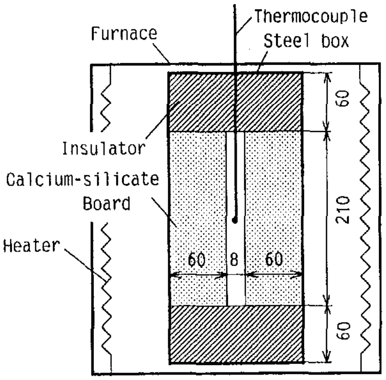

Fig. 5 Experimental setup for fire resistance test of calcium-silicate board

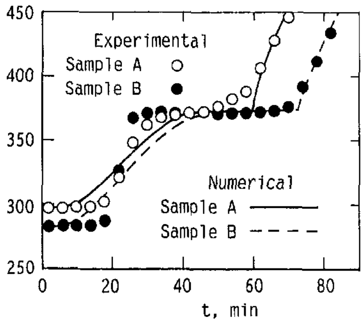

Fig. 6 Predicted and experimental results

The computations were conducted with $h_H = 50$ W/m^{2}K and $\epsilon_H = 0.9$ for the heated surface and with the insulated boundary condition for the opposite surface. The same values were used in the paper by Huang et al. (1991). However, some researchers (e.g., Sultan et al., 1986) adopted $h_H = 20 \sim 30$ W/m^{2}K for the computation instead of 50 W/m^{2}K. The surrounding temperature T_∞ which is calculated from Eq. (22) was also used for the computations. Note that the Eq. (22) is the approximation of the standard heating curve.

$$T_\infty = 1353 - 340e^{-0.8t/3600} - 130e^{-5t/3600} - 610e^{-19t/3600} \quad (22)$$

The initial temperatures of the boards of A and B were, respectively, 297.15 and 283.15 K. While the calculated temperature of T_∞ from Eq. (22) was lower than the initial temperature T_i, $T_\infty = Ti$ was assumed. The results are plotted in Fig. 6. The solid line and dashed line in the figure represent the numerical results. As seen in the figure, a discrepancy between the numerical and experimental results can be seen at the initiation of heating. However, the predicted time when the temperature rises again from 373.15 K almost coincides with the numerical results. The reason for this discrepancy is not clear since we can only observe the temperature. However, the fact is that the experimentally observed temperature rise is earlier than the numerical one. Since there are vapor vents on the periphery of the air gap, the vapor flow toward the inner direction may occur in the board.

The measurement of the permeability of the board B was also conducted using a 10 mm board. The obtained value is $k = 3 \times 10^{-15}$ m^2. Using this value, the estimated maximum pressure rise at the interface was 0.5×10^5 Pa when the liquid-vapor interface is located at $X_1 = 14$ mm. The saturation temperature rises 11 K due to the pressure rise.

Concluding Remarks

The simple one-dimensional numerical model to predict thermal responses of a fire wall which is made of a nonorganic insulator is developed. To verify the validity of the proposed model, fire resistance tests were performed for a sand wall and two calcium silicate boards. The results were compared with the numerical results. A discrepancy of the temperature responses can be seen at the initiation of heating. However, the predicted time when the temperature rises from 373.15 K agrees well with the numerical results.

References

Cao, Y., Faghri, A., and Chang, W. S., 1989, "A Numerical Analysis of Stefan Problems for Generalized Multi-dimensional Phase-Change Structures Using the Enthalpy Transforming Model," *Int. J. of Heat and Mass Transfer*, Vol. 32, No. 7, pp. 1289–1298.

Dayan, A., and Gluekler, E. L., 1982, "Heat and Mass Transfer within an Intensity Heated Concrete Slab," *International Journal of Heat and Mass Transfer*, Vol. 25, pp. 1461–1467.

Huang, C. L. D., and Ahmed, G. N., 1991, "Influence of Slab Thickness on Responses of Concrete Walls under Fire," *Numerical Heat Transfer*, Part A, Vol. 19, pp. 43–64.

Kunii, D., 1962, "Radiation Heat Transfer in Porous Material," *Journal of J.S.M.E.*, Vol. 65, No. 525, pp. 87–93.

Nield, D. A., and Bejan, A., 1992, *Convection in Porous Media*, Springer-Verlag, New York, p. 4.

Japan Society of Thermophysical Properties, 1990, *Thermophysical Properties Handbook*, Yokendo, Japan.

Sahota, M. S., and Pagni, P. J., 1979, "Heat and Mass Transfer in Porous Media Subject to Fires," *International Journal of Heat and Mass Transfer*, Vol. 22, pp. 1069–1081.

Sultan, M. A., Harmathy, T. Z., and Mehaffey, J. R., 1986, "Heat Transmission in Fire Test Furnaces," *Fire and Materials*, Vol. 10, pp. 47–55.

Tanaka, M., and Chisaka, F., 1990, "Effective Thermal Conductivity of Discontinuous and Continuous Solid System," *KagakuKogaku Ronbunshu*, Vol. 16, No. 1, pp. 168–173.

Tanaka, M., 1991, "Effective Thermal Conductivity of Wetted Granular Beds," *KagakuKogaku Ronbunshu*, Vol. 17, No. 2, pp. 445–447.

C. C. Wu
Associate Professor,
Department of Aeronautical Engineering,
Chung Cheng Institute of Technology,
Taoyuan 33509, Taiwan

G. J. Hwang[1]
Professor,
Department of Power
Mechanical Engineering,
National Tsing Hua University,
Hsinchu 30043, Taiwan
Fellow ASME

Flow and Heat Transfer Characteristics Inside Packed and Fluidized Beds

This paper investigates experimentally and theoretically the flow and heat transfer characteristics inside packed and fluidized beds. A single-blow transient technique combined with a thermal nonequilibrium two-equation model determined the heat transfer performances. Spherical particles were randomly packed in the test section for simulating the packed beds with porosity $\varepsilon = 0.38$ and 0.39. Particles were strung with different spaces for fluidized beds with $\varepsilon = 0.48 \sim 0.97$. The ranges of dominant parameters are the Prandtl number $Pr = 0.71$, the particle Reynolds number $Re_d = 200 \sim 7000$, and $\varepsilon = 0.38 \sim 0.97$. The results show that the heat transfer coefficient increases with the decrease in the porosity and the increase in the particle Reynolds number. The friction coefficients of the fluidized beds with $\varepsilon = 0.48$ and 0.53 have significant deviations from that of the packed bed with $\varepsilon = 0.38$ and 0.39. Due to fewer interactions among particles for $\varepsilon = 0.97$, the friction coefficient approaches the value of a single particle.

Introduction

Porous media have been employed widely in electronic cooling, thermal energy storage system, geothermal system and many other areas. Researchers have focused their attentions to the studies of drag and heat transfer in porous media for decades. For theoretical simulation of the transport phenomena in porous media, Vafai and Tien (1981) used a non-Darcian model to account for the boundary and inertia effects in forced convection. Vafai et al. (1985), Beckerman and Viskanta (1987), Cheng and Zhu (1987), and Renken and Poulikakos (1987, 1988) studied the forced convection in the porous media with the effects of flow inertia, thermal dispersion, variable porosity, and Brinkman friction. All the above-mentioned theoretical studies adopted the local thermal equilibrium assumption for formulating the energy equation. Generally, the values of thermal conductivity of the solid and fluid are not of the same order of magnitude. One should consider the heat transfer between the solid and the fluid phases for a better prediction of the heat transfer performance.

Koh and Colony (1974) and Koh and Stevens (1975) studied the forced convection in a porous channel filled with a high conductivity porous material by using the Darcy flow model. They reported that the wall temperature and the wall-to-coolant temperature difference decrease drastically in the channel with a constant heat flux. Vafai and Sozen (1990) presented an analysis of the forced gas flow through a packed bed of spherical particles. They used the fluid-to-solid heat transfer coefficients from an empirical correlation established by Gamson et al. (1943). The results showed that the local thermal equilibrium condition was very sensitive to the particle Reynolds number and the Darcy number. Chen and Yue (1991) studied theoretically and experimentally the thermal performance of packed capsules in an ice water storage system for air conditioning.

Hwang et al. (1994, 1995) found that the value of the heat transfer coefficient between the solid and the fluid phases might affect seriously the estimation of the heat transfer performance in a high conductivity porous channel. The structure and porosity of the porous media may also affect the flow patterns and thermal transport phenomena in the porous channels. Ergun (1952), Kuo and Nydegger (1978), Robbins and Gough (1978), and Jones and Krier (1983) investigated the channel flow drag with porosity from 0.38 to 0.65. Galloway and Sage (1970) and Rowe and Claxton (1965) measured the heat transfer performance in porous channels.

Howard (1964) presented a single-blow method including the effect of longitudinal heat conduction. Liang and Yang (1975) used the single-blow transient method to determine the heat transfer performance of perforated heat exchanger surfaces. This method measures the transient temperature response curves at the inlet and outlet sections. It requires a trial value of the heat transfer coefficient in numerical modeling for calculating the exit fluid temperature. If the calculated exit temperature does not match with the measured one, one should modify the trial value of the heat transfer coefficient.

A porous medium provides a large thermal dispersion and a solid-fluid contact area many times greater than the duct surface area, thus greatly enhancing the heat transfer. The purpose of this paper was to study the heat transfer performance of the porous channels by using the single-blow transient method combined with a thermal nonequilibrium two-equation model. This study set up a low-speed wind tunnel with an air heater and measurement systems of flow and temperature. When high-temperature air passed through the porous channel, a temperature recorder measured the transient inlet and outlet fluid temperatures for determining the internal heat transfer coefficients. The results show that the particle Reynolds number and porosity greatly affect the heat transfer coefficient.

Experimental Apparatus and Procedure

Experimental Apparatus. Figure 1 shows an experimental setup for flow drag and heat transfer measurements of packed and fluidized beds. It includes four major parts: (a) wind tunnel, (b) test section, (c) porous medium, and (d) data acquisition system. The details of the apparatus are depicted as follows:

(*a*) *Wind Tunnel:* It was an open-looped suction-type low-speed wind tunnel. Through a 1.1×1.1 m^2 bell mouth with a honeycomb straightener, air passed two contraction sections with

---

[1] To whom correspondence should be addressed.

Contributed by the Heat Transfer Division for publication in the JOURNAL OF HEAT TRANSFER and presented at '97 NHTC, Baltimore. Manuscript received by the Heat Transfer Division, June 17, 1997; revision received, Apr. 6, 1998. Keywords: Forced Convection, Measurement Techniques, Packed and Fluidized Beds. Associate Technical Editor: M. Kaviany.

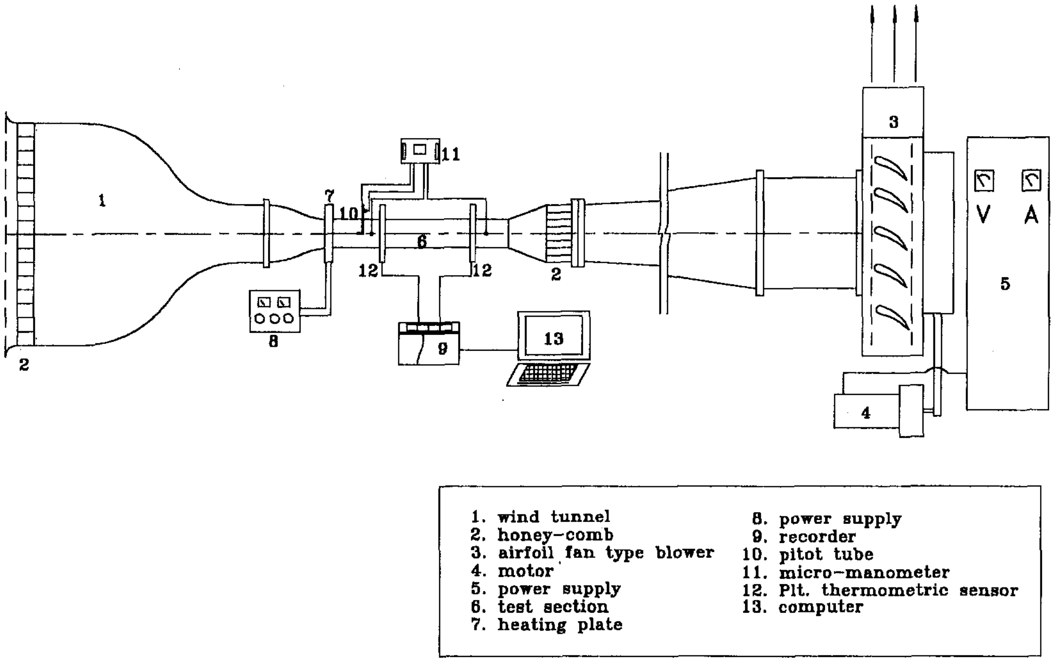

Fig. 1 Schematic of test system

ratios 30:1 and 4:1 for reducing the turbulence level. An airfoil fan-type blower could drive the air flow rate up to 144 m^3/min by a voltage-regulated power supply. To heat up the air flow before entering the test section, a specially designed plate heater was installed upstream of the test section. A 30 μm × 20 mm × 250 cm SUS304 stainless steel foil was wound around 24 times with 4 mm spacing in a bakelite frame to form the plate heater. The ends of the foil connected with brass bars on the outer surface of the frame. Electric power supplied through the brass bars by means of an electromagnetic switch, resulting in the inlet air temperature rising exponentially with time.

(b) Test Section: The test section was a square channel of cross section 10 × 10 cm^2 and length 30 cm. The tunnel walls were made of 20-mm thickness Plexiglas for observing the particle bed structure and reducing the heat loss. For the packed bed, the randomly arranged sphere particles filled up in the test section. Two stainless steel screens placed at the inlet and the outlet sections held the particles tightly in place. The fluidized bed was simulated by stringing nylon thread through the spherical particles in the test section. The nylon threads were fixed in 20 × 60 holes with a diameter of 1 mm. The holes were on two side walls of the test section, as shown in Fig. 2. The porosity can be adjusted by changing the particle size and the space between the particles. It is also noted in Fig. 2 that the number of particles is 10 × 10 × 30 for the case of d_p = 10 mm and ε = 0.48, and the number of particles is 19 × 19 × 60 for d_p = 5 mm and ε = 0.53. Due to the accumulated error in dimension, 20 × 20 particles with d_p = 5 mm cannot be fitted in the cross-sectional area of 10 × 10 cm^2. There were two cover plates for reducing flow leakage from the side walls of the test section. Two Pitot tubes of outside diameter 3.18 mm were installed at the upstream and the downstream of the test section for measuring the static pressure difference. The platinum wire resistance read the air flow average temperatures at the inlet and the outlet sections. The platinum wire of diameter 50 μm and length 1 m was wound with an equal spacing of 1 cm across the channel section to form a resistance temperature detector (RTD). Incorporated with a thermostat, a linear calibration curve correlated the temperature range from 20 to 60°C. Due to the wake effect, air temperature behind the porous bed was nonuniform and fluctuated. It is expected that the RTD may be more suitable for mean temperature measurement than the temperature grid by using a number of thermocouples jointed together.

Nomenclature

A = heat exchange area, m^2
C_1 = constant, = $m_s c_s / m_f c_f$
c = isobaric specific heat, J/kgK
C_f = friction coefficient
d_p = average bead diameter, m
Fv = friction factor
h = heat transfer coefficient, W/m^2K
k = thermal conductivity, W/mK
L = test section length, m
m = mass, kg
$\dot{m}$ = mass flow rate of fluid, kg/s
Nu = Nusselt number, = hd_p/k_f
P = pressure, N/m^2
Pr = fluid Prandtl number, = $c_f \mu_f / k_f$
Re_d = particle Reynolds number, = $\rho_f U d_p / \mu_f$
T = temperature, K
T_{final} = inlet fluid temperature, K
T_0 = initial temperature, K
t = time, sec
U = inlet average velocity, m/s
v_t = volume of total porous channel
X = dimensionless axial length
x = axial length, m

Greek symbols

ε = void fraction or porosity
μ = dynamic viscosity, kg/ms
θ = dimensionless temperature
ρ = density, kg/m^3
τ_i = time constant of inlet fluid temperature, sec
τ_{sys} = time constant of solid-fluid system, $m_s c_s / hA$

Subscripts

f = fluid
in = inlet
out = exit
s = solid

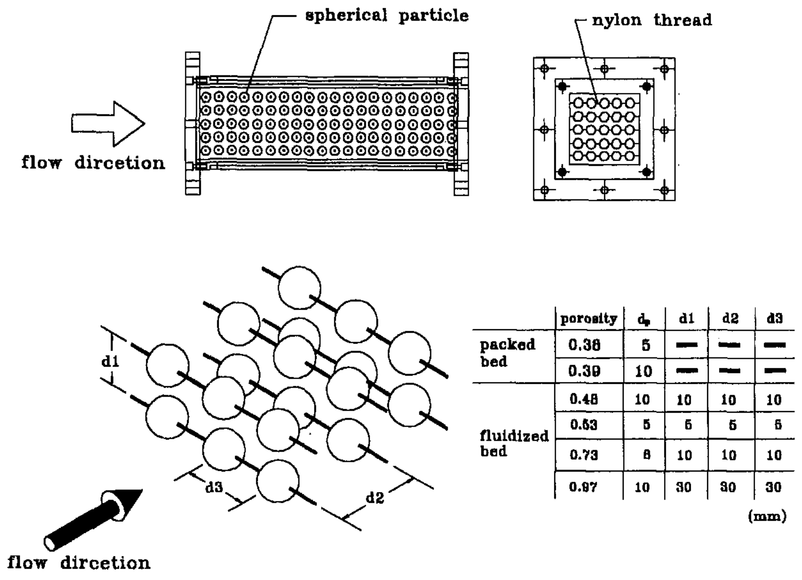

	porosity	d_p	d1	d2	d3
packed bed	0.38	5	—	—	—
	0.39	10	—	—	—
fluidized bed	0.48	10	10	10	10
	0.63	5	6	5	6
	0.73	8	10	10	10
	0.97	10	30	30	30

(mm)

Fig. 2 Packed and fluidized beds

(c) Porous Medium: The properties of solid an ABS particle are $\rho_s = 1190.$ kg/m^3, $k_s = 0.137$ W/mK and $c_s = 1255.$ J/kgK. The porosity of the packed bed was evaluated by using $\varepsilon = (v_t - v_s)/v_t$. In this expression, v_t is the volume of the total porous channel measured by its geometry, and $v_t - v_s$ is the difference of the total channel volume and particle volume. $v_t - v_s$ is also the volume of filling water. The porosity of the fluidized bed was obtained by calculation.

(d) Data Acquisition System: Pitot tubes measured the pressure drop and air velocity across the test channel. A digital manometer was for low-pressure difference (less than 2.02×10^3 N/m^2) and a U-tube Aq manometer was for high-pressure differences ($1.01 \times 10^3 \sim 1.01 \times 10^4$ N/m^2). Response for monitoring the air temperatures must be fast enough to collect enough data in the transient period. The time histories of the inlet and outlet air temperatures were recorded in a resistance mode by using a recorder. The circuits connected to a personal computer by using a GPIB interface and the conversion rate of the bridge circuits was 135 samples per sec.

Procedure. The air flow velocity determined by the upstream total and static pressure difference in the wind tunnel was kept constant for each run. The bead diameter and the average velocity defined the Reynolds number. The pressure drop, ΔP, was the static pressure difference between the inlet at position 4 cm in front of the test section and the exit at position 7 cm behind the test section. The heated inlet air had a temperature rise of around 20°C. A personal computer continuously recorded the time history of the air exit temperature until the temperature achieved a steady state. Before starting another test run, it took 20 to 30 minutes for the test section to cool down.

Analysis

Considering the heat transfer mechanism in a porous channel involves a complex thermal transport between the fluid and porous medium. The present study applied the single-blow transient method. A heated fluid flow supplied thermal energy to the heat transfer surface of the porous medium. The transient response of the outlet fluid temperature estimated the heat transfer coefficient between the fluid and the solid material. The following assumptions and simplifications are employed for facilitating the analysis of this problem.

1 The volumetric average fluid velocity in the porous channel is uniform.

2 The inlet fluid temperature is uniform. The temperatures of solid and fluid in the porous channel depend only on the position along the flow direction and time. Therefore, one is able to employ a one-dimensional transient heat transfer model.

3 The permeability is homogeneous and isotropic. The fluid thermophysical properties may be evaluated at the measured local average temperature.

4 There is no local thermal equilibrium between the solid and fluid phases.

5 The conduction and dispersion along the streamwise direction are neglected.

Thus, energy equations of the solid and fluid phases are

$$m_s c_s \frac{\partial T_s}{\partial t} = hA(T_f - T_s) \tag{1}$$

$$m_f c_f \frac{\partial T_f}{\partial t} + m_f c_f \frac{U}{\varepsilon} \frac{\partial T_f}{\partial x} = hA(T_s - T_f). \tag{2}$$

In the above equations, T_s and T_f indicate the volumetric average temperature of the solid and fluid phase, respectively, h is the heat transfer coefficient between the solid and fluid phase, and A is the heat exchange area. Equation (1) shows that the heat transferred from the fluid become the change of internal energy in solid. Equation (2) indicates that the enthalpy change of the fluid and the heat convection in the longitudinal direction balance the heat transfer to the solid phase. In the above equation, one neglects the axial thermal dispersion effect. By putting air velocity around 10 m/s, thermal dispersion around 50 times of the thermal diffusivity, and using the bead diameter as the characteristic length, one may find that the value of the advection term is about one order of magnitude higher than the axial thermal dispersion. Therefore, it is justified to use the above equations for the heat transfer analysis.

The associate initial and boundary conditions are

$$T_s(0, x) = T_f(0, x) = T_0 \tag{3}$$

$$T_f(t, 0) = T_0 + (T_{\text{final}} - T_0)(1 - e^{-t/\tau_i}) \tag{4}$$

where T_{final} is the inlet fluid steady-state temperature and τ_i is the experimentally determined time constant. The time constant is defined at $(T_f(t, 0) - T_0)/(T_{\text{final}} - T_0) = 0.632$.

The governing equations can be nondimensionalized by introducing the following variables:

$$\theta = \frac{T - T_0}{T_{\text{final}} - T_0}\,; \quad X = \frac{x}{\dot{m}_f c_f L/hA}\,;$$

$$\tau = \frac{t}{\tau_{\text{sys}}}\,; \quad \tau_{\text{sys}} = \frac{m_s c_s}{hA}\,; \quad C_1 = \frac{m_s c_s}{m_f c_f}$$

where L is the porous channel length, τ_{sys} is the time constant of solid-fluid system, and C_1 is the ratio of heat capacities of the solid and the fluid. The nondimensionalized equations, initial and boundary conditions are then expressed as follows:

$$\frac{\partial \theta_s}{\partial \tau} = \theta_f - \theta_s \tag{5}$$

$$\frac{\partial \theta_f}{\partial \tau} + C_1 \frac{\partial \theta_f}{\partial X} = C_1(\theta_s - \theta_f) \tag{6}$$

$$\theta_s(0, X) = \theta_f(0, X) = 0 \tag{7}$$

$$\theta_f = f(\tau) = 1 - e^{-\tau/\tau^*} \tag{8}$$

where τ^* is defined as τ_i/τ_{sys}. Using the prescribed values of geometric properties, the thermophysical properties, fluid inlet temperatures, mass flow rate and the guessed heat transfer coefficient h, one solves simultaneously the coupled Eqs. (5) to (8) for temperature distributions of solid and the fluid phases. One applies a finite difference explicit scheme to these equations. One has to ensure the stability of the numerical scheme by choosing a proper combination of $\Delta\tau = 0.05$ and $\Delta X = 0.1$ to obtain the temperature distributions. One also checked the result with that of finer meshes $\Delta\tau = 0.05$ and $\Delta X = 0.1$ with accuracy up to three significant figures.

The Determination of *h* and Error Analysis

One employed a modified single blow transient method developed by Liang and Yang (1975) for determining the heat transfer performance of the porous channel. This method requires only the transient response curves of the average inlet and outlet air temperatures. To match the exit air temperature, one guessed a trial value for the heat transfer coefficient, h. One modified the value of the heat transfer coefficient by keeping the difference between the predicted and the measured exit temperature less than 10^{-3}. One select six exit temperatures with an equal time interval along the measured response curve. The arithmetical mean value of the six heat transfer coefficients was the heat transfer coefficient for the porous channel with an air flow velocity. The maximum R.M.S. difference among the six measured air exit temperatures and the temperatures obtained from the average heat transfer coefficient was under 1.13 percent in the present study.

An uncertainty analysis (Kline and McClintock, 1953) was for evaluation of the accuracy of experimental measurements. Equation (2) was used for estimating the percentage of uncertainty. The percentage of uncertainty of m_f, c_f, ΔT_f, x, and A was 0.5, 0.5, 5, 0.2, and 1, respectively. Thus the uncertainty in the heat transfer coefficient was less than 5.2 percent.

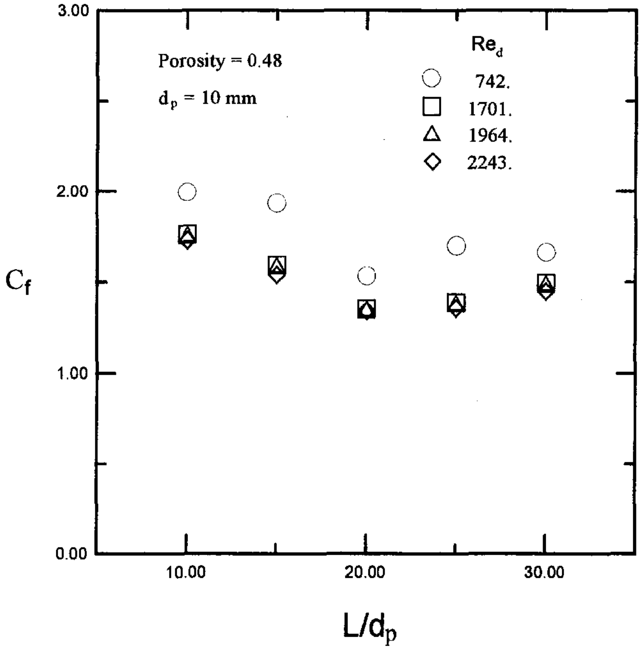

Fig. 3 The variation of C_f with Re_d and L/d_p

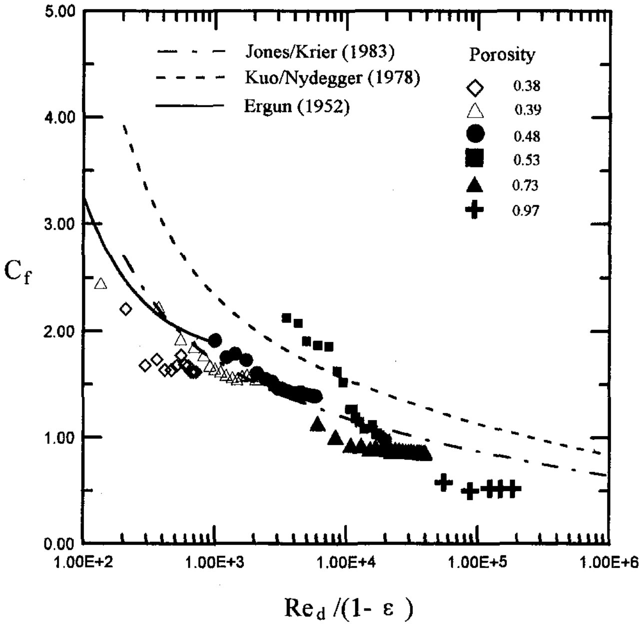

Fig. 4 The variation C_f with the effect of ε and Re_d

Results and Discussion

One may define the drag coefficient C_f in a porous channel as (Jones and Krier, 1983)

$$C_f = \left(\frac{\Delta P}{L}\right)\frac{d_p}{\rho U^2}\frac{\varepsilon^3}{(1-\varepsilon)}\,. \tag{9}$$

For correlating the relationship between C_f and Re_d, the following relation was the proposed friction factor, Fv (Kuo and Nydegger, 1978; Jones and Krier, 1983),

$$Fv = C_f \frac{Re_d}{(1-\varepsilon)}\,. \tag{10}$$

To reduce the entrance effect in the measurement of flow drag of the porous channel, one has to have a sufficient length of the test section. Figure 3 shows the variations of C_f with the length of the test section L/d_p for $Re_d = 742$, 1701, 1964, and 2243. It is seen that all the data of $Re_d = 1701$, 1964, and 2243 lie together. The data of $Re_d = 742$ presented higher C_f values than those of higher Reynolds number. It is seen in the definition of C_f that ΔP is in proportion to U^n, where $n < 2$ for $Re_d = 742$. The pressure difference ΔP is in proportion to U^2 at larger values of the Reynolds number. It is also seen that C_f decreases monotonously for $L/d_p \le 20$, and increases slightly when L/d_p

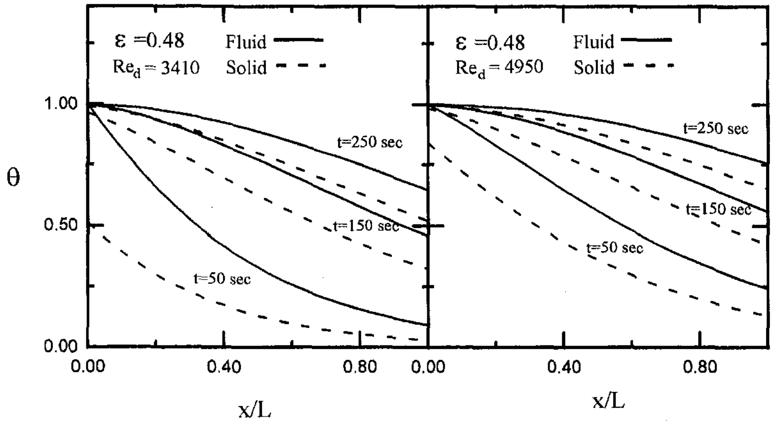

Fig. 5 The calculated Θ_f and Θ_s along the x direction at different time

$\gtrsim 25$. The value of C_f of $L/d_p = 30$ is about seven percent higher than that of $L/d_p = 20$. This may be due to the irregularity of the particle arrangement and then the development of velocity fluctuation along the downstream region. With this observation, one may conclude that a length of $L/d_p \gtrsim 20$ may be long enough for the measurement of a fully developed flow drag coefficient with a few percentage errors.

Figure 4 shows the measured value of friction coefficient C_f versus $\mathrm{Re}_d/(1-\varepsilon)$ for various ε. The value of C_f is evaluated by using Eq. (9). To correlate the values of C_f and Re_d, the formula defined in Eq. (10) is also presented graphically in this figure. The curve of Jones and Krier (1983), with $Fv = 150 + 3.89\,(\mathrm{Re}_d/(1-\varepsilon))^{0.87}$, and Kuo and Nydegger (1978), with $Fv = 276.23 + 5.05\,(\mathrm{Re}_d/(1-\varepsilon))^{0.87}$, are depicted. The measured data for each value of porosity approximately follow the trend of correlation of Eq. (10). The values of C_f for $\varepsilon = 0.38$ and 0.39 are below the curve of Jones and Krier (1983). The data of $\varepsilon = 0.48$ and 0.53 are seen on the opposite side of the curve. One may see the difference of C_f in the packed and fluidized beds. The values of C_f for 0.97 approach the value $C_f = 0.5$ for the single spherical particle and that lies below the curve of Jones and Krier (1983). The factor $\varepsilon^3/(1-\varepsilon)$ in Eq. (9) is greater than 1.0 when $\varepsilon > 0.682$, and is less than 1.0 when $\varepsilon < 0.682$. This increases the difference between C_f for small and large values of porosity, and makes C_f be displayed in linear scale as shown in Fig. 4. The factor $1/(1-\varepsilon)$ in Eq. (10) stretches the value of Re_d for large ε to avoid the data overlapping.

The fluid and the solid-phase temperature distributions along the flow direction at various times for $\varepsilon = 0.48$ are shown in Fig. 5. The results were obtained from the numerical calculation. When the high-temperature fluid flows through the low-temperature porous media, phenomena of thermal penetration are developed as shown in the figure. The flow with a higher Reynolds number shows a stronger thermal penetration. One also find that the temperature difference between the solid and the fluid decreases as time increases. From this figure, one can see the fluid and solid temperatures are far from each other. This clearly indicates the necessity of using the two-equation model.

Figure 6 shows the time history of the measured dimensionless inlet and outlet temperatures for various $\varepsilon = 0.39 \sim 0.97$ and $\mathrm{Re}_d = 1711 \sim 1815$. The simulated time constant and the corresponding inlet temperature curve are also plotted. The calculated outlet temperature distributions with the obtained average heat transfer coefficients are presented for comparison. The agreement between the measured and calculated data for $\varepsilon = 0.39 \sim 0.73$ is satisfactory. Only a small difference is observed between those for $\varepsilon = 0.97$. This proves the validity of the present transient technique. It is also seen that the value of the heat transfer coefficient increases with the decrease in the porosity. The time development of a dimensionless exit temperature for the cases of $\varepsilon = 0.73$ with $\mathrm{Re}_d = 920$, 1768 and 2530, is shown in Fig. 7. The agreement between the measured and calculated data for $\mathrm{Re}_d = 920$ and 1768 is also satisfactory. A small difference between those for $\mathrm{Re}_d = 2530$ is observed. This figure also depicts that the heat transfer coefficient increases with the increase in the Reynolds number.

Figure 8 summarizes the obtained Nusselt number, $\mathrm{Nu} = hd_p/k_f$, for $\varepsilon = 0.39 \sim 0.97$ and $\mathrm{Re}_d = 1000 \sim 6500$. The relationships of the Nusselt number and Reynolds number for $\varepsilon = 0.39 \sim 0.48$ and $\varepsilon = 0.73 \sim 0.97$ are not the same. One can see for $\varepsilon = 0.73$ and 0.97 that the value of Nu increases approximately in proportion to the value of Re_d. This may be explained by using the model of a single-sphere particle. For a fixed Reynolds number, a higher Nu for $\varepsilon = 0.73$ than that for $\varepsilon = 0.97$ is observed. This may be due to the higher local fluid velocity and the channeling effect for the $\varepsilon = 0.73$. An empirical formula of $\mathrm{Nu} = 0.0032\,\mathrm{Re}_d$ is proposed for $\varepsilon = 0.73$ and $\mathrm{Nu} = 0.0022\,\mathrm{Re}_d$ for $\varepsilon = 0.97$. Due to different mechanisms in transport phenomena, one has to use different correlation for different porosity. For $\varepsilon = 0.39$, the data may be correlated by using $\mathrm{Nu} = 0.32\,(\mathrm{Re}_d)^{0.59}$ that is similar to the correlation

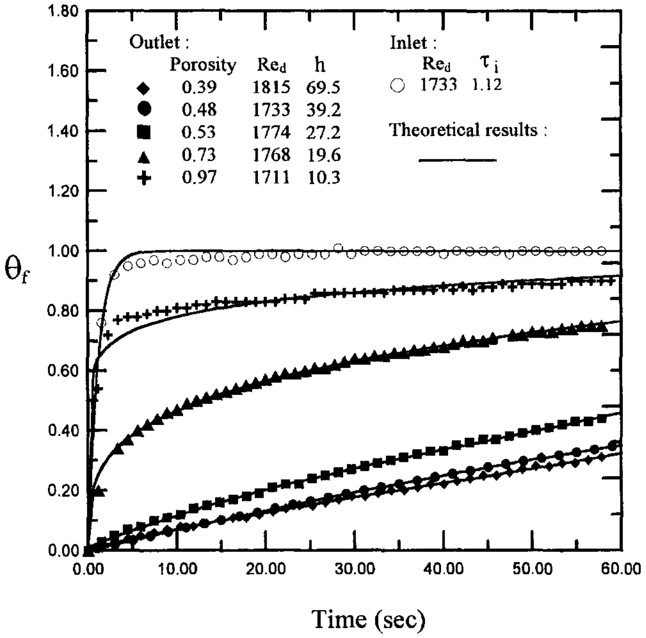

Fig. 6 The measured dimensionless inlet and outlet temperature for various ε and Re_d (h: W/m^{2}K)

proposed by Gamson et al. (1943). The data of $\varepsilon = 0.48$ varies linearly with Re_d. The correlation $Nu = 8 + 0.004\ Re_d$ may be used. All the measured data are within ten percent of the corresponding correlated curve. The data of Hwang et al. (1995), Galloway and Sage (1970), and Rowe and Claxton (1965) are also plotted for comparison. Due to different reasons, all these data yield higher values of the past Nusselt number than the present one. The data of Hwang et al. (1995) were obtained in a randomly packed sintered porous channel. The structures of solid and fluid phases were completely different from the present well-aligned particles. The irregularity of structure may yield a higher heat transfer rate. The data of Galloway and Sage (1970) and Rowe and Claxton (1965) were from an arrangement of staggered spheres. The fluid temperature was taken at a position behind the sphere. These were the reasons for higher values of the Nusselt number.

Concluding Remarks

1 This paper has studied the heat transfer performance of the porous channels by using the single-blow transient method combined with a thermal nonequilibrium two-equation model. The agreement between the measured data and calculated curve is satisfactory. This proves the validity of the present transient technique. The results show that the heat transfer coefficient is greatly affected by the particle Reynolds number and porosity.

2 To reduce the entrance effect in the measurement of flow drag of the porous channel, one has to have a sufficient length of the test section. This paper investigates the variations of C_f with the length of the test section L/d_p for $Re_d = 742$, 1701, 1964, and 2243. It is seen that C_f decreases monotonously for $L/d_p \leq 20$ and increases slightly when $L/d_p \geq 25$. The value of C_f of $L/d_p = 30$ is about seven percent higher than that of $L/d_p = 20$. With this observation, one may conclude that a length of $L/d_p \geq 20$ may be long enough for the measurement of a fully developed flow drag coefficient with a few percentage errors.

3 The measured drag coefficients for each porosity approximately follow the trend of correlation of Eq. (10). The values of C_f for $\varepsilon = 0.38$ and 0.39 lie below the curve of Jones and Krier (1983). The data of $\varepsilon = 0.48$ are seen on the opposite side of the curve. One may differentiate C_f from the packed and fluidized beds by this difference. The values of C_f for 0.97 approach the value $C_f = 0.5$ for the single spherical particle and that lies below the curve of Jones and Krier (1983).

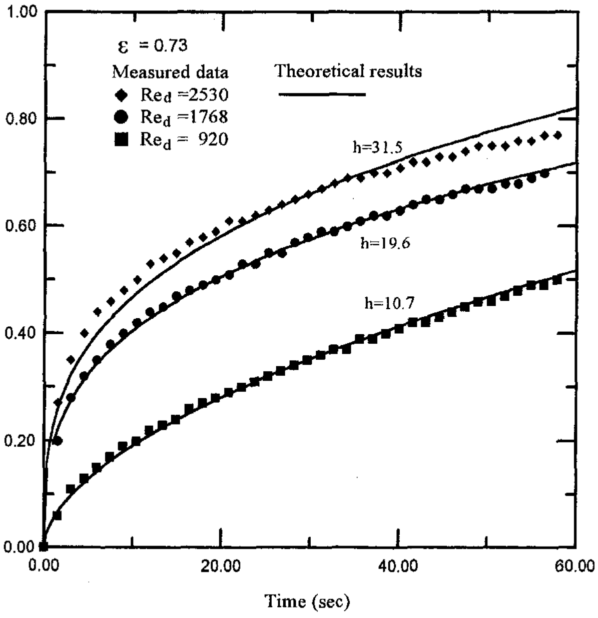

Fig. 7 The measured dimensionless outlet temperature for $\varepsilon = 0.73$ with various Re_d (h: W/m^2K)

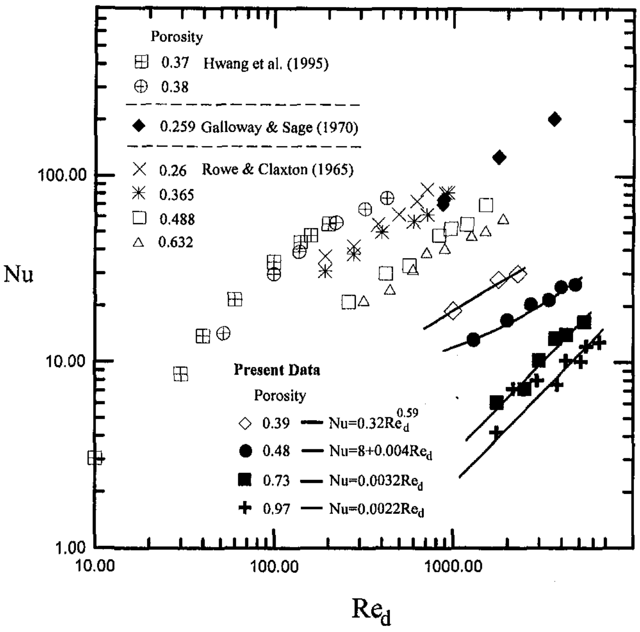

Fig. 8 Nessult number versus Re_d for various ε

4 For $\varepsilon = 0.73 \sim 0.97$, the value of the Nusselt number increases approximately in proportion to the value of Re_d. This may be explained by using the model of a single-sphere particle. For a fixed Reynolds number, a higher Nu for $\varepsilon = 0.73$ than that for $\varepsilon = 0.97$ is observed. An empirical formula of $Nu = 0.0032\ Re_d$ is proposed for $\varepsilon = 0.73$ and $Nu = 0.0022\ Re_d$ for $\varepsilon = 0.97$. Due to a different mechanism in transport phenomena, one has to use a different correlation for different porosity. For $\varepsilon = 0.39$, the data may be correlated by using $Nu = 0.32\ (Re_d)^{0.59}$ that is similar to the correlation proposed by Gamson et al. (1943). For $\varepsilon = 0.48$, the data are not in proportion to Re_d. The correlation $Nu = 8 + 0.004\ Re_d$ is used. All the measured data are within ten percent of the corresponding correlated curve.

Acknowledgment

The authors would like to thank the National Science Council, Taiwan (Grant No. NSC85-2623-D007-002) for their financial support of this work.

References

Beckerman, C., and Viskanta, R., 1987. "Forced Convection Boundary Layer Flow and Heat Transfer Along a Flat Plate Embedded in a Porous Medium," *Int. J. Heat Mass Transfer,* Vol. 30, No. 7, pp. 1547–1551.

Brinkman, H. C., 1947, "A Calculation of the Viscous Force Extended by a Flowing Fluid on a Dense Swarm of Particles," *Applied Science Research, Al.,* pp. 27–34.

Chen, S. L., and Yue, J. S., 1991, "Water Thermal Storage with Solidification," *Heat Recovery System & CHP,* Vol. 8, pp. 247–254.

Cheng, P., and Zhu, H., 1987, "Effects of Radial Thermal Dispersion on Fully Developed Forced Convection in Cylindrical Packed Bed," *Int. J. Heat Mass Transfer,* Vol. 30, pp. 2373–2383.

Ergun, S., 1952, "Fluid Flow Through Packed Columns," *Chemical Engineering Progress,* Vol. 48, pp. 89–94.

Galloway, T. R., and Sage, B. H., 1970, "A model of the Mechanism of Transport in Packed, Distended, and Fluidized Beds," *Chemical Engineering Science,* Vol. 25, pp. 495–516.

Gamson, B. W., Thodos, G., and Hougen, O. A., 1943, "Heat, Mass and Momentum Transfer in Flow of Gases," *Trans. AIChE,* Vol. 39, pp. 1–35.

Howard, C. P., 1964, "The Single Blow Problem Including the Effect of Longitudinal Conduction," presented at the Gas Turbine Conference and Product Show, Houston, TX, ASME Paper No. 64-GT2-11.

Hwang, G. J., and Chao, C. H., 1994, "Heat Transfer Measurement and Analysis for Sintered Porous Channels," ASME JOURNAL OF HEAT TRANSFER, Vol. 116, pp. 456–464.

Hwang, G. J., Wu, C. C., and Chao, C. H., 1995, "Investigation of Non-Darcian Forced Convection in an Asymmetrically Heated Sintered Porous Channel," ASME JOURNAL OF HEAT TRANSFER, Vol. 117, pp. 725–732.

Jones, D. P., and Krier, H., 1983, "Gas Flow Resistance Measurements Through Packed Beds at High Reynolds Numbers," ASME *Journal of Fluids Engineering,* Vol. 105, pp. 168–173.

Kline, S. J., and McClintock, F. A., 1953, "Describing the Uncertainties in Single-Sample Experiments," *ASME Mech. Eng.,* pp. 3–8.

Koh, J. C. Y., and Colony, R., 1974, "Analysis of Cooling Effectiveness for Porous Material in Coolant Passages," ASME JOURNAL OF HEAT TRANSFER, Vol. 96, pp. 324–330.

Koh, J. C. Y., and Stevens, R. L., 1975, "Enhancement of Cooling Effectiveness by Porous materials in Coolant Passage," ASME JOURNAL OF HEAT TRANSFER, Vol. 97, pp. 309–310.

Kuo, K. K., and Nydegger, C. C., 1978, "Flow Resistance Measurements and Correlation in a Packed Bed of WC 870 Ball Propellants," *Journal of Ballistics,* Vol. 2, No. 1, pp. 1–25.

Liang, C. Y., and Yang, W. J., 1975, "Modified Single-Blow Technique for Performance Evaluation on Heat Transfer Surfaces," ASME JOURNAL OF HEAT TRANSFER, Vol. 96, pp. 16–21.

Renken, K. J., and Poulikakos, D., 1987, "Forced Convection in Channel Filled with Porous Medium, Including the Effects of Flow Inertia, Variable Porosity, and Brinkman Friction," ASME JOURNAL OF HEAT TRANSFER, Vol. 109, pp. 880–888.

Renken, K. J., and Poulikakos, D., 1988, "Experiment and Analysis of Forced Convection Heat Transfer in a Packed Bed of Spheres," *Int. J. Heat Mass Transfer,* Vol. 31, pp. 1399–1408.

Robbins, R., and Gough, P. S., 1978, "Experimental Determination of Flow Resistance in Packed Beds of Gun Propellant," *Proceedings of 15th JANNAF Combustion Meeting,* CPIA pub. 297.

Rowe, P. N., and Claxton, K. T., 1965, "Heat and Mass Transfer From a Single Sphere to Fluid Flowing Through an Array," *Trans. Instn. Chem. Engrs.,* Vol. 43, pp. T321–T331.

Vafai, K., and Tien C. L., 1981, "Boundary and inertia effects on Flow and Heat Transfer in Porous Media," *Int. J. Heat Mass Transfer,* Vol. 24, pp. 195–203.

Vafai, K., Alkire, R. I. and Tien, C. L., 1985, "An Experimental Investigation of Heat Transfer in Variable Porosity Media," ASME JOURNAL OF HEAT TRANSFER, Vol. 107, pp. 642–647.

Vafai, K., and Sozen, M., 1990, "Analysis of the non-thermal equilibrium Condensing Flow of a Gas through a Packed Bed," *Int. J. Heat Mass Transfer,* Vol. 33, No. 6, pp. 1247–1261.

Transient Heat Transfer From a Particle With Arbitrary Shape and Motion

Zhi-Gang Feng[1]

E. E. Michaelides
Professor and Associate Dean,
e-mail: emichael@mailhost.tcs.tulane.edu
Mem. ASME

Department of Mechanical Engineering,
Tulane University,
New Orleans, LA 70118

A singular perturbation analysis and Green's second theorem are used in order to obtain a general expression for the heat transfer from a particle at low Peclet numbers, when advection and conduction are heat transfer modes of comparable magnitude. The particle may have arbitrary shape, and its motion in the fluid is not constrained to be Stokesian. In the ensuring analysis, the governing equations for the temperature fields at short and long times are derived. The expressions are combined to yield a general equation for the temperature field and for the total rate of heat transfer. The final results for the rate of heat transfer demonstrate the existence of a history integral, whose kernel decays faster than the typical history integrals of the purely conduction regime. As applications of the general results, analytical expressions for the Nusselt number are derived in the case of a sphere undergoing a step temperature change.

Introduction

There are several reasons for studying the problem of heat and mass transfer from a particle at small Peclet numbers (Pe): First, there are the practical applications of the subject and considerable engineering interest in processes such as evaporation of droplets, chemical reactors with solid particles, combustion, drying of solids, or diffusion of pharmaceuticals in biological fluids. Second, there is the fundamental question of what are the rates of heat or mass transfer in a given arbitrary transient temperature or concentration field and how the steady state is approached. Third, the problem is of intellectual interest, because until now Stokesian flow and pure conduction assumptions dominated all analytical studies. Fourth, analytical solutions are always useful because they assist in the derivation of numerical calculations, since they provide benchmarks for checking numerical solutions and robust boundary conditions.

Because of the complexity of the problem, there are no known general analytical solutions for the transient convection from a sphere at finite Pe. There are some numerical studies on the subject, which extend to large Pe. For example, Abramzon and Elata (1984) have provided numerical solutions to this problem, up to very high Pe for a sphere in a Stokesian flow field. A recent review article by Sirignano (1993) summarizes the correlations used in the case of droplets and presents the effects of several parameters on the rate of heat transfer. Oftentimes, modified steady-state models are being used for the determination of the instantaneous rate of heat transfer (Jacobs and Golafshani, 1989). However, the study by Gopinath and Mills (1993) indicates that this is not sufficient and that transient effects must be taken into account in cases of heat transfer from particles with acoustic excitations. An excellent monograph by Kaviani (1994) exposes the reader to the results of many pertinent studies on the (steady) heat transfer from particles.

Regarding the analytical studies on the subject, Michaelides and Feng (1994) performed an analysis analogous to those for the derivation of the equation of motion of the sphere. They derived a solution to the unsteady conduction problem from a sphere (Pe = 0) and discovered the existence of a history term, analogous to the "Basset" term in the equation of motion of a sphere. More recently, Feng and Michaelides (1996) obtained an asymptotic solution for the heat transfer from a sphere, which undergoes a step temperature change in a Stokesian velocity field. This manuscript extends the analytical methods used in the past and yields an analytical solution for the general problem of transient heat transfer from a particle with arbitrary shape in a transient temperature field. The velocity field is not restricted to be Stokesian, as in most of the previous studies. Hence, the motion of the particle may be arbitrary. The overall study delineates a new asymptotic method of singular perturbation analysis, which is used for the first time in the area of heat transfer and results in the inclusion of the advection terms in the energy and mass transfer equations of particles in fluids.

The heat and mass transfer equations are identical in their form. Therefore, the solutions obtained for the one apply to the other, as long as the boundary and initial conditions are similar. In order to avoid circumlocution, in the sections that follow we will use the terminology of the heat transfer processes. However, it must be remembered that all the results also apply to the mass transfer problems with similar boundary and initial conditions.

Problem Statement: Governing Equations

Consider a rigid particle moving with time-dependent velocity $\mathbf{V}_p(t)$ inside a viscous conducting fluid. The fluid velocity field, with respect to a fixed coordinate system $\mathbf{x}$, is denoted by $\mathbf{u}(\mathbf{x}, t)$. We may separate the fluid velocity field into two parts: the undisturbed field, $\mathbf{u}^\infty(\mathbf{x}, t)$, and the field $\mathbf{u}^D(\mathbf{x}, t)$ due to the disturbance induced by the presence and motion of the particle. The problem is posed with respect to a translating coordinate system, $\mathbf{r}$, whose origin is at the instantaneous position of the center of gravity of the particle. Thus, we have the following expressions for the coordinate system and the disturbance quantities:

$$\mathbf{r} = \mathbf{x} - \mathbf{Y}_P(t), \quad \mathbf{u}^D = \mathbf{u} - \mathbf{u}^\infty, \quad p^D = p - p^\infty. \qquad (1)$$

The vector $\mathbf{Y}_P(t)$ is the instantaneous position vector of the center of the particle in the fixed system of coordinates. Hence, the momentum and continuity equations for the flow field $\mathbf{u}^D(\mathbf{x}, t)$ in a coordinate system moving with the particle are as follows:

---

[1] Current address: Institute of Paper Science and Technology, Atlanta, GA.

Contributed by the Heat Transfer Division for publication in the JOURNAL OF HEAT TRANSFER. Manuscript received by the Heat Transfer Division, Aug. 16, 1996; revision received, Mar. 24, 1998. Keywords: Cumbustion, Evaporation, Multiphase Flows. Associate Technical Editor: S. Ramadhyani.

$$-\nabla p^D + \mu\nabla^2\mathbf{u}^{\mathrm{D}} = \rho\left(\frac{\partial \mathbf{u}^{\mathrm{D}}}{\partial t} + \mathbf{u}^{\mathrm{D}}\cdot\nabla\mathbf{u}^{\mathrm{D}} - \mathbf{u}^{\mathrm{S}}\cdot\nabla\mathbf{u}^{\mathrm{D}} + \mathbf{u}^{\mathrm{D}}\cdot\nabla\mathbf{u}^{\infty}\right)$$

$$\nabla\cdot\mathbf{u}^{\mathrm{D}} = 0, \qquad (2)$$

where $\mathbf{u}^{\mathrm{S}}(\mathbf{x}, t) = \mathbf{V}_{\mathrm{P}}(t) - \mathbf{u}^{\infty}(\mathbf{x}, t)$ is the relative velocity of the particle. The boundary conditions of the above equations are

$$\mathbf{u}^{\mathrm{D}} = \mathbf{u}^{\mathrm{S}} \quad \text{at} \quad S_P$$

$$\mathbf{u}^{\mathrm{D}}, \quad p^D \to 0 \quad \text{as} \quad |\mathbf{r}| \to \infty, \qquad (3)$$

where S_P is the surface of the particle, which may be of an arbitrary shape.

As in the case of the velocity field, we also decompose the temperature field, $\Theta(\mathbf{x}, t)$, into the undisturbed temperature field, $\Theta^{\infty}(\mathbf{x}, t)$, and the disturbance field, $\Theta^D(\mathbf{x}, t)$. The latter is the result of the energy transfer by conduction and advection from the particle $[\Theta^D(\mathbf{x}, t) = \Theta(\mathbf{x}, t) - \Theta^{\infty}(\mathbf{x}, t)]$. The temperature of the particle is denoted by the function $\Theta_P(t)$, which may be arbitrary. By taking the temperature of the particle to be uniform, we make the implicit assumption that the Biot number of the particle is very small. This assumption is consistent with the small Peclet number assumption and has been used in other studies on convection from a particle (Acrivos, 1980; Michaelides and Feng, 1996). Under these conditions, the energy equation of the disturbance field in the translating system of coordinates is as follows:

$$k\nabla^2\Theta^D = \rho c\left[\frac{\partial \Theta^D}{\partial t} + (\mathbf{u}^{\mathrm{D}} - \mathbf{u}^{\mathrm{S}})\cdot\nabla\Theta^D + \mathbf{u}^{\mathrm{D}}\cdot\nabla\Theta^{\infty}\right]. \qquad (4)$$

k, ρ, and c are, respectively, the thermal conductivity, density, and specific heat capacity of the fluid which are assumed to be constant. The boundary conditions of the energy equation are

$$\Theta^D = \Theta^S(t) = \Theta_P(t) - \Theta^{\infty} \quad \text{at} \quad S_P$$

$$\Theta^D \to 0 \quad \text{as} \quad |\mathbf{r}| \to \infty. \qquad (5)$$

The energy equation is rendered dimensionless by the introduction of the following variables, denoted by an asterisk (*):

$$\mathbf{u}^* = \frac{\mathbf{u}}{U_c}, \quad \mathbf{x}^* = \frac{\mathbf{x}}{L_c}, \quad \Theta^{D*} = \frac{\Theta^D(\mathbf{x}, t)}{\Theta_P(0) - \Theta^{\infty}(0, 0)},$$

$$t^* = \frac{t}{\tau_c}. \qquad (6)$$

U_c, L_c, and τ_c are the characteristic velocity, length scale, and time scale of the problem. The characteristic length scale is the radius (or the equivalent radius) of the particle, a. The characteristic time scale of the process is not as easily specified. In the problem at hand there are two significant time scales, which may be considered as the characteristic times of the process: During an established heat advection process, τ_c is of the order of L_c/U_c. During a purely unsteady conduction process, the characteristic time scale is $L_c^2\rho c/k$.

It is more convenient to discuss the phenomena pertaining to the time scales of the problem in terms of the equivalent length scales. This happens because in the analogous momentum transfer problem there is an agreed-upon length scale, sometimes referred to as "the Oseen distance," L_{Ose} $(=a\ \mathrm{Re}^{-1})$ which is perceived as the boundary between two regions, one where the purely diffusive processes dominate the momentum transfer and the other, where the process is dominated by the advection effects. Hinch (1993) in an appendix to the article by Lovalenti and Brady (1993) presents a lucid argument on the mechanisms of momentum transfer from a particle to the fluid regions inside and outside the Oseen distance. These arguments are based on the wake formed behind the particle, the magnitude of the mass defect in the wake (which may be represented by a sink), and the downstream spread of the wake. In the present study, we extend the concept of the Oseen distance to the heat transfer process by defining an analogous length scale, L_I, $(=a\ \mathrm{Pe}^{-1})$. Inside L_I conduction is the predominant mode of heat transfer to the fluid. In the fluid region near L_I the two modes of heat transfer by conduction and advection are of the same order. In this region the appropriate transport equation is the full convection equation. Far from L_I energy is predominantly advected downstream and the region is characterized by the existence of a thermal wake.

The dimensionless form of the energy Eq. (4) may be written as follows:

$$\nabla^{*2}\Theta^{D*} = \mathrm{PeSl}\,\frac{\partial \Theta^{D*}}{\partial t^*} + \mathrm{Pe}[\mathbf{u}^{*\mathrm{D}} - \mathbf{u}^{*\mathrm{S}}(t)]\cdot\nabla^*\Theta^{D*} + \mathrm{Pe}\mathbf{u}^{*\mathrm{D}}\cdot\nabla^*\Theta^{*\infty}. \qquad (7)$$

The two dimensionless numbers in (7) are, respectively, the Peclet and Strouhal numbers:

$$\mathrm{Pe} = \frac{U_c L_c \rho c}{k} \quad \text{and} \quad \mathrm{Sl} = \frac{L_c}{U_c \tau_c}. \qquad (8)$$

The Peclet number actually is the product of the Reynolds and

Nomenclature

$\mathbf{A}$ = vector defined in (44)
c = specific heat capacity
f = functional defining the governing equation
h = steady-state temperature
k = thermal conductivity
$\mathbf{k}$ = vector in Fourier space
L = length
$\mathbf{n}$ = outward vector
Nu = Nusselt number
p = pressure
Pe = Peclet number
Q = rate of heat transfer
$\mathbf{r}$ = coordinate system relative to particle
S = surface
Sl = Strouhal number
t, T = time
$\mathbf{V}$ = particle velocity
V = volume
$\mathbf{u}$, $\mathbf{U}$ = velocity
$\mathbf{x}$ = fixed coordinate system
$\mathbf{Y}$ = position vector of particle

Greek

α = thermal diffusivity
δ = Dirac delta
θ, Θ = temperature
τ = time scale

Superscripts

A = auxiliary
D = disturbance induced by particle
i = derived with advection terms retained
I = pertains to the equivalent Oseen distance
S = signifies relative velocity
T = total
∞ = pertains to undisturbed fields

Subscripts

0, 1 = order of gauge functions
c = characteristic
f = pertains to fluid
p = pertains to particle
∞ = pertains to undisturbed fields

Prandtl numbers. It must also be noted that Sl is defined above in terms of the advection time scale L_c/U_c.

During an unsteady heat transfer process Sl varies considerably. At the inception of an unsteady process, the characteristic time is the time elapsed since the commencement of the process and Sl is large. In this case, $\tau_c = L_c^2 \rho c/k$ and $\mathrm{Sl} = O(\mathrm{Pe}^{-1}) > 1$, reflecting the fact that unsteady conduction is the dominant mode of heat transfer. As the process develops, the advective terms become significant and the appropriate time scale is L_c/U_c. It appears, therefore, that definite values of Sl cannot be a priori identified. For this reason, we will retain this parameter in an explicit form in the rest of the study.

In order to simplify the writing and appearance of the equations, from now on the superscripts D and $*$ will be omitted from the disturbance temperature and velocity fields. The superscript $*$ will also be omitted from all the other dimensionless variables. It should be kept in mind, however, that in the following sections all the variables used are in dimensionless form.

For the solution of the problem we will use Green's second theorem (Kreysig, 1988), which may be written for two functions Θ and Θ^A as follows:

$$\int_{S_f} \Theta^A \nabla \Theta \cdot \mathbf{n} dS - \int_{V_f} \Theta^A f(\Theta, \mathbf{x}, t) dV = \int_{S_f} \Theta \nabla \Theta^A \cdot \mathbf{n} dS - \int_{V_f} \Theta f^A(\Theta^A, \mathbf{x}, t) dV, \quad (9)$$

where the surface S_f encloses the fluid volume V_f. Although the original version of Green's theorem pertains to harmonic functions, it may easily be proven that the theorem may be extended to functions $\Theta(\mathbf{x}, t)$ which satisfy a governing equation of the form:

$$\nabla^2 \Theta = f(\Theta, \mathbf{x}, t). \quad (10)$$

f is a functional which defines the governing equation of the field. In the case of steady-state conduction, $f = 0$, while in the general unsteady convection process, the functional f becomes

$$f(\Theta, \mathbf{x}, t) = \mathrm{PeSl} \frac{\partial \Theta}{\partial t} + \mathrm{Pe}[\mathbf{u} - \mathbf{u}^S(t)] \cdot \nabla \Theta + \mathrm{Pe}\mathbf{u} \cdot \nabla \Theta^\infty. \quad (11)$$

Heat Transfer at the Limit of Zero Peclet Numbers

A From a Particle of Arbitrary Shape. $\Theta^A(\mathbf{x}, t)$ is an auxiliary temperature field, which may be conveniently chosen in order to facilitate the calculation of the heat flux due to $\Theta(\mathbf{x}, t)$. We choose $\Theta^A(\mathbf{x}, t)$ to be the temperature field developed during the steady-state conduction from the particle in a stagnant fluid, when the surface temperature of the particle is equal to 1. Hence, we have the following conditions:

$$\Theta^A = \Theta^A(\mathbf{x}) \quad \text{and} \quad f^A(\Theta^A) = 0 \quad \text{with} \quad \Theta^A = 1 \quad \text{on} \quad S_P. \quad (12)$$

It must be noted that in the case of a spherical particle the solution is $\Theta^A = 1/r$.

The volume of the fluid V_f extends from the surface of the particle, S_P, to a surface at infinity S_∞. The boundary conditions indicate that the dimensionless disturbance temperature field, Θ, is zero at S_∞ and finite at S_P. Therefore, Θ must decay with r, for example as $\Theta = O(r^{-h})$, with $h > 0$. Hence, $\nabla\Theta = O(r^{-1-h})$. Since $\Theta^A = O(1/r)$, the contribution of the surface at S_∞ to the first surface integral of equation (9) is zero. By a similar argument we conclude that the contribution of S_∞ to the second surface integral is zero. Hence, Green's second theorem for a particle of arbitrary shape may be recast in the following form:

$$-\int_{S_P} \nabla \Theta \cdot \mathbf{n} dS = \int_{V_f} \Theta^A(\mathbf{r}) f(\Theta, \mathbf{r}, t) dV - \int_{S_P} \Theta(t) \nabla \Theta^A(\mathbf{r}) \cdot \mathbf{n} dS. \quad (13)$$

The total rate of heat transfer from the particle, Q^T, is the sum of the rates due to the disturbance field Θ and of the rate Q^∞ due to the undisturbed field $\Theta^\infty(\mathbf{x}, t)$. Since at the boundary we have $\Theta = \Theta_P - \Theta^\infty$, we may write the total dimensionless rate of heat transfer as follows:

$$Q^T = \int_{S_P} \nabla \Theta_P \cdot \mathbf{n} dS = Q^\infty + \int_{S_P} (\Theta_P - \Theta^\infty) \nabla \Theta^A \cdot \mathbf{n} dS - \int_{V_f} \Theta^A(\mathbf{r}) f(\Theta, \mathbf{r}, t) dV. \quad (14)$$

In general, Q^∞ may be given by the following expression:

$$Q^\infty = \int_{S_P} \nabla \Theta^\infty \cdot \mathbf{n} dS = \int_{V_f} \nabla^2 \Theta^\infty dV. \quad (15)$$

Since the undisturbed field $\Theta^\infty(\mathbf{x}, t)$ satisfies the equation

$$\nabla^2 \Theta^\infty = \mathrm{PeSl} \frac{\partial \Theta^\infty}{\partial t} - \mathrm{Pe}\mathbf{u}^S \cdot \nabla \Theta^\infty \equiv \frac{D\Theta^\infty}{Dt}, \quad (16)$$

it follows that the functional form of the total rate of heat transfer Q^T from a particle of arbitrary shape, subject to nonuniform and time-dependent fluid velocity and fluid temperature fields is

$$Q^T(t) = \int_{V_P} \frac{D\Theta^\infty}{Dt} dV + \int_{S_P} (\Theta_P - \Theta^\infty) \nabla \Theta^A \cdot \mathbf{n} dS - \int_{V_f} \Theta^A(\mathbf{r}) f(\Theta, \mathbf{r}, t) dV. \quad (17)$$

Therefore, the total rate of heat transfer from the particle is comprised of three contributions:

(a) the contribution of the undisturbed field, which is analogous to the similar term in the equation of motion of a particle;

(b) the steady-state conduction from the surface of the particle, which is analogous to the steady-state drag of the momentum equation; and

(c) the unsteady convection, which includes all the conduction and thermal advection effects inside the volume of the fluid. This last term is analogous to an integral, which yields the history and the so-called "Oseen correction terms" of the momentum equation.

Equation (17) is a general expression for the rate of heat transfer from a particle of arbitrary shape. In order to specifically determine the rate of heat transfer from a given particle, one must calculate the integrals in (17) and hence, one must have information on the geometry of the particle. In the following subsection we will calculate these integrals in the case of a sphere.

B Heat Transfer From a Sphere. We used a second-order Taylor expansion for the nonuniform temperature field Θ^∞ and calculated the first two integrals of Eq. (17) over a spherical geometry. The result for the total rate of heat transfer is

$$Q^T(t) = \frac{4\pi}{3}\left[\frac{D\Theta^\infty}{Dt} + \frac{1}{10}\nabla^2\left(\frac{D\Theta^\infty}{Dt}\right)\right]_{\mathbf{Y}_P} - 4\pi\left[(\Theta_P - \Theta^\infty) - \frac{1}{6}\nabla^2\Theta^\infty\right]_{\mathbf{Y}_P} - \int_{V_f} \frac{1}{r} f(\Theta, \mathbf{r}, t) dV, \quad (18)$$

where the functional $f(\Theta, \mathbf{r}, t)$ has been defined in Eq. (11). The first two terms of the last equation give explicitly the effects of the undisturbed temperature field and of the steady-state conduction to the total rate of heat transfer from the sphere. The last integral depends strongly on the particular problem at hand and the function f. It may not be explicitly evaluated in a general case.

We evaluated this integral term in the case of creeping flow ($\mathrm{Pe} \rightarrow 0$). Such cases have dominated the analytical studies of particle transfer processes in the past and all analytical expressions used in engineering practice are based on them. The volume integral yields a history term of the energy equation. The final equation derived for the transient rate of heat transfer from a sphere at zero Pe is

$$Q^T(t) = \frac{4\pi}{3}\left[\frac{D\Theta^\infty}{Dt} + \frac{1}{10}\nabla^2\left(\frac{D\Theta^\infty}{Dt}\right)\right]_{\mathbf{Y}_\mathbf{P}(t)} - 4\pi\left[(\Theta_P - \Theta^\infty) - \frac{1}{6}\nabla^2\Theta^\infty\right]_{\mathbf{Y}_\mathbf{P}(t)} - 4\sqrt{\pi\,\mathrm{PeSl}}\int_{-\infty}^{t}\frac{\dfrac{d}{d\tau}\left[(\Theta_P - \Theta^\infty) - \dfrac{1}{6}\nabla^2\Theta^\infty\right]_{\mathbf{Y}_\mathbf{P}(t)}}{\sqrt{t-\tau}}\,d\tau. \tag{19}$$

It must be pointed out that even in the limit $\mathrm{Pe} = 0$, the product PeSl is finite and equal to $a^2 k\rho / c\tau_c$. The last expression is essentially the same as the energy equation for a sphere, derived by Michaelides and Feng (1994) by a more cumbersome method. It also includes the second-order terms in the right-hand side, which account for the spatial nonuniformity of $\Theta^\infty(\mathbf{x}, t)$. It is of interest to note that the kernel of the history integral term decays as $t^{-1/2}$, which is typical of scalar diffusion processes. The history term is analogous (and very similar in its form) to the integral derived in the equation of motion of a sphere under creeping flow conditions, which is sometimes referred to as the "Basset term" (Maxey and Riley, 1983).

Heat Transfer from a Particle at Finite Peclet Numbers

In this section we will derive the rate of heat transfer from a particle of arbitrary shape at finite Pe, following a method similar to the singular perturbation method, which was developed by Proudman and Pearson (1956), Sano (1981), and Lovalenti and Brady (1993) in the case of the equation of motion of a particle. The following assumptions will be used:

(a) the undisturbed temperature field is unsteady but uniform, that is $\Theta^\infty = \Theta^\infty(t)$;

(b) the undisturbed velocity field is also uniform, that is $\mathbf{u}^\infty = \mathbf{u}^\infty(t)$; and

(c) Pe is small but nonzero.

Since the first two terms of (14) may easily be obtained from the geometry of the particle, the main objective of our analysis is to calculate the last integral, which represents the rate of heat transferred due to the combination of unsteady conduction and advection. For brevity, this term will be denoted as $Q^{(U)}(t)$. Since the functional f includes the effects of the disturbance field, $Q^{(U)}$ is affected by the heat transfer processes in both the inner and the outer field.

We will develop an asymptotic analysis based on the appropriate time scales and length scales of the process. Solutions will be sought for the short and long-time ranges. Because the process of determining a uniformly valid temperature field is complicated and several temperature fields will be mentioned, we will make use of the same notation as Lovalenti and Brady (1993): Time-dependent temperatures will be denoted by Θ; time-independent temperatures will be denoted by h; the subscript 0 will denote a leading-order temperature field; the subscript 1 will denote a first-order temperature field; the superscript p will denote a field produced by a point-source; the superscript i will indicate that the advective terms are retained in the governing equations; the superscript s will denote a solution in the short-time domain and the superscript L solutions in the long-time domain. Hence, we will develop an expression for the temperature field, which is uniformly valid in the whole space.

A Development of Uniformly Valid Temperature Fields.

A.1 Short-Time Domain. During this time domain, all energy exchange is confined to the vicinity of the particle, well inside the distance L_l and conduction is the dominant mode of heat transfer. There has not been sufficient time since the inception of the process for the thermal wake to be formed behind the particle. Hence, the advection term may be neglected in both the inner and the outer region. The characteristic time of this stage of the process is one, the heat diffusion scale, $L_c^2 \rho c / k$. In this case there is no region where the diffusive and the advective effects of the process are of the same order of magnitude. This feature of the heat transfer process is the result of the fact that any significant temperature gradients generated by the transport processes have not diffused into the region outside L_l. Because of this, a singular perturbation analysis is not necessary for this case. Hence, we may write the temperature field in the short-time domain, $\Theta^{(s)}$ by a regular perturbation method, as follows:

$$\Theta^{(s)} = \Theta_0 + \mathrm{Pe}\Theta_1 + o(\mathrm{Pe}^{1+}). \tag{20}$$

An order of magnitude analysis of the resulting governing equation reveals that the two terms of the temperature decomposition satisfy the following governing equations:

(a) The leading term Q_0

$$\nabla^2\Theta_0 = \mathrm{PeSl}\,\frac{\partial\Theta_0}{\partial t}, \tag{21}$$

with boundary conditions

$$\Theta_0 = \Theta_s(t) \quad \text{on} \quad S_P$$
$$\Theta_0 \rightarrow 0 \quad \text{as} \quad |\mathbf{r}| \rightarrow \infty; \tag{22}$$

(b) The first-order term Θ_1

$$\nabla^2\Theta_1 - \mathrm{PeSl}\,\frac{\partial\Theta_1}{\partial t} = [\mathbf{u} - \mathbf{u}^s(t)]\cdot\nabla\Theta_0, \tag{23}$$

with homogeneous boundary conditions.

It appears that the leading-order term for the short-time solution is independent of the velocity field, while the first-order solution Θ_1 depends on the relative velocity of the particle. In the case of a spherical particle, $\Theta_0(\mathbf{r})$ is symmetric and the boundary conditions for $\Theta_1(\mathbf{r})$ are homogeneous. In addition, if the disturbance velocity field $\mathbf{u}(\mathbf{r}, t)$ is symmetric, then $\Theta_1(\mathbf{r}, t)$ will be antisymmetric. Therefore, in this time domain the contribution of the first-order term $\Theta_1(\mathbf{r}, t)$ to the total rate of heat transfer from a sphere is zero.

A.2 Long-Time Domain. At long times after the commencement of the process, heat transfer by advection becomes important and the characteristic time of the process is L_c / U_c. However, close to the surface of the sphere, conduction dominates. Now there are two characteristic times, the conduction time scale, close to the surface of the sphere and the advection time scale, far from the sphere. Because of this, the problem cannot be solved by a regular perturbation method and, hence, a singular perturbation will be attempted. The basic notion of the singular perturbation method is to construct a uniform temperature field, which is valid (to the appropriate level of accuracy) in the inner region, then to add to it the outer temperature field and finally subtract the part in common at the region of overlap. In this case, we identify the inner fluid region within L_t and the outer region outside L_t.

In order to solve the analogous problem of the equation of motion Childress (1964) used the effects of a point force applied to the outer region, whose magnitude is the same as the force exerted from the inner region. Following the same method, we will use the point heat source equations to develop a solution in the outer region. The temperature field, which is in common to both regions, results from the point-source unsteady convection equation. This field must be eventually subtracted from the sum of the two temperature fields in order to avoid double counting of the contributions from the inner and outer regions.

At long times from the inception of the process, there is always a volume of the outer region, where the advective and conductive effects are equally important. The balance of the advection and conduction effects dictates the rescaling of the variables to be used. Order of magnitude arguments with respect to the rescaled variables (Feng and Michaelides, 1996) lead to the conclusion that in the long-time domain, the inner region is governed by a time-independent solution, which may be expressed as follows:

$$h(\mathbf{r}) = h_0(\mathbf{r}) + \mathrm{Pe}h_1(\mathbf{r}) + o(\mathrm{Pe}^{1+}). \tag{24}$$

The governing equations for the inner region solutions are given by the following expressions:

(a) For the leading-order equation,

$$\nabla^2 h_0 = 0; \tag{25}$$

(b) For the first-order equation,

$$\nabla^2 h_1 = \mathbf{u}\cdot\nabla h_0. \tag{26}$$

The thermal wake is predominately in the outer region. The effects of the inner region on the governing equation of the outer, are taken into account by using a point source of heat, whose intensity, Q^c, is equal to $-4\pi(\Theta_P - \Theta^\infty)$. Hence, the leading term for the temperature in the outer region obeys the following governing equation:

$$\nabla^2\Theta_0^{pi} = \mathrm{PeSl}\,\frac{\partial\Theta_0^{pi}}{\partial t} - \mathrm{Pe}\mathbf{u}^s(t)\cdot\nabla\Theta_0^{pi} - 4\pi(\Theta_P - \Theta^\infty)\delta(\mathbf{r}). \tag{27}$$

One may now proceed from the last equation, to construct a temperature field, valid in the entire space for the long-time domain. In order to construct the uniformly valid temperature field we add the two temperature fields Θ_0^{pi} and h_0 and subtract their component in common, h_0^p. Hence, the temperature field, which is valid in the entire domain at long times, is

$$\Theta^{(L)} = h_0 + \Theta_0^{pi} - h_0^p. \tag{28}$$

The governing equation of the component in common is given by the point-source solution in the inner region

$$\nabla^2 h_0^p = -4\pi(\Theta_p - \Theta^\infty)\delta(\mathbf{r}) = Q^c\delta(\mathbf{r}). \tag{29}$$

A.3 The Uniformly Valid Temperature Field for the Whole Time Domain. Having developed expressions for the temperature at the short and long-time domains, we will construct a uniformly valid temperature field for the whole time domain. At first glance it appears that we may only employ the temperature field given by (28). A moment's reflection, however, will convince us that it is more appropriate to construct a uniformly valid temperature field, which also includes the short-time effects. The reason for this is that heat first diffuses at short times around the particle and subsequently is convected to the outer region. The part in common of the two fields may be written as $\Theta^{(C)} = h_0 + \Theta_0^p - h_0^p + \mathrm{Pe}\Theta_1^p$. The governing equation of the leading-order unsteady term Θ_0^p is

$$\nabla^2\Theta_0^p = \mathrm{PeSl}\,\frac{\partial\Theta_0^p}{\partial t} + Q^c\delta(\mathbf{r}), \tag{30}$$

and for the first-order term Θ_1^p:

$$\nabla^2\Theta_1^p = \mathrm{PeSl}\,\frac{\partial\Theta_1^p}{\partial t} - \mathrm{Pe}\mathbf{u}^s(t)\cdot\nabla\Theta_0^p. \tag{31}$$

Therefore, the uniformly valid temperature field for both the space and time domain becomes

$$\begin{aligned}\Theta &= \Theta^{(s)} + \Theta^{(L)} - (h_0 + \Theta_0^p - h_0^p + \mathrm{Pe}\Theta_1^p)\\ &= \Theta_0 + \mathrm{Pe}\Theta_1 + \mathrm{Pe}\Theta_1^{pi} - \Theta_1^p\end{aligned} \tag{32}$$

where $\mathrm{Pe}\Theta_1^{pi} = \Theta_0^{pi} - \Theta_0^p$, and satisfies the following governing equation:

$$\nabla^2\Theta_1^{pi} = \mathrm{PeSl}\,\frac{\partial\Theta_1^{pi}}{\partial t} - \mathrm{Pe}\mathbf{u}^s(t)\cdot\nabla\Theta_1^{pi} - \mathbf{u}^S(t)\cdot\nabla\Theta_0^p. \tag{33}$$

B Heat Transfer From a Particle of Arbitrary Shape. Having obtained an expression for the uniformly valid temperature field Eq. (32) one may use Eq. (17) in order to obtain an analytic expression for the total rate of heat transfer from a particle of arbitrary shape. The resulting integrals may be further simplified by making the following observations:

(a) Since the contribution from the inner region is of lower order than $O(\mathrm{Pe})$, the precise form of $\Theta^A(r)$ in that region is not necessary to be evaluated. The far-field form of Θ^A, which is given to a leading order by an instantaneous point source Θ^{AP}, would be sufficient.

(b) Since Θ^A is replaced by the point source field Θ^{AP} and since the volume integrals of Θ_1^{pi} and Θ_1^p are nonsingular at the origin, we may extend the integration volume to include the volume of the particle. This is justified given the stated degree of accuracy, because both integrands decay slower than $O(r^{-2})$ as $r\to 0$. Upon integration over the particle volume, the resulting error is less than $O(\mathrm{Pe})$.

(c) The temperature field Θ_1^p is antisymmetric and Θ^{AP} is a symmetric one. Therefore, the part of the integrand, which includes the Θ_1^p field is antisymmetric and, when integrated over a spherical surface, its contribution vanishes.

Hence, the total rate of heat transfer from a particle of arbitrary shape, which moves with time-dependent velocity $\mathbf{u}^S(t)$, relative to an ambient fluid velocity $\mathbf{u}(t)$ in a uniform time-dependent temperature field $\Theta^\infty(t)$ is

$$\begin{aligned}Q^T = &\oint_{S_P}(\Theta_P - \Theta^\infty)\nabla\Theta^A\cdot\mathbf{n}dS\\ &- \int_{V_f}\mathrm{PeSl}\Theta^A\,\frac{\partial\Theta_0}{\partial t}\,dV + \mathrm{PeSl}V_P\,\frac{D\Theta^\infty}{Dt}\\ &- \mathrm{Pe}\int_{V_f}\Theta^A\left[\mathrm{PeSl}\,\frac{\partial\Theta_1}{\partial t} + (\mathbf{u} - \mathbf{u}^S)\cdot\nabla\Theta_0\right]dV\\ &- \mathrm{Pe}\int_{V_\infty}\Theta^A\left[\mathrm{PeSl}\,\frac{\partial\Theta_1^{pi}}{\partial t}\,\mathrm{Pe}\mathbf{u}^S\cdot\nabla\Theta_1^{pi}\right]dV.\end{aligned} \tag{34}$$

The first term of Eq. (34) represents that part of the dimensionless rate of heat transfer (or the Nusselt number), which is due to the steady conduction from the surface of the particle.

It is analogous to the steady-state drag of the equation of motion. The second term accounts for the regular perturbation due to the unsteady conduction. The analogue to this term in the equation of motion is the contribution from the regular perturbation to the unsteady Stokes problem. The third term is the contribution of the undisturbed temperature field. It has an analogous term in the equation of motion of the particle, very similar in form. The fourth and fifth terms, which appear as volume integrals, represent the combined advection and conduction effects to the fluid of the outer region. These integrals will yield the history terms of the heat transfer process. It is evident that details of the process as well as the geometric shape and the velocity field induced by the particle are needed for the completion of the calculations. In the following section we will perform these calculations in the case of a sphere, subject to a step increase of its surface temperature.

Heat Transfer From a Sphere With an Arbitrary Surface Temperature

A In the Short-Time Domain: In this section we restrict our analysis to the spherical geometry and develop an explicit form of the energy equation and the time-dependent Nusselt number. At the commencement of the heat transfer process, the conduction effects are confined to short distances from the sphere. Therefore, in the short-time domain $Q^{(U)}$ is negligible. The other terms of (34) yield an expression for the total rate of heat transfer from a sphere, which is essentially the same as (19) with the only difference that a uniform temperature field is applied in this case. From this solution we conclude that during the short-time domain, the creeping flow solution is accurate to $O(\mathrm{Pe}^{1+})$ if the induced velocity field is symmetric. It must be also pointed out that, in this time domain, the uniformly valid temperature field is $\Theta^{(s)} = \Theta_0 + \mathrm{Pe}\Theta_1 + O(\mathrm{Pe}^{1+})$.

B Heat Transfer Rate in the Long-Time Domain: In this case $Q^{(U)}$ must be explicitly evaluated. For the calculation of this integral we use the following convolution theorem:

$$Q^{(U)}(t) = -\int_{V_f} \overline{\Theta^A}(-\mathbf{k})\overline{f^{(\mathrm{out})}}(\Theta, \mathbf{k}, t)dV, \tag{35}$$

where the overline denotes the Fourier transform of a function and

$$f^{(\mathrm{out})} = \mathrm{PeSl}\,\frac{\partial \Theta_1^{pi}}{\partial t} - \mathrm{Pe}\mathbf{u}^s \cdot \nabla \Theta_1^{pi}. \tag{36}$$

The result of the calculations is as follows:

$$\begin{aligned} Q^U = &-\sqrt{\mathrm{PeSl}}\int_{-\infty}^{t} \frac{Q^c}{\sqrt{\pi(t-\tau)}}\,d\tau \\ &+ \frac{\mathrm{Pe}}{4\pi^{3/2}}\int_{-\infty}^{t}\int_{\Omega} \frac{(\mathbf{u}^S\cdot\mathbf{n})(\mathbf{A}\cdot\mathbf{n})}{t-\tau}\exp[-(\mathbf{A}\cdot\mathbf{n})^2]Q^c\,d\Omega d\tau \\ &+ \frac{\sqrt{\mathrm{PeSl}}}{4\pi}\int_{-\infty}^{t}\int_{\Omega} \frac{dQ^c/dt}{\sqrt{t-\tau}}\exp[-(\mathbf{A}\cdot\mathbf{n})^2]\,d\Omega d\tau \end{aligned} \tag{37}$$

where the integral around Ω represents the angular integration over a spherical surface, $\mathbf{n}$ is the outward unit vector normal to this surface, and the vector $\mathbf{A}$ is defined as follows:

$$\mathbf{A} = \frac{\mathrm{Pe}}{2}\left(\frac{t-\tau}{\mathrm{PeSl}}\right)^{1/2} \frac{\int_{\tau}^{t} \mathbf{u}^S(\xi)d\xi}{t-\tau}. \tag{38}$$

It is evident that the vector $\mathbf{A}$ scales as $(t-\tau)^{1/2}$.

We may assume without any loss of generality that the relative velocity vector of the particle $\mathbf{u}^S(t) = \mathbf{V_P}(t) - \mathbf{u}^\infty(t)$ is in the z-direction. Hence, the angular integration may be analytically accomplished and Eq. (37) may be simplified to yield the following for the total rate of heat transfer from a sphere:

$$\begin{aligned} Q^T(t) = &\frac{4\pi\mathrm{PeSl}}{3}\frac{d\Theta^\infty}{dt} - 4\pi(\Theta_P - \Theta^\infty) \\ &- 2\pi\sqrt{\mathrm{PeSl}}\int_{-\infty}^{t} \frac{\Theta_p - \Theta^\infty}{\sqrt{t-\tau}}\frac{\mathrm{erf}\,|\mathbf{A}|}{|\mathbf{A}|}\,d\tau \\ &- 2\,\mathrm{Pe}\sqrt{\pi}\int_{-\infty}^{t} \frac{(\Theta_p - \Theta^\infty)|\mathbf{u}^s|}{(t-\tau)|\mathbf{A}|}\left[\frac{\sqrt{\pi}}{2|\mathbf{A}|}\mathrm{erf}\,|\mathbf{A}| \right. \\ &\left. - \exp(-|\mathbf{A}|^2)\right]d\tau + o(\mathrm{Pe}^{1+}). \end{aligned} \tag{39}$$

The first term in (39) represents the contribution of the time-varying undisturbed temperature field. The second term is the usual steady-state conduction term. The third and fourth terms in the equation are history terms emanating from temperature gradients diffused and advected, since the inception of the heat transfer process. At the time domain under consideration $[t = O(\mathrm{Pe}^{-2})]$ these temperature gradients have been convected to distances greater than L_I. It should be pointed out that the last integrals do not diverge as $t \to \tau$ and that their kernel decays faster than $t^{-1/2}$, (which was the case in the creeping flow solution). The uniformly valid temperature field in this case is $\Theta^{(L)} = h_0 + \Theta_0^{pi} - h_0^p$.

C Heat Transfer From a Sphere Undergoing a Step Temperature Change. We now specify the cause of the heat transfer process and consider a sphere which undergoes a step temperature change from Θ^∞ to Θ^P in a fluid of uniform temperature. This case is analogous to the motion of a spherical particle, starting from rest, in an otherwise quiescent fluid (that is $\mathbf{u}^\infty = 0$). Its practical applications are Lagrangian methods of particle motion and energy exchange, such as the Monte-Carlo method, which successfully simulates turbulence effects (Michaelides et al., 1992). The process of the step temperature change is instantaneous. Because of this, we decided to take as the characteristic time of the process the time scale of conduction, which is the characteristic time of the diffusion of the thermal effects in the vicinity of the sphere. In this case PeSl = 1. Hence, we have the following relationships for the velocity field and the magnitude of the vector $\mathbf{A}$:

$$\mathbf{u}^S(t) = -\mathbf{e}_z \quad \text{and} \quad |\mathbf{A}| = \frac{\mathrm{Pe}}{2}(t-\tau)^{1/2}. \tag{40}$$

In the short-time domain we obtain the following expression for the total rate of heat transfer and the Nusselt number, valid for $t = O(1)$:

$$Q^T(t) = -4\pi(\Theta_P - \Theta^\infty) - 4\pi(\Theta_P - \Theta^\infty)\frac{1}{\sqrt{t}} + o(\mathrm{Pe}^{1+})$$

and

$$\mathrm{Nu}\,(t) = -\frac{Q^T}{2\pi(\Theta_P - \Theta^\infty)} = 2\left[1 + \frac{1}{\sqrt{t}}\right] + o(\mathrm{Pe}^{1+}). \tag{41}$$

The rate of approach to steady state is proportional to $t^{-1/2}$, as expected in this purely diffusion process and does not depend on Pe. Equation (41) features a singularity at $t = 0$. This is due to the energy impulse, which is required to achieve the implied step temperature change. However, this singularity is integrable and the total amount of energy exchange for the process is finite.

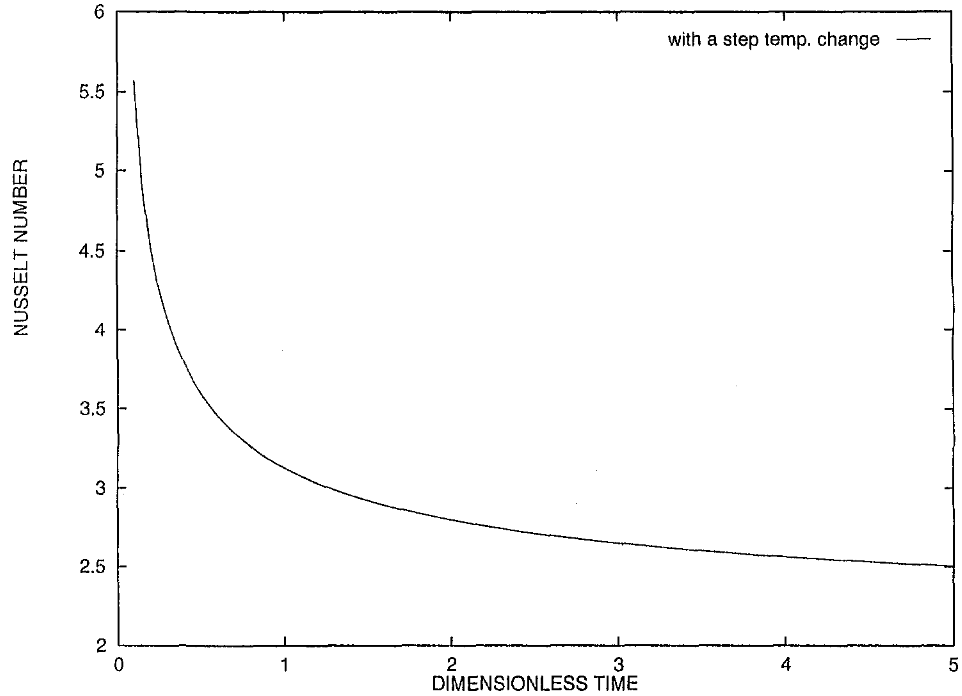

Fig. 1 Nusselt number versus dimensionless time for the conduction solution at short times (time is made dimensionless by using the conduction time-scale $a^2\rho c/k$)

In the long-time domain [$t = O(\mathrm{Pe}^{-2})$], the total rate of heat transfer and the Nusselt number for a sphere undergoing a step temperature change become

$$Q^T(t) = -4\pi(\Theta_P - \Theta^\infty) - 4\pi(\Theta_P - \Theta^\infty)\left[\frac{\exp\left(-\frac{\mathrm{Pe}^2}{4}t\right)}{\sqrt{\pi t}} + \sqrt{\frac{\mathrm{Pe}^2}{4}}\,\mathrm{erf}\sqrt{\frac{\mathrm{Pe}^2}{4}t}\right] + o(\mathrm{Pe}^{1+})$$

and

$$\mathrm{Nu}\,(t) = 2 + 2\left[\frac{\exp\left(-\frac{\mathrm{Pe}^2}{4}t\right)}{\sqrt{\pi t}} + \sqrt{\frac{\mathrm{Pe}^2}{4}}\,\mathrm{erf}\sqrt{\frac{\mathrm{Pe}^2}{4}t}\right] + o(\mathrm{Pe}^{1+}). \quad (42)$$

One will notice that the rate of approach to the steady-state solution during the long-time domain is $e^{-t}t^{-1/2}$. The approach to steady state during convection is faster than the approach during the purely conduction mode, which is $t^{-1/2}$, because the thermal wake is well formed in the outer region and is spreading by advection. The spread of the thermal wake facilitates the exchange of energy in the outer region of the fluid and, hence, accelerates the approach to steady state.

It is of interest to note that the steady-state solution obtained from Eq. (42) asymptotically for very large values of t is $\mathrm{Nu} = 2(1 + 0.5\,\mathrm{Pe})$. This asymptotic solution agrees very well with the expression (obtained asymptotically for low Pe) from the steady-state correlation of experimental data and previous analyses on the steady-state convection from a sphere (Bird et al., 1960).

Some numerical calculations were performed to determine the Nusselt number as functions of Pe in simple cases. Figure 1 shows the transient Nusselt number in the short-time domain in the case of a sphere in an otherwise quiescent fluid (that is $\mathbf{u}^\infty = 0$) for Pe = 0.25. Conduction dominates in this process. The temperature of the sphere undergoes a step temperature change at time $t = 0$. It is observed that Nu initially declines rapidly, and then approaches the steady-state solution (Nu = 2) at a very slow rate. After five characteristic times, the value of Nu is still 25 percent above the asymptotic value. Figure 2 depicts the case of a sphere moving with a relative velocity $\mathbf{u}^S = [1 + \cos(wt)]\mathbf{e}_z$. Time is made dimensionless in both figures by the characteristic time of conduction, $a^2\rho c/k$. Hence, the dimensionless frequency w is in effect the inverse of the Strouhal number of the velocity fluctuations (Sl_v). The surface temperature of the sphere undergoes the same step temperature change as in the previous case and, again Pe = 0.25. The three sinusoidal curves depict the Nusselt number, obtained from the solution of Eqs. (38) and (39), and the dotted curve represents the conduction solution from (41). It is observed that the inclusion of the advection effects enhances the Nusselt number by about five to ten percent, even at this low Pe. It is also observed that at the high value of the dimensionless frequency, w, the response of the particle is very weak, suggesting that at high frequencies for the velocity, the heat transfer from the sphere may not respond at all to the velocity fluctuations. This trend may be deduced from Eqs. (38) and (39), where it becomes evident that the influence of the velocity fluctuation on Nu comes through the magnitude of the vector **A** only. However, the fluctuations of **A** resulting from the velocity fluctuations are inversely proportional to w, as it may be easily observed from the evaluation of the vector **A** for the assumed velocity of the particle. Therefore, at high w the velocity fluctuations will generate proportionately lower magnitudes of fluctuations in the equations of the Nusselt number.

Conclusions

The heat transfer from a particle of arbitrary shape may be expressed in terms of integrals of an auxiliary temperature field and a functional, which defines the governing equation of the process. A history integral emerges from the solution of the

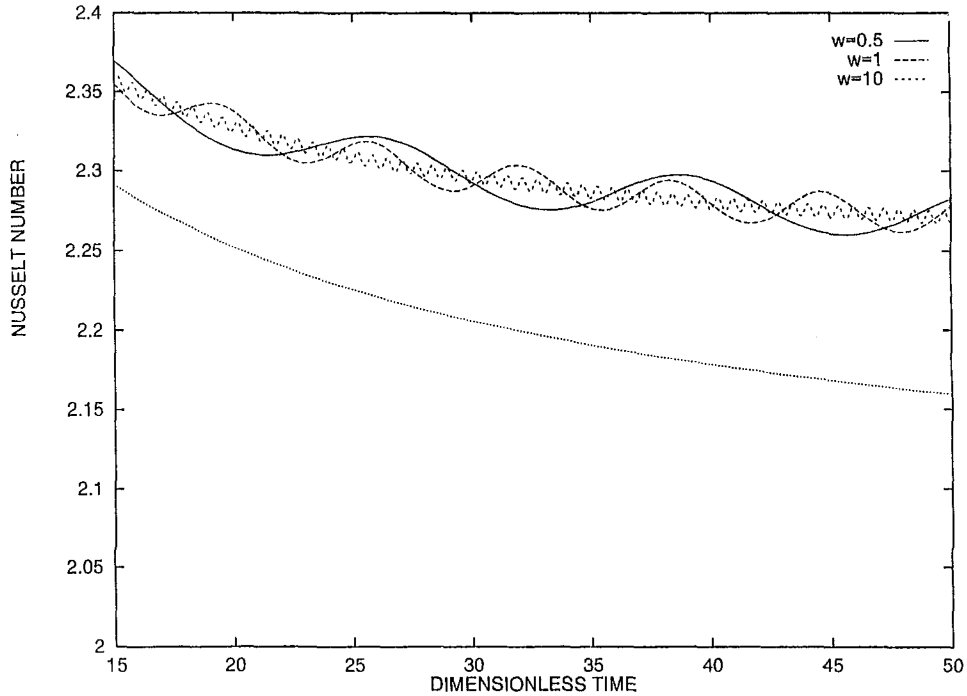

Fig. 2 Nusselt number versus dimensionless time for the convection solution at long times (time is made dimensionless by using the conduction time-scale $a^2\rho c/k$). The dotted line represents the conduction solution of Eq. (41).

governing equation. This is the result of diffused temperature gradients, which were created since the inception of the heat transfer process. The history integral is a special case of such integrals, which appear in more complex forms depending on the shape of the particle. In the case of convection at small Pe, the pertinent time scales span a large range, as the process evolves from pure diffusion to diffusion/advection. The length scale L_l, which is analogous to the Oseen distance of the momentum transfer problem, is the characteristic dimension for the conduction and convection domains. By the use of a singular perturbation method, one obtains uniformly valid temperature fields in both the short and the long-time domains. Hence, the total rate of heat transfer for a particle of arbitrary shape may be derived and expressed in a closed form, which includes an auxiliary temperature field, the temperature field of the fluid and the velocity of the particle and the fluid. Calculations are performed for a sphere, which undergoes a step temperature change. These results agree well with previously derived expressions for the transient heat transfer from a sphere at low Pe and asymptotic steady-state solutions.

Acknowledgments

This research was partly supported by grants from the NSF, NASA, and LEQSF to Tulane University. The authors are grateful for this support.

References

Abramzon, B., and Elata, C., 1984, "Heat Transfer from a Single Sphere in Stokes Flow," *Int. J. Heat and Mass Transfer.*, Vol. 27, pp. 687–695.

Acrivos, A., 1980, "A Note on the Rate of Heat or Mass Transfer from a Small Particle Freely Suspended in Linear Shear Field," *J. of Fluid Mechanics*, Vol. 98, p. 229.

Bird, R. B., Stewart, W. E., and Lightfoot, E. N., 1960, *Transport Phenomena*, John Wiley and Sons, New York, p. 409.

Childress, S., 1964, "The Slow Motion of a Sphere in a Rotating, Viscous Fluid," *J. of Fluid Mechanics*, Vol. 20, p. 305.

Feng, Z.-G., and Michaelides, E. E., 1996, "Unsteady Heat Transfer from a spherical Particle at finite Peclet Numbers," *J. of Fluids Engineering*, Vol. 118, pp. 96–102.

Gopinath, A., and Mills, A. F., 1993, "Conductive Heat Transfer From a Sphere due to Acoustic Streaming," ASME JOURNAL OF HEAT TRANSFER, Vol. 115, pp. 332–340.

Hinch, E. J., 1993, "The Approach to Steady State in Oseen Flows," *J. of Fluid Mechanics*, Vol. 256, p. 601.

Jacobs, H. R., and Golafshani, M., 1989, "A Heuristic Evaluation of the Governing Mode of Heat Transfer in a Liquid-Liquid Spray Column," ASME JOURNAL OF HEAT TRANSFER, Vol. 111, pp. 773–779.

Kaviani, M., 1994, *Principles of Convective Heat Transfer*, Springer-Verlag, New York.

Kreysig, E., 1988, *Advanced Engineering Mathematics*, 6th Ed., John Wiley and Sons, New York, p. 560.

Lovalenti, P. M., and Brady, J. F., 1993, "The Hydrodynamic Force on a Rigid Particle Undergoing Arbitrary time-dependent Motion at Small Reynolds Number," *J. of Fluid Mechanics*, Vol. 256, p. 561.

Maxey, M. R., and Riley, J. J., 1983, "Equation of Motion of a Small rigid Sphere in a Non-uniform Flow," *Phys. of Fluids*, Vol. 26, pp. 883–889.

Michaelides, E. E., and Feng, Z. G., 1994, "The Heat Transfer from a sphere in Non-uniform and Unsteady Velocity and Temperature Fields," *Int. J. Heat and Mass Transfer*, Vol. 37, p. 2069.

Michaelides, E. E., Liang, L., and Lasek, A., 1992, "The Effects of Turbulence on the Phase Change of Droplets and Particles under Non-Equilibrium Conditions," *Int. J. Heat and Mass Transfer*, Vol. 35, pp. 2069–2076.

Proudman, I. A., and Pearson, J. R. A., 1957, "Expansions at Small Reynolds Numbers for the Flow Past a Sphere and a Circular Cylinder," *J. of Fluid Mechanics*, Vol. 2, pp. 237–262.

Sano, T., 1981, "Unsteady Flow Past a Sphere at Low-Reynolds Number," *J. of Fluid Mechanics*, Vol. 112, pp. 433–441.

Sirignano, W. A., 1993, "Fluid Dynamics of Sprays," *J. of Fluids Engineering*, Vol. 115, pp. 345–378.

Effect of Drop Deformation on Heat Transfer to a Drop Suspended in an Electrical Field

M. A. Hader

M. A. Jog[1]
Mem. ASME

Department of Mechanical, Industrial,
and Nuclear Engineering,
University of Cincinnati,
P. O. Box 210072,
Cincinnati, OH 45221-0072

Heat transfer to a drop of a dielectric fluid suspended in another dielectric fluid in the presence of an electric field is investigated. We have analyzed the effect of drop deformation on the heat transport to the drop. The deformed drop shape is assumed to be a spheroid and is prescribed in terms of the ratio of drop major and minor diameter. Results are obtained for both prolate and oblate shapes with a range of diameter ratio b/a from 2.0 to 0.5. The internal problem where the bulk of the resistance to the heat transport is in the drop, as well as the external problem where the bulk of the resistance is in the continuous phase, are considered. The electrical field and the induced stresses are obtained analytically. The resulting flow field and the temperature distribution are determined numerically. Results indicate that the drop shape significantly affects the flow field and the heat transport to the drop. For the external problem, the steady-state Nusselt number increases with Peclet number for all drop deformations. For a fixed Peclet number, the Nusselt number increases with decreasing b/a. A simple correlation is proposed to evaluate the effect of drop deformation on the steady-state Nusselt number. For the internal problem, for all drop deformations, the maximum steady-state Nusselt number becomes independent of the Peclet number at high Peclet number. The maximum steady-state Nusselt numbers for an oblate drop are significantly higher than that for a prolate drop.

Introduction

When a uniform electric field is applied to a drop of dielectric liquid suspended in another immiscible fluid, the electric field induces stresses at the fluid interface. The normal stresses may deform the drop and the tangential stresses produce a circulatory motion inside the drop. This electrically induced motion can be used to enhance the heat/mass transfer from the drop and finds applications in development of compact direct-contact heat exchangers. To understand the effect of drop deformation on the heat transport to the drop, two limits based on the relative magnitude of the resistance to heat transfer in the continuous and the dispersed phase are considered. One limit where the bulk of the resistance to the heat transport is in the dispersed phase is known as the internal problem. The other extreme, where the resistance to heat transfer is mainly in the continuous phase is known as the external problem (Ayyaswamy, 1995). In general, the steady-state Nusselt number for a conjugate problem, where the heat transfer resistance in the two phases are comparable, can be estimated from the results for the internal and the external Nusselt numbers (Abramzon and Borde, 1980). Also, when the time scale for the external Nusselt number to reach its steady-state value is small compared to the time scale for temperature change in the drop interior, the heat transport in the continuous phase can be considered quasi-steady, and the steady-state results obtained here for the external problem would be applicable. Abramzon and Borde (1980) have shown that the heat transfer can be considered quasi-steady when $Nu_2 \gg ((\rho c_p)_1/(\rho c_p)_2)$. A detailed discussion on the internal as well as the external heat transfer problems with liquid drops and a review of the accomplished work is available in Ayyaswamy (1995) and in a recent monograph by Sadhal et al. (1997). Mathematical methods and numerical solutions in direct contact heat transfer studies with droplets are outlined in Ayyaswamy (1996).

Most of the work on heat transport to a liquid drop in an electric field has been carried out with an assumed spherical drop shape. Oliver et al. (1985) analyzed the internal heat transfer to a spherical liquid drop suspended in an electric field. They showed that for large Peclet numbers the Nusselt number for purely electrically driven flow becomes increasingly independent of the Peclet number. The maximum Nusselt number for the internal heat transfer is 29.8 (Oliver and DeWitt, 1993). The external heat transfer problem was studied by Sharpe and Morrison (1986) for a spherical drop. They found that the steady-state Nusselt number increased monotonically with the Peclet number. To validate our numerical model, we have compared our results for a nearly spherical drop ($b/a = 0.99$ and $b/a = 1.01$) to the results of Oliver et al. (1985) and Sharpe and Morrison (1986) for the internal and the external solution, respectively.

We note, that only for certain specific combinations of the electrothermophysical properties of the dispersed and the continuous phase, the drop may remain spherical (Taylor, 1966). Under these conditions the viscous stresses normal to the drop surface due to the induced circulatory flow exactly cancel the effect of the normal stress variation due to the electric field. In general, the nonuniformity in the normal stress at the drop surface leads to deformation of the drop. As the drop deforms, the electric field at the drop surface changes and the electrically induced surface stresses are altered (Feng and Scott, 1996). This results in a change in the flow field in the dispersed and the continuous phase. As a result, the heat transport to the drop is affected. Recently, we have studied the electrohydrodynamics and heat transfer for an oblate spheroid where the resistance to heat transfer was considered to be mainly in the dispersed phase (Jog and Hader, 1997). For an oblate drop, the surface velocity variation and the flow field were found to deviate from those for a sphere. The Nusselt numbers for oblate drops are higher than those for a sphere at high Peclet numbers.

---

[1] Corresponding author.

Contributed by the Heat Transfer Division for publication in the JOURNAL OF HEAT TRANSFER and presented at NHTC '97, Baltimore. Manuscript received by the Heat Transfer Division, Oct. 24, 1997; revision received, May 1, 1998. Keywords: Computational, Direct Contact, Droplet, Electric Fields, Heat Transfer. Associate Technical Editor: P. Ayyaswamy.

In this paper, we present a comprehensive analysis of the effect of drop deformation on the heat transport to a drop suspended in uniform electric field, in that both prolate and oblate deformations are studied, and the external as well as the internal heat transfer problems are considered. Analytical solutions are presented for the electric field and the electrically induced stresses. We have assumed the drop shape to be a spheroid. Taylor (1966) analytically showed that for small deformations the deformed drop shape is a spheroid. Numerous experimental studies (Allan and Mason, 1962; Taylor, 1966; Torza et al., 1971; Vizika and Saville, 1992) and computational study (Feng and Scott, 1996) have shown that the drop shape is very nearly spheroidal even for moderate deformations. The simplification of a spheroidal drop shape allows us to use an orthogonal coordinate system which conforms to the drop surface thereby reducing the computational efforts without much loss of accuracy. The electrically induced flow field is calculated by numerically solving the Navier-Stokes equations in the continuous and the dispersed phase. The temperature variation and the Nusselt number variations are obtained for both the internal and the external problem.

Results indicate that the drop deformation significantly affects the flow field and the heat transport to the drop. For the external problem, the steady-state Nusselt numbers for an oblate drop are higher, and those for prolate drop are lower, than the Nusselt numbers for a sphere at the same Peclet number. The steady-state Nusselt number increases with the Peclet number for all drop deformations. In the internal problem, for both prolate and oblate drops, the steady-state Nusselt number increases with the increasing Peclet number, and at a high Peclet number, becomes increasingly independent of the Peclet number. The maximum steady-state Nusselt numbers for oblate drops are significantly higher than those for prolate drops.

Problem Formulation

We consider a drop of a dielectric liquid suspended in another dielectric liquid in a uniform electric field. The drop may deform and acquire either a prolate or an oblate shape. Taylor's discriminating function (Φ) can be used to determine the type of drop deformation.

$$\Phi = S(R^2 + 1) - 2 + 3(SR - 1)\frac{2M + 3}{5M + 5}. \qquad (1)$$

$\Phi < 0$ indicates oblate deformations whereas $\Phi > 0$ results in prolate deformations. $\Phi = 0$ corresponds to a spherical drop. We use oblate/prolate spheroidal coordinates (ξ, η, ϕ) for computational convenience. The origin of the coordinate system is at the drop center as shown in Fig. 1. The drop surface corresponds to $\xi = \xi_a$. For sake of brevity, the formulation is presented in terms of the oblate spheroidal coordinates only. The corresponding expressions in terms of the prolate spheroidal coordinates can be readily obtained by substituting cosh ξ for i sinh ξ and sinh ξ for i cosh ξ. The oblate spheroidal coordinates are related to the cylindrical polar coordinates (r, z, θ) as $z = c \sinh \xi \cos \eta$, $r = c \cosh \xi \sin \eta$, and $\theta = \phi$ (Happel and Brenner, 1965). The formulation is axisymmetric. We note that although the two-dimensional cross sections of the oblate and the prolate spheroids appear to be similar in Fig. 1, the three-dimensional shapes are substantially different. At the extreme values of b/a, an oblate spheroid is disk-like whereas a prolate spheroid resembles a long cylinder.

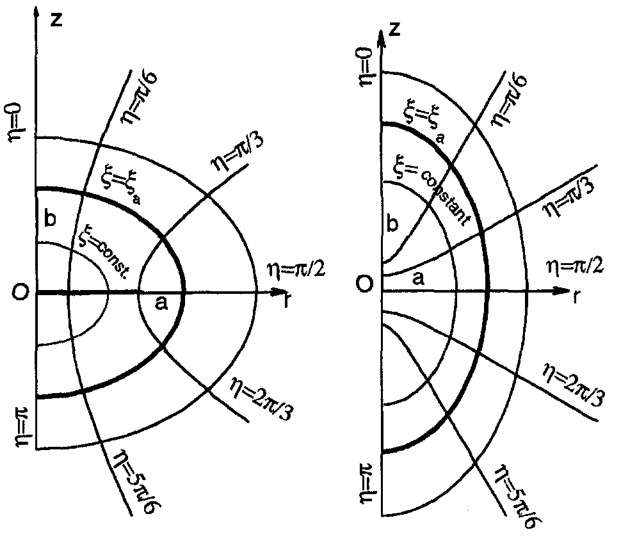

(a) (b)

Fig. 1 (*a*) Oblate spheroidal coordinates, and (*b*) prolate spheroidal coordinates

Governing Equations and Boundary Conditions. The electric field in both the phases is governed by the Laplace's equation and the flow is described by the Navier-Stokes equations. The temperature field can be calculated by the solution of the energy conservation equation. Note that the energy conservation equation in the drop interior must always be considered transient as no nontrivial steady-state solution exists. However, based on the timescales for momentum and heat diffusion,

Nomenclature

a = half of drop diameter perpendicular to the axis of symmetry
A_s = drop surface area
b = half of drop diameter along the axis of symmetry
E = electric field
k = dielectric constant
M = viscosity ratio (μ_1/μ_2)
Nu = Nusselt number based on drop diameter ($2a$)
p = pressure
Pe = Peclet number based on drop diameter ($2a$)
P_n = Legendre Polynomial of order n
Q = net heat flux to the drop
R = electric conductivity ratio (σ_1/σ_2)
Re = Reynolds number
(r, z, θ) = cylindrical polar coordinates
S = ratio of dielectric constants (k_1/k_2)
t = time
T = temperature
u = velocity
U = maximum surface velocity
V = electric potential
$\hat{V}$ = drop volume = $4/3\pi a^2 b$
w = vorticity

Greek Symbols

α = thermal diffusivity
γ = surface tension
μ = viscosity
ρ = density
σ = electrical conductivity
τ = stress
ψ = stream function
Φ = Taylor's discriminating function (Eq. (1))
(ξ, η, ϕ) = oblate spheroidal coordinates

Subscripts

0 = initial
1 = continuous phase
2 = dispersed phase
b = bulk
E = electrically induced
s = surface
∞ = far field

Superscripts

* = dimensional quantities

for liquids with moderate to high Prandtl number, the momentum transport can be regarded as quasi-steady (Sundararajan and Ayyaswamy, 1984).

We introduce the following dimensionless variables. Velocity is made dimensionless by the maximum surface velocity as $u = u^*/U$. Distances are nondimensionalized by a. The stresses and pressure are normalized by $\mu U/a$ and the Reynolds number is $\mathrm{Re} = \rho U 2a/\mu$. We define the dimensionless temperatures as $T_2 = (T_2^* - T_s^*)/(T_{2,0}^* - T_s^*)$, $T_1 = (T_1^* - T_\infty^*)/(T_s^* - T_\infty^*)$ and dimensionless time as $t = \alpha_2 t^*/a^2$. The Peclet number is given by $\mathrm{Pe} = 2Ua/\alpha$. The electric field is made dimensionless by $[\mu_2 U/(\epsilon_0 a)]^{1/2}$. The dimensionless governing equations are

$$\nabla \cdot \mathbf{u}_i = 0 \tag{2}$$

$$\mathrm{Re}_i \mathbf{u}_i \cdot \nabla \mathbf{u}_i = -\frac{1}{\rho_i} \nabla p_i + \nu_i \nabla^2 \mathbf{u}_i \tag{3}$$

$$\nabla \cdot \mathbf{E}_i = 0 \tag{4}$$

where $\mathbf{E} = -\nabla \mathbf{V}$ and $i = 1, 2$.

At the interface the following conditions are satisfied (Melcher and Taylor, 1969):

$$\mathbf{n} \cdot \mathbf{u}_i = 0, \quad u_{1\eta} = u_{2\eta}, \quad \mathbf{n} \cdot (\tau_E + \mu_1/\mu_2 \tau_1 - \tau_2) = \tau_\gamma,$$
$$V_1 = V_2 \quad \text{and} \quad R\mathbf{n} \cdot \nabla V_1 = \mathbf{n} \cdot \nabla V_2. \tag{5}$$

Here τ_E is the electrically induced stress at the drop surface, τ_γ is the stress due to surface tension, and $\mathbf{n}$ is a unit vector normal to the drop surface.

The symmetry condition is used along the z-axis and far away from the drop we have

$$\mathbf{u} \to 0, \quad p \to p_\infty, \quad \text{and} \quad V \to Ez. \tag{6}$$

The External Problem. The external problem represents the limit where the bulk of the resistance is in the continuous phase. The drop surface temperature is prescribed. For the external problem, the energy equation is

$$\frac{\mathrm{Pe}_1}{2} \mathbf{u}_1 \cdot \nabla T_1 = \nabla^2 T_1 \tag{7}$$

At the drop surface $T_1 = 1$ and far away from the drop surface $T_1 \to 0$.

The local Nusselt number is given by

$$\mathrm{Nu}_{1\eta} = -\frac{\cosh \xi_a}{(\cosh^2 \xi_a - \sin^2 \eta)^{1/2}} \left. \frac{\partial T_1}{\partial \xi} \right|_{\xi=\xi_a}. \tag{8}$$

The average Nusselt number is

$$\mathrm{Nu}_1 = \frac{4\pi a^2}{A_s} \int_0^\pi \sin \eta \left. \frac{\partial T_1}{\partial \xi} \right|_{\xi=\xi_a} d\eta. \tag{9}$$

The Internal Problem. The internal problem represents the limit where the bulk of the resistance to the heat transfer is in the drop. Therefore, the drop surface temperature can be considered equal to the freestream temperature. The temperature variation in the drop interior is governed by the transient energy equation

$$\frac{\partial T_2}{\partial t} + \frac{\mathrm{Pe}_2}{2} \mathbf{u}_2 \cdot \nabla T_2 = \nabla^2 T_2. \tag{10}$$

Initially the drop is uniformly at dimensionless temperature equal to 1. At the interface $T_2 = 0$.

The Nusselt number based on the drop major diameter is

$$\mathrm{Nu}_2 = \frac{Q2a}{A_s (T_s^* - T_b^*) k} = -\frac{2\hat{V}}{A_s a} \frac{1}{T_b} \frac{dT_b}{dt}. \tag{11}$$

The dimensionless bulk temperature for the dispersed phase can by calculated as

$$T_b = \frac{3}{2} \frac{1}{\sinh \xi_a \cosh^2 \xi_a} \int_0^{\xi_a} \int_0^\pi T_2 \cosh \xi \sin \eta \, (\cosh^2 \xi - \sin^2 \eta) d\eta d\xi. \tag{12}$$

Solution Technique

The general solution for the electric potential distribution can be obtained by the method of separation of variables as (Smythe, 1968)

$$V(\xi, \eta) = \sum_{n=0}^{\infty} [A_n P_n(\cos \eta) + B_n Q_n(\cos \eta)] \times [A_n' P_n(i \sinh \xi) + B_n' Q_n(i \sinh \xi)]. \tag{13}$$

The solutions which satisfy the appropriate boundary conditions are, for the continuous phase,

$$V_1 = \cos \eta [C_1 \sinh \xi + C_2 (\sinh \xi \cot^{-1} (\sinh \xi) - 1)], \tag{14}$$

and for the drop interior

$$V_2 = C_3 \cos \eta \sinh \xi \tag{15}$$

where

$$C_1 = E/\cosh \xi_a$$

$$C_2 = (E(1 - R) \tanh \xi_a (1 + \sinh^2 \xi_a))[(R - 1) \sinh \xi_a \times (1 + \sinh^2 \xi_a) \cot^{-1} (\sinh \xi_a) + \sinh^2 \xi_a - (1 + \sinh^2 \xi_a) R]^{-1}$$

$$C_3 = C_1 + C_2 (\sinh \xi_a \cot^{-1} (\sinh \xi_a) - 1)/\sinh \xi_a. \tag{16}$$

From the electrical potential variation the electrically induced shear stress can be calculated as

$$\tau_{E,\xi\eta} = (k_1 E_{1,\xi} E_{1,\eta} - k_2 E_{2,\xi} E_{2,\eta}). \tag{17}$$

To solve for the flow field in the continuous and the dispersed phase we introduce stream function ψ (nondimensionalized by Ua^2) such that

$$u_\xi = -\frac{\cosh^2 \xi_a}{(\cosh^2 \xi - \sin^2 \eta)^{1/2} \cosh \xi \sin \eta} \frac{\partial \psi}{\partial \eta} \tag{18}$$

$$u_\eta = \frac{\cosh^2 \xi_a}{(\cosh^2 \xi - \sin^2 \eta)^{1/2} \cosh \xi \sin \eta} \frac{\partial \psi}{\partial \xi} \tag{19}$$

and vorticity $\mathbf{w}$ (nondimensionalized by U/a) as

$$\mathbf{w} = \nabla \times \mathbf{u}. \tag{20}$$

As the formulation is axisymmetric, only the ϕ component of vorticity is nonzero. $\mathbf{w} = w\mathbf{i}_\phi$.

Vorticity can be expressed in terms of the stream function by substituting Eqs. (18) and (19) into Eq. (20). By taking curl of the momentum equation, the vorticity transport equation is obtained as

$$\mathbf{u} \cdot \nabla \mathbf{w} - \frac{2}{\mathrm{Re}} \nabla^2 \mathbf{w} = \mathbf{w} \cdot \nabla \mathbf{u}. \tag{21}$$

The governing equations for the stream function and vorticity transport (Eqs. (20) and (21)) were solved with appropriate boundary conditions (Eq. (5)) by a finite difference method with 61 × 61 node points in the drop interior and 101 × 61 node points in the surrounding fluid. These governing equations with the boundary conditions are given in oblate spheroidal coordinates in Jog and Hader (1997) and not repeated here for the sake of brevity. A hybrid differencing scheme (Patankar, 1980) was used to discretize the equations and an iterative procedure was used to obtain solutions. A guess for the surface velocity distribution is used to solve the stream function and vorticity equations in the continuous phase. The continuous phase solution provides the shear stress at the drop interface. Using the calculated interfacial shear stress, the flow field in the drop interior is obtained. This solution provides a new variation for the tangential velocity at the drop surface. The solution procedure is continued until the difference in both the tangential velocity and the shear stress obtained from the continuous and the dispersed phase are less than 1×10^{-6}. Transient temperature distributions inside the droplet were obtained using an alternating direction implicit (ADI) method with a tridiagonal algorithm. For the energy equation in the continuous phase, outflow boundary conditions were used to minimize the effect of finiteness of the far-field boundary as suggested by Sharpe and Morrison (1986). A typical run took about three hours on a HP 9000/712/80 workstation to determine the flow field. For a given Peclet number, the steady-state temperature distribution in the external problem required approximately two hours and the calculation of the transient temperature field in the drop interior required less than one hour. To study the effect of grid refinement, results for $b/a = 0.7$ and Pe = 200 as well as Pe = 1500 were obtained with doubling the node points in each direction. The change in the Nusselt number variation was found to be less than one percent for both the cases.

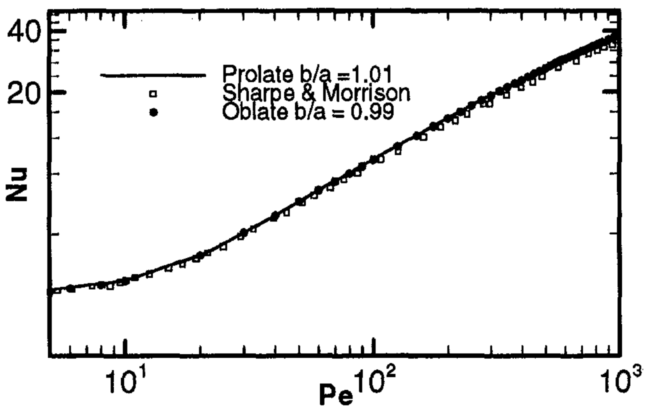

Fig. 2(*a*)

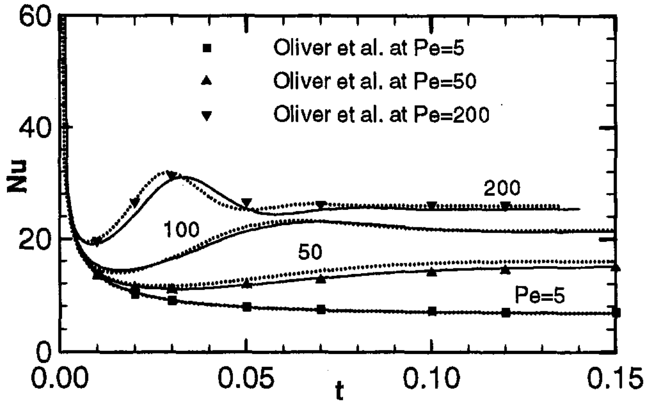

Fig. 2(*b*)

Fig. 2 Comparison of results for nearly spherical drops for model validation; (*a*) external problem and (*b*) internal problem

Results and Discussion

We have studied the effect of drop deformation on the heat transport in a drop suspended in a uniform electric field. A range of drop deformations is considered from $b/a = 2.0$ to $b/a = 0.5$. Results are obtained for both the internal and the external heat transfer problem. In all the earlier studies on heat transport in a spherical drop suspended in a uniform electric field, the assumption of Stokes flow ($Re \ll 1$) has been used. To make fruitful comparisons with the available results, we have used a value of drop Reynolds number as 0.1 in our computations. Under this condition the heat transport is governed by the drop Peclet number based on the maximum tangential velocity. A range of Peclet numbers from 1 to 1500 is considered. The following parameters are used in the numerical computations: $\rho_1/\rho_2 = 1$, $\mu_1/\mu_2 = 1$, $R = 0.1$, and $S = 2$.

To validate the computational model, results were first obtained for nearly spherical drops ($b/a = 1.01$ and 0.99) and were compared with the available results for a spherical drop. Figure 2(*a*) shows a comparison of the variation of Nusselt numbers with a Peclet number for the external problem with the results of Sharpe and Morrison (1986). It is seen from the figure that our results for nearly spherical drops match very well with the available results for a spherical drop at all Peclet numbers. The transient Nusselt number variations for the inner heat transfer problem are shown in Fig. 2(*b*) for a range of Peclet numbers. The figure shows that the transient Nusselt number variations calculated from our model for $b/a = 1.01$ and $b/a = 0.99$ agree well with the result of Oliver et al. (1985) for $b/a = 1$. The solutions for the stream function and the surface velocity for nearly spherical drops were also compared with Taylor's analytical solutions. Excellent agreements were observed. After validating the computational model, the flow fields in the continuous and the dispersed phase and the heat transfer characteristics for the internal and the external problems with deformed drops were calculated.

The flow field inside and outside the drop is shown in Figs. 3(*a*) and (*b*) for an oblate drop ($b/a = 0.7$) and a prolate drop ($b/a = 1.5$), respectively. As the flow is symmetric about the equatorial plane, only a quarter of the flow field is shown. The flow in the lower half moves in a direction opposite to that in the upper half. In the continuous phase, in a region near the pole, fluid is brought towards the drop. Fluid moves away from the drop in the vicinity of the equator. In the drop interior, the electrically induced flow forms circulatory vortex patterns with both the prolate and the oblate drop deformation. For a spherical drop, the center of the circulatory vortex pattern is located along a line making an angle of 45 deg with the vertical axis (Taylor 1966). For an oblate drop, with increasing drop deformation, the center of the circulatory vortex pattern moves towards the equatorial plane. The radial distance of the vortex center from the drop surface is also substantially less for a drop with $b/a = 0.7$ than that for a liquid sphere. For a prolate drop, the change in the circulatory vortex pattern from that in the sphere is smaller than that observed for an oblate drop. Similar differences in the circulatory motion with a prolate and an oblate drop shape are also reported by Feng and Scott (1996). Corresponding to the differences in the flow field in the dispersed phase for a deformed drop and that for a sphere, the location of the maximum surface velocity is located closer to the equatorial plane for a deformed drop than that for a sphere. Consequently, the flow field in the continuous phase for a deformed drop is altered from that for a spherical drop.

The External Problem. The isotherms for an oblate drop with $b/a = 0.7$ and for a prolate drop with $b/a = 1.5$ are shown in Figs. 4 and 5, respectively. Note that in these figures, the flow on the drop surface is from the pole to the equator. In both cases, as the Peclet number is increased, the isotherms get closer near the front stagnation point (pole) and move apart in the

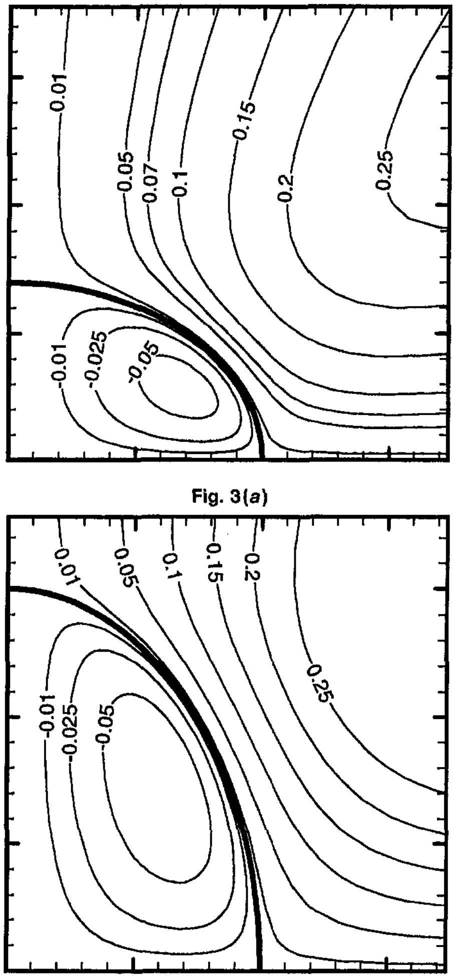

Fig. 3(*a*)

Fig. 3(*b*)

Fig. 3 Streamlines in the continuous and the dispersed phase; (*a*) oblate drop *b*/*a* = 0.7, and (*b*) prolate drop *b*/*a* = 1.5

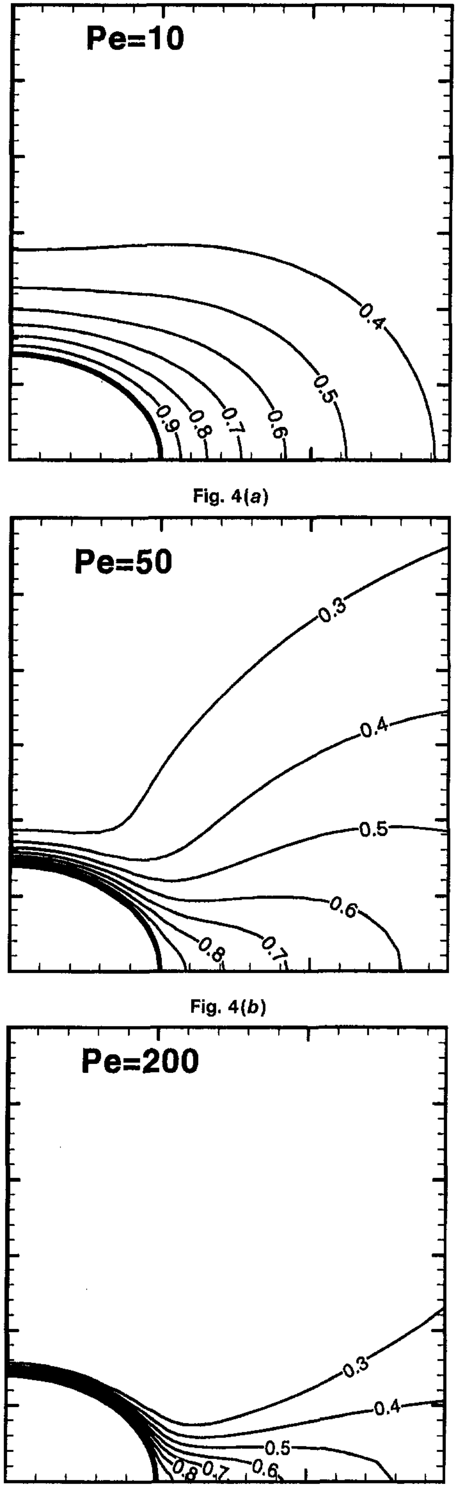

Fig. 4(*a*)

Fig. 4(*b*)

Fig. 4(*c*)

Fig. 4 Isotherms in the continuous phase for an oblate drop; (*a*) Pe = 10, (*b*) Pe = 50, and (*c*) Pe = 200

vicinity of the equator. The temperature gradients, and the corresponding local Nusselt numbers are higher in the front section of the drop than those near the equator. The local Nusselt number variation for a range of Peclet numbers is shown in Fig. 6. The solid lines show the variation for a prolate drop and the dashed lines for an oblate drop. The maximum Nusselt number increases with the Peclet number and occurs at the front stagnation point for both the prolate and the oblate drop deformations. The Nusselt number monotonically decreases from the front stagnation point (pole) to the equator. For a fixed Peclet number, the maximum local Nusselt number for a prolate drop is higher than that for an oblate drop. However, due to the much smaller surface area available for heat transfer near the front stagnation point (pole) compared to that in a region near the equator, the higher maximum Nusselt numbers do not translate to higher overall Nusselt numbers for a prolate drop.

The overall Nusselt number variation for a number of drop deformations is shown in Fig. 7. For all drop shapes, the overall steady-state Nusselt number increases with the Peclet number. For a given Peclet number, the Nusselt number increases with decreasing b/a, and the Nusselt number for an oblate drop is higher than that for a prolate drop. This is due to the larger surface area available with an oblate shape compared to a prolate shape for identical drop volumes. It can be seen from the figure that the difference in the Nusselt number for a spherical drop and that for a deformed drop is primarily a function of the drop shape (b/a). We propose a simple correlation to evaluate the deviation of the overall steady-state Nusselt number from that for a spherical drop.

$$\mathrm{Nu} = \mathrm{Nu}_{\mathrm{sphere}} \exp[-0.33*(b/a - 1)] \qquad (22)$$

Here Nu is the Nusselt number for a deformed drop and $\mathrm{Nu}_{\mathrm{sphere}}$ is the Nusselt number for a spherical drop at the same Peclet number. For the range of drop deformations shown here ($0.5 \le b/a \le 1.5$), the correlation fits the Nusselt number data

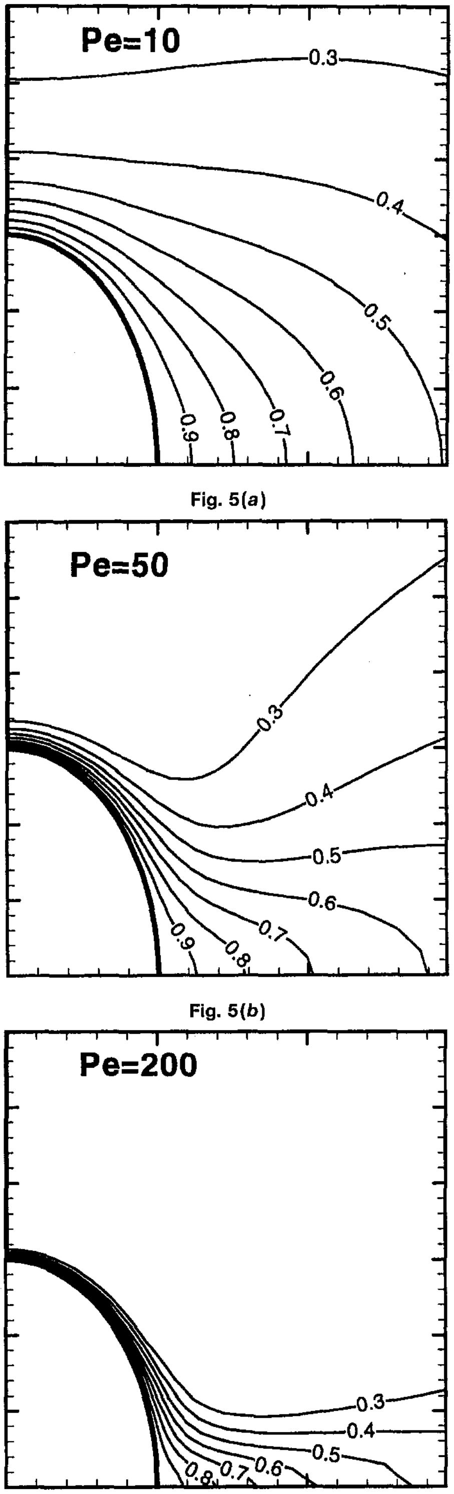

Fig. 5(*a*)

Fig. 5(*b*)

Fig. 5(*c*)

Fig. 5 Isotherms in the continuous phase for a prolate drop; (*a*) Pe = 10, (*b*) Pe = 50, and (*c*) Pe = 200

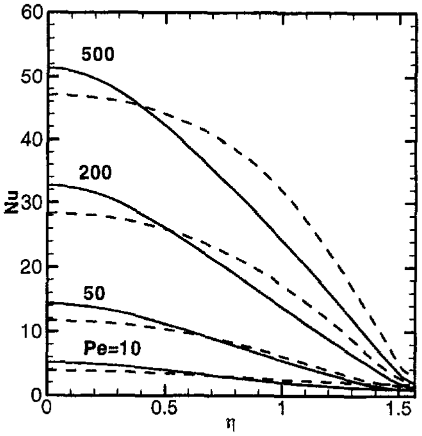

Fig. 6 Variation of local Nusselt number. Legend: Solid lines—prolate drop with b/a = 1.5 and dashed lines—oblate drop with b/a = 0.7.

within ±2 percent. Equation (22) can be used for engineering applications to estimate the effect of drop deformation on the steady-state Nusselt number for the external problem.

It has been shown by Sharpe and Morrison (1986) that the direction of flow influences the local Nusselt number variation. The maximum Nusselt number always occurs at the front stagnation point; however, it's value is different for an equator-to-pole flow and a pole-to-equator flow. For a spherical drop, the maximum local Nusselt number is higher for pole-to-equator flow than for a equator-to-pole flow. However, for flow at low Reynolds number, the *overall* Nusselt number is not a function of the flow direction (Brenner, 1967). Therefore, the above results for the overall Nusselt numbers are valid for both the equator-to-pole flow and pole-to-equator flow on the drop surface.

The Internal Problem. The transient Nusselt number variations for a prolate drop (b/a = 1.5) are shown in Fig. 8. For all Peclet numbers, for short times, conduction is the dominant heat transport mechanism as seen from the sharp initial drop in the Nusselt number. This is due to the steep temperature gradients near the drop surface. For low Peclet numbers, conduction remains to be the dominant mechanism at all times. For a higher Peclet number, the Nusselt number decreases for short times, but starts increasing thereafter as the cold fluid from the drop interior is brought near the drop surface due to the circulatory motion. The Nusselt number oscillations are more pronounced for high Peclet numbers. This is due to the shorter time scale for the circulatory motion in the drop interior at the high Peclet number. Eventually, as a result of the fluid convection, the temperature gradients along each stream line diminish. Then the heat transport is mainly in the direction perpendicular to the stream lines. Under this condition, the Nusselt number variation attains a steady state. The steady-state Nusselt number value increases as the Peclet number is increased. The transient Nusselt number variation was found to be qualitatively similar in prolate and oblate drops. However, for a given Peclet number,

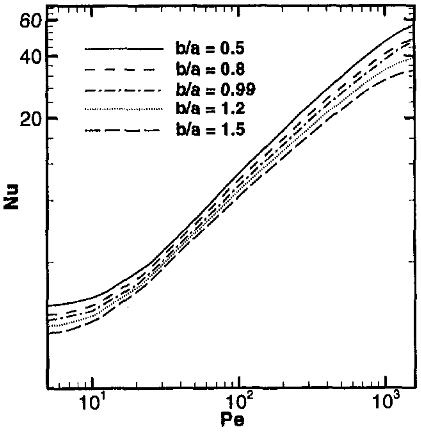

Fig. 7 Variation of overall external steady-state Nusselt number with Peclet number

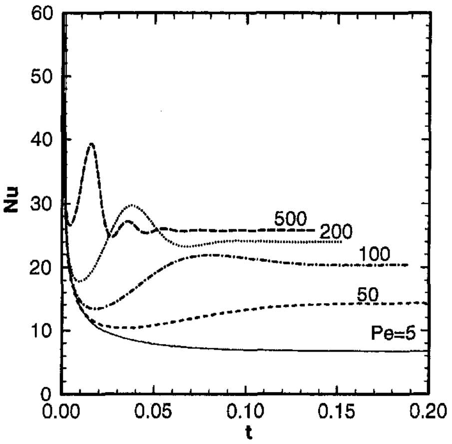

Fig. 8 Transient variation of internal Nusselt number for a prolate drop with $b/a = 1.5$

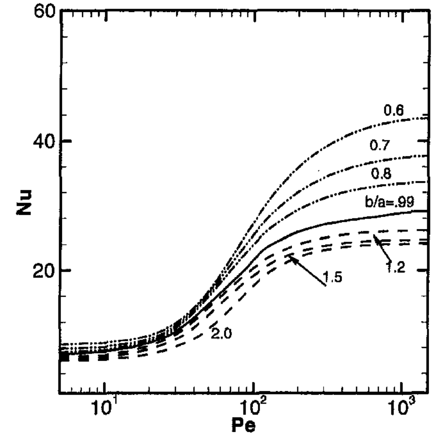

Fig. 9 Variation of internal Nusselt number with Peclet number for deformed drops

the steady-state Nusselt numbers for an oblate drop were higher than those for a prolate drop.

The variations of a steady-state Nusselt number with Peclet numbers is shown in Fig. 9 for a range of drop deformations. The Nusselt numbers for an oblate drop are higher than that for a spherical drop. At a small Peclet number, conduction is the most dominant mechanism of heat transport in the drop. Conduction of heat in a deformed drop is much faster than that in a sphere due to the smaller length scale and greater surface area for a deformed drop. For an oblate drop, the conduction length scale is the minor diameter b, which is smaller than the radius of a sphere of identical volume ($r = a^{2/3}b^{1/3}$). Therefore, for small Peclet numbers, the Nusselt numbers for an oblate drop are higher than those for a spherical drop. The Nusselt numbers for prolate drops are seemingly lower than those for oblate drops. We note that the Nusselt numbers reported here are based on the drop diameter $2a$. For an oblate drop $2a$ is the major diameter where as for a prolate drop it is the minor diameter. Therefore, the Nusselt numbers for a prolate drop are lower than that for oblate drops at low Peclet numbers.

At very large Peclet numbers, convection is the most dominant transport mechanism and the temperature gradients along each stream line diminish quickly. Therefore, after the initial transients, the heat transport is mainly in the direction perpendicular to the streamlines. For a given Peclet number, the resistance to the heat transport perpendicular to the stream lines will be inversely proportional to the distance between the drop surface and the center of the vortex. This distance is smaller in the case of an oblate drop than that for a sphere. This results in significantly higher steady-state Nusselt numbers for oblate drops at large Peclet numbers.

Although the variation of the Nusselt number with the Peclet number is qualitatively similar for oblate and prolate drops, the Nusselt numbers for prolate drops are significantly lower than that for oblate drops. As explained earlier, the Nusselt numbers for prolate drop are based on the minor diameter and those for the oblate drop are based on the major diameter. Also, the difference in the location of the circulatory vortex in prolate and oblate drops, is partly responsible for the lower values of the Nusselt number in prolate drops. Examination of Figs. 3(a) and (b) shows that the center of each vortex moves away from $\eta = \pi/4$ position as a drop deforms from a spherical shape. However, for a prolate drop, the movement of the vortex center is much smaller than that for an oblate drop. As a result of the difference in the flow field, the Nusselt numbers obtained for a prolate drop are closer to those for a spherical drop and lower than those for an oblate drop. Unlike the external problem, the difference in the Nusselt numbers for deformed drops and a liquid sphere, is not only a function of b/a but also a strong function of the Peclet number. As the effect of the Peclet number on the differences in the drop Nusselt number is nonuniform, no attempt was made to correlate the data in a form similar to Eq. (22).

Conclusions

We have studied the transient heat transport in a deformed drop suspended in a uniform electric field. An electrically induced flow field is determined for prolate and oblate drop shapes. The heat transfer results are obtained in the limits of the bulk of the resistance to the heat transport being in the drop (internal problem) and that in the continuous phase (external problem). From this study we can draw the following conclusions:

1 For the external problem, the overall steady-state Nusselt number increases with the Peclet number for all drop deformations. The steady-state Nusselt numbers for a sphere are lower than that for an oblate drop, and higher than that for a prolate drop, at all Peclet numbers.

2 For the range of drop shapes considered in this study, the effect of drop deformation on the steady-state Nusselt number for the external problem can be expressed as $\mathrm{Nu} = \mathrm{Nu}_{\mathrm{sphere}} \exp[-0.33*(b/a - 1)]$.

3 In the internal problem, for all drop deformations, the steady-state Nusselt numbers become increasingly independent of the Peclet number for large Peclet numbers.

4 The internal steady-state Nusselt numbers for an oblate drop are significantly higher than those for a prolate drop, for a given Peclet number.

5 As the steady-state Nusselt numbers for oblate drops are significantly higher than those for prolate drops for the internal as well as the external problem, the enhancement of direct contact heat/mass transfer is more effective for a combination of liquids for the continuous phase and the drop phase that leads to an oblate deformation of the drop under the application of an electric field.

Acknowledgments

The support for this work by the National Science Foundation under grant CTS-9409140 and under CAREER Award CTS-9733369 is thankfully acknowledged.

References

Abramzon, B., and Borde, I., 1980, "Conjugate unsteady heat transfer from a droplet in creeping flow," *AIChE J.*, Vol. 26, pp. 536–544.

Allan, R. S., and Mason, S. G., 1962, ''Particle behaviour in shear and electric fields, I. Deformation and burst of fluid drops,'' *Proc. R. Soc., London,* Vol. A267, pp. 45–61.

Ayyaswamy, P. S., 1995, ''Direct-contact transfer processes with moving liquid droplets,'' *Advances in Heat Transfer,* J. P. Hartnett and T. F. Irvine, eds., Vol. 26, pp. 1–104.

Ayyaswamy, P. S., 1996, ''Mathematical methods in direct-contact transfer studies with droplets,'' *Annual Review of Heat Transfer,* C.-L. Tien, ed., Vol. 7, pp. 245–331.

Brenner, H., 1967, ''On the Invariance of the Heat Transfer Coefficients to Flow Reversal in Stokes and Potential Streaming Flow Past Particle of Arbitrary Shape,'' *J. Mathematical and Physical Sciences,* Vol. 1, pp. 173–179.

Feng, J. Q., and Scott, T. C., 1996, ''A computational analysis of electrohydrodynamics of a leaky dielectric drop in an electric field,'' *J. Fluid Mech.,* Vol. 311, pp. 289–326.

Happel, J., and Brenner, H., 1965, *Low Reynolds number hydrodynamics,* Noordhoff International Publishing, Dordrecht, The Netherlands.

Jog, M. A., and Hader, M. A., 1997, "Transient Heat Transfer to a Spheroidal Drop Suspended in an Electric Field," *Int. J. Heat and Fluid Flow,* Vol. 18, pp. 411–418.

Melcher, J. R., and Taylor, G. I., 1969, ''Electrohydrodynamics: A review of the role of interfacial shear stresses,'' *Annual Reviews of Fluid Mechanics,* Vol. 1, pp. 111–146.

Oliver, D. L. R., Carleson, T. E., and Chung, J. N., 1985, ''Transient heat transfer to a fluid sphere suspended in an electric field,'' *Int. J. Heat Mass Transfer,* Vol. 28, pp. 1005–1009.

Oliver, D. L. R., and DeWitt, K. J., 1993, ''High Peclet number heat transfer from a droplet suspended in an electric field: Interior problem,'' *Int. J. Heat Mass Transfer,* Vol. 36, pp. 3153–3155.

Patankar, S. V., 1980, *Numerical Heat Transfer and Fluid Flow,* Hemisphere, Washington, DC.

Sadhal, S. S., Ayyaswamy, P. S., and Chung, J. N., 1997, *Transport Phenomena with Drops and Bubbles,* Springer-Verlag, New York.

Sharpe, L., Jr., and Morrison, F. A., Jr., 1986, ''Numerical Analysis of Heat and Mass Transfer From Fluid Sphere in an Electric Field,'' ASME JOURNAL OF HEAT TRANSFER, Vol. 108, pp. 337–342.

Smythe, W. R., 1968, *Static and Dynamics Electricity,* 3rd ed., McGraw-Hill, New York.

Sundararajan, T. S., and Ayyaswamy, P. S., 1984, ''Hydrodynamics and heat transfer associated with condensation on a moving drop for intermediate Reynolds numbers,'' *J. Fluid Mech.,* Vol. 149, pp. 33–58.

Taylor, G. I., 1966, ''Studies in Electrohydrodynamics, I. The circulation produced in a drop by an electric field,'' *Proc. R. Soc., London,* Vol. A291, pp. 159–166.

Torza, S., Cox, R. G., and Mason, S. G., 1971, ''Electrohydrodynamic deformation and burst of liquid drops,'' *Phil. Trans. R. Soc., London* Vol. A269, pp. 295–319.

Vizika, O., and Saville, D. A., 1992, ''The electrohydrodynamic deformation of drops suspended in liquids in steady and oscillatory electric fields,'' *J. Fluid Mechanics,* Vol. 239, pp. 1–21.

N. C. DeJong[1]
Research Assistant,
Department of Mechanical and
Industrial Engineering,
e-mail: n-dejon@uiuc.edu

L. W. Zhang[2]
Research Engineer,
Department of Mechanical and
Industrial Engineering,
Assoc. Mem. ASME.

A. M. Jacobi
Department of Mechanical and
Industrial Engineering,
Associate Professor,
Assoc. Mem. ASME.

S. Balachandar
Associate Professor,
Department of Theoretical
and Applied Mechanics.

D. K. Tafti
Senior Research Scientist,
National Center for
Supercomputing Applications,
Assoc. Mem. ASME.

University of Illinois,
Urbana, IL 61801

A Complementary Experimental and Numerical Study of the Flow and Heat Transfer in Offset Strip-Fin Heat Exchangers

A detailed analysis of experimental and numerical results for flow and heat transfer in similar offset strip-fin geometries is presented. Surface-average heat transfer and pressure drop, local Nusselt numbers and skin friction coefficients on the fin surface, instantaneous flow structures, and local time-averaged velocity profiles are contrasted for a range of Reynolds numbers using both prior and new experimental and numerical results. This contrast verifies that a two-dimensional unsteady numerical simulation captures the important features of the flow and heat transfer for a range of conditions. However, flow three-dimensionality appears to become important for Reynolds numbers greater than about 1300, and thermal boundary conditions are important for Reynolds numbers below 1000. The results indicate that boundary layer development, flow separation and reattachment, wake formation, and vortex shedding are all important in this complex geometry.

Introduction

In many liquid and refrigerant-to-air heat exchanger applications, interrupted surfaces are used to enhance the air-side heat transfer. Interrupted surfaces increase heat transfer via two mechanisms. First, they restart the boundary layers, thus taking advantage of the thin boundary layers—and hence high heat transfer—at the leading edges of fins. Second, above a certain critical Reynolds number, interrupted surfaces shed vortices which also enhance the heat transfer. Offset strip fins have found relatively common use for several decades, and a significant volume of research on this interrupted surface has been reported. The present research has been pursued through both experimental and numerical methods, and although a number of experimental and numerical studies have appeared in the literature, there have been few if any analyses that have taken advantage of the strengths of both approaches. The numerical and experimental approaches are complementary. Numerical simulations are well suited to parametric studies and provide a detailed description of the flow and thermal fields. However, while numerical simulations are often based on simplified models of geometry, flow, and heat transfer, such as perfect two-dimensionality, experimental studies reflect the full complexities of the three-dimensional geometry and account for the complex development of flow and heat transfer. Thus they provide verification for the numerical work. Owing to computational limitations, numerical simulations are best suited to investigate the fully developed flow and heat transfer in an infinite array of periodic plates while detailed experimental investigations model flow and thermal development through a finite array. A complementary experimental and numerical approach therefore offers many advantages in the study of such complex systems.

Manglik and Bergles (1995) provided a thorough review of the experimental literature on offset strip fins, and a related survey was very recently provided by DeJong and Jacobi (1997). Zhang et al. (1997a, b, c) provided surveys with a focus on progress in the numerical modeling of such flows. Because of these recent reviews, only a brief discussion of closely related research will be presented here.

Joshi and Webb (1987) used a combination of experimental and analytical techniques to develop correlations for the friction factor and the Colburn *j* factor in the laminar and turbulent flow regimes and to predict the transition between them. Using flow visualization, they were able to discern four different flow regimes. In the first regime, the flow was steady and laminar. In the second regime, the flow oscillated in the transverse direction near the upstream stagnation point of each fin. In the third regime, the flow oscillations encompassed the entire gap between the upstream and downstream fins, and in the fourth regime, the fins shed vortices. At the onset of the second regime, the laminar flow correlation of Joshi and Webb (1987) began to underpredict *j* and *f*. Therefore, they designated the Reynolds number at that point as the critical Reynolds number for transition between laminar and turbulent flow.

Xi et al. (1991) visualized the flow through an offset strip-fin arrangement with $\mathrm{Re}_b < 300$ by injecting ink in a water

---

[1] To whom correspondence should be addressed.

[2] Presently at Modine Manufacturing.

Contributed by the Heat Transfer Division for publication in the JOURNAL OF HEAT TRANSFER. Manuscript received by the Heat Transfer Division, Aug. 1, 1997; revision received, Apr. 13, 1998. Keywords: Finned Surfaces, Heat Exchangers, Numerical Methods. Associate Technical Editor: P. Simpkins.

tunnel. They used a hot and cold-wire anemometer probe to measure velocity and temperature fluctuations. Like Joshi and Webb (1987), they found that as the Reynolds number increased the flow went from steady laminar to a flow in which the wakes exhibited either roughly sinusoidal fluid motion or the formation of discrete vortices. Xi et al. (1991) suggested that heat transfer effects related to the formation of discrete vortices in the fin wakes caused j to deviate from the flat-plate solution. As the fin pitch decreased, the flow transitions occurred at lower Reynolds numbers. In 1990 Xi et al. analyzed the effect of fin thickness on heat transfer in offset fin arrays for the low Reynolds number range (characterized by free-forced mixed convection) and the middle Reynolds number range (dominated by forced convection). They presented local and row-by-row heat transfer data. It should be noted that their Nusselt number was based on the inlet fluid temperature rather than the local mixed-mean temperature and that this representation can lead to an erroneous interpretation of the results.

DeJong and Jacobi (1997) performed an experimental study of the flow and heat transfer in arrays of staggered parallel plates. Complementary flow visualization and local, row-by-row, and spatially averaged mass transfer experiments were conducted. They showed a direct link between vortex shedding and mass transfer enhancement. Rows in the array where the fins were shedding vortices, identified by flow visualization, showed a marked increase in Sherwood number. In the unsteady laminar regime, fins were noted to shed vortices from their leading edges.

In a numerical study, Sparrow and Liu (1979) examined the heat transfer on a series of parallel in-line and offset strip fins with negligible fin thickness by solving an approximate form of the steady Navier-Stokes and energy equations. They included the entrance and exit effects. Later, Patankar and Prakash (1981) modeled the flow and heat transfer in a periodic array of offset strip fins with finite fin thickness by solving the steady-state Navier-Stokes and energy equations. Suzuki et al. (1985) presented a combined numerical and experimental study of a two-dimensional offset strip model in free-forced mixed convection at low Reynolds numbers. These authors analyzed the effects of fin thickness and free-stream turbulence. The assumption of steady flow and thermal fields conceals the unsteady flow physics; unsteady numerical simulations of flows in grooved and communicating channels have shown that such effects can be significant (Ghaddar et al., 1986; Amon and Mikic, 1991). Recently, Zhang et al. (1997a, b) have shown that such effects can be very important when predicting heat transfer and friction loss for offset strip-fin heat exchangers, even under typical operating conditions.

The purpose of this paper is to present complementary experimental and numerical studies of the flow and heat transfer in offset strip fins. Earlier experimental measurements by DeJong and Jacobi (1997) as well as new experimental data will be contrasted with the unsteady numerical simulation of Zhang et al. (1997a, b, c). The complementary strengths of the experimental and numerical approaches will be used to improve understanding of the complex flow and heat transfer in the offset strip geometry. Both the experimental procedure and simulation methodology will be described here, followed by the results and conclusions.

Experimental Method

Mass transfer experiments were conducted to measure the local and spatially averaged surface convective behavior; local velocity experiments and flow visualization were used to obtain a clearer understanding of the flow field. The naphthalene sublimation technique was used for the mass transfer study (see Goldstein and Cho, 1995; Souza Mendes, 1991). The apparatus, instrumentation, specimen preparation method, and experimental procedures for these experiments have been discussed earlier

Nomenclature

A = area
b = fin thickness
C_f = skin friction factor
D = computational domain
D_{na} = mass diffusion coefficient of naphthalene in air
d_h = hydraulic diameter (see Eq. (2))
e_x = unit vector in streamwise (x) direction
f = friction factor (see Eq. (6))
f_v = vortex shedding frequency
h = local heat or mass transfer coefficient
$\bar{h}$ = average heat or mass transfer coefficient
H = half channel height between two fins (see Fig. 2)
j = modified Colburn j factor (see Eq. (5))
k = thermal conductivity of the fluid
L = plate length (see Fig. 1)
L_{core} = length of heat exchanger core
L_x = computational domain length in x-direction
L_y = computational domain length in y-direction
m = mass
n = outward normal unit vector on fin surfaces
N = number of local data acquired during a surface scan
Nu = local Nusselt number
p = modified perturbation pressure
P = total pressure
ΔP = mean pressure drop across a distance H unless otherwise noted
Pr = Prandtl number
q'' = specified constant heat flux
r = length along the fin periphery
Re = Reynolds number, based on hydraulic diameter unless otherwise noted (see Eq. (1))
s = transverse fin spacing (see Fig. 1)
Sc = Schmidt number, ν/D_{na}
Sh = local Sherwood number based on fin length (see Eq. (8))
$\overline{\text{Sh}}$ = average Sherwood number, based on hydraulic diameter unless otherwise noted (see Eq. (4))
Sr = Strouhal number
t = time
T = total temperature
u, v = velocity components in x and y directions
$\bar{u}$ = magnitude of the local velocity, time-averaged (see Eq. (25))
U = average velocity defined in Eq. (25)
U_{conv} = convective velocity of vortices
x^+ = dimensionless distance from the leading edge of a plate, x/L
y^+ = dimensionless transverse distance as defined in Figs. 2 and 8

Greek symbols

β = mean pressure gradient
δ_{sb} = local sublimation depth
γ = mean temperature gradient
λ = distance between vortices shed from a given side of the fin
μ = dynamic viscosity
ν = kinematic viscosity
θ = modified perturbation temperature
ρ = mass density

Subscripts and superscripts

c = evaluated at the minimum free-flow area of the heat exchanger
core = across the heat exchanger core
f = mass transfer surface
L = based on fin length
m = mass transfer
n, m = mixed-mean naphthalene
n, s = naphthalene in the solid phase
n, v = naphthalene in the vapor phase
ref = reference
τ = based on friction velocity
$*$ = dimensionless quantity

by DeJong and Jacobi (1997), so only a summary will be presented.

Apparatus and Instrumentation. An induction wind tunnel was used for the mass transfer and local velocity experiments. A test section with a 15.24 cm × 15.24 cm cross section was constructed of acrylic, and calibrated platinum RTDs and static pressure taps were located upstream and downstream of the test array. The test section could accommodate up to 92 fins in eight rows as shown in Fig. 1. Figure 1 also provides the geometric parameters for both the experimental and numerical arrays. All experimental fins had a height to length ratio of six. However, fin height was relatively unimportant since tests of local mass transfer showed the mass transfer not to be a function of vertical position on the fin. The test section included a combination of test specimens covered with naphthalene and dummy fins made of acrylic. The test specimens were placed in such a manner to simulate thermally developed conditions for downstream fins in some conditions whereas in others, the flow was thermally undeveloped. These conditions and terms will be discussed further in the results.

Local velocity data were acquired using a single-wire boundary layer hot-wire anemometer. The probe support was connected to a depth micrometer; the hot-wire was moved by turning the dial on the micrometer. Thus it was possible to determine the position of the hot-wire within ±.03 mm (compared to a value of s of 9.53 mm). Small holes were drilled through fins near the wind tunnel wall, and the probe was inserted through them to allow local velocity data to be acquired in the center of the array.

Flow visualization was performed by injecting ink into a water tunnel similar in configuration to the wind tunnel. The same array was used in both the wind and water tunnels.

Experimental Procedure. Before mass transfer experiments were conducted, the test specimens were weighed using an analytical balance (0–200 g, $\pm 5 \times 10^{-5}$ g). For cases where local data were obtained, the naphthalene surface profile was measured using a laser profilometer. This measurement system and its application to naphthalene sublimation have been described previously by Kearney and Jacobi (1996). A 60-by-20-point scanning grid was used to cover a 7.62 cm by 2.54 cm test area centered on the naphthalene surface. Thus, each surface measurement point was taken to represent a surface area element of approximately 1.6 mm^2. On the basis of repeated scans of a reference surface, these optical methods provided sublimation depths with a $2-\sigma$ uncertainty of ± 6 μm.

After the initial mass and surface profile data had been recorded, the specimens were placed in the test array and exposed to a controlled air flow. Upon removal from the wind tunnel, the specimens were weighed and scanned again. During each run, upstream and downstream temperatures were sampled every five seconds and averaged over the period of the test. The core pressure drop, pressure drop across an ASME standard orifice plate (to determine flow rate), relative humidity, barometric pressure, and exposure time were also recorded for each test.

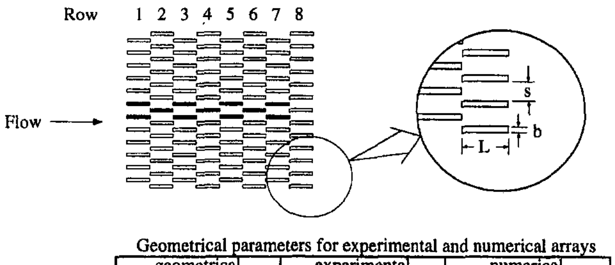

Geometrical parameters for experimental and numerical arrays

geometrical parameter	experimental geometry	numerical geometry
b/L	0.125	0.117
s/L	0.375	0.507

Fig. 1 Top view of the parallel plate array used for the experiments. The black fins were coated with naphthalene in most cases. The numerical simulation analyzed a similar, infinite array of plates. Geometric parameters for the two geometries are given in the table.

Before acquiring the local velocity data, the hot-wire anemometer was calibrated in an open test section. The local velocity data were acquired between adjacent fins at the leading edges and midpoints of the fins for the seventh row of the eight-row array. Each local velocity data point represents an average of 2000 measurements.

Data Reduction and Interpretation. The Reynolds number for flow through the test section was defined as

$$\mathrm{Re} = U_c d_h / \nu \tag{1}$$

where U_c is the flow velocity at the minimum free-flow area, and d_h is the hydraulic diameter

$$d_h = 2(s - b)L/(L + b). \tag{2}$$

To facilitate comparison between geometries with different hydraulic diameters, in some cases the Reynolds number was based on fin length, L, instead of hydraulic diameter.

The average mass transfer coefficient was determined through

$$\bar{h}_m = \Delta m / A_f \rho_{n,v} \Delta t \tag{3}$$

where Δm is the change in mass of the specimen and Δt is the exposure time. The sources of thermophysical properties are given in DeJong and Jacobi (1997). The average Sherwood number was calculated using

$$\overline{\mathrm{Sh}} = d_h \bar{h}_m / D_{na}. \tag{4}$$

Following the suggestion of Sparrow and Hajiloo (1980) for intermediate Schmidt numbers, a modified Colburn j factor was used to represent the spatially averaged mass transfer data

$$j = \overline{\mathrm{Sh}}/\mathrm{ReSc}^{0.4}. \tag{5}$$

The core pressure drop, ΔP_{core}, was interpreted using the conventional Fanning friction factor, f,

$$f = \frac{2\Delta P_{\text{core}}}{\rho U_c^2}\left(\frac{d_h}{4L_{\text{core}}}\right). \tag{6}$$

The local mass transfer coefficients were determined from the sublimation depths using the following relation:

$$h_m = \rho_{n,s}\delta_{sb}/\rho_{n,v}\Delta t. \tag{7}$$

Local Sherwood numbers (based on fin length) could then be determined from

$$\mathrm{Sh}_L = h_m L / D_{na}. \tag{8}$$

As a redundant check, the local Sherwood numbers were integrated and compared to the mass-averaged Sherwood numbers using the following approximation:

$$\overline{\mathrm{Sh}}_{\text{int}} = \frac{1}{A}\int_A \mathrm{Sh}\,dA \approx \frac{1}{N}\sum \mathrm{Sh}. \tag{9}$$

If $\overline{\mathrm{Sh}}_{\text{int}}$ for a particular experiment, as obtained through Eq. (9), were not within ten percent of $\overline{\mathrm{Sh}}_L$ as determined from the weight measurement, the local data for that run were rejected.

Heat transfer data could be inferred from the mass transfer data by employing the heat and mass analogy:

$$\mathrm{Nu} = \mathrm{Sh}(\mathrm{Pr}/\mathrm{Sc})^{n}. \qquad (10)$$

Again, a value of n of 0.4 is appropriate for the intermediate values of Schmidt number used here.

Strouhal numbers were calculated from flow visualization results using

$$\mathrm{Sr} = f_v b / U_c \qquad (11)$$

where $f_v = U_{\mathrm{conv}}/\lambda$. Here U_{conv} is the convective velocity of the vortices, which was approximated as the average velocity in the lateral gap s between adjacent fins in a row, and λ is the distance between vortices shed from a given side of a fin. This distance was determined from photographs recorded during flow visualization. Flow velocities were determined from the transit time required for an ink flow marker to pass through the array and from the free-flow to frontal area ratio.

Uncertainty. The uncertainties of the reduced data were determined by propagating the measurement uncertainties using standard methods (Kline and McClintock, 1953). The uncertainties in Re, $\overline{\mathrm{Sh}}$, modified Colburn j factor, and local Nusselt number were 2 percent, 5 percent, 5.5 percent, and 10 percent, respectively. The uncertainty in ΔP decreased as the Reynolds number increased because the uncertainty of the pressure measurement was fixed. Thus, the uncertainties in ΔP ranged from approximately 50 percent at very low Reynolds numbers to 0.2 percent at high Reynolds numbers. For Re $\geq$ 1000, the average uncertainty in ΔP was one percent, leading to an average uncertainty in f of about four percent. The calibration of the hot-wire resulted in a $2-\sigma$ uncertainty of nine percent.

Simulation Methodology

For the numerical simulation, the array is approximated as a periodic repetition of a basic unit, and the computational domain is limited to this basic unit. Thus, it has been assumed that the flow is both hydrodynamically and thermally fully developed in the fin array, and the effects of the entrance and exit have been neglected. The computational domain contains two fins and is periodically repeated in both the streamwise and transverse directions, as shown in Fig. 2.

The nondimensional Navier-Stokes, continuity and energy equations, which are shown below, are solved in two dimensions:

$$\frac{\partial u_i^*}{\partial t^*} + \frac{\partial}{\partial x_j^*}(u_i^* u_j^*) = -\frac{\partial P^*}{\partial x_i^*} + \frac{1}{\mathrm{Re}_\tau}\frac{\partial^2 u_i^*}{\partial x_j^{*2}} \quad \text{in} \quad D \qquad (12)$$

$$\frac{\partial u_i^*}{\partial x_i^*} = 0 \quad \text{in} \quad D \qquad (13)$$

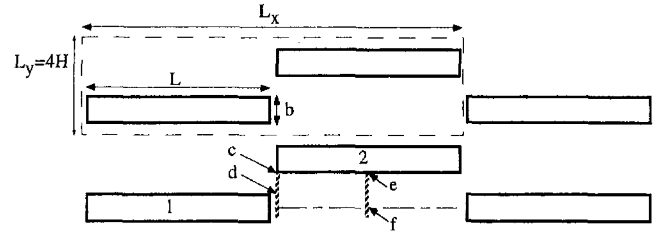

Fig. 2 Schematic of the fin arrangement for the computational simulation. The dashed line indicates the computational domain where $L/H = L^* = 6.41$, $L_x/H = L_x^* = 14.4$, $b/H = b^* = 0.75$. Letters c–f indicate locations of velocity measurements, as explained in Fig. 8.

$$\frac{\partial T^*}{\partial t^*} + \frac{\partial}{\partial x_j^*}(u_i^* T^*) = \frac{1}{\mathrm{Re}_\tau \, \mathrm{Pr}}\frac{\partial^2 T^*}{\partial x_j^{*2}} \quad \text{in} \quad D \qquad (14)$$

where D denotes the computational domain. It has been assumed that the flow is incompressible with constant properties, and the effects of viscous dissipation and buoyancy forces are neglected. The length scale is defined as the half distance between adjacent columns, H, while the pressure scale, ΔP, is chosen to be the applied pressure drop in the streamwise direction over a length of H. The velocity scale is the friction velocity, $u_\tau = (\Delta P/\rho)^{1/2}$. The temperature has been nondimensionalized by $q''H/k$, where q'' is the specified heat flux on the fin surface. Notice that two nondimensional parameters appear in the above equations as a result of this nondimensionalization: one is the Reynolds number based on the friction velocity, $\mathrm{Re} = u_\tau H/\nu$, and the other is the Prandtl number which is set to that of air, 0.7.

Since the present simulation assumes periodicity of the geometry over a basic unit, the following general periodic form can be applied for the velocity components:

$$u_i^*(x^* + mL_x^*, y^* + nL_y^*) = u_i^*(x^*, y^*) \qquad (15)$$

In Eq. (15) it is assumed that the resulting flow is periodic over m rows of fins in the x-direction and n columns of fins in the y-direction. For computational simplicity we assume that $m = n = 1$. The imposition of periodic conditions for the pressure and temperature requires some modifications. The pressure decreases monotonically in the flow direction while the temperature is expected to either decrease or increase monotonically in the flow direction, depending on the direction of heat transfer. Following Patankar et al. (1977), the nondimensional total pressure and temperature have each been subdivided into a linear component and a perturbation term:

$$P^*(x^*, y^*, t^*) = P_{\mathrm{in}}^* - \beta x^* + p^*(x^*, y^*, t^*) \qquad (16)$$

$$T^*(x^*, y^*, t^*) = T_{\mathrm{in}}^* - \gamma x^* + \theta(x^*, y^*, t^*) \qquad (17)$$

where β and γ are the mean streamwise pressure and temperature gradients. With such a decomposition, a periodic condition similar to Eq. (15) can be applied for the perturbation pressure, $p^*(x^*, y^*, t^*)$, and the perturbation temperature, $\theta(x^*, y^*, t^*)$. A detailed treatment of this approach can be found in Zhang et al. (1997a).

On the fin surfaces, no slip and no penetration boundary conditions are applied for the velocities while the Neumann boundary condition is applied for the modified nondimensional pressure and a modified heat flux condition for the temperature, as follows:

$$(\nabla p^*) \cdot \hat{n} = 0 \qquad (18)$$

$$(\nabla \theta) \cdot \hat{n} = 1 - \gamma \hat{e}_x \cdot \hat{n} \quad \text{on } \partial D_{\mathrm{fin}} \qquad (19)$$

where $\hat{n}$ is the outward unit vector normal to the fin surface and $\hat{e}_x$ is the unit vector in the x-direction.

The instantaneous Nusselt number based on the hydraulic diameter is defined as

$$\mathrm{Nu}\,(r, t) = q'' d_h / [T_f(r, t) - T_{\mathrm{ref}}(r, t)]k \qquad (20)$$

where T_f and T_{ref} are the dimensional fin surface temperature and local reference temperature and r is the length along the fin periphery. The above equation can also be expressed in nondimensional terms as

$$\mathrm{Nu}\,(r, t) = d_h^* / [\theta_f(r, t) - \theta_{\mathrm{ref}}(r, t)] \qquad (21)$$

with θ_{ref} defined as

$$\theta_{\text{ref}}(r, t) = \int \theta |u^*| dy^* \Big/ \int |u^*| dy^*. \qquad (22)$$

The global mean Nusselt number can be obtained be integrating Nu (r, t) around the fin surface and averaging over time.

The local skin friction factor is defined as

$$C_f = \frac{d_h \mu}{2H\rho U_c^2}\left[\frac{\partial u}{\partial y}\right]_{\text{wall}}. \qquad (23)$$

To quantify the accuracy of the calculations, a grid dependency study was performed at high Reynolds numbers (Zhang et al., 1997a). By doubling the grid from 128 × 32 to 256 × 64, the j and f factors reduced by nine percent and six percent, respectively. Further doubling the grid to 512 × 128 cells resulted in a nominal reduction of one percent and two percent for the f and j factors, respectively. In view of these results, the f and j factors on a 128 × 32 grid are expected to be overpredicted by five percent to ten percent in the high Reynolds number range. At each time step, the L_1 norm of the pressure equation was converged to $1 \times e^{-6}$. Further details regarding the spatial and temporal discretization and numerical implementation are presented in Zhang et al. (1997a), where computational performance and grid independence are also discussed.

Results

The results are divided into three sections. In each section, the experimental and numerical results are contrasted, and the physics of the flow and heat transfer are discussed. In the first section, overall heat transfer and pressure drop results, which are presented in the form of average j and f factors and Sherwood numbers, are presented. In the second, local time-averaged heat transfer results along the fins are presented to illustrate the local heat transfer characteristics. These results reveal the effects of both boundary layer growth and vortex shedding within the array. The third section contrasts the instantaneous flow structures and local time-averaged velocity results which reveal the flow behavior that causes the heat transfer characteristics.

Contrast of Overall Heat Transfer and Pressure Drop. The Colburn j and friction factors determined through the numerical simulation and the experiments are shown in Fig. 3 together with the correlations of Joshi and Webb (1987). The experimental friction factors are obtained using the pressure drop across the entire eight-row test section; however, the Colburn j factors are for the seventh row of the array. The numerical simulation assumes a large array of fins so that the entrance and exit effects can be neglected. The friction factor results reveal very similar performance. For the present numerical simulation, the ratio of the fin thickness to the gap between the fins is approximately 30 percent smaller than for the experiments (cf. Figs. 1 and 2). Different correlations indicate that this difference in geometries could cause the experimental and numerical results to differ by anywhere from −2 to −19 percent in the laminar regime (meaning the experimental values would be lower) and +15 to −21 percent in the turbulent regime (Wieting, 1975; Joshi and Webb, 1987; Manglik and Bergles, 1995). Figure 3 indicates that at low Reynolds numbers, this geometry difference has a small effect, but at higher Reynolds numbers the increased form drag of the thicker fins causes the experimental friction factors to be higher than those from the numerical simulation. The assumption of two-dimensionality and the neglect of entrance and exit effects in the present numerical simulation may have also attributed to this difference.

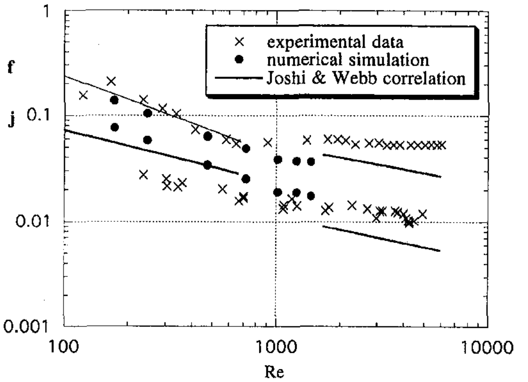

Fig. 3 Colburn j factors and friction factors as a function of Reynolds number. The correlation of Joshi and Webb (1987) is provided for comparison purposes.

For Reynolds numbers less than 1000, the Colburn j factors predicted by the numerical simulation are up to twice as large as the experimental measurements, but for Reynolds numbers greater than 1000, the numerical predictions are within ten percent of the experimental data. This behavior may be due in part to differences in the imposed boundary conditions (constant flux for the numerical simulations and constant fin temperature for the experiments). For example, the analytical solution for the Nusselt number for laminar flow over a flat plate with a constant heat flux is 36 percent higher than for the same plate with a constant surface temperature. For developed laminar flow in a flat duct the difference is only nine percent. At high Reynolds numbers the effect due to differing boundary conditions for both cases is small; for turbulent flow over a flat plate, the difference between the Nusselt numbers for the two boundary conditions is only about four percent. For the j factor results, the difference in boundary conditions would have a much larger effect than the difference in geometry. The correlations of Wieting (1975), Joshi and Webb (1987), and Manglik and Bergles (1995) indicate that the geometry difference could cause the experimental and numerical results to differ by −2 to +3 percent in the laminar regime and −2 to −10 percent in the turbulent regime.

Recent results by Zhang et al. (1997c) have shown that at sufficiently high Reynolds numbers, when in reality the flow is three-dimensional, a two-dimensional simulation tends to overpredict the overall heat transfer. For example, in an in-line array of fins, it was observed that at Re = 3500, the overprediction of the j factor in the two-dimensional simulation can be as high as 25 percent. This behavior is due to the three-dimensional flow effects not captured in the two-dimensional simulation—effects which tend to weaken the periodic shedding of vortices. Differences in pressure drop between two and three-dimensional simulations are much smaller; at Re = 3500, the friction factors agree to within four percent. A detailed exploration of the underlying three-dimensional mechanisms is discussed in Zhang et al. (1997c).

The experiments have the advantage of modeling developing flow with entrance and exit effects while the numerical simulation models developed flow through an infinite array of plates. Fig. 4 illustrates this difference. Experimental Sherwood numbers (which are analogous to Nusselt numbers) are shown for rows one through seven of the eight-row array. In Fig. 4, the solid lines connect data that have been corrected for the mixed-mean naphthalene concentration in the air using Eq. (24) while the dashed lines are the uncorrected data (where $\rho_{n,m}$ is assumed to be zero).

$$\bar{h}_m = \Delta m / A_f(\rho_{n,v} - \rho_{n,m})\Delta t \qquad (24)$$

The rate of naphthalene sublimation into the air stream was known. To determine the volume of air into which the naphthalene sublimed, a channel of width s was used for the odd-numbered rows while a channel of width $2s$ was used for the

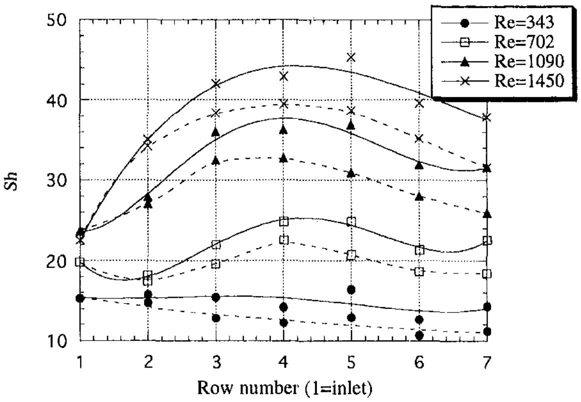

Fig. 4 Sherwood numbers for fins in successive rows of the eight-row experimental array. The solid lines have been corrected for mixed-mean naphthalene concentration, and the dashed lines are the uncorrected data.

even-numbered rows (see Fig. 1). It was also assumed that half of the naphthalene escaped out of this channel going from rows 2 to 3, 4 to 5, and 6 to 7. The reason for these somewhat conservative assumptions will be discussed later.

Figure 4 shows clearly that the fin's location within the array affects its heat transfer. At low Reynolds numbers, where the flow is laminar and no vortex shedding occurs, the Sherwood numbers remain approximately constant or decrease slightly for successive rows in the array. Since the flow is not well mixed, boundary layers from upstream plates may be carried onto downstream plates, decreasing their Sherwood numbers. As the Reynolds number is increased, vortex shedding begins in the downstream rows and moves upstream. Since shedding increases the convective transport, once a fin begins shedding vortices from its leading edge, its Sherwood number increases. Corresponding flow visualization presented in DeJong and Jacobi (1997) shows that the row number at which the Sherwood number shows a marked increase is that where significant vortex shedding begins. The two highest Reynolds numbers show a decrease of approximately 12 percent from row 5 to row 6. Since this decrease can be seen even in the data corrected for mixed-mean naphthalene concentration, the primary cause of this behavior may be that the exit of the array (following row 8) is affecting the flow and therefore naphthalene mass transfer upstream. If this is the case, then it would be better to compare experimental results for rows 3–5 with the simulation than to compare the results for row 7. For example, at a Reynolds numbers of 1450, the experimental Colburn j factors for row 7 are 13 percent lower (when not corrected for a nonzero mixed-mean naphthalene concentration) and four percent higher (for values that have been corrected) than the simulation, respectively. For rows 3–5, the uncorrected and corrected values are 7 percent and 20 percent higher, respectively.

To evaluate the effect of thermal development, in Fig. 5 Sherwood numbers for the seventh row of the eight-row array that have not been corrected for a nonzero mixed-mean naphthalene concentration are shown. For the data labeled ''thermally developed,'' naphthalene was present on the six upstream rows as well (see Fig. 1). For the data labeled ''thermally developing,'' naphthalene was present only on the seventh row of fins; dummy fins were placed upstream to ensure that the flow was hydrodynamically the same in both cases. Except for low Reynolds numbers (below 500), there is no appreciable difference between the two results. This result indicates that the overall effect of thermal development is insignificant. On the other hand, based on an estimate for the increase in the mixed-mean naphthalene concentration for the ''thermally developed'' case (similar to the one performed for Fig. 4), one would expect an 18 to 27 percent decrease in mass transfer for the ''thermally developed'' case. This contradiction can partially be resolved by noting that the concentration profile approaching the seventh fin is not uniform and that in fact the naphthalene concentration near the fin surface is lower than the mixed-mean concentration. Support for this assertion comes from the thermal profiles plotted at various downstream locations in Zhang et al. (1997b), and the behavior of the concentration profiles is expected to be the same. The effect of the reduced concentration adjacent to the fins is to increase the mass transfer.

Local Nusselt Number Behavior. Nusselt number distributions on the fin surface given by the numerical simulation and the experiments are shown in Fig. 6(*a*). Since the geometries have different hydraulic diameters, for comparison purposes, the Nusselt and Reynolds numbers are based on the fin length.

The experimental and numerical results reveal similar behavior. Average Nusselt numbers were obtained by integrating the local results over the fin surface. The experimental and numerical results agreed to within 3 percent and 12 percent for the low and high Reynolds number cases, respectively. Note that the use of L rather than d_h as the length scale has resulted in a much closer comparison. Considering an experimental uncertainty of ±10 percent for local Sherwood number and the differences between the experiments and the simulation, this agreement is excellent. Not only are the average Nusselt numbers predicted well by the simulation, but the similar trends reported along the length of the fin reveal the nature of the local flow structures and heat transfer.

The Nusselt number distributions for the low Reynolds number case show clear evidence of boundary layer growth. As expected, heat transfer is high at the leading edge of the fin and decreases further downstream, approaching an asymptotic value. Both distributions show a slight increase in the Nusselt number near the trailing edge of the fin. This increase is caused by acceleration of the flow as it passes through the minimum cross-sectional area. The high Reynolds number case shows that an additional flow feature is present in this case. Heat transfer is high at the leading edge and decreases over approximately the first ten percent of the fin. However, both the experimental and numerical results show a local maximum in the Nusselt number at a position approximately 30 percent downstream from the leading edge. The Nusselt number then decreases along the rest of the fin except for a slight increase at the end.

In order to explain this behavior of local Nusselt number, let us consider the local time-averaged skin friction coefficient on the top (or bottom) surface of the fin obtained from the computations at $\mathrm{Re}_L = 680$ ($\mathrm{Re}_{dh} = 474$) and $\mathrm{Re}_L = 2100$ ($\mathrm{Re}_{dh} = 1465$) and plotted in Fig. 6(*b*). While in the lower Re_L case

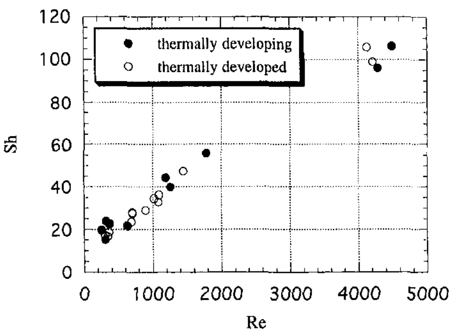

Fig. 5 Uncorrected Sherwood numbers for the seventh row of the array under two conditions. For the data labeled "thermally developed," naphthalene was present on the six upstream rows (see Fig. 1). For the data labeled "thermally developing," naphthalene was present only on the seventh row of fins; dummy fins were placed upstream. The flow was hydrodynamically identical in both cases.

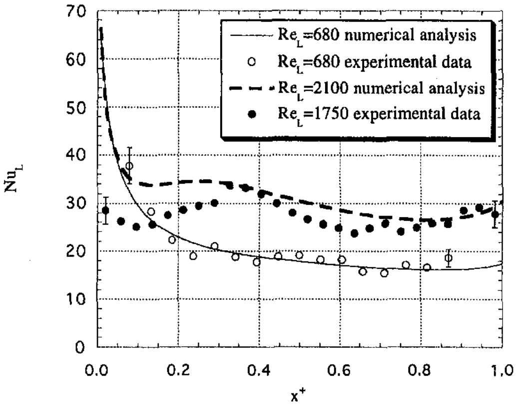

Fig. 6(*a*) Local Nusselt number distributions along a fin surface for a steady laminar and turbulent flow case where $x^+ = 0$ is the fin leading edge and $x^+ = 1.0$ the trailing edge. Typical error bars are shown on several data points. Note that the experimental fin pitch is smaller than the numerical fin pitch.

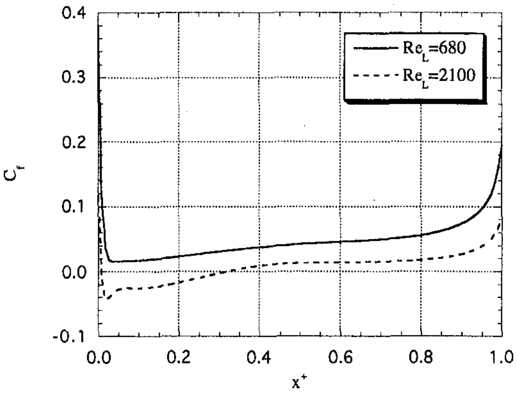

Fig. 6(*b*) Local time-averaged skin friction coefficient distributions along the top of the fin surface evaluated from the numerical simulation for a laminar and a turbulent flow case.

the local skin friction always remains positive, in the higher Re_L case the local skin friction is negative over the first 32 percent of the fin. This behavior suggests a recirculation region in the mean at the higher Reynolds number with the reattachment point around 32 percent of the fin length from the leading edge. This mean location where the separating shear layer impinges on the fin surface is in excellent agreement with the location of the local maxima in the Nusselt number. This observation agrees with earlier studies on separating and reattaching shear layers (Vogel and Eaton, 1985; Sparrow et al., 1987; Ota and Nishiyama, 1987) for flow over a backward-facing step and a blunt plate. In all of these studies it was found that a point of maximum heat transfer existed in the vicinity of the mean reattachment point.

It must be cautioned that the recirculation region is in the mean—the flow is unsteady, and vortices are shed from the leading edges of the fins. However, in a time-averaged sense, the flow is characterized by a recirculation zone. At the high Reynolds numbers considered (1750 and 2100), both Zhang et al. (1997b) and DeJong and Jacobi (1997) observed the flow to be turbulent with complex vortex shedding from the leading edges of fins. The recirculation region and the associated negative skin friction near the leading edge is a time-averaged effect. Although the instantaneous vortices are expected to influence both the local skin friction and heat transfer, the time-averaged cumulative effect of the vortices on the skin friction factor and Nusselt number may depend on the strength and complex dynamics of these vortices. The near coincidence of the peak in local Nusselt number and the mean reattachment point is somewhat fortuitous. At a somewhat lower Reynolds number, Zhang et al. (1997b) observed that while there was a recirculation region in the mean flow, no distinguishable local peak was observed in the Nusselt number. Nevertheless, it is clear that the effect of the vortices is to maintain a high Nusselt number over a significant portion of the fin.

Instantaneous Flow Structures and Velocity Profile Comparison. Instantaneous flow structures can be examined using the flow visualization shown in Fig. 7(*a*) and the numerically computed vorticity contour plot in Fig. 7(*b*). Figure 7(*b*) shows the magnitude of the vorticity plotted on a log scale for Re = 1018, and the flow visualization (Fig. 7(*a*)) shows streaklines for Re = 1060. While the dye helps to visualize regions of strong vorticity, it must be noted that dye exhibits a cumulative effect as it flows from upstream to downstream fins. The vorticity plot, on the other hand, presents a snapshot in time with no such cumulative effect. Although a direct comparison is difficult, one can see the similarity between the unsteady flow structures exhibited in the experiments and the simulation. Both plots show vortices shedding from the leading edges of the fins and a wavy wake downstream. Note the development effect illustrated in Fig. 7(*a*). Only a weak oscillation can be observed in the wake of row 1, but observations showed that vortices were shedding from the second and following rows of fins. This result corroborates the row-by-row Sherwood numbers plotted in Fig. 4 which show a marked increase in the Sherwood numbers from row 1 to row 2 at Re = 1090.

DeJong and Jacobi (1997) and Zhang et al. (1997b) report the transition between the steady and unsteady laminar flow regimes in the same Reynolds number range—between 460 and 550 for the former and between 474 and 720 for the latter. This unsteady laminar flow regime is characterized by the shedding of distinct vortices. DeJong and Jacobi report Sr ≈ 0.23 over a range of Reynolds numbers in the unsteady laminar regime. The corresponding Strouhal numbers observed by Zhang et al. increase slightly with Reynolds number and are in the range of 0.15 to 0.17. Thus, there is a 40 percent discrepancy between the experimental and computational results which may be due to several factors. First, the larger fin thickness and smaller fin pitch employed in the experimental array would affect the vortex shedding frequency. For an array of staggered cylinders, Chen (1968) reports the Strouhal number to vary with the cylinder diameter and also the transverse cylinder and streamwise cylinder spacing, reaching values as high as 0.7. Xi et al. (1991) report Strouhal numbers ranging from 0.1 to 0.38 for an array of offset plates five rows deep. Their vortex shedding frequencies vary with Reynolds number, fin length, fin thickness, and fin pitch. For a 25 percent decrease in fin pitch, Xi et al. saw increases in their Strouhal numbers by up to 40

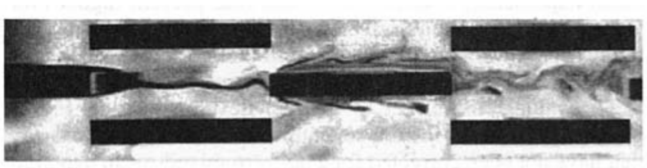

Fig. 7(*a*) Experimental streaklines at Re = 1060 for rows 1–4 of the experimental array

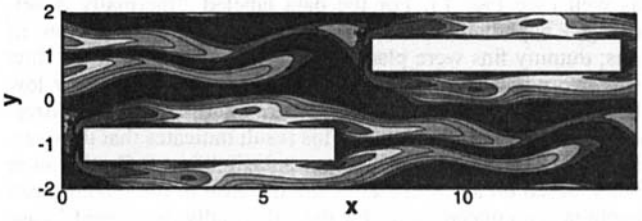

Fig. 7(*b*) Contours of vorticity magnitude obtained from the numerical simulation plotted on a log scale at Re = 1018

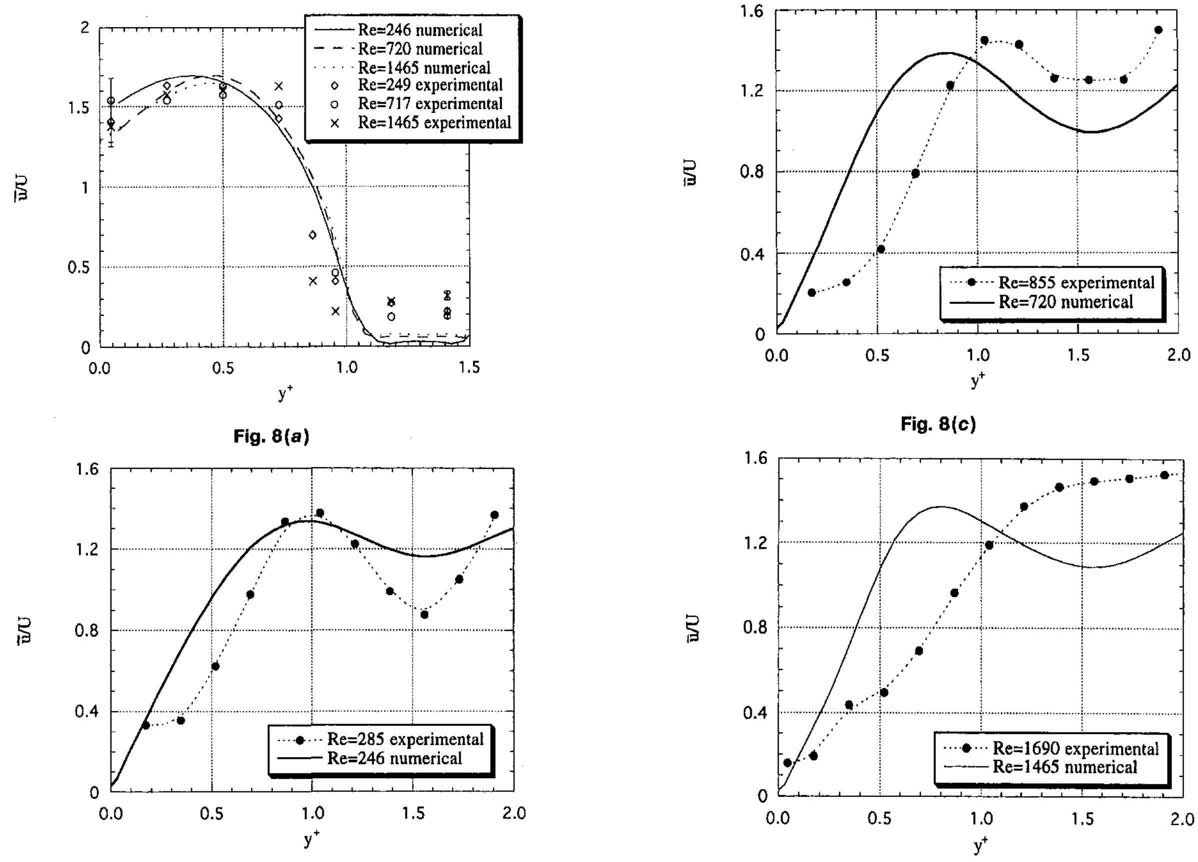

Fig. 8(*a*)

Fig. 8(*b*)

Fig. 8(*c*)

Fig. 8(*d*)

Fig. 8 Normalized local velocity results (*a*) at the fin leading edge for steady laminar, unsteady laminar, and turbulent flow cases with $y^+ = 0.0$ at *c* and $y^+ = 1.0$ at *d* in Fig. 2. Typical error bars are shown in (*a*) only. (*b*, *c*, *d*) at the fin midpoint $y^+ = 0.0$ at *e* and $y^+ = 1.5$ at *f* in Fig. 2 for (*b*) steady laminar flow, (*c*) unsteady laminar flow, and (*d*) turbulent flow.

percent. Second, the Strouhal number for an eight-row array may be different from that for an infinite array; Mochizuki and Yagi (1982) report that the Strouhal number can also vary with number of columns of plates for an offset plate array. Third, the two-dimensional limitation of the simulations may have contributed to the difference (see Zhang et al., 1997c). More importantly, the experimental Strouhal numbers are based on an approximation that the convective velocity of the vortices is equal to the average flow velocity. It has been reported in the literature that the convective velocity of the vortices can be as low as 80 percent of the mean velocity (Kiya and Sasaki, 1985). Use of this value would decrease the experimental Strouhal numbers to approximately 0.18, in closer agreement with the numerical simulations.

Local velocity results were acquired for three different Reynolds numbers at $x^+ = 0$ (the leading edge of the fin) and at $x^+ = 0.5$ (the fin midpoint). Results were recorded for positions along the hatched lines in Fig. 2. Because of geometrical differences, several interpretive measures were necessary to allow a meaningful comparison of the experimental and numerical findings. First, normalized velocities, $\bar{u}/U$, were presented. The normalizing parameter, U, is the average velocity across the gap given by

$$U = \frac{1}{s}\int_0^s \bar{u}dy \tag{25}$$

where $\bar{u}$ is the time-averaged magnitude of the velocity at a given position, and s is the lateral gap between two fins (see Fig. 1). Second, the position within the array was also normalized. Figure 8(*a*) shows measurements for the leading edge of the fin. Here $y^+ = 0.0$ and $y^+ = 1.0$ correspond to points *c* and *d* on Fig. 2. Figures 8(*b–d*) show measurements for the fin midpoint. Here $y^+ = 0.0$ and $y^+ = 1.5$ correspond to points *e* and *f* on Fig. 2.

Figure 8(*a*) shows that at the fin leading edge, the boundary layer is very thin—the increase in velocity from y^+ close to 0 to approximately $y^+ = 0.5$ is small. The small increase is due to residual effects of the wake of the upstream fin and distortion in the flow as it accelerates through the gap between neighboring fins. One can clearly see the low velocity in the wake downstream of fin 1 beginning at $y^+ = 1.0$. The numerical and experimental results show excellent agreement from $y^+ = 0.0$ to 1.0. In the wake the experimental velocities are slightly higher than the numerical predictions. This small difference notwithstanding, the experimental data and the numerical results clearly illustrate similar behavior.

Figures 8(*b–d*) show the results for the fin midpoint. In Figs. 8(*b*) and 8(*c*), the boundary layer is evident by the large increase in velocity beginning at $y^+ = 0.0$, and the velocity is smaller in the wake of the upstream fin (centered around $y^+ = 1.5$). The numerical predictions are in general agreement with the experimental results. However, at the highest Reynolds number an interesting discrepancy is evident (Fig. 8(*d*)). The numerical results still show effects of the upstream fin wake while the experimental results do not. This disparity may be caused by a combination of effects. Zhang et al. (1997a) show that three-dimensionality can have a large effect on wake size at high Reynolds numbers. The wake is much stronger in the numerical simulation due to the two-dimensionality of the calculations which results in strong coherence and less mixing. In reality, the wake size is much smaller (as in the experiments) because of enhanced mixing. Also, the slightly higher Reynolds number and the smaller fin pitch of the experiments would cause the flow to be more unsteady (see DeJong and Jacobi, 1997 and Xi et al., 1991). This increased unsteadiness results in more mixing which would smooth the velocity gradients in the wake.

Conclusion

The flow, heat transfer, and pressure drop results presented here are intimately coupled. The local heat transfer behavior on each fin is directly affected by the instantaneous flow structures and velocity profiles, as is the average heat transfer and pressure drop. The use of both experimental data and the results of a two-dimensional, unsteady numerical simulation draws upon the strengths of both methods. Numerical studies are faster and can provide detailed information about flow and heat transfer while experiments, which can be used to verify simulations, expose the effects of the complex, realistic conditions. Unsteady numerical simulations can more easily simulate developed flow while experiments exhibit developing flow with entrance and exit effects. Through this complementary study we have revealed the local heat transfer behavior of fins in both steady laminar and turbulent flow. In steady laminar flow, heat transfer behavior is determined mainly by boundary layer growth while at higher Reynolds numbers, vortex shedding is also important. Local time-averaged velocity data reveal a complex flow behavior.

Future work in this area should exploit the complementary nature of the experimental and numerical research by using identical geometries and boundary conditions. The unsteady laminar flow regime holds promise for a range of applications because high heat transfer rates can be attained with relatively low pressure drops. A deeper understanding of these complex flows can contribute to their effective exploitation in heat exchangers.

Acknowledgments

This research was performed under a grant from the Air Conditioning and Refrigeration Center at the University of Illinois at Urbana-Champaign. Computation time was provided by the National Center for Supercomputing Applications on the massively parallel CM-5.

References

Amon, C. H., and Mikic, B. B., 1991, "Spectral Element Simulations of Unsteady Forced Convective Heat Transfer: Application to Compact Heat Exchanger Geometries," *Numerical Heat Transfer, Part A*, Vol. 19, pp. 1–19.

Chen, Y. N., 1968, "Flow-Induced Vibration and Noise in Tube-Bank Heat Exchangers Due to von Karman Streets," *J. of Engineering for Industry*, Vol. 90(b), pp. 134–146.

DeJong, N. C., and Jacobi, A. M., 1997, "An Experimental Study of Flow and Heat Transfer in Parallel-Plate Arrays: Local, Row-by-Row and Surface Average Behavior," *Int. J. Heat Mass Transfer*, Vol. 40, No. 6, pp. 1365–1378.

Ghaddar, N. K., Karniadakis, G. E., and Patera, A. T., 1986, "A Conservative Isoparametric Spectral Element Method for Forced Convection: Application to Fully Developed Flow in Periodic Geometries," *Numerical Heat Transfer*, Vol. 9, pp. 277–300.

Goldstein, R. J., and Cho, H. H., 1995, "A Review of Mass Transfer Measurements Using Naphthalene Sublimation," *Exp. Thermal Fluid Sci.*, Vol. 10, pp. 416–434.

Joshi, H. M., and Webb, R. L., 1987, "Heat Transfer and Friction in the Offset Strip-Fin Heat Exchanger," *Int. J. Heat Mass Transfer*, Vol. 30, pp. 69–83.

Kearney, S. P., and Jacobi, A. M., 1996, "Local Convective Behavior and Fin Efficiency in Shallow Banks of Inline and Staggered, Annularly Finned Tubes," ASME JOURNAL OF HEAT TRANSFER, Vol. 118, pp. 317–326.

Kiya, M., and Sasaki, K., 1985, "Structure of Large-Scale Vortices and Unsteady Reverse Flow in the Reattaching Zone of a Turbulent Separation Bubble," *J. Fluid Mechanics*, Vol. 154, pp. 463–491.

Kline, S. J., and McClintock, F. A., 1953, "Describing Uncertainties in Single Sample Experiments," *Mechanical Engineering*, Vol. 75, pp. 3–8.

Manglik, R. M. and Bergles, A. E., 1995, "Heat Transfer and Pressure Drop Correlations for the Rectangular Offset Strip Fin Compact Heat Exchanger," *Exp. Thermal Fluid Sci.*, Vol. 10, pp. 171–180.

Ota, T., and Nishiyama, H., 1987, "A Correlation of Maximum Turbulent Heat Transfer Coefficient in Reattachment Flow Region," *Int. J. Heat Mass Transfer*, Vol. 30, pp. 1193–1200.

Patankar, S. V., and Prakash, C., 1981, "An Analysis of the Effect of Plate Thickness on Laminar Flow and Heat Transfer in Interrupted-Plate Passages," *Int. J. Heat Mass Transfer*, Vol. 24, pp. 51–58.

Souza Mendes, P. R., 1991, "The Naphthalene Sublimation Technique," *Exp. Thermal Fluid Sci.*, Vol. 4, pp. 510–523.

Sparrow, E. M., and Hajiloo, A., 1980, "Measurements of Heat Transfer and Pressure Drop for an Array of Staggered Plates Aligned Parallel to an Air Flow," ASME JOURNAL OF HEAT TRANSFER, Vol. 102, pp. 426–432.

Sparrow, E. M., Kang, S. S., and Chuck, W., 1987, "Relation Between the Points of Flow Reattachment and Maximum Heat Transfer for Regions of Flow Separation," *Int. J. Heat Mass Transfer*, Vol. 30, pp. 1237–1246.

Sparrow, E. M., and Liu, C. H., 1979, "Heat Transfer, Pressure Drop and Performance Relationships for In-Line, Staggered, and Continuous Plate Heat Exchangers," *Int. J. Heat Mass Transfer*, Vol. 22, pp. 1613–1624.

Suzuki, K., Hirai, E., and Miyake, T., 1985, "Numerical and Experimental Studies on a Two-Dimensional Model of an Offset-Strip-Fin Type Compact Heat Exchanger Used at Low Reynolds Number," *Int. J. Heat Mass Transfer*, Vol. 28, No. 4, pp. 823–836.

Vogel, J. C., and Eaton, J. K., 1985, "Combined Heat Transfer and Fluid Dynamic Measurements Downstream of a Backward-Facing Step," ASME JOURNAL OF HEAT TRANSFER, Vol. 107, pp. 922–929.

Wieting, A. R., 1975, "Empirical Correlations for Heat Transfer and Flow Friction Characteristics of Rectangular Offset-Fin Plate-Fin Heat Exchangers," ASME JOURNAL OF HEAT TRANSFER, Vol. 97, pp. 488–490.

Xi, G. N., Futagami, S., Hagiwara, Y., and Suzuki, K., 1991, "Flow and Heat Transfer Characteristics of Offset-Fin Array in the Middle Reynolds Number Range," *ASME/JSME Thermal Engineering Proceedings*, Vol. 3, pp. 151–156.

Xi, G. N., Suzuki, K., Hagiwara, Y., and Murata, T., 1990, "Experimental Study on Heat Transfer Characteristics of Offset Fin Arrays—Effect of Fin Thickness in the Low and Middle Ranges of Reynolds Number," *Heat Transfer 1990*, Vol. 4, pp. 81–86.

Zhang, L. W., Tafti, D. K., Najjar, F. M. and Balachandar, S., 1997a, "Computations of Flow and Heat Transfer in Parallel-Plate Fin Heat Exchangers on the CM-5: Effects of Flow Unsteadiness and Three-Dimensionality," *Int. J. Heat Mass Transfer*, Vol. 40, No. 6, pp. 1325–1341.

Zhang, L. W., Balachandar, S., Tafti, D. K., and Najjar, F. M., 1997b, "Heat Transfer Enhancement Mechanisms in Inline and Staggered Parallel-Plate Fin Heat Exchangers," *Int. J. Heat Mass Transfer*, Vol. 40, No. 10, pp. 2307–2325.

Zhang, L. W., Balachandar, S., and Tafti, D. K., 1997c, "Effect of Three-Dimensionality on Predicting Flow and Heat Transfer in Parallel-Plate Fin Heat Exchangers," *Num. Heat Transfer, Part A*, Vol. 31, pp. 327–353.

Heat and Moisture Transfer in Energy Wheels During Sorption, Condensation, and Frosting Conditions

C. J. Simonson

R. W. Besant[1]

Department of Mechanical Engineering,
University of Saskatchewan,
57 Campus Drive,
Saskatoon, SK S7N 5A9,
Canada

A numerical model for coupled heat and moisture transfer with sorption, condensation, and frosting in rotary energy exchangers is presented and validated with experimental data. The model is used to study condensation and frosting in energy wheels. Condensation/frosting increases with humidity and at some humidity level, water/frost will continually accumulate in the wheel. The sensitivity of condensation and frosting to wheel speed and desiccant type are studied. The energy wheel performance is also presented during both sorption and saturation conditions for a desiccant coating with a Type I sorption isotherm (e.g., molecular sieve) and a linear sorption isotherm (e.g., silica gel). Simulation results show that the desiccant with a linear sorption curve is favorable for energy recovery because it has better performance characteristics and smaller amounts of condensation/frosting for extreme operating conditions.

1 Introduction

Rotary heat exchangers that transfer sensible energy have been used for many years in gas turbine plants to recover thermal energy from the exhaust gases, thereby increasing the overall plant thermal efficiency (Harper and Rohsenow, 1953; Shah, 1981). Similarly, in HVAC application, energy recovery from the exhaust air of buildings to condition the supply ventilation air is possible and has frequently been accomplished with plate, heat-pipe, run-around, and rotary air-to-air heat exchangers. The current trend in North America is to use energy (or enthalpy) wheels, which transfer both sensible and latent energy to reduce the energy needed to condition ventilation air for buildings as compared to sensible heat exchangers (Stiesch et al., 1995; Rengarajan et al., 1996).

Rotary dehumidifiers can be compared with energy wheels because of their similar operation and function of transferring heat and moisture. Rotary dehumidifiers use an external heat source in conjunction with desiccant technology to remove moisture from the ventilation air in humid climates (Zheng and Worek, 1993). A collection of works by ASHRAE (1992), shows that the inclusion of desiccant dehumidifiers in HVAC systems for large and small office buildings and special applications such as supermarkets, ice rinks, and storage rooms is effective in reducing cooling loads. The benefits include reduced capital and operating costs together with improved building performance. Even more benefits are possible if properly designed and operated rotary energy exchangers are integrated into HVAC systems.

One problem that limits the practical application of energy wheels is condensation and frosting. Energy wheels are often selected and operated to avoid any condensation or frosting within the wheel. However, during hot and humid operating conditions, water may condense in the energy wheel, saturate the desiccant and finally run off. It is known that this type of uncontrolled condensation in energy wheels will damage the desiccant coating. This will result in poorer performance of the energy wheel and in extreme cases it can ruin the energy wheel. A similar problem exists during cold weather operation where frost may build up in the energy wheel, restrict the air flow and reduce the effectiveness of the wheel. The frosting problem has been the subject of numerical and experimental studies for both hygroscopic and nonhygroscopic regenerators (Holmberg, 1989, Leersum and Banks, 1977; Ruth et al., 1975). Heavy frosting in energy wheels will make a defrost cycle necessary and may even result in physical degradation of the desiccant by spalling. During defrost, the large amounts of water that run off the energy wheel may also remove the desiccant. Therefore, it is important to know under what operating conditions condensation and frosting occur in energy wheels and under what conditions condensation and frosting will alter the effectiveness and lead to uncontrolled accumulation. That is, small amounts of condensation and frosting may be a quasi-steady-state process but uncontrolled condensation and frosting needs to be avoided by some external control.

In this paper, a numerical model developed by Simonson and Besant (1997a, b) that models energy wheels during adsorption and desorption processes is expanded to include condensation and frosting. The numerical algorithm used to solve the governing equations during condensation and frosting is presented and a physically consistent method of numerically switching between sorption and saturation is given. The numerical model is used to show the transition from sorption to moderate condensation/frosting to uncontrolled condensation/frosting. The effectiveness of the energy exchanger is also presented during these transitions. The effect of wheel speed and desiccant type on condensation/frosting and energy wheel performance are also presented.

2 Numerical Model

The numerical model used in this paper has been presented by Simonson et al. (1997) and validated for a wide range of operating conditions by Simonson et al. (1998a). Figure 1(*a*) shows a rotary energy wheel operating in a counter flow arrangement and Figs. 1(*b*) and (*c*) show the details of the flow tubes in the wheel and the coordinate system used in the model. The numerical model solves the simultaneous heat and moisture

---

[1] To whom correspondence should be addressed.

Contributed by the Heat Transfer Division for publication in the JOURNAL OF HEAT TRANSFER. Manuscript received by the Heat Transfer Division, Sept. 3, 1997; revision received, Mar. 30, 1998. Keywords: Condensation, Heat Transfer, Heat Recovery, Moisture, Sorption. Associate Technical Editor: P. S. Ayyaswany.

transfer in one tube as it rotates around the axis of the wheel. A typical operating condition would be warm-moist supply air transferring energy and moisture to the matrix and energy and moisture being transferred from the matrix to the exhaust air during the second half of the cycle. In this analysis, the matrix of the wheel is made up of 0.044 mm thick aluminum, coated on both sides with 0.043 mm of molecular sieve desiccant. The height of the sine wave duct in Fig. 1(*b*) is 1.74 mm and the wavelength is 4.35 mm.

The governing equations for coupled heat and moisture transfer during adsorption and desorption processes in energy wheels are presented, discussed and simulated by Simonson and Besant (1997a, b):

$$\rho_g Cp_g A_g \frac{\partial T_g}{\partial t} + U\rho_g Cp_g A_g \frac{\partial T_g}{\partial x} - \dot{m}' h_{fg}\eta + hp(T_g - T_m) = 0, \tag{1}$$

$$\rho_m Cp_m A_m \frac{\partial T_m}{\partial t} - \dot{m}' h_{fg}(1 - \eta) - \dot{m}' Cp_w (T_g - T_m) - hp(T_g - T_m) = \frac{\partial}{\partial x}\left(k_{\mathrm{Al}} A_{\mathrm{Al}} \frac{\partial T_m}{\partial x}\right), \tag{2}$$

$$A_g \frac{\partial \rho_v}{\partial t} + \frac{\partial}{\partial x}(\rho_v U A_g) + \dot{m}' = 0, \tag{3}$$

$$\frac{\partial \rho_a}{\partial t} + \frac{\partial}{\partial x}(\rho_a U) = 0, \text{ and} \tag{4}$$

$$\dot{m}' = \rho_{d,\mathrm{dry}} A_d \frac{\partial u}{\partial t}, \tag{5}$$

where

$$\dot{m}' = h_m p(\rho_v - \rho_{v,m}), \tag{6}$$

and $\rho_{v,m}$ is calculated from the inverse of the sorption isotherm. During saturation conditions the density of the water vapor is calculated with

$$\rho_v = \rho_{v,\mathrm{sat}} = \frac{P_{v,\mathrm{sat}}}{R_v T_g}, \tag{7}$$

where $P_{v,\mathrm{sat}}$ is the saturation vapor pressure which is a function only of temperature.

The convective heat transfer coefficients are obtained from the literature (Shah and London, 1978) and the convective mass transfer coefficients are determined using the analogy between heat and mass transfer. Several thermodynamic and property relations are needed to complete the formulation and these can be found in Simonson and Besant (1997a) or Simonson et al. (1997). The effectiveness relations are given in Table 1 and differ slightly from those give in ASHRAE Standard 84-1991 because they are the average of the supply and exhaust side effectivenesses. These relations give the lowest uncertainty in the effectiveness value (Johnson et al., 1998). It is noted that the properties of water and the latent heat of phase change are assumed constant regardless if the temperature is above or below 0°C. Simulation results show that these assumptions affect the predicted effectiveness of the energy wheel by less than 0.5 percent. The energy of phase change during melting and freezing is neglected in this analysis because the heat of fusion is an order of magnitude lower than the heat of vaporization and the period or time for phase change to occur is small (1.5 s to 6 s at wheel speeds of 20 rpm to 5 rpm). This will be discussed further in Section 3.2.

The parameter η, in the energy equations, is the fraction of the energy of phase change that is convected directly into the

Nomenclature

A = cross-sectional area of each tube (m^2)
A_s = total heat transfer surface area on supply or exhaust side (m^2)
C = constant
Cp = specific heat (J/(kg·K))
Cr^* = dimensionless matrix capacity ($MCp_m\omega/(\dot{m}Cp_a)_{\min}$)
D_h = hydraulic diameter of one tube in the energy exchanger (mm)
H = total enthalpy per mass of dry air (J/kg_a or kJ/kg_a)
h = convective heat transfer coefficient (W/(m^2·K))
h_m = convective mass transfer coefficient (m/s)
h_{fg} = heat of vaporization (J/kg)
k = thermal conductivity (W/(m·K))
L = length of the energy wheel (m)
Le = Lewis number
M = total mass of the energy wheel (kg)
$\dot{m}$ = mass flow rate of dry air (kg_a/s)
$\dot{m}'$ = rate of phase change per unit length (kg/(s·m))
Nu = Nusselt number
NTU = number of transfer units $((1/(\dot{m}Cp_a)_{\min})[(1/(hA_s)_s) + (1/(hA_s)_e)]^{-1})$
P = pressure (Pa)
p = perimeter of each tube (m)
R = specific gas constant (J/(kg·K))
r = radial coordinate (m)
Re = Reynolds number
T = bulk temperature (K)
t = time (s)
U = mean air flow velocity in the tube (m/s)
u = mass fraction of water in the desiccant ($\mathrm{kg}_w/\mathrm{kg}_d$)
u_c = critical moisture content of the desiccant ($\mathrm{kg}_w/\mathrm{kg}_d$)
W = humidity ratio ($\mathrm{kg}_w/\mathrm{kg}_a$)
Wm = empirical coefficient used in the sorption isotherm describing the maximum moisture capacity of the desiccant ($\mathrm{kg}_w/\mathrm{kg}_d$)
x = axial coordinate (m)
ϵ_s = sensible heat transfer effectiveness
ϵ_l = latent heat transfer (or moisture) effectiveness
ϵ_t = total energy (enthalpy) effectiveness
ϕ = relative humidity
η = fraction of the phase change energy that enters the air directly
θ = rotational angle (deg)
ρ = density ($\mathrm{kg/m}^3$)
σ = volume fraction
ω = rotational speed (cycles/s)

Subscripts

Al = aluminum
a = air
d = desiccant
dry = dry properties
e = exhaust side
g = total gas phase (air and water vapor)
i = average inlet conditions
m = matrix (including aluminum, desiccant and moisture)
min = minimum
o = average outlet conditions
s = supply side
sat = saturation properties
v = water vapor
w = liquid water or frost

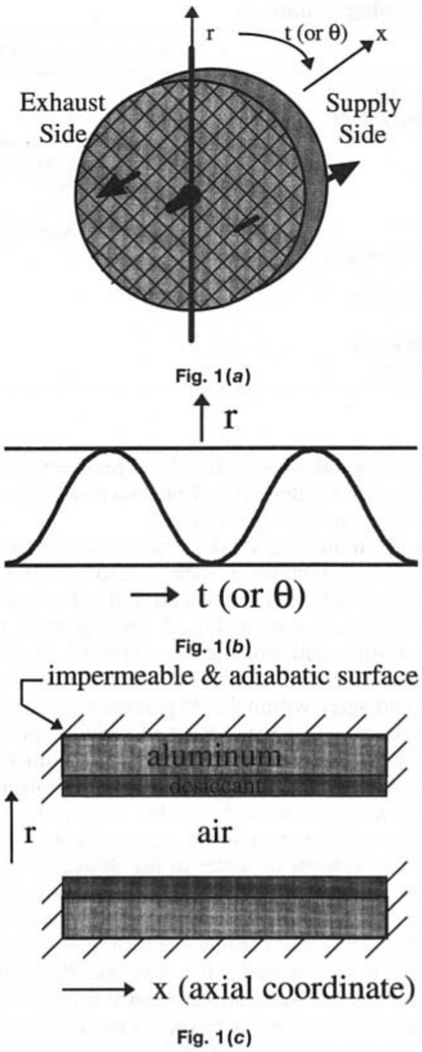

Fig. 1(*a*)

Fig. 1(*b*)

Fig. 1(*c*)

Fig. 1 Schematic of the energy wheel showing (*a*) the entire wheel, (*b*) the tube geometry cross section, and (*c*) a side view of one of the tubes

air. For the properties of the wheel used in this paper, η is expected to be about 0.05 (Simonson and Besant, 1997a), but for simplicity $\eta = 0$ is chosen. For extreme operating conditions of 40°C and 90 percent R.H., the sensible effectiveness would be decreased by 3.8 percent and 2.6 percent if $\eta = 0.05$ was chosen for simulation of the energy wheel coated with a desiccant having linear and Type I sorption isotherms, respectively.

The boundary conditions for the problem are the supply and exhaust inlet temperature, pressure and mass flow rate (see Tables 4 and 5). These allow the determination of the inlet boundary conditions for the dependent variables in the air stream (i.e., T_g, ρ_v, and U). The ends of the matrix are assumed to be impermeable and adiabatic which provides the boundary conditions for T_m and u. For the initial conditions, the wheel is assumed to be in equilibrium with the warm humid air at time 0. Initial conditions are not critical because the desired solution is typically the quasi-steady-state solution for an energy wheel rotating at constant speed with constant inlet conditions.

2.1 Numerical Algorithm.

The governing equations are discretized using an implicit finite volume method with a staggered grid (Patankar, 1980). Velocity is solved at the faces and all the remaining dependent variables and properties are solved at the nodes. The upwind differencing scheme is used for the air and the central differencing scheme is used for the matrix. The algebraic equations are solved using a Gauss-Seidel iteration technique with under relaxation and, to speed up convergence, the energy equation in the matrix (Eq. (2)) is solved using the Tridiagonal Matrix Algorithm (Patankar, 1980).

The algorithm used during sorption conditions is not the same as the algorithm used during saturation conditions as can be seen in Table 2. Each grid point can be saturated or unsaturated, independent of the rest of the grid points in the solution domain. This allows some regions of the wheel to be under saturation conditions while other regions are under sorption conditions. The algorithm uses a fixed grid; therefore, the saturation and sorption zones will change by finite steps equal to the grid size. A converged solution (see step 5 in Table 2) is obtained when the average absolute change in any dependent variable is less than 0.01 percent between iterations. Quasi-steady state (see step 7 in Table 2) is defined as the time when (a) the cyclic energy or moisture storage in the matrix of the energy wheel over one revolution wheel is less than 0.2 percent and (b) the rate of change of effectiveness is less than 0.01 percent.

2.2 Switching Between Saturation and Sorption.

The algorithm used in the numerical model is different for saturation conditions than for sorption conditions. For this reason, it is important that the numerical switching between algorithms be stable and, of course, physically correct. As a first attempt, the algorithm was changed implicitly and updated in the current time step. Although this method is more physically accurate, it tended to result in numerical oscillation for a fine grid mesh and small time steps. Therefore, to increase numerical stability, the algorithm is changed explicitly as indicated in step 6 of Table 2. The change from implicit to explicit switching changed the simulated effectiveness of the energy wheel by less than 0.5 percent.

A numerical switch from the sorption algorithm to the saturation algorithm is clear because the calculated relative humidity will exceed 100 percent when this switch is to be made. However, a numerical switch from the saturation algorithm to the sorption algorithm cannot be based on the air relative humidity falling below 100 percent because the saturation algorithm sets the air relative humidity to 100 percent. Therefore, the switch between algorithms is based on the phase-change rate (Simonson et al., 1997).

If moisture is being removed from the desiccant and the air flowing above the desiccant is saturated, the rate of evaporation phase change is such that the air relative humidity remains 100 percent. If the evaporation rate reduces, the air relative humidity will fall below 100 percent and sorption conditions will result. Similarly, as the condensation rate increases, the relative humidity of the air will fall below 100 percent. These cases mark the transition from saturation to sorption and therefore the numerical algorithm is changed from saturation to sorption when

$$\dot{m}'\,|_{\text{saturation algorithm}} < h_m p(\rho_v - \rho_{v,m}), \qquad (8)$$

where $\dot{m}'$ is positive for moisture accumulation (i.e., adsorption/condensation/ablimation) and $\dot{m}'$ is negative for moisture removal (i.e., desorption/evaporation/sublimation).

2.3 Numerical Validation.

In this section, the effectiveness predicted by the numerical model is compared with that measured experimentally on a commercial energy wheel. The

Table 1 Performance relations for energy wheels

$$W = \frac{\rho_v}{\rho_a} \qquad H = Cp_a(T - 273.15) + W(h_{fg} + Cp_v(T - 273.15)$$

$$\epsilon_s = \frac{\dot{m}_s(T_{s,i} - T_{s,o}) + \dot{m}_e(T_{e,o} - T_{e,i})}{2\dot{m}_{\min}(T_{s,i} + T_{e,i})}$$

$$\epsilon_t = \frac{\dot{m}_s(W_{s,i} - W_{s,o}) + \dot{m}_e(W_{e,o} - W_{e,i})}{2\dot{m}_{\min}(W_{s,i} - W_{e,i})}$$

$$\epsilon_t = \frac{\dot{m}_s(H_{s,i} - H_{s,o}) + \dot{m}_e(H_{e,o} - H_{e,i})}{2\dot{m}_{\min}(H_{s,i} - H_{e,i})}$$

Table 2 Algorithm used to solve the governing equations

Sorption ($\phi < 100\%$)	Common	Saturation ($\phi = 100\%$)
	1 Estimate the rate of phase change and the properties needed in the governing equations.	
2 Solve the T_m, $\boldsymbol{\rho}_v$, U, u, and T_g fields in order with Eqs. (2), (3), (4), (5), and (1), respectively.		2 Solve the T_m, $\dot{\mathbf{m}}'$, U, u, and T_g fields in order with Eqs. (2), (3), (4), (5) and (1) respectively.
	3 Update properties.	
4 Update the rate of phase change ($\dot{m}'$).		4 Update the water vapor density (ρ_v).
	5 Return to step 2 and iterate until a converged solution is reached.	
	6 Adjust, as necessary, the algorithm used in each grid for the next time-step.	
	7 Increment time, return to step 2 and iterate until a quasi-steady solution is obtained.	

properties of the molecular sieve coated energy wheel are given in Table 3 and were measured in our laboratory. Detailed validation of the numerical model requires a wide range of accurate experimental tests and has been done by Simonson et al. (1998a, b). However, comparison with a few experimental tests that include condensation and frosting conditions will show if the numerical model accurately models simultaneous heat and moisture transfer during sorption and saturation conditions.

In the laboratory experiments, the wheel was divided into quadrants and the air flowed through opposite quadrants. This reduced the crossover leakage between the two air streams and also reduced the required flow rate of air and consequently the size of the heating and cooling equipment and fans. Four fans were used in the tests to keep the pressure at the wheel near atmospheric pressure and thus minimize the leakage between the air streams and between the air streams and the surroundings. Leakage was measured by tracer gas tests to be usually less than two percent and always less than four percent of the flow rate for the complete range of flow rates.

The test setup and measurements were based on ASHRAE Standard 84-1991 with slight modifications. These changes did not increase the uncertainty in the calculated effectivenesses (Simonson et al., 1998b; Ciepliski et al., 1998). Air flow rate measurements were done with orifice plates designed according to ISO Standard 5167-1 (1991) and humidity measurements were made with capacitance and resistance relative humidity sensors that were calibrated against a calibrated chilled mirror dew point sensor and aqueous salt solutions. Flow rate and humidity measurements had bias uncertainties of ±2 to ±5 percent and ±2 percent R.H., respectively. Temperature measurements were performed with calibrated type T thermocouples which had a bias uncertainty of ±0.2°C. Experimental tests were run until steady state conditions were achieved and then more than 30 time-averaged data points were recorded to disk. During any test, the inlet temperatures, humidities, and flow rates varied by less than ±0.5°C, ±1 percent R.H., and ±0.5 percent, respectively.

The uncertainty of the measured effectiveness depends on the precision and bias errors of the sensors for flow, temperature, humidity, and barometric pressure and the difference between the supply and exhaust temperatures, humidity ratios, and enthalpies. The uncertainty in the measured effectiveness was determined with the method outlined in ASME Standard PTC 19.1-1985 using the 95 percent uncertainty limits with the added requirement that all the data must satisfy mass (dry air and water vapor) and energy balances within the experimental uncertainty limits as determined using the on-line data acquisition and analysis system (Simonson et al., 1998b).

To verify the numerical model, each of the three simulated effectivenesses are compared with measured effectivenesses and their associated 95 percent uncertainties for two rather extreme operating conditions in Fig. 2. During these test conditions, condensation and frosting are expected to occur in the energy wheel. The experimental and simulated results show the same trends and agree within the 95 percent uncertainty bounds.

In the hot tests, water was observed running off the energy wheel after about three hours of testing. The numerical model predicts run-off after about eight hours if the moisture content in the desiccant remains uniform due to capillary and drag forces and the maximum moisture content before run-off is 1 kg/kg. Axial movement of water in the desiccant is neglected in the model and excess moisture accumulation is predicted very near the supply inlet. Comparing the numerical and experimental results shows that capillary and drag forces may cause the condensed liquid moisture to move axially in the energy wheel. The excess moisture is likely distributed over about $\frac{1}{3}$ of the energy wheel before water begins to run off the wheel with increasing amounts towards the end of the supply cycle (i.e., near $\theta = 180$ deg). In the cold tests, the numerical model predicts uncontrolled frosting with frost blockage rates of 0 to 12 percent per hour depending on the flow rate. The method used to determine frost blockage rates is described in Section 3.3. The blockage rate of the wheel was not measured in the experiments but seemed to be small because the flow rate was constant during the four hours of cold testing. These results also helps to confirm the numerical model.

3 Numerical Results

In this section, simulation results are presented for both hot and cold outdoor conditions using the whole wheel. During the hot and humid outdoor conditions, water is expected to run off the wheel and during the cold outdoor conditions frost is expected to be accumulating in the wheel. The specific parameters of the energy wheel are given in Table 4 and the test conditions are given in Table 5. Uncontrolled condensation and frosting are unlikely for moderate outdoor temperatures of 30°C and −10°C (Simonson et al., 1997) and therefore this paper concentrates on more extreme outdoor temperatures of 40°C and −20°C. The mass flow rate of both supply and exhaust air is

Table 3 Geometry of the energy wheel

WHEEL	$M = 13.5$ kg	$L = 0.102$ m	diameter = 0.92 m
speed = 20 rpm	$D_h = 1.20$ mm	porosity = 82%	$Nu = 2.39$ (fully developed)
DESICCANT	$\rho = 350$ kg/m^3	$Cp = 615$ J/(kg·K)	mass fraction = 22%
$\sigma_d = 0.69$	$Wm = 0.13$	$C = 40$	$u = WmC\phi/(1 + C\phi)$

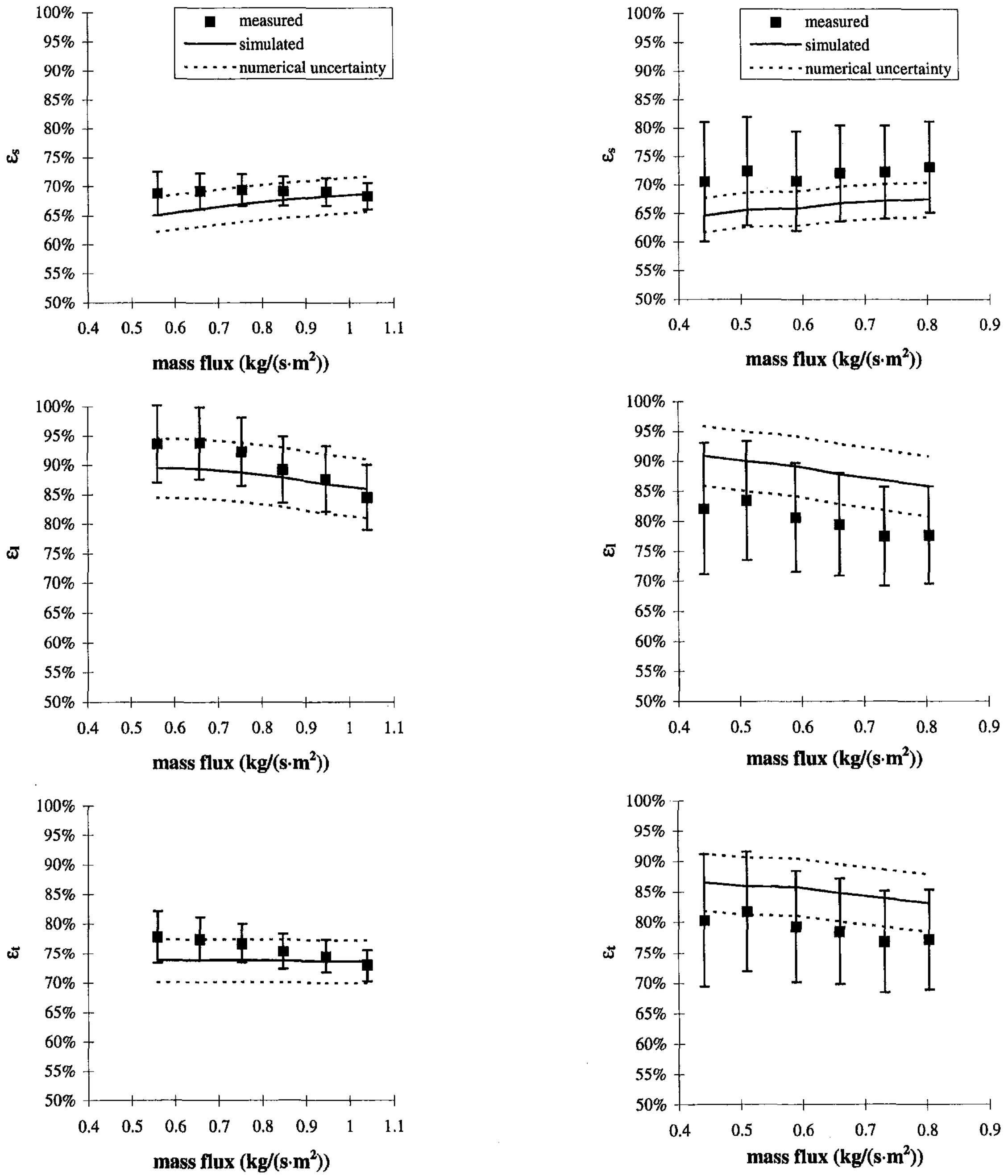

Fig. 2(a)

Fig. 2(b)

Fig. 2 Comparison of simulated and measured effectivenesses for inlet conditions of (*a*) 26°C and 40 percent R.H. and −20°C and 50 percent R.H. and (*b*) 40°C and 86 percent R.H. and 22°C and 15 percent R.H. with balanced flow rates. (Error bars indicate the 95 percent uncertainty in measured data.)

0.5 kg/s and standard atmospheric pressure (101 325 Pa) is used in all cases. Numerical results are presented for a desiccant with a Type I sorption isotherm (e.g., a molecular sieve desiccant) and a linear sorption isotherm (e.g., a silica gel desiccant). The accuracy of each calculated effectiveness is expected to be better than 0.5 percent because a grid size of 0.001 m and a time-step of 0.01 seconds are used in the simulations (Simonson and Besant, 1997a).

3.1 Onset of Saturation Conditions. It is important to know when the air in the energy wheel becomes saturated because at this time there is a risk of excessive moisture build up and degradation of the desiccant coating. The latent effectiveness can be used to determine when saturation conditions occur in the wheel (Simonson et al., 1997). Simonson et al. (1997) show that as the inlet relative humidity increases, ϵ_l decreases until saturation conditions occur. At this point, ϵ_l increases with increasing relative humidity. Two factors result in ϵ_l being higher during saturation conditions than during sorption conditions. First, the moisture storage capacity of the desiccant is not limited by the sorption curve during saturation conditions and, secondly, the rate of moisture transfer during saturation conditions is controlled by the mass flow rate of water vapor and the axial gradient of temperature (i.e., Eqs. (3) and (7)) not the radial diffusive moisture transport Eq. (6). Figure 3 shows the latent effectiveness as a function of relative humidity for desiccants with Type I and linear sorption isotherms at different wheel speeds.

The results in Fig. 3 show that saturation conditions exist at lower relative humidities for a Type I isotherm than for a linear

Table 4 Parameters used in the simulations

WHEEL	$M = 10.8$ kg	$L = 0.1$ m	diameter = 0.9 m
$\omega = 1$ to 20 rpm	$D_h = 1.5$ mm	$Re_{D_h} = 152$	porosity = 85%
Nu = 2.48*	Le = 1	$h = 43.5$ W/(m^2·K)*	$h_m = 0.036$ m/s*
NTU = 3.4	$Cr^* = 6.0$ @ 20 rpm	$U = 1.3$ to 1.7 m/s	$\dot{m} = 0.5$ kg/s
DESICCANT	$\rho_d = 350$ kg/m^3	$Cp_d = 615$ J/(kg·K)	mass fraction = 20%
$\sigma_d = 0.66$	$Wm = 0.2$	$C = 0.01$ or 1.0	$u = Wm/(1 - C + C/\phi)$

* fully developed.

isotherm. In the hot tests, saturation conditions begin for a Type I isotherm at supply inlet relative humidities of 60 percent to 65 percent, whereas saturation conditions exist only at extreme relative humidities of 95 percent to 100 percent for a linear isotherm. In the cold test, saturation conditions occur at $\phi_{e,i}$ = 25 percent to 30 percent for a Type I isotherm, but do not occur until $\phi_{e,i}$ = 35 percent to 40 percent for the linear sorption curve. These results show that saturation conditions are delayed when a desiccant with a linear sorption curve is used in place of a desiccant with a Type I sorption curve. This indicates that an energy wheel that is coated with silica gel will withstand more extreme operating conditions than a wheel that is coated with a molecular sieve desiccant.

Figure 3 illustrates the effect of the sorption curve on the latent energy transfer of the energy wheel. The latent effectiveness of a wheel coated with a linear sorption curve (e.g., silica gel) is significantly greater and less sensitive to the inlet relative humidity than one coated with a Type I sorption curve. It is possible that the effectiveness of the energy wheel coated with a Type I sorption curve could be increased to that with a linear sorption curve if the wheel speed was increased or the amount of desiccant coating was increased (Klein et al., 1990). However, for comparable wheel configurations and mass fraction of desiccant, the desiccant with a linear sorption curve is a preferable design selection for increased moisture transfer.

The latent effectiveness of the molecular sieve coated energy wheel decreases as the humidity increases during sorption conditions because the amount of moisture that must be stored in the matrix increases more rapidly with humidity than does the moisture storage capacity of the matrix for the Type I sorption curve. However, the latent effectiveness of the silica gel coated energy wheel remains constant with humidity during sorption conditions because the both the amount of moisture that must be stored in the matrix and the moisture storage capacity of the matrix increase linearly with inlet relative humidity for a linear sorption curve.

The effect of wheel speed is also evident in Fig. 3. Decreasing the wheel speed decreases the latent effectiveness, but only has a small effect on the onset of saturation conditions.

In Fig. 4 the inlet conditions where saturation conditions begin are presented on the psychrometric chart to emphasize

Table 5 Test conditions used in the simulations

	T (°C)	ϕ (%)	T (°C)	ϕ (%)
Supply	−20	50	40	40–100
Exhaust	24	10–50	24	50

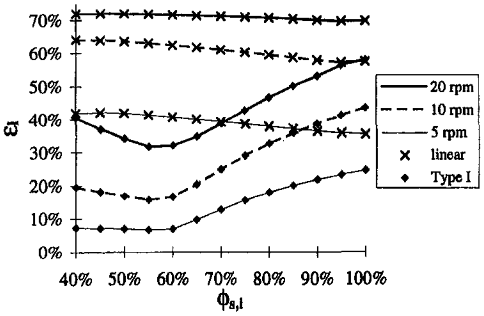

Fig. 3(*a*)

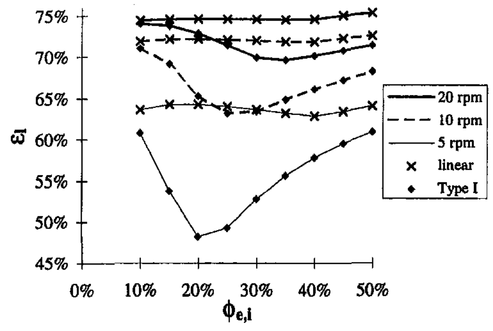

Fig. 3(*b*)

Fig. 3 Latent effectiveness as a function of the inlet relative humidity for (*a*) hot (40°C) and (*b*) cold (−20°C) test conditions

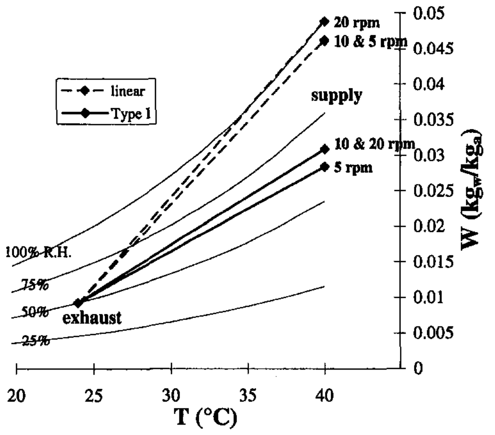

Fig. 4(*a*)

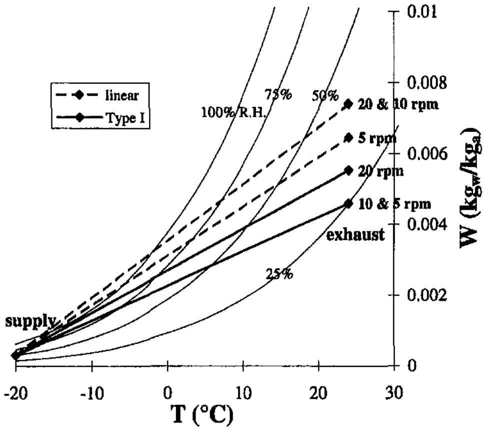

Fig. 4(*b*)

Fig. 4 Supply and exhaust inlet conditions for the (*a*) 40°C and (*b*) −20°C tests showing when saturation conditions begin

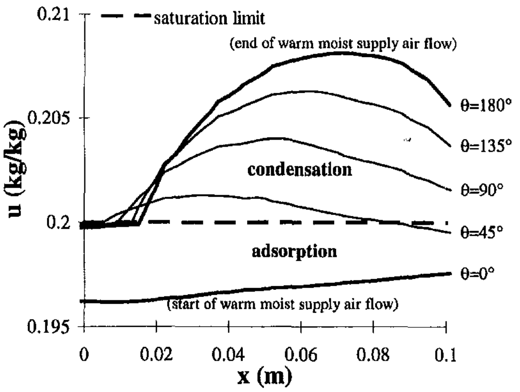

Fig. 5(*a*)

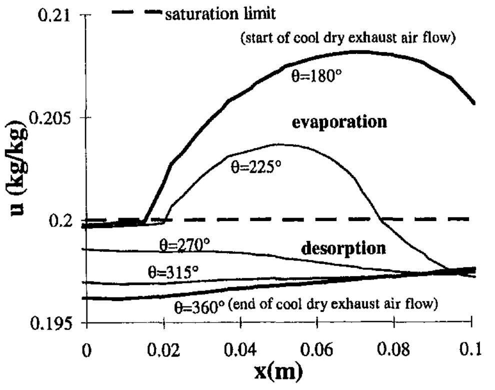

Fig. 5(*b*)

Fig. 5 Moisture content profiles in the Type I desiccant coating during (*a*) supply air flow (40°C and 80 percent R.H.) and (*b*) exhaust air flow (24°C and 50 percent R.H.) through the wheel

the fact that a desiccant with a linear sorption curve can be exposed to higher humidity conditions before saturation conditions begin. All inlet humidities above the lines in Fig. 4 will result in condensation and/or frosting in the wheel while those below will result in only sorption processes, indicating that the wheel will remain dry. Figure 4 shows that, in most cases, saturation conditions can be expected to begin when a straight line joining the inlet conditions touches the saturation line (Holmberg, 1989; Klein et al., 1990). The only exception to this rule is in the hot tests when the wheel is coated with a Type I isotherm. In this case, saturation conditions begin well before the straight line connecting the inlet conditions touches the saturation line.

3.2 Location of Condensation/Frosting. The location of condensation within the energy wheel coated with a Type I desiccant can be seen in Fig. 5 for supply air conditions of 40°C and 80 percent R.H. and several wheel rotational angles.

The results in Fig. 5 are for a wheel speed of 20 rpm and show that saturation and sorption conditions can coexist in the wheel. Phase change is due to adsorption at a rotational angle (θ) of 0 deg which is when the tube has just left the cool dry exhaust side and enters the warm moist supply side. At this point, the moisture content of the wheel is the lowest. As the wheel rotates, the moisture content of the desiccant increases and the relative humidity of the air increases. At a rotational angle of 45 deg, a large part of the wheel experiences condensation. The size of the condensation zone increases slightly as the wheel rotates but the moisture content of the desiccant increases significantly with angle up to 180 deg. At an angle of 180 deg, the condensation zone occupies 80 percent of the energy wheel. Figure 5(*b*) shows the removal of moisture by the cool and dry exhaust air as the wheel rotates from 180 deg to 360 deg. Here the transition from saturation to sorption conditions occurs later in the cycle than the transition from sorption to saturation occurred during the hot and humid supply air flow. It can be seen that condensation conditions are present for a longer time (over $\frac{3}{4}$ of the supply flow period) than evaporation conditions (less than $\frac{1}{2}$ of the exhaust flow period). The phase-change mechanism is clearly changing from adsorption to condensation then to evaporation and finally to desorption conditions during one cycle of the wheel, yet there is no uncontrolled condensation. The moisture that is accumulated on the supply side is removed on the exhaust side in a quasi-steady cyclic process.

Figure 6 shows the location of frosting for the cold test conditions when the indoor relative humidity is 35 percent, the desiccant has a Type I sorption isotherm and the wheel speed is 20 rpm. Here the moisture content profile does not change as much during one revolution as in the hot tests. The temperature profiles in the matrix are also included in Fig. 6 to show where condensation, frosting, melting, and freezing are expected to occur.

The zone of melting and freezing is sketched in Fig. 6 as a wavy line because the size of this zone is not exactly known. The size of this zone will depend on the amount of subcooling/superheating that is needed to freeze/melt the water in the matrix. If ±3°C are required, there will be no freezing and melting zone. In frost studies, it has been observed that small droplets of liquid water require up to 15 s of subcooling at temperatures of −10°C to −15°C before freezing occurs (Tao et al., 1993a). Also, Simonson et al. (1996) have reported significant subcooling of water during the cycling of moist fiberglass insulation between −20°C and +2°C. Therefore, the amount of water that freezes and melts during the 3 s period of the energy wheel is likely very small. At steady state, the wheel will have a zone of frozen water, a zone of liquid water and a very small zone that periodically changes phase between liquid and solid. For this reason, the latent heat of fusion (which is an order of magnitude smaller than the heat of vaporization) has been neglected in the energy equation for the matrix (Eq. (2)).

From Fig. 6 it can be seen that the majority of the moisture accumulation in the wheel is in the form of frost. The zone where significant frosting occurs makes up about 25 percent of the flow length of the energy wheel.

3.3 Uncontrolled Condensation/Frosting. Uncontrolled saturation exists when more moisture accumulates in the wheel from the warm-moist air than is removed by the cool-dry air. To study uncontrolled condensation and frosting, the net accumulation in the wheel at the end of the simulation is extrapolated for one hour to see how much moisture is accumulating in the wheel in the hot tests (Fig. 7(*a*)). The rate at which frost growth reduces the flow area for the cold tests can also be estimated from the model. The growth of frost is not included intrinsically in the model because the flow area of each tube is assumed to be constant. However, based on an average low-density frost (100 kg/m^3 - Tao et al., 1993b) and from moisture content profiles which show that the frost accumulates in about 25 percent of the tube (Fig. 6), the average blockage rate of the wheel can be predicted from the simulation results and is presented in Fig. 7(*b*). It should be noted that when there is a net accumulation of moisture in the wheel over time, the quasi-steady conditions stated in Section 2.1 cannot be met. In this case, the simulation was stopped when the typical quasi-steady time for similar test conditions was exceeded. When the quasi-steady conditions are satisfied, the net accumulation in the wheel can be assumed negligible.

The results in Fig. 7 show that reducing the wheel speed, significantly reduces uncontrolled condensation and frosting which is expected from the literature (Stiesch et al., 1995 and Holmberg, 1989). Lower wheel speeds are required to prevent

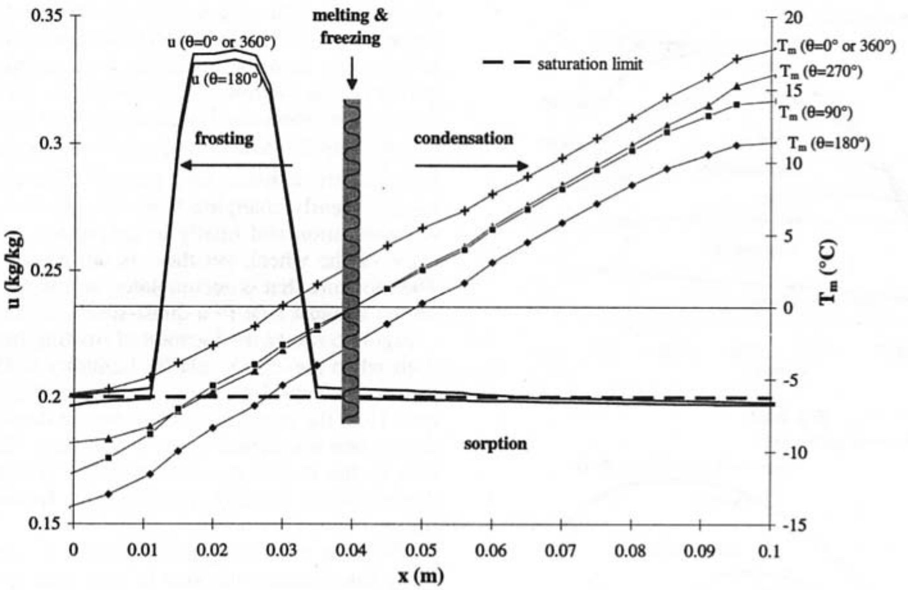

Fig. 6 Moisture content and matrix temperature profiles in the disiccant for supply conditions of −20°C and 35 percent R.H. and exhaust conditions of 24°C and 50 percent R.H.

uncontrolled frosting because the sensible effectiveness is higher in the cold tests than in the hot tests for the same wheel speed as shown in Fig. 8. The difference between a linear and Type I sorption isotherm is not as significant in the hot tests as in the cold tests. Figure 7(*b*) shows that an energy wheel, coated with a desiccant with a linear sorption curve (e.g., silica gel), has less frosting than the one coated with a Type I desiccant (e.g., molecular sieve).

In the hot test, the relative humidity of the supply air must be very high (greater than 95 percent) before water begins to accumulate in the wheel over time. Because desiccants have large moisture retention capacities (i.e., 1 kg/kg), it may take up to an hour of extreme operating conditions before water begins to run off the energy wheel. This implies that short-term exposure to high relative humidities, as during a rain storm, may not affect an energy wheel adversely. The large moisture accumulation shown in Fig. 7(*a*) for humidities greater than 95 percent would likely result in damage to the desiccant coating; however, these extreme operating conditions are almost never encountered in practice.

The cold tests, on the other hand, show that the moisture content can continuously increase for relatively moderate indoor

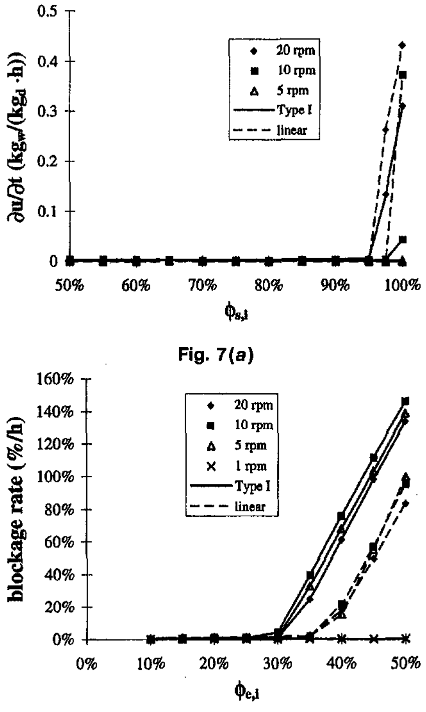

Fig. 7(*a*)

Fig. 7(*b*)

Fig. 7 Change in the average moisture content of the disiccant per hour during (*a*) the hot tests (40°C) and the estimated blockage rate of the wheel due to frost growth during (*b*) the cold tests (−20°C)

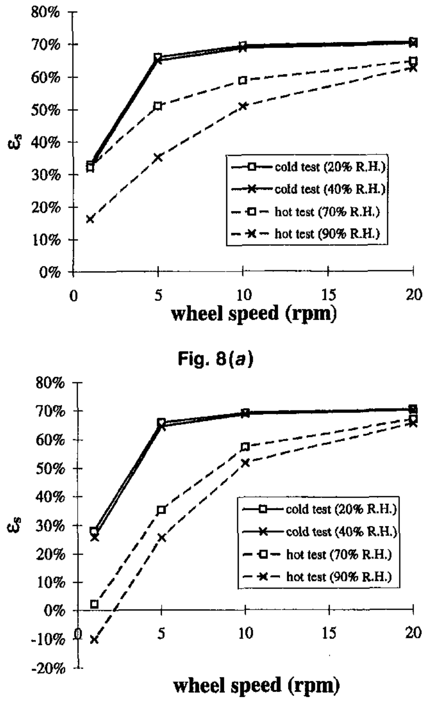

Fig. 8(*a*)

Fig. 8(*b*)

Fig. 8 Sensible effectiveness versus wheel speed for (*a*) Type I and (*b*) linear desiccants

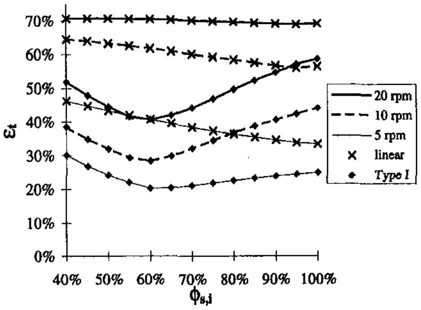

Fig. 9(*a*)

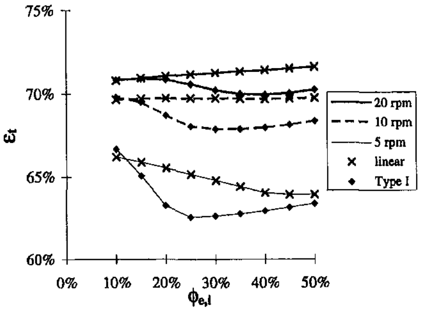

Fig. 9(*b*)

Fig. 9 Total effectiveness for supply temperatures of (*a*) 40°C and (*b*) −20°C

relative humidities. Blockage of the wheel occurs for wheel speeds of 5 to 20 rpm when the exhaust relative humidity is greater than 30 percent and 35 percent for the Type I and linear desiccant coatings, respectively. For a wheel speed of 1 rpm, no blockage is predicted even when the indoor relative humidity is 50 percent. When indoor conditions are 24°C and 40 percent R.H. and the wheel speed is 5 to 20 rpm, the blockage rate is 60 percent per hour when the coating is a Type I desiccant and 20 percent per hour when the coating is a linear desiccant. These results show that the energy wheel could be completely blocked with frost and require a defrost cycle after only a few hours of operation.

Figure 8 shows that the sensible effectiveness of the energy wheel decreases with increasing humidity and decreasing wheel speed. The calculated sensible effectivenesses for the cold tests conditions with a wheel speed of 1 rpm are comparable to those in the hot tests with a wheel speed of 5 rpm. This explains why the wheel speed needs to be reduced to 1 rpm or less in the cold tests to prevent uncontrolled frosting, while a wheel speed of 5 rpm prevents uncontrolled condensation in the hot tests. The sensible effectiveness decreases with increasing humidity because of the coupling between heat and moisture transfer.

3.4 Energy Wheel Performance. The physical phenomena of adsorption and desorption are different from condensation and evaporation (ablimation and sublimation below 0°C) which means that the performance of energy wheels may depend on the mode of phase change moisture transfer and the type of desiccant. To study this effect, Fig. 9 contains the predicted total effectiveness at different inlet humidities with different desiccants for the hot and cold tests.

The total effectiveness values in Fig. 9 are consistently higher for the linear isotherm than for the Type I isotherm. This shows that a desiccant with a linear sorption curve is preferable to a desiccant with an extreme Type I sorption curve. The total effectiveness of an energy wheel that is coated with a linear desiccant is less sensitive to the inlet relative humidity than the total effectiveness of an energy wheel that is coated with a Type I desiccant.

The effectiveness values presented in this paper (Figs. 2, 3, 8, and 9) show that effectiveness depends on the humidity and temperature of the energy wheel. This shows that the dimensionless groups that govern the heat and moisture transfer in energy wheels depend on the operating temperature and humidity as well as the wheel design (Simonson, 1998). There are no simple correlations in the literature that will predict energy wheel performance during condensation and frosting conditions. This could be an area of future studies.

4 Summary and Conclusions

In this paper, a one-dimensional and transient numerical model that predicts heat and sorption moisture transfer within desiccant coated rotary energy exchangers has been expanded to include condensation and frosting. The numerical algorithm that is used during sorption processes is necessarily different than the one used during saturation conditions. Numerical switching between these two algorithms must be physically correct and stable. The numerical algorithm is changed from sorption to saturation when the air relative humidity exceeds 100 percent and the algorithm is changed from saturation to sorption when the rate of phase change calculated from the saturation algorithm is less than that which would occur by molecular diffusion (Eq. (8)). Numerical stability is achieved by switching between algorithms in an explicit manner. Comparisons between experimental and numerical results show good agreement during condensation and frosting conditions.

The numerical results in this paper show that the onset of saturation conditions can be determined when a line connecting the inlet conditions on the psychrometric chart touches that saturation line. However, for an energy wheel that is coated with a desiccant that has a Type I sorption isotherm and exposed to hot and humid test conditions, saturation begins well before the straight line intersects the saturation line. Simulation results show that the adverse effects of uncontrolled condensation are expected to be minimal in hot climates, but frosting within energy wheels is expected to be very important in cold climates. Furthermore, because subcooling of water droplets may occur, experimental investigations of frosting within energy wheels should be done to complement these theoretical predictions of when uncontrolled frosting may occur.

Reducing the wheel speed reduces uncontrolled condensation and frosting. For the test conditions in this paper, uncontrolled condensation can be stopped by reducing the wheel speed to 5 rpm, while lower wheel speeds (1 rpm) were needed to prevent frosting.

A desiccant with a linear sorption curve (e.g., silica gel) appears to be more favorable for energy exchange applications than a desiccant with a Type I sorption curve (e.g., molecular sieve) because the linear sorption curve desiccant has better performance characteristics and smaller amounts of condensation/frosting. It is therefore expected that an energy wheel that is coated with a silica gel desiccant will operate better during more extreme operating conditions than an energy wheel that is coated with a molecular sieve desiccant.

Acknowledgments

Appreciation for financial assistance is expressed to the Natural Sciences and Engineering Research Council of Canada (NSERC), Petro-Canada and ASHRAE. Experimental measurements were performed by Dustin Ciepliski.

References

ASHRAE, 1992, *Desiccant cooling and dehumidification,* L. Harriman, ed., American Society of Heating, Refrigerating and Air Conditioning Engineers, Atlanta, GA.

ASHRAE, 1991, "Method of testing air-to-air heat exchangers," *American Society of Heating, Refrigerating and Air Conditioning Engineers Inc.*, Atlanta, GA, ASHRAE Standard 84-1991.

ASME, 1985, ''Measurement Uncertainty,'' *The American Society of Mechanical Engineers*, New York, ANSI/ASME Standard PTC 19.1-1985.

Ciepliski, D. L., Simonson, C. J., and Besant, R. W., 1998, ''Some recommendations for improvements to ASHRAE standard 84-1991,'' *ASHRAE Trans.*, Vol. 104, No. 1.

Harper, D. B., and Rohsenow, W. M., 1953, ''Effect of Rotary Regenerator Performance on Gas-Turbine Plant Performance,'' *Trans. ASME*, Vol. 75, pp. 759–765.

Holmberg, R. B., 1989, ''Prediction of condensation and frosting limits in rotary wheels for heat recovery in buildings,'' *ASHRAE Trans.*, Vol. 95, No. 1, pp. 64–69.

ISO, 1991, ''*Measurement of air flow by pressure differential devices—Part 1: orifice plates and venturi tubes inserted in circular conduits running full*,'' ISO Standard 5167-1, International Standards Organization, Geneva.

Johnson, A. B., Simonson, C. J., and Besant, R. W., 1998, ''Uncertainty analysis in the testing of air-to-air heat/energy exchangers installed in buildings,'' *ASHRAE Trans.*, Vol. 104, No. 1.

Klein, H., Klein, S. A., and Mitchell, J. W., 1990, ''Analysis of regenerative enthalpy exchangers,'' *Int. J. Heat Mass Transfer*, Vol. 33, pp. 735–744.

Leersum, J. G., and Banks, P. J., 1977, ''Equilibrium heat and mass transfer in regenerators in which condensation occurs,'' *Int. J. Heat Mass Transfer*, Vol. 20, pp. 927–934.

Patankar, S. V., 1980, *Numerical heat transfer and fluid flow*, Hemisphere, New York.

Rengarajan, K., Shirey, D. B., III, and Raustad, R. A., 1996, ''Cost-effective HVAC technologies to meet ASHRAE Standard 62-1989 in hot and humid climates,'' *ASHRAE Trans.*, Vol. 102, No. 1, pp. 166–182.

Ruth, D. W., Fisher, D. R., and Gawley, H. N., 1975, ''Investigation of frosting in rotary air-to-air heat exchangers,'' *ASHRAE Trans.*, Vol. 81, No. 2, pp. 410–417.

Shah, R. K., 1981, ''Thermal Design Theory for Regenerators,'' *Heat Exchangers: Thermal-Hydraulic Fundamentals and Design*, S. Kakaç, A. E. Bergles, and F. Mayinger, eds., Hemisphere, New York, pp. 721–763.

Shah, R. K., and London, A. L., 1978, *Advances in Heat Transfer: Laminar flow forced convection in ducts: A source book for compact heat exchanger analytical data*, T. F. Irvine, Jr. and J. P. Hartnett eds., Academic Press, New York.

Simsonson, C. J., 1998, ''Heat and Moisture Transfer in Energy Wheels,'' Ph.D. thesis, Mechanical Enbgineering, University of Saskatchewan, Saskatchewan, Canada.

Simonson, C. J., and Besant, R. W., 1997a, ''Heat and moisture transfer in desiccant coated rotary energy exchangers: Part I—Numerical model,'' *Int. J. HVAC&R Research*, Vol. 3, No. 4, pp. 325–350.

Simonson, C. J., and Besant, R. W., 1997b, ''Heat and moisture transfer in desiccant coated rotary energy exchangers: Part II—Validation and sensitivity studies,'' *Int. J. HVAC&R Research*, Vol. 3, No. 4, pp. 351–368.

Simonson, C. J., Besant, R. W., and Wilson, G. W., 1997, ''Condensation and frosting in energy wheels,'' *ASME Proceedings of the 32nd National Heat Transfer Conference*, Vol. 1, K. Vafai and J. L. S. Chen, eds., ASME, New York, pp. 161–169.

Simonson, C. J., Ciepliski, D. L., and Besant, R. W., 1998a, ''Determining the performance of energy wheels: Part II—Experimental data and numerical validation,'' *ASHRAE Trans.*, submitted for publication.

Simonson, C. J., Ciepliski, D. L., and Besant, R. W., 1998b, ''Determining the performance of energy wheels: Part I—Experimental and numerical methods,'' *ASHRAE Trans.*, submitted for publication.

Simonson, C. J., Tao, Y.-X., and Besant, R. W., 1996, ''Simultaneous Heat and Moisture Transfer in Fiber Glass Insulation with Transient Boundary Conditions,'' *ASHRAE Trans.*, Vol. 102, No. 1, pp. 315–327.

Stiesch, G., Klein, S. A., and Mitchell, J. W., 1995, ''Performance of rotary heat and mass exchangers,'' *Int. J. HVAC&R Research*, Vol. 1, No. 4, pp. 308–323.

Tao, Y.-X., Besant, R. W., and Mao, Y., 1993a, ''Characteristics of frost growth on a flat plate during the early growth period,'' *ASHRAE Trans.*, Vol. 99, No. 1, pp. 739–745.

Tao, Y.-X., Besant, R. W., and Rezkallah, K. S., 1993b, ''A mathematical model for predicting the densification of frost on a flat plate,'' *Int. J. Heat Mass Transfer*, Vol. 36, pp. 353–363.

Zheng, W., and Worek, W. M., 1993, ''Numerical simulation of combined heat and mass transfer processes in a rotary dehumidifier,'' *Numerical Heat Transfer*, Vol. 23A, pp. 211–232.

Heat Transfer-Friction Characteristic Comparison in Rectangular Ducts With Slit and Solid Ribs Mounted on One Wall

Jenn-Jiang Hwang
Associate Professor,
Department of Mechanical Engineering,
Chung-Hua University,
Hsinchu, Taiwan 30067, R. O. C.
e-mail: jjhwang@chu.edu.tw
Assoc. Mem. ASME

A comparison of fully developed heat transfer and friction characteristics has been made in rectangular ducts with one wall roughened by slit and solid ribs. The effects of rib void fraction and flow Reynolds number are examined. The rib height-to-duct hydraulic diameter and pitch-to-height ratios are fixed at $H/D_e = 0.167$ and $P_i/H = 10$, respectively. To understand the mechanisms of the heat transfer enhancement, smoke-wire flow visualization and measurements of mean velocity and turbulence intensity are conducted in the slit and solid-ribbed ducts. In addition, by separately measuring the floor and rib heat transfer, two contributive factors of heat transfer promotion, namely, the fin effect and the enhanced turbulence effect, have been isolated. Because of the greater turbulence-mixing effects the slit-ribbed geometry displays higher floor heat transfer than the solid-ribbed geometry. In addition, the fin effects for the slit rib are greater than that for the solid rib. The pressure drop across the slit ribs is lower than that across the solid ribs due to less duct blockage. Furthermore, slit ribs with larger void fractions in a lower flow Reynolds number range provide better thermal performance under a constant friction power constraint.

Introduction

The application of rib-type turbulators on the surfaces of high heat flux devices has attracted much attention for their significant enhancement in heat transfer (Webb, 1994). The use of solid ribs has been explored for applications such as gas-cooled nuclear reactors, electronic cooling devices, and heat exchangers. It is well known that the ribs can break up the viscous sublayer of the flow and more and promote local wall turbulence that, in turn, increases the heat transfer from the rib and the smooth surfaces. In addition, a thermally conductive rib attached to the heated wall provides a greater surface area for heat transfer over that of a ribless wall. Geometric parameters such as the duct aspect ratio, duct shape, duct blockage ratio (or rib height), rib angle-of-attack, rib shape, rib aspect ratio, and relative arrangement of the ribs (in-line, staggered, criss-cross, etc.) affect pronouncedly on both local and overall heat transfer coefficients by enhancing turbulence and/or adding heat transfer surface area. Some of these effects have been studied by several investigators such as Burggraf (1970), Webb et al. (1971), Han and his co-workers (Han et al., 1978, 1985; Han, 1988; Chandra and Han, 1989; Zhang et al., 1994), Metzger and Vedula (1987), Chyu and Wu (1989), Taslim and his co-workers (Taslim et al., 1991; Taslim and Wadsworth, 1994), Liou and Hwang (1992, 1993), and Archrya and his co-workers (Myrum et al., 1992; Archrya et al., 1993). The majority of these studies measure the overall heat transfer of the combination of ribs and the area between them. Some measure the heat transfer on the surfaces between the ribs (i.e., excluding rib heat transfer, which is referred to "floor heat transfer" in the following discussion). The heat transfer of the ribs themselves, however, has not been widely investigated. Note that the heat transfer measurements based on the mass transfer technique (e.g., naphthalene sublimation by Molki and Mostoufizadeh, 1989, and Chandra and Han, 1989) usually employ metallic ribs without a naphthalene coating mounted on the mass transfer surfaces. The ribs serve as turbulence promoters. The contribution of the additional rib surface area to the heat transfer enhancement is therefore not considered. In heat transfer experiments (e.g., Han, 1988; Hwang and Liou, 1994), the metallic ribs attached to the heat transfer surfaces are thermally active. Consequently, the heat transfer augmentation of the ribbed wall comes not only from the enhanced turbulence but also from the increased heat transfer area. The heat/mass transfer coefficients obtained using these two methods should be, to a certain extent, different. However, the technical literature contains little information about the distinction of the results obtained from the different boundary conditions of the ribbed wall.

The objective of this experimental study is to examine the heat transfer and friction characteristics in rectangular ducts with one wall roughened by slit or solid ribs. Slit ribs are of great interest since they cause substantially lower drag at the same rib height than do solid ribs and still provide greater heat transfer than a smooth-walled duct (Hwang and Liou, 1997). In addition, the different mechanism of heat transfer augmentation as compared to conventional solid ribs is of fundamental interest. Several issues are addressed by this study. First, experiments are conducted to examine the extent of heat transfer augmentation due to the enhanced turbulence and due to the extension in surface area for heat transfer on the ribbed walls, respectively. To achieve this, a test matrix is designed to measure the floor and rib heat transfer separately and simultaneously. In this way, the two factors that contribute to the promotion of the heat transfer become distinguishable. In the floor portion, the heat transfer augmentation should be attributed solely to turbulence-transport mechanisms, while the enhancement of heat transfer from the ribs themselves reflects the effects of the extension of the surface area (i.e., fin effect). Second, the effects of the rib void fraction and flow Reynolds number on the rib, floor, and overall heat transfer coefficients are also

---

Contributed by the Heat Transfer Division for publication in the JOURNAL OF HEAT TRANSFER. Manuscript received by the Heat Transfer Division, Apr. 22, 1997; revision received, May 4, 1998. Keywords: Augmentation and Enhancement, Finned Surfaces, Forced Convection, Heat Exchangers, Turbulence. Associate Technical Editor: J.-C. Han.

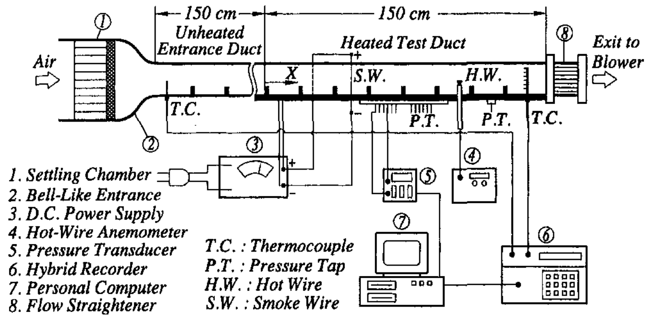

Fig. 1 Schematic drawing of flow system and instrumentation

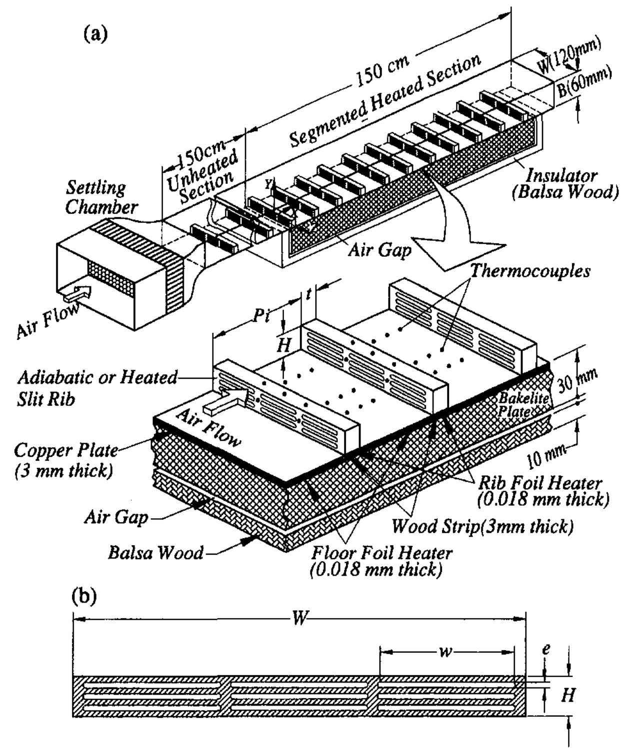

Fig. 2 Sketch of configurations of test section and slit rib

examined. Third, the local drag coefficient and the friction factor across the fully developed slit and solid-rib-duct flows are measured, and compared thereafter. Finally, using the overall heat transfer and friction data, pumping power performance comparison is made between solid and slit-ribbed ducts.

To confirm the heat transfer enhancement mechanisms mentioned above, the streamwise mean and fluctuating-velocity distributions in both solid and slit-ribbed ducts are measured and the structures of the flow over the slit and solid-ribbed walls are further visualized.

Description of Experiment

Experimental Apparatus. A horizontal low-speed wind tunnel operated in a suction mode is used, as shown schematically in Fig. 1. Air is drawn into the settling chamber from a temperature controlled laboratory room. This air flows into the bell-shaped duct entrance, through the unheated roughened duct, heated test section, flow straightener, flow meter, and is then exhausted by a 3 hp blower. The test duct is 1500 mm long with an aspect ratio of 2:1 (60 mm by 120 mm for YZ plane). The hydraulic (equivalent) diameter (D_e) of the test duct is 80 mm. As given in Fig. 2, the lower horizontal wall of the test section is heated and the remaining three duct walls (commercial plexiglas plates) are thermally insulated. Upstream of the test duct is an unheated roughened entrance section made of plexiglas with the same cross section and length as the test channel. This unheated duct provides a hydrodynamically fully

Nomenclature

A_{rib} = total heat transfer surface area of rib, i.e., the rib wetted area
A_{floor} = area of the duct wall between two ribs, i.e., $W \times (P_i - t)$
AR = duct aspect ratio, W/B
B = duct height
C_D = drag coefficient, Eq. (4)
C_f = Fanny friction factor, Eq. (5)
c_p = specific heat at constant pressure
D_e = duct hydraulic diameter without elements, $2B/(1 + B/W)$
e = slit height, Fig. 2
Gr = Grashof number
H = rib height
h = heat transfer coefficient based on total (wetted) heat transfer area
k_f = air thermal conductivity based on film temperature (T_f)
ΔL = duct length for fully developed pressure drop
m = mass flow rate
n = number of slits in a fence
N = index of rib number from the heated test section entrance
$\overline{\text{Nu}}$ = average rib or floor Nusselt number, $h \cdot D_e/k_f$
$\overline{\text{Nu}}_s$ = fully developed Nusselt number for the smooth duct
$\overline{\text{Nu}}_t$ = overall Nusselt number for the ribbed wall
P = pressure
P_i = rib pitch
Pr = Prandtl number
ΔP = fully developed pressure drop across the duct length ΔL
q_{rib} = net convective heat from rib surfaces to coolant (dissipated by rib heater)
q_{floor} = net convective heat from duct wall between ribs to coolant (dissipated by floor heater)
q_p = electrical power dissipated by the foil heater
q_l = total heat losses from the test section
Re = Reynolds number, $U_b \cdot D_e/\nu$
$\overline{T}_b$ = average air bulk mean temperature over a rib pitch
T_f = film temperature, $(\overline{T}_w + \overline{T}_b)/2$
T_{in} = air temperature at the inlet of the heated test section
$\overline{T}_w$ = average wall temperature of the rib or the floor
t = rib width
U = local (streamwise) mean velocity of air
U_b = bulk mean velocity of air in the smooth duct
u = local (streamwise) fluctuating velocity
W = duct width or rib length, Fig. 2
w = slit width
X = axial coordinate ($X = 0$ at heated test section inlet reference, Fig. 2)
X_N = axial coordinate ($X_N = 0$ at rib front edge)
Y = transverse coordinate, Fig. 2
Z = spanwise coordinate, Fig. 2

Greek Symbols

β = void fraction of the slit rib
ρ = air density
ν = kinematic viscosity of the air

Subscripts

b = bulk mean
l = loss
s = smooth
t = total
w = wall

developed (i.e., streamwise periodic) condition at the entrance of the heated test channel. The heat transfer surface, as shown schematically in Fig. 2(*a*), is constructed using 11 copper segments (120 mm by 125 mm by 3 mm) and 11 copper ribs (120 mm by 8 mm by 13.3 mm). They are fabricated onto a bakelite board (30 mm thick). Stainless-steel foil heaters, 0.018 mm thick are placed beneath each copper plate and rib. Each heater is connected directly to a d-c power supply to provide controllable wall heat flux. The surfaces of the copper plates and ribs are highly polished to minimize emissivity, hence radiative losses. In addition, to minimize the conductive heat losses, the backside surface of the Bakelite board is insulated using a 10-mm thick section of balsa wood with a 2-mm thick clearance (air gap) between them. The copper rib associated with the attached heater is mounted onto the wood strip (Fig. 2). The copper segments are spaced to ensure that no axial conduction occurs between them. Note that the ribs and the floors are heated individually by their own heaters. As shown in Fig. 2(*b*), a total of nine slits is perforated through each copper rib to facilitate the required void fraction (or open-area ratio). The rib void fraction is defined as $\beta = (n \cdot w \cdot e)/(W \cdot H)$, where n is the number slits distributed on the rib, w, the width of each slit, e, the height of each slit, W, the rib length, and H, the rib height. Detailed rib configurations and associated geometric parameters are listed in Table 1.

Forty-eight copper-constantan thermocouples are situated between $X/D_e = 10-15$ (across three rib pitches) for wall surface temperature measurements. As shown sketchily in Fig. 2, the floor and rib surfaces are instrumented with nine and seven thermocouples, respectively. The junction-beads (about 0.15 mm) of the thermocouples are carefully embedded into the walls and then ground flat to ensure that they are flush with the surfaces. In addition, a thermocouple probe and a thermocouple rake are placed at the test duct inlet and exit, respectively, for airflow temperature measurements. The temperature signals are transferred to a hybrid recorder (YOKOGAWA, DA 100), and subsequently sent to a Pentium computer via a multi-I/O interface. Preprocessing of the raw data is done with a built-in BASIC program where the nondimensional parameters are calculated. For the fluid-flow and static-pressure measurements, the bottom heated plate is replaced by a plexiglas plate. These experiments are carried out under unheated conditions. A hot-wire anemometer (DISA-56) with a normal single probe (I-type, 5 μm in diameter, 1 mm in length) is employed to measure the distributions of velocity and turbulence intensity. The probe is mounted on a motor-driven linear translation stage (Klinger UT-100, 10 μm in resolution), and inserted from the bottom plate to traverse across the section to any desired location in the flow. A total of 12 pressure taps are installed in the region $10 \leqq X/D_e \leqq 13$ along the spanwise centerline of the bottom plexiglas plate for local static wall pressure measurements. To reduce the possibility of spatial error, an additional pressure tap is positioned at $X/D_e = 17$ for fully developed friction factor measurements. Each tap is connected to a microdifferential transducer with accuracy up to 0.03 mm of water to amplify the pressure signals, which are subsequently transferred to a digital readout.

The parameters investigated include the Reynolds number (based on the duct hydraulic diameter and the ribless duct through-flow mean velocity), $8000 \leqq \mathrm{Re} \leqq 58{,}000$, and the rib void fractions, $\beta = 19$, 32, and 48 percent. The lowest void fraction selected here is to assure that the rib is permeable (Hwang and Liou, 1997), while the highest void fraction is limited by the machinability of the rib slit. The rib height-to-duct hydraulic diameter ratio and the rib spacing-to-height ratio are fixed at $H/D_e = 0.167$, and $P_i/H = 10$, respectively. In all the experiments performed, the maximum buoyancy parameter, $\mathrm{Gr}/\mathrm{Re}^2$ is below 0.02, suggesting that the flow and heat transfer are forced convection dominated.

Experimental Procedure and Data Reduction.

Heating Procedure. Since the ribs and floors are heated by their own heaters individually, three categories of average heat transfer coefficients could be determined during the measurement period, i.e., floor, rib, and overall heat transfer coefficients. Initially, each floor is heated with a fixed wall heat flux while the ribs keep adiabatic (i.e., without heating). The average floor heat transfer coefficient under adiabatic rib conditions is therefore obtained from and the measured average floor temperature and the known wall heat flux. Then, the ribs are heating while the floor wall heat flux remains essentially unaltered. Note that the heat flux supplied by the rib heater is adjusted until the rib and the nearby floor have the same average wall temperature. In general, the rib heat flux is always larger than the floor heat flux for satisfying the constant wall temperature boundary conditions. Such a heating process is required for the following reasons. First, local thermal equilibrium warrants that there be no axial conduction along the flow direction and subsequently ensures that the heat supplied by the floor heater and the rib heater (subtracting heat loss) is exactly convected from their own exposed surfaces. Second, during the heating procedure, the rib thermal boundary conditions are controlled either isothermally or adiabatically. The floor heat transfer coefficients under these two rib thermal boundaries are measured and compared.

Heat Transfer Coefficients. The fully developed average heat transfer coefficient for the floor portion, either with thermally active ribs or with adiabatic ribs, is determined by the ratio of floor heat flux to the difference between the floor and air bulk mean temperature, i.e.,

$$\begin{aligned} h &= q_{\text{floor}}/[A_{\text{floor}} \cdot (\bar{T}_w - \bar{T}_b)] \\ &= (q_p - q_l)/[A_{\text{floor}} \cdot (\bar{T}_w - \bar{T}_b)] \qquad (1) \end{aligned}$$

where q_{floor} represents the net heat transfer rate from the floor to coolant, and is calculated by subtracting the total heat loss from the electrical power dissipated by the floor heater ($q_p - q_l$). The electrical power generated from the floor foil heater is determined from the measured heater resistance and the current through the foil heater on each surface. Measuring the voltage drop across each foil heater can also check it. The total heat loss includes the conductive heat loss from the backside of the heated plate and the vertical adiabatic plates to the environment, and the radiative heat loss from the ribbed surface to its surroundings. By using one-dimensional conduction analysis, the first two are less than nine and six percent, respectively, of the total electrical power input for the range of Reynolds numbers tested. The last is less than 0.8 percent of the total electrical power input evaluated by a diffuse gray-surface network (Siegel and Howell, 1981). $\bar{T}_w$ is an average of the nine thermocouple readings on a single heated segment. In a typical run, the maximum variation for these nine wall temperatures is within 4°C. The local bulk mean air temperature, $\bar{T}_b$ is determined by measuring the bulk mean air temperatures at the duct inlet and outlet and assuming a linear rise along the test duct. The surface area used in Eq. (1) is the wall area between the ribs (i.e., rib base exclusive).

The average rib heat transfer coefficient can be obtained with the following equation:

$$h_{\text{rib}} = (q_{\text{rib}}/A_{\text{rib}})/(\bar{T}_w - \bar{T}_b). \qquad (2)$$

q_{rib} is the net heat transfer from the rib surface to the coolant and is calculated by subtracting the total heat loss from the dissipation of the electrical power from the rib foil heater. A_{rib} is the total rib heat transfer surface area (i.e., wetted area of the rib), and is listed in Table 1 in detail for the slit and solid ribs investigated.

Table 1 Configuration of the rib investigated

Rib type	Slit number (n)	Slit dimension ($w \times e$)	Void fraction (β)	Rib wetted area (A_{rib})
Slit rib #1	9	30 × 1.1 mm^2	19%	8.04×10^{-3} m^2
Slit rib #2	9	30 × 1.9 mm^2	32%	7.72×10^{-3} m^2
Slit rib #3	9	30 × 2.8 mm^2	48%	7.36×10^{-3} m^2
Solid	0	—	0	4.15×10^{-3} m^2

The overall heat transfer coefficient on the ribbed wall for the fully developed flow is deduced from the total heat transfer rate, the total heat transfer surface area and the average wall-to-fluid bulk temperature difference, i.e.,

$$h_{\text{overall}} = (q_{\text{rib}} + q_{\text{floor}})/[(A_{\text{rib}} + A_{\text{floor}})(\bar{T}_w - \bar{T}_b)]. \quad (3)$$

Local Drag Coefficient and Friction Factor. The local drag coefficient along the rib wall is defined as the ratio of the static-wall pressure drop to fluid dynamic pressure as

$$C_D = (P_x - P_o)/(\rho \cdot U_b^2/2) \quad (4)$$

where P_o is the reference pressure and is represented by the value at the first pressure tap and P_x, the static wall pressure at the axial position X. In a fully developed duct flow, the Fanning friction factor can be determined by measuring the pressure gradient across the duct and the mean velocity of the air. This is expressed as

$$C_f = [(-\Delta P/\Delta L)\cdot \text{De}]/(2\rho \cdot U_b^2). \quad (5)$$

Both the local drag coefficient and the friction factor are based on adiabatic conditions (i.e., test without heating).

Uncertainties. By using the uncertainty estimation method of Kline and McClintock (1953), the maximum uncertainties of the floor, rib, and overall heat transfer coefficients are less than 8.4, 8.6, and 8.6 percent, respectively, for Reynolds numbers larger than 8000. The maximum uncertainties for C_D and C_f are estimated to be less than 6.9 percent and 7.3 percent, respectively, for the Reynolds number larger than 8000. In addition, the individual contributions to the experimental uncertainties for the measured physical properties are as follows: m, ±2.7 percent; q_{rib} and q_{floor}, ±5.4 percent; $\bar{T}_w - \bar{T}_b$, ±6.4 percent; ΔP (or $P_x - P_o$), ±5.6 percent; U, ±2.4 percent; and $\sqrt{\overline{u^2}}$, ±8.2 percent.

Experimental Results and Discussion

Experimental Results of Smooth-Walled Ducts. Prior to the slit and solid-ribbed duct experiments, fully developed friction factors and heat transfer coefficients are measured for a smooth duct and compared with the results given in the literature, as shown in Fig. 3. The correlations selected for comparison includes the modified Dittus-Boelter equation for gas flow (McAdames, 1954) for heat transfer, and the Blasius equation (Kays and Crawfords, 1980) and the equation by Rehsenow and Choi (1969) for friction. All of these equations provide good representations of the data for a fully developed gas flow in smooth ducts. It can be seen from this figure that the present fully developed Nusselt numbers and friction factors compare well with the previous correlations. A satisfactory agreement in the above comparison has confirmed that the experimental procedure employed is adequate and the results obtained are reliable.

Fluid Flow Characteristics. Figure 4 shows a comparison of the flow patterns around the solid and slit (β = 32 percent) ribs, which are measured by the smoke-wire technique. The smoke wire is placed vertically along the duct center on the axial station of X_N/H = 1.8, and the flow is from left to right. As shown in Fig. 4(a), physically, the flow over the solid rib could be characterized as a turbulence shear flow, which is introduced from the upstream rib salient driving a recirculation cell attached to the rib downstream. Hence, the fluid flows upstream behind the solid rib. This reversed-flow phenomenon, however, is not observed in the slit-ribbed geometry in Fig. 4(b), indicating that the recirculating cell disappears when the solid rib is replaced with the slit rib. In addition, the flow structures behind the slit rib are rather different from those in the core portion. Behind the slit rib, the small and strong eddies of turbulence are observed. This results from the multi-mixing-layer interaction as the fluid passes through the slit rib.

Figures 5 and 6 show streamwise mean-velocity and turbulence-intensity profiles in the Y direction at the axial station of

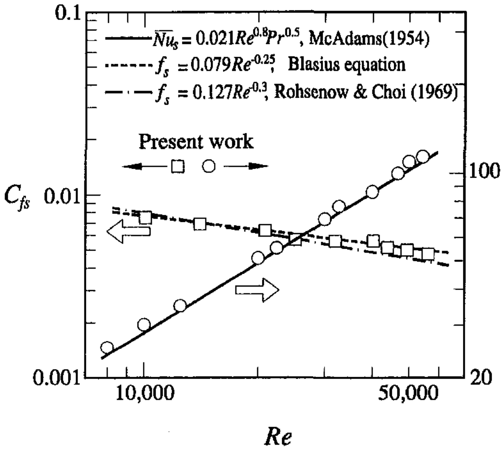

Fig. 3 Comparison of the smooth-wall friction factors and Nusselt numbers with previous correlations

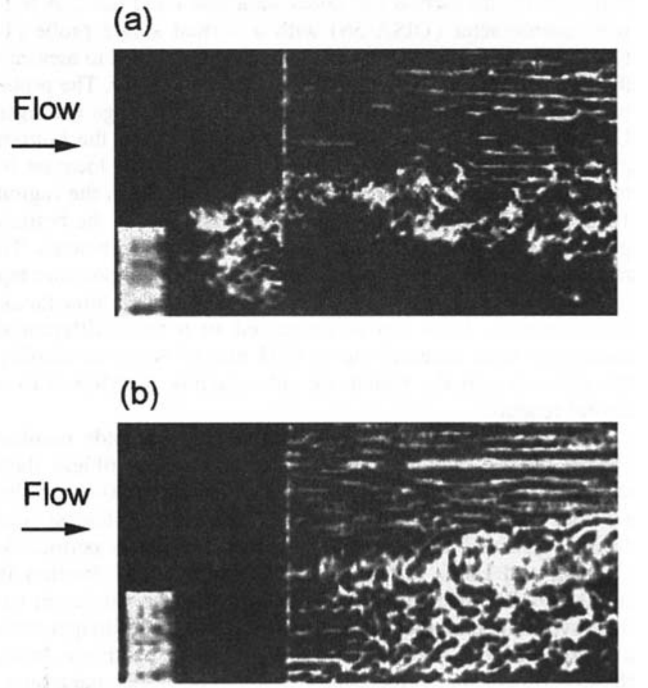

Fig. 4 Flow structure comparison between the slit and solid-ribbed-duct flows at Re = 8000; (a) solid-ribbed geometry, (b) slit-ribbed geometry

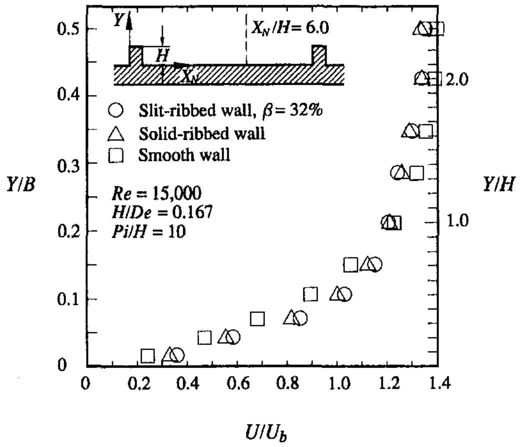

Fig. 5 Comparison of streamwise mean-velocity profiles for smooth, solid-fenced, and slit-ribbed channels at the axial station X_N/H = 6.0

$X_N/H = 6.0$ for the slit and solid-ribbed walls with Re = 15,000, and $P_i/H = 10$. Smooth-walled experiments are also conducted for comparison. Due to the turbulence mixing caused by the ribs, the velocity gradients near the walls for the slit-rib and solid-rib geometries are larger than that for the smooth wall. The velocity profiles are relatively flat for the solid-ribbed and slit-ribbed walls as compared to that for the smooth wall. The slit-ribbed wall has a flatter velocity profile than the solid-ribbed wall. A flatter velocity profile could enhance the convective heat transfer rate by enhancing the transfer of momentum and energy. As shown in Fig. 6, the turbulence intensity for the slit-ribbed wall is higher than the solid-ribbed and smooth walls, especially in $0 < Y/H < 1.0$.

The turbulence-intensity distributions along the streamwise direction of the channel centerline ($Z = 0$) are measured for three elevations, i.e., $Y/H = 0.5$, 1.0 and 2.0, which are shown in Fig. 7. The distribution of the turbulence intensity at the elevations of $Y/H = 1.0$ and 2.0 are found to be roughly similar for these two ribbed walls. But they are very different near the wall, i.e., $Y/H = 0.5$. At this elevation, the turbulence-intensity distribution along the slit-ribbed wall begins with a local maximum due to the turbulent mixing caused by a multijet flow emitting from the rear of the rib and then decreasing downstream. Along the solid-ribbed wall, the turbulence intensity distribution reveals a well-known trend (Chang, 1990), i.e., it begins with a local minimum because of the presence of the recirculation flow with a relatively stagnant fluid, increases to a local maximum near the midplane between the ribs due to the flow reattachment, and then decreases slightly before encountering the next rib. Globally, the turbulence intensity for the slit-ribbed wall is higher than that for the solid-ribbed wall, especially in the near-wall region.

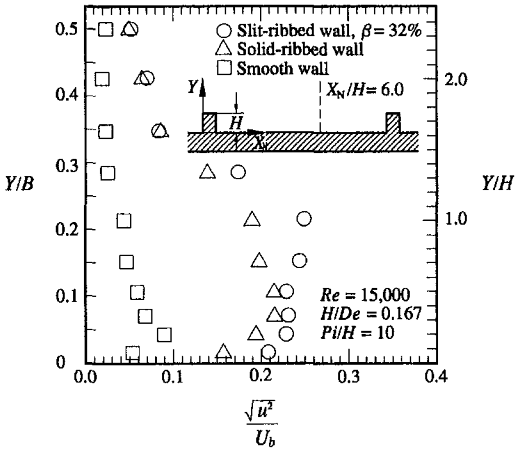

Fig. 6 Turbulence-intensity distributions at the axial station X_N/H = 6.0 along the direction normal to the ribbed wall

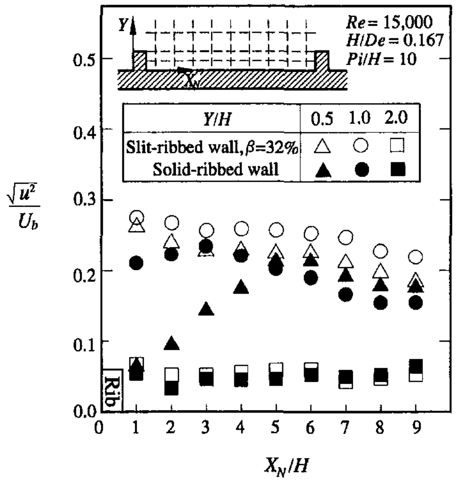

Fig. 7 Turbulence intensity distributions along streamwise direction for the solid and slit-ribbed walls

Average Heat Transfer Coefficient.

Floor Data. Figure 8 shows the average heat transfer for the area between two ribs (i.e., floor data) for the slit-ribbed and solid-ribbed walls. The smooth-duct results (centerline) are included for comparison. First, attention is focused on the effect of the thermal boundary condition for the rib on the floor heat transfer coefficient. Note that the solid symbols represent the results from the heated segments attached with adiabatic ribs, while the open reversed-triangular symbols are results from conditions that ribs and floors are heated simultaneously and isothermally. Obviously, the rib thermal boundary condition alters negligibly the floor heat transfer coefficient, typically within three percent. The floor heat transfer coefficient for the

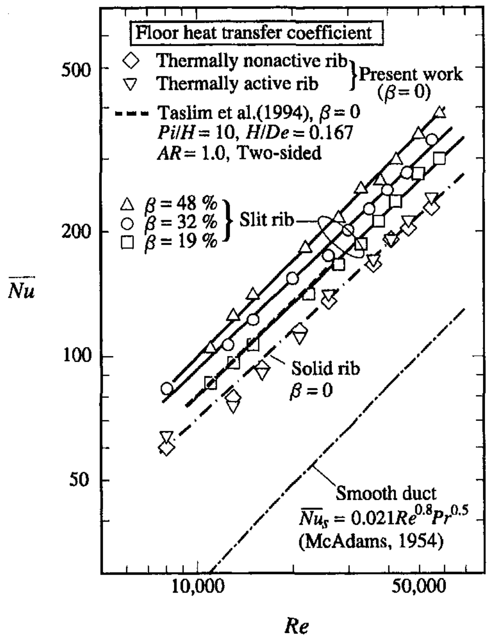

Fig. 8 Average floor heat transfer coefficients for the slit and solid ribbed walls

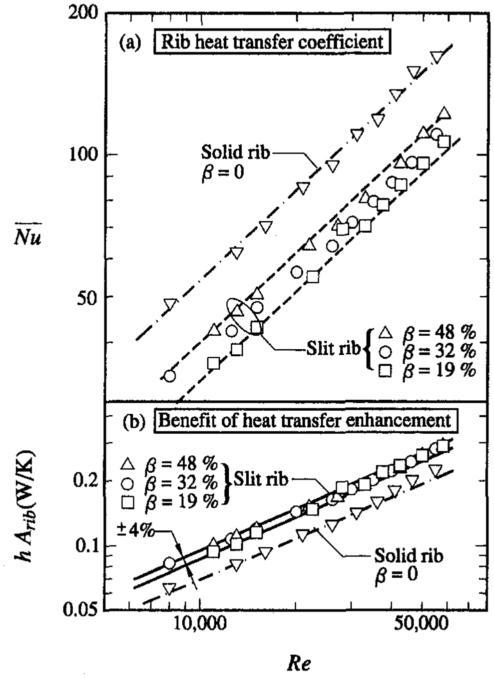

Fig. 9 (*a*) Average rib heat transfer coefficients for the slit and solid ribbed walls, (*b*) benefit of heat transfer enhancement for the slit and solid ribs

slit-ribbed wall is higher than the solid-ribbed and smooth walls. This implies that heat transfer enhancement through turbulence for the slit-ribbed wall is greater than that for the solid-ribbed wall, which is consistent with the measurements of turbulence-intensity distribution given in Figs. 5 and 6. Closer inspection of this figure further shows that the floor heat transfer increases with an increase of rib void fraction. This means that the more fluid that passes through a slit rib, the stronger the turbulence mixing between ribs. Previous floor results in Taslim et al. (1994) for a square duct of two opposite solid-ribbed walls are also given in Fig. 8 for comparison. Qualitatively, a good agreement between these two works is achieved. The higher duct blockage ratio ($2H/D_e = 0.334$) employed in Taslim et al. (1994) than the present ($H/D_e = 0.167$) would appear to explain the higher values of the average Nusselt number.

Copper Rib Data. Average rib heat transfer characteristics for the slit and solid-ribbed walls are displayed in Fig. 9. Figure 9(*a*) shows the comparison of the average rib Nusselt number between the slit and solid ribs. It is seen from this figure that the average Nusselt number for the slit rib decreases with a decreasing rib void fraction. Surprisedly, it is lower than that for the solid rib, typically by about 65–80 percent. This is not peculiar because the slit rib has a significantly higher heat transfer surface area than the solid ribs (Table 1). The average Nusselt number based on the large total heat transfer area (Eq. (2)) is therefore lower. Notably, the benefits of heat transfer enhancement for special surface geometries such as the finned walls discussed here utilize the value hA_{rib}, rather than the heat transfer coefficient itself (Webb, 1994). Thus, Fig. 9(*b*) compares the value of hA_{rib} between the slit and solid ribs at various Reynolds numbers. It is revealed that the slit rib, as expected, has a higher hA_{rib} per unit rib base surface than the solid rib, indicating that the slit rib has a greater fin effect than the solid rib. Furthermore, the hA_{rib} is affected negligibly by the rib void fraction, typically only four percent maximum for 19 percent $\leqq \beta \leqq 48$ percent. Although the incoming turbulence intensity may be higher for the higher rib void fraction, increasing the rib void fraction reduces the heat transfer surface area (Table 1). In addition, the flow acceleration between the rib top and the opposite duct wall decreases with an increase in the rib void fraction due to less duct blockage. Obviously, these counteracting factors result in comparable fin effects as the rib void fraction varies from 0.19 to 0.48.

Overall Heat Transfer Coefficient. The overall heat transfer coefficients on the rib-roughened wall deduced from Eq. (3) are shown by the average Nusselt number ratio in Fig. 10. Different lines for comparison also display the corresponding average floor heat transfer coefficients. In the case of the solid-ribbed wall, the overall heat transfer coefficient in which the rib heat transfer has been incorporated is slightly lower than the average floor heat transfer coefficient, typically within seven percent. This is an indication that the average heat transfer coefficient, based on the thermally active rib-walled boundary conditions, is not too different from that based on the thermally nonactive rib-walled boundary conditions which are analogous to those of the naphthalene-coated surfaces with glued-on metallic ribs (with surfaces from which no mass is transferred). As for the slit-ribbed wall, the overall heat transfer coefficients are significantly lower than the floor heat transfer coefficient, typically up to 20 percent. Further, this figure shows that the overall Nusselt number ratio for the slit-ribbed wall increases slightly with an increase in the rib void fraction. The average Nusselt number ratio for both the slit and solid-ribbed walls decreases slightly with increasing Reynolds number.

From the data given in Fig. 10, the effects of the Reynolds number and rib void fraction on the average Nusselt number in a rectangular duct with one slit-ribbed wall can be correlated by the following equation:

$$\overline{\mathrm{Nu}}_t = 0.067\,\mathrm{Re}^{0.742}(1-\beta)^{-0.297} \qquad (6)$$

where the coefficients are obtained with curved fitting, based on the least-squares method through the measured data shown in Fig. 10. The maximum deviations of the experimental data from Eq. (6) are 7.8 percent, 2.7 percent, and 4.1 percent for β = 19 percent, 32 percent, and 48 percent, respectively.

Several factors that affect the heat transfer mechanisms when the thermally active ribs are perforated with slits can be drawn from the data presented above. First, due to the existence of the slits within the rib, the effective thermal conductivity (or conduction capacity) of the slit rib should decrease. Then, due to the reduction in duct blockage, the local mean velocity between the rib top and the opposite duct wall is reduced. Both of these adversely affect rib heat transfer. Third, because of the flow through the slits, the extension in heat transfer surface area becomes significant (Table 1), which favors rib heat transfer. The last effect is caused by an alteration in the fluid-flow trans-

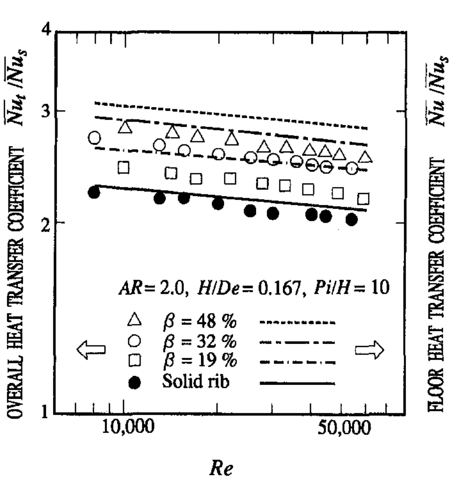

Fig. 10 Overall heat transfer coefficient of the ribbed wall versus Reynolds number

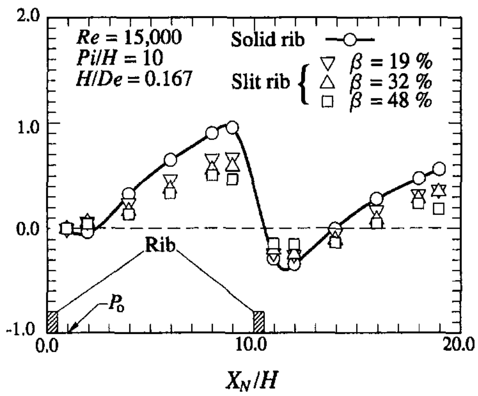

Fig. 11 Local drag-coefficient distributions along the slit and solid-ribbed walls

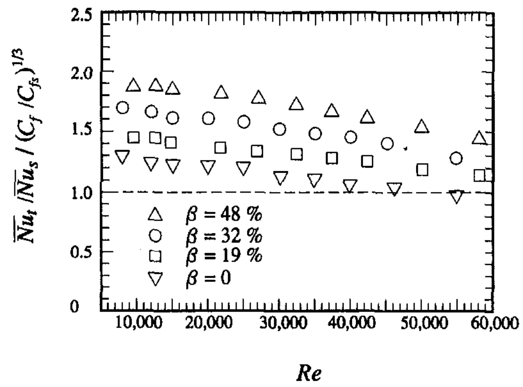

Fig. 13 Thermal performances of ribbed channels under constant pumping power condition

portation (Figs. 4 to 7). The first two factors compete with the third factor in influence on rib heat transfer. The last factor enhances both rib heat transfer and floor heat transfer.

Friction Characteristics. To examine the effects of flow permeability shown in Fig. 4 on the friction characteristics, static wall pressure measurements are undertaken in this research. From Eq. (4) the local drag-coefficient distributions are calculated and shown versus axial distance in Fig. 11. Generally, Fig. 11 shows that the local drag coefficient drops steeply across the solid rib (circular symbols) and then gradually recovers in the interrib region. The C_D distribution along the slit-ribbed wall is similar to but has less peak-to-peak variations than that along the solid-ribbed wall due to less form drag. It is further seen that the larger the rib void fraction is, the flatter the distribution of C_D becomes.

Figure 12 illustrates the combined effects of rib void fraction and flow Reynolds number on the fully developed friction factor for the slit and solid-ribbed geometries. From this figure the friction factor for the slit-ribbed duct is much higher than its counterpart for the smooth duct (Blasius correlation), but lower than that for the solid-ribbed duct (solid circular symbols). It is almost independent of the Reynolds number, i.e., "fully roughness". In comparison with the results of the solid-ribbed duct flows, the values of C_f are approximately 90 percent, 72 percent, and 60 percent for β = 19 percent, 32 percent, and 48 percent, respectively, in the range of the Reynolds number investigated. Perforating the rib with slit slots has two opposite effects on the friction factor. One is to decrease the form drag caused by distortion of the streamline by reducing the duct blockage. The other is to increase the surface drag due to the fluid going through the slits. Obviously, the former effect overcomes the latter. The results of similar duct blockages in the previous work are displayed in Fig. 12 for comparison. The dashed and center lines from Liou and Hwang (1992) are for two-opposite solid-rib walled ducts of blockage ratios $2H/D_e$ = 0.162, and 0.126, respectively. The former duct blockage is largely identical to that of the present one solid-rib walled duct with H/D_e = 0.167. The comparison shows a satisfactory agreement between these two ducts. In addition, the previous data of $2H/D_e$ = 0.126 (center line) fell reasonably into the region between the present data for one slit-rib walled ducts of β = 32 percent and 48 percent, which have blockage ratios 0.114 and 0.135, respectively.

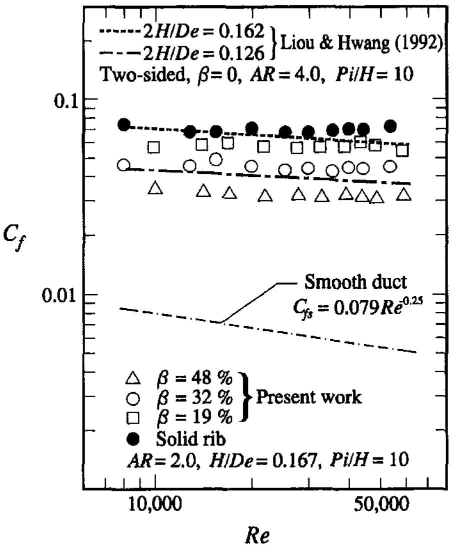

Fig. 12 Dependence of friction factor on the flow Reynolds number in ribbed channels

With the data presented in Fig. 12, the average friction factor for the duct flow with the slit ribs mounted on the wall can be correlated as below:

$$C_f = 0.0196\beta^{-0.671} \quad (7)$$

where the constants are obtained by curved fitting, based on the least-squares method through the data shown in Fig. 12. The maximum deviations of the experimental data from Eq. (7) are 2.1, 1.6, and 3.2 percent for β = 19 percent, 32 percent, and 48 percent, respectively.

Note that an additional experiment has been conducted to examine the effect of the rib conductivity on the friction factor under heated-wall conditions, which reveals that no difference in the friction factor, beyond experimental uncertainties, is observed between the thermally active and nonactive ribbed channels.

Pumping-Power Performance. One of the criteria for evaluating the performance of an enhanced surface is to compare the heat transfer of a ribbed duct to that of a smooth-walled duct under constant pumping power constraint as suggested by Webb and Eckert (1972) and Han et al. (1985). In view of their discussion, an efficiency index $(\overline{Nu}_r/\overline{Nu}_s)/(C_f/C_{fs})^{1/3}$, the equal pumping-power performance criterion, can decide whether or not a given ribbed surface is potentially gainful. From Fig. 13, where $(\overline{Nu}_r/\overline{Nu}_s)/(C_f/C_{fs})^{1/3}$ is plotted against Re, it can be seen that all ribbed ducts do show the same trend, i.e., higher values of $(\overline{Nu}_r/\overline{Nu}_s)/(C_f/C_{fs})^{1/3}$ at lower Reynolds numbers initially and then the monotonically decreasing values as Re increases. It is clear that the slit-ribbed duct has a higher performance than the solid-ribbed duct, especially for the larger void fraction. These results are very reasonable because of the moderately higher heat transfer enhancement (Fig. 10) and lower pressure-drop penalty (Fig. 12) for the slit-ribbed duct of higher rib void fraction.

Summary and Conclusions

The mechanisms of heat transfer augmentation have been studied experimentally in rectangular ducts with one wall roughened by slit or solid copper ribs. The rib height-to-channel hydraulic diameter ratio and rib pitch-to-height ratio are fixed at $H/D_e = 0.167$ and $P_i/H = 10$, respectively. The flow Reynolds number varies from Re = 8000 to 58,000, while the rib void fractions are $\beta = 19$, 32, and 48 percent. A specially designed heat transfer test rig has successfully measured the rib, floor, and overall heat transfer coefficients, respectively. The coupled contributing factors for heat transfer enhancement, i.e., turbulence effect and fin effect, are separated. Flow visualization, and the measurements of the velocity and turbulence distributions provide a better understanding of the heat-transfer-enhancement mechanisms in the ribbed duct. The main findings based on these experiments are as follows:

1 The slit and solid-ribbed walls produce flatter velocity profiles at $X_N/H = 6.0$ than a smooth wall. For a fixed Reynolds number, rib height and rib spacing, the slit-ribbed wall generates a relatively higher near-wall turbulence intensity than the solid-ribbed wall. The flatter velocity profile and higher turbulence intensity lead to higher heat transfer enhancement.

2 With greater turbulence-mixing effect, the slit-ribbed geometry provides better floor heat transfer coefficients than the solid-ribbed geometry. In addition, the slit rib has a more significant fin effect than the solid rib due to its larger heat transfer surface area.

3 For the solid-ribbed geometry, the overall heat transfer coefficient of the ribbed wall in which the rib heat transfer has been incorporated is about seven percent lower than the corresponding floor heat transfer coefficient. This adequately represents the discrepancy between the heat transfer measurement on the wall mounted with thermally active ribs and the mass transfer measurement with the metallic-ribbed surface discussed in the Introduction.

4 Increasing rib void fraction promotes floor heat transfer, but insignificantly affects rib heat transfer. The former is attributed solely to the effects of turbulence enhancement; while the latter is the result of the competing effects of the increase in incoming turbulence and the reduction of rib effective thermal conductivity and heat transfer surface area.

5 As compared to the solid-ribbed geometry, the slit-ribbed geometry has a flatter distribution of the local drag coefficient, indicating that the lower from drag occurs with slit-ribbed geometry. In addition, the fully developed friction factor for the slit ribbed duct is lower than that for the solid-ribbed duct, and decreases with increasing rib void fraction.

6 Pumping-power performance comparisons reveal that the slit-ribbed duct with larger rib void fractions in a lower Reynolds number range could perform superior heat transfer enhancement.

Acknowledgments

Support for this work was provided by the National Science Council of the Republic of China under contract No. NSC 87-2212-E-216-006.

References

Acharya, S., Dutta, S., Myrum, T. A., and Baker, R. S., 1993, "Periodically Developed Flow and Heat Transfer in a Ribbed Duct," *Int. J. Heat Mass Transfer,* Vol. 36, pp. 2069–2082.

Burggraf, F., 1970, "Experimental Heat Transfer and Pressure Drop With Two-Dimensional Discrete Turbulence Promoters Applied to Two Opposite Walls of a Square Tube," *Augmentation of Convective Heat and Mass Transfer,* A. E. Bergles and R. L. Webb, eds, ASME, New York, pp. 70–79.

Chandra, P. R., and Han, J. C., 1989, "Pressure Drop and Mass Transfer in Two-Pass Ribbed Channels," *AIAA, J. Thermophysics,* Vol. 3, pp. 315–320.

Chang, Y., 1990, "Three Dimensional Measurements of Turbulent Flows in a Rectangular Duct With Repeated Rectangular-Rib Pairs," Master thesis, National Tsing-Hua University, Taiwan.

Chyu, M. K., and Wu, L. X., 1989, "Combined Effects of Rib Angle-of-Attack and Pitch-to-Height Ratio on Mass Transfer From a Surface with Transverse Ribs," *Experimental Heat Transfer,* Vol. 2, pp. 291–308.

Han, J. C., Glicksman, L. R., and Rohsenow, W. H., 1978, "An Investigation of Heat Transfer and Friction for Rib-Roughness Surfaces," *Int. J. Heat Mass Transfer,* Vol. 21, pp. 1143–1156.

Han, J. C., Park, J. S., and Lei, C. K., 1985, "Heat Transfer Enhancement in Channels with Turbulence Promoters," ASME JOURNAL OF HEAT TRANSFER, Vol. 107, pp. 628–635.

Han, J. C., 1988, "Heat Transfer and Friction Characteristics in Rectangular Channels with Rib Turbulators," ASME JOURNAL OF HEAT TRANSFER, Vol. 110, pp. 321–328.

Hwang, J. J., and Liou, T. M., 1994, "Augmented Heat Transfer in a Rectangular Channel with Permeable Ribs Mounted on the Wall," ASME JOURNAL OF HEAT TRANSFER, Vol. 116, pp. 912–920.

Hwang, J. J., and Liou, T. M., 1997, "Heat Transfer Augmentation in a Rectangular Channel With Slit Rib-Turbulators on Two Opposite Walls," ASME *Journal of Turbomachinery,* Vol. 119, pp. 617–623.

Kays, W. M., and Crawford, M. E., 1980, *Convective Heat and Mass Transfer,* McGraw-Hill, New York.

Kline, S. J., and McClintock, F. A., 1953, "Describing Uncertainties on Single-Sample Experiments," *Mechanical Engineering,* Vol. 57, pp. 3–8.

Liou, T. M., and Hwang, J. J., 1992, "Turbulent Heat Transfer and Friction in Periodic Fully Developed Duct Flows," ASME JOURNAL OF HEAT TRANSFER, Vol. 114, pp. 56–64.

Liou, T. M., and Hwang, J. J., 1993, "Effects of Ridge Shapes on Turbulent Heat Transfer and Friction in a Rectangular Duct," *Int. J. Heat Mass Transfer,* Vol. 36, pp. 931–940.

Metzger, D. E., and Vedula, R. P., 1987, "Heat Transfer in Triangular Channels with Angled Roughness Ribs on Two Walls," *Experimental Heat Transfer,* Vol. 1, pp. 31–44.

Molki, M., and Mostoufizadeh, A. R., 1989, "Turbulent Heat Transfer in a Rectangular Duct With Repeated-Baffle Blockages," *Int. J. Heat Mass Transfer,* Vol. 32, pp. 1491–1499.

Myrum, T. A., Acharya, S., Inamdar, S., and Mehrotra, A., 1992, "Vortex Generator Induced Heat Transfer Augmentation in a heated Duct Air Flow," ASME JOURNAL OF HEAT TRANSFER, Vol. 114, pp. 280–284.

Rehsonow, W. M., and Choi, H. Y., 1969, *Heat, Mass, and Momentum Transfer,* Prentice-Hall, Englewood Cliffs, NJ.

Siegel, R., and Howell, J. R., 1981, *Thermal Radiation Heat Transfer,* 2nd Ed., McGraw-Hill, New York.

Taslim, M. E., Li, T., and Kercher, D. M., 1991, "An Experimental Investigation into the Effects Turbulator Profiles and Spacing Have on Heat Transfer Coefficient and Friction Factors in Small Cooled Turbine Airfoils," *27th AIAA/SAE/ASME Joint Propulsion Conference,* Sacramento, CA.

Taslim, M. E., and Wadsworth, C. M., 1994, "An Experimental Investigation of the Rib Surface-Averaged Heat Transfer in a Ribbed Roughened Square Passage," ASME paper 94-GT-162.

Webb, R. L., Eckert, E. R. G., and Goldstein, R. J., 1971, "Heat Transfer and Friction in Tubes with Repeated-Ribs Roughness," *Int. J. Heat Mass Transfer,* Vol. 14, pp. 601–617.

Webb, R. L., and Eckert, E. R. G., 1972, "Application of Rough Surfaces to Heat Exchanger Design," *Int. J. Heat Mass Transfer,* Vol. 15, pp. 1647–1658.

Webb, R. L., 1994, "Principles of Enhanced Heat Transfer," John Wiley and Sons, New York.

Zhang, Y. M., Gu, W. Z., and Han, J. C., 1994, "Heat Transfer and Friction in Rectangular Channels with Ribbed or Ribbed-Grooved Walls," ASME JOURNAL OF HEAT TRANSFER, Vol. 116, pp. 58–65.

M. Greiner
e-mail: greiner@moriah.ee.unr.edu.
Mem. ASME.

G. J. Spencer

Mechanical Engineering Department,
University of Nevada,
Reno, NV 89557

P. F. Fischer
Division of Applied Mechanics,
Brown University,
Providence, RI 02912

Direct Numerical Simulation of Three-Dimensional Flow and Augmented Heat Transfer in a Grooved Channel

Direct numerical simulations of three-dimensional flow and augmented convective heat transfer in a transversely grooved channel are presented for the Reynolds number range $140 < Re < 2000$. These calculations employ the spectral element technique. Multiple flow transitions are documented as the Reynolds number increases, from steady two-dimensional flow through broad-banded unsteady three-dimensional mixing. Three-dimensional simulations correctly predict the Reynolds-number-independent friction factor behavior of this flow and quantify its heat transfer to within 16 percent of measured values. Two-dimensional simulations, however, incorrectly predict laminar-like friction factor and heat transfer behaviors.

Introduction

Industrial heat transfer equipment employs a wide variety of augmented core configurations to enhance performance (Webb, 1994). Typical methods involve fins that extend the surface area or offset strips that promote thin boundary layers. These features are not specifically intended to modify the behavior of the flow field itself. In recent years, however, a number of numerical and experimental studies have been performed for passage configurations that excite flow instabilities leading to enhanced mixing. Transversely grooved channels (Ghaddar et al., 1986), passages with eddy promoters (Kozlu et al., 1988), and communicating channels (Amon et al., 1992) all promote the formation of inflections in the passage velocity profile. Kelvin-Helmholtz instabilities of these inflected profiles project energy onto the normally damped Tollmien-Schlichting waves of the outer channel, resulting in two-dimensional traveling waves at moderately low Reynolds numbers.

Fully developed heat transfer and pressure drop measurements using air in a rectangular cross-section channel with 46 transverse grooves on one wall were performed by Greiner et al. (1990, 1991). These grooves were right-triangular in shape and their depth normal to the flow and length parallel to the flow were both of the same order as the minimum wall-to-wall spacing. Visualizations showed that two-dimensional waves appeared at a Reynolds number of Re = 350 and the flow became three-dimensional at Reynolds numbers less than 1000. By comparison, flows in flat channels are steady up to Re = 2800 (Fox and McDonald, 1985). Moreover, for a given pumping power level, the grooved passage offered substantially higher heat transfer than a flat passage with the same minimum wall-to-wall spacing, even though the grooved passage operated at a lower Reynolds number.

Intentionally destabilized flows hold promise for enhancing the performance of exchange equipment. However, a wide variety of configurations must be investigated to optimize the heat transfer versus pumping power performance of these flows. Numerical simulations have become powerful tools in predicting the flow behavior and performance of exchange passages, as well as determining their sensitivity to geometric parameters. Two-dimensional spectral element simulations of grooved channels (Ghaddar et al., 1986; Roberts, 1994), passages with eddy promoters (Karniadakis et al., 1988), and communicating channels (Majumdar and Amon, 1997) have documented the evolution of the flow field and heat transfer augmentation. Recent two-dimensional simulations of flows in a channel with sine wave shaped grooves shows that the evolution of chaos follows the Ruelle-Takens-Newhouse scenario and that the predicted flow behavior is not significantly altered when three-dimensional simulations are performed (Guzman and Amon, 1994, 1996).

In contrast, the experiments by Greiner et al. with triangular-shaped grooves (whose length in the flow direction is roughly half that of the grooves studied by Guzman and Amon) show that no significant heat transfer augmentation is measured until the flow becomes three-dimensional. Other three-dimensional destabilized flows have been successfully studied using the spectral element technique (Amon and Patera, 1989; Amon, 1993; Blackburn et al., 1993). However, these studies do not report heat transfer results.

In this paper, direct numerical simulations of three-dimensional flow and augmented heat transfer in the same grooved passage configuration studied by Greiner et al. are presented and quantitatively benchmarked against the experimental results. The next section describes the computational domain and spectral element numerical technique employed in this work. The increasing complexity of the flow as the Reynolds number increases from 140 to 2000 is then described, along with the predicted heat transfer and friction factor. Finally, conclusions are drawn.

Numerical Method

Figure 1 shows the primary computational domain and spectral element mesh employed in the bulk of this work. The upper flat surface and lower V-shaped boundary are solid walls that impose no-slip velocity conditions. The minimum wall-to-wall spacing $H = 1$ cm, groove length $L = 2.4H$ and groove depth $D = 1.2H$ are designed to represent one periodicity cell of the continuously grooved passage of the earlier experimental study (Greiner et al., 1991).

A uniform body force per unit mass f_x, is applied to the fluid to drive the flow from left to right through the computation domain. This force is equivalent to a constant mean pressure

---

Contributed by the Heat Transfer Division for publication in the JOURNAL OF HEAT TRANSFER and presented at '96 NHTC. Manuscript received by the Heat Transfer Division, Oct. 16, 1996; revision received, Apr. 6, 1998. Keywords: Augmentation and Enhancement, Flow Transition, Heat Exchangers. Associate Technical Editor: S. Ramadhyani.

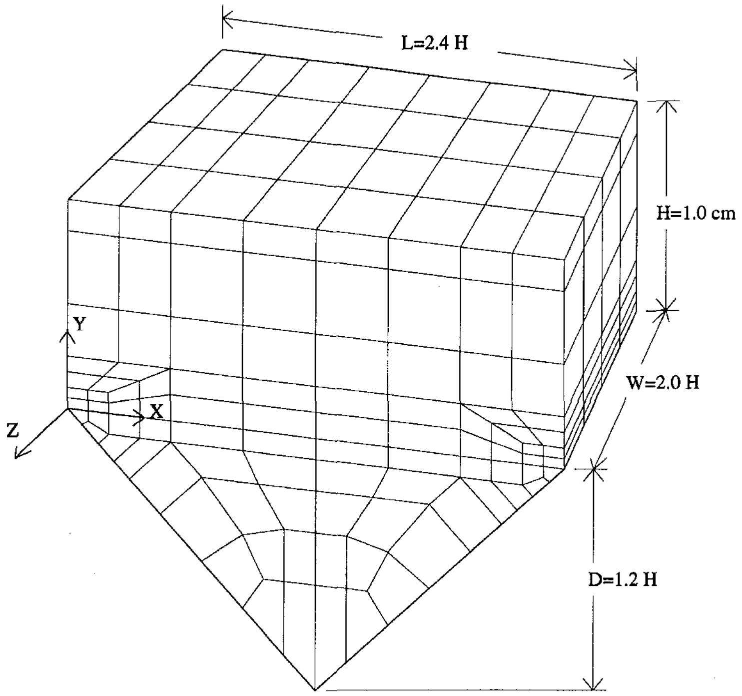

Fig. 1 Three-dimensional computational domain and spectral element mesh used to investigate a periodically grooved transport passage

gradient, $f_x = (-1/\rho)(\partial p/\partial x)$. Periodic boundary conditions are applied to the left and right surfaces of the domain ($x = 0$ and L) in order to model fully developed flow which, in this study, is assumed to be periodic from groove to groove.

Periodic boundary conditions are also applied to the front and back surfaces of the domain ($z = 0$ and $-W$). The choice of the z-direction periodicity length $W = 2.0$ cm is somewhat arbitrary. Another domain with $W = 3.0$ cm is employed to evaluate the sensitivity of the heat transfer and friction factor results to this parameter. A shortcoming of periodicity boundary conditions is that they do not admit a continuous spectrum of mode sizes. This technique only admits modal wavelengths such that an integer number of wavelengths exactly spans the periodicity length, that is, z-direction wavelengths of the form W/n, where n is an integer. This limitation is most severe when the dominant modes are larger than or roughly the same size as the domain. However, we will see that the eddy sizes generally decrease with increasing Reynolds number. As a result it is possible that the current simulations overpredict the Reynolds number where three-dimensional modes first appear. However, the limitation of using periodic boundary conditions in the z-direction is unimportant at higher Reynolds numbers.

The computational grid shown in Fig. 1 consists of four levels in the z-direction. Each level contains 96 hexahedral spectral elements (Patera, 1984; Maday and Patera, 1989), for a total of $K = 384$ elements. These elements are densely clustered near the peaks of the grooved surface and near the upper flat wall. Within each element, the solution, data, and geometry are represented by tensor-product polynomial bases of degree N in each spatial direction, corresponding to a total grid point count of roughly KN^3. As the fluid body force and Reynolds number are increased, spatial refinement is attained by increasing the spectral order from $N = 5$ to 9. A mesh with six z-levels is also used to evaluate grid independence of the heat transfer and friction factor results. The domain with $W = 3.0$ cm, which is used to assess the independence of the results to a larger domain

Nomenclature

A = area of flat surface
C_f = fanning friction factor, $C_f = (-\partial p/\partial x)(D_h/(2\rho u_m^2))$
D = groove depth, Fig. 1
D_h = minimum channel hydraulic diameter, $2H$
f = frequency
f_x = fluid body force in the x-direction per unit mass, $(-1/\rho)(\partial p/\partial x)$
H = minimum channel height, Fig. 1
k = fluid thermal conductivity
K = number of spectral elements
L = channel periodicity length, Fig. 1
N = spectral element order
Nu = Nusselt number, $q''D_h/T_m k$
Pr = Fluid Prandtl number
q'' = flat wall heat flux
Re = Reynolds number, $u_m D_h/\nu$
Re_{w_m} = Reynolds number based on w_m
t = time
T = temperature
T_m = mean flat surface temperature
u, v, w = velocity components in the x, y, and z directions
u_m = mean x-velocity passing through minimum channel cross section, V_r/WH
$\forall$ = volume of the computational domain
V_r = volume flow rate
W = width of the computational domain, Fig. 1
w_m = maximum z-velocity within the domain
x, y, z = coordinate directions, Fig. 1

Greek

ν = fluid kinematic viscosity
Ω = dimensionless frequency, fD_h/u_m
θ = dimensionless flat surface temperature, $T_m k/q''D_h$
ρ = fluid density

Marker

$\bar{\ }$ = averaged over time

width, also has six z-levels. A planar grid, equivalent to the face of the domain shown in Fig. 1, is used for two-dimensional simulations.

The present simulations are based upon a fractional step (or time-splitting) approach (Orszag and Kells, 1980; Fischer and Patera, 1992). In this technique, the coupled momentum equations are advanced by first computing the convection term, followed by the projection of the velocity onto a divergence-free space, followed by a viscous update which incorporates the velocity boundary conditions. The splitting results were compared against a more accurate approach based upon a consistent coupling of the viscous and pressure terms (Maday and Patera, 1989; Fischer and Ronquist, 1994). While the latter method more accurately predicts the onset of two-dimensional unsteadiness at low Reynolds numbers, both methods give essentially the same behavior at the higher Reynolds numbers central to the present investigation. Consequently, the less expensive splitting approach is used throughout this work.

Time-dependent simulations are performed for a range of applied body force levels, f_x. At each time step the x-velocity component, u, is integrated throughout the domain to determine the instantaneous volume flow rate, $V_r = (1/L)\int_{\forall} u d\forall$, where $\forall$ is the volume of the computational domain. In general, the velocity field and the integrated volume flow rate may vary with time, even for a steady body force. The resulting time-dependent Reynolds number is defined as $\text{Re} = u_m D_h/\nu$, where the mean x-velocity and hydraulic diameter through the minimum channel cross section are $u_m = V_r/HW$ and $D_h = 2H$, respectively, and ν is the fluid kinematic viscosity.

Time-dependent simulations are used to reach "steady-state" conditions. Depending on the Reynolds number, the volume flow rate for steady state is either steady, time periodic, or randomly varying about a constant mean value. Once steady-state conditions are reached, the time-averaged Reynolds number $\overline{\text{Re}} = \overline{u_m}D_h/\nu$ is evaluated, where $\overline{u_m}$ is the time average of u_m. The time-average Fanning friction factor is then determined from the expression $C_f = (f_x D_h)/(2\overline{u}_m^2)$.

With regard to thermal boundary conditions, the upper surface dissipates a uniform heat flux, q'', while the lower surface temperature is held constant and uniform at $T_0 = 0$. The flat surface temperature is integrated to determine its mean value, $T_m = (1/A)\int_A TdA$, where the area of the upper surface is A, and T is temperature. The time-dependent dimensionless temperature is defined as $\theta = T_m k/q''D_h$, where k is the fluid thermal conductivity. The mean flat surface temperature, in general, varies with time. The time-average flat surface temperature, $\overline{T_m}$, is determined after steady-state thermal conditions are reached and used in the time-averaged Nusselt number $\overline{\text{Nu}} = q''D_h/\overline{T_m}k$. This Nusselt number quantifies the thermal transport between the upper flat surface of the channel and its lower V-shaped boundary for a range of flow conditions. The fluid properties for most simulations are $k = 0.0334$ W/m·K, $\nu = 1.84 \times 10^{-5}$ m^2/sec, $\rho = 1.006$ kg/m^3, and a Prandtl number of $\text{Pr} = 0.56$. Runs are also made with $\text{Pr} = 0.71$ to allow direct comparisons with experimental data.

The three-dimensional results are computed in parallel on 128 i860-processors on the Intel Delta at Caltech (Fischer and Patera, 1991; Fischer and Ronquist, 1994). A typical simulation comprising 374,000 grid points ($K = 384$, $N = 9$) requires 15 seconds per time-step ($\Delta t = 0.00007$ sec). The two-dimensional simulations are performed using 32 processors. A typical calculation consisting of 3300 grid points ($K = 96$, $N = 5$) requires about five seconds per step ($\Delta t = 0.00025$ sec). All calculations are performed in 32-bit arithmetic.

Results

Flow Field. A series of two and three-dimensional simulations are now presented for body force levels of $f_x = 0.5$ to 8 N/kg to demonstrate the flow field and heat transfer behaviors for a range of Reynolds numbers. The initial simulation employs the two-dimensional mesh, which is equivalent to the face of the domain shown in Fig. 1. The body force for this calculation is $f_x = 0.5$ N/kg, and it uses fifth-order spectral elements. The initial temperature and velocity for this simulation with are both zero throughout the domain. After the body force is applied, the Reynolds number rises for roughly three seconds, as the volume flow rate increases, until it reaches a constant value of $\overline{\text{Re}} = 325$. The dimensionless temperature of the flat surface requires more than twice as much time to reach its steady-state value of $\theta = 0.59$.

Figure 2(a) shows the streamlines after steady state is reached. We see that the majority of the outer channel fluid moves parallel to the flat surface. The groove is filled by a slowly turning vortex, whose center is in the downstream portion of the groove. One second of flow time for this two-dimensional simulation requires roughly 0.8 hours of computational time. Three-dimensional simulations at this Reynolds number give essentially the same results, but one second of flow time requires 5.3 hours of computation.

Results from the simulation with $f_x = 0.5$ N/kg are used as initial conditions for two-dimensional simulations with $f_x = 1.0$ N/kg. Figure 3 shows the Reynolds number and the flat surface dimensionless temperature versus time t, after the body force is doubled. We see that Reynolds number increases and then develops periodic oscillations, with a time-average value of $\overline{\text{Re}} = 580$. The amplitude of the oscillatory component is two percent of the mean value and it has a dimensionless frequency of $\Omega = fD_h/\overline{u_m} = 0.52$, where f is the dimensional frequency. Once the steady periodic state is reached, the time-average dimensionless temperature drops to $\theta = 0.52$.

Figure 2(b) shows the streamlines of this flow at six equally spaced times during one oscillatory cycle. We see that the outer channel flow develops a traveling wave whose wavelength in the x-direction is equal to the channel periodicity length. The peak of this wave is seen moving to the right and then reenters the domain at the left-hand side. Simulations at lower Reynolds numbers, using the consistent viscous/pressure coupling method, show that these two-dimensional self-sustained oscillations first appear at a critical Reynolds number of $\text{Re} = 350$, in agreement with experimental observations (Greiner et al., 1991). These waves periodically push slow moving fluid from the grooved regions into the mainstream, retarding the flow. After each ejection the fluid in the channel re-accelerates until the next ejection occurs. This action accounts for the volume flow rate variations observed in Fig. 3. It also increases the

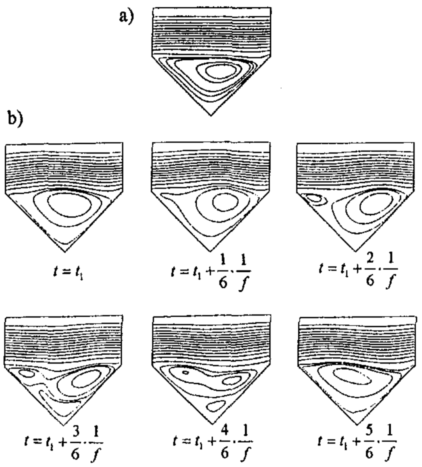

Fig. 2 Streamlines from two-dimensional simulations; (a) $f_x = 0.5$ N/kg, (b) $f_x = 1.0$ N/kg, at six equally spaced times during one oscillatory period

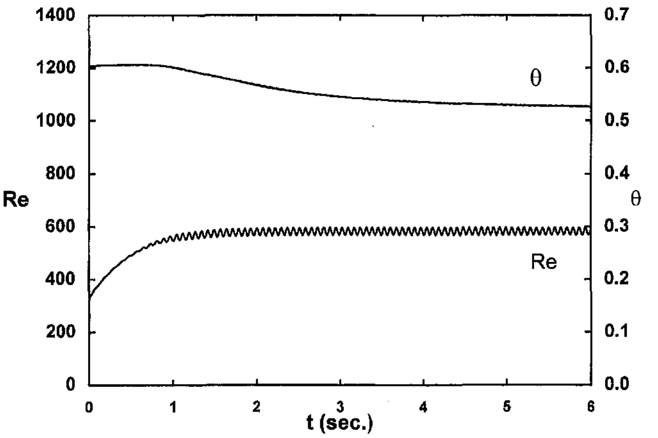

Fig. 3 Reynolds number and flat surface dimensionless temperature versus time for f_x = 1.0 N/kg, from two-dimensional simulations

thermal transport, which in turn reduces the dimensionless flat surface temperature.

The velocity and temperature fields calculated from the two-dimensional simulation are used as initial conditions for a three-dimensional calculation with the same imposed body force level, f_x = 1.0 N/kg. This is done by replicating the two-dimensional results at each z-station, and setting the initial z-velocity, w, to zero. These three-dimensional simulations employ seventh-order spectral elements. Figure 4 shows the time dependence of the Reynolds number, flat surface dimensionless temperature, and $\mathrm{Re}_{w_m} = w_m D_h/\nu$, where w_m is the maximum amplitude of z-velocity component within the domain. The data in this figure begins one second after the three-dimensional simulations begin. We see that w_m grows slowly at first, reaches a peak, and then exhibits regular oscillations. Peak values of w_m (Re_{w_m}) are more than 40 percent as large as $\overline{u_m}$ (Re), indicating that the flow has become highly three-dimensional.

Comparing the left and right-hand sides of Fig. 4 shows that once three-dimensional flow is fully established the flow behavior is markedly changed, even though the applied force level remains the same. We see that the time-average Reynolds number and dimensionless temperature decrease to $\overline{\mathrm{Re}} = 482$ and $\theta = 0.49$, respectively, indicating higher levels of predicted drag and thermal transport. Moreover, the oscillatory component of the flow rate (Re) decreases from 2 percent to only 0.12 percent of the time average value (this amplitude is too small to be visible in Fig. 4), and its dimensionless frequency increases from $\Omega = 0.52$ to 1.3.

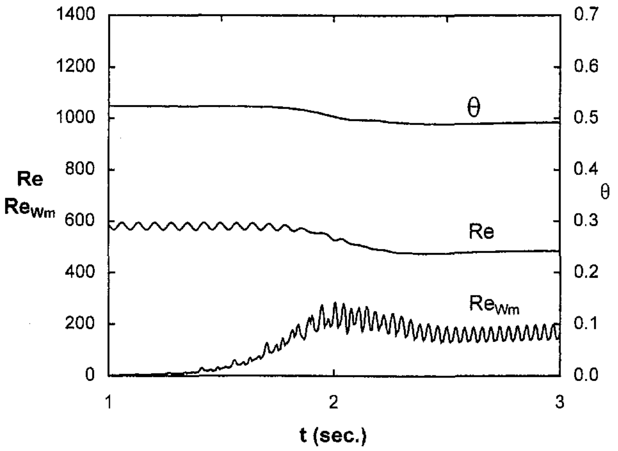

Fig. 4 Reynolds number, flat surface dimensionless temperature, and Reynolds number based on maximum w-velocity throughout the domain versus time for an applied fluid body force of f_x = 1.0 N/kg, from a three-dimensional simulation

To better understand these behaviors, we must consider the three-dimensional flow structure. Figure 5 shows the y-component of velocity v, in the outer channel for four different flow conditions. The curved surfaces are isometric views of v as a function of x and z on the plane $y/H = 0.25$. Points above the flat planes represent up-flow and points below show flow that is downward. These surfaces represent "snap-shots" of the flow at different instants in time. Snap-shots at different times show that the flow-field structures are traveling in the x-direction. The spacing between peaks and valleys in each surface is an indication of the eddy length scales within the flow. We note that these surfaces are merely intended to show the evolution of the flow structure, and that the velocity scale factor in each part of this figure is substantially different.

Figures 5(a) and 5(b) are both for f_x = 1.0 N/kg. Figure 5(a) is a snapshot of the outer channel two-dimensional traveling wave structure at a time before the flow becomes three-dimensional (left-hand side of Fig. 4). Figure 5(b) shows the corresponding structure once the flow has reached its three-dimensional, time-periodic state (right-hand side of Fig. 4). This flow has developed a traveling wave surface with variations in both the x and z-directions. Examination of the right-hand edge of Fig. 5(b) shows that the z-direction variation is

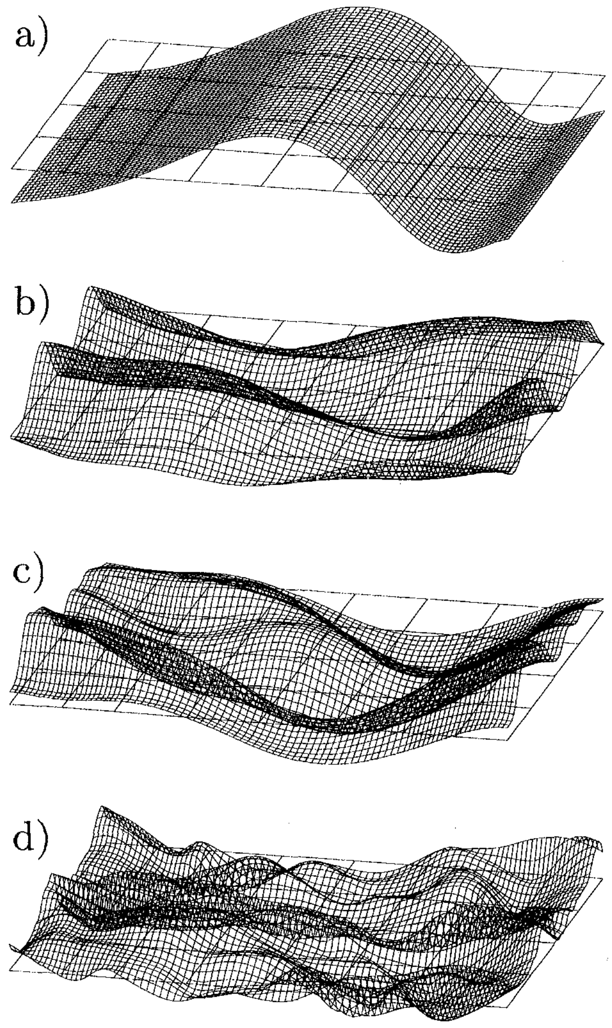

Fig. 5 Isometric views of v-velocity versus x and z on the plane y/H = 0.25 for four different conditions. (a) f_x = 1.0 N/kg, before three-dimensional structures develop; (b) f_x = 1.0 N/kg, after three-dimensional flow develops; (c) f_x = 2.0 N/kg; (d) f_x = 8.0 N/kg.

very regular. At this forcing level, the most unstable mode that is compatible with the imposed periodicity boundary conditions exhibits two waves in the imposed z-direction periodicity length. We point out that the imposed z-direction periodicity length $W = 2H$, was selected as a matter of convenience. The sensitivity of the transport data to variations in W is assessed later in this paper.

Comparing Figs. 5(a) and 5(b), we observe that the three-dimensional simulations develop structures with smaller length scales than those observed in two-dimensional calculations. Comparing the Re versus time curve on the left-hand side of Fig. 4 with the Re_{w_m} curve on the right-hand side, we see that the three-dimensional structures exhibit somewhat higher frequencies as well. Three-dimensional structures therefore advect material in the y-direction more continuously than the two-dimensional waves. This may cause the observed reduction in the channel volume flow rate oscillations, as well as the increases in heat and momentum transfer.

Figure 6 shows the time-history of Re, θ and Re_{w_m} for a three-dimensional simulation with an applied body force of $f_x = 2.0$ N/kg, after the system has reached steady state. These traces are much less regular than those for $f_x = 1.0$ N/kg. While their mean values appear to remain roughly constant, they exhibit large amplitude oscillations with a low dimensionless frequency of $\Omega_1 = 0.04$. Smaller amplitude oscillations are superimposed on the dominant unsteadiness in the Re_{w_m} time history with a higher dimensionless frequency of $\Omega_2 = 1.2$. These smaller oscillations have roughly the same dimensionless frequency as the dominant mode for three-dimensional flow at $f_x = 1.0$ N/kg. The time-average Reynolds number and dimensionless temperature are $\overline{\mathrm{Re}} = 757$ and $\theta = 0.41$.

Figure 5(c) shows an isometric view of the outer channel v-velocity at an instant in time after the three-dimensional flow is fully established. While this surface is similar to the surface for $f_x = 1.0$ N/kg (Fig. 5(b)), careful examination of the right-hand edge shows that its variation in the z-direction is not as regular. One second of flow time at this Reynolds number requires 15.6 hours of computing time.

Figure 7 shows the time history of the Reynolds number and upper surface dimensionless temperature for an applied fluid body force of $f_x = 8.0$ N/kg. These calculations employ ninth-order three-dimensional spectral elements. These traces are for a time period after three-dimensional flow has become fully established. Both of these time histories appear to oscillate randomly about their respective mean values of $\overline{\mathrm{Re}} = 1520$ and $\theta = 0.22$. The Reynolds number data, however, exhibit a wider range of oscillatory frequencies than the dimensionless temperature curve. One second of flow time at this forcing level requires 95 hours to compute.

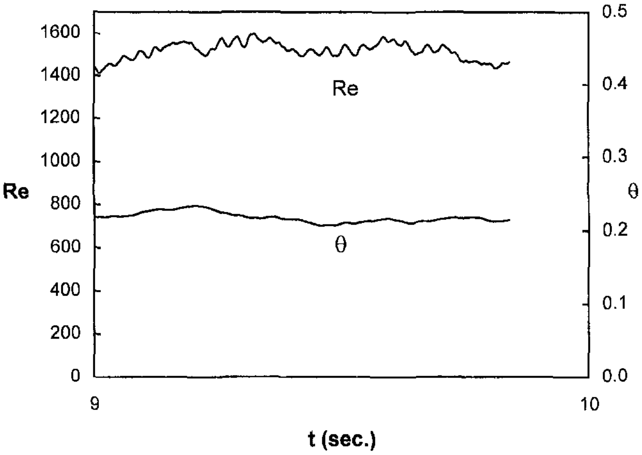

Fig. 7 Reynolds number and flat surface dimensionless temperature versus time for $f_x = 8.0$ N/kg, for a three-dimensional simulation

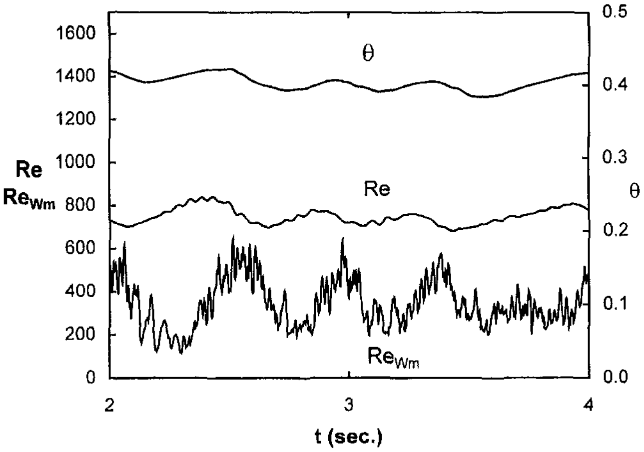

Fig. 6 Reynolds number, flat surface dimensionless temperature, and Reynolds number based on maximum w-velocity throughout the domain versus time for $f_x = 2.0$ N/kg, from a three-dimensional simulation

Figure 5(d) shows the v-velocity at $y/H = 0.25$ at one instant in time for $f_x = 8.0$ N/kg. We see that this surface is far less regular in the x and z-directions than any of the other surfaces in Fig. 5. Taken as a whole, Fig. 5 shows that smaller length scale and more contorted structures are observed as the Reynolds number is increased. Similarly, comparing Figs. 4, 6, and 7, a wider range of unsteady frequencies emerge with increasing flow rate.

We have seen that the current simulations predict that the grooved channel flow rate exhibits high levels of unsteadiness. No time-dependent flow rate measurements are currently available for grooved channels to benchmark these results. However, two factors suggest that the flow rate variations in the earlier experiments (Greiner et al., 1991) are smaller than the predicted unsteadiness. The first is that the current simulations employ periodic boundary conditions, which presume the flow in each groove is identical. In actuality, it is not likely that the flow in all 46 grooves of the experiment is synchronized. This would tend to decrease the unsteadiness of the flow rate passing through the channel. The second reason is that the inertia of nongrooved portions of the experimental apparatus would reduce the ability of the flow rate to vary with time. While the predicted flow rate unsteadiness cannot be compared to experimental results at this time, the predicted transport quantities are compared to experimental measurements in the next section.

Transport Quantities. Up to this point we have observed the increasing complexity of grooved channel flow as the Reynolds number is increased. We now quantitatively benchmark the current simulations against experimentally measured friction factor and Nusselt number data. The open symbols in Fig. 8 represent the numerically predicted Fanning friction factor for a range of Reynolds numbers from two and three-dimensional simulations. Experimentally measured grooved channel data (Greiner et al., 1991) are included using solid triangles. The solid line represents the laminar flow solution for parallel plates with the same *minimum* wall-to-wall spacing as the grooved channel.

Baseline two-dimensional simulations employ fifth-order spectral elements. These data are represented using diamonds in Fig. 8. The agreement between this data and the two-dimensional case run with seventh-order elements (square) implies that the results are insensitive to further spatial refinement. The majority of three-dimensional simulations employ the mesh in Fig. 1, with four levels in the z-direction, and seventh-order spectral elements (open up-pointing triangles). Data from alternate simulations, one with ninth-order elements (down-pointing

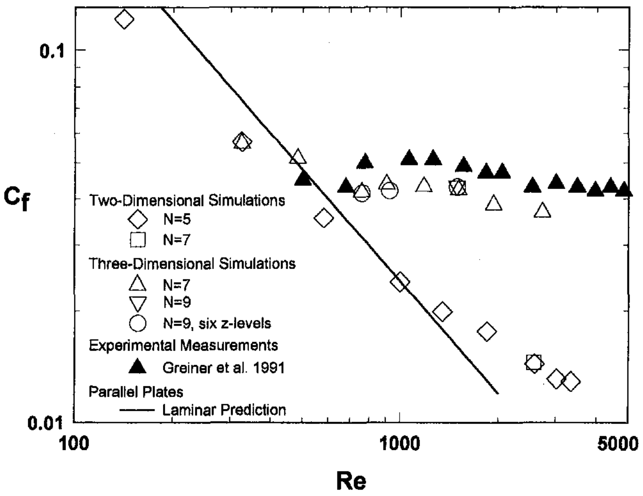

Fig. 8 Fanning friction factor versus Reynolds number from numerical simulations, experimental measurements, and theoretical predictions

triangle), and three with six z-levels (circle), are in close agreement with this data, indicating that further spatial refinements would not effect the friction factor predictions. Domain width independence is also assessed using a six z-level mesh with width $W = 3H$ at Re = 480 and 760. These results (not shown) are nearly identical with the other three-dimensional results. This suggests that the width $W = 2H$ is sufficiently large to admit all relevant flow structures at these Reynolds numbers.

For Reynolds numbers below 350, the calculated friction factors from two and three-dimensional simulations are identical. The friction factor versus Reynolds number behavior is parallel to, but slightly lower than, the dependence for a flat channel with the same *minimum* wall-to-wall spacing. Lower friction factors are expected at these low Reynolds numbers since the flow is steady and the grooves simply act to relax the no-slip boundary condition at $y = 0$.

For Re > 350, the flow is unsteady and the two and three-dimensional predictions diverge. This difference is 20 percent or greater for Re > 500. The two-dimensional simulations incorrectly predict that the friction factor decreases as the Reynolds number increases, in a similar manner to the characteristics of laminar (unmixed) flat passage flow. The three-dimensional simulations correctly predict that the friction factor is roughly independent of Reynolds number for Re > 450. The predicted constant friction factor is 20 percent lower than the measured values. The difference between the predicted and measured results may be due to the possible difference in flow rate unsteadiness mentioned at the end of the last section. From these results we conclude that three-dimensional simulations are required to accurately model the momentum transport of the current grooved passage for Reynolds numbers above Re = 500.

Figure 9 shows the predicted Nusselt number versus Reynolds number dependence from two and three-dimensional calculations. Data from the earlier experimental study, with Pr = 0.71, are also included. Most numerical results are for Pr = 0.56. Three points with Pr = 0.71 are included for direct comparison with the experimental data. The solid horizontal line in Fig. 9 represents a conduction solution, which represents the heat transfer between the top and bottom surface for no fluid motion, i.e., Re = 0.

The two and three-dimensional heat transfer results are virtually unaffected by variations in spectral order, mesh refinement and/or domain width, as observed with regard to the friction factor data. The two and three-dimensional simulation results are identical at Re = 325. These results diverge as the Reynolds number increases, and they are different by greater than 20 percent for Re > 600. The two-dimensional predictions are actually closer to the conduction solution than they are to the experimentally measured convection data.

The three-dimensional results, on the other hand, follow the same slope as the available measured data. The three numerical data points for Pr = 0.71 have higher Nusselt numbers than the data for Pr = 0.56. At Re = 1530 the Prandtl number dependence is $Pr^{0.4}$, in agreement with correlations for turbulent pipe flow. At Re = 1530, the numerical result is 16 percent lower than the experimental value.

The Nusselt number difference between the conduction solution (Re = 0) and the cases for Re > 0 represents the increased thermal transport from fluid motion. We have seen that for Re < 350, the flow is steady and two-dimensional, and the grooved region is filled with a slowly turning vortex. Figure 9 shows that for this Reynolds number range, transport is only slightly greater than that due to conduction alone. For Re > 350, two-dimensional simulations are unsteady. The resulting periodic injection of fluid from the outer channel to the groove, as well as the outer channel traveling wave motion, increases the heat transfer beyond the levels that would be expected from an extrapolation of the lower Reynolds number, steady results. Finally, three-dimensional mixing increases heat transfer beyond levels predicted from two-dimensional wave motion.

Summary and Conclusions

Direct numerical simulations of three-dimensional flow and augmented heat transfer in a continuously grooved passage are presented for the Reynolds number Range 140 < Re < 2000. These simulations employ the spectral element technique. At Re = 325 the flow is steady and two-dimensional, but it exhibits a series of transitions with increasing Reynolds number. At Re = 350, it exhibits two-dimensional traveling waves. For Re = 482, the flow is observed to have regular variations in the cross-stream (z) direction and to be time periodic. At Re = 748, the flow exhibits irregularities in the z-direction, and more than one dominant frequency is observed. Finally, for Re = 1530, the three-dimensional flow structure is very irregular and a broad band of flow frequencies is observed.

Two-dimensional simulations of grooved channel flows predict laminar-like (unmixed) friction factor and Nusselt number versus Reynolds number behaviors. Three-dimensional simulations are required to (1) correctly predict the Reynolds-number-independent friction factor of the current destabilized flow, and (2) accurately quantify the heat and momentum transport behavior for Re > 500.

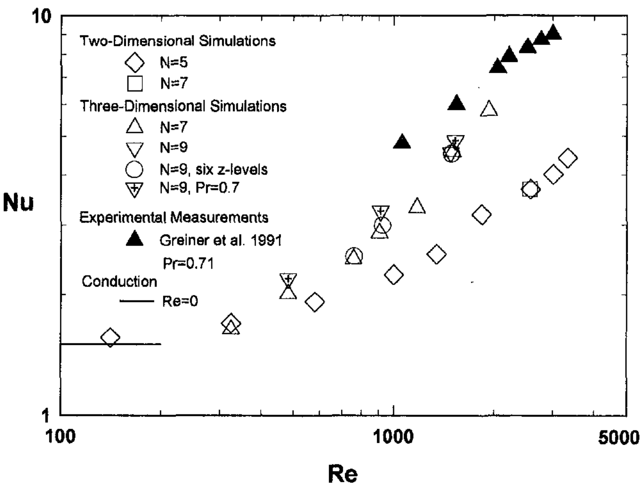

Fig. 9 Nusselt number versus Reynolds number from numerical simulations, experimental measurements, and theoretical predictions

Acknowledgments

This work is supported by National Science Foundation grant number CTS-9501502. The work of P. F. Fischer is supported in part by NSF Grant ASC-9405403. Caltech provides time on the Intel Delta under NSF Cooperative Agreement CCR-8809615.

References

Amon, C. H., 1993, "Spectral Element-Fourier Method of Transitional Flows in Complex Geometries," *AIAA Journal,* Vol. 31, pp. 42–48.

Amon, C. H., Majumdar, D., Herman, C. V., Mayinger, F., Mikic, B. B., and Sekulic, D. P., 1992, "Experimental and Numerical Investigation of Oscillatory Flow and Thermal Phenomena in Communicating Channels," *International J. Heat Mass Transfer,* Vol. 35, pp. 3115–3129.

Amon, C. H., and Patera, A. T., 1989, "Numerical Calculation of Stable Three-Dimensional Tertiary States in Groove-Channel Flow," *Physics of Fluids A,* Vol. 1, No. 12, pp. 2005–2009.

Blackburn, H. M., and Karniadakis, G. E., 1993, "Two- and Three-Dimensional Simulations of Vortex-Induced Vibrations of a Circular Cylinder," *Proceedings of the Third International Offshore and Polar Engineering Conference,* Singapore, pp. 715–720.

Fischer, P. F., and Patera, A. T., 1991, "Parallel Spectral Element Solutions of the Stokes Problem," *J. Comput. Phys.,* Vol. 92, pp. 380–421.

Fischer, P. F., and Patera, A. T., 1992, "Parallel Spectral Element Solutions of Eddy-Promoter Channel Flow," *Proceedings of the European Research Community on Flow Turbulence and Computation Workshop,* Lausanne, Switzerland, Cambridge University Press, Cambridge, UK, pp. 246–256.

Fischer, P. F., and Ronquist, E. M., 1994, "Spectral Element Methods for Large Scale Parallel Navier-Stokes Calculations," *Comp. Meth. Mech. Engr.,* pp. 69–76.

Fox, R. W. and McDonald, A. T., 1985, *Introduction to Fluid Mechanics,* John Wiley and Sons, New York.

Ghaddar, N. K., Korczak, K., Mikic, B. B., and Patera, A. T., 1986, "Numerical Investigation of Incompressible Flow in Grooved Channels. Part 1: Stability and Self-Sustained Oscillations," *J. Fluid Mech.,* Vol. 168, pp. 541–567.

Greiner, M., Chen, R.-F., and Wirtz, R. A., 1990, "Heat Transfer Augmentation Through Wall-Shaped-Induced Flow Destabilization," JOURNAL OF HEAT TRANSFER, Vol. 112, pp. 336–341.

Greiner, M., Chen, R.-F., and Wirtz, R. A., 1991, "Passive Heat Transfer Enhancement on a Flat Surface in a Grooved Channel," *Proceedings of the ASME/JSME Thermal Engineering Joint Conference,* Reno, NV, Vol. 3, pp. 97–101.

Guzman, A. H., and Amon, C. H., 1994, "Transition to chaos in converging-diverging channel flows: Ruelle-Takens-Newhouse scenario," *Phys. Fluids,* Vol. 6, pp. 1994–2002.

Guzman, A. H., and Amon, C. H., 1996, "Dynamical flow characterization of transitional and chaotic regimes in converging-diverging channels," *J. Fluid Mech.,* Vol. 321, pp. 25–57.

Karniadakis, G. E., Mikic, B. B., and Patera, A. T., 1988, "Minimum-Dissipation Transport Enhancement by Flow Destabilization: Reynolds Analogy Revisited," *J. Fluid Mech.,* Vol. 192, pp. 365–391.

Kozlu, H., Mikic, B. B., and Patera, A. T., 1988, "Minimum-dissipation heat removal by scale-matched flow destabilization," *Int. J. Heat Mass Transfer,* Vol. 10, pp. 2023–2032.

Maday, Y., and Patera, A. T., 1989, "Spectral Element Methods for the Navier-Stokes Equations," *State of the Art Surveys on Computational Mechanics,* A. K. Noor and J. T. Oden, eds., ASME, New York, pp. 71–143.

Majumdar, D., and Amon, C. H., 1997, "Oscillatory Momentum Transport Mechanisms in Transitional Complex Geometry Flows," ASME *Journal of Fluids Engineering,* Vol. 119, pp. 29–35.

Orszag, S. A. and L. C. Kells, 1980, "Transition to Turbulence in Plane Poiseuille Flow and Plan Couette Flow," *J. Fluid Mech.,* Vol. 96, pp. 159–205.

Patera, A. T., 1984, "A Spectral Element Method for Fluid Dynamics; Laminar Flow in a Channel Expansion," *J. Comput. Phys.,* Vol. 54, pp. 468–488.

Roberts, E. P. L., 1994, "A Numerical and Experimental Study of Transition Processes in an Obstructed Channel Flow," *J. Fluid Mech.,* Vol. 260, pp. 185–209.

Webb, R. L., 1994, *Principles of Enhanced Heat Transfer,* John Wiley and Sons, New York.

S. Acharya
Mem. ASME

S. Dutta

T. A. Myrum

Mechanical Engineering Department,
Lousiana State University,
Baton Rouge, LA 70803

Heat Transfer in Turbulent Flow Past a Surface-Mounted Two-Dimensional Rib

Heat transfer measurements and predictions are reported for a turbulent, separated duct flow past a wall-mounted two-dimensional rib. The computational results include predictions using the standard $k-\epsilon$ model, the algebraic-stress (A-S) functionalized $k-\epsilon$ model, and the nonlinear $k-\epsilon$ model of Speziale (1987). Three different prescriptions for the wall functions, WF I, WF II, and WF III given, respectively, by Launder and Spalding (1974), Chieng and Launder (1980), and Johnson and Launder (1982), are examined. The experiments include laser-Doppler flow measurements, temperature measurements, and local Nusselt number results. For WF I, the nonlinear model yielded improved predictions and displayed the most realistic predictions of the streamwise turbulence intensity and the mean streamwise velocities near the high-speed edge of the separated layer and downstream of reattachment. However, no significant improvements in the surface heat transfer predictions were obtained with the nonlinear model. With WF I and WF II, the models underpredicted the local Nusselt numbers and overpredicted the flow temperatures. With WF III, the predicted results agree with the experimental Nusselt numbers quite well up to reattachment, after which it substantially overpredicted the Nusselt numbers. The A-S functionalized model using only the high Re formulation and curvature corrections in Cartesian coordinates improved the temperature predictions substantially, with the predicted flow temperatures agreeing quite well with the measured temperatures.

Introduction

Ribs are commonly used in internal duct flows to enhance the heat transfer from the surface by providing a greater surface area for heat transfer and by periodically interrupting the wall boundary layer causing flow separation and reattachment. The focus of the present study is on the heat transfer for turbulent flow past a two-dimensional rib mounted on a horizontal heated surface. Measurements have been made of the surface heat transfer and temperature and of velocities and temperatures in the flow. Predictions are obtained with the standard $k-\epsilon$ model and two recently reported, improved variants of the standard $k-\epsilon$ model. Since near-wall effects play an important role in dictating the surface heat transfer, a number of wall functions are examined. All predictions are compared with the data of this study to provide a perspective on the performance of the two-equation model variants and the wall-function models that account for near-wall effects.

Numerous experimental studies have been reported for flows past two-dimensional ribs. Bergeles and Athanassiadis (1983) and Antoniou and Bergeles (1988) used a single-wire anemometer to study the flow past a two-dimensional rib. Flow visualizations conducted by Durst and Rastogi (1980) revealed that the length of the downstream recirculation region ranges from about 5 to 16 rib heights, depending on the rib shape and degree of flow blockage caused by the rib. Tropea and Gackstatter's (1985) laser-Doppler measurements behind fences and blocks essentially confirmed the findings of Bergeles and Athanassiadis (1983) and Durst and Rastogi (1980) for low-blockage ratios. The laser-Doppler measurements of Liou and Kao (1988) revealed that the peak turbulence intensity occurred within the downstream recirculation zone at about 1.5 rib heights upstream of reattachment. The measurements of Antoniou and Bergeles (1988), Phataraphruk and Logan (1979), and Castro (1979) showed that after reattachment, the development of the shear layer occurs over a long distance.

A number of numerical studies have also been performed in order to predict the flow past two-dimensional ribs. By incorporating streamline curvature effects in the linear $k-\epsilon$ model, Durst and Rastogi (1980) obtained improved predictions for the reattachment length. Benodekar et al. (1985) used a linear $k-\epsilon$ model which incorporated curvature correction through the functionalization of C_μ. Chung et al. (1987) and Park and Chung (1989) focused on developing a curvature correction to the linear $k-\epsilon$ model that took into account a number of experimental observations not previously accounted for. Lee et al. (1988) used the linear $k-\epsilon$ model with the curvature correction developed by Leschziner and Rodi (1981) to improve the predictions of the heat transfer and flow between successive ribs in the periodically developed region of a ribbed annulus.

Gooray (1982) and Gooray et al. (1982, 1983) took account of both the curvature of the flow and near-wall damping effects by equating the expressions for the Boussinesq approximations for the turbulent stresses with the corresponding algebraic-stress approximations, and functionalizing the expressions for some of the empirical model constants in the $k-\epsilon$ model (referred to as the algebraic-stress (A-S) functionalized $k-\epsilon$ model in this paper). They further proposed a double-pass procedure for the model in which a low Re version of the model is used downstream of reattachment and a high Re version of the model is used upstream of reattachment.

In an attempt to obtain better heat transfer predictions with the standard $k-\epsilon$ model, a number of investigators have employed wall functions to model the near-wall effects which govern the heat transport. For a separated flow through an abrupt pipe expansion, Chieng and Launder (1980) proposed an improvement over the standard wall function, proposed by Launder and Spalding (1974), by defining y^+ on the basis of the value of the turbulent kinetic energy k_v at the edge of the viscous sublayer. Johnson and Launder (1982) further corrected Chieng

---

Contributed by the Heat Transfer Division for publication in the JOURNAL OF HEAT TRANSFER. Manuscript received by the Heat Transfer Division, Jan. 13, 1997; revision received, Mar. 20, 1998. Keywords: Forced Convection, Modeling and Scaling, Turbulence. Associate Technical Editor: J. C. Han.

and Launder's (1980) work by making the sublayer Reynolds number Re_v a function of the change in the turbulent kinetic energy across the sublayer.

All of the studies just cited employed the linear $k-\epsilon$ model (Launder and Spalding, 1974) which is based on the Boussinesq approximation of the Reynolds stresses. The Boussinesq approximation retains only the first-order velocity derivatives and does not account for the nonisotropic behavior of the turbulent stresses. Thangam and Speziale (1991) found that nonisotropic effects play a strong role in the prediction of separated flow behavior. They also found that modifying the $k-\epsilon$ model to include higher-order nonisotropic effects yields good predictions for backstep flows. This involved using the nonlinear $k-\epsilon$ model of Speziale (1987) which accounts for nonisotropic effects by including the second-order derivatives of the main and cross-stream velocities. Improved predictions of separated flows past backsteps using the nonlinear $k-\epsilon$ model have also been obtained by Speziale and Ngo (1988) and Thangam and Hur (1991). Acharya et al. (1994) obtained improved flow predictions using the nonlinear model for flow past a rib.

The main objectives of the present investigation are (1) to obtain detailed measurements of the heat transfer and temperature in the flow past a wall-mounted, two-dimensional rib, (2) to evaluate the ability of the A-S functionalized $k-\epsilon$ model and the nonlinear $k-\epsilon$ model to predict the flow, temperature, and heat transfer behavior in the vicinity of the rib, and (3) to evaluate the performance of the wall functions of Launder and Spalding (1974) (WF I), Chieng and Launder (1980) (WF II), and Johnson and Launder (1982) (WF III) in predicting the heat transfer behavior.

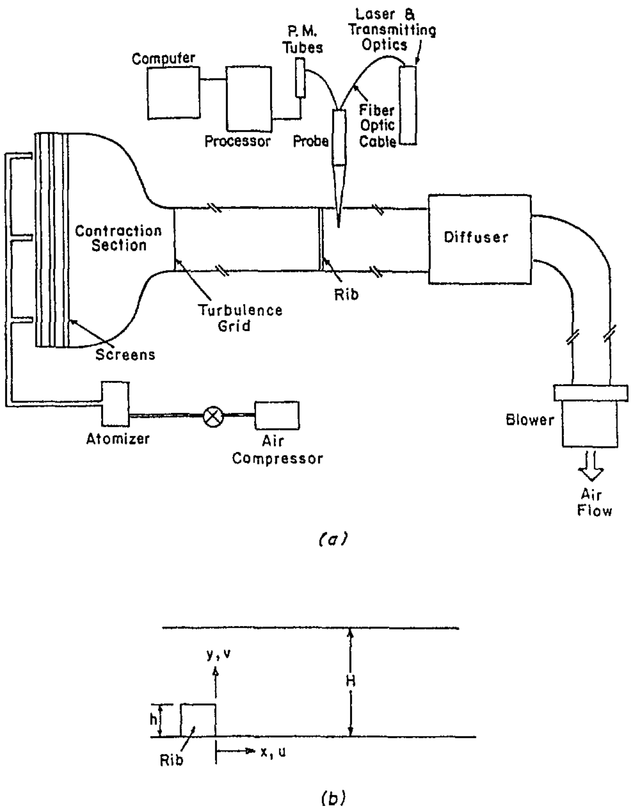

Fig. 1 (*a*) Schematic of the experimental setup (*b*) test section and computational domain

The Experimental Setup and Procedure

The experimental setup and flow measurement system are shown in Fig. 1(*a*). Air was drawn into the duct through a 5.25-to-1 contraction section containing a honeycomb baffle and four screens. The test section (see Fig. 1(*b*)) was placed 40 hydraulic diameters downstream of the duct inlet. It was 101.6 cm long, 30 cm wide, and 6.1 cm high, and was followed by an after-duct diffuser and a blower, operating in the suction mode. A 6.35 mm × 6.35 mm square rib was mounted on the lower wall, just downstream of the inlet to the test section, using double-sided tape.

The flow measurements were performed using a two-color DANTEC fiber optic LDV system. Each measurement consisted of 2000 samples at each location recorded at sampling rate that varied from 25 samples/s in the near-wall recirculating region to 1500 samples/s at the outer edge of the shear layer. Measurements

Nomenclature

C_1, C_2, C_μ = turbulence model constants; $C_1 = 1.44$, $C_2 = 1.92$, $C_\mu = 0.09$
C_{s1}, C_{s1w}, C_{s2}, C_{s2w}, C_w = A-S functionalized model constants (Table 2)
C_D = nonlinear turbulence model constant, $C_D = 1.68$
D = hydraulic diameter, $D = 101.6$ mm
$\bar{E}$, E^* = expressions/constants used in the low Re model
f_μ, f_ϵ = expression/constants used in the low Re model
h, H = rib height, channel height
k = turbulent kinetic energy
K = thermal conductivity of air
n = normal coordinate
Nu = local Nusselt number
P = production of turbulence kinetic energy, $\mu_t G$ (Eq. (5))
p = pressure
Pr, Pr_t = Prandtl number, turbulent Prandtl number
Q, q'' = total heat input, and surface heat flux, $Q = 85$ W, $q'' = 280$ W/m^2
R_c = radius of curvature
Re, Re_v, Re_t = Reynolds number, $\mathrm{Re} = U_o D/\nu$; sublayer Reynolds number, $\mathrm{Re}_v = y_v k_v^{1/2}/\nu$; Turbulence Reynolds number $\mathrm{Re}_t = \rho k^2/\epsilon\mu$
s = streamline coordinate
T = temperature
u, u' = streamwise velocity and its fluctuating component
U_o = freestream velocity, 3.6 m/s
v, v' = cross-stream velocity and its fluctuating component
x, y = Cartesian coordinates measured from the downstream corner of the rib
x^+, y^+ = x, y expressed in law-of-the-wall coordinates, $x^+ = x/\nu(C_\mu^{1/2}k)^{1/2}$, $y^+ = y/\nu(C_\mu^{1/2}k)^{1/2}$
x_R = reattachment length
ϵ = dissipation of kinetic energy
κ, κ^* = von Karman constant
$\kappa^* = \kappa C_\mu^{1/4}$
μ, μ_t, μ_{eff} = dynamic viscosity, turbulent viscosity, effective viscosity
ρ = density
ν = kinematic viscosity
σ_k, σ_ϵ = turbulence model constants, $\sigma_k = 1.0$, $\sigma_\epsilon = 1.3$
τ_{xx}, τ_{yy}, τ_{xy} = turbulent stresses

for sample sizes ranging from 2000 to 10,000 were performed at various locations with less than a one percent difference in the mean and rms values. As recommended by Driver and Seegmiller (1982, 1985), the mean velocities and Reynolds stresses were obtained by ensemble averaging without bias correction. The uncertainties were calculated to a 95 percent confidence level (Kline and McClintock, 1953); they were: ±3.5 percent and ±3 percent for the mean u and v velocities, ±5 percent and ±4.5 percent for the streamwise and cross-stream turbulence intensities and ±8 percent for the turbulent shear stress.

Measurements of the velocities at selected spanwise locations indicated that the flow was essentially two-dimensional in the midspan regions ($-18h < z/h < 18h$). All velocity measurements reported in this paper are at $z/h = 0$, the centerline of the wind tunnel.

For the heat transfer experiments, a constant heat flux boundary condition was simulated by dissipating dc current in a 0.025-mm thick (±10 percent) stainless steel shim epoxied to the upper surface of a plexiglass bottom wall. The rib, which spanned the entire test section width, was positioned with its upstream face flush with the leading edge of the shim. Chromel-constantan thermocouples (0.076-mm dia.), spot welded to the bottom of the shim at 5.1 mm intervals along the centerline, were used to measure the local shim temperatures. Thermocouples positioned at off-centerline locations confirmed that the spanwise temperature variation was less than four percent of the minimum shim-to-bulk-fluid temperature difference. The maximum effect of the heating current on the measured thermocouple voltage was less than 12 μV (0.2°C), which is within the uncertainty of the temperature measurement. A 0.076-mm diameter chromel-constantan thermocouple was also used to measure the flow temperatures to within a ten percent uncertainty.

Local Nusselt number results for the heated bottom wall of the test section were determined from the local convective heat flux and the measured shim temperatures. The local convective heat flux was determined by subtracting conduction and radiation heat losses from the local electric heat flux generation, which was determined from measurements of the current supplied to the shim and the temperature-dependent electrical resistivity of the shim. A finite difference procedure was used to compute the conduction losses. The temperatures measured along the shim and along the inner surfaces of the side walls and top wall of the test section were used as boundary conditions in the heat conduction code. Both the conduction and radiation heat losses were five percent of the local electric heat flux generation. The uncertainty in the local Nusselt numbers is ±5 percent.

Based on the measured temperatures, an estimate of $\mathrm{Gr}_H/\mathrm{Re}_H^2$ was made and found to be less than 0.002. This implies that the temperature differences, and therefore the associated density differences are small, and property variations and buoyancy effects can be neglected.

Modeled Equations

The Standard $k-\epsilon$ model. The equations expressing momentum conservation for an incompressible turbulent flow are given by

$$\rho u_j \frac{\partial u_i}{\partial x_j} = -\frac{\partial p}{\partial x_i} + \mu \frac{\partial}{\partial x_j}\left(\frac{\partial u_i}{\partial x_j}\right) + \frac{\partial \tau_{ij}}{\partial x_j} \qquad (1)$$

where τ_{ij} represent the turbulent stresses.

The standard $k-\epsilon$ model (Launder and Spalding, 1974) is based on the Boussinesq approximation:

$$\tau_{ij} = -\frac{2}{3}\rho k \delta_{ij} + \mu_t\left(\frac{\partial u_i}{\partial x_j} + \frac{\partial u_j}{\partial x_i}\right). \qquad (2)$$

The effective viscosity μ_{eff} is defined as

$$\mu_{\mathrm{eff}} = \mu + \mu_t, \quad \mu_t = \rho C_\mu\,|f_\mu|\,\frac{k^2}{\epsilon} \qquad (3)$$

where C_μ is a constant (typically 0.09) and f_μ is a near-wall damping factor. The quantities bounded by vertical bars in the above equation and in the equations that follow are included only in the low Re version of the model.

The modeled transport equations for the turbulent kinetic energy and its dissipation (k and ϵ) are expressed as

$$\rho u_j \frac{\partial k}{\partial x_j} = \frac{\partial}{\partial x_j}\left(\left(|\mu| + \frac{\mu_t}{\sigma_k}\right)\frac{\partial k}{\partial x_j}\right) + \mu_t G - \rho\epsilon - \left|2\mu\left(\frac{\partial k^{1/2}}{\partial y}\right)^2\right|$$

$$\rho u_j \frac{\partial \epsilon}{\partial x_j} = \frac{\partial}{\partial x_j}\left(\left(|\mu| + \frac{\mu_t}{\sigma_\epsilon}\right)\frac{\partial \epsilon}{\partial x_j}\right) + C_1\mu_t G\frac{\epsilon}{k}$$

$$- C_2\rho\frac{\epsilon^2}{k}\,|f_\epsilon| + \left|E\frac{\mu\mu_t}{\rho}\left(\frac{\partial^2 u}{\partial y^2}\right)^2\right|. \qquad (4)$$

In Eq. (4), the production of kinetic energy P ($= \mu_t G$), in Cartesian coordinates, is

$$\mu_t G = \tau_{ij}\left(\frac{\partial u_i}{\partial x_j}\right)$$

$$= \mu_t\left[2\left\{\left(\frac{\partial u}{\partial x}\right)^2 + \left(\frac{\partial v}{\partial y}\right)^2\right\} + \left(\frac{\partial u}{\partial y} + \frac{\partial v}{\partial x}\right)^2\right]. \qquad (5)$$

The modeled temperature transport equation is again based on the Boussinesq approximation, $\overline{-u_i'T'} = (\mu_t/\rho\ \mathrm{Pr}_t)(\partial T/\partial x_i)$, and is given by

$$\rho u\frac{\partial T}{\partial x} + \rho v\frac{\partial T}{\partial y} = \frac{\partial}{\partial x}\left(\mu_{\mathrm{eff}}\frac{\partial T}{\partial x}\right) + \frac{\partial}{\partial y}\left(\mu_{\mathrm{eff}}\frac{\partial T}{\partial y}\right) \qquad (6)$$

where the effective diffusion coefficient is $\mu_{\mathrm{eff}} = \mu/P_r + \mu_t/\mathrm{Pr}_t$.

To account for the near-wall effects in the standard high Re $k-\epsilon$ model, wall functions are used. In this work, three different wall functions, denoted by WF I, WF II, and WF III, will be considered in order to assess their effect on the heat transfer predictions:

WF I (Launder and Spalding, 1974): This requires the first interior grid point to be at a distance of $y^+ > 11.5$ from the wall and requires modifying the diffusion coefficient at the wall to satisfy the law-of-the-wall relationship. Thus, for the velocity component parallel to the wall, the diffusion coefficient at the wall is modified as

$$\mu_{\mathrm{eff\ at\ wall}} = \frac{\mu y^+}{2.5\ln(9y^+)} \quad \text{where} \quad y^+ = \rho\frac{y}{\mu}(C_\mu^{1/2}k)^{1/2} \qquad (7)$$

where y and k in the above equation are defined, respectively, as the normal distance from the wall and the turbulence kinetic energy at the first grid point away from the wall. This is tantamount to assuming Couette flow in equilibrium near the wall, with the velocity near the wall given by

$$\frac{u}{\sqrt{\tau_w/\rho}} = \frac{1}{\kappa}\ln \bar{E}\frac{y}{\nu}(C_\mu^{1/2}k)^{1/2}. \qquad (8)$$

Note that the wall function approach adopted in this paper, as specified by Eq. (7), requires the modification of the wall diffusion coefficient, and together with the specification of no-slip wall conditions, will yield wall-shear consistent with the Couette flow analysis. The normal distance from the wall, used in computing y^+ in Eq. (7) requires special attention near rib corners where the near-wall point is in the vicinity of two walls.

In these cases, an effective y, defined by Eq. (21) with y_1 and y_2 representing distances from the two walls, is first computed before Eq. (7) is used to calculate y^+.

WF II (Chieng and Launder, 1980): This defines y^+ on the basis of k_v (the value of k at the edge of the viscous sublayer) instead of k at the near-wall grid point. Thus, Eq. (8) is replaced by

$$\frac{uk_v^{1/2}}{\tau_w/\rho} = \frac{1}{\kappa^*} \ln E^* \frac{y}{\nu} (k_v)^{1/2}. \tag{9}$$

The sublayer thickness $y_v^+ = (y_v/\nu)(k_v)^{1/2}$ (which can also be interpreted to be the sublayer Reynolds number Re_v) is assumed to be a constant equal to 20. Special care has to paid to the evaluation of the production and dissipation rates of k at the near-wall node (Chieng and Launder, 1980). Sindir (1982) also details the implementation of this wall function for a flow past a backward-facing step. This procedure was followed in the present study.

WF III (Johnson and Launder, 1982): In WF II, the sublayer Reynolds number Re_v is taken as constant ($= 20$). Johnson and Launder (1982) have shown that WF II (with constant Re_v) does not improve upon the heat transfer predictions obtained using WF I. They redefined Re_v as

$$\mathrm{Re}_v = \frac{20}{1 + C_R\lambda}; \quad C_R = 3.1; \quad \lambda = \frac{k_v - k_w}{k_v} \tag{10}$$

where k_w is the value of k at wall obtained by extrapolation.

The same wall diffusion coefficient for the temperature is used for all three wall functions:

$$\frac{\mu_{\text{eff at wall}}}{\mathrm{Pr}_t} = \frac{\mu}{\mathrm{Pr}_t} \frac{y^+}{2.5 \ln (9y^+) + \mathrm{Pr}_{\mathrm{fn}}},$$

$$\mathrm{Pr}_{\mathrm{fn}} = \frac{9\left(\dfrac{\mathrm{Pr}}{\mathrm{Pr}_t} - 1\right)}{\left(\dfrac{\mathrm{Pr}}{\mathrm{Pr}_t}\right)^{1/4}}. \tag{11}$$

The near-wall dissipation value is prescribed from equilibrium as $\epsilon = C_\mu^{3/4} k^{3/2}/y$, and the wall gradients of k and ϵ are set to zero.

As noted earlier, the quantities f_μ, f_ϵ, and E are used in the low Re model. Two common choices for these quantities have been proposed by Jones and Launder (1987) and Nagano and Hishida (1987), and are tabulated in Table 1. Unless otherwise noted, the prescription of Jones and Launder (1972) has been used in the present work.

The Nonlinear k–ϵ Model. The nonlinear k–ϵ model of Speziale (1987) retains the tensorially invariant eddy viscosity of the standard k–ϵ model and adds the second-order derivatives of the streamwise and cross-stream velocities to the Boussinesq approximation to account for the nonisotropic behavior in the turbulent stresses. These extra second-order terms are incorporated as source terms in the momentum equations and in the k and ϵ transport equations. The source terms are kept frame indifferent, and they can be included in a standard computer program that solves Navier-Stokes-type equations.

For two-dimensional flows, the individual components of the stress terms in the nonlinear model (Speziale, 1987) can be written in Cartesian coordinates as

$$\tau_{xx} = -\frac{2}{3}\rho k + 2\rho C_\mu \frac{k^2}{\epsilon}\frac{\partial u}{\partial x} + 4C_D\rho C_\mu^2 \frac{k^3}{\epsilon^2}\left[-\frac{1}{3}\left(\frac{\partial u}{\partial x}\right)^2 - \frac{7}{12}\left(\frac{\partial u}{\partial y}\right)^2 - \frac{1}{6}\left(\frac{\partial u}{\partial y}\frac{\partial v}{\partial x}\right) + \frac{5}{12}\left(\frac{\partial v}{\partial x}\right)^2 + t_1\right] \tag{12}$$

$$\tau_{yy} = -\frac{2}{3}\rho k + 2\rho C_\mu \frac{k^2}{\epsilon}\frac{\partial v}{\partial y} + 4C_D\rho C_\mu^2 \frac{k^3}{\epsilon^2}\left[-\frac{1}{3}\left(\frac{\partial v}{\partial y}\right)^2 - \frac{7}{12}\left(\frac{\partial v}{\partial x}\right)^2 - \frac{1}{6}\left(\frac{\partial u}{\partial y}\frac{\partial v}{\partial x}\right) + \frac{5}{12}\left(\frac{\partial u}{\partial y}\right)^2 + t_2\right] \tag{13}$$

$$\tau_{xy} = \rho C_\mu \frac{k^2}{\epsilon}\left(\frac{\partial u}{\partial y} + \frac{\partial v}{\partial x}\right) + 4C_D\rho C_\mu^2 \frac{k^3}{\epsilon^2}\left[-\frac{\partial u}{\partial y}\frac{\partial v}{\partial y} - \left(\frac{\partial u}{\partial x}\frac{\partial v}{\partial x}\right) + t_3\right] \tag{14}$$

where

$$t_1 = \frac{\partial}{\partial x}\left(u\frac{\partial u}{\partial x}\right) + \frac{\partial}{\partial y}\left(v\frac{\partial u}{\partial x}\right);$$

$$t_2 = \frac{\partial}{\partial x}\left(u\frac{\partial v}{\partial y}\right) + \frac{\partial}{\partial y}\left(v\frac{\partial v}{\partial y}\right);$$

$$t_3 = \frac{\partial}{\partial x}\left(u\frac{1}{2}\left(\frac{\partial u}{\partial y} + \frac{\partial v}{\partial x}\right)\right) + \frac{\partial}{\partial y}\left(v\frac{1}{2}\left(\frac{\partial u}{\partial y} + \frac{\partial v}{\partial x}\right)\right). \tag{15}$$

The nonlinear model also requires that wall functions be used to account for near-wall effects. In this study, only WF I (Eq. (7)) was used for the nonlinear model.

The predictions by the nonlinear model showed minor kinks in the profiles of the turbulent stresses when t_1, t_2, and t_3 were included in Eqs. (12), (13), and (14), respectively. Speziale and Ngo (1988) observed that dropping these terms from the expressions for turbulent stresses in the nonlinear k–ϵ model reduced the predicted recirculation length downstream of the backstep by 6.25 percent but had a relatively small effect on

Table 1 Low Re model parameters

Parameter	Jones and Launder, 1972	Nagano and Hishida, 1987
f_μ	$\exp\left(-\frac{A_m}{1+\mathrm{Re}_t A_r}\right)$	$\left(1-\exp\left(-\frac{y^+}{26.5}\right)\right)^2$
f_ϵ	$1-0.222\exp\left(-\frac{\mathrm{Re}_t^2}{36}\right)$	$1-0.222\exp\left(-\frac{\mathrm{Re}_t^2}{36}\right)$
E	2	$1-f_\mu$

the turbulent stress intensity. In the present study, a 5.4 percent decrease was noted in the predicted recirculation length by neglecting the second-order derivatives and no significant changes in the rms velocity fluctuations (less than one percent) were observed. Therefore, for the results presented in this paper, t_1, t_2, and t_3 are dropped from Eqs. (12)–(14), respectively.

Algebraic Stress (A-S) Based Functionalized $k-\epsilon$ Model. In deriving the equations for the A-S functionalized model, this study follows the approach of Gooray (1982) in equating the algebraic stress expressions for the turbulent shear stress with the corresponding Boussinesq approximation. This is done in both the streamline (s, n) coordinate system for flow upstream of reattachment, and in (x, y) coordinate system for flow downstream of reattachment. However, unlike Gooray (1982), a coordinate transformation was used to obtain the stress expressions in the s-n coordinate system, and further, all expressions and constants for the individual stress components are consistent with those given by Launder et al. (1975). The A-S functionalized expressions in the present model are therefore different, and more consistent, compared to those presented by Gooray (1982).

The Boussinesq approximation for the turbulent shear stress in s-n coordinates is given by

$$-\overline{u_s'u_n'} = C_\mu \frac{k^2}{\epsilon}\left(\frac{\partial u_s}{\partial n} - \frac{u_s}{R_c}\right) \tag{16}$$

where R_c is the local radius of curvature. The corresponding algebraic stress expression (Launder, 1971), in s-n coordinates, obtained following a coordinate transformation, is given by (see Dutta and Acharya, 1993; Lee et al., 1988)

$$-\overline{u_s'u_n'} = \frac{\frac{2}{3}(k^2/\epsilon)\Lambda'[\Lambda'(P/\epsilon) - 1]\left[\frac{\partial u_s}{\partial n} - \frac{u_s}{R_c}\right]}{S_4} \tag{17}$$

where

$$S_4 = 1 + \frac{k^2}{\epsilon^2}\left\{8\Lambda'^2 \frac{u_s}{R_c}\left(\frac{\partial u_s}{\partial n} + \frac{u_s}{R_c}\right) + 4\Lambda''(\Lambda' + \Lambda'')\left(\frac{\partial u_s}{\partial n} + \frac{3u_s}{R_c}\right)^2\right\} \tag{18}$$

$$\Lambda' = \frac{1 - C_{S2}}{\frac{P}{\epsilon} - 1 + C_{S1} - C_{S1w}f\left(\frac{l}{x}\right)},$$

$$\Lambda'' = \frac{C_{S2w}f\left(\frac{l}{x}\right)\Lambda'}{1 - C_{S2}} \tag{19}$$

and C_{S1}, C_{S2}, C_{S1w}, C_{S2w} are model constants (Table 2). From dimensional and intuitive arguments, $f(l/x)$ which represents a function that accounts for near wall viscous damping, can be written as

$$f\left(\frac{l}{x}\right) = \frac{1}{C_w}\frac{k^{3/2}}{\epsilon}\left[\left(\frac{1}{x}\right)^{1/m} + \left(\frac{1}{y}\right)^{1/m}\right]^m \tag{20}$$

where x is the distance from the vertical rib face ($1/x$ is set to zero if the location of interest is above the rib) and y is the effective mean of y_1 and y_2, the vertical distances from the lower and upper walls, calculated as

$$\left(\frac{1}{y}\right)^{1/m} = \left(\frac{1}{y_1}\right)^{1/m} + \left(\frac{1}{y_2}\right)^{1/m}. \tag{21}$$

The constants C_w and m are also given in Table 2.

Table 2 Constants for A-S functionalized $k-\epsilon$ model

Constant	Value	Reference
C_{S1}	1.8	Sindir, 1982
C_{S2}	0.6	Sindir, 1982
C_{S1w}	0.305	Launder, Reece and Rodi, 1975
C_{S2w}	0.037	Launder, Reece and Rodi, 1975
C_W	2.44	Gooray, 1982
C_{T1}	3.2	Amano and Chai, 1988
C_{T2}	0.5	Amano and Chai, 1988
C_{T1w}	0.244	Amano and Chai, 1980
A_m	3.4	Gooray, 1982
A_r	0.02	Jones and Launder, 1972
m	2.0	Gooray, 1982

Equating $-\overline{u_s'u_n'}$, from Eq. (16) (the Boussinesq approximation), with Eq. (17) (the algebraic stress expressions) leads to a functionalized expression for C_μ:

$$C_\mu = \frac{2}{3}\Lambda'\left[\Lambda'\left(\frac{P}{\epsilon}\right) - 1\right]\Big/ S_4. \tag{22}$$

Note that the expression for S_4 (Eq. (18)) used in Eq. (22) above is different from that reported by Gooray and co-workers. The difference is due to the fact that in the present work, a coordinate transformation has been used to express the shear stress $-\overline{u_s'u_n'}$, while Gooray and co-workers directly expressed $-\overline{u_s'u_n'}$ from the Cartesian expression for $-\overline{u_i'u_j'}$ by replacing the (i, j) indices with (s, n) indices.

In the x-y coordinate system, a similar approach to that above leads to the following expression for C_μ (Dutta and Acharya 1993):

$$C_\mu = \frac{\frac{2}{3}\left(\Lambda'\frac{P}{\epsilon} - 1\right)\left\{-\Lambda' - 2\Lambda'' + \Lambda'\frac{k}{\epsilon}2A\left(\frac{\partial v}{\partial x} - \frac{\partial u}{\partial y}\right)\Big/\left(\frac{\partial u}{\partial y} + \frac{\partial v}{\partial x}\right)\right\}}{1 - \frac{k^2}{\epsilon^2}\frac{2\alpha\beta}{\left(1 + \frac{k}{\epsilon}2A\right)} - \frac{k^2}{\epsilon^2}\frac{2\alpha\beta}{\left(1 - \frac{k}{\epsilon}2A\right)}\left\{1 - \left(\frac{k}{\epsilon}2A\right)^2\right\}} \tag{23}$$

where

$$A = -\Lambda'\frac{\partial v}{\partial y} - 2\Lambda''\frac{\partial v}{\partial y}; \quad \alpha = -\Lambda'\frac{\partial v}{\partial x} - \Lambda''\left(\frac{\partial v}{\partial x} + \frac{\partial u}{\partial y}\right);$$

$$\beta = -\Lambda'\frac{\partial u}{\partial y} - \Lambda''\left(\frac{\partial v}{\partial x} + \frac{\partial u}{\partial y}\right). \tag{24}$$

The values of all constants used in the above model are given in Table 2, and it should be noted that no attempt has been made to change any of the constants from the accepted values in the literature (Launder, 1971).

Since the algebraic stress model accounts for the streamline curvature, pressure-strain interactions, and near-wall damping, the functionalized forms for $C\mu$ (Eqs. (22) and (23)), therefore, incorporate these effects. The use of these A-S functionalized forms is, therefore, a better choice than the constant value of 0.09 commonly employed.

The functionalization of the turbulent Prandtl number follows the procedure described above. The Boussinesq approximation for the turbulent scalar flux, $-\rho\overline{u_n'T'}$ in s-n coordinates and

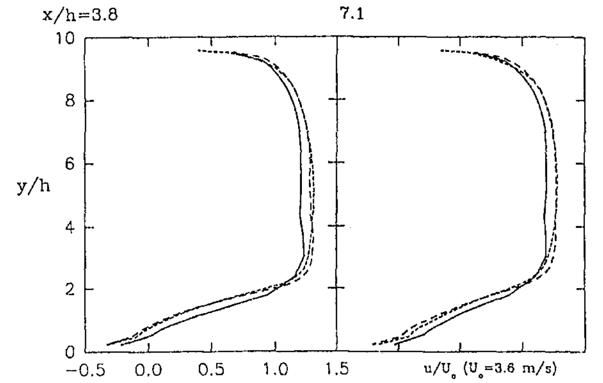

Fig. 2 u/U_o **plots for different grid distributions; standard k-ϵ model case III (——— 75 × 28, --- 175 × 88, ----- 275 × 150)**

$-\rho\overline{v'T'}$ in x-y coordinates, is equated with the algebraic stress approximation, and an expression for the turbulent Prandtl number is derived (Dutta and Acharya 1993). The expression in s-n coordinates is

$$\mathrm{Pr}_t = C_\mu \frac{ST_1}{ST_2} \tag{25}$$

where

$$ST_1 = 1 + 2\left(\phi'_T \frac{k}{\epsilon}\right)^2 \frac{u_s}{R_c}\left(\frac{\partial u_s}{\partial n} + \frac{u_s}{R_c}\right);$$

$$\phi'_T = \phi_T(1 - C_{T2});$$

$$\phi_T = \frac{1}{C_{T1} + C_{T1w} f\left(\frac{l}{x}\right) + \frac{1}{2}\left(\frac{P}{\epsilon} - 1\right)} \tag{26}$$

$$ST_2 = -2\,\frac{\phi_T}{\epsilon}\left[\frac{C_\mu k^2}{\epsilon}\left(\frac{\partial u_s}{\partial n} - \frac{u_s}{R_c}\right)\left(\frac{u_s}{R_c}(2\Lambda' + \phi'_T)\right.\right.$$
$$\left.\left. + \left(\frac{\partial u_s}{\partial n} + \frac{3u_s}{R_c}\right)\Lambda''\right) + \frac{1}{3}\epsilon\left(\Lambda'\frac{P}{\epsilon} - 1\right)\right]. \tag{27}$$

In x-y coordinate system, the expression for Pr_t is given by

$$\mathrm{Pr}_t = \frac{C_\mu\left[\left(1 + \frac{k}{\epsilon}\phi'_T\frac{\partial v}{\partial y}\right)\left(1 + \frac{k}{\epsilon}\phi'_T\frac{\partial u}{\partial x}\right) + \left(\phi'_T\frac{k}{\epsilon}\right)^2\frac{\partial v}{\partial x}\frac{\partial u}{\partial y}\right]}{\frac{\phi_T}{k}\overline{v'^2}\left(1 + \phi'_T\frac{k}{\epsilon}\frac{\partial u}{\partial x}\right) - \phi'_T\phi_T\frac{1}{\epsilon}\frac{\partial v}{\partial x}\overline{u'v'}}. \tag{28}$$

The values of the constants C_{T1}, C_{T2}, and C_{T1w} are based on those reported in the literature and are given in Table 2.

It is important to note that the A-S functionalized model presented here has been derived from first principles using consistent expressions. The model has been implemented in two forms. In the first form, the model has been used with the high Re formulation using wall functions. In its second form, the model has been implemented in a double-pass procedure, where in the first pass, a high Re standard k-ϵ formulation is used to predict the reattachment location, and in the second pass, downstream of reattachment, a low Re A-S functionalized formulation is used, and upstream of reattachment, the high Re A-S functionalized formulation is employed. The rationale for the double-pass approach, as explained by Gooray et al. (1985), is that while the low Re model has been noted to perform well in developing boundary layer-type situations, it does not do well in separated regions. In fact, Chieng and Launder (1980), and Yap (1987) both used the low Re model for an abrupt pipe expansion and report Nusselt numbers five to seven times higher than those measured in the vicinity of reattachment. While source terms corrections to the dissipation equation have been proposed to remedy this problem, this approach has not been used here. Rather, the two-pass formulation is used, where in the second pass, the high Re model is used in the separated region, and the low Re formulation is used only downstream of reattachment.

Computational Domain and Boundary Conditions. The computational domain is shown in Fig. 1(b). Measured inlet boundary conditions were provided for the computations. The inlet and outlet positions relative to the rib were given as $-15h/30h$. The measured velocity profile at $-15h$ (inlet) consisted of turbulent boundary layers on the top and bottom surfaces and a turbulent potential-core region in the middle. The turbulent boundary layers on the top and bottom surfaces were found to match the empirical expressions for a turbulent flat-plate velocity profile. Therefore, the following inlet profile was specified for the computations

$$\frac{u}{U_o} = \left(\frac{y}{\delta_u}\right)^{1/5.6} \quad \text{if} \quad y/\delta_u < 1 \quad \text{and} \quad y/\delta_u > \left(\frac{H}{\delta_u} - 1\right);$$

$$\frac{u}{U_o} = 1 \quad \text{if} \quad 1 \le y/\delta_u \le \left(\frac{H}{\delta_u} - 1\right) \tag{29}$$

where the boundary layer thickness δ_u and the channel height H were specified as $3.3h$ and 61 mm, respectively. The specified velocity profile fit the measured profiles to within five percent.

The measured k profile (assuming $\overline{w'^2} = \frac{1}{2}(\overline{u'^2} + \overline{v'^2})$) was used directly and the inlet ϵ profiles was specified using a com-

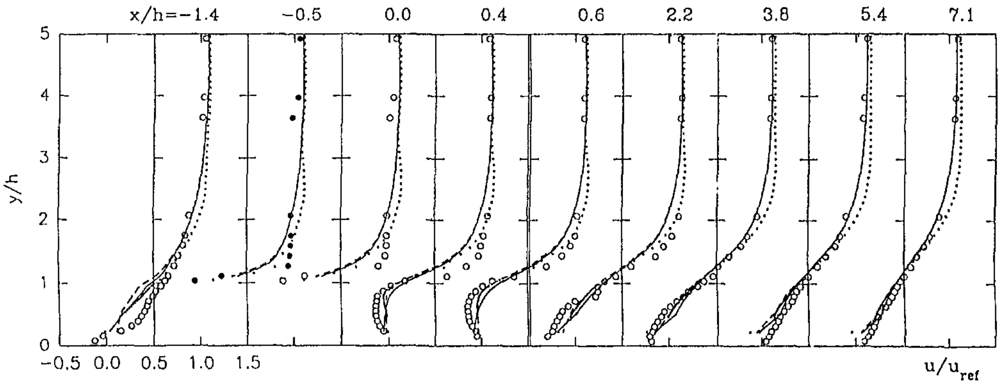

Fig. 3 Mean streamwise velocity at different x/h locations (0 experimental data, ——— standard k-ϵ model, ... nonlinear model, --- functionalized model)

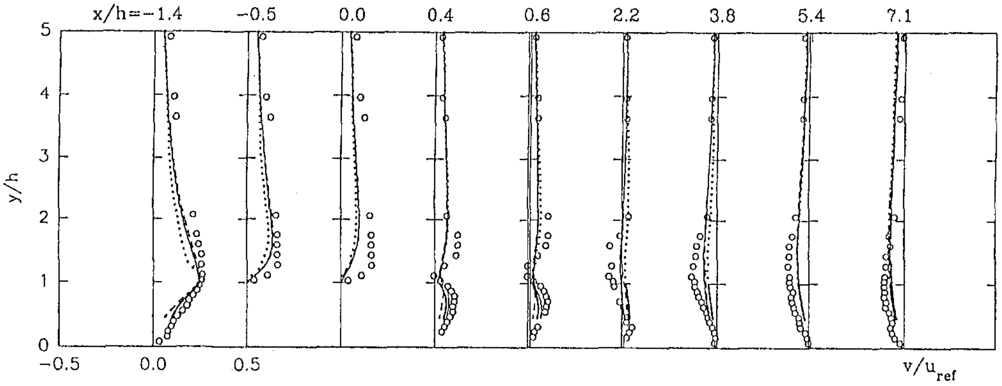

Fig. 4 Mean cross-stream velocities at different *x/h* locations (Legend: see Fig. 3).

monly employed empirical expression ($\epsilon = C_D k^{1.5}/\lambda$, where λ is a length scale and C_D is a constant) as $\epsilon = k^{1.5}/H$.

At the outlet, zero-gradient flow conditions were specified for all quantities. No-slip conditions for the velocity and the wall conditions for the turbulence quantities were specified at all of the bounding surfaces, including the rib surfaces.

For the temperature equation, the constant heat flux value measured in the present experiments was specified for the heated bottom wall, starting at the downstream face of the rib. Recall, for the experiments, the start of the heated wall coincided with the upstream face of the rib. The incoming flow was assumed to be at room temperature and zero-gradient conditions were imposed at the outlet and the top wall.

Computational Details

Numerical Scheme. The numerical solutions were obtained using the control-volume-based formulation of Patankar (1980). In this procedure, the domain is discretized by a series of control volumes, with each control volume containing a grid point. Each differential equation is expressed in an integral manner over the control volume, and profile approximations are made in each coordinate direction, leading to a system of algebraic equations that can be solved in an iterative manner. Pressure-velocity interlinkages are handled by the SIMPLER formulation (Patankar, 1980).

A box filter (Clark et al., 1979) was necessary in computing the source terms for the nonlinear model to smooth out the shear stress and velocity profiles. The velocity field was filtered once before calculating the velocity gradients that appear in the source terms. The shear stress terms were filtered three times before using them in the source or generation terms.

In the double-pass model, at the reattachment point a transition has to be made from the high Re model used upstream of the reattachment point to the low Re model. Since, in the low Re model, grid points have to be placed in the viscous sublayer ($y^+ \leq 11.5$), these grid points at the reattachment plane do not have corresponding upstream grid points in the recirculation region where wall functions that require the first grid point to be outside the viscous layer are used. Thus, for the points in the viscous sublayer that are in the reattachment plane, the profiles for all variables have to be based on the variable values outside the sublayer, computed from the high Re model calculations up to the reattachment point. For the u velocity, the law of the wall $u^+ = y^+$ is used up to the first point outside the viscous sublayer. The cross-stream velocity is assumed to be zero, k is interpolated linearly from a zero value at the wall to the value computed outside the viscous sublayer, and ϵ is specified to be a uniform value obtained from the equilibrium relationship.

Grid-Independence Studies. Grid-independence studies were performed for all three models. With the standard and nonlinear $k-\epsilon$ models, results for grid sizes of 75 × 28, 175 × 88, and 275 × 150 were obtained. In all cases, a single-block grid was used, and the grid spacing in both the x and y-directions were reduced in a smooth, monotonic manner toward the rib faces. However, the y^+ value of the first grid point away from the surface has to be maintained at a value of 11.5 or greater, and this required a few trial runs and iterative adjustments of the near-wall grid points. Additional details on the grid distributions are given in Dutta (1991).

The recirculation lengths predicted by the nonlinear model on the 175 × 88 and 275 × 150 meshes were within nine percent of each other; the corresponding deviation for the standard $k-\epsilon$ model is six percent. The predictions for u/U_o at two locations, for the different grid sizes are shown in Fig. 2 for the standard $k-\epsilon$ model. Note, the agreement between two profiles

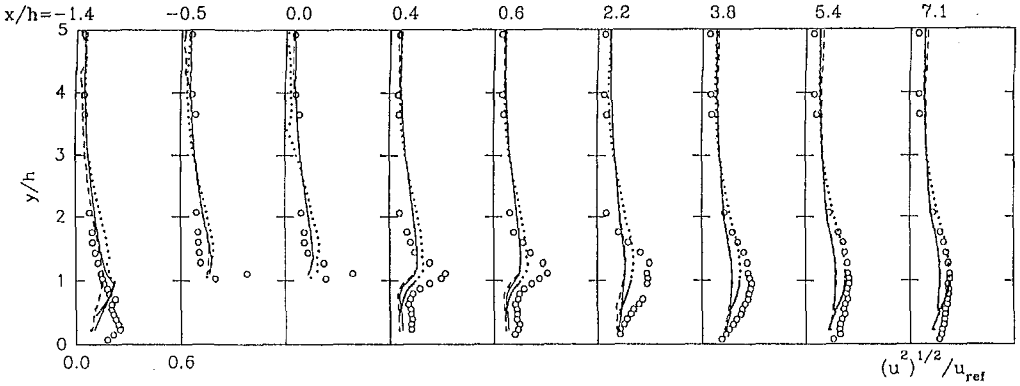

Fig. 5 Streamwise turbulence intensity at different *x/h* locations (Legend: See Fig. 3).

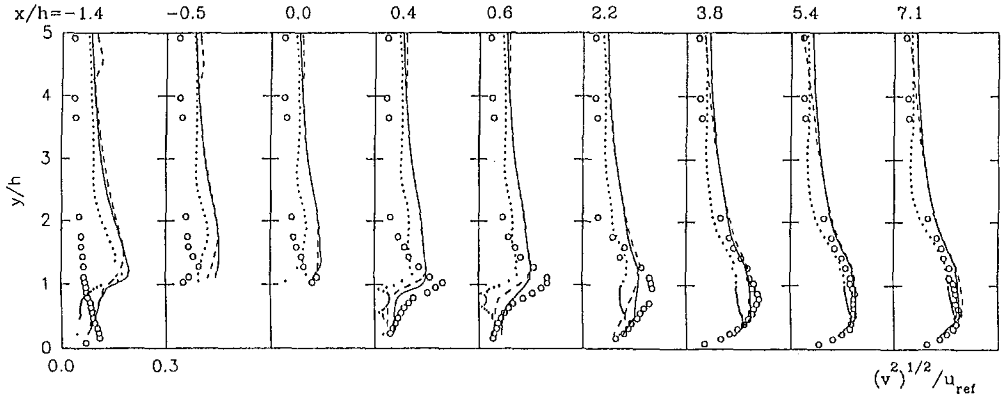

Fig. 6 **Cross-stream turbulence intensities at different *x/h* locations (Legend: See Fig. 3).**

on the 175 × 88 mesh and 275 × 150 mesh is quite good. Although the solutions on the 175 × 88 grid appear to be grid independent, all of the solutions presented in this paper were obtained using the 275 × 150 grid.

With the A-S functionalized model, results were obtained with a 115 × 49 mesh (with six grid points in the viscous sublayer) and with a 165 × 75 mesh (with 11 grid points in the viscous sublayer). The reattachment lengths predicted by the two meshes are found to be within six percent of each other. Comparisons of individual profiles on the two meshes showed excellent agreement. All A-S functionalized model results presented in this paper are from the 165 × 75 mesh calculations.

Results and Discussion

Flow Results. Figure 3 shows the measured streamwise velocity in the vicinity of the rib ($-1.4 \leq x/h \leq 7.1$), and the predictions obtained with the three turbulence models. In addition to the flow separation upstream and downstream of the rib, the measurements indicate a separated flow region blanketing the rib surface.

All three models predict the mean streamwise velocities quite well, with the nonlinear model showing the best agreement with the experimental data, particularly on the high-speed side of the separated shear layer. In the separated flow regions, before and after the rib, all three models underpredict the magnitude of the velocities, with the standard $k-\epsilon$ model showing the largest degree of error. In the downstream separated regions, the nonlinear and the A-S functionalized model predictions are in reasonably good agreement with each other. The standard $k-\epsilon$ model overpredicts the growth of the separated shear layer and leads to reattachment lengths that are smaller than experimentally observed. This behavior is consistent with that observed in flow past backsteps. The nonlinear model, as noted earlier, predicts the growth of the separated shear layer on the high-speed side particularly well, but on the low-speed side of the separated flow region, the rate of growth lags the measured growth rate, and the predicted reattachment is downstream of that observed experimentally. The A-S functionalized model predictions lie between the nonlinear model and the standard $k-\epsilon$ model predictions.

The measured cross-stream velocities (Fig. 4) indicate a large streamline curvature close to the rib. All three models consistently underpredict the magnitude of the v velocity, and also the streamwise evolution of the flow. Except in the near-field of the downstream separated region ($0 \leq x/h \leq 0.6$, $y/h \leq 1$), the model predictions are generally in good agreement with each other.

The reattachment length has been widely used in the literature as a measure of a model's performance. Depending on the matrix of measurement locations, there is, however, considerable uncertainty associated with the reported value for the reattachment point. In the present study, the measured reattachment is estimated to be at $x_R/h = 6.3 \pm 0.9$. Within the limits of numerical uncertainty, the model predictions yield the following values for reattachment: $x_R/h = 5.9$ for the standard $k-\epsilon$ model, $x_R/h = 7.5$ for the nonlinear model, and $x_R/h = 7$ for the A-S functionalized model. In view of the uncertainty associated with the measured reattachment value, it would be difficult to make a definitive conclusion on the performance of the models. What can be said, however, is that the standard $k-\epsilon$ model underpredicts the reattachment length (due to an overprediction of turbulent viscosity), as is widely reported in the literature pertaining to flow over backsteps, and that both the nonlinear and the A-S functionalized model correct this behavior resulting in larger values of the predicted reattachment lengths (associated with smaller values of the turbulent viscosity).

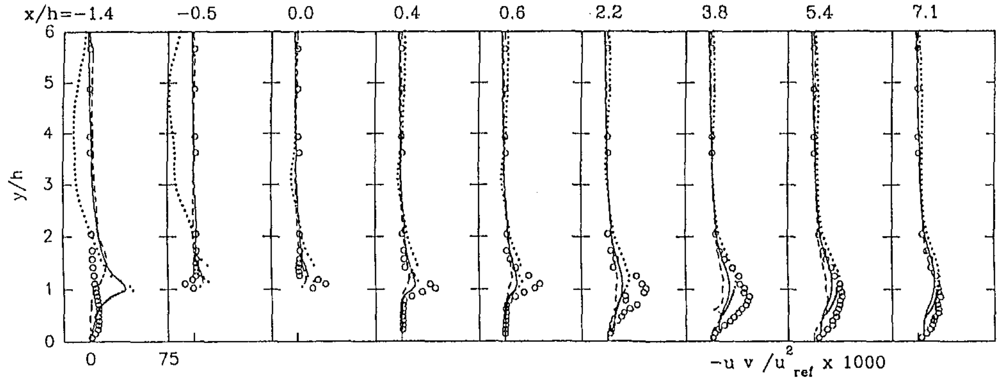

Fig. 7 **Turbulent Shear Stress at different *x/h* locations (Legend: See Fig. 3).**

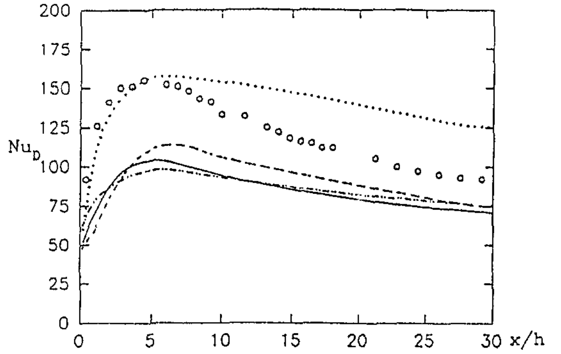

Fig. 8 Local Nusselt numbers (○ experimental data; standard $k-\epsilon$ model (——— WF I, – · · – · · – WF II, · · · WF III); --- nonlinear model, WF I)

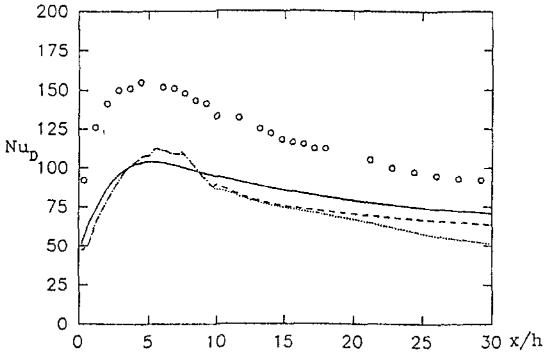

Fig. 10 Local Nusselt numbers at downstream locations of the rib (○ experimental data; ——— standard $k-\epsilon$ model; --- double pass (low-Re model; Jones and Launder, 1972); · · · · · · double pass (low-Re model; Nagano and Hishida, 1987)).

The streamwise turbulence intensity is shown in Fig. 5. The largest values of the turbulence intensities are measured directly above the rib, with near-wall peak values as high as four times the freestream value. Downstream of the rib, the peak values decay and the profiles expectedly become more uniform. Although the general features of the flow-field are similar to those for backstep flows, there are notable differences. The most important difference is that the streamwise turbulence peaks directly above the rib and not immediately downstream of the rib backface as in backstep flows (Chandrasuda and Bradshaw, 1981). This is due to the fact that in the ribbed-duct flow, the flow separates upstream of the rib leading to regions of high mean-flow gradients and increased turbulence production directly above the rib. In backstep flows, there is no analogous flow separation upstream of the step face, and therefore the turbulence flow-field, and its development in the near-field of the step face, is different than that observed here for a ribbed-duct flow.

All three models underpredict the measured values, but the nonlinear model predictions are superior to the predictions of the other two models. In the vicinity of reattachment ($5.4 \leq x/h \leq 7.1$), the nonlinear model results are in reasonable agreement (within ten percent) with the measurements, except close to the wall. With the standard $k-\epsilon$ and the A-S functionalized $k-\epsilon$ models, the deviations of the predictions from the measured values are much greater, with the peak values underpredicted by nearly 30 percent.

It is well known that the near-wall turbulence intensities have a significant effect on the surface heat transfer. However, the near-wall predictions of all three models are comparable, and the nonlinear model which, compared to the other two models, shows improvements away from the wall, does not show any significant improvements close to the heated surface.

The cross-stream turbulence intensities (Fig. 6) are considerably smaller than the streamwise intensities close to the rib ($-1.4 \leq x/h \leq 2.2$), indicating the nonisotropic nature of the separated flow. Downstream of reattachment, the cross-stream and streamwise turbulence intensities become more comparable in magnitude. In general, the models overpredict the measured values on the high-speed side, and underpredict them in the separated flow regions. The standard $k-\epsilon$ model predicts the largest magnitudes of the cross-stream intensity; the nonlinear model predicts the lowest values, and the A-S functionalized model predicts values that are between the other two predictions. The nonlinear model, due to its nonisotropic nature, attempts to correct the predictions of the linear isotropic Boussinesq model for the stresses used in the standard $k-\epsilon$ model. Although these corrections improve the predictions (the nonlinear model predictions are in the best agreement with the measured values on the high-speed side, $y/h > 1.5$), the comparisons in the separated flow region are, however, not very satisfactory. In the vicinity of reattachment, and downstream of it ($5.4 \leq x/h \leq 7.1$), the model predictions are in good agreement with the measured values, with the nonlinear model showing the best agreement.

The measured shear stresses (Fig. 7) downstream of the rib are consistent with those reported for flow past a step. Past the downstream separation point ($x/h = 0$), the peak value is consistently underpredicted. Again, the nonlinear model shows the best agreement, with all models showing good agreement with the measured values downstream of the reattachment point.

Heat Transfer and Temperature Results. Figure 8 presents the local Nusselt number results obtained from the standard model using wall functions WF I, II, and III, the nonlinear

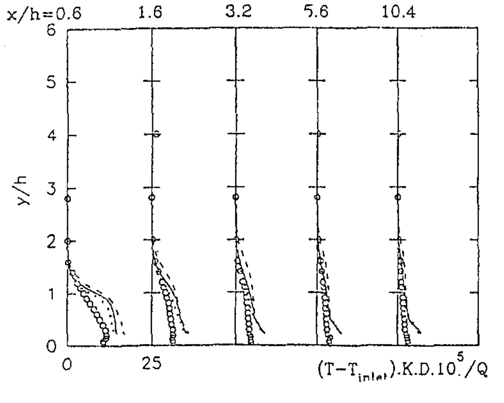

Fig. 9 Mean temperatures (○ experimental data; standard $k-\epsilon$ model (——— WF I, · · · · WF III); --- nonlinear model, WF I)

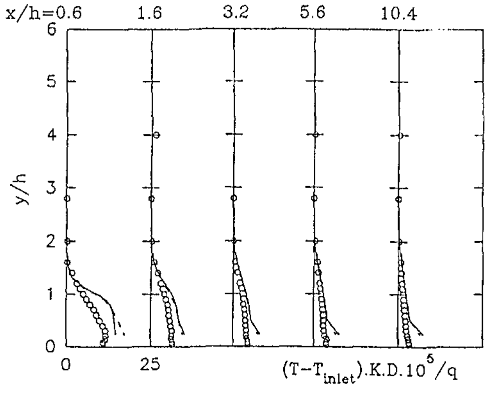

Fig. 11 Mean temperature at different downstream locations of the rib (○ experimental data; ——— standard $k-\epsilon$ model; --- double pass).

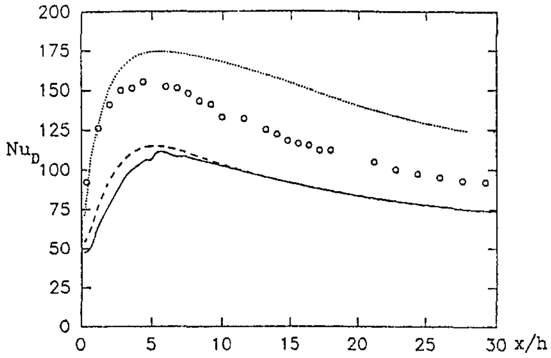

Fig. 12 Local Nusselt numbers at downstream locations of the rib (○ experimental data; ——— *s-n* c.c. (WF I); --- *x-y* c.c. (WF I); · · · *x-y* c.c. (WF III)).

model using WF I, and the experiments. The local Nusselt number is calculated as Nu $= q''D/(K(T_w(x) - T_b(x))$, where D is the hydraulic diameter and K is the thermal conductivity based on $(T_w(x) + T_b(x)/2$. It should be emphasized that the heat transfer data were taken in a duct nearly identical to the cold-flow duct used for the flow measurements.

Figure 8 shows that for WF I, the maximum Nusselt number is underpredicted by both the standard and the nonlinear models, with the standard model performing better up to about $x/h = 4$ and the nonlinear model performing better downstream of $x/h = 4$. It is seen that the peaks are achieved at different locations: $x/h = 4.4$ (± 0.4), 5.0 and 6.3, for the experiments, the standard model, and the nonlinear model, respectively. This is because of the different reattachment lengths. The peak locations upstream of the reattachment point are roughly 1.9, 0.9, and 1.2 rib heights for the experiments, standard model, and nonlinear model, respectively. The predicted peak values for the two models were found to coincide with the location of the highest near-wall turbulent kinetic energy value, so the peak in the surface heat transfer is correlated directly to the near-wall turbulence levels generated by the separation of the flow.

The underprediction of the peak Nusselt number by both the models can be attributed, in part, to the handling of the near-wall effects using WF I and the assumption of equilibrium of turbulence in the near-wall region. The equilibrium assumption is valid for a plane channel flow, but in a separated shear layer flow, the production and dissipation of turbulent fluxes are not in equilibrium at all locations (Acharya et al., 1994).

In order to examine the role of the near-wall assumptions on the Nu predictions, results are also presented in Fig. 8 for the standard model using WF II and III. The figure shows that the use of WF II has a minimal effect on the Nu predictions. Recall that Johnson and Launder (1982) found that the use of WF II did not improve significantly upon the heat transfer predictions of WF I; consequently, they proposed WF III. It is seen that the use of WF III yields predictions that are in excellent agreement with the experiments up to the peak Nu location. However, beyond this point, the use of WF III results in a substantial overprediction of Nu.

Figure 9 shows the mean temperature profiles in the fluid. The WF II results were identical to those of WF I and are omitted. The calculations overpredict the measured temperatures, regardless of the model or wall function used. Overprediction of the temperatures implies larger μ_t/Pr_t values in the computations than in the experiments. However, the predictions show a thinner thermal shear layer than the experiments. These observations point to the inappropriateness of a constant Pr_t assumption. For WF I, the standard model performs better than the nonlinear model at $x/h = 0.6$, but the predictions merge together, and they all do a better job of predicting the measured values as the shear layer develops. In keeping with the local Nusselt number data, the use of WF III results in improved temperature predictions, especially near the rib ($x/h = 0.6$ and 1.6). At larger values of x/h, the WF III predictions merge together with the other predictions and the experimental results.

Figure 10 shows the predictions of the A-S functionalized double-pass model. Up to the peak Nu position, the A-S functionalized double-pass model predictions show trends similar to the nonlinear model predictions. Compared to the standard $k-\epsilon$ model, the A-S functionalized double-pass model better predicts the peak Nu value, but in the developing region, the double-pass model predictions fall even below the standard $k-\epsilon$ model predictions. The use of Nagano and Hishda's (1987) low Re formulation in the double-pass model leads to lower Nu predictions in the developing regions ($20 \le x/h \le 30$) compared to those obtained with the Jones and Launder's (1972) low Re formulation. The temperature predictions shown in Fig. 11 also indicate no noticeable improvements with the double-pass model.

The observations in Fig. 10 indicate that the use of a low Re model in a double-pass formulation is unsuitable for the ribbed-duct flow configuration, and that a high Re model is better suited for such flows. Since, in Fig. 8, the use of WF III wall functions led to substantial improvements in the heat transfer predictions up to the reattachment point, results were obtained with the A-S functionalized high Re formulation with both WF I and WF III. The results shown in Fig. 12 indicate that the A-S functionalized high Re model shows improvements over the double pass model, but still it does not considerably improve the standard $k-\epsilon$ model predictions. Streamline curvature corrections based on Cartesian coordinates (*x-y/c-c*) everywhere appears to yield slightly better predictions than the use of curvature corrections based on streamline coordinates (*s-n/c-c*) upstream of reattachment. The use of WF III again improves the predictions up to the reattachment point, but overestimates the measured values beyond this point.

Temperature predictions shown in Fig. 13 indicate substantial improvements obtained with the *x-y/c-c* version of the model. The predictions have been obtained with both WF I and WF III versions. In fact, these model predictions virtually overlap the measured values. Recall that with the standard and the nonlinear models, where a constant Pr_t is used (Fig. 9), the temperature predictions were rather poor. Clearly, with Pr_t functionalized as in the *x-y/c-c* version of the model, more realistic estimates of (μ_t/Pr_t) are computed. The observed discrepancy in the Nusselt number is, therefore, attributable to the inability of the wall function approximations to correctly reproduce the near-wall turbulence in the vicinity of a rib.

Conclusions

Predictions of the flow, temperatures, and local Nusselt numbers in a duct flow past a wall-mounted two-dimensional rib

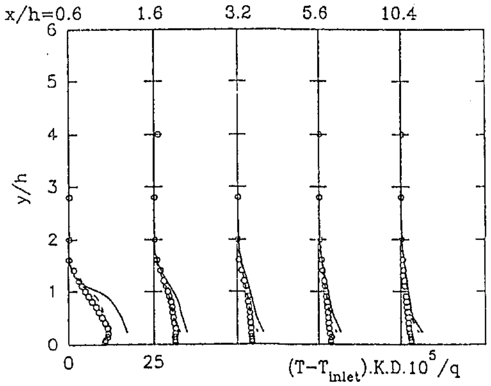

Fig. 13 Mean temperature at different downstream locations of the rib (○ experimental data; ——— *s-n* c.c. (WF I, WF III); --- *x-y* c.c. (WF I, WF III)).

were obtained with the standard $k-\epsilon$, the A-S functionalized $k-\epsilon$, and the nonlinear $k-\epsilon$ turbulence models using the wall function (WF I) proposed by Launder and Spalding (1974). Additional flow, temperature, and Nusselt number predictions were obtained using the wall functions (WF II and III) proposed by Chieng and Launder (1980) and Johnson and Launder (1982), respectively. The performance of the various models was assessed through comparisons with the laser-Doppler flow measurements and experimental flow, temperature, and Nusselt number results obtained for the present investigation.

For WF I, the use of the nonlinear model resulted in improved predictions of the mean velocities near the upper edge of the shear layer. It also resulted in considerable improvements in the prediction of the streamwise turbulence intensity and shear stress. The A-S functionalized model showed only marginal improvements over the standard $k-\epsilon$ model predictions.

In predicting the surface heat transfer, none of the model predictions were very satisfactory. The local Nusselt number results showed that for WF I, both the standard and nonlinear models resulted in severe underpredictions of the local Nusselt numbers. In general, the nonlinear model predictions were better than those of the standard model; however, the standard model predicted the peak Nusselt number location better than the nonlinear model. The use of WF II was observed to have only a small effect on the local Nusselt number predictions, while the use of WF III resulted in good agreement with the experimental results up to the peak Nu location. Downstream of the peak Nu value, WF III substantially overpredicted the Nu values. The temperature results showed that all of the models overpredicted the flow temperatures close to the rib, with the results of the predictions and those of the experiments merging together as the shear layer developed. Heat transfer predictions with the A-S functionalized double pass model showed only marginal improvements over the standard $k-\epsilon$ model up to the reattachment point. However, the temperature predictions with the high Re A-S functionalized model, incorporating curvature corrections in Cartesian coordinates, showed substantial improvements, and agreed very well with the experimental data.

Acknowledgment

This work was supported by a grant from the National Science Foundation and the Cornell Supercomputing Facility. Their support is gratefully acknowledged. The help provided by Mr. S. Baker and Ms. X. Qiu in the experimental effort is also acknowledged.

References

Acharya, S., Dutta, S., Myrum, T. A., and Baker, R. S., 1994, "Turbulent Flow Past a Surface Mounted Two-Dimensional Rib," ASME *Journal of Fluids Engineering,* Vol. 116, pp. 238–246.

Amano, R. S., and Chai, J. C., 1988, "Transport Models of the Turbulent Velocity—Temperature Products for Computations of Recirculating Flow," *Numerical Heat Transfer,* Vol. 14, pp. 75–95.

Antoniou, J., and Bergeles, G., 1988, "Development of the Reattachment Flow Behind Surface-mounted Two-Dimensional Prisms," ASME *Journal of Fluids Engineering,* Vol. 110, pp. 127–133.

Benodekar, R. W., Goddard, A. J. H., Gosman, A. D., and Issa, R. I., 1985, "Numerical Prediction of Turbulent Flow Over Surface-Mounted Ribs," *AIAA Journal,* Vol. 23, No. 3, pp. 359–366.

Bergeles, G., and Athanassiadis, N., 1983, "The Flow Past a Surface-Mounted Obstacle," ASME *Journal of Fluids Engineering,* Vol. 105, pp. 461–463.

Castro, I. P., 1979, "Relaxing Wakes Behind Surface-Mounted Obstacles in Rough Wall Boundary Layers," *Journal of Fluid Mechanics,* Vol. 93, pp. 631–659.

Chandrsuda, C., and Bradshaw, P., 1981, "Turbulence Structure of a Reattaching Mixing Layer," *Journal of Fluid Mechanics,* Vol. 110, pp. 171–194.

Chieng, C. C., and Launder, B. E., 1980, "On the Calculation of Turbulent Heat-Transport Downstream from an Abrupt Pipe Expansion," *Numerical Heat Transfer,* Vol. 3, pp. 189–207.

Chung, M. K., Park, S. W., and Kim, K. C., 1987, "Curvature Effect on Third-Order Velocity Correlations and Its Model Representation," *Physics of Fluids,* Vol. 30, No. 3, pp. 626–628.

Clark, R. A., Ferziger, J. H., and Reynolds, W. C., 1979, "Evaluation of Subgrid-Scale Models Using an Accurately Simulated Turbulent Flow," *Journal of Fluid Mechanics,* Vol. 91, Part 1, pp. 1–16.

Driver, D. M., and Seegmiller, H. L., 1985, "Features of a Reattaching Turbulent Shear Layer in Divergent Channel Flow," *AIAA Journal,* Vol. 23, No. 2, pp. 163–171.

Driver, D. M., and Seegmiller, H. L., 1982, "Features of a Reattaching Turbulent Shear Layer Subject to an Adverse Pressure Gradient," AIAA/ASME 3rd Joint Thermophysics, Fluids, Plasma and Heat Transfer Conference, June 7–11, St. Louis, MO.

Durst, F., and Rastogi, A. K., 1980, "Turbulent Flow over Two-Dimensional Fences," *Turbulent Shear Flows, 2,* Bradbury et al., eds., Berlin, Springer-Verlag, Berlin, pp. 218–231.

Dutta, S., 1991, "Turbulence Modeling of Unsteady Separated Flows," M. S. thesis, Mechanical Engineering Department, Louisiana State University, Baton Rouge, LA, May.

Dutta, S., and Acharya, S., 1993, "Heat Transfer and Flow Past a Backstep with a Nonlinear $k-\epsilon$ and a Modified $k-\epsilon$ Model," *Numerical Heat Transfer,* Vol. 23, No. 3, pp. 281–302.

Gooray, A. M., 1982, "Numerical Calculation of Turbulent Recirculating Heat Transfer Beyond Two-Dimensional Backsteps and Sudden Pipe Expansions," Ph.D. dissertation, Howard University, Washington, DC.

Gooray, A. M., Watkins, C. B., and Aung, W., 1982, "$k-\epsilon$ Calculations of Heat Transfer in Redeveloping Turbulent Boundary Layers Downstream of Reattachment," AIAA/ASME Fluids, Plasma and Heat Transfer Conference, St. Louis, MO, ASME Paper 82-HT-77.

Gooray, A. M., Watkins, C. B., and Aung, W., 1983, "A Two-Pass Procedure for the Calculation of Heat Transfer in Recirculating Turbulent Flow," *Numerical Heat Transfer,* Vol. 6, pp. 423–440.

Gooray, A. M., Watkins, C. B., and Aung, W., 1985, "Turbulent Heat Transfer Computations for Rearward-facing Steps," ASME JOURNAL OF HEAT TRANSFER, Vol. 107, pp. 70–76.

Johnson, R. W., and Launder, B. E., 1982, "Discussion of 'On the Calculation of Turbulent Heat Transfer Downstream From an Abrupt Pipe Expansion," *Numerical Heat Transfer,* Vol. 5, pp. 493–496.

Kline, S. J., and McLintock, F. A., 1953, "Describing Uncertainties in Single-Sample Experiments," *Mechanical Engineering,* Vol. 75, pp. 3–8.

Launder, B. E., 1971, "An Improved Algebraic Stress Model of Turbulence," Mech. Engg. Rep. TMTN/A19 Imperial College.

Launder, B. E., and Spalding, D. B., 1974, "The Numerical Computation of Turbulent Flows," *Computer Methods in Applied Mechanics and Engineering,* Vol. 3, 1974, pp. 269–289.

Launder, B. E., Reece, G. J., and Rodi, W., 1975, "Progress in the Development of a Reynolds-Stress Turbulence Closure," *Journal of Fluid Mechanics,* Vol. 68, pp. 537–566.

Lee, B. K., Cho, N. H., and Choi, Y. D., 1988, "Analysis of Periodically Fully Developed Turbulent Flow and Heat Transfer by $k-\epsilon$ Equation Model in Artificially Roughened Annulus," *International Journal of Heat and Mass Transfer,* Vol. 31, No. 9, pp. 1797–1806.

Leschziner, M. A., and Rodi, W., 1981, "Calculation of Annular and Twin Parallel Jets Using Various Discretization Schemes and Turbulence Model Variations," ASME *Journal of Fluids Engineering,* Vol. 103, pp. 352–360.

Liou, T. M., and Kao, C. F., 1988, "Symmetric and Asymmetric Turbulent Flows in a Rectangular Duct with a Pair of Ribs," ASME *Journal of Fluids Engineering,* Vol. 110, pp. 373–379.

Nagano, Y., and Hishida, M., 1987, "Improved Form of the $k-\epsilon$ Model for Turbulent Shear Flows," ASME *Journal of Fluids Engineering,* Vol. 109, pp. 156–160.

Park, S. W., and Chung, M. K., 1989, "Curvature-Dependent Two-Equation Model for Prediction of Turbulent Recirculating Flows," *AIAA Journal,* Vol. 27, pp. 340–344.

Patankar, S. V., 1980, *Numerical Heat Transfer and Fluid Flow,* Hemisphere, Bristol, PA, p. 133.

Phataraphruk, P., and Logan, E., Jr., 1979, "Turbulent Pipe Flow Past a Rectangular Roughness Element," *Turbulent Boundary Layers,* H. E. Weber, ed., ASME, New York.

Sindir, M. M. S., 1982, "A Numerical Study of Turbulent Flows in Backward Facing Step Geometries," Ph.D. dissertation, University of California, Davis, CA.

Sparrow, E. M., and Tao, W. Q., 1983, "Enhanced Heat Transfer in a Flat Rectangular Duct with Streamwise Periodic Disturbances at one Principal Wall," ASME JOURNAL OF HEAT TRANSFER, Vol. 105, pp. 851–861.

Speziale, C. G., 1987, "On Nonlinear $k-l$ and $k-\epsilon$ Models of Turbulence," *Journal of Fluid Mechanics,* Vol. 178, pp. 459–475.

Speziale, C. G., and Ngo, T., 1988, "Numerical Solution of Turbulent Flow Past a Backward Facing Step Using a Nonlinear $k-\epsilon$ Model," *International Journal of Engineering Sciences,* Vol. 26, pp. 1099–1112.

Thangam, S., and Hur, N., 1991, "A Highly-Resolved Numerical Study of Turbulent Separated Flow Past a Backward-Facing Step," *International Journal of Engineering Services,* Vol. 29, pp. 607–615.

Thangam, S., and Speziale, C. G., 1991, "Turbulent Separated Flow Past a Backward-Facing Step: A Critical Evaluation of Two-Equation Turbulence Models," NASA Contractor Report, ICASE Report No. 91-23.

Tropea, C. D., and Gackstatter, R., 1985, "The Flow over Two-Dimensional Surface-Mounted Obstacles at Low Reynolds Numbers," ASME *Journal of Fluids Engineering,* Vol. 107, pp. 489–494.

Yap, C., 1987, "Turbulent Heat and Momentum Transfer in Recirculating and Impinging Flows," Ph.D. Thesis, University of Manchester, Manchester, UK.

Liwei Lin[1]
Department of Mechanical Engineering
and Applied Mechanics,
University of Michigan,
Ann Arbor, MI 48109-2125
Mem. ASME

A. P. Pisano

V. P. Carey

Department of Mechanical Engineering,
University of California at Berkeley,
Berkeley, CA 94720

Thermal Bubble Formation on Polysilicon Micro Resistors

Thermal bubble formation in the microscale is of importance for both scientific research and practical applications. A bubble generation system that creates individual, spherical vapor bubbles from 2 to 500 μm in diameter is presented. Line shape, polysilicon resistors with a typical size of $50 \times 2 \times 0.53$ μm^3 are fabricated by means of micromachining. They function as resistive heaters and generate thermal microbubbles in working liquids such as Fluorinert fluids (inert, dielectric fluids available from the 3M company), water, and methanol. Important experimental phenomena are reported, including Marangoni effects in the microscale; controllability of the size of microbubbles; and bubble nucleation hysteresis. A one-dimensional electrothermal model has been developed and simulated in order to investigate the bubble nucleation phenomena. It is concluded that homogeneous nucleation occurs on the microresistors according to the electrothermal model and experimental measurements.

1 Introduction

The emerging technology of MEMS (microelectromechanical systems) is shrinking mechanical devices into micro and nanometer scales. The trend of miniaturization has brought unprecedented research opportunities in conventional areas of mechanical engineering. Many engineering challenges are expected to be encountered when innovative microdevices are introduced. For example, the commercial success of bubble jet printers (Nielsen, 1985) has inspired many researchers to apply bubble formation mechanism as the operation principle in different microsystems (Zdeblick and Angell, 1987; Sniegowski, 1993; Evans, Liepmann, and Pisano, 1997; Tseng et al., 1996). It is important to study the bubble nucleation and heat transfer processes powered by MEMS microheaters before any of these microdevices may be optimally designed and operated.

This paper addresses bubble nucleation mechanism and heat transfer processes generated by micro-polysilicon line resistors with a typical size of $50 \times 2 \times 0.53$ μm^3. Experiments are recorded under a microscope by passing electrical power through the microresistive heaters while immersing them in subcooled working liquids. Several unprecedented bubble formation phenomena are observed, including stable and controllable bubble sizes during the formation processes and bubble nucleation hysteresis. A one-dimensional electrothermal model is established based on the conservation of energy to help analyzing the heat transfer process. In order to characterize the bubble nucleation mechanism, theories for both heterogeneous and homogeneous nucleation are investigated.

1.1 Previous Works. Boiling phenomenon have been investigated for centuries. Notable experimental investigations may date back to late 1960s. Clark, Strenge, and Westwater (1959) reported that pits with diameters of 0.0003 to 0.003 in. (8 to 76 μm) on a heated surface were active sites for nucleate boiling. Gaertner (1965) later conducted a series of photographic studies and proposed a sequence for nucleate boiling. Other experimental and theoretical studies have followed (Hahne and Grigull, 1977; Stralen and Cole, 1979; Carey, 1992; Stephan, 1992). However, little work can be found in the literature for bubble formation using IC-processed micro resistors.

Several researchers have studied bubble nucleation phenomena by small wire-type heating elements. For example, Pitts and Leppert (1966) used heated wires with a diameter of 0.0005 to 0.051 in. (13 to 1200 μm) in boiling experiments. Sun and Lienhard (1970) investigated the boiling process on horizontal Nichrome cylinders with a diameter of 0.0005 to 0.081 in. (130 to 2060 μm). Bakhru and Lienhard (1972) studied boiling phenomena from small platinum cylinders of 0.001 to 0.004 in. (25 to 102 μm) in diameter. Bubble formation from very short heaters has also been investigated. Baker (1972; 1973) studied the heater length effects for single-phase force convection in pool boiling. Ma and Bergles (1986) used a 1500-μm long heater to study forced boiling convection phenomena. Recently, Lee and Simon (1988) used a 250×2000 μm^2 heated patch to study the phase change process in a subcooled, fully developed turbulent flow. Nagasaki et al. (1993) examined the local heating process by using microresistive heaters. All of the above studies contributed different aspects of bubble nucleation processes generated by small heaters. However, these heaters are relatively large when compared with the polysilicon microline resistors presented in this paper.

Analytical theories have also been developed for years to explain the boiling phenomena. For example, Zuber (1961) developed a model for bubble growth in a nonuniform temperature field near a heated surface. Hsu (1962) proposed a model that predicts the size range of active nucleation cavities on a heated surface. Mikic, Rohsenow, and Griffith (1970) established a model for predicting the initial radius of a vapor embryo. All of these models are based on pool boiling conditions for macroscale boiling processes. Therefore, they are generally not applicable for the microscale sub-cooled boiling tests as presented in this paper. Modifications or new theoretical derivations would be required.

2 Experiments

Measurements are performed in a "probe station" apparatus that consists of an optical microscope and several micromanipulators as shown in Fig. 1. Electrical probes are placed right on the contact pads with the help of the micromanipulators. These probes provide electrical interconnections from the power supply and instrument to the microdevices. In order to clearly illustrate the microheater and the two contact pads, Fig. 1 is not drawn to scale. The actual size of the microheater ranges from

---

[1] Address for correspondence: Department of Mechanical Engineering and Applied Mechanics, University of Michigan, 2350 Hayward Street, Ann Arbor, MI 48109-2121. e-mail: lwlin@engin.umich.edu.

Contributed by the Heat Transfer Division for publication in the JOURNAL OF HEAT TRANSFER. Manuscript received by the Heat Transfer Division, Jan. 6, 1997; revision received, Mar. 6, 1998. Keywords: Bubble Growth, Phase Change, Thermocapillary, Thermophysics, Thin Films. Associate Technical Editor: M. Modest.

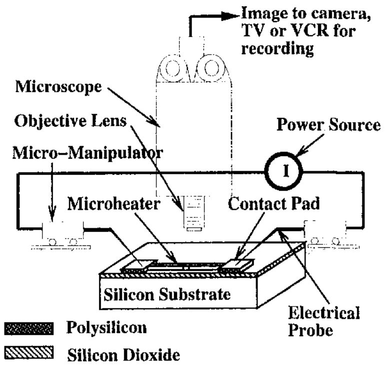

Fig. 1 Schematic drawing of test apparatus

15 to 50 μm in length. The line resistor functions as a resistive heater when an electrical current is applied. Silicon dioxide underneath the resistor is used for electrical and thermal insulation. Silicon substrate, which has a thermal conductivity nearly 100 times higher than that of silicon dioxide, acts as a heat sink.

Two types, standard and irregular, microline resistors have been designed and fabricated. The standard-type resistor has a line shape and its length is 50 ± 0.1 μm; width is 2 ± 0.1 μm; and thickness is 0.53 ± 0.003 μm. The irregular resistor has two different widths, 3 μm (10 μm in length) and 2 μm (5 μm in length), respectively, as shown in Fig. 2. This irregular-shape resistor is designed and fabricated in order to compare and study different thermophysical aspects with respect to the lineshape resistors. Particularly, the thinner portion is expected to endure higher current density such that a higher temperature is expected.

MEMS fabrication technologies are used to fabricate these microdevices. Process details have been described previously (Lin, 1993). Figure 2 shows a scanning electron microscope (SEM) micrograph of a fabricated irregular resistor which is ready for testing. A small beaker is used to hold the working liquid and the fabricated microdevices are immersed at the bottom. The depth of the liquid is about 5 mm. Fluorinert liquids (3M, 1991), DI (Deionized) water, and methanol have been successfully tested as the working liquids to generate thermal bubbles. Although other liquids can certainly be applied, it is noted that if the liquid is not electrically inert, the electrolysis process, instead of thermal bubble formation process, may occur. Therefore, the majority experimental data gathered in this paper are based on the FC liquids which are electrically inert. The experiments are carried out at room temperature and under one atmospheric pressure. Images of the experiments are taken by Polaroid films and recorded on a video tape.

2.1 General Observations. Both a-c and d-c voltage sources have been applied to generate thermal bubbles. The peak values of less than 10 V are found sufficient in bubble formation experiments. Since a small contact resistance exists between the electrical probes and the contact pads, electrical currents, instead of voltages, are measured in major tests to diminish experimental errors. When an a-c source is applied to the microresistor and the driving frequencies are less than 10 Hz, bubbles are formed at twice the signal frequency. It is found that bubble formation does not follow the input frequency greater than about 100 Hz at which the bubble forms and persists. The liquid surrounding the resistor gradually turns into bright color when a d-c input is applied. An individual, spherical shape microbubble is formed when a specific magnitude of input current, ''activation current,'' is applied. After the bubble is nucleated, it grows very quickly until its diameter reaches the length of the resistor. The whole process, including bubble nucleation and growth, takes place in less than one second.

After the initial bubble is formed, three ways of inputing electrical power have been explored. First, the input current is kept at the same level or increased to a higher value than the activation current. The microbubble grows continuously and eventually departs. Second, the current is reduced abruptly after the initial bubble is nucleated. The original bubble is found to collapse and transform into liquid instantly. Third, the input current is reduced gradually after the initiation of bubble formation. In this case, the size of the microbubble will decrease and the bubble stays on the top of the resistor. It is possible to control the bubble size by adjusting the input current. For example, it takes about 10 mW to maintain a stable microbubble on a 50 × 2 × 0.53 μm^3 standard resistor in FC 43 liquid. A great portion of this power input actually dissipates down to the substrate. When the input power is further reduced, the size of the bubble continues to diminish. If the bubble is less than 3 μm in diameter, it drifts around the center of the resistor. It is very difficult to control the stability of the bubble at this stage and any reduction of input power will kill the bubble.

These microresistors are very small such that the pool boiling condition has never been established during the experiments. The microresistor creates a local temperature field that may have profound effects to the local flow patterns. For example, the Marangoni effect (Collier, 1981) can be clearly identified which prevents nucleated microbubbles from floating up into the working liquid. In the extreme case, the microbubble tends to stick to the microresistor despite attempts to dislodge it via an electrical probe. Moreover, the bubble may physically move

Nomenclature

A = notation for $(2\sigma_l T_{\text{sat}}/h_{\lambda\upsilon} d_\upsilon)$ in Hsu's analysis
C = constant in Hsu's analysis
d = density, kg m^{-3}
F = thermal conductive shape factor
I = current, Amp
J = current density, Amp m^{-2}
L = length, m
T = temperature, °C
c = specific heat, W m^{-1} $°\text{C}^{-1}$
$h_{\lambda\upsilon}$ = latent heat of evaporation, cal kg^{-1}
k = thermal conductivity, W m^{-1} $°\text{C}^{-1}$
R = resistance, ohm
r = cavity radius in Hsu's analysis, m
t = time, s
V = voltage, V
w = width, m
x = coordinate, m
z = thickness, m

Greek Symbols

α = thermal diffusivity, m^2 s^{-1} $°\text{C}^{-1}$
δ = thickness of the limiting thermal layer in Hsu's analysis, m
ϵ = a combined variable in the heat equation, °C m^{-2}
ρ = resistivity, ohm-cm
σ = surface tension, N m^{-1}
θ = temperature difference with respect to bulk, °C
ξ = resistivity coefficient with respect to temperature, $°\text{C}^{-1}$

Subscript

ave = average
c = critical
l = working liquid
o = silicon dioxide
p = polysilicon
ref = reference
s = silicon
sat = saturation
ss = steady state
ts = transient
υ = vapor of working liquid
w = wall (surface)
∞ = ambient, bulk

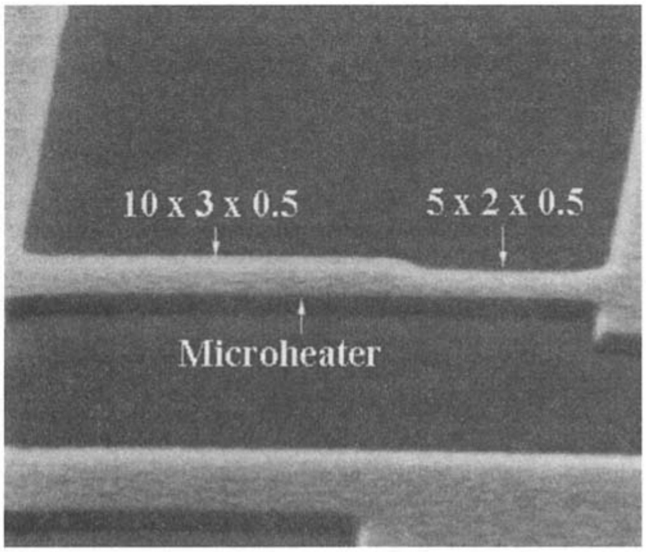

Fig. 2 SEM micrograph of an irregular microresistor

around the substrate by controlling the input current (Lin and Pisano, 1991).

2.2 Bubble Formation on the Irregular Resistor. Experiments on the irregular resistors are conducted and compared with the standard straight-line resistors. Figures 3 to 5 show several steady-state microbubbles generated by the irregular resistor. These experiments are performed in FC 43 liquid and input currents are monitored and recorded. When the input current is less than 12 mA, there is no bubble nucleation. If the input current is larger than 12 mA, a microbubble is nucleated. After bubble nucleation, the input current is reduced to 9.5 mA. A stable microbubble can be maintained as seen in Fig. 3. The two dark objects at both sides of the microphoto are the tips of electrical probes. The microbubble stays at the narrower portion of the resistor and has a diameter of about 2 μm. If the input current is increased, the microbubble grows larger. Figure 4 shows a microbubble with a diameter of 5 μm and the input current is 10 mA. When the input current reaches 12 mA, the size of the microbubble is no longer controllable and the bubble keeps growing. A big microbubble of 500 μm in diameter is seen before detaching in Fig. 5. The objective lens of the microscope has been changed in this photo.

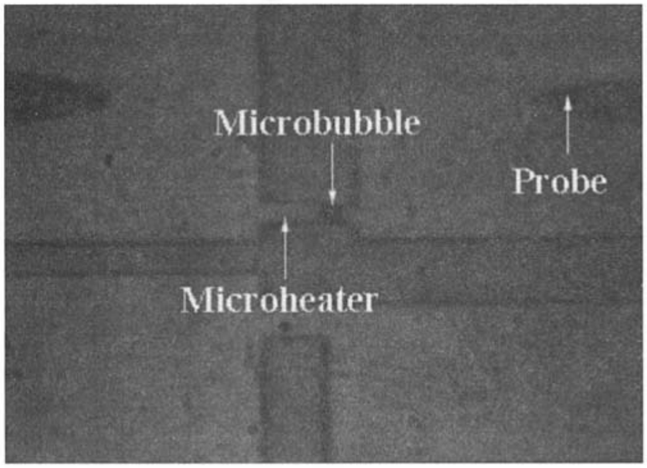

Fig. 3 A single bubble of 2 μm in diameter under a 9.5 mA input current

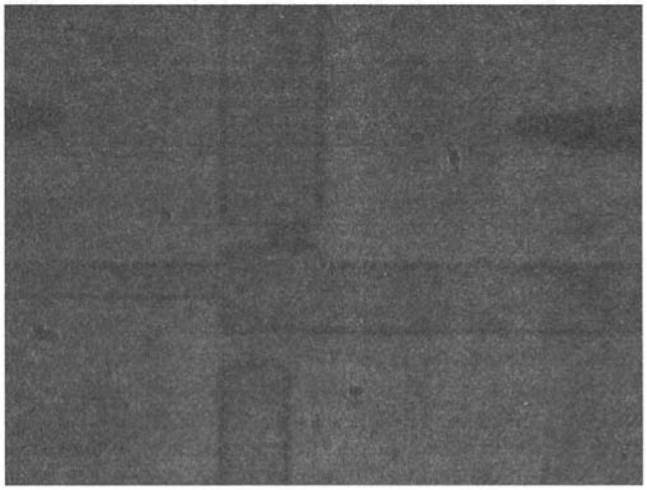

Fig. 4 A microbubble of 5 μm in diameter under a 10 mA input current

3 Electrothermal Modeling

3.1 Thermal Model. The lumped one-dimensional electrothermal model has been derived by the law of energy conservation. A second-order partial differential heat equation can be established as (Lin and Pisano, 1991)

$$\frac{\partial^2 T}{\partial x^2} = \frac{1}{\alpha_p}\frac{\partial T}{\partial t} + \epsilon(T - T_{\mathrm{ref}}) \tag{1}$$

in which T is the temperature along the microline resistor, t is time, and α_p is the thermal diffusivity of polysilicon. Both ϵ and T_{ref} are functions of resistor dimensions and thermal properties. They are summarized below:

$$\alpha_p = \frac{k_p}{c_p d_p} \tag{2}$$

$$\epsilon = \frac{k_o F}{k_p z_p z_o} - \frac{J^2 \rho_p \xi_p}{k_p} \tag{3}$$

$$T_{\mathrm{ref}} = T_\infty + \frac{J^2 \rho_p}{k_p \epsilon}\,. \tag{4}$$

An excessive shape factor, F, is used to account for the heat conduction losses to the substrate and environment. The shape factor is defined as

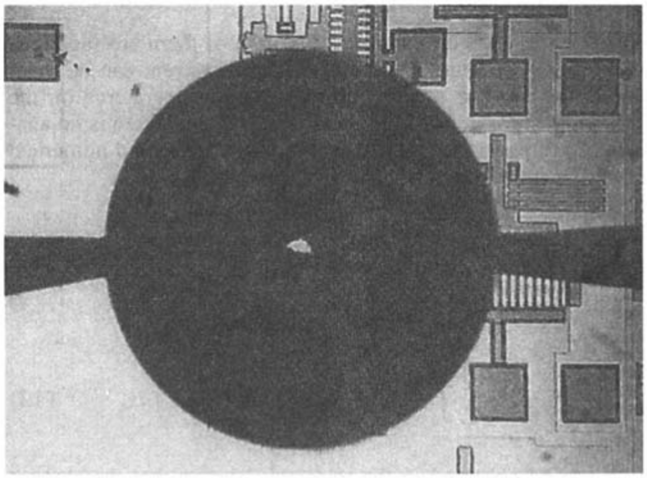

Fig. 5 The final stage of a microthermal bubble before detaching

Table 1 Shape factors for different widths of microresistors in FC43 liquid

Width	Shape Factor
1μm	1.74
2μm	1.30
5μm	1.04

$$F = \frac{\text{total heat flux per unit length}}{\dfrac{wk_o(T - T_\infty)}{z_o}} \tag{5}$$

where the denominator represents the heat flux going directly under the width of the resistor. In order to calculate the shape factor, a two-dimensional finite element simulation has been implemented (Ansoft, 1990). For example, the isotherms around a 2-μm wide microresistor are analyzed and plotted in Fig. 7. The shape factors are calculated accordingly. Some of the numbers with respect to different microresistors are listed in Table 1.

The solutions of Eq. (1) are solved subject to the initial and boundary conditions. It is assumed that the resistor is initially at ambient temperature before heating and both ends of the resistor remain at the ambient temperature. Validation of these assumptions has been proven previously (Lin and Pisano, 1991).

$$T(x = 0, t) = T_\infty \tag{6}$$

$$T(x = L, t) = T_\infty \tag{7}$$

$$T(x, t = 0) = T_\infty \tag{8}$$

The steady-state solution along the micro resistor is derived as

$$T(x)_{ss} = T_{\text{ref}} - (T_{\text{ref}} - T_\infty)\frac{\cosh\left[\sqrt{\epsilon}\left(x - \dfrac{L}{2}\right)\right]}{\cosh\left(\sqrt{\epsilon}\,\dfrac{L}{2}\right)}. \tag{9}$$

The maximum temperature that occurs at the center of the standard resistor is derived as

$$T(x)_{\text{ssmax}} = T_{\text{ref}} - (T_{\text{ref}} - T_\infty)\frac{1}{\cosh\left(\sqrt{\epsilon}\,\dfrac{L}{2}\right)}. \tag{10}$$

$T(x)_{\text{ssmax}}$ depends on ϵ and T_{ref} and both of them are functions of the input current. Therefore, the input current can be measured and used to predict the maximum temperatures on the microline resistor. For irregular-shape resistors, there is no analytical expression for the maximum temperature and numerical analyses are required.

The transient solutions are derived as

$$T(x, t)_{ts} = e^{-\alpha_p \epsilon t} \sum_{n=1}^{\infty} B_n \sin\left(\frac{n\pi x}{L}\right) e^{-\alpha_p t (nx/L)^2} \tag{11}$$

where

$$B_n = \frac{2}{L}\int_0^L [T_\infty - T(x)_{ss}] \sin\left(\frac{n\pi x}{L}\right) dx. \tag{12}$$

It can be observed in the transient solution that the slowest transient decay time ($n = 1$) is in the order of 10 microseconds for a 50-μm long line resistor. For an input source with frequency less than 10 kHz, the temperature of the microline resistor reaches steady state without significant transient delay. This transient decay time can be represented as

$$t_{\text{decay}} = \left(\frac{L}{n\pi}\right)^2 \frac{1}{\alpha_p}. \tag{13}$$

3.2 Electrical Model. The electrical model, including voltage and current, can be derived based on the resistance changes with respect to the temperature.

$$R = \int_0^L dR(T) \tag{14}$$

$$= \frac{\rho_p L}{w z_p}(1 + \xi_p(T_{\text{ave}} - T_\infty)), \tag{15}$$

where T_{ave} is the average temperature of the line resistor and is expressed as

$$T_{\text{ave}} = \frac{1}{L}\int_0^L T dx \tag{16}$$

$$= T_{\text{ref}} - (T_{\text{ref}} - T_\infty)\frac{\tanh\left(\dfrac{\sqrt{\epsilon}L}{2}\right)}{\dfrac{\sqrt{\epsilon}L}{2}}. \tag{17}$$

Therefore, the voltage across the microline resistor is expressed as

$$V = I\frac{\rho_p L}{wz}(1 + \xi_p(T_{\text{ave}} - T_\infty)). \tag{18}$$

This equation is useful to characterize fundamental electrical characteristics of the microline resistors. Figure 6 is the experimental measurements of voltage-current curves for microline resistors. The theoretical predictions as drawn in solid lines are consistent with the experimental data. However, it should be noted that the thermal properties of these thin films are functions of temperature. The above models are only moderately accurate for temperatures less than 300°C which satisfies the operation range of current bubble formation experiments. Modifications are required for high-temperature applications.

3.3 Numerical Simulations. A one-dimensional finite element program, including time responses, has been established to analyze the heat transfer processes of these resistors. This

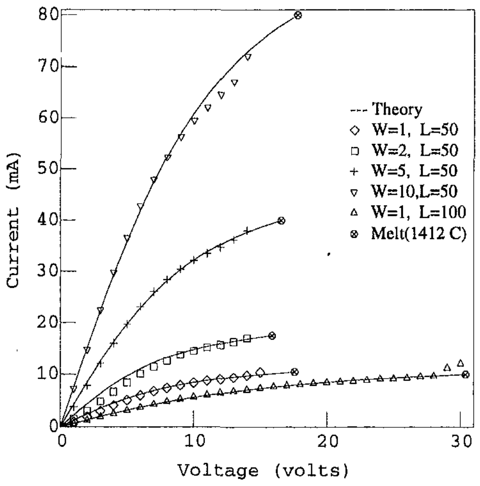

Fig. 6 Comparison between experimental and theoretical *I-V* curves

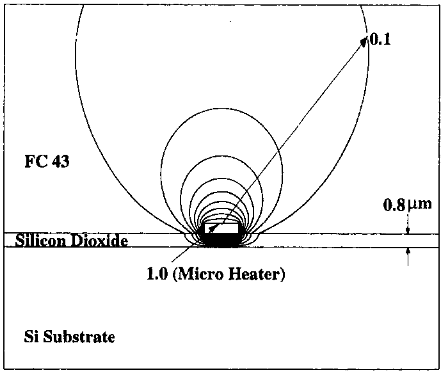

Fig. 7 Cross-sectional view of isotherms around a 2-μm wide microline resistor

finite element model uses 99 nodal points and 49 quadratic elements. It has been built based on Eq. (1) and solved with initial and boundary conditions.

3.3.1 Steady-State and Transient Responses. Figure 8 shows the simulation results of the steady-state temperature profile of a standard line resistor. FC 43 liquid is used in this simulation. It is observed that a relatively uniform, high-temperature region appears at the central region of the line resistor. Moreover, the temperature drops quickly at both ends of the resistor to ambient temperature. The highest current used in this simulation is 11 mA which can create a high temperature of about 300°C. This is a more than enough temperature to nucleate thermal bubbles in most liquids.

The transient analysis is incorporated into the finite element model by using the backward Euler method. Figure 9 is the simulation result that shows the heating process under a step input current of 11 mA. It is observed that steady state is reached in only about 10 microseconds. This number is consistent with the theoretical prediction in Eq. (13). Although 10 microseconds are needed for this microline resistor to reach steady state, only 3 microseconds can bring the resistor temperature over 250°C as shown in this figure.

The cooling process is simulated in Fig. 10. This simulation is conducted by removing the input current of 11 mA. It is noted that only 2 microseconds are needed to cool the resistor to 50°C.

3.3.2 Irregular Microresistor. This finite element model is also used to simulate irregular microresistors. Temperature distributions of the irregular resistor are plotted in Fig. 11. The highest temperature occurs at the narrower portion, 11.6 μm from the left contact pad. This simulation is consistent with the experimental result of Fig. 3, where a microbubble is attached to this hottest spot due to Marangoni effect.

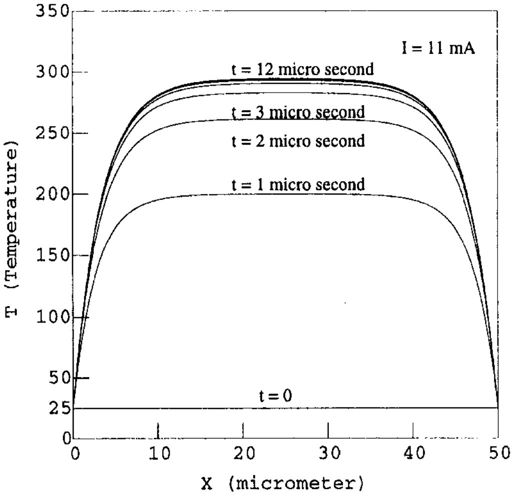

Fig. 9 Heating process of a standard resistor

4 Discussions

Experiments, theories, and numerical simulations for bubble formation on microline resistors have been addressed in this paper. They are foundations for characterizing bubble formation on microline resistors. Bubble formation mechanisms and new bubble formation phenomena are discussed in this section based on these analyses and experiments.

4.1 Bubble Formation Mechanisms. Two bubble nucleation mechanisms are examined. For heterogeneous nucleation, bubbles are formed at nucleation sites that are typically provided by surface defects. This type of nucleation can occur for a wide range of superheat temperature. The exact bubble nucleation temperature depends on the size of the cavity and whether vapor is present. Since the microfabrication process is capable of making a very smooth surface, possible surface defects on these microresistors are expected to be extremely small. On the other hand, homogeneous nucleation occurs when liquid approaches the superheated limit such that the liquid phase penetrates the metastable region to a progressively greater degree. In order to

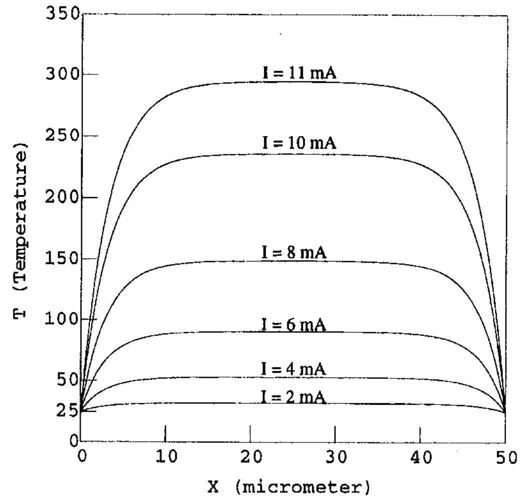

Fig. 8 Steady-state temperature profile of a standard microline resistor

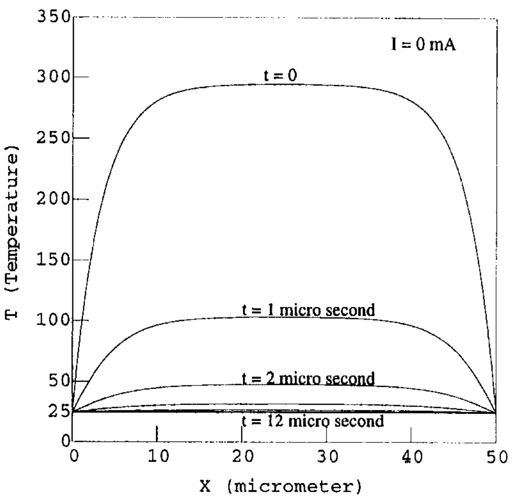

Fig. 10 Cooling process of a standard resistor

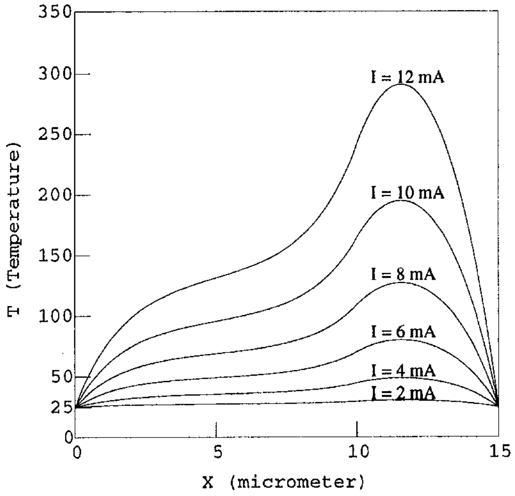

Fig. 11 Temperature distribution of a irregular microresistor

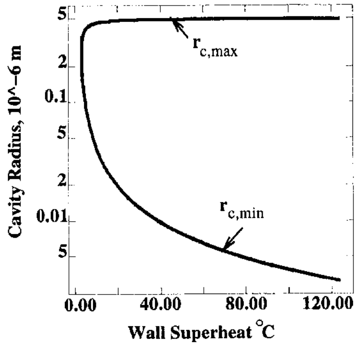

Fig. 13 Range of cavity sizes with respect to superheat temperature based on Hsu's analysis

investigate the bubble formation mechanism, the "activation current" is measured. Analytical theories developed in this paper are then used to calculate the bubble nucleation temperatures. Figure 12 shows the experimental results of bubble activation currents and temperatures in three different kinds of Fluorinert liquids (FC 43, FC 75, and FC 72). Microresistors with different widths of 1 to 5 μm and length of 50 μm have been tested. The experimental results suggest that the "activation temperatures" are close to the superheat limits of individual liquids (294°C for FC 43, 227°C for FC 75 and 178°C for FC 72 (3M, 1991)). Similar results are found for DI water and methanol in a previous report that investigated microbubble formation in confined and unconfined microchannels (Lin, Udell, and Pisano, 1993). Both heterogeneous and homogeneous nucleation mechanisms are discussed with the help of these experiments.

4.1.1 Heterogeneous Nucleation. There are several analytical theories that describe the heterogeneous bubble nucleation mechanisms. However, most of these analyses are based on saturated liquid under the pool-boiling condition and they are not directly applicable to the current microboiling experiments. In an effort to address the microscale, subcooled boiling phenomena, a macroscale theory developed by Hsu (1962) is discussed here as the limiting case. According to Hsu's theory, the effective cavity size for saturated pool-boiling should fall into the following range on a heated surface:

$$r_c = \frac{\delta}{2C_1}\left[1 - \frac{\theta_{\rm sat}}{\theta_w} \pm \sqrt{\left(1 - \frac{\theta_{\rm sat}}{\theta_w}\right)^2 - \frac{4AC_3}{\delta\theta_w}}\right] \quad (19)$$

where A is expressed as the following:

$$A = \frac{2\sigma_l T_{\rm sat}}{h_{\lambda v} d_v}. \quad (20)$$

For simplicity, the cavity mouth is assumed to be a perfect circle and $C_1 = 2$, $C_3 = 1.6$ as described by Hsu (1962). The limiting thermal-layer thickness is estimated to be 1 μm. The surface tension, σ, is estimated to be 2.3 dynes per centimeter according to a previous report that describes microbubble-powered actuators (Lin, Pisano and Lee, 1991). The simulation results are plotted in Fig. 13. It is observed that a superheat temperature of about 20°C is required for bubble nucleation if the cavity is 0.5 μm in radius.

Figure 14 shows the close-view SEM microphoto of a 2-μm wide microline resistor. It is noted that the possible cavities on the surface of the microresistor have a size much less than 0.5 μm in radius. AFM (Atomic Force Microscope) surface analyses are conducted and Fig. 15 shows the scanning result for an area of 0.6 × 0.5 μm^2 on top of the microresistor. The RMS (Root Mean Square) roughness is found to be 6.5 nanometers. A "cavity"-like structure may be identified at the right center of Fig. 15 and a horizontal scan passing through the cavity is drawn at the bottom. The measured peak-to-valley roughness

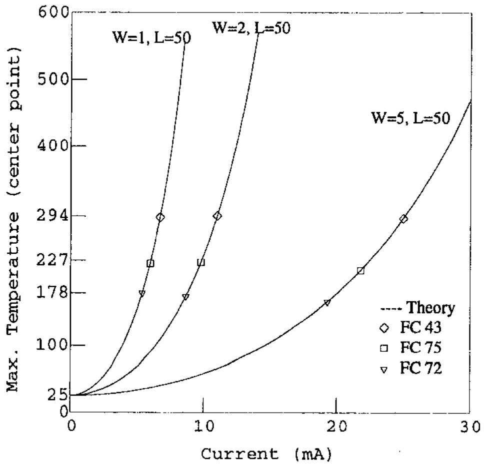

Fig. 12 Experimental results of nucleation currents with respect to temperature

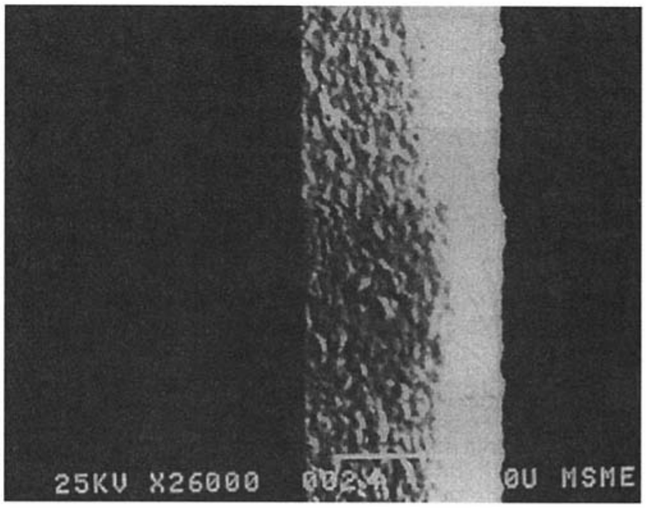

Fig. 14 Close-view SEM photo of a microheater with width of 2 μm

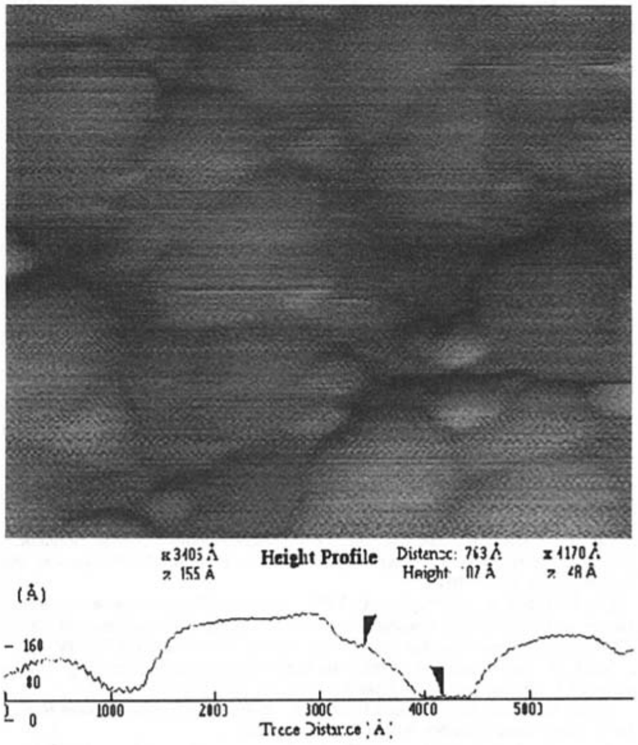

Fig. 15 AFM scanning result on a microresistor

of the cavity is about 10.7 nanometers. If a cavity of this size, 0.01 μm in radius, as suggested by the AFM measurement is actually activated, a superheat temperature of about 80°C should be reached according to Hsu's theory in Fig. 13. However, it should be noted that Hsu's analysis is the limiting case for bubble formation in the microboiling experiments. Further investigations, including modification or derivation of new theories, are required.

4.1.2 Homogeneous Nucleation. Homogeneous nucleation theories with experimental verifications have been derived for many years. There are two spinodal limits, van der Waals spinodal and Berthelot spinodal (Carey, 1992), which predict the thermodynamic limit of superheat. Blander et al. (Blander, Hengstenberg, and Katz, 1971; Blander and Katz, 1975) have demonstrated that the measured superheat limits are higher than the prediction of van der Waals spinodal but lower than that of Berthelot spinodal in their boiling experiments. For the working liquids used in this paper, Table 2 lists the calculation results of both spinodals at one atmospherical pressure. The measured ''activation temperatures'' as shown in Fig. 12 are clearly close to the superheat limits and spinodals rather than their boiling temperatures. Therefore, the experimental result strongly suggests that homogeneous nucleation occurs on these microline resistors.

4.2 Bubble Formation Phenomena.

4.2.1 Stable and Controllable Bubbles. In pool-boiling experiments, bubble forms and departs. The whole process can be monitored but the reverse of the process, including maintaining a stable bubble or controlling the size of the bubble, is not achievable. Microline resistors provide a unique opportunity to stabilize and control the growing bubble since they can quickly change the temperature field in a confined region. When a microbubble is nucleated, there are two thermal processes that dominate the thermal equilibrium condition: the evaporation process and the condensation process. The evaporation process is related to the input power from the microline resistor. The condensation process is dominated by the liquid/vapor contact interface where vapor is condensed when it meets with cool liquid. In order to reach steady state, these two processes must reach equilibrium. The overall thermodynamic reaction requires complicated three-dimensional analyses, including energy loss to the substrate, the latent heat transfer through the condensation process and simulations for the nonuniform temperature field. A preliminary first-order observation is provided in this paper. According to the energy law, the electrical power is roughly proportional to the square of the input current. On the other hand, the condensation process is roughly dominated by the area of the liquid/vapor interface that is proportional to the square of the bubble diameter. Therefore, under the first-order approximation, the size of the microbubble should change linearly with respect to the input current. Experimentally this trend has been observed (Lin, 1993).

4.2.2 Nucleation Hysteresis. Another important phenomenon to be discussed is the ''nucleation hysteresis.'' The name of nucleation hysteresis follows the report by Bakhru and Lienhard (1972). In Bakhru and Lienhard's experiments, small metal wires (0.001 to 0.004 in. in diameter) were used as the heaters and bubble nucleation tests were conducted in saturated liquids. They found that bubble will nucleate at one temperature while decrease at a lower temperature. The phenomenon is explained based on macroscale heterogeneous bubble nucleation theories. They suggested that larger nucleation sites are initially filled with liquid and do not function at the beginning of bubble nucleation. Small cavities which are filled with vapor nucleate first at an overshooting temperature. After the initial bubble nucleation, large cavities are filled with vapor and they are functional during the power decreasing process at a lower temperature. Therefore, nucleation hysteresis occurs.

The microscale boiling experiments suggest a different mechanism for nucleation hysteresis. First of all, the cavity theories for pool-boiling experiments are not generally applicable for microboiling experiments as discussed in the previous section. According to the cross-sectional simulation of isotherms as shown in Fig. 7, a thin layer of superheated liquid exists around the microline resistor. When the temperature is high enough such that homogeneous nucleation occurs, the bubble embryo grows with the help of the highly energized, superheated liquid. The stored energy helps the evaporation process during the initiation of the bubble formation and contributes the fast growing of the microbubble as observed in the experiments. After the first stage of bubble formation, the condensation process eventually catches up with the evaporation process as the bubble grows and becomes larger. By lowering the input power, an equilibrium state may be achieved when the evaporation process is in equilibrium with the condensation process. The bubble size becomes controllable at this stage. This explains the reason that the bubble only decreases at a lower temperature which causes nucleation hysteresis.

5 Conclusions

The combination of MEMS technologies and thermal bubble formation provides unique theoretical and experimental challenges. This paper has developed an electrothermal model for microline resistors which can be used as the foundation for further investigations. Experimentally, bubble formation processes are observed and discussed. Based on the established

Table 2 Superheat limits (T/T_c) for FC liquids and water

Liquid	FC 43	FC 72	FC 75	Water
van der Waals	85.5%	85.0%	85.2%	84.5%
Berthelot	92.4%	92.2%	92.3%	91.9%

model and experimental measurements, the bubble "activation temperatures" are close to the critical temperatures of the working liquids. Therefore, it is concluded that homogeneous nucleation occurs on these microline resistors. Several important thermophysical phenomena have been demonstrated:

1 Individual, spherical vapor bubbles with diameters from 2 to 500 μm have been generated by *locally* heating of working fluids.
2 Stable, controllable thermal microbubbles have been demonstrated by microboiling.
3 Strong Marangoni effects have prevented thermal bubbles from floating into working liquids.

Although this paper addresses the fundamentals of bubble formation on microline resistors, many scientific issues and techniques should be further investigated. If clear understanding of boiling phenomena generated by IC-processed microresistors can be achieved, both MEMS fluidic and thermal devices will benefit from these investigations. Specific areas to be explored are: local temperature measurements; models for bubble incipience mechanisms; transport process of vaporization and condensation; and three-dimensional thermal and fluidic models in the microscale.

Acknowledgment

The authors would like to thank Prof. K. S. Udell, Mechanical Engineering Department, U.C. Berkeley for valuable discussions. The devices were fabricated in the U.C. Berkeley Microfabrication Laboratory and this work was supported by Berkeley Sensor and Actuator Center, an NSF/Industry/University Cooperative Research Center. We acknowledge the support by an NSF CAREER Program (ELS-9734421).

References

3M, C., 1991, *Fluorinert Electronic Liquids Product Manual,* 3M Industrial Chemical Production Division, St. Paul, MN.

Ansoft, C., 1990, "Maxwell Solver," 4 Station Square, 660 Commerce Court Building, Pittsburgh, PA, v. 4.33.

Baker, E., 1972, "Liquid Cooling of Microelectronic Devices by Free and Forced Convection," *Microelectronics and Reliability,* Vol. 11, pp. 213–222.

Baker, E., 1973, "Liquid Immersion Cooling of Small Electronic Devices," *Microelectronics and Reliability,* Vol. 12, pp. 163–173.

Bakhru, N., and Lienhard, J., 1972, "Boiling from Small Cylinders," *Int. J. of Heat Mass Transfer,* Vol. 15, pp. 2011–2025.

Blander, M., Hengstenberg, D., and Katz, J. L., 1971, "Bubble Nucleation in *n*-Pentane, *n*-Hexane, *n*-Pentane + Hexadecane Mixtures and Water," *The Journal of Physical Chemistry,* Vol. 75, pp. 3613–3619.

Blander, M., and Katz, J., 1975, "Bubble Nucleation in Liquids," *AIChE Journal,* Vol. 21, pp. 833–848.

Carey, V., 1992, *Liquid-Vapor Phase-Change Phenomena,* Hemisphere Pub. Corp., Washington, DC.

Clark, H., Strenge, P., and Westwater, J., 1959, "Active Sites for Nucleate Boiling," *Chem. Eng. Prog. Symposium,* Vol. 55, pp. 103–110.

Collier, J., 1981, "Convective Boiling and Condensation," 2nd Ed., McGraw-Hill, New York.

Evans, J., Liepmann, D., and Pisano, A. P., 1997, "Planar Laminar Mixer," *Proceedings of IEEE Micro Electro Mechanical Systems (MEMS97),* pp. 96–101.

Gaertner, R., 1965, "Photographic Study of Nucleate Pool Boiling on a Horizontal Surface," ASME JOURNAL OF HEAT TRANSFER, Vol. 87, pp. 17–29.

Hahne, E., and Grigull, U., 1977, *Heat Transfer in Boiling,* Academic Press, New York.

Hsu, Y., 1962, "On the Size Range of Active Nucleation Cavities on a Heating Surface," ASME JOURNAL OF HEAT TRANSFER, Vol. 84C, pp. 207–216.

Lee, T., Simon, T., and Bar-Cohen, A., 1988, "An Investigation of Short Heating Length Effect on Flow Boiling Critical Heat Flux in a Subcooled Turbulent Flow," *Cooling Technology for Electronic Equipment,* Hemisphere, Washington, DC, pp. 435–450.

Lin, Liwei, 1993, "Selective Encapsulations of MEMS: Micro Channels, Needles, Resonators and Electromechanical Filters," Ph.D. dissertation, Mechanical Engineering Department, University of California at Berkeley, Berkeley, CA.

Lin, L., and Pisano, A., 1991, "Bubble Forming on a Micro Line Heater," *Micromechanical Sensors, Actuators and Systems,* ASME, New York, pp. 147–163.

Lin, L., Pisano, A., and Lee, A., 1991, "Microbubble Powered Actuator," *Digest of Transducers '91,* International Conference on Solid-State Sensors and Actuators, pp. 1041–1044.

Lin, L., Udell, K., and Pisano, A., 1993, "Vapor Bubble Formation on a Micro Heater in Confined and Unconfined Micro Channels," *Proceedings of ASME 1993 National Heat Transfer Conference,* ASME, New York, pp. 85–94.

Ma, C.-F., and Bergles, A., 1986, "Jet Impringement Nucleate Boiling," *International J. of Heat and Mass Transfer,* Vol. 29, pp. 1095–1011.

Mikic, B., Rohsenow, W., and Griffith, P., 1970, "On Bubble Growth Rate," *Int. J. Heat Mass Transfer,* Vol. 13, pp. 657–666.

Nielsen, N. J., 1985, "History of Thinkjet Printerhead Development," *HP Journal,* Vol. 36, No. 5, pp. 12–13.

Nagasaki, T., Hijikata, K., et al., 1993, "Boiling Heat Transfer from a Small Heating Element," *Proceedings of the 1993 ASME Winter Annual Meeting,* Vol. HTD-262, pp. 15–22.

Pitts, C., and Lepert, G., 1966, "The Critical Heat Flux for Electrically Heated Wires in Saturated Pool Boiling," *Int. J. Heat Mass Transfer,* Vol. 9, pp. 365–377.

Sniegowski, J., 1993, "A Micro Actuation Mechanism Based on Liquid-Vapor Surface Tension," *Digest of Late News of Transducers '93,* International Conference on Solid-State Sensors and Actuators, pp. 12–13.

Stephan, K., 1992, *Heat Transfer in Condensation and Boiling,* Springer-Verlag, New York.

Stralen, S., and Cole, R., 1979, *Boiling Phenomena: Physicochemical and Engineering Fundamentals and Applications,* Hemisphere, Washington, DC.

Sun, K., and Lienhard, J., 1970, "The Peak Pool Boiling Heat Flux on Horizontal Cylinders," *Int. J. Heat Mass Transfer,* Vol. 13, pp. 1425–1439.

Tseng, F.-G., Linder, C., Kim, C. J., and Ho, C.-M., 1996, "Control of Mixing with Micro Injectors for Combustion Application," *ASME International Mechanical Engineering Congress and Exposition,* Vol. DSC-59, pp. 183–187.

Zdeblick, M. J., and Angell, J. B., 1987, "A Microminiature Electric-to-Fluidic Valve," *Digest of Transducers '87,* International Conference on Solid-State Sensors and Actuators, pp. 827–829.

Zuber, 1961, "Vapor Bubbles in Non-uniform Temperature Field," *Int. J. Heat Mass Transfer,* Vol. 2, p. 83.

Capillary Performance of Evaporating Flow in Micro Grooves: An Approximate Analytical Approach and Experimental Investigation

G. P. Peterson[1]
Executive Associate Dean,
e-mail: GPP5386@teesmail.tamu.edu
Fellow ASME

J. M. Ha
Research Associate,
Mem. ASME.

Department of Mechanical Engineering,
Texas A&M University,
College Station, TX 77843-3123

The capillary flow along a microgroove channel was investigated both analytically and experimentally. In order to obtain insight into the phenomena, and because the governing equation had the form of a nonlinear differential equation, an analytical solution and approximate algebraic model were developed rather than using numerical methods. Approximating the governing equation as a Bernoulli differential equation resulted in an analytical solution for the radius curvature as the cube root of an exponential function. The axial variation of the radius of curvature profile as determined by this method was very similar to the numerical result as was the algebraic solution. However, the analytical model predicted the meniscus dryout location to be somewhat shorter than either the numerical results or the results from the algebraic solution. To verify the modeling results, the predictions for the axial capillary performance were compared to the results of the experimental investigation. The results of this comparison indicated that the experimentally measured wetted length was approximately 80 percent of the value predicted by the algebraic expression. Not only did the prediction for the dryout location from the algebraic equation show good agreement with the experimental data, but more importantly, the expression did not require any experimentally correlated constants. A nondimensionalized expression was developed as a function of just one parameter which consists of the Bond number, the Capillary number, and the dimensionless groove shape geometry for use in predicting the flow characteristics in this type of flow.

Introduction

Phase-change processes utilizing small capillary grooves are often incorporated in the design of heat transfer equipment to increase the effective liquid-vapor interfacial area for evaporation or the effective solid-vapor surface area for condensation. These capillary grooves allow the liquid to coalesce and promote the flow of liquid either away from the condensing region or towards the evaporating region, decreasing the average film thickness. Recently, increased interest in the use of phase-change heat transfer processes for the thermal control of electronic components, either through traditional methods (Peterson and Ortega, 1990) or more innovative methods involving the use of microscale devices (Peterson, 1992) has resulted in the need for a better understanding of the liquid film behavior in these grooves.

When a liquid contacts a flat surface, the extended meniscus is typically divided into three regions. The intrinsic meniscus region, dominated by the capillary forces; the evaporating thin film region, which has the combined effects of both capillarity and disjoining pressure; and the adsorbed layer region, where the disjoining forces dominate, inhibiting vaporization. The junction of the evaporating thin film region and the adsorbed layer is referred to as the interline region, and it is here that a majority of the heat transfer occurs due to the very thin film thickness. Thus, the magnitude of heat transfer is strongly affected by the pressure and magnitude of the interline region, which can be varied by controlling the number, length, and shape of the grooves. However, determination of the mechanism and parameters that govern the extended meniscus formed in the capillary grooves is still underway (Ha and Peterson, 1996).

A number of analytical and experimental investigations have been conducted to better understand the evaporating thin film formed on flat plates (DasGupta et al., 1993; Mirzamoghadam and Catton, 1988a, b; Potash and Wayner, 1972; Schonberg and Wayner, 1992; Sujanani and Wayner, 1991; Wayner et al., 1976), or associated with capillary feeder (Moosman and Homsy, 1980; Renk et al., 1978; Renk and Wayner, 1979a, 1970b). These studies, however, are all two-dimensional, and as a result are most helpful in understanding the evaporating flow along the groove wall. Additionally, two-dimensional analyses have been conducted by Holm and Goplen, (1979) and Stephan and Busse, (1992) for a fixed cross section in the groove. However, to completely understand the flow field through capillary grooves, the axial flow characteristics occurring in the intrinsic meniscus must also be investigated.

As reported previously, Stroes et al. (1992) conducted an experimental study of the evaporating flow through small grooves and compared the capillary forces in rectangular and triangular channels, and Xu and Carey (1990) conducted a combined analytical and experimental investigation of the liquid behavior in micro grooves. Following this, Ha and Peterson (1994) developed an approximate analytical solution for the axial dryout location, as a function of the input heat flux, the thermophysical properties, and the geometric parameters of the

---

[1] Address correspondence to Professor G. P. "Bud" Peterson, Engineering Program Office, 301 Wiesenbaker Engineering Research Center, Texas A&M University, College Station, TX 77843-3126.

Contributed by the Heat Transfer Division for publication in the JOURNAL OF HEAT TRANSFER. Manuscript received by the Heat Transfer Division, Sept. 23, 1997; revision received, Apr. 20, 1998. Keywords: Heat Transfer, Multiphase, Thin Films, Transient. Associate Technical Editor: P. Simpkins.

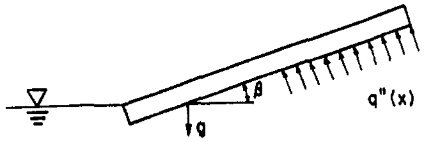

Fig. 1(*a*) Schematics of view side considered in the model

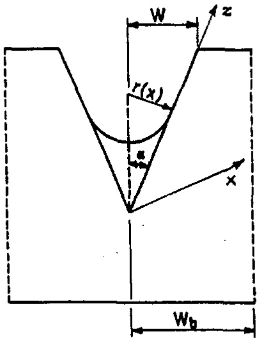

Fig. 1(*b*) Groove geometry

grooves. More recently, Ha and Peterson (1996) developed an analytical model for very small tilt angles using a perturbation method.

The present investigation is a continuation of this previous study, and was undertaken in an effort to better understand the axial capillary performance and the location of the axial dryout point. The objective of the current study is to predict the dryout location in a closed-form solution as a function of the governing parameters and verify the results by comparison with experimental data.

Theoretical Formulation

The current investigation considers thin liquid films flowing through V-shaped micro grooves as illustrated in Figs. 1(*a*) and 1(*b*). One end of the grooves was immersed in a pool of liquid and held stationary at a small inclination angle, β, while heat was supplied to a portion of the underside of the plate. For the current investigation, the capillary forces act against the gravitational body and frictional force, and determine the axially wetted length. An adiabatic region was included between the point where the plate emerges from the liquid pool and the upper region of the plate to which a known uniform heat flux is applied, as illustrated in Fig. 1(*a*).

For a very small groove, it can be assumed that the capillary radius of the intrinsic meniscus is constant at a given cross section. When heat is added to the plate, the radius of curvature of the intrinsic meniscus decreases gradually along the axial direction. As the liquid recedes further and further towards the apex of the groove, the liquid film thins, finally reaching a point where the disjoining force becomes strong enough to retard evaporation. The capillary pumping or wicking action is the result of this decrease in the radius of curvature.

In addition to promoting flow along the groove, this meniscus variation promotes flow up the groove sidewall. Above the intrinsic meniscus region of the groove wall, the film behavior is dominated by the dispersion forces. Since the resistance to flow in the evaporating thin film and adsorbed layer regions of the extended thin film is much larger than in the intrinsic meniscus region, it can be assumed that the majority of the axial flow is confined to the intrinsic meniscus region.

Based on the above arguments, several assumptions are made for determining the axial dryout point (Ha and Peterson, 1996). These are

(i) the axial flow along the groove in the x-direction occurs primarily in the intrinsic meniscus region;
(ii) the radius of curvature of the intrinsic meniscus is constant at a given location, x, but the radius of curvature varies axially along the groove, and the capillary pressure gradient due to this decreasing radius drives the liquid flow in the x-direction;
(iii) the disjoining pressure gradient due to the variation of the film thickness along the z-direction drives the film flow up the groove wall, and evaporation occurs primarily in the thin film region; and
(iv) the vapor pressure is constant, and the Kelvin effect was assumed to be negligible.

Since the convective term in the force-momentum equation can be neglected due to the low flow rate, the governing equation for steady, laminar flow in the x-direction can be simplified as

$$\frac{dP_l}{dx} + \rho_l g \sin \beta + F_v = 0 \qquad (1)$$

where β is the angle between the gravitational vector and a line normal to the grooved surface. If the vapor pressure, P_v, is assumed to be constant, the liquid pressure gradient can be expressed in terms of the radius of curvature by the Young-Laplace equation assuming a contact angle of 0 deg,

$$\frac{dP_l}{dx} = -\frac{d}{dx}(P_v - P_l) = -\frac{d}{dx}\left(\frac{\sigma}{r(x)}\right). \qquad (2)$$

Following the procedure originally proposed by Xu and Carey

Nomenclature

A = constant defined in Eq. (8)
B = constant defined in Eq. (8)
Bo = Bond number
c_3 = constant in Eq. (4)
Ca = Capillary number
D = dimensionless grove geometry defined in Eq. (29)
F = frictional coefficient
g = gravitational acceleration
h_{fg} = latent heat of vaporization
K = parameter in Eq. (3)
P = pressure
$q''(x)$ = heat flux normal to the bottom plate at x
$r(x)$ = radius of curvature in the intrinsic meniscus at x
R = dimensionless r in Eq. (33)
T = temperature
w = half of the top groove width
w_b = half of the bottom width
x = coordinate along the groove channel
X = dimensionless x in Eq. (33)
z = coordinate up the groove wall

Greek

α = half the vertex angle of the groove
β = slope of the plate with respect to gravity
Γ_c = mass flow rate per cross section in x-direction
ϵ = perturbation parameter
ν = kinematic viscosity
χ = dimensionless capillary performance in Eq. (28)
ρ = density
σ = surface tension

Subscript

j = junction of the adiabatic and evaporating regions
l = liquid
max = maximum of axial or groove side direction length
$m\beta0$ = maximum value in case of $\beta = 0$
v = vapor
o = origin or reference
sat = saturation

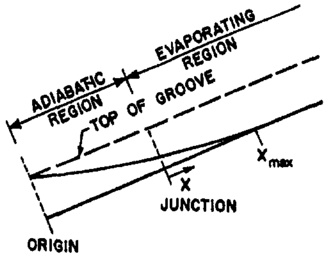

Fig. 2 Centerline film profile along the axial direction

(1990), Eq. (1) can be modified to represent a balance between viscous, surface tension, and gravitational forces to be

$$\frac{d}{dx}\left(\frac{\sigma}{r(x)}\right) = \frac{2K\nu_l}{c_3 r(x)^4}\Gamma_c + \rho_l g \sin\beta \tag{3}$$

where

$$c_3 = 4\tan^2\alpha\left(\frac{1}{\tan\alpha} + \alpha - \frac{\pi}{2}\right)^3. \tag{4}$$

In this expression, Γ_c is the mass flow rate through a given cross section of groove, and the parameter K, originally determined by Ayyaswamy et al. (1974), is a function of the groove half-angle α and the liquid contact angle. Note that Eq. (3) is valid for both the adiabatic and evaporating regions.

Evaporating Region. If the liquid in the evaporating region is assumed to be saturated, and the heat flux along the x-direction is given by $q''(x)$ the mass flow rate at position x, can be expressed as

$$\Gamma_c = \int_0^{\Gamma_c} d\Gamma_c = \frac{2w_b}{h_{fg}}\int_x^{\max} q''(x)dx \tag{5}$$

where the value of $x_{\max}$ is the point farthest from the liquid pool at which the intrinsic meniscus could still be considered to exist. The mass flow rate is zero at the dryout point $x_{\max}$, the location of which, as shown in Fig. 2, is measured from the junction between the heated and adiabatic regions of the plate.

For a uniform heat flux, $q''(x)$ will be a constant represented by q_b'', and the mass flow rate, Γ_c, in Eq. (5) at x can be expressed as

$$\Gamma_c = \int_0^{\Gamma_c} d\Gamma_c = \frac{2}{h_{fg}} q_b'' w_b (x_{\max} - x). \tag{6}$$

Combining Eq. (3) with Eq. (6) yields

$$r(x)^2\frac{dr}{dx} = -A(x_{\max} - x) - Br(x)^4 \tag{7}$$

where

$$A = \frac{4K\nu_l q_b'' w_b}{c_3\sigma h_{fg}} \quad \text{and} \quad B = \frac{\rho_l g \sin\beta}{\sigma}. \tag{8}$$

Equation (7) represents the general equation for $r(x)$ with a uniform heat flux and, as a nonlinear first-order ordinary differential equation with respect to x, can be solved numerically. However, Eq. (7) has an exact solution for the case of $B = 0$ (the case of zero inclination angle) which is

$$r(x)^2\frac{dr}{dx} = -A(x_{\max} - x). \tag{9}$$

Using the separation of variables method, the solution for $r(x)$ can be shown to be

$$r^3 = \tfrac{3}{2}A(x_{\max} - x)^2. \tag{10}$$

This equation for tilt angle $\beta = 0$ is expected to produce the longest axial wetted length. In the above solution, the boundary condition at the dryout point was used; ($r = 0$ at $x = x_{\max}$. Using the boundary condition at the junction ($r = r_j$ at $x = 0$), the expression for $x_{\max}$ with no inclination is given by

$$x_{m\beta 0} = \sqrt{\frac{2r_j}{3A}}\, r_j. \tag{11}$$

It is apparent that if r_j, is known, $x_{m\beta 0}$ for zero inclination angle can be predicted in a closed form. This value of $x_{m\beta 0}$ can be used as a reference length which characterizes the longest wetted length for a given set of geometric and thermophysical parameters.

For the general case of a finite tilt angle, i.e., $\beta \neq 0$, Eq. (7) becomes a nonlinear differential equation with no analytical solution, and must be solved numerically. However, numerical computation shows only the final discrete results and does not provide any information about the relationship between the various parameters being investigated. It is, however, possible to approximate Eq. (7) in order to obtain an analytical solution for $x_{\max}$ in a closed form.

Consider again the nonlinear expression given in Eq. (7).

$$\frac{dr}{dx} + Br^2 = -A(x_{\max} - x)r^{-2} \tag{12}$$

Based on the known boundary conditions, Ha and Peterson (1994) approximated the term dr/dx in the left-hand side of Eq. (12) as

$$\frac{dr(x)}{dx} = \frac{2r_j}{x_{\max}^2}(x - x_{\max}). \tag{13}$$

By substituting Eq. (13) into Eq. (12), the nonlinear differential equation was changed to an algebraic equation in r

$$2r(x)^2 r_j\left(\frac{x - x_{\max}}{x_{\max}^2}\right) = -A(x_{\max} - x) - Br(x)^4. \tag{14}$$

Using the boundary condition $r = r_j$ at $x = 0$, Eq. (14) yielded the following explicit expression for $x_{\max}$:

$$x_{\max} = \frac{r_j}{2A}\left(-Br_j^3 + \sqrt{B^2 r_j^6 + 8Ar_j}\right). \tag{15}$$

This equation developed by Ha and Peterson (1994) indicates that the axial location of the dryout point, $x_{\max}$, is a function of r_j, A, and B.

As an alternative to the previous method, the method proposed here for obtaining a closed form of solution is to modify $r(x)$ rather than dr/dx in Eq. (13). To do so, the following boundary conditions can be considered:

$$\text{at} \quad x = x_{\max}, \quad r \approx 0 = 0$$
$$\text{at} \quad x = 0, \quad r = r_j. \tag{16}$$

From only two boundary conditions, the simplest form of a linear profile for $r(x)$ can be obtained as

$$r(x) = \frac{r_j}{x_{\max}}(x_{\max} - x). \tag{17}$$

Substituting this expression for one of $r(x)$ terms in the $r(x)^2$ term on the left-hand side of Eq. (12) results in a modified form of Eq. (12)

$$\frac{dr}{dx} + \frac{Br_j}{x_{\max}}(x_{\max} - x)r = -A(x_{\max} - x)r^{-2}. \qquad (18)$$

This is still a nonlinear differential equation, but this nonlinear form is well known as the Bernoulli differential equation and can be reduced to a linear form by a suitable change of the dependent variable, i.e., by letting $r(x)^3$ be $u(x)$, which yields

$$\frac{du(x)}{dx} + \frac{3Br_j}{x_{\max}}(x_{\max} - x)u(x) = -3A(x_{\max} - x). \qquad (19)$$

Equation (19) has a solution of the following form:

$$u(x) = e^{-h}\left\{\int e^{h} 3Axdx + c\right\} \qquad (20)$$

where

$$h = \int \frac{-3Br_j}{2x_{\max}} xdx. \qquad (21)$$

The integration constant, c, can be determined by using the boundary condition $r = 0$ at $x = x_{\max}$. Returning to the original notation yields the following expression for $r(x)$:

$$r(x)^3 = \frac{-Ax_{\max}}{Br_j}\left\{1 - \exp\left(\frac{3Br_j}{2x_{\max}}(x_{\max} - x)^2\right)\right\}, \qquad (22)$$

and using the boundary condition $r = r_j$ at $x = 0$, the above equation yields an expression for $x_{\max}$ of

$$x_{\max}\left\{\exp\left(\frac{3Br_j}{2}x_{\max}\right) - 1\right\} = \frac{B}{A}r_j^4. \qquad (23)$$

This equation again indicates that $x_{\max}$ is dependent upon r_j, A, and B, but here values of r_j can be found by analyzing the liquid flow behavior in the adiabatic region. It is interesting to note that as B approaches zero the solution to Eq. (23) approaches Eq. (11), provided e^x is expanded as a series in x and is truncated at B^1.

Adiabatic Region. In the adiabatic region, the axial mass flow rate at any position is constant and equal to the total mass flow rate evaporated over the entire length of the evaporating region, which for uniform heat flux in the adiabatic region can be expressed as a function of $x_{\max}$ as

$$\Gamma_c = \Gamma_j = \Gamma_o = \frac{2q_b'' w_b}{h_{fg}} x_{\max}. \qquad (24)$$

Substituting this expression into the governing equation, Eq. (7), and rearranging yields

$$\frac{dr}{dx'} = -\frac{Ax_{\max}}{r(x')^2} - Br(x')^2, \qquad (25)$$

which must be solved numerically. Assuming that the thin liquid of the meniscus completely fills the V-groove at the origin results in a boundary condition of the form

$$r(x) = r_o = \frac{w}{\cos\alpha} \quad \text{at} \quad x' = 0. \qquad (26)$$

The radius of curvature at the junction r_j can be calculated from Eq. (25) with the boundary condition shown in Eq. (26), but the length of the adiabatic region must be given. It is important to note that the value of r_j used in Eq. (23) comes from the calculation through the adiabatic region; i.e., from $x' = 0$ not from $x = 0$.

An initial value of r_j less than $w/\cos\alpha$ is assumed as the first estimate to obtain an initial value of $x_{\max}$ using Eq. (23). This value is then substituted into Eq. (25) to obtain a second value for r_j, which in turn results in a second value for $x_{\max}$. This iterative procedure continues until r_j and $x_{\max}$ converge within a predetermined allowable accuracy. After having determined the value of $x_{\max}$, Eq. (22) is used to obtain $r(x)$.

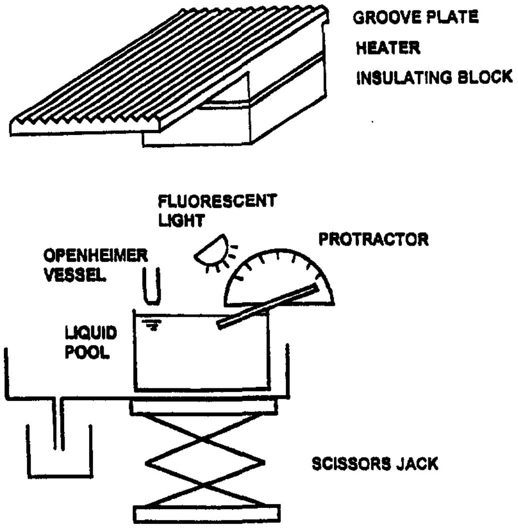

Fig. 3 Groove plate system and test apparatus

Experimental Description

In order to validate the assumptions and procedures used in the development of the analytical model a series of experiments were conducted. For the evaporating meniscus phenomena in a grooved channel it is typically possible to detect the overall characteristics, such as the axial wetted length and plate temperature. However, because of the small physical dimensions—usually micrometers or smaller in magnitude that are associated with a meniscus—it is extremely difficult to determine the *local* experimental data such as film thickness near the interline region.

Experimental work in the measurement of micro scale meniscus phenomena has been carried out by Wayner's research group (Sujanani and Wayner, 1991; DasGupta et al., 1993; etc.), but these were all for two-dimensional problems, i.e., thin film profiles on a horizontal substrate. For grooved channels, no experimental data are available in which local measurements of the microscale meniscus have been made. The experimental system described here was constructed to measure two characteristics: the evaporating wetted length in the axial direction and the local plate temperature.

Figure 3 illustrates the grooved plate system and test apparatus. Due to the visibility problems associated with a closed chamber system, the current experiments were conducted in an open air environment. Similar experiments were conducted by Stroes et al. (1992), but these did not measure the plate temperature. In an open air experiment, the plate temperature is equal to, or more important than the applied heat flux in determining the saturation pressure. A thin flexible heater was attached to the bottom of the grooved plate, and covered by an insulating block. The entire grooved plate system was mounted on a baseplate whose angle of inclination could be adjusted. One end of the plate was immersed in the liquid pool. An overflow method by continuous dripping from an Openheimer vessel was used to maintain the liquid level at a constant value. A controllable fluorescent lamp was placed over the grooved plate to enhance the visibility of the dryout point and to allow detection of the end of the evaporating meniscus.

The focus of the experimental apparatus is a copper plate with a series of triangular V-shape grooves machined into the surface. As shown in Fig. 4, the plate had a groove width of $w = w_b = 0.19$ mm, and an apex half-angle of $\alpha = 30$ deg. The detailed dimensions of the plate are given in Fig. 5. In the heated region, four small diameter holes were drilled perpendicular to the heat flux direction, and special limit of error, 30 gage, T-type thermocouples with an experimental uncertainty of ±0.2°C were embedded to measure the temperature of the heated region 0.1 mm below the grooves.

The adiabatic region was comparatively thin; whereas the heated region was quite thick to avoid conduction heat losses to the adiabatic region, and to allow the applied heat flux from the heater to be distributed uniformly. A flexible thermofoil heater was used to supply a uniform heat flux, and was attached with a thin layer of silicon cement on the bottom of the heated portion. The input power was measured using a digital multimeter, which produced an uncertainty of ±0.001 watts.

In order to ensure that the applied heat was only dissipated through evaporation, insulation was applied to the liquid pool reservoir and the backside of the heater. To reduce axial conduction through the plate, the liquid temperature in the pool was held constant at the same temperature as that of the heated region.

To prevent heat losses from the liquid pool to the environment, a heating system was inserted in the liquid pool. As shown in Fig. 6, two heaters were used to enhance both the temperature stability and the circulation of the liquid. This allowed the coolant temperature to be controlled to within ±0.5°C. A large heater was placed at the lower zone and connected to a variable transformer power supply and a smaller heater was connected to a d-c power supply, and was controlled by a temperature controller to maintain the liquid temperature to within ±0.5°C of the temperature of the heated region. A thin film RTD was used to monitor the temperature of the reservoir.

A 1-cm layer of silicone rubber sealant with a thermal conductivity of 0.208 W/m K was used to insulate the backside of the grooved plate, and two thermocouples were embedded in the two surfaces of the insulating block to calculate the conduction heat loss through the insulation. All the thermocouples from the grooved plate and the insulating block were connected to a data logger to monitor and record the corresponding temperatures.

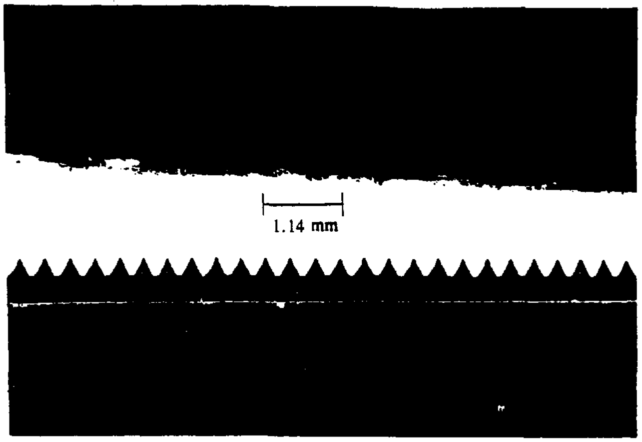

Fig. 4 Micrograph of the triangular groove surface

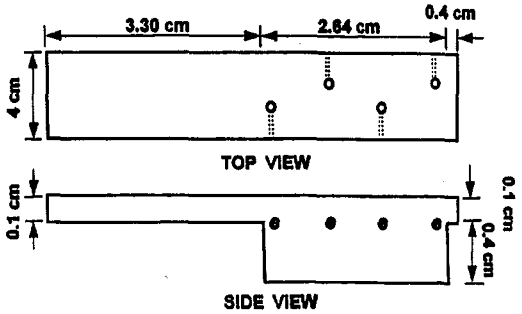

Fig. 5 Top and side views of groove plate

The axial wetted length was measured to within ±1.0 mm for various combinations of heat fluxes, tilt angles, and fluid properties. Prior to conducting the experiment, cleaning of the grooved copper plate was repeated several times. The plate was immersed in an acetone pool for approximately five minutes to remove any oils on the surface, then in a 20 percent nitric acid solution for about ten minutes to remove any surface oxides, and finally, rinsed in pure distilled water. The grooved plate system (grooved plate with heater, and insulating block) was then mounted on the baseplate and the angle was adjusted. One end of the grooved plate was immersed in the liquid pool and the working fluid wicked up into the grooves, with the length of the unheated portion of the groove adjusted until the dry out point reached the end of the heated region. Tests were conducted using methanol and ethanol, both of which have good wettability on copper surfaces.

Because the experiment was conducted in the open air, the vaporization did not occur into a pure vapor, hence the vapor was not at the saturation pressure. In order to calculate the partial pressure of the working fluid vapor, it was assumed that the measured plate temperature was equal to the temperature of the grooved substrate on which the evaporation occurred, and that the substrate temperature was at the vapor saturation temperature. Given that there was nearly continuous vapor production, that the liquid film was very thin, and that there is negligible diffusion into the air, this assumption was justified. Once the saturation temperature had been determined, the saturation pressure and fluid properties could be obtained. Preliminary tests were conducted to ensure that the measured temperatures were nearly the same along the entire length of the channel. To further ensure that all the fluid wicked up along the axial direction was at saturation conditions, a HUGHES Probeye TVS 3000 infrared thermal imaging system was used which provided temperature resolutions to within 0.01°C. This system verified a nearly constant temperature distribution (±0.5°C) of the interface along the entire length of the axial channel and indicated no measurable temperature variation in the axial direction.

After reaching steady state, and the desired conditions, (i.e., dryout at the axial end of the channel and a pool temperate equal to the temperature of the heated region), all the temperatures were recorded. Using the temperature of the heated region the saturation pressure and fluid properties were calculated, as was the heat loss through the backside of the heater. The heat loss through the plate to the liquid pool could be neglected, since the temperature of the liquid pool was held at a temperature equal to that of the heated region. The adiabatic length was measured using a cold stainless steel vernier scale, and a fluorescent lamp was used to help detect the dryout point. To obtain the net heat utilized in the evaporation process, the heat loss through the backside of the heater was subtracted from the applied heat. Using the procedure described above, the wetted length and the working fluid temperature were measured to within 0.01 mm and 0.2°C, respectively, for a variety of working fluids, tilt angles, and input heats.

Results and Discussion

Applying the numerical calculation of Euler to the nonlinear differential governing equation produces a meniscus profile, a radius of curvature, and $x_{\max}$. The approximate analytical method described previously was used to determine the radius of curvature r and the location of the dryout point $x_{\max}$. The governing equation was then transformed into the well-known Bernoulli differential equation, to produce a closed-form exact

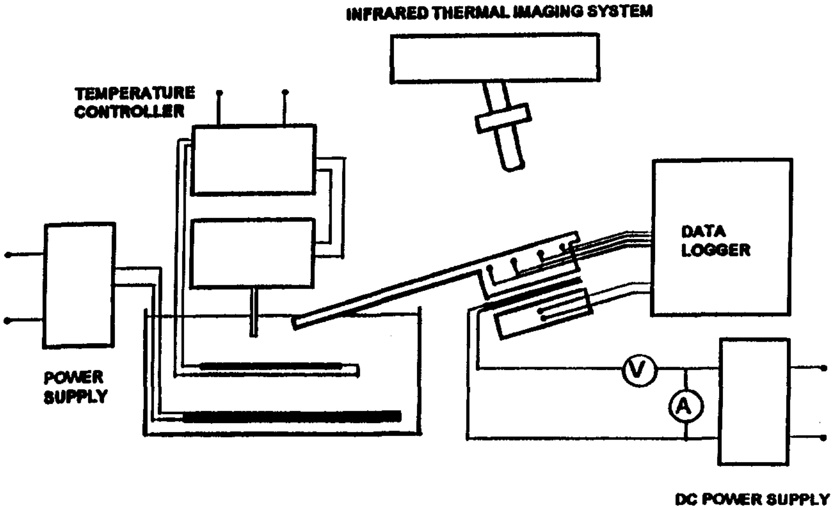

Fig. 6 Schematics of the experimental system

solution for r expressed as the cube root of an exponential function.

In the theoretical predictions, property values at a saturation pressure of 1 atm were used, and r_j was set equal to r_o for simplicity, i.e., no adiabatic region along the x-direction. For a given set of conditions, $x_{\max}$ was first calculated from Eq. (23), and then the value of r was obtained directly from Eq. (22). The axial profiles for $r(x)$ calculated by the numerical method and those found using Bernoulli's equation are plotted in Figs. 7(*a*) and 7(*b*) for the case of methanol, with $w = w_b = 0.19$ mm, $\alpha = 30$ deg, $\beta = 15$ deg and 25 deg; at two different thermal loads; $q_b'' = 5{,}000$ W/m^2 and $q_b'' = 10{,}000$ W/m^2, respectively. Increasing the heat flux and/or the tilt angle, forces $x_{\max}$ to be shortened. For every case, under the same conditions, the profiles obtained from Bernoulli's equation demonstrates a shorter value for $x_{\max}$ than those obtained from the numerical method, due to the steep slope of $r(x)$ in Bernoulli's equation, caused by the exponential function in Eq. (22). However, the form of $r(x)$ displayed similar features in the convex form to those obtained using the numerical solution technique. This result confirms that the characteristic shape of the $r(x)$ profile obtained from the numerical calculation can be approximated as an exponential function as shown in Eq. (22).

It is interesting to compare the values of $x_{\max}$ obtained from the algebraic equation presented previously by Ha and Peterson (1994) to those obtained here using the numerical method and Bernoulli's equation. The values of $x_{\max}$ with respect to the

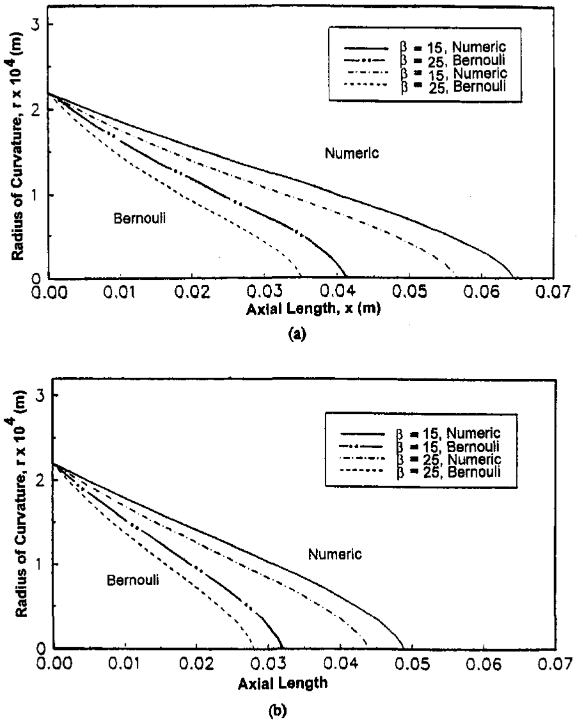

Fig. 7 Radius of curvature versus axial length of several approaches for methanol, $w = 0.19$ mm, $\alpha = 30$ deg; and (*a*) $q_b'' = 5.0$ Kw/m^2, (*b*) $q_b'' = 10.0$ KW/m^2

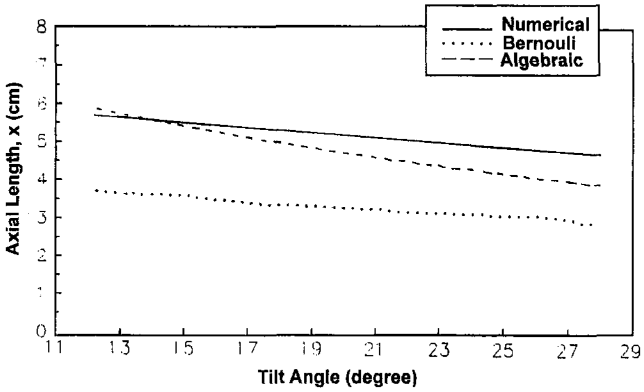

Fig. 8(*a*) $x_{\max}$ versus β for methanol, $w = 0.19$ mm, $\alpha = 30$ deg, $q_b'' = 7.5$ KW/m^2

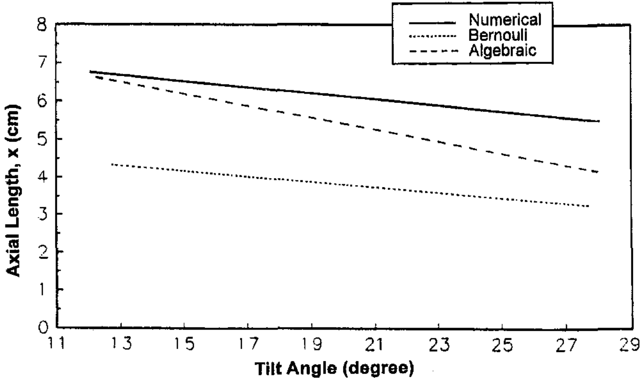

Fig. 8(*b*) $x_{\max}$ versus β for methanol, $w = 0.19$ mm, $\alpha = 30$ deg, $q_b'' = 5.0$ KW/m^2

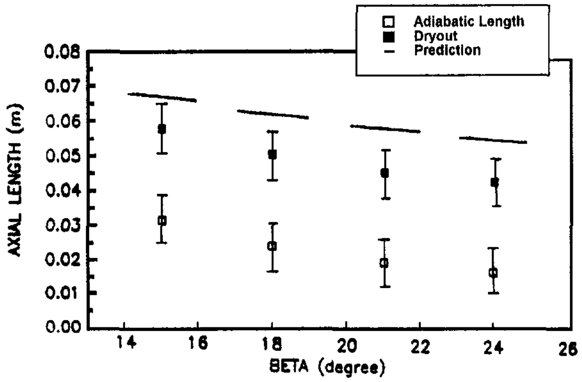

Fig. 9(*a*) Wetted axial length for methanol, $w = 0.19$ mm, $q_b'' = 5.87$ KW/m^2, $T_{sat} = 46°$C

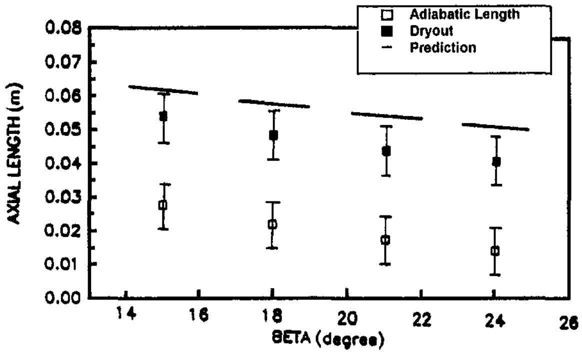

Fig. 9(*b*) Wetted axial length for methanol, $w = 0.19$ mm, $q_b'' = 7.20$ KW/m^2, $T_{sat} = 49°$C

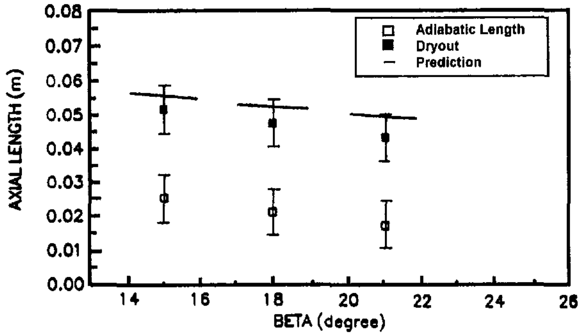

Fig. 9(*c*) Wetted axial length for methanol, $w = 0.19$ mm, $q_b'' = 9.58$ KW/m^2, $T_{sat} = 52°$C

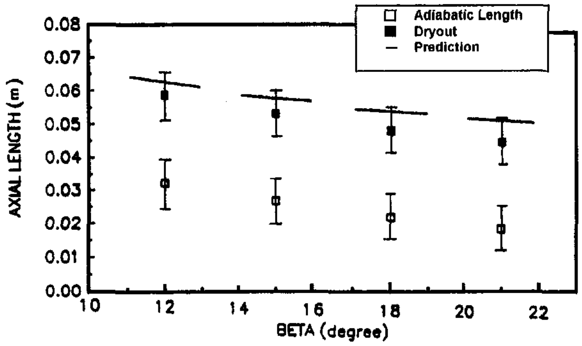

Fig. 9(*d*) Wetted axial length for ethanol, $w = 0.19$ mm, $q_b'' = 4.42$ KW/m^2, $T_{sat} = 49°$C

varying tilt angle for the case of $q_b'' = 7{,}500$ W/m^2 and $w = w_b = 0.19$ mm and $\alpha = 30$ deg are plotted in Fig. 8(*a*). As illustrated, the difference of $x_{\max}$ between the numerical method and the Bernoulli equation is nearly constant for every tilt angle,

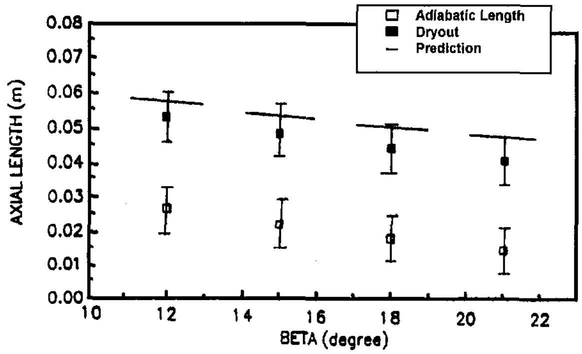

Fig. 9(*e*) Wetted axial length for ethanol, $w = 0.19$ mm, $q_b'' = 5.61$ KW/m^2, $T_{sat} = 57°$C

while the values of $x_{\max}$ from the numerical method are significantly larger than those from the Bernoulli equation. This tendency is also apparent in Fig. 8(*b*) for $q_b'' = 5{,}000$ W/m^2.

Comparison of Figs. 8(*a*) and 8(*b*) illustrates the effect of heat flux, with a smaller heat flux inducing a longer wetted length. For every case shown in Figs. 8(*a*) and 8(*b*) the values of $x_{\max}$ from the numerical method are larger than those obtained from the Bernoulli equation, and are nearly the same as those obtained from the algebraic equation.

By comparing these predictions with the experimental data the most applicable model can be identified. As described previously, the experimental system was designed to control the length of the adiabatic region, yet maintain a constant length of the heated region. The experimental data for a variety of cases are plotted in Figs. 9(*a*) through 9(*e*) with predictions from Eq. (15) also shown. The capillary performance, i.e., the axial wetted lengths, with respect to tilt angle and applied heat flux, were measured for two working fluids, methanol and ethanol. The range of tilt angles and heat fluxes was limited due to the dimensions of the grooved plate.

The controlled length of the adiabatic region is denoted by the empty box □, and the location of dryout on the groove plate is denoted by the solid box ■. For all cases, the variations of the measured value was within ±1.0 mm. The data denoted by the symbols □ and ■ represent the mean value of the maximum and minimum wetted axial lengths observed for each set of conditions. As the applied heat flux was increased, the thinning of the fluids along the groove became less abrupt, and continued gradually, ending in a region that was partially dried and wet over time. As expected, the capillary performance for the fluids decreased with increased tilt angles and/or increased heat flux.

The predicted values of $x_{\max}$, calculated from Eq. (15) are plotted and denoted by the dashed line. In the calculation of $x_{\max}$, the length of the adiabatic region used was the measured value, and for this adiabatic length, some of the values of the calculated $x_{\max}$ values are plotted. For example, in Fig. 9(*a*), for a given heat flux at $\beta = 21$ deg, the dryout point meets the end of the heated region with an adiabatic length of 2 cm. Some $x_{\max}$ values for an adiabatic length of 2 cm are calculated from Eq. (15) for the range of $\beta = 20$ deg to 22 deg. Figures 9(*a*) through 9(*c*) illustrate the results for methanol at three heat fluxes while Figs. 9(*d*) and 9(*e*) show ethanol at two heat fluxes. For the same conditions, the measured value of $x_{\max}$ for methanol were slightly greater than those for ethanol. Under the same heat flux and groove size, methanol induced a longer wetted length than ethanol because the latent heat of methanol is larger. For all cases, the plate temperature of the heated region was used as the saturation temperature of the working fluid, as explained previously.

The predicted values for all cases are slightly higher than the experimental data. The measured values are from 80 percent to 90 percent of the predicted values of algebraic equation. In considering the results of Figs. 8(*a*) and 8(*b*), Bernoulli's equation yields a slightly smaller value than those obtained from the algebraic equation. Thus, prediction by Bernoulli's equation, at first glance, seems to more closely predict the experimental data than does the algebraic equation. However, the slightly overpredicted value obtained from the algebraic equation may be preferable because the possible existence of wall contamination and evaporation in the adiabatic region may hinder the capillary performance. In practice, the triangular grooves were not quite triangular in shape as seen in Fig. 4, while the theory assumes a pin-point sharp triangular groove. This geometrical effect of the grooves as well as the surface roughness may have hindered the wicking action.

From these observations it is apparent that the prediction from the algebraic equation, Eq. (15), is preferable when predicting the capillary performance.

It is important to note that the expression given in Eq. (15) has no empirical constants, yet the capillary performance is in very good agreement with the experimental data. As a result, it is worthwhile to reexamine Eq. (15). By scaling Eq. (15) with r_o, Ha and Peterson (1994) presented a physical explanation of the capillary performance using dimensionless parameters such as the Bond number, Bo (the ratio of gravitational and surface tension forces), and the capillary number, Ca (the ratio of viscous and surface tension forces) as follows:

$$\chi_{\max} = \frac{-\mathrm{Bo}\sin\beta R_j^4}{D\mathrm{Ca}} + \sqrt{\left(\frac{\mathrm{Bo}\sin\beta R_j^4}{D\mathrm{Ca}}\right)^2 + \frac{4R_j^3}{D\mathrm{Ca}}} \quad (27)$$

where

$$\chi_{\max} = \frac{x_{\max}}{r_o}, \quad R_j = \frac{r_j}{r_o} \quad (28)$$

and

$$\mathrm{Bo} = \frac{\rho g r_o^2}{\sigma}, \quad \mathrm{Ca} = \frac{\nu_l q_b''}{\sigma h_{fg}}, \quad D = \frac{8Kw_b \cos\alpha}{c_3 w}. \quad (29)$$

Because r_o defined in Eq. (26) characterizes not only the groove width but the groove depth, it was used as the reference length for Bo and $\chi_{\max}$. In Eq. (27), $\chi_{\max}$ is expressed by R_j, sin β and three dimensionless variables, Bo, Ca, and D. The first of these, R_j, accounts for the length of the adiabatic region, sin β for the inclination angle, Bo for some of the fluid properties, Ca for the combined effect of the remaining fluid properties and the heat input, and D for the groove shape. Here, Eq. (27) can be changed into a more concise and simple form.

Equation (27) scaled by $x_{m\beta 0}$ in Eq. (11) has the form

$$\chi_{\max} = -\tfrac{3}{4}R_j\epsilon + \sqrt{(\tfrac{3}{4}R_j\epsilon)^2 + 3} \quad (30)$$

where

$$\chi_{\max} = \frac{x_{\max}}{x_{m\beta 0}}, \quad \epsilon = x_{m\beta 0} r_o B. \quad (31)$$

In this expression, $\chi_{\max}$ is described in a closed form by only two dimensionless variables, R_j and ϵ. Here, it is useful to consider the physical meaning of the term of ϵ defined in Eq. (31).

Equation (7) scaled by $x_{m\beta 0}$ has the following equivalent form:

$$\begin{aligned} R^2 \frac{dR}{dX} &= \frac{x_{m\beta 0}^2}{r_o^3} A(X - \chi_{\max}) - x_{m\beta 0} r_o B R^4 \\ &= \frac{2}{3} R_j^3 (X - \chi_{\max}) - \epsilon R^4 \end{aligned} \quad (32)$$

where

$$R = r/r_o, \quad X = x/x_{m\beta 0}. \quad (33)$$

The second term in the right-hand side in Eq. (32), ϵR^4, represents the effect of the gravitational term which causes the governing equation to change from a linear differential equation to a nonlinear differential equation. Thus, ϵ can be interpreted as a perturbation parameter. Introducing this perturbation parameter, a physical explanation of ϵ is possible and can be represented as a group of dimensionless parameters as follows:

$$\begin{aligned} \epsilon = x_{m\beta 0} r_o B &= \frac{\rho g}{\sigma} \sqrt{\frac{2r_j}{3A}}\, r_j r_o \sin\beta \\ &= 2R_j \sqrt{\frac{R_j}{3\mathrm{Ca}D}}\, \mathrm{Bo} \sin\beta. \end{aligned} \quad (34)$$

In Eq. (34), ϵ is expressed as a function of R_j, sin β and three dimensionless variables, Bo, Ca, and D. In other words, it is possible that R_j, sin β, Bo, Ca, and D can be combined into a parameter ϵ in Eq. (34). If there is no adiabatic region, then $R_j = 1$, and $X_{\max}$ can be expressed in a very concise form as a function of only one variable, ϵ. That is,

$$\chi_{\max} = -\tfrac{3}{4}\epsilon + \sqrt{(\tfrac{3}{4}\epsilon)^2 + 3}. \quad (35)$$

Conclusion

In analyzing the capillary flow in a microgroove channel the analysis of the intrinsic meniscus in the axial direction is important, due to the size of the evaporating thin film region on the *groove* wall. For the intrinsic meniscus region, the capillary pressure difference was assumed to be caused by the receding of the intrinsic meniscus, which resulted in the axial liquid flow along the groove. Because the governing equation had the form of a nonlinear differential equation, approximate analytical solutions rather than a numerical calculation were used to obtain insight into the phenomena.

Approximating the governing equation as a Bernoulli differential equation yielded a solution for the radius curvature as the cube root of an exponential function and the axial profile of the radius of curvature was similar to the numerical results. The current model, however, predicts the dryout location to be somewhat shorter than that of the numerical model or the algebraic equation solution.

These predictions for the axial capillary performance were compared to experimental data obtained in an open air environment. The results demonstrated that the prediction from the algebraic equation slightly overpredicts the wetted length and that the experimental data is approximately 80 percent of the algebraic prediction. The expression for the dryout location obtained from the algebraic equation showed good agreement with experimental data, and perhaps more importantly, required no experimentally correlated constants. The equation was nondimensionalized, and expressed as a function of just one parameter which consists of the Bond number, the Capillary number, and the dimensionless groove shape geometry.

References

Ayyaswamy, P. S., Catton, I., and Edwards, D. K., 1974, "Capillary Flow in Triangular Grooves," ASME *Journal of Applied Mechanics*, Vol. 41, pp. 332–336.

DasGupta, S., Schonberg, J. A., and Wayner, P. C., Jr., 1993, "Investigation of an Evaporating Extended Meniscus Based on the Augmented Young-Laplace Equation," ASME JOURNAL OF HEAT TRANSFER, Vol. 115, pp. 201–214.

Ha, J. M., and Peterson, G. P., 1994, "Analytical Prediction of the Axial Dryout Point for Evaporating Liquids in Triangular Microgrooves," ASME JOURNAL OF HEAT TRANSFER, Vol. 116, pp. 498–503.

Ha, J. M., and Peterson, G. P., 1996, "Capillary Performance of Evaporating Flow in Micro Grooves; An Analytical Approach for Very Small Tilt Angles," ASME JOURNAL OF HEAT TRANSFER, submitted for publication.

Holm, F. W., and Goplen, S. P., 1979, "Heat Transfer in the Meniscus Thin-Film Transition Region," ASME JOURNAL OF HEAT TRANSFER, Vol. 101, pp. 498–503.

Moosman, S., and Homsy, G. M., 1980, "Evaporating Menisci of Wetting Fluids," *J. of Colloid and Interface Science*, Vol. 73, No. 1, pp. 212–223.

Mirzamoghadam, A., and Catton, I., 1988a, "A Physical Model of the Evaporating Meniscus," ASME JOURNAL OF HEAT TRANSFER, Vol. 110, pp. 201–207.

Mirzamoghadam, A., and Catton, I., 1988b, "Holographic Interferometry Investigation of Enhanced Tube Meniscus Behavior," ASME JOURNAL OF HEAT TRANSFER, Vol. 110, pp. 208–213.

Peterson, G. P., and Ortega, A., 1990, "Thermal Control of Electronic Equipment and Devices," *Advances in Heat Transfer*, Vol. 20, J. P. Hartnett and T. F. Irvine, eds., Pergamon Press, New York, pp. 181–314.

Peterson, G. P., 1992, "An Overview of Micro Heat Pipe Research," invited review article, ASME *Applied Mechanics Reviews*, Vol. 45, pp. 175–189.

Potash, M., and Wayner, P. C., Jr., 1972, "Evaporation from a Two-dimensional Extended Meniscus," *Int. J. Heat and Mass Transfer*, Vol. 15, pp. 1851–1863.

Renk, F., Wayner, P. C., Jr., and Homsy, C. M., 1978, "On the Transition between a Wetting Film and a Capillary Meniscus," *J. of Colloid and Interface Science*, Vol. 67, pp. 408–414.

Renk, F. J., and Wayner, P. C., Jr., 1979a, "An Evaporating Ethanol Meniscus, Part I: Experimental Studies," ASME JOURNAL OF HEAT TRANSFER, Vol. 101, pp. 55–58.

Renk, F. J., and Wayner, P. C., Jr., 1979b, "An Evaporating Ethanol Meniscus, Part II: Analytical Studies," ASME JOURNAL OF HEAT TRANSFER, Vol. 101, pp. 59–62.

Schonberg, J. A., and Wayner, P. C., Jr., 1992, "Analytical Solution for the Integral Contact Line Evaporative Heat Sink," *J. Thermophysics*, Vol. 6, 170.1, pp. 128–134.

Stephan, P. C., and Busse, C. A., 1992, "Analysis of the Heat Transfer Coefficient of Grooved Heat Pipe Evaporator Walls," *Int. J. Heat & Mass Transfer*, Vol. 35, No. 2, pp. 383–391.

Stroes, G., Rohloff, T., and Catton, I., 1992, "An Experimental Study of the Capillary Forces in Rectangular Channels vs. Triangular Channels," Vol. HTD 301. ASME, New York, pp. 1–8.

Sujanani, M., and Wayner, P. C., Jr., 1991, "Spreading and Evaporative Processes in Thin Films," *J. Colloid and Interface Science*, Vol. 143, No. 2, pp. 472–488.

Wayner, P. C., Jr., Kao, Y. K., and LaCroix, L. V., 1976, "The Interline Heat-Transfer Coefficient of an Evaporating Wetting Film," *Int. J. Heat & Mass Transfer*, Vol. 19, pp. 487–492.

Xu, X., and Carey, V. P., 1990, "Film Evaporation from a Micro-Grooved Surface—An Approximate Heat Transfer Model and its Comparison with Experimental Data," *AIAA J. of Thermophysical and Heat Transfer*, Vol. 4, No. 4, pp. 512–520.

Chun-Liang Lai[1]

Wen-Lang Tang

Department of Mechanical Engineering,
National Taiwan University,
Taipei, Taiwan 106, R.O.C.

Transient Thermocapillary Flows Induced by a Droplet Translating in an Electric Field

A spherical dielectric droplet translating steadily in another dielectric liquid with a uniform electric field imposed in the translational direction of the droplet is studied theoretically. With the small Reynolds number and large Peclet number assumptions, analytic solutions are obtained for the stream function with a term involving the interfacial temperature distribution which is then computed numerically. The results indicate that the interfacial temperature distribution is indeed nonuniform and the thermocapillarity might exist thereby. The induced thermocapillary flows in the droplet are usually of multiple cells with which the heat transfer rate may increases or decreases depending on whether the original flow is enhanced or suppressed. For the example calculated in the present study, the heat transfer rate is decreased by the thermocapillary effect.

Introduction

Since Taylor (1966) analyzed the circulation inside a droplet caused by the interaction of a uniform electric field with the electric charge distribution induced along the droplet interface, the enhancement of heat transfer rate between a droplet and its surroundings by applying an electric field has been extensively studied. Qualitative and Quantitative results have been applied in many engineering systems such as compact direct-contact heat exchangers, spray cooling, extraction processes, etc.

Circulation inside a droplet can be induced not only by applying an electric field but also by the translational motion of the droplet itself. The transport phenomena of a droplet induced by the above-mentioned hybrid fluid motion have been widely studied theoretically and numerically. Specifically, self-similar solutions have been obtained by Chang et al. (1982) among others (Johns et al., 1966; Morrison, 1977; Chang et al., 1985) for the transient heat and mass transfer of a droplet translating in an electric field with a low Reynolds number and a high Peclet number. The thin thermal boundary layer model employed by the previous investigators resulted in a uniform interfacial temperature distribution which is quite restrictive in the realistic situations. However, with convective heat transfer, the interfacial temperature distributions are necessarily nonuniform. This nonuniformity of interfacial temperature distribution will then induce a thermocapillary flow and influence the transient heat transfer. This phenomenon has never been investigated previously. The present study is therefore aimed at resolving this deficiency and analyzing the thermocapillary effects on the transient heat transfer.

By assuming a small Reynolds number and a large Peclet number, analytic solutions are obtained for the stream function with a term involving the interfacial temperature distribution which is then computed numerically. With such semi-analytic solutions, the transient thermocapillary flows and its effects on the heat transfer are analyzed and discussed.

Mathematical Formulation

Physical Modeling and Assumptions. Consider a spherical dielectric droplet of radius a which is translating steadily at a velocity U_∞ in another dielectric medium with a uniform electric field imposed in the translational direction of the droplet. Initially, the temperature of the droplet is T_o and the infinite ambient medium is at temperature T_∞. The schematic diagram and associated coordinate system employed are shown in Fig. 1. According to the proposed physical model the flow is axisymmetric with respect to the axis in the translational direction.

Because of the temperature difference between the droplet and the ambient medium and the hybrid fluid motion resulted from the effects due, respectively, to the droplet translational motion and the imposed electric field, transient heat transfer between the dispersed phase (the droplet) and the continuous phase (the ambient fluid) is induced. During the heat transfer process, the surface temperature distribution of the droplet has to be nonuniform as a result of the convective effect surrounding it. This nonuniformity of interfacial temperature distribution will then induce a surface tension gradient due to the thermocapillary effect which, in turn, results in a so-called thermocapillary flow. The fluid motion and the associated transport phenomena will be further influenced thereby. The present study is aimed at studying semi-analytically the thermocapillary flow so induced and its effect on the transient heat transfer of a single droplet translating in an electric field.

However, in order to simplify the problem for the convenience of theoretical analysis, the following assumptions are necessary.

1 Only a single droplet with a constant migration speed U_∞ is considered and the flow field is axisymmetric as shown in Fig. 1.

2 Both the droplet and ambient medium are incompressible Newtonian fluids.

3 The magnetic and convective effects due to the electric field are neglected.

4 Buoyancy effect is neglected under the microgravity environment.

5 The Joule effect and viscous dissipation are neglected in the energy equation.

6 All the thermodynamic properties are assumed constant except the surface tension which is considered as a monotonically decreasing function of temperature.

7 The thermocapillary effects on the droplet migration speed and surface deformation are negligible.

8 Transport phenomena with a small Reynolds number and a large Peclet number are assumed.

---

[1] To whom correspondence should be addressed.

Contributed by the Heat Transfer Division for publication in the JOURNAL OF HEAT TRANSFER and presented at the '97 ASME Fluids Engineering Division Summer Meeting, Vancouver. Manuscript received by the Heat Transfer Division, Oct. 10, 1997; revision received, Mar. 16, 1998. Keywords: Heat Transfer. Associate Technical Editor: R. Douglass.

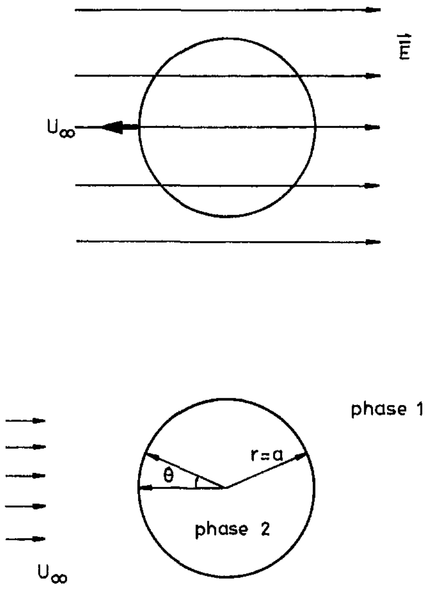

Fig. 1 The schematic diagram of the physical model and coordinate system

9 The time scale of the electric field is assumed smaller than that of the velocity field which, in turn, is smaller than that of the temperature field. Therefore, when the temperature distribution and the associated heat transfer are considered, both the electric and velocity fields can be assumed asymptotically steady.

Most of the above assumptions were more or less employed in the previous studies explicitly or implicitly.

Nondimensionalization Scheme and Relevant Parameters. Before presenting the equations and solutions, the following nondimensionalization scheme is introduced first for the convenience of analysis.

$$t \sim \frac{a^2}{\alpha_1}, \quad \mathbf{V} \sim U_\infty, \quad r \sim a$$

$$P_i \sim \rho_i U_\infty^2, \quad E \sim \bar{E}, \quad T_i - T_\infty \sim T_o - T_\infty$$

In the above expressions, $\bar{E}$ represents the imposed electric field strength and the subscript $i = 1$ (continuous phase) and 2 (dispersed phase).

Based on the above scheme, several parameters which will appear in the nondimensional equations and boundary conditions are presented in the following:

Re_i = Reynolds number = $U_\infty a/\nu_i$
Pe_i = Peclet number = $U_\infty a/\alpha_i$
R_σ = surface tension Reynolds number = $\sigma_T(T_o - T_\infty)a/\mu_1\nu_1$
R = ratio of electric conductivities = $\sigma_{e_2}/\sigma_{e_1}$
S = ratio of permitivities = e_1/e_2
X = ratio of viscosities = μ_2/μ_1

Stream Functions. By the assumptions (8) and (9), the dimensionless Stokes' stream functions for steady, creeping flow in both the continuous phase (phase 1) and dispersed phase (phase 2) are described by

$$\left[\frac{\partial^2}{\partial r^2} + \frac{\sin\theta}{r^2}\frac{\partial}{\partial\theta}\left(\frac{1}{\sin\theta}\frac{\partial}{\partial\theta}\right)\right]^2 \psi_i = 0; \quad i = 1.2 \qquad (1)$$

with the following boundary conditions:

$$\psi_1 \to \tfrac{1}{2} r^2 \sin^2\theta \quad \text{as } r \to \infty \qquad (2)$$

$$\frac{1}{r^2 \sin\theta}\frac{\partial\psi_2}{\partial\theta}, \frac{1}{r\sin\theta}\frac{\partial\psi_2}{\partial r} = \text{finite} \quad \text{at} \quad r = 0 \qquad (3)$$

$$\psi_1 = \psi_2 = 0 \quad \text{at} \quad r = 1 \qquad (4)$$

$$\frac{\partial\psi_1}{\partial r} = \frac{\partial\psi_2}{\partial r} \quad \text{at} \quad r = 1 \qquad (5)$$

$$\left[\frac{\partial V_{\theta_1}}{\partial r} - \frac{V_{\theta_1}}{r} + \frac{1}{r}\frac{\partial V_{r_1}}{\partial\theta}\right] - \frac{\mu_2}{\mu_1}\left[\frac{\partial V_{\theta_2}}{\partial r} - \frac{V_{\theta_2}}{r} + \frac{1}{r}\frac{\partial V_{r_2}}{\partial\theta}\right]$$

$$+ \frac{U_E}{U_\infty}\tau_{r\theta_E} = \frac{R_\sigma}{\mathrm{Re}_1}\frac{dT}{d\theta} \quad \text{at} \quad r = 1. \qquad (6)$$

The last condition is the balance of the tangential stress at the droplet interface with (Tang, 1994; Taylor, 1966)

$$\tau_{r\theta_E} = \frac{-9\bar{E}^2 a e_2(SR - 1)\sin\theta\cos\theta}{\mu_1 U_\infty (2 + R)^2}$$

$$= \text{dimensionless electrohydrodynamic stress} \qquad (7)$$

and

$$U_E = \frac{e_1\bar{E}^2 a}{\mu_1}. \qquad (8)$$

The general solutions of Eq. (1) are (Happel et al., 1965)

$$\psi_1 = \sum_{n=2}^{\infty}(A_n r^n + B_n r^{-n+1} + C_n r^{n+2} + D_n r^{-n+3}) \,\mathrm{In}\,(\zeta) \qquad (9)$$

$$\psi_2 = \sum_{n=2}^{\infty}(A'_n r^n + B'_n r^{-n+1} + C'_n r^{n+2} + D'_n r^{-n+3}) \,\mathrm{In}\,(\zeta) \qquad (10)$$

Nomenclature

a = radius of droplet
$\bar{E}$ = strength of electric field
Nu = Nusselt number
P = pressure
Pe = Peclet number
R = ratio of electric conductivities, $\sigma_{e_2}/\sigma_{e_1}$
Re = Reynolds number
R_σ = surface tension Reynolds number
r = radial coordinate
S = ratio of permitivities, e_1/e_2
T = temperature
T_o = initial temperature of droplet
T_∞ = ambient temperature
t = time
U_∞ = migration speed of droplet
u_s = surface velocity of droplet
V = characteristic velocity induced by electric field
W = relative importance of electric field and translational motion
X = ratio of viscosities, μ_2/μ_1
α = thermal diffusivity
e = permitivity
μ = dynamic viscosity
ν = kinematic viscosity
ρ = density
σ = surface tension
σ_e = electric conductivity
σ_T = derivative of surface tension with respect to temperature
θ = tangential coordinate

Subscripts

1 = continuous phase
2 = dispersed phase

wherein $\ln(\zeta)$ represents the first kind Gegenbaurer functions of order n and degree $-\frac{1}{2}$ with $\zeta = \cos\theta$. The coefficients are then determined from the boundary conditions. The final solutions are as follows (Tang, 1994):

$$\psi_1 = \left\{ \frac{r^2}{2} - \frac{2+3X}{4(1+X)} r + \frac{X}{4(1+X)} \frac{1}{r} \right\} \sin^2\theta + \frac{W}{4(1+X)} \left(1 - \frac{1}{r^2}\right) \sin^2\theta \cos\theta + \frac{1}{4(1+X)} \frac{R_\sigma}{\mathrm{Re}_1} \sum_{n=2}^{\infty} n(n-1) \left(\frac{1}{r^{n-3}} - \frac{1}{r^{n-1}} \right) \ln(\zeta) \int_0^\pi \left. \frac{dT_1}{d\theta} \right|_{r=1} \ln(\zeta) d\theta \quad (11)$$

$$\psi_2 = \frac{1}{4(1+X)} (r^4 - r^2) \sin^2\theta + \frac{W}{4(1+X)} (r^5 - r^3) \sin^2\theta \cos\theta + \frac{1}{4(1+X)} \frac{R_\sigma}{\mathrm{Re}_1} \sum_{n=2}^{\infty} n(n-1)(r^{n+2} - r^n) \ln(\zeta) \int_0^\pi \left. \frac{dT_1}{d\theta} \right|_{r=1} \ln(\zeta) d\theta. \quad (12)$$

In the above expressions

$$W = \frac{4V(1+X)}{U_\infty} \quad (13)$$

with

$$V = \frac{9\bar{E}^2 a e_2 (1 - SR)}{10\mu_1 (1+X)(2+R)^2}. \quad (14)$$

The physical meaning of W is the relative importance of the electric field with respect to the translation of the droplet and V is the maximum surface velocity induced solely by the electric field.

The surface velocity of the droplet modified by the thermocapillary effect becomes

$$u_s = \frac{\sin\theta}{2(1+X)} + \frac{W}{2(1+X)} \sin\theta\cos\theta + \frac{1}{2\mu_1(1+X)U_\infty} \times \sum_{n=2}^{\infty} n(n-1) \frac{\ln(\zeta)}{\sin\theta} \int_0^\pi \sigma_T \left. \frac{dT_1}{d\theta} \right|_{r=1} \ln(\zeta) d\theta. \quad (15)$$

It is obvious that, in order to determine completely the velocity field, the temperature distribution has to be found.

Temperature Distribution. By assuming the thermocapillary effect is small, i.e., $R_\sigma/\mathrm{Re}_1 = \epsilon \ll 1$, the stream function and temperature are expanded with respect to ϵ as follows:

$$\psi_i = \psi_i^0 + \epsilon\psi_i^1 + \ldots; \quad i = 1, 2 \quad (16)$$

$$T_i = T_i^0 + \epsilon T_i^1 + \ldots; \quad i = 1, 2. \quad (17)$$

In the expansions, ψ_i^0 and T_i^0 are solutions without considering the thermocapillary effects.

With the solutions for ψ_i obtained in the previous section, we have

$$\psi_1 = \psi_1^0 + \epsilon\psi_1^1 = \left\{ \frac{r^2}{2} - \frac{2+3X}{4(1+X)} r + \frac{X}{4(1+X)} \frac{1}{r} \right\} \sin^2\theta + \frac{W}{4(1+X)} \left(1 - \frac{1}{r^2}\right) \sin^2\theta\cos\theta + \frac{\epsilon}{4(1+X)} \sum_{n=2}^{\infty} n \times (n-1) \left(\frac{1}{r^{n-3}} - \frac{1}{r^{n-1}} \right) \mathrm{In}(\zeta) \int_0^\pi \left. \frac{dT_1^0}{d\theta} \right|_{r=1} \mathrm{In}(\zeta) d\theta \quad (18)$$

$$\psi_2 = \psi_2^0 + \epsilon\psi_2^1 = \frac{1}{4(1+X)} (r^4 - r^2) \sin^2\theta + \frac{W}{4(1+X)} (r^5 - r^3) \sin^2\theta\cos\theta + \frac{\epsilon}{4(1+X)} \sum_{n=2}^{\infty} n(n-1)(r^{n+2} - r^n) \ln(\zeta) \int_0^\pi \left. \frac{dT_1^0}{d\theta} \right|_{r=1} \ln(\zeta) d\theta. \quad (19)$$

With such expansions, the flow field is then modified by T_i^0 through ψ_i^1 taking into account the thermocapillary effect. Such a disturbance in the flow field will, in turn, affect the temperature distribution resulting in the term T_i^1.

In the following, the differential equations and the initial and boundary conditions for T_i^0 and T_i^1 are given. The numerical method employed to solve these equations will be described in a later section.

$$\epsilon^0: \frac{\partial T_i^0}{\partial t} + \mathrm{Pe}_i \left(V_{r_i}^0 \frac{\partial T_i^0}{\partial r} + \frac{V_{\theta_i}^0}{r} \frac{\partial T_i^0}{\partial \theta} \right) = \left(\frac{\partial^2 T_i^0}{\partial r^2} + \frac{2}{r} \frac{\partial T_i^0}{\partial r} + \frac{\cot\theta}{r^2} \frac{\partial T_i^0}{\partial\theta} + \frac{1}{r^2} \frac{\partial^2 T_i^0}{\partial\theta^2} \right); \quad i = 1, 2. \quad (20)$$

$$T_1^0 = 0,\ T_2^0 = 1; \quad t = 0 \quad (21)$$

$$T_2^0 = \text{finite}; \quad r = 0 \quad (22)$$

$$T_1^0 = 0; \quad r \to \infty \quad (23)$$

$$T_1^0 = T_2^0; \quad r = 1 \quad (24)$$

$$\frac{\partial T_1^0}{\partial r} = \frac{k_2}{k_1} \frac{\partial T_2^0}{\partial r}; \quad r = 1 \quad (25)$$

$$\epsilon^1: \frac{\partial T_i^1}{\partial t} + \mathrm{Pe}_i \left(V_{r_i}^0 \frac{\partial T_i^1}{\partial r} + \frac{V_{\theta_i}^0}{r} \frac{\partial T_i^1}{\partial\theta} \right) = \left(\frac{\partial^2 T_i^1}{\partial r^2} + \frac{2}{r} \frac{\partial T_i^1}{\partial r} + \frac{\cot\theta}{r^2} \frac{\partial T_i^1}{\partial\theta} + \frac{1}{r^2} \frac{\partial^2 T_i^1}{\partial\theta^2} \right) - \mathrm{Pe}_i \left(V_{r_i}^1 \frac{\partial T_i^0}{\partial r} + \frac{V_{\theta_i}^1}{r} \frac{\partial T_i^0}{\partial\theta} \right); \quad i = 1, 2 \quad (26)$$

$$T_1^1 = 0,\ T_2^1 = 0; \quad t = 0 \quad (27)$$

$$T_2^1 = \text{finite}; \quad r = 0 \quad (28)$$

$$T_1^1 = 0; \quad r \to \infty \quad (29)$$

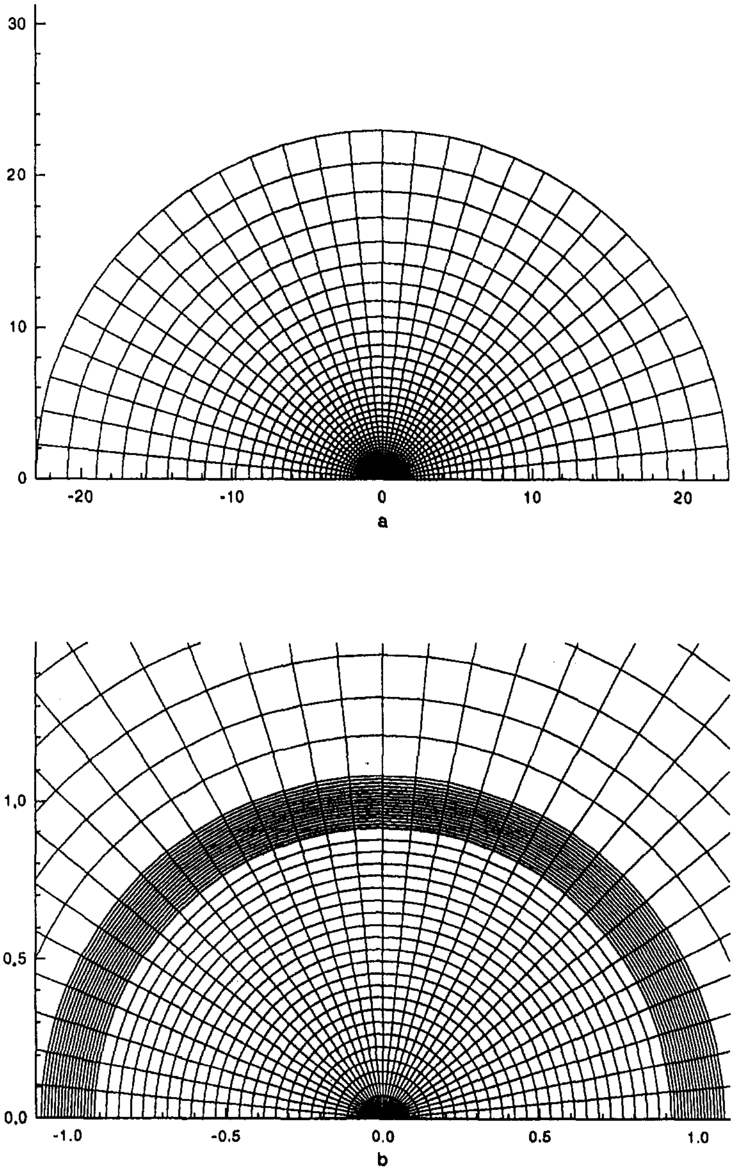

Fig. 2 (73 × 33) grid system used for calculation

$$T_1^1 = T_2^1; \quad r = 1 \tag{30}$$

$$\frac{\partial T_1^1}{\partial r} = \frac{k_2}{k_1}\frac{\partial T_2^1}{\partial r}; \quad r = 1. \tag{31}$$

The velocity fields $(V_{r_i}^0, V_{\theta_i}^0)$ and $(V_{r_i}^1, V_{\theta_i}^1)$ are obtained, respectively, from the stream functions ψ_i^0 and ψ_i^1 with

$$V_{r_i}^{0,1} = -\frac{1}{r^2 \sin\theta}\frac{\partial \psi_i^{0,1}}{\partial \theta} \tag{32}$$

and

$$V_{\theta_i}^{0,1} = \frac{1}{r \sin\theta}\frac{\partial \psi_i^{0,1}}{\partial r}. \tag{33}$$

To find the analytical solutions for the temperature distributions is a formidable task. Therefore, it has to be solved numerically.

Nusselt Number. For the convenience of discussion of the transient heat transfer between the droplet and the surrounding liquid, the Nusselt number is defined as follows.

$$\mathrm{Nu} = -\int_0^\pi \left.\frac{\partial T_1}{\partial r}\right|_{r=1} \sin\theta d\theta \tag{34}$$

Therefore,

$$\mathrm{Nu}^0 = -\int_0^\pi \left.\frac{\partial T_1^0}{\partial r}\right|_{r=1} \sin\theta d\theta \tag{35}$$

and

$$\mathrm{Nu}^1 = -\int_0^\pi \left.\frac{\partial T_1^1}{\partial r}\right|_{r=1} \sin\theta d\theta. \tag{36}$$

Numerical Calculations

The governing equations for the temperature with the appropriate initial and boundary conditions are solved numerically using the SIMPLE method developed by Patanka (1980). Several important aspects about the numerical calculations are stated as follows. (1) The real-time marching scheme is employed to simulate the transient heat transfer phenomena. Ini-

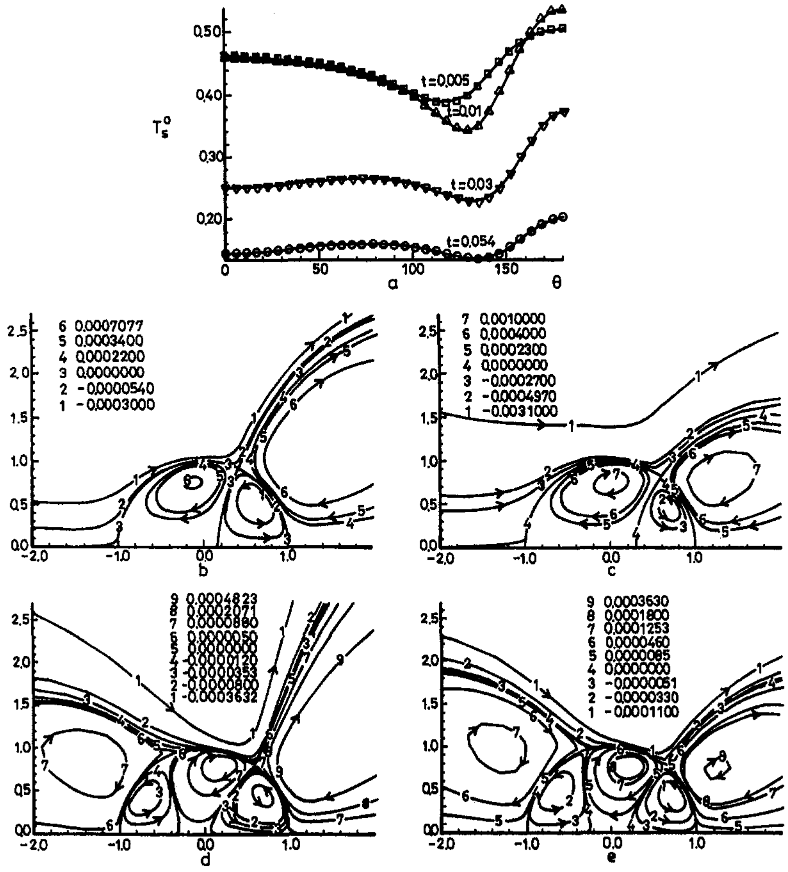

Fig. 3 The interfacial temperature distributions and stream functions at t = 0.005, 0.01, 0.03, and 0.054; Pe_1 = 100, Pe_2 = 1000, X = 1., W = 1.414, and k_2/k_1 = 0.333

tially, the time step is 10^{-4} with convergence criterion of 10^{-6} in the relative error. As the asymptotically steady state is approached, the time-step is changed to 10^{-2} with the convergence criterion in relative error less than 5×10^{-6}. (2) The ADI method is employed to facilitate the calculations. (3) A nonuniform grid system in the continuous phase is used for the calculations. The grid spaces near the droplet are much closer than those away from the droplet to simulate appropriately the temperature variation therein. The grid inside the droplet and in the θ-direction are uniformly spaced. (4) Only the upper portion, $0 \leq \theta \leq \pi$, is calculated and presented for discussion because of the symmetry of the problem itself. (5) The outer boundary

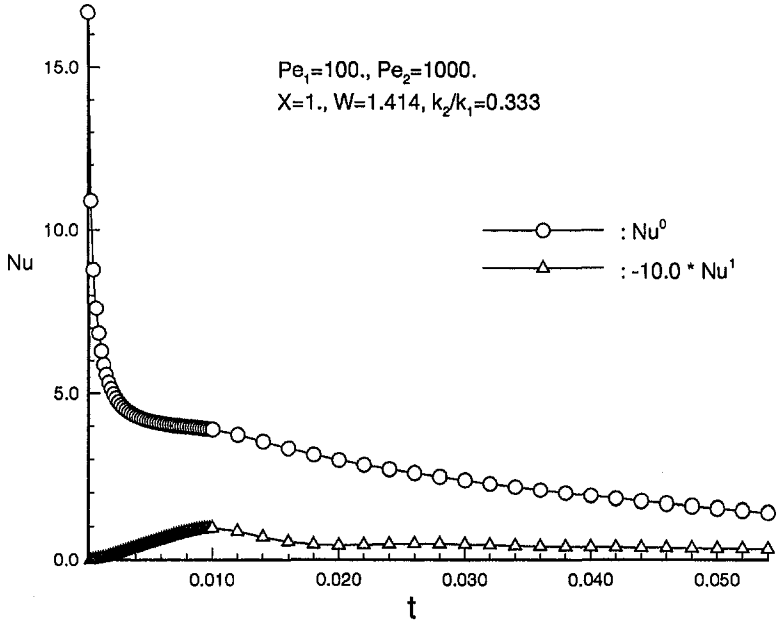

Fig. 4 Variation of Nusselt number versus time

for the numerical domain is located, after a series of tests, at $r = 22.98$ where the variation of velocity field is negligibly small. (6) To demonstrate, as an example, the thermocapillary effects on the transient heat transfer, the following parameters are chosen for the calculations: $\mathrm{Pe}_1 = 100$, $\mathrm{Pe}_2 = 1000$, $X = 1$, $W = 1.414$, and $k_2/k_1 = 0.333$, which are also within the parametric range studied by Abramzon and Borde (1980) and Chung and Oliver (1990). (7) Supplementary numerical calculations performed on various grid systems suggested that satisfactory grid independence could be achieved using a biased 73×33 grid with 73 grids in the r-direction and 33 grids in the θ-direction. Among the 73 grids in the r-direction, 32 grids are inside the droplet and 41 grids are in the ambient liquid. The schematic diagram is shown in Fig. 2. (8) The numerical calculations have been verified through comparisons with the results computed by Abramzon and Borde (1980). Good agreement between them has been achieved. (9) The asymptotic nature of the infinite series for the stream function has also been tested. Since the effect due to the seventh term of the series is of order $10^{-5} \sim 10^{-6}$, within the parametric range of the present study, only the first six terms are used for the calculations. (10) The perturbation parameter used in the computation is $\epsilon = 0.1$.

Results and Discussion

In this section the thermocapillary effects on the flow structure and transient heat transfer will be presented and discussed. The flow situation to be studied is $\mathrm{Pe}_1 = 100$, $\mathrm{Pe}_2 = 1000$, $X = 1$, $W = 1.414$, and $k_2/k_1 = 0.333$.

The basic flow structure, i.e., ψ_i^0, before taking into account the thermocapillary effect is qualitatively similar to all those presented by other researchers mentioned in the previous sections. Therefore, it is of no interest to repeat herein. However, the corresponding surface temperature distribution of the droplet i.e., T_s^0, is essential to the existence of thermocapillarity. It is then necessary to present the droplet surface temperature distribution before getting into the main discussion.

Shown in Fig. 3(a) are the basic temperature distributions along the droplet surface, T_s^0, at different times. It can be seen that T_s^0 has a minimum around $\theta = 120$ deg in the beginning, i.e., at $t = 0.005$, and has its maximum at the rear stagnation point. At $t = 0.01$, the nonuniformity of the surface temperature distribution becomes more obvious with the local minimum moving toward $\theta \approx 130$ deg. However, as time goes on, e.g., at $t = 0.03$ and $t = 0.054$, the nonuniformity tends to diminish with the local minimum moving further toward the rear stagnation point; it is then around $\theta \approx 135$ deg. In addition, there seems to have another local maximum around $\theta \approx 80$ deg at $t = 0.03$ and 0.054. These nonuniform surface temperature distributions at different times will therefore induce secondary flows, i.e., ψ_i^1, through the thermocapillary effect. The corresponding flow structures are shown in Figs. 3(b)–(e).

Since in the present study it is assumed that the surface tension is larger in the lower-temperature region and smaller in the higher-temperature region, it can be seen that, at $t = 0.005$, a counterclockwise flow motion is induced in the right portion of the droplet and a clockwise flow motion in the left portion according to the surface temperature distribution at that time. At $t = 0.01$, as the local minimum of the surface temperature distribution moves toward $\theta = 130$ deg and the nonuniformity becomes stronger, the counterclockwise cellular motion in the right portion of the droplet becomes smaller but stronger. On the other hand, the clockwise cellular motion in the left portion of the droplet becomes larger and stronger. Interesting changes of the flow structure occur when the second local maximum appears around $\theta \approx 80$ deg at $t = 0.03$ and 0.054. It can be seen in Figs. 3(d) and 3(e) that the flow structure now changes from two-cellular motion to three-cellular motion. It is counterclockwise in the portions near the front and rear stagnation points and clockwise in the central. The flow strength becomes weaker as the nonuniformity of the surface temperature distribution becomes milder.

Shown in Fig. 4 are the transient heat transfer rates without and due solely to the thermocapillary effects, as indicated by Nu^0 and Nu^1. The line with circles represents that without and the line with triangles represents that due solely to the thermocapillary effects. It can be seen that although Nu^0, the heat transfer rate without thermocapillary effects, decreases as time proceeds, $|\mathrm{Nu}^1|$, the heat transfer rate due sole to the thermocapillary effect, reaches a maximum before it gradually decreases. For the present example calculated, the maximum value of $|\mathrm{Nu}^1|$ occurs around $t \approx 0.010$ when the surface temperature distribution becomes most nonuniform.

Conclusions

A single spherical dielectric droplet translating steadily in another dielectric medium with a uniform electric field imposed in the translational direction of the droplet is studied semi-analytically. With the small Reynolds number and large Peclet number assumptions, analytic solutions are obtained for the stream function with a term involving the interfacial temperature distribution which is then computed numerically. The following conclusions can be drawn from the study.

1 The interfacial temperature distributions are indeed nonuniform and the thermocapillarity might exist thereby.

2 The induced thermocapillary flow structures are of multiple cells in accordance with the nonuniformity of the interfacial temperature distributions.

3 With the thermocapillary effects, the heat transfer rate may increase or decrease depends on whether the original flow is enhanced or suppressed. For the example calculated in the present study, the heat transfer rate is decreased due to thermocapillary effect.

4 $|\mathrm{Nu}^1|$, the heat transfer rate due solely to the thermocapillary effect reaches a maximum when the surface temperature distribution becomes most nonuniform.

Acknowledgment

The financial support of the R.O.C. National Science Council through Grant NSC83-0401-E-002-121 at National Taiwan University is gratefully acknowledged.

References

Abramzon, B., and Borde, I., 1980, "Conjugate Unsteady Heat Transfer from a Droplet in Creeping Flow," *AIChE J.*, Vol. 26, No. 4, pp. 536–544.

Chang, L. S., and Berg, J. C., 1985, "The Effect of Interfacial Tension Gradients on the Flow Structure of Single Drops or Bubbles Translating in an Electric Field," *AIChE J.*, Vol. 31, No. 4, pp. 551–557.

Chang, L. S., Charleson, T. E., and Berg, J. C., 1982, "Heat and Mass Transfer to a Translating Drop in an Electric Field," *Int. J. Heat Mass Transfer*, Vol. 25, pp. 1023–1030.

Chung, J. N., and Oliver, D. L. R., 1990, "Transient Heat Transfer in a Fluid Sphere Translating in an Electric Field," ASME JOURNAL OF HEAT TRANSFER, Vol. 112, pp. 84–91.

Happel, J., and Brenner, H., 1965, *Low Reynolds Number Hydrodynamics*, Prentice-Hall, Englewood Cliffs, NJ.

Johns, L. E., Jr., and Beckmann, R. B., 1966, "Mechanisms of Dispersed-Phase Mass Transfer in Viscous, Single-Drop Extraction Systems," *AIChE J.*, Vol. 12, pp. 10–16.

Morrison, F. A., Jr., 1977, "Transient Heat and Mass Transfer to a Drop in an Electric Field," ASME JOURNAL OF HEAT TRANSFER, Vol. 99, pp. 269–273.

Patankar, S. V., 1980, *Numerical Heat Transfer and Fluid Flow*, Hemisphere, Washington, DC.

Tang, W. L., 1994, "Thermocapillary Effects on Transient Heat Transfer in a Droplet Translating in an Electric Field," M.S. thesis, Department of Mechanical Engineering, National Taiwan University, R.O.C.

Taylor, G. I., 1966, "Studies in Electrohydrodynamics, I. The Circulation Produced in a Drop by an Electric Field," *Proc. Roy. Soc., Lond.*, Vol. 291A, pp. 159–166.

Y. Kamotani
e-mail: yxk@po.cwru.edu
Mem. ASME

S. Ostrach
Department of Mechanical and
Aerospace Engineering,
Case Western Reserve University,
Cleveland, OH 44106

Theoretical Analysis of Thermocapillary Flow in Cylindrical Columns of High Prandtl Number Fluids

Steady and oscillatory thermocapillary flows of high Prandtl number fluids in the half-zone configuration are analyzed theoretically. Scaling analysis is performed to determine the velocity and length scales of the basic steady flow. The predicted scaling laws agree well with the numerically computed results. The physical mechanism of oscillations is then discussed. It is shown that the deformation of free surface plays an important role for the onset of oscillations in that it alters the main thermocapillary driving force of the flow by changing the temperature field near the hot-corner region. This phenomenon triggers oscillation cycles in which the surface flow undergoes active and slow periods. Based on that concept a surface deformation parameter is derived by scaling analysis. The deformation parameter correlates available data for the onset of oscillations well.

Introduction

Thermocapillary flow or heat-induced surface-tension-driven flow becomes oscillatory under certain conditions. Ever since the oscillation phenomenon was discovered by Schwabe et al. (1978) and Chun and Wuest (1979) experimentally in the so-called half-zone configuration, in which a liquid column is suspended between two differentially heated rods, many investigators have studied the phenomenon under various conditions both experimentally and theoretically. Masud et al. (1997) discussed some past studies pertinent to the present work. Despite those studies the cause of oscillations and the dimensionless parameter(s) to specify the onset of oscillations are not yet fully understood. Dimensional analysis shows that the only parameter that represents the thermocapillary driving force is the Marangoni number, Ma, or the surface-tension Reynolds number, $R\sigma$, if the free surface is assumed to be rigid. Based on that, many investigators use a critical Ma to specify the onset of oscillations.

Much experimental data are available on the onset conditions in the half-zone configuration but they tend to be confusing and contradictory because of the possibility of additional effects, such as buoyancy, liquid column shape, and heat loss at the liquid free surface. For that reason, Masud et al. (1997) carefully investigated those effects experimentally on the onset of oscillations. Their data, when those effects are minimized, together with available data taken in microgravity, show clearly that Ma alone cannot specify the onset of oscillations: There is an order of magnitude difference in the critical Ma between our ground-based data with small zones (2 and 3 mm dia.) and the data taken in microgravity with much larger zones (30 to 60 mm dia.). Such a large difference cannot be attributed to those effects mentioned above. Similar results were obtained with cylindrical containers by comparing our experiments on the ground and those in microgravity (Kamotani et al., 1994, 1995).

Therefore, experimentally it is clear that Ma is not sufficient to specify the onset of oscillations. At present that finding is limited to high Prandtl (Pr) fluids (Pr > 5). Not enough experimental data are available for other Pr fluids. The objective of the present work is to identify the additional parameter for the half-zone configuration by theoretical analysis. We will start with the hypothesis that free-surface deformation plays an important role in the oscillation mechanism and discuss the physical mechanism. Finally we will derive a parameter to represent the free-surface deformation, which will be shown to correlate available experimental data on the onset of oscillations well.

Oscillatory Flow in a Half-Zone

The half-zone configuration investigated herein is sketched in Fig. 1. A vertical liquid bridge is formed between two differentially heated metal rods. In the present work it is assumed that (i) the static liquid free surface is flat, (ii) buoyancy is negligible, and (iii) the heat loss from the free surface is negligible. Under those conditions the important dimensionless parameters for steady flow are surface-tension Reynolds number ($R\sigma$), Prandtl number (Pr), and aspect ratio (Ar). The Marangoni number is defined as $\mathrm{Ma} = R\sigma\mathrm{Pr}$. If free surface deformation is important, the capillary number (Ca) must also be included.

Before the appearance of oscillations, the flow in the liquid column is axisymmetric and recirculates in a toroidal pattern with the fluid moving from the hot to the cold end along the free surface. Once the imposed temperature difference between the hot and the cold rod (ΔT) reaches a certain value (ΔT_{cr}), the flow becomes time-periodic and three-dimensional. During oscillations a nonaxisymmetric flow pattern travels around the zone and at a given instant of time the pattern varies in a periodic manner in the azimuthal direction (Preisser et al., 1983). An important feature is that in a fixed radial plane (rz-plane in Fig. 1) the surface flow becomes alternately fast and slow in one cycle of oscillations (Lee, 1991). During the period when the surface flow is strong, called the active period herein, the surface temperature along the free surface increases due to increased convection. The active period is followed by a period of weak surface motion, called the slow period, in which the surface temperature decreases. We have investigated oscillatory thermocapillary flows in other configurations, namely, in cylindrical containers (Kamotani et al., 1992) and in rectangular containers (Lee and Kamotani, 1991). The structure of the oscillatory flow

---

Contributed by the Heat Transfer Division for publication in the JOURNAL OF HEAT TRANSFER. Manuscript received by the Heat Transfer Division, Oct. 15, 1997; revision received, Mar. 13, 1998. Keywords: Heat Transfer, Microgravity, Thermocapillary. Associate Technical Editor: R. Douglass.

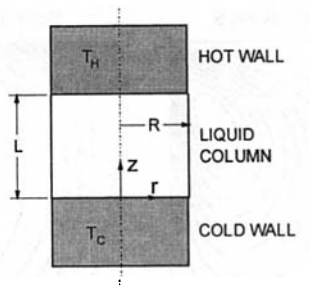

Fig. 1 Schematic of half-zone configuration

varies substantially depending on the geometry but a common feature is the presence of active and slow periods.

We are interested in the physical mechanism of oscillations and the parameter(s) to specify the onset. Near the onset conditions the value of Ca is usually much less than unity, which suggests that free surface deformation is very small. In fact, it is very difficult to see the flow-induced free-surface deformation experimentally without magnification. If, then, the free-surface deformation can be neglected, Ma is the only parameter containing ΔT. Ma represents convection heat transfer in the zone relative to conduction. As discussed by Masud et al. (1997), available data show that Ma must be larger than about 7×10^3 for the oscillations to occur, which means convection is an important factor. However, that condition is a necessary but not sufficient condition, namely, Ma alone cannot specify the onset of oscillations even when Ma is large: Available experimental data show that for given Pr and Ar, the critical Ma varies with the zone diameter, which should not be true if Ma were the only critical parameter. This strong effect of zone diameter cannot be attributed to the effect of buoyancy nor to that of heat loss from the free surface (Masud et al., 1997). Therefore, we have to consider an additional feature and a parameter associated with it to explain the oscillation phenomenon. Before we discuss the additional feature, it is useful to understand the basic steady flow field.

Analysis of Basic Flow Field

A scaling analysis of the steady thermocapillary flow in the half-zone is presented herein to determine what forces are important in the flow and to derive the important velocity and length scales. Since detailed experimental data are very limited, a numerical analysis is also performed to check the scaling laws as well as to give some guidance to the scaling analysis. The analysis is limited to high Pr fluids, namely, Pr = 10–100. For simplicity, we consider only the case with Ar = 0.7 (a typical value in many experiments). The free surface is assumed to be flat and undeformable in this steady flow analysis. The effects of buoyancy and heat loss from the free surface are not considered.

The numerical analysis is based on the SIMPLER algorithm (Patankar, 1980) as in our past work on steady thermocapillary flows (Kamotani et al., 1994, 1995). The flow is assumed to be laminar, incompressible, and axisymmetric. The fluid properties are considered to be constant in the analysis except for surface tension which varies linearly with temperature. The cylindrical coordinate system adopted herein is shown in Fig. 1. The velocity and stream function are nondimensionalized by $\sigma_T \Delta T/\mu$ and $\sigma_T \Delta T R^2/\mu$, respectively (Kamotani et al., 1996). The temperature is made dimensionless as $(T - T_c)/\Delta T$. A nonuniform grid is employed with meshes graded toward the hot and cold walls and toward the free surface. The computed surface velocity and temperature distributions are presented in Fig. 2 for the conditions of Ar = 0.7, Pr = 100, and Ma = 1.5×10^5 (the maximum Ma studied in the present numerical analysis). The computed values are obtained with three different grids, 60×80 ($r \times z$), 90×120, and 120×160, with the smallest radial mesh sizes next to the hot and cold walls being 0.0004, 0.0002, and 0.0001, respectively. With those grids the computed maximum surface velocities near the hot wall are 0.0275, 0.0277, and 0.0277, respectively, and the maximum stream functions are 1.15×10^{-3}, 1.02×10^{-3}, and 1.01×10^{-3}, respectively. As Fig. 2 shows, the surface velocity and temperature distributions computed with the last two grid systems are nearly indistinguishable. Based on the comparison, the 90×120 grid is the finest grid system used in the present work. As Fig. 2 shows, there exists a very large surface velocity peak next to the cold wall. Since the cold wall peak occurs very close to the wall when Ma is large, one needs to use a finer mesh than used herein to resolve that peak very accurately (the computed peak cold wall velocities with the above three grids are, 0.101, 0.0884, and 0.0856, respectively). However, the cold wall peak is highly localized when Ma is large, as will be discussed later, so that the other flow quantities can be predicted accurately without an accurate resolution of the cold wall peak, as can be seen in Fig. 2.

The computed surface temperature and velocity distributions are presented in Fig. 3 for four different values of Ma. The surface temperature distribution is especially important because it is directly related to the driving force of the flow. When Ma = 100, the surface temperature decreases gradually from the hot to the cold wall, which means that the thermocapillary driving force exists more or less uniformly over the surface and, consequently, the velocity distribution increases and then decreases monotonically with the axial location.

Nomenclature

Ar = zone aspect (length/diameter) ratio
k = thermal conductivity
L = zone length
L_H = extent of hot corner (Fig. 5)
Ma = Marangoni number, $\sigma_T \Delta T L/\mu\alpha$
Nu = Nusselt number
Pr = Prandtl number, ν/α
R = zone radius
(r, z) = coordinate system defined in Fig. 1
Rσ = Reynolds number, $\sigma_T \Delta T L/\mu\nu$
S = S-parameter defined by Eq. (13)
T = temperature
T_C = cold wall temperature
T_H = hot wall temperature
U_0 = characteristic flow velocity in hot corner
U_0^* = dimensionless characteristic hot corner velocity, $\mu U_0/\sigma_T \Delta T$
α = thermal diffusivity
Δ = length scale defined in Fig. 5
ΔT = temperature difference, $T_H - T_C$
ΔT_{cr} = critical temperature difference for onset of oscillations
ΔT_H = surface temperature variation in region Δ
δ_s = free-surface deformation in region Δ
δ_{TC} = thermal boundary layer thickness along cold wall
δ_{TH} = thermal boundary layer thickness along hot wall
δ_{TS} = thermal boundary layer thickness along free surface in hot corner (Fig. 5)
μ = dynamic viscosity
ν = kinematic viscosity
ρ = density
σ = surface tension
σ_T = temperature coefficient of surface tension
$\Psi_{\max}$ = maximum stream function
$\Psi_{\max}^*$ = dimensionless maximum stream function, $\mu\Psi_{\max}/\sigma_T \Delta T R^2$

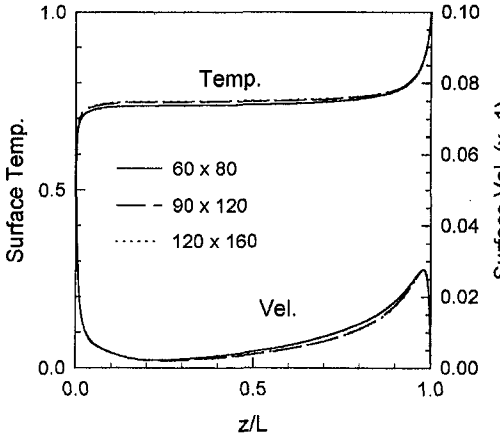

Fig. 2 Surface velocity and temperature distributions computed with various grid systems (Ma = 1.5×10^5, Ar = 0.7, and Pr = 100)

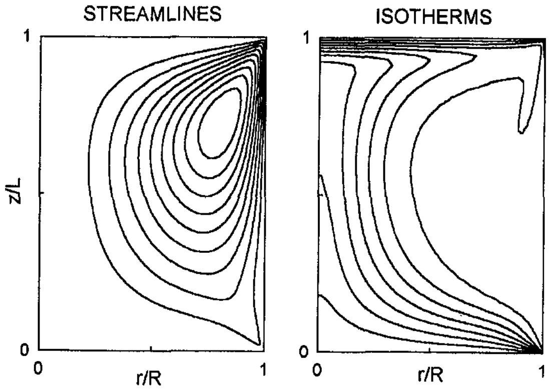

Fig. 4 Computed streamlines and isotherms for Ma = 1.1×10^5, Ar = 0.7, and Pr = 50

With increasing Ma, convection causes large surface temperature changes near the hot and cold walls, called the hot and cold corner regions herein, with a relatively uniform temperature region in between. As a consequence, large driving forces exist mainly in those corner regions and the velocity has a peak in each of those regions. The corner regions shrink as Ma increases. One important consequence of the fact that the large driving force appears mainly in those corner regions which shrink with increasing flow speed is that the overall flow remains viscous-dominated even when Rσ is much larger than unity (Masud et al., 1997). Oscillations are known to appear when the basic flow has such surface temperature and velocity distributions, and in our concept of the oscillation mechanism, which will be discussed later, the hot corner region plays the primary role. Therefore, it is important to understand what is happening in the hot corner, as well as to know the proper length and velocity scales of the problem when Ma is large. Typical streamline and isotherm patterns are shown in Fig. 4 for a large Ma, which will be referred to in the scaling analysis.

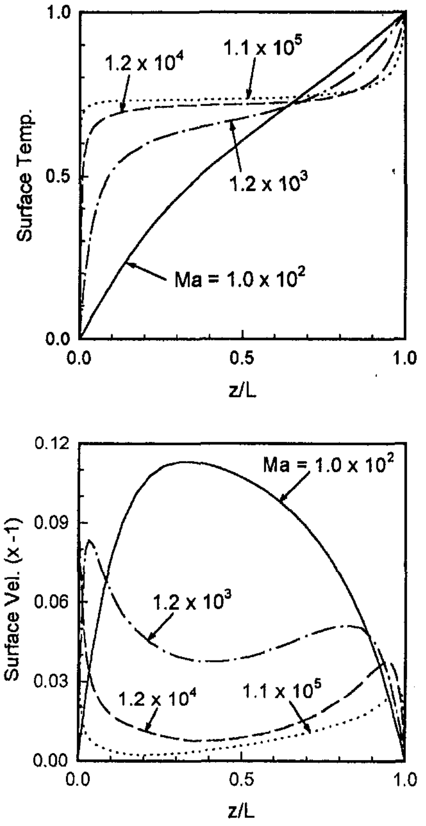

Fig. 3 Computed surface velocity and temperature distributions at various Ma for Ar = 0.7 and Pr = 50

The scaling analysis given below is similar to the one we performed for cylindrical containers (Kamotani et al., 1996). Since Ar is assumed to be constant, only one overall length scale (L) is used. The analysis presented herein is limited to the viscous-dominated regime (the range of Rσ for this regime will be discussed later), which means that Ma is the only parameter.

Although the thermocapillary driving force exists mainly in the two corner regions, the driving force in the hot corner becomes more important for the overall flow as Ma becomes large, as will be shown later. As can be seen in the streamline pattern in Fig. 4, the overall flow pattern is unicellular, and the center of the cell is located close to the hot corner because the main driving force exists there. As sketched in Fig. 5, the important quantities in the hot corner region are the location of the velocity peak Δ, the thermal boundary layer δ_{TH}, and the peak velocity value U_0, which represents the characteristic velocity of the region. The region defined by Δ is very important because it determines the velocity scale. Balancing the shear stress with the thermocapillary driving force at the free surface over Δ one obtains

$$\mu \frac{U_0}{\Delta} \sim \sigma_T \frac{\Delta T_H}{\Delta} \tag{1}$$

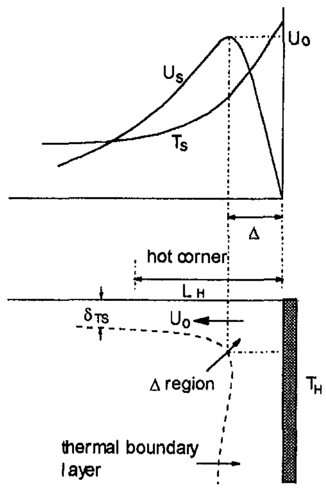

Fig. 5 Velocity and temperature distributions and various length scales in hot corner (U_S = surface velocity, T_S = surface temperature)

where ΔT_H is the temperature variation over Δ. The fact that the length scales in the r and z-directions are the same in viscous turning flow is utilized in the above balance.

As illustrated in Fig. 5, a thermal boundary layer exists along the hot wall since Ma is large. The fluid velocity along the hot wall varies from 0 at $r = 0$ to U_0 near the free surface so that the average velocity scales with U_0. Then, by balancing the convection and conduction in the thermal boundary layer one obtains

$$\frac{\delta_{TH}}{L} \sim \left(\frac{\alpha}{U_0 L}\right)^{1/2}. \tag{2}$$

Within region Δ the surface temperature gradient is large and nearly constant (Fig. 5), and the velocity increases almost linearly there. Such a large and nearly constant temperature gradient is created because the convection along the hot wall into Δ is balanced by the conduction in that region, namely

$$U_0 \frac{\Delta T}{L} \sim \alpha \frac{\Delta T_H}{\Delta^2}. \tag{3}$$

One must balance the overall heat transfer rate at the hot and cold walls. As seen in Fig. 4, most of the flow generated in the hot corner toward the cold region turns before it gets close to the cold wall. The turning flow generates a thermal boundary layer along the cold wall. A balance of convection and conduction in the boundary layer gives

$$U_0 \frac{\delta_{TC}}{L} \frac{\Delta T}{L} \sim \alpha \frac{\Delta T}{\delta_{TC}^2} \tag{4}$$

where the velocity scale is modified by the factor δ_{TC}/L near the thermal boundary layer because the flow velocity decreases gradually toward the cold wall. In the present cylindrical configuration, the heat transfer near the free surface contributes more to the overall transfer rate than that in the region near the centerline, because the former region occupies a larger area. As the isotherms of Fig. 4 show, the bulk fluid temperature just outside the hot wall thermal boundary layer in the region $r/R > 0.5$ is relatively large and uniform. Thus, the temperature drop across δ_{TH} is considered to scale with ΔT_H in the heat transfer analysis. By balancing the overall heat transfer rate at the hot and cold walls one obtains

$$k \frac{\Delta T_H}{\delta_{TH}} L \sim k \frac{\Delta T}{\delta_{TC}} L. \tag{5}$$

The extent of the hot corner, L_H, can be estimated by balancing the total heat transfer along the hot wall and the heat flux through the thermal boundary layer δ_{TS} in the hot corner,

$$\alpha \frac{\Delta T_H}{\delta_{TH}} L \sim U_0 \Delta T \delta_{TS} \sim U_0 \Delta T \left(\frac{\alpha L_H}{U_0}\right)^{1/2}. \tag{6}$$

Since a relatively large surface temperature gradient exists only over L_H, the flow is mainly driven over that region. Therefore, the total volume flux, or the maximum stream function, scales with $U_0 L_H L$.

The quantities U_0, Δ, δ_{TH}, δ_{TC}, ΔT_H, and L_H can be determined from Eqs. (1)–(6). The dimensionless heat transfer rate (Nusselt number) can be expressed as Nu $\sim L/\delta_{TC}$. As explained above, the dimensionless maximum stream function can be computed as $\Psi^*_{\max} \sim U_0^* L_H/L$. One then obtains the following scaling laws:

$$U_0^* \sim \Delta T_H/\Delta T \sim \mathrm{Ma}^{-1/7} \tag{7}$$

$$\Delta/L \sim \mathrm{Ma}^{-1/2} \tag{8}$$

$$\mathrm{Nu} \sim L/\delta_{TC} \sim \mathrm{Ma}^{2/7} \tag{9}$$

$$\Psi^*_{\max} \sim U_0^* L_H/L \sim \mathrm{Ma}^{-3/7} \tag{10}$$

Cowley and Davis (1983) analyzed viscous thermocapillary convection at high Marangoni number and they derived various scaling laws for the hot corner. The main difference between their analysis and the present one is that the overall flow is mainly driven in the hot corner in the present analysis, while the surface temperature drop in the Cawley and Davis analysis is only a fraction of ΔT. Despite this difference, Cowley and Davis obtained the same scaling laws for Nu and U_0^* as in the present analysis.

For the cold corner region, the location of the peak velocity in that region can be determined by balancing the convection along the free surface and the conduction in the same direction, with the result that the extent of that region relative to L scales with Ma^{-1} (Ostrach et al., 1985; Canright, 1994). Therefore, the cold corner is a relatively small region compared to the hot corner whose extent ($\sim L_H/L$) scales with $\mathrm{Ma}^{-2/7}$ (Eq. (10)), which is due to the flow being accelerated toward the wall in the cold corner. As a result, the large-velocity peak in the cold corner disappears quickly away from the free surface when Ma is large (Masud et al., 1997).

The quantities U_0^*, Δ/L, Nu, and $\Psi^*_{\max}$ can be determined from the numerical analysis. The scaling laws (Eqs. (7)–(10)) are compared with the present numerical results in Fig. 6. They are in good agreement above Ma $> 1.5 \times 10^3$ and up to certain Reynolds numbers to be discussed below. The present scaling laws are based on the assumption that the flow is viscous-

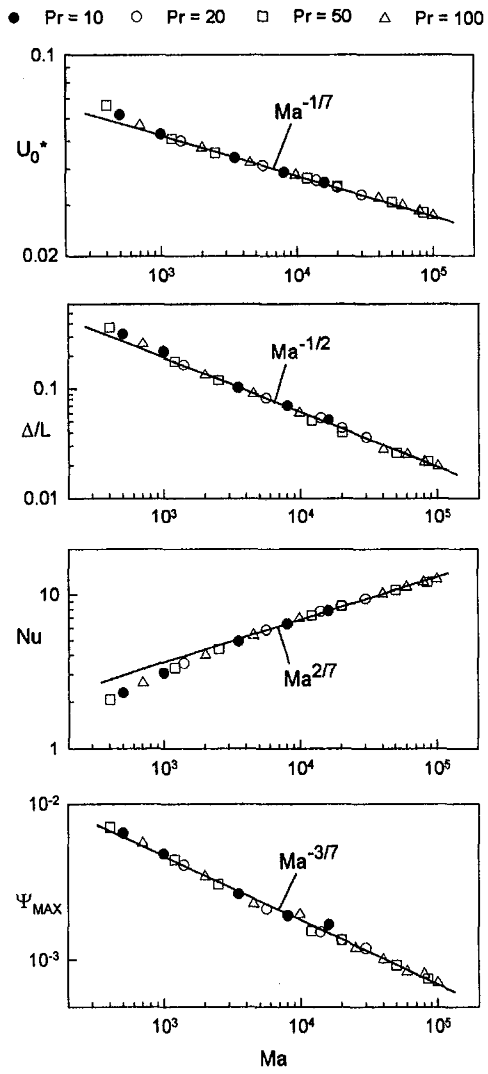

Fig. 6 Comparisons of scaling laws with computed results

dominated. Therefore, the upper limit of validity of those scaling laws is determined by the $R\sigma$ limit for viscous flows. The quantity $\Psi^*_{\max}$ is found to deviate first from the viscous scaling law because it is associated with the bulk flow while the other quantities are associated more with the flow near the hot wall. According to the present numerical analysis the computed $\Psi_{\max}$ deviates from the scaling law beyond about $R\sigma$ of 1000 for $Pr = 10$ and 1500 for $Pr = 20$. The $R\sigma$ limits for larger Pr fluids are beyond the maximum $R\sigma$ computed. Since the flow is known to become oscillatory mostly in the range of Fig. 6, the viscous scaling laws will be used in the following analysis of the oscillation phenomenon. The fact that the flow is viscous-dominated is very important because it means that the oscillation phenomenon is not due to a hydrodynamic instability where inertia forces play an important role.

Physical Mechanism of Oscillations

Based on our past extensive analyses and experiments, we now describe our concept of the oscillation mechanism which involves a nonlinear coupling among the surface temperature distribution, velocity field, and free-surface deformation. Since it is a complex mechanism involving free-surface deformation, a few important basic elements are discussed first. In the following discussion, the flow along the free surface toward the cold wall is called the surface flow and the flow toward the hot wall in the interior is called the return flow.

First, it is important that Ma is large enough so that the hot corner region exists. The major driving force exists in that relatively small region and what happens there can influence the entire flow field. A balance exists in the hot corner between strong convection by the surface flow and that by the return flow when the flow is steady. However, in a transient situation if they are not balanced at any moment, the unbalance could change the surface temperature distribution substantially and, consequently, the entire flow field.

Secondly, the surface flow is driven by thermocapillarity but the return flow is driven by the pressure gradients generated by the surface flow. Therefore, since the pressure near the free surface is determined by the free-surface shape, the return flow is closely related to the free surface shape. Consequently, when the surface flow is changed (e.g., accelerated) locally, there is a finite time lag before the return flow responds to the change because it takes a finite time to change the free surface shape, which results in the aforementioned transient unbalance between them.

We now put those elements together to explain the oscillation phenomenon. Although the observed oscillatory flows are generally three-dimensional, we will concentrate on the activity in one radial plane (r-z plane) for simplicity. As described earlier, the surface flow goes through active and slow periods in one radial plane.

According to our flow observations the oscillations start in the hot corner and spread toward the cold corner. The active period is initiated in the following way. The most important process occurs in the region defined by Δ. Suppose that the surface flow in that region becomes somewhat stronger for some reason (e.g., a change in the heat input) so that the surface velocity increases by a finite amount. The return flow does not respond immediately to the change because of a time lag due to free-surface deformation. Because of the deformation, a small amount of the fluid is removed from region Δ and transported downstream along the free surface (Fig. 7(a)). The removal of the fluid in region Δ exposes the slightly cooler fluid below the surface and, consequently, the surface temperature gradient becomes larger there (Fig. 7(b)). At the same time, the hot fluid transported out of Δ increases the surface temperature gradient just outside that region (Fig. 7(b)). As a result, the overall thermocapillary driving force in the hot corner increases and thus the surface flow velocity increases further. The surface velocity in the hot corner continues to increase until the return flow catches up with the surface flow change. Eventually, the whole flow field becomes active and temperature increases over most of the free surface. This is the active period for this radial plane.

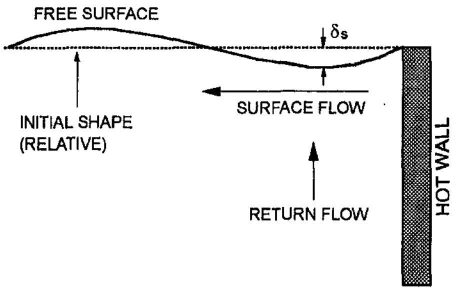

Fig. 7(a) Free-surface shape change

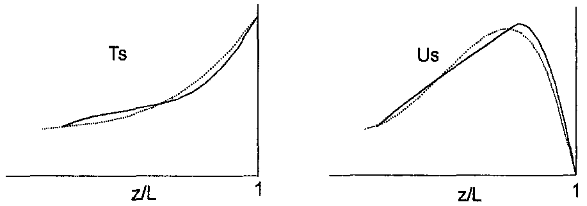

Fig. 7(b) Surface velocity and temperature variations (T_S = surface temperature, U_S = surface velocity

Fig. 7 Variations of free surface shape and surface velocity and temperature distributions in hot corner at the beginning of an active period. Dotted and solid lines represent initial and transient states, respectively.

The return flow eventually begins to cool the surface flow, which then begins to slow down. This is the beginning of the slow period. The hot region retreats toward the hot wall in the slow period. Both surface and return flows slow down in this period. When the surface flow goes back to the original state near the end of this period, the return flow lags behind it because the surface must deform in order to slow down the return flow. Consequently, the return flow becomes somewhat stronger than the surface flow in region Δ, and the surface temperature begins to decrease. The increased surface temperature gradient in Δ revitalizes the surface flow and the whole process repeats.

In summary, the oscillation phenomenon is a nonlinear phenomenon in which the driving force is continuously altered by the flow. Free-surface deformation is important because it causes the important time lag in the region Δ to initiate an active period.

Important Parameters for Oscillations

Finally, we discuss the conditions for the onset of oscillations and the dimensionless parameters associated with it. It was mentioned earlier that Ma is an important parameter and it has to be larger that a certain value (about 7×10^3) to have oscillations but another parameter is required to describe the onset of oscillations. In our concept of the oscillation mechanism the other parameter is associated with free-surface deformation. From the earlier discussion of the oscillation mechanism the free-surface deformation plays two important roles. First, it causes a time lag between the surface and return flows in the region defined by Δ. Second, it changes the surface temperature distribution in the region Δ (hence the thermocapillary driving force) as hot fluid is removed from the surface. In what follows the amount of surface deformation in the region Δ is estimated. Since the surface flow thickness is Δ, if the surface deformation is comparable with Δ, there would be a substantial change in convection and, as a result, the driving force would be altered significantly, which would lead to oscillations. Therefore, we will seek the condition that the free-surface deformation becomes comparable to Δ in the following discussion. We focus on the conditions near the onset of oscillations so that the velocity and length scales obtained for the basic flow are still valid.

The surface deformation of interest, δ_s (see Fig. 7(a)), causes a time lag of order δ_s/U_0, since it takes that long to deform the surface by the local velocity scale U_0. After the time lag, the return flow responds to the change in the surface flow, which means that the deformation must create a sufficient pressure gradient for the response. As will be seen later, the time lag is very small compared to the viscous diffusion time. Therefore, we have to include the unsteady term in the equation of motion to estimate the amount of free-surface deformation. Assuming that the free-surface deformation is small compared to the overall length scale, the pressure at the free surface caused by δ_s in the region Δ scales with $\sigma\delta_s/\Delta^2$. As discussed above, the free-surface deformation of interest generates a pressure gradient over the region Δ to change the return flow velocity by a finite amount after the time δ_s/U_0. The amount of deformation is estimated by balancing the pressure gradient generated in the region Δ and the unsteady term in the momentum equation, namely

$$\rho \frac{U_0}{\delta_s/U_0} \sim \sigma \frac{\delta_s}{\Delta^2}\frac{1}{\Delta} \qquad (11)$$

from which one obtains

$$\left(\frac{\delta_s}{\Delta}\right)^2 \sim \frac{\rho U_0^2 \Delta}{\sigma}. \qquad (12)$$

From the above discussion the condition to start the oscillation process is that the ratio δ_s/Δ be of order unity. To be consistent with our past work we call the square of the ratio (as in Eq. (12)) a surface deformation parameter or S-parameter. Using the scaling laws for U_0 and Δ given in Eqs. (7) and (8) the S-parameter can be written as

$$S = \left(\frac{\delta_s}{\Delta}\right)^2 = \frac{\sigma_T \Delta T}{\sigma}\frac{1}{\mathrm{Pr}}\mathrm{Ma}^{3/14}. \qquad (13)$$

In our earlier work for the half-zone (Kamotani et al., 1984) we obtained a similar expression for S empirically but without the Ma dependence, because it was based on ground-based data taken in a limited Ma range.

Based on the above results the time scale of the deformation δ_s/U_0 relative to the viscous diffusion time can be expressed as $(\mathrm{Pr}\sigma_T\Delta T/\sigma)^{1/2}/\mathrm{Ma}^{5/4}$, which is much less than unity near the onset of oscillations. That is the reason for the use of the unsteady term to estimate the deformation in the above analysis. Note also that the deformation causes a time lag between the surface and return flows and, as such, it is important only in the oscillatory flow.

We now correlate the available experimental data in terms of Ma and S. In Fig. 8 representative existing data for the onset of oscillations are correlated in terms of S and Ma. In the above analysis Ar is assumed to be constant, so the data in Fig. 8 are chosen in a limited range of Ar ($0.5 \leq \mathrm{Ar} \leq 1.5$). It is noted that within that Ar range there is no consistent trend of Ar in the data given in Fig. 8. Experimental data taken in one-g are all somewhat scattered around $\mathrm{Ma} = 10^4$. There are more data available in that region but they are not shown here because they simply bunch up in the same region. If we include the microgravity data to cover a wider range of Ma, Fig. 8 suggests that the flow becomes oscillatory when S is larger than about 0.01 (or the ratio δ_s/Δ is larger than 0.1).

Although more microgravity data for a larger Ma range are needed, based on what is presently available, the S-parameter seems to specify the onset conditions well. In order to validate our concept of oscillations further, we are investigating the coupling among the free-surface deformation, surface temperature distribution, and velocity field during oscillations in our microgravity experiments performed in 1995, but the data are still being analyzed so that they are not discussed here.

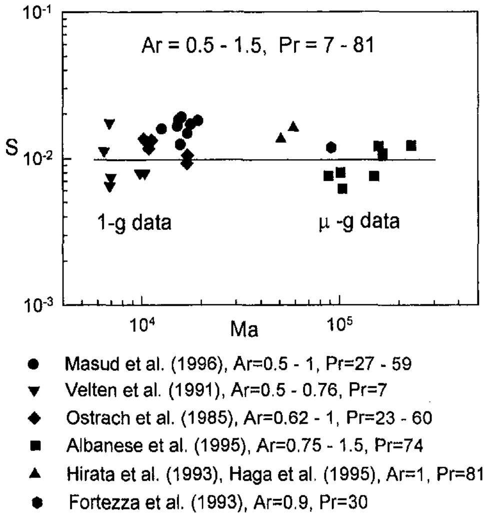

Fig. 8 Correlation of available experimental conditions for onset of oscillations in terms of Ma and S

Conclusions

In thermocapillary flow of a high Prandtl number fluid in a half-zone there appears, when Ma is large, a hot-corner region next to the hot wall where the flow is mainly driven. Because the hot corner region shrinks with increasing Ma, the flow remains viscous-dominated even when the Reynolds number is large. The present analysis shows that free-surface deformation plays an important role in oscillatory thermocapillary flow in high Pr fluids. The deformation induces a small time lag before the return flow responds to a change in the surface flow and alters the the driving force in the hot corner, which triggers oscillation cycles in which the surface flow becomes alternately fast and slow. Based on that concept the surface deformation parameter (S-parameter) is derived by scaling analysis. When the parameter becomes larger than a certain value, the free-surface deformation in the hot corner becomes large enough to change the temperature field there substantially to initiate oscillations. Available data, which cover wide ranges of conditions, are shown to be correlated by the S-parameter reasonably well.

Acknowledgments

This work is supported by NASA under Grant NAG3-1568. We thank Dr. Masud for his help in preparing this manuscript.

References

Canright, D., 1994, "Thermocapillary Flow Near a Cold Wall," *Physics of Fluids*, Vol. 6, No. 4, pp. 1415–1424.

Chun, C.-H., and Wuest, W., 1979, "Experiments on the Transition from Steady to the Oscillatory Marangoni Convection of a Floating Zone under Reduced Gravity Effect," *Acta Astronautica*, Vol. 6, pp. 1073–1082.

Cowley, S. J., and Davis, S. H., 1983, "Viscous Thermocapillary Convection at High Marangoni Number," *Journal of Fluid Mechanics*, Vol. 135, pp. 175–188.

Haga, M., Maekawa, T., Kuwahara, K., Ohara, A., Kawasaki, K., Harada, T., Yoda, S., and Nakamura, T., 1995, "Effect of Electric Field on Marangoni Convection under Microgravity," *Journal of the Japan Society of Microgravity Application*, Vol. 12, No. 1, pp. 19–26.

Hirata, A., Nishizawa, S., Imaishi, N., Yasuhiro, S., Yoda, S., and Kawasaki, K., 1993, "Oscillatory Marangoni Convection in a Liquid Bridge under Microgravity by Utilizing TR-1A Sounding Rocket," *Journal of the Japan Society of Microgravity Application*, Vol. 10, No. 4, pp. 241–250.

Kamotani, Y., Ostrach, S., and Vargas, M., 1984, "Oscillatory Thermocapillary Flow in a Simulated Floating-Zone Configuration," *Journal of Crystal Growth*, Vol. 66, pp. 83–90.

Kamotani, Y., Lee, J. H., Ostrach, S., and Pline, A., 1992, "An Experimental Study of Oscillatory Thermocapillary Convection in Cylindrical Containers," *Physics of Fluids A*, Vol. 4, pp. 955–962.

Kamotani, Y., Ostrach, S., and Pline, A., 1994, "Analysis of Velocity Data Taken in Surface Tension Driven Convection Experiment in Microgravity," *Physics of Fluids*, Vol. 6, No. 11, pp. 3601–3609.

Kamotani, Y., Ostrach, S., and Pline, A., 1995, "A Thermocapillary Convection Experiment in Microgravity," ASME JOURNAL OF HEAT TRANSFER, Vol. 117, pp. 611–618.

Kamotani, Y., Chang, A., and Ostrach, S., 1996, "Effects of Heating Mode on Steady Axisymmetric Thermocapillary Flows in Microgravity," ASME JOURNAL OF HEAT TRANSFER, Vol. 118, pp. 191–197.

Lee, K. J., 1991, "Experiments on Oscillatory Thermocapillary Flow in Simulated Floating-Zone Configurations," Ph.D. thesis, Department of Mechanical and Aerospace Engineering, Case Western Reserve University, Cleveland, OH.

Lee, K. J., and Kamotani, Y., 1991, "Combined Thermocapillary and Natural Convection in Rectangular Enclosures," *Proceedings of the 3rd ASME/JSME Thermal Engineering Conference*, Reno, NV, pp. 115–120.

Masud, J., Kamotani, Y., and Ostrach, S., 1997, "Oscillatory Thermocapillary Flow in Cylindrical Columns of High Prandtl Number Fluids," *Journal of Thermophysics and Heat Transfer*, Vol. 11, No. 1, pp. 105–111.

Monti, R., Albanese, C., Carotenuto, L., Castagnolo, D., and Evangelista, G., 1995, "An Investigation on the Onset of Oscillatory Marangoni Flow," *Advances in Space Research*, Vol. 16, No. 7, pp. 87–94.

Ostrach, S., Kamotani, Y., and Lai, C. L., 1985, "Oscillatory Thermocapillary Flows," PCH PhysicoChemical Hydrodynamics, Vol. 6, pp. 585–599.

Patankar, S. V., 1980, *Numerical Heat Transfer and Fluid Flow* Hemisphere, Washington, DC.

Preisser, F., Schwabe, D., and Scharmann, A., 1983, "Steady and Oscillatory Thermocapillary Convection in Liquid Columns with Free Cylindrical Surface," *Journal of Fluid Mechanics*, Vol. 126, pp. 545–567.

Schwabe, D., Scharmann, A., Preisser, F., and Oeder, R., 1978, "Experiments on Surface Tension Driven Flow in Floating Zone Melting," *Journal of Crystal Growth*, Vol. 43, pp. 305–312.

Velten, R., Schwabe, D., and Scharmann, A., 1991, "The Periodic Instability of Thermocapillary Convection in Cylindrical Liquid Bridges," *Physics of Fluids A*, Vol. 3, pp. 267–279.

L. M. Phinney[1]
Graduate Student Researcher,
Assoc. Mem. ASME

Chang-Lin Tien
NEC Distinguished Professor
of Engineering,
Honorary Mem. ASME

Department of Mechanical Engineering,
University of California,
Berkeley, CA 94720-1740

Electronic Desorption of Surface Species Using Short-Pulse Lasers

New methods of removing surface contaminants from microelectronic and microelectromechanical systems (MEMS) devices are needed since the decreasing size of their components is reducing the allowable contamination levels. By choosing the pulse duration and fluence to optimize electronic rather than thermal desorption in short-pulse laser processing, surface species can be removed without exceeding maximum temperature constraints. A two-temperature model for short-pulse laser heating of, and subsequent desorption from, metal surfaces is presented. A scaling analysis indicates the material properties and laser parameters on which the ratio of electronic to thermal desorption depends. Regimes of predominantly electronic and thermal desorption are identified, and predicted desorption yields from gold films show that electronic desorption is the primary desorption mechanism in certain short-pulse laser processes.

Introduction

The decreasing size of microelectronic components and devices is resulting in the establishment of more stringent requirements on allowable levels of surface contamination during fabrication and prior to packaging. Surface contaminants like water and ionic atmospheric species corrode electronic materials in the same way that bridges, automobiles, and pipelines are corroded. The small dimensions of microelectronic devices, however, mean that even a few nanograms of corrosion can cause significant damage and even complete device failure (Comizzoli et al., 1986). Electrical leakage, oxidation, and contamination are among the undesirable effects of residual moisture entrapment in electronic assemblies (Leech, 1994). Therefore, it is now necessary to remove very small amounts of adsorbed molecules from metal and semiconductor surfaces. A technological challenge to removing smaller amounts of contaminants is that the adhesion forces become greater as the amount of coverage of the contaminant is decreased. For example, Prybyla et al. (1992) remarked in their study of the removal of carbon monoxide from copper that when the coverage was a third of a monolayer or less, it was significantly harder to remove the carbon monoxide molecules. A monolayer film is one atom or molecule thick over the entire surface.

Small amounts of liquid molecules also create substantial problems in microelectromechanical systems (MEMS) manufacturing. Stiction is the permanent attachment of one part of a microstructure to another, typically the fusion of a slender component, such as a cantilever or membrane, to the underlying substrate layer. Stiction reduces device yields and useful operating lifetimes and is one of the major barriers to large-scale MEMS production and marketability (Walsh et al., 1995). A common stiction failure involves the collection of small amounts of liquid underneath a cantilever. When the liquid is removed, the surface tension forces deform the cantilever. The cantilever may come into contact with the underlying substrate and permanently adhere, thus making the device inoperable (Legtenberg et al., 1994).

Since the allowable levels of surface contamination are decreasing, new methods and processes need to be developed and implemented to achieve these higher standards. Since 1990, several experimenters have used short-pulse lasers to desorb or remove undesirable molecules from metal and semiconductor surfaces. There are several advantages of laser-based contaminant removal processes, including that they are noncontact, do not require the use of toxic chemicals, can achieve high spatial resolutions, and can remove very small contaminants which have high adhesion forces (Park et al., 1994). One of the key features of ultrashort-pulse desorption experiments is that they have enhanced desorption yields over that of nanosecond laser pulses of comparable fluence (Busch et al., 1995). Fushinobu et al. (1996) proposed an ultrashort-pulse laser process for recovering stiction-failed microstructures based on the premise that liquids trapped between a cantilever and the substrate could be desorbed. Tien et al. (1996) later demonstrated that this technique could be used to recover failed microstructures. Thus, short-pulse laser contaminant removal processes are viable and should be investigated.

The important materials in microelectronics and MEMS are metals and semiconductors. This paper examines the removal of undesirable surface species from metals using short-pulse lasers. A two-temperature model of short-pulse laser heating and desorption is presented and used to predict desorption yields from gold films of two thicknesses for a range of laser pulse durations and fluences. Of particular interest are the relative contributions from electronic and thermal desorption mechanisms. Regimes of thermal and electronic desorption are identified, and implications for optimum laser surface contaminant removal are presented.

Short-Pulse Laser-Induced Desorption

Three mechanisms exist by which a laser can desorb, or remove, unwanted molecules from the surface of a substrate: resonant excitation of the adsorbate, thermally induced desorption, and electronically induced excitations (Cavanagh et al., 1990). A brief summary of these mechanisms is provided in this section. If the species on the surface are excited by the incoming laser irradiation directly, they can resonantly absorb enough energy to leave the surface. For a very thin layer of weakly absorbing contaminants, it is usually not possible for enough energy to be absorbed by the surface species for them to desorb (Zhu, 1994). In a thermal desorption process, the

---

[1] Current address: Department of Mechanical and Industrial Engineering, University of Illinois at Urbana-Champaign, 140 Mechanical Engineering Building, MC-244, Urbana, IL 61801.

Contributed by the Heat Transfer Division for publication in the JOURNAL OF HEAT TRANSFER. Manuscript received by the Heat Transfer Division, July 16, 1997; revision received, Apr. 23, 1998. Keywords: Analytical, Microscale, Laser, Desorption, Heat Transfer. Associate Technical Editor: M. Pinar Menguc.

substrate absorbs the incoming radiation and is heated. Lattice vibrations, phonons, then transfer sufficient vibrational energy to the adsorbates on the surface for desorption.

In electronically induced desorption processes, the laser radiation is also absorbed by the substrate, but the energy is transferred to the surface species through excited electrons in the substrate which change the electronic state of the adsorbate-surface bond. In the excited electronic state, the surface species can acquire the necessary energy to leave the surface. One significant advantage of an electronic desorption mechanism is that surface species can be removed without significantly heating the substrate material. Most microelectronic and MEMS devices should not be significantly heated after the metallization processing has been completed. Since electronic desorption mechanisms can be used to remove adsorbates without heating the substrate, processes utilizing this technique could be employed without damaging devices or structures.

Ultrafast lasers have pulse durations on the order of or less than a picosecond, 10^{-12} s, and have been used to create energetic electrons in metals for the purpose of electronically desorbing surface species. Prybyla et al. (1990) desorbed nitric oxide, NO, molecules from a palladium surface using subpicosecond laser irradiation. Since then, several other investigators have similarly removed surface species using laser pulses on the order of a hundred femtoseconds, fs, 10^{-15} s (Prybyla et al., 1992; Kao et al., 1993a, b; Busch et al., 1995). The laser wavelength in the these experiments was usually 620 nm, but experiments were also performed at 310 nm.

Modeling of Short-Pulse Laser-Induced Desorption

In order to correctly model short-pulse laser heating of (and subsequent desorption from) metals, it is necessary to understand the energy absorption, transport, and storage phenomena. A metal can be represented schematically as a sea of electrons surrounding the ion cores arranged in a crystalline lattice structure. When the metal is irradiated by a laser, the radiant energy is first absorbed by the electrons. The electrons then transfer the energy to the metal lattice.

The electron-lattice relaxation time, t_c, is the time scale in which the transfer of energy from the electrons to the lattice occurs and is on the order of a picosecond for metals (Qiu and Tien, 1994). When the duration of the laser pulse, t_p, is on the order of or shorter than the relaxation time, a substantial nonequilibrium can occur between the electron and lattice temperatures, T_e and T_l, respectively. An additional time scale, the thermalization time, specifies the amount of time necessary to fully establish an electron temperature; before this time the electron temperature is only an approximation. Fann et al. (1992) measured the time necessary to establish an electron temperature in gold to be 800 fs.

It should be noted that there is some inconsistency in the literature with regards to the thermalization and relaxation time terminology, with some authors calling the time for the electrons to transfer their energy to the lattice the thermalization time. The convention followed in this paper is that the time for the electrons to reach an equilibrium temperature is called the thermalization time and the time for the electrons to transfer energy to the lattice is called the relaxation time. Also, thermal diffusion throughout the metal becomes important at longer times, typically times on the order of tens of picoseconds.

A two-temperature, or two-step, model of heat diffusion was originally proposed by Anisimov et al. (1974) and later derived from the Boltzmann equation by Qiu and Tien (1993a) for short-pulse laser heating of metals. Qiu and Tien (1993a) showed that conventional models, which assume instantaneous transfer of energy to the lattice, ignore the time required for energy transfer and therefore predict higher lattice temperatures, lower electron temperatures, and smaller heat affected regions. Consequently, conventional models cannot be used for short-pulse laser interactions with metals when the electron-lattice relaxation time is considered. Thus, the two-temperature model is used in the present investigation.

Since the size of the laser beam is large compared to the laser penetration depth, short-pulse laser heating of metals can be modeled as one-dimensional. The electron and lattice energy equations are (Anisimov et al., 1974)

$$C_e(T_e)\frac{\partial T_e}{\partial t} = \nabla\cdot(\kappa\nabla T_e) - G(T_e - T_l) + S \qquad (1)$$

$$C_l\frac{\partial T_l}{\partial t} = G(T_e - T_l) \qquad (2)$$

where κ is the thermal conductivity. The electron-phonon coupling factor, G, transfers energy from the electrons to the lattice and is considered independent of temperature (Kaganov et al., 1957; and Schoenlein et al., 1987). The linear variation of the electronic specific heat with T_e is written as $C_e(T_e) = \gamma T_e$ for temperatures much below the Fermi temperature, which is around 60,000 K for gold (Kittel, 1986). The thermal conductivity of the electrons is much larger than that of the lattice. Thus, the majority of the energy is transported by the electrons, and conduction through the lattice can be neglected. For example, in gold at room temperature, 99 percent of the energy transfer is through the electrons (Klemens and Williams, 1986). Equations (1) and (2) are valid below the melting temperature of the metal, which is 1338 K for gold (Kittel, 1986).

The laser source term, S, in Eq. (1) is

$$S = \alpha I, \qquad (3)$$

Nomenclature

A = scaling factor in the desorption rate equation, molecules/(m^2 s)
C = specific heat per unit volume, J/(m^3K)
E = activation energy for desorption, J or eV
G = electron-lattice coupling factor, W/(m^3 K)
I = laser intensity as a function of time and space, W/m^2
J = laser fluence per pulse, J/m^2
k = Boltzmann's constant = $1.381\cdot10^{-23}$, J/K
L = thickness of the metal layer, m
n = surface concentration, molecules/m^2
R = reflectivity
S = energy source term in the carrier energy equation, W/m^3
T = temperature, K
T_0 = initial temperature, K
t = time, s
t_c = electron-lattice relaxation time, s
t_p = pulse duration (full-width at half-maximum), s
x = spatial coordinate, m
Y = yield, molecules/m^2

Greek

α = absorption coefficient, m^{-1}
γ = electronic specific heat coefficient, J/(m^3 K^2)
κ = thermal conductivity, W/(m K)
δ = radiation penetration depth, m
ΔT_c = temperature nonequilibrium between the electrons and the lattice, K
ΔT_{th} = temperature increase due to thermal heating, K

Subscripts

e = electron
el = electronic
l = lattice
th = thermal

where I is the laser intensity and α the absorption coefficient of the metal. The absorption coefficient of the metal is the inverse of the radiation penetration depth, δ. For a spatially uniform and temporally Gaussian laser pulse, with a full-width at half-maximum (FWHM) pulse duration of t_p centered at time $t = 0$, the intensity is

$$I = \frac{2\sqrt{\ln(2)}J}{\sqrt{\pi}t_p}(1 - R)\exp\left(-\int_0^x \alpha d\eta\right) \times \exp\left\{-4\ln(2)\left(\frac{t}{t_p}\right)^2\right\}. \quad (4)$$

In Eq. (4), J is the laser fluence and R the reflectivity of the metal. The thin layer of surface contaminants is assumed not to absorb or interfere with the incoming laser radiation or change the optical constants of the metal. This assumption is justified for thin layers of weakly absorbing species on metal and semiconductor surfaces (Zhu, 1994).

An Arrhenius expression is assumed for the desorption rate (time rate of change of the surface concentration, n) of the surface contaminants. The desorption rate is then written as

$$-\frac{dn}{dt} = A_{el}\exp\left(\frac{-E_{el}}{kT_e(x = 0)}\right) + A_{th}\exp\left(\frac{-E_{th}}{kT_l(x = 0)}\right) \quad (5)$$

where k is the Boltzmann constant and E_{el} and E_{th} are the activation barriers to electronically and thermally induced desorption, respectively. Thus, the desorption rate depends on the surface temperatures of the electrons and lattice, T_e $(x = 0)$ and T_l $(x = 0)$. The factors A_{el} and A_{th} are scaling factors and can vary with coverage and temperature. The first term on the right-hand side is an Arrhenius equation for the electronically induced desorption, and the second term represents the desorption due to lattice heating. Using an Arrhenius equation to model thermal desorption is well established (Woodruff and Delchar, 1994). Prybyla et al. (1990), Budde et al. (1991), and Kao et al. (1993b) use an Arrhenius equation to phenomenologically model the electronic desorption of various surface species from metal surfaces induced by femtosecond laser pulses. An Arrhenius model for the electronic desorption does not capture all of the physics occurring in such a process but can provide a first-order estimate of the desorption rate. The desorption yield, Y, at a particular time is found by integrating the desorption rate over the corresponding temperature profile.

Thermal and Electronic Desorption Regimes

Due to restrictions on the maximum temperature, T_l, which can be achieved during processing for certain applications, the relative contributions to the total desorption yield from electronically and thermally induced desorption need to be established for varying laser conditions and material properties. The temporal history of the surface electron and lattice temperatures determines the amount of electronic and thermal desorption, respectively. The amount of electron-lattice nonequilibrium during laser irradiation determines the extent to which these two temperatures will differ. For conditions of laser irradiation in which energy propagation in the material is neglected, Qiu (1993) presents expressions for ΔT_c, the maximum temperature difference between the electrons and lattice, and t_c as

$$\Delta T_c = S/G \quad (6)$$

and

$$t_c = C_e/G. \quad (7)$$

For a metal film of thickness L, energy conservation requires that, ΔT_{th}, the increase in temperature of the film due to a deposition of laser energy, would be

$$\Delta T_{th} = \frac{(1 - R)J}{C_l L_d} \quad (8)$$

assuming no losses. The heat penetration depth, L_d, represents the amount of material thermally heated or the heat affected zone and is typically the laser penetration depth, δ. For laser pulses shorter than t_c, however, the heat penetration depth should be estimated from $L_d = \sqrt{\kappa t_c/C_e}$. For gold at room temperature, the heat penetration depth is then 110 nm which is over seven times larger than the laser penetration depth of 15 nm (Qiu and Tien, 1993b). The ΔT_{th} predicted from Eq. (8) would represent the peak lattice temperature increase which would occur before the energy could diffuse throughout a film thicker than L_d. For very thin films, $L < L_d$, the boundary condition at the rear surface would affect peak temperature. For an insulated boundary, the film thickness, L, could be used to estimate the extent of the thermal heating.

A scaling analysis of ΔT_c and ΔT_{th} provides insight into the magnitude of the temperature nonequilibrium compared to the amount of thermal heating. The ratio of these two quantities is

$$\frac{\Delta T_c}{\Delta T_{th}} = \frac{S}{G}\left(\frac{C_l L_d}{(1 - R)J}\right). \quad (9)$$

This ratio is a measure of how much relative desorption would be expected due to the two mechanisms. The magnitude of the desorption event is not predicted by Eq. (9), but the relative contributions are. Four energy regimes of desorption are identified and shown schematically in Fig. 1. The energy scale in Fig. 1 provides insight into the amount of desorption which would occur; low energies correspond to small amounts of (or no) desorption and high energies correspond to significant desorption. The upper two regimes in the figure correspond to a substantial nonequilibrium in temperatures, and desorption due to electronic desorption is significant in these regimes. As the energy is increased, the thermal heating of the metal film increases. Thermal desorption is therefore significant in the two regimes on the right in Fig. 1. The regime of particular interest in Fig. 1 is the upper left regime in which the nonequilibrium is significant but thermal heating is not. By using laser conditions corresponding to this regime, desorption could be sustained without significant heating.

Using $S = ((1 - R)J)/(\delta t_p)$ and Eq. (7), Eq. (9) is rewritten as

$$\frac{\Delta T_c}{\Delta T_{th}} = \left(\frac{C_l}{C_e}\right)\left(\frac{t_c}{t_p}\right)\left(\frac{L_d}{\delta}\right). \quad (10)$$

The ratio of the nonequilibrium during laser heating to the peak lattice temperature is thus a product of three terms: the ratio of

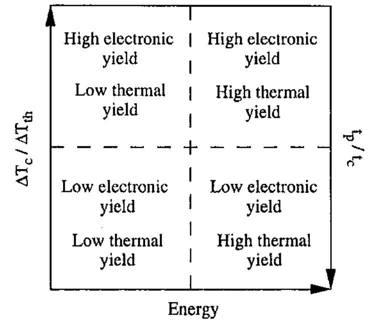

Fig. 1 **Regimes of electronic and thermal desorption**

the lattice and electron specific heats, a characteristic time, and a characteristic length. The lattice specific heat is one to two orders of magnitude greater than the electron specific heat in most metals at room temperature (Klemens and Williams, 1986). Calculations for short-pulse laser heating of gold films assuming constant C_l/C_e indicate that, for a given t_p and L, the ratio of $\Delta T_c/\Delta T_{th}$ remains constant even when the fluence varies by two orders of magnitude; however, the electron specific heat varies linearly with T_e and C_l/C_e will decrease as T_e increases. At elevated electron temperatures, larger fluences are required to continue increasing T_e, and the relaxation time will increase according to Eq. (7).

The ratio of the lattice to the electron specific heat at room temperature is listed in Table 1 for several metals in order to predict the amount and probability of electronic desorption. The electronic specific heat was calculated from $C_e(T_e) = \gamma T_e$ with the values for γ taken from Kittel (1986). The lattice specific heat is equal to the difference between the total specific heat values at room temperature, C_p (Incropera and Dewitt, 1990), and C_e. The electron-phonon coupling factor is also listed in Table 1. Higher values of C_l/C_e indicate more electronic excitation for a given amount of energy and thus final lattice temperature rise. It can be seen that gold, copper, and silver would be expected to have the greatest electronic temperatures from this criterion. The value of G is also important because the larger the electron-phonon coupling factor the more efficient the energy transfer between the electrons and the lattice. For prolonged electronic excitations leading to more electronic desorption, low values of G are desired. On this basis, gold and silver are expected to have the longest lasting and largest degree of electronic excitation for a given energy input. The electronic excitation in vanadium and niobium would be present for the shortest amount of time. Thus, gold and silver are predicted to be two of the best metals for electronic desorption due to their high C_l/C_e ratios and low electron-phonon coupling factors.

The characteristic time, the ratio of t_c/t_p, relates the relaxation time to the laser pulse duration. For laser pulses on the order of or less than the relaxation time, a significant nonequilibrium develops between the electron and lattice temperatures making electronic desorption possible. The ratio of the thermal and radiation penetration depths also gives insight into the type of desorption likely to occur. Films with larger thermal penetration depths achieve lower lattice temperatures for a given amount of energy which increases the ratio of $\Delta T_c/\Delta T_{th}$, indicating that the contribution from electronic desorption would be more significant if desorption occurs. It should be noted, however, that by increasing only the ratio of L_d to δ it is not possible to initiate electronic desorption processes even though the ratio of $\Delta T_c/\Delta T_{th}$ increases.

The time and length scale regimes for electronic and thermal desorption from a metal surface due to irradiation with a short-pulse laser are delineated and depicted in Fig. 2. An electron-lattice relaxation time of 1 ps is assumed. The time scale on Fig. 2 corresponds to a range of laser pulse durations from 100 fs to 100 ps. Energy propagation through the material becomes important starting at times around 10 ps in metals and needs to considered in order to extend the current scaling to longer pulse durations. The lines representing $\Delta T_c/\Delta T_{th} = 1$ for $C_l/C_e = 100$ and $C_l/C_e = 10$ are shown on Fig. 2. For gold, if the lattice temperature remains constant at room temperature, $T_l = 300$ K, $C_l/C_e = 100$ at $T_e = 375$ K, and $C_l/C_e = 10$ at $T_e = 3750$ K.

Table 1 C_l/C_e ratio at room temperature and G for various metals

Metal	$\frac{C_\ell(300K)}{C_e(300K)}$	G $W/(m^3 \cdot K)$
Chromium (Cr)	54	42 ± 5^a
Copper (Cu)	117	4.8 ± 0.7^a, 10^b
Gold (Au)	115	2.8 ± 0.5^a
Lead (Pb)	29	12.4 ± 1.4^a
Niobium (Nb)	9.5	387 ± 36^a
Palladium (Pd)	8.2	50^c
Silver (Ag)	130	2.8^d
Vanadium (V)	8.0	523 ± 37^a, 170^e
Tungsten (W)	61	26 ± 3^b

Superscripts: a Brorson et al., 1990 b Esayed-Ali et al., 1987
c Prybyla et al., 1990 d Groeneveld et al., 1990
c Yoo et al., 1990

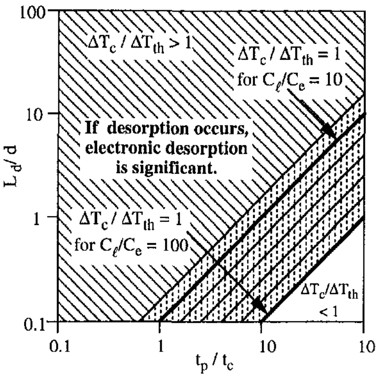

Fig. 2 Time and length scale regimes of electronic and thermal desorption in short-pulse laser processing

Numerical Results

The model for short-pulse laser heating of and desorption from metals was used to investigate the type of desorption expected from a gold surface subject to a range of laser conditions. Gold is one of the metals used for interconnects and bonds in microelectronics and MEMS devices. Additional advantages to studying gold films are the expected electronic effects due to high C_l/C_e and low G, availability of property data, and presence of numerous studies of short-pulse laser interactions with gold in the scientific literature (Schoenlein et al., 1987; Brorson et al., 1990; Fann et al., 1992; and Qiu and Tien, 1993a). Using the control volume approach and implicit solver presented in Patankar (1980), a finite difference scheme was used to calculate the electron and lattice temperatures and desorption rates from Eqs. (1), (2), and (5).

A schematic of the computational domain, a gold film of thickness L, is shown in Fig. 3. The initial and boundary conditions correspond to a constant initial temperature and insulated surfaces due to the short time of the laser pulse. The initial time was chosen as five pulse durations prior to the maximum of the pulse, at which time the source term in Eq. (3) is negligibly small compared to its peak value. The initial and boundary conditions are thus

$$T_e(x, -5t_p) = T_l(x, -5t_p) = T_0 \tag{11}$$

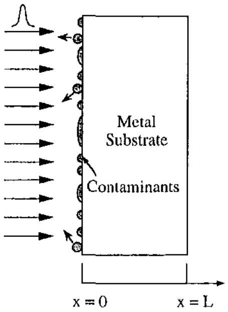

Fig. 3 Laser irradiation of a metal substrate with surface contaminants

Table 2 Physical properties of gold used in the calculations

Reflectivity: R	0.93 †
Absorption coefficient: α	$6.54\text{x}10^7$ m^{-1} †
Thermal conductivity: κ	315.0 W/(m K) †
Electron specific heat: C_e	$C_e = \gamma T_e$ J/(m^3 K) *
Electronic specific heat coefficient: γ	66.6 J/(m^3 K^2) *
Lattice specific heat: C_ℓ	$2.5\text{x}10^6$ J/(m^3 K) †
Electron-lattice coupling factor: G	$2.6\text{x}10^{16}$ W/(m^3 K) #
Activation energy for electronic desorption: E_{el}	$6.4\text{x}10^{-20}$ J (0.4 eV) ‡
Activation energy for thermal desorption: E_{th}	$6.4\text{x}10^{-20}$ J (0.4 eV) ‡

† Grey, 1972 * Kittel, 1986 # Brorson et al., 1990 ‡ Kao et al., 1993b

and

$$\left.\frac{\partial T_e}{\partial x}\right|_{x=0} = \left.\frac{\partial T_l}{\partial x}\right|_{x=0} = \left.\frac{\partial T_e}{\partial x}\right|_{x=L} = \left.\frac{\partial T_l}{\partial x}\right|_{x=L} = 0 \qquad (12)$$

where T_0 is the initial temperature. The spatial discretization and time steps in the calculation were varied to verify that the calculated results are independent of their values. Also, the increase in the internal energy of the system was compared to the absorbed laser fluence and agreed within one percent for all cases.

The optical and material properties were assumed to remain constant during the short-pulse laser heating process and are listed in Table 2. The optical properties are typical of those for visible light (600 nm) irradiation of gold. The temperature effects on the reflectivity and absorptivity were neglected (Scouler, 1967; Pells and Shiga, 1969). Typical thermal activation energies range from 0.4 to 1.7 eV for coverages below a monolayer approaching zero (Zhdanov, 1991), where 1 electron volt, eV, equals $1.60219 \cdot 10^{-19}$ J. The activation energy of 0.4 eV is typical for the energies observed during femtosecond desorption experiments of CO from Cu (Prybyla et al., 1992) and O_2 from Pt (Kao et al., 1993b). Kao et al. (1993b) also observed that the electronic desorption activation energy which they determined from their measurements is very close to the activation energy needed to thermally remove O_2 from Pt. Thus, the activation energies can be on the same order for thermal and electronic desorption in some systems, and an activation energy of 0.4 eV was assumed for both thermal and electronic desorption. The thermal energy corresponding to 0.4 eV, $E = kT$, yields a temperature of 4640 K. The constants, A_{el} and A_{th}, in Eq. (5) are usually determined empirically in a fit to the available data. In this study, they were assumed to be equal. Further, the desorption rates and yields were normalized canceling out the scaling factor value.

To test the numerical procedure, the predicted electron temperatures at the front and rear surfaces of a 100 nm gold film were compared to the experimental results of Brorson et al.'s (1987) experiment. The predicted values agreed with the experimental values reasonably well (Phinney, 1997), with the electron temperature decay at the front surface and rear surfaces predicted to occur slightly faster and slower than experimentally measured, respectively. This means that the predicted values will yield a conservative estimate for the electronic desorption from the front surface as the actual decay is somewhat slower than the calculations predict.

The range of laser pulse widths and fluences was then chosen to correspond to situations in which significant electronic desorption is expected. The laser pulse durations, t_p, and fluences, J, ranged from 100 fs to 10 ps and 1 mJ/cm^2 to 10 mJ/cm^2, respectively. The corresponding range in intensity is $1 \cdot 10^{12}$ to $1 \cdot 10^{15}$ W/m^2. Qiu (1993) predicts a ΔT_e of at least 100 K starting at intensities of $1 \cdot 10^{12}$ W/m^2 for gold. The time-steps used in the calculations were 2 fs, 20 fs, and 200 fs, for t_p equal to 100 fs, 1 ps, and 10 ps, respectively. Two film thicknesses, 100 and 20 nm, were used. Due to the smaller volume to be heated, the 20 nm film is heated more than the 100 nm film. The spatial steps were 0.25 nm for the 100 nm and 0.05 nm for the 20 nm films.

Figure 4 shows the electron and lattice temperatures calculated for a 100 nm gold film irradiated by a laser with $J = 10$ mJ/cm^2 and $t_p = 100$ fs, 1 ps, or 10 ps. A substantial nonequilibrium between the electron and lattice temperatures occurs for the 100 fs and 1 ps calculations with the electron temperatures reaching 2510 K and 1460 K, respectively. The lattice temperatures only increase by 30 K for all three pulse widths. Due to the substantial nonequilibrium and low level of lattice heating, desorption would be expected to occur due to electronic mechanisms. Figure 5 shows the normalized desorption rates for these systems. The desorption clearly occurs during the time in which the electron temperatures are elevated. Thus, surface contaminants could be desorbed without damaging the material due to high lattice heating. Figure 5 also shows that the reduction in the maximum electron temperatures for the longer pulse width calculations results in even larger reductions in the desorption rates due to the Arrhenius form of Eq. (5). The desorption rate for $t_p = 10$ ps is barely visible on Fig. 5; the symbols are slightly elevated at $t = 0$ seconds. In contrast, the maximum electron temperature for the $t_p = 10$ ps calculation can be clearly seen on Fig. 4.

Figure 6 shows the pulse width dependence of the normalized desorption yields for two film thicknesses irradiated by laser pulses with fluences of 1 mJ/cm^2 or 10 mJ/cm^2. The total desorption yields were calculated by integrating the desorption rates over the appropriate temperature profiles from $t = -5t_p$

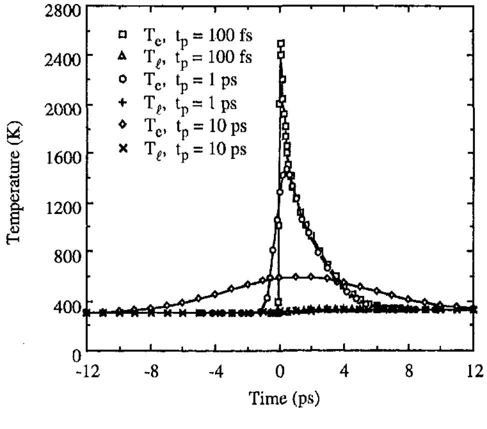

Fig. 4 Surface electron and lattice temperatures for 100 nm gold films irradiated with $J = 10$ mJ/cm^2 and $t_p = 100$ fs, 1 ps, or 10 ps

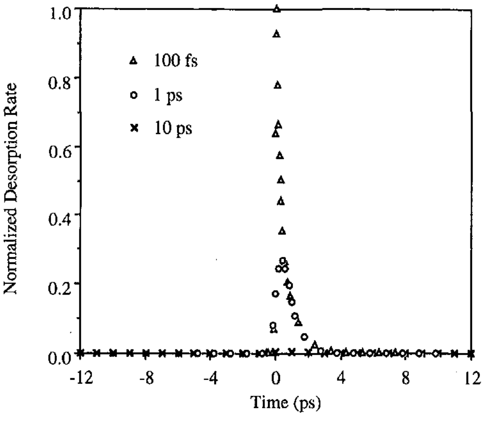

Fig. 5 Normalized desorption rates from 100 nm gold films irradiated with $J = 10$ mJ/cm^2 and $t_p = 100$ fs, 1 ps, or 10 ps

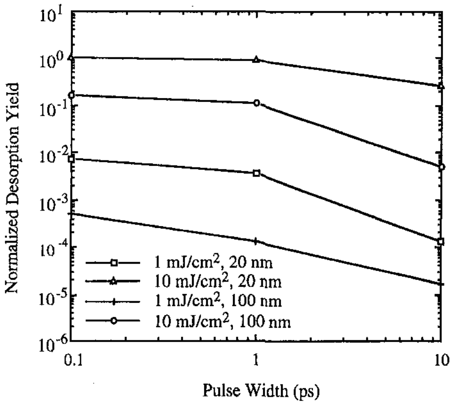

Fig. 6 Normalized desorption yields as a function of pulse width

to 50 ps. The maximum desorption yield was obtained for the 20 nm film irradiated with the 100 fs pulse of 10 mJ/cm^2 and was used to normalize the yields. The desorption yields from the 20 nm films are greater than that from the 100 nm films subject to the same fluence. This difference is partially due to the increased thermal heating but occurs mainly because the temperature nonequilibrium and relaxation times were larger in these cases. This is seen by comparing the temperature profiles calculated for 20 nm films shown in Fig. 7 to those for 100 nm films in Fig. 4. Brorson et al. (1987) also observed in their experiments that the front surface reflectivity decay time increased as the sample dimensions decreased. The absorption depth in gold is 15 nm so a 20 nm film is only slightly larger than δ. In the 100 nm film, the energetic electrons diffuse throughout the film as well as transferring their energy to the lattice, thereby lowering the surface electron temperature. In the 20 nm films, the electrons are only able to lower their energy by transferring their energy to the lattice.

The larger electronic desorption yield for the 20 nm films is inconsistent with Eq. (10), which was derived for conditions neglecting diffusion, and therefore is not able to predict the lower electronic temperatures for the 100 nm films. The higher electron temperatures for the smaller films result in a greater percentage of the desorption being due to electronic desorption as shown in Table 3. For all of the cases calculated, the majority of the desorption was due to electronic desorption. The electronic desorption percentage decreases with pulse width as expected from Eq. (10). Figure 6 also shows that the desorption yield dependence on pulse width changes as the laser fluence is increased. For low fluences, the desorption yield increases substantially with decreasing pulse width. As the fluence is increased, the pulse width variation becomes less significant.

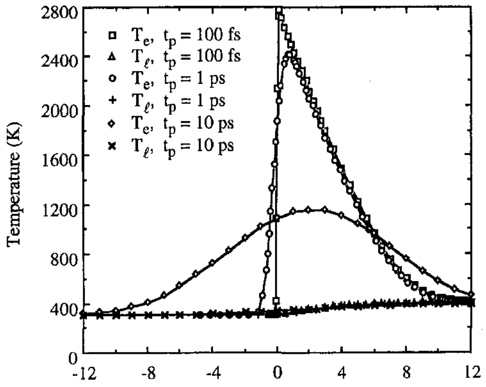

Fig. 7 Surface electron and lattice temperatures for 20 nm gold films irradiated with J = 10 mJ/cm^2 and t_p = 100 fs, 1 ps, or 10 ps

Table 3 Percentage of the total desorption due to electronic desorption

Fluence mJ/cm^2	Film Thickness nm	Pulse Width (FWHM) 100 fs	1 ps	10 ps
1	20	99.6	99.2	90.7
1	100	96.3	85.7	80.4
10	20	99.9	99.9	99.7
10	100	99.9	99.9	98.8

Conclusions

Due to the need to remove increasingly small amounts of surface contaminants, a short-pulse laser desorption process is investigated. In short-pulse laser heating of materials, a nonequilibrium occurs between the electron and lattice temperatures for laser pulse durations on the order of or less than the electron-lattice relaxation time. The high electron temperatures are conducive to electronically induced desorption as well as desorption due to thermal heating. A desorption model is presented which includes contributions from both electronic and thermal desorption. A scaling analysis comparing the expected nonequilibrium in temperatures and increase in the lattice temperature indicates the dependence of the relative desorption yields on three ratios: the lattice and electron specific heats, the electron-lattice relaxation time and laser pulse duration, and the heat and radiation penetration depths. Regimes of predominantly electronic and thermal desorption are then identified. For very short laser-pulse durations, fluence levels below those required to significantly heat the material can be used to remove contaminants, which is important for processes with constraints on the amount of temperature increase. Calculations of laser-induced desorption indicate that significant desorption can result from electronic excitations.

Acknowledgments

Support from DOE and NSF grants is gratefully acknowledged.

References

Anisimov, S. I., Kapeliovich, B. L., and Perel'man, T. L., 1974, "Electron Emission from Metal Surfaces Exposed to Ultrashort Laser Pulses," *Soviet Physics JETP*, Vol. 39, pp. 375–377.

Brorson, S. D., Fujimoto, J. G., and Ippen, E. P., 1987, "Femtosecond Electronic Heat-Transport Dynamics in Thin Gold Films," *Physical Review Letters*, Vol. 59, pp. 1962–1965.

Brorson, S. D., Kazeroonian, A., Moodera, J. S., Face, D. W., Cheng, T. K., Ippen, E. P., Dresselhaus, M. S., and Dresselhaus, G., 1990, "Femtosecond Room-Temperature Measurement of the Electron-Phonon Coupling Constant λ in Metallic Super-conductors," *Physical Review Letters*, Vol. 64, pp. 2172–2175.

Budde, F., Heinz, T. F., Loy, M. M. T., Misewich, J. A., de Rougemont, F., and Zacharias, H., 1991, "Femtosecond Time-Resolved Measurement of Desorption," *Physical Review Letters*, Vol. 66, pp. 3024–3027.

Busch, D. G., Gao, S., Pelak, R. A., Booth, M. F., and Ho, W., 1995, "Femtosecond Desorption Probed by Time-Resolved Velocity Measurements," *Physical Review Letters*, Vol. 75, pp. 673–676.

Cavanagh, R. R., Buntin, S. A., Richter, L. J., and King, D. S., 1990, "Laser Induced Desorption of Molecules from Surfaces," *Comments on Atomic and Molecular Physics*, Vol. 24, pp. 365–376.

Comizzoli, R. B., Frankenthal, R. P., Milner, P. C., and Sinclair, J. D., 1986, "Corrosion of Electronic Materials and Devices," *Science*, Vol. 234, pp. 340–345.

Elsayed-Ali, H. E., Norris, T. B., Pessot, M. A., and Mourou, G. A., 1987, "Time-Resolved Observation of Electron-Phonon Relaxation in Copper," *Physical Review Letters*, Vol. 58, pp. 1212–1215.

Fann, W. S., Storz, R., Tom, H. W. K., and Bokor, J., 1992, "Direct Measurement of Nonequilibrium Electron-Energy Distributions in Subpicosecond Laser-Heated Gold Films," *Physical Review Letters*, Vol. 68, pp. 2834–2837.

Fushinobu, K., Phinney, L. M., and Tien, N. C., 1996, "Ultrashort-Pulse Laser Heating of Silicon to Reduce Microstructure Adhesion," *International Journal of Heat and Mass Transfer*, Vol. 39, pp. 3181–3186.

Grey, D. E., ed., 1972, *American Institute of Physics Handbook*, 3rd Ed., McGraw-Hill, New York.

Groeneveld, R. H. M., Sprik, R., and Lagendijk, A., 1990, "Ultrafast Relaxation of Electrons Probed by Surface Plasmons at a Thin Silver Film," *Physical Review Letters*, Vol. 64, pp. 784–787.

Incropera, F. P., and DeWitt, D. P., 1990, *Fundamentals of Heat and Mass Transfer*, 3rd Ed., John Wiley and Sons, New York.

Kaganov, M. I., Lifshitz, I. M., and Tanatarov, L. V., 1957, "Relaxation between Electrons and the Crystalline Lattice," *Soviet Physics JETP*, Vol. 4, pp. 173–178.

Kao, F.-J., Busch, D. G., Gomes da Costa, D., and Ho, W., 1993a, "Femtosecond versus Nanosecond Surface Photochemistry: O_2 + CO on Pt(111) at 80 K," *Physical Review Letters*, Vol. 70, pp. 4098–4101.

Kao, F.-J., Busch, D. G., Cohen, D., Gomes da Costa, D., and Ho, W., 1993b, "Femtosecond Laser Desorption of Molecularly Adsorbed Oxygen from Pt(111)," *Physical Review Letters*, Vol. 71, pp. 2094–2097.

Kittel, C., 1986, *Introduction to Solid State Physics*, 6th Ed., John Wiley and Sons, New York.

Klemens, P. G., and Williams, R. K., 1986, "Thermal Conductivity of Metals and Alloys," *International Metals Reviews*, Vol. 31, pp. 197–215.

Leech, C. S., 1994, "Removing Moisture from Electronic Components and Assemblies," *Circuit Assembly*, Vol. 5, pp. 34–37.

Legtenberg, R., Tilmans, H. A. C., Elders, J., and Elwenspoek, M., 1994, "Stiction of Surface Micromachined Structures after Rinsing and Drying: Model and Investigation of Adhesion Mechanisms," *Sensors and Actuators A*, Vol. 43, pp. 230–238.

Park, H. K., Grigoropoulos, C. P., Leung, W. P., and Tam, A. C., 1994, "A Practical Excimer Laser-Based Cleaning Tool for Removal of Surface Contaminants," *IEEE Transactions on Components, Packaging, and Manufacturing Technology-Part A*, Vol. 17, pp. 631–643.

Patankar, S. V., 1980, *Numerical Heat Transfer and Fluid Flow*, Hemisphere, New York.

Pells, G. P., and Shiga, M., 1969, "The Optical Properties of Copper and Gold as a Function of Temperature," *Journal of Physics C*, Vol. 2, pp. 1835–1846.

Phinney, L. M., 1997, "Electronic Desorption and Microstructure Adhesion Reduction Using Ultrashort-Pulse Lasers," Ph.D. thesis, University of California, Berkeley, CA.

Prybyla, J. A., Heinz, T. F., Misewich, J. A., Loy, M. M. T., and Glownia, J. H., 1990, "Desorption Induced by Femtosecond Laser Pulses," *Physical Review Letters*, Vol. 64, pp. 1537–1540.

Prybyla, J. A., Tom, H. W. K., and Aumiller, G. D., 1992, "Femtosecond Time-Resolved Surface Reaction: Desorption of CO from Cu(111) in <325 fsec," *Physical Review Letters*, Vol. 68, pp. 503–506.

Qiu, T. Q., 1993, "Energy Deposition and Transport during High-Power and Short-Pulse Laser-Metal Interactions," Ph.D. thesis, University of California, Berkeley, CA.

Qiu, T. Q., and Tien, C. L., 1993a, "Heat Transfer Mechanisms during Short-Pulse Laser Heating of Metals," ASME JOURNAL OF HEAT TRANSFER, Vol. 115, pp. 835–841.

Qiu, T. Q., and Tien, C. L., 1993b, "Size Effects on Nonequilibrium Laser Heating of Metal Films," ASME JOURNAL OF HEAT TRANSFER, Vol. 115, pp. 842–847.

Qiu, T. Q., and Tien, C. L., 1994, "Femtosecond Laser Heating of Multi-Layer Metals—I. Analysis," *International Journal of Heat and Mass Transfer*, Vol. 37, pp. 2789–2797.

Schoenlein, R. W., Lin, W. Z., Fujimoto, J. G., and Eesley, G. L., 1987, "Femtosecond Studies of Nonequilibrium Electronic Processes in Metals," *Physical Review Letters*, Vol. 58, pp. 1680–1683.

Scouler, W. J., 1967, "Temperature-Modulated Reflectance of Gold from 2 to 10 eV," *Physical Review Letters*, Vol. 18, pp. 445–448.

Shumay, W. C., 1987, "Corrosion in Electronics," *Advanced Materials and Processes*, Vol. 132, pp. 73–77.

Tien, N. C., Jeong, S., Phinney, L. M., Fushinobu, K., and Bokor, J., 1996, "Surface Adhesion Reduction in Silicon Microstructures Using Femtosecond Laser Pulses," *Applied Physics Letters*, Vol. 68, pp. 197–199.

Walsh, S. T., Boylan, R., and Bart, S. F., 1995, "Overcoming Stiction in MEMS Manufacturing," *Micro*, Vol. 13, pp. 49–50, 52, 54, 56, 58.

Woodruff, D. P., and Delchar, T. A., 1994, *Modern Techniques of Surface Science*, 2nd Ed., Cambridge University Press, Cambridge, England.

Yoo, K. M., Zhao, X. M., Siddique, M., Alfano, R. R., Osterman, D. P., Radparvar, M., and Cunniff, J., 1990, "Rate of Electron-Phonon Relaxation in Niobium," *Ultrafast Phenomena VII*, C. B. Harris et al., ed., Springer-Verlag, Berlin, pp. 357–359.

Zhdanov, V. P., 1991, "Arrhenius Parameters for Rate Processes on Solid Surfaces," *Surface Science Reports*, Vol. 12, pp. 183–242.

Zhu, X.-Y., 1994, "Surface Photochemistry," *Annual Review of Physical Chemistry*, Vol. 45, pp. 113–144.

Journal of Heat Transfer
Technical Notes

This section contains shorter technical papers. These shorter papers will be subjected to the same review process as that for full papers.

A Periodic Transient Method Using Liquid Crystals for the Measurement of Local Heat Transfer Coefficients

J. W. Baughn,[1,5] J. E. Mayhew,[2]
M. R. Anderson[3,5] and R. J. Butler[4,6]

Nomenclature

c = specific heat of model (Plexiglas)
f = frequency of periodic freestream temperature
h = local convective heat transfer coefficient
h_T = local convective heat transfer coefficient for a uniform temperature boundary condition
k = thermal conductivity of model (Plexiglas)
Nu_x = Nusselt number (hx/k)
Pr = Prandtl number
Re_x = Reynolds number (based on x)
x = distance from leading edge
y = distance into model from the surface
t = time
T^* = nondimensional surface temperature, Eq. (3)
T_M = mean fluid temperature
T_s = local surface temperature
T_{wi} = initial wall temperature
T_∞ = freestream air temperature
α = thermal diffusivity of model (Plexiglas)
θ = nondimensional surface temperature change, Eq. (6)
γ = variable in Eq. (3), defined by Eq. (4)
ρ = density of model (Plexiglas)

Introduction

There are many different methods for measuring local convective heat transfer coefficients. One common category is transient methods. Liquid crystals have been used extensively for the surface temperature measurements with transient methods. They provide global information on the surface temperature distribution allowing contour maps of local heat transfer coefficients.

Both narrow-band and broad-band liquid crystals have been used for heat transfer coefficient measurements. With the narrow band liquid crystals, typically a single color (usually yellow, between the red-green transition) is used to find a particular isotherm (Baughn, 1995). With the broad band the hue is calibrated against temperature and is used to obtain a series of isotherms (Camci et al., 1992, 1993). Hay and Hollingsworth (1996) discuss the calibration of the hue versus temperature for liquid crystals. The effect of illumination on calibration is described by Farina et al. (1993).

In transient methods, the transient temperature of the surface of a model is used to deduce the local heat flux and heat transfer coefficient. In most transient methods, the difference in temperature between the model and the surrounding fluid involves a step change. We will refer to these as ''step transient'' methods.

The basic principles and data reduction for the step transient method are described by Ireland and Jones (1985, 1986). When the surface has a low thermal diffusivity (e.g., Plexiglas) a one-dimensional assumption is often a good approximation. In this case the surface temperature response is limited to a thin layer near the surface and lateral conduction is small.

There are a variety of techniques used to accomplish the fluid temperature change relative to the surface temperature for the step transient. For example, Clifford et al. (1983), Ireland and Jones (1985, 1986), Metzger and Larson (1986), and Metzger et al. (1991) all use an ambient temperature model and suddenly raise the temperature of their fluid using switching valves. Jones and Hippensteele (1987) preheat the wall of their wind tunnel and then initiate their flow using a diverter door. O'Brien et al. (1986) use a preheated cylinder and insert it into place across a channel with an ambient temperature fluid. Baughn and Yan (1991) remove a shield blocking a heated flat surface from an impinging jet. For measurements on the wall in a duct, Baughn et al. (1994) use an insertion technique. Another variation is the use of in-situ heating described by Butler and Baughn (1995) where a shroud acts as an in-situ heater and is suddenly removed to expose the model to the flow. This shroud technique has been used to investigate the effect of thermal boundary conditions on measurements with the step transient method (Butler and Baughn, 1996).

The present paper introduces a new type of transient method called the periodic transient method. In this method, the freestream temperature is periodically heated while the local surface temperature change of a model is measured. The local heat transfer coefficient can be determined from the frequency of the periodic change in the freestream temperature, the ratio of the surface temperature change to the freestream temperature change and the model thermal properties. Measurements on a Plexiglas flat plate with a laminar boundary layer are presented as a demonstration of this method. The results are compared to

---

[1] Professor. e-mail: jwbaughn@ucdavis.edu. Fellow ASME.
[2] Assistant Professor.
[3] Graduate Student.
[4] Associate Professor.
[5] Department of Mechanical and Aeronautical Engineering, University of California, Davis, One Shields Avenue, Davis, CA 95616.
[6] Department of Aeronautics, United States Air Force Academy, CO 80840.

Contributed by the Heat Transfer Division for publication in the JOURNAL OF HEAT TRANSFER and presented at '97 IMECE, Dallas. Manuscript received by the Heat Transfer Division, Aug. 26, 1997; revision received, Feb. 24, 1998. Keywords: Experimental, Heat Transfer, Measurement Techniques, Periodic, Transient. Associate Technical Editor: T. Bergman.

earlier measurements by Butler and Baughn (1996) and show that the periodic transient method is effective at measuring local heat transfer coefficients. The primary advantage of the periodic transient method is that it approximates a uniform temperature thermal boundary condition (which is often not the case for the step transient). Another advantage is that radiation effects tend to be self-canceling. It is also not necessary to control or measure the initial wall temperature. Its disadvantage is the complexity and power requirements for periodically heating the freestream, which may limit the size of the wind tunnel or the freestream velocity.

Step Transient Theory

The heat transfer coefficient in the step transient method is determined from the response of the surface temperature to a step change in the difference between the surface and the freestream temperature. This response can be determined by solving the one-dimensional transient conduction equation for the wall,

$$\frac{\partial T}{\partial t} = \alpha \frac{\partial^2 T}{\partial y^2} \tag{1}$$

using a convective boundary condition at the surface,

$$-k \left.\frac{\partial T}{\partial y}\right|_{y=0} = h[T(y = 0, t) - T_\infty] \tag{2}$$

where T_∞ is the freestream temperature (or the local bulk temperature in the case of a duct).

Assuming T_∞ is constant after the step change, h is constant, a semi-infinite wall with constant properties, and a uniform initial temperature of T_{wi}, the solution for the temperature at the surface is

$$T^* = \frac{T_\infty - T_s}{T_\infty - T_{wi}} = e^{\gamma^2} erfc(\gamma) \tag{3}$$

where the parameter γ is defined as

$$\gamma = \frac{h\sqrt{t}}{\sqrt{\rho c k}}. \tag{4}$$

This solution is valid for both step transients with a heated freestream (Fig. 1(*a*)) and step transients with a preheated model (Fig. 1(*b*)).

Measurements with the step transient method are made by determining the time, t, for the surface temperature, $T_s(t)$, to produce a particular liquid crystal color. From T^*, t, and the wall thermal properties, Eqs. (3) and (4) are used to obtain the local heat transfer coefficient (a polynomial fit can be used to determine γ from T^*). It may be (and usually is) necessary to correct this heat transfer coefficient for thermal radiation.

Periodic Transient Theory

For the periodic transient method the freestream temperature (T_∞) is a periodic function of time. In this case Eq. (1) is solved using a time-dependent convective boundary condition,

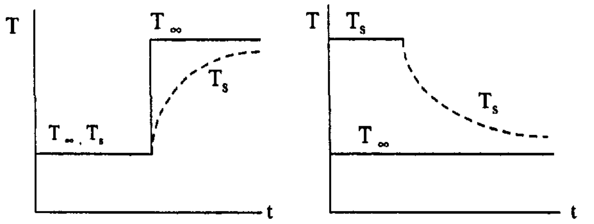

a) Heated Freestream b) Preheated Model

Fig. 1 Surface temperature for a step transient

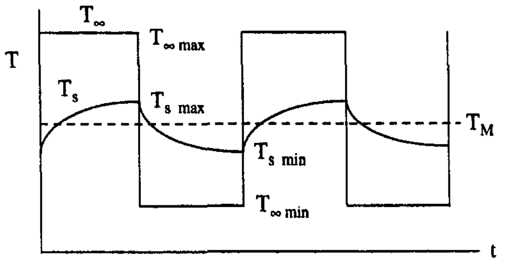

Fig. 2 Surface temperature variation for a periodic freestream temperature (sustained solution)

$$-k \left.\frac{\partial T}{\partial y}\right|_{y=0} = h[T(y = 0, t) - T_\infty(t)]. \tag{5}$$

Numerical solutions of the transient temperature in a Plexiglas wall have been done for a square wave periodic freestream temperature. The periodic surface temperature is attenuated from that of the freestream as shown in Fig. 2.

We define the attenuation, θ, as the ratio of the difference between the maximum and minimum surface temperatures to the difference between the maximum and minimum freestream temperatures,

$$\theta = \frac{T_{s,\max} - T_{s,\min}}{T_{\infty,\max} - T_{\infty,\min}} = \frac{\Delta T_s}{\Delta T_\infty}. \tag{6}$$

The attenuation is dependent on the heat transfer coefficient, the frequency of the periodic freestream temperature, and the wall thermal properties.

Figure 3 shows numerical results for the heat transfer coefficient corresponding to different levels of attenuation as a function of the frequency of the square wave periodic freestream temperature. These results are for the surface temperature after a long period of time (sustained or quasi-steady solution). In this case the mean temperature of the Plexiglas substrate becomes the same as the mean temperature of the periodic freestream. These results show that the local heat transfer coefficient can be determined if the frequency of the periodic freestream temperature and the surface temperature attenuation are measured. The attenuation requires measurement of the maximum and minimum temperatures of the surface and the freestream.

These results have been fit to the following equation:

$$h = \lfloor 1290.9\theta^2 + 787.5\theta + 10.062 \rfloor f^{0.5}. \tag{7}$$

For the range $20 \leq h \leq 200$ this equation fits the numerical

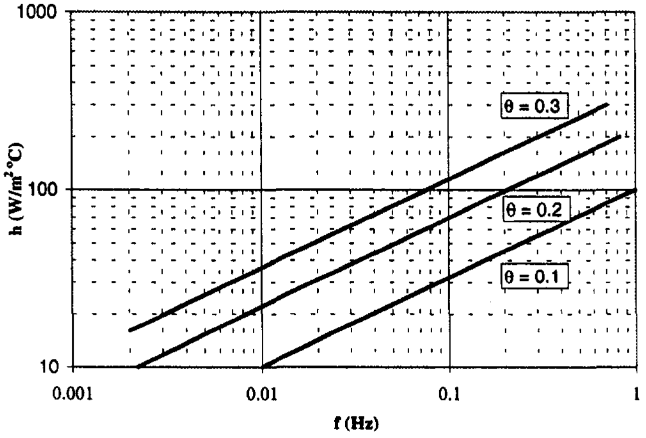

Fig. 3 Numerical results for the heat transfer coefficient as a function of frequency of the periodic freestream temperature (square wave) and surface temperature attenuation (Plexiglas wall)

results within one percent for $0.1 \leq \theta \leq 0.2$ and within 1.8 percent for $0.2 < \theta \leq 0.3$. Equation (7) for the periodic transient method is analogous to Eq. (3) for the step transient method with θ analogous to T^* and f analogous to time. It should be noted that it may not have been necessary to do a numerical solution (although it was convenient to do so) since an analytical solution for the square wave is possible. However, since the solution would be implicit, a fit would still be necessary (as is usually done with Eq. (3)). Equation (7) can be used to determine h using the periodic transient method in the same manner Eq. (3) is used for the step transient method.

To use Eq. (7) it is necessary that the wall be thick enough that the semi-infinite solution is valid. The effective penetration depth of the periodic temperature change after reaching the sustained (quasi-steady) solution has been calculated numerically for the range of h's and θ's for which Eq. (7) is valid. The penetration depth is less for high h's and for lower values of θ, which correspond to higher frequencies (i.e., less time to penetrate). It ranges from less than 1 mm for high h's, low θ's to as much as 1 cm for low h's, high θ's.

It is necessary to wait a sufficiently long time to reach the sustained (quasi-steady) solution. The time for θ to approach its final value depends on the wall thickness, h and θ and has also been calculated numerically. For the range of Eq. (7) and a 0.6 cm wall, times range from ten minutes to one hour.

Thermal Boundary Condition Effect

It is commonly understood that local heat transfer coefficients depend on the thermal boundary condition upstream of the location of interest. However, this important effect is often neglected in the measurement and reporting of heat transfer coefficients.

For the step transient method the upstream thermal boundary condition is changing with time and thus the local h also changes with time. In general the amount of change in h during the transient is not known. For the special simple case of a laminar boundary layer on a flat plate Butler and Baughn (1996) suggest a correlation to correct the measured h from the step transient method to the value h_T which would occur for uniform temperature boundary condition. Their correlation is a function of T^* and the local Reynolds number:

$$h_T = h[(T^*)^{4.9/\mathrm{Re}_x^{0.2}}]. \qquad (8)$$

To understand why this correction is necessary, it is helpful to consider the surface temperature distribution at various times after the transient begins. This is shown in Fig. 4(a) for the case of a preheated model. Initially the plate is uniform in temperature at t_1. As the plate cools more rapidly upstream, due to the higher h upstream, the temperature looks like that at t_2 and later t_3. At these later times the cooler upstream surface temperature results in a thinner thermal boundary layer at a location downstream than would occur with a uniform temperature boundary condition. Thus the downstream heat transfer coefficient increases with time as the upstream surface cools more rapidly than the downstream location. The local heat transfer coefficient determined using Eq. (3) is a time-average value which is higher than the value for a uniform temperature boundary condition (h_T). A similar argument can be made for the case of a step increase in the freestream temperature (ambient temperature model) which also causes a higher h to be measured with the step transient method.

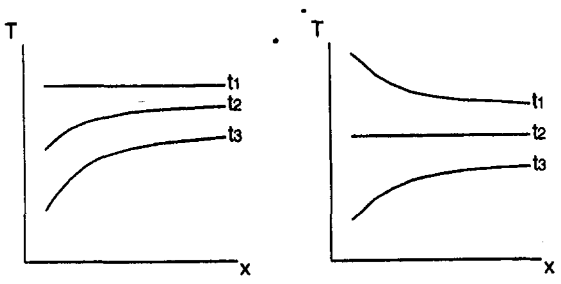

a) step transient

b) periodic transient

Fig. 4 Surface temperature distributions during transients

For the laminar boundary layer on a flat plate the correction from Eq. (8) can be substantial. For turbulent boundary layers the effect is expected to be less, but Butler and Baughn (1996) point out that in cases where there are large heat transfer gradients (for example, near regions of separation), the effects could be significant. This unknown effect is one of the limitations of the step transient method.

For the periodic transient method a similar effect occurs, but it tends to cancel out. To understand this, it is again helpful to consider the surface temperature distribution at various times during the transient. This is shown in Fig. 4(b). The surface temperature distribution at time t_1 represents the distribution at the beginning of the cooling part of the cycle. During the time interval between t_1 and t_2 the warmer upstream surface temperatures result in a thicker thermal boundary layer at a location downstream than would have occurred for a uniform temperature boundary condition and therefore an h lower than h_T. As the upstream plate temperature decreases below the mean plate temperature (between times t_2 and t_3) the cooler upstream temperatures result in a thinner thermal boundary layer at a location downstream than would have occurred for a uniform temperature boundary condition and therefore an h higher than h_T. These effects tend to cancel out. A similar argument can be made for the heating part of the cycle. The time-averaged heat transfer coefficient measured with the periodic transient method is therefore close to the value that would occur for the uniform temperature boundary condition.

Thermal Radiation Effect

During a transient the surface temperature is usually different from the temperature of the surroundings. This generally requires a radiation correction to the measured heat transfer coefficient.

For the step transient the radiation correction usually involves simply subtracting the equivalent radiation heat transfer coefficient from the value obtained from Eq. (3). This approach is valid when the surroundings are at the same temperature as the air or fluid (it is more difficult if they are different). This radiation correction contributes to the uncertainty in the results.

For the periodic transient method, the radiation correction is more complex, but is generally smaller. This is because thermal radiation during the cycle tends to skew the maximum and minimum temperatures of the surface in the same direction (up or down depending on whether the surroundings are at a higher or lower temperature) by approximately the same amount. Since the heat transfer coefficient is determined from the difference between the maximum and minimum temperatures (embodied in θ), which is generally much smaller than the difference between the surface and surroundings, the radiation effect tends to be self-canceling.

Experiment to Demonstrate Periodic Transient Method

An experiment was designed and performed to demonstrate the use of the periodic transient method for measuring local heat transfer coefficients. A laminar boundary layer on a flat plate was selected since this is a simple case with a well-established analytical solution (Pohlhausen's Equation) and has been used to study the step transient (Butler and Baughn, 1996). A diagram of the apparatus is shown in Fig. 5.

The apparatus uses a wind tunnel with a 30.5-cm square straight test section. The entrance to the test section was covered

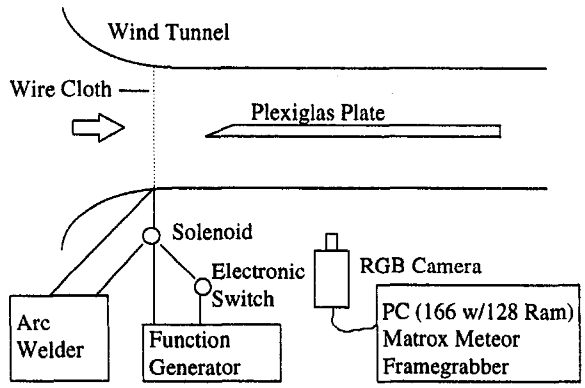

Fig. 5 Diagram of apparatus for periodic transient method measurements on a flat plate

with a fine mesh wire cloth (128 wires per cm) made of stainless steel wire (diameter of 28 μm.). The periodic freestream temperature change was produced by electrically heating this wire cloth with a high current (up to 225 amps) from an arc welder power supply. The current was switched on and off using an automotive starter solenoid, which was activated by a 12 VDC power supply and an electronic switch connected to a function generator. This allowed the switching of the solenoid (and heating) at any desired frequency. The flow-field and turbulence intensity (approximately 0.5 percent) were not significantly affected by the wire cloth.

The time constant of the wire cloth heater is a function of the air velocity and was determined by measuring the transient temperature of the flowing air. For the air velocity used here the time constant was approximately 0.12 seconds. A frequency of 8.33 mHz (60 seconds on and 60 seconds off) was used in this demonstration experiment because of the low h's involved (power limitations kept the velocity low). Higher frequencies can be used for higher h's. For this frequency the freestream temperature can be approximated as a square wave.

In addition to the time delay for heating and cooling the wire cloth there is also a delay associated with the transit time between the wire cloth and the test location. For the measurements presented below, a velocity of 7.3 m/sec is used. The screen is approximately 5 cm upstream of the leading edge of a test plate (a transit time less than 10 msec), and the region of testing is approximately 7 cm (another 10 msec). These times are negligible.

The test plate is Plexiglas (1.24 cm thick) with a sharp leading edge. A slight angle of attack (test surface windward) was used to ensure that flow separation did not occur at the sharp leading edge. A Pitot tube and fast response thermocouple (type K) were mounted in the freestream above the test surface. The test surface was airbrushed with black paint and a medium band liquid crystal (Hallcrest 23C5W). Off-axis lighting was used which tends to narrow the useful range of the liquid crystal.

During the periodic transient, the freestream temperature is continuously recorded and RGB images of the liquid crystal on the surface are captured at the times when the heating current is turned on (minimum surface temperatures) and off (maximum surface temperatures). From these two images the minimum and maximum temperatures can be determined from the liquid crystals as described below. The images were captured using an RGB camera (Sony XC-003) and a Matrox Meteor RGB-framegrabber in a PC (Micron 166 MHz with 128 MB RAM).

The difference between the maximum and minimum surface temperatures at various locations can be determined from the liquid crystal images using a hue analysis. The image files from the Matrox Meteor framegrabber are 24-bit color RGB matrices ($640 \times 480 \times 3$) in TIFF format. A median filter (5×5 block) is used on these RGB matrices, then $640 \times 480 \times 1$ hue matrices are produced using the MATLAB 5.0 RGB2HSV conversion. This conversion has been compared to and gives essentially identical results (while requiring less computational time) to the hue equation recommended by Hay and Hollingsworth (1996):

$$\text{hue} = \arctan\left(\frac{\sqrt{3}\,(G - B)}{2R - G - B}\right). \tag{9}$$

The hue variation with x was determined by averaging the hue from 20 adjoining pixels (0.25 cm) perpendicular to the flow near the location of the freestream thermocouple. To convert this hue variation into a temperature distribution, and ultimately a heat transfer coefficient distribution, an in-situ calibration of hue versus temperature was done. The hue to temperature conversion was done using a linear interpolation between four calibration points.

Experimental Results

The freestream velocity used for these measurements (7.3 m/sec) produced a Reynolds number of approximately 18,600 at a location 5.0 cm downstream of the leading edge. Thus along most of the plate, a laminar boundary layer is expected. The Pohlhausen equation for the heat transfer coefficient for a laminar boundary layer on a flat plate is

$$\text{Nu}_x = 0.332\ \text{Re}_x^{0.5}\ \text{Pr}^{0.333}. \tag{10}$$

The heat transfer coefficient for this relation is plotted in Fig. 6 as a function of Re_x on the plate for the temperature and pressure conditions which existed during the test runs.

The step transient data from Butler and Baughn (1996) is shown in Fig. 6 for two different values of T^* (the strong effect of T^* is evident). Their step transient data is not corrected here for the effect of thermal boundary conditions using Eq. (8). This correction would collapse the data very close to the Pohlhausen curve (Butler and Baughn, 1996). However, their data is corrected for thermal radiation.

The periodic transient method data is also shown in Fig. 6. The values for θ ranged from 0.2 to 0.3. No radiation correction is included for the periodic data (see discussion above).

It is clear from Fig. 6 that the periodic transient results are closer to Pohlhausen's equation (well within the uncertainty discussed below) than the step transient results (without thermal boundary layer correction). Pohlhausen's equation assumes a uniform temperature boundary condition and as discussed above, the periodic transient method approximates this boundary condition well.

Uncertainty Analysis

For the periodic transient method the local heat transfer coefficient is determined from the surface temperature attenuation (θ), the frequency (f), and the thermal properties,

$$h = \phi(\theta, f, \sqrt{\rho c k}). \tag{11}$$

In this case, the uncertainty in h is given by

$$\frac{\delta h}{h} = \sqrt{\left(\frac{1}{h}\frac{\partial h}{\partial \theta}\,\delta\theta\right)^2 + \left(\frac{1}{h}\frac{\partial h}{\partial f}\,\delta f\right)^2 + \left(\frac{1}{h}\frac{\partial h}{\partial \sqrt{\rho c k}}\,\delta\sqrt{\rho c k}\right)^2}. \tag{12}$$

The individual contributions to the total uncertainty in h for the periodic transient method measurements are given in Table 1 for an h of 30 W/m^2°C. In this table θ is broken up into two parts in accordance with its definition in Eq. (6). These uncertainties are determined using standard uncertainty methods with odds of 20:1.

The uncertainty in h is quite high for the reported demonstration measurements with the periodic transient method. The uncertainty in the surface temperature change (and thus in θ) is

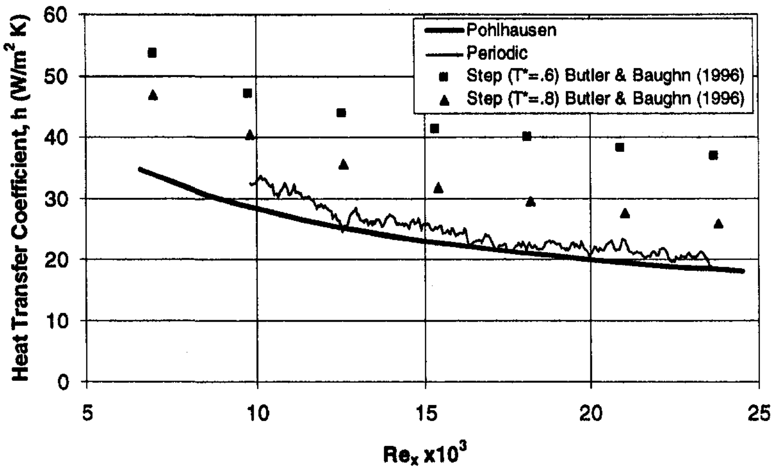

Fig. 6 Heat transfer measurements on a flat plate

the major contribution to this uncertainty. In this demonstration experiment a relatively small surface temperature change was used because of limited heater power. This resulted in a range of θ's from 0.2 to 0.3. To examine the effect of θ on the uncertainty more closely we can look at its contribution to the uncertainty in h given by

$$\frac{\delta h}{h} \approx \frac{1}{h}\frac{\partial h}{\partial \theta}\delta\theta. \tag{13}$$

Using the definition of θ (Eq. (6)), and noting that the uncertainty in the freestream temperature change is small relative to that of the surface temperature change, the uncertainty in θ can be approximated as

$$\frac{\delta\theta}{\theta} = \sqrt{\left(\frac{\delta\Delta T_s}{\Delta T_s}\right)^2 + \left(\frac{\delta\Delta T_\infty}{\Delta T_\infty}\right)^2} \approx \frac{\delta\Delta T_s}{\Delta T_s}. \tag{14}$$

Substituting Eq. (14) into Eq. (13), gives the following approximation for the uncertainty in h for the periodic transient method:

$$\frac{\delta h}{h} \approx \frac{1}{h}\frac{\partial h}{\partial \theta}\theta\frac{\delta\Delta T_s}{\Delta T_s}. \tag{15}$$

Using Eq. (7) this becomes

$$\frac{\delta h}{h} \approx \left(\frac{2581.8\theta^2 + 787.5\theta}{1290.9\theta^2 + 787.5\theta + 10.062}\right)\frac{\delta\Delta T_s}{\Delta T_s} \tag{16}$$

For $0.1 \leq \theta \leq 0.3$ the parenthetic term varies from 1 to 1.3, respectively. Thus the uncertainty can be reduced by using a lower value of θ as well as reducing the uncertainty in the surface temperature change. The lower value of θ can be obtained by using a larger freestream temperature change; this will require a higher frequency to measure the same h (see Fig. 3). The uncertainty in the measurement of the surface temperature change can be reduced by selecting a liquid crystal with a useful range which closely matches the selected surface temperature change. With current hue methods and careful calibration the change in temperature could be measured within approximately seven percent of the useful color range. For these conditions the potential uncertainty could be reduced to eight percent or less for the same h shown in Table 1. Improvements in methods for measuring the surface temperature (better hue methods) could reduce the uncertainty to levels similar to that of the step transient method (typically six percent).

Table 1 Uncertainty of periodic transient method (presented experiment—h = 30 W/m^2°C)

Measurement	Typical Value	δ (±)	% Uncertainty
$\sqrt{\rho c k}$	575 $W\sqrt{sec/m^2\,°C}$	25	4.4
$T_{s,max}$-$T_{s,min}$	0.7 °C	0.1	18
$T_{\infty,max}$-$T_{\infty,min}$	2.5 °C	0.1	5.4
f	8.3 mHz	0.1	0.6
Fit Equation	--	--	1.8
		Total	19

Conclusions

This research has investigated a new variation on the step transient method that uses a periodic freestream temperature. An analysis of the relationship between the local heat transfer coefficient, frequency and surface temperature attenuation has been presented. An experimental demonstration has shown that this periodic transient method can be used to determine local heat transfer coefficients from measurements of the periodic freestream temperature and surface temperature.

The primary advantage of the periodic transient method is that it approximates a uniform temperature thermal boundary condition, eliminating the need for a thermal boundary condition correction. This overcomes one of the limitations of the step transient method where the correction is usually not known and can be significant (Butler and Baughn, 1996). Another advantage is that its radiation correction is small. Also it is not necessary to control or measure the initial wall temperature. Its disadvantage is the complexity and power requirements for periodically heating the freestream which may limit the size of the wind tunnel or the freestream velocity.

Acknowledgments

The support of the Air Force Office of Scientific Research, which provided a University Resident Researcher Program grant for the assignment of Professor Baughn to the USAF Academy, is gratefully acknowledged. We would also like to acknowledge the support and advice of Dr. Richard Rivir of the USAF Wright Laboratory, Aeropropulsion and Power Directorate. Captain John Jumper of the USAFA provided invaluable help by writing the program to drive our frame grabber. Prof. Aaron Byerley (Mercer University) read our manuscript and made many useful suggestions. Discussions with Prof. Terry Jones (Oxford University) and Prof. J. Michael Owen (University of Bath), who visited the USAF Academy under an EOARD WOS grant, were helpful and are appreciated. The assistance of Cadets First Class Jeremy Fischman and James Maxwell of the USAF Academy, who participated in the early part of this research as part of the their USAFA Aeronautics Laboratory course, is also gratefully acknowledged.

References

Baughn, J. W., and Yan, X., 1991, "A Preheated-Wall Transient Method for Measurements of the Heat Transfer to an Impinging Jet," Eurotherm Seminar No. 25, pp. 1–7.

Baughn, J. W., Yan, X., and Roby, Jon L., 1994, "An Insertion Technique Using the Transient Method with Liquid Crystals for Enhanced Heat Transfer Measurements in Ducts," *Enhanced Heat Transfer,* Vol. 1, No. 2, pp. 179–180.

Baughn, J. W., 1995, "Liquid Crystal Methods for Studying Turbulent Heat Transfer," *International Journal of Heat and Fluid Flow,* Vol. 16, pp. 365–375.

Butler, R. J., and Baughn, J. W., 1995, "A Shroud Technique Using the Transient Method for Local Heat Transfer Measurements," *Experimental Heat Transfer,* Vol. 8, No. 1, pp. 17–32.

Butler, R. J., and Baughn, J. W., 1996, "The Effect of the Thermal Boundary Condition on Transient Method Heat Transfer Measurements on a Flat Plate With a Laminar Boundary Layer," ASME JOURNAL OF HEAT TRANSFER, Vol. 118, pp. 831–837.

Camci, C., Kim, K., and Hippensteele, S. A., 1992, "A New Hue Capturing Technique for the Quantitative Interpretation of Liquid Crystal Images Used in Convective Heat Transfer Studies," ASME *Journal of Turbomachinery,* Vol. 114, pp. 765–775.

Camci, C., Kim, K., Hippensteele, S. A., and Poinsatte, P. E., 1993, "Evaluation of a Hue Capturing Based Transient Liquid Crystal Method for High-Resolution Mapping of Convective Heat Transfer on Curved Surfaces," ASME JOURNAL OF HEAT TRANSFER, Vol. 115, pp. 311–318.

Clifford, R. J., Jones, T. V., and Dunne, S. T., 1983, "Techniques for Obtaining Detailed Heat Transfer Coefficient Measurements Within Gas Turbine Blade and Vane Cooling Passages," ASME Paper 83-GT-58.

Farina, D. J., Hacker, J. M., Moffat, R. J., and Eaton, J. K., 1993, "Illuminant Invariant Calibration of Thermochromic Liquid Crystals," *Visualization of Heat Transfer Processes,* Vol. 252, 252, J. J. Simoneau and B. F. Armaly, eds., pp. 1–11.

Hay, J. L., and Hollingsworth, D. K., 1996, "A Comparison of Trichromic Systems for Use in the Calibration of Polymer-Dispersed Thermochromic Liquid Crystals," *Exp. Thermal Fluid Science,* Vol. 12, pp. 1–12.

Ireland, P. T., and Jones, T. V., 1985, "The Measurement of Local Heat Transfer Coefficients in Blade Cooling Geometries," *AGARD Conference Proceedings,* No. 390, Paper 28.

Ireland, P. T., and Jones, T. V., 1986, "Detailed Measurements of Heat Transfer On and Around a Pedestal in Fully Developed Passage Flow," *8th International Heat Transfer Conference,* Vol. 3, pp. 975–980.

Jones, T. V., and Hippensteele, S. A., 1987, "High-Resolution Heat-Transfer Coefficient Maps Applicable to Compound Curve Surfaces Using Liquid Crystals in a Transient Wind Tunnel," *Development in Experimental Technique in Heat Transfer and Combustion,* (also NASA TM-89855, 1988).

Metzger, D. E., and Larson, E. E., 1986, "Use of Melting Point Surface Coatings for Local Convective Heat Transfer Measurements in Rectangular Channel Flows With 90-Deg. Turns," ASME JOURNAL OF HEAT TRANSFER, Vol. 108, pp. 48–54.

Metzger, D. E., Bunker, R. S., and Bosch, G., 1991, "Transient Liquid Crystal Measurement of Local Heat Transfer on a Rotating Disk With Jet Impingement," ASME *Journal of Turbomachinery,* Vol. 113, pp. 52–59.

O'Brien, J. E., Simoneau, R. J., LaGraff, J. E., and Morehouse, K. A., 1986, "Unsteady Heat Transfer and Direct Comparison for Steady-State Measurements in a Rotor-Wake Experiment," *8th International Heat Transfer Conference,* San Francisco, pp. 1243–1248.

Thermal Diffusivity Determination of High-Temperature Levitated Oblate Spheroidal Specimen by a Flash Method

F. Shen[1,3] **and J. M. Khodadadi**[2,3]

In extending the range of applicability of a recently developed method, a single-step containerless flash technique for determining the thermal diffusivity of levitated oblate spheroidal samples is proposed. The flash method is modeled as an axisymmetric transient conduction heat transfer problem within the oblate spheroid. It is shown that by knowing the sample geometric parameters and recording the temperature rise history at least at two different points on the surface simultaneously, the thermal diffusivity can be determined without knowing the heat loss parameter. The appropriate coefficients needed for determining the thermal diffusivity of oblate spheroidal samples are provided.

Nomenclature

Bi = Biot number, defined as $(4\epsilon_{\mathrm{eff}}\sigma F T_{\mathrm{sur}}^3 + h)R/k$
c_p = specific heat at constant pressure, J/kg · K
h = convection heat transfer coefficient, $\mathrm{W/m^2 \cdot K}$
k = thermal conductivity, W/m · K
Q = uniform incident energy flux, $\mathrm{J/m^2s}$
R = equivalent radius of a spherical sample, m
t = time, s
$t_{1/4}$ = rise time to quarter-maximum temperature, s
$t_{3/4}$ = rise time to three quarter-maximum temperature, s
t^* = dimensionless time, defined as $\alpha t/R^2$
T = temperature, K
T_i = initial temperature, K
T_{sur} = temperature of the surroundings, K

Greek Symbols

α = thermal diffusivity, defined as $k/\rho c_p$, $\mathrm{m^2/s}$
η = oblate spheroids coordinate surface in oblate spherical coordinate system
θ = hyperboloids coordinate surface in oblate spheroidal coordinate system
Θ^* = dimensionless temperature, defined as $(T - T_{\mathrm{sur}})/(Q\tau/\rho c_p R)$
$[\Theta^*]_\infty$ = spatially uniform value of the dimensionless temperature at $t \to \infty$, when $\mathrm{Bi} = 0$
ρ = density of the sample, $\mathrm{kg/m^3}$
τ = time duration of the laser pulse, s

1 Introduction

Thermal diffusivity of high-temperature liquid metals, alloys, and electronic materials is a crucial parameter in melting, solidification, crystal growth, casting, and welding processes. However, the thermal diffusivity data for high-temperature liquids are still far from complete although a large amount of data is available on thermal diffusivity of solids over a wide range of temperatures. The main difficulties associated with the thermal diffusivity determination are due to the presence of convection within the molten material and the need for a container to hold the sample. Nowadays, the availability of levitation technology and space-related advances make it possible to solve these problems by levitating the specimen on the ground or in the microgravity environment of outer space.

2 Background

There are several ways to measure the thermal diffusivity, among which the flash (or pulse) technique is the most popular one. This measurement method was introduced by Parker et al. (1961). Using this technique, thermal diffusivity values in the range of 10^{-7} to 10^{-3} $\mathrm{m^2/s}$ have been reported in the temperature range of 100 to 3300 K. However, nearly all the different variations of the flash method up to now were developed to measure the thermal diffusivity of solids and low-temperature liquids. Shen et al. (1997) have proposed two extensions of the flash technique which are applicable to levitated high-temperature spherical samples. For the *single-*

---

[1] Graduate Research Assistant. Currently with Adapco, Inc., Melville, NY.

[2] Associate Professor. Mem. ASME.

[3] Department of Mechanical Engineering, Auburn University, 201 Ross Hall, Auburn, AL 36849-5341.

Contributed by the Heat Transfer Division for publication in the JOURNAL OF HEAT TRANSFER. Manuscript received by the Heat Transfer Division, Apr. 14, 1997; revision received, Mar. 18, 1998. Keywords: Conduction, Liquid Metals, Thermophysical Properties. Associate Technical Editor: T. Tong.

are appreciated. The assistance of Cadets First Class Jeremy Fischman and James Maxwell of the USAF Academy, who participated in the early part of this research as part of the their USAFA Aeronautics Laboratory course, is also gratefully acknowledged.

References

Baughn, J. W., and Yan, X., 1991, "A Preheated-Wall Transient Method for Measurements of the Heat Transfer to an Impinging Jet," Eurotherm Seminar No. 25, pp. 1–7.

Baughn, J. W., Yan, X., and Roby, Jon L., 1994, "An Insertion Technique Using the Transient Method with Liquid Crystals for Enhanced Heat Transfer Measurements in Ducts," *Enhanced Heat Transfer,* Vol. 1, No. 2, pp. 179–180.

Baughn, J. W., 1995, "Liquid Crystal Methods for Studying Turbulent Heat Transfer," *International Journal of Heat and Fluid Flow,* Vol. 16, pp. 365–375.

Butler, R. J., and Baughn, J. W., 1995, "A Shroud Technique Using the Transient Method for Local Heat Transfer Measurements," *Experimental Heat Transfer,* Vol. 8, No. 1, pp. 17–32.

Butler, R. J., and Baughn, J. W., 1996, "The Effect of the Thermal Boundary Condition on Transient Method Heat Transfer Measurements on a Flat Plate With a Laminar Boundary Layer," ASME JOURNAL OF HEAT TRANSFER, Vol. 118, pp. 831–837.

Camci, C., Kim, K., and Hippensteele, S. A., 1992, "A New Hue Capturing Technique for the Quantitative Interpretation of Liquid Crystal Images Used in Convective Heat Transfer Studies," ASME *Journal of Turbomachinery,* Vol. 114, pp. 765–775.

Camci, C., Kim, K., Hippensteele, S. A., and Poinsatte, P. E., 1993, "Evaluation of a Hue Capturing Based Transient Liquid Crystal Method for High-Resolution Mapping of Convective Heat Transfer on Curved Surfaces," ASME JOURNAL OF HEAT TRANSFER, Vol. 115, pp. 311–318.

Clifford, R. J., Jones, T. V., and Dunne, S. T., 1983, "Techniques for Obtaining Detailed Heat Transfer Coefficient Measurements Within Gas Turbine Blade and Vane Cooling Passages," ASME Paper 83-GT-58.

Farina, D. J., Hacker, J. M., Moffat, R. J., and Eaton, J. K., 1993, "Illuminant Invariant Calibration of Thermochromic Liquid Crystals," *Visualization of Heat Transfer Processes,* Vol. 252, 252, J. J. Simoneau and B. F. Armaly, eds., pp. 1–11.

Hay, J. L., and Hollingsworth, D. K., 1996, "A Comparison of Trichromic Systems for Use in the Calibration of Polymer-Dispersed Thermochromic Liquid Crystals," *Exp. Thermal Fluid Science,* Vol. 12, pp. 1–12.

Ireland, P. T., and Jones, T. V., 1985, "The Measurement of Local Heat Transfer Coefficients in Blade Cooling Geometries," *AGARD Conference Proceedings,* No. 390, Paper 28.

Ireland, P. T., and Jones, T. V., 1986, "Detailed Measurements of Heat Transfer On and Around a Pedestal in Fully Developed Passage Flow," *8th International Heat Transfer Conference,* Vol. 3, pp. 975–980.

Jones, T. V., and Hippensteele, S. A., 1987, "High-Resolution Heat-Transfer Coefficient Maps Applicable to Compound Curve Surfaces Using Liquid Crystals in a Transient Wind Tunnel," *Development in Experimental Technique in Heat Transfer and Combustion,* (also NASA TM-89855, 1988).

Metzger, D. E., and Larson, E. E., 1986, "Use of Melting Point Surface Coatings for Local Convective Heat Transfer Measurements in Rectangular Channel Flows With 90-Deg. Turns," ASME JOURNAL OF HEAT TRANSFER, Vol. 108, pp. 48–54.

Metzger, D. E., Bunker, R. S., and Bosch, G., 1991, "Transient Liquid Crystal Measurement of Local Heat Transfer on a Rotating Disk With Jet Impingement," ASME *Journal of Turbomachinery,* Vol. 113, pp. 52–59.

O'Brien, J. E., Simoneau, R. J., LaGraff, J. E., and Morehouse, K. A., 1986, "Unsteady Heat Transfer and Direct Comparison for Steady-State Measurements in a Rotor-Wake Experiment," *8th International Heat Transfer Conference,* San Francisco, pp. 1243–1248.

Thermal Diffusivity Determination of High-Temperature Levitated Oblate Spheroidal Specimen by a Flash Method

F. Shen[1,3] and J. M. Khodadadi[2,3]

In extending the range of applicability of a recently developed method, a single-step containerless flash technique for determining the thermal diffusivity of levitated oblate spheroidal samples is proposed. The flash method is modeled as an axisymmetric transient conduction heat transfer problem within the oblate spheroid. It is shown that by knowing the sample geometric parameters and recording the temperature rise history at least at two different points on the surface simultaneously, the thermal diffusivity can be determined without knowing the heat loss parameter. The appropriate coefficients needed for determining the thermal diffusivity of oblate spheroidal samples are provided.

Nomenclature

Bi = Biot number, defined as $(4\epsilon_{\mathrm{eff}}\sigma F T_{\mathrm{sur}}^3 + h)R/k$
c_p = specific heat at constant pressure, J/kg · K
h = convection heat transfer coefficient, $\mathrm{W/m^2 \cdot K}$
k = thermal conductivity, W/m · K
Q = uniform incident energy flux, $\mathrm{J/m^2 s}$
R = equivalent radius of a spherical sample, m
t = time, s
$t_{1/4}$ = rise time to quarter-maximum temperature, s
$t_{3/4}$ = rise time to three quarter-maximum temperature, s
t^* = dimensionless time, defined as $\alpha t/R^2$
T = temperature, K
T_i = initial temperature, K
T_{sur} = temperature of the surroundings, K

Greek Symbols

α = thermal diffusivity, defined as $k/\rho c_p$, $\mathrm{m^2/s}$
η = oblate spheroids coordinate surface in oblate spherical coordinate system
θ = hyperboloids coordinate surface in oblate spheroidal coordinate system
Θ^* = dimensionless temperature, defined as $(T - T_{\mathrm{sur}})/(Q\tau/\rho c_p R)$
$[\Theta^*]_\infty$ = spatially uniform value of the dimensionless temperature at $t \to \infty$, when Bi = 0
ρ = density of the sample, $\mathrm{kg/m^3}$
τ = time duration of the laser pulse, s

1 Introduction

Thermal diffusivity of high-temperature liquid metals, alloys, and electronic materials is a crucial parameter in melting, solidification, crystal growth, casting, and welding processes. However, the thermal diffusivity data for high-temperature liquids are still far from complete although a large amount of data is available on thermal diffusivity of solids over a wide range of temperatures. The main difficulties associated with the thermal diffusivity determination are due to the presence of convection within the molten material and the need for a container to hold the sample. Nowadays, the availability of levitation technology and space-related advances make it possible to solve these problems by levitating the specimen on the ground or in the microgravity environment of outer space.

2 Background

There are several ways to measure the thermal diffusivity, among which the flash (or pulse) technique is the most popular one. This measurement method was introduced by Parker et al. (1961). Using this technique, thermal diffusivity values in the range of 10^{-7} to 10^{-3} $\mathrm{m^2/s}$ have been reported in the temperature range of 100 to 3300 K. However, nearly all the different variations of the flash method up to now were developed to measure the thermal diffusivity of solids and low-temperature liquids. Shen et al. (1997) have proposed two extensions of the flash technique which are applicable to levitated high-temperature spherical samples. For the *single-*

---

[1] Graduate Research Assistant. Currently with Adapco, Inc., Melville, NY.

[2] Associate Professor. Mem. ASME.

[3] Department of Mechanical Engineering, Auburn University, 201 Ross Hall, Auburn, AL 36849-5341.

Contributed by the Heat Transfer Division for publication in the JOURNAL OF HEAT TRANSFER. Manuscript received by the Heat Transfer Division, Apr. 14, 1997; revision received, Mar. 18, 1998. Keywords: Conduction, Liquid Metals, Thermophysical Properties. Associate Technical Editor: T. Tong.

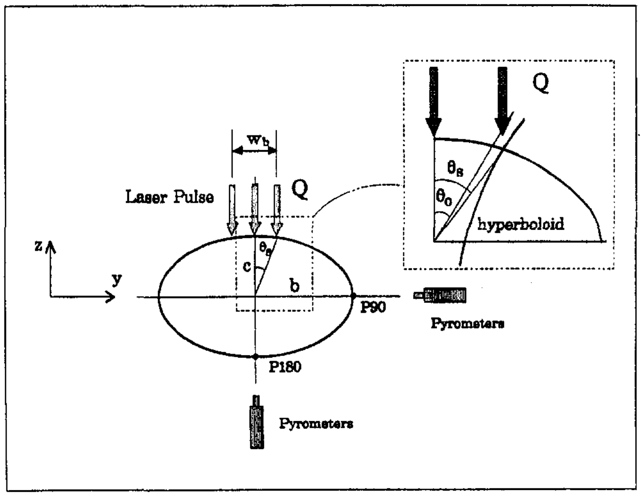

Fig. 1 Schematic diagram of the proposed technique

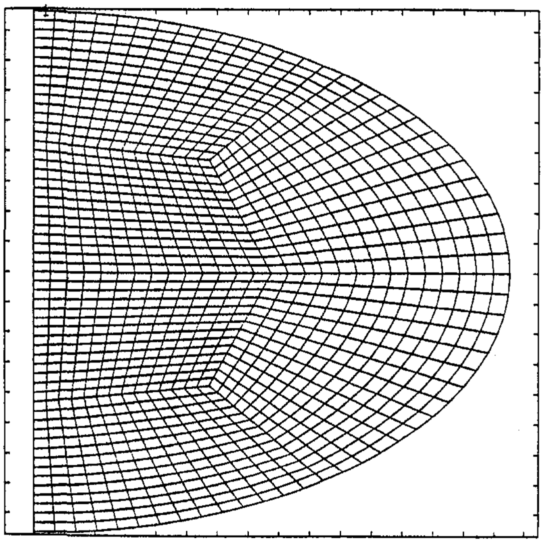

Fig. 2 Computational elements used in the finite element analysis

step method, the only parameters needed to determine the thermal diffusivity are the diameter of the sample and the temperature rise history at two different points on the surface. Experimental verification of the single-step method was conducted by Shen et al. (1997) for spherical solid samples of nickel and Inconel 718 superalloy near their melting temperatures. The thermal diffusivity values which were determined using the single-step method agreed very well with published data in the literature.

Although near-perfect spherical geometry is known to be attainable in low-gravity environments, levitation experiments have shown that the specimen can assume other shapes as well, among which the shape of an *oblate spheroid* is the most common. Trinh (1990) levitated oblate spheroidal samples with characteristic horizontal-to-vertical axial ratios ranging from 1 (sphere case) to 2. In light of this and in order to extend the recent work of Shen et al. (1997), a single-step containerless flash technique which is applicable to levitated high-temperature spheroidal samples is proposed in this paper. The advantages of the single-step method of Shen et al. (1997) are still retained for the spheroidal specimen. Finally, it should be noted that very few studies dealing with oblate geometries are found in the literature (e.g., Niven, 1880; Asako et al., 1991).

3 Overview of the Proposed Method

The proposed technique will utilize the components shown schematically in Fig. 1. The levitated sample is heated up to a uniform initial temperature (T_i) by an external heating device. The sample is then subjected to a very short burst of high-power radiant energy (beam energy flux of Q and beam diameter of w_b). Pyrometers are placed to detect the surface temperature rise history at least at two points. Transient temperature rise data are collected by using a digital data acquisition system or a digital oscilloscope. Thermal diffusivity is then determined using the simple relation proposed in this paper.

4 Mathematical Formulation

The oblate spheroidal coordinate system (η, θ, ψ) is the natural orthogonal coordinate system for studying the heat transport within an oblate spheroid (Moon and Spencer, 1988). The Cartesian coordinates (x, y, z) of the surface of an oblate spheroid is given by

$$\frac{x^2}{a^2\cosh^2\eta}+\frac{y^2}{a^2\cosh^2\eta}+\frac{z^2}{a^2\sinh^2\eta}=1 \qquad (1)$$

where a is the focal distance. The horizontal (y) axial distance of the oblate spheroid is $b = a\cdot\cosh\eta$, and the vertical (z) axial distance is $c = a\cdot\sinh\eta$ (Fig. 1). The shape of an oblate spheroid is determined by the ratio of these two distances, which is a function of η (i.e., $b/c = 1/\tanh\eta$). Also, it is easy to show that the volume of the oblate spheroid is

$$V_{\text{oblate}}=\tfrac{4}{3}\,\pi\,(a\cosh\eta)^2(a\sinh\eta). \qquad (2)$$

For comparison purposes with the spherical shape, the total droplet volume V is kept constant as the ratio b/c is varied. Since the volume is dependent upon η, the focal length is adjusted accordingly for each axial ratio. Uniformity is maintained by defining all the dimensionless quantities in terms of R, i.e., the radius of an equivalent sphere of the same volume V. Thus, R can be expressed as $R = a\,(\cosh^2\eta_0\cdot\sinh\eta_0)^{1/3}$, where a given value of η_0 defines the surface of a particular spheroid.

Governing Equation, Boundary, and Initial Conditions. The following assumptions are made: (a) The spheroidal sample is homogeneous and the thermophysical properties are independent of temperature. (b) The duration of the radiation burst is short compared to the characteristic rise time being sought, and the energy flux is assumed to be uniform over the width of the beam. (c) Thermocapillary convection resulting from the temperature dependence of the surface tension is neglected. Shen (1996) has established the conditions under which this assumption is valid. (d) The droplet is opaque and its surface acts as a diffuse gray body to the irradiant energy. Upon subjecting the specimen to the beam, heat will diffuse through the sample. This phenomenon is governed by the heat conduction equation:

Table 1 Values of the angles θ_0 and θ_s for different spheroids

b/c	1.1	1.2	1.3	1.4	1.5	1.6	1.7	1.8	1.9	2.0
θ_0	3.007	2.921	2.844	2.775	2.712	2.654	2.601	2.552	2.506	2.463
θ_s	3.307	3.504	3.696	3.882	4.064	4.242	4.416	4.587	4.754	4.918

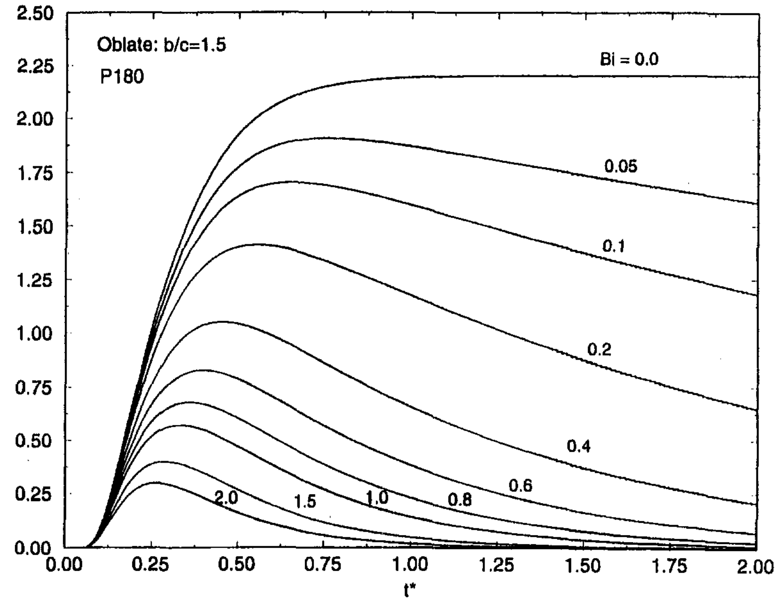

Fig. 3 Dimensionless transient temperature rise curves at P180, on the surface of the oblate spheroid (*b/c* = 1.5)

$$\frac{1}{a^2(\cosh^2\eta - \sin^2\theta)}\left(\frac{\partial^2\Theta}{\partial\eta^2} + \tanh\eta\,\frac{\partial\Theta}{\partial\eta} + \frac{\partial^2\Theta}{\partial\theta^2} + \cot\theta\,\frac{\partial\Theta}{\partial\theta}\right) = \frac{1}{\alpha}\frac{\partial\Theta}{\partial t} \quad (3)$$

where $\Theta = T - T_{\text{sur}}$. This process is modeled as an axisymmetric transient heat conduction problem in the oblate spheroidal coordinate system. Both radiative and convective heat losses are taken into account on the entire surface of the spheroid, where the radiation boundary condition is linearized:

$$\left[-\frac{R}{a(\cosh^2\eta - \sin^2\theta)^{1/2}}\frac{\partial\Theta}{\partial\eta}\right]_{\eta=\eta_0} = \frac{(4\epsilon_{\text{eff}}\sigma F T_{\text{sur}}^3 + h)R}{k}\,\Theta|_{\eta=\eta_0} = \text{Bi}\,\Theta|_{\eta=\eta_0} \quad (4)$$

which is valid for $t \geq 0$. The linearization assumption is subject to the condition $|\Theta(\eta_0, \theta, t)| \ll T_{\text{sur}}$. The Biot number (Bi) is a measure of both convective and radiative surface heat losses. In the case of no heat loss, the Biot number equals zero. In addition, the boundary condition which accounts for the absorbed portion of the beam on the irradiated part of the surface can be written as

$$\left[-k\,\frac{1}{a(\cosh^2\eta - \sin^2\theta)^{1/2}}\frac{\partial\Theta}{\partial\eta}\right]_{\eta=\eta_0} = Q_{\text{abs}}\cdot\cos\theta \quad 0 \leq \theta \leq \theta_0, \quad 0 \leq t \leq \tau \quad (5)$$

where Q_{abs} is the absorbed portion of the incident energy flux and the incidence angle θ_0 characterizes the width of the pulse in the oblate spheroidal coordinate system (Fig. 1). To account

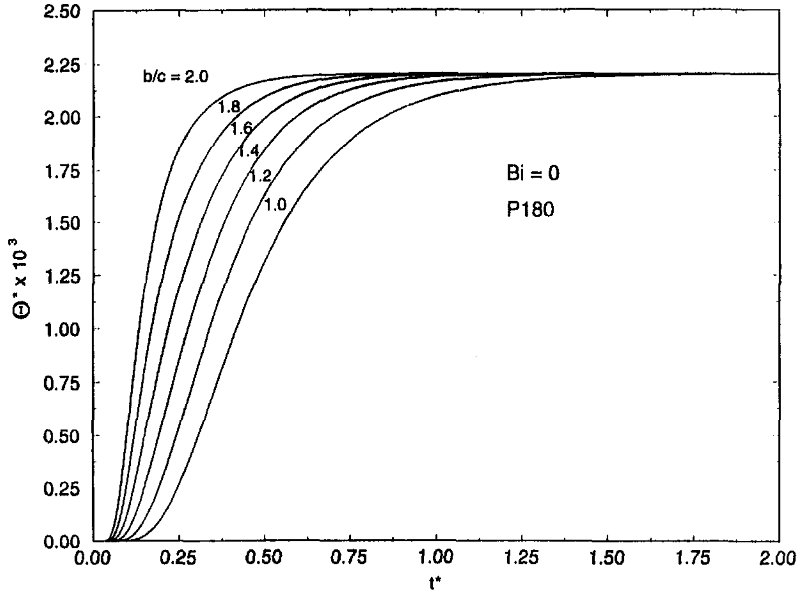

Fig. 4 Dimensionless transient temperature rise curves at P180 for different geometric shapes (Bi = 0)

Table 2 Values of coefficients m, n, M, and N in Eq. (7)

	P90		P180			
b/c	m_1	n_1	m_2	n_2	M	N
1.0	0.115232	0.625436	0.290427	0.896588	0.01366	2.30659
1.1	0.110939	0.611875	0.269234	0.875877	0.01421	2.31769
1.2	0.108803	0.606113	0.253212	0.871385	0.01579	2.28512
1.3	0.108134	0.606076	0.240047	0.881347	0.01868	2.20174
1.4	0.108601	0.610531	0.227271	0.899141	0.02277	2.11542
1.5	0.109921	0.618325	0.212504	0.913683	0.02765	2.09348
1.6	0.111761	0.627378	0.194271	0.913340	0.03323	2.19392
1.7	0.114026	0.638112	0.172351	0.991263	0.05405	1.80691
1.8	0.116566	0.649568	0.147961	0.827594	0.04883	3.64873
1.9	0.119318	0.661302	0.123663	0.737711	0.08755	8.65477
2.0	0.122191	0.673085	0.102370	0.631667	0.00688	-16.251

for the change in curvature as b/c increases, the incidence angle θ_0 must be adjusted. Corresponding to the angle $\theta_0 = 3.1046$ deg for the sphere case ($b/c = 1$), the values of θ_0 for different spheroids are given in Table 1, where the units of the angles θ_0 and θ_s are degrees and the angle θ_s is the physical incidence angle of the beam as identified in Fig. 1.

Finally, the initial condition is $\Theta_i(\eta, \theta, 0) = 0$, where the assumption $T_i = T_{\text{sur}}$ is utilized, which implies that a "hot-wall" experimental setup is demanded for the proposed method.

Limiting Case of Bi = 0. For the case of Bi = 0, all the incident energy is absorbed by the sample. After a reasonably long time, the temperature distribution within the spheroid becomes uniform. A lumped heat balance analysis can be performed to find this uniform temperature denoted as $[\Theta^*]_\infty$:

$$[\Theta^*]_\infty = \frac{\cosh^{8/3}\eta_0}{2\sinh^{2/3}\eta_0}\left[1 - \left(1 - \frac{\sin^2\theta_0}{\cosh^2\eta_0}\right)^{3/2}\right]. \quad (6)$$

For the present investigation, we have $[\Theta^*]_\infty = 0.0022$, which is a constant for every case studied, since the incident energy and volume of the spheroid were kept constant.

Computational Details. Although an analytic solution of the problem formulated above is possible (Shen, 1996) following the work of Moon and Spencer (1988), the evaluation and presentation of the results is very time-consuming. In view of this, the finite element computer code TOPAZ2D (Shapiro and Edwards, 1990) was utilized to simulate the transient conduction heat transfer process. Grid-independence of the results was established by using a number of grid densities. A typical grid layout (28 × 28) is shown in Fig. 2. The time-step Δt was chosen to be 0.02 seconds. The pulse time is set equal to one time-step.

5 Results and Discussion

In order to observe the general features of the surface temperature rise history, the variation of the dimensionless temperature (Θ^*) versus dimensionless time (t^*) for two points, P90 ($\theta = 90$ deg) and P180 ($\theta = 180$ deg), on the oblate spheroidal surface were explored. A typical set of surface temperature rise curves are shown in Fig. 3, which correspond to the point P180 on the surface of an oblate spheroid with $b/c = 1.5$. The characteristics of temperature response at the rear surface is similar to that of spherical samples (Shen et al., 1997). The effect of the incident flash is sensed with a time delay which depends on both the measurement point and shape of the spheroid. This is followed by a monotonic rise to a maximum temperature, its value being dependent on the heat loss parameter (Bi). After a long time, due to the heat exchange with the surroundings, the dimensionless temperature goes to zero for all the cases with Bi ≠ 0. In general, the bigger the Biot number, the greater the heat loss, and the maximum temperature decreases accordingly. At the same time, greater the heat loss from the spheroid means smaller the value of the dimensionless rise time. Temperature at every point in the spheroid approaches a constant value as indicated before when there are no heat losses (Bi = 0). The asymptotic value attained for the Bi = 0 case in Fig. 3 was in extremely close proximity to the lumped analysis result (Eq. (6)) and this also served as a check for the accuracy of the computational results. The temperature rise curves at the point P180 when there are no heat losses for various spheroids are given in Fig. 4. Even though all the spheroids asymptotically reach $[\Theta^*]_\infty$, the spheroid with greater ratio b/c reaches that temperature faster since the distance between the laser incidence point and the point P180 is getting shorter and shorter, as b/c is increased.

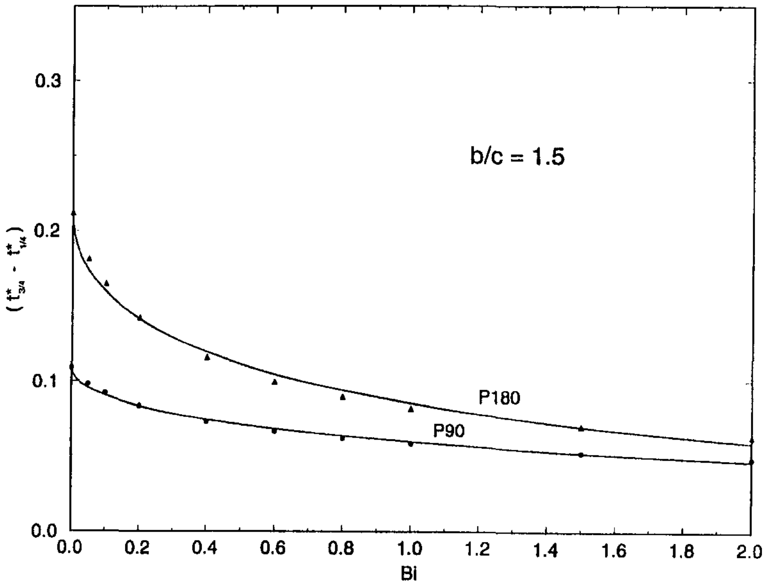

Fig. 5 The relationship between $(t^*_{3/4} - t^*_{1/4})$ and the Biot Number for $b/c = 1.5$

6 Determination of Thermal Diffusivity

Given a temperature-rise history, it was found that the exponential function fitted the relationship between characteristic dimensionless time $(t^*_{3/4} - t^*_{1/4})$ and the Biot number well (see Fig. 5). Variables $t^*_{3/4}$ and $t^*_{1/4}$ represent dimensionless rise times to reach quarter-maximum and three quarter-maximum temperatures, respectively. The form of the dependence was $(t^*_{3/4} - t^*_{1/4}) = me^{-n\sqrt{\mathrm{Bi}}}$. The parameters m and n for different geometric shapes and different measurement locations are listed in Table 2. By following the same steps as for spherical samples (Shen et al., 1997), the formula to determine the thermal diffusivity can be derived assuming the temperature rise at points P_1 and P_2 have been recorded. The pertinent relation is

$$\alpha = \left[\frac{m_1^{n_2}}{m_2^{n_1}}\right]^{[1/(n_2-n_1)]} \frac{[t_{3/4} - t_{1/4}]_2^{(n_1/(n_2-n_1))}}{[t_{3/4} - t_{1/4}]_1^{1+[n_1/(n_2-n_1)]}} R^2$$

$$= \mathrm{M} \frac{[t_{3/4} - t_{1/4}]_2^{N}}{[t_{3/4} - t_{1/4}]_1^{1+N}} R^2. \quad (7)$$

The only physical quantities which need to be known are the size of the specimen and the simultaneously recorded temperature rise curves at least at two different points on the surface of the specimen. It is recommended that the temperature rise histories be measured at points P_1 = P90 and P_2 = P180. The parameters m_1, m_2, n_1, n_2, M, and N in Eq. (7) to be used for these two points are summarized in Table 2.

Experimental validation of the technique proposed here has only been made for the case of spherical specimen ($b/c = 1$) by Shen et al. (1997). Given the success of that experimental study for the limiting case of the present analysis, it appears that the current technique will be capable of providing reliable thermal diffusivity measurements. However, direct experimental validations are not available at the present time.

7 Conclusions

In order to determine the thermal diffusivity of high-temperature materials, extension of a recently validated containerless single-step flash technique for levitated oblate spheroidal specimen is proposed. The thermal diffusivity is determined by knowing the sample size and recording the temperature rise at least at two different points on the surface of the oblate spheroid simultaneously. The main advantage of this method is that the thermal diffusivity can be determined without the necessity of knowing the heat loss parameter. The appropriate coefficients for oblate spheroidal samples are provided.

Acknowledgments

The work reported in this paper was supported by the NASA's Office of Commercial Programs under Grant NAGW-1192.

References

Asako, Y., Nakamura, H., Toyoda, S., and Faghri, M., 1991, "Numerical Analysis of Two-Dimensional Transient Freezing in a Spheroidal Capsule," ASME JOURNAL OF HEAT TRANSFER, Vol. 113, pp. 1017–1020.

Moon, P. H., and Spencer, D. E., 1988, *Field Theory Handbook: Including Coordinate Systems, Differential Equations and Their Solutions*, 2nd Ed., Springer-Verlag, Berlin.

Niven, C., 1880, "On the Conduction of Heat in Ellipsoids of Revolution," *Philosophical Transactions of the Royal Society of London (Series A)*, pp. 117–151.

Parker, W. J., Jenkins, R. J., Butler, C. P., and Abbott, G. L., 1961, "Flash Method of Determining Thermal Diffusivity, Heat Capacity, and Thermal Conductivity," *J. Appl. Phys.*, Vol. 32, pp. 1679–1684.

Shapiro, A. B., and Edwards, A. L., 1990, "TOPAZ2D Heat Transfer Code Users Manual and Thermal Property Data Base," University of California, Lawrence Livermore National Laboratory, Report UCRL-ID-104558.

Shen, F., 1996, "Novel Pulse Techniques for Containerless Thermal Diffusivity Determination: Development of Methods and Numerical Analysis of Thermocapillary and Buoyant Flows," Ph.D. thesis, Department of Mechanical Engineering, Auburn University, Auburn, AL.

Shen, F., Khodadadi, J. M., Woods, M. C., Weber, J. K. R., and Li, B. Q., 1997, "Containerless Thermal Diffusivity Determination of High-Temperature Levitated Spherical Specimen by Extended Flash Methods: Theory and Experimental Validation," ASME JOURNAL OF HEAT TRANSFER, Vol. 119, pp. 210–219.

Trinh, E. H., 1990, "Fluid Dynamics and Solidification of Levitated Drops and Shells," *Progress in Astronautics and Aeronautics* (Vol. 130, Low-Gravity Fluid Dynamics and Transport Phenomena), J. N. Koster and R. L. Sani, eds., AIAA, pp. 515–536.

Effective Thermal Conductivity Model of Flame Spread Over a Shallow Subflash Liquid Fuel Layer

M. Epstein[1] **and J. P. Burelbach**[1]

Nomenclature

Bo = Bond number $(g\rho\beta\delta^2/\sigma')$
c_p = specific heat of the liquid fuel
g = gravitational acceleration
k_e = effective conductivity transport coefficient
q = heat flux transmitted horizontally through the liquid layer
q_o = heat flux transmitted from flame to the underlying fuel (Fig. 1)
T = local surface temperature of fuel layer
T_{fp} = flash point temperature of liquid fuel (Fig. 1)
$T_{\max}$ = maximum temperature of fuel layer surface beneath flame (Fig. 1)
T_∞ = ambient temperature
U = flame spreading velocity
x = horizontal coordinate measured from the flame front (Fig. 1)
$x_{\max}$ = distance behind flame front at which $T = T_{\max}$
x_∞ = location ahead of flame at which $T = T_\infty$

Greek Letters

α = thermal diffusivity of liquid fuel
β = liquid fuel volumetric expansion coefficient
δ = fuel layer thickness (depth)
$\theta(x, T_1)$ = function defined by Eq. (11)
$\theta(0, T_{\mathrm{fp}})$ = function $\theta(x, T_1)$ evaluated at flame front (x = 0), see Eq. (12)
μ = absolute viscosity of liquid fuel
ρ = density of liquid fuel
σ = surface tension of liquid fuel
σ' = absolute variation of σ with temperature, $|d\sigma/dT|$

Subscripts

1 = beneath the flame
2 = ahead of the flame

---

[1] Fauske & Associates, Inc., 16W070 West 83rd Street, Burr Ridge, IL 60521.

Contributed by the Heat Transfer Division for publication in the JOURNAL OF HEAT TRANSFER. Manuscript received by the Heat Transfer Division, Mar. 10, 1997; revision received, Mar. 8, 1998. Keywords: Combustion, Fire/Flames, Thermocapillary Flows. Associate Technical Editor: S. Ramadhyani.

6 Determination of Thermal Diffusivity

Given a temperature-rise history, it was found that the exponential function fitted the relationship between characteristic dimensionless time $(t^*_{3/4} - t^*_{1/4})$ and the Biot number well (see Fig. 5). Variables $t^*_{3/4}$ and $t^*_{1/4}$ represent dimensionless rise times to reach quarter-maximum and three quarter-maximum temperatures, respectively. The form of the dependence was $(t^*_{3/4} - t^*_{1/4}) = me^{-n}\sqrt{\mathrm{Bi}}$. The parameters m and n for different geometric shapes and different measurement locations are listed in Table 2. By following the same steps as for spherical samples (Shen et al., 1997), the formula to determine the thermal diffusivity can be derived assuming the temperature rise at points P_1 and P_2 have been recorded. The pertinent relation is

$$\alpha = \left[\frac{m_1^{n_2}}{m_2^{n_1}}\right]^{[1/(n_2-n_1)]} \frac{[t_{3/4} - t_{1/4}]_2^{(n_1/(n_2-n_1))}}{[t_{3/4} - t_{1/4}]_1^{1+[n_1/(n_2-n_1)]}} R^2$$

$$= \mathrm{M}\, \frac{[t_{3/4} - t_{1/4}]_2^N}{[t_{3/4} - t_{1/4}]_1^{1+N}} R^2. \quad (7)$$

The only physical quantities which need to be known are the size of the specimen and the simultaneously recorded temperature rise curves at least at two different points on the surface of the specimen. It is recommended that the temperature rise histories be measured at points P_1 = P90 and P_2 = P180. The parameters m_1, m_2, n_1, n_2, M, and N in Eq. (7) to be used for these two points are summarized in Table 2.

Experimental validation of the technique proposed here has only been made for the case of spherical specimen ($b/c = 1$) by Shen et al. (1997). Given the success of that experimental study for the limiting case of the present analysis, it appears that the current technique will be capable of providing reliable thermal diffusivity measurements. However, direct experimental validations are not available at the present time.

7 Conclusions

In order to determine the thermal diffusivity of high-temperature materials, extension of a recently validated containerless single-step flash technique for levitated oblate spheroidal specimen is proposed. The thermal diffusivity is determined by knowing the sample size and recording the temperature rise at least at two different points on the surface of the oblate spheroid simultaneously. The main advantage of this method is that the thermal diffusivity can be determined without the necessity of knowing the heat loss parameter. The appropriate coefficients for oblate spheroidal samples are provided.

Acknowledgments

The work reported in this paper was supported by the NASA's Office of Commercial Programs under Grant NAGW-1192.

References

Asako, Y., Nakamura, H., Toyoda, S., and Faghri, M., 1991, "Numerical Analysis of Two-Dimensional Transient Freezing in a Spheroidal Capsule," ASME JOURNAL OF HEAT TRANSFER, Vol. 113, pp. 1017–1020.

Moon, P. H., and Spencer, D. E., 1988, *Field Theory Handbook: Including Coordinate Systems, Differential Equations and Their Solutions,* 2nd Ed., Springer-Verlag, Berlin.

Niven, C., 1880, "On the Conduction of Heat in Ellipsoids of Revolution," *Philosophical Transactions of the Royal Society of London (Series A),* pp. 117–151.

Parker, W. J., Jenkins, R. J., Butler, C. P., and Abbott, G. L., 1961, "Flash Method of Determining Thermal Diffusivity, Heat Capacity, and Thermal Conductivity," *J. Appl. Phys.,* Vol. 32, pp. 1679–1684.

Shapiro, A. B., and Edwards, A. L., 1990, "TOPAZ2D Heat Transfer Code Users Manual and Thermal Property Data Base," University of California, Lawrence Livermore National Laboratory, Report UCRL-ID-104558.

Shen, F., 1996, "Novel Pulse Techniques for Containerless Thermal Diffusivity Determination: Development of Methods and Numerical Analysis of Thermocapillary and Buoyant Flows," Ph.D. thesis, Department of Mechanical Engineering, Auburn University, Auburn, AL.

Shen, F., Khodadadi, J. M., Woods, M. C., Weber, J. K. R., and Li, B. Q., 1997, "Containerless Thermal Diffusivity Determination of High-Temperature Levitated Spherical Specimen by Extended Flash Methods: Theory and Experimental Validation," ASME JOURNAL OF HEAT TRANSFER, Vol. 119, pp. 210–219.

Trinh, E. H., 1990, "Fluid Dynamics and Solidification of Levitated Drops and Shells," *Progress in Astronautics and Aeronautics* (Vol. 130, Low-Gravity Fluid Dynamics and Transport Phenomena), J. N. Koster and R. L. Sani, eds., AIAA, pp. 515–536.

Effective Thermal Conductivity Model of Flame Spread Over a Shallow Subflash Liquid Fuel Layer

M. Epstein[1] **and J. P. Burelbach**[1]

Nomenclature

Bo = Bond number $(g\rho\beta\delta^2/\sigma')$
c_p = specific heat of the liquid fuel
g = gravitational acceleration
k_e = effective conductivity transport coefficient
q = heat flux transmitted horizontally through the liquid layer
q_o = heat flux transmitted from flame to the underlying fuel (Fig. 1)
T = local surface temperature of fuel layer
T_{fp} = flash point temperature of liquid fuel (Fig. 1)
$T_{\max}$ = maximum temperature of fuel layer surface beneath flame (Fig. 1)
T_∞ = ambient temperature
U = flame spreading velocity
x = horizontal coordinate measured from the flame front (Fig. 1)
$x_{\max}$ = distance behind flame front at which $T = T_{\max}$
x_∞ = location ahead of flame at which $T = T_\infty$

Greek Letters

α = thermal diffusivity of liquid fuel
β = liquid fuel volumetric expansion coefficient
δ = fuel layer thickness (depth)
$\theta(x, T_1)$ = function defined by Eq. (11)
$\theta(0, T_{\mathrm{fp}})$ = function $\theta(x, T_1)$ evaluated at flame front ($x = 0$), see Eq. (12)
μ = absolute viscosity of liquid fuel
ρ = density of liquid fuel
σ = surface tension of liquid fuel
σ' = absolute variation of σ with temperature, $|d\sigma/dT|$

Subscripts

1 = beneath the flame
2 = ahead of the flame

---

[1] Fauske & Associates, Inc., 16W070 West 83rd Street, Burr Ridge, IL 60521.

Contributed by the Heat Transfer Division for publication in the JOURNAL OF HEAT TRANSFER. Manuscript received by the Heat Transfer Division, Mar. 10, 1997; revision received, Mar. 8, 1998. Keywords: Combustion, Fire/Flames, Thermocapillary Flows. Associate Technical Editor: S. Ramadhyani.

Introduction

The rather extensive literature on the rate at which a flame spreads over the free surface of a liquid fuel layer has been reviewed thoroughly by Ross (1994). Relative to the present paper it is noteworthy that scaling analyses have provided some simple formulas for the spreading rate (see, e.g., Williams, 1985; and Quintiere, 1988), although these expressions contain a characteristic surface flow length that is not known a priori. Advanced numerical models due to Di Blasi et al. (1990) and Schiller et al. (1993) account for thermal convection in the fuel layer and in the overlying gas space, liquid fuel vaporization, and finite-rate gas-phase kinetics. These models represent significant contributions as they are capable of explaining and predicting flame spread behavior over alcohol fuels when the initial fuel temperature is not too far below the flash point (near-flash regime).

Our goal is to obtain a convenient closed-form expression for the flame-spreading velocity over a shallow liquid fuel layer whose initial temperature is very low relative to the fuel flash point. (This situation is of interest in ongoing weapons site cleanup and safety studies.) Thermocapillary and to a lesser extent thermogravitational flow in the liquid phase are assumed to be the controlling mechanisms of flame propagation. The effective thermal conductivity concept (Burelbach et al., 1996) is exploited to transform this combined natural convection flame-spread problem into a nonlinear conduction-like problem. It is recognized that Burgoyne and Roberts (1968) also proposed a flame spread model in which the convective heat transfer in the liquid fuel layer was described in terms of effective thermal conductivities. However, their effective thermal conductivities were unknown and had to be determined from experiment. This is not the case in the effective thermal conductivity model presented here.

Physical Model

As is usual in the treatment of one-dimensional steady-state flame propagation, we consider a system of coordinates in which the flame position is fixed and the fuel layer of thickness δ moves with flame front velocity U in the negative x-direction (see Fig. 1). The position of the flame front coincides with the origin $x = 0$. The rate of liquid phase energy transport in the region $0 < x < x_\infty$ ahead of the flame is sufficient to raise the surface temperature of the fuel from the ambient temperature T_∞ (at $x = x_\infty$) to the flash point temperature T_{fp} at the flame front. The surface temperature of the fuel continues to increase behind the flame front in the region $-x_{\max} < x < 0$. At the distance $x_{\max}$ behind the flame front the liquid surface temperature is assumed to reach a maximum value $T_{\max}$, which lies somewhere between T_{fp} and the boiling point of the fuel. We will see later that it is not necessary to know the exact value of $T_{\max}$ in order to derive a useful formula for the flame spreading rate. The heat flux q_o from the flame to the fuel segment $-x_{\max} < x < 0$ beneath the flame is assumed to be spatially uniform and a known quantity. Thermophysical properties of the fuel layer are assumed to take on constant mean values. Heat losses from the fuel layer to the rigid substrate beneath the fuel are neglected. Finally, radiative heat transfer from the flame to the fuel surface ahead of the flame is ignored, as is thermocapillary deformation (thinning) of the fuel layer in the vicinity of the flame front.

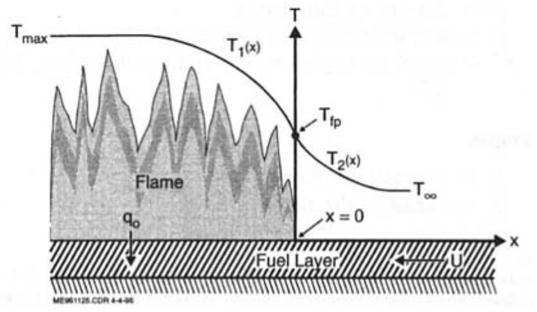

Fig. 1 Schematic diagram of physical model; indicating fuel-surface temperature profile and nomenclature

Model Equations and Solution

We begin construction of the flame propagation model by adopting the following nonlinear Fourier conduction-type expression derived by Burelbach et al. (1996) that relates the local x-directed heat flux q within the shallow fuel layer to the temperature gradient dT/dx along the surface of the layer:

$$q = -k_e \left(\frac{dT}{dx} \right)^3 . \tag{1}$$

The quantity q is the rate of heat transport by surface flow away from the flame minus the rate of heat transport by the subsurface flow toward the flame. In the above equation k_e is an effective thermal conductivity coefficient (in W m K^{-3}) which accounts for both thermocapillary and thermogravitational convection, and is given by

$$k_e = \frac{\rho c_p (\sigma')^2 \delta^4}{1680\, \alpha\, \mu^2} \left(1 + \frac{7}{24}\, \mathrm{Bo} + \frac{19}{864}\, \mathrm{Bo}^2 \right) . \tag{2}$$

The symbols are defined in the Nomenclature list. For typical liquid fuels Eq. (1) is formally valid as long as the layer thickness δ is less than about 6 mm. Equation (1) does not account for inertial effects which become increasingly important as the fuel depth is increased above 6 mm. Equations (1) and (2) have been used successfully to predict the local rise in liquid surface temperature beneath a heat source (Burelbach et al., 1996) and the liquid surface temperature as a function of distance from the heat source (Epstein et al., 1997).

Armed with Eq. (1) we may now treat the flame spread problem as a conduction problem, much like the problem of flame propagation over a solid fuel surface. A thermal energy balance on a surface-segment of lateral dimension dx beneath the flame results in

$$\rho U c_p \frac{dT_1}{dx} + k_e \frac{d}{dx} \left(\frac{dT_1}{dx} \right)^3 + \frac{q_o}{\delta} = 0 \quad -x_{\max} < x < 0. \tag{3}$$

Note that in writing Eq. (3) we assume that the temperature gradient dT_1/dx is constant over the depth of the fuel layer, an approximation that is consistent with the derivation of Eq. (1) (Burelbach et al., 1996). Similarly, the energy balance for a surface-segment ahead of the flame front is

$$\rho U\, c_p \frac{dT_2}{dx} + k_e \frac{d}{dx} \left(\frac{dT_2}{dx} \right)^3 = 0 \quad 0 < x < x_\infty . \tag{4}$$

In the above differential equations $T_1(x)$ is the temperature profile along the surface of the fuel layer beneath the flame, and $T_2(x)$ is the surface temperature profile in the region ahead of the flame front. At the flame front ($x = 0$) we have the matching conditions

$$T_1 = T_2 = T_{\mathrm{fp}}, \quad \frac{dT_1}{dx} = \frac{dT_2}{dx} . \tag{5}$$

In accord with the physical model described previously, we also have the boundary conditions

$$T_1 = T_{\max}, \quad \frac{dT_1}{dx} = 0 \quad \text{at} \quad x = -x_{\max} \tag{6}$$

$$T_2 = T_\infty, \quad \frac{dT_2}{dx} = 0 \quad \text{at} \quad x = x_\infty. \tag{7}$$

The solution of Eq. (4) that satisfies the first condition in Eq. (5) and the boundary conditions given by Eq. (7) is

$$\frac{T_2 - T_\infty}{T_{\mathrm{fp}} - T_\infty} = \left(1 - \frac{x}{x_\infty}\right)^{3/2}; \quad 0 < x < x_\infty \tag{8}$$

where the length x_∞ of the heat transfer zone ahead of the flame is

$$x_\infty = \frac{3}{2}\left[\frac{k_e(T_{\mathrm{fp}} - T_\infty)^2}{\rho\, U\, c_p}\right]^{1/3}. \tag{9}$$

Solving Eq. (3) and requiring that the result satisfy conditions (5) and (6) yields the following implicit relationship for $T_1(x)$:

$$\ln\left[1 - \theta(x, T_1)\right] + \theta(x, T_1) + \frac{1}{2}\left[\theta(x, T_1)\right]^2$$

$$= -\frac{1}{3}\left[\theta(0, T_{\mathrm{fp}})\right]^3\left(\frac{T_{\max} - T_\infty}{T_{\mathrm{fp}} - T_\infty}\right)\left(1 + \frac{x}{x_{\max}}\right);$$

$$-x_{\max} < x < 0. \tag{10}$$

The function $\theta(x, T_1)$ that appears in Eq. (10) is defined as

$$\theta(x, T_1) = \theta(0, T_{\mathrm{fp}})\left[\left(\frac{T_{\max} - T_\infty}{T_{\mathrm{fp}} - T_\infty}\right)\frac{x}{x_{\max}} + \frac{T_1 - T_\infty}{T_{\mathrm{fp}} - T_\infty}\right]^{1/3};$$

$$-x_{\max} < x < 0 \tag{11}$$

where the quantity $\theta(0, T_{\mathrm{fp}})$ is the dimensionless flame speed

$$\theta(0, T_{\mathrm{fp}}) = \frac{(\rho\, U\, c_p)^{4/3}\,\delta(T_{\mathrm{fp}} - T_\infty)^{1/3}}{q_o k_e^{1/3}}. \tag{12}$$

The length $x_{\max}$ of the heat transfer zone beneath the flame is

$$x_{\max} = \frac{\rho\, U\, c_p \delta}{q_o}(T_{\max} - T_\infty). \tag{13}$$

It follows from Eq. (10) that $\theta(0, T_{\mathrm{fp}})$ is given by the transcendental equation

$$\ln\left[1 - \theta(0, T_{\mathrm{fp}})\right] + \theta(0, T_{\mathrm{fp}}) + \frac{1}{2}\left[\theta(0, T_{\mathrm{fp}})\right]^2$$

$$= -\frac{1}{3}\left[\theta(0, T_{\mathrm{fp}})\right]^3\left(\frac{T_{\max} - T_\infty}{T_{\mathrm{fp}} - T_\infty}\right). \tag{14}$$

Combining Eqs. (12) and (14) yields the desired closed-form expression for the flame spreading rate U.

Results and Comparison With Experiment

Examination of Eqs. (10), (11), and (14) reveals that the dimensionless liquid surface temperature profile beneath the flame is strictly a function of the dimensionless maximum temperature $(T_{\max} - T_\infty)/(T_{\mathrm{fp}} - T_\infty)$. The temperature profile beneath the flame is found by first solving Eq. (14) for $\theta(0, T_{\mathrm{fp}})$ for a fixed value of $(T_{\max} - T_\infty)/(T_{\mathrm{fp}} - T_\infty)$. Once $\theta(0, T_{\mathrm{fp}})$ is determined, Eqs. (10) and (11) can be solved numerically for the dimensionless surface temperature $(T_1 - T_\infty)/(T_{\mathrm{fp}} - T_\infty)$ at dimensionless location $x/x_{\max}$.

The dimensionless flame spreading velocity (see Eq. (12)) is also a function only of the dimensionless maximum temperature. It is apparent from the solution of Eq. (14) for $\theta(0, T_{\mathrm{fp}})$ versus $(T_{\max} - T_\infty)/(T_{\mathrm{fp}} - T_\infty)$ that if $(T_{\max} - T_\infty)/(T_{\mathrm{fp}} - T_\infty)$ is sufficiently large, the dimensionless flame velocity is given by the asymptotic result

$$\frac{(\rho\, U\, c_p)^{4/3}\delta\,(T_{\mathrm{fp}} - T_\infty)^{1/3}}{q_o k_e^{1/3}} \simeq 1.0 \tag{15}$$

which is a practical limit since the liquid surface temperature under the flame probably approaches the boiling point of the fuel. For example, identifying $T_{\max}$ with the boiling point of n-decane (174°C) the ratio $(T_{\max} - T_\infty)/(T_{\mathrm{fp}} - T_\infty) = 5.9$, where $T_{\mathrm{fp}} = 46°\mathrm{C}$ and the ambient temperature is taken to be $T_\infty = 20°\mathrm{C}$. At this value of $(T_{\max} - T_\infty)/(T_{\mathrm{fp}} - T_\infty)$ the solution $\theta(0, T_{\mathrm{fp}})$ is within 5.0 percent of its asymptotic limit of unity. Even if $T_{\max}$ beneath a decane flame is as low as 120°C, Eq. (15) would overestimate the flame speed U by only ten percent relative to the numerical solution of Eq. (14). Thus, to a good approximation we have the following simple flame speed result obtained by solving Eq. (15) for U:

$$U = \frac{1}{\rho\, c_p}\left[\frac{q_o^3\, k_e}{\delta^3(T_{\mathrm{fp}} - T_\infty)}\right]^{1/4}. \tag{16}$$

There has been little experimentation in the regime where Eq. (16) is applicable, namely flame spread on cold, shallow fuel layers. In this regime the vapor pressure exerted by the fuel is low and the controlling mechanism is convective heat transfer through the liquid fuel layer. We believe that the experimental results of Mackinven et al. (1970) for flame spread over shallow pools of n-decane are appropriate for comparison with Eq. (16). Their experimental results of flame speed as a function of fuel depth are represented by open circles in Fig. 2. The experiments were carried out in a tray that was demonstrated to be large enough to preclude scale effects. The theoretical curve in the figure was produced using Eq. (16) combined with Eq. (2) for k_e. The curve is dashed beyond $\delta = 6.0$ mm because the assumptions employed in deriving Eqs. (1) and (2) are not valid for thicker layers (see Burelbach et al., 1996). The thermophysical properties used to construct the curve correspond to decane at 35°C, which is the arithmetic mean of the flash point ($T_{\mathrm{fp}} = 46°\mathrm{C}$) and the ambient temperature ($T_\infty = 23°\mathrm{C}$). The heat flux q_o from the fire to the fuel layer was identified with the heat flux that would be measured during a nonspreading decane pool (pan) fire. The pool-fire burning rate

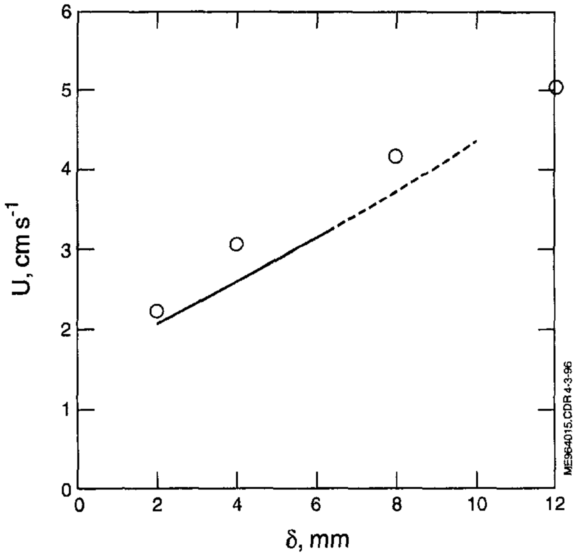

Fig. 2 Flame spreading velocity versus fuel depth for n-decane at T_∞ = 23°C; comparison of measurements (Mackinven et al., 1970) with theory

correlation of Burgess et al. (1961) yields $q_o = 4 \times 10^4$ W m^{-2} for decane.

The theory is in surprisingly good agreement with the experimental data considering the simplicity of the model relative to the complex behavior of the actual flame/fuel layer system (Mackinven et al., 1970).

References

Burelbach, J. P., Epstein, M., and Plys, M. G., 1996, "The Temperature Rise at the Surface of a Liquid Layer Subject to a Concentrated Heat Source Placed Above the Layer," ASME JOURNAL OF HEAT TRANSFER, Vol. 118, pp. 374–380.

Burgess, D. S., Grumer, J., and Wolfhard, H. G., 1961, "Burning Rates of Liquid Fuels in Large and Small Open Trays," *Proc. Int'l Symp. on the Use of Models in Fire Research,* Publication 786, National Academy of Sciences, Washington, DC, pp. 68–75.

Burgoyne, J. H., and Roberts, A. F., 1968, "The Spread of Flame Across a Liquid Surface III. A Theoretical Model," *Proc. Roy. Soc. London,* Vol. A308, pp. 69–79.

Di Blasi, C., Crescitelli, S., and Russo, G., 1990, "Model of Pulsating Flame Spread Across Liquid Fuels," *23rd Symposium on Combustion,* The Combustion Institute, pp. 1669–1675.

Epstein, M., Burelbach, J. P., and Plys, M. G., 1997, "Surface Temperature Profiles Due to Radiant Heating in a Thermocapillary Channel Flow," ASME JOURNAL OF HEAT TRANSFER, Vol. 119, pp. 137–141.

Mackinven, R., Hansel, J. G., and Glassman, I., 1970, "Influence of Laboratory Parameters on Flame Spread Across Liquid Fuels," *Combustion Sci. and Tech.,* Vol. 1, pp. 293–306.

Quintiere, J. G., 1988, "Surface Flame Spread," *SFPE Handbook of Fire Protection Engineering,* 1st Ed., National Fire Protection Assoc., Quincy, MA, pp. 360–367.

Ross, H. D., 1994, "Ignition of and Flame Spread Over Laboratory-Scale Pools of Pure Liquid Fuels," *Prog. Energy Combust. Sci.,* Vol. 20, pp. 17–63.

Schiller, D. N., Ross, H. D., and Sirignano, W. A., 1993, "Computational Predictions of Flame Spread over Alcohol Pools," Presented at 31st Aerospace Sciences Mtg. & Exhibit, Jan. 11–14, Reno, NV, Paper No. AIAA-93-0825.

Williams, F. A., 1985, *Combustion Theory,* 2nd Ed., Benjamin/Cummings, Menlo Park, CA, Chapter 12.

Thermal Transport Phenomena in Turbulent Gas Flow Through a Tube at High Temperature Difference and Uniform Wall Temperature

Shuichi Torii[1] and Wen-Jei Yang[2]

A numerical study is performed to investigate thermal transport phenomena in turbulent gas flow through a tube heated at high temperature difference and uniform wall temperature. A k-ϵ turbulence model is employed to determine the turbulent viscosity and the turbulent kinetic energy. The turbulent heat flux is expressed by a Boussinesq approximation in which the eddy diffusivity of the heat is determined by a t^2-ϵ_t heat transfer model. The governing boundary layer equations are discretized by means of a control-volume finite difference technique and are numerically solved using a marching procedure. It is disclosed from the study that (i) laminarization takes place in a turbulent gas flow through a pipe with high uniform wall temperature just as it does in a pipe with high uniform wall heat flux, and (ii) the flow in a tube heated to high temperature difference and uniform wall temperature is laminarized at a lower heat than that under the uniform heat flux condition.

Nomenclature

c_p = specific heat at constant pressure, J/(kg K)
D = diameter, m
G = mass flux of gas flow, kg/(m^2 s)
k = turbulent kinetic energy, m^2/s^2
L = heating length, m
Pr = Prandtl number
Pr$_t$ = turbulent Prandtl number
q_w = wall heat flux, W/m^2, Eq. (2)
q^+_{in} = dimensionless heat flux parameter, Eq. (1)
r = radial coordinate, m
Re = Reynolds number, $u_m D/\nu$
St = Stanton number, $q_w/(\rho c_p u_m (T_w - T_b))$
T = time-averaged temperature, K
t = fluctuating temperature component, K
$\overline{t^2}$ = temperature variance, K^2
U = time-averaged velocity components in axial direction, m/s
u_m = mean velocity over tube cross section
x = axial coordinate, m

Greek Symbols

ϵ = turbulent energy dissipation rate, m^2/s^3
ϵ_t = dissipation rate of t^2, K/s^2
λ = molecular thermal conductivities, W/(K m)
ν = fluid kinematic viscosity, m^2/s

Subscripts

b = bulk
in = inlet
w = wall

Superscripts

- = time-averaged value
′ = fluctuation value

Introduction

When gas flowing in a channel is heated by high uniform wall heat flux, a transition from turbulent to laminar patterns occurs at higher Reynolds numbers than at the usual critical value. This phenomenon is often referred to as laminarization. Experimental study on the criteria for its occurrence and heat transfer characteristics has been undertaken and reported by several investigators (Bankston, 1970; Coon and Perkins, 1970; McEligot et al., 1970; Perkins et al., 1973; Mori and Watanabe, 1979; Ogawa et al., 1982; Koshizuka et al., 1995). In order to further understand the transport phenomena in a laminarizing flow, Kawamura (1979), Torii et al. (1990), Fujii et al. (1991), and Torii et al. (1993) analyzed the flow structure by means of k-kL, k-ϵ, k-kL-$\overline{uv}$, and Reynolds stress turbulence models, respectively. In all of these numerical simulations, the turbulent heat flux in the energy equation was modeled by the classical Boussinesq approximation. The unknown turbulent thermal conductivity λ_t was obtained from the correlation of the specific heat c_p, the known turbulent viscosity μ_t and the turbulent Prandtl number Pr$_t$ ($\lambda_t = c_p \mu_t/\text{Pr}_t$). However, results obtained through this approach failed to provide detailed information on the thermal field, such as temperature fluctuation and turbulent heat flux. This motivated Torii and Yang (1997) to employ the two-equation heat transfer model to determine the turbulent heat flux in the energy equation. Their study disclosed that (i) once

---

[1] Associate Professor, Department of Mechanical Engineering, Kagoshima University, 1-21-40 Korimoto, Kagoshima 890, Japan. e-mail: torii@mech.kagoshima-u.ac.jp.

[2] Professor, Department of Mechanical Engineering and Applied Mechanics, University of Michigal, Ann Arbor, MI 48109. e-mail: wjyang@engin.umich.edu. Fellow ASME.

Contributed by the Heat Transfer Division for publication in the JOURNAL OF HEAT TRANSFER. Manuscript received by the Heat Transfer Division, Jan. 28, 1997; revision received, May 1, 1998. Keywords: Flow Transition, Forced Convection, High-Temperature Phenomena, Numerical Methods, Turbulence. Associate Technical Editor: J.-C. Han.

correlation of Burgess et al. (1961) yields $q_o = 4 \times 10^4$ W m^{-2} for decane.

The theory is in surprisingly good agreement with the experimental data considering the simplicity of the model relative to the complex behavior of the actual flame/fuel layer system (Mackinven et al., 1970).

References

Burelbach, J. P., Epstein, M., and Plys, M. G., 1996, "The Temperature Rise at the Surface of a Liquid Layer Subject to a Concentrated Heat Source Placed Above the Layer," ASME JOURNAL OF HEAT TRANSFER, Vol. 118, pp. 374–380.

Burgess, D. S., Grumer, J., and Wolfhard, H. G., 1961, "Burning Rates of Liquid Fuels in Large and Small Open Trays," *Proc. Int'l Symp. on the Use of Models in Fire Research,* Publication 786, National Academy of Sciences, Washington, DC, pp. 68–75.

Burgoyne, J. H., and Roberts, A. F., 1968, "The Spread of Flame Across a Liquid Surface III. A Theoretical Model," *Proc. Roy. Soc. London,* Vol. A308, pp. 69–79.

Di Blasi, C., Crescitelli, S., and Russo, G., 1990, "Model of Pulsating Flame Spread Across Liquid Fuels," *23rd Symposium on Combustion,* The Combustion Institute, pp. 1669–1675.

Epstein, M., Burelbach, J. P., and Plys, M. G., 1997, "Surface Temperature Profiles Due to Radiant Heating in a Thermocapillary Channel Flow," ASME JOURNAL OF HEAT TRANSFER, Vol. 119, pp. 137–141.

Mackinven, R., Hansel, J. G., and Glassman, I., 1970, "Influence of Laboratory Parameters on Flame Spread Across Liquid Fuels," *Combustion Sci. and Tech.,* Vol. 1, pp. 293–306.

Quintiere, J. G., 1988, "Surface Flame Spread," *SFPE Handbook of Fire Protection Engineering,* 1st Ed., National Fire Protection Assoc., Quincy, MA, pp. 360–367.

Ross, H. D., 1994, "Ignition of and Flame Spread Over Laboratory-Scale Pools of Pure Liquid Fuels," *Prog. Energy Combust. Sci.,* Vol. 20, pp. 17–63.

Schiller, D. N., Ross, H. D., and Sirignano, W. A., 1993, "Computational Predictions of Flame Spread over Alcohol Pools," Presented at 31st Aerospace Sciences Mtg. & Exhibit, Jan. 11–14, Reno, NV, Paper No. AIAA-93-0825.

Williams, F. A., 1985, *Combustion Theory,* 2nd Ed., Benjamin/Cummings, Menlo Park, CA, Chapter 12.

Thermal Transport Phenomena in Turbulent Gas Flow Through a Tube at High Temperature Difference and Uniform Wall Temperature

Shuichi Torii[1] and Wen-Jei Yang[2]

A numerical study is performed to investigate thermal transport phenomena in turbulent gas flow through a tube heated at high temperature difference and uniform wall temperature. A k-ε turbulence model is employed to determine the turbulent viscosity and the turbulent kinetic energy. The turbulent heat flux is expressed by a Boussinesq approximation in which the eddy diffusivity of the heat is determined by a t^2-ϵ_t *heat transfer model. The governing boundary layer equations are discretized by means of a control-volume finite difference technique and are numerically solved using a marching procedure. It is disclosed from the study that (i) laminarization takes place in a turbulent gas flow through a pipe with high uniform wall temperature just as it does in a pipe with high uniform wall heat flux, and (ii) the flow in a tube heated to high temperature difference and uniform wall temperature is laminarized at a lower heat than that under the uniform heat flux condition.*

Nomenclature

c_p = specific heat at constant pressure, J/(kg K)
D = diameter, m
G = mass flux of gas flow, kg/(m^2 s)
k = turbulent kinetic energy, m^2/s^2
L = heating length, m
Pr = Prandtl number
Pr_t = turbulent Prandtl number
q_w = wall heat flux, W/m^2, Eq. (2)
q_{in}^+ = dimensionless heat flux parameter, Eq. (1)
r = radial coordinate, m
Re = Reynolds number, $u_m D/\nu$
St = Stanton number, $q_w/(\rho c_p u_m (T_w - T_b))$
T = time-averaged temperature, K
t = fluctuating temperature component, K
$\overline{t^2}$ = temperature variance, K^2
U = time-averaged velocity components in axial direction, m/s
u_m = mean velocity over tube cross section
x = axial coordinate, m

Greek Symbols

ϵ = turbulent energy dissipation rate, m^2/s^3
ϵ_t = dissipation rate of $\overline{t^2}$, K/s^2
λ = molecular thermal conductivities, W/(K m)
ν = fluid kinematic viscosity, m^2/s

Subscripts

b = bulk
in = inlet
w = wall

Superscripts

- = time-averaged value
' = fluctuation value

Introduction

When gas flowing in a channel is heated by high uniform wall heat flux, a transition from turbulent to laminar patterns occurs at higher Reynolds numbers than at the usual critical value. This phenomenon is often referred to as laminarization. Experimental study on the criteria for its occurrence and heat transfer characteristics has been undertaken and reported by several investigators (Bankston, 1970; Coon and Perkins, 1970; McEligot et al., 1970; Perkins et al., 1973; Mori and Watanabe, 1979; Ogawa et al., 1982; Koshizuka et al., 1995). In order to further understand the transport phenomena in a laminarizing flow, Kawamura (1979), Torii et al. (1990), Fujii et al. (1991), and Torii et al. (1993) analyzed the flow structure by means of k-kL, k-ϵ, k-kL-$\overline{uv}$, and Reynolds stress turbulence models, respectively. In all of these numerical simulations, the turbulent heat flux in the energy equation was modeled by the classical Boussinesq approximation. The unknown turbulent thermal conductivity λ_t was obtained from the correlation of the specific heat c_p, the known turbulent viscosity μ_t and the turbulent Prandtl number Pr_t ($\lambda_t = c_p \mu_t/\mathrm{Pr}_t$). However, results obtained through this approach failed to provide detailed information on the thermal field, such as temperature fluctuation and turbulent heat flux. This motivated Torii and Yang (1997) to employ the two-equation heat transfer model to determine the turbulent heat flux in the energy equation. Their study disclosed that (i) once

---

[1] Associate Professor, Department of Mechanical Engineering, Kagoshima University, 1-21-40 Korimoto, Kagoshima 890, Japan. e-mail: torii@mech.kagoshima-u.ac.jp.

[2] Professor, Department of Mechanical Engineering and Applied Mechanics, University of Michigal, Ann Arbor, MI 48109. e-mail: wjyang@engin.umich.edu. Fellow ASME.

Contributed by the Heat Transfer Division for publication in the JOURNAL OF HEAT TRANSFER. Manuscript received by the Heat Transfer Division, Jan. 28, 1997; revision received, May 1, 1998. Keywords: Flow Transition, Forced Convection, High-Temperature Phenomena, Numerical Methods, Turbulence. Associate Technical Editor: J.-C. Han.

laminarization takes place, the time-averaged wall temperature gradient across the whole tube cross section diminishes along the flow, resulting in an attenuation in the temperature variance and the turbulent heat flux, (ii) although both velocity and temperature dissipation time scales are substantially amplified in the laminarizing flow, their ratio is only slightly increased, and (iii) consequently, the turbulent heat flux is diminished due to a decrease in the turbulent kinetic energy over the pipe cross section, which results in the deterioration of heat transfer performance. These numerical and experimental results may be applied to heat transfer in nuclear-powered space vehicles with gaseous flow of the propellant. In the design of reactors operating on turbulent flows at higher Reynolds numbers, this regime plays an important role in reactor shutdown/restart and a quasi-steady transient in partial loss of coolant accidents, which occurs under uniform heat flux conditions.

It is well known that the actual situation in internal convection lies between two limiting cases: uniform wall heat flux and uniform wall temperature. The purpose of the present study is to investigate thermal transport phenomena of a turbulent gas flow through a pipe at high temperature difference with uniform wall temperature. Both the k-ϵ turbulence model (Torii et al., 1990) and the two-equation heat transfer model (Torii and Yang, 1997) are appropriate for capturing the fluid flow and heat transfer characteristics in the turbulent-to-laminar transition region. They are employed to investigate the mechanism of transport phenomena. Consideration is given to the streamwise variation of the flow and to thermal fields in a strongly heated gas flow, including turbulent kinetic energy, temperature variance and velocity, and temperature profiles.

Governing Equations and Numerical Method

Consider turbulent gas flows in a circular tube at high temperature difference and uniform wall temperature. Since the governing equations and numerical methods are the same as those used by Torii and Yang (1997), the details are omitted here. In the present study, both the k-ϵ-Pr_t model (Torii et al., 1990) and k-ϵ-t^2-ϵ_t model (Torii and Yang, 1997) were employed to investigate the mechanism of transport phenomena. Let the k-ϵ-Pr_t and k-ϵ-t^2-ϵ_t models be referred to as "Model A" and "Model B," respectively. Models A and B can predict both the transition from turbulent to laminar flow and the flow and heat transfer characteristics in a laminarizing flow in a tube with high heat flux (Torii et al., 1990; Torii and Yang, 1997).

The hydrodynamically fully developed isothermal circular tube flow is assumed at the starting point of the heated section. The following boundary conditions are maintained at the wall:

$$r = 0 \text{ (center line):} \quad \frac{\partial U}{\partial r} = \frac{\partial k}{\partial r} = \frac{\partial \epsilon}{\partial r} = \frac{\partial T}{\partial r} = \frac{\partial \overline{t^2}}{\partial r} = \frac{\partial \epsilon_t}{\partial r} = 0$$

$$r = D/2 \text{ (wall):} \quad U = k = \epsilon = \overline{t^2} = \epsilon_t = 0,$$

$$T = T_w \text{ (uniform wall temperature).}$$

For the laminarizing gas flow in a channel with high heat flux, the nondimensional heat flux parameter, q_{in}^+, is defined as

$$q_{\mathrm{in}}^+ = \frac{q_w}{(Gc_pT)_{\mathrm{in}}}, \tag{1}$$

and is employed to indicate the magnitude of heat flux at the tube wall. However, that parameter cannot be used here because wall heat flux varies along the flow under the uniform wall temperature condition, as shown in the following. In the present study, wall heat flux, q_w, (in Eq. (1)) is defined as

$$q_w = \frac{1}{L}\int_0^L \left(\lambda \frac{\partial T}{\partial r}\right)_w dx, \tag{2}$$

namely, an average heat flux over the whole heated wall surface. Here, it is assumed that the wall temperature is uniform around the tube periphery. The ranges of the parameters are nondimensional heat flux parameter $q_{\mathrm{in}}^+ < 0.0050$; Reynolds number at the onset of heating $\mathrm{Re}_{\mathrm{in}} = 6000 \sim 10{,}000$; and inlet gas (nitrogen) temperature $T_{\mathrm{in}} = 273$ K.

Results and Discussion

The local heat transfer coefficients in a strongly heated gas flow obtained by means of Models A and B are illustrated in Fig. 1 in the form of Stanton number St_b versus Reynolds number Re_b, with q_{in}^+ as the parameter. The inlet bulk Reynolds number is fixed at 8500. There is no experimental data pertinent to the fluid flow and heat transfer characteristics in a tube heated to a very high-temperature difference and uniform wall temperature. The measured results of Bankston (1970) under a uniform wall heat flux condition, denoted by hollow circles and triangles, are superimposed in Fig. 1 for reference. In addition, the Dittus-Boelter's turbulent heat transfer correlation equation (McAdams, 1954) and the theoretical solutions for heat transfer in laminar flow under a uniform wall temperature condition (Kays and Crawford, 1983) are presented in the figure as straight solid lines. As the flow proceeds downstream, the bulk Reynolds number decreases gradually from the inlet value as a result of an increase in the molecular viscosity due to heating. Hence, a reduction in the bulk Reynolds number is equivalent to a change in the axial location, as shown by the arrow sign. It is observed that for $q_{\mathrm{in}}^+ = 0.001$, the calculated Stanton number decreases in the thermal entrance region followed by an upturn and approaches the fully developed turbulent correlation downstream. This is a nonlaminarizing flow. Here, the predicted values appear to exceed the turbulent heat transfer correlation at $\mathrm{Re}_{\mathrm{in}}$ of 8500. This is because the thermal boundary layer is developing. When a turbulent gas flow at the entrance is strongly heated at $q_{\mathrm{in}}^+ = 0.0026$, the flow has undergone a transition from turbulent to laminar fashion exhibiting laminar heat transfer characteristics at certain distance from the entrance, a phenomenon called laminarization. This phenomenon does not happen to the $q_{\mathrm{in}}^+ = 0.001$ case and hence laminarization fails to occur. However, at a higher wall temperature of $q_{\mathrm{in}}^+ = 0.0026$, the numerical results depart completely from the turbulent correlation from the onset and advance toward the laminar correlation as the flow proceeds downstream. It is of interest that the predicted change from turbulent to laminar flow (i.e., the laminarization process) with a uniform wall temperature at $q_{\mathrm{in}}^+ = 0.0026$

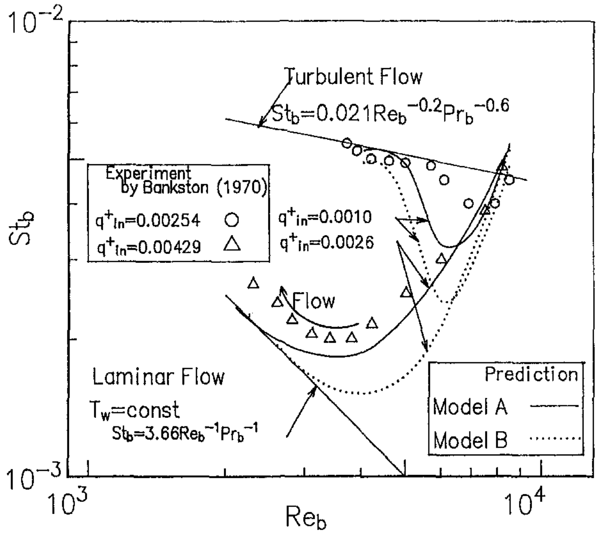

Fig. 1 Predicted local heat transfer performance in the form of Stanton number St_b versus Reynolds number Re_b as a function of nondimensional heat flux parameter, q_{in}^+, for $\mathrm{Rei}_n = 8500$

follows closely the laminarization trend of Bankston's experimental data for $q^+_{\mathrm{in}} = 0.00429$ under a uniform wall heat flux condition. A substantial reduction in the local Stanton number is ascribed to the occurrence of laminarization. However, the experimental data of Bankston (1970) at $q^+_{\mathrm{in}} = 0.00254$ with a uniform wall heat flux shows no evidence of laminarization. Thus, the numerical predictions of Models A and B have revealed that a gas flow in a tube with a high uniform wall temperature is always laminarized, just as it is when heated with a uniform high wall heat flux.

An attempt is made to determine the criterion for the laminarization of flow in a tube with uniform wall temperature. First of all, conditions should be specified under which the flow is necessarily laminarized. Torii et al. (1990) established the criterion for flow laminarization in a tube with high wall heat flux using the k-ϵ turbulence model. The criterion is for the turbulent kinetic energy at $x/D = 150$ to be lower than one-tenth of its inlet value. The same idea has been adopted for the uniform wall temperature case because the streamwise variation of a turbulent kinetic energy in the laminarizing flow (not shown) was similar to that under the uniform heat flux condition (Torii et al., 1990). The criteria established under a uniform wall temperature using Models A and B are depicted in Fig. 2. In all of the numerical calculations, the number of control volumes is selected between 62 and 98, resulting in no appreciable difference between the criteria established by each model. In other words, the numerical results, with different grid spacing, show almost the same values over the inlet Reynolds number ($\mathrm{Re}_{\mathrm{in}}$) region discussed here. Thus the confidence level of Models A and B is maintained to a certain degree. For reference, the existing criteria under the uniform heat wall flux condition are superimposed in Fig. 2, because there is no experimental data for gas flows in a tube heated at a very high temperature difference and uniform wall temperature. As for the experiment data in Fig. 2, the uncertainty in the criterion for occurrence of laminarization is strongly affected by that of the local Stanton number, which is dependent on the uncertainty in the heat transfer coefficients. At the same time, it strongly depends on the accuracy of local heat flux and inner wall temperature. That is, each test section was individually calibrated by determining the local resistivity of the tube wall and the local effective heat-exchange coefficient between the outer wall of the tube and the environment. The inner wall temperature of the tube was calculated using measured outside wall temperature, in which the uncertainty was reduced by taking into account radial and axial conductions (including the effects of temperature-dependent thermal conductivity, electrical resistivity, and the diameter of the tube) and radiation from the outer surface of the tube. It is observed that the criteria established discovered using Models A and B are lower than those under a uniform heat flux condition over a wide range of Reynolds numbers. Therefore, a flow in a tube heated at high-temperature difference and uniform wall temperature seems to be laminarized at a lower heat level than that under the uniform heat flux condition, although there remains a quantitative ambiguity, i.e., whether or not the criteria obtained here are true, because there is no experimental data with which to compare them.

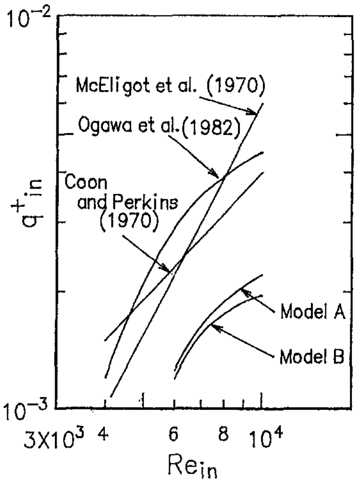

Fig. 2 A comparison of criteria for the occurrence of flow laminarization under uniform wall heat flux condition

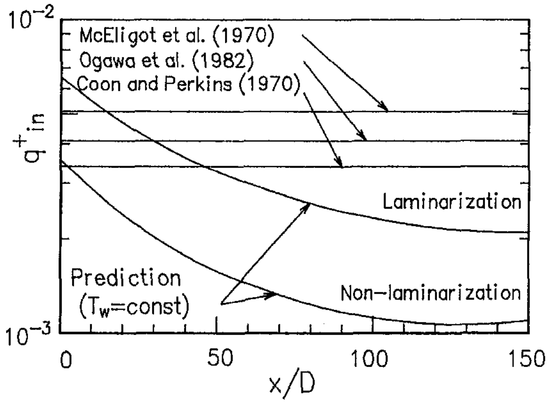

Fig. 3 Streamwise variation of local nondimensional heat flux parameter q^+_{in} in nonlaminarizing and laminarizing flows at $\mathrm{Re}_{\mathrm{in}} = 8500$

What causes a gas flow to be laminarized at a slight temperature difference between the wall and the bulk of the fluid under a uniform wall temperature than the uniform wall heat flux case? Figure 3 illustrates the streamwise variation of the local nondimensional wall heat-flux parameter, q^+_{in}, for both the nonlaminarizing and laminarizing flow cases at $\mathrm{Re}_{\mathrm{in}} = 8{,}500$. For comparison, the existing criteria for laminarization under the uniform wall heat flux condition obtained by Coon and Perkins (1970), McEligot et al. (1970), and Ogawa et al. (1982) are superimposed in the figure as solid straight lines. Here, the local wall heat flux, q_w, as shown in Eq. (2), is nondimensionalized to obtain q^+_{in} in Eq. (1). It is observed that the predicted q^+_{in} for both the nonlaminarizing and laminarizing flows gradually decreases in the flow direction, as mentioned previously. Of importance is that the magnitude of q^+_{in} for the laminarizing flow agrees with the existing criteria in the entrance region (x/D less than 50). In other words, gas flow in the entrance region is strongly heated by the local wall heat flux whose level induces laminarization even with uniform wall heat flux. In summary, a flow in a tube heated at high-temperature difference and a uniform wall temperature is substantially accelerated due to gas expansion, resulting in a deterioration in turbulence in the velocity field, and consequently, laminarizing the flow.

Summary

k-ϵ-Pr_t and k-ϵ-$\overline{t^2}$-ϵ_t models have been employed to numerically investigate fluid flow and heat transfer in a tube with uniform wall temperature. Consideration is given to whether or not the flow is laminarized as well as the uniform heat flux case. The results are summarized as follows:

1 Both Models A and B predict laminarization to take place accompanied by the substantial reduction in the local Stanton number in a strongly heated gas flow.

2 The predicted criterion for the occurrence of laminarization where there is uniform wall temperature is lower than that for the uniform wall flux heating over the wide range of the Reynolds number, if Eq. (1) is employed as the nondimensional heat flux parameter.

References

Bankston, C. A., 1970, "The Transition from Turbulent to Laminar Gas Flow in a Heated Pipe," *Trans. ASME*, Ser. C, Vol. 92, pp. 569–579.

Coon, C. W., and Perkins, H. C., 1970, "Transition from the Turbulent to the Laminar Regime for Internal Convective Flow with Large Property Variations," *Trans. ASME*, Ser. C, Vol. 92, pp. 506–512.

Fujii, S., Akino, N., Hishida, M., Kawamura, H., and Sanokawa, K., 1991, "Numerical Studies on Laminarization of Heated Turbulent Gas Flow in Annular Duct," *J. Atomic Energy Soc. Jpn.*, Vol. 33, No. 12, pp. 1180–1190 (in Japanese).

Kawamura, H., 1979, "Prediction of Strongly Heated Turbulent Flow of Gas in a Circular Tube Using a Two-Equation Model of Turbulence," *Trans. Jpn. Soc. Mech. Eng.*, Vol. 45, No. 395B, pp. 1038–1046 (in Japanese).

Kays, W. M., and Crawford, M. E., 1983, *Convective Heat and Mass Transfer*, McGraw-Hill, New York.

Koshizuka, S., Takano, N., and Oka, Y., 1995, "Numerical Analysis of Deterioration Phenomena in Heat Transfer to Supercritical Water," *Int. J. Heat Mass Transfer*, Vol. 38, pp. 3077–3084.

McAdams, W. H., 1954, *Heat Transfer*, McGraw-Hill, New York.

McEligot, D. M., Coon, C. M., and Perkins, H. C., 1970, "Relaminarization in Tubes," *Int. J. Heat Mass Transfer*, Vol. 13, pp. 431–433.

Mori, Y., and Watanabe, K., 1979, "Reduction in Heated Transfer Performance due to High Heat Flux," *Trans. Jpn. Soc. Mech. Eng.*, Vol. 45, No. 397B, pp. 1343–1353 (in Japanese).

Ogawa, M., Kawamura, H., Takizuka, T., and Akino N., 1982, "Experimental on Laminarization of Strongly Heated Gas Flow in Vertical Circular Tube," *J. Atomic Energy Soc. Jpn.*, Vol. 24, No. 1, pp. 60–67 (in Japanese).

Perkins, K. R., Schade, K. W., and McEligot, D. M., 1973, "Heated Laminarizing Gas Flow in a Square Duct," *Int. J. Heat and Mass Transfer*, Vol. 16, pp. 897–916.

Torii, S., Shimizu, A., Hasegawa, S., and Higasa, M., 1990, Laminarization of Strongly Heated Gas Flows in a Circular Tube (Numerical Analysis by Means of a Modified k-ϵ Model), *JSME Int. J.*, Ser. II, Vol. 33, No. 33, pp. 538–547.

Torii, S., Shimizu, A., and Hasegawa, S., 1993, "Numerical Analysis of Laminarizing Tube Flows by Means of a Reynolds Stress Turbulence Model," *Heat Transfer-Japanese Research*, Vol. 22, No. 2, pp. 154–170.

Torii, S., and Yang, W-J., 1997, "Laminarization of Turbulent Gas Flow Inside a Strongly Heated Tube," *Int. J. Heat Mass Transfer*, Vol. 40, No. 13, pp. 3105–3117.

Means to Improve the Heat Transfer Performance of Air Jet Arrays Where Supply Pressures are Limiting

H. S. Sheriff[1,3] **and D. A. Zumbrunnen**[2,3]

Nomenclature

A_N = flow pulsation amplitude at discharge point in terms of the root-mean square of periodic velocity fluctuations
h = convective heat transfer coefficient, W/m^{2}K
H = vertical distance between nozzle or orifice opening and impingement surface, m
k_f = thermal conductivity of fluid, W/mK
Nu = Nusselt number = hd/k_f
Re$_d$ = Reynolds number referenced to diameter of orifice or nozzle opening and evaluated at film temperature = $u_N d/\nu$
S_d = Strouhal number = $f\,d/u_N$
u_N = mean centerline axial velocity at one diameter downstream of nozzle or orifice exit, m/s
ν = kinematic viscosity, m^2/s

Introduction

Because of ease of construction, large arrays of air jets are most commonly formed by discharging air through orifices drilled or stamped in thin plates. However, pressure drops across orifices can be significantly greater than those across convergent nozzles and may restrict maximum flow rates or require costly air supply systems using compressors and piping. If pressure drops can be kept small, blowers and low-cost ducting can be used in air supply systems which can readily provide large flow rates. The use of blowers and ducting is especially advantageous where air consumption is necessarily large such as when numerous or large jet arrays are needed for heating, cooling, or drying in materials processing applications. Automated machining and manufacturing methods now make practical the production of arrays of convergent nozzles. For example, large convergent nozzle arrays can be readily machined in automated milling operations from thick, single metallic or plastic plates in lieu of being assembled from separate parts.

An example of a convergent nozzle array is shown in Fig. 1. A recent trend in jet arrays has been to replace orifices with tubes (Gundappa et al., 1989) as it allows a larger corridor for venting the spent jet from the vicinity of the target surface. The use of convergent nozzles in place of tubes also has this advantage. Because such arrays can now be economically produced and given resulting opportunities to reduce costs associated with air supply systems, the heat transfer characteristics of arrays of convergent nozzles and arrays of orifices have been compared under the constraint of fixed pressure drop. Results demonstrate that arrays of nozzles provide higher and more uniform heat transfer rates in applications where low-pressure air supply sources are preferred. Because jets emerging from orifices do not readily generate large-scale vortical structures that are observed in submerged jets issuing from convergent nozzles (Michalke, 1972; Popiel and Trass, 1991), results are also presented for pulsating flow conditions that are known to alter coherent flow structures and might lead to changes in convective heat transfer. For example, although the natural frequency for vortex formation of a typical submerged jet is very high such that only small-pulsation amplitudes can be induced (Mladin and Zumbrunnen, 1997), a jet can be forced with large pulsation magnitudes at forcing frequencies much lower than

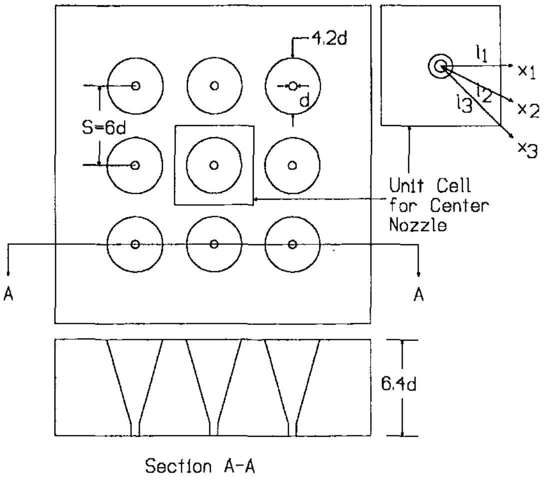

Fig. 1 Detail of the convergent nozzle plate and unit cell within jet array

---

[1] Graduate Assistant.

[2] Professor, Mem. ASME. e-mail: zdavid@ces.clemson.edu. To whom all correspondence should be addressed.

[3] Laboratory for Materials Processing, Mixing, and Environmental Studies, Department of Mechanical Engineering, Clemson University, Clemson, SC 29634-0921. Web site: www.ces.clemson.edu/~mmpl/.

Contributed by the Heat Transfer Division for publication in the JOURNAL OF HEAT TRANSFER. Manuscript received by the Heat Transfer Division, Feb. 10, 1997; revision received, Mar. 20, 1998. Keywords: Forced Convection, Jets, Materials Processing and Manufacturing Process. Associate Technical Editor: J. C. Han.

References

Bankston, C. A., 1970, "The Transition from Turbulent to Laminar Gas Flow in a Heated Pipe," *Trans. ASME*, Ser. C, Vol. 92, pp. 569–579.

Coon, C. W., and Perkins, H. C., 1970, "Transition from the Turbulent to the Laminar Regime for Internal Convective Flow with Large Property Variations," *Trans. ASME*, Ser. C, Vol. 92, pp. 506–512.

Fujii, S., Akino, N., Hishida, M., Kawamura, H., and Sanokawa, K., 1991, "Numerical Studies on Laminarization of Heated Turbulent Gas Flow in Annular Duct," *J. Atomic Energy Soc. Jpn.*, Vol. 33, No. 12, pp. 1180–1190 (in Japanese).

Kawamura, H., 1979, "Prediction of Strongly Heated Turbulent Flow of Gas in a Circular Tube Using a Two-Equation Model of Turbulence," *Trans. Jpn. Soc. Mech. Eng.*, Vol. 45, No. 395B, pp. 1038–1046 (in Japanese).

Kays, W. M., and Crawford, M. E., 1983, *Convective Heat and Mass Transfer*, McGraw-Hill, New York.

Koshizuka, S., Takano, N., and Oka, Y., 1995, "Numerical Analysis of Deterioration Phenomena in Heat Transfer to Supercritical Water," *Int. J. Heat Mass Transfer*, Vol. 38, pp. 3077–3084.

McAdams, W. H., 1954, *Heat Transfer*, McGraw-Hill, New York.

McEligot, D. M., Coon, C. M., and Perkins, H. C., 1970, "Relaminarization in Tubes," *Int. J. Heat Mass Transfer*, Vol. 13, pp. 431–433.

Mori, Y., and Watanabe, K., 1979, "Reduction in Heated Transfer Performance due to High Heat Flux," *Trans. Jpn. Soc. Mech. Eng.*, Vol. 45, No. 397B, pp. 1343–1353 (in Japanese).

Ogawa, M., Kawamura, H., Takizuka, T., and Akino N., 1982, "Experimental on Laminarization of Strongly Heated Gas Flow in Vertical Circular Tube," *J. Atomic Energy Soc. Jpn.*, Vol. 24, No. 1, pp. 60–67 (in Japanese).

Perkins, K. R., Schade, K. W., and McEligot, D. M., 1973, "Heated Laminarizing Gas Flow in a Square Duct," *Int. J. Heat and Mass Transfer*, Vol. 16, pp. 897–916.

Torii, S., Shimizu, A., Hasegawa, S., and Higasa, M., 1990, Laminarization of Strongly Heated Gas Flows in a Circular Tube (Numerical Analysis by Means of a Modified k-ϵ Model), *JSME Int. J.*, Ser. II, Vol. 33, No. 33, pp. 538–547.

Torii, S., Shimizu, A., and Hasegawa, S., 1993, "Numerical Analysis of Laminarizing Tube Flows by Means of a Reynolds Stress Turbulence Model," *Heat Transfer-Japanese Research*, Vol. 22, No. 2, pp. 154–170.

Torii, S., and Yang, W-J., 1997, "Laminarization of Turbulent Gas Flow Inside a Strongly Heated Tube," *Int. J. Heat Mass Transfer*, Vol. 40, No. 13, pp. 3105–3117.

Means to Improve the Heat Transfer Performance of Air Jet Arrays Where Supply Pressures are Limiting

H. S. Sheriff[1,3] and D. A. Zumbrunnen[2,3]

Nomenclature

A_N = flow pulsation amplitude at discharge point in terms of the root-mean square of periodic velocity fluctuations
h = convective heat transfer coefficient, W/m^{2}K
H = vertical distance between nozzle or orifice opening and impingement surface, m
k_f = thermal conductivity of fluid, W/mK
Nu = Nusselt number = hd/k_f
Re$_d$ = Reynolds number referenced to diameter of orifice or nozzle opening and evaluated at film temperature = $u_N d/\nu$
S_d = Strouhal number = $f\,d/u_N$
u_N = mean centerline axial velocity at one diameter downstream of nozzle or orifice exit, m/s
ν = kinematic viscosity, m^2/s

Introduction

Because of ease of construction, large arrays of air jets are most commonly formed by discharging air through orifices drilled or stamped in thin plates. However, pressure drops across orifices can be significantly greater than those across convergent nozzles and may restrict maximum flow rates or require costly air supply systems using compressors and piping. If pressure drops can be kept small, blowers and low-cost ducting can be used in air supply systems which can readily provide large flow rates. The use of blowers and ducting is especially advantageous where air consumption is necessarily large such as when numerous or large jet arrays are needed for heating, cooling, or drying in materials processing applications. Automated machining and manufacturing methods now make practical the production of arrays of convergent nozzles. For example, large convergent nozzle arrays can be readily machined in automated milling operations from thick, single metallic or plastic plates in lieu of being assembled from separate parts.

An example of a convergent nozzle array is shown in Fig. 1. A recent trend in jet arrays has been to replace orifices with tubes (Gundappa et al., 1989) as it allows a larger corridor for venting the spent jet from the vicinity of the target surface. The use of convergent nozzles in place of tubes also has this advantage. Because such arrays can now be economically produced and given resulting opportunities to reduce costs associated with air supply systems, the heat transfer characteristics of arrays of convergent nozzles and arrays of orifices have been compared under the constraint of fixed pressure drop. Results demonstrate that arrays of nozzles provide higher and more uniform heat transfer rates in applications where low-pressure air supply sources are preferred. Because jets emerging from orifices do not readily generate large-scale vortical structures that are observed in submerged jets issuing from convergent nozzles (Michalke, 1972; Popiel and Trass, 1991), results are also presented for pulsating flow conditions that are known to alter coherent flow structures and might lead to changes in convective heat transfer. For example, although the natural frequency for vortex formation of a typical submerged jet is very high such that only small-pulsation amplitudes can be induced (Mladin and Zumbrunnen, 1997), a jet can be forced with large pulsation magnitudes at forcing frequencies much lower than

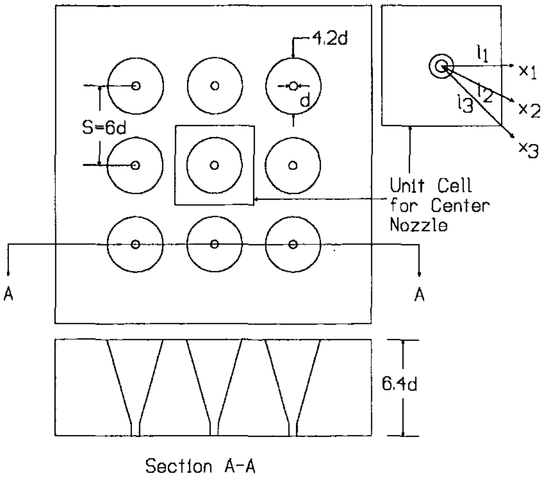

Fig. 1 Detail of the convergent nozzle plate and unit cell within jet array

---

[1] Graduate Assistant.

[2] Professor, Mem. ASME. e-mail: zdavid@ces.clemson.edu. To whom all correspondence should be addressed.

[3] Laboratory for Materials Processing, Mixing, and Environmental Studies, Department of Mechanical Engineering, Clemson University, Clemson, SC 29634-0921. Web site: www.ces.clemson.edu/~mmpl/.

Contributed by the Heat Transfer Division for publication in the JOURNAL OF HEAT TRANSFER. Manuscript received by the Heat Transfer Division, Feb. 10, 1997; revision received, Mar. 20, 1998. Keywords: Forced Convection, Jets, Materials Processing and Manufacturing Process. Associate Technical Editor: J. C. Han.

the natural jet frequency to develop large vortices, so that heat transfer conditions can become changed.

Experimental Apparatus and Procedures

Details of the entire apparatus have been presented by Sheriff (1997). After first entering a plenum chamber, dehumidified and filtered air proceeded through a laminarizing flow element to either a plate containing a square array of nine convergent nozzles or to a plate with a square array of nine sharp-edge orifices. The diameter *d* of each nozzle opening and the nozzle-to-nozzle spacing S, which were identical to those used for the orifice array, were 6 mm and 6*d*, respectively. The spacing corresponded to a maximum heat transfer condition for the orifice array as documented by Martin (1977). It should be noted that comparisons of heat transfer performance thereby favor the orifice array. The specific configuration for arrays of convergent nozzles that provides optimal heat transfer performance remains a topic of future investigations. The array of convergent nozzles, which is shown in Fig. 1, was machined in a plastic plate of 38.1-mm thickness. Each nozzle had an inlet opening of 25.4-mm diameter and a linear contraction contour. A 3.2-mm long transition section was provided at the nozzle exit to straighten the flow prior to discharge.

The jets from the orifices or convergent nozzles discharged vertically upward onto a test cell composed essentially of a heated test plate with instrumentation to measure local convective heat transfer. The test plate consisted of two separate aluminum sections with 25.4-mm diameter semicircular slots designed to accommodate a 25.4-mm diameter aluminum nitride substrate containing a heat flux microsensor (Model HFM-1A-AIN-B, Vatell Corporation, Christiansburg, VA). The test plate was firmly mounted on a thin metallic electric foil heater which rested on an electrically insulative substrate. The heating foil was attached to bus bars that were connected to a direct current power supply. The test cell was mounted on a linear traversing mechanism to control the vertical separation between the test plate and the nozzle or orifice plate. The heat flux microsensor had a heat flux sensing element of less than 2 microns thickness and was fabricated directly on the aluminum nitride substrate by a vapor deposition and masking process. The sensing element consisted of a 1 μm-thick layer of silicon monoxide thermal resistance and multiple nickel-nichrome thermocouple layers which formed a differential thermopile. A platinum resistance sensor was located adjacent to the thermopile to measure the surface temperature. The combined sensing elements had overall dimensions of 2.29 mm by 1.78 mm. The surface temperatures along the test plate exhibited less than four percent temporal and spatial variations due to the high thermal conductivities of the substrate and test plate. The thermal boundary condition of the experiment was therefore nearly that of a spatially uniform and temporally constant surface temperature. Given the sensor's small size and the constant surface temperature, local heat transfer measurements within the jet array were made within the unit cell in Fig. 1 by changing the relative position of the sensor with respect to the axis of the central jet. The sensor temperature was maintained between 45°C and 70°C and the heat flux ranged from 0.2 W/cm^2 to 1.0 W/cm^2. To generate a pulsed jet, a portion of the air supply was directed through a motor-driven ball valve. Pulsation frequencies (10 Hz $< f <$ 65 Hz) were well below the rated frequency response of the sensor (100 kHz).

As simple analyses show for incompressible flow conditions such as are common in industrial applications of gas jets or submerged liquid jets, pressure drops across nozzles and orifices are nearly identical when jet centerline velocities are equal. This equality in pressure drops was confirmed experimentally to be within three percent by using a differential water manometer connected across the nozzle or orifice plates. The jet Reynolds number Re_d of this study was therefore referenced to the centerline velocity of the central jet (Fig. 1) at a distance equal to one diameter *d* from the nozzle or orifice opening within the jet potential core in order to provide comparisons of heat transfer performance for identical pressure drops. Heat transfer measurements were performed for $2500 < \mathrm{Re}_d < 10000$. Flow velocities were measured using a TSI (St. Paul, MN) IFA-100 anemometer fitted with a hot-film probe (TSI Model 1240-20). The temperature of the air at the nozzle inlet was measured using an ANSI Type T thermocouple. This temperature was within 0.1°C of the temperature of the discharged air. Local convective heat transfer coefficients were calculated from Newton's law of cooling with the adiabatic wall temperature as the reference temperature to account for possible entrainment effects (Bouchez and Goldstein, 1975). The adiabatic wall temperature was measured using the surface temperature sensor after a required flow had been established, but with no electrical power supplied to the heater strip and with the test cell initially at ambient temperature. Heat transfer coefficients were corrected for any contribution from radiative heat transfer by considering the test surface as a gray, diffuse body exchanging heat with black surroundings. All thermophysical properties for heat transfer measurements were evaluated at the local film temperature. Experimental uncertainty was determined using the method presented by Kline and McClintock (1953). The uncertainties at a 95 percent confidence level in the Reynolds number and Nusselt number were 4.6 percent and 8.9 percent, respectively. The repeatability in the local Nusselt numbers in the present investigation was two percent. Since comparative data are presented in this study, the repeatability reflects how well differences could be discerned between heat transfer performances.

Results and Discussion

Heat transfer measurements were recorded within the central unit cell shown in Fig. 1 at discrete locations on the impingement plate along the axes x_1, x_2, and x_3. The axis x_2 formed an angle of 22.5 deg with x_1 and x_3. The local time-averaged Nusselt number distributions for the convergent nozzle array and orifice array are presented in Fig. 2 along these axes for $H/d = 2$ and 6. The results for $H/d = 4$ were intermediate to these distributions (Sheriff, 1997). Although Fig. 2 pertains to $\mathrm{Re}_d = 5000$, results are representative for other Reynolds numbers considered. Heat transfer

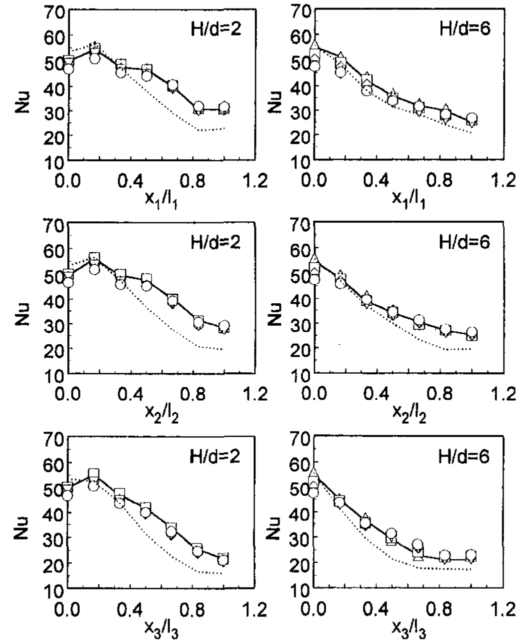

Fig. 2 Convective heat transfer distributions for arrays with convergent nozzles with $\mathrm{Re}_d \cong 5{,}000$, $f = 10$ Hz, $S_d \cong 0.0044$ (... Steady Orifice Jets, — Steady Convergent Jets; △A_N = 10 percent, □ A_N = 25 percent, ◇ A_N = 40 percent, ∇ A_N = 50 percent, ○ A_N = 60 percent)

rates in terms of local Nusselt numbers for the convergent nozzles were significantly greater than for the orifices away from the stagnation region. Since greater heat transfer rates occurred in regions adjacent to the stagnation region, local heat transfer distributions with the convergent nozzles were also more uniform. Such improved uniformity is highly desirable in air jet applications to mitigate hot, cold, or wet spots. The greater heat transfer rates were larger for $H/d = 2$ in comparison to those for $H/d = 6$ and occurred along all three axes. It has been observed in steady jets that secondary vortices on the impingement surface resulting from incident coherent flow structures do not form for $H/d > 6$ (Fox et al., 1993). Evidence of incident coherent flow structures in the flows of this study have been documented by Sheriff (1997). Consequently, the larger increases for $H/d = 2$ and more uniform distribution may indicate the presence of more effective secondary vortices near the boundary layer. For $H/d = 2$ and $0.6 < x_1/l_1 < 1.0$, local Nusselt numbers were between 34 percent and 38 percent larger than those for the orifice array. The largest difference at all separation distances occurred for $x_1/l_i > 0.3$. The spatially averaged heat transfer for the nozzle array was 26.2 percent higher than the results for the orifice array and 36 percent higher than given by the correlation of Martin (1977) for arrays of short straight tubes. It should be noted that these tubes were referred to as nozzles by Martin (1977), but differ from the convergent nozzles of this study. For $H/d = 6$, the spatially averaged heat transfer with the convergent nozzles was 16 percent and 48.9 percent higher than values for the orifice and from the short tube correlation, respectively.

Small off-center peaks in Nusselt number are evident in Fig. 2 on either side of the stagnation point at $x_1/l_1 = x_2/l_2 = x_3/l_3 \approx 0.2$. Locations agreed with the locations of off-center peaks observed experimentally in jet arrays with orifices (Huber and Viskanta, 1994) and numerically within laminar jet arrays (Chen et al., 1994). Since both of the jet flows in these cited studies did not contain coherent flow structures, it can be discerned that the peaks are related to boundary layer development in the stagnation region and not to the interaction of incident flow structures with the surface. Reductions in stagnation point Nusselt numbers due to pulsating flow conditions are also evident in Fig. 2, where $S_d = 0.0044$. Reductions became greater with increasing pulse magnitude and have been theoretically explained by a nonlinear dynamics model of the hydrodynamic and thermal boundary layer responses to a periodic incident flow velocity (Mladin and Zumbrunnen, 1995). Flow pulsations were found to effectively increase the time-averaged thermal boundary layer thickness and lead to reduced heat transfer in a stagnation region. Convective heat transfer distributions thereby became still more uniform. However, at higher pulsation frequencies within the frequency range of this study, a more abundant succession of incident vortices was produced in the pulsed jet so that nonlinear dynamical boundary layer effects became secondary to improved mixing (Sheriff, 1997). Nusselt numbers for the nozzle array were as much as ten percent larger as a consequence than those for the corresponding steady flow case. When orifices were used, a higher initial turbulence level was generated in the discharging jet and coherent flow structure development was impeded even under pulsating flow conditions. Measurable enhancements in Nusselt numbers were therefore not obtained with the orifice arrays even at the highest Strouhal number considered.

Acknowledgment

Support for this work has been provided by the National Science Foundation of the United States under grant number CMS-9253640 in conjunction with a Presidential Faculty Fellow Award to D. A. Zumbrunnen.

References

Bouchez, J.-P., and Goldstein, R. J., 1975, "Impingement Cooling from a Circular Jet in a Cross Flow," *International Journal of Heat and Mass Transfer*, Vol. 18, pp. 719–730.

Chen, J., Wang, T., and Zumbrunnen, D. A., 1994, "Numerical Analysis of Convective Heat Transfer from a Moving Plate Cooled by an Array of Submerged Planar Jets," *Numerical Heat Transfer*, Vol. 26, pp. 141–160.

Fox, M. D., Kurosaka, M., Hedges, L., and Hirano, K., 1993, "The Influence of Vortical Structures on the Thermal Fields of Jets," *Journal of Fluid Mechanics*, Vol. 255, pp. 447–472.

Gundappa, M., Hudson, J. F., and Diller, T. E., 1989, "Jet Impingement Heat Transfer from Jet Tubes and Orifices," Presented at the National Heat Transfer Conference, Philadelphia, PA, Aug. 6–9, HTD-Vol. 107, Heat Transfer in Convective Flows, pp. 43–50.

Huber, A. M., and Viskanta, R., 1994, "Convective Heat Transfer to a Confined Impinging Array of Air Jets with Spent Air Exits," ASME JOURNAL OF HEAT TRANSFER, Vol. 116, pp. 570–576.

Kline, S. J., and McClintock, F. A., 1953, "Describing Uncertainties in Single-Sample Experiments," *Mechanical Engineering*, Vol. 75, pp. 3–8.

Martin, H., 1977, "Heat and Mass Transfer Between Impinging Gas Jets and Solid Surfaces," *Advances in Heat Transfer*, Vol. 13, pp. 1–60.

Michalke, A., 1972, "The Instability of Free Shear Layers," *Progress in Aerospace Sciences*, Vol. 12, pp. 213–239.

Mladin, E. C., and Zumbrunnen, D. A., 1995, "Dependence of Heat Transfer to a Pulsating Stagnation Flow on Pulse Characteristics," *Journal of Thermophysics and Heat Transfer*, Vol. 9, pp. 181–192.

Mladin, E. C., and Zumbrunnen, D. A., 1997, "Local Convective Heat Transfer to Submerged Pulsating Jets," *International Journal of Heat and Mass Transfer*, Vol. 40, pp. 3305–3321.

Popiel, C. O., and Trass, O., 1991, "Visualization of a Free and Impinging Round Jet," *Experimental Thermal and Fluid Science*, Vol. 4, pp. 253–264.

Sheriff, H. S., 1997, "Convective Heat Transfer to Arrays of Jets with and without Flow Pulsations," Ph.D. dissertation, Clemson University, Clemson, SC.

Enhancement of Saturated Flow Boiling Heat Transfer on Cylinders Using Interference Sleeves

S. Madhusudana Rao[1] **and**
A. R. Balakrishnan[2]

Introduction

Many techniques have been developed in recent years to enhance boiling heat transfer. Bergles (1988), Thome (1990), and Webb (1994) have reviewed most of these enhancement techniques for both pool boiling and flow boiling. Abhat and Seban (1974) studied the effect of copper mesh around a cylinder in water. Hasegawa et al. (1975) studied various woven meshes for boiling water on a plate. Asakavicius et al. (1979) examined surfaces with several layers of copper screen for boiling water, R-113 and ethanol. Typical enhancements were not very large, about 100 percent at low heat fluxes and much less at high heat fluxes. A recent experimental study on pool boiling by Shimada et al. (1991) showed that an interference plate (a plate with small holes located on a given pitch) placed with a small clearance over a copper heating surface traps the vapor bubbles stably. These holes in the interference plate facilitates smooth the exchange of vapor-liquid and thereby higher heat

---

[1] Research Scholar, Department of Chemical Engineering, Indian Institute of Technology, Madras, Chennai 600 036, India.

[2] To whom correspondence should be addressed. Professor, Department of Chemical Engineering, Indian Institute of Technology, Madras, Chennai 600 036, India. e-mail: chmcl!arb@iitm.ernet.in. Mem. ASME.

Contributed by the Heat Transfer Division for publication in the JOURNAL OF HEAT TRANSFER. Manuscript received by the Heat Transfer Division, July 25, 1996; revision received, Apr. 14, 1998. Keywords: Augmentation and Enhancement, Boiling, Forced Convection. Associate Technical Editor: R. D. Boyd.

rates in terms of local Nusselt numbers for the convergent nozzles were significantly greater than for the orifices away from the stagnation region. Since greater heat transfer rates occurred in regions adjacent to the stagnation region, local heat transfer distributions with the convergent nozzles were also more uniform. Such improved uniformity is highly desirable in air jet applications to mitigate hot, cold, or wet spots. The greater heat transfer rates were larger for $H/d = 2$ in comparison to those for $H/d = 6$ and occurred along all three axes. It has been observed in steady jets that secondary vortices on the impingement surface resulting from incident coherent flow structures do not form for $H/d > 6$ (Fox et al., 1993). Evidence of incident coherent flow structures in the flows of this study have been documented by Sheriff (1997). Consequently, the larger increases for $H/d = 2$ and more uniform distribution may indicate the presence of more effective secondary vortices near the boundary layer. For $H/d = 2$ and $0.6 < x_1/l_1 < 1.0$, local Nusselt numbers were between 34 percent and 38 percent larger than those for the orifice array. The largest difference at all separation distances occurred for $x_1/l_i > 0.3$. The spatially averaged heat transfer for the nozzle array was 26.2 percent higher than the results for the orifice array and 36 percent higher than given by the correlation of Martin (1977) for arrays of short straight tubes. It should be noted that these tubes were referred to as nozzles by Martin (1977), but differ from the convergent nozzles of this study. For $H/d = 6$, the spatially averaged heat transfer with the convergent nozzles was 16 percent and 48.9 percent higher than values for the orifice and from the short tube correlation, respectively.

Small off-center peaks in Nusselt number are evident in Fig. 2 on either side of the stagnation point at $x_1/l_1 = x_2/l_2 = x_3/l_3 \approx 0.2$. Locations agreed with the locations of off-center peaks observed experimentally in jet arrays with orifices (Huber and Viskanta, 1994) and numerically within laminar jet arrays (Chen et al., 1994). Since both of the jet flows in these cited studies did not contain coherent flow structures, it can be discerned that the peaks are related to boundary layer development in the stagnation region and not to the interaction of incident flow structures with the surface. Reductions in stagnation point Nusselt numbers due to pulsating flow conditions are also evident in Fig. 2, where $S_d = 0.0044$. Reductions became greater with increasing pulse magnitude and have been theoretically explained by a nonlinear dynamics model of the hydrodynamic and thermal boundary layer responses to a periodic incident flow velocity (Mladin and Zumbrunnen, 1995). Flow pulsations were found to effectively increase the time-averaged thermal boundary layer thickness and lead to reduced heat transfer in a stagnation region. Convective heat transfer distributions thereby became still more uniform. However, at higher pulsation frequencies within the frequency range of this study, a more abundant succession of incident vortices was produced in the pulsed jet so that nonlinear dynamical boundary layer effects became secondary to improved mixing (Sheriff, 1997). Nusselt numbers for the nozzle array were as much as ten percent larger as a consequence than those for the corresponding steady flow case. When orifices were used, a higher initial turbulence level was generated in the discharging jet and coherent flow structure development was impeded even under pulsating flow conditions. Measurable enhancements in Nusselt numbers were therefore not obtained with the orifice arrays even at the highest Strouhal number considered.

Acknowledgment

Support for this work has been provided by the National Science Foundation of the United States under grant number CMS-9253640 in conjunction with a Presidential Faculty Fellow Award to D. A. Zumbrunnen.

References

Bouchez, J.-P., and Goldstein, R. J., 1975, "Impingement Cooling from a Circular Jet in a Cross Flow," *International Journal of Heat and Mass Transfer*, Vol. 18, pp. 719–730.

Chen, J., Wang, T., and Zumbrunnen, D. A., 1994, "Numerical Analysis of Convective Heat Transfer from a Moving Plate Cooled by an Array of Submerged Planar Jets," *Numerical Heat Transfer*, Vol. 26, pp. 141–160.

Fox, M. D., Kurosaka, M., Hedges, L., and Hirano, K., 1993, "The Influence of Vortical Structures on the Thermal Fields of Jets," *Journal of Fluid Mechanics*, Vol. 255, pp. 447–472.

Gundappa, M., Hudson, J. F., and Diller, T. E., 1989, "Jet Impingement Heat Transfer from Jet Tubes and Orifices," Presented at the National Heat Transfer Conference, Philadelphia, PA, Aug. 6–9, HTD-Vol. 107, Heat Transfer in Convective Flows, pp. 43–50.

Huber, A. M., and Viskanta, R., 1994, "Convective Heat Transfer to a Confined Impinging Array of Air Jets with Spent Air Exits," ASME JOURNAL OF HEAT TRANSFER, Vol. 116, pp. 570–576.

Kline, S. J., and McClintock, F. A., 1953, "Describing Uncertainties in Single-Sample Experiments," *Mechanical Engineering*, Vol. 75, pp. 3–8.

Martin, H., 1977, "Heat and Mass Transfer Between Impinging Gas Jets and Solid Surfaces," *Advances in Heat Transfer*, Vol. 13, pp. 1–60.

Michalke, A., 1972, "The Instability of Free Shear Layers," *Progress in Aerospace Sciences*, Vol. 12, pp. 213–239.

Mladin, E. C., and Zumbrunnen, D. A., 1995, "Dependence of Heat Transfer to a Pulsating Stagnation Flow on Pulse Characteristics," *Journal of Thermophysics and Heat Transfer*, Vol. 9, pp. 181–192.

Mladin, E. C., and Zumbrunnen, D. A., 1997, "Local Convective Heat Transfer to Submerged Pulsating Jets," *International Journal of Heat and Mass Transfer*, Vol. 40, pp. 3305–3321.

Popiel, C. O., and Trass, O., 1991, "Visualization of a Free and Impinging Round Jet," *Experimental Thermal and Fluid Science*, Vol. 4, pp. 253–264.

Sheriff, H. S., 1997, "Convective Heat Transfer to Arrays of Jets with and without Flow Pulsations," Ph.D. dissertation, Clemson University, Clemson, SC.

Enhancement of Saturated Flow Boiling Heat Transfer on Cylinders Using Interference Sleeves

S. Madhusudana Rao[1] **and**
A. R. Balakrishnan[2]

Introduction

Many techniques have been developed in recent years to enhance boiling heat transfer. Bergles (1988), Thome (1990), and Webb (1994) have reviewed most of these enhancement techniques for both pool boiling and flow boiling. Abhat and Seban (1974) studied the effect of copper mesh around a cylinder in water. Hasegawa et al. (1975) studied various woven meshes for boiling water on a plate. Asakavicius et al. (1979) examined surfaces with several layers of copper screen for boiling water, R-113 and ethanol. Typical enhancements were not very large, about 100 percent at low heat fluxes and much less at high heat fluxes. A recent experimental study on pool boiling by Shimada et al. (1991) showed that an interference plate (a plate with small holes located on a given pitch) placed with a small clearance over a copper heating surface traps the vapor bubbles stably. These holes in the interference plate facilitates smooth the exchange of vapor-liquid and thereby higher heat

---

[1] Research Scholar, Department of Chemical Engineering, Indian Institute of Technology, Madras, Chennai 600 036, India.

[2] To whom correspondence should be addressed. Professor, Department of Chemical Engineering, Indian Institute of Technology, Madras, Chennai 600 036, India. e-mail: chmcl!arb@iitm.ernet.in. Mem. ASME.

Contributed by the Heat Transfer Division for publication in the JOURNAL OF HEAT TRANSFER. Manuscript received by the Heat Transfer Division, July 25, 1996; revision received, Apr. 14, 1998. Keywords: Augmentation and Enhancement, Boiling, Forced Convection. Associate Technical Editor: R. D. Boyd.

Table 1 Sleeve geometries used in the present study

Sleeve no.	Hole diameter *d*, mm	Pitch *p*, mm	Clearance δ, mm	Wall thickness *t*, mm	No. of holes per m^2 (N/A)
1	1	4	0.36	2.78	8.8×10^4
2	1	8.3	0.36	2.78	2.0×10^4
3	1	14.3	0.36	2.78	7.0×10^3
4	1, 2 (comb.)	4, 8 (comb.)	0.36	2.78	5.8×10^4 2.7×10^4
5	1	4	0.92	3.58	9.1×10^4
6	1	4	2.3	2.25	9.1×10^4
7	1, 2 (comb.)	14.3, 24.8 (comb.)	0.36	2.78	4.5×10^3 1.6×10^3
8	2	4	0.36	2.78	8.8×10^4

fluxes at lower wall superheats between the heating surface and the liquid are achieved. Shimada et al. (1991) claim that the performance of this arrangement was comparable and sometimes even better than some of the commercially available high-performance boiling heat transfer surfaces. In their study, a 6-mm thick polycarbonate sheet was used as the interference plate with varying hole geometries (size and pitch) and clearance above the heated surface. The Shimada et al. (1991) study showed that the "best" boiling curve was obtained when combination holes of 1 mm and 4 mm diameter were used with 8.1 mm and 14 mm pitch (respectively) and with 0.12 mm clearance. The primary advantage of using an interference plate over a boiling surface as a heat transfer enhancement technique over other enhancement techniques is the easy cleaning of the heat transfer surface of fouling deposits. This is particularly important in certain process applications such as desalination. Secondly, preparation of the enhanced surfaces does not require any complicated mechanical processing.

Rao and Balakrishnan (1997) studied subcooled flow boiling over a horizontal heated tube (flow in the axial direction) covered with an interference sleeve having holes in a triangular pitch. The sleeves were made of aluminum. The liquid boiled was distilled water at atmospheric pressures. They found that the various parameters which influence the boiling heat transfer performance are sleeve geometry (hole geometry and the clearance between the heating cylinder and the interference sleeve), mass velocity of the boiling liquid and the liquid inlet subcooling. Furthermore, it was found that the heat transfer enhancement factor is greatly reduced with higher subcoolings. In the present study, experiments have been carried out at saturated conditions.

The details of the experimental setup, the test section, and the arrangement of the sleeve on the heating cylinder have been presented elsewhere (Rao and Balakrishnan, 1997). In the experiments, the applied heat flux was varied and the temperatures of the heating cylinder and the liquid were measured. Since the vapor qualities encountered in the present study are small (up to a maximum value of 0.01), the results are presented in a format similar to those used in subcooled boiling and in pool boiling. Eight perforated sleeves were used to examine the sleeve geometries. The geometrical details of these sleeves are given in Table 1.

Results and Discussion

Figure 1(*a*) shows the effect of hole pitch on boiling heat transfer at the inlet liquid mass velocity of 577 kg/m^{2}s. The hole diameter and the gap clearance are also maintained constant at 1 mm and 0.36 mm, respectively. At all heat flux levels the boiling curve for sleeve 1 gives lower wall superheats compared to plain tubes. In the case of sleeve 2 (with a hole pitch of 8.3 mm), there is no enhancement in the heat flux range from 1.3×10^4 W/m^2 to 3×10^4 W/m^2. Increasing the heat flux to a value above 1.4×10^5 W/m^2 results in the wall temperature shooting up which leads to film formation. For sleeve 3 (with a hole pitch of 14.3 mm), the enhancement in heat flux is several times that of a plain tube. Transition to film boiling is observed at a heat flux of about 4.6×10^4 W/m^2. As the pitch of the holes is increased from 8.3 mm to 14.3 mm, the film transition heat flux decreases from 1.4×10^5 W/m^2 to 4.6×10^4 W/m^2. The boiling curve obtained with sleeve 4 (with combination holes of 1 mm and 4 mm diameter on 4 mm and 8 mm pitch

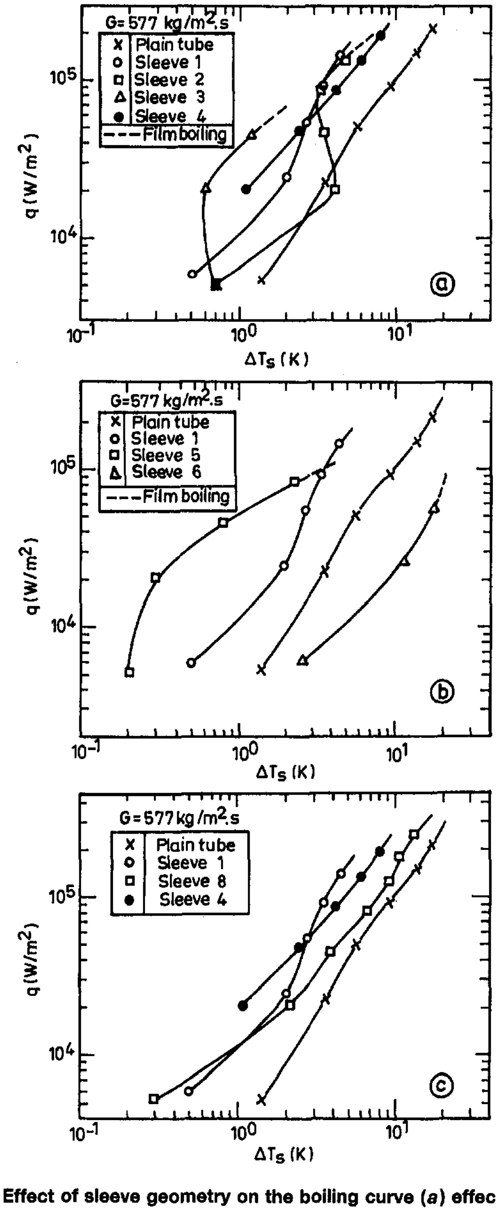

Fig. 1 Effect of sleeve geometry on the boiling curve (*a*) effect of hole pitch; (*b*) effect of gap clearance; (*c*) effect of hole diameter

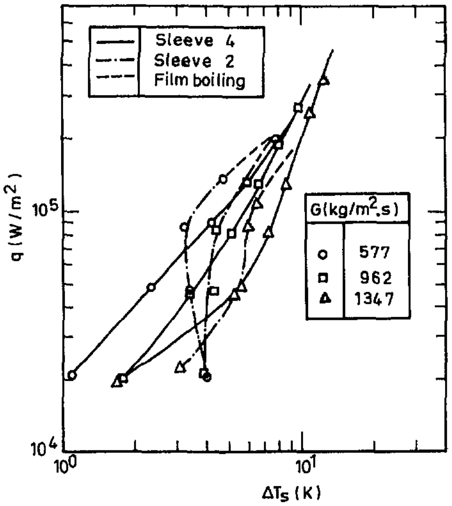

Fig. 2 Effect of liquid inlet mass velocity on the boiling curve using sleeve 2 and sleeve 4 geometries

respectively) are also shown in the figure. This shape of this curve is typical of standard boiling curves and there is no tendency towards transition to film boiling.

Figure 1(*b*) shows the effect of gap clearance at an inlet mass velocity of 577 kg/m^{2}s. Three gap clearances 0.36, 0.92, and 2.3 mm were used. The hole diameter and the pitch of the holes are the same at 1 mm and 4 mm, respectively. The results show that at all heat fluxes sleeve 5 (0.92 mm clearance) gave better enhancement compared to sleeve 1 (with 0.36 mm clearance). This is most likely due to the larger coalescence of the vapor bubbles. According to Ishibashi and Nishikawa (1969), the coalesced bubble regime gives rise to higher heat transfer coefficients than the isolated bubble regime. For sleeve 5, transition to film boiling occurred at a heat flux of 9 × 10^4 W/m^2. This transition occurs because as the heat flux is increased, the number of holes may be insufficient to discharge the large amount of vapour generated and it accumulates in the large gap clearance causing the vapor-liquid exchange equilibrium to be disturbed. In the case of sleeve 6 (gap clearance of 2.3 mm) the situation is quite different. Sleeve 6 always gave larger wall superheats compared to the plain tube. This is due to the existence of a vapor layer in the large gap. Visual observations showed that at low heat fluxes, vapor was coming from the top part of the sleeve intermittently in slugs. At higher heat fluxes the vapor slugs are seen all around the sleeve. At a heat flux of 5.6 × 10^4 W/m^2, the gap clearance was completely filled with vapor.

Figure 1(*c*) shows the boiling curves for three sleeves, one with 1 mm diameter holes (sleeve 1), one with 2-mm dia. holes (sleeve 8) and one with combination holes of 1 mm and 2 mm on 4 mm and 8 mm pitch, respectively (sleeve 4). It can be observed that the boiling curve with 2-mm diameter holes shifts towards the left of that obtained with a sleeve of 1-mm diameter holes until a heat flux value of 1.2 × 10^4 W/m^2. This is due to lower incipient heat fluxes required with larger hole diameters. Film boiling and unusual boiling behavior (decreasing wall superheat with increase in heat flux) are not observed with sleeves with 2-mm diameter holes. The boiling behavior obtained with sleeve 4 (combination holes) is even superior to sleeves with 2 mm holes at heat flux levels beyond 1.2 × 10^4 W/m^2.

Three inlet mass velocity 577 kg/m^{2}s, 962 kg/m^{2}s, and 1347 kg/m^{2}s were used to obtain data. Figure 2 shows the effect of mass velocity on the boiling curve using sleeve 2 geometry. It can be observed that as the mass velocity increases from 577 kg/m^{2}s to 1347 kg/m^{2}s the boiling curve shifts towards the larger ΔT_s values. It can be also observed that the film boiling occurs at a heat flux value of about 1.3 × 10^5 W/m^2 for the three mass velocities considered. Similar results were noticed for sleeve 3 also. It can therefore be concluded that the film transition heat fluxes are not affected by the mass velocity at least for sleeve 2 and sleeve 3 geometries. This is different from the observations on subcooled flow boiling over interference sleeves (Rao and Balakrishnan; 1997) where it was seen that the film transition heat fluxes are delayed with increasing mass velocity. Figure 2 also shows the boiling curves obtained with sleeve 4 (combination holes geometry). The effect of mass velocity is similar to that obtained with sleeve 2, but the shape of the boiling curves are similar to standard boiling curves and there is no tendency towards transition to film boiling.

Enhancement Factors. Figure 3 shows the enhancement factors of the eight sleeves used in the present study at different heat flux values where the enhancement factor "*E*" is defined as the ratio of the excess temperature of the plain tube to that of a sleeve at a given heat flux and mass velocity. The figure shows that sleeve 3 has enhancement factors ranging from 8 to as high as 13. But it has the disadvantage of film formation at a heat flux of 4.6 × 10^4 W/m^2. The enhancement factors seen with sleeves 5 and 6 are not more than 3. In addition, there is the disadvantage of film formation. Film formation was not

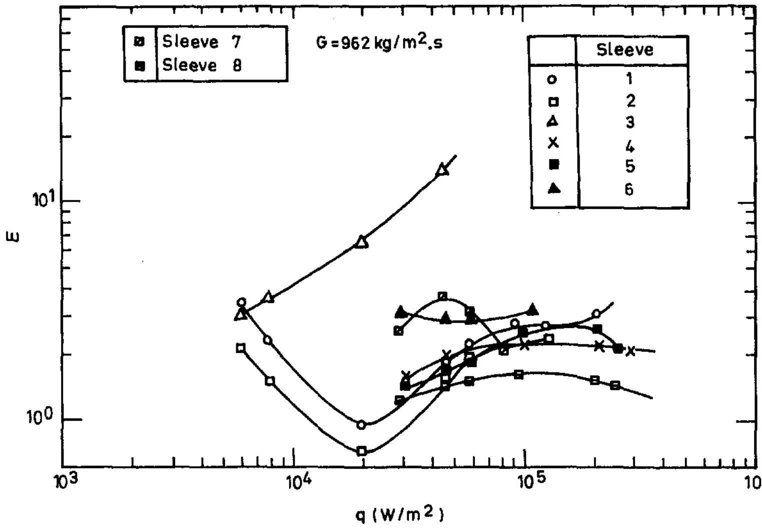

Fig. 3 Enhancement factors at various heat flux values at a mass velocity of 962 kg/m^{2}s for the eight sleeves used in this study

encountered with sleeves 1 and 4. Sleeve 4 has enhancement factors ranging from 1.5 to 2.2 and these values are almost constant with heat flux. Sleeve 2 shows a maximum enhancement factor of 2.2 just before film boiling occurs. Sleeve 8 gives a maximum enhancement factor of 1.6 without film formation. All the data in Fig. 3 are at a mass velocity of 962 kg/m^{2}s. At these flow rates, the maximum enhancement factors encountered under subcooled conditions were about two (Rao and Balakrishnan, 1997). In fact, at higher subcoolings (around 20 K), the enhancement factors were less than one indicating poorer performance than with plain tubes.

Conclusions

The perforated interference sleeve, as a boiling heat transfer enhancement technique, gives larger enhancement factors at saturated flow conditions compared to subcooled flow conditions. High enhancement factors were encountered with large hole pitch sleeves but with the disadvantage of an early transition to film boiling conditions. This transition heat flux is not influenced by the liquid mass velocity. Sleeves with large gap clearance of 2.3 mm gave poor performance at 577 kg/m^{2}s mass velocities; i.e., at all heat flux levels they gave high ΔT_s values. The "best" boiling curve with high enhancement factors and with high film transition heat fluxes at low heat flux levels, was obtained with the sleeves with 2 mm holes. The best boiling curve at higher heat fluxes was obtained using sleeves with 1 mm, 2 mm combination holes on 4 mm, 8 mm pitch, respectively.

References

Abhat, A., and Seban, R. A., 1974, "Boiling and Evaporation from Heat Pipe Wicks with Water and Acetone," ASME JOURNAL OF HEAT TRANSFER, Vol. 96, pp. 331–337.

Asakavicius, J. P., Zukauskas, A. A., Gaigolis, V. A., and Eva, V. K., 1979, "Heat Transfer from Freon-113, Ethyl Alcohol and Water with Screen Wicks," *Heat Transfer-Soviet Research*, Vol. 11, pp. 92–100.

Bergles, A. E., 1988, "Some Perspectives on Enhanced Heat Transfer—Second Generation Heat Transfer Technology," ASME JOURNAL OF HEAT TRANSFER, Vol. 110, pp. 1082–1096.

Hasegawa, S., Echigo, R., and Irie, S., 1975, "Boiling Characteristics and Burnout Phenomena on a Heating Surface covered with Woven Screens," *Journal of Nuclear Science and Technology*, Vol. 12, pp. 722–724.

Ishibashi, E., and Nishikawa, K., 1969, "Saturated Boiling Heat Transfer in Narrow Spaces," *International Journal of Heat and Mass Transfer*, Vol. 12, pp. 863–894.

Rao, S. M., and Balakrishnan, A. R., 1997, "Enhancement of Sub-cooled Flow Boiling Heat Transfer on Cylinders using Interference Sleeves," *Journal of Enhanced Heat Transfer*, Vol. 4, pp. 203–215.

Shimada, R., Komai, J., Hirono, Y., Kumagai, S., and Takeyama, T., 1991, "Enhancement of Boiling Heat Transfer in a Narrow Space Restricted by an Interference Plate with Holes," *Experimental Thermal and Fluid Science*, Vol. 4, pp. 587–593.

Thome, J. R., 1990, *Enhanced Boiling Heat Transfer*, Hemisphere, Washington, DC.

Webb, R. L., 1994, *Principles of Enhanced Heat Transfer*, John Wiley and Sons, New York.

A New Method for Tracking Radiative Paths in Monte Carlo Simulations

B. M. Shaughnessy[1,3] and
M. Newborough[2,3]

Nomenclature

c = elements of matrix $\mathbf{C}$
$\mathbf{C}$ = matrix of cumulative density functions
F_{ij} = exchange factor from surface i to surface j
n = number of surfaces
N = number of energy bundles tracked
p_{ij} = transition probability from surface i to surface j
p_{ijk} = transition probability from surface i to surface k via a single reflection from surface j
$\mathbf{P}$ = matrix of transition probabilities
R = uniformly generated (pseudo) random number ($0 \le R \le 1$)
s = specularity parameter (Eq. (5))
$z_{\alpha/2}$ = percentage point of the Standard Normal Distribution
ϵ = emissivity
θ = polar angle, rad

Subscripts

e = enclosure
i, j, k = surface indices
I = incident
o = obstruction
R = reflected

Introduction

The Monte Carlo (MC) approach is a powerful means of solving radiative heat transfer problems involving realistic geometries and properties. As described elsewhere (e.g., Siegel and Howell, 1972; Modest, 1993), radiation exchange factors, F_{ij}, between surfaces in an enclosure are calculated by ray-tracing (or tracking) the paths of a large number of "energy bundles" according to probability functions that describe emission, reflection, and absorption. Unfortunately, the time penalty associated with computing ray-surface intersections is high, and this inhibits high-accuracy solutions. This article presents a new method for tracking the reflected paths of energy bundles, which is much faster than traditional ray-tracing approaches (Shaugh-

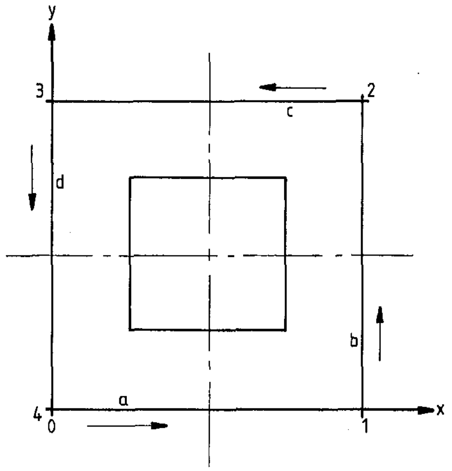

Fig. 1 Two-dimensional enclosure with central obstruction. The faces *a*, *b*, *c*, and *d*, and the dimensionless wall location around the enclosure perimeter are indicated.

---

[1] Research Assistant. e-mail: b.m.shaughnessy@cranfield.ac.uk.

[2] Senior Lecturer. e-mail: m.newborough@cranfield.ac.uk. Assoc. Mem. ASME.

[3] School of Mechanical Engineering, Cranfield University, Bedford MK43 0AL, UK.

Contributed by the Heat Transfer Division for publication in the JOURNAL OF HEAT TRANSFER. Manuscript received by the Heat Transfer Division, Jan. 6, 1997; revision received, Mar. 23, 1998. Keywords: Computer Codes, Numerical Methods, Radiation. Associate Technical Editor: T. Tong.

encountered with sleeves 1 and 4. Sleeve 4 has enhancement factors ranging from 1.5 to 2.2 and these values are almost constant with heat flux. Sleeve 2 shows a maximum enhancement factor of 2.2 just before film boiling occurs. Sleeve 8 gives a maximum enhancement factor of 1.6 without film formation. All the data in Fig. 3 are at a mass velocity of 962 kg/m^{2}s. At these flow rates, the maximum enhancement factors encountered under subcooled conditions were about two (Rao and Balakrishnan, 1997). In fact, at higher subcoolings (around 20 K), the enhancement factors were less than one indicating poorer performance than with plain tubes.

Conclusions

The perforated interference sleeve, as a boiling heat transfer enhancement technique, gives larger enhancement factors at saturated flow conditions compared to subcooled flow conditions. High enhancement factors were encountered with large hole pitch sleeves but with the disadvantage of an early transition to film boiling conditions. This transition heat flux is not influenced by the liquid mass velocity. Sleeves with large gap clearance of 2.3 mm gave poor performance at 577 kg/m^{2}s mass velocities; i.e., at all heat flux levels they gave high ΔT_s values. The "best" boiling curve with high enhancement factors and with high film transition heat fluxes at low heat flux levels, was obtained with the sleeves with 2 mm holes. The best boiling curve at higher heat fluxes was obtained using sleeves with 1 mm, 2 mm combination holes on 4 mm, 8 mm pitch, respectively.

References

Abhat, A., and Seban, R. A., 1974, "Boiling and Evaporation from Heat Pipe Wicks with Water and Acetone," ASME JOURNAL OF HEAT TRANSFER, Vol. 96, pp. 331–337.

Asakavicius, J. P., Zukauskas, A. A., Gaigolis, V. A., and Eva, V. K., 1979, "Heat Transfer from Freon-113, Ethyl Alcohol and Water with Screen Wicks," *Heat Transfer-Soviet Research*, Vol. 11, pp. 92–100.

Bergles, A. E., 1988, "Some Perspectives on Enhanced Heat Transfer—Second Generation Heat Transfer Technology," ASME JOURNAL OF HEAT TRANSFER, Vol. 110, pp. 1082–1096.

Hasegawa, S., Echigo, R., and Irie, S., 1975, "Boiling Characteristics and Burnout Phenomena on a Heating Surface covered with Woven Screens," *Journal of Nuclear Science and Technology*, Vol. 12, pp. 722–724.

Ishibashi, E., and Nishikawa, K., 1969, "Saturated Boiling Heat Transfer in Narrow Spaces," *International Journal of Heat and Mass Transfer*, Vol. 12, pp. 863–894.

Rao, S. M., and Balakrishnan, A. R., 1997, "Enhancement of Sub-cooled Flow Boiling Heat Transfer on Cylinders using Interference Sleeves," *Journal of Enhanced Heat Transfer*, Vol. 4, pp. 203–215.

Shimada, R., Komai, J., Hirono, Y., Kumagai, S., and Takeyama, T., 1991, "Enhancement of Boiling Heat Transfer in a Narrow Space Restricted by an Interference Plate with Holes," *Experimental Thermal and Fluid Science*, Vol. 4, pp. 587–593.

Thome, J. R., 1990, *Enhanced Boiling Heat Transfer*, Hemisphere, Washington, DC.

Webb, R. L., 1994, *Principles of Enhanced Heat Transfer*, John Wiley and Sons, New York.

A New Method for Tracking Radiative Paths in Monte Carlo Simulations

B. M. Shaughnessy[1,3] **and**
M. Newborough[2,3]

Nomenclature

c = elements of matrix $\mathbf{C}$
$\mathbf{C}$ = matrix of cumulative density functions
F_{ij} = exchange factor from surface i to surface j
n = number of surfaces
N = number of energy bundles tracked
p_{ij} = transition probability from surface i to surface j
p_{ijk} = transition probability from surface i to surface k via a single reflection from surface j
$\mathbf{P}$ = matrix of transition probabilities
R = uniformly generated (pseudo) random number ($0 \le R \le 1$)
s = specularity parameter (Eq. (5))
$z_{\alpha/2}$ = percentage point of the Standard Normal Distribution
ϵ = emissivity
θ = polar angle, rad

Subscripts

e = enclosure
i, j, k = surface indices
I = incident
o = obstruction
R = reflected

Introduction

The Monte Carlo (MC) approach is a powerful means of solving radiative heat transfer problems involving realistic geometries and properties. As described elsewhere (e.g., Siegel and Howell, 1972; Modest, 1993), radiation exchange factors, F_{ij}, between surfaces in an enclosure are calculated by ray-tracing (or tracking) the paths of a large number of "energy bundles" according to probability functions that describe emission, reflection, and absorption. Unfortunately, the time penalty associated with computing ray-surface intersections is high, and this inhibits high-accuracy solutions. This article presents a new method for tracking the reflected paths of energy bundles, which is much faster than traditional ray-tracing approaches (Shaugh-

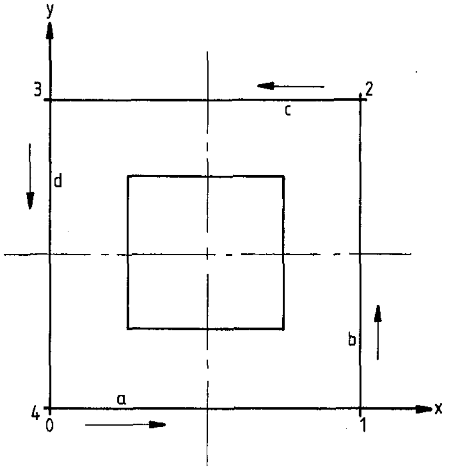

Fig. 1 Two-dimensional enclosure with central obstruction. The faces *a*, *b*, *c*, and *d*, and the dimensionless wall location around the enclosure perimeter are indicated.

---

[1] Research Assistant. e-mail: b.m.shaughnessy@cranfield.ac.uk.

[2] Senior Lecturer. e-mail: m.newborough@cranfield.ac.uk. Assoc. Mem. ASME.

[3] School of Mechanical Engineering, Cranfield University, Bedford MK43 OAL, UK.

Contributed by the Heat Transfer Division for publication in the JOURNAL OF HEAT TRANSFER. Manuscript received by the Heat Transfer Division, Jan. 6, 1997; revision received, Mar. 23, 1998. Keywords: Computer Codes, Numerical Methods, Radiation. Associate Technical Editor: T. Tong.

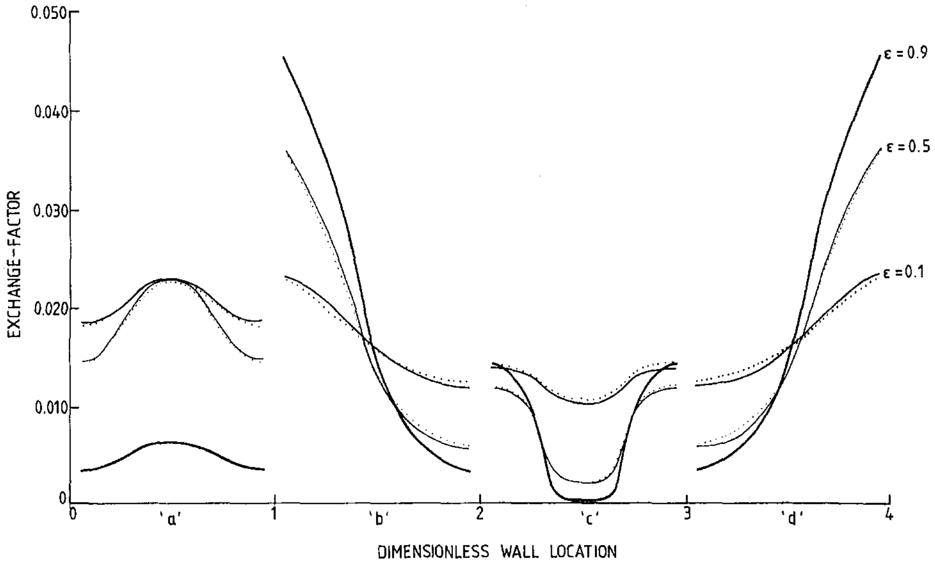

Fig. 2 Exchange factor distribution between face "*a*" and all enclosure surfaces in a diffusely reflecting enclosure by MC (solid lines) and DFMC (dotted lines)

nessy, 1996). It is referred to here as "Discrete Function Monte Carlo" (DFMC).

Formulation

In the proposed approach, the directional emission and reflection functions (for a system of n surfaces) are described in terms of discrete transition probabilities, p_{ij}. For each surface i, the set of transition probabilities (for $1 \le j \le n$) defines a probability density function (PDF). This PDF therefore characterizes the direction of each energy bundle, emitted or reflected from surface i, in terms of the surfaces that it may directly intercept. By randomly sampling the PDFs for each intercepted surface (in sequence), a representative path for each energy bundle (from emission to absorption) can be determined. Exchange factors can then be calculated by repeating this process.

The transition probabilities for directional emission and reflection between each of the n surfaces are given in terms of the $n \times n$ matrix $\mathbf{P}$:

$$\mathbf{P} = \begin{bmatrix} p_{11} & \cdots & p_{1n} \\ \vdots & \ddots & \vdots \\ p_{n1} & \cdots & p_{nn} \end{bmatrix} \quad \text{where} \quad \sum_{j=1}^{n} p_{ij} = 1, \quad \text{for each } i. \quad (1)$$

For the case of diffuse emission or reflection each transition probability is identical to the view factor.

Bi-directional (including specular) reflections have a magnitude that is dependent on the incident and reflected directions of radiation. To accurately calculate bi-directional reflections the exact path of radiation from emission to absorption must therefore be traced. In this investigation the "n-bounce" approximation of Bevans and Edwards (1965) was employed to calculate three-point transition probabilities, p_{ijk}. To calculate reflection from each bi-directional surface j, a PDF must be derived corresponding to each "previous" surface i. As the accuracy of this approximation of p_{ijk} depends upon the directional distribution of the radiation leaving surface i, it can be improved by increasing the number of radiation bounces before surface i is intercepted.

Table 1 Relative performance of the DFMC solutions for the diffuse enclosures

Emissivity, ϵ ($\epsilon_e = \epsilon_o$)	Relative Performance	Emissivity, ϵ ($\epsilon_e = \epsilon_o$)	Relative Performance
0.05	6.6	0.6	3.0
0.1	4.4	0.7	3.5
0.2	3.1	0.8	4.5
0.3	2.7	0.9	6.9
0.4	2.6	0.95	10.4
0.5	2.7		

To sample destination locations from the PDFs, cumulative density functions (CDFs) must be derived from the transition probabilities. For Eq. (1) the CDF is

$$c_{ik} = \sum_{j=1}^{k} p_{ij} \quad (1 \le k \le n). \quad (2)$$

Because it is a cumulative expression of probabilities, the CDF is nondecreasing and has a value of unity when $k = n$. In matrix form the CDF is

$$\mathbf{C} = \begin{bmatrix} c_{1,1} & \cdots & c_{1,n-1} & 1 \\ \vdots & \ddots & & 1 \\ c_{n,1} & \cdots & c_{n,n-1} & 1 \end{bmatrix}. \quad (3)$$

Matrix $\mathbf{C}$ is sampled to yield the index number of the destination surface by means of a uniformly generated random number R. For radiation leaving surface i, the destination j is such that $c_{i,j-1} < R \le c_{i,j}$.

Example Simulations

To demonstrate the performance and accuracy of the new approach, results are presented for a square two-dimensional enclosure with a concentric obstruction (Fig. 1). The enclosure was divided into equally sized surfaces ($n_e = 40$), while each face of the obstruction was considered as a single surface ($n_o = 4$). Emission from the enclosure and the obstruction was considered diffuse; and diffuse, specular, and bi-directional reflections were studied (exchange factors for the diffuse enclosure may be more efficiently calculated directly from the transition probabilities; however, the diffuse case was included to demonstrate the capability of the method to model directional reflection characteristics).

A MC ray-tracing model was written to provide reference solutions. The ray-tracing kernel from this model was implemented in the DFMC model to evaluate transition probabilities. These models were considered to have comparable computa-

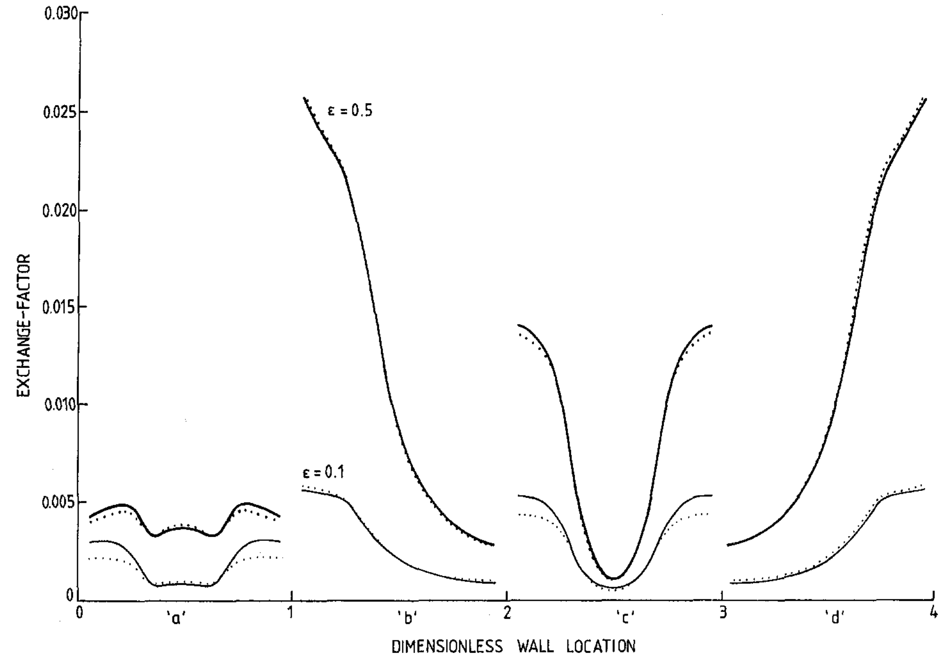

Fig. 3 Exchange factor distribution between face "*a*" and all enclosure surfaces in a specularly reflecting enclosure by MC (solid lines) and DFMC (dotted lines)

tional efficiencies, but, as computation times are dependent upon hardware and software implementation, only relative timings are presented here. In each considered case, exchange factors between each of the surfaces of the enclosure were calculated. The "relative-performance" of the DFMC approach was defined as the ratio of computation time for a MC simulation to that for a DFMC simulation (which involves calculating the transition probabilities and tracking the energy bundles).

The uncertainties in the exchange factors were calculated from (Weiner et al., 1965; Maltby and Burns, 1991)

$$\Delta F_{ij} = z_{\alpha/2} \frac{\sqrt{F_{ij}(1 - F_{ij})}}{\sqrt{(N_i - 1)}} \tag{4}$$

where there is a 99 percent confidence that the true value of F_{ij} is within $\pm\Delta F_{ij}$ of F_{ij} when $z_{\alpha/2} = 2.58$. Equation (4) was implemented in the models as an algorithm to increment N until the average uncertainty in the exchange factors had converged to within ±5 percent.

Diffuse Reflections. Emissivities within the range $0.05 \leq \epsilon \leq 0.95$ were examined ($\epsilon_e = \epsilon_o$). The differences in the DFMC and MC predictions for individual exchange factors were well within the expected uncertainty of ±5 percent. The strong agreement between the two approaches is illustrated in Fig. 2.

The DFMC method was between 2.6 and 10.4 times faster than MC for the enclosures investigated (Table 1). The greatest improvements in computational speed are attained when the number of rays to track is high. That is, when either the reflectivity is high or when many energy bundles must be projected

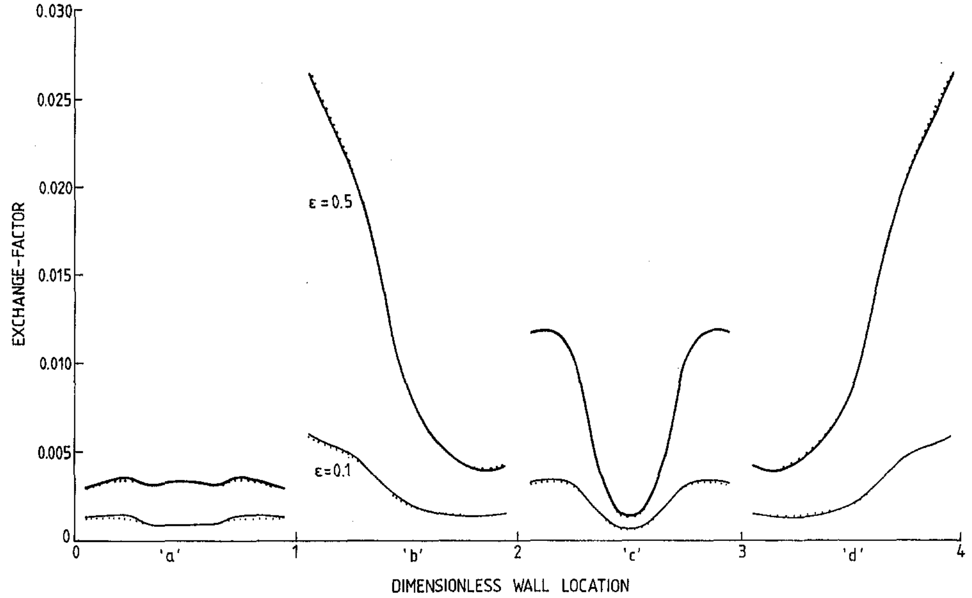

Fig. 4 Exchange factor distribution between face "*a*" and all enclosure surfaces in a bi-directionally reflecting enclosure by MC (solid lines) and DFMC (dotted lines)

to ensure convergence of small exchange factors (which applies for the high-emissivity enclosures studied here).

Specular and Bi-directional Reflections. These were examined for $\epsilon_e = 0.1$ and $\epsilon_e = 0.5$, with $\epsilon_o = 0.9$. A one-bounce approximation was used to calculate the transition probabilities. An analytic bi-directional reflection function presented by Billings et al. (1991) was employed:

$$f(\theta_I, \theta_R) = \frac{(s^2 + 1)\cos(\theta_R) e^{-s|\theta_I + \theta_R|}}{2s\cos(\theta_I) + e^{-s(\pi/2+\theta_I)} + e^{-s(\pi/2-\theta_I)}}$$

$$-\pi/2 \geq \theta \geq \pi/2. \qquad (5)$$

The parameter s controls the specularity of the reflected radiation. Setting $s = 0$ results in diffuse reflection, but as $s \rightarrow \infty$ reflection becomes increasingly specular. Simulations were performed with $s = 4$, which yields a "directional-diffuse" reflection characteristic.

To calculate exchange factors (in MC) and transition probabilities (in DFMC) directions need to be sampled from the CDF of Eq. (5). The CDF must be inverted and stored as a lookup table of reflected directions corresponding to possible incident directions and random number values (Maltby and Burns, 1991; Modest, 1993). Cubic spline interpolation (Press et al., 1992) was employed to tabulate reflected directions in degree intervals of incident direction and percent intervals in random number values. Actual angles of reflection were obtained by linear interpolation from the lookup table.

For specular reflection DFMC was approximately eight times faster than MC, while for bi-directional reflection this increase was sixfold when $\epsilon_e = 0.1$ and about threefold when $\epsilon_e = 0.5$. Again, there is strong agreement between the two approaches (Figs. 3 and 4). For specular reflection, there is a slight difference in the exchange factors calculated by each method to faces "*a*" and "*c*" (Fig. 3). The accuracy of these results could be improved by increasing the number of bounces of radiation when calculating the transition probabilities or by optimising the surface sizes.

Conclusion

A numerical approach has been presented that offers faster calculation of exchange factors in nonblack enclosures. For the studied cases, predictions from the DFMC and MC methods are in close agreement, and computational speeds were improved by factors of between 2.6 and 10.4 by using the DFMC method. The DFMC model is easy to implement, and transition probabilities can be determined by existing computer codes. Furthermore, because the transition probabilities represent directional exchange between surfaces they can be reused. This provides a significant advantage if the surface absorptivities, or the directional properties of only a few surfaces, are altered for the purpose of analysis.

Work is continuing with the development of the method in three areas. First, to provide a broader understanding of its performance characteristics (particularly when applied to realistic three-dimensional geometries). Secondly, to investigate means for optimizing the calculation of specular and bi-directional reflections. And thirdly, because the present approach is memory intensive (particularly for calculations including bi-directional reflections), to develop improved algorithms for managing the CDF matrices (e.g., sparse matrix routines, data compression, and function approximation).

References

Bevans, J. T., and Edwards, D. K., 1965, "Radiation Exchange in an Enclosure with Directional Wall Properties," ASME JOURNAL OF HEAT TRANSFER, Vol. 87, pp. 388–396.

Billings, R. L., Barnes, J. W., and Howell, J. R., 1991, "Markov Analysis of Radiative Transfer in Enclosures With Bidirectional Reflections," *Numerical Heat Transfer*, Part A, Vol. 19, pp. 313–326.

Maltby, J. D., and Burns, P. J., 1991, "Performance, Accuracy, and Convergence in a Three-Dimensional Monte Carlo Radiative Heat Transfer Simulation," *Numerical Heat Transfer*, Part B, Vol. 19, pp. 191–209.

Modest, M. F., 1993, *Radiative Heat Transfer*, McGraw-Hill, New York.

Press, W. H., Flannery, B. P., Teukolsky, S. A., and Vetterling, W. T., 1992, *Numerical Recipes*, 2nd. Ed., Cambridge University Press, Cambridge, England.

Shaughnessy, B. M., 1996, "Radiative Heat Transfers in Low-Emissivity Enclosures," Ph.D. thesis, School of Mechanical Engineering, Cranfield University, England.

Siegel, R., and Howell, J. R., 1972, *Thermal Radiation Heat Transfer*, McGraw-Hill, New York.

Weiner, M. M., Tindall, J. W., and Candell, L. M., 1965, "Radiative Interchange Factors by Monte-Carlo," ASME Paper No. 65-WA/HT-51.

Heat Transfer Coefficient Enhancement With Perforated Baffles

S. Dutta,[1,2] P. Dutta,[1] R. E. Jones,[1] and J. A. Khan[1,2]

Introduction

Primarily there are three popular techniques to enhance heat transfer coefficient in channels: (i) boundary layer disturbance that is created by periodically placed ribs on the heat transfer surface; (ii) impingement cooling that uses high velocity jets to cool the surface of interest; and (iii) internal flow swirls or tape twisters that create a significant amount of bulk flow disturbance. Inclined solid baffles may be considered as a combination of ribs and channel inserts. Baffles are big enough to disturb the core flow, but like ribs, they are mounted on or near the heat transfer surface and can be spatially periodic. Perforations in inclined baffles create multiple jet impingement condition, and thus create a situation where all three major heat transfer coefficient enhancement techniques work in unison. In the past, experimental results were published with baffle plates perpendicular to the flow direction. Habib et al. (1994) have investigated heat transfer and flow over perpendicular baffles of various heights. Unlike previous publications, in our present study, we investigate heat transfer enhancement using an *inclined* baffle. The baffle plate is oriented in both stream aligned and stream opposed directions. In addition, jet impingement is added by using multiple jet hole arrays. Since the baffle is inclined, the jets can be directed toward the heat transfer surface. Characteristic friction factors and average Nusselt numbers with these inclined baffles are discussed in Dutta et al. (1997).

Experimental Facility

A suction mode blower is used to draw air through a rectangular cross-sectioned wind tunnel. The cross section of the smooth wind tunnel is 24.92 cm × 4.92 cm (channel height, H = 4.92 cm). Air enters the tunnel through a contraction and flow straighteners, and then the flow develops through a 31 H-long unheated entrance. The exit is at a 22.2 H distance downstream of the heated test section. The heated test section is 19.2 H

---

[1] Department of Mechanical Engineering, University of South Carolina, Columbia, SC 29208.

[2] Mem. ASME.

Contributed by the Heat Transfer Division for publication in the JOURNAL OF HEAT TRANSFER and presented at '97 IMECE, Dallas. Manuscript received by the Heat Transfer Division, Aug. 1, 1997; revision received, Mar. 20, 1998. Keywords: Enclosure Flows, Flow Separation, Forced Convection, Heat Exchangers, Turbulence. Associate Technical Editor: J. C. Han.

to ensure convergence of small exchange factors (which applies for the high-emissivity enclosures studied here).

Specular and Bi-directional Reflections. These were examined for $\epsilon_e = 0.1$ and $\epsilon_e = 0.5$, with $\epsilon_o = 0.9$. A one-bounce approximation was used to calculate the transition probabilities. An analytic bi-directional reflection function presented by Billings et al. (1991) was employed:

$$f(\theta_I, \theta_R) = \frac{(s^2 + 1)\cos(\theta_R) e^{-s|\theta_I + \theta_R|}}{2s \cos(\theta_I) + e^{-s(\pi/2+\theta_I)} + e^{-s(\pi/2-\theta_I)}}$$

$$-\pi/2 \geq \theta \geq \pi/2. \quad (5)$$

The parameter s controls the specularity of the reflected radiation. Setting $s = 0$ results in diffuse reflection, but as $s \to \infty$ reflection becomes increasingly specular. Simulations were performed with $s = 4$, which yields a "directional-diffuse" reflection characteristic.

To calculate exchange factors (in MC) and transition probabilities (in DFMC) directions need to be sampled from the CDF of Eq. (5). The CDF must be inverted and stored as a lookup table of reflected directions corresponding to possible incident directions and random number values (Maltby and Burns, 1991; Modest, 1993). Cubic spline interpolation (Press et al., 1992) was employed to tabulate reflected directions in degree intervals of incident direction and percent intervals in random number values. Actual angles of reflection were obtained by linear interpolation from the lookup table.

For specular reflection DFMC was approximately eight times faster than MC, while for bi-directional reflection this increase was sixfold when $\epsilon_e = 0.1$ and about threefold when $\epsilon_e = 0.5$. Again, there is strong agreement between the two approaches (Figs. 3 and 4). For specular reflection, there is a slight difference in the exchange factors calculated by each method to faces "*a*" and "*c*" (Fig. 3). The accuracy of these results could be improved by increasing the number of bounces of radiation when calculating the transition probabilities or by optimising the surface sizes.

Conclusion

A numerical approach has been presented that offers faster calculation of exchange factors in nonblack enclosures. For the studied cases, predictions from the DFMC and MC methods are in close agreement, and computational speeds were improved by factors of between 2.6 and 10.4 by using the DFMC method. The DFMC model is easy to implement, and transition probabilities can be determined by existing computer codes. Furthermore, because the transition probabilities represent directional exchange between surfaces they can be reused. This provides a significant advantage if the surface absorptivities, or the directional properties of only a few surfaces, are altered for the purpose of analysis.

Work is continuing with the development of the method in three areas. First, to provide a broader understanding of its performance characteristics (particularly when applied to realistic three-dimensional geometries). Secondly, to investigate means for optimizing the calculation of specular and bi-directional reflections. And thirdly, because the present approach is memory intensive (particularly for calculations including bi-directional reflections), to develop improved algorithms for managing the CDF matrices (e.g., sparse matrix routines, data compression, and function approximation).

References

Bevans, J. T., and Edwards, D. K., 1965, "Radiation Exchange in an Enclosure with Directional Wall Properties," ASME JOURNAL OF HEAT TRANSFER, Vol. 87, pp. 388–396.

Billings, R. L., Barnes, J. W., and Howell, J. R., 1991, "Markov Analysis of Radiative Transfer in Enclosures With Bidirectional Reflections," *Numerical Heat Transfer*, Part A, Vol. 19, pp. 313–326.

Maltby, J. D., and Burns, P. J., 1991, "Performance, Accuracy, and Convergence in a Three-Dimensional Monte Carlo Radiative Heat Transfer Simulation," *Numerical Heat Transfer*, Part B, Vol. 19, pp. 191–209.

Modest, M. F., 1993, *Radiative Heat Transfer*, McGraw-Hill, New York.

Press, W. H., Flannery, B. P., Teukolsky, S. A., and Vetterling, W. T., 1992, *Numerical Recipes*, 2nd. Ed., Cambridge University Press, Cambridge, England.

Shaughnessy, B. M., 1996, "Radiative Heat Transfers in Low-Emissivity Enclosures," Ph.D. thesis, School of Mechanical Engineering, Cranfield University, England.

Siegel, R., and Howell, J. R., 1972, *Thermal Radiation Heat Transfer*, McGraw-Hill, New York.

Weiner, M. M., Tindall, J. W., and Candell, L. M., 1965, "Radiative Interchange Factors by Monte-Carlo," ASME Paper No. 65-WA/HT-51.

Heat Transfer Coefficient Enhancement With Perforated Baffles

S. Dutta,[1,2] P. Dutta,[1] R. E. Jones,[1] and J. A. Khan[1,2]

Introduction

Primarily there are three popular techniques to enhance heat transfer coefficient in channels: (i) boundary layer disturbance that is created by periodically placed ribs on the heat transfer surface; (ii) impingement cooling that uses high velocity jets to cool the surface of interest; and (iii) internal flow swirls or tape twisters that create a significant amount of bulk flow disturbance. Inclined solid baffles may be considered as a combination of ribs and channel inserts. Baffles are big enough to disturb the core flow, but like ribs, they are mounted on or near the heat transfer surface and can be spatially periodic. Perforations in inclined baffles create multiple jet impingement condition, and thus create a situation where all three major heat transfer coefficient enhancement techniques work in unison. In the past, experimental results were published with baffle plates perpendicular to the flow direction. Habib et al. (1994) have investigated heat transfer and flow over perpendicular baffles of various heights. Unlike previous publications, in our present study, we investigate heat transfer enhancement using an *inclined* baffle. The baffle plate is oriented in both stream aligned and stream opposed directions. In addition, jet impingement is added by using multiple jet hole arrays. Since the baffle is inclined, the jets can be directed toward the heat transfer surface. Characteristic friction factors and average Nusselt numbers with these inclined baffles are discussed in Dutta et al. (1997).

Experimental Facility

A suction mode blower is used to draw air through a rectangular cross-sectioned wind tunnel. The cross section of the smooth wind tunnel is 24.92 cm × 4.92 cm (channel height, H = 4.92 cm). Air enters the tunnel through a contraction and flow straighteners, and then the flow develops through a 31 H-long unheated entrance. The exit is at a 22.2 H distance downstream of the heated test section. The heated test section is 19.2 H

---

[1] Department of Mechanical Engineering, University of South Carolina, Columbia, SC 29208.

[2] Mem. ASME.

Contributed by the Heat Transfer Division for publication in the JOURNAL OF HEAT TRANSFER and presented at '97 IMECE, Dallas. Manuscript received by the Heat Transfer Division, Aug. 1, 1997; revision received, Mar. 20, 1998. Keywords: Enclosure Flows, Flow Separation, Forced Convection, Heat Exchangers, Turbulence. Associate Technical Editor: J. C. Han.

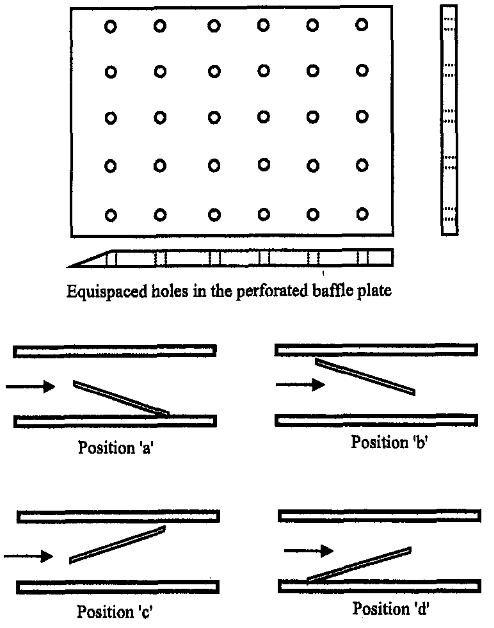

Fig. 1 Perforated baffle plate and four different inclined baffle positions

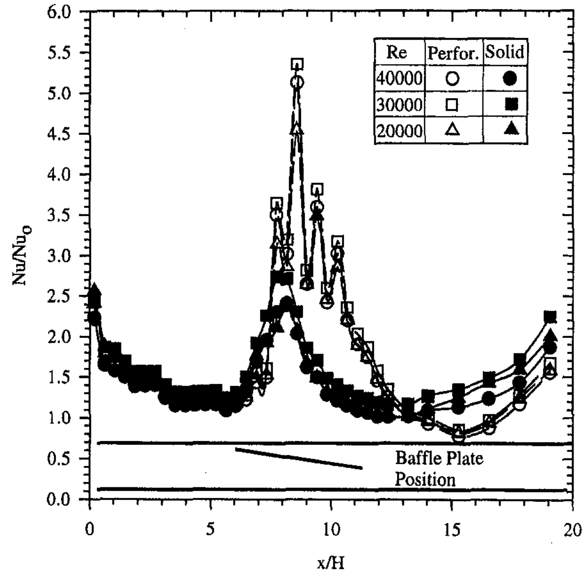

Fig. 3 Local Nusselt number ratio distribution along the channel centerline for perforated and solid baffles at position "*b*"

long, and the top surface is heated and instrumented. Other three sides are unheated and insulated. Stainless steel foil heaters are aligned perpendicular to the flow direction, similar to the configuration used by Han (1988). The thermocouples are laid along the centerline of the channel, and each strip is equipped with one thermocouple. Seven-mm diameter turbulators are located at 1.55 H upstream and 2.3 H downstream of the test section.

The solid and perforated baffle plates used are 28.9 cm long, 5 mm thick, and span the entire channel (24.92 cm). Leading edges of the baffle plates are kept sharp to reduce the flow disturbance by the protruding edge. Perforations hole diameters are $D = 1.07$ cm and center to center hole spacing is 3.56 D. Four different baffle plate positions with respect to the top heated surface are used. The baffle plate and its various positions are shown in Fig. 1. The heating starts at 6H upstream of the leading edge of the inclined baffle. The angle of inclination is 5 deg. When the baffle is mounted near the top heated surface, a gap of 3 mm between the heater surface and the baffle is maintained to avoid flow stagnation where the baffle plate contacts the channel wall. The solid baffle creates a blockage ratio of 65 percent and perforated baffles create a lower blockage due to the holes in the baffle.

The local centerline heat transfer coefficient, h, is calculated from heat flux, and wall and bulk fluid temperatures. The heat flux, q'', is the supplied electrical power divided by the total heater surface area. The heat loss is estimated from a separate heat loss experiment done on the test facility without airflow. A characteristic heat loss curve is developed for each thermocouple location. It is found that the maximum local heat flux loss, q''_{loss}, is less than six percent of the total supplied local heat flux, q''. The centerline wall temperatures are measured directly by thermocouples; and the bulk temperature is calculated by control volume energy balance technique (heat carried by the air stream). The channel centerline Nusselt number is

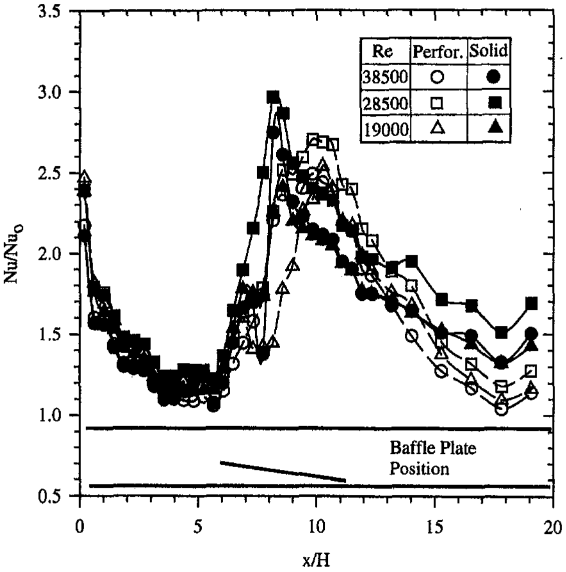

Fig. 2 Local Nusselt number ratio distribution along the channel centerline for perforated and solid baffles at position "*a*"

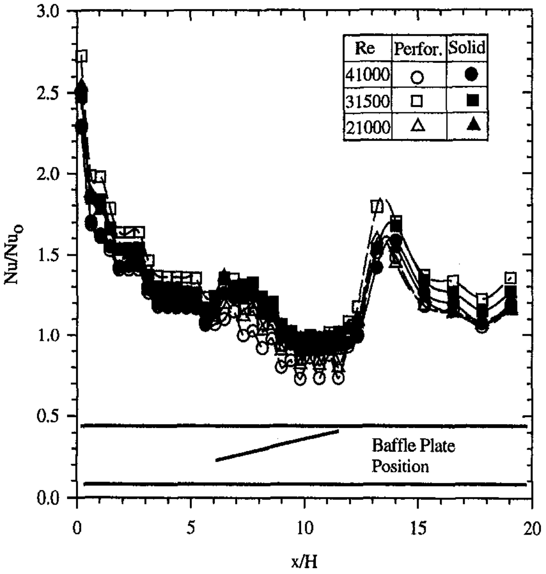

Fig. 4 Local Nuselt number ratio distribution along the channel centerline for perforated and solid baffles at position "c"

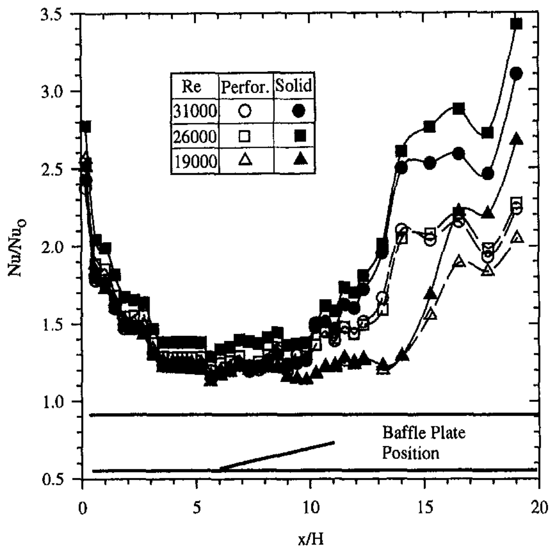

Fig. 5 **Local Nusselt number ratio distribution along the channel centerline for perforated and solid baffles at position "d"**

calculated from the heat transfer coefficient and the channel height as: $Nu = hH/K_{air}$. The Nusselt numbers are normalized to minimize the Reynolds number effect by Nu_o, Nusselt number for fully developed pipe flow at the same Reynolds number, Re. The Nu_o is a function of Re and Prandtl number, Pr, and given by Dittus-Boelter Equation as $Nu_o = 0.023\ Re^{0.8}\ Pr^{0.4}$ (Incropera and DeWitt, 1990). Maximum uncertainty estimate on the flow Reynolds number, based on channel centerline velocity and channel height, is ±2 percent and maximum uncertainty in Nusselt number, Nu, is ±3 percent.

Results and Discussion

Figures 2 to 5 show the Nusselt number ratios, Nu/Nu_o, for different baffle plate orientations. Four different positions of the baffle plate are considered, as shown in the figures (also see Fig. 1). Both solid and perforated plate results are plotted in the same graph. The Nusselt number ratio presented signifies the amount of improvement in the heat transfer coefficient obtained by the flow disturbance promoters. While verifying the test facility and instrumentation, a smooth channel Nusselt number ratio profile showed that the developed channel centerline Nusselt number ratio was within 1.1 and 1.2 at locations downstream of $x/H = 5$ at $Re = 30{,}000$. Figure 2 shows the Nusselt number distribution along the centerline of the channel for orientation "a." Initially high values of the Nusselt number ratio are due to the start of the thermal boundary layer. The Nusselt number ratio gradually decreases to nearly fully developed value before being affected by the baffle plate. The heat transfer coefficient enhancement starts immediately upstream of the baffle plate location. Results with the solid plate are higher than the perforated plate for the given configuration. The solid plate creates a flow blockage and increases the local flow velocity at the start of the baffle plate. The Nusselt number ratio peaks downstream of the maximum flow blockage. It can be argued that the flow separates in the diverging channel, and therefore, the heat transfer coefficient increases. The diverging portion of the channel indicates an increased heat transfer coefficient. The perforated plate allows some fluid to pass through the plate and increases mixing in the core flow. The maximum Nusselt number location shifts downstream with the addition of perforation and the magnitude of the Nusselt number ratio is also low in most locations with the perforated baffle plate compared to that with the solid baffle.

Figure 3 shows results for configuration "b" of the baffle plate. Unlike other three configurations, perforations improve the heat transfer coefficient in this baffle orientation. In the perforated plate, flow through holes act as impingement jets and heat transfer coefficient is significantly improved. Interestingly, the heat transfer downstream of the baffle plate is higher for the solid plate. The higher heat transfer coefficients at the end of the test section may be due to flow reattachment downstream of the baffle plate.

Figure 4 shows that the blockage created by the baffle in orientation "c" is not favorable for heat transfer enhancement. The flow leaks through the gap between the baffle plate and the heat transfer surface and there is a local peak near the end of the baffle plate. Perforated plate performs worse than the solid plate at the plate bounded region. Figure 5 shows configuration "d" of the baffle plate. The flow accelerates due to the channel constriction created by the inclined baffle. However, the Nusselt number ratio is higher in all downstream locations of the inclined baffle. Heat transfer coefficient enhancement at the downstream locations may be coupled to the wake shed by the baffle. The perforated plate performs poorly compared to the solid plate in heat transfer augmentation. Since the perforated holes allow the flow to leak through the blockage, wakes shed by perforated baffle plate are weaker than wakes generated by the solid baffle.

References

Dutta, S., Dutta, P., Jones, R. E., and Khan, J. A., 1997, "Experimental Study of Heat Transfer Coefficient Enhancement with Inclined Solid and Perforated Baffles," ASME IMECE, Dallas, TX, Nov. 16–21, ASME Paper No. 97-WA/HT-4.

Habib, M. A., Mobarak, A. M., Sallak, M. A., Abdel Hadi, E. A., and Affify, R. I., 1994, "Experimental Investigation of Heat Transfer and Flow Over Baffles of Different Heights," ASME JOURNAL OF HEAT TRANSFER, Vol. 116, pp. 363–368.

Han, J. C., 1988, "Heat Transfer and Friction Characteristics in Rectangular Channels With Rib Turbulators," ASME JOURNAL OF HEAT TRANSFER, Vol. 110, pp. 321–328.

Incropera, F. P., and DeWitt, D. P., 1990, *Fundamentals of Heat and Mass Transfer*, 3rd Ed., John Wiley and Sons, New York, p. 496.

Second-Law Analysis on Wavy Plate Fin-and-Tube Heat Exchangers

W. W. Lin[1] and D. J. Lee[1,2]

Second-law analysis on the herringbone wavy plate fin-and-tube heat exchanger was conducted on the basis of correlations of Nusselt number and friction factor proposed by Kim et al. (1997), from which the entropy generation rate was evaluated. Optimum Reynolds number and minimum entropy generation rate were found over different operating conditions. At a fixed heat duty, the in-line layout with a large tube spacing along streamwise direction was recommended. Furthermore, within the valid range of Kim et al.'s correlation, effects of the fin spacing and the tube spacing along spanwise direction on the second-law performance are insignificant.

---

[1] Department of Chemical Engineering, National Taiwan University, Taipei, Taiwan 10617, R. O. China.

[2] Corresponding author. e-mail: djlee@ccms.ntu.edu.tw.

Contributed by the Heat Transfer Division for publication in the JOURNAL OF HEAT TRANSFER. Manuscript received by the Heat Transfer Division, Dec. 15, 1997; revision received, May 4, 1998. Keywords: Finned Surfaces, Heat Transfer, Optimization, Thermodynamics. Associate Technical Editor: B. T. F. Chung.

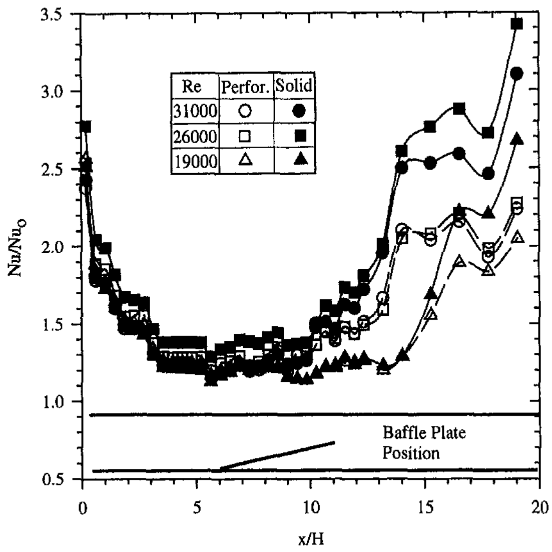

Fig. 5 Local Nusselt number ratio distribution along the channel centerline for perforated and solid baffles at position "*d*"

calculated from the heat transfer coefficient and the channel height as: $Nu = hH/K_{air}$. The Nusselt numbers are normalized to minimize the Reynolds number effect by Nu_o, Nusselt number for fully developed pipe flow at the same Reynolds number, Re. The Nu_o is a function of Re and Prandtl number, Pr, and given by Dittus-Boelter Equation as $Nu_o = 0.023\ Re^{0.8}\ Pr^{0.4}$ (Incropera and DeWitt, 1990). Maximum uncertainty estimate on the flow Reynolds number, based on channel centerline velocity and channel height, is ±2 percent and maximum uncertainty in Nusselt number, Nu, is ±3 percent.

Results and Discussion

Figures 2 to 5 show the Nusselt number ratios, Nu/Nu_o, for different baffle plate orientations. Four different positions of the baffle plate are considered, as shown in the figures (also see Fig. 1). Both solid and perforated plate results are plotted in the same graph. The Nusselt number ratio presented signifies the amount of improvement in the heat transfer coefficient obtained by the flow disturbance promoters. While verifying the test facility and instrumentation, a smooth channel Nusselt number ratio profile showed that the developed channel centerline Nusselt number ratio was within 1.1 and 1.2 at locations downstream of $x/H = 5$ at Re = 30,000. Figure 2 shows the Nusselt number distribution along the centerline of the channel for orientation "*a*." Initially high values of the Nusselt number ratio are due to the start of the thermal boundary layer. The Nusselt number ratio gradually decreases to nearly fully developed value before being affected by the baffle plate. The heat transfer coefficient enhancement starts immediately upstream of the baffle plate location. Results with the solid plate are higher than the perforated plate for the given configuration. The solid plate creates a flow blockage and increases the local flow velocity at the start of the baffle plate. The Nusselt number ratio peaks downstream of the maximum flow blockage. It can be argued that the flow separates in the diverging channel, and therefore, the heat transfer coefficient increases. The diverging portion of the channel indicates an increased heat transfer coefficient. The perforated plate allows some fluid to pass through the plate and increases mixing in the core flow. The maximum Nusselt number location shifts downstream with the addition of perforation and the magnitude of the Nusselt number ratio is also low in most locations with the perforated baffle plate compared to that with the solid baffle.

Figure 3 shows results for configuration "*b*" of the baffle plate. Unlike other three configurations, perforations improve the heat transfer coefficient in this baffle orientation. In the perforated plate, flow through holes act as impingement jets and heat transfer coefficient is significantly improved. Interestingly, the heat transfer downstream of the baffle plate is higher for the solid plate. The higher heat transfer coefficients at the end of the test section may be due to flow reattachment downstream of the baffle plate.

Figure 4 shows that the blockage created by the baffle in orientation "*c*" is not favorable for heat transfer enhancement. The flow leaks through the gap between the baffle plate and the heat transfer surface and there is a local peak near the end of the baffle plate. Perforated plate performs worse than the solid plate at the plate bounded region. Figure 5 shows configuration "*d*" of the baffle plate. The flow accelerates due to the channel constriction created by the inclined baffle. However, the Nusselt number ratio is higher in all downstream locations of the inclined baffle. Heat transfer coefficient enhancement at the downstream locations may be coupled to the wake shed by the baffle. The perforated plate performs poorly compared to the solid plate in heat transfer augmentation. Since the perforated holes allow the flow to leak through the blockage, wakes shed by perforated baffle plate are weaker than wakes generated by the solid baffle.

References

Dutta, S., Dutta, P., Jones, R. E., and Khan, J. A., 1997, "Experimental Study of Heat Transfer Coefficient Enhancement with Inclined Solid and Perforated Baffles," ASME IMECE, Dallas, TX, Nov. 16–21, ASME Paper No. 97-WA/HT-4.

Habib, M. A., Mobarak, A. M., Sallak, M. A., Abdel Hadi, E. A., and Affify, R. I., 1994, "Experimental Investigation of Heat Transfer and Flow Over Baffles of Different Heights," ASME JOURNAL OF HEAT TRANSFER, Vol. 116, pp. 363–368.

Han, J. C., 1988, "Heat Transfer and Friction Characteristics in Rectangular Channels With Rib Turbulators," ASME JOURNAL OF HEAT TRANSFER, Vol. 110, pp. 321–328.

Incropera, F. P., and DeWitt, D. P., 1990, *Fundamentals of Heat and Mass Transfer*, 3rd Ed., John Wiley and Sons, New York, p. 496.

Second-Law Analysis on Wavy Plate Fin-and-Tube Heat Exchangers

W. W. Lin[1] and D. J. Lee[1,2]

Second-law analysis on the herringbone wavy plate fin-and-tube heat exchanger was conducted on the basis of correlations of Nusselt number and friction factor proposed by Kim et al. (1997), from which the entropy generation rate was evaluated. Optimum Reynolds number and minimum entropy generation rate were found over different operating conditions. At a fixed heat duty, the in-line layout with a large tube spacing along streamwise direction was recommended. Furthermore, within the valid range of Kim et al.'s correlation, effects of the fin spacing and the tube spacing along spanwise direction on the second-law performance are insignificant.

---

[1] Department of Chemical Engineering, National Taiwan University, Taipei, Taiwan 10617, R. O. China.

[2] Corresponding author. e-mail: djlee@ccms.ntu.edu.tw.

Contributed by the Heat Transfer Division for publication in the JOURNAL OF HEAT TRANSFER. Manuscript received by the Heat Transfer Division, Dec. 15, 1997; revision received, May 4, 1998. Keywords: Finned Surfaces, Heat Transfer, Optimization, Thermodynamics. Associate Technical Editor: B. T. F. Chung.

Nomenclature

A = overall surface area (fins and tubes), m^2
A_c = minimum area of flow path, m^2
B = dimensionless group defined in Eq. (10*b*)
D = tube outer diameter, m
D_{hv} = volumetric hydraulic diameter, m
f = fanning friction factor
Gz = Graetz number
h = average heat transfer coefficient, W/m^2 K
k = thermal conductivity of liquid, W/m K
$\dot{m}$ = mass flow rate defined in Eq. (2), kg/s
N = number of rows of tubes
N_s = entropy generation number defined in Eq. (7)
$N_{s,F}$ = fluid flow irreversibility defined in Eq. (9)
$N_{s,H}$ = heat transfer irreversibility defined in Eq. (8)
$N_{s,\min}$ = minimum entropy generation number
Nu = Nusselt number
P_d = fin pattern depth, peak-to-valley excluding fin thickness, m
P_l = tube spacing in streamwise direction, m
Pr = Prandtl number
P_t = tube spacing in spanwise direction, m
ΔP = pressure drop, Pa
q = heat flow rate, W
Re_D = Reynolds number
$\mathrm{Re}_{D,\mathrm{opt}}$ = optimum Reynolds number
S = space between adjacent fins, m
S_{gen} = entropy generation rate, W/K
T = temperature, K
ΔT = temperature difference, K
t = fin thickness, m
$u_{\max}$ = maximum velocity base on A_c, m/s
X_f = projected fin pattern length for one-half wave length, m
ρ = density of fluid, kg/m^3
β = geometric parameter
μ = viscosity of fluid, kg/m s

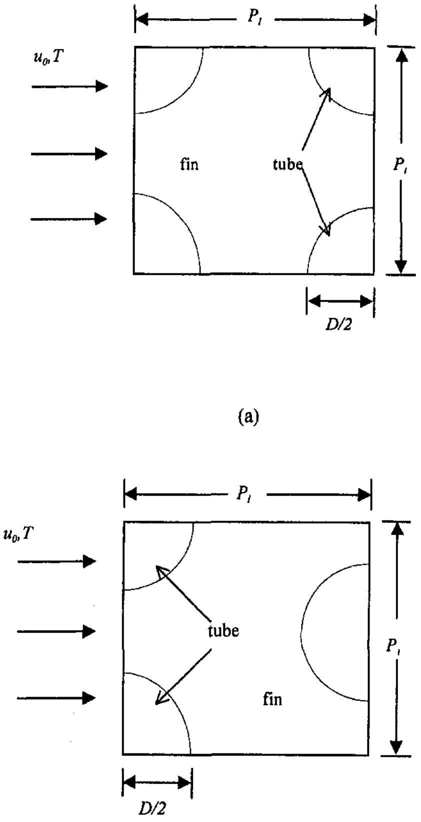

(a)

(b)

Fig. 1 Basic elements considered for wavy fin geometry; (*a*) in-line layout, (*b*) staggered layout

Introduction

Second-law analysis has influenced the design methodology of various heat and mass transfer systems (Bejan, 1996). The major concern for the second-law analysis is the entropy generation rate (or system irreversibility), while to minimize the total process entropy production is equivalent to maximize system available work. Lin and Lee (1997) conducted the second-law analysis on pin-fin arrays performance under a forced flow condition. They found that an optimal Reynolds number exists over a wide operating condition. On the basis of entropy generation rate minimization, comparisons between the staggered and the in-line pin-fin alignments were made, from which the optimal operational/design conditions were evaluated.

The fin-and-tube heat exchanger is commonly used in industry. Previous experimental works on the heat transfer and pressure drop characteristics of the herringbone wavy plate fin geometry was recently reviewed by Kim et al. (1997), in which an up-to-date correlation was derived for future usage. We considered in this Note the second-law analysis on the performance of the herringbone wavy plate fin-and-tube heat exchanger on the basis of Kim's correlation. Within the valid range of their correlation, optimum Reynolds number and the corresponding minimum entropy generation rate were evaluated at different fin/tube geometry.

Analysis

Figures 1(*a*) and 1(*b*) depict schematically the alignment of the fin-and-tube heat exchanger. A fluid (pure substance) of velocity u_0 and temperature T is flowing across the fin assembly. Assuming $\Delta T/T \ll 1$ and a negative pressure gradient, the entropy generation rate for fluid flowing across the element has been stated as (Bejan, 1996)

$$S_{\mathrm{gen}} = \frac{q\Delta T}{T^2} + \frac{\dot{m}|\Delta P|}{\rho T}, \tag{1}$$

where ΔT is the average temperature difference between solid surface and bulk fluid; $|\Delta P|$ is the pressure difference across the element,

$$\dot{m} = u_{\max}[(P_t - D)S]\rho, \tag{2}$$

in which $u_{\max}$ is the maximum average fluid velocity occurring at the minimum cross-section area available for fluid flow (A_c); and q, the total heat exchange rate through heat transfer area (A), where

$$q = hA\Delta T, \tag{3}$$

and h is the average heat transfer coefficient of the element.

ΔP in Eq. (1) can be described by defining the friction factor as follows:

$$\Delta P = f\left(\frac{A}{A_c}\right)\left(\frac{\mathrm{Gz}^2}{2\rho}\right), \tag{4}$$

where the ratio A/A_c is

$$\frac{A}{A_c} = \frac{2(1-\beta)\left(\frac{P_t}{P_l}\right)\left(\frac{P_l}{D}\right)^2 + \pi\left(\frac{S}{D}\right)}{\left(\frac{S}{D}\right)\left[\left(\frac{P_t}{P_l}\right)\left(\frac{P_l}{D}\right) - 1\right]}, \qquad (5)$$

and Gz is the Graetz number defined as (Kim et al., 1997)

$$\mathrm{Gz} = \frac{\mathrm{Re}_D\left(\frac{D_{hv}}{D}\right)^2 \mathrm{Pr}\left[1 - \frac{1}{(P_t/P_l)(P_l/D)}\right]}{N\left(\frac{P_l}{D}\right)(1-\beta)}. \qquad (6)$$

Pr in Eq. (6) is the fluid's Prandtl number, D_{hv} is the volumetric hydraulic diameter and parameter β is the fraction of the channel volume occupied by the tube (defined in Kim et al., 1997). Substituting Eqs. (2)–(6) into Eq. (1) yields the dimensionless entropy generation number

$$N_s = \frac{S_{\mathrm{gen}}}{\left(\frac{q^2}{kDT^2}\right)} = N_{s,H} + N_{s,F}, \qquad (7)$$

where $N_{s,H}$ is the entropy generation rate owing to heat transfer irreversibility,

$$N_{s,H} = \frac{(D_{hv}/D)}{\mathrm{Nu}}\left[2(1-\beta)\left(\frac{P_t}{P_l}\right)\left(\frac{P_l}{D}\right)^2 + \pi\left(\frac{S}{D}\right)\right]^{-1}, \qquad (8)$$

and $N_{s,F}$ is due to the fluid flow irreversibility,

$$N_{s,F} = \frac{1}{2} Bf\,\mathrm{Re}_D\,\mathrm{Gz}^2\left(\frac{A}{A_c}\right)\left[\left(\frac{P_t}{P_l}\right)\left(\frac{P_l}{D}\right) - 1\right]\left(\frac{S}{D}\right). \qquad (9)$$

Some undefined dimensionless groups appearing in Eqs. (8)–(9) are as follows:

$$\mathrm{Re}_D = \frac{\rho u_{\max} D}{\mu}; \quad B = \frac{D^2 \mu k T}{\rho^2 q^2}; \quad \mathrm{Nu} = \frac{hD_{hv}}{k}. \qquad (10a\text{–}c)$$

Correlations for the Nusselt number (Nu) and friction factor (f) were available in Kim et al. (1997) and were not listed here for brevity's sake. (Note: In Kim et al.'s paper, for staggered and in-line configurations, the equations corresponding to correlations for the Nusselt number were Eqs. (13)–(14) and (21)–(22), and for the friction factor, Eq. (20) and Eq. (23), respectively.)

The entropy generation number, N_s, is thereby a function of operational parameters (Re_D, B), fluid property (Pr), and fin-and-tube heat exchanger parameters (N, P_t/P_l, P_l/D, S/D, P_d/X_f, P_d/S). Since the correlation by Kim et al. (1997) is limited to the following constraints, $N = 4$, $P_t/P_l = 1$, $P_d/X_f = 1/4.083$ and $\mathrm{Pr} = 0.705$ (air), the remaining control parameters are Re_D, B, P_l/D, S/D, and P_d/S. As a result, at a fixed heat duty (B) and a prescribed geometry, the minimum of N_s with respect to Re_D can be evaluated by solving $\partial N_s/\partial\,\mathrm{Re}_D = 0$ graphically, while the corresponding optimal $\mathrm{Re}_{D,\mathrm{opt}}$ can be subsequently obtained.

Results and Discussion

Optimal Reynolds Number. Figure 2 illustrates an example of the N_s versus Reynolds number plot for the staggered and the in-line tube layout at a fixed heat duty and geometry. $N_{s,H}$ ($N_{s,F}$) decreases (increases) with an increase in Re_D for the staggered layout (bold curves) and the in-line layout (dashed curves). Notably, both the $N_{s,H}$ and $N_{s,F}$ are greater for staggered layout than for the in-line layout, thereby giving a higher N_s for the former. The minimum entropy generation number (and hence the optimum Reynolds number) are read out from the figure. The results are, for staggered layout, $\mathrm{Re}_{D,\mathrm{opt}} = 3065$ and $N_{s,\min} = 4.34 \times 10^{-3}$; and for in-line layout, $\mathrm{Re}_{D,\mathrm{opt}} = 3020$ and $N_{s,\min} = 7.56 \times 10^{-4}$. Although the $N_{s,\min}$ is five times higher for the staggered layout, the corresponding $\mathrm{Re}_{D,\mathrm{opt}}$'s are alike.

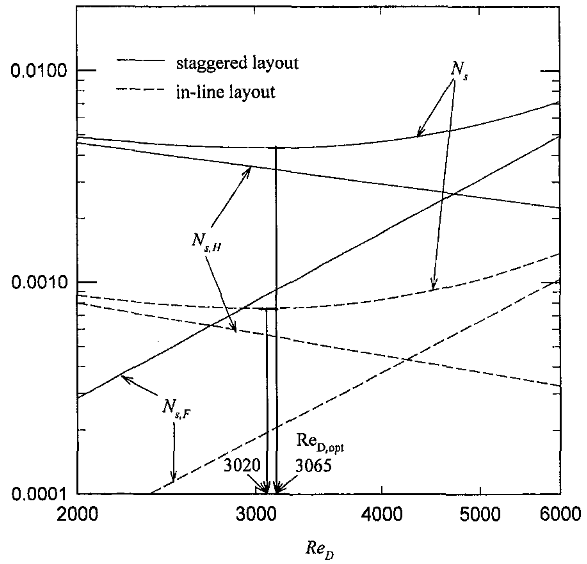

Fig. 2 N_s, $N_{s,F}$, and $N_{s,H}$ versus Reynolds number. $B = 1 \times 10^{-12}$, $\mathrm{Pr} = 0.705$, $N = 4$, $P_t/P_l = 1$, $P_l/D = 2$, $S/D = 0.32$, $P_d/X_f = 1/4.083$, $P_d/S = 0.5$.

In the following discussion we will focus on the effects of the heat duty and geometry of tube-and-fin heat exchanger on the $\mathrm{Re}_{D,\mathrm{opt}}$ and $N_{s,\min}$.

Effects of Heat Duty and Geometry. Figures 3(a) and 3(b) depict the $\mathrm{Re}_{D,\mathrm{opt}}$ and $N_{s,\min}$ versus B plot, with P_l/D as a parameter. Notably, a greater B value increases only the fluid flow rather than heat transfer irreversibility (Eqs. (9)) that favors lower flow velocity. The $\mathrm{Re}_{D,\mathrm{opt}}$ is thereby reduced. The total amount of irreversibility increases with B, as evidenced by the greater $N_{s,\min}$ in Fig. 3(b).

An increase in tube spacing (P_l/D) would markedly reduce $N_{s,H}$, since the fin area increases accordingly. On the other hand, owing to the same reasoning, the effects on $N_{s,F}$ is relatively less. As a result, the system favors a greater Reynolds number for delivering more heat by paying for a similar pressure drop, which leads to a less $\mathrm{Re}_{D,\mathrm{opt}}$ and a lower $N_{s,\min}$ at elevated P_l/D.

Figures 4(a) and 4(b) illustrate the effects of fin spacing (S/D) and wave height (P_d/S). Larger S/D leads to a higher $\mathrm{Re}_{D,\mathrm{opt}}$ and a (slightly) less $N_{s,\min}$. This is attributed to the lesser pressure drop (with $N_{s,F}$) at the greater fin spacing. The influence on heat transfer is insignificant since the total heat transfer area is almost unchanged. Consequently, a smaller $N_{s,F}$ and nearly constant $N_{s,H}$ at elevated S/D yields a greater $\mathrm{Re}_{D,\mathrm{opt}}$ and a smaller $N_{s,\min}$. However, the effect is relatively insignificant as compared to those depicted in Fig. 3.

A larger wave height (P_d/S) would lead to a higher $\mathrm{Re}_{D,\mathrm{opt}}$ and a greater $N_{s,\min}$ for staggered layout, but has no effect on in-line layout. For a staggered layout, a larger P_d/S at fixed S/D (with all the other geometrical factors fixed) implies a lesser fin spacing (S) with a lesser tube diameter (D). The effects of the latter is more important than that of the former, and the net result is to give an increasing $N_{s,H}$. Furthermore, the effect on $N_{s,F}$ is almost negligible. This corresponds to the higher $\mathrm{Re}_{D,\mathrm{opt}}$ and $N_{s,\min}$ noted in Fig. 4. Once again, as compared with Fig. 3, the influence is as well relatively small.

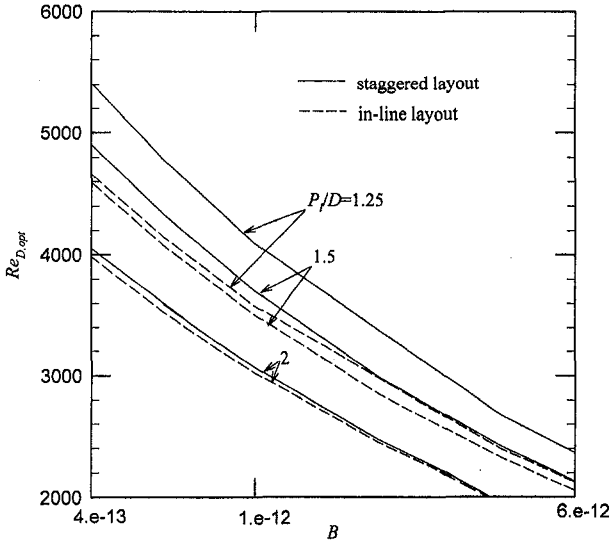

Fig. 3(*a*) $Re_{D,opt}$ versus *B* plot with P_l/D as a parameter. Pr = 0.705, *N* = 4, P_t/P_l = 2, *S*/*D* = 0.32, P_d/X_f = 1/4.083, P_d/S = 0.5.

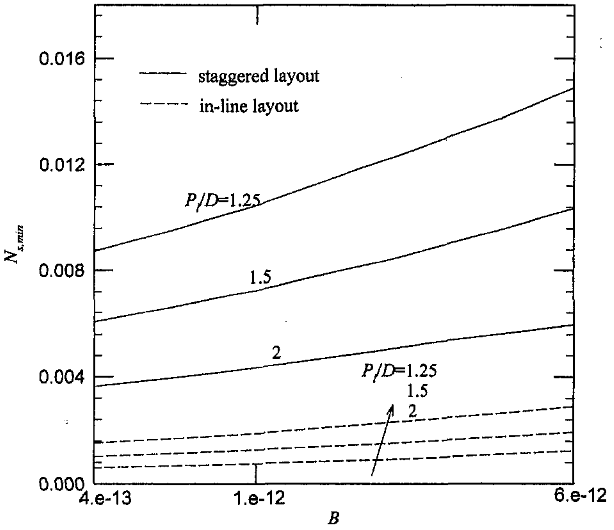

Fig. 3(*b*) $N_{s,min}$ versus *B* plot with P_l/D as a parameter. Pr = 0.705, *N* = 4, P_t/P_l = 2, *S*/*D* = 0.32, P_d/X_f = 1/4.083, P_d/S = 0.5.

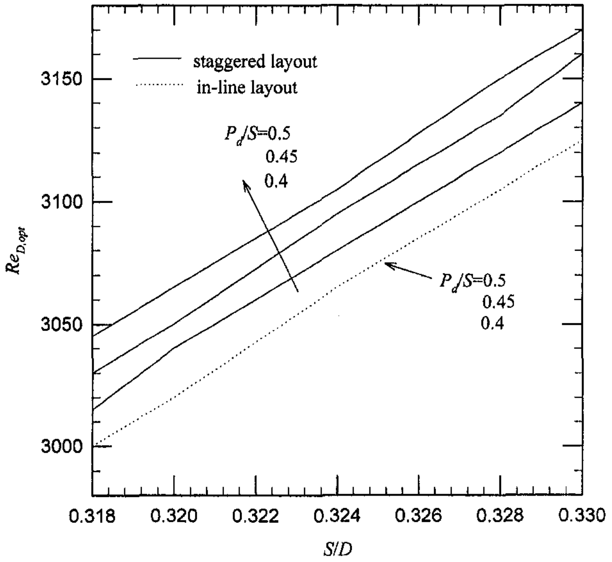

Fig. 4(*a*) $Re_{D,opt}$ versus *S*/*D* plot with P_d/S as a parameter. *B* = 1 × 10^{-12}, Pr = 0.705, *N* = 4, P_t/P_l = 1, P_l/D = 2, P_d/X_f = 1/4.083.

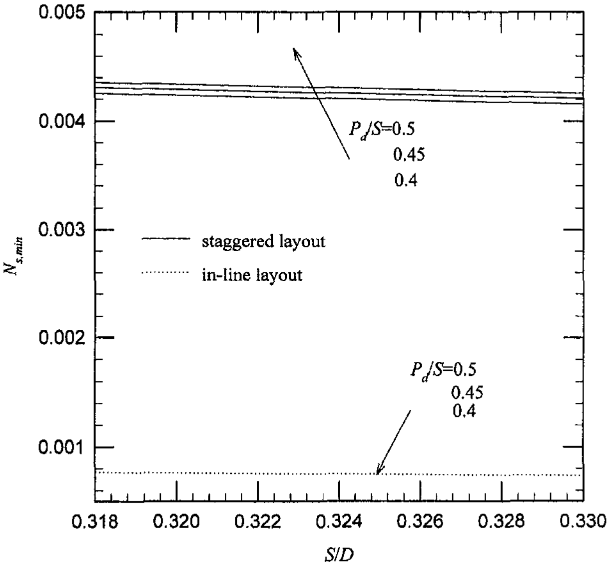

Fig. 4(*b*) $N_{s,min}$ versus *S*/*D* plot with P_d/S as a parameter. *B* = 1 × 10^{-12}, Pr = 0.705, *N* = 4, P_t/P_l = 1, P_l/D = 2, P_d/X_f = 1/4.083.

For the in-line layout, however, the only significant geometrical factor in Kim et al.'s (1997) correlation for the Nusselt number is S/D, not P_d/S. As a result, we found no dependence of P_d/S on data depicted in Fig. 4.

On the basis of the second-law analysis, at a fixed heat duty, a herringbone wave plate fin-and-tube heat exchanger of an in-line layout with a large P_l/D was recommended. On the other hand, the effects of P_d/S and S/D are insignificant over the range where Kim et al.'s correlation is valid. However, inasmuch as the range for S/D (0.318 to 0.33) covered by their correlation is relatively narrow (four percent), the significance of changing S/D over a wide range remains unclear.

Conclusions

Second-law analysis on herringbone wave plate fin-and-tube heat exchanger was conducted on the basis of correlations proposed by Kim et al. (1997), from which the entropy generation rate was evaluated. Increase in the fluid velocity not only enhances heat transfer rate (reduces heat transfer irreversibility) but also raises the pressure drop (increases fluid flow irreversibility). An optimum Reynolds number thereby exists over wide operating conditions. On the basis of second-law analysis, at a fixed heat duty, the in-line layout with a large P_l/D was recommended. Effects of P_d/S and S/D are insignificant over the range where Kim et al.'s correlation is valid. This last conclusion requires further investigation inasmuch as their correlation is valid over a narrow range of S/D.

Acknowledgment

This work is supported by National Science Council, R.O.C.

References

Bejan, A., 1996, *Entropy Generation Minimization,* CRC Press, Boca Raton, FL.

Kim, N.-H., Yun, J.-H., and Webb, R. L., 1997, "Heat Transfer and Friction Correlations for Wavy Plate Fin-and-Tube Heat Exchangers," ASME JOURNAL OF HEAT TRANSFER, Vol. 119, pp. 560–567.

Lin, W. W., and Lee, D. J., 1997, "Second-Law Analysis on a Pin-Fin Array Under Crossflow," *Int. J. Heat Mass Transfer,* Vol. 40, pp. 1937–1945.

Journal of Heat Transfer

Discussion

Analysis of Matrix Heat Exchanger Performance[1]

V. Ahuja[2] and R. K. Green[3]. *Recently, a new numerical scheme for solving the equations governing matrix heat exchanger thermal performance was published in this journal. It was found that this scheme does not include the full effect of longitudinal heat transfer in the said heat exchangers. This effect is demonstrated by correcting the parameter related to longitudinal heat transfer in the approximate analytical solution for the balanced flow case and finding it to deviate considerably from the numerically calculated result.*

Nomenclature

A = heat transfer surface area, m^2
A_{cr} = spacer area, m^2
A_{fr} = frontal area, m^2
b = separator width, m
C = mc_p, J/s·K
c_p = specific heat, fluid, J/kg·K
G_o = fluid mass velocity in perforation, kg/s·m^2
G = $G_o p$, fluid mass velocity in header, kg/s·m^2
H_f = fin height, m
k_{ax} = axial conductivity, W/m·K
k_p = conductivity, perforated plate, W/m·K
k_{plate} = conductivity, plate material, W/m·K
k_s = conductivity, spacer material, W/m·K
m = mass flow rate, kg/s
n = number of plates in matrix heat exchanger
Ntu = Number of transfer units
p = plate porosity
s = separator thickness, m
U = overall heat transfer coefficient, W/m^2·K
W = Plate width, m
β = surface area per unit volume, m^2/m^3
δ = plate thickness, m
λ = overall axial conduction parameter, Eq. (3)
λ_p = plate conduction parameter, Eq. (5)
ν = heat capacity rate ratio
ϕ = $\text{Ntu}_{p,i}/\text{Ntu}_{f,i}$

Subscripts

D = design
eff = effective
f = fluid
i = channel number (1 or 2)
o = overall
p = plate (perforated)

Review

Venkatarathnam and Sarangi (1991) derived equations governing the heat transfer in a matrix heat exchanger. These equations were reduced to two second-order ordinary differential equations and four algebraic equations describing the energy balance and heat transfer for every plate, based on the assumption that the axial temperature gradient in the plate is negligible and hence the full temperature drop takes place across the spacer. They describe a new numerical scheme to solve these equations. This analysis accounts for the discrete plate-spacer pair set structure of the matrix heat exchanger, and nonunity fin effectiveness. Details of this work and a listing of the program incorporating this numerical scheme are covered in Venkatarathnam's Ph.D. thesis (1991).

Venkatarathnam (1996) has subsequently published an approximate analytical solution for the matrix heat exchanger governing equations. The approximate analytical solution for the equations for energy balance and heat transfer, accounting for the heat transfer coefficient, axial conduction, number of plates, and fin effectiveness in the matrix heat exchangers, for balanced flow is shown in Eq. (1).

$$\text{Ntu}_{\text{eff}} = \frac{n(1-\alpha_1)(1-\alpha_2)}{\lambda n(1-\alpha_1)(1-\alpha_2) + 1 - \alpha_1\alpha_2 + (1-\alpha_1)(1-\alpha_2)/\text{Ntu}_{po}} \quad (1)$$

where

$$\alpha_i = e^{-\text{Ntu}_{f,i}} \quad (2)$$

$$\lambda = \frac{k_s b W}{n s C}, \quad (3)$$

and Ntu_{po}, the overall plate Ntu, is defined as

$$\frac{1}{\text{Ntu}_{po}} = \frac{1}{\lambda_p} + \frac{1}{3\phi_1 \text{Ntu}_{f,1}} + \frac{\nu}{3\phi_2 \text{Ntu}_{f,2}} \quad (4)$$

with

$$\lambda_p = \frac{k_{\text{plate}} \delta W}{bC} \quad (5)$$

$$\phi = \frac{\text{Ntu}_{p,i}}{\text{Ntu}_{f,i}} = \frac{k_p}{h\beta H_f^2} \quad (6)$$

$$k_p = k_{\text{plate}} \left(\frac{1-p}{1+p}\right). \quad (7)$$

---

[1] Venkatarathnam, G., and Sarangi, S., 1991, "Analysis of Matrix Heat Exchanger Performance," ASME Journal of Heat Transfer, Vol. 113, pp. 830–836.

[2] CSIRO Manufacturing Science and Technology, Locked Bag 9 (cnr. Albert and Raglan Streets), Preston, Victoria 3072, Australia. e-mail: vikas.ahuja@mlb.dmt.csiro.au

[3] Directorate, Otago Polytechnic, Private Bag 1910, Denedin, New Zealand. e-mail: rgreen@tekotago.ac.nz

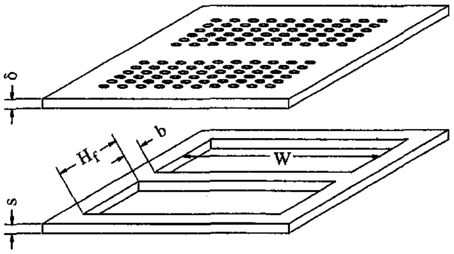

Fig. 1 Perforated plate and spacer dimensions

Plate and spacer dimensions relevant to these equations are shown in Fig. 1.

Longitudinal Conduction

The control volume for which the energy balance is considered for deriving the governing equations does not include the area over which longitudinal conduction occurs other than the separator. The axial conduction parameter defined in Eq. (3) incorporates a spacer area equivalent only to that of the separator (bW). The parameters λ_p and $\lambda_s = n\lambda$ are derived from the energy balance for the separator, for the numerical solution. Venkatarathnam has then applied λ to the approximate analytical solution as the overall axial conduction parameter to account for axial conduction as done by Kroeger (1969). However, Kroeger has used the overall axial conductivity and total area for axial conduction to define this axial conduction parameter λ as

$$\lambda = \frac{k_{ax}A_{cr}}{n(\delta + s)C} \tag{8}$$

where

$$k_{ax} = \frac{\delta + s}{\dfrac{\delta}{k_{\text{plate}}} + \dfrac{s}{k_s}} . \tag{9}$$

Venkatarathnam's use of λ thus represents a small proportion of the area over which axial conduction occurs, and the net axial conductivity. The effect of taking λ from (3) or (8) is shown in Fig. 2.

Venkatarathnam's results were presented as Ntu_{eff} versus Ntu_D graphs for constant ϕ and λ. A matrix heat exchanger of given geometry at one flow condition would represent a single point on such a graph. Figure 2 shows Ntu_{eff} versus Ntu_D plotted for given constant geometric parameters. Venkatarathnam's approximate analytical and numerical solutions only show agreement provided λ is calculated for the separator alone. If λ is taken as the overall axial conduction parameter, the approximate analytical solution deviates considerably from the numerical solution. As to whether the numerical solution can take into account axial conduction in the heat exchanger body other than in the separator is uncertain.

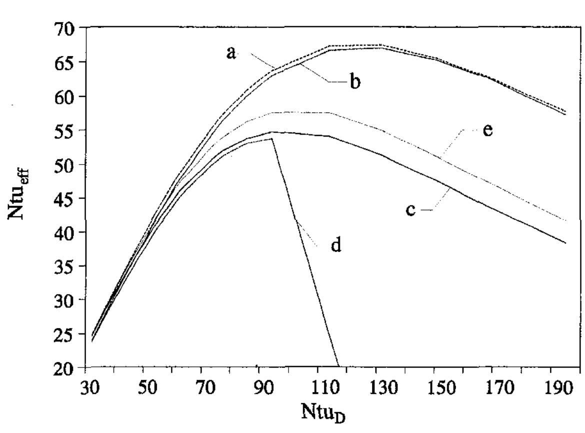

Fig. 2 Ntu_{eff} **versus** Ntu_D **for *a*: Venkatarathnam, analytical; *b*: Venkatarathnam, numerical; *c*: analytical, using** λ **from (8); *d*: numerical, using** λ **from (8); *e*: analytical solution using Fleming's (1969) equation for fin effectiveness and Kroeger's method for longitudinal conduction**

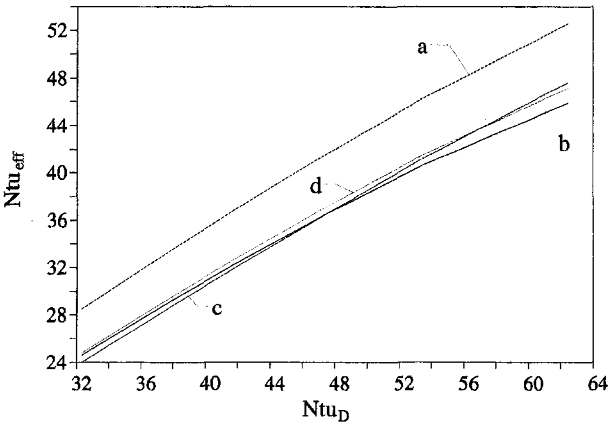

Fig. 3 Ntu_{eff} **versus** Ntu_D **for *a*: Venkatarathnam, analytical with** $\lambda_p = \infty$**; *b*: this work, with finite values for** λ_p**; *c*: Venkatarathnam, numerical; *d*: analytical solution using Fleming's equation for fin effectiveness and Kroeger's method for longitudinal conduction**

The source code of the program incorporating Venkatarathnam's numerical solution for the energy balance and heat transfer equations, as presented in his thesis, does not run. A running version of the program in his thesis was obtained through correspondence with the author (1995). He stated that the program included in his thesis is a pared down version of a larger program and suggested changes to the listed source code. The modified version gives results which concur with the graphs presented in his various papers and thesis. However, the modified version still produces absurd results (negative values of Ntu_{eff}) if the axial conduction parameter is proportionately higher than some undefined limit. An example of this is shown in Fig. 2, by taking a value of λ comparable to that from (8) for the numerical solution. The efficacy of this numerical solution and associated program is thus questionable.

Lateral Conduction

Venkatarathnam has used the simplification of neglecting transverse resistance in the separator by assuming the plate conduction parameter $\lambda_p = \infty$. Thus for $\alpha_1 = \alpha_2$

$$\text{Ntu}_{\text{eff}} = \frac{n(1 - \alpha_i)}{n\lambda(1 - \alpha_i) + (1 + \alpha_i) + \dfrac{(1 - \alpha_i)}{\text{Ntu}_{po}}} , \tag{10}$$

and from

$$\text{Ntu}_D = n\left(\frac{1}{\text{Ntu}_{f,1}} + \frac{1}{\text{Ntu}_{f,2}} + \frac{1}{\lambda_p}\right)^{-1} \tag{11}$$

$$\text{Ntu}_{f,i} = \frac{2Ntu_D}{n} \tag{12}$$

$$\text{Ntu}_{po} = \frac{3}{2}\,\text{Ntu}_{p,i} = \frac{3k_p\delta}{2G_o pc_p H_f^2} . \tag{13}$$

The effect of taking $\lambda_p = \infty$ is shown in Fig. 3. The convection heat transfer coefficients for the matrix heat exchanger are much higher than those normally associated with gaseous heat transfer media. It is apparent that the simplification of $\lambda_p = \infty$ may not be justifiable for the low Reynolds number flows which are characteristic of matrix heat exchangers.

Sizing Equation

The analytical solution for the balanced flow case lends itself to further simplification. For design purposes a sizing equation can be derived from Eq. (1) by re-arranging the terms and solving by substitution. The sizing equation gives the surface area required for any known desired Ntu. From (1), (2), (8), and (13), neglecting conduction resistance

$$\mathrm{Ntu}_{\mathrm{eff}} = \frac{n}{\dfrac{k_{ax}A_{cr}}{(\delta + s)C} + \dfrac{1 + e^{-\mathrm{Ntu}_{f,i}}}{1 - e^{-\mathrm{Ntu}_{f,i}}} + \dfrac{2G_o p c_p H_f^2}{3k_p\delta}}. \quad (14)$$

Taking the number of plates as

$$n = \frac{A}{\beta A_{fr}\delta}, \quad (15)$$

Eq. (14) can be solved as

$$A = \left[e^{2\tanh^{-1}(-h\beta\delta/Gc_p)} + \frac{k_{ax}A_{cr}}{(\delta + s)C} + \frac{2Gc_pH_f^2}{3k_p\delta}\right]\beta W H_f \delta \mathrm{Ntu}_{\mathrm{eff}}. \quad (16)$$

If conduction resistance is included then

$$\mathrm{Ntu}_{po} = \frac{3k_p\delta W}{C\left(2H_f + 3\left(\dfrac{1 - p}{1 + p}\right)b\right)} \quad (17)$$

giving

$$A = \left[e^{2\tanh^{-1}(-h\beta\delta/Gc_p)} + \frac{k_{ax}A_{cr}}{(\delta + s)C} + \frac{GH_fc_p\left(2H_f + 3\left(\dfrac{1 - p}{1 + p}\right)b\right)}{3k_p\delta}\right]\beta W H_f \delta \mathrm{Ntu}_{\mathrm{eff}}. \quad (18)$$

Conclusion

The new numerical scheme developed by Venkatarathnam and Sarangi (1991) for solving the equations governing heat transfer in matrix heat exchangers has been shown to neglect the full effect of longitudinal heat transfer. The efficacy of the program listing available in open literature, which incorporates this numerical scheme, is questionable. It is recommended that for matrix heat exchanger performance analysis, the analytical solution be used with the corrected axial conduction parameter.

References

Fleming, R. B., 1969, "A compact perforated plate heat exchanger," *Advances in Cryogenic Engineering*, Vol. 14, pp. 197–204.

Kroeger, P. G., 1967, "Performance deterioration in high effectiveness heat exchangers due to axial conduction effects," *Advances in Cryogenic Engineering*, Vol. 12, pp. 363–372.

Venkatarathnam, G., 1991, "Matrix heat exchangers," Ph.D. thesis, Indian Institute of Technology, Kharagpur, India.

Venkatarathnam, G., 1995, private correspondence, Indian Institute of Technology, Madras, India.

Venkatarathnam, G., 1996, "Effectiveness N_{tu} relationship in perforated plate matrix heat exchangers," *Cryogenics*, Vol. 36, No. 4, pp. 235–241.

Venkatarathnam, G. and Sarangi, S., 1991, "Analysis of Matrix Heat Exchanger Performance," ASME JOURNAL OF HEAT TRANSFER, Vol. 113, pp. 830–836.

Authors' Closure

Vikas Ahuja has discussed the need to include the full cross-sectional area of the walls that separate the streams from the environment as well as that which separates the streams from one another in calculating the longitudinal conduction parameter originally presented by the authors. He has also raised some points on the accuracy of the work. The salient features of the methods proposed by us are reviewed and the points raised by Ahuja have been answered in this closure.

Introduction

Ahuja has compared the effective number of transfer units (effectiveness) estimated using a numerical scheme presented by the authors in the *Journal of Heat Transfer* (Venkatarathnam and Sarangi, 1991) and an analytical solution presented by Venkatarathnam (Venkatarathnam, 1996) recently in *Cryogenics.* The main point raised by Ahuja is that the definition of the longitudinal heat conduction parameter should include the total foot print area of the low conductivity spacer that separates the copper perforated plates, and not the area of the wall that separates the two streams alone, as defined in our paper. He has also compared the performance when the lateral resistance of the wall is neglected, and has stressed the need for accounting for the same. The points raised by Ahuja are answered in this closure.

Longitudinal Heat Conduction

The walls of the perforated plate matrix heat exchanger are formed by bonding a stack of alternating low thermal conductivity (plastic/stainless steel) spacers and copper perforated plates to form a monolithic block (Fig. 1). The walls that separate the streams from the environment and that which separate the two streams are thus interconnected. In deriving the governing equations, it was assumed that the longitudinal heat conduction occurs only through the walls that separate the streams, to simplify the analysis. This assumption has been made by many workers (Kroeger, 1967) who have studied the performance degradation due to longitudinal heat conduction through the walls of heat exchangers. These assumptions are meant only to simplify the analysis and make the problem tractable. While analyzing the performance of any real heat exchanger it is necessary to take the longitudinal heat conduction through all the walls. In most cases, the performance of the heat exchanger will be slightly underpredicted if the longitudinal heat conduction through the outer walls is accounted for by adding the cross-sectional areas of the outer and inner walls, and assuming that all the longitudinal heat conduction occurs only through the inner wall alone (Narayanan, 1997).

It is well known that the longitudinal heat conduction parameter should be estimated using the area of all the walls of any exchanger, including perforated plate matrix heat exchangers. To demonstrate the basic principles of heat exchangers, Mills (1996) used the total foot print area to evaluate the longitudinal heat conduction parameter and predict the performance degradation due to longitudinal heat conduction in perforated plate heat exchangers. Thus, the suggestion made by Ahuja is not new.

Figure 2 shows the temperature profile in the wall separating the streams. Because of the small thickness of the copper perforated plates (typically 0.2 to 1.0 mm thick), the temperature of any copper perforated plate will essentially be uniform in the longitudinal direction (Sarangi and Barclay, 1984, Venkatarathnam and Sarangi, 1991). The total temperature drop across the wall is almost totally sustained by the low conductivity (plastic or stainless steel) spacers separating the copper perforated

---

[1] G. Venkatarathnam, Department of Mechanical Engineering, Indian Institute of Technology, Chennai 600 036, India and S. Sarangi, Cryogenic Engineering Centre, Indian Institute of Technology, Kharagpur 721 302, India.

be justifiable for the low Reynolds number flows which are characteristic of matrix heat exchangers.

Sizing Equation

The analytical solution for the balanced flow case lends itself to further simplification. For design purposes a sizing equation can be derived from Eq. (1) by re-arranging the terms and solving by substitution. The sizing equation gives the surface area required for any known desired Ntu. From (1), (2), (8), and (13), neglecting conduction resistance

$$\mathrm{Ntu}_{\mathrm{eff}} = \frac{n}{\dfrac{k_{ax}A_{cr}}{(\delta + s)C} + \dfrac{1 + e^{-\mathrm{Ntu}_{f,i}}}{1 - e^{-\mathrm{Ntu}_{f,i}}} + \dfrac{2G_o p c_p H_f^2}{3k_p\delta}}. \quad (14)$$

Taking the number of plates as

$$n = \frac{A}{\beta A_{fr}\delta}, \quad (15)$$

Eq. (14) can be solved as

$$A = \left[e^{2\tanh^{-1}(-h\beta\delta/Gc_p)} + \frac{k_{ax}A_{cr}}{(\delta + s)C} + \frac{2Gc_pH_f^2}{3k_p\delta}\right]\beta W H_f \delta \mathrm{Ntu}_{\mathrm{eff}}. \quad (16)$$

If conduction resistance is included then

$$\mathrm{Ntu}_{po} = \frac{3k_p\delta W}{C\left(2H_f + 3\left(\dfrac{1 - p}{1 + p}\right)b\right)} \quad (17)$$

giving

$$A = \left[e^{2\tanh^{-1}(-h\beta\delta/Gc_p)} + \frac{k_{ax}A_{cr}}{(\delta + s)C} + \frac{GH_fc_p\left(2H_f + 3\left(\dfrac{1 - p}{1 + p}\right)b\right)}{3k_p\delta}\right]\beta W H_f \delta \mathrm{Ntu}_{\mathrm{eff}}. \quad (18)$$

Conclusion

The new numerical scheme developed by Venkatarathnam and Sarangi (1991) for solving the equations governing heat transfer in matrix heat exchangers has been shown to neglect the full effect of longitudinal heat transfer. The efficacy of the program listing available in open literature, which incorporates this numerical scheme, is questionable. It is recommended that for matrix heat exchanger performance analysis, the analytical solution be used with the corrected axial conduction parameter.

References

Fleming, R. B., 1969, "A compact perforated plate heat exchanger," *Advances in Cryogenic Engineering*, Vol. 14, pp. 197–204.

Kroeger, P. G., 1967, "Performance deterioration in high effectiveness heat exchangers due to axial conduction effects," *Advances in Cryogenic Engineering*, Vol. 12, pp. 363–372.

Venkatarathnam, G., 1991, "Matrix heat exchangers," Ph.D. thesis, Indian Institute of Technology, Kharagpur, India.

Venkatarathnam, G., 1995, private correspondence, Indian Institute of Technology, Madras, India.

Venkatarathnam, G., 1996, "Effectiveness N_{tu} relationship in perforated plate matrix heat exchangers," *Cryogenics*, Vol. 36, No. 4, pp. 235–241.

Venkatarathnam, G. and Sarangi, S., 1991, "Analysis of Matrix Heat Exchanger Performance," ASME JOURNAL OF HEAT TRANSFER, Vol. 113, pp. 830–836.

Authors' Closure

Vikas Ahuja has discussed the need to include the full cross-sectional area of the walls that separate the streams from the environment as well as that which separates the streams from one another in calculating the longitudinal conduction parameter originally presented by the authors. He has also raised some points on the accuracy of the work. The salient features of the methods proposed by us are reviewed and the points raised by Ahuja have been answered in this closure.

Introduction

Ahuja has compared the effective number of transfer units (effectiveness) estimated using a numerical scheme presented by the authors in the *Journal of Heat Transfer* (Venkatarathnam and Sarangi, 1991) and an analytical solution presented by Venkatarathnam (Venkatarathnam, 1996) recently in *Cryogenics.* The main point raised by Ahuja is that the definition of the longitudinal heat conduction parameter should include the total foot print area of the low conductivity spacer that separates the copper perforated plates, and not the area of the wall that separates the two streams alone, as defined in our paper. He has also compared the performance when the lateral resistance of the wall is neglected, and has stressed the need for accounting for the same. The points raised by Ahuja are answered in this closure.

Longitudinal Heat Conduction

The walls of the perforated plate matrix heat exchanger are formed by bonding a stack of alternating low thermal conductivity (plastic/stainless steel) spacers and copper perforated plates to form a monolithic block (Fig. 1). The walls that separate the streams from the environment and that which separate the two streams are thus interconnected. In deriving the governing equations, it was assumed that the longitudinal heat conduction occurs only through the walls that separate the streams, to simplify the analysis. This assumption has been made by many workers (Kroeger, 1967) who have studied the performance degradation due to longitudinal heat conduction through the walls of heat exchangers. These assumptions are meant only to simplify the analysis and make the problem tractable. While analyzing the performance of any real heat exchanger it is necessary to take the longitudinal heat conduction through all the walls. In most cases, the performance of the heat exchanger will be slightly underpredicted if the longitudinal heat conduction through the outer walls is accounted for by adding the cross-sectional areas of the outer and inner walls, and assuming that all the longitudinal heat conduction occurs only through the inner wall alone (Narayanan, 1997).

It is well known that the longitudinal heat conduction parameter should be estimated using the area of all the walls of any exchanger, including perforated plate matrix heat exchangers. To demonstrate the basic principles of heat exchangers, Mills (1996) used the total foot print area to evaluate the longitudinal heat conduction parameter and predict the performance degradation due to longitudinal heat conduction in perforated plate heat exchangers. Thus, the suggestion made by Ahuja is not new.

Figure 2 shows the temperature profile in the wall separating the streams. Because of the small thickness of the copper perforated plates (typically 0.2 to 1.0 mm thick), the temperature of any copper perforated plate will essentially be uniform in the longitudinal direction (Sarangi and Barclay, 1984, Venkatarathnam and Sarangi, 1991). The total temperature drop across the wall is almost totally sustained by the low conductivity (plastic or stainless steel) spacers separating the copper perforated

---

[1] G. Venkatarathnam, Department of Mechanical Engineering, Indian Institute of Technology, Chennai 600 036, India and S. Sarangi, Cryogenic Engineering Centre, Indian Institute of Technology, Kharagpur 721 302, India.

plates. Therefore, it is appropriate to define the longitudinal heat conduction parameter in terms of the resistance of the insulating spacers only. The step-wise temperature profile in the wall also makes it unique, and makes the performance of the perforated plate matrix heat exchangers a strong function of the number of perforated plates in the exchanger.

Ahuja has suggested the use of combined resistance of both the copper and stainless steel/plastic spacers in evaluating the longitudinal and lateral thermal resistance of the walls. This approach is, as such, very old and had been used by all Russian workers in the past, who considered the matrix heat exchanger to be a normal heat exchanger with the perforated plates serving as fins and with the wall having different thermal conductivity in the lateral and longitudinal directions, without due consideration to the stepwise temperature profile, and the effect of finite number of plates in the heat exchanger. A detailed discussion on the papers that adopted such an approach has been presented elsewhere (Venkatarathnam and Sarangi, 1990, 1991). The importance of our approach in considering the step-wise temperature profile and the effect of finite number of plate-spacer pairs has been recognized by other workers not only for estimating the steady-state performance but also for reducing the transient test data (Rodrigues and Mills, 1988).

In any case, when the longitudinal heat conduction parameter is estimated using the total resistance of the plate, the performance of the heat exchanger must decrease only marginally and not as shown by Ahuja in his discussion (Fig. 2) because of the large difference in the magnitude of thermal conductivity of copper and stainless steel/plastics. In that figure Ahuja compared the performance using the method suggested by us but using only the area of the inner wall with that using the entire wall area and the combined resistance of the plates and spacers and arrived at the wrong conclusion that the longitudinal heat conduction parameter defined by us needs a correction. It is our belief that the step-wise temperature profile should be taken into account, while defining the longitudinal and lateral heat conduction parameters.

Lateral Heat Conduction Through the Wall

Ahuja states that we have used the simplification of neglecting the lateral (transverse) resistance of the separating wall, by assuming that the plate conduction parameter $lp = Y$. The accompanying equations (Eqs. (1)–(4) of Ahuja) derived by us and presented by Ahuja do contain the expressions for effective number of transfer units (effectiveness) as a function of lp! The resistance of the perforated plate as well as that of the wall was neglected by Sarangi and Barclay (1984) and was not in any of our subsequent papers as mentioned by Ahuja. The main contribution of our paper in this Journal (Venkatarathnam and Sarangi, 1991) was in accounting for all the resistances and the finite number of plate-spacer pairs in the heat exchanger including the above resistances, and suggesting a numerical scheme for solving all the differential equations simultaneously. The conclusion of Ahuja that the lateral thermal resistance of the wall has been neglected by us is thus misplaced.

Ahuja showed the importance of not neglecting the lateral thermal resistance of the wall (Fig. 3 of Ahuja). It is well known that the resistances normally neglected in low effectiveness heat exchangers, such as longitudinal heat conduction, cannot be neglected in high effectiveness heat exchangers. No serious worker will ever ignore this effect if his analysis or experiment is aimed at a precision finer than this effect. Still, Dr. Ahuja's reminder can benefit new entrants to the field.

Numerical Method for Solving the Differential Equations

Ahuja has questioned the efficacy of the computer program that incorporates the numerical method suggested by us to solve the set of differential equations. The numerical method was suggested and tested by us for a large number of practical cases. Ahuja's study (Fig. 2 of Ahuja) shows that our program did work well and the results with our numerical method (program) were comparable to that obtained with our analytical methods suggested more recently and did not work only for modifications made by him. Also, Ahuja states that the program produces wrong results if the longitudinal heat conduction parameter is large. The main reason for providing a large number of low conductivity spacers is to reduce the longitudinal heat conduction! The program in question is a part of the Ph.D. thesis of Venkatarathnam and is not a part of the paper presented by us in this Journal. As stated by Ahuja, it is a reduced version of the program that was originally developed by us.

Sizing of the Heat Exchanger

Ahuja presented a simple equation for determining the heat transfer area of the heat exchanger. Using this equation (Eq. (18) of Ahuja), it is possible to determine the total heat transfer area, provided the exchanger height and width are known, and the exchanger is assumed to be of balanced design (equal thermal resistance on either side). The sizing of a perforated plate exchanger essentially involves determining the height, width, and length (number of plates) of the heat exchanger. This information required in Eq. (18) of Ahuja is therefore not known in advance! Also, the thermal resistance will never be the same on the two sides since the thermal resistance of the cold (low-pressure) stream is always much larger than that of the hot (high-pressure) stream for perforated plate exchangers used in any cryogenic system. The determination of the height, width, and number of plates of a perforated plate matrix heat exchanger is somewhat more difficult than the method suggested by Ahuja. An analytical method for determining the size of a matrix heat exchanger of unbalanced design, based on the Lagrangian optimization technique, has recently been presented by Venkatarathnam (1997).

Conclusions

Most of the suggestions made by Ahuja are those available in standard text books, or those already made by other workers in the past.

Since the thermal gradient between the two ends of the heat exchanger is sustained by the insulating spacers, the longitudinal heat conduction parameter should be based on the thermal resistance of the spacers only. Similarly, since negligible lateral heat transfer takes place through the spacers, it is appropriate to define the lateral heat conduction parameter in terms of the conduction resistance of the perforated plates.

The doubts raised by Ahuja regarding assuming the conduction resistance of the plates to be negligible is applicable only to the work of Sarangi and Barclay (1984) presented in an ASME conference and not applicable to our work published subsequently in this Journal. In fact, that is the very basis of the work presented in this Journal. It should be pointed out that the work of Sarangi and Barclay (1984) aimed at studying the effect of a finite number of plates. It would have been unwise of them to include the finite plate conductivity which would have eclipsed the effect they were studying.

Closed-form analytical solutions are always preferable to any numerical method, even if they are slightly less accurate for any preliminary study. Hence, it is recommended that the analytical solutions presented by us (Venkatarathnam, 1996) be used for quick design and optimization studies only, and not for precision work as suggested by Ahuja. For final design work and when the variation of properties of the fluid with temperature is large (as in cryogenic systems), it is recommended that the numerical approach presented by us in this Journal (Venkatarathnam and Sarangi, 1991) be used.

The data presented by Ahuja do not raise any questions regarding the efficacy of the program presented in the thesis of

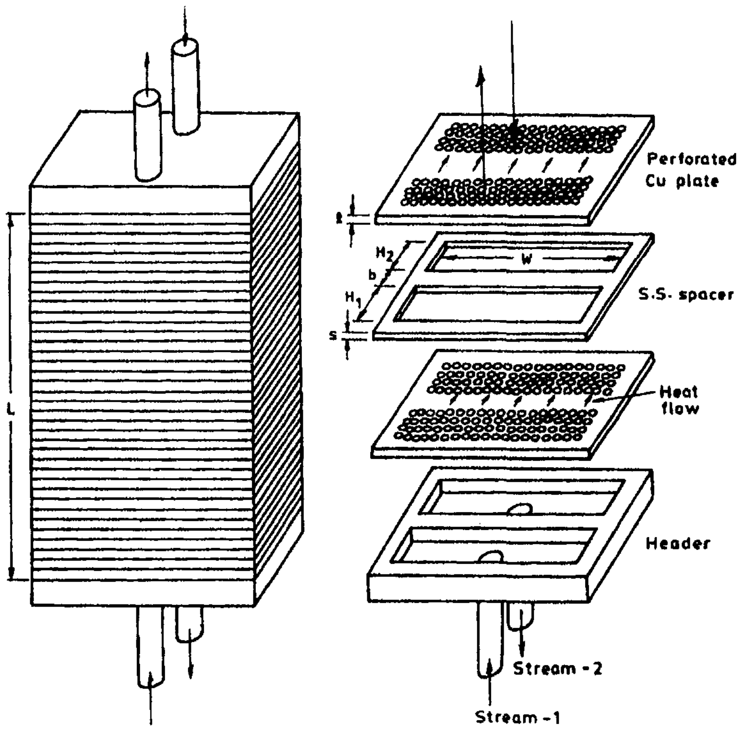

Fig. 1 Schematic of a perforated plate matrix heat exchanger

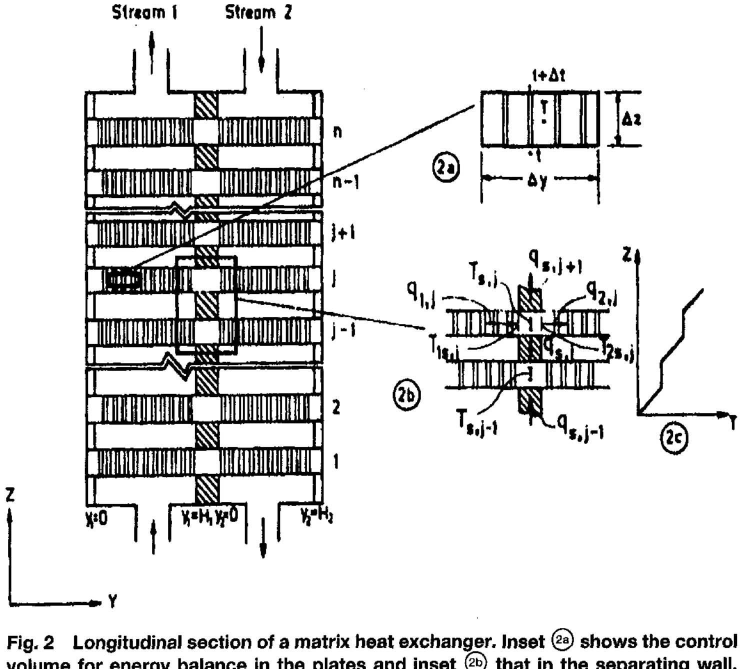

Fig. 2 Longitudinal section of a matrix heat exchanger. Inset (2a) shows the control volume for energy balance in the plates and inset (2b) that in the separating wall. Figure (2c) shows the temperature profile along the centerline.

one of the authors. The Journal space may be better utilized to discuss serious technical issues than a trivial problem encountered while modifying and using a reduced version program presented in the appendix of a Ph.D. thesis, particularly when the complete program was made available to whoever asked for it.

References

Kroeger, P. G., 1967, "Performance deterioration in high effectiveness heat exchangers due to axial conduction effects," *Advances in Cryogenic Engg*, Vol. 12, pp. 363–372.

Narayanan, S. P., 1997, "Analysis of Performance of Heat Exchangers Used in Micro Miniature Refrigerators," M.S. thesis, Indian Institute of Technology, Madras, India.

Rodriguez, J. I., and Mills, A. F., 1990, "Analysis of Single-Blow Transient Testing of Perforated Plate Heat Exchangers," *Int J. Heat Mass Transfer,* Vol. 33, pp. 1969–1976.

Sarangi, S., and Barclay, J., 1984, "An analysis of Compact Heat Exchanger Performance," *Cryogenic Processes and Equipment–1984,* P. J. Kerney et al., eds., ASME, New York, pp. 37–44.

Venkatarathnam, G., 1991, "Matrix Heat Exchangers," Ph.D. thesis, Indian Institute of Technology, Kharagpur, India.

Venkatarathnam, G., and Sarangi, S., 1991, "Analysis of Matrix Heat Exchanger Performance," ASME JOURNAL OF HEAT TRANSFER, Vol. 113, pp. 830–836.

Venkatarathnam, G., 1996, "Effectiveness Ntu relationship in perforated plate matrix heat exchangers," *Cryogenics,* Vol. 36, pp. 235–241.

Venkatarathnam, G., 1998, "A Straight forward method for the sizing of perforated plate matrix heat exchangers," presented at the Cryogenic Engineering Conference, July 28–Aug. 1, Portland, OR, accepted for publication in *Advances in Cryogenic Engg,* Vol. 43.